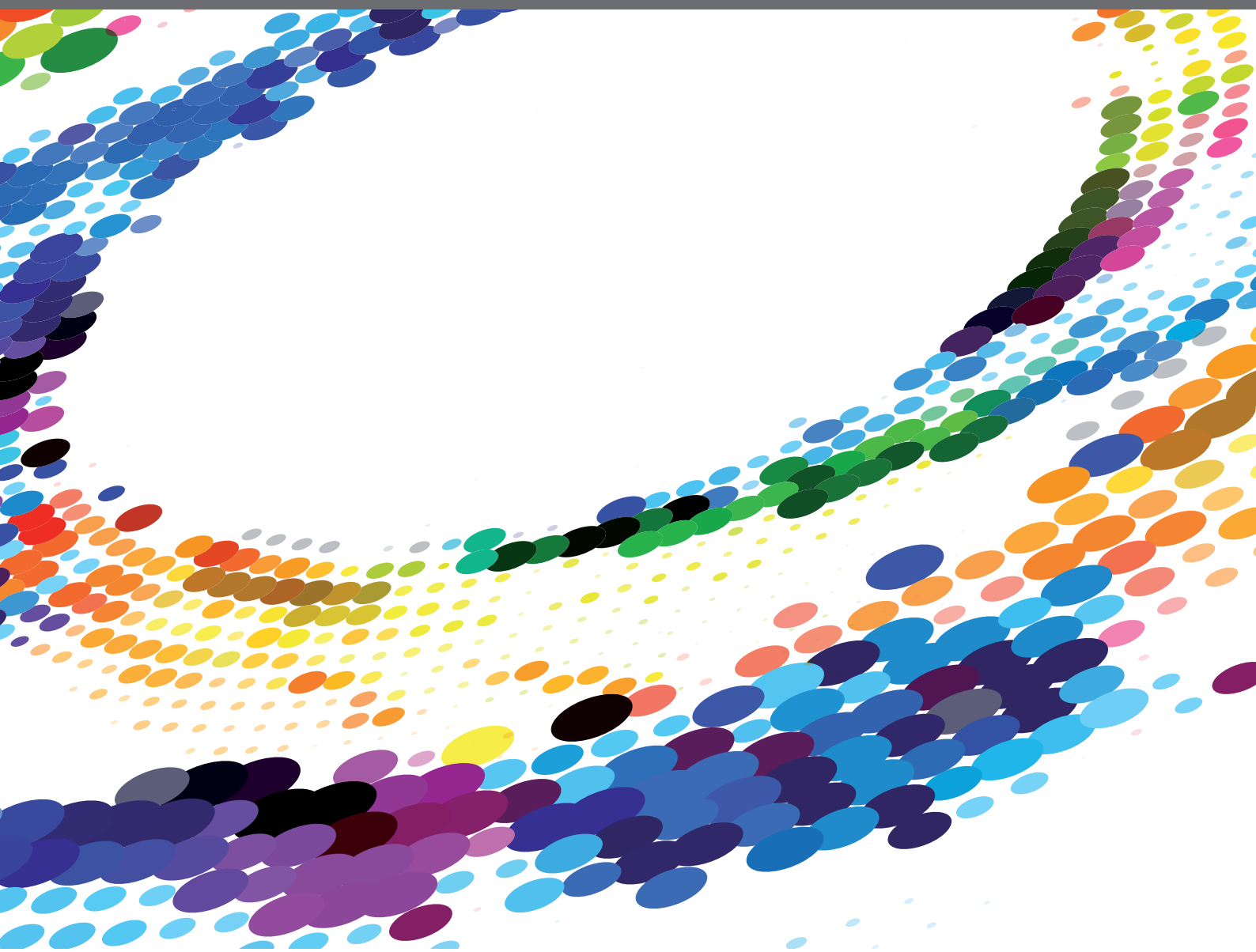
COUPLED FEEDBACK MECHANISMS IN THE MAGNETOSPHERE-IONOSPHERE SYSTEM

EDITED BY: Scott Alan Thaller, Jean-Francois Ripoll, Toshi Nishimura and Philip J. Erickson
PUBLISHED IN: Frontiers in Astronomy and Space Sciences and Frontiers in Physics



frontiers Research Topics



frontiers

Frontiers eBook Copyright Statement

The copyright in the text of individual articles in this eBook is the property of their respective authors or their respective institutions or funders. The copyright in graphics and images within each article may be subject to copyright of other parties. In both cases this is subject to a license granted to Frontiers.

The compilation of articles constituting this eBook is the property of Frontiers.

Each article within this eBook, and the eBook itself, are published under the most recent version of the Creative Commons CC-BY licence. The version current at the date of publication of this eBook is CC-BY 4.0. If the CC-BY licence is updated, the licence granted by Frontiers is automatically updated to the new version.

When exercising any right under the CC-BY licence, Frontiers must be attributed as the original publisher of the article or eBook, as applicable.

Authors have the responsibility of ensuring that any graphics or other materials which are the property of others may be included in the CC-BY licence, but this should be checked before relying on the CC-BY licence to reproduce those materials. Any copyright notices relating to those materials must be complied with.

Copyright and source acknowledgement notices may not be removed and must be displayed in any copy, derivative work or partial copy which includes the elements in question.

All copyright, and all rights therein, are protected by national and international copyright laws. The above represents a summary only. For further information please read Frontiers' Conditions for Website Use and Copyright Statement, and the applicable CC-BY licence.

ISSN 1664-8714
ISBN 978-2-83250-556-4
DOI 10.3389/978-2-83250-556-4

About Frontiers

Frontiers is more than just an open-access publisher of scholarly articles: it is a pioneering approach to the world of academia, radically improving the way scholarly research is managed. The grand vision of Frontiers is a world where all people have an equal opportunity to seek, share and generate knowledge. Frontiers provides immediate and permanent online open access to all its publications, but this alone is not enough to realize our grand goals.

Frontiers Journal Series

The Frontiers Journal Series is a multi-tier and interdisciplinary set of open-access, online journals, promising a paradigm shift from the current review, selection and dissemination processes in academic publishing. All Frontiers journals are driven by researchers for researchers; therefore, they constitute a service to the scholarly community. At the same time, the Frontiers Journal Series operates on a revolutionary invention, the tiered publishing system, initially addressing specific communities of scholars, and gradually climbing up to broader public understanding, thus serving the interests of the lay society, too.

Dedication to Quality

Each Frontiers article is a landmark of the highest quality, thanks to genuinely collaborative interactions between authors and review editors, who include some of the world's best academicians. Research must be certified by peers before entering a stream of knowledge that may eventually reach the public - and shape society; therefore, Frontiers only applies the most rigorous and unbiased reviews.
Frontiers revolutionizes research publishing by freely delivering the most outstanding research, evaluated with no bias from both the academic and social point of view. By applying the most advanced information technologies, Frontiers is catapulting scholarly publishing into a new generation.

What are Frontiers Research Topics?

Frontiers Research Topics are very popular trademarks of the Frontiers Journals Series: they are collections of at least ten articles, all centered on a particular subject. With their unique mix of varied contributions from Original Research to Review Articles, Frontiers Research Topics unify the most influential researchers, the latest key findings and historical advances in a hot research area! Find out more on how to host your own Frontiers Research Topic or contribute to one as an author by contacting the Frontiers Editorial Office: frontiersin.org/about/contact

COUPLED FEEDBACK MECHANISMS IN THE MAGNETOSPHERE-IONOSPHERE SYSTEM

Topic Editors:
Scott Alan Thaller, Atmospheric and Space Technology Research Associates (United States), United States
Jean-Francois Ripoll, CEA DAM Île-de-France, France
Toshi Nishimura, Boston University, United States
Philip J. Erickson, Haystack Observatory, Massachusetts Institute of Technology, United States

Citation: Thaller, S. A., Ripoll, J.-F., Nishimura, T., Erickson, P. J., eds. (2022). Coupled Feedback Mechanisms in the Magnetosphere-Ionosphere System. Lausanne: Frontiers Media SA. doi: 10.3389/978-2-83250-556-4

Table of Contents

05 ***Editorial: Coupled Feedback Mechanisms in the Magnetosphere-Ionosphere System***
Scott Thaller, Jean-Francois Ripoll, Toshi Nishimura and Phil Erickson

10 ***Machine Learning Applications to Kronian Magnetospheric Reconnection Classification***
Tadhg M. Garton, Caitriona M. Jackman, Andrew W. Smith, Kiley L. Yeakel, Shane A. Maloney and Jon Vandegriff

24 ***Modeling and Prediction of Near-Earth Plasma Sheet Parameters Using the Rice Convection Model and the Recurrent Neural Network***
Shishir Priyadarshi, Jian Yang and Weiqin Sun

39 ***Counterstreaming Cold H^+, He^+, O^+, and N^+ Outflows in the Plasmasphere***
J. Krall and J. D. Huba

49 ***Propagation and Dispersion of Lightning-Generated Whistlers Measured From the Van Allen Probes***
J.-F. Ripoll, T. Farges, D. M. Malaspina, G. S. Cunningham, G. B. Hospodarsky, C. A. Kletzing and J. R. Wygant

67 ***Two-Dimensional Structure of Flow Channels and Associated Upward Field-Aligned Currents: Model and Observations***
Larry. R. Lyons, Yukitoshi Nishimura, Chih-Ping Wang, Jiang Liu and William. A. Bristow

78 ***Thermospheric Neutral Winds as the Cause of Drift Shell Distortion in Earth's Inner Radiation Belt***
Solène Lejosne, Mariangel Fedrizzi, Naomi Maruyama and Richard S. Selesnick

88 ***Impact of Storm-Enhanced Density (SED) on Ion Upflow Fluxes During Geomagnetic Storm***
Shasha Zou, Jiaen Ren, Zihan Wang, Hu Sun and Yang Chen

106 ***The Predictive Capabilities of the Auroral Electrojet Index for Medium Energy Electron Precipitation***
H. Nesse Tyssøy, N. Partamies, E. M. Babu, C. Smith-Johnsen and J. A. Salice

119 ***Electron Microbursts Induced by Nonducted Chorus Waves***
Lunjin Chen, Xiao-Jia Zhang, Anton Artemyev, Liheng Zheng, Zhiyang Xia, Aaron W. Breneman and Richard B. Horne

134 ***Estimating Precipitating Energy Flux, Average Energy, and Hall Auroral Conductance From THEMIS All-Sky-Imagers With Focus on Mesoscales***
Christine Gabrielse, Toshi Nishimura, Margaret Chen, James H. Hecht, Stephen R. Kaeppler, D. Megan Gillies, Ashton S. Reimer, Larry R. Lyons, Yue Deng, Eric Donovan and J. Scott Evans

151 ***Reproducibility of the Geomagnetically Induced Currents at Middle Latitudes During Space Weather Disturbances***
Takashi Kikuchi, Yusuke Ebihara, Kumiko. K. Hashimoto, Kentaro Kitamura and Shin-Ichi Watari

168 ***On the Saturation (or Not) of Geomagnetic Indices***
Joseph E. Borovsky

182 ***Direct Connection Between Auroral Oval Streamers/Flow Channels and Equatorward Traveling Ionospheric Disturbances***
Larry R. Lyons, Yukitoshi Nishimura, Shunrong Zhang, Anthea Coster, Jiang Liu, William A. Bristow, Ashton S. Reimer, Roger H. Varney and Don L. Hampton

197 ***Mesoscale Features in the Global Geospace Response to the March 12, 2012 Storm***
Mayowa Adewuyi, Amy M. Keesee, Yukitoshi Nishimura, Christine Gabrielse and Roxanne M. Katus

208 ***The Role of Mesoscale Plasma Sheet Dynamics in Ring Current Formation***
K. A. Sorathia, A. Michael, V.G. Merkin, A.Y. Ukhorskiy, D. L. Turner, J.G. Lyon, J. Garretson, M. Gkioulidou and F.R. Toffoletto

224 ***Links of the Plasmapause With Other Boundary Layers of the Magnetosphere: Ionospheric Convection, Radiation Belt Boundaries, Auroral Oval***
V. Pierrard, E. Botek, J.-F. Ripoll, S. A. Thaller, M. B. Moldwin, M. Ruohoniemi and G. Reeves

251 ***Early-Time Non-Equilibrium Pitch Angle Diffusion of Electrons by Whistler-Mode Hiss in a Plasmaspheric Plume Associated with BARREL Precipitation***
R. M. Millan, J.-F. Ripoll, O. Santolík and W. S. Kurth

262 ***Pitch-Angle Diffusion in the Earth's Magnetosphere Organized by the Mozer-Transformed Coordinate System***
Joseph E. Borovsky, Gian Luca Delzanno and Kateryna N. Yakymenko

268 ***Radial Transport of Energetic Electrons as Determined From the "Zebra Stripes" Measured in the Earth's Inner Belt and Slot Region***
Solène Lejosne, Bela G. Fejer, Naomi Maruyama and Ludger Scherliess

278 ***Statistical Analysis of Bifurcating Region 2 Field-Aligned Currents Using AMPERE***
H. K. Sangha, S. E. Milan, B. J. Anderson and H. Korth

288 ***Machine Learning Methods Applied to the Global Modeling of Event-Driven Pitch Angle Diffusion Coefficients During High Speed Streams***
G. Kluth, J.-F. Ripoll, S. Has, A. Fischer, M. Mougeot and E. Camporeale

310 ***Imaging Low-Energy Ion Outflow in the Auroral Zone***
Douglas Rowland, Michael Collier, John Keller, Robert Pfaff, Jeffrey Klenzing, Jason McLain, James Clemmons and James Hecht

326 ***Kelvin-Helmholtz Vortices as an Interplay of Magnetosphere-Ionosphere Coupling***
K.-J. Hwang, J. M. Weygand, D. G. Sibeck, J. L. Burch, M. L. Goldstein, C. P. Escoubet, E. Choi, K. Dokgo, B. L. Giles, C. J. Pollock, D. J. Gershman, C. T. Russell, R. J. Strangeway and R. B. Torbert

frontiers | Frontiers in Astronomy and Space Sciences

TYPE Editorial
PUBLISHED 06 October 2022
DOI 10.3389/fspas.2022.1011217

Check for updates

OPEN ACCESS

EDITED AND REVIEWED BY
Julio Navarro,
University of Victoria, Canada

*CORRESPONDENCE
Scott Thaller,
thaller1@gmail.com

SPECIALTY SECTION
This article was submitted to Space Physics,
a section of the journal
Frontiers in Astronomy and Space Sciences

RECEIVED 03 August 2022
ACCEPTED 26 August 2022
PUBLISHED 06 October 2022

CITATION
Thaller S, Ripoll J-F, Nishimura T and Erickson P (2022), Editorial: Coupled feedback mechanisms in the magnetosphere-ionosphere system. *Front. Astron. Space Sci.* 9:1011217. doi: 10.3389/fspas.2022.1011217

COPYRIGHT
© 2022 Thaller, Ripoll, Nishimura and Erickson. This is an open-access article distributed under the terms of the Creative Commons Attribution License (CC BY). The use, distribution or reproduction in other forums is permitted, provided the original author(s) and the copyright owner(s) are credited and that the original publication in this journal is cited, in accordance with accepted academic practice. No use, distribution or reproduction is permitted which does not comply with these terms.

Editorial: Coupled feedback mechanisms in the magnetosphere-ionosphere system

Scott Thaller[1]*, Jean-Francois Ripoll[2,3], Toshi Nishimura[4] and Phil Erickson[5]

[1]Laboratory for Atmospheric and Space Physics, University of Colorado Boulder, Boulder, CO, United States, [2]CEA DAM Île-de-France, Bruyères-le-Châtel, France, [3]UPS, CEA, LMCE, Bruyères-le-Châtel, France, [4]Boston University, Boston, MA, United States, [5]Haystack Observatory, Massachusetts Institute of Technology, Cambridge, MA, United States

KEYWORDS

magnetosphere–ionosphere interactions, aurora, radiation belts, currents and electric fields, GIC, plasmasphere, ring current

Editorial on the Research Topic
Coupled feedback mechanisms in the magnetosphere-ionosphere system

The dynamics of the inner-magnetosphere and ionosphere are coupled through complex feedback mechanisms involving waves, DC electric fields, particle flows, and field aligned currents. A full understanding of the behavior of either the magnetosphere or ionosphere requires an account of the other. These magnetosphere-ionosphere (M-I) coupling processes and dynamics may be driven not only by the solar wind and its influence on the outer-magnetosphere, but from the thermosphere through the action of neutral winds. Today, current interests are brought on any processes contributing to the transport of energy into and out from the ionosphere. This includes general advection/convection in the ionosphere and inner-magnetosphere, and, particularly, meso-scale convective subauroral phenomena, including subauroral polarization streams (SAPS) and subauroral ion drifts (SAIDS). Luminous manifestations in the lower ionosphere such as Strong Thermal Emission Velocity Enhancement (STEVE), SAR arcs, diffuse electron and proton aurora, and discrete aurora, are key to the analysis and understanding the particle and fields dynamics. In this Research Topic, we have collected a wide variety of studies that contribute to understanding the magnetosphere-ionosphere-thermosphere as a coupled feedback system, from either satellite or ground-based data sets, theory, modeling, simulations, and studies involving machine learning. These studies are sorted according to the following sub-categories: radiation belts, mesoscale phenomenon, aurora, current systems, ion outflows and geomagnetic indices. Their main results are briefly contextualized and discussed in following.

Radiation belts

Convection, electric field, and boundary motion

Investigating the origins of the large-scale electric field and their dissymmetry causing observed radiation belt distortion, Lejosne et al. use the RCM model coupled with the Coupled Thermosphere-Ionosphere-Plasmasphere-electrodynamics (CTIPe) model. The objective is to assess whether or not neutral wind dynamo, i.e., dynamo electric fields produced by tidal motion of upper atmospheric winds (Richmond, 1989) that flows across the Earth's magnetic field lines, could cause these distortions and be at the origins of the local time asymmetry of the equatorial electron intensity occurring from dawn to dusk observed in the inner radiation belt (Selesnick et al., 2016). Measured equatorial electron intensity (100–400 keV) and *in-situ* electric field combined with wind dynamo modeling results lead to an estimation of 6–8 kV for the average dawn-to-dusk electric potential variation from neutral wind dynamo, making these fields main drivers of the drift shell distortion in the Earth's inner radiation belt. By tracing the drift of trapped energetic electrons (10–100 keV), Lejosne et al. further show electric field disturbances coherently transport radially this population over hundreds to thousands of kilometers in the inner belt. Results of the Rice Convection Model (RCM) (Toffoletto et al., 2003) code suggests that the electric field disturbances are likely greater than empirical estimates and that electron radial transport driven by prompt magnetospheric convection varies as L to the power 3, though the magnitude of this transport remains to be determined. Another study involving RCM (Priyadarshi et al.) investigates interactions between Earth's magnetotail and the inner magnetosphere, which play an important role in the transport of mass and energy in the ionosphere–magnetosphere coupled system. They simulate injection events and extract the flux-tube entropy parameter, the dawn-to-dusk electric field component, and the cumulative magnetic flux transport in the central plasma sheet. Recurrent neural networks are then trained to learn these results and to predict the solution for the successive tens of minutes. Predictions are successively and successfully validated against subsequent RCM simulation results. In Pierrard et al., the equatorward motion of the plasmapause projected in the ionosphere is related to the equatorward edge motion of the auroral oval that goes to lower latitudes during storms due to the geomagnetic perturbation as well as to the electron outer radiation belt. The links between these different regions are investigated during quiet periods, for which the plasmasphere is widely extended, as well as during geomagnetic storms; tremendous differences in flux associated with the pitch angle dependence are shown in both cases.

Electromagnetic waves

Electromagnetic waves produced by lightning strokes in the atmosphere and travelling through the ionosphere up to the magnetosphere produces the scattering of trapped particle in the inner belt. The propagation of these waves is studied from Earth to space in Ripoll et al. They find the electric field wave power decays with distance mostly quadratically in space, while the magnetic field wave power decays mostly linearly in space. These waves measured by the Van Allen Probes are rare on the dayside. Their mean wave-normal angle is 41.6° +/-24°, with a strong MLT-dependence. Their smaller refractive index during Northern hemisphere summer for L-shells above 1.8 is inconsistent with Chapman ionization theory and consistent with the so-called winter/seasonal anomaly (Liu et al., 2009). The wave normal angle and refractive index are found anti-correlated. High power attenuation is correlated with large refractive index and anti-correlated with small wave normal angle.

Microbursts are short-lived electron precipitation observed in the lower ionosphere by LEO satellites. They are thought to contribute significantly to the losses of energetic electrons in the outer radiation belt and to be caused by whistler mode chorus waves. The quantification of microbursts often relies on the assumption that chorus waves are ducted along the magnetic field line. Chen et al. develop a new nonducted chorus wave model integrated in the HOTRAY ray tracing code (Horne, 1989). Test particle simulations further show that nonducted waves tend to produce electron microbursts at lower energy, over a shorter duration, and over a broader L-shell region, and, as such, can trigger different resonance mechanisms.

Wave particle interaction and electron precipitation

The chemical imprint of the energetic electron precipitation on the atmosphere is a part of the natural forcing of the climate system (van de Kamp et al., 2016), with important questions on quantifying energetic electron precipitation flux in terms of timing and intensity. In that context, Nesse Tyssøy et al. create a new medium energy electron (MEE) (30–300 keV) flux proxy by accumulating the AE activity over multiple days and combining observations from NOAA/POES and EUMETSAT/MetOp spacecraft, as well as pitch angle diffusion by wave-particle interaction to estimate the precipitating fluxes. Their results indicate that AE based proxies can predict at least 70% of the observed MEE precipitation variance at all energies.

Intense precipitation observed at 37 km of altitude over Sweden from the Balloon Array for Radiation belt Relativistic Electron Losses (BARREL) are explained in Millan et al. by wave particle interaction occurring in dense plasma plumes at GEO

orbits. In these plumes, whistler-mode hiss with electromagnetic power 3–4 times above the median power are found. The induced pitch angle scattering is far from equilibrium with short apparent decay rates of the electron flux in space of the order of ~12 min at 74 keV and persisting during ~30 min, exceeding by a factor ~10 the electron lifetime. The energy of the precipitating electrons is estimated to be ~50–100 keV. The prevalence of plasmaspheric plumes and detached plasma regions suggests whistler-mode hiss waves could be an important driver of electron loss even at high L-value (L~6), outside of the main plasmasphere. Pitch angle diffusion coefficients that are essential for computing precipitations can be embedded in a Deep Neural Network as done in Kluth et al. in order to create a parametrized model easily usable for simulating and predicting the effect of solar high-speed streams on the radiation belts. Pitch angle diffusion of protons, either produced by plasma-wave scattering or by field-line-curvature (FLC) scattering is further demonstrated by Borovsky et al. as better organized in a transformed coordinate system, called the "Mozer transform" from Mozer (1966).

Mesoscale and auroral phenomenon

Meso-scale structures in the plasma sheet and auroral oval play an important role in plasma transport. Lyons et al. test the 2-days structure of plasma sheet flow bursts predicted by the Rice Convection Model (RCM) using aurora and flow observations. They find that RCM predictions of the azimuthal spread of a low-entropy plasma sheet plasma and its associated field-aligned currents and flows give a realistic physical description of the structure of plasma sheet flow bursts. Lyons et al. examines a connection between such flow bursts and large-scale traveling ionospheric disturbances (LSTIDs). The observations show a direct connection between a group of streamers and flow channels to TIDs propagating equatorward from the equatorward boundary of the auroral oval. Ionospheric currents associated with the aurora, however, must be sufficiently large to result in LSTIDs. Garton et al. derives a neural network model fed by satellite observations of the magnetic field components to identify evidence of reconnection in the magnetosphere, based on a classification of the events as plasmoids, traveling compression regions, and dipolarization fronts. This model allows a full cataloging and examination of magnetic reconnection. Although it is initially built for Saturn, its method can generally be applied to any planet's magnetosphere.

Remote sensing techniques for aurora and energetic neutral atoms (ENA) have revealed fundamental plasma processes in the magnetosphere-ionosphere system. Gabrielse et al. present a new method that utilizes the 2D array of all-sky-imagers to estimate auroral scale sizes of intense precipitating energy fluxes and the associated Hall conductances. They find that mesoscale aurora contributes up to ~80% of the total energy flux immediately after onset during the early expansion phase of substorms. A sounding rocket mission by Rowland et al. investigated the factors leading to ion outflow following a geomagnetic substorm. ENA emissions were most intense in the auroral zone, and were dominated there by upgoing ENAs, indicating a strong interaction between the energetic ions and the neutral atmosphere. They suggest large regions of efficient wave particle heating up to a few keV. Adewuyi et al. presented temperature maps using satellite-based ENA observations of a storm event. In coordination with *in-situ* and auroral observations, they find that mesoscale features in the magnetotail are observed throughout the storm and suggested to be a dominant process that leads to pressure buildup in the inner magnetosphere.

Interaction between the magnetotail/aurora and inner magnetosphere is another key process in Geospace. Sorathia et al. investigate the relative importance of mesoscale flow structures and effects of ion non-adiabaticity on the ring current. Flow bursts produced by the simulation reproduce thermodynamic and magnetic statistics from *in-situ* measurements. Mesoscale bubbles, localized depleted entropy regions, and species-dependent particle gradient drifts are critical for ion transport. Pierrard et al. compared plasmapause positions measured by Van Allen Probes and a model. Inward motion of the outer radiation belt was related to the plasmapause erosion and equatorward edge motion of the auroral oval. Importance of the magnetic field topology and of convection electric field was suggested.

Ion outflows

Outflows from the ionosphere, and the general details of plasmasphere field-aligned flows, are very important processes as they can populate the inner magnetosphere with cold plasma, influencing many subsequent dynamic responses. Krall and Huba provide the latest in a long string of hydrodynamic and kinetic model investigations of plasmasphere outflows stretching back to SUPIM (Bailey et al., 1997) and FLIP (Young et al., 1980). Using the SAMI3 model from US Naval Research Laboratory the work examined all relevant topside species - H^+, He^+, N^+, and O^+ - and their thermal outflows during storm conditions. The study finds that counterstreaming cold ion populations occur in all cases as material streams outward from both hemispheres following large scale plasmasphere reconfiguration, with particular emphasis on afternoon/dusk sector counterstreaming in areas of large ring current heating. Zou et al. focus on the significant impact on ion outflows caused by another well-known mass transport stormtime signature, the storm enhanced density (SED) plume (Foster, 1993). During a moderate intensity storm, SED formation into the cusp fed the creation of polar cap patches anti-sunward, and these high-density structures triggered large cold ionospheric ion upward

fluxes reaching 3 x 10^{14} m^{-2} s^{-1}. Such intense upward fluxes are important mechanisms for populating the inner magnetosphere with low energy ions.

Current systems

One of the major coupling mechanisms in the IM system are field aligned current systems. Hwang et al. use observations from the Cluster and MMS missions to identify solar wind driven Kelvin-Helmholtz (KH) vortices on the dusk and dawn flanks of the magnetosphere. The twisting magnetic fields result in field aligned currents that are upward from (downward into) the ionosphere, consistent that are with the Region-1 currents, ground and low-altitude spacecraft observations. Thus, showing that the KH vortices at the plasmapause are a driver of this current system. Sangha et al. presents a statistical study using AMPERE data of the bifurcation of the region-2 current system on the dawn and dusk sides. They show that this phenomenon exhibits seasonal and UT trends, with the bifurcated region two currents occurring preferably in the summer hemisphere at dusk, which may be due to enhanced ionospheric conductivity there. The authors point out a possible relation to SAPS. Field aligned currents play an important role in Zou et al. wherein they present a study using both remote and *in situ* observations of the ionosphere-thermosphere system, along with solar wind, IMF data and Sym-H index to demonstrate the crucial role that Storm Enhanced Densities (SED), structures of high ionospheric density, have in creating large upward ion fluxes. The FAC help contextualize the state of the magnetospheric driver in terms of its impact on the ionosphere.

Ionospheric currents, through their associated magnetic field induce current in the ground. Kikuchi et al. investigate the correlation of the measured surface magnetic field with ground induced currents (GIC) on various timescales from ~ 1 min to ~1 day. They show that the induced electric field calculated from the surface magnetic field and semi-infinite one- and two-layer conductivity models correlates well with the GIC for periods from 1 min to 24 h. These models, combined with global magnetospheric simulations, would allow for the prediction of GIC during space weather disturbances.

Geomagnetic indices

Geomagnetic indices are proxies for various magnetospheric/ionospheric current systems. Borovsky investigates the saturation, or non-saturation, of various geomagnetic indices, exploring the topics of whether the nature of the index matters, the relation of the saturation of the index to that of the polar cap potential, and any role the choice of solar wind driver function has. Borovsky shows, among other things, that the degree of saturation depends on the solar wind driver function, that different indices show different degrees of saturation, that the polar-cap function can sometimes correct for the saturation, and that the nature of the index measurement matters.

Geomagnetic indices can also serve as good proxies for other processes, such as precipitating MEE as described above (Nesse Tyssøy et al.) The link between the AE and MEE precipitation is likely to be the substorm dynamics, as these both crease the currents that produce the magnetic disturbances from which AE is determined, and directly inject both source and seed particles for MEE, some of which will precipitate.

As is clear from the above aggregation of the articles comprising this Research Topic, the processes, mechanism, and investigatory techniques used to further our understanding of the complex coupling in the magnetosphere-ionosphere-thermosphere system is an extremely rich area of research. The articles contained herein advance our knowledge of this very complex system-of-systems, and help point direction to promising avenues of exploration for future studies.

Author contributions

ST planned, wrote portions of, synthesized, and edited the manuscript. J-FR conceptualized, wrote parts of, and edited the manuscript, TN wrote portions of the manuscript and help in editing, PE wrote portions of the manuscript and helped with editing. Substantial contributions were made by all authors.

Conflict of interest

The authors declare that the research was conducted in the absence of any commercial or financial relationships that could be construed as a potential conflict of interest.

Publisher's note

All claims expressed in this article are solely those of the authors and do not necessarily represent those of their affiliated organizations, or those of the publisher, the editors and the reviewers. Any product that may be evaluated in this article, or claim that may be made by its manufacturer, is not guaranteed or endorsed by the publisher.

References

Bailey, G. J., Balan, N., and Su, Y. Z. (1997). The sheffield University plasmasphere ionosphere model—A review. *J. Atmos. Sol. Terr. Phys.* 59, 1541–1552. doi:10.1016/s1364-6826(96)00155-1

Foster, J. C. (1993). Storm time plasma transport at middle and high latitudes. *J. Geophys. Res.* 98 (A2), 1675–1689. doi:10.1029/92JA02032

Horne, R. B. (1989). Path-integrated growth of electrostatic waves: The generation of terrestrial myriametric radiation. *J. Geophys. Res.* 94, 8895–8909. doi:10.1029/ja094ia07p08895

Liu, L., Zhao, B., Wan, W., Ning, B., Zhang, M-L., and He, M. (2009). Seasonal variations of the ionospheric electron Densities retrieved from constellation observing system for meteorology, ionosphere, and climate mission radio occultation measurements. *J. Geophys Res.* 114, A02302. doi:10.1029/2008JA013819

Mozer, F. S. (1966). Proton trajectories in the radiation belts. *J. Geophys. Res.* 71, 2701–2708. doi:10.1029/jz071i011p02701

Richmond, A. D. (1989). Modeling the ionosphere wind dynamo: A review. *PAGEOPH* 131, 413–435. doi:10.1007/BF00876837

Selesnick, R. S., Su, Y. J., and Blake, J. B. (2016). Control of the innermost electron radiation belt by large-scale electric fields. *JGR. Space Phys.* 121, 8417–8427. doi:10.1002/2016JA022973

Toffoletto, F., Sazykin, S., Spiro, R., and Wolf, R. (2003). Inner magnetospheric modeling with the Rice convection model. *Space Sci. Rev.* 107, 175–196. doi:10.1007/978-94-007-1069-6_19

van de Kamp, M., Seppälä, A., Clilverd, M. A., Rodger, C. J., Verronen, P. T., and Whittaker, I. C. (2016). A model providing long-term data sets of energetic electron precipitation during geomagnetic storms. *J. Geophys. Res. Atmos.* 121, 12520–12540. doi:10.1002/2015JD024212

Young, E. R., Torr, D. G., and Richards, P. G. (1980). A flux preserving method of coupling first and second order equations to simulate the flow of plasma between the protonosphere and the ionosphere. *J. Comput. Phys.* 38, 141–156. doi:10.1016/0021-9991(80)90050-9

frontiers in Astronomy and Space Sciences

ORIGINAL RESEARCH
published: 10 March 2021
doi: 10.3389/fspas.2020.600031

Machine Learning Applications to Kronian Magnetospheric Reconnection Classification

Tadhg M. Garton[1], Caitriona M. Jackman[1,2], Andrew W. Smith[3], Kiley L. Yeakel[4], Shane A. Maloney[2] and Jon Vandegriff[4]*

[1]Department of Physics and Astronomy, Space Environment Physics Group, University of Southampton, Southampton, England, [2]School of Cosmic Physics, Dublin Institute for Advanced Studies, Dublin, Ireland, [3]Mullard Space Science Laboratory, Department of Space and Climate Physics, University College London, London, England, [4]Johns Hopkins University Applied Physics Laboratory, Laurel, MD, United States

The products of magnetic reconnection in Saturn's magnetotail are identified in magnetometer observations primarily through characteristic deviations in the north–south component of the magnetic field. These magnetic deflections are caused by traveling plasma structures created during reconnection rapidly passing over the observing spacecraft. Identification of these signatures have long been performed by eye, and more recently through semi-automated methods, however these methods are often limited through a required human verification step. Here, we present a fully automated, supervised learning, feed forward neural network model to identify evidence of reconnection in the Kronian magnetosphere with the three magnetic field components observed by the Cassini spacecraft in Kronocentric radial–theta–phi coordinates as input. This model is constructed from a catalog of reconnection events which covers three years of observations with a total of 2093 classified events, categorized into plasmoids, traveling compression regions and dipolarizations. This neural network model is capable of rapidly identifying reconnection events in large time-span Cassini datasets, tested against the full year 2010 with a high level of accuracy (87%), true skill score (0.76), and Heidke skill score (0.73). From this model, a full cataloging and examination of magnetic reconnection events in the Kronian magnetosphere across Cassini's near Saturn lifetime is now possible.

Keywords: machine learning, magnetic reconnection, planetary magnetospheres, magnetotail, plasmoid

OPEN ACCESS

Edited by:
Scott Alan Thaller, University of Colorado Boulder, United States

Reviewed by:
Octav Marghitu, Space Science Institute, Romania
Arnaud Masson, European Space Astronomy Centre (ESAC), Spain
Enrico Camporeale, University of Colorado Boulder, United States

****Correspondence:***
Tadhg M. Garton
t.m.garton@soton.ac.uk

Specialty section:
This article was submitted to Space Physics, a section of the journal Frontiers in Astronomy and Space Sciences

Received: *28 August 2020*
Accepted: *19 November 2020*
Published: *10 March 2021*

Citation:
Garton TM, Jackman CM, Smith AW, Yeakel KL, Maloney SA and Vandegriff J (2021) Machine Learning Applications to Kronian Magnetospheric Reconnection Classification. Front. Astron. Space Sci. 7:600031. doi: 10.3389/fspas.2020.600031

1. INTRODUCTION

Magnetic reconnection is the primary process whereby magnetic fields under strain can reconfigure and energy within their structure can transfer. On the dayside, incoming plasma and magnetic fields can reconnect, opening previously closed planetary magnetic field lines. At planets like Earth, day-side (between 6 and 18 local time) reconnection is considered to play a primary role in energy and mass transportation between a planet's magnetic field and the interplanetary magnetic field (Milan et al., 2007). Similarly, on the night-side (0–6 and 18–24 local time), open planetary magnetic field lines become distended in an extended planetary magnetotail, within which field lines may reconnect to again form closed field lines (Dungey, 1961; Dungey, 1965). This cyclic transition between open and closed field configurations allows the transfer of mass, both in and out, of the planetary

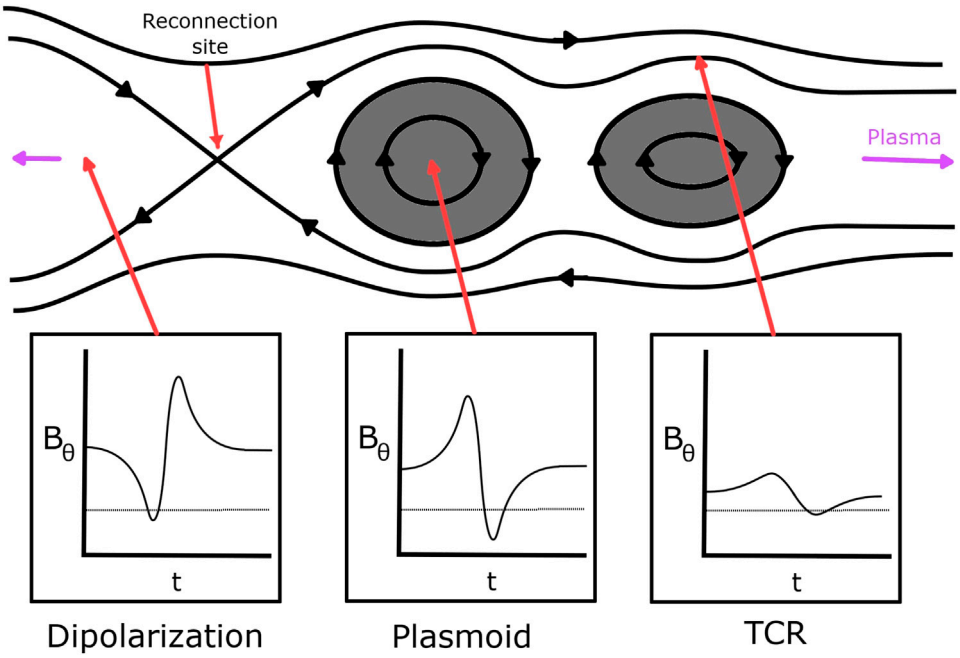


FIGURE 1 | Model north-south magnetic field (B_θ) measurements for a spacecraft as it passes through a dipolarization, plasmoid and TCR associated with a magnetic reconnection event. Notably, a significant deflection occurs as the spacecraft travels through the center of this region, with directionality of the field even possibly being reversed (going from positive to negative).

magnetosphere system. Alternatively, reconnection can further occur for rapidly rotating planets which involves no change in overall magnetic flux. For example, at Jupiter and Saturn fast rotation rates and significant internal mass sources result in the operation of the Vasyliunas cycle. In this cycle mass is lost down the magnetotail through the reconnection of centrifugally stretched, mass loaded field lines (Vasyliunas, 1983).

On a global scale reconnection can facilitate an energy balance, dynamic equilibrium between the planetary field and the interplanetary field, and serve as a way to balance the mass budget for magnetospheres where there is a significant amount of internal plasma loading, e.g., from volcanic moons. However, on a small scale it produces local fluctuations of energy and unstable closed magnetic field systems of plasma. These small scale products can be identified by *in-situ* spacecraft through measurements of magnetic field topology and changes in plasma flow. For this study, focus will be on reconnection signatures at Saturn, as identified from the Cassini magnetometer and now classified through machine learning. Reconnection for Saturn has long focused on the planetary magnetotail whereby two types of reconnection signatures are typically reported: dipolarizations and plasmoid ejections. Dipolarizations occur on the planetside of the reconnection site where previously stretched magnetic field lines relax, under a reconnection event, to a more dipole-like magnetic field (Bunce et al., 2005; Russell et al., 2008; Jackman et al., 2013; Jackman et al., 2015; Yao et al., 2017; Smith et al., 2018a; Smith et al., 2018b). On the tailside of the reconnection site, closed magnetic field systems encompassing a trapped bubble of plasma known as plasmoids are created during reconnection, which are rapidly ejected down-tail. These events were first identified in Earth's magnetosphere (Hones, 1977), but have since been identified in Saturn's magnetosphere (Jackman et al., 2007; Hill et al., 2008). Observations of these reconnection related structures can be further identified indirectly in magnetic field measurements in the adjacent magnetotail lobes through compressions in the magnetic field. These features are known as traveling compression regions (TCRs; Slavin et al. (1984)) due to their close following of plasmoid and dipolarization features. Notably, this indirect method of identification gives no insight to the internal structure of the plasmoid but do at least indicate reconnection occurring and hence can be used to estimate reconnection rates.

Typically signatures of reconnection may be identified by a rapid deflection in the north-south magnetic field component, as observed in **Figure 1**. At Saturn, plasmoids moving are expected to exhibit a south to north deflection and vice versa (north to south deflection) for planetward-moving dipolarizations. For plasmoids in particular, it is important to recognize the true velocity of the signature may have some azimuthal/corotational component following release (McAndrews et al., 2009; Thomsen et al., 2013; Neupane et al., 2019; Kane et al., 2020). The nature and magnitude of magnetic field deflection depends not only on the intensity of incoming reconnection event, but also on the orientation and direction of travel of the observing spacecraft through this region (Cowley et al., 2015). Spacecraft traveling through the center of reconnection signatures observe stronger deviations from the background north–south component of magnetic field, and vice versa. Without *a priori* knowledge of

reconnection, these signatures are the principal identifiable feature in magnetic field data, and any deviation in north-south field component present a potential indication of magnetic reconnection. Notably, this is not a definitive method of classification as random turbulent motion in the magnetosphere or waves in the plasma sheet can reproduce similar signatures in the magnetic field observations (Nakagawa and Nishida, 1989; Jackman et al., 2009; Martin and Arridge, 2017).

Only recently has there been sufficient data to catalog and identify large numbers of reconnection events in Saturn's magnetosphere. During 2006 the Cassini spacecraft executed a series of tail orbits to a maximum downtail distance of 68 R_S (1 R_S = 60,268 km) and reconnection signatures from these data were cataloged by Jackman et al. (2007), Hill et al. (2008). These catalogs were built upon in Jackman et al. (2011), where 34 additional plasmoid signatures were identified in the 2006 orbit, and again expanded in Jackman et al. (2014) which reported a total of 99 events, 86 of which are identified moving tailward. Estimations of mass loss from large-scale events in this catalog could not balance the mass gain in the system from Enceladus and other sources (Bagenal and Delamere, 2011). Multiple theories have been submitted to account for this imbalance including unobserved mass loss in the magnetospheric flanks (Burkholder et al., 2017; Ma et al., 2017), through small scale processes (Bagenal and Delamere, 2011), simply that the definition of reconnection event duration under-accounted for the mass in a plasma structure (Cowley et al., 2015), or unaccounted for reconnection on the day-side may balance the mass transfer budget (Guo et al., 2018). Most recently, Smith et al. (2016) attempted to more fully quantify the mass imbalance through the creation of a more comprehensive model and catalog of tail reconnection events. This model was applied to the equatorial dawn flank orbits and midnight tail orbits of 2006, the dusk flank orbits of 2009, and similar low latitude dusk orbits throughout 2010. Across this observing window 2093 individual events were identified and validated forming a substantial catalog of reconnection events for Saturn's magnetosphere. However, their semi-automated technique required the selection of observationally defined limits and thresholds.

Here, we apply established methods of machine learning (ML) to planetary magnetospheric reconnection classification to expand these previous surveys to spatially cover the entire Kronian magnetosphere and temporally cover all of Cassini's near Saturn lifetime. ML is an application of artificial intelligence that allows computers the ability to learn from large datasets and experience without being explicitly programmed. This method aides in the prevention of biases and limitations that would otherwise be imposed by a human created model, such as event size and spatial constraints. Furthermore, these models perform well at identifying underlying structures that humans otherwise would not, or could not, that are essential for classification and can be extrapolated to identify features in previously unobserved datasets and have already been implemented across the field of astrophysics to solve a variety of problems (Ruhunusiri, 2018; Ruhunusiri et al., 2018; Waldmann and Griffith, 2019).

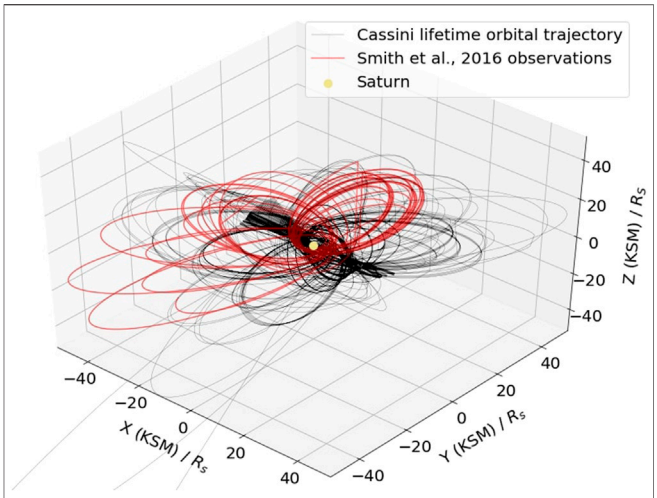


FIGURE 2 | Lifetime trajectory (black) of Cassini around Saturn (yellow). The Cassini trajectories during the observing window employed in the creation of the Smith et al. (2016) catalog of magnetic reconnection are highlighted in red for comparison. For the creation of a machine learning training set, observations of events are taken from the Smith catalog and null events are randomly taken from a variety of local times and radial distances during the Smith catalog observing window.

2. DATASET AND OBSERVATION

The datasets used in this study are magnetic field component measurements as observed by the Cassini magnetometer (MAG; Dougherty et al., 2004) instrument. Cassini was launched onboard a Titan IV rocket in 1997 and following Saturn Orbit Insertion in July 2004, it orbited the planet until 2017. During its lifetime it observed a variety of environments within the Kronian magnetosphere which can be used to gain a greater understanding of Saturn's magnetic processes. For this research, Kronocentric radial, theta, phi (KRTP) coordinates are used as this coordinate system has been shown to be useful in distinguishing reconnection related events from turbulent motion in the hinged current sheet (Jackman et al., 2009). In this spherical coordinate system the radial component (B_r) is positive outward from Saturn, the meridional component (B_θ) is positive southward (at the equator), and the azimuthal component (B_ϕ) is positive in the direction of corotation (prograde). Furthermore, 1 min cadence observations are analyzed as it has been shown that reconnection events last an average duration of ~ ~10–20 min and can be accurately identified at this cadence (Jackman et al., 2014; Smith et al., 2016).

Figure 2 illustrates the near-Saturn lifetime trajectory of Cassini in Kronocentric solar magnetospheric coordinates. This Cartesian coordinate system is oriented such that the x axis points toward the Sun, the x–z plane contains the planetary dipole axis, and the y component completes the right-handed set. The trajectories of Cassini during the Smith et al. observing window is highlighted in red for comparison. The full 13 years dataset shows the various magnetic environments about Saturn that the Cassini satellite has explored. Similarly, the trajectories during the highlighted observations cover much of these varied

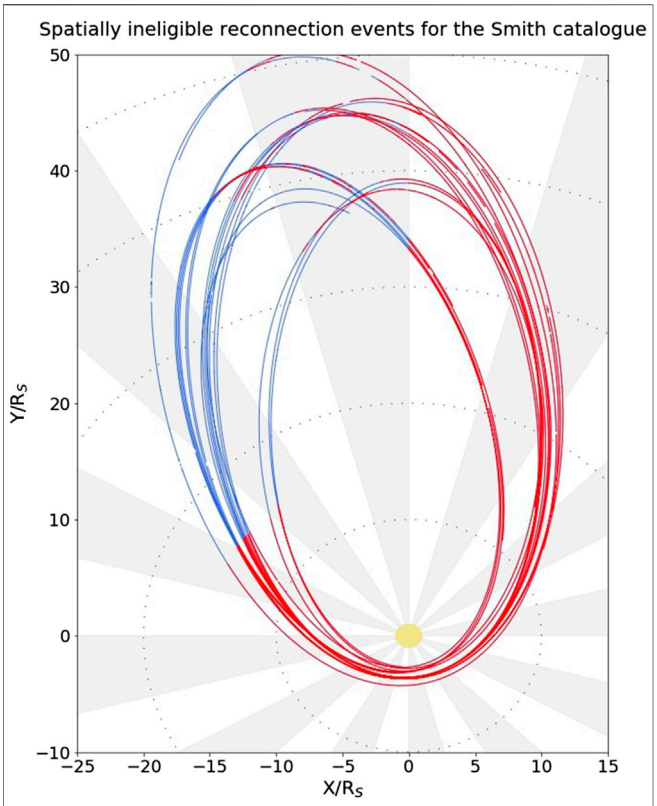


FIGURE 3 | 2010 trajectory of Cassini about Saturn (yellow) separated by color into regions where the S16 could identify reconnection events (blue) and the trajectories that were spatially ineligible for identification (red). Notably, at large distances ($>35\ R_S$) eligibility appears to be very patchy, this is due to the changing position of the magnetopause boundary under the varying balance between solar wind dynamic pressure and internal plasma pressure.

environments, however are focused primarily on longer observation times of Saturn's magnetotail within the equatorial plane. Furthermore, this observing window covered times when Saturn's night-side current sheet was hinged upward (southern hemisphere summer), was parallel to the equatorial plane (e.g., equinox; Khurana et al., 2009), or even hinged downward (northern hemisphere summer) later in the mission (Arridge et al., 2011). By allowing for identification across the entire Cassini lifetime, more accurate statistical investigations can be performed on reconnection occurrence across the entire morphology of Saturn's magnetosphere.

For the construction of a supervised ML model, a previous, labeled database is required for the model to learn the parametric identifiers of the magnetic reconnection class, and to test against to validate the model's accuracy. The Smith et al. (2016) catalog (hereafter S16) of reconnection is selected as this classified dataset due to its large number of samples, variety of orbital trajectories sampled, and its final human based verification step. However, to utilize this catalog, the limitations of its selection criteria must be understood. This catalog was constructed from a semi-automated model with many hard-coded limitations. Excluding the aforementioned temporal limitations of observation window selection, this model further includes spatial and magnetic parametric limitations. Spatially, this model is defined within a 'viewing region' where events are strictly only identified within the night-side, at distances greater than 15 R_S from Saturn, and strictly within the magnetosphere. **Figure 3** demonstrates the spatial constraints on the S16. This figure illustrates the entire 2010 trajectory of he Cassini instrument seperated into spatial constraints where the S16 could identify reconnection events (blue) and those where identifications are spatially ineligible (red). This catalog has similar magnetic parametric limitations. Primarily events are identified from the background through a quadratic fit to B_θ polarity crossings with a least squared goodness of fit value of $r^2 \geq 0.9$. Identified candidates are then verified through

$$\frac{|\Delta B_\theta|}{B_\theta^{RMS}} \geq 1.5 \tag{1}$$

where $|\Delta B_\theta|$ is the magnitude of deflection during the event and the root-mean-square (RMS) of B_θ is calculated for a period extending 30 min both sides on the candidate. A secondary validation step follows this such that:

$$|\Delta B_\theta| \geq 0.25\ nT \tag{2}$$

where symbols have their previous meaning. These validation steps are imposed as it is difficult for humans to verify candidates that fall below these parametric limitations due to a signal to noise ratio problem. Through these identification and validation methods, the Smith et al. model identifies 2094 (1083 planetward and 1011 tailward) reconnection signatures within their observation window.

These events identify the temporal windows which act as a labeled dataset for a supervised training ML method. However, training of a ML model requires a collection of input parameters, from which the ML model learns the association of parameters to events. For this research, exclusively magnetic observations in the three spatial components of the KRTP coordinate systems are used for identification. This selection is made due to the coverage of Cassini's lifetime that the MAG instrument remained operational. While signatures of planetary reconnection exist in other property observations such as plasma density, MAG data is used as a predominant identifier for human based identifications. Furthermore, the Cassini plasma spectrometer (CAPS; Young et al., 2004) did not remain operational across the entirety of Cassini's near Saturn lifetime, being permanently inactive post-2012, nor did it provide a full 3D picture of the plasma environment, and so may miss any reconnection related jets due to pointing in the 'wrong' direction. A model for identifying magnetic reconnection signatures using only magnetic field component data would also ease possible transitions, and transfer learning of a ML model to use with new satellites and for different planetary magnetic fields. Hence, plasma property observations for these reconnection events are not used in this research, however, plasma observations could and should be used in any future implementation where the plasma measurements are comprehensive in both time and 3D viewing. Finally, it is envisioned that the construction of a catalog using

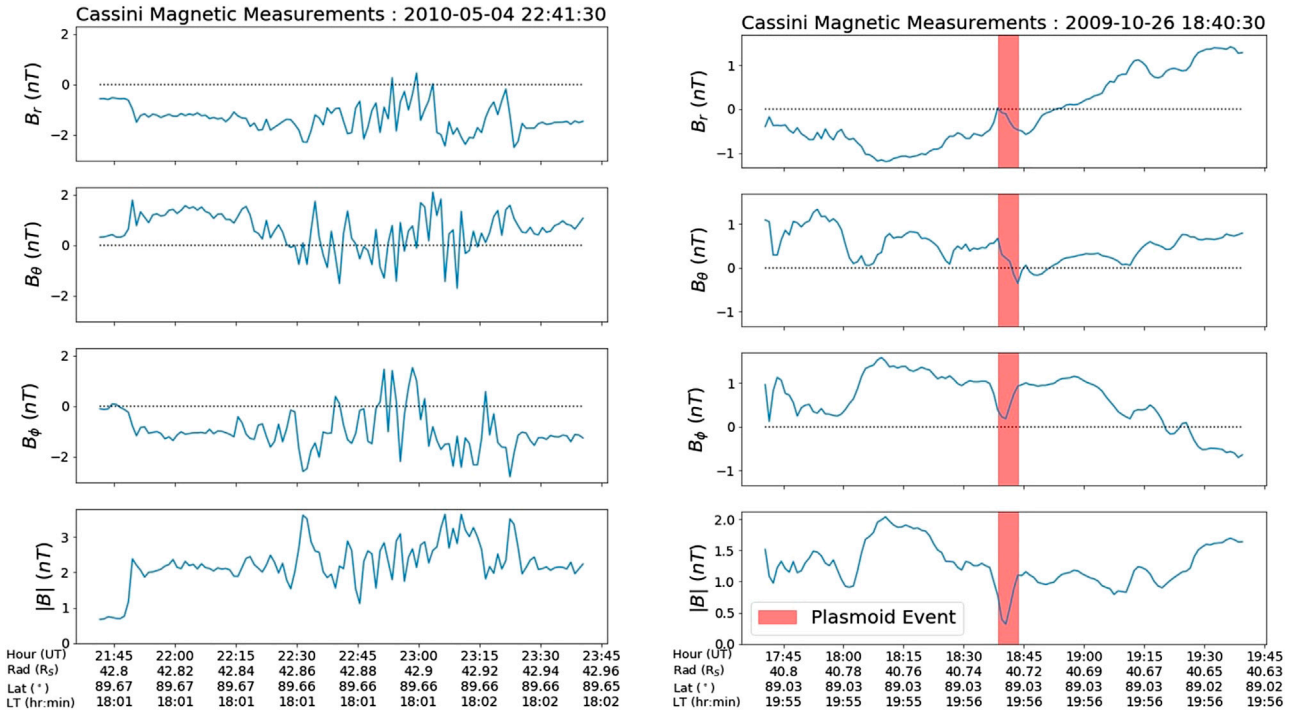


FIGURE 4 | Examples of magnetometer data for a non event **(left)** and event **(right)** used to train a machine learning algorithm. Titles of these plots denote the time at center of these observing windows in a YYYY-MM-DD format.

this method across the entire Cassini dataset will enable the examination of numerous case studies of reconnection using multiple instruments.

Figure 4 illustrates example magnetic time series across the three KRTP spatial components as well as the total magnetic field, $|B|$, used during training as a null classification (left) and an event classification (right). The X-axis of these plots denotes the time of observation and the spacecraft ephemeris data for Cassini at that time. The time constraint of ML training is highly dependant on the size of input parameters, hence, only the three elementary components of magnetic field measurements from Cassini are used as inputs for ML training in this study.

$$|B| = \sqrt{B_r^2 + B_\theta^2 + B_\phi^2} \tag{3}$$

3. MACHINE LEARNING ARCHITECTURE

3.1. Class Balancing and Data Augmentation

The greatest risk for poorly constructed ML identification of relatively rare features is the possibility of a class imbalance (Buda et al., 2017). For this case, magnetic reconnection events are only identified occupying $\sim <1$–10% of the total observing time dependant on the identification method, hence, ML training with this ratio will exhibit bias toward the majority class (Guo et al., 2008; Johnson and Khoshgoftaar, 2019). Hence, an unbalanced ratio of non-events to events will cause the ML algorithm, in its interest of maximizing its accuracy, to simply classify all inputs as nulls to obtain an accuracy of $\sim 90\%$ without truly learning underlying identifying signatures. To alleviate this issue, a randomized under-sampling of non-reconnection events is used to balance with the $\sim 2{,}000$ events in the S16. This renders $\sim 4{,}000$ total observations to construct training, test and validation sets, which is a low number of samples to perform ML methods to and expect the overarching reconnection features to be accurately identified, rather than the ML model simply memorizing the training set.

The issue of a small sample size can be solved through data augmentation, such as data synthesis, or the transformation of already existing data (Mikołajczyk and Grochowski, 2018; Fawaz et al., 2018). Data synthesis is simply the creation of data through the combination of a model with some overlying noise in an attempt to create real-like datasets, however this method can be inaccurate if predictive models are inaccurate, or missing some underlying understanding. Data transformation takes already existing data and applies some kind of transformation, such as adding noise or filters over the existing measurements or translating the data either spatially or temporally. Since the signatures of magnetic reconnection occur across a number of minutes, averaging ~ 8 min (Smith et al., 2016), it is possible to increase our number of samples by considering every minute of an event as a unique positive identification. Hence, a single event lasting 5 min would be considered as five consecutive positive

labeled identifications every minute between the start and end time of an event. This method increases the total available observations to ~32,000 (16,000 positive labels and 16,000 randomly selected negative labels). This increased number of samples allows for more complex ML architectures and a more robust final model. In this instance, nulls are selected randomly from the S16 observing window with the same spatial limitations of the S16, e.g., at distances greater than 15 R_S from Saturn, etc. Finally, since these events occur and are identified across multiple minutes of magnetic data, due to their temporal structure, for the ML model to identify these events, it must have a time window of magnetic measurements as input. 15 min both before and after the central label in the three KRTP spatial magnetic field components ($B_r, B_\theta, and\, B_\phi$) are used as this window is wide enough to cover the longer duration events in the S16 catalog, but short enough to identify label changes occurring between event clusters. This renders a total of 90 magnetic property inputs for each of the 32,000 labels for any given ML model.

3.2. Machine Learning Types

A variety of ML models exist, ranging in complexity to allow for identification of more elaborate and subtle features within datasets. This research focuses on identification of features within three singular dimension magnetic field time series, hence, only relatively simple supervised learning ML methods will be investigated, namely: support vector classifier with a linear (LSVC) and non-linear kernel (NLSVC), random forest classifier (RFC), and a simple artificial feed forward neural network (ANN). All of these models are available in the sklearn python packages (Buitinck et al., 2013) and the TensorFlow libraries (Abadi et al., 2015). A LSVC creates a multi-dimensional hyperspace of observed parameters. The labeled data are then input into this hyperspace and a linear hyperplane is created as a decision boundary to optimally separate data of opposing labels with the widest possible margins. This hyperplane seperator is then stored and used to predict the labels of new datasets. A NLSVC behaves similarly to its linear variant, by creating some hyperplane as a decision boundary, however, the kernel function utilized by a NLSVC can non-linearly transform the feature space such that the classes become separable. RFC similarly creates a multi-dimensional hyper space, but instead of separating data by a continuous hyperplane, a vast array of Boolean decision tree networks, of variable depth, are created to segment a training dataset non-linearly. New data sets are then input into this array of decision trees and a classification is judged by majority vote outcome. The final type, ANNs, rely on the creation of input (parameters) and output (labels) neural nodes, interconnected by a collection of initially random weights and biases. This method of ML is optimized through tuning of various hyperparameters such as: the non-linear activation function on each of the nodes, the number of nodes within each layer, the loss and optimization functions, and the number of hidden layers within the architecture. These hidden layers of neural nodes between the input and output nodes have no true observable parameter, however they enable more complex feature identification by the ANN. To judge which of these models is optimal for identification of reconnection signatures, each must be trained and the model that exhibits the highest accuracy can be selected for further fine tuning. It is important to note that model accuracy is not typically the greatest indicator of a model's performance, and many other metrics will be discussed later, however this metric is significant enough to indicate a single ML model that can be best improved, and hence will be further investigated in this research. **Table 1** indicates the accuracy for these 4 ML models to identify the signatures of magnetic reconnection using only the three KRTP magnetic field components observed by Cassini for times within the spatial and temporal limitations of the S16. Overfitting of these models was prevented by standard methods of train/test/validation splitting, principle component analysis and algorithm complexity limitations. The train/test/validation split had a weighted random assignment across all years in the S16 catalog with no temporal disjoint. This means the training set was composed of events from 2006, 2009, and 2010 allowing it to learn the structure of reconnection from varied spacecraft orbits and trajectories. However, set assignment was performed on a reconnection event basis, meaning all minutes of observations associated with an individual reconnection event are assigned to a single set. Most notably, ANNs exhibit the highest accuracy rating, likely due to their allowed higher complexity when compared to the other methods mentioned. Hence, ANNs are further utilized for this research.

TABLE 1 | Comparison of validation set accuracy for ML event classification using a linear support vector classifier (LSVC), a non-linear support vector classifier (NLSVC), a random forrest classifier (RFC), and artificial neural network (ANN).

ML type	Accuracy
LSVC	0.73
NLSVC	0.75
RFC	0.87
ANN	0.90

This accuracy value is calculated as the ratio of correctly identified samples to total samples.

3.3. Artificial Neural Networks

Figure 5 demonstrates the architecture of a simple ANN created and trained during this research to identify signatures of magnetic reconnection. In this architecture, input properties are directed into the architecture in the input layer. Operations are performed on these parameters between each interconnected layer, with the goal being to accurately recreate the desired outputs in the output layer. ANNs are generally optimized and fine tuned through a process of trial and error, however some simple rules for their creation exist to prevent overfitting of training data. Generally, the number of free parameters must not exceed the number of samples used for training, i.e.,

$$N_S > N_{FP} = \sum_{i=1}^{i} ((N_{i-1} \times N_i) + N_i) \tag{4}$$

where N_S is the number of training samples, N_{FP} is the number of free parameters, and N_i describes the number of nodes in the ith layer. No strict consensus exists to decide the number of nodes in

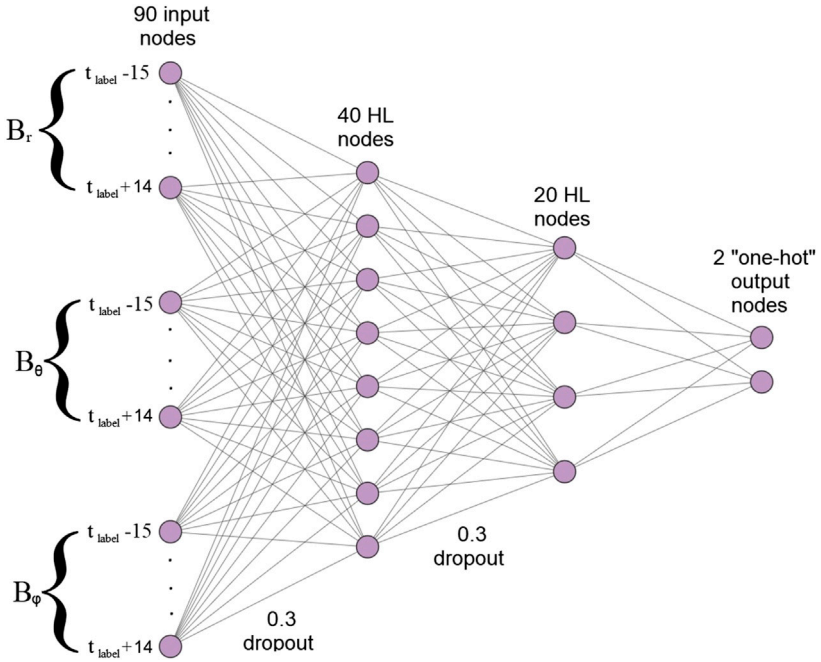


FIGURE 5 | NN architecture used to train to identify reconnection signatures in Cassini magnetometer data. This structure shows 90 input nodes composed of three 30 min time windows centered on the label time (t_{label}), in the three KRTP magnetic field components (B_r, B_θ, and B_ϕ). These nodes are then fed into a 40 node hidden layer (HL) with a 0.3 dropout, which feeds into a 20 node HL with a 0.3 dropout. This final HL is then categorized using a 2 node, one-hot classification system. During training, every epoch, the weights and biases interconnecting each layer are varied to under a gradient descent to optimize the accuracy of classifications.

TABLE 2 | Confusion matrices for a feed-forward neural network classification of magnetic reconnection within the Kronian magnetosphere

	Train		**Test**	
	Pred. Null	*Pred. Event*	*Pred. Null*	*Pred. Event*
Obs. Null	26690 (0.92)	2278 (0.08)	3272 (0.94)	226 (0.06)
Obs. Event	1564 (0.16)	8092 (0.84)	672 (0.19)	2826 (0.81)
	Validation		**2010**	
	Pred. Null	*Pred. Event*	*Pred. Null*	*Pred. Event*
Obs. Null	3020 (0.93)	232 (0.07)	486400 (0.94)	32954 (0.06)
Obs. Event	614 (0.19)	2638 (0.81)	1134 (0.18)	5111 (0.82)

ANN hidden layers, however it is generally accepted for the number of nodes in a hidden layer to be approximately half way between the number of nodes in the previous and next layers. Through trial and error, it was found that a two hidden layer ANN architecture was most efficient at identifying magnetic reconnection in the training set, however Huang (2003) proved an upper limit to the total available hidden nodes available in this system to be

$$N_H \leq \frac{2}{\alpha}\sqrt{(N_O + 2)N_S} \tag{5}$$

where N_S has its previous meaning, N_H represents the total available hidden nodes, N_O is the number of output nodes, and α is a robustness factor usually between one and ten. From **Eqs. 4** and **5**, and the aforementioned 32,000 samples, it is possible to train the robust two hidden layer neural network in **Figure 5**: 90 input nodes with a dropout of 0.3 connected by a rectified linear units (relu) activation function to 40 first hidden layer nodes, which are in turn connected with a dropout of 0.3 and a relu activation function to 20 s hidden layer nodes, which connects fully with a softmax activation function to two output nodes representing a Boolean classification of reconnection occurring. After each training epoch, the model was trained toward improving a binary cross entropy accuracy metric. During training, however, it was observed that a significant number of events were identified outside the magnetosphere, along portions of Cassini's orbit in the magnetosheath and solar wind. This is likely due to the ML algorithm never encountering observations from these magnetic regions during training. Since these regions are unique classifications and differ from null training samples within the magnetosphere, they can be included in training as a unique classification of nulls. This means our number of samples will

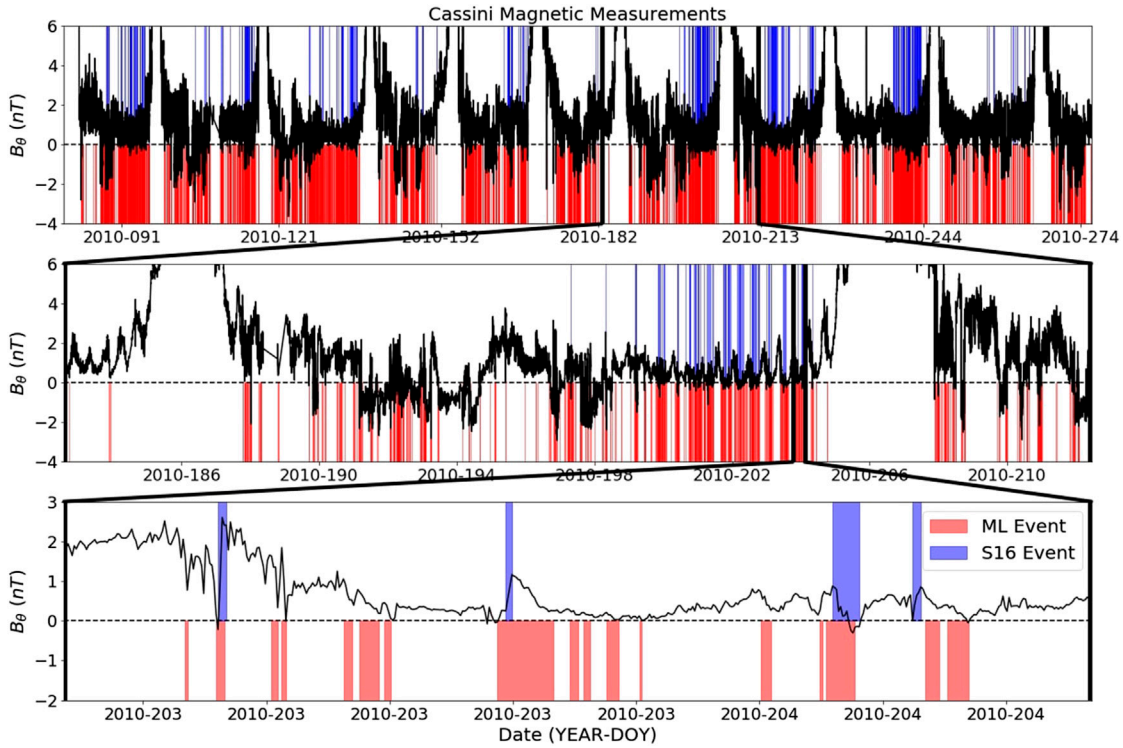


FIGURE 6 | Output of reconnection signatures identified by a feed forward neural network (red areas) across half of 2010 compared to identifications from the Smith catalog (blue areas) for the same period. These areas are overplot onto the B_θ component of the magnetic field, where reconnection signatures are easiest identified by eye. Each successive plot examines zoomed in windows to observe finer structure in magnetic field measurements and identifications.

TABLE 3 | Confusion matrices of neural network classification considering only events that the Smith et al. catalog could have identified.

	2010	
	Pred. Null	*Pred. Event*
Obs. Null	1008 (0.82)	208 (0.17)
Obs. Event	58 (0.07)	741 (0.93)

increase to ~ 16,000 reconnection events, ~ 16,000 magnetosphere nulls, ~ 16,000 magnetosheath nulls, and ~ 16,000 solar wind nulls. Given a train-test-validation split of 60–20–20, ~ 38,400 samples are available for training.

The relative effectiveness of this architecture is displayed in **Table 2** through four confusion matrices. A confusion matrix exists for each of the training, test and validation set, and a fourth confusion matrix illustrates the effectiveness of the ANN to identify reconnection events across the entirety of 2010, replicating how the model will perform on large continuous datasets. The year 2010 was selected for this comparison as it is one of two full years which the S16 covered, along with 2006. 2010 was selected between these two years as the trajectory of Cassini for this year included a wider sampling of varied magnetic environments, hence being the most stringent full year comparison possible. It is important to recognize that this 2010 confusion matrix includes identifications from the training, test, and validation datasets. Across each of these confusion matrices an accuracy of ~ 90% is attained and the training, test, and validation sets have high skill metrics: the Heidke skill score (HSS; 0.75; Heidke, 1926), the true skill statistic (TSS; 0.76), and the threat score (TS; 0.68). It is important to reinstate, the final step of the S16 catalog's final step is a human verification, hence our comparison in the validation confusion matrix shows the effectiveness of the ML model against human verified data. However, in the 2010 confusion matrix, the number of false positives (FP; 32,954) significantly outweigh the number of true positives (TP; 5,111) leading to a high false alarm ratio. Hence the imbalance in this confusion matrix is represented in its HSS; 0.21, TSS; 0.75, and TS; 0.13. These skill score metrics quantifiably describe the ability of this model to replicate the observable data. The HSS measures the fractional improvement of the forecast over a standard forecast and ranges from $-\infty$ to 1, with 1 being perfectly skillful, a value of 0 representing no skill, and a value of 0.3 being considered of good skill. The TSS, also known as the Peirce's skill score, compares classification to a random selection classifier and ranges from −1 to 1, with 1 being considered perfectly skillful, and 0 having no skill. TS measures the fraction of observed and/or classified events that were correctly identified and ranges from 0 to 1, with 0 having no threat detecting capabilities and 1 being a perfect identifier. The imbalance of these classifications is illustrated in **Figure 6** which compares identification of magnetic reconnection across 2010 by the ANN architecture compared to the S16. In this

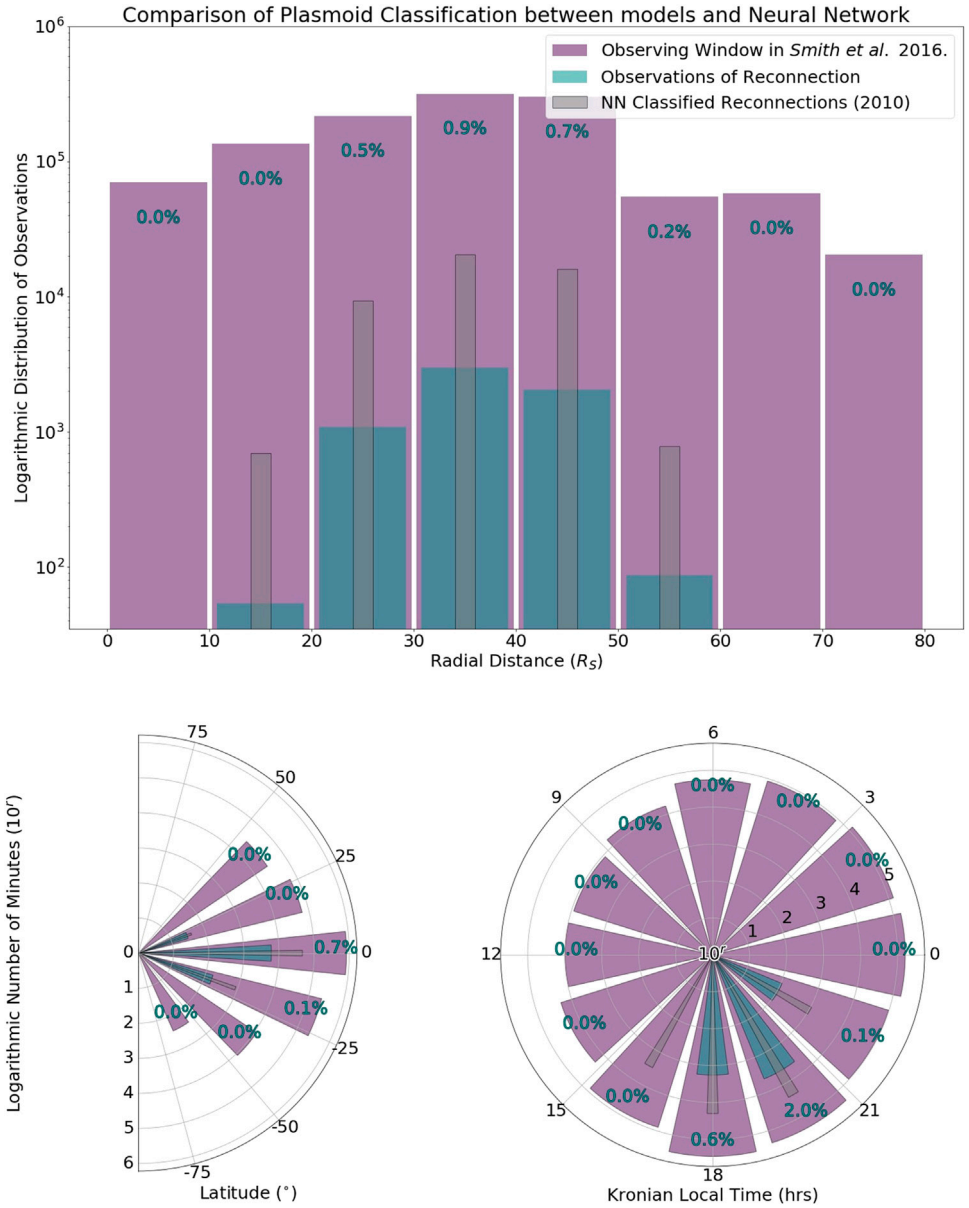


FIGURE 7 | Total time of Cassini observations of Saturn's magnetosphere during the 2010 observing window (purple) with radius, latitude and local time respectively. This distribution is compared to the time classified as magnetic reconnection signatures by Smith et al. (blue) and as classified by a neural network method (grey). Percentiles indicate relative time spent near reconnection events as found in the Smith et al. catalog to the total window.

figure, events are highlighted over underlying B_θ magnetic components as measured by Cassini. Events from the S16 are highlighted in blue, whereas events classified by the ML algorithm are highlighted in red.

4. DISCUSSION

The results and corresponding skill scores from **Table 2** would imply a significant bias of the neural network to mis-classify null observations, as classified by the S16 catalog, as events. Investigations into the spatial distribution of events to identify the cause of this large number of mis-classification are illustrated in **Figure 7**. This figure demonstrates the distribution of total time during the observation window of Smith et al. (2016) (purple) across radial distance, latitude and the Kronian local time. Additionally, the time spent observing reconnection related events as stated by the S16 (blue) and the time spent observing reconnection products as classified by the ANN (gray) are displayed for comparison. Blue percentile values illustrate the percentage of total time of a given distribution spent observing reconnection as found by S16. As is illustrated, the ANN

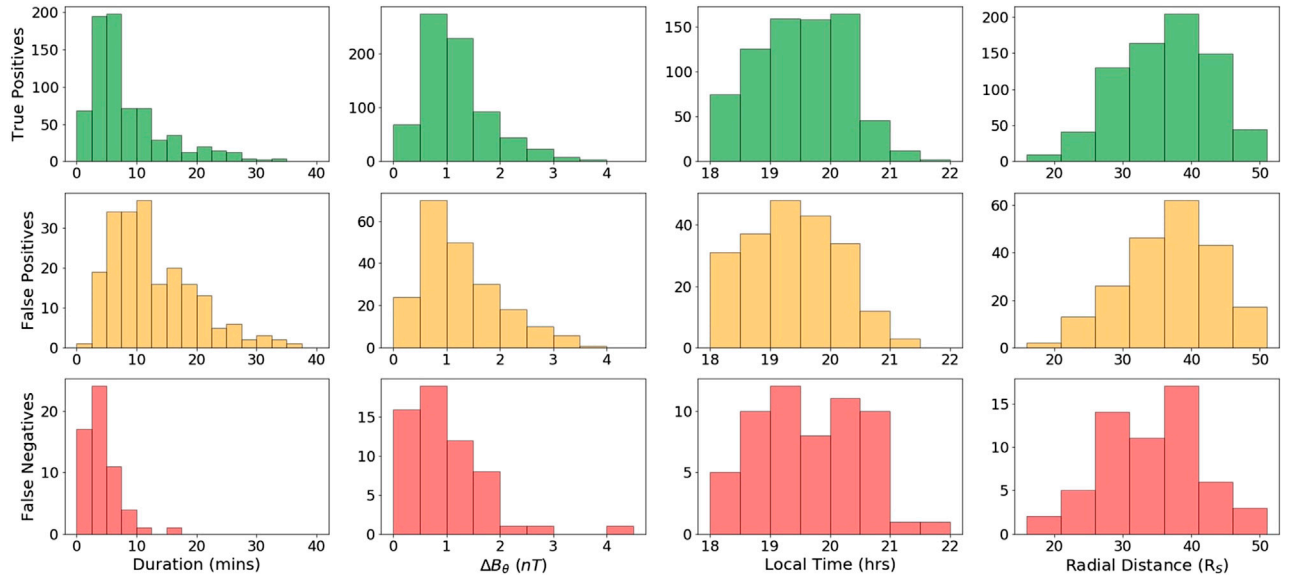


FIGURE 8 | Temporal, magnetic and spatial properties of reconnection events that are classified as true positives (green), false positives (orange), and false negatives (red) when comparing the neural network classifications to those of the S16.

observations have a similar spatial distribution of identifications to the S16, simply the ANN recognizes more minutes of reconnection occurring due to more events being identified. In the local time distribution, all events identified by both S16 and the ANN for 2010 are located on the planetary dusk side due to the orbital trajectory of the Cassini spacecraft at this time, being very close to the planet ($< 15 R_S$) at other local times. Most notably, the local time distribution of the ANN identifications shows a non-zero rate of reconnection on the day-side of Saturn, while the Smith et al. model maintained a strict cut-off of dayside events due to its hard coded spatial limitations. Evidence for dayside reconnection has been identified previously (Delamere et al., 2015; Guo et al., 2018), hence, inclusion of dayside reconnection identification within this catalog allows for more future exploratory research to be performed.

4.1. Evaluation of ANN Performance and Identifications

As previously mentioned, the S16 is constructed from numerous hard coded spatial and magnetic limitations within their semi-automatic identification method that significantly limit their identifications. In the ML model, these limitations are not in place, which leads to a substantial number of ML identifications that cannot otherwise be identified by the S16 method, thus leading to our abundance of apparent FPs. Hence, the confusion matrix for 2010 in **Table 2** does not accurately compare the results of the neural network to the S16, and it must be corrected. By examining only the neural network reconnection identifications that could be recognized by the S16 (i.e. events with $\delta B_\theta \geq 0.25\, nT$, and a significant signal to noise ratio: $\delta B_\theta / B_{rms} \geq 1.5$), and comparing events as a whole, by considering sequential positive minute-by-minute classifications as part of the same event, a new confusion matrix is obtained for the entirety of 2010. **Table 3** demonstrates the corrected confusion matrix for 2010, only comparing events that the S16 could identify. This enables us to more fairly assess the performance of our approach. To calculate the value of true negatives (TN; 1008), the same method could not be used as TN measurements are not considered discrete events, and are not privy to the same parametric limitations that events are. To obtain this value, TNs are considered to be all of the periods when a TP, FP, or FN is not applicable, hence:

$$TN = TP + FP + FN + 1 = 1008 \tag{6}$$

This corrected confusion matrix for eligible 2010 events has a significant increase in accuracy (87.0%), HSS (0.73), TSS (0.76), and TS (0.74). **Figure 8** displays distributions of temporal (duration), magnetic (B_θ deflections), and spatial (radial distance and local time of event) properties of TP, FP, and FN events from **Table 3**. No significant discrepancy is evident between these categories spatially or magnetically, however, the differences between the ANN and Smith et al. method is visible in the distributions of event duration. The ANN identifies a higher number of longer duration events, while finding difficulty in identifying short duration events (< 10 min). However, as evident by the distribution of ΔB_θ for FNs, these missed events represent smaller deflections, which are least likely to be identified by eye, and most likely to be spurious identifications. The plotted distribution of FPs is very similar to TPs, excluding the longer average durations (~ 10 min). This discrepancy may be due the quadratic fitting and identification method of the Smith et al. model, coupled with their model not identifying the inclining and declining phases of reconnection which implies a shorter average duration of identifications. Hence, the neural network is considered to accurately identify magnetic reconnection events solely from magnetic field component measurements, not only under the

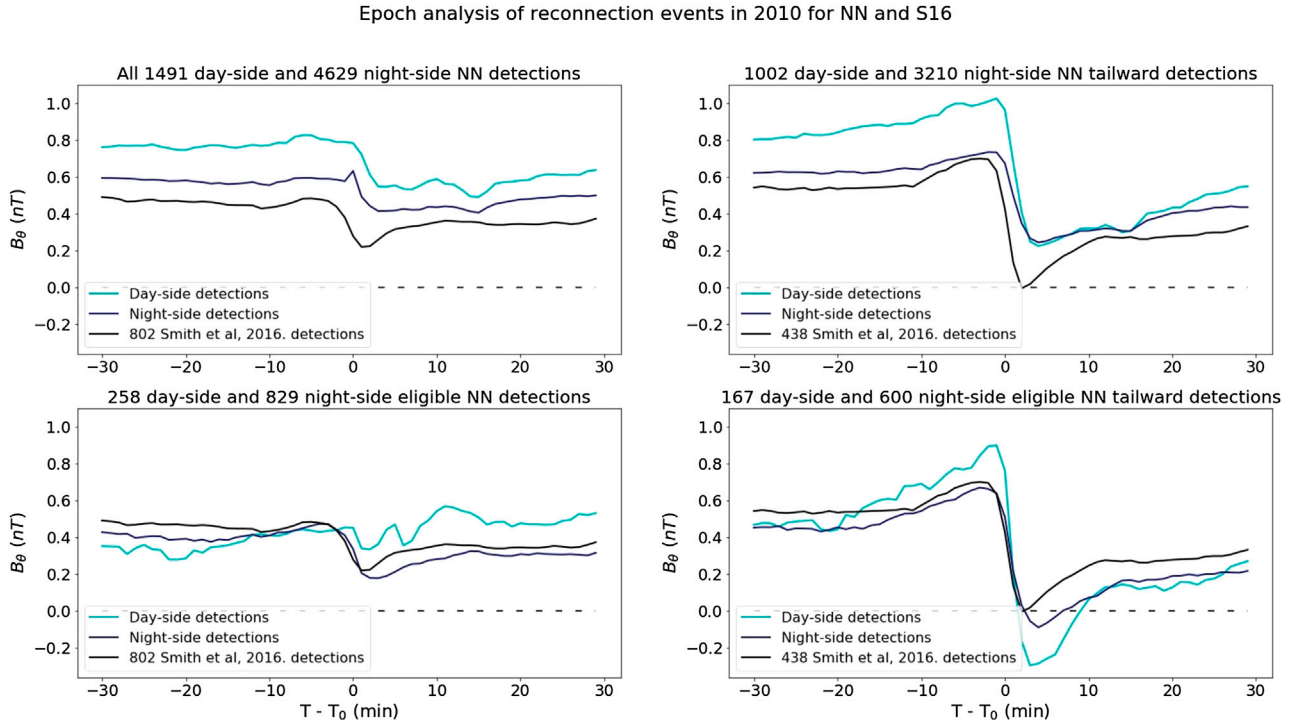


FIGURE 9 | Epoch analysis of all 2010 events (top left), tailward events (top right), all 2010 events that meet the S16 criteria (bottom left), and meet the S16 criteria while also being tailward (bottom right) identified by the NN. Identifications are split onto the day-side (light blue) and night-side (dark blue) and are compared to the average of events from the S16 for 2010 (left) and tailward. (right)

same restrictions as the S16, but also across the total spatial and magnetic domain of Cassini's lifetime.

Figure 9 displays an epoch analysis for events classified by this NN for both day-side (light blue) and night side detections (dark blue) compared to the events from the S16 (black). These events are compared across 4 criteria: all events for 2010 (top left), all tailward event for 2010 (top right), all event for 2010 that all within the human built thresholds for S16 (bottom right) and all tailward events that fall within this threshold (bottom right). The term tailward here is defined as a reconnection event occurring with a negative slope in the deflection phase $(B_\theta(t_0) > B_\theta(t_1))$. The average day-side and average night-side epochs are similar in all panels. The main difference between the two is the higher average B_θ in the day-side events and the larger ΔB_θ deflections, however this is more likely due to the Cassini spacecraft being closer to the planet on the day-side on average for 2010, and hence within a stronger magnetic field region. The ANN epochs have a similar structure compared to the Smith et al. epoch, however the ANN epochs do not become negative auntil the S16 criteria is applied. This is likely due to the more numerous small scale B_θ deflections ($\Delta B_\theta < 0.5$ nT) occurring within a relatively strong magnetic field regions ($B_\theta > 1$ nT) for the ANN method than the S16 model, which skews the average. Similarly, events identified by the ANN have higher average B_θ than events identified by the S16, however this is likely due to the ANN not spatially limiting its detections. Interestingly, a secondary deviation is visible in both top panels (no limitations on identifications) at $T \approx 12$ min after the central deviation. This deviation may imply a propensity for reconnection events to occur in clusters with a ~ 12 min delay. However, it is uncertain if this secondary deviation is simply a statistical anomaly in the data, or if this ~ 12 min delay is related to the orbital trajectory of Cassini for 2010, particulary since this feature is not visible in the bottom panels (S16 limits in place).

5. CONCLUSION

Here, the operations and effectiveness of ML approaches to magnetic reconnection identification have been discussed. A new ANN model has been constructed to identify reconnection signatures in Saturn's magnetosphere through spherical magnetic field measurements with a HSS ~ 0.73, and hence is considered an effective identifier. This ML approach identifies deflections in the B_θ field component with no hard-coded limitations that a human-built model may otherwise impose and can identify small scale B_θ deflections that a human, or human made model, would find difficult. This new model has been used across the entire Cassini near-Saturn lifetime to identify $\sim 46{,}000$ reconnection events and their associated properties which have been compiled and cataloged. This model and associated reconnection catalog is available at Garton (2020).

Further study is required on events within this catalog to identify statistical properties and spatial likelihood of magnetic

reconnection in Saturn's magnetosphere to improve predictive modeling. The 13 years catalog created from this research can be used to identify long-term magnetospheric trends and create a statistical predictive model of reconnection occurence for extreme and rare events. This ANN was constructed using a limited sample of events (~ 2000) which may be insufficient to cover the spectrum of reconnection signatures, hence this model can be further improved through the inclusion of additional samples of manually selected reconnection signatures, or through the inclusion of additional particle property observations, should they be available. Furthermore, the training of this ANN involved the inclusion of additional null sets which corresponded to non-reconnection events within the magnetosphere, the magnetosheath and the solar wind. It is possible other such unique magnetic environments exist that could cause spurious identifications where characteristic magnetic field deflections are observed, such as during a Cassini flyby of Titan (Simon et al., 2010) or Enceledus (Dougherty et al., 2006). Hence, inclusion of datasets within these environments as nulls in the training set could improve the overall accuracy and skill of the ANN. Finally, through transfer learning, it is possible to retrain this model to identify similar reconnection signatures in other planetary magnetospheres given fewer training samples of identification. Through this established method it is possible to create a similar operational ML model to identify reconnection signatures at Mercury, or Earth. It is our intention to explore such approaches in future, to realize the full capability of ML for uncovering reconnection signatures for a variety of planetary magnetospheres. Datasets observing various planetary magnetospheres is abundant, e.g. MESSENGER (Solomon et al., 2001) at Mercury, and Galileo (Young, 1998)/Juno (Bagenal et al., 2017) at Jupiter, however, exploration of these datasets has only been partially completed by the wider community. This insufficient exploration is partly due to the required time to manually investigate the datasets and the lack of manpower available. ML infrastructure, of the kind discussed in this paper, will enable the processing and full exploration of these large datasets with minimal required human intervention. Furthermore, ML identification methods allow the extrapolation of catalogs and allow for an investigation of more diverse events at different locations, and even make more accurate estimations of the mass budget of magnetospheres. As we rapidly approach a period of data flooding, developing tools to address this issue before it arises is essential for the future of planetary research (Azari et al., 2020).

DATA AVAILABILITY STATEMENT

The datasets presented in this study can be found in online repositories. The names of the repository/repositories and accession numbers can be found below: https://zenodo.org/record/3978252#.X0kgADV7nb0.

AUTHOR CONTRIBUTIONS

TG was responsible for development and application of machine learning methods to create a neural network reconnection classifier. CJ sourced datasets and applied physical insights into the model's creation. AS applied physical insights into the model's creation and laid groundwork for its creation. KY validated machine learning methods and applied insight into machine learning theory. SM validated machine learning methods and applied insight into machine learning theory. JV validated machine learning methods and applied physical insights into the model's creation.

FUNDING

TG's work is supported by the Science and Technology Facilities Council Opportunities Fund Grant ST/T002255/1. CJ's work at Southampton was supported by the STFC Ernest Rutherford Fellowship ST/L004399/1. AS was supported by STFC Consolidated Grant ST/S000240/1 and NERC Grant NE/P017150/1.

REFERENCES

Abadi, M., Agarwal, A., Barham, P., Brevdo, E., Chen, Z., Citro, C., et al. (2015). TensorFlow: large-scale machine learning on heterogeneous systems. Software available from tensorflow.org.

Arridge, C. S., André, N., Khurana, K. K., Russell, C. T., Cowley, S. W. H., Provan, G., et al. (2011). Periodic motion of saturn's nightside plasma sheet. *J. Geophys. Res.: Space Physics* 116. 14. doi:10.1029/2011JA016827

Azari, A. R., Biersteker, J. B., Dewey, R. M., Doran, G., Forsberg, E. J., Harris, C. D. K., et al. (2020). Integrating machine learning for planetary science: perspectives for the next decade. *White Paper Sub. Decad. Surv. Planet. Sci. Astrobiol.* 12, 2023–2032. doi:10.1787/9789264028586-en

Bagenal, F., Adriani, A., Allegrini, F., Bolton, S. J., Bonfond, B., Bunce, E. J., et al. (2017). Magnetospheric science objectives of the juno mission. *Space Sci. Rev.* 213, 219–287. doi:10.1007/s11214-014-0036-8

Bagenal, F., and Delamere, P. A. (2011). Flow of mass and energy in the magnetospheres of jupiter and saturn. *J. Geophys. Res.: Space Phys.* 116. doi:10.1029/2010JA016294

Buda, M., Maki, A., and Mazurowski, M. A. (2017). A systematic study of the class imbalance problem in convolutional neural networks. *Neural Netw.* 106, 249–259. doi:10.1016/j.neunet.2018.07.011

Buitinck, L., Louppe, G., Blondel, M., Pedregosa, F., Mueller, A., Grisel, O., et al. (2013). "API design for machine learning software: experiences from the scikit-learn project," in ECML PKDD workshop: languages for data mining and machine learning, 108–122.

Bunce, E. J., Cowley, S. W. H., Wright, D. M., Coates, A. J., Dougherty, M. K., Krupp, N., et al. (2005). *In situ* observations of a solar wind compression-induced hot plasma injection in saturn's tail. *Geophys. Res. Lett.* 32. 121–127. doi:10.1029/2005GL022888

Burkholder, B., Delamere, P. A., Ma, X., Thomsen, M. F., Wilson, R. J., and Bagenal, F. (2017). Local time asymmetry of saturn's magnetosheath flows. *Geophys. Res. Lett.* 44, 5877–5883. doi:10.1002/2017GL073031

Cowley, S. W. H., Nichols, J. D., and Jackman, C. M. (2015). Down-tail mass loss by plasmoids in jupiter's and saturn's magnetospheres. *J. Geophys. Res.: Space Phys.* 120, 6347–6356. doi:10.1002/2015JA021500

Delamere, P. A., Otto, A., Ma, X., Bagenal, F., and Wilson, R. J. (2015). Magnetic flux circulation in the rotationally driven giant magnetospheres. *J. Geophys. Res.* 120, 4229–4245. doi:10.1002/2015JA021036

Dougherty, M., Kellock, S., Southwood, D., Balogh, A., Smith, E., Tsurutani, B., et al. (2004). The cassini magnetic field investigation. *Space Sci. Rev.* 114, 331–383. doi:10.1007/s11214-004-1432-2

Dougherty, M. K., Khurana, K. K., Neubauer, F. M., Russell, C. T., Saur, J., Leisner, J. S., et al. (2006). Identification of a dynamic atmosphere at enceladus with the cassini magnetometer. *Science* 311, 1406–1409. doi:10.1126/science.1120985

Dungey, J. W. (1961). Interplanetary magnetic field and the auroral zones. *Phys. Rev. Lett.* 6, 47–48. doi:10.1103/PhysRevLett.6.47

Dungey, J. W. (1965). The length of the magnetospheric tail. *J. Geophys. Res.* 70, 1753. doi:10.1029/JZ070i007p01753

Fawaz, H. I., Forestier, G., Weber, J., Idoumghar, L., and Muller, P. (2018). Data augmentation using synthetic data for time series classification with deep residual networks. *Stud. Classif. Data Anal. Knowl. Org. Classif. Data Anal.* 7, 345–352. doi:10.1007/978-3-642-60126-2_43

Garton, T. M. (2020). *Machine learning identification of reconnection in cassini mag data programs*. Berlin: Springer. doi:10.5281/zenodo.3978252

Guo, R. L., Yao, Z. H., Wei, Y., Ray, L. C., Rae, I. J., Arridge, C. S., et al. (2018). Rotationally driven magnetic reconnection in saturn's dayside. *Nat. Astronom.* 2, 640–645. doi:10.1038/s41550-018-0461-9

Guo, X., Yin, Y., Dong, C., Yang, G., and Zhou, G. (2008). "On the class imbalance problem," in Fourth international conference on natural computation, ICNC '084. doi:10.1109/ICNC.2008.871

Heidke, P. (1926). Berechnung des erfolges und der güte der windstärkevorhersagen im sturmwarnungsdienst. *Geogr. Ann.* 8, 301–349. doi:10.1080/20014422.1926.11881138

Hill, T. W., Thomsen, M. F., Henderson, M. G., Tokar, R. L., Coates, A. J., McAndrews, H. J., et al. (2008). Plasmoids in saturn's magnetotail. *J. Geophys. Res.: Space Phys.* 113. 33–39. doi:10.1029/2007JA012626

Hones, J., E. W. (1977). Substorm processes in the magnetotail: comments on 'On hot tenuous plasmas, fireballs, and boundary layers in the Earth's magnetotail' by L. A. Frank, K. L. Ackerson, and R. P. Lepping. *J. Geophys. Res.* 82, 5633. doi:10.1029/JA082i035p05633

Huang, G.-B. (2003). Learning capability and storage capacity of two-hidden-layer feedforward networks. *IEEE Trans. Neural Netw.* 14, 274–281. doi:10.1109/TNN.2003.809401

Jackman, C. M., Achilleos, N., Cowley, S. W., Bunce, E. J., Radioti, A., Grodent, D., et al. (2013). Auroral counterpart of magnetic field dipolarizations in saturn's tail. *Planet. Space Sci.* 82-83, 34–42. doi:10.1016/j.pss.2013.03.010

Jackman, C. M., Arridge, C. S., McAndrews, H. J., Henderson, M. G., and Wilson, R. J. (2009). Northward field excursions in saturn's magnetotail and their relationship to magnetospheric periodicities. *Geophys. Res. Lett.* 36, 111–134. doi:10.1029/2009GL039149

Jackman, C. M., Russell, C. T., Southwood, D. J., Arridge, C. S., Achilleos, N., and Dougherty, M. K. (2007). Strong rapid dipolarizations in saturn's magnetotail: in situ evidence of reconnection. *Geophys. Res. Lett.* 34, 77–79. doi:10.1029/2007GL029764

Jackman, C. M., Slavin, J. A., and Cowley, S. W. H. (2011). Cassini observations of plasmoid structure and dynamics: implications for the role of magnetic reconnection in magnetospheric circulation at saturn. *J. Geophys. Res.: Space Phys.* 116, 43–49. doi:10.1029/2011JA016682

Jackman, C. M., Slavin, J. A., Kivelson, M. G., Southwood, D. J., Achilleos, N., Thomsen, M. F., et al. (2014). Saturn's dynamic magnetotail: a comprehensive magnetic field and plasma survey of plasmoids and traveling compression regions and their role in global magnetospheric dynamics. *J. Geophys. Res.: Space Phys.* 119, 5465–5494. doi:10.1002/2013JA019388

Jackman, C. M., Thomsen, M. F., Mitchell, D. G., Sergis, N., Arridge, C. S., Felici, M., et al. (2015). Field dipolarization in saturn's magnetotail with planetward ion flows and energetic particle flow bursts: evidence of quasi-steady reconnection. *J. Geophys. Res.: Space Phys.* 120, 3603–3617. doi:10.1002/2015JA020995

Johnson, J. M., and Khoshgoftaar, T. M. (2019). Survey on deep learning with class imbalance. *J. Big Data* 6, 27. doi:10.1186/s40537-019-0192-5

Kane, M., Mitchell, D. G., Carbary, J. F., Dialynas, K., Hill, M. E., and Krimigis, S. M. (2020). Convection in the magnetosphere of saturn during the cassini mission derived from mimi inca and chems measurements. *J. Geophys. Res.: Space Phys.* 125, e2019JA027534. doi:10.1029/2019JA027534

Khurana, K. K., Mitchell, D. G., Arridge, C. S., Dougherty, M. K., Russell, C. T., Paranicas, C., et al. (2009). Sources of rotational signals in saturn's magnetosphere. *J. Geophys. Res.: Space Phys.* 114, 24. doi:10.1029/2008JA013312

Ma, X., Delamere, P., Otto, A., and Burkholder, B. (2017). Plasma transport driven by the three-dimensional kelvin-helmholtz instability. *J. Geophys. Res.: Space Phys.* 122 (10382–10), 395. doi:10.1002/2017JA024394

Martin, C. J., and Arridge, C. S. (2017). Cassini observations of aperiodic waves on saturn's magnetodisc. *J. Geophys. Res.: Space Physics* 122, 8063–8077. doi:10.1002/2017JA024293

McAndrews, H., Thomsen, M., Arridge, C., Jackman, C., Wilson, R., Henderson, M., et al. (2009). Plasma in saturn's nightside magnetosphere and the implications for global circulation. *Planet. Space Sci.* 57, 1714–1722. doi:10.1016/j.pss.2009.03.003

Mikołajczyk, A., and Grochowski, M. (2018). Data augmentation for improving deep learning in image classification problem. *Curr. Bioinform.* 14, 117–122. doi:10.1109/IIPHDW.2018.8388338

Milan, S. E., Provan, G., and Hubert, B. (2007). Magnetic flux transport in the dungey cycle: a survey of dayside and nightside reconnection rates. *J. Geophys. Res.: Space Phys.* 112, 153. doi:10.1029/2006JA011642

Nakagawa, T., and Nishida, A. (1989). Southward magnetic field in the neutral sheet produced by wavy motions propagating in the dawn-dusk direction. *Geophys. Res. Lett.* 16, 1265–1268. doi:10.1029/GL016i011p01265

Neupane, B. R., Delamere, P. A., Wilson, R. J., and Ma, X. (2019). Quantifying mass and magnetic flux transport in saturn's magnetosphere. *J. Geophys. Res.: Space Phys.* 124, 1916–1926. doi:10.1029/2018JA026022

Ruhunusiri, S., Halekas, J. S., Espley, J. R., Eparvier, F., Brain, D., Mazelle, C., et al. (2018). An artificial neural network for inferring solar wind proxies at mars. *Geophys. Res. Lett.* 45 (10855–10), 865. doi:10.1029/2018GL079282

Ruhunusiri, S. (2018). Identification of plasma waves at saturn using convolutional neural networks. *IEEE Trans. Plasma Sci.* 46, 3090–3099. doi:10.1007/978-1-4899-7687-1_100342

Russell, C. T., Jackman, C. M., Wei, H. Y., Bertucci, C., and Dougherty, M. K. (2008). Titan's influence on saturnian substorm occurrence. *Geophys. Res. Lett.* 35. 121. doi:10.1029/2008GL034080

Simon, S., Wennmacher, A., Neubauer, F. M., Bertucci, C. L., Kriegel, H., Saur, J., et al. (2010). Titan's highly dynamic magnetic environment: a systematic survey of Cassini magnetometer observations from flybys TA-T62. *Planet. Space Sci.* 58, 1230–1251. doi:10.1016/j.pss.2010.04.021

Slavin, J. A., Smith, E. J., Tsurutani, B. T., Sibeck, D. G., Singer, H. J., Baker, D. N., et al. (1984). Substorm associated traveling compression regions in the distant tail: Isee-3 geotail observations. *Geophys. Res. Lett.* 11, 657–660. doi:10.1029/GL011i007p00657

Smith, A. W., Jackman, C. M., Thomsen, M. F., Lamy, L., and Sergis, N. (2018a). Multi-instrument investigation of the location of saturn's magnetotail x-line. *J. Geophys. Res.: Space Phys.* 123, 5494–5505. doi:10.1029/2018JA025532

Smith, A. W., Jackman, C. M., and Thomsen, M. F. (2016). Magnetic reconnection in saturn's magnetotail: a comprehensive magnetic field survey. *J. Geophys. Res. Space Physics* 121, 2984–3005. doi:10.1002/2015JA022005

Smith, A. W., Jackman, C. M., Thomsen, M. F., Sergis, N., Mitchell, D. G., and Roussos, E. (2018b). Dipolarization fronts with associated energized electrons in saturn's magnetotail. *J. Geophys. Res.: Space Phys.* 123, 2714–2735. doi:10.1002/2017JA024904

Solomon, S., McNutt, R., Gold, R., Acuña, M., Baker, D., Boynton, W., et al. (2001). The messenger mission to mercury: scientific objectives and implementation. *Planet. Space Sci.* 49, 1445–1465. doi:10.1016/S0032-0633(01)00085-X

Thomsen, M. F., Wilson, R. J., Tokar, R. L., Reisenfeld, D. B., and Jackman, C. M. (2013). Cassini/caps observations of duskside tail dynamics at saturn. *J. Geophys. Res.: Space Phys.* 118, 5767–5781. doi:10.1002/jgra.50552

Vasyliunas, V. M. (1983). *Plasma distribution and flow*. Cambridge: Cambridge Cambridge University Press, 395–453. doi:10.1017/CBO9780511564574.013

Waldmann, I. P., and Griffith, C. A. (2019). Mapping saturn using deep learning. *Nat. Astronom.* 3, 620–625. doi:10.1038/s41550-019-0753-8

Yao, Z. H., Grodent, D., Ray, L. C., Rae, I. J., Coates, A. J., Pu, Z. Y., et al. (2017). Two fundamentally different drivers of dipolarizations at saturn. *J. Geophys. Res.: Space Phys.* 122, 4348–4356. doi:10.1002/2017JA024060

Young, D. T., Berthelier, J. J., Blanc, M., Burch, J. L., Coates, A. J., Goldstein, R., et al. (2004). Cassini plasma spectrometer investigation. *Space Sci. Rev.* 114, 1–112. doi:10.1007/s11214-004-1406-4

Young, R. E. (1998). The galileo probe mission to jupiter: science overview. *J. Geophys. Res.: Plan* 103, 22775–22790. doi:10.1029/98JE01051

Conflict of Interest: The authors declare that the research was conducted in the absence of any commercial or financial relationships that could be construed as a potential conflict of interest.

Copyright © 2021 Garton, Jackman, Smith, Yeakel, Maloney and Vandegriff. This is an open-access article distributed under the terms of the Creative Commons Attribution License (CC BY). The use, distribution or reproduction in other forums is permitted, provided the original author(s) and the copyright owner(s) are credited and that the original publication in this journal is cited, in accordance with accepted academic practice. No use, distribution or reproduction is permitted which does not comply with these terms.

frontiers in Astronomy and Space Sciences

ORIGINAL RESEARCH
published: 09 June 2021
doi: 10.3389/fspas.2021.691000

Modeling and Prediction of Near-Earth Plasma Sheet Parameters Using the Rice Convection Model and the Recurrent Neural Network

Shishir Priyadarshi[1]*, *Jian Yang*[1]* and *Weiqin Sun*[1,2]

[1]Department of Earth and Space Sciences, Southern University of Science and Technology, Shenzhen, China, [2]School of Atmospheric Sciences, Sun Yat-Sen University, Zhuhai, China

Interaction between Earth's magnetotail and its inner magnetosphere plays an important role in the transport of mass and energy in the ionosphere–magnetosphere coupled system. A number of first-principles models are devoted to understanding the associated dynamics. However, running these models, including both magnetohydrodynamic models and kinetic drift models, can be computationally expensive when self-consistency and high spatial resolution are required. In this study, we exploit an approach of building a parallel statistical model, based on the long short-term memory (LSTM) type of recurrent neural network, to forecast the results of a first-principles model, called the Rice Convection Model (RCM). The RCM is used to simulate the transient injection events, in which the flux-tube entropy parameter, dawn-to-dusk electric field component, and cumulative magnetic flux transport are calculated in the central plasma sheet. These key parameters are then used as initial inputs for training the LSTM. Using the trained LSTM multivariate parameters, we are able to forecast the plasma sheet parameters beyond the training time for several tens of minutes that are found to be consistent with the subsequent RCM simulation results. Our tests indicate that the recurrent neural network technique can be efficiently used for forecasting numerical simulations of magnetospheric models. The potential to apply this approach to other models is also discussed.

Keywords: machine learning, substorm injections, numerical simulation, plasma sheet, M-I coupling

OPEN ACCESS

Edited by:
Jean-Francois Ripoll,
CEA DAM Île-de-France, France

Reviewed by:
Alexei V. Dmitriev,
Lomonosov Moscow State University, Russia
Binbin Tang,
National Space Science Center (CAS), China

***Correspondence:**
Jian Yang
yangj36@sustech.edu.cn
Shishir Priyadarshi
priyadarshi@sustech.edu.cn

Specialty section:
This article was submitted to Space Physics, a section of the journal Frontiers in Astronomy and Space Sciences

Received: *05 April 2021*
Accepted: *17 May 2021*
Published: *09 June 2021*

Citation:
Priyadarshi S, Yang J and Sun W (2021) Modeling and Prediction of Near-Earth Plasma Sheet Parameters Using the Rice Convection Model and the Recurrent Neural Network. Front. Astron. Space Sci. 8:691000. doi: 10.3389/fspas.2021.691000

KEY POINTS

1. Simulation results of the RCM (a physics-based model) are used as inputs for training the LSTM-based RNN model for the forecast of the longer duration.
2. The approach is applied to multiple simulations of idealized low-entropy bubble injection events.
3. There is a great consistency between the LSTM-based forecast and the RCM results beyond the training time.

INTRODUCTION

Data in Earth's magnetosphere are less available than in other regions (e.g., the ionosphere, the lower atmosphere, and ground-based observations of the upper atmosphere) based on their

spatial and temporal continuity. Therefore, for developing a machine learning model, the output from a physics-based model can serve as an input asset due to the continuous temporal/spatial availability of their outputs. Besides, it is always good to train a machine learning model using a known and stable environment (e.g., an existing model in our case). This allows the machine learning model to learn the time series quickly and understand the underlying relationship among the time series of several physics-based models' output parameters.

Previous works have adapted artificial neural networks (ANNs) to study space weather. For example, Koon and Gorney (1991) used Los Alamos National Laboratory (LANL) particle data for the prediction of daily averaged electrons with an energy of >3 MeV. Stringer et al. (1996) used ANNs on GOES-7 data for nowcasting 1-h geosynchronous orbit electron flux at energies of 3–5 MeV. The work of Stringer et al. (1996) was extended to one-day forecast by Ukhorskiy et al. (2004) and Kitamura et al. (2011). A relativistic electron flux at a geosynchronous orbit––forecasting neural network (NN) model was developed by Ling et al. (2010). They used historical electron flux values and daily summed values of the planetary K_p index over two neurons, and their neural network model showed better prediction than the Relativistic Electron Forecast Model (REFM) developed by Baker et al. (1990). The NNs were also used on solar wind inputs to predict geosynchronous electron distributions over wide energy ranges and for a number of time resolutions (Shin et al., 2016; Wei et al., 2018). Wiltberger et al. (2017) used machine learning analysis of the magnetosphere–ionosphere field-aligned current (FAC) patterns and found out that the ratio of Region 1 (R1) to Region 2 (R2) current decreases as the simulation resolution increases. This application of machine learning to the FAC analysis helped establish a better agreement in the simulation results than the Weimer 2005 model (Weimer, 2005). They used a Python-based open source Scikit-Learn algorithm package developed by Pedregosa et al. (2011), which allows supervised and unsupervised machine learning algorithms. Other space weather–related research that uses machine learning techniques has also been reviewed by Camporeale (2019). Recently, Pires de Lima et al. (2020) used a convolution neural network (CNN) to build a predictive model for the MeV electrons inside Earth's outer radiation belt. The model of Pires de Lima and Lin, known as PreMevE 2.0, is a supervised machine learning model, and it can forecast the onset of MeV electron events in 2 days. The Pires de Lima and Lin model uses electron data observed by the particle instruments of RBSP spacecraft, one geo-satellite of the Los Alamos National Laboratory (LANL), and one NOAA Polar Operational Environmental Satellite (POES) for the time duration from February 2013 to August 2016.

A recurrent neural network (RNN) is a state-of-the-art approach that combines several algorithms to enable them to learn the time series of datasets (Connor et al., 1994; Graves et al., 2013). However, due to the limited memory, the error becomes larger when the longer (e.g., more than a hundred data time steps) training datasets in the RNN are used. The wait function, which is a statistical and analytical tool used to characterize input parameters' influence on the prediction, also becomes erroneous with time (Graves and Schmidhuber, 2005). On the other hand, a long short-term memory (LSTM)–based neural network is a kind of recurrent neural network which can memorize time series datasets with very long duration and also forget them if some part of the dataset is not necessary. The LSTM uses the sigmoid function for keeping things in its memory and TANH functions if the LSTM states decide to remove the memory after finding it useless for future time series forecasting (Eck and Schmidhuber, 2002). The sigmoid functions are best for modeling the physical processes that start with the small beginnings but attain a high saturated value over time as the specific models often fail to reproduce such processes (Gers et al., 2000).

LSTM has already been used in robot control, speech recognition, rhythm learning, music composition, grammar learning, handwriting recognition, human language recognition, sign language translation, and many more scientific and nonscientific disciplines. The LSTM-based models can be made scientific by sensibly choosing the input datasets and the training and testing periods of time. To do this, one has to first think about what are the most suitable inputs and in what order they should be fed in the LSTM algorithm to bring satisfactory outputs. Once the inputs and the training/testing periods are defined, the final LSTM model can be fitted to the entire dataset. The magnetosphere is a region where only sparse numbers of *in situ* measurements exist so far. A machine learning model can prove them to be an asset to better understand, analyze, and forecast the evolution and dynamics of magnetosphere physics during different kinds of space weather events or simulations. First-principles models reflect purely physics-based laws, and such models are generally represented by mathematical equations. They can be effectively converted into a machine learning statistical model by creating a multivariate time series of the variables used in the mathematical equations of the parameters we are going to model.

The phenomenon we will study in this article is the earthward injection of plasma sheet bubbles. A plasma sheet bubble has a lower flux-tube entropy parameter, $PV^{5/3}$, than its neighbors (Pontius and Wolf, 1990). Here, P is the plasma pressure and $V = \int ds/B$ is the flux-tube volume per unit magnetic flux. Dependent on their observational signatures, they are also called earthward flow channels or bursty bulk flows (BBFs) (Angelopoulos et al., 1992). They are found to be associated with enhanced energetic particle flux near the geosynchronous orbit (McIlwain 1972, 1974; Yang et al., 2010a, Yang et al., 2010b; 2011 and references therein). These earthward flows are associated with the dipolarized northward magnetic field B_z, and they also lead to pulses of the enhanced dawn-to-dusk electric field component E_y (Nakamura et al., 2002; Runov et al., 2009; Liu et al., 2013; Khotyaintsev et al., 2011; Birn et al., 2019). As a consequence,

the magnetic flux transport is earthward with a positive E_y. Here, the cumulative magnetic flux transport (CMFT) is defined (Birn et al., 2019) as follows:

$$\phi = \int_0^t Ey \ dt. \tag{1}$$

The Rice Convection Model (RCM) is a first-principles physics-based model of the inner magnetosphere and the plasma sheet which can simulate drifts of different isotropic particles using the many-fluid formalism (Toffoletto et al., 2003 and references therein). It has been widely used to simulate the bubble injections and flow channels associated with substorm activities (Zhang et al., 2008; Yang et al., 2011; Lemon et al., 2004). Although the computational speed has been greatly improved by using Message Passing Interface (MPI) parallel programming in the RCM and the coupled MHD code (Yang et al., 2019; Silin et al., 2013), it is still computation-heavy. On the other hand, LSTM-based RNN models learn from the time series and multivariate inputs, and the underlying relationship between different variables can make the LSTM learn the relative simultaneous changes in the different input variables with time and it boosts the LSTM forecast capabilities. Therefore, combining the RCM with the LSTM technique can be a nice attempt at converting a first-principles physics-based model into a statistical model that abides by scientific laws used in the RCM.

In the next section, we will discuss the methodology, the boundary condition in the RCM, and our RNN modeling approach. In the third section, we will validate RNN results by comparing them with the RCM outputs. A detailed error analysis is discussed in the "*LSTM Forecast Error Analysis*" section for all the three runs by dividing the entire simulation region into four sectors. The last section will conclude the presented study and discuss our future plans for developing the statistical model using the well-established magnetospheric models.

METHODOLOGY AND MODEL SETUP

Setup of RCM Simulations

In this study, we performed three different RCM runs. The initial conditions are set the same way as in Yang et al. (2011), in which the plasma distribution and the magnetic field configuration are specified according to empirical models driven by idealized solar wind parameters. In all the RCM runs used in this study, the solar wind condition is assumed to be steady; IMF B_z is −5 nT and Bx and By are assumed to be zero. The solar wind velocity Vx = −400 km/s, and the other components are assumed to be zero. The solar wind proton number density is 5 cm^{-3}, and the solar dynamic pressure is 1.34 nPa. The IRI-90 (International Reference Ionosphere) empirical ionospheric model plus conductance enhancement due to the electron precipitation is used to calculate the ionospheric conductance. An ellipse is set in the equatorial plane as the outer boundary of the RCM simulation region. The total potential drop across the RCM boundary is set to 30 kV (Yang et al., 2015; Yang et al., 2016).

Boundary Conditions for a Single Bubble Injection

A bubble is launched from the tailward boundary centered at X = −18.0 R_e and Y = 0 R_e. The entropy parameter $PV^{5/3}$ is uniformly reduced to 2% in 10 min between 23.5 and 0.5 h MLT. The magnetic local time noon 12 MLT corresponds to Φ = 0 radians; 18 MLT, 0 MLT, and 6 MLT correspond to Φ = $\pi/2$, π, and 1.5π radians, respectively. The boundary condition for the flux-tube content η_s^e is written as follows:

$$\eta_s^e(\lambda s) = \begin{cases} \eta_s^g(\lambda s), & (\Phi_E < \Phi \text{ or } \Phi_W > \Phi, \\ 0.02\ \eta_s^g(\lambda s), & (\Phi_W \le \Phi \le \Phi_E \text{ and } 1 \le T \le 10) \\ \eta_s^g(\lambda s), & (T \ge 10) \end{cases} \text{and } 1 \le T \le 10).$$

(2)

Here, η_s^g is the plasma flux-tube content in the initial (background) condition; the single bubble simulation starts at zero minutes, and we do not include the growth phase in our run; and λs is the energy invariant ($\lambda s = E_S V^{2/3}$, and E_S is the particle

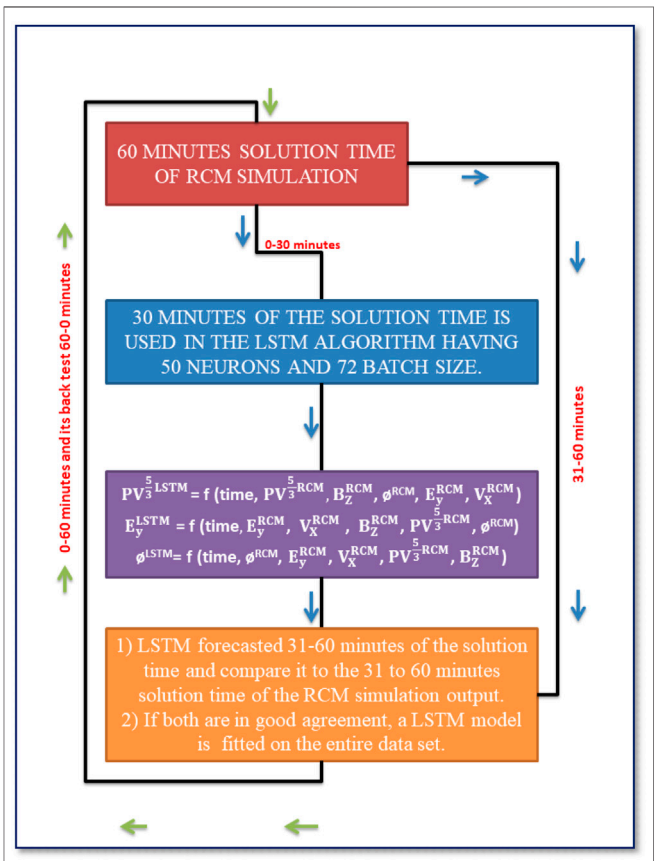


FIGURE 1 | Scheme for RNN-based LSTM modeling of cumulative magnetic flux (CMFT) ϕ in Wb/R_e; dawn-to-dusk electric field E_y in mV/m; and entropy parameter $PV^{5/3}$ in nPa $[R_e/nT]^{5/3}$ using the first 0–30 min of the RCM simulation as inputs.

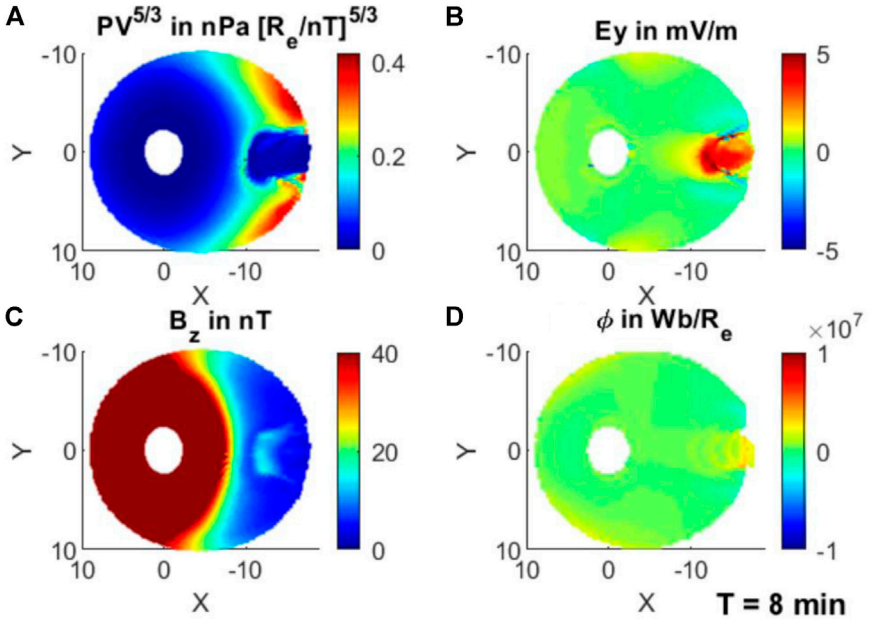


FIGURE 2 | Single bubble run at $T = 8$ min; **(A)** entropy parameter $PV^{5/3}$ in nPa $[R_e/nT]^{5/3}$; **(B)** dawn-to-dusk component of the electric field E_y in mV/m; **(C)** B_Z in nT; and **(D)** cumulative magnetic flux transport ϕ in Wb/R_e. X and Y are in Earth's radii (R_e) units. The Sun is to the left.

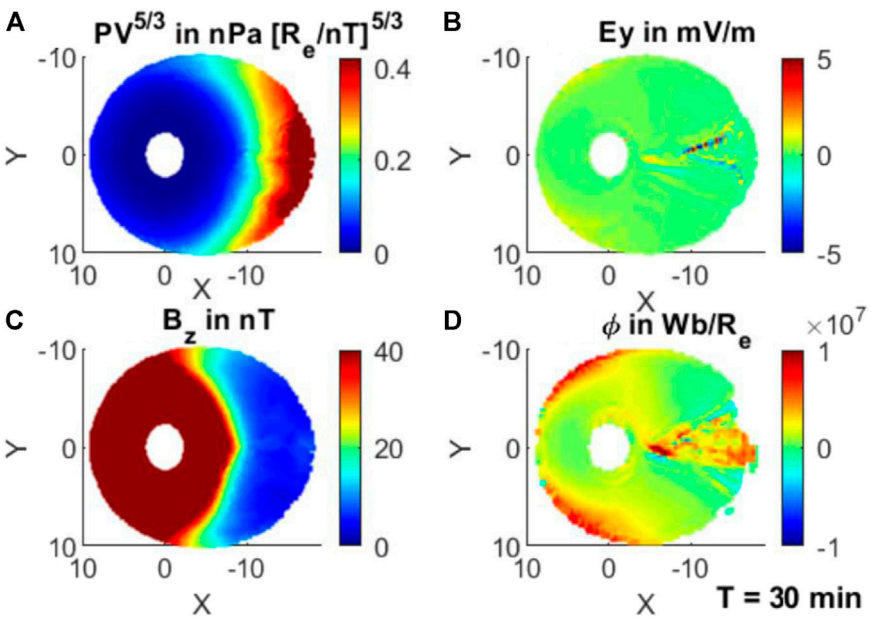


FIGURE 3 | Single bubble run at $T = 30$ min; **(A)** entropy parameter $PV^{5/3}$ in nPa $[R_e/nT]^{5/3}$; **(B)** dawn-to-dusk component of the electric field E_y in mV/m; **(C)** B_Z in nT; and **(D)** cumulative magnetic flux transport ϕ in Wb/R_e.

kinetic energy). The "T" in **Eq. 2** is the simulation solution time in minutes. The westward boundary of the bubble $\Phi_W = 11.5/12\ \pi$, and the eastward boundary of the bubble $\Phi_E = 12.5/12\ \pi$.

Boundary Conditions for a Single Flow Channel

In this run, the depletion in $PV^{5/3}$ is sustained until $T = 59$ min. The flow channel is centered at midnight with a width of 0.5 h in

local time, that is, from $\Phi_W = 11.75/12\ \pi$ to $\Phi_E = 12.25/12\ \pi$. The boundary condition for the flux-tube content η_s^e is written as follows:

$$\eta_s^e(\lambda s) = \begin{cases} \eta_s^g(\lambda s), & (\Phi_E < \Phi \text{ or } \Phi_W > \Phi, \text{ and } T \le 1) \\ 0.3\eta_s^g(\lambda s), & (\Phi_W \le \Phi \le \Phi_E, \ 1 \le T \le 59) \\ \eta_s^g(\lambda s), & (T \ge 59) \end{cases}. \tag{3}$$

Boundary Conditions for Three Flow Channels

Out of the three flows, one flow is centered at midnight with a width of 0.5 h in local time, that is, from $\Phi_W = 11.75/12\ \pi$ to $\Phi_E = 12.25/12\ \pi$, and the other two are at $\Phi_W = 7/9\ \pi$ to $\Phi_E = 5/6\ \pi$ and $\Phi_W = 7/6\ \pi$ to $\Phi_E = 11/9\ \pi$. The flux-tube content η_s^e is like that in **Eq. 3**.

We run the RCM simulation for 60 min. Out of several output parameters, we have used the entropy parameter, dawn-to-dusk electric field component, and cumulative magnetic flux for the presented LSTM modeling of the three plasma sheet parameters. The 1-h RCM simulations output these parameters every minute.

LSTM–RNN–Based Modeling

We use Python's Keras (https://keras.io/) deep learning library to prepare and fit the LSTM forecast based on the RCM's outputs. To train the LSTM, 50 neurons are used in the first hidden layer and one neuron is used for the output layer. After several experiments, we found that 30 training epochs and 72 batch sizes are good enough for the internal state of our LSTM model. We have developed three independent LSTM models for $PV^{5/3}$, *Ey*, and cumulative magnetic flux ϕ. We cannot model the magnetic field in the RCM-MHD code using LSTM, as for now, it is hard to include additional constraint to the LSTM to ensure the divergence-free nature of the magnetic field. On the other hand, it is challenging to include some additional constraints in the LSTM to make it satisfy the MHD force balance equation for B_z and V_x. Due to these issues, we decided to model only $PV^{5/3}$, E_y, and ϕ. We use simulation time for indexing the time series data, and we use the multivariate LSTM to train the RCM boundary condition–dependent machine learning model about the time series and the underlying relationship of the different input parameters used in our algorithm. All RCM and LSTM variables in the following equations are in two dimensions (i.e., in X and Y coordinates, which are in R_e units).

$$\mathbf{PV}^{\frac{5}{3}\,\mathbf{LSTM}} = f\left(\text{time},\ \mathbf{PV}^{\frac{5}{3}\mathbf{RCM}},\ \mathbf{B_Z^{RCM}},\ \phi^{\mathrm{RCM}},\ \mathbf{E_y^{RCM}},\ \mathbf{V_x^{RCM}}\right), \tag{4}$$

$$\mathbf{E_y^{LSTM}} = f\left(\text{time},\ \mathbf{E_y^{RCM}},\ \mathbf{V_x^{RCM}},\ \mathbf{B_Z^{RCM}},\ \mathbf{PV}^{\frac{5}{3}\mathbf{RCM}},\ \phi^{\mathrm{RCM}}\right), \tag{5}$$

$$\phi^{\mathrm{LSTM}} = f\left(\text{time},\ \phi^{\mathrm{RCM}},\ \mathbf{E_y^{RCM}},\ \mathbf{V_x^{RCM}},\ \mathbf{PV}^{\frac{5}{3}\mathbf{RCM}},\ \mathbf{B_Z^{RCM}}\right). \tag{6}$$

The above input datasets are the best combination of the input variables in terms of their order in the given function, as we get the minimal root mean square error (RMSE) and minimal training and test loss between the RCM and the LSTM for these input combinations. From the left to the right in the RHS of each equation, the weight of the variable gradually decreases.

Figure 1 shows the scheme of our LSTM model. This scheme demonstrates that we have 61 steps (0–60 min) of RCM simulation, out of which we use 0–30 min of simulation to train three independent multivariate time series LSTM models. Using these models, we forecast 31–60 min of the RCM simulation, and then we compare the LSTM forecast with the

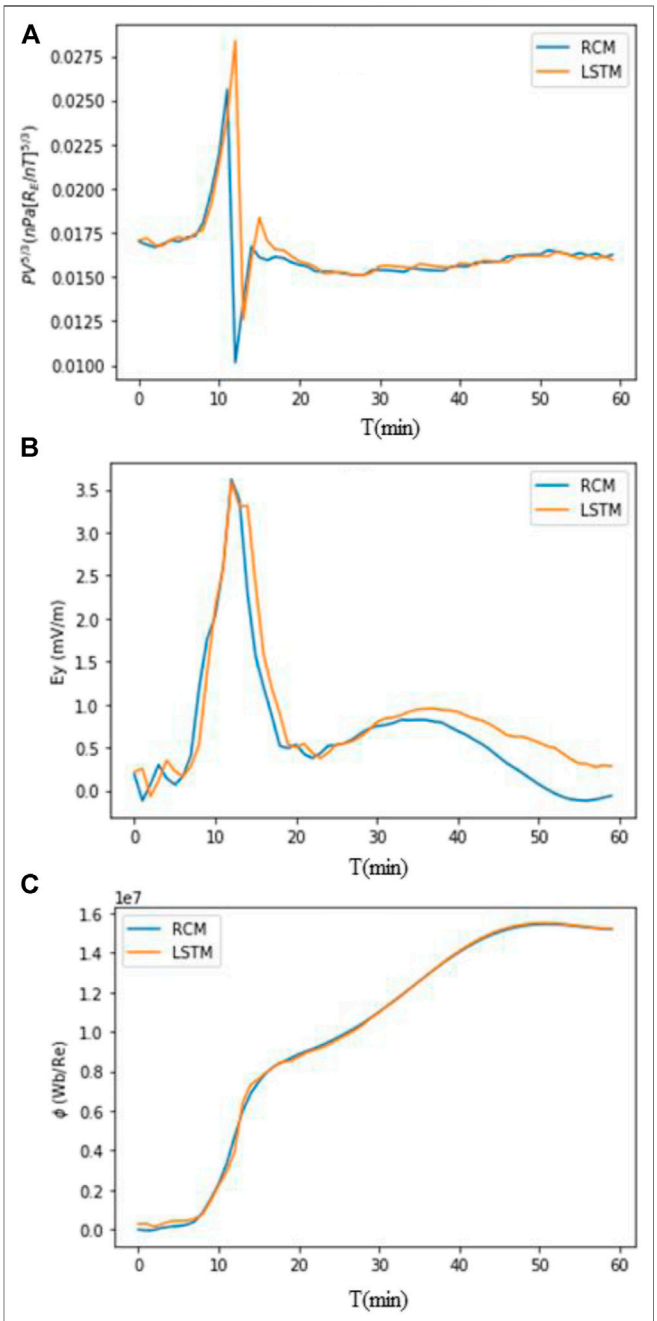


FIGURE 4 | Single-point comparison of the RCM single bubble run with the LSTM-based RNN model at X = −9.9 and Y = −1.1; **(A)** $PV^{5/3}$ in nPa $[R_e/nT]^{5/3}$; **(B)** E_y in mV/m; and **(C)** ϕ in Wb/R_e.

31–60 min of RCM simulation during three different runs. If there is a good agreement between the LSTM forecast and the RCM simulation for 31–60 min of the solution time, we fit the same model for the entire data length of the time series, that is, from 0 to 60 min of solution time. Using this LSTM model, we have forecasted the entire series. As a final check after the model fitting, we see if the final LSTM forecast is ±10% (in our case) of the RCM simulation, in which case the LSTM forecast meets our expectations, and we can forecast the entire RCM runs' data time series. Although the RCM simulation is in 2D (X and Y both are in the unit of Earth radii–R_e) coordinates, we do not use the X and Y coordinates as an input parameter in our LSTM model. The LSTM model for the presented three parameters is represented by **Eqs 4–6**, and it is also presented as a scheme diagram in **Figure 1**. The order of input parameters for forecasting different inner magnetosphere and plasma sheet variables will be according to their modeling in **Eqs 4–6**.

Model Validation

In this section, we will use an example of the single bubble run to demonstrate the consistency between the RCM simulation results and the LSTM forecast at a given location.

Figure 2 shows the RCM simulation results at $T = 8$ min of the single bubble event. **Figure 2A** shows a single low-entropy bubble centered at the midnight region of the plasma sheet. At the same time, E_y is significantly enhanced (**Figure 2B**), which is around 1 mV/m at the edge of the bubble, and it has a peak value of >2 mV/m inside the bubble. The northward component of the magnetic field B_z is enhanced to ~20 nT (**Figure 2C**) at the leading head of the bubble, and the cumulative magnetic flux ϕ (**Figure 2D**) shows enhancement with respect to the surrounding background.

Figure 3 shows the RCM simulation of the same event at the solution time $T = 30$ min, where $PV^{5/3}$ on the tailward boundary is already recovered to the value prior to the injection. $PV^{5/3}$ increases tailward. The most significant enhancement is ϕ, and this enhancement is aligned with the direction of the launch of the bubble and its vicinity where the ϕ is increasing with time. In summary, this single bubble simulation shows features of typical injections, which can cause abrupt changes in the magnetotail parameters.

Using **Eqs 4**, **5** and **6**, we have developed three independent LSTM-based RNN models for ϕ, E_y, and $PV^{5/3}$. To perform this action, we trained our LSTM RNN model with the first 30 min of

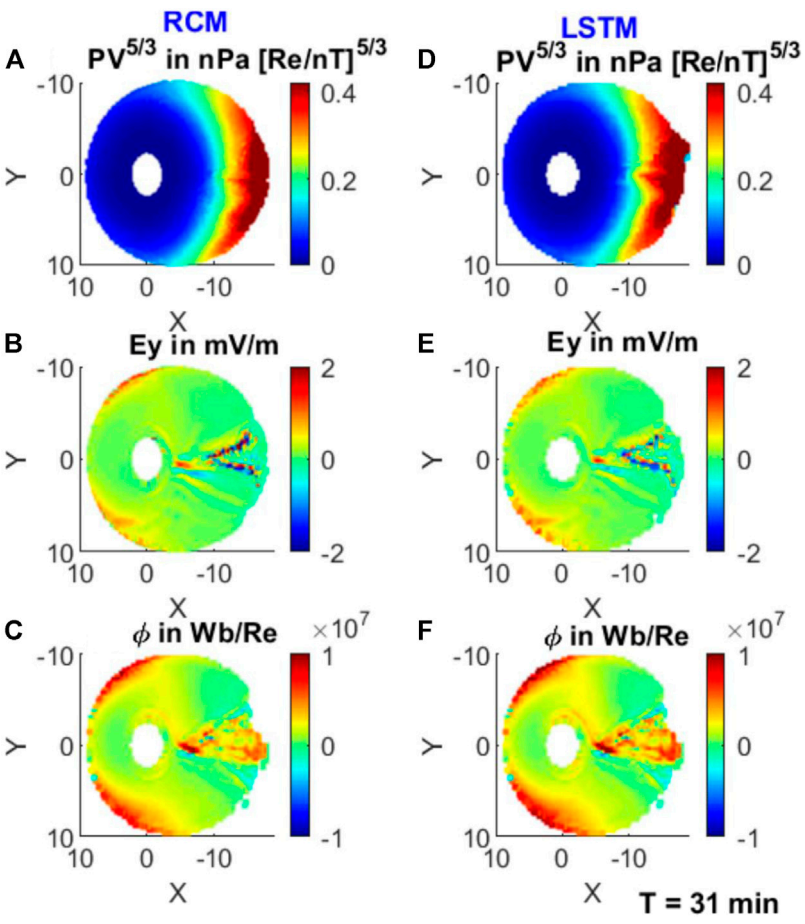


FIGURE 5 | Comparison of the RCM single bubble injection run **(left)** with the LSTM forecast **(right)**. From top to bottom are $PV^{5/3}$, E_y, and ϕ at $T = 31$ min.

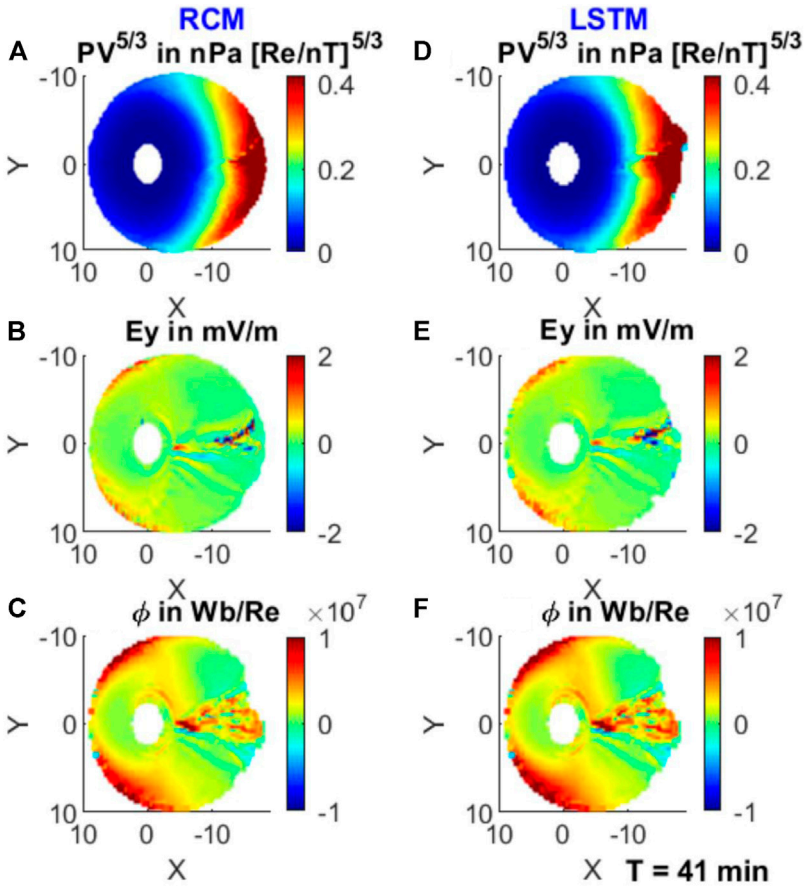


FIGURE 6 | Similar to **Figure 5**, but for T = 41 min.

the RCM simulation. The trained LSTM is used to reproduce the 60-min single bubble injection. Now, we will compare the entire 60 min between the RCM and the LSTM results. **Figure 4** shows the comparison of the single bubble RCM simulation (blue line) to the LSTM forecast (orange line) for the single point at X = −9.9 R_e and Y = −1.1 R_e. A satisfactory agreement is obtained between the model and the forecast for the ϕ (**Figure 4C**), which demonstrates the LSTM caliber in learning from the multivariate time series input data (which is the first 30 min of the RCM single bubble simulation output in our case). Following **Eq. 6**, the LSTM model for E_y learned the time series using the first 30 min of the RCM simulation outputs in the order E_y followed by V_X, B_Z, $PV^{5/3}$, and ϕ, respectively. The variations in the RCM and the LSTM only differ slightly. The entropy parameter $PV^{5/3}$ (**Figure 4A**) obtained from the RCM and the LSTM is in good agreement as well. This location was inside the bubble, so it is reflecting the injection of the bubble for the first 20 min. Minutes before the bubble arrives, $PV^{5/3}$ increases; then, the bubble arrival causes a sudden enhancement in the E_y and a sharp reduction in the $PV^{5/3}$. The CMFT ϕ with a little hump between 15 and 20 min keeps on increasing. All these features are consistent with typical features of bubble injection (Yang et al., 2011). After this validation in **Figure 4**, in the next section, we will compare the 2D maps of the RCM and the LSTM forecast at three different solution times.

In general, CMFT shows a better match between the LSTM and the RCM simulation; however, there are some tiny timescale deviations between the LSTM and the RCM for E_y and $PV^{5/3}$. In all the solution times presented in this section, we see that the CMFT is the only parameter that steadily grows along the bubble propagation path with time. The LSTM-based algorithms have minimal errors while learning the time series trends of the parameters which start from a small or zero numerical value and tend to achieve a high numerical value with time (Eck and Schmidhuber, 2002).

RESULTS

In this section, we will compare the LSTM forecast with the RCM single bubble simulation in the entire 2-D equatorial plane for all three simulations, focusing on the latter 30 min.

Figure 5 shows the single bubble injection run for T = 31 min. At this time, the bubble injection has already been completed in the plasma sheet, although variations in $PV^{5/3}$ (**Figure 5A**) and E_y (**Figure 5B**) are still visible along the injection path. **Figure 5C**

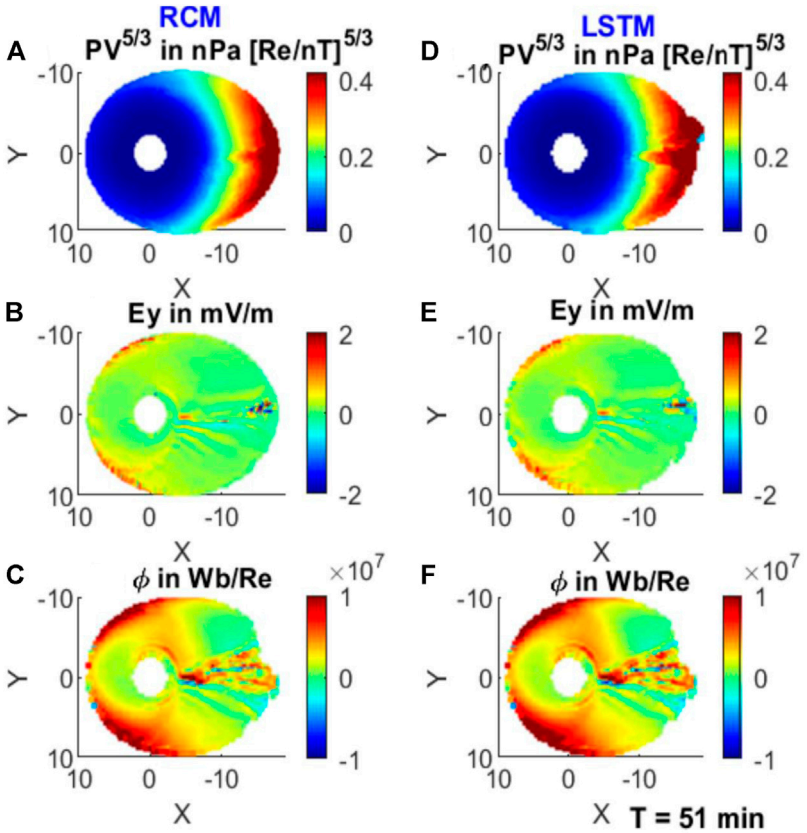


FIGURE 7 | Similar to **Figure 5**, but for T = 51 min.

shows a significant enhancement in the CMFT in yellow-red color from X = −5 to X = −16 R_e. The LSTM modeling reproduces the distribution of these three key parameters very well, even for the small-scale fluctuations. In order to check the forecast and the quality of prediction, we also compare the RCM and the LSTM model at different solution times to check if the LSTM forecast is updating and able to track the changes that are evolving in the RCM simulation with time. **Figures 6**, **7** compare the two modeling results, 11 and 21 min after the training solution time, respectively. The LSTM forecasts reasonably resemble the RCM simulation. It can be seen that the residual fluctuations in the electric field E_y and the associated structures in the CMFT ϕ can also be reproduced in the LSTM model.

Furthermore, we would like to compare the LSTM forecast with the RCM results at the end of the simulation time. The LSTM model has used part of the RCM simulation as an input; therefore, the LSTM forecast performance must be checked beyond the 30 min training solution time and up to the end of the RCM simulation. Comparison of the end solution time of the single bubble RCM simulation to the LSTM forecast will boost the confidence of the LSTM-based RNN model for its further development and extensive use in parallel to the RCM simulation. Similar to previous times, the LSTM forecast is very consistent with the RCM results, as shown in **Figure 8**.

Similar to the above case, we have applied the same approach to predict the RCM simulation results for the single-flow-channel run and the three-flow-channel run. Again, we have trained the LSTM model for the first 30 min and forecasted the next 30 min. **Figures 9A–D** and **Figures 9E–H** are similar to **Figure 2** and **Figure 3**. This figure compares the single flow channel and the three flow channels at T = 7 min. In **Figures 8A–D**, the changes in the modeled parameters appear at one point near the magnetic midnight in the equatorial plane. However, for the three flow channels (**Figures 9E–H**), the changes related to the launch of the three flow channels are present at the three points, and it is consistent in all four modeled parameters. This figure is also useful as it is reproducing the RCM simulation for the two different cases whose simulation time is within the boundary condition for both the runs.

As discussed earlier, for the single bubble run, the LSTM and the forecast have to be compared at different times for the single-flow-channel and three-flow-channel runs. **Figures 10**, **11** compare the four RCM parameters as compared in **Figures 5–8**. But this time, we compared the $PV^{5/3}$ at T = 32 min, E_y at T = 41 min, and CMFT at T = 49 min. The inputs provided within the simulation boundary conditions triggered LSTM

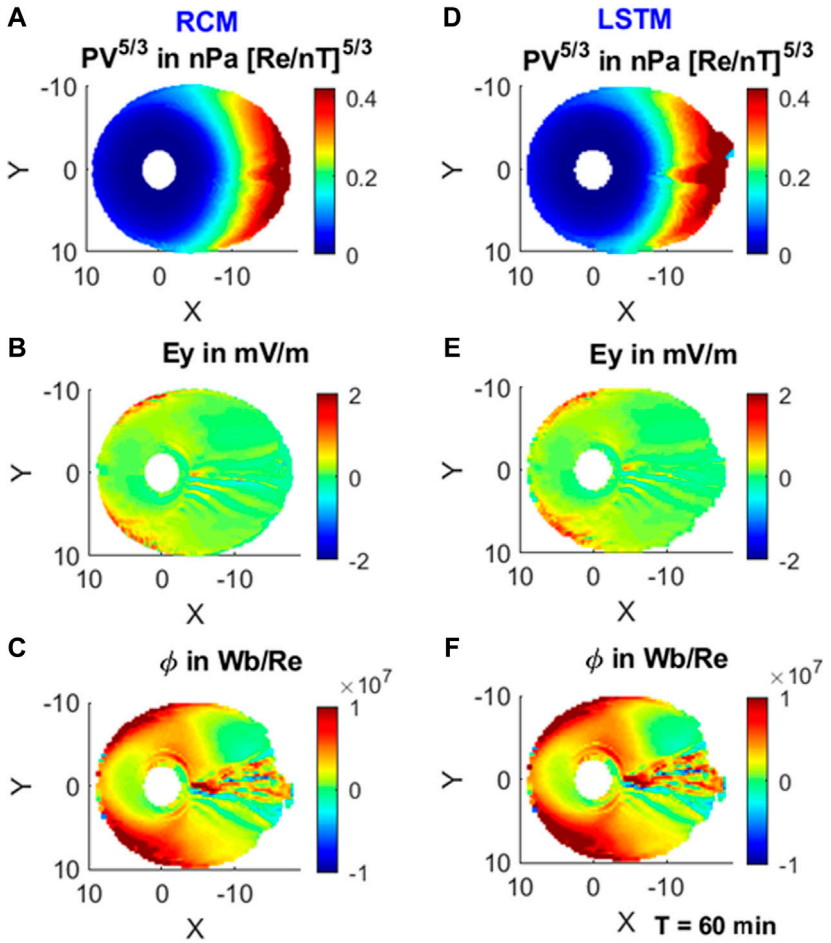


FIGURE 8 | Similar to **Figure 5**, but for T = 60 min.

fast learning of the correlation between different parameters and the degree and order of their mutual variance. We also train the LSTM model a little beyond the boundary condition of the LSTM, which allows the forget gate to classify the frequency of spatial and temporal vanishing gradients among the input parameters in the time series. LSTM forecasts were fully replicating the changes in the modeled parameters at and around the flow channel existence regions, at the boundary layer and near the geosynchronous orbit. In all the three simulation times and the runs presented in the study, there is a good agreement between the RCM simulation and the LSTM forecast for the three modeled parameters. These comparative pieces of evidence indicate that the LSTM is a strong data learning tool when it comes to learning large time series multivariate data trends, in particular when the variables in the data trends are related to each other by well-defined physics. LSTM's supervised learning algorithm makes it capable of extracting the degree of underlying correlation among many variables of a multiparameter data series through clustering, dimensionality reduction, structured prediction, and reinforcement learning.

LSTM FORECAST ERROR ANALYSIS

To check and quantify the error in the LSTM prediction of the RCM simulations during three different runs, we have calculated the correlation coefficient (Corr), which is used to study the statistical relationship between two parameters: the mean absolute error (MAE), which is an arithmetic average of the absolute error, and the mean squared error or mean squared deviation (MSE), which is the mean of the squares of the errors and is used for checking the quality of a procedure or method to predict an observed/simulated quantity (Chai and Draxler, 2014). The root mean square error (RMSE) is widely used to measure the difference between the predicted or estimated value, using a model or an estimator with respect to the observed or simulated value. The RMSE is the square root of the second sample moment of the difference between predicated and observed/simulated values or the quadratic mean of these differences (Chai and Draxler, 2014 and references therein). We calculated the Corr, MAE, MSE, and RMSE for the 30–60 min of the RCM simulation and the LSTM forecast all through the three simulations presented. We have divided the space/time into four sectors using the magnetic local time (MLT) range. The four sectors

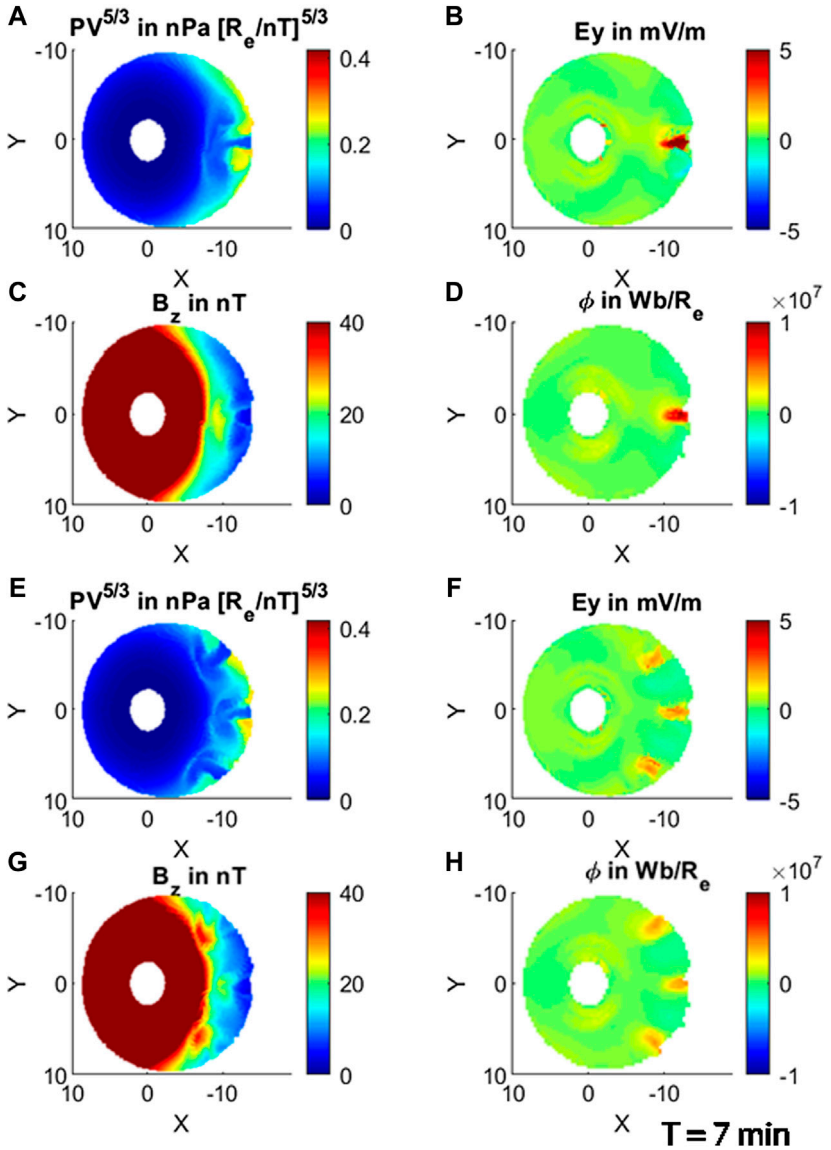


FIGURE 9 | Similar to **Figure 2** or **Figure 3**, from **A–D** is for the single flow channel and **E–H** is for the three flow channels at T = 7 min.

are magnetic dawn (03:00–09:00 MLT), magnetic noon (09:00–15:00 MLT), magnetic dusk (15:00–21:00 MLT), and magnetic midnight (21:00–03:00 MLT). **Table 1** shows the calculated error for the single bubble run. Similarly, **Tables 2**, **3** show the Corr, MAE, MSE, and RMSE for the 30–60 min for the single-flow-channel run and the three-flow-channel run.

The Corr for all the runs and for all the parameters is more than 0.80, which indicates that the LSTM forecast is in a good statistical coherence to the RSM simulations. The Corr for the CMFT is comparatively high as it is overall positive, and it has an increasing trend from a very low value, which makes it easier for LSTM to learn and reproduce the variation trend as compared to the E_y and $PV^{5/3}$. The correlation coefficient is close to 1, which also indicates the linear statistical relationship between the LSTM forecast and the RCM simulation.

RMSE and MAE are two variables used to measure the accuracy between the two continuous variables, and RMSE and MAE can vary between 0 and ∞. The MAE uses the absolute difference between the observation and prediction. The numerical value of the MAE and the RMSE is considered well for a prediction if it is close to zero. The MAE is highly dependent on the magnitude of the two continuous variables for which the MAE is calculated. The RMSE uses the quadratic scoring rule, and it also measures the error. Both the MAE and the RMSE measure the average model prediction error regardless of considering the direction of prediction. The RMSE and MAE are always in the unit of the predicted/observed variable. If we compare the MAE and RMSE values for E_y, $PV^{5/3}$, and ϕ, they seem to be in coherence with these three plasma sheet parameters.

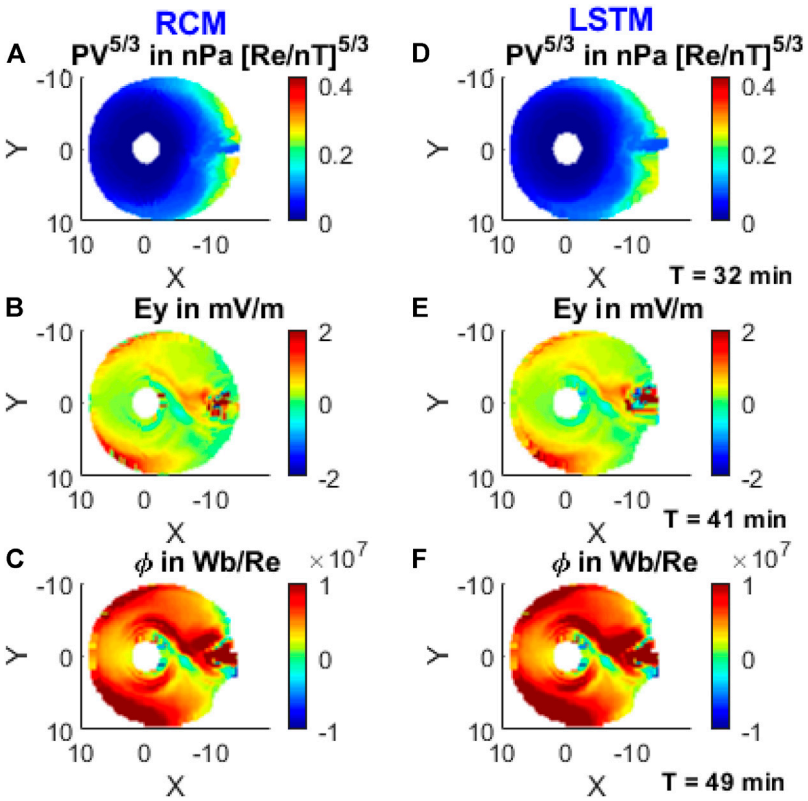


FIGURE 10 | From top to bottom are comparison of the RCM and LSTM forecasts during the single-flow-channel run for $PV^{5/3}$ at $T = 32$ min, E_y at $T = 41$ min, and ϕ at $T = 49$ min.

RMSE values are generally higher than those of the MAE because the RMSE uses the squared errors before averaging; therefore, it gives more weight to the higher value errors. It is hard to see any trend in the RMSE and MAE for the three different runs at the four MLT sectors that are discussed in the study; however, it is noticeable that with the increased number of flow channels, the RMSE, MSE, and MAE have increased significantly. This enhancement indicates that with an increasing number of flow channels, it becomes challenging for the LSTM model to forecast the RCM simulation. It is because each flow channel or each bubble influences the entire modeled region and when there is a greater number of flow channels and bubbles, LSTM-based models need to assess the influence due to all the flow channels, considering their launch location and the duration they exist for. We have also used the MSE, which is generally used to evaluate the quality of the predictor or estimator. The MSE is in the squared unit of the observed parameter, as it is the second moment of the errors. The MSE shows the variance of the estimator or model and shows the error as the square of the quantity being measured. In all the cases and MLT sectors, the MSE is close to the square of the RMSE, which is consistent with all the other error analyses in the presented study.

CONCLUDING REMARKS AND SUMMARY

The presented LSTM method is applied to build a parallel statistical model using a physics-based magnetospheric model like the RCM. There are other kinds of models which rely on the observation data from the satellite and/or coupled with the ground-based observation. The LSTM-based models can be applicable to both physics-based models and analytical models dependent on the observational data.

The three case studies (i.e., single bubble, one flow channel, and three flow channels) presented in this article reflect that just after LSTM was trained with the initial simulation results from the RCM LSTM model, it was able to accurately replicate the 60 min RCM simulations. All the three LSTM models were able to forecast temporal and spatial variations in entropy parameter $PV^{5/3}$, dawn-to-dusk electric field E_y, and CMFT ϕ. The LSTM forecast quality was very satisfactory from the beginning until the end of the forecast. The performance of the LSTM model for the near-Earth plasma sheet parameter forecast in this study demonstrates that the LSTM is a powerful RNN tool that can be applied to any time series scientific data to learn the underlying relationship among many scientific parameters and to forecast

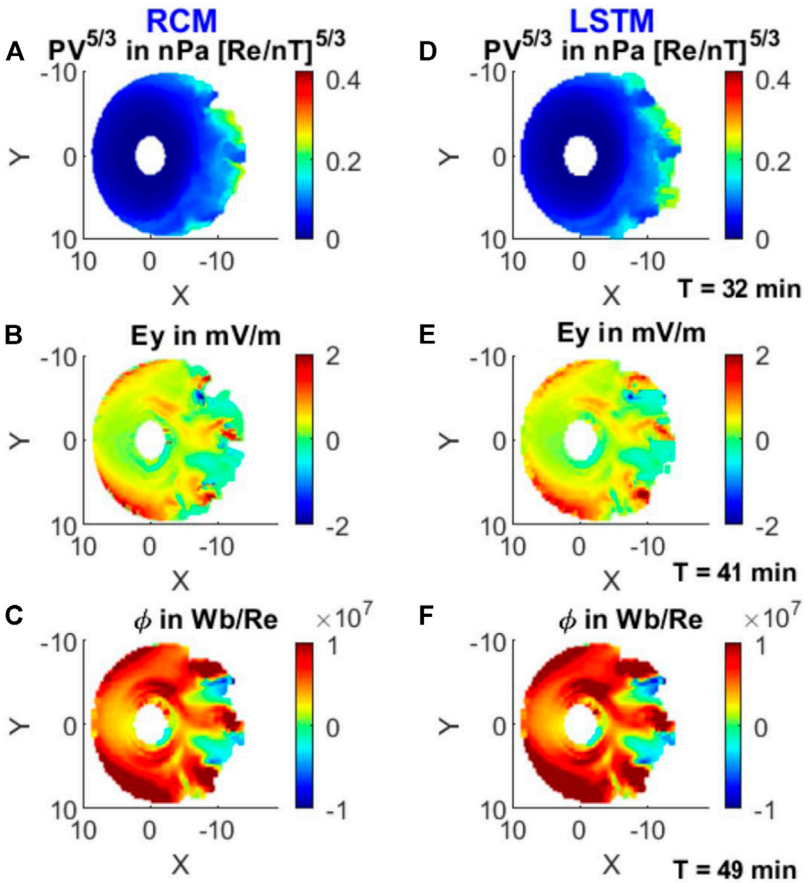


FIGURE 11 | Similar to **Figure 10**, but for the three-flow-channel run.

any desired scientific parameters until the produced forecasts fully abide by the scientific laws.

The main limitation of the LSTM models is their dependence on the input data that come from real observation or a physics-based model's simulation. Besides this, if the LSTM model is multivariate (as in our case), one must find the best sequence of the input parameters in terms of the degree of their dependence on the parameter to be predicted. On the other hand, once these two discussed steps are accomplished, the LSTM multivariate algorithm is powerful in learning the underlying trends among the input variables. However, these LSTM models must still be trained up to the boundary condition implementation in the RCM simulation, in order to produce reasonable and reliable forecasts. Beyond the RCM simulation's boundary condition, the LSTM models are great in producing similar variation trends to the RCM simulations.

In both cases, LSTM will need a significant amount of the model inputs. The first step before training the LSTM algorithm is to logically choose the best inputs and their order, which influence model outputs the most. It can be done in two ways. First, if the physical parameters we are going to model can be written in the form of mathematical equations, then we know on what it depends the most, and we prepare the input order accordingly. But, in case there are two or more input parameters, we can use different combinations of their orders and compare the root mean square error (RMSE) of all the outputs. The input combination with the least RMSE is the best model. For training the LSTM algorithm in parallel to an existing model, it is challenging and crucial to choose the appropriate training and test duration. The modeler should make sure that all the boundary conditions must fall within the training duration for the model, and they should also train the model by allowing it to learn the underlying relationship between the different inputs once all the boundary conditions are defined. In the presented case studies, all the boundary conditions are defined within the first quarter of simulation time, and the LSTM model is trained for the initial 30 min. Now, at this point, we can test the model by splitting the entire dataset into the train and test periods, which means we train the LSTM model with part of the data and then forecast the remaining time series, which is compared to the input data beyond the training time limit. If there is a good match in the forecast and observation, we can fit this model for the entire dataset, and the last LSTM product would be the final model, which can forecast the entire data series.

Here, the readers should keep in mind that the presented LSTM approach is to study an RCM simulation and not the

TABLE 1 | Error Analysis for Single Bubble injection.

Single bubble event: magnetic dawn (03:00–09:00 MLT)				
Parameter	**Corr [−1 to 1]**	**MAE [0 to ∞]**	**MSE [0 to ∞]**	**RMSE [0 to ∞]**
E_y	0.8500	0.5200	0.3137	0.5600
$PV^{5/3}$	0.8300	0.0065	0.0005	0.0077
Φ	0.8900	6.8345	73.6009	8.5791
Single bubble event: magnetic noon (09:00–15:00 MLT)				
Time	Corr	MAE	MSE	RMSE
E_y	0.8300	0.4700	0.2615	0.5100
$PV^{5/3}$	0.8200	0.0028	0.0002	0.0032
Φ	0.8500	7.4265	86.7133	9.3120
Single bubble event: magnetic dusk (15:00–21:00 MLT)				
Time	Corr	MAE	MSE	RMSE
E_y	0.8500	0.4100	0.2075	0.4500
$PV^{5/3}$	0.8200	0.0057	0.0005	0.0075
Φ	0.8600	6.3853	71.7544	8.4708
Single bubble event: magnetic midnight (21:00–03:00 MLT)				
Time	Corr	MAE	MSE	RMSE
E_y	0.8800	0.4900	0.2811	0.5300
$PV^{5/3}$	0.8200	0.0123	0.0029	0.0171
Φ	0.8900	7.1538	70.9772	8.4248

TABLE 3 | Error Analysis for Three Flow Channel.

Three flow channel: magnetic dawn (03:00–09:00 MLT)				
Parameter	**Corr**	**MAE**	**MSE**	**RMSE**
E_y	0.8000	0.2200	0.1189	0.3449
$PV^{5/3}$	0.8500	0.00017	0.0004	0.0020
Φ	0.8800	19.2648	532.6864	23.0800
Three flow channel: magnetic noon (09:00–15:00 MLT)				
Time	Corr	MAE	MSE	RMSE
E_y	0.8400	0.2300	0.0614	0.2478
$PV^{5/3}$	0.8600	0.0058	0.0006	0.0078
Φ	0.8000	21.7847	648.7922	25.4714
Three flow channel: magnetic dusk (15:00–21:00 MLT)				
Time	Corr	MAE	MSE	RMSE
E_y	0.8100	0.5800	0.4111	0.6412
$PV^{5/3}$	0.8800	0.0017	0.0004	0.0022
Φ	0.8300	17.5739	477.6585	21.8554
Three flow channel: magnetic midnight (21:00–03:00 MLT)				
Time	Corr	MAE	MSE	RMSE
E_y	0.8500	0.6900	0.6012	0.7754
$PV^{5/3}$	0.8100	0.0029	0.0001	0.0035
Φ	0.8600	19.6746	484.1452	22.0033

general trend of variation of the inner magnetosphere and/or plasma sheet parameters. Therefore, for a distinct kind of RCM simulation (or other physics-based models), we must develop the distinct input datasets and fit the LSTM model over it. For the analytical model, it can prove itself to be more superior by learning the long-term data trend during the different kinds of solar activity, and it can be developed to forecast a few years of the data in a few easy steps. For example, there is a time delay in the ionospheric response for dayside and nightside as when the interplanetary magnetic field (IMF) turns from northward to southward, the IMF is measured at the dayside (Tenfjord et al., 2017). Therefore, if we have real-time solar wind data, LSTM can be used to develop an alarm for the hazardous events before an hour or so. The physics-based model and the analytical model dependent on observations are costlier in terms of their computational costs and the huge amount of time and resources spent in developing and maintaining them. On the other hand, the LSTM-based modeling algorithm is purely statistical and nonscientific in general. But the LSTM can be made scientific by training it to learn the underlying relationship of any existing models' inputs. Once we are sure that the LSTM outputs satisfy the scientific conditions and the produced outputs are satisfactory to our goals, it can be used as a parallel forecasting/nowcasting system to any space weather or magnetospheric model.

TABLE 2 | Error Analysis for Single Flow Channel.

Single flow channel: magnetic dawn (03:00–09:00 MLT)				
Parameter	**Corr**	**MAE**	**MSE**	**RMSE**
E_y	0.8300	0.3700	0.2116	0.4600
$PV^{5/3}$	0.8600	0.0026	0.0014	0.0038
Φ	0.8700	6.9527	72.8786	8.5369
Single flow channel: magnetic noon (09:00–15:00 MLT)				
Time	Corr	MAE	MSE	RMSE
E_y	0.8200	0.3500	0.1521	0.3900
$PV^{5/3}$	0.8500	0.0021	0.0005	0.0024
Φ	0.8800	8.1437	91.1356	9.5465
Single flow channel: magnetic dusk (15:00–21:00 MLT)				
Time	Corr	MAE	MSE	RMSE
E_y	0.8800	0.2200	0.0961	0.3100
$PV^{5/3}$	0.8100	0.0029	0.0011	0.0034
Φ	0.8600	6.3572	68.8186	8.2957
Single flow channel: magnetic midnight (21:00–03:00 MLT)				
Time	Corr	MAE	MSE	RMSE
E_y	0.8100	0.1900	0.0729	0.2700
$PV^{5/3}$	0.8300	0.0024	0.0007	0.0027
Φ	0.8800	7.3645	67.5437	8.2185

Three RCM simulation (single bubble, single flow channel, and three flow channels) runs' 50% data are used to train a multivariate LSTM model for the three plasma sheet parameters. The LSTM forecast is tested within the boundary condition and beyond the boundary condition of the 60 min simulation. For all the simulation times, there was a good agreement between the RCM simulation and LSTM forecast. All the major and minor fluctuations in the RCM parameters were fully noticeable at all the times and regions of the RCM simulation. The inner magnetospheric data are limited, and it is hard to build a statistical model using the available satellite data (e.g., THEMIS, MMS, ERG, and Cluster II). On the other hand, the RCM is a well-established physics-based model, and we can produce any type of

the run according to our need and concern. The RCM-simulated results are stable for the deep learning–based statistical modeling, and the input environment is well known. These merits of the RCM simulation boundary conditions make them suitable inputs for the LSTM-based RNN model of the inner magnetospheric parameters. Here in this study, it is the very first time a magnetospheric modeled output is being used in the recurrent neural network for forecasting. We have used RCM single bubble, single flow channel, and multiple flow channel runs for the initial 30-min simulation to train our LSTM model. We developed three independent deep learning models for entropy parameter, dawn-to-dusk electric field, and cumulative magnetic flux transport. We have validated the LSTM model by comparing its single point's prediction time series with the RCM single bubble, one-flow-channel, and three-flow-channel runs, the single-point time series simulations. We found a great coherence in both the models (RCM and LSTM). Later, we used 2D maps in the X and Y coordinates to compare the LSTM forecast to the RCM simulation at distinct solution times. In all the solution times, the LSTM forecasts demonstrate a good agreement with the RCM output for all three inner magnetospheric parameters modeled.

The CMFT comes out as the only parameter that steadily grows along the bubble propagation path with time. The LSTM-based algorithms are more appropriate for modeling such parameters which start from a small numerical value and have a tendency to achieve a high numerical value with time. Overall, the LSTM predicted that all parameters are in good prediction range as compared to the RCM simulations. The most significant part of the presented modeling approach was that the prediction efficiency did not compromise with time. The LSTM forecast's efficiency was very satisfactory within and beyond the boundary condition run time. The forecasted parameters through the LSTM were spatially evolving in the same way as in the RCM simulation, and we are confident that the LSTM can be used to train and predict different sophisticated runs of the inner magnetospheric parameters in the future.

DATA AVAILABILITY STATEMENT

The raw data supporting the conclusions of this article will be made available by the authors, without undue reservation.

AUTHOR CONTRIBUTIONS

SP planned the research, developed the LSTM and RCM code, and wrote the manuscript. JY helped in editing the manuscript, revising it, and reshaped several of its sections. WS helped in the plasma bubble simulation launch and provided technical details related to it.

FUNDING

This work at the Southern University of Science and Technology was supported by grant no. 41974187 of the National Natural Science Foundation of China (NSFC) and grant no. XDB41000000 of the Strategic Priority Research Program of the Chinese Academy of Science.

REFERENCES

Angelopoulos, V., Baumjohann, W., Kennel, C. F., Coroniti, F. V., Kivelson, M. G., Pellat, R., et al. (1992). Bursty Bulk Flows in the Inner central Plasma Sheet. *J. Geophys. Res.* 97 (A4), 4027–4039. doi:10.1029/91JA02701

Baker, D. N., McPherron, R. L., Cayton, T. E., and Klebesadel, R. W. (1990). Linear Prediction Filter Analysis of Relativistic Electron Properties at 6.6 RE. *J. Geophys. Res.* 95 (15), 133. doi:10.1029/ja095ia09p15133

Birn, J., Liu, J., Runov, A., Kepko, L., and Angelopoulos, V. (2019). On the Contribution of Dipolarizing Flux Bundles to the Substorm Current Wedge and to Flux and Energy Transport. *J. Geophys. Res. Space Phys.* 124, 5408–5420. doi:10.1029/2019JA026658

Camporeale, E. (2019). The Challenge of Machine Learning in Space Weather: Nowcasting and Forecasting. *Space Weather* 17, 1166–1207. doi:10.1029/2018SW002061

Chai, T., and Draxler, R. R. (2014). Root Mean Square Error (RMSE) or Mean Absolute Error (MAE)? - Arguments against Avoiding RMSE in the Literature. *Geosci. Model. Dev.* 7, 1247–1250. doi:10.5194/gmd-7-1247-2014

Connor, J. T., Martin, R. D., and Atlas, L. E. (1994). Recurrent Neural Networks and Robust Time Series Prediction. *IEEE Trans. Neural Netw.* 5 (2), 240–254. doi:10.1109/72.279188

Eck, D., and Schmidhuber, J. (2002). A First Look at Music Composition Using LSTM Recurrent Neural Networks. *Istituto Dalle Molle Di Studi Sull Intelligenza Artificiale* 103, 1–11.

Gers, F. A., Schmidhuber, J., and Cummins, F. (2000). Learning to Forget: Continual Prediction with LSTM. *Neural Comput.* 12 (10), 2451–2471. doi:10.1162/089976600300015015

Graves, A., Mohamed, A.-R., and Hinton, G. (2013). "Speech Recognition with Deep Recurrent Neural Networks," in 2013 IEEE International Conference on Acoustics, Speech and Signal Processing, Vancouver, BC, Canada, May 26–31, 2013 (IEEE), 6645–6649.

Graves, A., and Schmidhuber, J. (2005). Framewise Phoneme Classification with Bidirectional LSTM and Other Neural Network Architectures. *Neural Networks* 18 (5-6), 602–610. doi:10.1016/j.neunet.2005.06.042

Khotyaintsev, Y. V., Cully, C. M., Vaivads, A., André, M., and Owen, C. J. (2011). Plasma Jet Braking: Energy Dissipation and Nonadiabatic Electrons. *Phys. Rev. Lett.* 106 (16), 165001. doi:10.1103/PhysRevLett.106.165001

Kitamura, K., Nakamura, Y., Tokumitsu, M., Ishida, Y., and Watari, S. (2011). Prediction of the Electron Flux Environment in Geosynchronous Orbit Using a Neural Network Technique. *Artif. Life Robotics* 16 (3), 389–392. doi:10.1007/s10015-011-0957-1

Koon, H. C., and Gorney, D. J. (1991). A Neural Network Model of the Relativistic Electron Flux at Geosynchronous Orbit. *J. Geophys. Res.* 96, 5549–5559. doi:10.1029/90JA02380

Lemon, C., Wolf, R. A., Hill, T. W., Sazykin, S., Spiro, R. W., Toffoletto, F. R., et al. (2004). Magnetic Storm Ring Current Injection Modeled with the Rice Convection Model and a Self-Consistent Magnetic Field. *Geophys. Res. Lett.* 31, L21801, 1–4. doi:10.1029/2004GL020914

Ling, A. G., Ginet, G. P., Hilmer, R. V., and Perry, K. L. (2010). A Neural Network-Based Geosynchronous Relativistic Electron Flux Forecasting Model. *Space Weather* 8, S09003, 1–14. doi:10.1029/2010SW000576

Liu, J., Angelopoulos, V., Runov, A., and Zhou, X.-Z. (2013). On the Current Sheets Surrounding Dipolarizing Flux Bundles in the Magnetotail: The Case for Wedgelets. *J. Geophys. Res. Space Phys.* 118, 2000–2020. doi:10.1002/jgra.50092n

McIlwain, C. E. (1972). "Plasma Convection in the Vicinity of the Geosynchronous Orbit," in *Earth's Magnetospheric Processes*. Editor B. M. McCormac (Dordrecht, Netherlands: D. Reidel), 268–279.

McIlwain, C. E. (1974). "Substorm Injection Boundaries," in *Magnetospheric Physics*. Editor B. M. McCormac (Dordrecht, Netherlands: D. Reidel), 143–154.

Nakamura, R., Baumjohann, W., Klecker, B., Bogdanova, Y., Balogh, A., Rème, H., et al. (2002). Motion of the Dipolarization Front during a Flow Burst Event Observed by Cluster. *Geophys. Res. Lett.* 29 (20), 3–1. doi:10.1029/2002GL015763

Pedregosa, F., Varoquaux, G., Gramfort, A., Michel, V., Thirion, B., Grisel, O., et al. (2011). Scikit-learn: Machine Learning in python. *J. Mach. Learn. Res.* 12, 2825–2830.

Pires de Lima, R., Chen, Y., and Lin, Y. (2020). Forecasting Megaelectron-Volt Electrons inside Earth's Outer Radiation Belt: PreMevE 2.0 Based on Supervised Machine Learning Algorithms. *Space Weather* 18, e2019SW002399. doi:10.1029/2019SW002399

Pontius, D. H., Jr., and Wolf, R. A. (1990). Transient Flux Tubes in the Terrestrial Magnetosphere. *Geophys. Res. Lett.* 17 (1), 49–52. doi:10.1029/GL017i001p00049

Runov, A., Angelopoulos, V., Sitnov, M. I., Sergeev, V. A., Bonnell, J., McFadden, J. P., et al. (2009). THEMIS Observations of an Earthward-Propagating Dipolarization Front. *Geophys. Res. Lett.* 36, L14106. doi:10.1029/2009GL038980

Shin, D.-K., Lee, D.-Y., Kim, K.-C., Hwang, J., and Kim, J. (2016). Artificial Neural Network Prediction Model for Geosynchronous Electron Fluxes: Dependence on Satellite Position and Particle Energy. *Space Weather* 14 (4), 313–321. doi:10.1002/2015SW001359

Silin, I., Toffoletto, F., Wolf, R., and Sazykin, S. Y. (2013). "Calculation of Magnetospheric Equilibria and Evolution of Plasma Bubbles with a New Finite-volume MHD/magnetofriction Code," in American Geophysical Union, Fall Meeting 2013, San Francisco, December 9–13, 2013, SM51B-2176.

Stringer, G. A., Heuten, I., Salazar, C., and Stokes, B. (1996). *Artificial Neural Network (ANN) Forecasting of Energetic Electrons at Geosynchronous Orbit*. Washington, DC, USA: American Geophysical Union, 291–295. doi:10.1029/GM097p0291

Tenfjord, P., Østgaard, N., Strangeway, R., Haaland, S., Snekvik, K., Laundal, K. M., et al. (2017). Magnetospheric Response and Reconfiguration Times Following IMF B Y Reversals. *J. Geophys. Res. Space Phys.* 122, 417–431. doi:10.1002/2016JA023018

Toffoletto, F., Sazykin, S., Spiro, R., and Wolf, R. (2003). Inner Magnetospheric Modeling with the Rice Convection Model. *Space Sci. Rev.* 107, 175–196. doi:10.1007/978-94-007-1069-6_19

Ukhorskiy, A. Y., Sitnov, M. I., Sharma, A. S., Anderson, B. J., Ohtani, S., and Lui, A. T. Y. (2004). Data-derived Forecasting Model for Relativistic Electron Intensity at Geosynchronous Orbit. *Geophys. Res. Lett.* 31 (9), L09806, 1–4. doi:10.1029/2004GL019616

Wei, L., Zhong, Q., Lin, R., Wang, J., Liu, S., and Cao, Y. (2018). Quantitative Prediction of High-Energy Electron Integral Flux at Geostationary Orbit Based on Deep Learning. *Space Weather* 16 (7), 903–916. doi:10.1029/2018SW001829

Weimer, D. R. (2005). Improved Ionospheric Electrodynamic Models and Application to Calculating Joule Heating Rates. *J. Geophys. Res.* 110, A05306. doi:10.1029/2004ja010884

Wiltberger, M., Rigler, E. J., Merkin, V., and Lyon, J. G. (2017). Structure of High Latitude Currents in Magnetosphere-Ionosphere Models. *Space Sci. Rev.* 206, 575–598. doi:10.1007/s11214-016-0271-2

Yang, J., Toffoletto, F. R., Erickson, G. M., and Wolf, R. A. (2010a). Superposed Epoch Study ofPV5/3during Substorms, Pseudobreakups and Convection Bays. *Geophys. Res. Lett.* 37, L07102, 1–5. doi:10.1029/2010GL042811

Yang, J., Toffoletto, F. R., and Song, Y. (2010b). Role of Depleted Flux Tubes in Steady Magnetospheric Convection: Results of RCM-E Simulations. *J. Geophys. Res.* 115, A00I11, 1–10. doi:10.1029/2010JA015731

Yang, J., Toffoletto, F. R., and Wolf, R. A. (2016). Comparison Study of Ring Current Simulations with and without Bubble Injections. *J. Geophys. Res. Space Phys.* 121, 374–379. doi:10.1002/2015JA021901

Yang, J., Toffoletto, F. R., Wolf, R. A., and Sazykin, S. (2011). RCM-E Simulation of Ion Acceleration during an Idealized Plasma Sheet Bubble Injection. *J. Geophys. Res.* 116, A05207. doi:10.1029/2010JA016346

Yang, J., Toffoletto, F. R., Wolf, R. A., and Sazykin, S. (2015). On the Contribution of Plasma Sheet Bubbles to the Storm Time Ring Current. *J. Geophys. Res. Space Phys.* 120, 7416–7432. doi:10.1002/2015JA021398

Zhang, J. C., Wolf, R. A., Sazykin, S., and Toffoletto, F. R. (2008). Injection of a bubble into the inner magnetosphere. *Geophys. Res. Lett.* 35, L02110. doi:10.1029/2007GL032048

Yang, J., Wolf, R. A., Toffoletto, F. R., Sazykin, S., Wang, W., and Cui, J. (2019). The Inertialized Rice Convection Model. *J. Geophys. Res. Space Phys.* doi:10.1029/2019JA026811

Conflict of Interest: The authors declare that the research was conducted in the absence of any commercial or financial relationships that could be construed as a potential conflict of interest.

Copyright © 2021 Priyadarshi, Yang and Sun. This is an open-access article distributed under the terms of the Creative Commons Attribution License (CC BY). The use, distribution or reproduction in other forums is permitted, provided the original author(s) and the copyright owner(s) are credited and that the original publication in this journal is cited, in accordance with accepted academic practice. No use, distribution or reproduction is permitted which does not comply with these terms.

frontiers in Astronomy and Space Sciences

ORIGINAL RESEARCH
published: 04 August 2021
doi: 10.3389/fspas.2021.712611

Counterstreaming Cold H^+, He^+, O^+, and N^+ Outflows in the Plasmasphere

J. Krall[1]* *and J. D. Huba*[2]

[1]Plasma Physics Division, Naval Research Laboratory, Washington, DC, United States, [2]Syntek Technologies, Fairfax, VA, United States

The Naval Research Laboratory (NRL) Sami3 is Also a Model of the Ionosphere (SAMI3) ionosphere/plasmasphere code is used to examine H^+, He^+, N^+, and O^+ thermal outflows during a storm. Here, H^+ and He^+ outflows are associated with refilling while O^+ and N^+ outflows are associated with ring current heating. An improved model of counterstreaming H^+ outflows from the two hemispheres is presented, using an implementation of SAMI3 with two fluid species for H^+. The two-fluid H^+ model avoids nonphysical high-altitude "top-down refilling" density peaks seen in one-fluid H^+ simulations. Counterstreaming cold ion populations are found in all cases. In these fully three-dimensional simulations with realistic magnetosphere boundary conditions, nonphysical top-down refilling density peaks were milder than those found in previous single-field-line or single-magnetic-longitude simulations. In the present two-fluid H^+ case, "bottom-up refilling" density peaks were so mild as to be difficult to detect. For O^+ and N^+, the nonphysical high-altitude density peak is a brief (1–2 h) transient that occurs when heating-driven northward and southward flows first meet. In general, He^+ outflows mimic H^+ outflows while N^+ outflows mimic O^+ outflows.

Keywords: ionosphere, plasmasphere, magnetosphere, oxygen torus, oxygen shell, cold plasma, ionosphere outflow

OPEN ACCESS

Edited by:
Scott Alan Thaller, University of Colorado Boulder, United States

Reviewed by:
W. K. Peterson, University of Colorado Boulder, United States
Ildiko Horvath, The University of Queensland, Australia

***Correspondence:**
J. Krall
jonathan.krall@nrl.navy.mil

Specialty section:
This article was submitted to Space Physics, a section of the journal Frontiers in Astronomy and Space Sciences

Received: *20 May 2021*
Accepted: *21 July 2021*
Published: *04 August 2021*

Citation:
Krall J and Huba J D (2021) Counterstreaming Cold H^+, He^+, O^+, and N^+ Outflows in the Plasmasphere. Front. Astron. Space Sci. 8:712611. doi: 10.3389/fspas.2021.712611

1 INTRODUCTION

Because the plasmasphere (Carpenter, 1966; Nishida, 1966) is an important component of space weather (Lichtenberger et al., 2013), there is significant interest (Gallagher and Comfort, 2016) in the development of predictive models. First-principles plasmasphere simulations, beginning with single field-line models (Banks et al., 1971; St.-Maurice and Schunk, 1977; Richards et al., 1983) and progressing to global simulations (Bailey et al., 1997; Huba et al., 2005; Codrescu et al., 2012; Maruyama et al., 2016), commonly employ fluid equations, with one fluid representing each ion species. In single-field-line simulations, multi-fluid (Rasmussen and Schunk, 1988), semi-kinetic (Lin et al., 1992; Wilson et al., 1992; Wang et al., 2015), and kinetic (Liemohn et al., 1999; Marchaudon and Blelly, 2015) approaches have also been used.

One problem with fluid-code plasmasphere simulations is that the H^+ fluid tends to outflow from the north and south, colliding nonphysically near the apex (Banks et al., 1971; Richards et al., 1983; Singh et al., 1986). These outflows occur during the refilling of plasmasphere flux tubes (Sojka and Wrenn, 1985; Su et al., 2001; Dent et al., 2006; Sandel and Denton, 2007) following the erosion (Park, 1973; Foster et al., 2014) of the plasmasphere by a geomagnetic storm. In fact, the two outflowing proton streams normally pass through each other (Rasmussen and Schunk, 1988). In a single-fluid description of H^+, the northward and southward velocities cancel when the two streams collide near the apex of the field line, producing a nonphysical density peak (Singh et al., 1986). While a

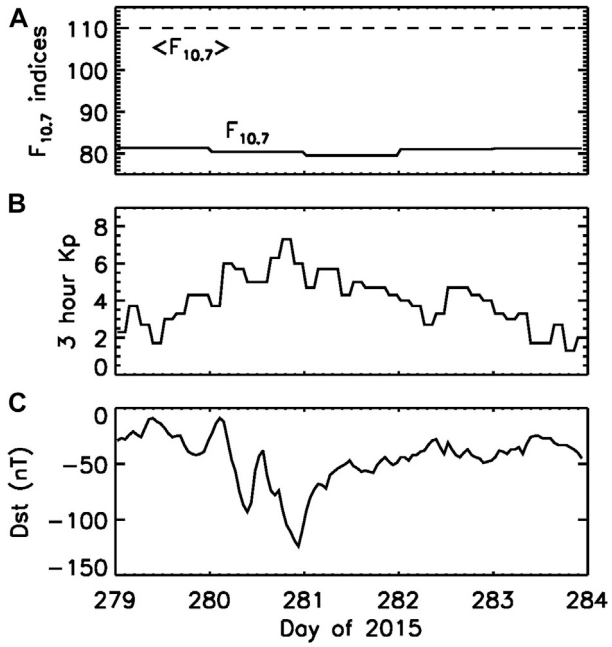


FIGURE 1 | Simulation inputs **(A)** $F_{10.7}$ EUV index and $F_{10.7A}$, its 81-days average value, **(B)** decimal Kp index, and **(C)** Dst index. During the model storm, magnetospheric convection is driven by Kp and ring-current heating of electrons is driven by Dst.

comparison of fluid and semi-kinetic modeling (Singh et al., 1994) shows that this is a problem only during early-stage refilling, it is still a problem. Test runs (Krall and Huba, 2019) using the Naval Research Laboratory (NRL) Sami2 is Another a Model of the Ionosphere (SAMI2) ionosphere/plasmasphere code (Huba et al., 2000b) code show that a two-fluid description of H^+ dramatically improves modeling of early-stage refilling in comparison to the usual one-fluid description.

In this brief study, we revisit this issue using the NRL Sami3 is Also a Model of the Ionosphere (SAMI3) global ionosphere/plasmasphere code (Huba and Krall, 2013). We consider SAMI3 simulations of a specific storm event, including plasmasphere erosion, refilling, and H^+, He^+, N^+ and O^+ outflows. In these simulations, O^+ (and N^+) outflows are driven by ring-current heating, as in Krall et al. (Krall et al., 2020). These results confirm past findings (Roberts et al., 1987; Craven et al., 1995) that the He^+ density generally mimics H^+ (Craven et al., 1997; Goldstein et al., 2003) and that N^+ generally mimics O^+ (Ilie and Liemohn, 2016).

We seek answers to the following two questions: does a two-fluid description of H^+ improve SAMI3 modeling of early-stage refilling? and do single-fluid model O^+ outflows, like single-fluid model H^+ outflows, collide nonphysically?

We answer "yes" to both questions. In the simulations presented below, we show that two-fluid H^+ does indeed improve the modeling, but the effect is not as dramatic as that found in the test-case modeling of Krall and Huba 2019 and the prior single-field-line simulations of Banks et al. 1971 and Singh et al. (1986). We also show that, model O^+ outflows do collide nonphysically as outflows from the north and south meet each other at high altitudes. The result is a transient high-altitude density enhancement that fades within 1–2 h. Coincident N^+ outflows similarly collide, producing a brief transient.

2 THE 7 OCTOBER 2015 STORM

Figure 1 shows ground-based observations, Kp and Dst indices, for the October 7, 2015 (day 280) geomagnetic storm. Also shown is the extreme ultraviolet (EUV) $F_{10.7}$ index and its 81-days average, $F_{10.7A}$. These indices affect the strength of the ionosphere and the state of the background thermosphere.

Figure 1 represents some of the inputs used in the SAMI3 modeling presented below. In addition to the EUV indices already described, the Kp index is used to determine the stormtime convection potential as in Volland (Volland, 1973), Stern (Stern, 1975) and Maynard and Chen (Maynard and Chen, 1975). The Dst index is used to determine ring-current heating of ionosphere and plasmasphere electrons as in Krall et al. (Krall et al., 2020).

3 SAMI3 RESULTS: HYDROGEN AND HELIUM IONS

We now present SAMI3 simulations of the 5-days pre-storm, storm, and recovery period shown in **Figure 1**. SAMI3 (Huba et al., 2005; Huba and Krall, 2013) simulates H^+, He^+, O^+, N^+, O_2^+, N_2^+, and NO^+ ions in the ionosphere and plasmasphere, with one fluid used for each ion. Below, we refer to this version of SAMI3 as either "SAMI3 (one fluid H^+)" or, simply, "SAMI3." We also present simulations of this same time period using SAMI3 (two-fluid H^+), also called "two-stream SAMI3." As in two-stream SAMI2 (Krall and Huba, 2019), two-stream SAMI3 represents the H^+ ion component of the ionosphere and plasmasphere using two model fluids, one with a source only south of the magnetic equator, the other only north of the magnetic equator. During quiet times, these two fluids combine diffusively to mimic the model H^+ density of SAMI3 (one fluid H^+).

The storm simulated here is the same as that in Krall et al. (2020). To ensure that the only differences between SAMI3 and two-stream SAMI3 reflect an updated treatment of the H^+ ions, we began by repeating that previous work with the latest version of the SAMI3 code. We then modified the code to implement two-fluid H^+ and repeated the simulation. As expected, the new SAMI3 run of the same storm is virtually identical to that presented in Krall et al. (2020). Because, as we shall see below, the effect of counterstreaming is not dramatic, results from the new two-stream SAMI3 run are also quite similar to those presented in Krall et al. (2020). However, our attention in that prior work was on O^+, not H^+.

Let us now turn our attention to H^+ and He^+. **Figure 2** compares SAMI3 (left column) to two-stream SAMI3 (right column) at identical times. Shown are color contours of electron density n_e at longitude 0. Each plot is near midnight local time, where "empty" flux tubes convect in from the tailward boundary. Based on model-data comparisons at geosynchronous orbit (Krall et al., 2018), the H^+ density boundary value is set to

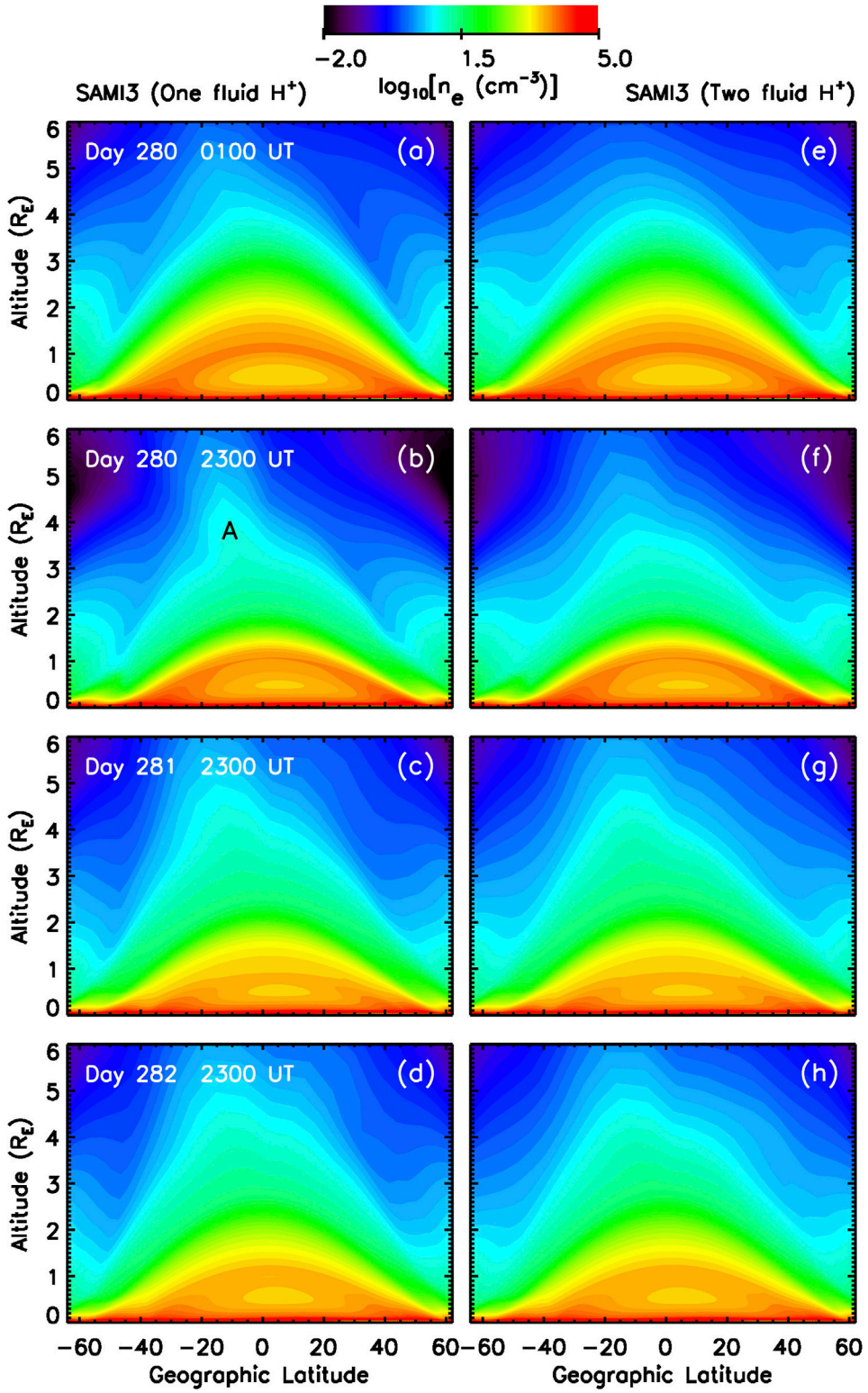


FIGURE 2 | Color contours of the log of the electron density are shown at times **(A,E)** 0100 UT Day 280 (before the storm), **(B,F)** 2300 UT Day 280 (during the storm), **(C,G)** 2300 UT Day 281 and **(D,H)** 2300 UT Day 282. Plots **(A–D)** are from SAMI3; plots **(E–H)** are from two-stream SAMI3. The density peak ('A') in panel **(B)** is caused by colliding H^+ streams from the two hemispheres. While a weaker version of feature A seems to be present in the two-stream SAMI3 result, panel **(F)**, analysis shows that panel **(F)** also includes a second, much weaker peak. Two days later, panels **(D)** and **(H)**, SAMI3 and two-stream SAMI3 come into closer agreement.

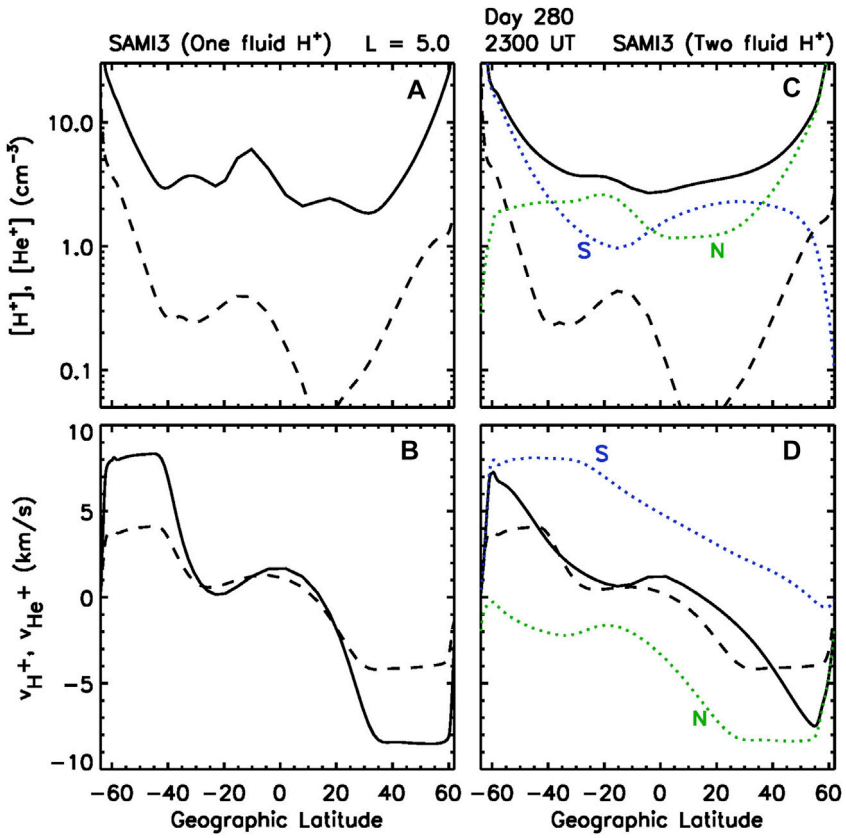


FIGURE 3 | (A, C) H^+ (solid) and He^+ (dashed) ion densities and **(B, D)** H^+ (solid) and He^+ (dashed) ion velocities plotted versus latitude along a fixed-longitude (0.3°) L = 5 field line from **(A, B)** SAMI3 and **(C, D)** two-stream SAMI3. The density peak near the equator (-10°) in panel **(A)** largely disappears in the two-stream SAMI3 simulation **(C)**. Panels **(C, D)** also show the separate H^+_N (H^+ with its source in the north) and H^+_S fluids. We see that H^+ from the south rushes northward ($v > 0$) while H^+ from the north rushes southward ($v < 0$). This is at the same time as panels (b,f) of **Panel 2**.

0.1 cm^{-3}. These times are chosen to include the peak of the storm, panels (b) and (f), where and when counterstreaming H^+ outflows from the ionosphere are strongest.

Figure 2, panel (b), shows the one-fluid colliding upflow effect, with a prominent peak in the electron density near the apex of the geomagnetic field for altitudes > $3R_E$. This peak, labeled "A" in panel (b), appears to be significantly reduced (and shifted slightly southward) in the two-stream SAMI3 result, panel (f). This will be examined further below. Two days after the storm, panels (d, h), SAMI3 and two-stream SAMI3 give nearly identical results. Because these plots are near local midnight, the topside ionosphere electron hole described by Huba et al. (2000a) is evident at altitude 0.5 R_E in each panel.

We now consider plots versus position along an L = 5 field line at the same fixed longitude, where L is the McIlwain parameter (McIlwain, 1961). **Figure 3** shows the colliding-upflow effect, with a peak in the H^+ density, panel (a), at latitude −10°. This is the same as feature A in **Figure 2B**. The corresponding velocity, panel (b), shows a region of near-zero H^+ velocity between high-speed (8 km/s) upflows from the north and south. Here, a positive velocity is northward.

Dashed lines in **Figure 3** indicate He^+. These show that, as expected from past modeling and observations, the He^+ density is generally coincident with the H^+ density. Interestingly, this coincidence includes the nonphysical, but likely insignificant, He^+ density peak at latitude −12° in panel (a). Similar to the way that the He^+ density mimics the H^+ density in panel (a), the He^+ velocity mimics the H^+ velocity in panel (b).

Two-stream SAMI3 results are shown in **Figures 3C,D**. Here, separate south and north components of H^+ are shown as dotted curves. In panels (c, d), we see that H^+ from the north (green dotted curve) moves southward at a high velocity. The velocity falls to zero as it moves southward. As a result, H^+ ions from the north accumulate in the south, creating a peak at latitude −20°. This is the density peak, seen in **Figure 2F** that appears to correspond to the much stronger peak of **Figure 2B**. In fact this peak in H^+_N is one of two H^+ peaks, the other being a peak in H^+_S at latitude 25°. In the latter case, H^+ ions from the south accumulate in the north. The H^+ velocity shown in **Figure 3D**, a density-weighted average of the two separate H^+ fluid velocities, shows that the two-fluid model of H^+ affects both densities and velocities.

4 SAMI3 RESULTS: OXYGEN AND NITROGEN IONS

Figure 4 again compares SAMI3 (left column) to two-stream SAMI3 (right column) at the same times as in **Figure 2**. Shown

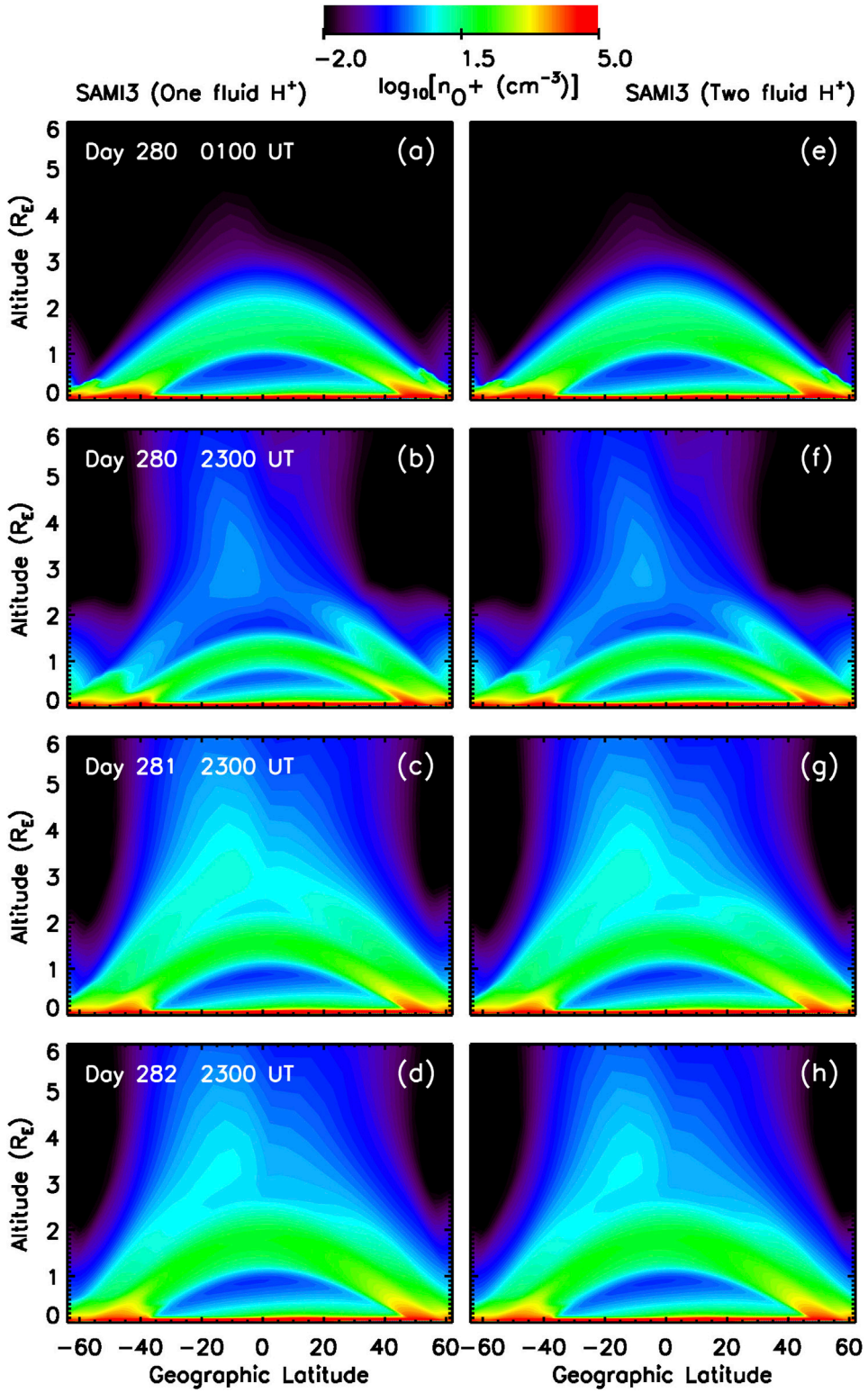


FIGURE 4 | Color contours of the log of the O^+ density are shown at the same times as in **Panel 2** for SAMI3 **(left column)** and two-stream SAMI3 **(right column)**. While the density peak at high altitude implies that O^+ is also affected by the colliding-fluid issue, analysis shows that this is not the case.

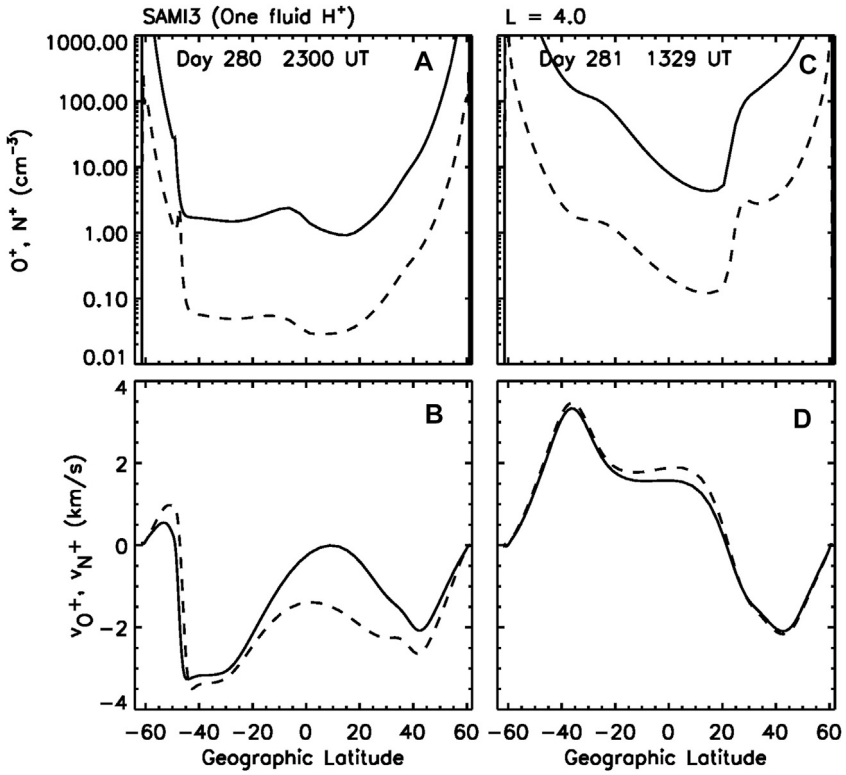


FIGURE 5 | O^+ (solid) and N^+ (dashed) ion densities **(A, C)** and velocities **(B, D)** plotted versus latitude along a fixed-longitude (0.5°) L = 4 field line at Day 280 2300 UT **(A,B)** and Day 281 1329 UT **(C, D)** from the SAMI3 (one fluid H^+) simulation. Panels **(A, B)** are at the same time as panel **(B)** of **Panel 4**. The weak high altitude density peak in panel **(A)** (and **Panel 4B**) occurs at a time when the upward daytime flows have not yet entirely reversed, panel **(B)**.

are color contours of O^+ density at longitude 0. In both cases O^+ is represented by a single fluid; in two-stream SAMI3, only H^+ is represented by two fluids.

Figure 4 shows a weak, local O^+ density peak at nearly the same latitude as the H^+ peak of **Figure 2B**. This seems to suggest that converging O^+ outflows from the north and south are colliding at this point, but this is misleading. In fact, these plots are near local midnight, where O^+ velocities are often downward. Unsurprisingly, a comparison between the left hand panels (SAMI3) and the right hand panels (two-stream SAMI3) of **Figure 4** shows that the two-fluid treatment of H^+ has little effect on O^+. For this reason, we presently focus our analysis of O^+ dynamics on the SAMI3 results.

Figure 4C shows significant O^+ density at $L > 3.5$, with densities exceeding 100 cm^{-3}. This is the O^+ "shell/torus" (Horwitz et al., 1986; Roberts et al., 1987) that was first identified (Chappell, 1982) using the Retarding Ion Mass Spectrometer (RIMS) instrument on the Dynamics Explorer (DE) spacecraft. This aspect of these model results was discussed at length in Krall et al. (2020) [note: Krall et al. (2020) incorrectly states that the heating was applied only at high altitudes; in fact the heating was applied along the entirety of each field line; this issue will be explored further in the near future].

To discern the source of the high-altitude peak in the O^+ density, **Figure 4B**, we examine the dynamics along an L = 4 field line at the time of **Figure 4B** and at a time 14.5 h later, when ring-current heating of ionosphere and plasmasphere electrons is driving significant O^+ outflows. **Figure 5** shows O^+ and N^+ densities and velocities along an L = 4 field line at these two times. In the afternoon sector and soon after the peak of the storm, **Figures 5C,D**, the ring current heating of plasmasphere electrons *via* Coulomb collisions with ring current ions is strongest. At this time the tendency of O^+ to be contained by gravity is overcome and upflows from the north and south are evident in panel (d). The converging velocity pattern and the local jump in the O^+ and N^+ densities at latitude 22° in **Figures 5C,D** suggest that these outflows might be better described using two fluids, as with H^+ in two-stream SAMI3. This will be discussed further below.

After dusk, velocities in the south reverse, panel (b). Here, downward flows in the south are growing while upward flows in the north persist. Near the apex, the velocity is close to zero. Profiles of O^+ density and velocity in **Figures 5A,B** show that the density peak near the apex, visible only in panel (a), is not associated with simultaneous converging upflows. We speculate that the O^+ density peak near the apex of the field line in **Figures 4B**, **5A** represents density that is slowest to descend at night. Dashed lines in **Figure 5** show that N^+ generally mimics O^+, but with a lower density.

5 DISCUSSION: BOTTOM-UP REFILLING

Based on past work, we expect a two-stream treatment of H^+ to replace "top-down" refilling, seen in one-fluid models (Banks

et al., 1971), with "bottom-up" refilling (Rasmussen and Schunk, 1988). With top-down refilling, the initial peak is at high altitude. With bottom-up refilling, two initial peaks occur at lower altitude. In **Figure 3**, the top-down peak is in panel (a) at latitude −10°. In the two-stream SAMI3 result, panel (c), only one peak is clearly visible; it is located at −20°. In fact, there are two H^+ peaks in panel (c), the northern peak being at 25°. This can be seen in **Figure 3**, panel (c), where the separate H_S^+ (H^+ coming from the south, blue) and H_N^+ (green) densities are shown as dotted curves. These are the two peaks expected for bottom-up refilling.

In **Figure 3C**, H_S^+, has high values in the south (<−40°), where it is the main component of the total H^+ density, and in the north (25°), where it is contributing to the bottom-up refilling process. Similarly, H_N^+ has high values in the north (>40°), where it is the main component of the total H^+ density, and in the south (−20°). The H_S^+ and H_N^+ field-aligned velocities, panel (d), confirm that H_S^+ is rushing northward from the south while H_N^+ is rushing southward from the north. In bottom-up refilling we expect the two peaks to form initially at lower altitudes (higher latitudes) and then move upward and equatorward as the flux tube fills(Rasmussen and Schunk, 1988) (**Figure 3**). Plots of H_S^+ and H_N^+ densities at other times, not shown, follow this pattern.

It is notable that neither the one top-down peak, **Figure 3A**, nor the two bottom-up peaks, **Figure 3C**, are nearly as dramatic as the corresponding features found in test-case numerical models of refilling [e.g. 42, 23]. In fact, differences between these SAMI3 and two-stream SAMI3 results are confined to the midnight sector at high altitudes where the top-down density peak in SAMI3 exceeds the two-stream SAMI3 density by only a factor of 2. Otherwise, results from the two simulations are quite similar. While observations of low-energy ion outflows (Sagawa et al., 1987; Liemohn et al., 2005) and plumes (Borovsky et al., 2014; Lee et al., 2016) often show counterstreaming ion populations, corresponding "bottom-up" (or discredited "top-down") density enhancements have yet to be detected.

These runs illustrate the importance of multidimensional simulations for the purpose of accurately simulating refilling events. Specifically, our present runs differ from prior one-dimensional (single field line) simulations [e.g. 42, 37] and our own prior two-dimensional SAMI2 (one magnetic longitude) simulations (Krall et al., 2008; Krall and Huba, 2019) in that the low-density pre-refilling conditions imposed in those low-dimensionality simulations are not present here. The "empty" field lines that are convected into a global plasmasphere simulation are not empty at all. They instead represent the cold plasma component of the tailward magnetosphere. In this case, we represented that plasma by imposing a minimum density of 0.1 cm^{-3}. Further, these inward-convecting field lines develop low-density counterstreaming ion flows as soon as they enter the simulation. While it might be possible to capture some of these features by imposing convection drifts and a tailward boundary condition on a SAMI2 simulation, a complete numerical description, including zonal convection drifts, are obtainable only via three-dimensional simulation. Ultimately, such modeling will need to be placed into the context of a global magnetosphere simulation, such as by Glocer et al. (2020).

6 DISCUSSION: COUNTERSTREAMING OUTFLOWS

To be clear, in this study of H^+, He^+, O^+, and N^+ counterstreaming outflows, only H^+ counterstreaming is simulated, and only in the two-stream SAMI3 case. He^+, O^+, and N^+ are represented using a single fluid per ion species. In the latter cases, would-be counterstreaming flows are indicated by simultaneous converging upflows, such as in **Figures 3B**, **5D**, with corresponding density peaks, **Figures 3A**, **5C**.

From previous studies, we expect that the He^+ and H^+ components of the plasmasphere are generally co-located. For example, remote and *in situ* measurements show that the He^+ and H^+ components of the plasmapause are closely aligned (Goldstein et al., 2003). These results, specifically **Figure 3**, are consistent with this past understanding. They suggest that counterstreaming He^+ outflows, like H^+ outflows, occur during refilling (Richards et al., 1983). However, given the lack of dramatic differences between these SAMI3 and two-stream SAMI3 results, and that the He^+ density is typically less than 10% of the H^+ density, we speculate that counterstreaming He^+ outflows are not significant.

In the case of O^+, we find simultaneous converging high-altitude upflows only during the day and during the storm, when the ring current heating outflow is further supported by the tendency of the ionosphere and plasmasphere to swell during the day (Galvan et al., 2008). In **Figure 5D** we find nearly identical converging upflow velocities for O^+ (solid curve) and N^+ (dashed curve). These converge at latitude 22°, where the field-aligned velocity crosses zero. At this point both the O^+ and N^+ densities jump by an order of magnitude and N^+ has a local density peak. The O^+ density curve at latitude 25° might also be interpreted as a local density peak.

Figure 6 further examines the colliding outflow that is apparent in **Figure 5D**. O^+ density contours (left column) and corresponding O^+ and N^+ density profiles along the $L = 4$ field line (right column) show that the density jump of **Figure 5C**, also shown in **Figure 6F**, occurs just as the north and south O^+ outflows meet at high altitude.

Figures 6A,E, 30 min earlier, shows that these two relatively high density (100 cm^{-3}) outflows have not yet connected. **Figures 6C,G**, 1 hour later, and (d, h), 2 hours later, show that the localized density peak dissipates very quickly. Velocity profiles (not shown) at these same times demonstrate that the coincidence of the velocity zero-crossing and the local density peak, see in **Figures 5C,D**, does not persist.

These results suggest that counterstreaming O^+ ions are both likely be present at high altitude during a storm and likely to be only a transient effect. We speculate that a two-fluid model of O^+ might not exhibit the same density jump as in **Figure 5D**; instead one might obtain a different, but similarly brief, transient density structure.

Unfortunately these O (1 eV) outflows are very difficult to measure. For example, Sagawa et al. (1987) uses Dynamics Explorer 1 data to simultaneously measure composition and pitch angle distribution, but only for energies >10 eV. Using these same data, Lin et al. (1982) infer counterstreaming Maxwellian ion populations such as simulated here. Lee et al.

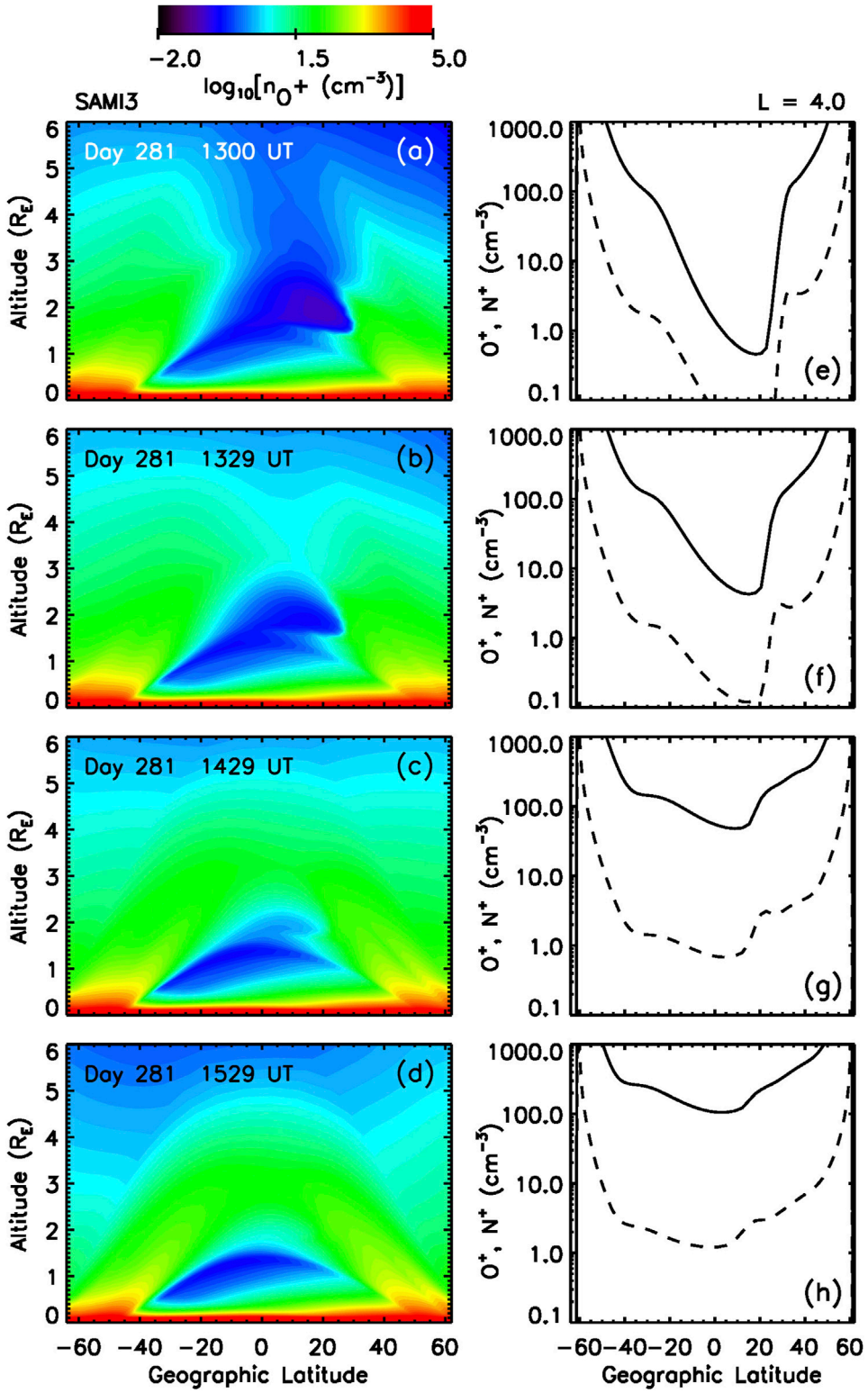


FIGURE 6 | Color contours of the log of the O^+ density **(A–D)** versus latitude and altitude and O^+ (solid) and N^+ (dashed) ion densities **(E–H)** versus latitude on an L = 4 field line at various times from the SAMI3 (one fluid H^+) simulation. Panels **(B,F)** are at the same time as **Panels 5C,D**.

(2016) uses measurements to infer numerous plume or outflow occurrences. However, because measurements used in that study cannot access ion energies below 5 eV, the cold plumes and outflows could not be described in detail. Nevertheless, even within the limitations of current observations, model/data comparison and analysis of well-measured events could provide a useful evaluation of these results.

7 CONCLUSION

As in past modeling studies (Richards et al., 1983), we find evidence for stormtime counterstreaming H^+ and He^+ outflows. In this global simulation of an actual storm, however, such counterstreaming is notable only in the midnight sector. Results also suggest the occurrence of stormtime, high-altitude O^+ and N^+ counterstreaming in the afternoon sector, where the ring-current heating that drives the outflow is strongest (Krall et al., 2020). In these simulations, where O^+ and N^+ are each modeled using a single fluid (only H^+ was modeled using two fluids), converging O^+ and N^+ produce small density peaks (less than an order of magnitude over background values), **Figure 6F**. These density enhancements dissipate rapidly, **Figures 6G,H**. In **Figure 6F**, the local N^+ density peak is on an $L = 4$ field line at latitude 28°.

While two-stream SAMI3 (SAMI3 with a two-fluid model of H^+) leads to minor changes in the results at plasmasphere altitudes, the biggest effect is the avoidance of a small, nonphysical H^+ density peak near the equator, in the midnight sector, during early-stage refilling. At lower altitudes ($<2R_E$), this effect is less significant. For a strong storm, however, low-density flux tubes might convect in from the tail quickly enough to bring flux tubes to low L values while still undergoing early-stage refilling; this might produce stronger density peaks. In all cases simulated here, nonphysical high-altitude density peaks were quite mild, with the nonphysical density peak exceeding the expected result by less than a factor of 10. In this global simulation of an actual storm event, non-physical one-fluid-model density peaks were not nearly as pronounced as those seen in past refilling test-case studies (Singh et al., 1986; Rasmussen and Schunk, 1988; Krall et al., 2008; Krall and Huba, 2019).

DATA AVAILABILITY STATEMENT

The datasets presented in this study can be found in online repositories. The names of the repository/repositories and accession number(s) can be found below: https://doi.org/10.5281/zenodo.4771210.

AUTHOR CONTRIBUTIONS

Both authors, JK and JH contributed to this manuscript.

FUNDING

This research was supported by NRL base Funds, NASA Grand Challenge award NNH17AE97I, and NASA Living with a Star award 80NSSC19K0089.

ACKNOWLEDGMENTS

We thank Mei-Ching Fok of NASA Goddard Space Flight Center for helpful discussions.

REFERENCES

Bailey, G. J., Balan, N., and Su, Y. Z. (1997). The Sheffield University Plasmasphere Ionosphere Model-A Review. *J. Atmos. Solar-Terrestrial Phys.* 59, 1541–1552. doi:10.1016/S1364-6826(96)00155-1

Banks, P. M., Nagy, A. F., and Axford, W. I. (1971). Dynamical Behavior of thermal Protons in the Mid-latitude Ionosphere and Magnetosphere. *Planet. Space Sci.* 19, 1053–1067. doi:10.1016/0032-0633(71)90104-8

Borovsky, J. E., Welling, D. T., Thomsen, M. F., and Denton, M. H. (2014). Long-lived Plasmaspheric Drainage Plumes: Where Does the Plasma Come from? *J. Geophys. Res. Space Phys.* 119, 6496–6520. doi:10.1002/2014JA02022810.1002/2014ja020228

Carpenter, D. L. (1966). Whistler Studies of the Plasmapause in the Magnetosphere: 1. Temporal Variations in the Position of the Knee and Some Evidence on Plasma Motions Near the Knee. *J. Geophys. Res.* 71, 693–709. doi:10.1029/JZ071i003p00693

Chappell, C. R. (1982). Initial Observations of thermal Plasma Composition and Energetics from Dynamics Explorer-1. *Geophys. Res. Lett.* 9, 929–932. doi:10.1029/GL009i009p00929

Codrescu, M. V., Negrea, C., Fedrizzi, M., Fuller-Rowell, T. J., Dobin, A., Jakowsky, N., et al. (2012). A Real-Time Run of the Coupled Thermosphere Ionosphere Plasmasphere Electrodynamics (CTIPe) Model. *Space Weather* 10, a–n. doi:10.1029/2011SW000736

Craven, P. D., Comfort, R. H., Richards, P. G., and Grebowsky, J. M. (1995). Comparisons of Modeled N^+, O^+, H^+, and He^+ in the Midlatitude Ionosphere with Mean Densities and Temperatures from Atmosphere Explorer. *J. Geophys. Res.* 100, 257–268. doi:10.1029/94JA02306

Craven, P. D., Gallagher, D. L., and Comfort, R. H. (1997). Relative Concentration of He^+ in the Inner Magnetosphere as Observed by the DE 1 Retarding Ion Mass Spectrometer. *J. Geophys. Res.* 102, 2279–2289. doi:10.1029/96JA02176

Dent, Z. C., Mann, I. R., Goldstein, J., Menk, F. W., and Ozeke, L. G. (2006). Plasmaspheric Depletion, Refilling, and Plasmapause Dynamics: A Coordinated Ground-Based and IMAGE Satellite Study. *J. Geophys. Res.* 111, A03205. doi:10.1029/2005JA011046

Foster, J. C., Erickson, P. J., Coster, A. J., Thaller, S., Tao, J., Wygant, J. R., et al. (2014). Storm Time Observations of Plasmasphere Erosion Flux in the Magnetosphere and Ionosphere. *Geophys. Res. Lett.* 41, 762–768. doi:10.1002/2013GL059124

Gallagher, D. L., and Comfort, R. H. (2016). Unsolved Problems in Plasmasphere Refilling. *J. Geophys. Res. Space Phys.* 121, 1447–1451. doi:10.1002/2015JA02227910.1002/2015ja022279

Galvan, D. A., Moldwin, M. B., and Sandel, B. R. (2008). Diurnal Variations in Plasmaspheric He^+ Inferred from Extreme Ultraviolet Images. *J. Geophys. Res. Space Phys.* 113, A09216. doi:10.1029/2007JA01301310.1029/2007ja013013

Glocer, A., Welling, D., Chappell, C. R., Toth, G., Fok, M. C., Komar, C., et al. (2020). A Case Study on the Origin of Near-Earth Plasma. *J. Geophys. Res. Space Phys.* 125, e2020JA028205. doi:10.1029/2020JA028205

Goldstein, J., Spasojevic, M., Reiff, P. H., Sandel, B. R., Forrester, W. T., Gallagher, D. L., et al. (2003). Identifying the Plasmapause in IMAGE EUV Data Using IMAGE RPI *In Situ* Steep Density Gradients. *J. Geophys. Res.* 108, 1147. doi:10.1029/2002JA009475

Horwitz, J. L., Brace, L. H., Comfort, R. H., and Chappell, C. R. (1986). Dual-spacecraft Measurements of Plasmasphere-Ionosphere Coupling. *J. Geophys. Res.* 91, 11203–11216. doi:10.1029/JA091iA10p1120310.1029/ja091ia10p11203

Huba, J. D., Joyce, G., and Fedder, J. A. (2000). Sami2 Is Another Model of the Ionosphere (Sami2): A New Low-Latitude Ionosphere Model. *J. Geophys. Res.* 105, 23035–23053. doi:10.1029/2000JA00003510.1029/2000ja000035

Huba, J. D., Joyce, G., and Fedder, J. A. (2000). The Formation of an Electron Hole in the Topside Equatorial Ionosphere. *Geophys. Res. Lett.* 27, 181–184. doi:10.1029/1999GL010735

Huba, J. D., Joyce, G., Sazykin, S., Wolf, R., and Spiro, R. (2005). Simulation Study of Penetration Electric Field Effects on the Low- to Mid-latitude Ionosphere. *Geophys. Res. Lett.* 32, L23101. doi:10.1029/2005GL024162

Huba, J., and Krall, J. (2013). Modeling the Plasmasphere with Sami3. *Geophys. Res. Lett.* 40, 6–10. doi:10.1029/2012GL054300

Ilie, R., and Liemohn, M. W. (2016). The Outflow of Ionospheric Nitrogen Ions: A Possible Tracer for the Altitude-dependent Transport and Energization Processes of Ionospheric Plasma. *J. Geophys. Res. Space Phys.* 121, 9250–9255. doi:10.1002/2015JA022162

Krall, J., Huba, J. D., and Borovsky, J. E. (2018). Sami3 Simulations of a Persistent Plasmasphere Plume. *Geophys. Res. Lett.* 45, 3374–3381. doi:10.1002/2017GL076448

Krall, J., Huba, J. D., and Fedder, J. A. (2008). Simulation of Field-Aligned H+ and He+ Dynamics during Late-Stage Plasmasphere Refilling. *Ann. Geophys.* 26, 1507–1516. doi:10.5194/angeo-26-1507-2008

Krall, J., Huba, J. D., and Fok, M. C. (2020). Does Ring Current Heating Generate the Observed O + Shell? *Geophys. Res. Lett.* 47, e2020GL088419. doi:10.1029/2020GL088419

Krall, J., and Huba, J. D. (2019). Simulation of Counterstreaming H + Outflows during Plasmasphere Refilling. *Geophys. Res. Lett.* 46, 3052–3060. doi:10.1029/2019GL082130

Lee, S. H., Zhang, H., Zong, Q. G., Otto, A., Rème, H., and Liebert, E. (2016). A Statistical Study of Plasmaspheric Plumes and Ionospheric Outflows Observed at the Dayside Magnetopause. *J. Geophys. Res. Space Phys.* 121, 492–506. doi:10.1002/2015JA021540

Lichtenberger, J., Clilverd, M. A., Heilig, B., Vellante, M., Manninen, J., Rodger, C. J., et al. (2013). The Plasmasphere during a Space Weather Event: First Results from the PLASMON Project. *J. Space Weather Space Clim.* 3, A23. doi:10.1051/swsc/2013045

Liemohn, M. W., Khazanov, G. V., Craven, P. D., and Kozyra, J. U. (1999). Nonlinear Kinetic Modeling of Early Stage Plasmaspheric Refilling. *J. Geophys. Res.* 104, 10295–10306. doi:10.1029/1999JA90010410.1029/1999ja900104

Liemohn, M. W., Moore, T. E., Craven, P. D., Maddox, W., Nagy, A. F., and Kozyra, J. U. (2005). Occurrence Statistics of Cold, Streaming Ions in the Near-Earth Magnetotail: Survey of Polar-TIDE Observations. *J. Geophys. Res.* 110, A07211. doi:10.1029/2004JA010801

Lin, C. S., Burch, J. L., Winningham, J. D., Menietti, J. D., and Hoffman, R. A. (1982). DE-1 Observations of Counterstreaming Electrons at High Altitudes. *Geophys. Res. Lett.* 9, 925–928. doi:10.1029/GL009i009p00925

Lin, J., Horwitz, J. L., Wilson, G. R., Ho, C. W., and Brown, D. G. (1992). A Semikinetic Model for Early Stage Plasmasphere Refilling: 2, Effects of Wave-Particle Interactions. *J. Geophys. Res.* 97, 1121–1134. doi:10.1029/91JA02729

Marchaudon, A., and Blelly, P. L. (2015). A New Interhemispheric 16-moment Model of the Plasmasphere-ionosphere System: IPIM. *J. Geophys. Res. Space Phys.* 120, 5728–5745. doi:10.1002/2015JA021193

Maruyama, N., Sun, Y. Y., Richards, P. G., Middlecoff, J., Fang, T. W., Fuller-Rowell, T. J., et al. (2016). A New Source of the Midlatitude Ionospheric Peak Density Structure Revealed by a New Ionosphere-Plasmasphere Model. *Geophys. Res. Lett.* 43, 2429–2435. doi:10.1002/2015GL067312

Maynard, N. C., and Chen, A. J. (1975). Isolated Cold Plasma Regions: Observations and Their Relation to Possible Production Mechanisms. *J. Geophys. Res.* 80, 1009–1013. doi:10.1029/JA080i007p01009

McIlwain, C. E. (1961). Coordinates for Mapping the Distribution of Magnetically Trapped Particles. *J. Geophys. Res.* 66, 3681–3691. doi:10.1029/JZ066i011p0368110.1029/jz066i011p03681

Nishida, A. (1966). Formation of Plasmapause, or Magnetospheric Plasma Knee, by the Combined Action of Magnetospheric Convection and Plasma Escape from the Tail. *J. Geophys. Res.* 71, 5669–5679. doi:10.1029/JZ071i023p05669

Park, C. G. (1973). Whistler Observations of the Depletion of the Plasmasphere during a Magnetospheric Substorm. *J. Geophys. Res.* 78, 672–683. doi:10.1029/JA078i004p00672

Rasmussen, C. E., and Schunk, R. W. (1988). Multistream Hydrodynamic Modeling of Interhemispheric Plasma Flow. *J. Geophys. Res.* 93, 14557–14565. doi:10.1029/JA093iA12p14557

Richards, P. G., Schunk, R. W., and Sojka, J. J. (1983). Large-scale Counterstreaming of H+and He+along Plasmaspheric Flux Tubes. *J. Geophys. Res.* 88, 7879–7886. doi:10.1029/JA088iA10p07879

Roberts, W. T., Horwitz, J. L., Comfort, R. H., Chappell, C. R., Waite, J. H., Jr., and Green, J. L. (1987). Heavy Ion Density Enhancements in the Outer Plasmasphere. *J. Geophys. Res.* 92, 13499–13512. doi:10.1029/JA092iA12p13499

Sagawa, E., Yau, A. W., Whalen, B. A., and Peterson, W. K. (1987). Pitch Angle Distributions of Low-Energy Ions in the Near-Earth Magnetosphere. *J. Geophys. Res.* 92, 12241–12254. doi:10.1029/JA092iA11p1224110.1029/ja092ia11p12241

Sandel, B. R., and Denton, M. H. (2007). Global View of Refilling of the Plasmasphere. *Geophys. Res. Lett.* 34, L17102. doi:10.1029/2007GL03066910.1029/2007gl030669

Singh, N., Schunk, R. W., and Thiemann, H. (1986). Temporal Features of the Refilling of a Plasmaspheric Flux Tube. *J. Geophys. Res.* 91, 13433–13454. doi:10.1029/JA091iA12p13433

Singh, N., Wilson, G. R., and Horwitz, J. L. (1994). Comparison of Hydrodynamic and Semikinetic Treatments for a Plasma Flow along Closed Field Lines. *J. Geophys. Res.* 99, 11495–11506. doi:10.1029/93JA0302710.1029/93ja03027

Sojka, J. J., and Wrenn, G. L. (1985). Refilling of Geosynchronous Flux Tubes as Observed at the Equator by GEOS 2. *J. Geophys. Res.* 90, 6379–6385. doi:10.1029/JA090iA07p06379

St.-Maurice, J.-P., and Schunk, R. W. (1977). Diffusion and Heat Flow Equations for the Mid-latitude Topside Ionosphere. *Planet. Space Sci.* 25, 907–920. doi:10.1016/0032-0633(77)90003-4

Stern, D. P. (1975). The Motion of a Proton in the Equatorial Magnetosphere. *J. Geophys. Res.* 80, 595–599. doi:10.1029/JA080i004p00595

Su, Y.-J., Thomsen, M. F., Borovsky, J. E., and Lawrence, D. J. (2001). A Comprehensive Survey of Plasmasphere Refilling at Geosynchronous Orbit. *J. Geophys. Res.* 106, 25615–25629. doi:10.1029/2000JA00044110.1029/2000ja000441

Volland, H. (1973). A Semiempirical Model of Large-Scale Magnetospheric Electric fields. *J. Geophys. Res.* 78, 171–180. doi:10.1029/JA078i001p0017110.1029/ja078i001p00171

Wang, Y., Tu, J., and Song, P. (2015). A New Dynamic Fluid-kinetic Model for Plasma Transport within the Plasmasphere. *J. Geophys. Res. Space Phys.* 120, 8486–8502. doi:10.1002/2015JA021345

Wilson, G. R., Horwitz, J. L., and Lin, J. (1992). A Semikinetic Model for Early Stage Plasmasphere Refilling: 1, Effects of Coulomb Collisions. *J. Geophys. Res.* 97, 1109–1119. doi:10.1029/91JA01459

Conflict of Interest: Author JH was employed by the company Syntek Technologies.

The remaining author declares that the research was conducted in the absence of any commercial or financial relationships that could be construed as a potential conflict of interest.

Publisher's Note: All claims expressed in this article are solely those of the authors and do not necessarily represent those of their affiliated organizations, or those of the publisher, the editors and the reviewers. Any product that may be evaluated in this article, or claim that may be made by its manufacturer, is not guaranteed or endorsed by the publisher.

Copyright © 2021 Krall and Huba. This is an open-access article distributed under the terms of the Creative Commons Attribution License (CC BY). The use, distribution or reproduction in other forums is permitted, provided the original author(s) and the copyright owner(s) are credited and that the original publication in this journal is cited, in accordance with accepted academic practice. No use, distribution or reproduction is permitted which does not comply with these terms.

frontiers in Physics

ORIGINAL RESEARCH
published: 19 August 2021
doi: 10.3389/fphy.2021.722355

Propagation and Dispersion of Lightning-Generated Whistlers Measured From the Van Allen Probes

J.-F. Ripoll[1,2], T. Farges[1], D. M. Malaspina[3,4], G. S. Cunningham[5], G. B. Hospodarsky[6], C. A. Kletzing[6] and J. R. Wygant[7]*

[1]CEA, DAM, DIF, Bruyères-le-Châtel, France, [2]UPS, CEA, LMCE, Bruyères-le-Châtel, France, [3]Department of Astrophysical and Planetary Sciences, University of Colorado, Boulder, CO, United States, [4]Laboratory for Atmospheric and Space Physics, University of Colorado, Boulder, CO, United States, [5]Space Science and Applications Group, Los Alamos National Laboratory, Los Alamos, NM, United States, [6]Department of Physics and Astronomy, University of Iowa, Iowa City, IA, United States, [7]School of Physics and Astronomy, University of Minnesota, Minneapolis, MN, United States

We study the propagation and attenuation of lightning-generated whistler (LGW) waves in near-Earth space (L ≤ 3) through the statistical study of three specific quantities extracted from data recorded by NASA's Van Allen Probes mission, from 2012 to 2019: the LGW electric and magnetic power attenuation with respect to distance from a given lightning stroke, the LGW wave normal angle in space, and the frequency-integrated LGW refractive index. We find that LGW electric field wave power decays with distance mostly quadratically in space, with a power varying between -1 and -2, while the magnetic field wave power decays mostly linearly in space, with a power varying between 0 and -1. At night only, the electric wave power decays as a quadratic law and the magnetic power as a linear law, which is consistent with electric and magnetic ground measurements. Complexity of the dependence of the various quantities is maximal at the lowest L-shells ($L < 1.5$) and around noon, for which LGW are the rarest in Van Allen Probes measurements. In-space near-equatorial LGW wave normal angle statistics are shown for the first time with respect to magnetic local time (MLT), L-shell (L), geographic longitude, and season. A distribution of predominantly electrostatic waves is peaked at large wave normal angle. Conversely, the distribution of electromagnetic waves with large magnetic component and small electric component is peaked at small wave normal angle. Outside these limits, we show that, as the LGW electric power increases, the LGW wave normal angle increases. But, as the LGW magnetic power increases, the LGW wave normal angle distribution becomes peaked at small wave normal angle with a secondary peak at large wave normal angle. The LGW mean wave-normal angle computed over the whole data set is 41.6° with a ~24° standard deviation. There is a strong MLT-dependence, with the wave normal angle smaller for daytime (34.4° on average at day and 46.7° at night). There is an absence of strong seasonal and continental dependences of the wave-normal angle. The statistics of the LGW refractive index show a mean LGW refractive index is 32 with a standard deviation of ~26. There is a strong MLT-dependence, with larger refractive index for daytime 36) than for nighttime (28). Smaller refractive index is found during Northern hemisphere summer for L-shells above 1.8, which is inconsistent with Chapman ionization theory and consistent with the so-called winter/seasonal anomaly. Local minima of the mean refractive index are

OPEN ACCESS

Edited by:
Ioannis A. Daglis, National and Kapodistrian University of Athens, Greece

Reviewed by:
Yuri Shprits, German Research Centre for Geosciences, Helmholtz Centre Potsdam, Germany
Arnaud Masson, European Space Astronomy Centre (ESAC), Spain

***Correspondence:**
J.-F. Ripoll
jean-francois.ripoll@cea.fr

Specialty section:
This article was submitted to Space Physics, a section of the journal Frontiers in Physics

Received: *08 June 2021*
Accepted: *29 July 2021*
Published: *19 August 2021*

Citation:
Ripoll J-F, Farges T, Malaspina DM, Cunningham GS, Hospodarsky GB, Kletzing CA and Wygant J R (2021) Propagation and Dispersion of Lightning-Generated Whistlers Measured From the Van Allen Probes. Front. Phys. 9:722355. doi: 10.3389/fphy.2021.722355

observed over the three continents. Cross-correlation of these wave parameters in fixed (MLT, L) bins shows that the wave normal angle and refractive index are anti-correlated; large (small) wave normal angles correspond with small (large) refractive indexes. High power attenuation during LGW propagation from the lightning source to the spacecraft is correlated with large refractive index and anti-correlated with small wave normal angle. Correlation and anti-correlation show a smooth and continuous path from one regime (i.e. large wave normal angle, small refractive index, low attenuation) to its opposite (i.e. small wave normal angle, large refractive index, large attenuation), supporting consistency of the results.

Keywords: lightning-generated whistlers, wave propagation, wave-normal angle, refractive index, attenuation laws, WWLLN database, radiation belts, Van Allen Probes

INTRODUCTION

Cloud-to-ground lightning flashes emit powerful electromagnetic radiation over a broad spectrum of electromagnetic waves, including waves in very low frequency (VLF) band (~100 Hz - ~20 kHz), which propagates with successive reflections within the Earth-ionosphere waveguide. Some of this power escapes into the magnetosphere in the form of VLF lightning-generated whistlers (LGW) (e.g. [1,2]). These waves travel in the magnetosphere from their injection point to the satellite location along different paths, with or without one or more magnetospheric reflections at the northern and/or southern hemisphere [3]. Lightning-generated whistlers interact through resonant wave-particle interactions with the trapped electrons in the inner magnetosphere ($L \leq 3$), causing pitch angle diffusion and ultimately the scattering of those electrons into the atmosphere (e.g. [4–7]; [8,9, 51]). In doing so, LGW diminish the radiation levels encountered by satellites in low Earth orbits. Pitch angle diffusion is quantified through quasi-linear diffusion coefficients (e.g. [10]), which are directly proportional to the wave (electric or magnetic) power (defined as the square of the wave amplitude). Dependence of pitch angle diffusion coefficients on parameters treated in this article, including wave power but also wave-normal angle are discussed in Albert [11] (see also [12]). Recent derivation of LGW diffusion coefficients was carried by Albert et al. [9] based on the low Earth orbit (LEO) Detection of Electro-Magnetic Emissions Transmitted from Earth-quake Regions (DEMETER) micro-satellite [13, 14] measured LGW power in Colman and Starks [15] and the computation by ray-and-power tracing of the propagation of LGW through the ionosphere and into the magnetosphere [16]. Our work attempts to bypass the numerical complexity and cost of ray tracing simulation through the derivation of empirical attenuation laws (cf. section *Electric and Magnetic Wave Power Attenuation Laws*). More references on radiation belt physics and wave-particle interactions can be found in the review of Ripoll et al. [17].

The first detailed knowledge and variation of the LGW power in space [6] originates from measurements from the Combined release and Radiation Effects Satellite (CRRES), which sampled a limited range of magnetic local times. At that time, conversion from electric to magnetic field was made assuming a zero wave-normal angle (**Eq. 3** of [6]) due to lack of knowledge of the LGW wave-normal angle. Our study will show that, in reality, LGW mean wave-normal angle is 42° with a standard deviation of 24°.There exists a strong and complex dependence of LGW properties including wave normal angle with respect to L-shell, magnetic local time (MLT), longitude and seasons. Median power spectral density measured by both the DEMETER satellite and the Van Allen Probes are discussed in Zahlava et al. [18]. Electric and magnetic field wave amplitudes of LGW measured by the two probes of the NASA Van Allen Probes mission (initially named the Radiation Belt Storm Probes (RBSP) mission) in the near-equatorial magnetic region during their entire mission, from 2012 to 2019, have been analyzed in Ripoll et al. [19]. Their study revealed strong dayside ionospheric damping of the LGW electric field. LGW amplitudes drop below $L = 2$, contrary to the Earth's intense equatorial lightning activity (e.g [20, 21]) when mapped onto the projection of the Earth's magnetic field lines at 100 km [22]. A related study focuses on the quantification of the electromagnetic power radiated on Earth and in space by extremely powerful lightning strokes, called superbolts [23].

In this study, we focus on LGW electromagnetic power propagation and attenuation in the near-Earth space, defined here as $L < 3$ within ± 20°degrees of the magnetic equator. We use observations from the two Van Allen Probes over their entire mission in order to assess LGW electric and magnetic wave power, similarly to Ripoll et al. [19, 23], although here we increase the planarity threshold criteria for the selected LGW in order to improve the accuracy of the wave-normal angle computation. Our analysis uses the World-Wide Lightning Location Network (WWLLN) databases (e.g. Dowden et al., 2002; [24–26]) established using ground VLF receiver stations. WWLLN provides the location and estimated VLF energy of the lightning source for waves later sensed in space by the Van Allen Probes, as is commonly done (19, 23, 27, 28, 50). Combining both datasets, we generate empirical electric and magnetic attenuation laws according to the distance (between the lightning source on Earth and the closest magnetic footprint of the spacecraft) and energy of the lightning source identified by WWLLN. We also present and discuss, for the first time, LGW wave-normal angle statistics from Van Allen Probes and their variation with respect to L-shell, magnetic local time (MLT), longitude and season. From the knowledge of the electric and magnetic field amplitudes as well as the wave-normal angle, we are able to generate statistics

of the measured (frequency-integrated) LGW refractive index as defined from the ratio of the magnetic amplitude with the electric amplitude. Correlations between attenuation law parameters, wave normal angles and refractive index are also determined.

MATERIALS AND METHODS

Van Allen Probes Data

Data from the Van Allen Probes mission [29] are used in this study. The Van Allen Probes are twin spin-stabilized spacecraft (A and B) that orbited Earth in similar geotransfer orbits (nominal perigee and apogee altitudes of ~618 km and ~5.8 Earth radii, respectively). The spacecraft launched in August of 2012. Probes A and B were decommissioned in July 2019 and October 2019, respectively. During their mission, they completed more than three full precessions about MLT. Their orbital period was ~9 h, and spin period ~11 s. Their orbits stayed within ~20° of the geomagnetic equator.

This study makes use of data from the Electric and Magnetic Field Instrument Suite and Integrated Science (EMFISIS) instrument suite [30] and the Electric Fields and Waves (EFW) instrument [31]. The specific data used include the DC-coupled magnetic field from the Fluxgate Magnetometer (FGM) and AC-coupled magnetic fields from the Search Coil Magnetometer (SCM). EMFISIS calculates spectra and cross-spectra on-board using the SCM magnetic field data and electric field data from the EFW sensors as inputs. Differential electric field measurements are used. Specifically, we use the sum of the power spectra from the two spin-plane axes (orientated within ~15°degrees of to perpendicular to the spacecraft-Sun line). Spin-axis electric field data are not used because of contamination by broadband spikes due to frequent shadowing of the anti-sunward sensor by spacecraft structures. All three orthogonal axes of SCM data are used. The survey spectral data consist of power spectral densities averaged over the first 0.5 s of every 6 s. The native sample rate of these data is 35,000 Samples/s. The on-board calculated spectra and cross-spectra span ~2 Hz to ~11 kHz, distributed in 65 pseudo-logarithmically spaced frequency bins.

Data Processing

The Van Allen Probes' data described above are processed to isolate signatures of VLF plasma waves associated with lightning. This processing has several steps that are described in detail in Ripoll et al. [19] and only briefly summarized here: 1) noise floors are derived following a similar procedure to Malaspina et al. [32], 2) a signal to noise ratio (SNR) metric is used to determine whether or not it is possible to conclusively identify VLF plasma waves in a given frequency bin at a given time, 3) VLF wave observations are considered possible for SNR ≥5 magnetic field wave power spectral density data and SNR ≥13 electric field wave power spectral density data, 4) contaminated measurements of electric fields on Probe A by spacecraft-generated noise in several frequency bins (e.g. 2,243, 3555, 3988, 5633, and 7,956 Hz) are not used in this study.

To quantify the power of lightning-related VLF waves, we integrate the electric (magnetic) wave power spectral density between ~2 kHz and ~11 kHz, multiplied by the frequency bandwidth in each bin, to obtain a single frequency-integrated electric (magnetic) power for each sample. All wave data beyond L = 3 are excluded from consideration due to lower lightning activity and a decay of the lightning power as ~1/L [22]. This study uses electric and magnetic field measurements made after October 1, 2012. We do not use magnetic power spectra after May 31, 2018 on Probe B and after June 30, 2018 on Probe A. We do not use electric power spectra data after June 30, 2019 for Probe B and after June 30, 2016 for Probe A. Data from thruster firings, intense spacecraft charging, and EFW calibration bias sweeps are always excluded.

Method for Associating Lightning-Generated Whistlers Observed by Van Allen Probes With Lightning Sources on Earth

We use the WWLLN database (e.g Dowden et al., 2002; [24–26,33]) to obtain the lightning location on Earth and its estimated energy. For each measurement {i} of the Van Allen Probes (abbreviated RBSP in the following equation subscripts) survey spectral database for which both the electric and magnetic power are defined, we seek all lightning strokes in the WWLLN files that existed during *dt* around their time of occurrence, $t_{RBSP}\{i\}$, and could have caused the wave, with *dt* defined by:

$$dt = t_{WWLLN} - t_{RBSP}\{i\} + t_{delay}, \quad (1)$$

$$t_{delay} = 0.277 \times L_{RBSP}\{i\} - 0.255 \; and \; |dt| < 0.25s. \quad (2)$$

The expression of t_{delay} as a function of the Van Allen Probes L-shell, $L_{RBSP}\{i\}$, of event {i} is taken from time delays that are observed when receiving superbolt wave signals, for which there is high confidence of the signal source due to the extreme power and low occurrence of superbolts on Earth [23]. We then only retain in the statistics the Van Allen Probes measurements for which there is a single lightning stroke identified within *dt* in order to guarantee a unique source. For every lightning stroke that is retained, we compute *d* that is the distance between the lightning stroke location on Earth given by WWLLN and the closest (North or South) magnetic footprint (MFP) of the satellite. We also store WWLLN energy for the {i} event. Events for which $d > 7{,}000$ km are disregarded. Later in the document (cf. **Table 1** and related discussion), we will explain why the maximal distance needs to also be defined as a function of (L, MLT) and further reduced.

The full Van Allen Probes VLF wave database has 9,561 997 (8,346 691) survey measurements, but a large number of them fall below the SNR thresholds. Among these measurements, we find ~2.5 M (~1.4 M) electric (magnetic) measurements that exceed the respective SNR threshold and allow a power to be defined. Of these ~1.8 M (~0.9 M) are associated with a unique WWLLN source satisfying $|dt| < 0.25$ *s*.

TABLE 1 | Maximal distance, d_{max} (in km) used for fitting the (M) magnetic power distribution and the (E) electric power distribution for a given L-MLT bin (for all seasons).

	L\MLT	0–3	3–6	6–9	9–12	12–15	15–18	18–21	21–24
E	1.1	5,000	2,500	2,500	2000	1,500	2,500	3,500	3,500
E	1.3	5,000	3,500	3,500	3,500	2,000	2,500	5,000	4,000
E	1.5	5,000	4,000	3,500	3,500	2,000	3,000	5,000	4,000
E	1.7	5,000	4,500	2,500	2,500	3,500	3,500	5,000	4,000
E	1.9	5,000	3,500	5,000	3,000	3,500	5,000	5,000	5,000
E	2.1	5,000	5,000	5,000	5,000	4,500	5,000	5,000	5,000
E	2.3	5,000	5,000	4,000	5,000	5,000	5,000	5,000	5,000
E	2.5	5,000	5,000	5,000	5,000	5,000	5,000	5,000	5,000
E	2.7	5,000	4,000	5,000	5,000	4,000	5,000	5,000	5,000
M	1.1	2,500	2,500	3,000	1,500	2,000	2000	3,000	2,500
M	1.3	4,000	4,000	2,500	1,500	2,000	2,500	3,000	3,500
M	1.5	4,000	4,500	3,000	2,000	2,500	3,000	5,000	4,000
M	1.7	5,000	4,500	4,000	2,000	2,500	3,500	5,000	4,000
M	1.9	5,000	4,000	2,500	2,500	2,500	2,500	5,000	3,500
M	2.1	5,000	4,000	4,000	2,500	3,000	5,000	5,000	3,500
M	2.3	5,000	3,500	4,000	5,000	4,000	5,000	5,000	3,500
M	2.5	5,000	3,500	5,000	5,000	4,000	5,000	5,000	3,500
M	2.7	3,500	3,500	4,000	5,000	5,000	5,000	5,000	2,500

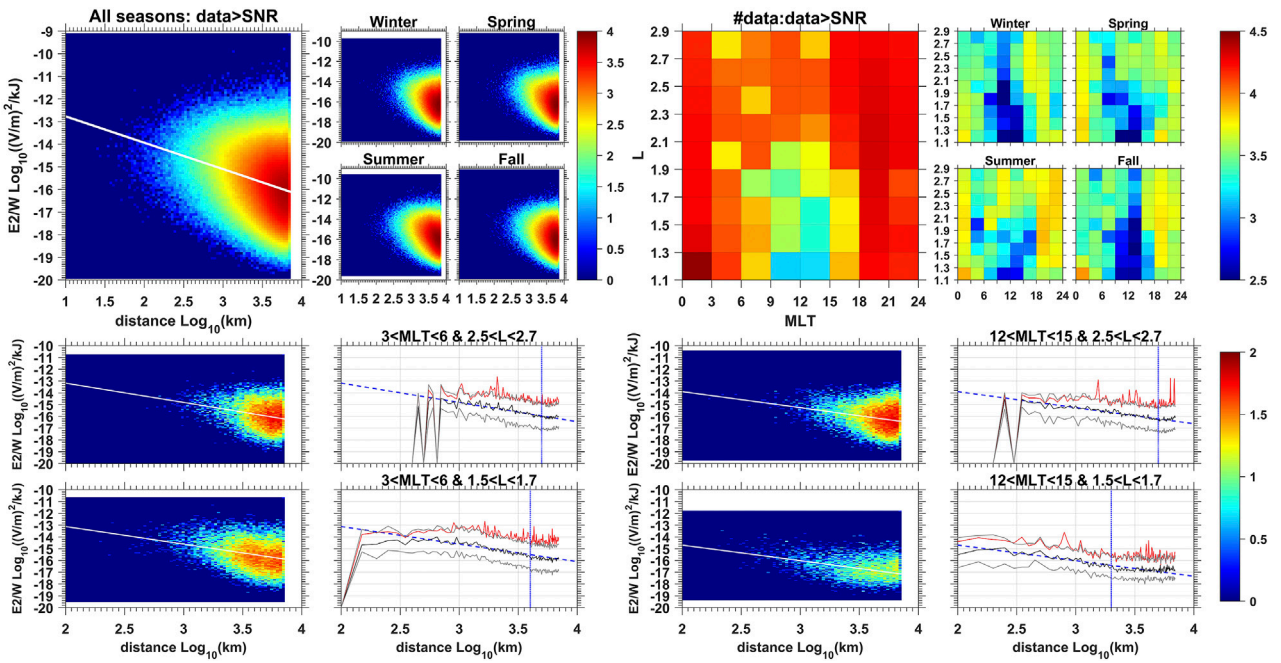


FIGURE 1 | (top left) Statistics of LGW Electric power $(V/m)^2$ (in log10 of number of events), rescaled by WWLLN lightning energy (kJ) and plotted versus distance between the lightning location (from WWLLN) and the spacecraft for the full database of Van Allen Probe A and B mission (2012–2019), with full distribution and distribution per season. The distribution is spread over many orders of magnitude due to the different behaviors in (L, MLT) (top right) Number of events (in log10) sorted by (L, MLT) and (season, L, MLT) (bottom) Same statistics (in log10) as top left but limited to (left) a night bin of at MLT = [3,6] and L = [2.5,2.7] and [1.5,1.7] and (right) a day bin at MLT = [12,15] and L = [2.5,2.7] and [1.5,1.7]. White line plots represent linear regression (left bottom panels only). Line plots represent (black) the median, (grey) the upper (84%) and lower (16%) quartiles defining one sigma, (red) the mean, (blue) the linear regression which equates the median. We find the mean equates the median plus one sigma. The vertical blue dashed line indicates the maximal distance used for the fits given in **Table 1**.

RESULTS

Electric and Magnetic Wave Power Attenuation Laws

We assume that the wave power (normalized by the lightning energy) follows a decaying power law as it travels from its source to the satellite footprint. Two applications of these empirical attenuation laws are 1) to provide a predictive law for the electric and magnetic VLF wave power that will be sensed in space (near the equator) at a given L-shell and MLT (equivalently LT) for a given season from a source of energy (W in kJ) located at d km from the magnetic footprint and 2) to provide a way to rescale lightning power at a given location in space from WWLLN activity to derive the mean lightning magnetic power over a drift period and to be able to compute mean LGW effects on trapped electrons [22].

Such a power law with respect to the distance from the stroke to the closest spacecraft magnetic footprint 4) was derived by Burkholder et al. [28] based on the measurements of the electric wave power by the Communication/Navigation Outage Forecast System satellite (C/NOFS). The power law derived by Burkholder et al. [28], with power, −2.34, is valid for nighttime MLT (see also [27]). Similar power laws have been also derived from DEMETER observations for daytime and nighttime in [50], with a power of −1.76 (less attenuation than Burkholder's law). Ripoll et al. [23] derived specifically attenuation power laws of superbolt electric power both on the ground (power of −2) and in space (power of −1.7) from Van Allen Probes as well as an attenuation power law for superbolt magnetic power in space from Van Allen Probes (power between −1.2 and −1.6).

The Burkholder et al. [28] power law is used in Ripoll et al. [22] to connect the total lightning power on Earth (see a world-wide map in their **Figure 1**(top)) with an estimation of the electromagnetic power that should be sensed by the Van Allen Probes (see the map in their **Figure 1**(middle)). One parameter of this law was later modified in Ripoll et al. [19] to include MLT dependence extracted from the day/night differences observed in Van Allen Probes LGW measurements in order to better agree with these observations and to account for the strong effect of the dayside ionosphere on lightning wave attenuation (e.g. [34]). None of these aforementioned laws had a dependence on L-shell while the L-shell dependence of both the electric and magnetic power is anticipated to be strong and complex (e.g. [35]). None of the previously derived empirical power laws had either a fine MLT (or LT) resolution or a seasonal variation, while both parameters have a significant importance on the wave amplitude [19]. Fiser's and Burkholder's attenuation laws also concern only the electric wave power but not the magnetic power (not measured by C/NOFS, for instance). Current understanding is that VLF wave magnetic power decays linearly on Earth [36], while VLF wave electric power decays quadratically both on Earth and in space (23, 27, 28, 50).

The goal of this article is thus to derive empirical electric and magnetic LGW attenuation laws with a dependence on local time, L-shell, and seasons from Van Allen Probes and WWLN measurements. The Van Allen Probes measurements are near-equatorial measurements, within ±20° latitude, so that the attenuation laws may differ from the ones derived from LEO satellites due to the propagation between the footprint and the satellite position at the magnetic equator. Attenuation laws are taken to have the common form

$$\frac{X^2\,(L, MLT, s)}{W} = 10^{Log_{10}\beta\,(L,MLT,s)} \times d^{\alpha\,(L,MLT,s)}, \qquad (3)$$

with a law for each of the electric or magnetic power, $X^2 = E^2$ *or* B^2 (in $\mu V^2/m^2$ or pT^2), and with the energy of the WWLLN-identified stroke, W in kJ, the distance between WWLLN lightning stroke location and the nearest probe MFP of the Van Allen Probes, d (in km). The α and $log_{10}\beta$ main parameters are, for the first time, dependent on L, MLT, and the season, s.

Figures 1, **2** (top left) give the global distribution of E^2/W and B^2/W with respect to the distance d to the WWLLN lightning location. The distribution is spread over many orders of magnitude, too many to make the mean or any regression law to be relevant. This is in agreement with the wide standard deviation shown in Burkholder et al. [28]. The wide spread is caused by mixing measurements taken at all (*L, MLT, s*) and indicates that there is too much variation if a single law is derived without differentiating for L-shell, MLT, and seasons. When separation in (*L, MLT*) is applied, as shown in the bottom row of **Figures 1**, **2**, the variability is reduced significantly. The top-right panels of **Figures 1**, **2** confirm that the resolution (i.e. number of events per bin) remains sufficient for relevant statistics. The smallest data set (few hundreds of events) is found at the lowest L-shells ($L < 1.5$) and around noon, for which LGW are the rarest in Van Allen Probes measurements [19].

Interestingly, these statistics show that the mean (red line plot in **Figures 1**, **2** bottom) of the distribution is equal to the median (black line plot) plus one standard deviation (grey line plot) at a given distance for all (*L, MLT*) bins (only shown for four bins in **Figures 1**, **2** bottom row). This is a property of log-normal distributions and could thus indicate the distribution follows a log-normal law. The regressions with respect to distance in log-log space (blue line plot) generally agree with and fit with the median of the distribution. Regressions are performed up to a maximal distance, d_{max} (L,MLT) (vertical dashed line in **Figures 1**, **2**) after which we see the distribution becomes flat (as visible in **Figures 1**, **2**).

Statistics are binned by (*L, MLT, s*) and a power law following **Eq. 1** is fitted for each bin, yielding the α(*L, MLT, s*) and $Log_{10}\beta$ (*L, MLT, s*) fitted values in **Figure 3**, with the electric (magnetic) attenuation law parameters shown on the top (bottom). **Table 1** gives the d_{max} that is used for fitting the power law in each (L, MLT) bin. For daytime (defined as MLT = 6–18) and low L-shell bins this distance is as low as 1,500 km, while it could exceed 7,000 km for nighttime and $1.3 < L < 2.5$, though we limit d_{max} to 5,000 km. As a comparison, Fiser et al. (50) used 2000 km, Burkholder et al. [28] and Ripoll et al. [19, 22]) used 10,000 km, and Ripoll et al. [23] used 7,000 km. Here, we found that using a constant value of d_{max} for all (L, MLT)

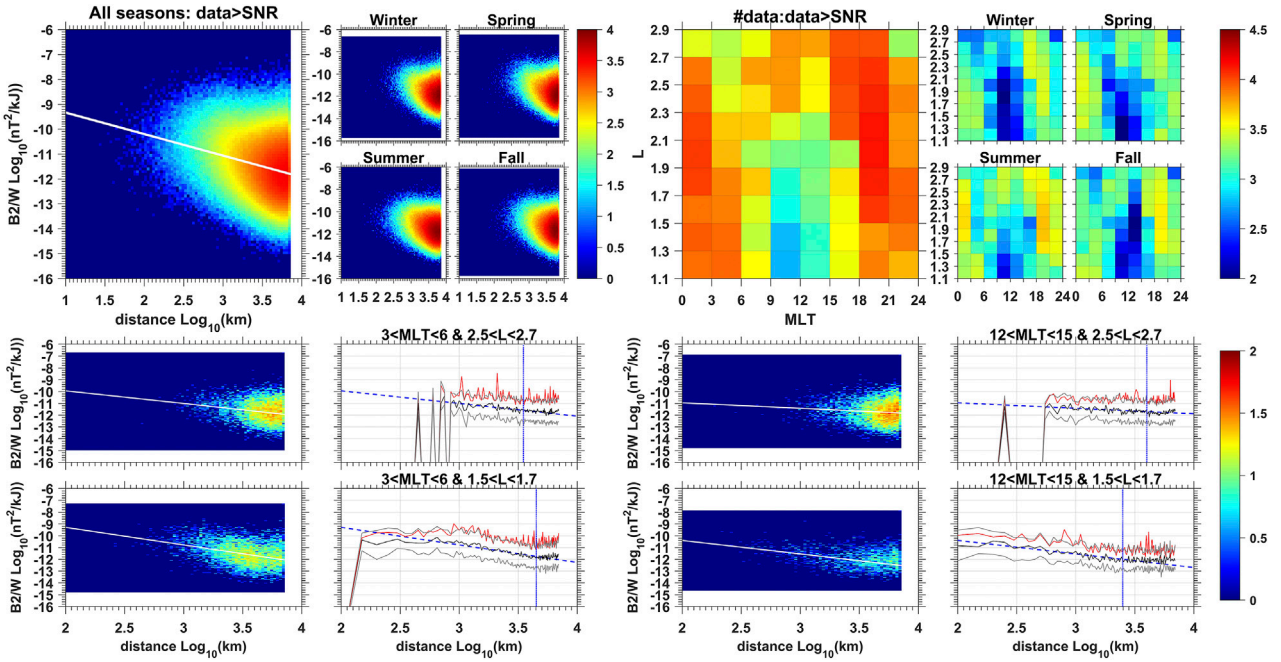


FIGURE 2 | Same as **Figure 1** for the LGW magnetic power (in nT^2).

bins was causing unjustifiable variability of the α and β parameters. A careful inspection of the distribution for each bin was required to perform an accurate fit. Low value of d_{max} are already indicative of the most complex bins, i.e. the lowest and highest L-shell bins (L < 1.5 and L > 2.5) and during the daytime (MLT = 9–12 and 12–15). Seasons are differentiated in the smaller figures. We find the electric power decays mostly quadratically in space, with α(*L, MLT, s*) varying between -1 and -2 (from blue to green), while the magnetic power decays mostly linearly in space, with α(*L, MLT, s*) varying between 0 and -1 (from green to red). Variation with seasons is visible in **Figure 3** but is not too strong so we perform the remainder of the analysis with data from all seasons combined together for simplicity. This choice reduces the complexity by one dimension but conversely introduces more variability of the (α, β) parameters. The strong attenuation of the power during daytime (MLT = 6–18) (due to the denser ionosphere) is demonstrated by the 2D color plots of **Figure 3**. The mean value with respect to all (*L, MLT, s*) of α is −1.4 for the electric field power (−1.3 for day and −1.5 for night only) and −1.1 for the magnetic field power (−0.95 for day only and −1.2 for night only). On average over all (*L, MLT, s*), we find a decay of the β (*L, MLT, s*) parameter by one order of magnitude but local variation at fixed L-shell is greater, with orders of magnitude variations. We also see a change of regime in the α power. The α power could have been expected to be lower during daytime–more attenuation–but the opposite occurs, both for E^2 and B^2 (with the α power increasing from ∼−2 at night to ∼ −1 at day for E^2 and from ∼−1 at night to ∼0 at day for B^2). However, the β scaling factor falls down by one to two order of magnitude during daytime compared with nighttime (**Figures 3E,K**). In these laws, the β scaling factor plays thus the main role of causing strong attenuation during daytime. **Figures 3C,E,I,K** show the opposite behavior of α and β with respect to MLT. Values of the α power for both E^2 and B^2 are however consistent with ground measurements only at night, during which E^2 decays as a quadratic law (e.g. [28]) and B^2 as a linear law [36].

Statistics of the Wave-Normal Angle of Lightning-Generated Whistlers Observed by the Van Allen Probes

The wave normal angle is the angle between the wave vector of a given emitted LGW at a frequency, f, and the magnetic field vector at the point of observation. In a homogeneous/isotropic medium, the wave normal angle points in the direction of propagation of the wave energy. In the magnetosphere, which is an inhomogeneous/anisotropic medium, the wave energy propagates in the ray direction, which differs from the direction pointed by the wave normal angle (e.g. [3]).

LGW wave normal angles are taken from Level 4 EMFISIS data. Their computation relies on the Singular Value Decomposition method [37, 38], which requires high wave planarity, applied on on-board calculated cross-spectral data. Data described in section *Materials and Methods* 2 and in the subsection Electric and Magnetic Wave Power Attenuation Laws of the section *Results* 3 are thus down-selected such that the LGW planarity, P(f), remains above 0.5 for each frequency bin. This leads to a slightly reduced set of 9,324,651 values compared with the database used in section *Electric and Magnetic Wave Power Attenuation Laws*. In order to compute the wave normal angle, both electric and magnetic components have to be defined

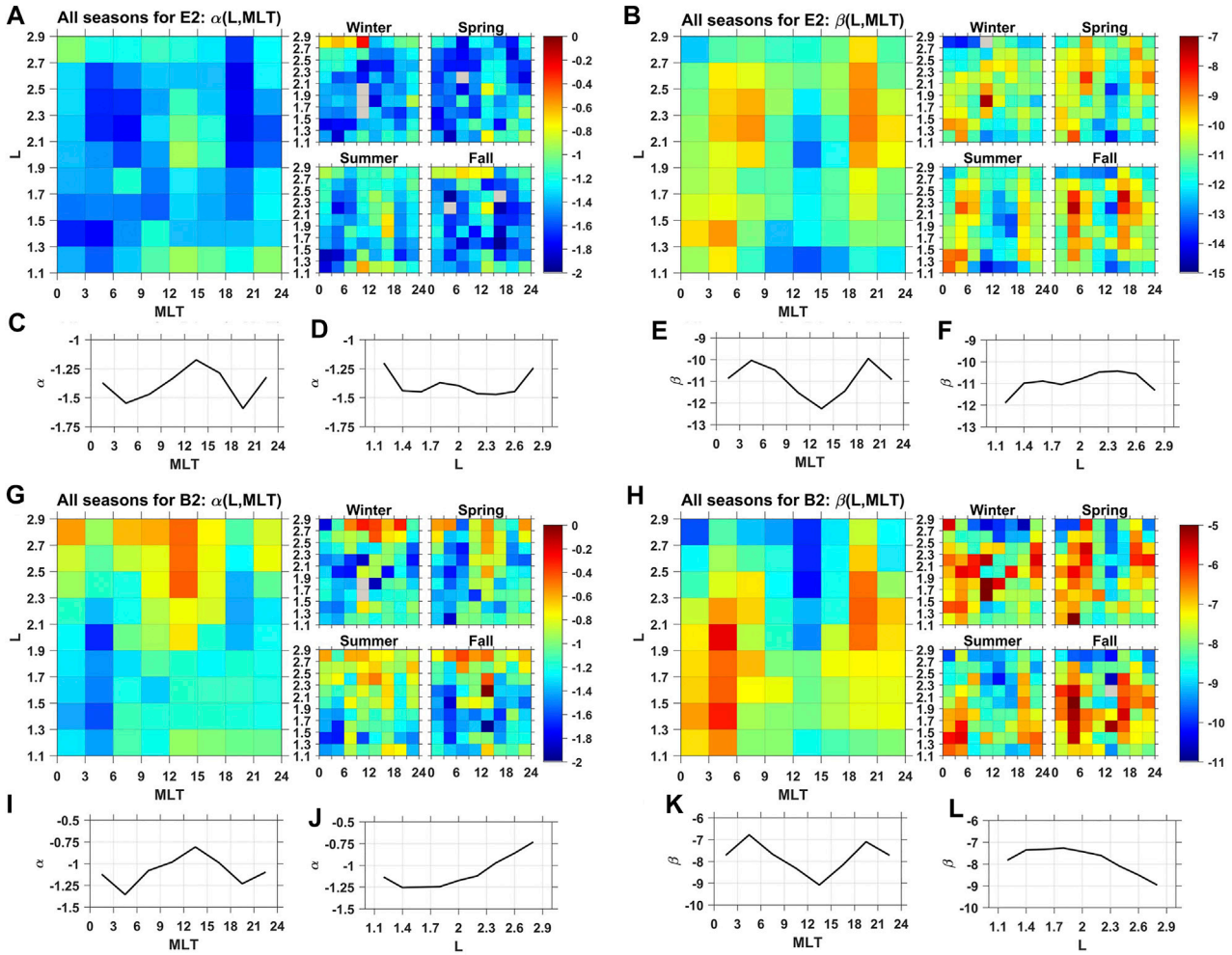


FIGURE 3 | (A–F) Electric and **(G-I)** magnetic attenuation law parameters **(A,G)** α and **(B,H)** β parameters of the attenuation laws for **(A,B)** (E^2/W) **(D)** and **(G,H)** (B^2/W) **(D)** attenuation laws. Unidimentional plots show the average with respect to **(C,E,I,K)** L-shell and **(D,F,J,L)** MLT of the **(C,D,I,J)** α and **(E,F,K,L)** β parameters. Decay of E^2/W follows more a quadric law, with ~−2<α<~−1 (blue to green in a). Decay of B^2/W follows more a linear law, with ~−1<α<~0 (green to red in g). Day/night difference is well-marked. The α and β parameters behave oppositely in MLT as shown in **C,E,I,K**.

simultaneously and be above their respective SNR thresholds. This reduces the time period of the data to November 1, 2012 to May 31, 2018 for Probe B and to November 1, 2012 to June 30, 2016 for Probe A. Taking then both electric and magnetic power above SNR reduces the data to 1,781,179 measurements (~20% of the wave power database). Such a large reduction in number is expected due to the low number of lightning-generated VLF waves in space caused by their natural occurrence rate on Earth, explaining the large number of values having low SNR. Lightning occurrence rate is seven stroke per second according to WWLLN (e.g. [22]), which measures the strongest strokes reaching space, and ~7 times more (~50 #/s) observed by the Lightning Imaging Sensor on board the TRMM satellite (e.g., [20, 39]). The mean amplitude of the electric field measurements that pass the planarity and SNR thresholds is 48.1 μV/m, with a standard deviation of 132 μV/m and median of 28.5 μV/m. The minimum (threshold) electric field amplitude associated with the noise level is 2 μV/m (cf [32]. for the noise floor definition).

TABLE 2 | electric and magnetic field threshold values and number of electric and magnetic field data for a given percentile of the data.

Percentile	E (μV/m)	#E data	B (pT)	#B Data
1	2.33	18,278	0.57	8,995
5	3.12	91,489	0.65	44,963
25	8.03	457,483	1.25	224,994
50	17.18	915,027	2.30	449,996
75	36.38	1,372,585	4.37	675,017
95	114.9	1,738,606	11.67	855,031
99	281.4	1,811,812	27.41	891,034

The sample mean of the magnetic field distribution is 3.77 pT with a standard deviation of 6.23 pT and the median is 2.16 pT. The minimum (threshold) magnetic field amplitude associated with the noise level is 0.5 pT. Differences between these sample statistics and the ones in Ripoll et al. [19] are due to 1-the change

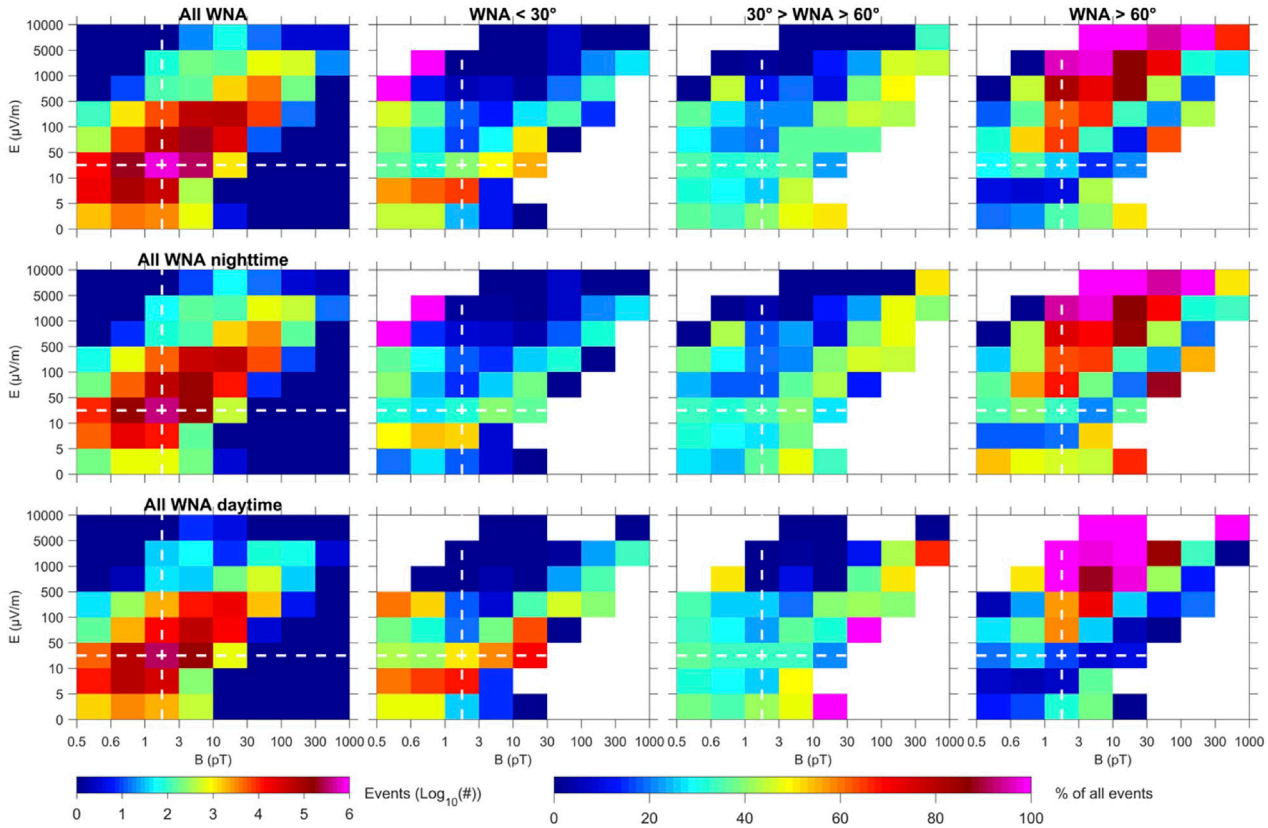


FIGURE 4 | Distributions of the wave-normal angle with respect to electric field and magnetic field amplitudes for (column 1) all ($0° \le \overline{\theta} < 90°$), (column 2) low ($\overline{\theta} \le 30°$), (column 3) moderate ($30° < \overline{\theta} \le 60°$), and (column 4) large ($\overline{\theta} > 60°$) wave normal angles and for (row 1) all times, (row 2) nighttime only, and (row 3) daytime only. (1 column) numbers of data is plotted while (two to four columns) the percentage of data is shown. While lines indicate the mean of the all times and all wave normal angle data in the top left corner. These white lines are replicated on all plots for facilitating the comparisons.

of planarity threshold from 0.2 to 0.5 (without great impact), two-the absence of considering the zeros (measurements with data below the SNR threshold) for both E and B (i.e. the sample statistics in this article are conditioned on the signals passing the SNR threshold whereas the statistics in the previous work are not) in order to be able to compute the wave-normal angle. The last change causes the mean magnetic power to be ~3 times larger on average than in Ripoll et al. [19]. Percentile and associated values of the statistics are given in **Table 2**.

The wave normal angle as a function of frequency for a single wave is further processed by integration over frequency, from f_{min} = 2 kHz to f_{max} = 12 kHz, using a power weighted integral, $\overline{\theta} \sim \int_{f_{min}}^{f_{max}} \theta(f) P_B(f) df$, with P_B the LGW magnetic power spectral density (e.g. [40]).

Figure 4 bins the power-averaged wave normal angle ($\overline{\theta}$) statistics sorted per bins of both by the root-mean-square (rms) electric and magnetic field amplitude for all ($0° \le \overline{\theta} < 90°$), low ($\overline{\theta} \le 30°$), moderate ($30° < \overline{\theta} \le 60°$), and large ($\overline{\theta} > 60°$) wave normal angle. The mean of the distribution (computed at all times and all $\overline{\theta}$) is shown with a white dashed line. The peak of the distribution is always far from the noise level. There is a shift up of the diagonal of the distribution toward higher E for higher wave normal angle compared with the lower wave normal angle distribution that we will comment on more below. Waves with larger E are more numerous at large wave normal angle. The distributions indicate a similar behavior during day and night, with two competing effects. Propagation is facilitated during nighttime due to the lower local electron density but lightning activity is reduced (the maximum of lightning activity is from 14 to 19 local time). Propagation is reduced during daytime but lightning activity is maximal (e.g. [15]). For instance, WWLLN total lightning energy for the 2018 years is reparteed in 38% for nighttime and 62% for daytime, with a similar averaged energy per flash ratio during the day. Further analysis is required to better understand the trends of these distributions. **Figure 5** shows the wave normal angle ($\overline{\theta}$) distributions sorted by bins of (left) electric and (right) magnetic amplitudes. This is equivalent to the sum of the values of **Figure 4** along one axis, while increasing wave normal angle resolution to 1°. The peak distribution is reached for amplitudes that are much larger than the noise level. **Figure 5**(left) shows LGW with large electric amplitudes have a large wave normal angle and LGW with small electric amplitudes have a rather small wave normal angle. This means the wave becomes more electrostatic as its wave normal angle increases, which is consistent with expected whistler-mode wave behavior in cold plasma wave theory [41].

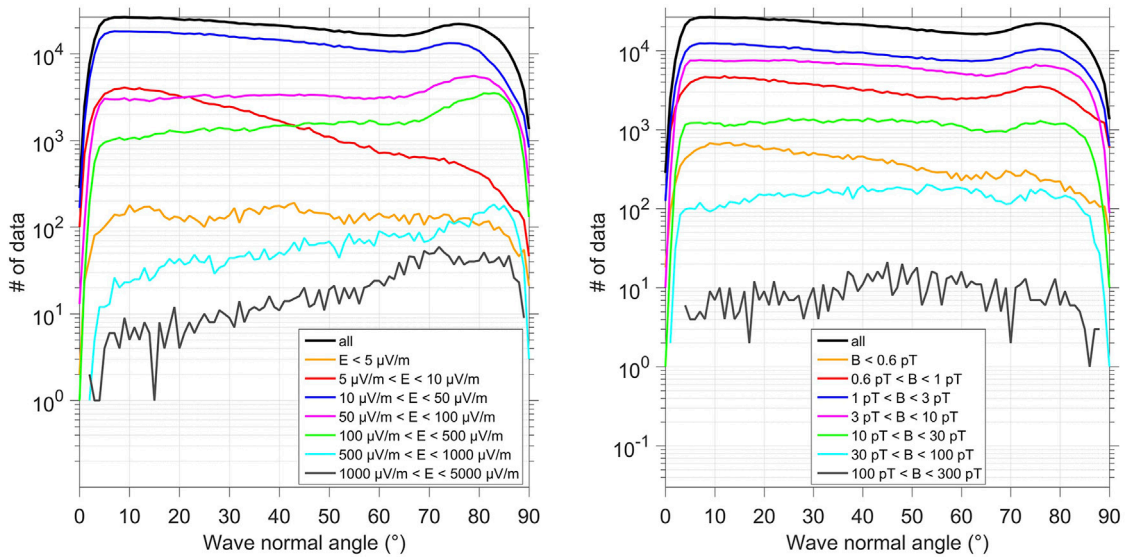


FIGURE 5 | Distribution (log10) of wave normal angle values sorted with respect to (left) the electric amplitude and (right) the magnetic amplitude for different bins of amplitude.

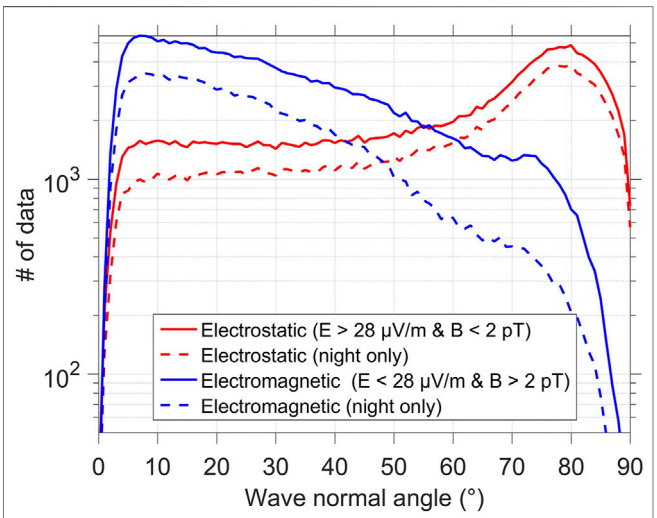


FIGURE 6 | Distribution (log10) of wave normal angle values for (red) electrostatic and (blue) electromagnetic waves. Electrostatic (electromagnetic) waves are more oblique (field-aligned). Dashed line is the distribution for nighttime only.

The situation with the magnetic amplitude is not as simple. LGW with small magnetic amplitudes were expected to be quasi-parallel or less oblique. We do see a main peak of small wave normal angle for the small magnetic amplitude waves. However, the distribution also shows a second peak of oblique waves for small magnetic amplitudes. The first peak is centered at 5–20° while the second peak is centered at 75°. Conversely, LGW with large magnetic amplitudes were expected to have a small wave normal angle. They rather have a distribution spread toward a broad range of wave normal angles. Thus, as the wave becomes electromagnetic, the wave normal angle distribution is peaked at small wave normal angle but also has a second peak at large wave normal angle.

To further investigate the variation of the wave normal angle with respect to the wave properties, we determine the statistics of electrostatic waves, defined such that their electric amplitude is large, i.e. values are above the 50 percentile (cf. **Table 1**), and their magnetic amplitude is small, i.e. values are below the 50 percentile. Similarly, we define a subpart of electromagnetic waves such that they have a large magnetic amplitude (above the 50 percentile) and a small electric amplitude (below the 50 percentile). These two double conditioned distributions are presented in **Figure 6**. Note also for the discussion on the refractive index in section 3.3 that the electrostatic limit implies a low refractive index (low B/E ratio) and the electromagnetic waves with both large/small magnetic/electric amplitudes implies a high refractive index (large B/E ratio). **Figure 6** unambiguously shows large wave-normal angles are preferred for electrostatic waves. Conversely, electromagnetic waves with a large magnetic amplitude and small electric amplitude primarily have small wave-normal angles. However, the plots in **Figure 6** represent only a small portion of the total data: 11% of the waves are electrostatic and 13% are electromagnetic waves using the definition above. The distributions of **Figure 5** are thus made more complex by inclusion of data for which E and B are both of the same order (as shown in **Figure 4**). In other words, electrostatic LGW are more oblique and electromagnetic LWG are more field aligned. Another quantity to explore is the proportion of electrostatic waves at day and night. The dashed-line distributions of **Figure 6** show 75% of electrostatic waves occur for nighttime and 43% of the electromagnetic waves

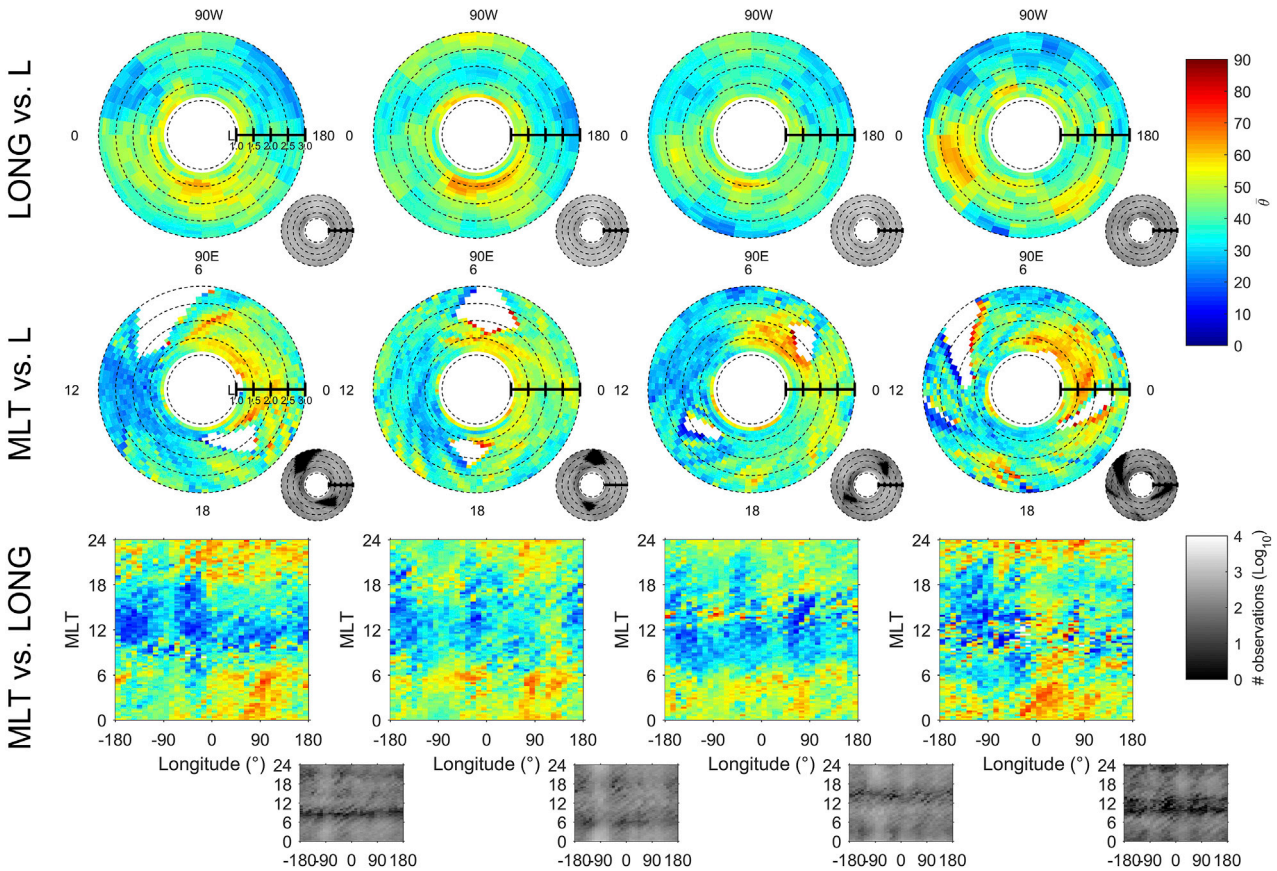


FIGURE 7 | Column table of graphic pairs. Each pair has a large map depicting the Van Allen Probes mean wave-normal angle ($\bar{\theta}$) of lightning-generated whistlers (in °), a lower right auxiliary map depicting the Probes coverage in number of observations. Columns correspond to four seasons (with M/A/M for March/April/May, etc.), and rows show the wave normal angle marginalized over MLT (i.e. plotted versus longitude and L-shell), longitude, and L-shell respectively.

with a large magnetic power and small electric power occur for daytime. These nighttime distributions determine the shape of the total distribution with respect to wave-normal angle. For daytime (not shown), and although either the electric or magnetic component are above the average value, the distribution develops a small tail of the opposite behavior with respect to wave normal angle. This signifies the dense daytime atmosphere complicates the distributions. With about twice more lightning for daytime than for nighttime, one reason could be that more different waves are locally mixed and sensed.

Full statistics are presented in **Figure 7** with a column table of graphic duos. Each duo has a large map depicting the Van Allen Probes mean wave normal angle and a lower right auxiliary map depicting data coverage. Columns correspond to four seasons, and rows show the Van Allen Probes mean wave normal angle marginalized over MLT (i.e., plotted versus longitude and L-shell), longitude, and L-shell, respectively. Statistics are generated per 10° longitude, 0.1L, 3 months, and 0.25 MLT. Such statistics can directly be used in the computation of pitch angle diffusion coefficients (e.g. [7]; [40]; [49]) that are used afterward in Fokker-Planck codes for space weather predictions.

Although **Figure 7** presents average values, the high (L, MLT, s) resolution of **Figure 7** is auspicious for event-driven simulations of pitch angle diffusion (e.g. [40, 42, 51]) as one can choose the average conditions for an event occurring at a given (L, MLT) for a given season.

Wave normal angles cover the whole range from 0 to 90° in **Figure 7**. White regions are the rare regions not covered during the ~7 years of the Van Allen Probes mission. Assuming a zero wave-normal angle (as in **Eq. (3)** of [6]) in the conversion from CRRES electric to magnetic field to generate LGW magnetic power cannot be justified from the simple observation point of view. Larger wave-normal angles are found at lower L-shells (but not only), with an overall complex L-shell dependence. Larger wave-normal angles at lower L-shells seem to be consistent with the magnetic field being more oblique to the ionospheric density gradient at lower L. Over America (90 W°), the wave normal angle is rather field aligned, mostly below 40° for L > 1.5, with smaller values in winter and larger in summer (**Figure 7** top row). On the contrary, wave normal angles are large over Africa (20 E°) and Asia (120 E°) in winter. The strong diurnal dependence with the wave normal angle smaller for daytime is the most apparent

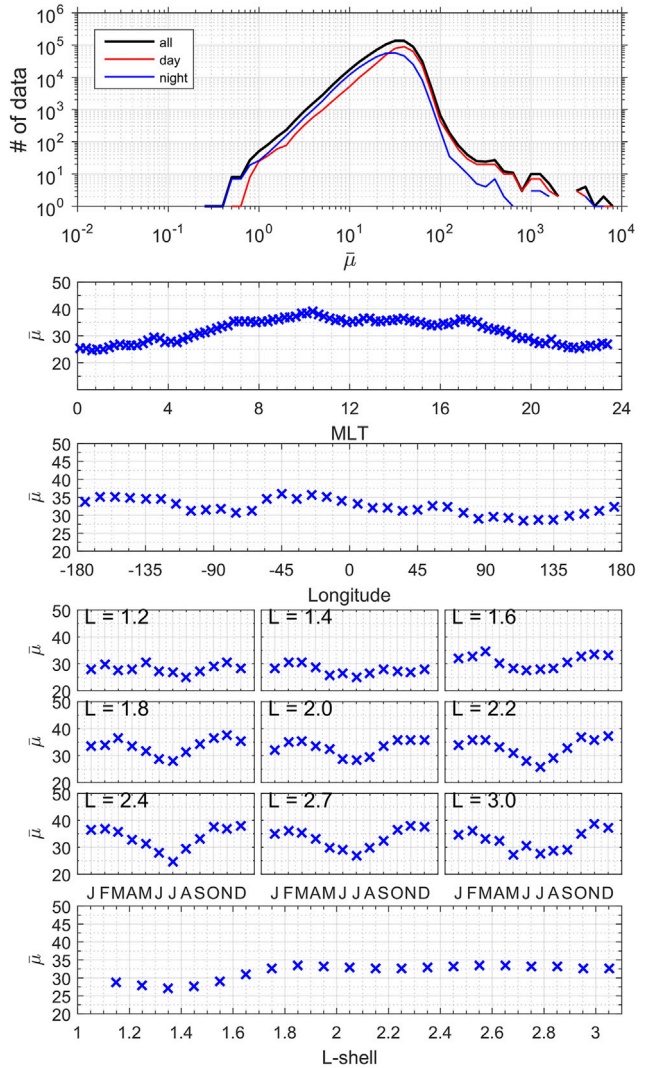


FIGURE 8 | (first panel) Distributions of the wave normal angle (WNA) (in °) at (red) day (6–17 ML T), (blue) night (18–5 ML T), (black) all times. Wave normal angle is plotted versus (second panel) MLT and (third panel) longitude. The day/night differences appear clearly but not the continental dependence (fourth panel) Monthly and (fifth panel) total average of wave normal angle versus L-shell. No simple seasonal dependence is found.

variation (**Figure 7** middle and bottom rows). This is confirmed in **Figure 8** in which more global averages are plotted. Daytime LGW (6–17 MLT) are more field-aligned and nighttime LGW (18–5 MLT) are more oblique, by up to 20° on average. The statistics is oriented toward smaller wave normal angle on average for daytime since we just showed (cf. **Figure 5**) that small electric amplitude of LGW are predominantly field aligned. Wave normal angles of LGW are similarly larger during nighttime because larger electric amplitude are propagated in space during the night (cf. **Figure 1** in [19]), which shifts the wave normal angle statistics toward large wave normal angles (from **Figure 5**). Next section will address the variation of B/E. The fact that the LGW wave normal distribution sorted by magnetic amplitude has two peaks seems to indicate that the magnetic amplitude does not strongly correspond to the value of the wave-normal angle. The LGW mean wave-normal angle computed over the whole data set is 41.6° (34.4° at day and 46.7° at night), a ~12° difference between day and night on average, and its median is 39.1° (29.7° at day and 47.3° at night). The standard deviation is: 24.5° (22.8° at day and 24.6° at night).

There is an absence of strong seasonal dependence of the wave-normal angle in **Figures 7**, **8**. This should be compared with the dependence of E (and B) shown in **Figure 1** (and 2) of Ripoll et al. [19], where it was shown that a seasonal dependence is evident for the electric amplitude, with larger electric amplitude during Northern hemisphere summer. This earlier work might lead one to expect larger wave normal angles in Northern hemisphere summer. We do see larger wave normal angle in Northern hemisphere summer at some L-shells ($L \leq 1.4$ and for $L \geq 2.7$), but not all of them. The seasonal dependence of the magnetic amplitude is much weaker than the electric amplitude, with only a slight increase in Northern hemisphere summer (cf. **Figure 2** in [19]). The combination of both leads to wave-normal angle statistics without an emerging clear seasonal dependence.

The continental dependence is well marked for both the LGW electric and magnetic amplitudes with larger amplitudes over the American (90 W°), African (20 E°), and Asian/Australian continents (120 E°) (**Figures 1**, **2** of [19]). Both electric and magnetic amplitudes being large over continents, this cannot skew the wave-normal angle statistics predominantly toward either large or small wave-normal angles. This causes an undetermined behavior of the wave normal angle statistics over continents in **Figure 7** with LGW wave normal angle that can be as large over seas than over land.

Statistics of the Refractive Index of Near-Equatorial Magnetospheric Plasma When Lightning-Generated Whistlers are Observed by the Van Allen Probe

The refractive index, μ, is defined by $\mu(\omega, \theta, L) = c \times k\,(\omega, \theta, L)/\omega$, where θ is the wave normal angle, c is the speed of light, k is the wave number, and $\omega = 2\pi f$ is the wave pulsation for a frequency f [41]. In general and using cold plasma theory, the refractive index is only expressed in terms of the ambient plasma density, Ne(L), in which a wave of frequency, f, travels with a wave normal angle θ(f) within a given background magnetic field. That way $\mu = \mu(f, \theta, Ne(L))$ with μ that is proportional to Ne(L). The refractive index is then determined from the ambient media only and whistler-mode wave electric and magnetic components can be computed, for instance, by ray tracing (e.g. [3]). Thanks to cold plasma theory, the refractive index of whistler-mode waves can also be written as a function of E and B when the wave is known. Such refractive index becomes then a probe of the local environment. For parallel waves, $\theta(f) \sim 0$, the refractive index can simply and equivalently be computed as μ(f)~B(f)/E(f) (in cgs units), with B (in G) = 10^{-5} B (in pT) and E (in statvolt/cm) = $1/3 \times 10^4$ E (μV/m).

Here, we will compute $\overline{\mu} = \overline{B}/\overline{E}$ in which $\overline{E}$ and $\overline{B}$ are the LGW electric and magnetic amplitude used in the computation of the wave-normal angle, i.e. the electric (magnetic) power spectral

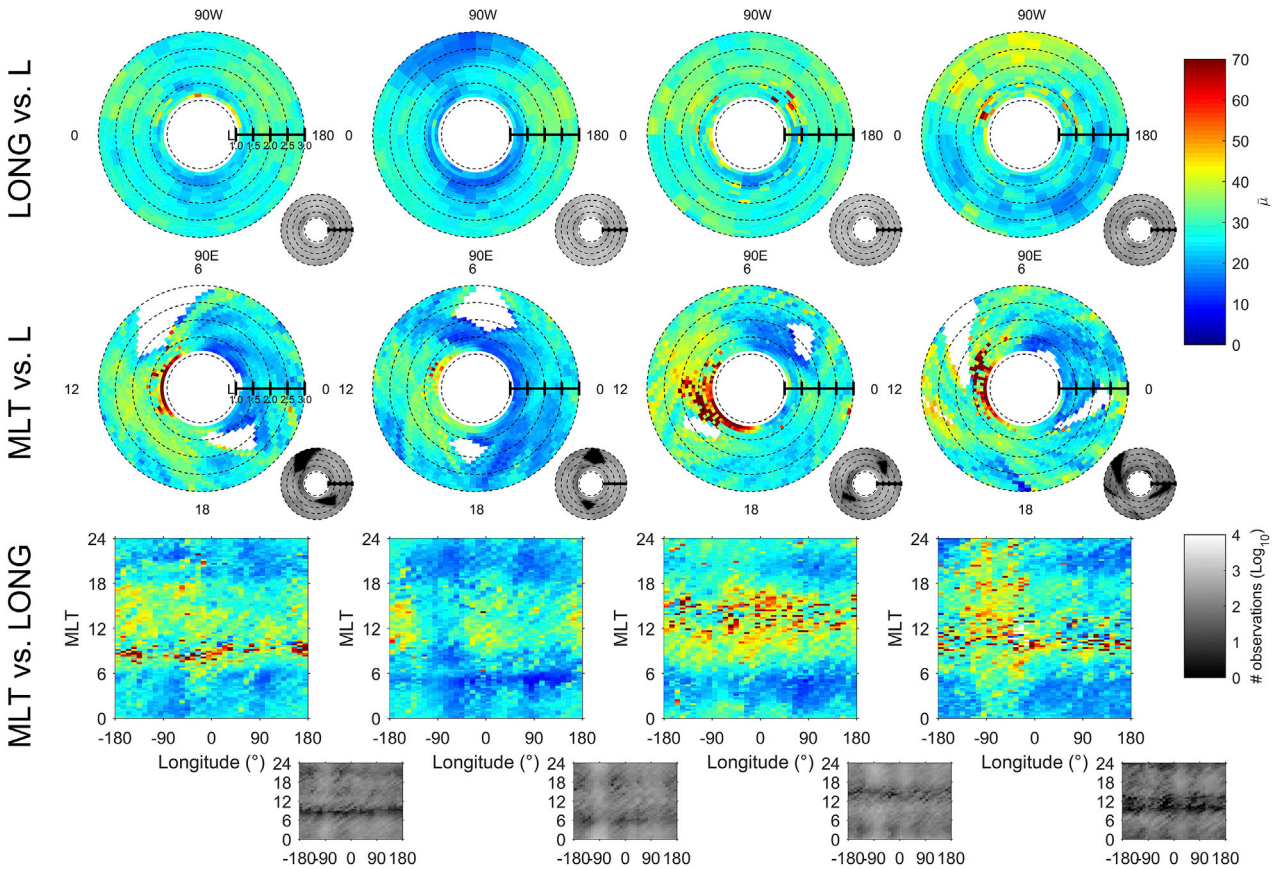


FIGURE 9 | Column table of graphic pairs. Each pair has a large map depicting the Van Allen Probes refractive index, $\overline{\mu}$, and a lower right auxiliary map depicting the probes coverage in number of observations. Columns correspond to four seasons (with M/A/M for March/April/May, etc.), and rows show the Van Allen Probes refractive index marginalized over MLT (i.e., plotted versus longitude and L-shell), longitude, and L-shell, respectively.

density of a given LGW integrated from 2 to 12 kHz. The variation with respect to frequency is thus removed. Therefore, the refractive index we discuss here is representative of mean LGW, with a mean frequency between 2 and 12 kHz. If readers are uncomfortable with this approximation, they can simply consider that this section discusses the ratio of B with E of the LGW studied in section 3.1 and 3.2 in order to establish how/why/when this ratio evolves and correlates with the variation of wave normal angle and the propagation parameters α and β. In order to guarantee the validity of the parallel approximation in the $\overline{\mu}$ expression, we also filter the previous E and B distributions to select only the (frequency-integrated) wave normal angle, $\overline{\theta}$, below 30°, for which $\overline{\mu} = \overline{B}/\overline{E}$ is appropriate. This lowers the number of measurements to 688,613, which remains high enough to produce statistics.

The advantages of selecting only field aligned waves is double. First, the law is significantly more complex for general wave-normal angles as it involves the full dispersion relation [41]. Second, the validity of the SVD method requires the plane wave approximation, which does not apply for large wave normal angle [38]. This leads to the choice of computing the refractive index only for small wave normal angles. The refractive index statistics presented and discussed in **Figures 9**, **10** below constitute an improvement of the refractive index published in the Supplementary Information of Ripoll et al. [19] (Figures S4 and S5) in which the refractive index was also computed with the use of μ~B/E but without filtering for small wave-normal angle because wave-normal data was unavailable at that time. Comparing both allows to understand the bias caused by large wave-normal angle in the statistics of Figures S4 and S5 of Ripoll et al. [19].

Refractive index statistics are presented with respect to (L, MLT, Longitude, seasons) in **Figure 9** (same format as **Figure 7**). The most apparent difference is the diurnal dependence. There is larger refractive index for daytime than for nighttime (**Figure 9**, middle/bottom rows), with highest indexes in Northern hemisphere Fall for daytime. This is consistent with μ~Ne(L) and a higher electron density for daytime. There is no clear continental dependence visible in **Figure 9** (both E and B that are large over continents). Largest refractive indexes are found over the continental North America

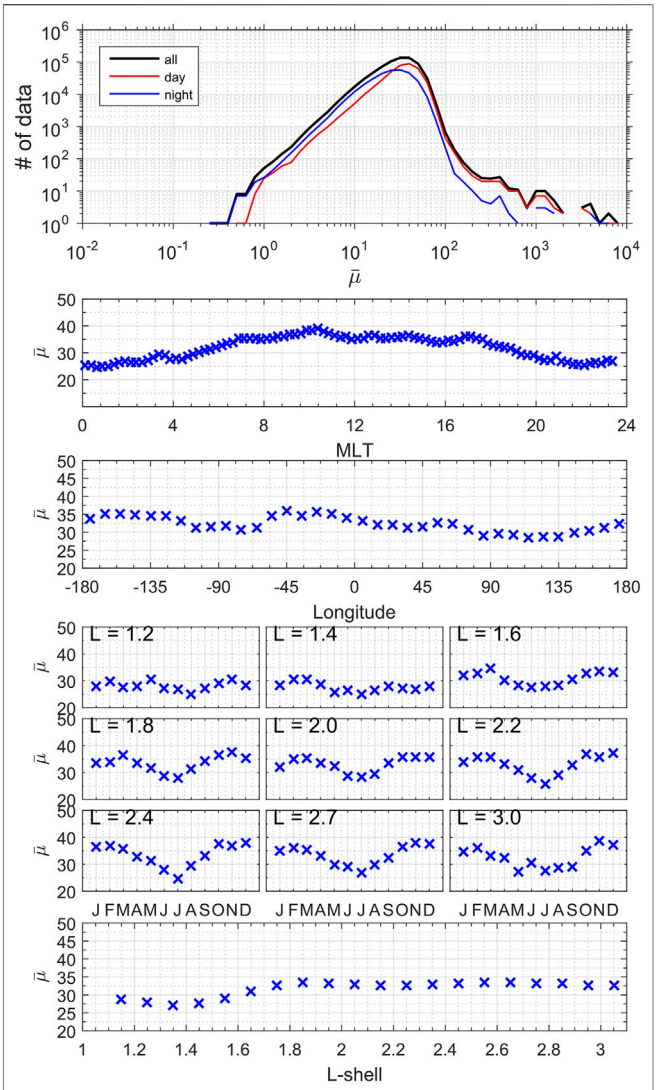


FIGURE 10 | (first panel) Distributions of the refractive index ($\bar{\mu}$) at (red) day, (blue) night, (black) all times. Refractive index is plotted versus (second panel) MLT and (third panel) longitude (fourth panel) Monthly and (fifth panel) total average of wave normal angle versus L-shell.

and its coastal regions (20–120 W) during winter (**Figure 9** first row) and smallest refractive index are found over the same geographic region during summer. If one expects higher electron density in Northern hemisphere summer than in Northern hemisphere winter from Chapman ionization theory, this result is inconsistent with μ~Ne(L). However, this result becomes consistent with what is referred as the winter anomaly. The winter (a.k.a seasonal) anomaly occurs when the electron density in the F_2 layer of the ionosphere is not controlled by the solar zenith angle, which leads to an electron density abnormally greater in winter than in summer, as we observe. This anomaly is widely reported in the literature (e.g. [43] and references in it; [44, 45]). The winter anomaly is stronger during solar maximum period and almost nonexistent at solar minimum [46], with our data (2012–2018) covering indistinctly a range of solar activity (solar maximum from 2012 to 2016).

Figure 10 presents more global statistics (same format as **Figure 8**). The mean refractive index of LGW varies between 25–30 at night and 40–45 at day, consistent with μ~Ne(L). For comparison, refractive indexes between 10 and 100 are considered for LGW in Bortnik et al. [3]. There is a well-marked seasonal variation with smaller refractive index (by a factor ~1.5–2) during summer for L-shells above 1.8. An extremum in summer is consistent with the LGW electromagnetic power which peaks in August (L ≥ 1.8) and Earth lightning activity. However, a minimum of refractive index during summer is only consistent with the seasonal anomaly discussed above. The mean continental dependence remains complex but it shows local minima, between ~30 and ~35 are reached over the three continents, at 90W°, 20 E° and 120°E. The mean annual refractive index shows two regimes of variation with respect to L-shell. There is first a decay with respect to L-shell decreasing for L-shells below 2. This decay has to be related to the observed decay of both E and B at L < 2 (**Figure 3** in [19]) that is attributed to a difficulty of lightning VLF waves to penetrate, or/and to propagate, or/and to remain at low L-shells. The mean refractive index also decays with respect to L-shell increasing from L = 2 to L = 3 as both E and B do [19]. Mean refractive index computed over the whole data set is 32.2 (35.7 at day and 28.0 at night) with a standard deviation of 26 (27.3 at day and 23.6 at night). Median refractive index is 30.1 (34.9 at day and 26.2 at night).

DISCUSSION

This section is devoted to the cross-comparison of the above quantities based on the recognition that both L and MLT are determinant parameters in order to perform a synthesis of the various observations. **Figure 11** represents the wave normal angle and the refractive index on a (MLT,L) grid similarly to the attenuation laws shown in **Figure 3**. Plotting the refractive index as a function of the wave normal angle for a given (MLT,L) bin in **Figure 11** (bottom) shows a distinct high anti-correlation between both, with a high Pearson correlation coefficient R^2 = -80% (-89% if waves below L = 1.3 are excluded), with small wave normal angle found at large refractive index (or equivalently large ratio of B over E) and vise-versa. This is consistent with the limits discussed in section *Electric and Magnetic Wave Power Attenuation Laws*: the electrostatic limit implies a low refractive index and had a distribution peaked at large wave-normal and the limit of electromagnetic waves with both large/small magnetic/electric amplitudes implies a high refractive index and had a distribution peaked at large wave-normal (cf. **Figure 6**). This means the peak of distribution of electrostatic waves will fall in the lower right corner (small $\bar{\mu}$, large $\bar{\theta}$) of **Figure 11** while the peak of distribution of electromagnetic waves with both large/small magnetic/electric amplitudes falls in the upper left corner (large $\bar{\mu}$, small $\bar{\theta}$) of **Figure 11**. The coloring by MLT or L-shell shows that data are better organized with MLT than with L-shell. **Figure 11** also shows the LGW energy density defined as

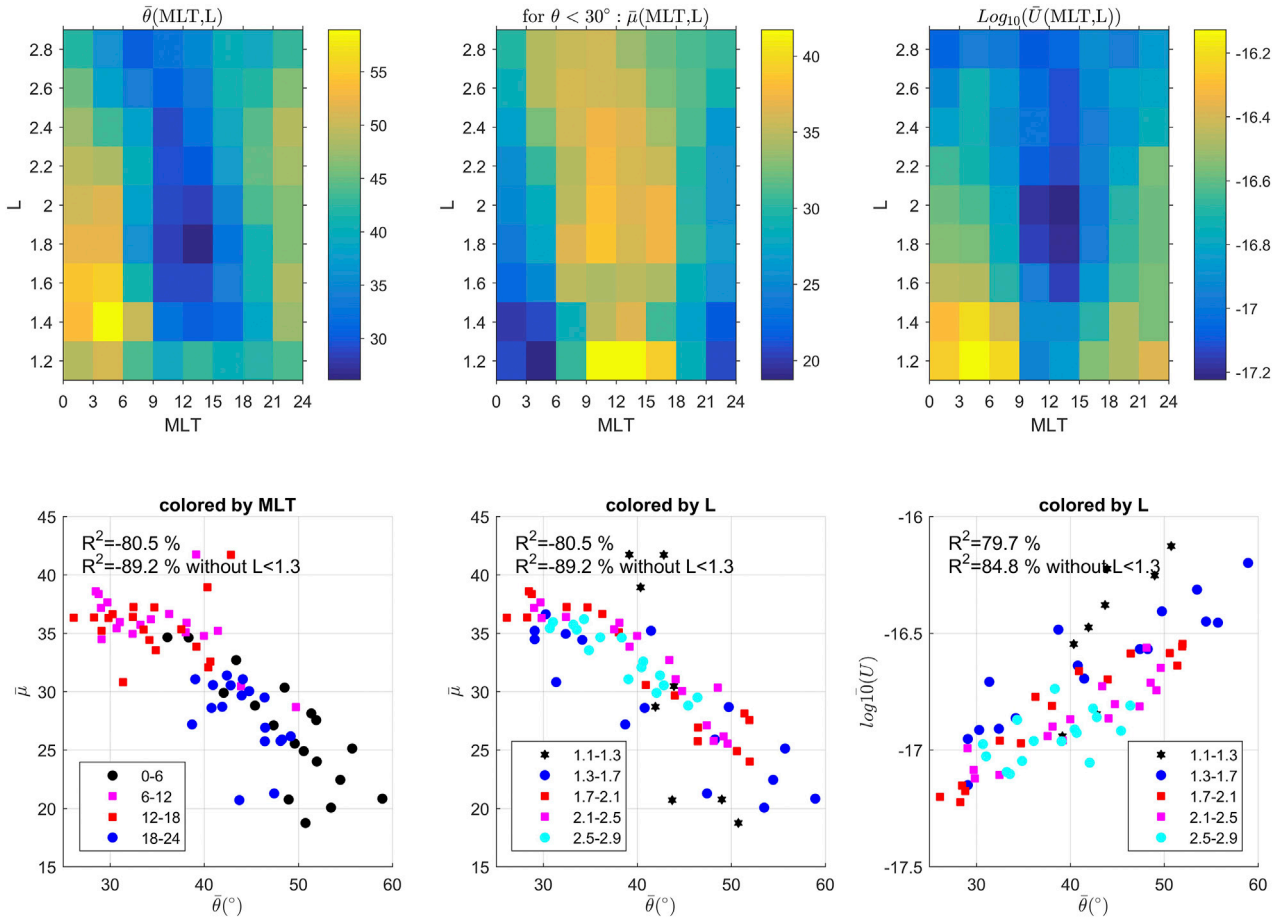


FIGURE 11 | (top, left) Wave normal angle ($\bar{\theta}$), (top, center) refractive index ($\bar{\mu}$), and (top, right) wave energy density (U) binned by (MLT, L) (bottom) refractive index as a function of wave normal angle (for a given (MLT, L) bin colored by (left) MLT and (center) L-shell. Dark colors (blue and black) are used for night sectors and low L-shells. There is a high anti-correlation (-80%) between $\bar{\mu}$ and $\bar{\theta}$, with small wave normal angle at large refractive index and vise-versa. The peak of distribution of electromagnetic waves with both large/low magnetic/electric amplitudes will fall in the upper left corner. The peak of distribution of electrostatic waves will fall in the lower right corner (bottom, right) LGW energy density as a function of wave normal angle for a given (MLT, L) bin colored by L-shell. There is a high correlation (-80%) between $\bar{U}$ and $\bar{\theta}$, with small wave normal angle at low energy density and vise-versa.

$\bar{U} = \frac{1}{2}(\varepsilon_0 \bar{E}^2 + \bar{B}^2/\mu_0)$, with higher energy density at night and at low L-shell. There is a high correlation (-80%) between $\bar{U}$ and $\bar{\theta}$ with small wave normal angle at low energy density and vise-versa, therefore an anti-correlation of $\bar{U}$ and $\bar{\mu}$. The coloring by L-shell indicates lowest L-shell have preferably high wave-normal angle and high energy density.

Figure 12 shows the α and β parameters of the power law attenuation generated in section 3.1 plotted with respect of wave-normal and the refractive index, with the Pearson correlation coefficient given. The two first row of **Figure 12** show the same data as the two last rows of **Figure 12**, with only the color code changing to illustrate the (top) L-shell and (bottom) MLT dependence.

Some correlations and anti-correlations are visible although the Pearson coefficients are much smaller. On average, the Pearson correlation in **Figure 12** is 45%. Limiting the data to above L = 1.3 and below 2.7, the mean Pearson correlation between the α and β parameters and the wave normal angle increases to 53% but it remains at 42% for the refractive index. The correlation coefficients therefore deteriorate below L = 1.3, which have their own regime, and by the winter anomaly affecting the refractive index. Limiting the refractive index to low wave normal angle may also deteriorate the correlations. These overall low correlation factors indicate no direct and strict correlations between the (α, β) parameters and the ($\bar{\mu}$, $\bar{\theta}$). However, the consistent behavior of these quantities with both MLT and L-shell make them related and with apparent trends visible in **Figure 12**.

Figure 12 shows large absolute values of the β scaling factor occurring for daytime (more attenuation) are correlated with large refractive index and anti-correlated with small wave normal angles. Small absolute values of the β scaling factor occurring for nighttime (less attenuation) are correlated with small refractive index and anti-correlated with large wave normal angles.

The α power factor, which attenuates more the wave for large absolute values, shows opposite correlations to the β scaling factor. The large absolute values of the α power factor

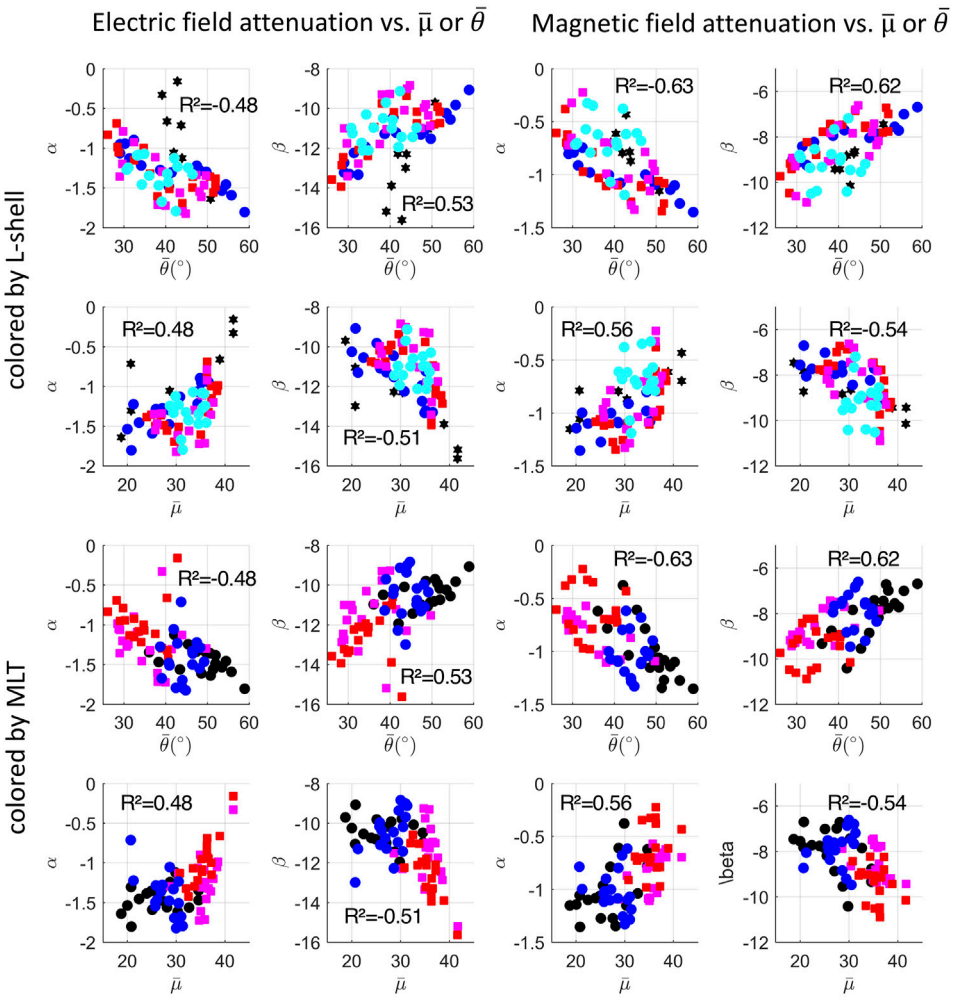


FIGURE 12 | (four left of two first rows) Electric and (four right of two first rows) magnetic α-β-parameters of the attenuation laws plotted with respect to (first row) the wave normal angle and (second row) the refractive index colored by (2 first row) MLT. (2 last rows) Figures of the two first rows are repeated but colored by L-shell. Pearson correlation coefficient R^2 is given for each figure. Colored codes are given in **Figure 10** with dark colors for night sectors and small L-shells.

occurring for nighttime (more attenuation) are correlated large refractive index and anti-correlated with small wave normal angles. Small absolute values of the α power factor occurring for daytime (less attenuation) are correlated with small refractive index and anti-correlated with large wave normal angles. As discussed above, the α power factor behave inversely to what could be expected with more attenuation at night than at day, but with a law that matches the attenuation behavior on Earth at night. Nevertheless, we can conclude high attenuation (regardless if caused from large absolute values of either the β scaling factor for daytime or the α power factor for nighttime) is more correlated with large refractive index and more anti-correlated with small wave normal angles. Correspondence between large (low) refractive index with large (low) attenuation is consistent with μ~Ne(L). This means the winter anomaly, which exists in our statistics (cf. section 3.3), is not strong enough in order to reverse the global dependence (but likely contributes to lower the Pearson correlation coefficients). Interestingly, using a single constant d_{max} of 5,000 km or 7,000 km (results not shown) causes to include a flat tail (more pronounced for complex (L, MLT) regions) which lowers the slope of the fits and increases the role of (L, MLT). As a consequence, the (α, β) parameters vary more within their respective range and all the Pearson correlation coefficients of **Figure 12** increase by +10% on average. This confirms the correlation coefficients only illustrate the consistent dependence of all quantities with respect to (L, MLT). Finally, deducing an effective ambient plasma density from the computed refractive index is possible. First attempts show the obtained density falls in the range of commonly known values (e.g. [47, 48]) and this subject is left for another contribution.

CONCLUSION

We presented the analysis of propagation, attenuation, and dispersion of lightning-generated whistlers (LGW) observed

from the two spacecraft of the NASA Van Allen Probes mission, from 2012 to 2019, through the statistic of three specific quantities; the (electric and magnetic) LGW power decay with distance from the lightning source, the LGW wave-normal angle, and the LGW refractive index.

Attenuation (power) laws of both the electric and magnetic field power of LGW, E^2/W and B^2/W, rescaled by the WWLLN-estimated lightning energy, W, are derived. We conserve the L-shell, magnetic local time (with MLT ~ LT), and seasonal dependences in these laws as these parameters are highly influential, which generalizes existing global laws (23, 27, 28, 50). The derived attenuation laws (**Eq. (2)** with parameters given in **Figure 3**) can serve to provide a prediction of LGW power present in space (near the equator) for a source of energy (*W* in kJ) located at *d* km away from the closest satellite magnetic footprint. These laws are also useful to derive the mean lightning power in space over a drift period at constant L-shell as done with Burkholder's law in [22]. We find that the LGW electric power decays mostly quadratically in space, with $\alpha(L, MLT, s)$ in **Eq. 2** varying between $\alpha = -1$ and $\alpha = -2$, while the magnetic power decays mostly linearly in space, with $\alpha(L, MLT, s)$ varying between $\alpha = 0$ and $\alpha = -1$. At night, E^2 decays as a quadratic law and B^2 as a linear law, which is consistent with ground measurements (cf. section *Electric and Magnetic Wave Power Attenuation Laws*). This is the first time, to our knowledge, that the characterization of the magnetic power decay in space is performed. There is a strong attenuation of the (electric and magnetic) power during daytime (MLT = 9–18) due to the denser ionosphere, with a strong decay of the scaling factor of the power law (i.e. $log_{10}\beta$ in **Eq. (2)**). Power law complexity is maximal at the lowest L-shells ($L < 1.5$) and around noon, for which LGW are the rarest in Van Allen Probes measurements [19].

Statistics of the LGW wave-normal angle, i.e. the angle between the emitted wave and the Earth magnetic field line, which is a key parameter in the computation of pitch angle diffusion coefficients for radiation belt physics, are presented for the first time. We find that, as the wave becomes more electrostatic its wave normal angle increases. As the wave becomes electromagnetic, the wave normal angle distribution is peaked at small wave normal angle but also has a second peak at large wave normal angle. Predominantly electrostatic waves and electromagnetic waves with large magnetic amplitude and small electric amplitude are both well-identified at night. The distribution of electrostatic waves is peaked at large wave normal angle while the distribution of electromagnetic waves with large/small magnetic/electric amplitudes is peaked at small wave normal angle. LGW wave normal angles cover the whole range from 0 to 90°. The LGW mean wave-normal angle computed over the whole data set is 41.6° (34.4° at day and 46.7° at night) with a ~24° standard deviation. The strong diurnal dependence is the clearest dependence, with the wave normal angle smaller for daytime. There is an absence of strong seasonal and continental dependences of the wave-normal angle in comparison with the well-marked dependence of both the Van Allen Probes electric and magnetic amplitude with seasons/continents.

We also analyze the statistics of an approximated LGW refractive index (frequency integrated), with this quantity computed for the first time with the knowledge of the wave-normal angle, which allows to compute $\overline{\mu} = \overline{B}/\overline{E}$ only where this expression is valid, i.e. for small wave normal angles (<30°). Mean LGW refractive index is 32 with a standard deviation of ~26. The most apparent difference is the diurnal dependence, with larger refractive index for daytime (36 on average) than for nighttime (28 on average), consistent with a refractive index proportional to the ambient electron density. However, there is a well-marked seasonal variation, with smaller refractive index (by a factor ~1.5–2) during summer for L-shells above 1.8, which is inconsistent with Chapman ionization theory and consistent with the so-called winter/seasonal anomaly. The mean continental dependence remains complex but it shows local minima, between ~30 and ~35 are reached over the three continents.

Cross-correlation established at fixed (MLT, L) bins shows that there is a direct high anti-correlation between wave normal angle and refractive index; large (small) wave normal angle anti-correlates with small (large) refractive index. We find overall low Pearson correlation factors (~50%) between the (α, β) parameters of the attenuation laws and the $(\overline{\mu}, \overline{\theta})$, which indicate no direct and strict correlations between attenuation and a given value of $(\overline{\mu}, \overline{\theta})$. However, there is a consistent behavior of (α, β, $\overline{\mu}$, $\overline{\theta}$) with both MLT and L-shell, which make them well related and with apparent trends. The MLT-coloring in **Figure 12** (dark colors for night) is, for instance, explicit of the different comportment we observe for daytime and nighttime. High attenuation (regardless whether it is caused by large absolute values of either the β scaling factor for daytime or the α power factor for nighttime in **Eq. (2)**) is correlated with large refractive index and anti-correlated with small wave normal angles. Correlation and anti-correlation show a smooth and continuous path from one regime (i.e. large wave normal angle, small refractive index, low attenuation) to its opposite (i.e. small wave normal angle, large refractive index, high attenuation), attesting of the great consistency of the variation, the data, and ultimately indicative of the measurements' quality from both probes of the Van Allen Probes over 7 years.

DATA AVAILABILITY STATEMENT

The datasets presented in this study can be found in online repositories. The names of the repository/repositories and accession number(s) can be found below: http://www.space.umn.edu/rbspefw-data/, https://emfisis.physics.uiowa.edu/data/index, https://www.rbsp-ect.lanl.gov/science/DataDirectories.php.

AUTHOR CONTRIBUTIONS

J-FR led the study, performed the data analysis, and wrote the manuscript. TF processed WWLLN and Van Allen Probes data, and performed the data analysis. DM treated the EFW and EMFISIS survey data and contributed to the analysis of Van Allen Probes data. GC contributed to the data analysis. GH and CK contributed to the quality check of EMFISIS data used in this

article. JW contributed to the quality check of EFW data. TF, DM, EL, GC, GH, CK, and JW contributed to writing of the manuscript through reviews and edits.

FUNDING

DM was supported for this work by NASA grant 80NSSC18K1034. The work of GSC was supported in part by the Defense Threat Reduction Agency (DTRA).

ACKNOWLEDGMENTS

The authors wish to thank the World Wide Lightning Location Network (http://wwlln.net), a collaboration among over 50 universities and institutions, for providing the lightning location data used in this paper. We thank the Satellite Situation Center Locator operated on-line by NASA for providing Van Allen Probes trajectories. This work was performed under the auspices of an agreement between CEA/DAM and NNSA/DP on cooperation on fundamental science. The authors acknowledge the International Space Sciences Institute (ISSI) and the participants in a 2020 ISSI workshop in Bern. The authors thank the entire Van Allen Probes team, and especially the EFW and EMFISIS teams for their support. The EMFISIS wave data (survey-mode magnetic and electric power and L4 wave normal angle) used in this work are accessible from https://emfisis.physics.uiowa.edu/data/index. The EFW wave data (survey-mode magnetic and electric power) used in this work are accessible from http://www.space.umn.edu/rbspefw-data/.

REFERENCES

1. Carpenter DL. Ducted Whistler-Mode Propagation in the Magnetosphere; a Half-Gyrofrequency Upper Intensity Cutoff and Some Associated Wave Growth Phenomena. *J Geophys Res* (1968) 73(9):2919-28. doi:10.1029/ja073i009p02919
2. Helliwell RA. Low-Frequency Waves in the Magnetosphere. *Rev Geophys* (1969) 7(1):2. doi:10.1029/rg007i001p00281
3. Bortnik J, Inan US, and Bell TF. Temporal Signatures of Radiation Belt Electron Precipitation Induced by Lightning-Generated MR Whistler Waves: 1. Methodology. *J Geophys Res* (2006) 111:A02204. doi:10.1029/2005JA011182
4. Abel B, and Thorne RM. Electron Scattering Loss in Earth's Inner Magnetosphere: 1. Dominant Physical Processes. *J Geophys Res* (1998) 103: 2385–96. doi:10.1029/97JA02919
5. Rodger CJ, Brundell JB, Holzworth RH, and Lay EH. Growing Detection Efficiency of the World Wide Lightning Location Network. In: NB Crosby, T-Y Huang, and MJ Rycroft, editors. *CP1118, Coupling of Thunderstorms and Lightning Discharges to Near-Earth*. American Institute of Physics (2009). 978-0-7354-0657-5/09.
6. Meredith NP, Horne RB, Glauert SA, and Anderson RR. Slot Region Electron Loss Timescales Due to Plasmaspheric Hiss and Lightning-Generated Whistlers. *J Geophys Res* (2007) 112:A08214. doi:10.1029/2007JA012413
7. Meredith NP, Horne RB, Glauert SA, Baker DN, Kanekal SG, and Albert JM. Relativistic Electron Loss Timescales in the Slot Region. *J Geophys Res* (2009) 114:A03222. doi:10.1029/2008JA013889
8. Ripoll J-F, Chen Y, Fennell JF, and Friedel RHW. On Long Decays of Electrons in the Vicinity of the Slot Region Observed by HEO3. *J Geophys Res Space Phys* (2014) 120:460–78. doi:10.1002/2014JA020449
9. Albert JM, Starks MJ, Selesnick RS, Ling AG, O'Malley S, and Quinn RA. VLF Transmitters and Lightning-Generated Whistlers: 2. Diffusion of Radiation Belt Electrons. *J Geophys Res Space Phys* (2020) 125:e2019JA027030. doi:10.1029/2019JA027030
10. Albert JM. Evaluation of Quasi-Linear Diffusion Coefficients for Whistler Mode Waves in a Plasma with Arbitrary Density Ratio. *J Geophys Res* (2005) 110:A03218. doi:10.1029/2004JA010844
11. Albert JM. Dependence of Quasi-Linear Diffusion Coefficients on Wave Parameters. *J Geophys Res* (2012) 117:A09224. doi:10.1029/2012JA017718
12. Ripoll J-F, Albert JM, and Cunningham GS. Electron Lifetimes from Narrowband Wave-Particle Interactions within the Plasmasphere. *J Geophys Res Space Phys* (2014) 119:8858–80. doi:10.1002/2014JA020217
13. Parrot M, Berthelier JJ, Lebreton JP, Treumann R, and Rauch JL. DEMETER Observations of EM Emissions Related to Thunderstorms. *Space Sci Rev* (2008) 137:511–9. doi:10.1007/s11214-008-9347-y
14. Berthelier JJ, Godefroy M, Leblanc F, Malingre M, Menvielle M, Lagoutte D, et al. ICE, the Electric Field experiment on DEMETER. *Planet Space Sci* (2006) 54:456–71. doi:10.1016/j.pss.2005.10.016
15. Colman JJ, and Starks MJ. VLF Wave Intensity in the Plasmasphere Due to Tropospheric Lightning. *J Geophys Res Space Phys* (2013) 118:4471–82. doi:10.1002/jgra.50217
16. Starks MJ, Albert JM, Ling AG, O'Malley S, and Quinn RA. VLF Transmitters and Lightning-Generated Whistlers: 1. Modeling Waves from Source to Space. *J Geophys Res Space Phys* (2020) 125:e2019JA027029. doi:10.1029/2019JA027029
17. Ripoll JF, Claudepierre SG, Ukhorskiy AY, Colpitts C, Li X, Fennell JF, et al. Particle Dynamics in the Earth's Radiation Belts: Review of Current Research and Open Questions. *J Geophys Res Space Phys* (2020) 125:e2019JA026735. doi:10.1029/2019JA026735
18. Záhlava J, Němec F, Santolík O, Kolmašová I, Hospodarsky GB, Parrot M, et al. Lightning Contribution to Overall Whistler Mode Wave Intensities in the Plasmasphere. *Geophys Res Lett* (2019) 46:8607–16. doi:10.1029/2019GL08391810.1029/2019gl083918
19. Ripoll JF, Farges T, Malaspina DM, Lay EH, Cunningham GS, Hospodarsky GB, et al. Analysis of Electric and Magnetic Lightning-Generated Wave Amplitudes Measured by the Van Allen Probes. *Geophys Res Lett* (2020) 47:e2020GL087503. doi:10.1029/2020GL087503
20. Christian HJ, Blakeslee RJ, Boccippio DJ, Boeck WL, Buechler DE, Driscoll KT, et al. Global Frequency and Distribution of Lightning as Observed from Space by the Optical Transient Detector. *J Geophys Res* (2003) 108(D1):4005. doi:10.1029/2002JD002347
21. Cecil DJ, Buechler DE, and Blakeslee RJ. TRMM LIS Climatology of Thunderstorm Occurrence and Conditional Lightning Flash Rates*. *J Clim* (2015) 28(16):6536–47. doi:10.1175/JCLI-D-15-0124.1
22. Ripoll JF, Farges T, Lay EH, and Cunningham GS. Local and Statistical Maps of Lightning-Generated Wave Power Density Estimated at the Van Allen Probes Footprints from the World-Wide Lightning Location Network Database. *Geophys Res Lett* (2019) 46:4122–33. doi:10.1029/2018GL081146
23. Ripoll J-F, Farges T, Malaspina DM, Lay EH, Cunningham GS, Hospodarsky GB, et al. Electromagnetic Power of Lightning Superbolts from Earth to Space. *Nat Commun* (2021) 12:3553. doi:10.1038/s41467-021-23740-6
24. Holzworth RH, McCarthy MP, Brundell JB, Jacobson AR, and Rodger CJ. Global Distribution of Superbolts. *J Geophys Res Atmos* (2019) 124: 9996–10005. doi:10.1029/2019jd030975
25. Hutchins ML, Holzworth RH, Brundell JB, and Rodger CJ. Relative Detection Efficiency of the World Wide Lightning Location Network. *Radio Sci* (2012) 47:RS6005. doi:10.1029/2012RS005049
26. Hutchins ML, Holzworth RH, Rodger CJ, and Brundell JB. Far-Field Power of Lightning Strokes as Measured by the World Wide Lightning Location Network. *J Atmos Oceanic Technol* (2012) 29:1102–10. doi:10.1175/JTECH-D-11-00174.1

27. Jacobson AR, Holzworth RH, Pfaff RF, and McCarthy MP. Study of Oblique Whistlers in the Low-Latitude Ionosphere, Jointly with the C/NOFS Satellite and the World-wide Lightning Location Network. *Ann Geophys* (2011) 29: 851–63. doi:10.5194/angeo-29-851-2011
28. Burkholder BS, Hutchins ML, McCarthy MP, Pfaff RF, and Holzworth RH. Attenuation of Lightning-Produced Sferics in the Earth-Ionosphere Waveguide and Low-Latitude Ionosphere. *J Geophys Res Space Phys* (2013) 118:3692–9. doi:10.1002/jgra.50351
29. Mauk BH, Fox NJ, Kanekal SG, Kessel RL, Sibeck DG, and Ukhorskiy A. Science Objectives and Rationale for the Radiation Belt Storm Probes Mission. *Space Sci Rev* (2013) 179(1–4):3–27. doi:10.1007/s11214-012-9908-y
30. Kletzing CA, Kurth WS, Acuna M, MacDowall RJ, Torbert RB, Averkamp T, et al. The Electric and Magnetic Field Instrument Suite and Integrated Science (EMFISIS) on RBSP. *Space Sci Rev* (2013) 179:127–81. doi:10.1007/s11214-013-9993-6
31. Wygant JR, Bonnell JW, Goetz K, Ergun RE, Mozer FS, Bale SD, et al. The Electric Field and Waves Instruments on the Radiation Belt Storm Probes Mission. *Space Sci Rev* (2013) 179:183–220. doi:10.1007/s11214-013-0013-7
32. Malaspina DM, Jaynes AN, Hospodarsky G, Bortnik J, Ergun RE, and Wygant J. Statistical Properties of Low-Frequency Plasmaspheric Hiss. *J Geophys Res Space Phys* (2017) 122:8340–52. doi:10.1002/2017JA024328
33. Holzworth RH, McCarthy MP, Pfaff RF, Jacobson AR, Willcockson WL, and Rowland DE. Lightning-generated Whistler Waves Observed by Probes on the Communication/Navigation Outage Forecast System Satellite at Low Latitudes. *J Geophys Res* (2011) 116:A06306. doi:10.1029/2010JA016198
34. Němec F, Santolík O, Parrot M, and Rodger CJ. Relationship between Median Intensities of Electromagnetic Emissions in the VLF Range and Lightning Activity. *J Geophys Res* (2010) 115:A08315. doi:10.1029/2010JA015296
35. Bortnik J, Inan US, and Bell TF. Ldependence of Energetic Electron Precipitation Driven by Magnetospherically Reflecting Whistler Waves. *J Geophys Res* (2002) 107(A8):1150. doi:10.1029/2001JA000303
36. Chang S-C, Hsu R-R, Huang S-M, Su H-T, Kuo C-L, Chou J-K, et al. Characteristics of TLE-Producing Lightning in a Coastal Thunderstorm. *J Geophys Res Space Phys* (2014) 119:9303–20. doi:10.1002/2014JA019819
37. Santolík O, Pickett JS, Gurnett DA, and Storey LRO. Magnetic Component of Narrowband Ion Cyclotron Waves in the Auroral Zone. *J Geophys Res* (2002) 107(A12):17–1. doi:10.1029/2001JA000146
38. Santolík O, Parrot M, and Lefeuvre F. Singular Value Decomposition Methods for Wave Propagation Analysis. *Radio Sci* (2003) 38(1):1010. doi:10.1029/2000RS002523
39. Cecil DJ, Buechler DE, and Blakeslee RJ. Gridded Lightning Climatology from TRMM-LIS and OTD: Dataset Description. *Atmos Res* (2014) 135-136:404–14. doi:10.1016/j.atmosres.2012.06.028
40. Ripoll JF, Santolík O, Reeves GD, Kurth WS, Denton MH, Loridan V, et al. Effects of Whistler Mode Hiss Waves in March 2013. *J Geophys Res Space Phys* (2017) 122:7433–62. doi:10.1002/2017JA024139
41. Stix TH. *The Theory of Plasma Waves*. New York: McGraw-Hill (1962).
42. Ripoll J-F, Loridan V, Denton MH, Cunningham G, Reeves G, Santolík O, et al. Observations and Fokker-Planck Simulations of the L-Shell, Energy, and Pitch Angle Structure of Earth's Electron Radiation Belts during Quiet Times. *J Geophys Res Space Phys* (2019) 124, 1125–42. doi:10.1029/2018ja026111
43. Liu L, Zhao B, Wan W, Ning B, Zhang M-L, and He M. Seasonal Variations of the Ionospheric Electron Densities Retrieved from Constellation Observing System for Meteorology, Ionosphere, and Climate mission Radio Occultation Measurements. *J Geophys Res* (2009) 114:A02302. doi:10.1029/2008JA013819
44. Tulasi Ram S, Su S-Y, and Liu CH. FORMOSAT-3/COSMIC Observations of Seasonal and Longitudinal Variations of Equatorial Ionization Anomaly and its Interhemispheric Asymmetry during the Solar Minimum Period. *J Geophys Res* (2009) 114:A06311. doi:10.1029/2008JA013880
45. Sai Gowtam V, and Tulasi Ram S. Ionospheric Annual Anomaly-New Insights to the Physical Mechanisms. *J Geophys Res Space Phys* (2017) 122:8816–30. doi:10.1002/2017JA024170
46. Burns AG, Wang W, Qian L, Solomon SC, Zhang Y, Paxton LJ, et al. On the Solar Cycle Variation of the winter Anomaly. *J Geophys Res Space Phys* (2014) 119:4938–49. doi:10.1002/2013JA019552
47. Gallagher DL, Craven PD, and Comfort RH. Global Core Plasma Model. *J Geophys Res* (2000) 105(18):18819–33. doi:10.1029/1999JA000241
48. Ozhogin P, Tu J, Song P, and Reinisch BW. Field-Aligned Distribution of the Plasmaspheric Electron Density: An Empirical Model Derived from the IMAGE RPI Measurements. *J Geophys Res* (2012) 117:A06225. doi:10.1029/2011JA017330
49. Ripoll J-F, Reeves GD, Cunningham GS, Loridan V, Denton M, Santolík O, et al. Reproducing the Observed Energy-Dependent Structure of Earth's Electron Radiation Belts during Storm Recovery with an Event-specific Diffusion Model. *Geophys Res Lett* (2016) 43:5616–25. doi:10.1002/2016GL068869
50. Fiser JC, Diendorfer G, Parrot M, and Santolik O Whistler intensities above thunderstorms. *Ann Geophys* (2010) 28:37–46.
51. Kim K-C, Shprits Y, Subbotin D, and Ni B Understanding the dynamic evolution of the relativistic electron slot region including radial and pitch-angle diffusion. *J Geophys Res* (2011) 116:A10214. doi:10.1029/2011JA016684

Conflict of Interest: The authors declare that the research was conducted in the absence of any commercial or financial relationships that could be construed as a potential conflict of interest.

Publisher's Note: All claims expressed in this article are solely those of the authors and do not necessarily represent those of their affiliated organizations, or those of the publisher, the editors and the reviewers. Any product that may be evaluated in this article, or claim that may be made by its manufacturer, is not guaranteed or endorsed by the publisher.

Copyright © 2021 Ripoll, Farges, Malaspina, Cunningham, Hospodarsky, Kletzing and Wygant. This is an open-access article distributed under the terms of the Creative Commons Attribution License (CC BY). The use, distribution or reproduction in other forums is permitted, provided the original author(s) and the copyright owner(s) are credited and that the original publication in this journal is cited, in accordance with accepted academic practice. No use, distribution or reproduction is permitted which does not comply with these terms.

frontiers in Astronomy and Space Sciences

ORIGINAL RESEARCH
published: 31 August 2021
doi: 10.3389/fspas.2021.737946

Two-Dimensional Structure of Flow Channels and Associated Upward Field-Aligned Currents: Model and Observations

Larry. R. Lyons[1]*, *Yukitoshi Nishimura*[2], *Chih-Ping Wang*[1], *Jiang Liu*[1,3] and *William. A. Bristow*[4]

[1]Department of Atmospheric and Oceanic Sciences, University of California Los Angeles, Los Angeles, CA, United States, [2]Center for Space Physics and Department of Electrical and Computer Engineering, Boston University, Boston, MA, United States, [3]Department of Earth, Planetary, and Space Sciences, University of California Los Angeles, Los Angeles, CA, United States, [4]Department of Meteorology and Atmospheric Science, 621 Walker Building, The Pennsylvania State University, State College, PA, United States

OPEN ACCESS

Edited by:
Jiansen He,
Peking University, China

Reviewed by:
Yiqun Yu,
Beihang University, China
Alexei. V. Dmitriev,
Lomonosov Moscow State University, Russia

***Correspondence:**
Larry. R. Lyons
larry@atmos.ucla.edu

Specialty section:
This article was submitted to Space Physics, a section of the journal Frontiers in Astronomy and Space Sciences

Received: 07 July 2021
Accepted: 12 August 2021
Published: 31 August 2021

Citation:
Lyons LR, Nishimura Y, Wang C-P, Liu J and Bristow WA (2021) Two-Dimensional Structure of Flow Channels and Associated Upward Field-Aligned Currents: Model and Observations. Front. Astron. Space Sci. 8:737946. doi: 10.3389/fspas.2021.737946

Flow bursts are a major component of transport within the plasma sheet and auroral oval (where they are referred to as flow channels), and lead to a variety of geomagnetic disturbances as they approach the inner plasma sheet (equatorward portion of the auroral oval). However, their two-dimensional structure as they approach the inner plasma sheet has received only limited attention. We have examined this structure using both the Rice Convection Model (RCM) and ground-based radar and all sky imager observations. As a result of the energy dependent magnetic drift, the low entropy plasma of a flow burst spreads azimuthally within the inner plasma sheet yielding specific predictions of subauroral polarization stream (SAPS) and dawnside auroral polarization stream (DAPS) enhancements that are related to the field-aligned currents associated with the flow channel. Flow channels approximately centered between the dawn and dusk large-scale convection cells are predicted to give significant enhancements of both SAPS and DAPS, whereas flow channel further toward the dusk (dawn) convection cell show a far more significant enhancement of SAPS (DAPS) than for DAPS (SAPS). We present observations for cases having good coverage of flow channels as they approach the equatorward portion of the auroral oval and find very good qualitative agreement with the above RCM predictions, including the predicted differences with respect to flow burst location. Despite there being an infinite variety of flow channels' plasma parameters and of background plasma sheet and auroral oval conditions, the observations show the general trends predicted by the RCM simulations with the idealized parameters. This supports that RCM predictions of the azimuthal spread of a low-entropy plasma sheet plasma and its associated FAC and flow responses give a realistic physical description of the structure of plasma sheet flow bursts (auroral oval flow channels) as they reach the inner plasma sheet (near the equatorward edge of the auroral oval).

Keywords: flow channels, flow bursts, saps, dawnside polarization stream, convection, aurora

INTRODUCTION

Bursts of flows with an equatorward component are seen within the nightside auroral oval (Sergeev et al., 1990; Kauriste et al., 1996; Yeoman & Lühr, 1999), these being the ionospheric counterpart of earthward flow bursts in the plasma sheet (Angelopoulos et al., 1992). Within flow bursts, flux tubes with lower total entropy than the surrounding plasma are brought earthward via interchange motion as seen in both theory (e.g., Pontius & Wolf, 1990; Yang et al., 2011) and observations (e.g., Angelopoulos et al., 1994; Dubyagin et al., 2010; Panov et al., 2010; Xing et al., 2010; Sergeev et al., 2012).

Flow bursts in the ionosphere (often referred to "meso-scale" flow channels) drive convergence of ionospheric currents to the right of their the flow direction. This convergence is related via current continuity to upward field-aligned currents (FACs) that can require magnetic-field-aligned electric fields that energize electrons and form discrete aurora (e.g., Lyons, 1981). This gives rise to intensifications along the poleward boundary of the auroral oval (de la Beaujardière et al., 1994; Lyons et al., 1999; Zesta et al., 2000) that are the most common auroral disturbance and have become referred to as poleward boundary intensifications (PBIs). PBIs can extend equatorward from the poleward boundary of the auroral oval along with the meso-scale flow bursts and become elongated in very roughly the north-south direction forming what are referred to as streamers (Rostoker et al., 1987; Nakamura et al., 1993; Gallardo-Lacourt et al., 2014).

Flow bursts in the ionosphere have also been observed to lead to a variety of other important geomagnetic disturbances as the reach to near the equatorward boundary of the auroral oval, which maps to the inner plasma sheet. These disturbances include thin substorm growth phase aurora arc formation or intensification (Nishimura et al., 2011), substorm onset (e.g., Nishimura et al., 2010), and omega bands (Henderson et al., 2002; Liu et al., 2018). Flow bursts moving earthward/equatorward are also important because they can give particle injections (Gabrielse et al., 2014; Liu et al., 2016), including into the storm-time ring current e.g., Gkioulidou et al. (2014) and radiation belts (e.g., Kim et al., 2021).

Thus the physics of flow bursts as they move earthward within the plasma sheet is of critical importance to understanding geomagnetic activity. Evaluation of flow bursts from an ideal MHD perspective e.g., Birn and Hesse (2013), Birn and Hesse (2014) has yielded much insight into flow burst dynamics in the more distant magnetotail, but is not appropriate for investigation of what happens as the flowing plasma encounters the inner plasma sheet where magnetic drift becomes significant. In ideal MHD, flow bursts come to rest where the flux tube integrated entropy of the plasma within the flow burst equals that of the background plasma (Wolf et al., 2012). However, the energy dependence of magnetic drift should dramatically change this result. As predicted by the Rice Convection Model (RCM), the low entropy plasma should spread azimuthally, be accompanied by substantial azimuthal drift (Yang et al., 2014; Yu et al., 2017), and lead to a substantial reduction of flux tube integrated entropy as plasma moves earthward (Lyons et al., 2009; Wang et al., 2018a; Wang et al., 2020).

This paper provides an observational test of the RCM predictions of the fate of the reduced entropy, flow burst plasma as it enters the near-Earth plasma sheet. We base our test on the Wang et al. (2018) RCM results. The model gives predictions of azimuthal flow relative to upward FAC regions when a localized plasma perturbation is introduced into the outer plasma sheet and leads to a reduced entropy plasma bubble. The model also shows important differences in response when these perturbations are introduced at three different MLTs relative to the near midnight model boundary between the large-scale dusk and dawn convection cells. Our test uses observations of upward FACs and flows within the ionosphere. The upward FACs are inferred from the aurora obtained primarily from the Time History of Events and Macroscale Interactions during Substorms (THEMIS) white-light all sky imager (ASI) array, which offers continent-scale coverage of the North American auroral zone with high temporal and spatial resolution (Mende et al., 2008). Poker Flat 557.7 nm ASI observations are included for events over Alaska. Flows are identified from Super Dual Auroral Radar Network (SuperDARN) observations, and presented as maps of flow vectors obtained with the Bristow et al. (2016) technique. This technique gives spatial resolution set by that of the underlying measurements and not by the smoothing from the global fits that are typically used for global SuperDARN convection maps. The resulting vectors are determined by the local line-of-sight (LOS) observations and the divergence-free condition. They are not strongly influenced by information beyond a distance of a few grids, so that localized steep gradients can be represented without influencing the remainder of the domain. Flow vector maps are available every 2 min.

RCM RESULTS

The RCM (Harel et al., 1981; Toffoletto et al., 2003) computes species- and energy-dependent particle transport and convection electric field self-consistently using the bounce–averaged electric drift and magnetic curvature/gradient drift. Drift due to the induced electric field, which is associated with magnetic field changes, are included in computing motions in the magnetosphere. Particles are released from the RCM outer/tail boundary, proton loss by charge exchange and electrons loss by precipitation are considered, and the RCM computes electric field potential in the ionosphere self-consistently through the requirement for current continuity. Conductance includes Solar-EUV-generated conductance and Hall and Pedersen auroral conductance computed from the simulated particle spectra and precipitation loss rates based on (Robinson et al., 1987). The cross polar-cap potential is the external driver of the large-scale convection.

In the RCM simulations presented in this study (Wang et al., 2018b), the UCLA version of the RCM, UCLA-RCM, is used. Three modules developed separately have been incorporated in the UCLA-RCM: (1) observation-based tail particle boundary

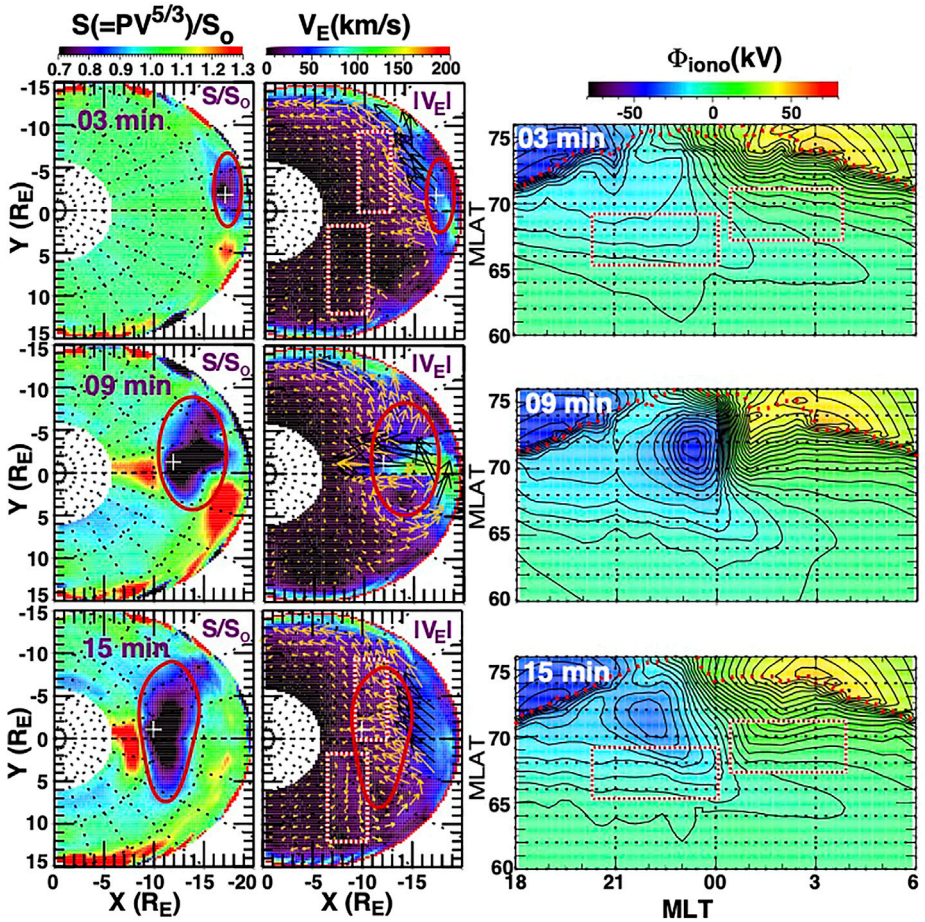


FIGURE 1 | UCLA-RCM results in the equatorial plane and ionosphere from Run one of Wang et al. (2018a) for times 3, 9, and 15 min after a meso-scale perturbation with a 1 h in MLT width and centered at 24 MLT was imposed on the RCM outer boundary A cross-polar cap potential drop of 90 keV was used. The perturbation had a density decrease by a factor of six and a temperature increase by a factor of 6. The left column shows the ratio of flux tube integrated entropy S to the integrated entropy S_o at t = 0, and the middle column shows the electric field drift velocity V_E. Both are of these columns are in the equatorial plane. In the left panel, a crimson curve outlines the approximate boundary of the expanding bubble for each of the three times. In the middle column, red and white rectangles are drawn to help identify the locations for comparing V_E at t = 3 and t = 15 min. Electric potential and equipotential contours are shown in the right column.

conditions (Wang et al., 2011), (2) force-balanced magnetic field (Liu et al., 2006; Gkioulidou et al., 2011), and (3) observation-based electron loss rates (Chen & Schulz, 2001; Gkioulidou et al., 2012).

Figure 1 shows UCLA-RCM results in the equatorial plane and ionosphere from Run one of Wang et al. (2018b) for times 3, 9, and 15 min after a meso-scale perturbation with a 1 h in MLT width and centered at 24 MLT was imposed on the RCM outer boundary, which is near X = −20 R_E at midnight. A cross-polar cap potential drop of 90 kV was used. The perturbation had a density decrease by a factor of six and a temperature increase by a factor of 6, so that the bubble was created by the heat flux vector divergence due to the higher magnetic drift speeds of the hotter particles relative to those of the cooler background. As the bubble moves earthward, the lower energy ions tend to follow the electric field drift (along equipotentials, which are shown in the ionosphere as the black contours in the right column), while the higher energy ions magnetic drift more duskward. As a result, the bubble spreads in longitude, consistent with magnetotail observations (Liu et al., 2015), and its entropy decreases and as it moves earthward. The spreading can very clearly be seen in the left column of **Figure 1**, which shows the ratio of flux tube integrated entropy S to the integrated entropy S_o at t = 0 ($S = PV^{5/3}$, where P is plasma pressure and V is flux tube volume). A crimson curve outlines the approximate boundary of the expanding bubble for each of the three times. S typically has a tailward gradient in the plasma sheet. However, the bubble spreading leads to an approximately azimuthal-aligned decrease in the tailward gradient in S at t = 15 min. As shown in Lyons et al. (2021a), there are enhancements of the Region 1 and 2-sense FACs as the bubble moves earthward (t = 9 min), and these FACs become longitudinally broad Region 1 and Region 2-sense currents as the bubble moves earthward to the inner plasma sheet. The enhanced Region 1-sense FACs are located approximately within the bubble itself, whereas the enhanced Region 2-

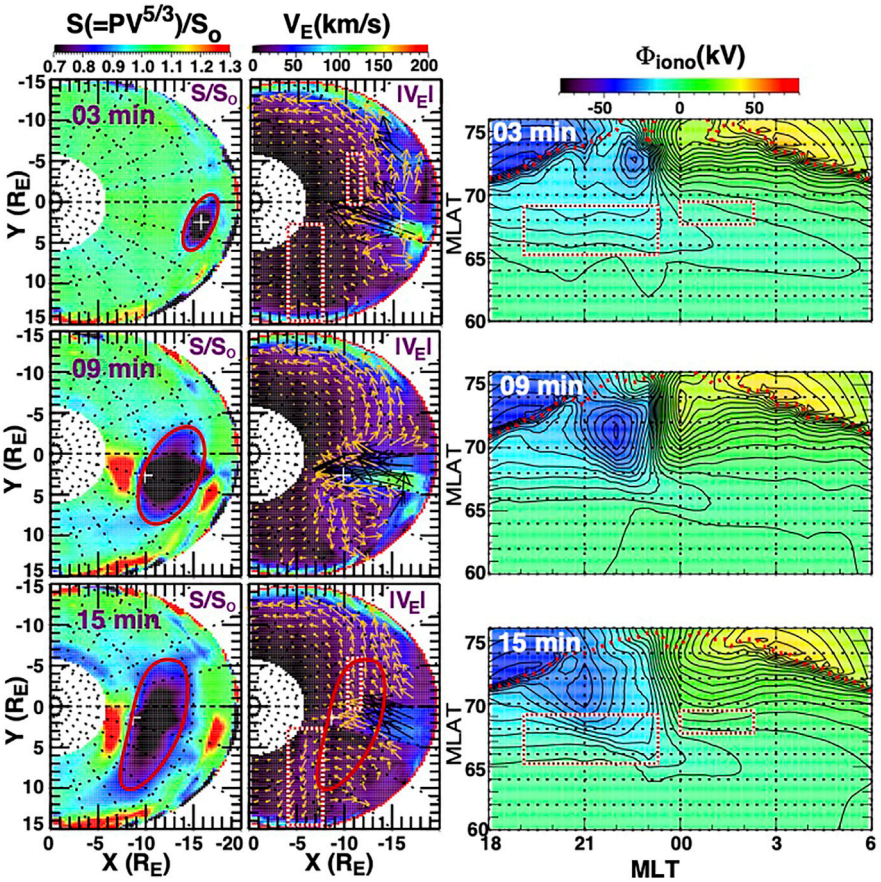


FIGURE 2 | UCLA-RCM results in the equatorial plane and ionosphere from Run two of Wang et al. (2018b). Format is the same as **Figure 1**, and all model parameters were the same except the perturbation with centered at 23 MLT.

sense FACs are earthward of the bubble, consistent with magnetotail observations (Liu et al., 2013; Sun et al., 2013).

The electric field changes as the FACs develop to maintain current continuity in both the ionosphere and magnetosphere. These changes can be seen in the middle row of **Figure 1** as azimuthal turnings of the electric field drift vector (V_E) as the flow channel moves earthward (t = 9 min). By t = 15 min, the electric field changes give significant enhancements in the subauroral polarization stream (SAPS) and dawnside polarization stream (DAPS) Liu et al. (2020) flows in the regions of the enhanced downward FACs, where conductivities are substantially lower than in the upward FAC regions. These enhancements can be seen by comparing the equatorial-plane electric field drift velocities in the middle column and the spacing of ionospheric equipotentials in the right column at t = 3 and t = 15 min. Red and white rectangles in **Figure 1** are drawn to help identify the locations for making this comparison, and comparison with the crimson curve shows that the DAPS increase is within the plasma sheet bubble, while the SAPS increase is adjacent to the equatorward boundary of the bubble. (The nightside auroral oval and plasma sheet can have both the well-known SAPS region and an analogous DAPS' region as discussed in Liu et al. (2020). SAPS are strong westward flows in the low conductivity region of downward (duskside) Region two field-aligned currents (FACs) that lies just equatorward of the electron auroral oval. DAPS consist of strong eastward flows in the more poleward, downward (dawnside) Region one FAC portion of the dawnside auroral oval, where auroral precipitation Lyons and Fennell (1986), Zou et al. (2009) and thus conductivities are much lower than within the more equatorward dawnside upward Region two FAC portion of the dawnside auroral oval.)

The bubble in **Figure 1** was approximately centered between the dawn and dusk large-scale convection cells. Run 2, shown in **Figure 2**, is for the same conditions as Run 1 except the perturbation leading to the bubble was centered at 23 MLT and thus further toward the dusk convection cell. The important differences from Run 1 are that the bubble expands further towards dusk and less towards dawn, leading to a stronger SAPS region flow enhancement and a substantially smaller and weaker DAPS region for enhancement. Run 3, shown in **Figure 3** is also for the same conditions as Run 1 except the perturbation leading to the bubble was centered at 01 MLT and thus further within the dawn convection cell. This bubble expanded further dawnward than did the bubble in Run 1, and led to a substantial DAPS region flow enhancement but no discernable enhancement of SAPS.

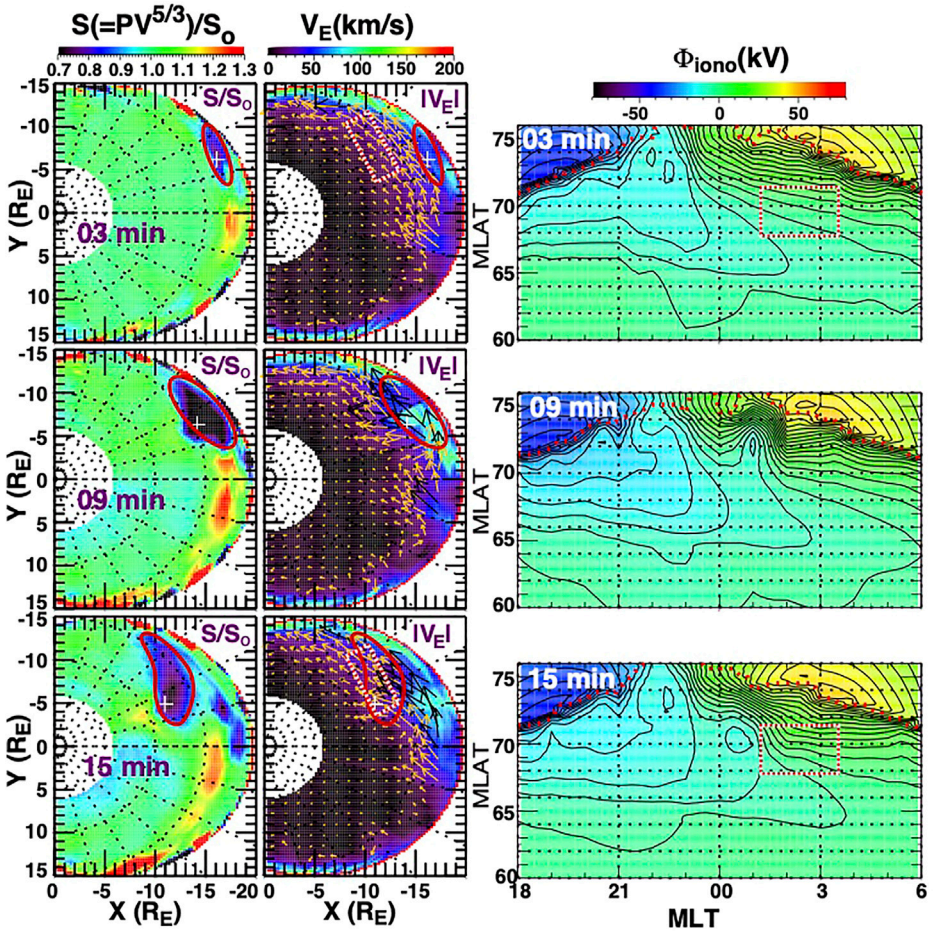


FIGURE 3 | UCLA-RCM results in the equatorial plane and ionosphere from Run three of Wang et al. (2018b). Format is the same as **Figure 1**, and all model parameters were the same except the perturbation with centered at 01 MLT

ANALYSIS

We started with 14 nights that were selected for having good auroral viewing from Poker Flat, Alaska that we have used in previous studies [most in Lyons et al. (2021a); Lyons et al. (2021b)], and identified six flow channel events having good auroral viewing conditions and good radar coverage of flows moving to the equatorward portion of the auroral oval and of their connection to azimuthal flows. We first show two examples with a flow channel that appears to be near the boundary between the dusk-side and dawn-side convection cells, approximately corresponding to the RCM model run in **Figure 1**. We then show one example each of a flow channel that appears to be more within the dusk-side or dawn-side convections cells, resembling the RCM model runs in **Figures 2**, **3**, respectively. This is followed by examples with two or more flow channels.

We only examine the two-dimensional structure of the flow channels, its location relative to upward FACs as indicated by bright auroral arcs, and the dependence on whether the flow channel is between the two large-scale convection cells or more within the dusk or dawn cell. We do not have the combination of time resolution with consistent echo coverage to consistently see the evolution of flow channels as they move equatorward within the auroral oval. We do, however, show sequences of flow and ASI measurement to show that the two-dimensional pattern is maintained for several minutes and is not just a coincidental pattern seen during a single measurement interval, and to also show that the flow channel appears to come in from higher latitudes (probably the polar cap).

November 11, 2012 and February 20, 2014: Between-Cell Examples

Figure 4 shows 557.7 nm images from the Poker Flat ASI, with THEMIS ASI image mosaics for the region surrounding the Poker image FOV, for a flow channel near midnight (cyan line) on November 11, 2012. This flow channel appears to be in the region that separates the dawnside and duskside large-scale convection cells. Images are shown every 2–4 min, and SuperDARN flow vectors are overlaid on the images in each panel. The magnitude of each vector is shown by both its length and its color, the foot of the arrow being at the location of the

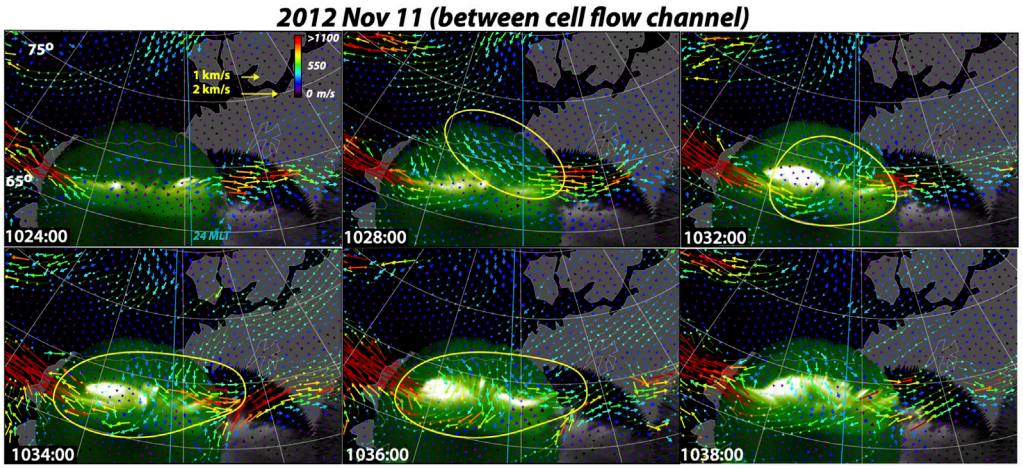


FIGURE 4 | 557.7 nm images from the Poker Flat ASI, with THEMIS ASI image mosaics for the region surrounding the Poker image FOV for a flow channel near midnight (cyan line) on November 11, 2012. SuperDARN flow vectors are overlaid on the images in each panel. Vectors are scaled both by length and by color, the foot of the arrow being at the location of the measurement. Heavier flow vector arrows are at points with a LOS flow measurement. The further from a region of heavier arrows, the more the flows shown with the lighter arrows revert to a statistical model. Closed yellow curve approximately encircles the region where flows were enhanced relative to that seen at 1024 UT.

measurement. Heavier flow vector arrows are at points with a LOS flow measurement. The further from a region of heavier arrows, the more the flows shown with the lighter arrows revert to a statistical model.

The first panel (1024 UT) shows conditions just before the start of a period of several consecutive 2 min SuperDARN maps showing a connection of the flow channel to flows within the equatorward portion of the auroral oval. Very weak flows are seen between 23 and 24 MLT, with westward/eastward flows at earlier/later MLTs. The stronger and more equatorward/poleward of these flow are SAPS/DAPS. In the next panel (1028 UT), a longitudinally localized region of enhanced flows (i.e., a flow channel) can be seen approaching the poleward boundary of the auroral oval at ~23 to 24 MLT. The flow is equatorward with a significant eastward component, and it can be seen to connect to and enhance the eastward flows. (Flow direction variations are common for polar-cap flows approaching the auroral poleward boundary.). The eastward flows are poleward of a bright aurora arc on the dawnside, consistent them being DAPS. A closed yellow curve approximately encircles the region of the equatorward directed flow channel and DAPS flow that were enhanced relative to that seen at 1024 UT. There was not sufficient radar echo coverage at 1028 UT to determine if the flow channel connected to the SAPS region.

In the next three panels, we have sufficient measurement vectors to see that the flow channel simultaneously directly connected to, and enhanced, the duskside westward and dawnside eastward flows. The westward flows are equatorward of the brighter auroral emissions and within the region of uniform 557.7 nm emissions that results from the proton precipitation within the SAPS region (Zou et al., 2009; Lyons et al., 2015). The eastward flows are at distinctly higher latitudes than the westward flows. The dawnside aurora remains clear for this event, and the strongest eastward flows can be seen to lie adjacent to, but poleward of the dawnside bright auroral arc. This is characteristic of DAPS. Again, a closed yellow curve approximately encircles the region of the equatorward directed flow channel and SAPS and DAPS flows that were enhanced relative to that seen at 1024 UT. These are just the flows and location relative to the brighter auroral emissions expected from the near-midnight flow channel run of the RCM in **Figure 1**.

A second example of a flow channel in the region between the two large scale convection cells, on February 20, 2014, is shown in **Figure 5**. This channel is centered at ~22.5 h in MLT. However, based on the background flow pattern, this flow channel appears to lie near the boundary between the large-scale dusk and dawn convection cells. At 0800 UT, some of the southeastward flows of the flow channel show a connection to strong DAPS flows just poleward of the lower latitude region of brighter morning aurora and an auroral arc identified by a magenta arrow. For this time, the flow channel appears to be partially within the dawn convection cell. However, in the next three panels, we see enhanced equatorward flow channels coming into the auroral oval from higher latitudes, and there are sufficient echoes to show a connection to both DAPS and SAPS at the next three times. The flow channel appears most clearly as between the convection cells in the 0808 UT panel. The closed yellow curve approximately encircles the region where flows were enhanced relative to that seen at 0800 UT. The flow speeds and echo coverage decrease by the times of the 0808 and 0810 UT panels. We see the flow connection to both SAPS and DAPS for ~6 min in this case, and for ~6–10 min for the case in **Figure 4**. These are reasonable durations for a flow channel, and their two-dimensional structure is as predicted by the RCM, including the predicted SAPS and DAPS enhancement location relative to the upward FAC as indicated by the bright auroral arcs.

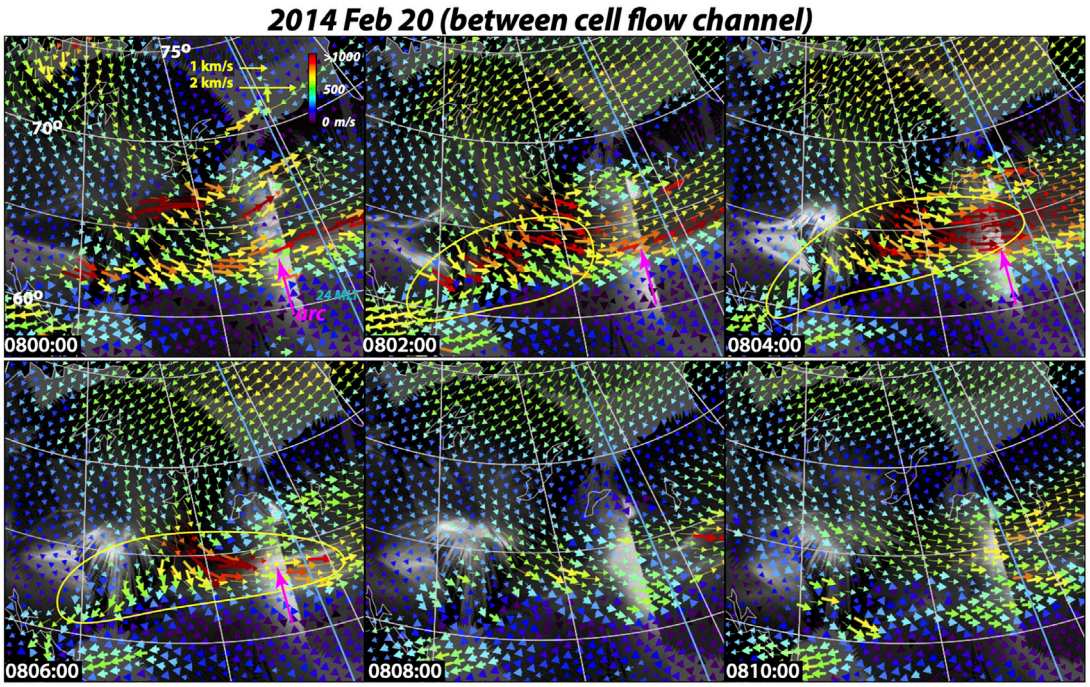


FIGURE 5 | Same as **Figure 4**, except for a between cell flow channel on February 20, 2014, and the closed yellow curve approximately encircles the region where flows were enhanced relative to that seen at 0800 UT.

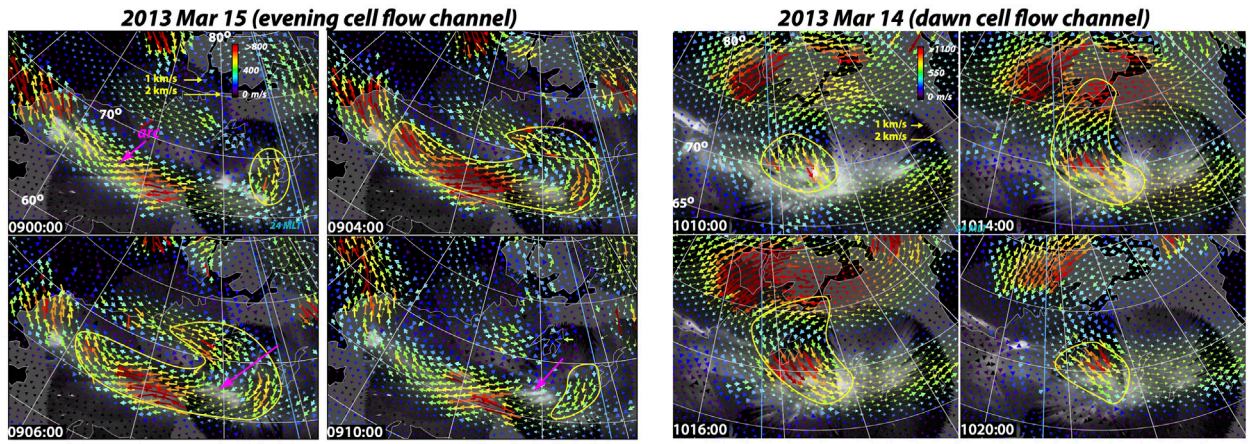


FIGURE 6 | Same as **Figure 4**, except the left- and right-hand sides, respectively, show an example of a flow channel appearing to enter the auroral oval from the polar cap and becoming primarily within the dusk (March 15, 2013) and dawn (March 14, 2013) convection cell. The closed yellow curves approximately encircle the region of the equatorward flows and where flows were enhanced relative to that seen in the first panel for each event.

March 14, and 15 2013: Two-Dimensional TEC Coverage: Dusk and Dawn Cell Examples

The left- and right-hand sides, respectively, of **Figure 6** show an example where an observed flow channel appears to enter the auroral oval from the polar cap and become primarily within the dusk or the dawn convection cell. We choose these examples in part because there are at least some echoes toward the dusk and dawn sides of the equatorward portion of the flow channel that show a decrease in flow speed. This indicates that the strongest flow of the channel did not extend more broadly in MLT, and, in particular, did not extend in MLT from the dusk/dawn cell to the dawn/dusk. In this figure, the closed yellow curves approximately encircle the region of the equatorward flows and where flows were enhanced relative to that seen in the first panel for each event.

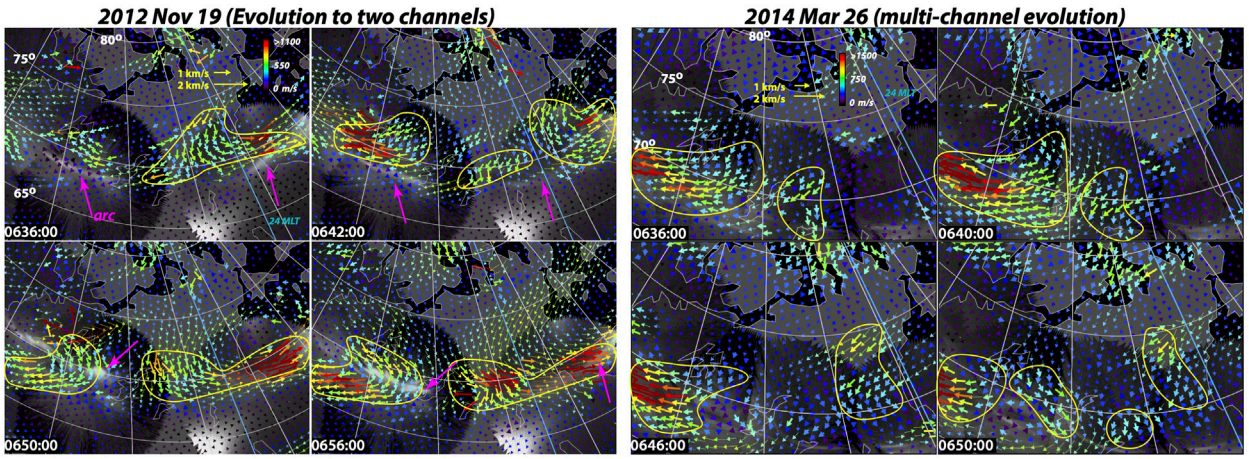


FIGURE 7 | Same as **Figure 4**, except for two events (**left**: November 19, 2012; **right**: March 26, 2014) showing flow evolution to two or more flow channels. Yellow curves approximately encircle the identified flow channels in each panel.

The equatorward flow channel on March 15, 2013 is seen in the 0900 UT panel. In the next two panels, the flows of the channel can be seen turning azimuthally towards the west, becoming connected to, and leading to an enhancement of, the SAPS flows. These flows lie equatorward of an auroral arc that was seen at 0900 UT as identified with a magenta arrow. At the later times shown, that arc was no longer visible, but the flows are within the region of uniform 557.7 nm emissions that results from the proton precipitation within the SAPS region. They were also equatorward of an arc observed to the east of the largest flows There are several radar echoes to the east of the flow channel, and they show only very weak flows with no evidence for a connection to DAPS flows. These observations are consistent with the pattern expected from the RCM results for a dusk cell flow channel in **Figure 2**. The flow channel then started to decrease as seen in the 0910 UT panel. The dawn cell flow channel on March 14, 2013 is first seen in the 1010 UT panel. It then increased and further turned towards the east, and then started to decrease by the time of the last panel shown (1020 UT). The flows turning toward the east are likely DAPS, though the auroral signature is not clear. Weak, diffuse auroral emissions are seen within the region of the flows on the dawn side. However, there may be brighter emissions towards the equatorward boundary of the ASIs FOVs, but this region of the FOVs is partially obscured by trees. Also, there are several radar echoes to the west of the flow channel, and they show only very weak flows with no evidence for a connection to SAPS flows This dawn cell example is consistent with the RCM pattern for a dawn cell flow channel in **Figure 3**.

As mentioned above, in neither the dusk-cell or dawn-cell examples in **Figure 6** do we see a turning of the flows of the flow channel to the other azimuthal direction, that being to the east on 15 March and to the west on 14 March. This is a distinct difference to the connections to both SAPS and DAPS flow enhancements seen in the between cell examples in **Figures 4**, **5**, showing further consistency with the RCM predictions in **Figures 1**–**3**.

Nov 19, 2012 and March 26, 2014: Evolution to Two or More Flow Channels

We identified single flow channels in the above events. Since there can be more than one streamer within the auroral oval at a given time (e.g., Lyons et al., 2012), we would expect there to often be more than one flow channel simultaneously within the oval. We thus turn attention to the two examples in **Figure 7**. Observations from November 19, 2012 are shown in the left portion of **Figure 7**. As outlined by the yellow curves, here we see a clear between-cell flow channel in the first panel (0636 UT), which then evolves into very distinct and separated dusk- and dawn-cell flow channels by the time times of the 0,650 and 0,656 panels. Observations from March 26, 2014 are in the right portion of the figure. As outlined by the yellow curves, in the first panel (0636 UT) we see a nice dusk-cell flow channel and a small equatorward flow channel to the east. The subsequent panels then show that the flows evolved toward four identifiable flow channels, with a dusk cell always being seen and three additional small equatorward flow channels appearing at 0650 UT. (Auroral features are difficult to identify for this event.)

We thus see that the idealized representations of a single flow channel that we have simulated with the RCM give patterns that compare remarkably well with the observations in examples with a single flow channel. However, the situation when there are multiple flow channels requires consideration and simulation of substantially more complicated scenarios where multiple bubbles are imposed on the RCM outer boundary.

SUMMARY AND CONCLUSION

While flow bursts are a major component of plasma sheet and auroral oval transport, and lead to a variety of other geomagnetic disturbances when they reach the inner plasma sheet (equatorward portion of the auroral oval), their two-dimensional structure as they approach the inner plasma sheet has not received much attention

beyond that which is seen in ideal MHD simulations. We have examined this structure using both the RCM and ground-based radar and ASI observations. Specifically, we first presented the RCM predictions, and then tested these predictions using upward FACs identified from ASI images of the aurora and SuperDARN observations presented as maps of flow vectors obtained with the Bristow et al. (2016) technique. We used only observations for cases having good coverage of flow channels as they approach the equatorward portion of the auroral oval and the regions of possible connection to the azimuthal flows of SAPS and DAPS.

The energy dependence of magnetic drift becomes crucial within the inner plasma sheet, and as predicted by the RCM, the low entropy plasma of a flow burst should spread azimuthally and be accompanied by substantial azimuthal drift. We have taken advantage of the RCM results of Wang et al. (2018b) who ran three RCM simulations that were identical except for the MLT of a plasma perturbation applied at the model outer boundary that gives rise to a low-entropy plasma bubble. The results gave specific predictions of azimuthal flow enhancements in the SAPS and DAPS regions and their relation to flow-channel FACs that are associated with the azimuthal spreading of flow channels' low entropy plasma as the flows reach to near the equatorward boundary of the auroral oval. We find consistency between the RCM pattern and the patterns seen in the observation results when a single flow channel is observed. The results also show clear response distinctions based on a flow channel's location relative to the dusk-side and dawn-side large-scale convection cells, as seen in the RCM results of **Figures 1–3** and the observations in **Figures 4–6**. The flow channels in **Figures 1**, **4**, **5** were approximately centered between the dawn and dusk large-scale convection cells and gave significant flow enhancements of both SAPS and DAPS. The flow channels in **Figure 2** and the left side of **Figure 6** were further toward the dusk convection cell, and showed a far more significant enhancement of SAPS than for DAPS. The flow channels in **Figure 3** and the right side of **Figure 6** were further within the dawn convection cell. The low entropy plasma within these flow channels expanded further dawnward than did the between cell flow channels, and led to a substantial DAPS region flow enhancement but no discernable enhancement of SAPS.

It needs to be remembered that there is an infinite variety of flow channels plasma parameters and of background plasma sheet and auroral oval conditions. That the observations show the general trends predicted by the RCM simulations with the idealized parameters of Wang et al. (2018a) gives strong support that the azimuthal spread of a low-entropy plasma sheet plasma and its associated FAC and flow responses gives a realistic two-dimensional physical description of the structure of plasma sheet flow bursts (auroral oval flow channels) as they reach the inner plasma sheet (near the equatorward edge of the auroral oval).

That the structure of the flow bursts becomes approximately azimuthally aligned within the inner plasma sheet (equatorward portion of the auroral oval) may be quite important. For example, this alignment is likely critical for understanding the disturbances of the magnetosphere-ionosphere system that have east-west alignment, such as growth-phase auroral arcs, substorm onset, and dawnside auroral omega bands. Based on the few cases presented here, the auroral oval flow channels have a typical duration of several minutes. Also, based on the observations in **Figure 7**, the character of a flow channel can evolve with time, and more than one flow channel can significantly affect the plasma sheet and auroral oval at any specific time. Such evolution and the effects of multiple flow channels warrant further consideration, as does other effects of MLT location of bubble injection such as seen in (Nishimura et al., 2020).

DATA AVAILABILITY STATEMENT

Publicly available datasets were analyzed in this study. This data can be found here: SuperDARN data is accessible *via* http://vt.superdarn.org/tiki-index.php?page = Data+Access. The University of Alaska ASI data is available from http://optics.gi.alaska.edu/optics/, and the THEMIS ASI data from http://themis.ssl.berkeley.edu/themisdata/.

AUTHOR CONTRIBUTIONS

LL: All aspects of paper YN: Data coordination, analysis, and interpretation C-PW: Rice Convection Model simulations JL: Data analysis and interpretation WB: Two-dimensional radar flows and their interpretation.

FUNDING

Work at UCLA has been supported by NSF grant 1907483, NASA grant 80NSSC20K1314 and AFOSR FA9559-16-1-0364, at Boston University by AFOSR FA9559-16-1-0364, NASA NNX17AL22G, NSF AGS-1737823, and AFOSR FA9550-15-1-0179. SuperDARN work at Penn State was supported by AFOSR FA9559-16-1-0364. SuperDARN is a collection of radars funded by national scientific funding agencies of Australia, Canada, China, France, Italy, Japan, Norway, South Africa, United Kingdom and the United States of America. Operation of the Kodiak and Adak radars, and processing of the SuperDARN data for this study was supported by NSF grant AGS1934410 to the University of Alaska Fairbanks.

REFERENCES

Angelopoulos, V., Baumjohann, W., Kennel, C. F., Coroniti, F. V., Kivelson, M. G., Pellat, R., et al. (1992). Bursty Bulk Flows in the Inner Central Plasma Sheet. *J. Geophys. Res.* 97 (A4), 4027–4039. doi:10.1029/91JA02701

Angelopoulos, V., Kennel, C. F., Coroniti, F. V., Pellat, R., Kivelson, M. G., Walker, R. J., et al. (1994). Statistical Characteristics of Bursty Bulk Flow Events. *J. Geophys. Res.* 99 (A11), 280. doi:10.1029/94ja01263

Birn, J., and Hesse, M. (2013). The Substorm Current Wedge in MHD Simulations. *J. Geophys. Res. Space Phys.* 118 (6), 3364–3376. doi:10.1002/jgra.50187

Birn, J., and Hesse, M. (2014). The Substorm Current Wedge: Further Insights from MHD Simulations. *J. Geophys. Res. Space Phys.* 119 (5), 3503–3513. doi:10.1002/2014JA019863

Bristow, W. A., Hampton, D. L., and Otto, A. (2016). High-spatial-resolution Velocity Measurements Derived Using Local Divergence-Free Fitting of SuperDARN Observations. *J. Geophys. Res. Space Phys.* 121 (2), 1349–1361. doi:10.1002/2015JA021862

Chen, M. W., and Schulz, M. (2001). Simulations of Storm Time Diffuse aurora with Plasmasheet Electrons in strong Pitch Angle Diffusion. *J. Geophys. Res.* 106 (A2), 1873–1886. doi:10.1029/2000JA000161

de la Beaujardière, O., Lyons, L. R., Ruohoniemi, J. M., Friis-Christensen, E., Danielsen, C., Rich, F. J., et al. (1994). Quiet-Time Intensifications along the Poleward Auroral Boundary Near Midnight. *J. Geophys. Res.* 99 (A1), 287–298. doi:10.1029/93JA01947

Dubyagin, S., Sergeev, V., Apatenkov, S., Angelopoulos, V., Nakamura, R., McFadden, J., et al. (2010). Pressure and Entropy Changes in the Flow-Braking Region during Magnetic Field Dipolarization. *J. Geophys. Res.* 115, a–n. doi:10.1029/2010JA015625

Gabrielse, C., Angelopoulos, V., Runov, A., and Turner, D. L. (2014). Statistical Characteristics of Particle Injections throughout the Equatorial Magnetotail. *J. Geophys. Res. Space Phys.* 119 (4), 2512–2535. doi:10.1002/2013JA019638

Gallardo-Lacourt, B., Nishimura, Y., Lyons, L. R., Zou, S., Angelopoulos, V., Donovan, E., et al. (2014). Coordinated SuperDARN THEMIS ASI Observations of Mesoscale Flow Bursts Associated with Auroral Streamers. *J. Geophys. Res. Space Phys.* 119 (1), 142–150. doi:10.1002/2013JA019245

Gkioulidou, M., Ukhorskiy, A. Y., Mitchell, D. G., Sotirelis, T., Mauk, B. H., and Lanzerotti, L. J. (2014). The Role of Small-Scale Ion Injections in the Buildup of Earth's Ring Current Pressure: Van Allen Probes Observations of the 17 March 2013 Storm. *J. Geophys. Res. Space Phys.* 119, 7327–7342. doi:10.1002/2014JA020096

Gkioulidou, M., Wang, C.-P., and Lyons, L. R. (2011). Effect of Self-Consistent Magnetic Field on Plasma Sheet Penetration to the Inner Magnetosphere: Rice Convection Model Simulations Combined with Modified Dungey Force-Balanced Magnetic Field Solver. *J. Geophys. Res.* 116 (A12), a–n. doi:10.1029/2011JA016810

Gkioulidou, M., Wang, C.-P., Wing, S., Lyons, L. R., Wolf, R. A., and Hsu, T.-S. (2012). Effect of an MLT Dependent Electron Loss Rate on the Magnetosphere-Ionosphere Coupling. *J. Geophys. Res. Space Phys.* 117 (A11), n/a. doi:10.1029/2012JA018032

Harel, M., Wolf, R. A., Reiff, P. H., Spiro, R. W., Burke, W. J., Rich, F. J., et al. (1981). Quantitative Simulation of a Magnetospheric Substorm 1. Model Logic and Overview. *J. Geophys. Res.* 86 (A4), 2217–2241. doi:10.1029/JA086iA04p02217

Henderson, M. G., Kepko, L., Spence, H. E., Connors, M., Sigwarth, J. B., Frank, L. A., and singer, H. J. (2002). "The Evolution of north-south Aligned Auroral Forms into Auroral Torch Structures: The Generation of omega Bands and Ps6 Pulsations via Flow Bursts," in Sixth International Conference on Substorms. Editor R. M. Winglee (Seattle: The University of Washington), 169–174.

Kauristie, K., Sergeev, V. A., Pulkkinen, T. I., Pellinen, R. J., Angelopoulos, V., and Baumjohann, W. (1996). "Study of the Ionospheric Signatures of the Plasma Sheet Bubbles," in *Substorms 3* (Noordwijk: European Space Agency Publications Division), 93.

Kim, H. J., Lee, D. Y., Wolf, R., Bortnik, J., Kim, K. C., Lyons, L., et al. (2021). Rapid Injections of MeV Electrons and Extremely Fast Step-Like Outer Radiation Belt Enhancements. *Geophys. Res. Lett.* 48 (9), e2021GL093151. doi:10.1029/2021GL093151

Liu, J., Angelopoulos, V., Runov, A., and Zhou, X.-Z. (2013). On the Current Sheets Surrounding Dipolarizing Flux Bundles in the Magnetotail: The Case for Wedgelets. *J. Geophys. Res. Space Phys.* 118 (5), 2000–2020. doi:10.1002/jgra.50092

Liu, J., Angelopoulos, V., Zhang, X. J., Turner, D. L., Gabrielse, C., Runov, A., et al. (2016). Dipolarizing Flux Bundles in the Cis-geosynchronous Magnetosphere: Relationship between Electric fields and Energetic Particle Injections. *J. Geophys. Res. Space Phys.* 121 (2), 1362–1376. doi:10.1002/2015JA021691

Liu, J., Angelopoulos, V., Zhou, X.-Z., Yao, Z.-H., and Runov, A. (2015). Cross-tail Expansion of Dipolarizing Flux Bundles. *J. Geophys. Res. Space Phys.* 120 (4), 2516–2530. doi:10.1002/2015JA020997

Liu, J., Lyons, L. R., Archer, W. E., Gallardo-Lacourt, B., Nishimura, Y., Zou, Y., et al. (2018). Flow Shears at the Poleward Boundary of Omega Bands Observed during Conjunctions of Swarm and THEMIS ASI. *Geophys. Res. Lett.* 45 (3), 1218–1227. doi:10.1002/2017GL076485

Liu, J., Lyons, L. R., Wang, C. P., Hairston, M. R., Zhang, Y., and Zou, Y. (2020). Dawnside Auroral Polarization Streams. *J. Geophys. Res. Space Phys.* 125 (8), e2019JA027742. doi:10.1029/2019JA027742

Liu, S., Chen, M. W., Schulz, M., and Lyons, L. R. (2006). Initial Simulation Results of Storm-Time Ring Current in a Self-Consistent Magnetic Field Model. *J. Geophys. Res.* 111 (A4). doi:10.1029/2005JA011194

Lyons, L. R., and Fennell, J. F. (1986). Characteristics of Auroral Electron Precipitation on the Morningside. *J. Geophys. Res.* 91 (A10), 11225–11234. doi:10.1029/JA091iA10p11225

Lyons, L. R., Liu, J., Nishimura, Y., Reimer, A. S., Bristow, W. A., Hampton, D. L., et al. (2021b). Radar Observations of Flows Leading to Substorm Onset over Alaska. *J. Geophys. Res. Space Phys.* 126 (2), e2020JA028147. doi:10.1029/2020JA028147

Lyons, L. R., Liu, J., Nishimura, Y., Wang, C. P., Reimer, A. S., Bristow, W. A., et al. (2021a). Radar Observations of Flows Leading to Longitudinal Expansion of Substorm Onset over Alaska. *J. Geophys. Res. Space Phys.* 126 (2), e2020JA028148. doi:10.1029/2020JA028148

Lyons, L. R., Nagai, T., Blanchard, G. T., Samson, J. C., Yamamoto, T., Mukai, T., et al. (1999). Association between Geotail Plasma Flows and Auroral Poleward Boundary Intensifications Observed by CANOPUS Photometers. *J. Geophys. Res.* 104 (A3), 4485–4500. doi:10.1029/1998JA900140

Lyons, L. R., Nishimura, Y., Gallardo-Lacourt, B., Nicolls, M. J., Chen, S., Hampton, D. L., et al. (2015). Azimuthal Flow Bursts in the Inner Plasma Sheet and Possible Connection with SAPS and Plasma Sheet Earthward Flow Bursts. *J. Geophys. Res. Space Phys.* 120 (6), 5009–5021. doi:10.1002/2015JA021023

Lyons, L. R., Nishimura, Y., Xing, X., Runov, A., Angelopoulos, V., Donovan, E., et al. (2012). Coupling of Dipolarization Front Flow Bursts to Substorm Expansion Phase Phenomena within the Magnetosphere and Ionosphere. *J. Geophys. Res.* 117 (A2), a–n. doi:10.1029/2011JA017265

Lyons, L. R. (1981). "The Field-Aligned Current versus Electric Potential Relation and Auroral Electrodynamics," in *Geophysical Monograph Series*. Editors S. I. Akasofu and J. R. Kan (Washington, D. C: American Geophysical Union), Vol. 25, 252–259. Available at: http://www.agu.org/books/gm/v025/GM025p0252/GM025p0252.shtml.

Lyons, L. R., Wang, C.-P., Gkioulidou, M., and Zou, S. (2009). Connections between Plasma Sheet Transport, Region 2 Currents, and Entropy Changes Associated with Convection, Steady Magnetospheric Convection Periods, and Substorms. *J. Geophys. Res.* 114 (A9), a–n. doi:10.1029/2008JA013743

Mende, S. B., Harris, S. E., Frey, H. U., Angelopoulos, V., Russell, C. T., Donovan, E., et al. (2008). The THEMIS Array of Ground-Based Observatories for the Study of Auroral Substorms. *Space Sci. Rev.* 141 (1–4), 357–387. doi:10.1007/s11214-008-9380-x

Nakamura, R., Oguti, T., Yamamoto, T., and Kokubun, S. (1993). Equatorward and Poleward Expansion of the Auroras during Auroral Substorms. *J. Geophys. Res.* 98 (A4), 5743–5759. doi:10.1029/92JA02230

Nishimura, Y., Lyons, L. R., Angelopoulos, V., Kikuchi, T., Zou, S., and Mende, S. B. (2011). Relations between Multiple Auroral Streamers, Pre-onset Thin Arc Formation, and Substorm Auroral Onset. *J. Geophys. Res.* 116 (A9), a–n. doi:10.1029/2011JA016768

Nishimura, Y., Lyons, L., Zou, S., Angelopoulos, V., and Mende, S. (2010). Substorm Triggering by New Plasma Intrusion: THEMIS All-Sky Imager Observations. *J. Geophys. Res.* 115 (A7). doi:10.1029/2009JA015166

Nishimura, Y., Yang, J., Weygand, J. M., Wang, W., Kosar, B., Donovan, E. F., et al. (2020). Magnetospheric Conditions for STEVE and SAID: Particle Injection, Substorm Surge, and Field-Aligned Currents. *J. Geophys. Res. Space Phys.* 125 (8), e2020JA027782. doi:10.1029/2020JA027782

Panov, E. V., Nakamura, R., Baumjohann, W., Angelopoulos, V., Petrukovich, A. A., Retinò, A., et al. (2010). Multiple Overshoot and Rebound of a Bursty Bulk Flow. *Geophys. Res. Lett.* 37 (8), n/a. doi:10.1029/2009GL041971

Pontius, D. H., and Wolf, R. A. (1990). Transient Flux Tubes in the Terrestrial Magnetosphere. *Geophys. Res. Lett.* 17 (1), 49–52. doi:10.1029/GL017i001p00049

Robinson, R. M., Vondrak, R. R., Miller, K., Dabbs, T., and Hardy, D. (1987). On Calculating Ionospheric Conductances from the Flux and Energy of Precipitating Electrons. *J. Geophys. Res.* 92 (A3), 2565. doi:10.1029/JA092iA03p02565

Rostoker, G., Lui, A. T. Y., Anger, C. D., and Murphree, J. S. (1987). North-south Structures in the Midnight Sector Auroras as Viewed by the Viking Imager. *Geophys. Res. Lett.* 14 (4), 407–410. doi:10.1029/GL014i004p00407

Sergeev, V. A., Aulamo, O. A., Pellinen, R. J., Vallinkoski, M. K., Bösinger, T., Cattell, C. A., et al. (1990). Non-substorm Transient Injection Events in the Ionosphere and Magnetosphere. *Planet. Space Sci.* 38 (2), 231–239. doi:10.1016/0032-0633(90)90087-7

Sergeev, V., Nishimura, Y., Kubyshkina, M., Angelopoulos, V., Nakamura, R., and Singer, H. (2012). Magnetospheric Location of the Equatorward Prebreakup Arc. *J. Geophys. Res.* 117 (A1), A01212. doi:10.1029/2011JA017154

Sun, W. J., Fu, S. Y., Parks, G. K., Liu, J., Yao, Z. H., Shi, Q. Q., et al. (2013). Field-aligned Currents Associated with Dipolarization Fronts. *Geophys. Res. Lett.* 40 (17), 4503–4508. doi:10.1002/grl.50902

Toffoletto, F., Sazykin, S., Spiro, R., and Wolf, R. (2003). Inner Magnetospheric Modeling with the Rice Convection Model. *Space Sci. Rev.* 107 (1), 175–196. doi:10.1007/978-94-007-1069-6_19

Wang, C.-P., Gkioulidou, M., Lyons, L. R., Wolf, R. A., Angelopoulos, V., Nagai, T., et al. (2011). Spatial Distributions of Ions and Electrons from the Plasma Sheet to the Inner Magnetosphere: Comparisons between THEMIS-Geotail Statistical Results and the Rice Convection Model. *J. Geophys. Res.* 116, a–n. doi:10.1029/2011JA016809

Wang, C. P., Gkioulidou, M., Lyons, L. R., and Wolf, R. A. (2018a). Spatial Distribution of Plasma Sheet Entropy Reduction Caused by a Plasma Bubble: Rice Convection Model Simulations. *J. Geophys. Res. Space Phys.* 123 (5), 3380–3397. doi:10.1029/2018JA025347

Wang, C. P., Gkioulidou, M., Lyons, L. R., and Wolf, R. A. (2018b). Spatial Distribution of Plasma Sheet Entropy Reduction Caused by a Plasma Bubble: Rice Convection Model Simulations. *J. Geophys. Res. Space Phys.* 123 (5), 3380–3397. doi:10.1029/2018JA025347

Wang, C. P., Yang, J., Gkioulidou, M., Lyons, L. R., and Wolf, R. A. (2020). Generation and Evolution of Two Opposite Types of Mesoscale Plasma Sheet Bubbles. *J. Geophys. Res. Space Phys.* 125 (9), e2020JA028072. doi:10.1029/2020JA028072

Wolf, R. A., Chen, C. X., and Toffoletto, F. R. (2012). Thin Filament Simulations for Earth's Plasma Sheet: Interchange Oscillations. *J. Geophys. Res. Space Phys.* 117 (A2), n/a. doi:10.1029/2011JA016971

Xing, X., Lyons, L., Nishimura, Y., Angelopoulos, V., Larson, D., Carlson, C., et al. (2010). Substorm Onset by New Plasma Intrusion: THEMIS Spacecraft Observations. *J. Geophys. Res.* 115, a–n. doi:10.1029/2010JA015528

Yang, J., Toffoletto, F. R., and Wolf, R. A. (2014). RCM-E Simulation of a Thin Arc Preceded by a north-south-aligned Auroral Streamer. *Geophys. Res. Lett.* 41 (8), 2695–2701. doi:10.1002/2014GL059840

Yang, J., Toffoletto, F. R., Wolf, R. A., and Sazykin, S. (2011). RCM-E Simulation of Ion Acceleration during an Idealized Plasma Sheet Bubble Injection. *J. Geophys. Res.* 116. doi:10.1029/2010JA016346

Yeoman, T. K., and Lühr, H. (1999). CUTLASS/IMAGE Observations of High-Latitude Convection Features during Substorms. *Ann. Geophys.* 15 (6), 692–702. doi:10.1007/s00585-997-0692-z

Yu, Y., Cao, J., Fu, H., Lu, H., and Yao, Z. (2017). The Effects of Bursty Bulk Flows on Global-scale Current Systems. *J. Geophys. Res. Space Phys.* 122 (6), 6139–6149. doi:10.1002/2017JA024168

Zesta, E., Lyons, L. R., and Donovan, E. (2000). The Auroral Signature of Earthward Flow Bursts Observed in the Magnetotail. *Geophys. Res. Lett.* 27 (20), 3241–3244. doi:10.1029/2000gl000027

Zou, S., Lyons, L. R., Nicolls, M. J., Heinselman, C. J., and Mende, S. B. (2009). Nightside Ionospheric Electrodynamics Associated with Substorms: PFISR and THEMIS ASI Observations. *J. Geophys. Res. Space Phys.* 114 (A12), n/a. doi:10.1029/2009JA014259

Conflict of Interest: The authors declare that the research was conducted in the absence of any commercial or financial relationships that could be construed as a potential conflict of interest.

Publisher's Note: All claims expressed in this article are solely those of the authors and do not necessarily represent those of their affiliated organizations, or those of the publisher, the editors and the reviewers. Any product that may be evaluated in this article, or claim that may be made by its manufacturer, is not guaranteed or endorsed by the publisher.

Copyright © 2021 Lyons, Nishimura, Wang, Liu and Bristow. This is an open-access article distributed under the terms of the Creative Commons Attribution License (CC BY). The use, distribution or reproduction in other forums is permitted, provided the original author(s) and the copyright owner(s) are credited and that the original publication in this journal is cited, in accordance with accepted academic practice. No use, distribution or reproduction is permitted which does not comply with these terms.

frontiers in Astronomy and Space Sciences

ORIGINAL RESEARCH
published: 01 September 2021
doi: 10.3389/fspas.2021.725800

Thermospheric Neutral Winds as the Cause of Drift Shell Distortion in Earth's Inner Radiation Belt

Solène Lejosne[1]*, *Mariangel Fedrizzi*[2,3], *Naomi Maruyama*[2,3] *and Richard S. Selesnick*[4]

[1]Space Sciences Laboratory, University of California, Berkeley, Berkeley, CA, United States, [2]Cooperative Institute for Research in Environmental Sciences, University of Colorado, Boulder, CO, United States, [3]NOAA Space Weather Prediction Center, Boulder, CO, United States, [4]Space Vehicles Directorate, Air Force Research Laboratory, Kirtland AFB, Albuquerque, NM, United States

Recent analysis of energetic electron measurements from the Magnetic Electron Ion Spectrometer instruments onboard the Van Allen Probes showed a local time variation of the equatorial electron intensity in the Earth's inner radiation belt. The local time asymmetry was interpreted as evidence of drift shell distortion by a large-scale electric field. It was also demonstrated that the inclusion of a simple dawn-to-dusk electric field model improved the agreement between observations and theoretical expectations. Yet, exactly what drives this electric field was left unexplained. We combine *in-situ* field and particle observations, together with a physics-based coupled model, the Rice Convection Model (RCM) Coupled Thermosphere-Ionosphere-Plasmasphere-electrodynamics (CTIPe), to revisit the local time asymmetry of the equatorial electron intensity observed in the innermost radiation belt. The study is based on the dawn-dusk difference in equatorial electron intensity measured at L = 1.30 during the first 60 days of the year 2014. Analysis of measured equatorial electron intensity in the 150–400 keV energy range, *in-situ* DC electric field measurements and wind dynamo modeling outputs provide consistent estimates of the order of 6–8 kV for the average dawn-to-dusk electric potential variation. This suggests that the dynamo electric fields produced by tidal motion of upper atmospheric winds flowing across Earth's magnetic field lines - the quiet time ionospheric wind dynamo - are the main drivers of the drift shell distortion in the Earth's inner radiation belt.

Keywords: Earth's inner radiation belt, thermospheric neutral winds, ionospheric wind dynamo, electric fields, radial transport

OPEN ACCESS

Edited by:
Jean-Francois Ripoll,
CEA DAM Île-de-France, France

Reviewed by:
Paul O'Brien,
The Aerospace Corporation,
United States
Margaret Chen,
The Aerospace Corporation,
United States

***Correspondence:**
Solène Lejosne
solene@berkeley.edu

Specialty section:
This article was submitted to Space Physics, a section of the journal Frontiers in Astronomy and Space Sciences

Received: *15 June 2021*
Accepted: *13 August 2021*
Published: *01 September 2021*

Citation:
Lejosne S, Fedrizzi M, Maruyama N and Selesnick RS (2021) Thermospheric Neutral Winds as the Cause of Drift Shell Distortion in Earth's Inner Radiation Belt. Front. Astron. Space Sci. 8:725800. doi: 10.3389/fspas.2021.725800

1. INTRODUCTION

The Van Allen Probes (Mauk et al., 2013) have provided unprecedented amounts of high quality energetic (10–100 keV) electron flux measurements near the magnetic equator in the inner belt and slot region (Reeves et al., 2016) below an equatorial altitude of about 3 Earth Radii ($L < 3$). These new measurements confirmed known dynamical features such as "zebra stripe" patterns in the spectrograms of energetic electrons (Imhof and Smith, 1965; Ukhorskiy et al., 2014) and energetic electron injections deep into the inner magnetosphere (Pfitzer and Winckler, 1968; Turner et al., 2015). Electron flux measurements in the 100–400 keV energy range from the Magnetic Electron Ion Spectrometer (MagEIS) instruments (Blake et al., 2013) also revealed a surprisingly persistent local time asymmetry of the equatorial electron intensity below $L = 1.4$ during geomagnetically quiet times, with higher radiation belt electron intensities near dawn (Selesnick et al., 2016).

Radiation belt particles are magnetically trapped high energy particles whose motion exhibits three quasi-periodic types of motion occurring on three distinct timescales (e.g., Northrop and Teller, 1960). The slowest periodicity corresponds to a drift motion around the planet that is the combination of an energy-independent electric drift and a gradient-curvature magnetic drift proportional to the particle's momentum. Radiation belt particles' drift motion defines closed surfaces known as drift shells. At high enough energies (>100 keV), the role played by large-scale electric fields is usually omitted: Radiation belt particles' momentum is expected to be conserved along a drift shell and the flux is expected to be constant at a fixed L value in the absence of any significant source or loss mechanism (e.g. Roederer, 1967). The observed local time asymmetry of the equatorial electron intensity at fixed L values below $L = 1.4$ challenged the latter, suggesting a drift shell distortion by a quasi-static electric field.

Even during geomagnetically quiet times, large-scale electric fields of the inner magnetosphere are more complex than the simple superposition of 1) a corotation electric field due to the rigid corotation of a perfectly conducting ionosphere and 2) a convection electric field set up by the coupling between the solar wind and the magnetosphere (e.g. Wolf et al., 2006). Dynamo electric fields produced by tidal motion of upper atmospheric winds flowing across the Earth's magnetic field lines—the ionospheric wind dynamo (Richmond, 1989)—are usually larger than subauroral convection electric fields below L ~ 2 (e.g., Figure 1 in the review by Mozer (1973). Longitudinal, seasonal, and solar cycle variations of the mid- and low-latitude ionospheric electric fields have been reported, together with a large day-to-day variability present even during geomagnetically quiet times (e.g., Fejer, 1993; Chau et al., 2010; Pfaff et al., 2010).

The objective of this study is to re-examine the time interval analyzed by Selesnick et al. (2016) in order to determine the origin of the large-scale electric field causing the observed radiation belt distortion. Observational and modeling resources are introduced in **Section 2** to describe the electric field properties associated with the drift shell distortion observed. In particular, we present a method to infer electric field properties directly from an analysis of asymmetries measured in differential directional fluxes. Experimental, numerical and analytical experiments provide consistent electric potential variation estimates, of the order of 6 – 8 kV between the dawn and dusk sectors at the magnetic equator of $L = 1.30$, i.e. at a magnetic latitude of ~ 29° at the ionospheric field line footpoint (**Section 3**). The similarities between experimental data analysis and outputs from a quiet time run by the Rice Convection Model (RCM) Coupled Thermosphere-Ionosphere-Plasmasphere-electrodynamics (CTIPe) model suggests that the electric potential variation results mainly from the quiet time wind dynamo.

2. MATERIALS AND METHODS

Leveraging Liouville's theorem and adiabatic invariant theory, we conduct an analysis of energetic electron directional differential fluxes measured by the Van Allen Probes to infer electric field properties in the inner belt. The resulting electric field properties are compared with outputs from Van Allen Probes field measurements and from a physics-based coupled model, RCM-CTIPe.

2.1. Field and Particle Measurements Onboard the Van Allen Probes

The time interval of the study corresponds to the first 60 days of the year 2014. This time interval was also selected for the study by Selesnick et al. (2016) because 1) the two orbital legs are near dawn and dusk at $L = 1.3$ and 2) it is geomagnetically quiet. Although some moderate (Echer et al., 2006) geomagnetic activity occurs towards the end of February, the time interval contains no significant inner belt injection. Additional details on the geomagnetic conditions associated with this time interval are provided in **Section 4**.

The Van Allen Probes (Fox and Burch, 2014) were twin spacecraft with similar highly elliptical orbits (perigee at ~ 600 km, apogee at ~ 5.8 R_E), an orbital period of about 9 h, and an inclination close to 10°. Spacecraft apogees drifted slowly so that it took a bit less than 2 years for spacecraft apogees to scan all local time sectors (precession rate of about 210° per year). Successive inbound and outbound crossings of $L = 1.3$ occurred fast, within 30 min. During the first 60 days of 2014, inbound crossings of $L = 1.3$ are in the dusk-premidnight region (20–22 MLT) while outbound crossings are in the dawn sector (4-6 MLT) for both Van Allen probes. The geographic longitudes of the crossings depend on time (UT).

In this study, we rely primarily on the directional differential fluxes provided by the MagEIS instrument (processed to level 3). Electric field measurements are also analyzed to compare and contrast with proposed electric field models. Experimental electric field information comes from measurements by the Electric Field and Waves (EFW) instrument (Wygant et al., 2013) and by the Electric and Magnetic Field Instrument Suite and Integrated Science (EMFISIS) (Kletzing et al., 2013). Field and particle measurements immediately following spacecraft maneuvers are omitted.

2.1.1. Differential Fluxes for Equatorial Electrons

The analysis focuses on equatorial electron intensity in the 150–400 keV energy range. MagEIS data below 400 keV is normally well above background. We follow the approach developed by Selesnick et al. (2016) to determine fluxes of equatorially mirroring electrons. MagEIS pitch-angle resolved measurements are extrapolated when the spacecraft is close to the magnetic equator. Specifically, directional differential fluxes are extrapolated to determine the equatorial electron intensity, j_o, when the local field magnitude, B, is such that $B_o \leq B < 1.08B_o$, where B_o is the equatorial magnetic field calculated according to the International Geomagnetic Reference Field to which Olson and Pfitzer, 1977 Quiet is superimposed (Olson and Pfitzer, 1977).

We define the magnetic shell parameter, L, following the definition provided by McIlwain (1961). For equatorial particles, the parameter L is such that:

$$L = (B_E/B_o)^{1/3} \quad (1)$$

where $B_E = 30,000\,nT$ is the magnetic equatorial field at the surface of the Earth. This definition guarantees that constant L values define curves of constant equatorial magnetic field amplitude, i.e., $(B_o = cst.) \Leftrightarrow (L = cst.)$, even in non-dipolar fields.

When experimental information is required at a fixed L value, we interpolate as a function of L using adjacent measurements within $\pm 0.025\,L$ when available. Linear interpolations of adjacent logarithmic flux measurements are also performed to estimate partial derivatives with respect to L and kinetic energy, T (with window sizes of $\pm 0.025\,L$ and $\pm 155\,keV$, respectively).

2.1.2. Electric Drift Measurements

Electric drift measurements are pre-processed following the approach developed over the years by Lejosne and Mozer (2016a, 2016b, 2019) and briefly described below. After a slight correction applied to the orientation of the magnetometer axes (Lejosne and Mozer, 2016a), the spin-averaged ($\sim 12\,s$) electric drift measurement is reformulated in a local orthonormal frame of reference $(\boldsymbol{e_\rho}, \boldsymbol{e_b}, \boldsymbol{e_\varphi})$ set by the measured magnetic field direction: $\boldsymbol{e_b} = -\boldsymbol{B}/\|\boldsymbol{B}\|$, $\boldsymbol{e_\varphi} = (\boldsymbol{B}\times\boldsymbol{r})/\|\boldsymbol{B}\times\boldsymbol{r}\|$ and $\boldsymbol{e_\rho} = \boldsymbol{e_\varphi}\times\boldsymbol{B}/\|\boldsymbol{B}\|$, where $\boldsymbol{B}$ is the magnetic field vector at the location $\mathbf{r}$. $\boldsymbol{e_\rho}$ and $\boldsymbol{e_\varphi}$ indicate the radial and azimuthal directions, respectively. The shorting factor is calibrated to a value very close to 1 (Lejosne and Mozer, 2019). Once corotation is subtracted, the electric drift measurement is projected to the magnetic equator assuming equipotential field lines. The magnetic field model is set to the International Geomagnetic Reference Field for the Earth's internal field. The choice of the external magnetic field model is unimportant when mapping at L = 1.30. During data processing, the Kp-driven Tsyganenko (1989) magnetic field model was superimposed (Lejosne and Mozer, 2016b).

2.2. Numerical Model RCM-CTIPe

Electric potential and electric field values at 100 km altitude are provided by the Rice Convection Model (RCM) Coupled Thermosphere-Ionosphere-Plasmasphere-electrodynamics (CTIPe) model. This self-consistently coupled model of the magnetosphere, ionosphere and thermosphere is composed of three physical models: 1) the Coupled Thermosphere-Ionosphere-Plasmasphere with self-consistent electrodynamics (CTIPe) model (Fuller-Rowell et al., 1996; Millward et al., 2001, 1996); 2) the Rice Convection Model—RCM (Toffoletto et al., 2003; Wolf, 1983); and 3) the global electrodynamic solver based on the National Center for Atmospheric Research Thermosphere-Ionosphere Electrodynamics General Circulation Model—NCAR-TIEGCM (Richmond and Maute, 2014). The model includes the electrodynamic coupling, interactions, and feedback between the inner magnetosphere and the thermosphere-ionosphere-magnetosphere system. A detailed description of the model coupling can be found in the article by Maruyama et al. (2011).

2.3. Theoretical Framework for the Inference of Electric Field Properties From Directional Differential Flux Analysis

The objective of this section is to show how to infer information on electric field properties from measured variations of differential fluxes of equatorially trapped particles. This theoretical framework is similar to the one developed by Lejosne and Mozer (2020) for the analysis of zebra stripe patterns. It is adapted below to the case of drift shell distortion by quasi-static electric fields.

Leveraging Liouville's theorem and adiabatic invariant theory, the variation of equatorial electron fluxes measured at different local times along the same $B_o = cst.$ curve is related to trapped particle kinetic energy variation (**Section 2.3.1.**). **Section 2.3.2.** details the relationship between trapped particle kinetic energy variation and electric potential variation. **Section 2.3.3.** provides the equation implemented hereafter and summarizes the assumptions underlying the overall approach.

2.3.1. Link Between Fluctuations in Directional Differential Fluxes of Equatorially Trapped Particles and Kinetic Energy Variations

According to Liouville's theorem, the phase space density, $f = j_o/p^2$, is constant along the continuous trajectories of the system in phase space, i.e., along the dynamical path of particles, in the absence of any source or loss. Thus, any variation of the trapped population momentum, dp/p, is related to a variation of the directional differential flux, dj_o/j_o along the drift shell:

$$\frac{dj_o}{j_o} = 2\frac{dp}{p} \quad (2)$$

This equation can also be rewritten in terms of kinetic energy, T, and kinetic energy variation, dT, since:

$$\frac{dp}{p} = \frac{\gamma}{\gamma+1}\frac{dT}{T} \quad (3)$$

where $\gamma = (T + mc^2)/mc^2$ is the Lorentz factor and $mc^2 = 511\,keV$ is the rest mass energy for an electron. Assuming conservation of the first invariant, $p^2/2mB_o = cst.$, any variation of the momentum is related to a variation in the equatorial magnetic field along the drift shell:

$$2\frac{dp}{p} = \frac{dB_o}{B_o} \quad (4)$$

Noting that $B_o = B_E/L^3$(**Eq. 1**), the combination of **Eqs 3**, **4** also relates trapped particle energization, dT, and radial motion, dL:

$$\frac{dT}{T} = -\frac{3}{2}\left(1+\gamma^{-1}\right)\frac{dL}{L} \quad (5)$$

The variations discussed above occur along the same equatorial drift shell, i.e.:

$$dj_o = j_o\left(T + dT, B_o + dB_o, \varphi_2\right) - j_o\left(T, B_o, \varphi_1\right) \quad (6)$$

where (T, B_o, φ_1) and $(T + dT, B_o + dB_o, \varphi_2)$ are coordinates along the same equatorial drift shell. The phases φ_1 and φ_2 represent the magnetic local times of an L-crossing during consecutive inbound and outbound passes, respectively. In practice, the shape of the distorted drift shell is unknown, and what is measured is in fact the fluctuation in differential equatorial flux at fixed kinetic energy, T, and different magnetic local times along the same $B_o = cst.$ curve. In other words, the fluctuation measured is:

$$\delta j_o = j_o(T, B_o, \varphi_2) - j_o(T, B_o, \varphi_1) \tag{7}$$

Assuming small distortions of the field, the fluctuation measured, δj_o, is related to the fluctuation along the dynamical path of particles, dj_o, in the following way:

$$\delta j_o = dj_o - dT\frac{\partial j_o}{\partial T} - dB_o\frac{\partial j_o}{\partial B_o} \tag{8}$$

Combining **Eqs 3**, **4** and **8**, and noting that $dx/x = d\ln x$, we obtain the relationship between the variation of equatorial electron differential fluxes measured at different local times along the same $B_o = cst.$ curve, δj_o, and trapped particle energy variation, dT:

$$\frac{\delta j_o}{j_o} = \left(\frac{2\gamma}{\gamma+1}\left(1 - \frac{\partial \ln j_o}{\partial \ln B_o}\right) - \frac{\partial \ln j_o}{\partial \ln T}\right)\frac{dT}{T} \tag{9}$$

2.3.2. Link Between Kinetic Energy Variation and Electric Potential Variation

The time rate of change of the average kinetic energy of a guiding center of charge q is provided by the energy equation (Roederer and Zhang, 2014):

$$\frac{dT}{dt} = \frac{M}{\gamma}\frac{\partial B}{\partial t} + \boldsymbol{V}\cdot(q\boldsymbol{E} + \boldsymbol{F}) \tag{10}$$

where $\boldsymbol{V}$ refers to the drift velocity of the guiding center and $\boldsymbol{F}$ is an external non-electromagnetic force that is omitted hereafter. The electric field, $\boldsymbol{E}$, is described here as the sum of a corotation electric field and a subauroral electrostatic field:

$$E = -(\boldsymbol{\Omega}\times\mathbf{r})\times\mathbf{B} - \nabla U \tag{11}$$

where $\boldsymbol{\Omega}$ is the angular velocity vector of the Earth's rotation, and U is the electrostatic potential associated with the subauroral electrostatic field. Noting that $\partial B/\partial t = -(\boldsymbol{\Omega}\times\boldsymbol{r})\cdot\nabla B$, it follows from the combination of **Eqs 10**, **11** in the case of energetic electrons ($q < 0$) that a variation in kinetic energy, dT, along the dynamical path of particles is related to a variation in electrostatic potential, dU:

$$dT = e(1 - \varsigma(T))dU \tag{12}$$

where $e = |q| > 0$ is the elementary charge and $\varsigma(T)$ corresponds to the ratio between electric and total (magnetic + electric) angular drift velocities

$$\varsigma(T) \cong e\frac{2}{3}\left(\frac{\gamma}{\gamma+1}\right)\frac{\Omega B_E R_E^2}{TL} \ll 1 \tag{13}$$

where $R_E = 6,370\,km$ is one Earth radius. **Eq. 12** describes the conservation of the total energy of the guiding center along the drift shell (e.g., Whipple, 1978).

2.3.3. Summary of the Theoretical Framework

A change of variables from B_o to L (**Eq. 1**) and the combination of **Eqs 9**, **12** provides the relationship between a measured fluctuation in the equatorial electron intensity, δj_o, and an electrostatic potential variation, dU. Let us emphasize that the variations measured are between the magnetic local times of the inbound (φ_1) and outbound (φ_2) crossings of the same $B_o = cst.$ curve:

$$dU = \frac{T(1+\varsigma(T))}{e}\left(\frac{2\gamma}{\gamma+1}\left(1 + \frac{1}{3}\frac{\partial \ln j_o}{\partial \ln L}\right) - \frac{\partial \ln j_o}{\partial \ln T}\right)^{-1}\frac{\delta j_o}{j_o} \tag{14}$$

where $\delta j_o = j_o(T, B_o, \varphi_2) - j_o(T, B_o, \varphi_1)$, and the partial derivatives are computed outbound at (T, B_o, φ_2).

Theoretically, the electric potential variation, dU, on the left side of **Eq. 14**, is a quantity independent of the kinetic energy of the trapped population considered, T. Thus, the right side of **Eq. 14** is expected to be independent of the variable T as well.

The assumptions underlying this equation are that there is no significant source or loss mechanism on the time scale of the equatorially trapped population drift period, no external non-electromagnetic force, no parallel electric field, no other significant source of magnetic field time variation besides Earth's rotation, and no significant time variation of the electric potential on the timescale of the electron drift period (this includes the timescale of spacecraft motion from the inbound to the outbound crossings of $L = 1.3$, which is of the order of 30 *min*).

3. RESULTS

Section 3.1. presents experimental information on the electric potential variation between dawn and dusk at $L = 1.30$ (magnetic latitude of $\sim 29°$ at the corresponding ionospheric field line footpoint), leveraging field and particle measurements independently. **Section 3.2.** compares these results with estimates from analytical and numerical models. **Section 3.3.** *Conclusion of the Experimental Analysis* summarizes our findings.

3.1. Experimental Results

3.1.1. Experimental Information on the Electric Potential Variation Between Dawn and Dusk Based on Measured Equatorial Electron Intensity Asymmetry

Figure 1 is an introduction to the approach. During the first 60 days of 2014, the Van Allen Probes crossings of $L = 1.30$ are in the dusk-premidnight region (20–22 MLT) during inbound, φ_1, and in the dawn (4-6 MLT) sector during outbound, φ_2 (**Figure 1A**). The equatorial intensity of 226 keV electrons at $L = 1.30$ measured by Van Allen Probes A (RBA) is ~40% higher at dawn (in red **Figure 1B**) than dusk (in blue **Figure 1B**). The

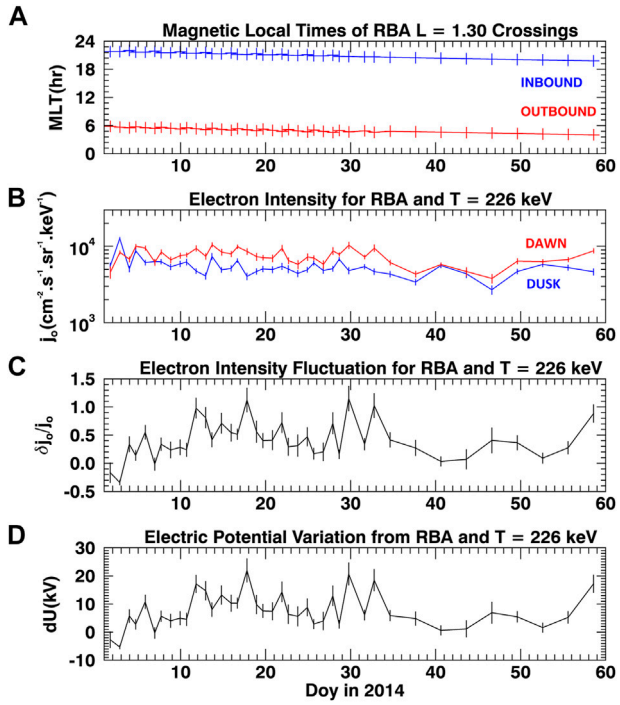


FIGURE 1 | The variation of electric potential between the inbound and outbound locations of the same L = 1.30 value is inferred directly from an analysis of asymmetries in measured energetic electron fluxes. **(A)** Magnetic local times of the Van Allen Probes A, RBA, during (blue) inbound and (red) outbound crossings of L = 1.30; **(B)** Equatorial electron intensity at 226 keV during (blue) inbound and (red) outbound crossings of L = 1.30, derived from measurements at 226 keV by the MagEIS instrument onboard Van Allen Probes A; **(C)** Corresponding fluctuations in directional differential fluxes of equatorially trapped 226 keV electrons; and **(D)** Corresponding electric potential variation at L = 1.30 between dawn and dusk, the local times of the outbound and inbound crossings, respectively. The 1-sigma error bars are derived from statistical error in each measured j value.

corresponding equatorial intensity fluctuation at 226 keV and L = 1.30, $\delta j_o/j_o$, is evaluated by subtracting the outbound electron intensity (the red line **Figure 1B**) from the inbound electron intensity (the blue line **Figure 1B**), and normalizing by the inbound value. This was done for 40 different consecutive sequences of near equatorial inbound/outbound crossings of L = 1.3 during the 60 days considered (**Figure 1C**). The partial derivatives of $\ln j_o$ with respect to $\ln L$ and $\ln T$ were computed locally to provide a time series for the electric potential variation, dU, between the inbound and outbound local times of L = 1.30 following **Eq. 14** (**Figure 1D**).

The time variation of the electric potential variation, $dU(t)$, is similar to the time variation of the intensity fluctuation, $\delta j_o/j_o(t)$, because the coefficient by which $\delta j_o/j_o$ is multiplied to obtain dU (**Eq. 14**) does not vary significantly (<10%) during the time interval considered. Analysis of the 226 keV equatorial electron intensity measured by Van Allen Probes A during the first 60 days of 2014 suggests that the average electric potential variation between dawn and dusk is $7.6 \pm 2.7\,kV$.

The approach is extended to both Van Allen Probes, and to all four MagEIS energy channels between 150 and 400 keV. The results are presented **Figure 2**. While the times series for the electric potential variations seem to depend on the measuring spacecraft (**Figures 2A,B**), the averages, and standard deviations of the electric potential variation, dU, appear independent of the energy channel (**Figure 2C**). That the statistical characteristics of the electric potential do not depend on MagEIS energy channel is consistent with theoretical expectations (**Section 2.3.3.**).

The analysis suggests that the average value for the electric potential variation between dawn and dusk is $dU = 8 \pm 4\,kV$ during the first 60 days of 2014. In terms of average electrostatic field, since $dU = -\int_{\varphi_1}^{\varphi_2} \boldsymbol{E}.\boldsymbol{dl} \cong -\int_{\varphi_1}^{\varphi_2} E_\varphi r_o d\varphi$, the electric potential variation corresponds to an average radial electric field between dusk (φ_1) and dawn (φ_2) of $[E_\varphi] = -0.5 \pm 0.2\,mV/m$ at the magnetic equator of L = 1.3.

3.1.2. Experimental Information on the Electric Potential Between Dawn and Dusk Based on Electric Field Measurements

While Van Allen Probes only provide local electric field samples at $L = 1.3$ at precisely dusk (φ_1) and dawn (φ_2) during the time interval considered, it is possible to obtain another estimate of the electric potential variation between dawn and dusk by considering Van Allen Probes electric field measurements over a longer time interval. **Figure 3** provides experimental information on the characteristics of the DC electric field measured by the Van Allen Probes during the years 2013 and 2014 at $L = 1.3 \pm 0.05$ during geomagnetically quiet times ($Kp < 3$). The local time averages and standard deviations are computed over running windows of 1 hour size and they are represented by a black line and a shaded area, respectively. Assuming that the electrostatic electric field ($-\nabla U$) is quasi-stationary, the 24 hr-MLT average of the electric field components should be zero. Experimentally, the 24 hr-MLT averages of the radial and azimuthal electric field components measured are $0.02\,mV/m$ and $0.20\,mV/m$, respectively. These small offsets could be due to small residual calibration errors (e.g. Lejosne and Mozer, 2019). They could also be due to the irregular seasonal and longitudinal samplings. These small offsets have been subtracted from the datasets before estimating the average electric field between dusk and dawn and the corresponding electric potential variation between dawn and dusk. In that context, the average azimuthal component of the electric field between dusk and dawn is $-0.4 \pm 0.1\,mV/m$, and the corresponding variation of the electric potential is $7 \pm 2\,kV$. These are comparable to the estimates provided by the particle data analysis (**Section 3.1.1.**).

3.2. Model-Observation Comparison for the Electric Potential and Electric Field Components

In this section, we provide electric potential variation between dawn and dusk predicted by analytic and numerical models.

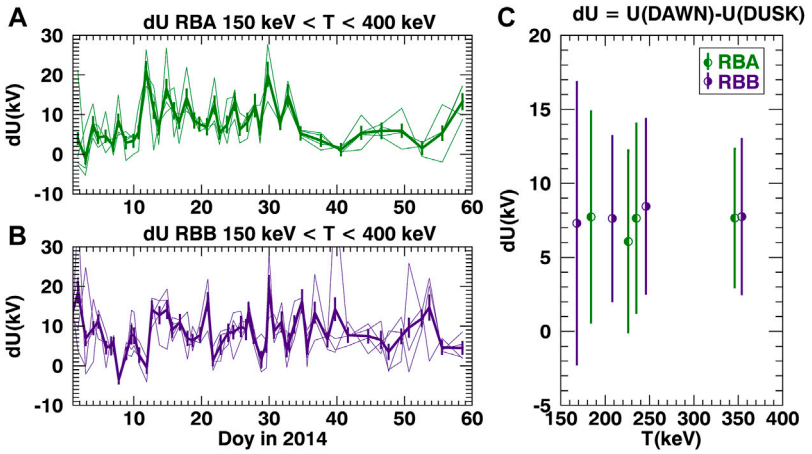


FIGURE 2 | (A) Time series of electric potential variations according to four MagEIS channels comprised between 150 and 400 keV onboard the Van Allen Probes A (RBA). The time series inferred from each individual energy channel are represented by thin lines while the average over all four energy channels is represented by a thick solid green line. **(B)** Time series of electric potential variations according to four MagEIS channels comprised between 150 and 400 keV onboard the Van Allen Probes B (RBB). The time series for each energy channel are represented by thin lines while the average over all four energy channels is represented by a thick solid purple line. **(C)** Medians and standard deviations for the electric potential variation between dawn and dusk at L = 1.3 during the first 60 days of the year 2014 according to four MagEIS channels measuring differential direction fluxes for kinetic energies, T, comprised between 150 and 400 keV, onboard (green) Van Allen Probes A and (purple) Van Allen Probes B.

3.2.1. Comparison With an Analytical Expression for the Electric Potential Variation

The simple electrostatic potential proposed by Selesnick et al. (2016), U_s, is:

$$U_s = E_c L R_E \sin\varphi \tag{15}$$

where $E_c = 0.4\,mV/m$. The magnitude of E_c was set in order to correctly represent the average distortion observed during the first 50 days of 2014. Under that model, the electric potential variation between dawn and dusk is of the order of $6\,kV$ and the average azimuthal electric field component between dusk and dawn is $-0.3\,mV/m$.

3.2.2. Comparison With Numerical Values During a Quiet Time Run With RCM-CTipe

24 h worth of electric field values during a quiet-time run with the RCM-CTIPe are provided in **Figure 4**. The quiet time run corresponds to a day in spring (set to March 17, 2013) during which the solar wind-magnetosphere dynamo is artificially forced to 0. In that context, the electric fields are driven solely by the quiet time wind dynamo. Because the magnetic local time (MLT) is a combination of universal time (UT) and longitude, the time variations observed at a given MLT are also representative of the longitudinal dependence of the electric field. Ionospheric values have been projected to the magnetic equator along dipolar equipotential field lines. This projection means that the radial (poleward) ionospheric component of the electric field has been multiplied by a factor ~ 0.52 while the azimuthal (eastward) ionospheric component of the electric field has been multiplied by a factor ~ 0.67 to obtain the corresponding amplitudes at the magnetic equator of $L = 1.3$ (see also Lejosne and Mozer, 2016b, Section 2.1.3 for analytic expressions regarding electric field mapping). The modeled average electric potential variation due to the wind dynamo between dawn and dusk is $7 \pm 1\,kV$ according to RCM-CTIPe and the average azimuthal electric field component between dusk and dawn is $-0.4 \pm 0.1\,mV$. This first estimate is consistent with simulated values for the MLT distribution of the electric potential resulting solely from the quiet time motion of the neutral atmosphere of (Yamazaki and Maute, 2017, their Figure 8).

3.3. Conclusion of the Experimental Analysis

The different estimates for the dawn-dusk electric potential variation at $L = 1.3$ are summarized in **Table 1**, together with the method and the time interval considered.

Table 1 shows that different methods provide consistent estimates for the electric potential variation between dawn and dusk, with a magnitude of the order of 6–8 kV. The similarity is remarkable given that: 1) the neutral winds and associated wind dynamo vary from day to day and 2) every method was applied under a unique set of conditions.

An electric potential variation of 6–8 kV between dawn and dusk is ~15 times greater than would be predicted by the usual Maynard and Chen (1975) parametrization of the Volland (1973) - Stern (1975) convection electric field model during quiet geomagnetic activity ($Kp = 2$), suggesting that the solar wind-magnetosphere dynamo is unlikely to be the main of cause of the observed drift shell distortion.

Van Allen probes electric field measurements and simulations by RCM-CTIPe are in qualitative agreement, despite differences in their time intervals. These similarities confirm that the electric potential variation results mainly from the quiet time wind dynamo. Comparing **Figures 3**, **4** also demonstrates that the Van Allen Probes can resolve the effects of neutral winds on global electric fields.

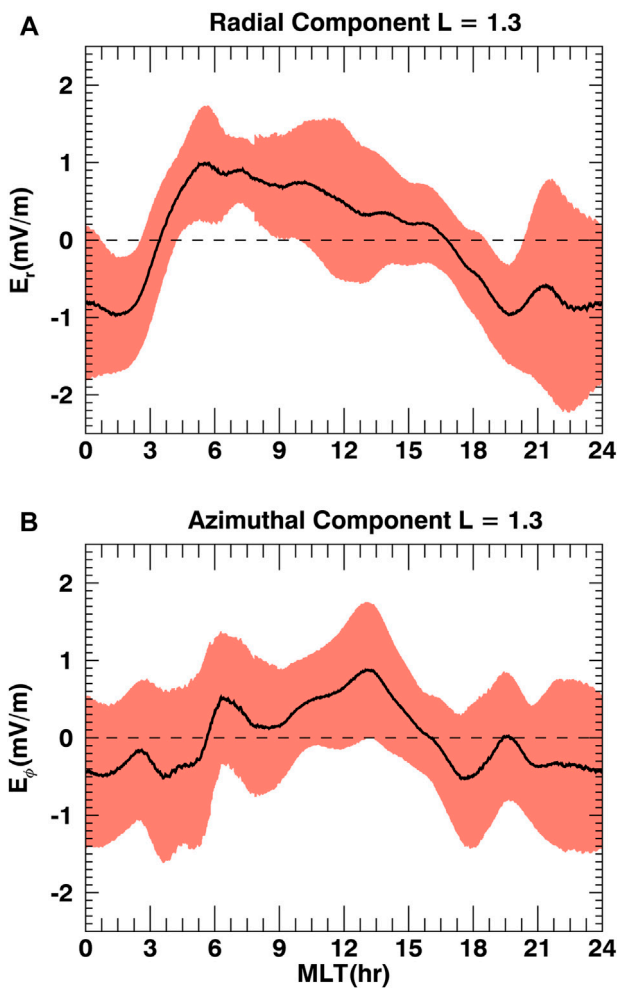


FIGURE 3 | Characteristics of the **(A)** radial and **(B)** azimuthal components of the electric field measured by both Van Allen Probes and projected to the magnetic equator during crossings of L = 1.3 in the years 2013 and 2014. The solid black lines are the 1hr-MLT running averages of the data points. The standard deviation computed over the same 1 hr-MLT running window is represented by the shaded area. The 24 hr-MLT experimental averages of the radial and azimuthal electric field components, of 0.02 mV/m and 0.20mV/m, respectively, have been subtracted from the datasets for calibration purposes.

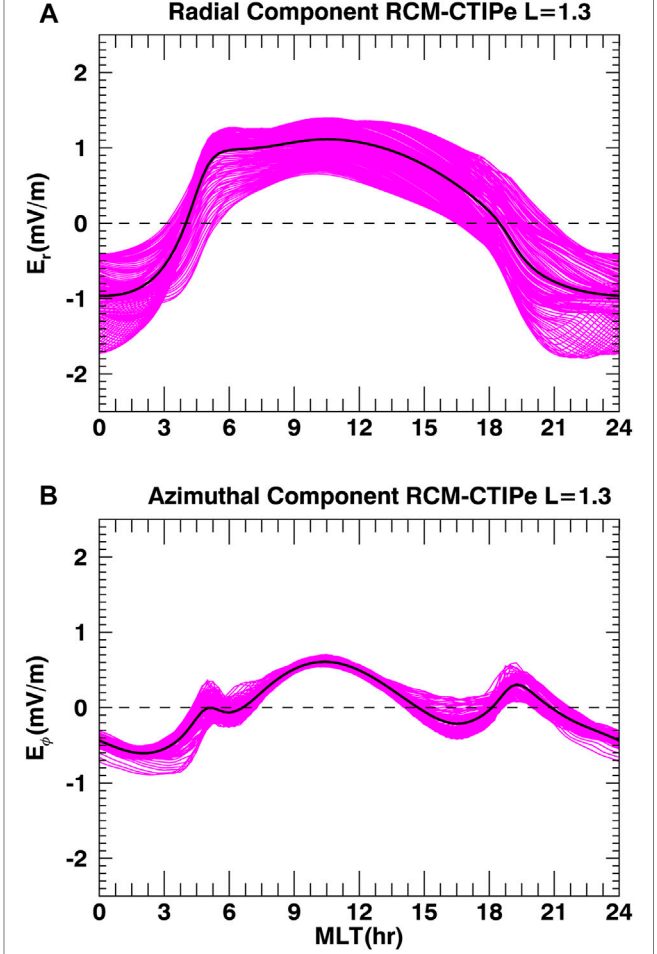


FIGURE 4 | Characteristics of the **(A)** radial and **(B)** azimuthal components of the electric field projected to the magnetic equator of L = 1.3 according to 24 h of quiet time run by the RCM-CTIPe model. The MLT variations of the electric field vary as a function of the time of the day, and they are represented every 10 min *via* solid magenta lines. The solid black lines represent the electric field daily averages.

4. DISCUSSION: TIME VARIATIONS OF THE ELECTRIC POTENTIAL VARIATION AS DETERMINED BY THE MEASURED ASYMMETRY IN THE EQUATORIAL ELECTRON INTENSITY

While the modeling and experimental results provide similar estimates for the average magnitude of the dawn-dusk electric potential variation, they do not explain the high variability revealed by the particle data analysis. The time series of dawn-dusk electric potential variation, $dU(t)$, has a standard deviation of the order of $7\,kV$ (**Figure 2C**). On the other hand, 1 day of quiet time run by RCM-CTIPe provides a standard deviation of the order of $1\,kV$ only, including possible longitudinal effects.

Data analyses similar to the one presented **Section 3.1.1.** were performed 1) using measurements by the Radiation Belt Storm Probes Ion Composition Experiment (Mitchell et al., 2013) in place of MagEIS, and/or 2) at higher L values (specifically, L = 1.5, and L = 1.7). While quantitative analysis of RBSPICE data is incomplete, similar trends for the time variations of the dawn-dusk electric potential were observed. These findings suggest that the time variations observed correspond to real geophysical information.

We searched for possible dependencies of the time series, $dU(t)$, by performing correlation analyses with various indicators. We looked for possible correlations between the

TABLE 1 | Estimates of the electric potential variation between dawn and dusk, and average azimuthal electric field component between the dusk and dawn regions of the magnetic equator of L = 1.3 according to different experimental, numerical and analytical methods.

Method	Time interval considered	Electric potential variation $dU(kV)$ between dusk (φ_1) and dawn (φ_2) at the magnetic equator of $L = 1.3$	Average azimuthal electric field [E_φ] between dusk (φ_1) and dawn (φ_2) at the magnetic equator of L = 1.3
Local asymmetries in radiation belt intensity ($\delta j_o/j_o$)	94 crossings of L = 1.3 during the first 60 days in 2014	$8 \pm 4kV$	$-0.5 \pm 0.2mV/m$
Van Allen Probes DC electric field measurements	2 years of data (2013–2014) with at L = 1.3 (9 h orbit)	$7 \pm 2kV$	$-0.4 \pm 0.1\,mV$
Analytic expressions developed by Selesnick et al. (2016)	DOY 1-53 in 2014	$6kV$	$-0.3mV/m$
Numerical Model RCM-CTIPe	24 h of artificial quiet time run (Mar 17, 2013)	$7 \pm 1kV$	$-0.4 \pm 0.1mV$

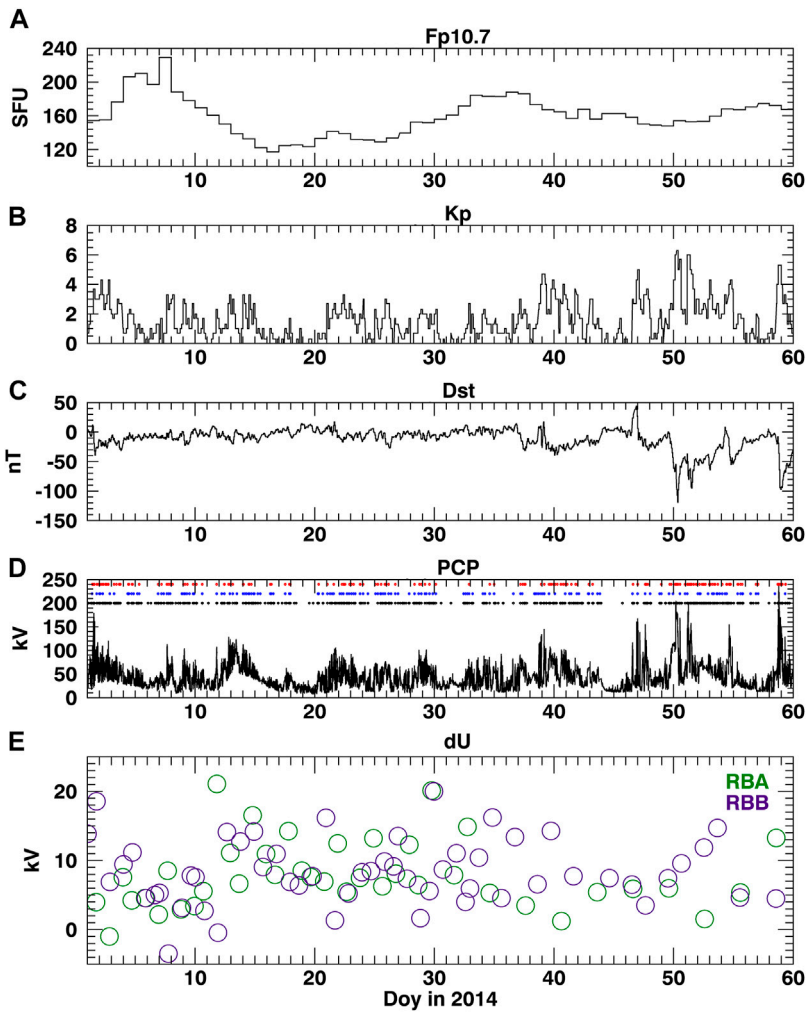


FIGURE 5 | Various indicators [**(A)** F10.7, **(B)** Kp, **(C)** Dst and **(D)** Polar Cap Potential PCP] for the electromagnetic conditions associated with **(E)** the time dependence of the dawn-dusk electric potential variation, dU. The SuperMag substorm lists from Forsyth et al. (2015), Newell and Gjerloev (2011) and Ohtani and Gjerloev (2020) are indicated Panel **(D)** in black, blue and red, respectively.

sampled electric potential variation, $dU(t)$, and the spacecraft longitudinal positions at the time, t, of measurements (UT). We also looked for possible variations based on a variety of indicators (presented in **Figure 5**), such as F10.7, Kp, Dst, and the polar cap potential, PCP, computed according to the formula by Boyle et al. (1997). We also considered substorm onsets as defined by Forsyth et al. (2015), Newell and Gjerloev (2011) and Ohtani and Gjerloev (2020). Regardless of the parameter considered, no obvious dependency was found.

Realistic modeling of the subauroral electric field evolution is required to further investigate the origin of the variability reported here.

DATA AVAILABILITY STATEMENT

Publicly available datasets were analyzed in this study. This data can be found here: The Van Allen Probes electric field data are in public access in the RBSP/EFW database: www.space.umn.edu/rbspefw-data. The MagEIS and magnetic ephemeris data are available from the ECT Science Operations and Data Center, https://rbsp-ect.newmexicoconsortium.org/rbsp_ect.php Simulation outputs can be obtained by contacting NM.

AUTHOR CONTRIBUTIONS

The first author is the lead and corresponding author. All other authors are listed in alphabetical order. We describe contributions to the paper using the CRediT (Contributor Roles Taxonomy) categories (Brand et al., 2015). Conceptualization and Funding Acquisition: SL and NM. Resources: SL, MF, NM, and RS. Methodology, Software, Validation, Formal Analysis and Investigation: SL and RS. Writing-Original Draft, Visualization and Project Administration: SL. Writing-Review and Editing: SL, RS, and MF.

FUNDING

SL work was performed under JHU/APL Contract No. 922613 (RBSP-EFW), NASA Grant Awards 80NSSC18K1223 and 80NSSC20K1351. RS work is supported by the Space Vehicles Directorate of the Air Force Research Laboratory.

ACKNOWLEDGMENTS

The authors are grateful to Seth Claudepierre, the MAGEIS team, and the RBSPICE team for insightful discussions.

REFERENCES

Blake, J. B., Carranza, P. A., Claudepierre, S. G., Clemmons, J. H., Crain, W. R., Dotan, Y., Fennell, J. F., Fuentes, F. H., Galvan, R. M., George, J. S., Henderson, M. G., Lalic, M., Lin, A. Y., Looper, M. D., Mabry, D. J., Mazur, J. E., McCarthy, B., Nguyen, C. Q., O'Brien, T. P., Perez, M. A., Redding, M. T., Roeder, J. L., Salvaggio, D. J., Sorensen, G. A., Spence, H. E., Yi, S., and Zakrzewski, M. P. (2013). The Magnetic Electron Ion Spectrometer (MagEIS) Instruments Aboard the Radiation Belt Storm Probes (RBSP) Spacecraft. *Space Sci Rev* 179, 383–421. doi:10.1007/s11214-013-9991-8

Boyle, C. B., Reiff, P. H., and Hairston, M. R. (1997). Empirical polar cap potentials. *J. Geophys. Res.* 102 (A1), 111–125. doi:10.1029/96JA01742

Brand, A., Allen, L., Altman, M., Hlava, M., and Scott, J. (2015). Beyond authorship: attribution, contribution, collaboration, and credit. *Learn. Pub.* 28, 151–155. doi:10.1087/20150211

Chau, J. L., Aponte, N. A., Cabassa, E., Sulzer, M. P., Goncharenko, L. P., and González, S. A. (2010). Quiet time ionospheric variability over Arecibo during sudden stratospheric warming events. *J. Geophys. Res.* 115, a–n. doi:10.1029/2010JA015378

Echer, E., Gonzalez, W. D., and Alves, M. V. (2006). On the geomagnetic effects of solar wind interplanetary magnetic structures. *Space Weather* 4, a–n. doi:10.1029/2005SW000200

Fejer, B. G. (1993). F region plasma drifts over Arecibo: Solar cycle, seasonal, and magnetic activity effects. *J. Geophys. Res.* 98 (A8), 13645–13652. doi:10.1029/93JA00953

Forsyth, C., Rae, I. J., Coxon, J. C., Freeman, M. P., Jackman, C. M., Gjerloev, J., and Fazakerley, A. N. (2015). A new technique for determining Substorm Onsets and Phases from Indices of the Electrojet (SOPHIE). *J. Geophys. Res. Space Physics* 120 (10), 10,592. doi:10.1002/2015JA021343

Fox, N., and Burch, J. L. (2014). "The Van Allen Probes Mission," in *Physics and Astronomy* (Boston, MA: Springer). doi:10.1007/978-1-4899-7433-4

Fuller-Rowell, T. J., Rees, D., Quegan, S., Moffett, R. J., Codrescu, M. V., and Millward, G. H. (1996). "A coupled thermosphere ionosphere model (CTIM)," in *STEP: Handbook of ionospheric models*. Editor R. W. Schunk (Boulder, CO: Science Communication on Solar-Terrestrial Physics), 239–279.

Kletzing, C. A., Kurth, W. S., Acuna, M., MacDowall, R. J., Torbert, R. B., Averkamp, T., Bodet, D., Bounds, S. R., Chutter, M., Connerney, J., Crawford, D., Dolan, J. S., Dvorsky, R., Hospodarsky, G. B., Howard, J., Jordanova, V., Johnson, R. A., Kirchner, D. L., Mokrzycki, B., Needell, G., Odom, J., Mark, D., Pfaff, R., Phillips, J. R., Piker, C. W., Remington, S. L., Rowland, D., Santolik, O., Schnurr, R., Sheppard, D., Smith, C. W., Thorne, R. M., and Tyler, J. (2013). The Electric and Magnetic Field Instrument Suite and Integrated Science (EMFISIS) on RBSP. *Space Sci Rev* 179, 127–181. doi:10.1007/s11214-013-9993-6

Imhof, W. L., and Smith, R. V. (1965). Observation of Nearly Monoenergetic High-Energy Electrons in the Inner Radiation Belt. *Phys. Rev. Lett.* 14, 885–887. doi:10.1103/PhysRevLett.14.885

Lejosne, S., and Mozer, F. S. (2016a). Van Allen Probe measurements of the electric drift E × B/B 2 at Arecibo's L = 1.4 field line coordinate. *Geophys. Res. Lett.* 43, 6768–6774. doi:10.1002/2016GL069875

Lejosne, S., and Mozer, F. S. (2016b). Typical values of the electric drift E × B/B 2 in the inner radiation belt and slot region as determined from Van Allen Probe measurements. *J. Geophys. Res. Space Physics* 121 (12), 12,014. doi:10.1002/2016JA023613

Lejosne, S., and Mozer, F. S. (2019). Shorting Factor In-Flight Calibration for the Van Allen Probes DC Electric Field Measurements in the Earth's Plasmasphere. *Earth and Space Science* 6, 646–654. doi:10.1029/2018ea000550

Lejosne, S., and Mozer, F. S. (2020). Inversion of the Energetic Electron "Zebra Stripe" Pattern Present in the Earth's Inner Belt and Slot Region: First Observations and Interpretation. *Geophys. Res. Lett.* 47, e2020GL088564. doi:10.1029/2020GL088564

Maruyama, N., Fuller-Rowell, T. J., Codrescu, M. V., Anderson, D., Richmond, A. D., Maute, A., et al. (2011). "Modeling the storm time electrodynamics," in *Aeronomy of the Earth's atmosphere and ionosphere, IAGA Special Sopron Book Series*. Editors M. Abdu and D. Pancheva (Dordrecht: Springer), Vol. 2. doi:10.1007/978-94-007-0326-1_35

Mauk, B. H., Fox, N. J., Kanekal, S. G., Kessel, R. L., Sibeck, D. G., and Ukhorskiy, A. (2013). Science Objectives and Rationale for the Radiation Belt Storm Probes Mission. *Space Sci Rev* 179, 3–27. doi:10.1007/s11214-012-9908-y

Maynard, N. C., and Chen, A. J. (1975). Isolated cold plasma regions: Observations and their relation to possible production mechanisms. *J. Geophys. Res.* 80, 1009–1013. doi:10.1029/ja080i007p01009

McIlwain, C. E. (1961). Coordinates for mapping the distribution of magnetically trapped particles. *J. Geophys. Res.* 66 (11), 3681–3691. doi:10.1029/JZ066i011p03681

Millward, G. H., Rishbeth, H., Fuller-Rowell, T. J., Aylward, A. D., Quegan, S., and Moffett, R. J. (1996). IonosphericF2layer seasonal and semiannual variations. *J. Geophys. Res.* 101, 5149–5156. doi:10.1029/95JA03343

Millward, G. H., Müller-Wodarg, I. C. F., Aylward, A. D., Fuller-Rowell, T. J., Richmond, A. D., and Moffett, R. J. (2001). An investigation into the influence of tidal forcing onFregion equatorial vertical ion drift using a global ionosphere-thermosphere model with coupled electrodynamics. *J. Geophys. Res.* 106, 24733–24744. doi:10.1029/2000JA000342

Mitchell, D. G., Lanzerotti, L. J., Kim, C. K., Stokes, M., Ho, G., Cooper, S., Ukhorskiy, A., Manweiler, J. W., Jaskulek, S., Haggerty, D. K., Brandt, P., Sitnov, M., Keika, K., Hayes, J. R., Brown, L. E., Gurnee, R. S., Hutcheson, J. C., Nelson, K. S., Paschalidis, N., Rossano, E., and Kerem, S. (2013). Radiation Belt Storm Probes Ion Composition Experiment (RBSPICE). *Space Sci Rev* 179, 263–308. doi:10.1007/s11214-013-9965-x

Mozer, F. S. (1973). Electric fields and plasma convection in the plasmasphere. *Rev. Geophys.* 11 (3), 755–765. doi:10.1029/RG011i003p00755

Newell, P. T., and Gjerloev, J. W. (2011). Substorm and magnetosphere characteristic scales inferred from the SuperMAG auroral electrojet indices. *J. Geophys. Res.* 116, a–n. doi:10.1029/2011JA016936

Northrop, T. G., and Teller, E. (1960). Stability of the adiabatic motion of charged particles in the Earth's field. *Phys. Rev.* 117 (1), 215–225. doi:10.1103/PhysRev.117.215

Ohtani, S., and Gjerloev, J. W. (2020). Is the substorm current wedge an ensemble of wedgelets?: Revisit to midlatitude positive bays. *J. Geophys. Res. Space Physics* 125, e2020JA027902. doi:10.1029/2020JA027902

Olson, W. P., and Pfitzer, K. A. (1977). *Magnetospheric magnetic field modeling, Annual Sci. Rep. contract F44620-75-C-0033, Air Force Office of Scientific Research*. Huntington Beach, California: McDonnell Douglas Astronautics Co.

Pfaff, R., Rowland, D., Freudenreich, H., Bromund, K., Le, G., Acuña, M., Klenzing, J., Liebrecht, C., Martin, S., Burke, W. J., Maynard, N. C., Hunton, D. E., Roddy, P. A., Ballenthin, J. O., and Wilson, G. R. (2010). Observations of DC electric fields in the low-latitude ionosphere and their variations with local time, longitude, and plasma density during extreme solar minimum. *J. Geophys. Res.* 115, a–n. doi:10.1029/2010JA016023

Pfitzer, K. A., and Winckler, J. R. (1968). Experimental observation of a large addition to the electron inner radiation belt after a solar flare event. *J. Geophys. Res.* 73 (17), 5792–5797. doi:10.1029/JA073i017p05792

Reeves, G. D., Friedel, R. H. W., Larsen, B. A., Skoug, R. M., Funsten, H. O., Claudepierre, S. G., Fennell, J. F., Turner, D. L., Denton, M. H., Spence, H. E., et al. (2016). Energy-dependent dynamics of keV to MeV electrons in the inner zone, outer zone, and slot regions. *J. Geophys. Res. Space Physics* 121, 397–412. doi:10.1002/2015JA021569

Richmond, A. D. (1989). Modeling the ionosphere wind dynamo: A review. *PAGEOPH* 131, 413–435. doi:10.1007/BF00876837

Richmond, A. D., and Maute, A. (2014). "Ionospheric electrodynamics modeling," in *Modeling the ionosphere–thermosphere system*. Editors J. Huba, R. Schunk, and G. Khazanov, 57–71. doi:10.1002/9781118704417.ch6

Roederer, J. G. (1967). On the adiabatic motion of energetic particles in a model magnetosphere. *J. Geophys. Res.* 72 (3), 981–992. doi:10.1029/JZ072i003p00981

Roederer, J. G., and Zhang, H. (2014). "Dynamics of Magnetically Trapped Particles," in *Foundations of the Physics of Radiation Belts and Space Plasmas, Astrophysics and Space Science Library* (Berlin, Heidelberg: Springer-Verlag). doi:10.1007/978-3-642-41530-2

Selesnick, R. S., Su, Y. J., and Blake, J. B. (2016). Control of the innermost electron radiation belt by large-scale electric fields. *J. Geophys. Res. Space Physics* 121, 8417–8427. doi:10.1002/2016JA022973

Stern, D. P. (1975). The motion of a proton in the equatorial magnetosphere. *J. Geophys. Res.* 80, 595–599. doi:10.1029/ja080i004p00595

Toffoletto, F., Sazykin, S., Spiro, R., and Wolf, R. (2003). Inner magnetospheric modeling with the Rice Convection Model. *Space Sci. Rev* 107, 175–196. doi:10.1007/978-94-007-1069-6_19

Tsyganenko, N. A. (1989). A magnetospheric magnetic field model with a warped tail current sheet. *Planetary and Space Science* 37 (1), 5–20. doi:10.1016/0032-0633(89)90066-4

Turner, D. L., Claudepierre, S. G., Fennell, J. F., O'Brien, T. P., Blake, J. B., Lemon, C., Gkioulidou, M., Takahashi, K., Reeves, G. D., Thaller, S., Breneman, A., Wygant, J. R., Li, W., Runov, A., and Angelopoulos, V. (2015). Energetic electron injections deep into the inner magnetosphere associated with substorm activity. *Geophys. Res. Lett.* 42, 2079–2087. doi:10.1002/2015GL063225

Ukhorskiy, A. Y., Sitnov, M. I., Mitchell, D. G., Takahashi, K., Lanzerotti, L. J., and Mauk, B. H. (2014). Rotationally driven 'zebra stripes' in Earth's inner radiation belt. *Nature* 507, 338–340. doi:10.1038/nature13046

Volland, H. (1973). A semiempirical model of large-scale magnetospheric electric fields. *J. Geophys. Res.* 78, 171–180. doi:10.1029/ja078i001p00171

Whipple, E. C. (1978). (U, B, K) Coordinates: A natural system for studying magnetospheric convection. *J. Geophys. Res.* 83 (A9), 4318–4326. doi:10.1029/JA083iA09p04318

Wolf, R. A. (1983). "The Quasi-Static (Slow-Flow) Region of the Magnetosphere," in *Solar-terrestrial physics: Principles and theoretical foundations*. Editors R. L. Carovillano and J. M. Forbes (Norwell, MA: D. Reidel), 303–368. doi:10.1007/978-94-009-7194-3_14

Wolf, R. A., Spiro, R. W., Sazykin, S., and Toffoletto, F. R. (2007). How the Earth's inner magnetosphere works: An evolving picture. *Journal of Atmospheric and Solar-Terrestrial Physics* 69 (3), 288–302. doi:10.1016/j.jastp.2006.07.026

Wygant, J. R., Bonnell, J. W., Goetz, K., Ergun, R. E., Mozer, F. S., Bale, S. D., Ludlam, M., Turin, P., Harvey, P. R., Hochmann, R., Harps, K., Dalton, G., McCauley, J., Rachelson, W., Gordon, D., Donakowski, B., Shultz, C., Smith, C., Diaz-Aguado, M., Fischer, J., Heavner, S., Berg, P., Malsapina, D. M., Bolton, M. K., Hudson, M., Strangeway, R. J., Baker, D. N., Li, X., Albert, J., Foster, J. C., Chaston, C. C., Mann, I., Donovan, E., Cully, C. M., Cattell, C. A., Krasnoselskikh, V., Kersten, K., Brenneman, A., and Tao, J. B. (2013). The Electric Field and Waves Instruments on the Radiation Belt Storm Probes Mission. *Space Sci Rev* 179, 183–220. doi:10.1007/s11214-013-0013-7

Yamazaki, Y., and Maute, A. (2017). Sq and EEJ-A Review on the Daily Variation of the Geomagnetic Field Caused by Ionospheric Dynamo Currents. *Space Sci Rev* 206, 299–405. doi:10.1007/s11214-016-0282-z

Conflict of Interest: The authors declare that the research was conducted in the absence of any commercial or financial relationships that could be construed as a potential conflict of interest.

Publisher's Note: All claims expressed in this article are solely those of the authors and do not necessarily represent those of their affiliated organizations, or those of the publisher, the editors and the reviewers. Any product that may be evaluated in this article, or claim that may be made by its manufacturer, is not guaranteed or endorsed by the publisher.

Copyright © 2021 Lejosne, Fedrizzi, Maruyama and Selesnick. This is an open-access article distributed under the terms of the Creative Commons Attribution License (CC BY). The use, distribution or reproduction in other forums is permitted, provided the original author(s) and the copyright owner(s) are credited and that the original publication in this journal is cited, in accordance with accepted academic practice. No use, distribution or reproduction is permitted which does not comply with these terms.

frontiers in Astronomy and Space Sciences

ORIGINAL RESEARCH
published: 23 September 2021
doi: 10.3389/fspas.2021.746429

Impact of Storm-Enhanced Density (SED) on Ion Upflow Fluxes During Geomagnetic Storm

Shasha Zou[1]*, *Jiaen Ren*[1], *Zihan Wang*[1], *Hu Sun*[2] and *Yang Chen*[2]

[1]Department of Climate and Space Sciences and Engineering, University of Michigan, Ann Arbor, MI, United States, [2]Department of Statistics, University of Michigan, Ann Arbor, MI, United States

The impact of the dynamic evolution of the Storm-Enhanced Density (SED) on the upward ion fluxes during the March 06, 2016 geomagnetic storm is studied using comprehensive multi-scale datasets. This storm was powered by a Corotating Interaction Region (CIR), and the minimum Sym-H reached ~−110 nT. During the ionospheric positive storm phase, the SED formed and the associated plume and polar cap patches occasionally drifted anti-sunward across the polar cap. When these high-density structures encountered positive vertical flows, large ion upward fluxes were produced, with the largest upward flux reaching $3 \times 10^{14}\,m^{-2}s^{-1}$. These upflows were either the type-1 ion upflow associated with fast flow channels, such as the subauroral polarization stream (SAPS) channel, or the type-2 ion upflow due to soft particle precipitations in the cusp region. The total SED-associated upflow flux in the dayside cusp can be comparable to the total upflow flux in the nightside auroral zone despite the much smaller cusp area compared with the auroral zone. During the ionospheric negative storm phase, the ionospheric densities within the SED and plume decreased significantly and thus led to largely reduced upward fluxes. This event analysis demonstrates the critical role of the ionospheric high-density structures in creating large ion upward fluxes. It also suggests that the dynamic processes in the coupled ionosphere-thermosphere system and the resulting state of the ionospheric storm are crucial for understanding the temporal and spatial variations of ion upflow fluxes and thus should be incorporated into coupled geospace models for improving our holistic understanding of the role of ionospheric plasma in the geospace system.

Keywords: storm-enhanced density (SED), SED plume, ion upflow, ionospheric convection, field-aligned currents, magnetosphere-ionosphere-thermosphere coupling

OPEN ACCESS

Edited by:
Philip J. Erickson, Massachusetts Institute of Technology, United States

Reviewed by:
John C. Foster, Massachusetts Institute of Technology, United States
Alexei V. Dmitriev, Lomonosov Moscow State University, Russia

***Correspondence:**
Shasha Zou
shashaz@umich.edu

Specialty section:
This article was submitted to Space Physics, a section of the journal Frontiers in Astronomy and Space Sciences

Received: *23 July 2021*
Accepted: *13 September 2021*
Published: *23 September 2021*

Citation:
Zou S, Ren J, Wang Z, Sun H and Chen Y (2021) Impact of Storm-Enhanced Density (SED) on Ion Upflow Fluxes During Geomagnetic Storm. Front. Astron. Space Sci. 8:746429. doi: 10.3389/fspas.2021.746429

INTRODUCTION

The Earth's ionosphere is a crucial plasma source for the magnetosphere, in particular for heavy ions such as O^+ (e.g., Yau et al., 2011; Moore and Horwitz, 2007; Lotko 2007; Welling et al., 2015; Chappell, 2015 and references therein). Once arriving the magnetosphere, these heavy ions have been shown to be able to regulate the magnetospheric dynamics (Kronberg et al., 2014 and references therein), such as increasing the heavy ion concentration in the ring current (e.g., Daglis et al., 1999 and references therein) and modulating the magnetotail dynamics (e.g., Garcia et al., 2010). The influence of the ionospheric O^+ outflow on magnetospheric dynamics is found to depend on the source location (Yu and Ridley, 2013).

Ion upflow in the F-region and topside ionosphere is a critical first step for the ion outflow into the magnetosphere. The velocities of the upward moving ions at these altitudes typically have not

reached their escaping values yet, and thus these ion flows are termed upflow and not outflow. The ion upflow pumps plasmas to higher altitudes (>~1,000 km) and then additional energization processes at those altitudes can further accelerate plasmas to reach their escape velocities (e.g., Strangeway, 2005). Since those additional energization processes seem common, (Nilsson et al., 2008; Nilsson, 2011) suggested that the eventual ion ouflow is mainly determined by the initial ion upflow process. Besides the upward lifting, ion downward flows have also been observed in the F-region and topside ionosphere, which can push plasma to lower altitudes where the recombination rate is higher thereby resulting in enhanced losses (e.g., Loranc et al., 1991; Buchert et al., 2004; Ogawa et al., 2009; Ren et al., 2019, 2020). The downward flows can occur independently or together with upflows, i.e., divergent flows (e.g., Zou et al., 2017). Understanding the physical processes in the coupled ionosphere-thermosphere regime that could regulate the ion upflow fluxes is of central importance for understanding the mass, momentum and energy flow in the geospace system.

During geomagnetic storms, the ionospheric responses are often termed as positive/negative ionospheric storms phases. They refer to the period when the storm-time ionospheric density or TEC changes are positive/negative when comparing against the quiet-time values. During positive ionospheric storm phase, there are a few important high-density structures in the mid-to high-latitude ionosphere that could affect the ion upflow fluxes, such as the storm-enhanced density (SED) and SED plumes (e.g., Foster et al., 2005; Zou et al., 2013; Zou et al., 2014; Heelis, 2016; Foster et al., 2021), as well as polar cap patches (e.g., Zhang et al., 2013; Zhang et al., 2016; Ren et al., 2019, Ren et al., 2020; Zou et al., 2021). In this study, the SED base refers to the broadly distributed mid-latitude density enhancement, and the SED plume refers to the narrow and poleward extending portion of the SED, including when it is carried by the anti-sunward convection flows moving towards the nightside. Convective transport of such high-density structures into regions with enhanced precipitating particle fluxes or enhanced convection flows has been suggested to be an important mechanism of generating large ion upflow fluxes (Lotko, 2007 and references therein; Yau et al., 2011 and reference therein). Without energization, the field-aligned plasma flows within these high-density structures are usually downward (Zou et al., 2014; Ren et al., 2019; Ren et al., 2020). When these high-density structures drift poleward following the convection flows to regions, such as the dayside cusp and the nightside auroral zone, intense upflow fluxes and even divergent fluxes can form.

Large ion upflow fluxes that associated with the polar cap patches and SEDs have been observed before (Semeter et al., 2003; Yuan et al., 2008; Zhang et al., 2016). Semeter et al. (2003) used Sondrestrom incoherent scatter radar (ISR) and attributed a strong ion upflow flux event, i.e., ~$1.0 \times 10^{14}\,m^{-2}s^{-1}$, with a drifting polar cap patch. When the SED plume reached the nightside polar cap boundary, large vertical ion fluxes of ~$1.2 \times 10^{14}\,m^{-2}s^{-1}$ were measured by the DMSP satellite (Yuan et al., 2008). More recently, using the Poker Flat ISR (PFISR), (Zou et al., 2017) reported an event that the open-closed field-line boundary expanded equatorward into a SED plume and produced an intense upflow flux reaching ~$1.9 \times 10^{14}\,m^{-2}s^{-1}$ at 600 km. Using numerical simulations, (Zeng and Horwitz, 2007; Zeng and Horwitz, 2008) compared the efficiency of the O^+ outflow produced by soft electron precipitation and the SED plasma and found that they can produce a comparable amount of outflow flux. Recently, (Cohen et al., 2015) found that increased initial density before the onset of precipitation leads to smaller electron temperature increases, lower upflow speeds, and longer upflow timescales but larger upflow fluxes. These observations and numerical simulation studies indicate the importance and efficiency of the high-density structures in producing large ion upflow fluxes.

Recent studies revealed considerable variations within the SED and SED plume, and that the dynamics of SED during storms is mainly determined by the dynamic interplay between the convection electric field and the thermospheric wind pattern during the positive ionospheric storm phase (Lu et al., 2012; Zou et al., 2013; Zou et al., 2014; Liu et al., 2016) and by the thermospheric composition change during the negative ionospheric storm phase (e.g., Prölss, 2008; Wang et al., 2021). In addition, the SED has large longitudinal variations because of the miss-match between the geomagnetic and geographic poles (Coster et al., 2007; Thomas et al., 2016). Coster et al. (2007) found that SED are usually stronger in the Northern America sector. In addition, high-density structures in the polar region are found to occur more frequently between 12 and 24 UT and during winter times (David et al., 2016). Since the SED and plume are highly dynamic during storms and they can significantly affect the ion upflow fluxes, it is critical to evaluate the mutual evolution of the SED and the upflow fluxes during storms.

In this study, we analyzed the evolution of the SED and plume using global TEC, convection and field-aligned currents (FACs) data, and its impact on the ion upflow fluxes measured by the DMSP satellites during March 06, 2016, geomagnetic storm. *Datasets and Methodology* describes the major datasets that we use in this study. *Results* describes the results of the event and our analyses and interpretations. We summarize and conclude the study in *Summary and Conclusion*.

DATASETS AND METHODOLOGY

GNSS TEC

Ionospheric TEC can be calculated using the different delays of two transmitted frequencies from multi-frequency GNSS, including GPS. Recent years have witnessed an increased interest in investigating the ionospheric density variations during geomagnetic disturbances due to the fast-growing number of ground-based GPS receivers and the resulting regional or even global scale 2-D GPS TEC maps. We use the world-wide GNSS Vertical TEC (VTEC) data distributed in the publicly available CEDAR Madrigal database. The processed and binned VTEC data have a spatial resolution of $1^\circ \times 1^\circ$ in geographical coordinates and a temporal resolution of 5 min. Detailed information about the data processing procedure has been described in Rideout and Coster (2006).

The Madrigal TEC data were ingested into the recently developed TEC matrix completion tool called VISTA (Video Imputation with SoftImpute, Temporal smoothing and Auxiliary data) (Sun et al., 2021). The VISTA algorithm is based on the SoftImpute software and contains two extensions of temporal smoothing and auxiliary data. In this case, the auxiliary data is the spherical harmonic fitting of the Madrigal TEC data. The VISTA model is able to provide completed TEC map and preserves the meso-scale TEC features in the final output, which is important for tracking high-density structures in our study.

SuperDARN

The SuperDARN is an international collaboration operating high-frequency (HF) coherent radars in both the Northern and Southern Hemispheres (Greenwald et al., 1995; Chisham et al., 2007). They enable us to image the large-scale ionospheric convection and thus electric fields with high temporal resolution (~1–2 min). The SuperDARN radars operate 24 h a day, 365 days a year and have been generating a large amount of data.

AMPERE

Based on measurement of magnetic field perturbations from the Iridium Communications constellation of more than 70 satellites at low Earth orbits (~780 km), Active Magnetosphere and Planetary Electrodynamics Response Experiment (AMPERE) can provide a global view of Birkeland FACs in the high-latitude ionosphere. The orbits of the satellites form 12 longitudinal planes equally spaced by 2 h, and the satellites along each track are separated by 9 min. The magnetic field perturbation data are calibrated and then used in spherical harmonic inversion (Anderson et al., 2000). The FACs are derived by taking the curl of the fitted perturbations and are provided in the Altitude Adjustment Corrected GeoMagnetic (AACGM) coordinates on a 1 h local time by 1° latitude grid. More detailed description of the data product can be found in Anderson et al. (2014) and references therein.

DMSP

DMSP satellites are equipped with comprehensive instruments that can measure the precipitating particles from the solar wind and magnetosphere as well as the ionospheric thermal plasma characteristics. DMSP SSIES (Special Sensor for Ions, Electrons, and Scintillation) plasma instrument package is mainly used in this study and can measure the ionospheric thermal ion and electron temperatures, ion density and composition, as well as cross-track and vertical drifts. The DMSP horizontal velocities are shown in the inertial reference frame. In the auroral and polar region, vast majority of the ions at the DMSP altitude is O^+ and the total ion density or plasma density is essentially the same as the O^+ density. The product of the plasma density and vertical drift is used to study the vertical flux in the polar region (e.g., Coley et al., 2006). DMSP SSJ (Special Sensor J) precipitating particle instrument are also used to analyzing the generation mechanism of upflows. They can measure precipitating electrons and protons from 30 eV to 30 keV.

PFISR

The PFISR radar is part of the NSF-supported advanced modular incoherent scatter radar (AMISR) facility that is used to conduct studies of the upper atmosphere and to observe space weather events. It can simultaneously measure the altitude profiles of important ionospheric parameters, such as electron density, electron/ion temperatures, and line-of-sight ion velocity. PFISR was in the four-beam low-duty cycle mode during this period. Two types of pulses were transmitted, a long pulse and an alternating code pulse. The former is appropriate for F-region measurements (>175 km) and the latter for the E region (<175 km). Electron density measurements from these two pulses were combined to produce the altitude profiles in this study. The convection flows are calculated using the method described in Heinselman and Nicolls (2008).

TIMED GUVI

The Global Ultraviolet Imager (GUVI) onboard NASA TIMED can yield global maps of thermospheric composition, including maps of the ratio between the O and N_2 column densities, which can monitor the neutral composition changes during geomagnetic activities (Strickland et al., 1995; Zhang et al., 2004). During this storm, the TIMED satellite was in the early afternoon to postmidnight orbital plane, which is ideal to observe the thermosphere composition change impact on the SED.

RESULTS

Solar Wind and IMF

Figure 1 shows the solar wind and IMF conditions for this geomagnetic storm together with the AE and Sym-H indices at the bottom. During this storm, the Sym-H minimum reached ~−110 nT, and thus this storm should be classified as an intense geomagnetic storm. During these 2 days, the solar wind speed gradually increased from ~360 km/s to ~600 km/s but no shock formed, and the IMF had large fluctuations during the velocity increasing period, which are classical signatures of corotating interaction region (CIR). The three vertical lines highlight the three important times. The first vertical line indicates the sudden negative IMF By increase (t1: ~11:25 UT on March 06, 2016) and the beginning of the enhanced geomagnetic activities signaled by the gradually elevated AE. The IMF southward turning occurred at ~15 UT and led to the rapid Sym-H decrease and supersubstorm with AE reaching 1,500 nT. The second vertical line indicates the time when the Sym-H reached minimum (t2: ~21:20 UT on March 06, 2016). The last vertical line highlights the decline of the enhanced solar wind driving (t3: 06 UT on March 07), signaled by the solar wind dynamic pressure decrease and the reduction in the IMF fluctuation magnitude.

Evolution of SED During Storm

The TEC, SuperDARN convection and AMPERE FACs were combined and plotted in **Figure 2** at a cadence of every 3 h starting at 11 UT on March 06. These combined data are shown in the magnetic local time (MLT) and magnetic latitude coordinates and reveal the mutual evolution of the ionospheric

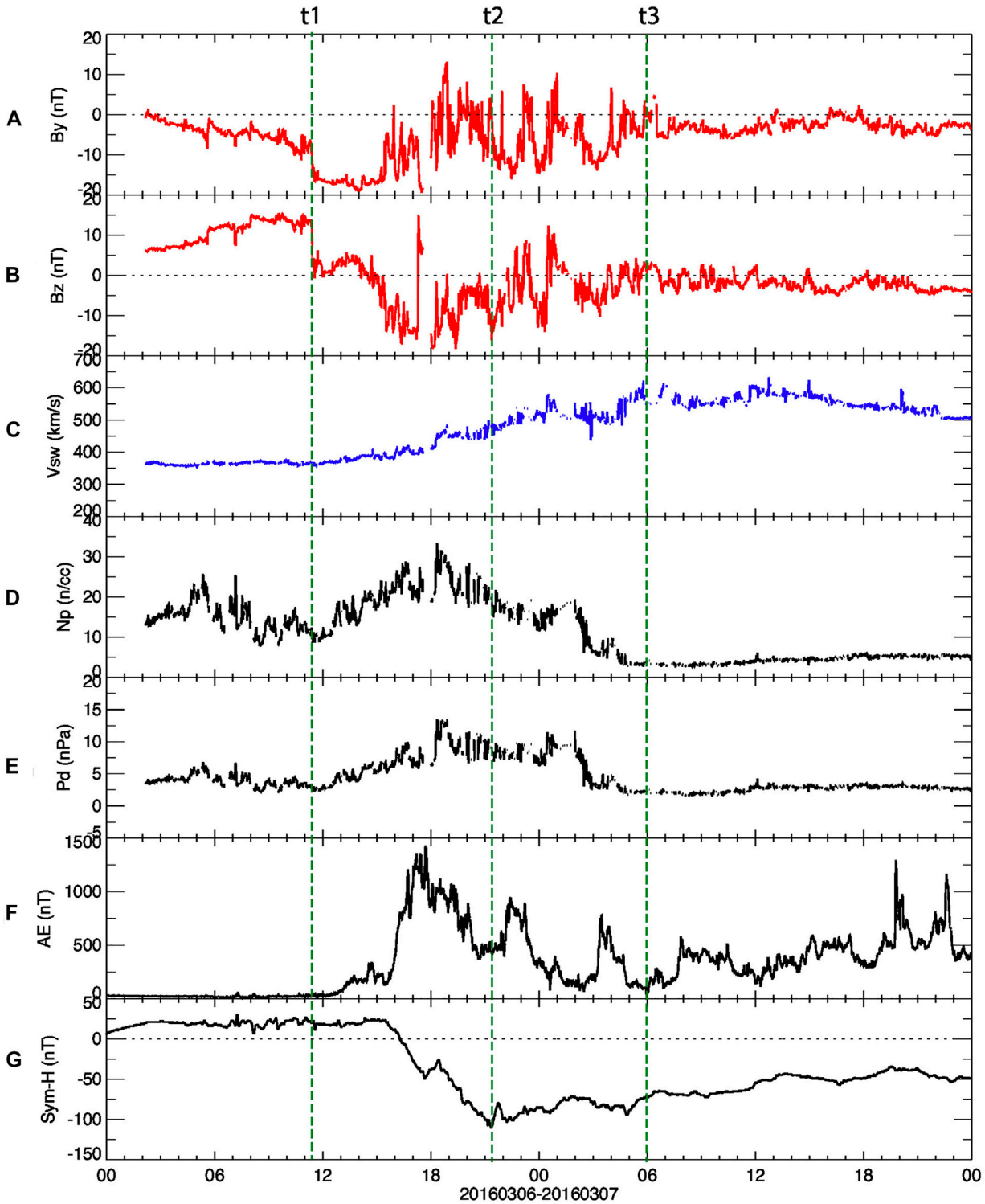


FIGURE 1 | Solar wind and IMF observations for March 06–07, 2016. From top to bottom, **(A)** IMF By, **(B)** IMF Bz, **(C)** solar wind speed, **(D)** proton number density, **(E)** dynamic pressure, **(F)** auroral electrojet index (AE), and **(G)** Sym-H index are shown. The IMF components are shown in Geocentric Solar Magnetospheric (GSM) coordinates. The three vertical lines indicate the times of sudden IMF By increase (t1: 11:47 UT on March 06, 2016), Sym-H reaching minimum (t2: 21:20 UT on March 06, 2016), and ending of large IMF fluctuation (t3: 06 UT on March 07).

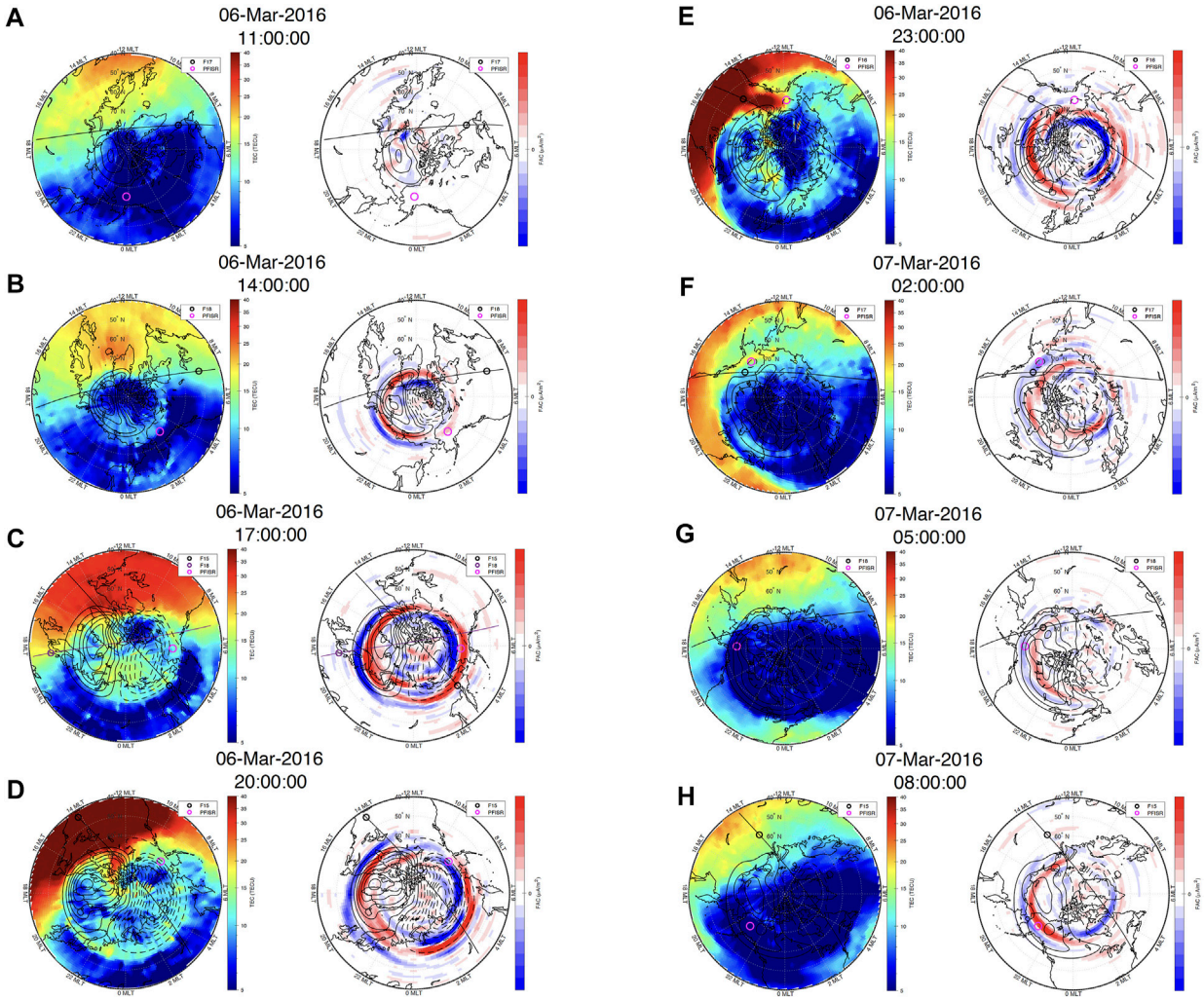


FIGURE 2 | Polar view of the northern hemisphere TEC, SuperDARN convection, and AMPERE FACs in the MLT and magnetic latitude coordinates at a cadence of every 3 h starting at 11 UT on March 06. The low latitude boundary in each panel is 40° mlat. In addition, trajectories of the DMSP satellites and their locations (circles) at the time of the plot are shown. Upward FACs are positive and in red colors, while downward FACs are negative and in blue colors.

TEC and the electrodynamics resulted from the magnetosphere-ionosphere coupling processes. A supplementary movie in the same format as **Figure 2** is also provided at a time cadence of every 2 min. **Figure 2A** shows the conditions just before the enhanced solar wind driving t1, and the TEC map shows the quiet time typical diurnal pattern with higher TEC on the day side and lower TEC on the night side. The convection and FACs were consistent with the quiet-time patterns confined near the pole. After t1 (**Figure 2B**), the convection and FACs started to expand to lower latitudes, and the SED began to develop in the early afternoon sector. Following the IMF southward turning, solar wind energy continuously entered the geospace system and the convection and FACs kept expanding to low latitudes (**Figure 2C**). Near the peak of the storm time t2 (**Figure 2D**), the Region-2 FAC system reached below 60° mlat in the afternoon sector and close to 55° mlat in the premidnight sector. During this period, the SED further developed and multiple polar cap patches and the SED plume entered the polar cap and drifted anti-sunward. **Figures 2E–H** show the decay of solar wind driving signaled by the shrinking of convection and weakening of the FACs. The impact of the negative ionospheric storm also became clear first in the morning sector and then gradually expanded to later local times. In particular, the SED plume narrowed, the TEC values decreased, and the plume eventually completely disappeared.

In order to capture the FACs and SED dynamics in a single plot, the time series of the TEC and FACs at 14 MLT from 40° mlat to 90° mlat are shown in **Figure 3**. The three vertical lines indicate the same important times as shown in **Figure 1**. As one can see, the FACs at 14 MLT strengthened and expanded equatorward after t1 and retreated to higher latitudes after t2 during the recovery phase of the storm. After that, their strength and location were relatively steady until the end of March 07. Several SED plume and polar cap patches can be seen extending

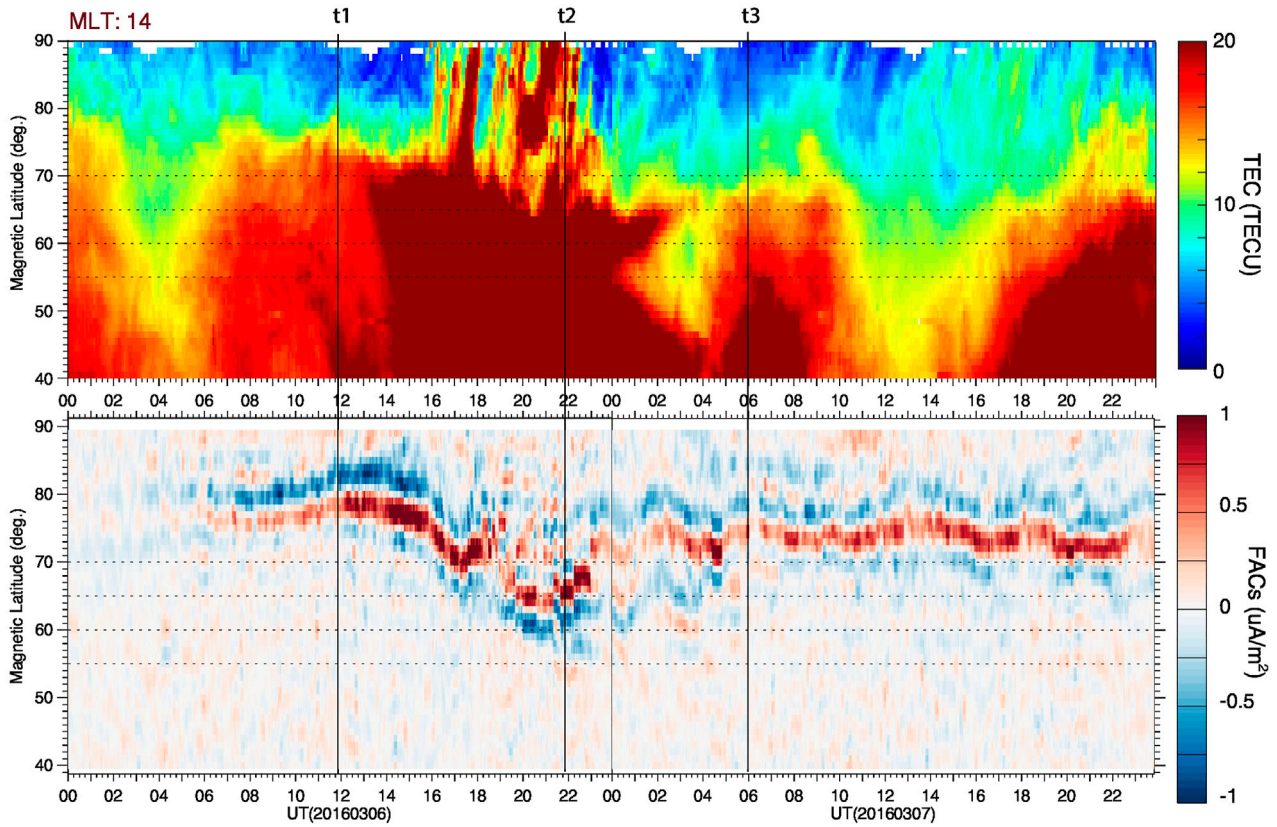


FIGURE 3 | Time series of TEC and FACs at 14 MLT are shown for March 06–07 storm. Upward FACs are positive and in red colors, while downward FACs are negative and in blue colors.

to the pole, including two wide plumes drifting anti-sunward at ~17 UT, 20 UT.

The SED and plume disappeared during the ionospheric negative storm phase due to the large-scale thermosphere composition change. The daily TIMED GUVI O/N_2 ratio of March 05–07 is shown in **Figures 4A–C** in geographic latitude and longitude coordinates. The quiet time values on March 05 were subtracted from the storm day values, and the delta O/N_2 ratios are plotted in **Figures 4D,E**. In each panel, the trajectories of the TIMED satellite are shown and the UTs when the satellite crossed the 60° geographic latitude in the Northern Hemisphere are labeled at the top horizontal axis. The quiet time map reveals the classical hemispheric asymmetry of the O/N_2 ratio with higher values in the winter hemisphere, i.e., the Northern Hemisphere. During storm time, in the low and mid-latitude regions, the O/N_2 ratio increased during the storm, while in the auroral latitudes, the thermosphere O/N_2 ratio change became negative after ~17 UT on March 06, first in the Northern Hemisphere and then extended to low latitude in both hemispheres on March 07. This equatorward expansion of reduced O/N_2 ratio was seen for all sectors except near 120° W in the Southern Hemisphere due to the dipole tilt effect and low magnetic latitudes comparing with other regions with similar geographic latitudes. The expansion of the negative O/N_2 ratio change to low latitude is a classical signature for thermosphere composition change during a storm and the major reason for the negative ionospheric storm in the auroral and mid-latitude regions (Prölss, 2008; Fuller-Rowell, 2011; Wang et al., 2021). The impact of the thermosphere composition change on the ionospheric TEC can be seen clearly in **Figures 2E–H** and the supplementary movie.

PFISR was right underneath the dayside SED plume during the early storm recovery phase (**Figure 2E**) and observed the altitude profiles of the SED plume during its decay phase. As shown **Figures 2E,F** and in the supplementary movie, the width of the SED plume rapidly reduced after 00 UT on March 07. This width reduction mainly happened near the poleward boundary of the plume and was associated with the horizontal transport of lower density plasma from later MLTs due to the enhanced convection driven by the short-lived but intense southward IMF Bz after 23:30 UT on March 06. **Figure 5** shows the PFISR observations from 17 UT on March 06 to 06 UT on March 07 and the TEC/FAC map at 01 UT on March 07. From top to bottom, **Figures 5B-G** show the direction, magnitude and vector of convection flows, vertical flow due to a combination of the convection and field-aligned flow, and altitude profiles of electron densities from beam 4 and beam 2. In **Figure 5A**, the magenta circle indicates the location of PFISR at 01 UT, right near the poleward edge of the SED plume. In **Figure 5G**, the density profiles of the SED plume,

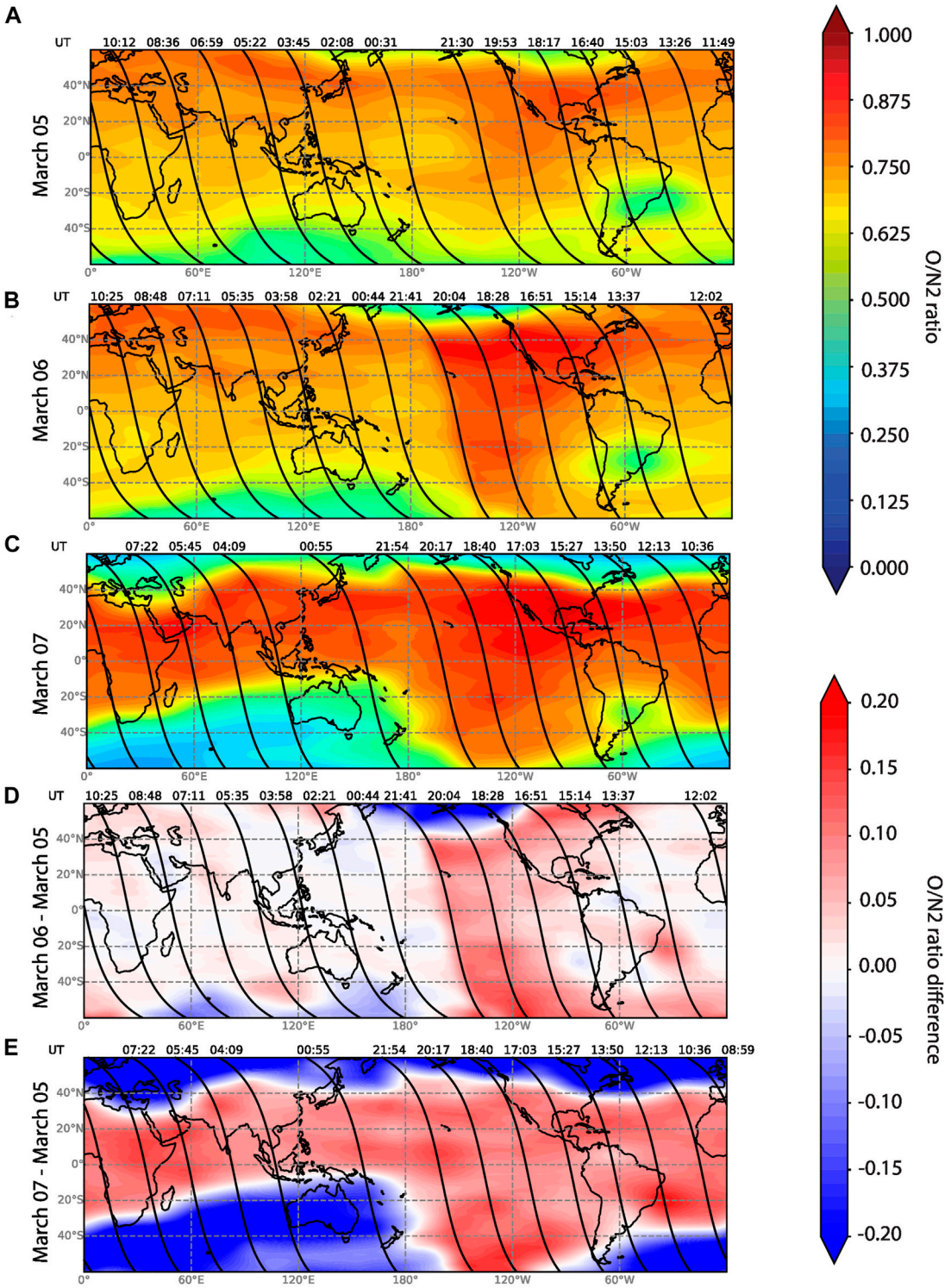


FIGURE 4 | The TIMED GUVI O/N_2 ratio of March 05–07 are shown in panels **(A–C)** in geographic coordinates. The quiet time O/N_2 values on March 05 were subtracted from the storm day values and the delta O/N_2 are plotted in panels **(D–E)**. In each panel, the trajectories of the TIMED satellite are shown and the UTs when the satellite crossed the 60° latitude in the Northern Hemisphere are labeled at the top horizontal axis.

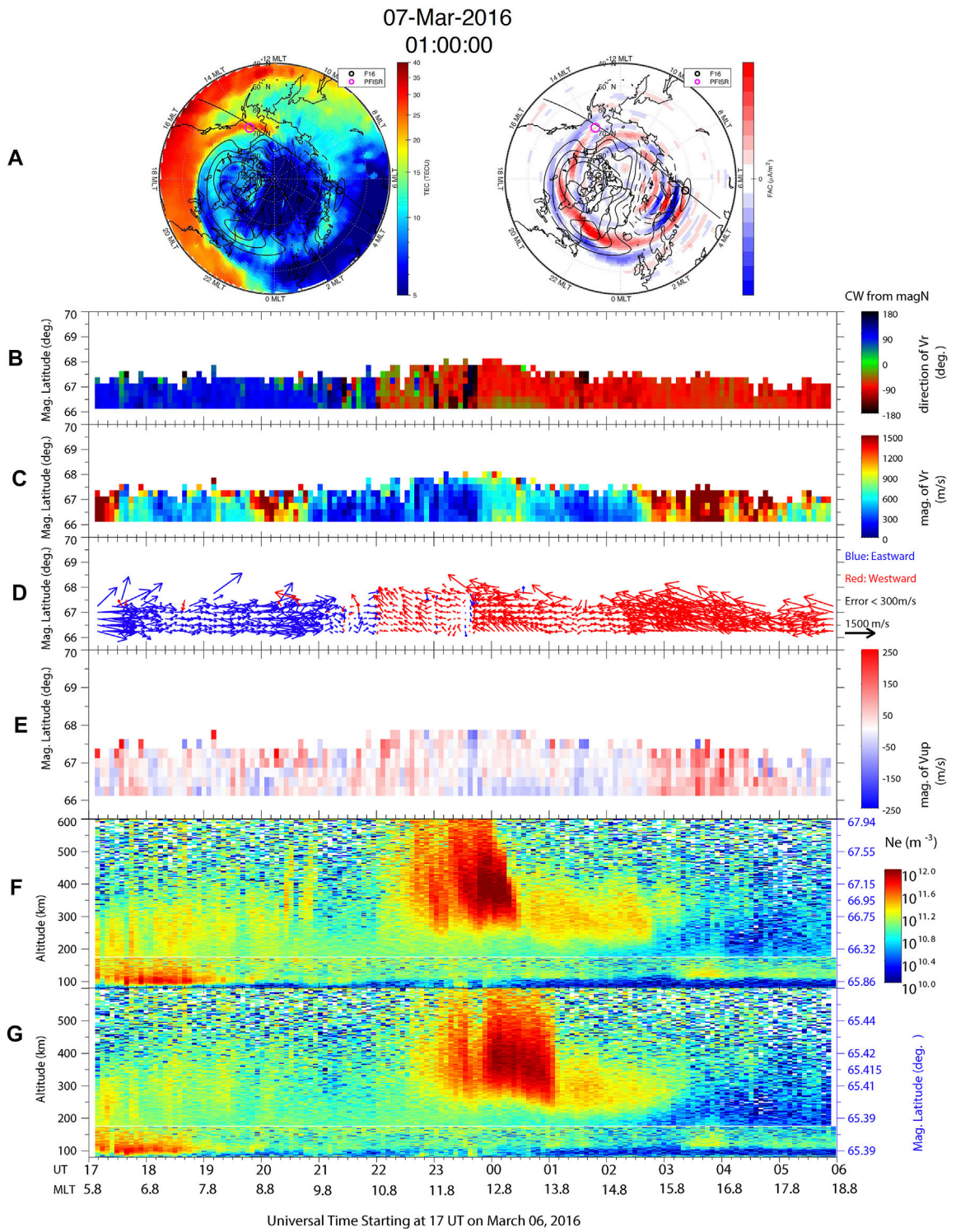


FIGURE 5 | PFISR observations from 17 UT on March 06 to 06 UT on March 07. TEC/convection/FAC maps at 01 UT on March 07 are shown at the top in **(A)**. The top three panels show **(B)** the convection flow direction with 0 means northward and positive means eastward, **(C)** the magnitude of the convection flow, **(D)** vector plots of the convection flows, **(E)** vertical flow due to a combination of the E x B convection and field-aligned flow. The bottom two panels show the altitude profiles of the ionosphere density observed by beam 4 **(F)** and beam 2 (**G**, field-aligned). The SED plume, its poleward shoulder, and the mid-latitude trough were observed by these two beams.

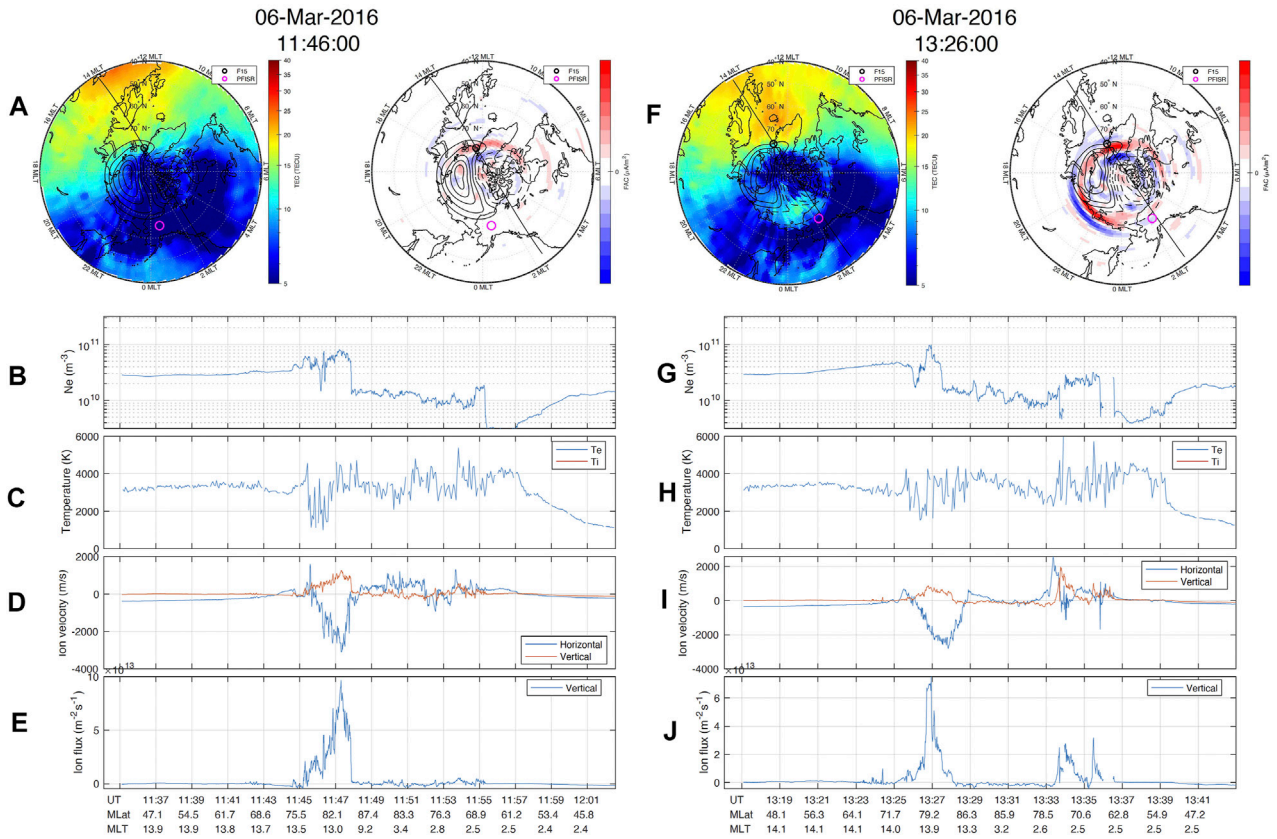


FIGURE 6 | Two periods of DMSP F15 measurements during the large negative IMF By period, i.e., 11:35–12:01 UT **(A–E)** and 13:17–13:41 UT **(F–J)**. Two selected TEC/convection/FAC polar view plots at 11:46 UT and 13:26 UT are also shown at the top **(A , F)**. From top to bottom, the DMSP observations include plasma density, electron temperature, horizontal (blue) and vertical drift (red), and the vertical flux, which is the product of plasma density and vertical flow. The trajectory of the DMSP satellite during this period is shown in the polar view plot.

the low-density plasma from later MLTs at the poleward shoulder of the SED plume (~01–03 UT) and the mid-latitude trough (after ~03 UT) revealed large density gradients near the poleward edge of the SED plume. The PFISR beam looking at higher latitudes and with lower elevation angle observed the poleward edge earlier at ~00: 30 UT. The peak SED electron density exceeded ~10^{12} m^{-3} at ~400 km at ~00 UT on March 07.

During this decay phase of the SED plume, the accompanied plasma convection flows were weakly northwestward (**Figures 5A,C**), while the vertical flows due to the combined E × B convection and field-aligned flow component turned negative near the low latitude boundary of PFISR and weakly positive near 67° mlat (**Figure 5D**). These observations are consistent with the SED decay phase observations shown in Zou et al. (2014). Downward plasma flows can push plasma to lower altitudes with denser neutrals and thus speed up the loss process, more specifically, the charge exchange reactions during the first step of the dissociative recombination. The large westward convection flows observed after 03 UT were subauroral polarization streams (SAPS) accompanied with proton precipitations based on the DMSP F17 observations (not shown).

DMSP Observations of Ion Upflow Flux

Four DMSP satellites (F15, F16, F17, F18) operated during this period and provided the precipitating particles and thermal plasma measurements in the polar ionosphere. In particular, DMSP F15 was in the 14-02 MLT orbital plane, which is the most suitable for detecting the SED contribution to ion upflow fluxes among the available satellites. **Figure 6** shows two periods of DMSP F15 measurements during the large negative IMF By period, i.e., 11:35-12:01 UT (A-E) and 13:17-13:41 UT (F-J). Two selected TEC/convection/FAC polar view plots at 11:46 UT and 13:26 UT are also shown at the top. These two periods were at the beginning of the enhanced solar wind driving, and the SED TEC in the dayside mid-latitude and subauroral regions just started to increase. In **Figures 6B, G**, the topside SED plasma, characterized by enhanced density and relatively low electron temperature, were measured by DMSP F15 at ~11:47 UT and ~13:27 UT. The accompanied anti-sunward horizontal convection flows in **Figures 6D, I** were larger than ~2 km/s and sandwiched by the large negative By related upward and downward FACs near noon (**Figures 6A, F**), while the vertical flows were elevated to several hundred m/s and exceeded ~1 km/s at 11: 47 UT. The combination of the high density and large vertical

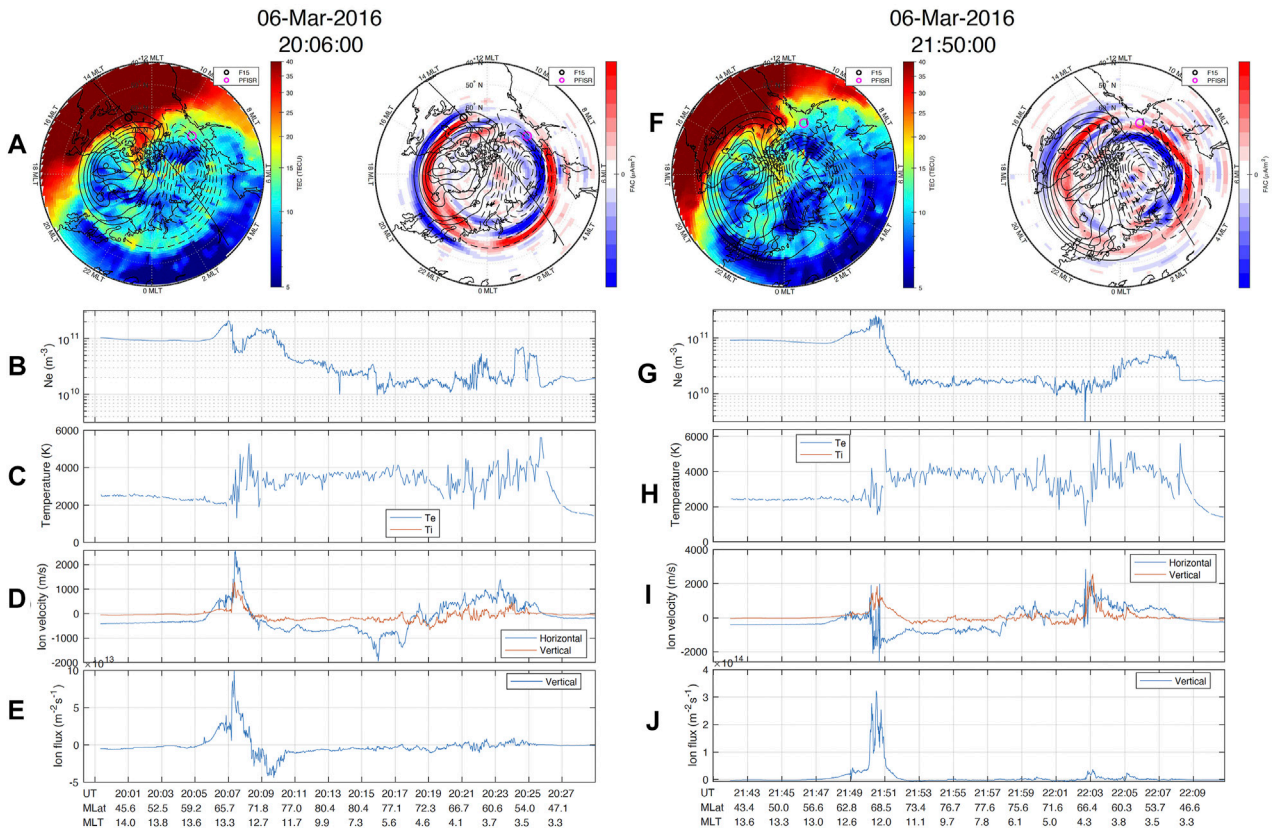


FIGURE 7 | The same format as **Figure 6** but near the peak of the storm time.

flow produced the upward flux reaching ~0.8–1 × 10^{14} $m^{-2}s^{-1}$ during these periods. The second DMSP orbit shown in **Figure 6** also observed relatively enhanced densities at ~13:35 UT at 2.5 MLT and produced ~3 × 10^{13} $m^{-2}s^{-1}$ upward fluxes. Based on the movie, these enhanced densities were likely the remnant of the SED plasma transported to this location.

After the IMF Bz southward turning, clear Region-1 and Region-2 FACs and two-cell convection patterns developed. The TEC values within the SED continued to increase and then multiple patches and the SED plume were seen moving anti-sunward. **Figure 7** shows the DMSP F15 measurements during the peak of the storm from 20:01 to 20:27 UT (A-E) and from 21:43 to 22:09 UT (F-J) on March 06. In the same format as **Figure 6**. In **Figures 7A, F**, the high-latitude convection and FACs had already expanded to beyond 60° mlat. The large SED density was observed near 65.7° mlat at ~20:07 UT, and the plume was observed at ~ 71.8° mlat (**Figure 7B**). The horizontal convection flows associated with SED were sunward, peaking at ~2.5 km/s, and the vertical flows exceeded ~1.2 km/s. The peak upward flux again reached ~1 × 10^{14} $m^{-2}s^{-1}$ near the poleward shoulder of the SED. Interestingly, the ion fluxes within the SED plume at ~ 71.8° mlat were downward, similar to previous observations deep in the polar cap (Ren et al., 2019). One orbit later, DMSP F15 observed the fully grown SED plasma, and the topside density at 850 km reached ~2 × 10^{11} m^{-3}, tripled the value at the beginning of the storm in **Figure 6B**. In addition, the largest upflow fluxes during this storm was observed, exceeding 3 × 10^{14} $m^{-2}s^{-1}$ at ~12 MLT.

Figure 8 shows the DMSP F15 measurements during the negative ionospheric storm phase from 02:56 to 03:14 UT (A-E) and from 04:34 to 04:56 UT (F-J) on March 07. In the same format as **Figures 6**, **7**. Evident in the TEC polar view plot, the TEC values in the Northern Hemisphere gradually reduced first in the noon sector and later in the pre-midnight sector. The topside ionosphere density shown in **Figures 8B,G** reduced to about 30% of the peak topside density shown in **Figure 7**. Despite the large vertical flows, i.e., several hundred m/s, due to the reduced ionospheric density, the upflow fluxes dropped to ~2-3 x 10^{13} $m^{-2}s^{-1}$. When comparing the second DMSP orbit in **Figure 8** with the first orbit in **Figure 6**, one can see that the convection flows (**Figure 8I** and **Figure 6D**) and the electron temperature (**Figure 8H** and **Figure 6H**) during these two time periods were nearly identical, while the upward fluxes differed significantly due to the status of the ionospheric storm and the change of the topside ionosphere condition.

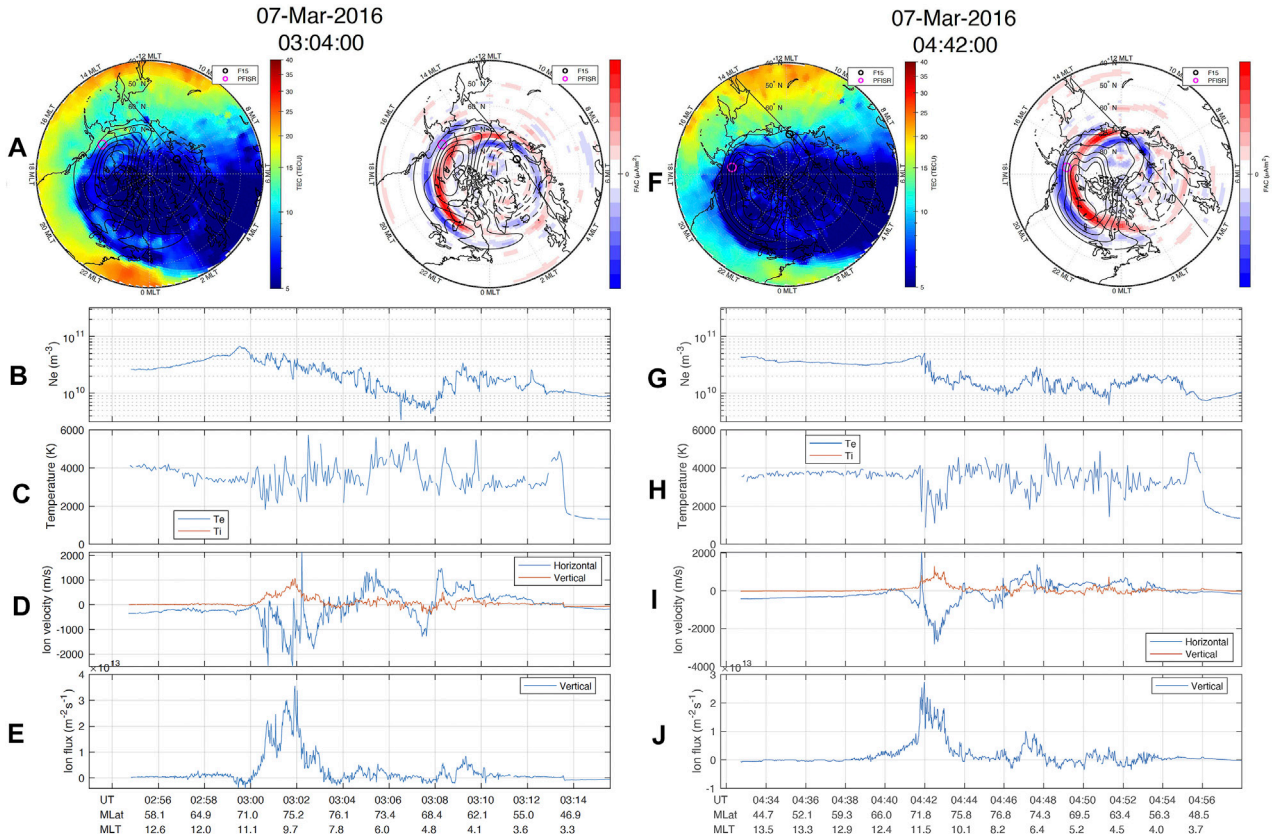


FIGURE 8 | The same format as **Figure 7** but during the ionospheric negative storm phase.

Generation Mechanism of Intense Ion Upflow Fluxes

Based on the plasma temperature associated with the ion upflow in the F region and the topside ionosphere, ion upflow events have been conventionally classified into two categories, type 1 and type 2 (Wahlund et al., 1992). The type 1 ion upflows are related to strong perpendicular electric fields, enhanced and anisotropic ion temperatures, and low electron densities below 300 km. The enhanced ion temperature results in pressure gradients that propel the ions to higher altitudes. The type 2 ion upflows are related to electron precipitation, electron temperature increase, and reduced or unaffected topside electron density. The largely increased electron temperature in the topside ionosphere leads to an increased ambipolar electric field and thus ions are pulled upward together with the expanding electrons. The type 2 ion upflows can sometimes be accompanied by enhanced ion temperature as well.

In order to analyze the generation mechanism of the intense ion upflow fluxes and the associated precipitating particles, selected DMSP F16 passes are shown in **Figures 9–11**. DMSP F16 was in the 15-03 MLT orbital plane. The format of these three figures is the same, and from top to bottom shows the TEC/FAC map (a), precipitating electron (b) and proton (c) energy fluxes in log scale, *in situ* density (d), plasma temperature €, horizontal and vertical velocities (f), and vertical fluxes (g). In **Figure 9**, DMSP F16 crossed the afternoon sector SED base before 19:37 UT and observed the increased *in situ* density of ~10^{11} m^{-3}, with a small peak near the equatorward edge of the proton precipitation and the SAPS flow region (highlighted by a dashed line). The density peak was clearly associated with the peak upflow flux, ~6 × 10^{13} $m^{-2}s^{-1}$, and the SAPS. The westward flux transported by this SAPS channel was ~2 × 10^{14} $m^{-2}s^{-1}$, comparable to the previous reported values (Erickson et al., 2011).

Both electron and ion temperatures associated with this SAPS upflow were lower than the surrounding region. The fact that this peak upflow flux was collocated with SAPS suggests that this is likely a type 1 upflow. The type 1 ion upflows are usually associated with strong perpendicular electric field (e.g., Sellek et al., 1991; Heelis et al., 1993). Sellek et al. (1991) used an ionosphere and plasmasphere model to study the effect of frictional heating due to a 2 km/s westward drift. Their results showed that the O^+ temperature profile increases from ~1000 to ~3200 K between 200 and 500 km, decreases rapidly from ~3200 to ~2000 K between 500 and 750 km, and no enhancement above 750 km. Similarly, Heelis et al. (1993) studied the effect of frictional heating of a 2 km/s horizontal drift on O^+ temperature and upflow velocity with a focus on their transient dynamic evolution. Their simulation results showed a negative temperature gradient between 300 and 1,000 km about

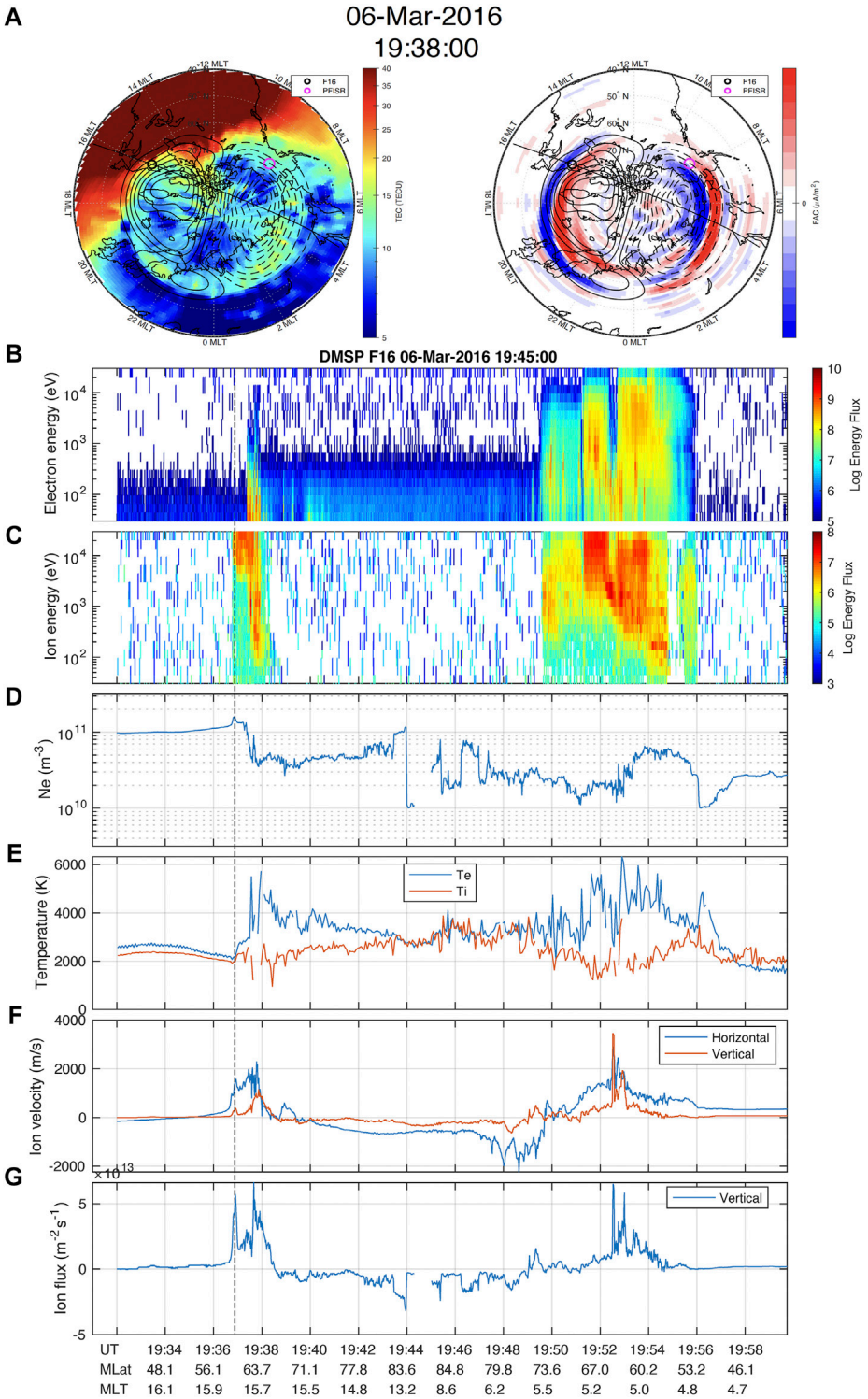


FIGURE 9 | DMSP F16 measurements from 19:32 to 19:58 UT on March 06 revealing the SAPS-associated upflow fluxes. TEC/convection/FAC polar view plots at 19:38 UT are also shown at the top **(A)**. From top to bottom, the DMSP observations include precipitating electron **(B)** and proton **(C)** fluxes, plasma density **(D)**, electron (blue) and ion (red) temperature **(E)**, horizontal (blue) and vertical drift (red) **(F)**, and the vertical flux **(G)**, which is the product of plasma density and vertical flow. The trajectory of the DMSP satellite during this period is shown in the polar view plot.

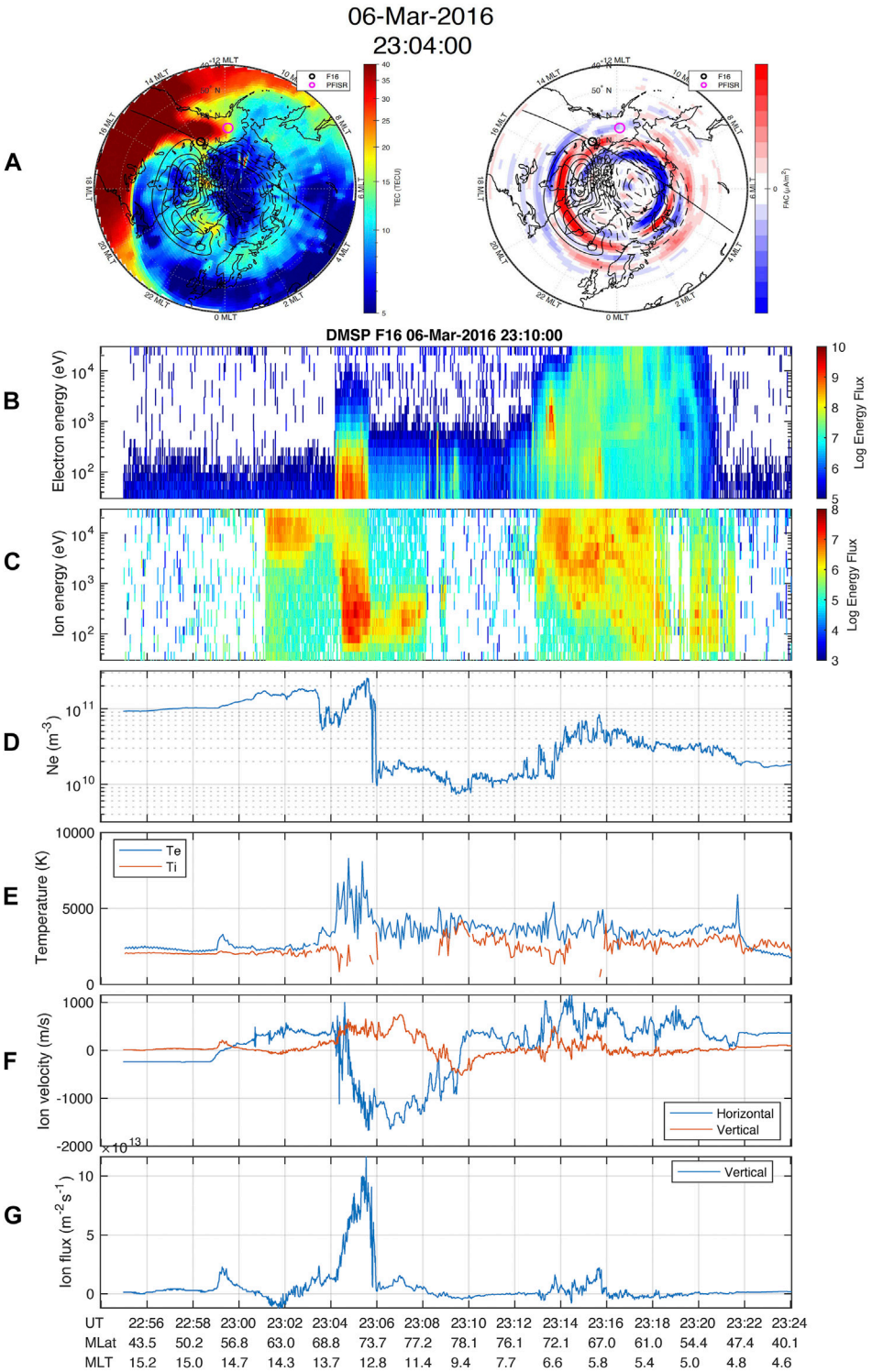


FIGURE 10 | The same format as **Figure 9** but the large upflow fluxes were associated with the fully grown SED plume.

several minutes after reaching the peak velocity. Therefore, it is not unexpected that there was no clear ion temperature enhancement signature associated with this SAPS upflow at the DMSP altitude.

Figures 10, **11** show the DMSP passes crossing the SED plume during its peak and its decaying phase, respectively. In **Figure 10**, the peak upflow fluxes increased to ~10^{14} $m^{-2}s^{-1}$ at ~23:05 UT, when the SED plume met with intense soft electron

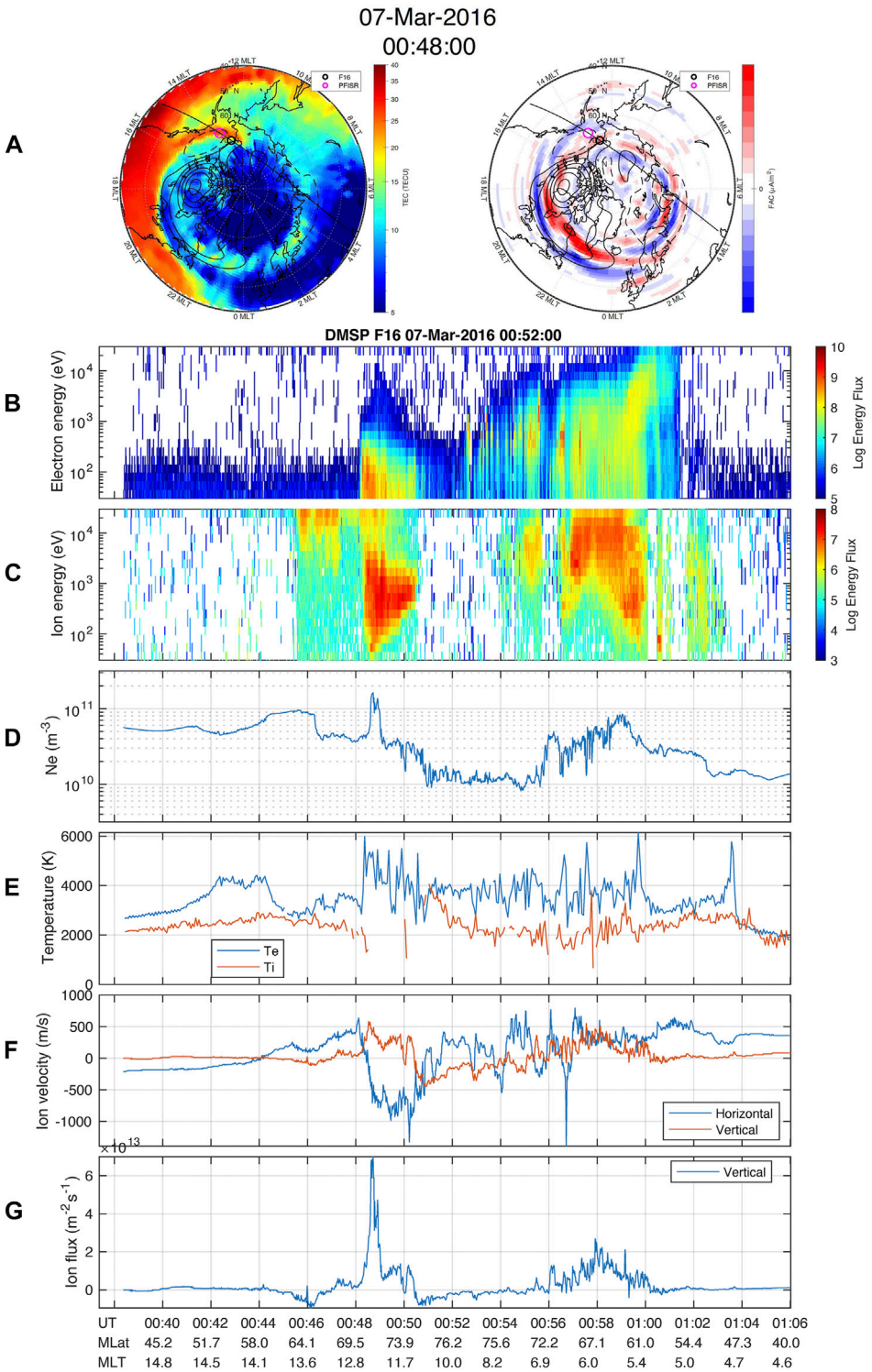


FIGURE 11 | The same format as **Figure 9** but the large upflow fluxes were associated with the SED plume during its decaying phase.

and proton precipitations. These soft particle precipitation signatures are classic cusp precipitations that directly coming from the equatorial magnetosheath. In **Figure 11**, the SED plume continued to contribute to the large ion upflow fluxes even during its decaying phase. DMSP F16 encountered the SED plume at ~00:46–00:48 UT and observed the narrow

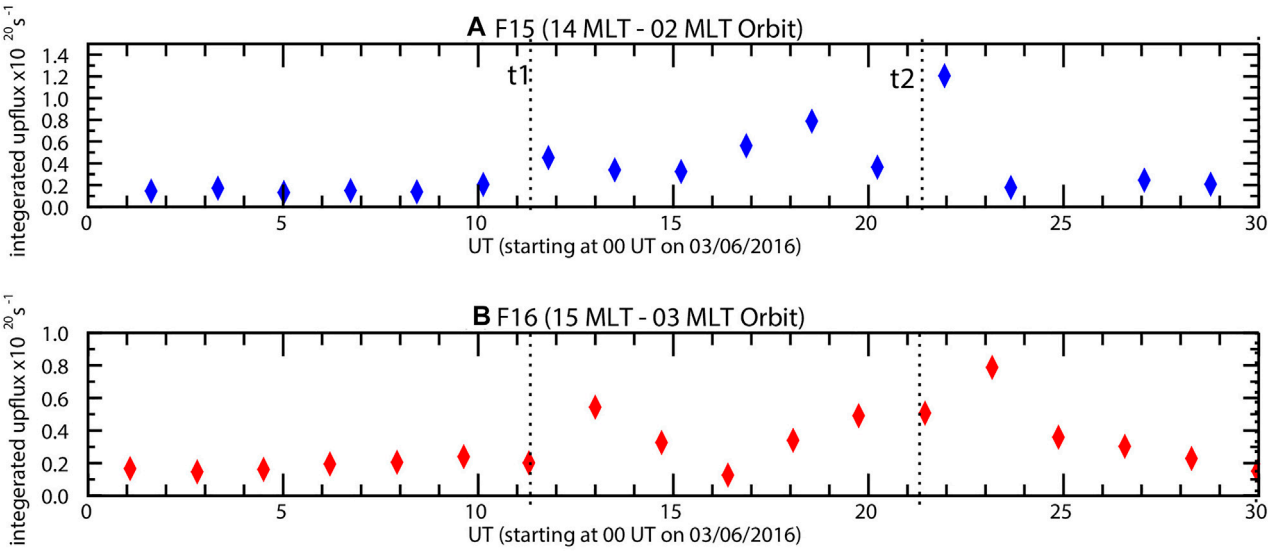


FIGURE 12 | The upward fluxes in the Northern Hemisphere for DMSP F15 and F16 satellites were integrated along the trajectories when the satellite was poleward of 45° mlat and assuming a unit length in the cross-track direction. The upward flux values were normalized to 1×10^{20} s^{-1}. DMSP F15 pass at ~01:16 UT on March 07 was not included due to large data gaps.

plume contribution to the large upflow fluxes there. Like **Figure 10**, the precipitating soft electron and ion signatures indicate again this was near the dayside cusp region. Together with the signature of largely elevated electron temperature, the large ion upflowes shown in **Figures 10**, **11** should be classified as type 2 ion upflow seeded by the SED plume plasma. It is interesting to note that in **Figures 10**, **11**, the ion vertical fluxes associated with the SED at lower latitudes were downward (before 23:02 UT in **Figure 10** and at ~00:46 UT in **Figure 11**), consistent with the PFISR observations described in the previous section and earlier studies (Zou et al., 2014; Ren et al., 2020).

Temporal Evolution of the Integrated Upflow Fluxes

In order to show the temporal evolution of integrated upward fluxes, we integrated the upward fluxes above 45° mlat in the Northern Hemisphere for all DMSP F15 and F16 satellites and created the time series of integrated upflow flux in **Figure 12**. DMSP 15 and DMSP 16 have similar orbits, i.e., covering afternoon and postmidnight sectors, and their observations are also comparable. The integrated fluxes gradually increased during the positive ionospheric storm, due to a combination of the elevated SED plasma density and the increased vertical flow speed. The hemispheric integrated flux reached its peak at ~22-23 UT, shortly after the ring current attainded its peak and the Sym-H approached its minimum. After the ionospheric negative storm initiated due to the thermospheric composition change, the integrated flux decreased significantly, despite the fact that the vertical flow speed was comparable to that during the earlier positive storm condition. These observations clearly demonstrate the importance of the ionospheric storm phase and status in determining the total available ion upflow fluxes. DMSP F17 and F18 were close to each other in the dusk and dawn orbital plane, and the SED contributions to the upflow fluxes there are difficult to quantify. Because at these two local times, the SED plasmas usually have already traveled a long distance from the dayside convection throat to the nightside auroral zone and on the way back to the dayside *via* the return convection flows. High quality convection flow pattern would be required to trace the SED plasma parcel to ensure that the enhanced densities observed at the dusk and dawn auroral zone are indeed part of the SED remnant. Therefore, the DMSP F17 and F18 observations are not shown here and further studies regarding the contribution of SED plasmas to the ion upflow fluxes in the return flow region of the auroral zone should be performed.

A back-of-the-envelope estimation of the SED contribution to the integrated upflow fluxes in the dayside cusp region is performed and compared with the integrated upflow fluxes in the nightside auroral zone. In Ren et al. (2020) paper, the average ion upflow fluxes observed by PFISR in the nightside auroral zone is ~ $2\text{-}3 \times 10^{13}$ $m^{-2}s^{-1}$. So, the SED-associated upflow fluxes in the cusp can be ~5–10 times larger than the average upflow fluxes observed in the nightside auroral zone. If we assume the typical dayside cusp is located at 75° mlat and covers 2 h of MLT and 2° mlat, as suggested by the statistical picture shown in Newell, (2004), and the SED contributed upflow flux is ~$1\text{-}2 \times 10^{14}$ $m^{-2}s^{-1}$, the integrated upflow flux in the cusp with SED contribution could be ~ $2\text{-}4 \times 10^{25}$ s^{-1}. Similarly, if assuming the nightside auroral zone is located at ~65° mlat and covers 6 h of

MLT and 5° mlat and the upflow flux is ~2-3 × 10^{13} $m^{-2}s^{-1}$, the total auroral zone upflow flux could be ~4-6 × 10^{25} s^{-1}. Based on the above estimations, the SED-associated upflow fluxes in the dayside cusp is comparable to the total upflow fluxes in the nightside auroral zone despite the much-limited spatial coverage of cusp.

SUMMARY AND CONCLUSION

In this study, we evaluated the impact of the SED dynamic evolution on the upward ion fluxes during the March 06, 2016 geomagnetic storm using comprehensive multi-scale datasets. Large-scale TEC, convection, and FACs were combined to reveal the mutual evolution of the ionospheric TEC and the high-latitude electrodynamics. The TIMED GUVI observations were used to monitor the thermosphere neutral composition change. In addition, localized ISR and *in situ* DMSP satellite observations were used to study the detailed ionospheric plasma property. During the ionospheric positive storm phase, large ion upward fluxes were produced when the high-density SED plasma encountered the dayside fast flow channel and soft particle precipitations. The peak upward flux observed was about 3 × 10^{14} $m^{-2}s^{-1}$ with the topside ionospheric density reaching 2 × 10^{11} m^{-3} in the dayside cusp region. During the ionospheric negative storm phase, the thermospheric O/N_2 ratio was reduced at the high latitude region due to neutral upwelling from lower altitudes, and this perturbation gradually propagated to lower latitudes. The ionospheric density was significantly reduced (e.g., the SED and plume disappeared), and thus the upward fluxes were severely suppressed. Even under similar convection and particle precipitation conditions, the reduced ionospheric density during the negative storm phase led to weakened upward fluxes. This event analysis demonstrates the critical role of the SED and SED plume in creating large ion upward fluxes. It also suggests that the dynamic coupling of the ionosphere-thermosphere and the resulting state of the ionospheric storm are crucial for understanding the temporal and spatial variations of ion upflow dynamics. Appropriately specifying these lower boundary conditions are important for global geospace models to fully evaluate the dynamic evolution of ion outflows and their impact on geospace system dynamics.

DATA AVAILABILITY STATEMENT

The original contributions presented in the study are included in the article/**Supplementary Material**, further inquiries can be directed to the corresponding author.

AUTHOR CONTRIBUTIONS

SZ oversaw and designed the research plan, analyzed the multi-instrument data, and wrote the manuscript. JR created the polar view plots and movie of the TEC, convection, and FACs, as well as visualized the DMSP data. ZW created the TIMED GUVI O/N2 plots. HS and YC produced the VISTA TEC data.

FUNDING

SZ, JR, and ZW at the University of Michigan are supported by NASA 80NSSC20K1313, 80NSSC20K0190, and 80NSSC20K0600. HS and YC are supported by NASA 80NSSC20K0600.

ACKNOWLEDGMENTS

We acknowledge Dr. Anthea Coster and her colleagues at MIT Haystack to make the TEC data available on Madrigal database. We thank Patricia Doherty for making the DMSP data available on Madrigal database. The solar wind and IMF data are obtained from the OMNI web. The PFISR data are obtained from the SRI AMISR website. The SuperDARN data are obtained from the SuperDARN group at the Virginia Tech. We thank the AMPERE team and the AMPERE Science Center for providing the Iridium derived data products.

SUPPLEMENTARY MATERIAL

The Supplementary Material for this article can be found online at: https://www.frontiersin.org/articles/10.3389/fspas.2021.746429/full#supplementary-material

REFERENCES

Anderson, B. J., Korth, H., Waters, C. L., Green, D. L., Merkin, V. G., Barnes, R. J., et al. (2014). Development of Large-Scale Birkeland Currents Determined from the Active Magnetosphere and Planetary Electrodynamics Response Experiment. *Geophys. Res. Lett.* 41, 3017–3025. doi:10.1002/2014gl059941

Anderson, B. J., Takahashi, K., and Toth, B. A. (2000). Sensing Global Birkeland Currents with Iridium Engineering Magnetometer Data. *Geophys. Res. Lett.* 27 (24), 4045–4048. doi:10.1029/2000gl000094

Buchert, S. C., Ogawa, Y., Fujii, R., and van Eyken, A. P. (2004). Observations of Diverging Field-Aligned Ion Flow with the ESR. *Ann. Geophys.* 22 (3), 889–899. doi:10.5194/angeo-22-889-2004

Chappell, C. R. (2015). The Role of the Ionosphere in Providing Plasma to the Terrestrial Magnetosphere-An Historical Overview. *Space Sci. Rev.* 192 (1-4), 5–25. doi:10.1007/s11214-015-0168-5

Chisham, G., Lester, M., Milan, S. E., Freeman, M. P., Bristow, W. A., Grocott, A., et al. (2007). A Decade of the Super Dual Auroral Radar Network (SuperDARN): Scientific Achievements, New Techniques and Future Directions. *Surv. Geophys.* 28 (1), 33–109. doi:10.1007/s10712-007-9017-8

Cohen, I. J., Lessard, M. R., Varney, R. H., Oksavik, K., Zettergren, M., and Lynch, K. A. (2015). Ion Upflow Dependence on Ionospheric Density and Solar Photoionization. *J. Geophys. Res. Space Phys.* 120 (11), 10039–10052. doi:10.1002/2015JA021523

Coley, W. R., Heelis, R. A., and Hairston, M. R. (2006). Characteristics of High-Latitude Vertical Plasma Flow from the Defense Meteorological Satellite Program. *J. Geophys. Res.* 111 (A11). doi:10.1029/2005JA011553

Coster, A. J., Colerico, M. J., Foster, J. C., Rideout, W., and Rich, F. (2007). Longitude Sector Comparisons of Storm Enhanced Density. *Geophys. Res. Lett.* 34 (18). doi:10.1029/2007GL030682

Daglis, I. A., Thorne, R. M., Baumjohann, W., and Orsini, S. (1999). The Terrestrial Ring Current: Origin, Formation, and Decay. *Rev. Geophys.* 37 (4), 407–438. doi:10.1029/1999RG900009

David, M., Sojka, J. J., Schunk, R. W., and Coster, A. J. (2016). Polar Cap Patches and the Tongue of Ionization: A Survey of GPS TEC Maps from 2009 to 2015. *Geophys. Res. Lett.* 43 (6), 2422–2428. doi:10.1002/2016GL068136

Erickson, P. J., Beroz, F., and Miskin, M. Z. (2011). Statistical Characterization of the American Sector Subauroral Polarization Stream Using Incoherent Scatter Radar. *J. Geophys. Res.* 116, A00J21. doi:10.1029/2010JA015738

Foster, J. C., Coster, A. J., Erickson, P. J., Holt, J. M., Lind, F. D., Rideout, W., et al. (2005). Multiradar Observations of the Polar Tongue of Ionization. *J. Geophys. Res.* 110, A09S31. doi:10.1029/2004JA010928

Foster, J. C., Zou, S., Heelis, R. A., and Erickson, P. J. (2021). ch6, in *Ionosphere Dynamics and Applications*. Editors C. Huang, G. Lu, Y. Zhang, and L. J. Paxton. doi:10.1002/9781119815617

Fuller-Rowell, T. J. (2011). "Storm-Time Response of the Thermosphere-Ionosphere System," in *Aeronomy of the Earth's Atmosphere and Ionosphere, IAGA Spec. Sopron Book Ser.* Editors M. A. Abdu and D. Pancheva (Dordrecht, Netherlands: Springer), Vol. 2419, 435–434. doi:10.1007/978-94-007-0326-1_32

Garcia, K. S., Merkin, V. G., and Hughes, W. J. (2010). Effects of Nightside O+outflow on Magnetospheric Dynamics: Results of Multifluid MHD Modeling. *J. Geophys. Res.* 115 (A12), a–n. doi:10.1029/2010JA015730

Greenwald, R. A., Baker, K. B., Dudeney, J. R., Pinnock, M., Jones, T. B., Thomas, E. C., et al. (1995). DARN/SuperDARN. *Space Sci. Rev.* 71 (1-4), 761–796. doi:10.1007/BF00751350

Heelis, R. A., Bailey, G. J., Sellek, R., Moffett, R. J., and Jenkins, B. (1993). Field-Aligned Drifts in Subauroral Ion Drift Events. *J. Geophys. Res.* 98 (A12), 21493–21499. doi:10.1029/93JA02209

Heelis, R. A. (2016). "Longitude and Hemispheric Dependencies in Storm-Enhanced Density," in *Geophysical Monograph Series*. Editors T. Fuller-Rowell, E. Yizengaw, P. H. Doherty, and S. Basu (Hoboken, NJ, USA: John Wiley & Sons), 59–70. doi:10.1002/9781118929216.ch5

Heinselman, C. J., and Nicolls, M. J. (2008). A Bayesian Approach to Electric Field andE-Region Neutral Wind Estimation with the Poker Flat Advanced Modular Incoherent Scatter Radar. *Radio Sci.* 43, a–n. doi:10.1029/2007RS003805

Kronberg, E. A., Ashour-Abdalla, M., Dandouras, I., Delcourt, D. C., Grigorenko, E. E., Kistler, L. M., et al. (2014). Circulation of Heavy Ions and Their Dynamical Effects in the Magnetosphere: Recent Observations and Models. *Space Sci. Rev.* 184 (1-4), 173–235. doi:10.1007/s11214-014-0104-0

Liu, J., Wang, W., Burns, A., Solomon, S. C., Zhang, S., Zhang, Y., et al. (2016). Relative Importance of Horizontal and Vertical Transports to the Formation of Ionospheric Storm-enhanced Density and Polar Tongue of Ionization. *J. Geophys. Res. Space Phys.* 121, 8121–8133. doi:10.1002/2016JA022882

Loranc, M., Hanson, W. B., Heelis, R. A., and St.-Maurice, J.-P. (1991). A Morphological Study of Vertical Ionospheric Flows in the High-latitudeFregion. *J. Geophys. Res.* 96 (A3), 3627. doi:10.1029/90JA02242

Lotko, W. (2007). The Magnetosphere-Ionosphere System from the Perspective of Plasma Circulation: A Tutorial. *J. Atmos. Solar-Terrestrial Phys.* 69 (3), 191–211. doi:10.1016/j.jastp.2006.08.011

Lu, G., Goncharenko, L., Nicolls, M. J., Maute, A., Coster, A., and Paxton, L. J. (2012). Ionospheric and Thermospheric Variations Associated with Prompt Penetration Electric fields. *J. Geophys. Res.* 117, a–n. doi:10.1029/2012JA017769

Moore, T. E., and Horwitz, J. L. (2007). Stellar Ablation of Planetary Atmospheres. *Rev. Geophys.* 45 (3), a–n. doi:10.1029/2005RG000194

Newell, P. T. (2004). Maps of Precipitation by Source Region, Binned by IMF, with Inertial Convection Streamlines. *J. Geophys. Res.* 109, A10206. doi:10.1029/2004JA010499

Nilsson, H. (2011). "Heavy Ion Energization, Transport, and Loss in the Earth's Magnetosphere," in *The Dynamic Magnetosphere*. Editors W. Liu and M. Fujimoto (Dordrecht: Springer Netherlands), 315–327. doi:10.1007/978-94-007-0501-2_17

Nilsson, H., Waara, M., Marghitu, O., Yamauchi, M., Lundin, R., Rème, H., et al. (2008). Transients in Oxygen Outflow above the Polar Cap as Observed by the Cluster Spacecraft. *Ann. Geophys.* 26 (11), 3365–3373. doi:10.5194/angeo-26-3365-2008

Ogawa, Y., Buchert, S. C., Fujii, R., Nozawa, S., and van Eyken, A. P. (2009). Characteristics of Ion Upflow and Downflow Observed with the European Incoherent Scatter Svalbard Radar. *J. Geophys. Res.* 114 (A5), a–n. doi:10.1029/2008JA013817

Prölss, G. W. (2008). "Ionospheric Storms at Mid-Latitude: A Short Review," in *Geophysical Monograph Series*. Editors P. M. Kintner, A. J. Coster, T. Fuller-Rowell, A. J. Mannucci, M. Mendillo and R. Heelis (Washington, DC: American Geophysical Union), 181, 9–24. doi:10.1029/181GM03

Ren, J., Zou, S., Lu, J., Giertych, N., Chen, Y., Verney, R., et al. (2020). Statistical Study of Ion Upflow and Downflow Observed by the Poker Flat Incoherent Scatter Radar (PFISR). *J. Geophys. Res. Space Phys.* 125, e2020JA028179. doi:10.1029/2020ja028179

Rideout, W., and Coster, A. (2006). Automated GPS Processing for Global Total Electron Content Data. *GPS Solut.* 10 (3), 219–228. doi:10.1007/s10291-006-0029-5

Sellek, R., Bailey, G., Moffett, R., Heelis, R., and Anderson, P. (1991). Effects of Large Zonal Plasma Drifts on the Subauroral Ionosphere. *J. Atmos. Terrestrial Phys.* 53 (6-7), 557–565. doi:10.1016/0021-9169(91)90083-J

Semeter, J., Heinselman, C. J., Thayer, J. P., Doe, R. A., and Frey, H. U. (2003). Ion Upflow Enhanced by driftingF-Region Plasma Structure along the Nightside Polar Cap Boundary. *Geophys. Res. Lett.* 30 (22). doi:10.1029/2003GL017747

Strangeway, R. J. (2005). Factors Controlling Ionospheric Outflows as Observed at Intermediate Altitudes. *J. Geophys. Res.* 110 (A3). doi:10.1029/2004JA010829

Strickland, D. J., Evans, J. S., and Paxton, L. J. (1995). Satellite Remote Sensing of Thermospheric O/N2and Solar EUV: 1. Theory. *J. Geophys. Res.* 100, 12217. doi:10.1029/95ja00574

Sun, H., Hua, Z., Ren, J., Zou, S., Sun, Y., and Chen, Y. (2021). Matrix Completion Methods for the Total Electron Content Video Reconstruction. *Ann. Appl. Stat.,* 15 (3).

Thomas, E. G., Baker, J. B. H., Ruohoniemi, J. M., Coster, A. J., and Zhang, S. R. (2016). The Geomagnetic Storm Time Response of GPS Total Electron Content in the North American Sector. *J. Geophys. Res. Space Phys.* 121, 1744–1759. doi:10.1002/2015JA022182

Wahlund, J.-E., Opgenoorth, H. J., Häggström, I., Winser, K. J., and Jones, G. O. L. (1992). EISCAT Observations of Topside Ionospheric Ion Outflows during Auroral Activity: Revisited. *J. Geophys. Res.* 97 (A3), 3019–3037. doi:10.1029/91JA02438

Welling, D. T., André, M., Dandouras, I., Delcourt, D., Fazakerley, A., Fontaine, D., et al. (2015). The Earth: Plasma Sources, Losses, and Transport Processes. *Space Sci. Rev.* 192 (1-4), 145–208. doi:10.1007/s11214-015-0187-2

Yau, A. W., Peterson, W. K., and Abe, T. (2011). "Influences of the Ionosphere, Thermosphere and Magnetosphere on Ion Outflows," in *The Dynamic Magnetosphere*. Editors W. Liu and M. Fujimoto (Dordrecht: Springer Netherlands), 283–314. doi:10.1007/978-94-007-0501-2_16

Yu, Y., and Ridley, A. J. (2013). Exploring the Influence of Ionospheric O + Outflow on Magnetospheric Dynamics: Dependence on the Source Location. *J. Geophys. Res. Space Phys.* 118 (4), 1711–1722. doi:10.1029/2012JA018411

Yuan, Z.-G., Deng, X.-H., and Wang, J.-F. (2008). DMSP/GPS Observations of Intense Ion Upflow in the Midnight Polar Ionosphere Associated with the SED Plume during a Super Geomagnetic Storm. *Geophys. Res. Lett.* 35, L19110. doi:10.1029/2008GL035462

Zeng, W., and Horwitz, J. L. (2007). Formula Representation of Auroral Ionospheric O+outflows Based on Systematic Simulations with Effects of Soft Electron Precipitation and Transverse Ion Heating. *Geophys. Res. Lett.* 34 (6). doi:10.1029/2006GL028632

Zeng, W., and Horwitz, J. L. (2008). Storm Enhanced Densities (SED) as Possible Sources for Cleft Ion Fountain Dayside Ionospheric Outflows. *Geophys. Res. Lett.* 35 (4). doi:10.1029/2007GL032511

Zhang, Q.-H., Zhang, B.-C., Lockwood, M., Hu, H.-Q., Moen, J., Ruohoniemi, J. M., et al. (2013). Direct Observations of the Evolution of Polar Cap Ionization Patches. *Science* 339, 1597–1600. doi:10.1123/science.123148710.1126/science.1231487

Zhang, Q. H., Zong, Q. G., Lockwood, M., Heelis, R. A., Hairston, M., Liang, J., et al. (2016). Earth's Ion Upflow Associated with Polar Cap Patches: Global and *In Situ* Observations. *Geophys. Res. Lett.* 43 (5), 1845–1853. doi:10.1002/2016GL067897

Zhang, Y., Paxton, L. J., Morrison, D., Wolven, B., Kil, H., Meng, C.-I., et al. (2004). O/N2changes during 1-4 October 2002 Storms: IMAGE SI-13 and TIMED/GUVI Observations. *J. Geophys. Res.* 109, A10308. doi:10.1029/2004JA010441

Zou, S., Moldwin, M. B., Ridley, A. J., Nicolls, M. J., Coster, A. J., Thomas, E. G., et al. (2014). On the Generation/decay of the Storm-Enhanced Density Plumes: Role of the Convection Flow and Field-Aligned Ion Flow. *J. Geophys. Res. Space Phys.* 119 (10), 8543–8559. doi:10.1002/2014JA020408

Zou, S., Perry, G. W., and Foster, J. C. (2021). "Recent Advances in Polar Cap Density Structure Research," in *Ionosphere Dynamics and Applications*. Editors C. Huang, G. Lu, Y. Zhang, and L.J. Paxton, 67–82. doi:10.1002/9781119815617.ch4

Zou, S., Ridley, A., Jia, X., Boyd, E., Nicolls, M., Coster, A., et al. (2017). PFISR Observation of Intense Ion Upflow Fluxes Associated with an SED during the 1 June 2013 Geomagnetic Storm. *J. Geophys. Res. Space Phys.* 122, 2589–2604. doi:10.1002/2016JA023697

Zou, S., Ridley, A. J., Moldwin, M. B., Nicolls, M. J., Coster, A. J., Thomas, E. G., et al. (2013). Multi-instrument Observations of SED during 24-25 October 2011 Storm: Implications for SED Formation Processes. *J. Geophys. Res. Space Phys.* 118 (12), 7798–7809. doi:10.1002/2013JA018860

Conflict of Interest: The authors declare that the research was conducted in the absence of any commercial or financial relationships that could be construed as a potential conflict of interest.

The handling editor declared a past co-authorship with one of the authors SZ.

Publisher's Note: All claims expressed in this article are solely those of the authors and do not necessarily represent those of their affiliated organizations, or those of the publisher, the editors and the reviewers. Any product that may be evaluated in this article, or claim that may be made by its manufacturer, is not guaranteed or endorsed by the publisher.

Copyright © 2021 Zou, Ren, Wang, Sun and Chen. This is an open-access article distributed under the terms of the Creative Commons Attribution License (CC BY). The use, distribution or reproduction in other forums is permitted, provided the original author(s) and the copyright owner(s) are credited and that the original publication in this journal is cited, in accordance with accepted academic practice. No use, distribution or reproduction is permitted which does not comply with these terms.

frontiers in Astronomy and Space Sciences

ORIGINAL RESEARCH
published: 04 October 2021
doi: 10.3389/fspas.2021.714146

The Predictive Capabilities of the Auroral Electrojet Index for Medium Energy Electron Precipitation

H. Nesse Tyssøy[1]*, *N. Partamies*[1,2], *E. M. Babu*[1], *C. Smith-Johnsen*[1] and *J. A. Salice*[1]

[1]Birkeland Centre for Space Science, Department of Physics and Technology, University of Bergen, Bergen, Norway, [2]Department of Arctic Geophysics, The University Centre in Svalbard (UNIS), Longyearbyen, Norway

The chemical imprint of the energetic electron precipitation on the atmosphere is now acknowledged as a part of the natural forcing of the climate system. It has, however, been questioned to which degree current proxies are able to quantify the medium energy electron (MEE) (≳30 keV) precipitation and the associated daily and decadal variability. It is particularly challenging to model the high energy tail (≳300 keV) of MEE, both in terms of the intensity as well as the timing. This study explores the predictive capabilities of the AE index for the MEE precipitation. MEE measurements from the NOAA/POES over a full solar cycle from 2004 to 2014 are applied. We combine observations from the MEPED 0° and 90° detectors together with theory of pitch angle diffusion by wave-particle interaction to estimate the precipitating fluxes. To explore the energy dependent time scales, each of the MEPED energy channels, > 43, >114, and >292 keV are evaluated independently. While there is a strong correlation between the daily resolved AE index and >43 keV fluxes, it is a poor predictor for the >292 keV fluxes. We create new AE based MEE proxies by accumulating the AE activity over multiple days, including terms counting for the associated lifetimes. The results indicate that AE based proxies can predict at least 70% of the observed MEE precipitation variance at all energies. The potential link between the AE index, substorms and the MEE precipitation is discussed.

Keywords: energetic electron precipitation, medium energy electrons, outer radiation belt, auroral electrojet index, substorms

OPEN ACCESS

Edited by:
Scott Alan Thaller, University of Colorado Boulder, United States

Reviewed by:
Victor Sergeev, Saint Petersburg State University, Russia
Ingmar Sandberg, Space Applications and Research Consultancy (SPARC), Greece

***Correspondence:**
H. Nesse Tyssøy
hilde.nesse@uib.no

Specialty section:
This article was submitted to Space Physics, a section of the journal Frontiers in Astronomy and Space Sciences

Received: *24 May 2021*
Accepted: *15 September 2021*
Published: *04 October 2021*

Citation:
Tyssøy HN, Partamies N, Babu EM, Smith-Johnsen C and Salice J (2021) The Predictive Capabilities of the Auroral Electrojet Index for Medium Energy Electron Precipitation. Front. Astron. Space Sci. 8:714146. doi: 10.3389/fspas.2021.714146

1 INTRODUCTION

Precipitating auroral electrons (≲ 30 keV) and protons (≲ 1 MeV) from the plasma sheet will ionize the lower thermosphere and upper mesosphere. Medium energy electrons (MEE) (≳ 30 keV) from the radiation belts have sufficient energy to penetrate deep into the mesosphere (Turunen et al., 2009). The associated ionization enhances the production rate of NOx and HOx gasses, which in turn can reduce ozone in catalytic processes (e.g., Sætre et al., 2004; Andersson et al., 2012; Sinnhuber et al., 2016; Zawedde et al., 2016). During polar winter, the chemical impact can be long lasting and influence temperatures, winds, and wave propagation. This chain of reactions can impact the strength of the stratospheric polar vortex, causing a dynamical signal that may propagate all the way down to the surface (Seppälä et al., 2013; Maliniemi et al., 2016). To account for this natural solar forcing of the atmosphere, a parametrization of energetic electron precipitation is – for the first time – part of the official input to the Coupled Model Intercomparison Project phase 6 (CMIP 6) going into the Intergovernmental Panel on

Climate Change sixth assessment report (Matthes et al., 2017). The MEE ionization rate dataset therein is based on observations from the Medium Energy Proton and Electron Detector (MEPED) instrument on board the NOAA/Polar Orbiting Environmental Satellites (POES), and the geomagnetic Ap index is used as a proxy to provide an extended time series beyond the satellite observation period (van de Kamp et al., 2016). There is, however, an active discussion to what extent this approach gives a representative flux and ionization rate level (Mironova et al., 2019; Nesse Tyssøy et al., 2019; Pettit et al., 2019; Clilverd et al., 2020). The CMIP6 flux is a general underestimate, largely ascribed to the use of the vertical (0°) detector on MEPED which only covers a small fraction of the loss cone (Nesse Tyssøy et al., 2019). Recent studies, however, also point out that the role of substorms in driving MEE precipitation is not readily explained by a single magnetic index value. Hence, substorms is one of the main unknowns in the existing proxies when considering the MEE precipitation and especially its high energy tail ($\gtrsim$ 300 keV) (Partamies et al., 2021).

Several processes in the magnetosphere contribute to the driving of the MEE precipitation. A globally induced electric field during southward interplanetary magnetic field accelerates and transports electrons from the magnetotail into the inner magnetosphere where they become a part of the radiation belts. In parallel, localized transient-induced electric fields, created from the magnetotail collapse during substorm activity, also energize and increase the MEE population in the radiation belts. So-called seed particles of 10–100 s keV can be directly injected into the inner magnetosphere during a substorm (Li et al., 2009; Jaynes et al., 2015). Further acceleration also occurs as the injection of source particles (tens of keV) gives rise to Very Low Frequency (VLF) wave growth, which may resonantly interact and accelerate radiation belt electrons to MEE (Borovsky & Yakymenko, 2017). Repeated substorm activity has been shown to be particularly important for MEE fluxes (Rodger et al., 2016; Partamies et al., 2021), possibly due the induction electric field directly energizing the trapped electrons as they drift across the nightside during substorm expansion phases (Dai et al., 2014). Partamies et al. (2021) identified the substorm occurrence by a regional AE index and used cosmic noise absorption enhancement as a measure of the MEE precipitation. They showed that for multi-night substorm events, the first night was rarely associated with the most intense absorption. Instead, the high-energy electron population, needed to cause the strongest absorption, was built up over one to two additional nights of substorm activity. This was further confirmed by MEPED *in situ* particle spectra. In the expansion phases the bulk of the spectra showed a local maximum flux in the range of a few keV to 10 keV, while in the recovery phases higher fluxes were seen in the range of tens of keV to hundreds of keV. Based on the SuperMAG substorm event list, Rodger et al. (2016) constructed a superposed epoch analysis differing between isolated and recurrent events. Even though their main focus was the trapped MEE fluxes, they also showed higher precipitating MEE fluxes in the epoch analysis for the recurrent events compared to isolated events, in particular with respect to the high energy tail (>300 keV). Although not commented on, Figure A1 in Rodger et al. (2016) showed an instant effect as well as a gradual build-up over the consecutive days. Seppälä et al. (2015) used the substorm model developed by Beharrell et al. (2015) to investigate the production of HOx and NOx and the subsequent depletion of mesospheric ozone with the Sondakylä Ion and Neutral Chemistry model (Turunen et al., 2009). The peak loss of mesospheric ozone was observed during the third and fourth day in the period of the repetitive substorm activity. This implies that the creation of MEE precipitation involves processes with various time constants and potentially accumulated effects, where there are increasing delays in flux buildup with energy (Boynton et al., 2016; Ødegaard et al., 2017; Stepanov et al., 2021).

Out of the International Association of Geomagnetism and Aeronomy (IAGA) recognized magnetic indices, the Auroral Electrojet (AE) index best corresponds to substorm activity. The AE index goes back to the 1960s and is constructed from the horizontal magnetic field component recorded with 1-min time resolution at 10–13 magnetic observatories located under the average auroral oval in the Northern Hemisphere (NH) (geomagnetic latitudes 60°–70°) (Davis & Sugiura, 1966; Kauristie et al., 2017, and references therein). The upper and lower envelope curves are defined to be the AU and AL indices which characterize the intensity of eastward and westward electrojets, respectively. The difference, AU—AL, defines the AE-index (Davis & Sugiura, 1966). The magnetotail energy release associated with the substorm expansion phase affects the intensity and spatial distribution of electric currents in the auroral oval region. In particular, the substorm current wedge causes sudden enhancements in the westward electrojet (Kauristie et al., 2017).

In this study, we explore the prediction capability of AE in regard to MEE precipitating fluxes. We combine observations from both the MEPED 0° and 90° detectors together with the theory of pitch angle diffusion by wave-particle interaction to quantify the MEE flux in the bounce loss cone. We treat the MEPED energy channels, > 43, >114, and >292 keV, independently to explore their associated time delays in respect to the geomagnetic activity. The objective is to determine the potential of AE as a proxy for MEE precipitating fluxes with a particular focus on the high energy tail. The paper is organised as follows: **Section 2** describes the MEPED detectors and the methods applied to estimate the loss cone fluxes. It provides a short introduction to the AE index followed by a comparison between the AE index and the SuperMAG substorms list from the period 2004–2014. **Section 3** starts with a simple inspection of the correlation between the AE index and the MEE fluxes, where the investigation of time delays and build-up effects points toward a more advanced model. **Section 4** provides a discussion of the implication of the results and the potential role of substorms as the physical process linking the AE based proxies and the MEE fluxes.

2 DATA AND METHODS

2.1 The Medium Energy Electrons Loss Cone Fluxes

The MEPED instrument is mounted on the NOAA/POES series and three EUMETSAT/MetOp spacecraft (Evans & Greer, 2004). The satellites are Sun-synchronous, low-altitude (~ 850 km), polar orbiting spacecrafts. Their orbital period is about 100 min, resulting in 14–15 orbits for each satellite each day. The combined measurements offer a long, near continuous observation of MEE from 1979 until today. During the latest decades a constellation of up to six operating satellites has allowed for a more global magnetic local time coverage.

The MEPED instrument consists of two directional electron telescopes and two directional proton telescopes, as well as an omni-directional detector for very energetic protons measured over a wide range of angles (Evans & Greer, 2004). The field of view of both the 0° and 90° telescopes is 30° full width. The nominal energy limits of the MEPED telescopes are given as > 30, >100, and >300 keV. The true detector efficiency, however, will depend on the incoming energy spectrum (Yando et al., 2011). Ødegaard et al. (2017) utilize the geometric factors given in Yando et al. (2011) to determine new optimized effective integral energy limits >43, >114, and >292 keV and associated geometric factors based on a series of realistic power law and exponential spectra. Furthermore, the spurious response to contaminating protons is accounted for. The observed proton fluxes are first corrected for degradation due to radiation damage by applying correction factors derived by Sandanger et al. (2015) and Ødegaard et al. (2016). Subsequently, a monotonic piecewise cubic Hermite interpolating polynomial is applied to the corrected proton fluxes. The proton flux in the energy ranges known to impact the respective electron channels (Evans & Greer, 2004), are then retrieved and subtracted from the original measured electron fluxes.

A detailed discussion on which radiation belt populations the 0° and 90° telescopes measure has been presented in Appendix A in Rodger et al. (2010). In general, it shows that at middle and high latitudes the 0° telescopes measure particle fluxes that will be lost to the atmosphere, whereas the 90° telescopes detect precipitating particle fluxes and/or trapped particles in the radiation belts. This implies that in the frequent case of pitch angle anisotropy the 0° detector will underestimate, while the 90° detector will overestimate the flux of precipitating electrons (Nesse Tyssøy et al., 2016; Nesse Tyssøy et al., 2019). A more realistic estimate can be achieved by combining fluxes from both the 0° and 90° telescopes together with electron pitch angle distributions from theory of wave-particle interactions in the magnetosphere. We solve the Focker-Planck equation for particle diffusion (Kennel & Petschek, 1966; Theodoridis & Paolini, 1967) for a wide range of diffusion coefficients (The specific equations are also given in Nesse Tyssøy et al. (2016)). The solutions are then transformed to the satellite altitude and saved in a look-up table. When comparing the theoretical pitch angle distributions with the measured particle fluxes the procedure is as follows:

- Determine the pitch angles of center look directions of the 0° and 90° telescopes.
- Calculate the ratio between of the fluxes detected by the 0° and 90° detector.
- Calculate the ratio between the fluxes for the theoretical pitch angle distributions taking into account the look directions.
- Determine which of the theoretical pitch angle distributions best corresponds to the observed ratio.

Finally, the size of the loss cone, predicted based on the International Geomagnetic Reference Field (IGRF) model, are applied to estimate the precipitating fluxes. The loss cone flux estimate is done separately for each energy channel as the level of particle diffusion will vary with energy. A detail explanation of the method can be found in Nesse Tyssøy et al. (2016).

We use MEE precipitation estimates from a full solar cycle from 2004 to 2014. This includes the active years in the declining phase of cycle 23, the extreme minimum, and the moderate maximum of cycle 24. **Figure 1** illustrates the number of NOAA and MetOp satellites applied throughout the 11 years alongside the MLT coverage in the NH. Although, the combination of satellites has a near global coverage on a daily scale, it is not equally distributed in terms of MLT. In particular, the evening sector and midnight sector are poorly represented in the NH. The daily average of the fluxes is therefore first calculated for four separate MLT sectors, 0–6 MLT, 6–12 MLT, 12–18 MLT, and 18–24 MLT over the CGM latitude band 55°–70°. Thereafter, a daily MEE flux is achieved as the average of the four MLT regions to ensure that the MEE flux is weighted equally in respect to MLT. **Figure 2** shows the resulting daily integral fluxes for the energies >43 keV (blue line), >114 keV (red line), and >292 keV (black line) over the full solar cycle. The values are given as the logarithm of the flux value, illustrating that the flux of the high energy tail >292 keV are typically two order of magnitude less than the >43 keV fluxes.

2.2 The Auroral Electrojet Index

The AE-index is designed by Davis and Sugiura (1966) to monitor the electrojet activity. The link to substorm activity was assumed from the very beginning as the substorm current system lies in the ionosphere. However, its deficiency with respect to coarse geographic latitude and longitude coverage was quickly pointed out. The observations, limited to a geomagnetic latitude band of 60°–70°N, could not always detect the dynamic auroral oval, both expanding equatorward and contracting poleward of the 12–13 stations. Short-term and localized events in the midnight sector, such as substorms, can easily be missed by the coarse network of stations. Besides substorms, pseudo-breakups, steady magnetospheric convection events, sawtooth injections, poleward boundary intensifications, or a mixture of these modes have been recognized in the AE data (McPherron, 2015). To overcome some of these challenges, regional electrojet-indices have been created (Tanskanen, 2009), and multiple regional magnetometer chains have been combined to compile globally denser network of stations (Gjerloev, 2012). Analysis have been performed to identify individual substorms. However, no generally accepted

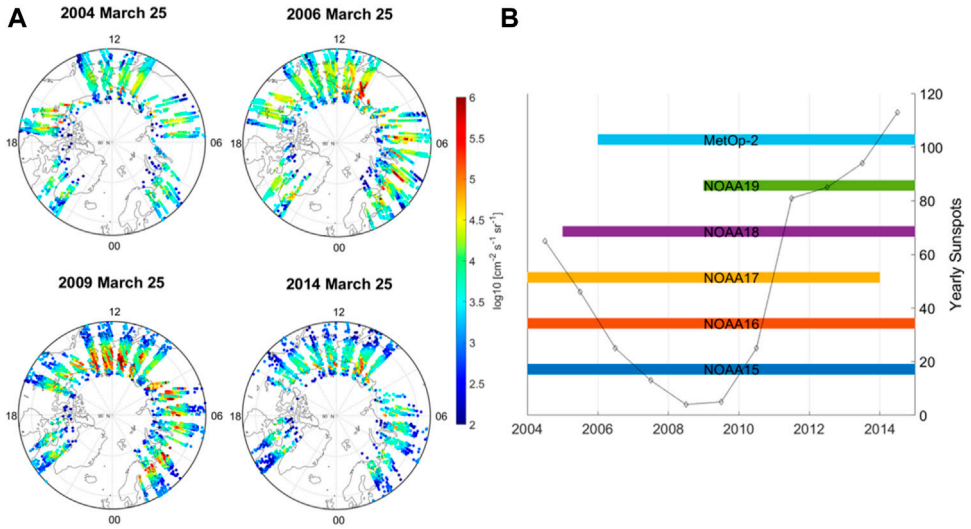


FIGURE 1 | (A): The POES and MetOp satellite MLT coverage over a full day during March 25th in 2004, 2006, 2009 and 2014. **(B)**: The POES and MetOp satellite coverage over a full solar cycle from 2004 to 2014.

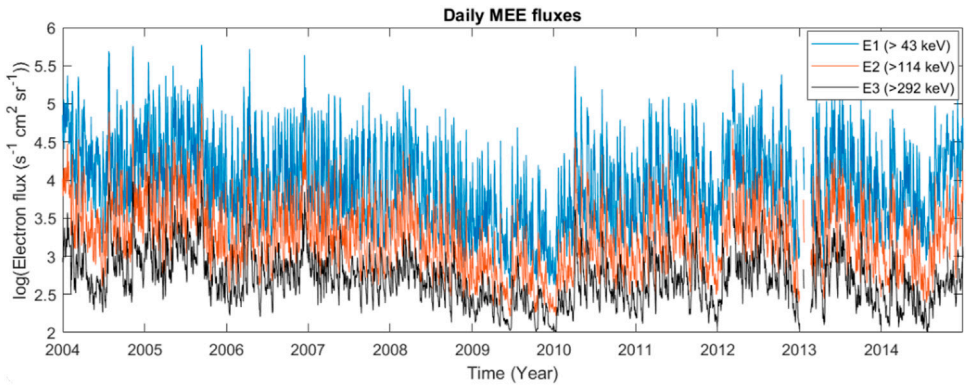


FIGURE 2 | Daily MEE of >43 keV (blue line), >114 keV (red line), and >292 keV (black line) from 2004 to 2014. The fluxes are averaged over all MLT and the CGM latitude band 55°–70°N.

method exists to identify substorm events from auroral electrojet indices, and different sets of criteria are used in different studies (e.g., Tanskanen et al., 2002; Newell & Gjerloev, 2011).

Figure 3 shows the daily averaged AE index alongside the daily number of substorms identified by Newell and Gjerloev (2011) from 2004 to 2014. The Pearson correlation coefficient, r, between the two datasets over the entire solar cycle is 0.89, giving $r^2 = 0.79$. It should, however, be emphasized that using the AE index on a daily scale makes identification of substorm/non-substorm modes problematic in particular for long active periods. Therefore, **Figure 3** shows a potential (but not proven) link between the daily averaged AE index and substorms.

We note that the daily AE index has a pronounced seasonal bias where the AU and AL indices maximize during summer and equinoctial months, respectively (Ahn et al., 2000). The equinox bias is due to the seasonal bias of solar wind driving which also applies to MEE. While the summer maxima, clearly evident in **Figure 3**, is due to increased background ionization from UV. This implies that the relation between the AE index and other parameters such as the number of substorms or MEE flux will vary with season. It also means that if AE, based on observations only from NH, is to be used as a global proxy for both hemispheres the seasonal bias needs to be addressed. In the MEE_{proxy} developed in this study, we remove the seasonal trend by subtracting the minimum daily AE value found in a moving window of ±14 days from the daily resolved AE index.

3 RESULTS

The daily AE index vary by three orders of magnitude over the 11 years. The daily fluxes of >43, >114, and >292 keV loss cone

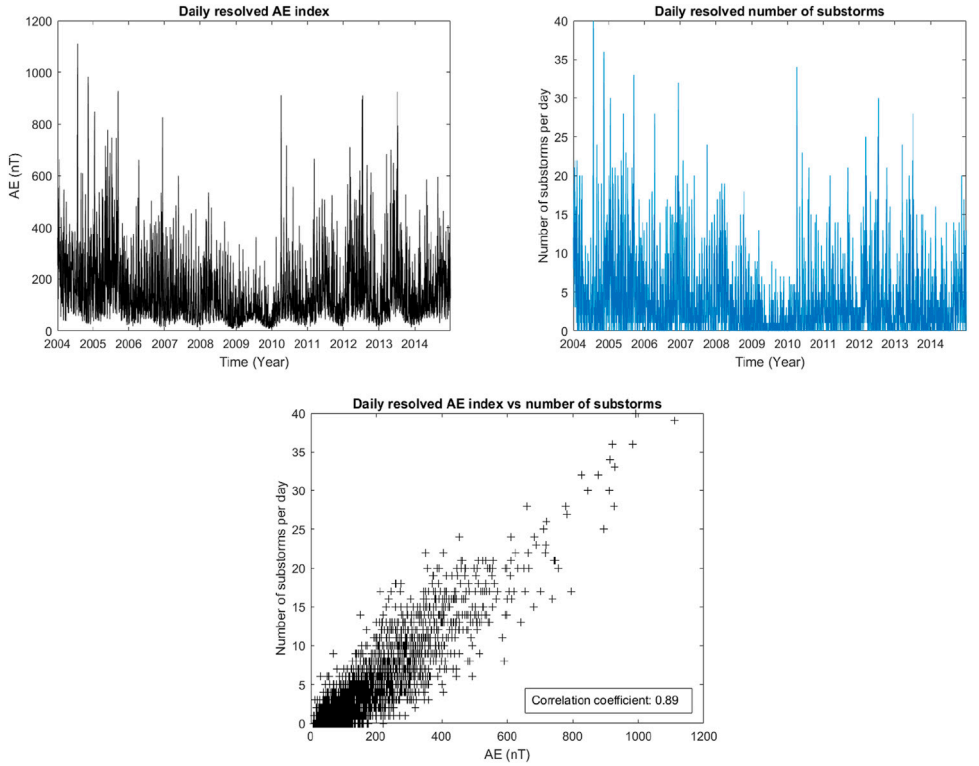


FIGURE 3 | Upper left plot: Daily resolved AE index (black line). **Upper right plot:** The number of substorms per day (blue line) based on Newell and Gjerloev (2011). **Upper right plot:** Scatter plot of the number of substorms per day and the daily resolve AE index. All panels include the period from 2004 to 2014.

fluxes over the 55°–70° CGM latitude band varies by five, four, and three orders of magnitude over the same period, respectively. **Figure 4** shows the scatter plots of a linear fit for 1) the linear value of the daily AE index and linear value of the daily >43 keV fluxes (Linear-Linear), 2) the linear value of the daily AE index and logarithmic value of the daily >43 keV fluxes (Linear-Logarithmic), and 3) the logarithmic value of the daily AE index and logarithmic value of the daily >43 keV fluxes (Logarithmic-Logarithmic). Despite a fairly good correlation of 0.83, the predictability of the Linear-Linear comparison is quite poor for low flux values. The Linear-Logarithmic and Logarithmic-Logarithmic comparison ensure equal weighting of errors associated to high and low flux values. Nevertheless, despite a high correlation coefficient of 0.81, the Linear-Logarithmic comparison systematically overestimates the high flux values and underestimate the low flux values. The Logarithmic-Logarithmic fit shows a clear linear dependence with the highest correlation coefficient of 0.88. As such, it is evident both in the correlation coefficients, and the scatter plots that using both the logarithmic values of the AE and the fluxes, ensures the strongest correspondence.

Table 1 lists the Pearson correlation coefficient between the daily resolved logarithmic value of the AE index and the logarithmic value of >43, >114, and >292 keV The square value of the correlation coefficients of 0.88 and 0.73 implies that the AE regression models fit with 77% and 53% of the variability of the >43 keV and >114 keV fluxes, respectively. The correlation coefficient decreases with energy, where a value of 0.47 implies that the AE regression model can only fit 22% of the variability of the >292 keV fluxes. This might reflect that a larger fraction of the >43 keV and >114 keV electron fluxes are directly injected during the substorm activity, while relatively fewer electrons >292 keV are part of the initial seed population. **Table 1** also shows that the AE index is best correlated with >43 keV and >114 keV electron fluxes in the post-midnight MLT sector which supports the link to substorm nightside injection and the subsequent eastward electron drift around the Earth and westward electrojet enhancements. The MLT bias is, however, not as prominent for >292 keV electron fluxes.

Figure 5A shows the Pearson correlation coefficients between the logarithmic value of the AE index 0–8 days prior to the logarithmic value of the observed MEE fluxes. The highest correlation is found on day zero, zero, and two for >43, >114, and >292 keV fluxes, respectively. The increasing offset as a function of energy substantiates that time is a prerequisite for the MEE high energy tail. The broad correlation peak and gradual decay further suggest that the MEE fluxes are influenced by the geomagnetic activity level of several days. **Figure 5B** shows the correlation between the logarithmic value of the AE index accumulated over consecutive longer periods prior to the logarithmic value of the observed MEE fluxes. The correlation coefficients between the accumulated AE index and the >43 keV fluxes peaks at 0.88 when both the zero and first preceding day are taken into account, which based on r-squared corresponds to

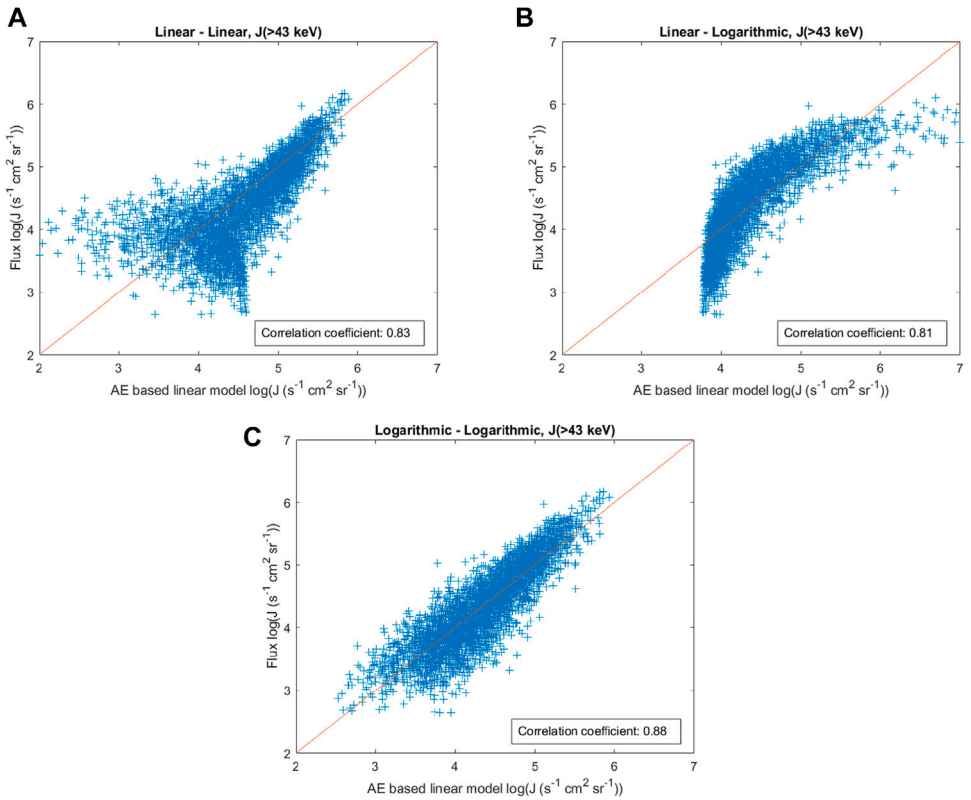


FIGURE 4 | Scatter plots and a linear fit of **(A)** the linear value of the daily AE index and linear value of the daily >43 keV fluxes (Linear-Linear), **(B)** the linear value of the daily AE index and logarithmic value of the daily >43 keV fluxes (Linear-Logarithmic), and **(C)** the logarithmic value of the daily AE index and logarithmic value of the daily >43 keV fluxes (Logarithmic-Logarithmic).

TABLE 1 | The Pearson correlation coefficient between daily resolved AE index and the logarithmic value of >43 > 114, and >292 keV loss cone fluxes over the 55°–70° CGM latitude band for the years 2004–2014.

Correlation coefficient between the AE index and MEE fluxes					
Energy	**0–6 MLT**	**6–12 MLT**	**12–18 MLT**	**18–24 MLT**	**All MLT**
>43 keV	0.86	0.86	0.85	0.74	0.88
>114 keV	0.73	0.75	0.73	0.65	0.73
>292 keV	0.48	0.46	0.45	0.47	0.47

approximately 77% of the flux variability. The correlation coefficient of the AE index for the >114 keV fluxes reaches about 0.83 when 3–4 days are accumulated, increasing the predictive capability of AE index from about 53% to 69%. The correlation coefficient between the accumulated AE index and the >292 keV fluxes increases rapidly the first few days and as many as seven preceding days are required for it to reach its peak of 0.81. Now, the predictive capability of the AE index has increased from about 22% to 66%.

Based on the correlation coefficients shown in **Figure 5A** is unlikely that each of the preceding days are equally important as assumed in this simple model shown in **Figure 5B**. As time evolves the seed population injected during a specific substorm is not only accelerated, but it is likely to be lost to the atmosphere or to the magnetopause. A more realistic model, where the AE index is weighted in respect to lifetimes of the particle population, could increase the predictive capability of the AE index even more. We assume the following weighting of geomagnetic activity:

$$MEE_{proxy} = \sum_{i=0}^{10} AE_i \cdot e^{\left(\frac{-i}{\tau}\right)} \quad (1)$$

where i refers to the preceding days and τ is the assumed lifetime. Due to the broad peak found in **Figure 5** for the >292 keV fluxes, the equation includes ten offset days. Furthermore, **Figure 3** shows a clear seasonal trend in the daily AE index which could impact the correlation with the MEE fluxes. As described in **Section 2.2**, we remove the seasonal trend in the AE index by subtracting the minimum daily AE value found in a moving window of ±14 days from all AE values. Now, the maximum correlation coefficients increases to 0.91, 0.89, and 0.84, using the optimized lifetime, τ, of one, three, and 9 days for >43 keV, > 114 keV, and >292 keV, respectively.

For the >43 keV fluxes a correlation coefficient of 0.91 is a small improvement from the 0.88 found in **Figure 5**. In addition, to better model low and high extremes, we fit two separate linear equations based on the logarithmic value of the MEE_{proxy}. The optimized separating boundary and the associated model equations are achieved by stepwise moving the limit over the

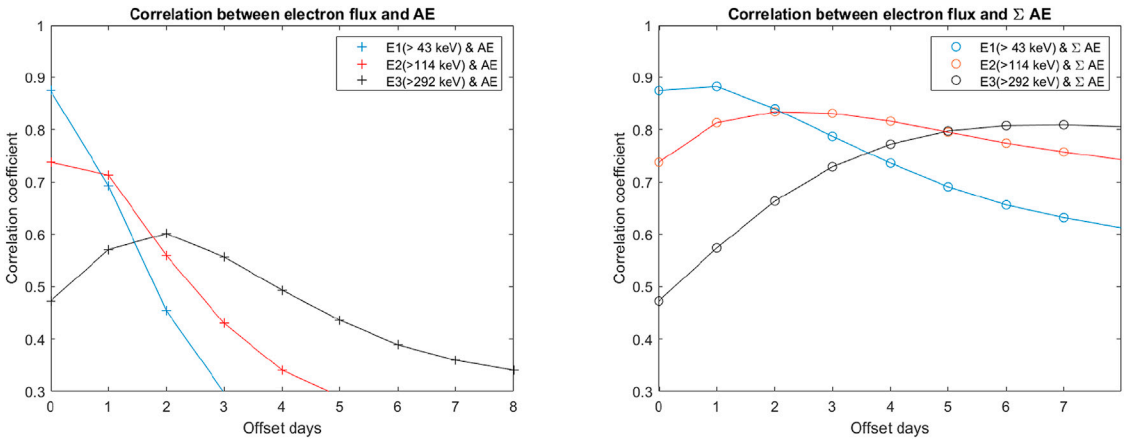


FIGURE 5 | The Pearson correlation coefficients between the logarithmic value of the electron fluxes >43 keV (blue line), >114 keV (red line), and >292 keV (black line) and the logarithmic value of the AE index (left plot) and the logarithmic value of the accumulated AE values (right plot).

TABLE 2 | The MEE_{proxy} models for two separate MEE_{proxy} intervals. The models give the logarithmic value of >43, >114, and >292 keV loss cone fluxes over the 55°–70° CGM latitude band.

The MEE_{proxy} model			
Energy	**MEE_{proxy}**	**Linear Model 1**	**Linear Model 2**
>43 keV	$\sum_{i=0}^{10} AE_i \cdot e^{(\frac{-i}{7})}$	$MEE_{proxy} < 66nT$: $a \cdot log(MEE_{proxy}) + b$, a = 0.6481, b = 2.634	$MEE_{proxy} \geq 66nT$: $a \cdot log(MEE_{proxy}) + b$, a = 1.733, b = 0.6631
>114 keV	$\sum_{i=0}^{10} AE_i \cdot e^{(\frac{-i}{3})}$	$MEE_{proxy} < 224nT$: $a \cdot log(MEE_{proxy}) + b$, a = 0.9654, b = 0.9843	$MEE_{proxy} \geq 224nT$: $a \cdot log(MEE_{proxy}) + b$, a = 1.752, b = -0.8791
>292 keV	$\sum_{i=0}^{10} AE_i \cdot e^{(\frac{-i}{9})}$	$MEE_{proxy} < 984nT$: $a \cdot log(MEE_{proxy}) + b$, a = 0.7717, b = 0.6536	$MEE_{proxy} \geq 984nT$: $a \cdot log(MEE_{proxy}) + b$, a = 1.414, b = -0.9869

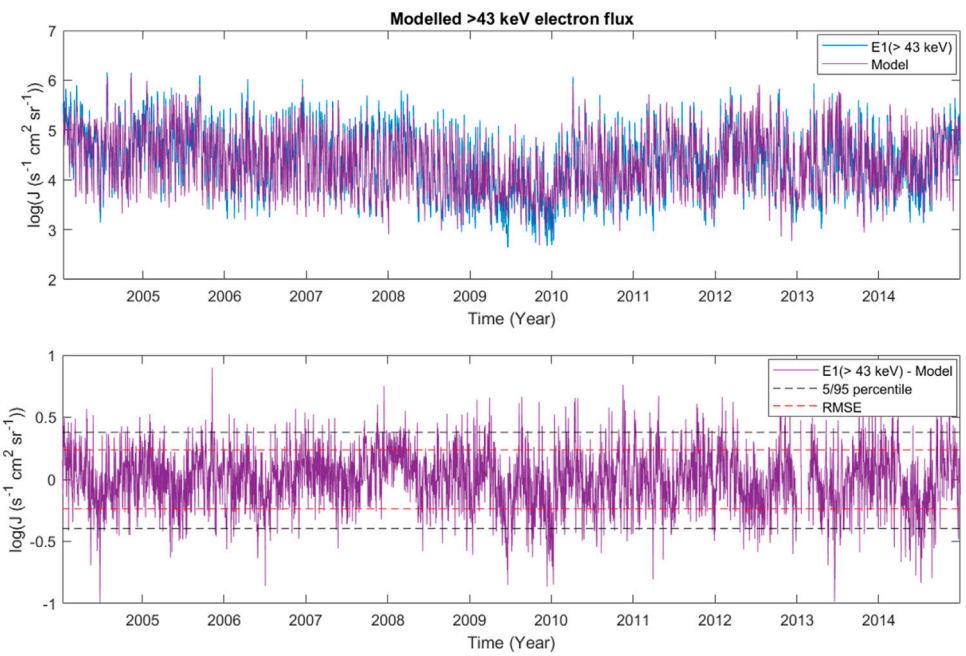


FIGURE 6 | The upper panel shows the observed (blue) and modelled (purple) daily resolved fluxes >43 keV in the period from 2004 to 2014. The lower panel shows the difference between the observed and modelled fluxes.

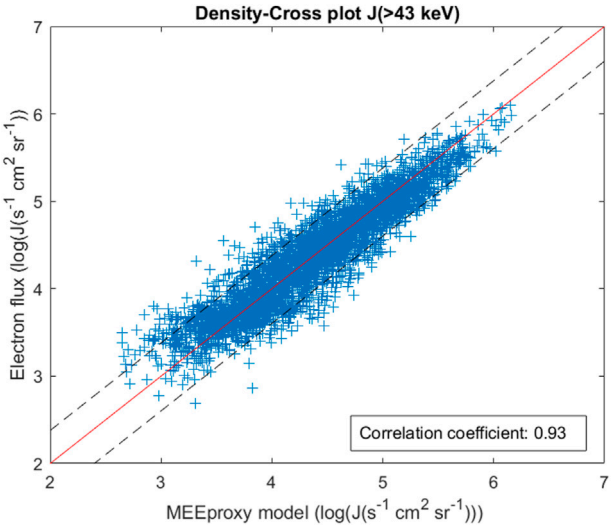


FIGURE 7 | Scatter plot of a linear fit of the logarithmic value of the optimized MEE_{proxy} and logarithmic value of the daily >43 keV fluxes. The black, dashed lines show the 95 and 5 percentile of the model errors.

entire MEE_{proxy} interval while performing two independent linear regression fits for the fluxes associated with the MEE_{proxy} values below and above the limit. The boundary giving the highest correlation coefficient and smallest RMSE for the two model fits combined are selected. An overview of the AE based MEE_{proxy}, including the mathematical expressions, lifetime τ, and linear equations are given in **Table 2** (Note that the limits are based on the MEE_{proxy} and not the daily AE values.) These simple measures increase the correlation coefficients to 0.93, 0.90, and 0.85 for >43 keV, > 114 keV, and >292 keV, respectively. This implies that about 86%, 81% and 72% of the daily flux variability, considering all MLTs and the full solar cycle, can be accounted for by the MEE_{proxy} models.

The upper panel in **Figure 6** shows the resulting linear fits to the AE-based MEE_{proxy} for >43 keV electron fluxes. The model captures the day-to-day fluctuations. The lower panel shows the differences between the observed and modelled fluxes. Similarly to the flux, the error are given as log [J $(s^{-1}cm^2sr^{-1})$], which implies that values larger than one would correspond to one order of magnitude difference. The 5/95 percentile black, dashed lines demonstrate that the typical error is less than 0.4 log [J $(s^{-1}cm^2sr^{-1})$], corresponding to the value $10^{0.40} \sim 2.5$. This means that for 90% of the days the model predicts fluxes that deviates from the observed fluxes by less than a factor of 2.5. The largest error found is 0.99 which correspond to a factor of 9.8. Hence, all values are within one order of magnitude of the observed fluxes. We note, however, specific periods in time where the model appears to have a bias. In the declining phase the model underestimates the flux level, while the opposite occurs for the extreme solar minimum year of 2009. There also appear to be a seasonal bias where the model overestimate/underestimate the flux values during summer/winter. **Figure 7** shows the scatter plot of the MEE_{proxy} model vs the observed >43 keV electron flux. It illustrates that the largest errors are found during low to moderate activity. Compared to **Figure 4** the improvement using the MEE_{proxy} model on a detrended AE index is readily evident.

Figure 8 shows the resulting linear fits to the AE-based MEE_{proxy} for >114 keV electron fluxes. The accuracy and weaknesses of the modelled >114 keV fluxes are similar to the modelled >43 keV fluxes as shown in **Figure 8**. However, **Figure 9** shows a tendency of the MEE_{proxy} model to overestimate the fluxes during high activity. **Figure 10** and **Figure 11** confirm a similar trend for the modelled >292 keV fluxes. All correlation coefficients, including the MLT dependence are listed in **Table 3**.

4 DISCUSSION AND CONCLUSION

There is increasing evidence that substorms are key in driving MEE precipitation (Beharrell et al., 2015; Partamies et al., 2021). Nevertheless, the substorms remain partly unresolved in the existing proxies when considering the MEE precipitation (van de Kamp et al., 2016). In this study, we have explored the prediction capability of AE in regard to MEE precipitation on a daily scale over a full solar cycle. The potential link between the AE index, substorms, and MEE precipitation will be discussed, alongside the progressive time delay between the geomagnetic activity and the MEE precipitation.

The initial correlation study, summarized in **Figure 5**, reveals a high coherence between the daily AE index with zero lag and >43 keV precipitating electron fluxes. Similarly, **Figure 3** suggests a strong coherence with the daily AE index and the daily number of substorms. The magnetotail dipolarization during substorms will directly inject source and seed particles in this energy range, some of which will precipitate into the atmosphere. It is therefore a realistic physical link between the AE intensity and >43 keV fluxes, despite the fact that the >43 keV fluxes deposit their energy below 100 km and do not directly contribute to the intensity of the electrojets. The strong correlation between the AE index and >43 keV fluxes is in agreement with recent studies of the trapped radiation belt electrons. Based on an extensive database of 16 years of corrected MEE flux observations (40–400 keV) from the Research with Adaptive Particle Imaging Detector (RAPID)/Imaging Electron Spectrometer (IES) instrument on board the Cluster mission, Smirnov et al. (2019) reveal that the variability of the outer belt electrons (L-shell 4–6) exhibits a pattern very close to the AE index. Furthermore, Katsavrias et al. (2021) confirm, based on 9 years of electron measurements from GOES-13, 14 and 15, that the trapped electron fluxes at energies in the interval 10–100 keV are well correlated with the AE index consistent with substorm injected source particles.

In the case of the high energy tail of the MEE precipitation, **Figure 5** suggests that only 22% of the >292 keV flux variability are described by the daily AE variability. Ødegaard et al. (2017) shows that these higher energy electrons typically peak 1–2 days after the onset of a geomagnetic storm. The progressive time delays of relativistic electrons has also been identified by e.g., Boynton et al. (2016) and Mourenas et al. (2019). The delay implies that it takes time to accelerate the injected seed electrons

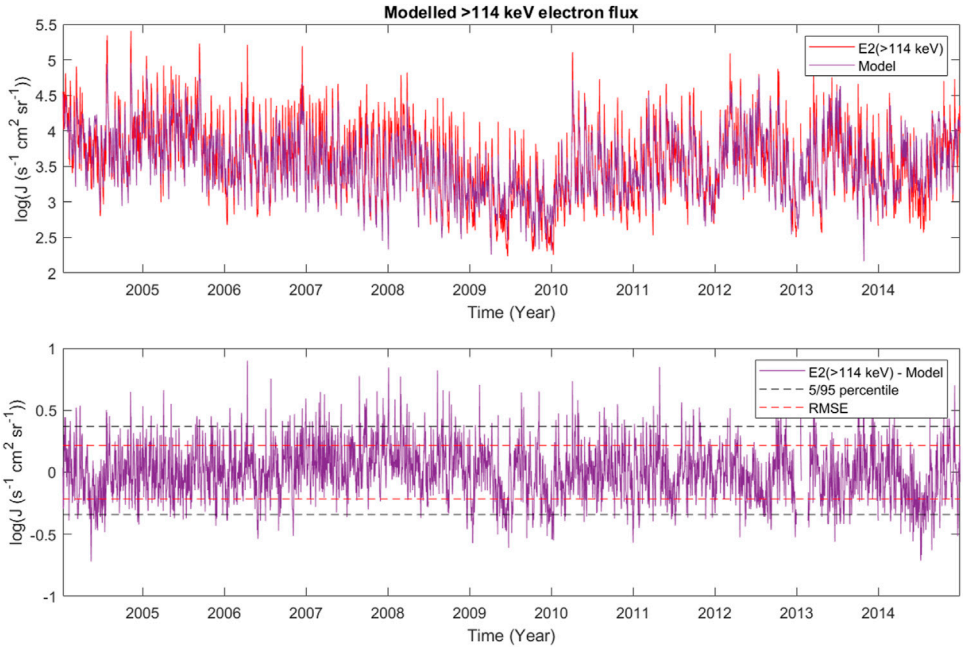


FIGURE 8 | The upper panel shows the observed (red) and modelled (purple) daily resolved fluxes >114 keV in the period from 2004 to 2014. The lower panel shows the difference between the observed and modelled fluxes.

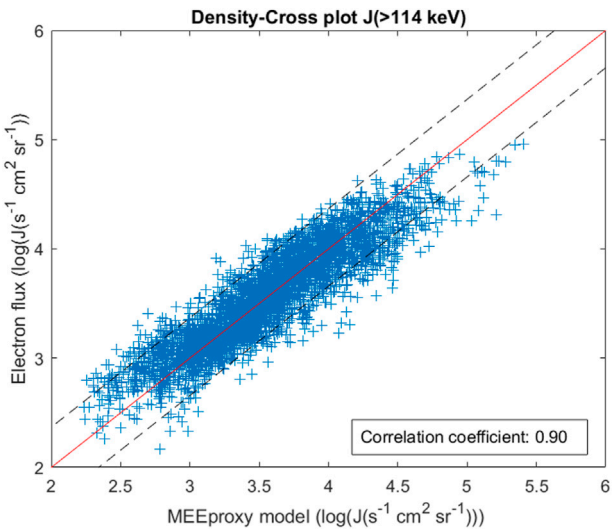


FIGURE 9 | Scatter plot of a linear fit of the logarithmic value of the optimized MEE_{proxy} and logarithmic value of the daily >114 keV fluxes. The black, dashed lines show the 95 and 5 percentile of the model errors.

into several 100 s keV. It will also require a continuous acceleration mechanism. This could be provided during repeated substorm activity, as the source particles will fuel VLF waves and the injected seed particles can be energized as they drift across the substorm induced electric field on the nightside. This means that the precipitating >292 keV fluxes are a product of both the ongoing activity, as well as the substorm activity during the previous days. This potential link is made viable by the simple accumulation of the AE values in **Figure 5B**. However, the identification of substorm/non-substorm modes might be problematic using the daily resolved AE index, in particular for long active geomagnetic periods. Moreover, VLF acceleration and scattering are not limited to substorm periods.

Katsavrias et al. (2021) also find a reduced correlation between 100–350 keV trapped electron flux and the AE index compared to the 10–100 keV electrons. These higher energies display, however, a strong dependence on the solar wind speed. They suggest that it implies that the acceleration and loss of the seed energies are not purely substorm driven but rather depend on convection driven by the fast solar wind and/or ULF driven inward diffusion. Smirnov et al. (2019) demonstrate a high positive correlation between the 40–400 keV radiation belt electrons and the AE index and solar wind dynamic pressure. Furthermore, Stepanov et al. (2021) confirm the role of solar wind speed as one of the most important predictors for transporting electron fluxes from the plasmasheet to the radiation belt region. Similarly, Ødegaard et al. (2017) show how the >292 keV flux variability depends on the Akasufos's coupling function. Boynton et al. (2016) developed forecast models for MEE and highly relativistic electrons using the coupling function proposed by (Boynton et al., 2011) and the Dst index. The latter confirms the solar wind dependence while simultaneously accounting for the direction of the Northward interplanetary field direction. Neither the solar wind dependence, nor the coupling function dependence does, however, exclude substorms and the associated VLF wave generation as the working mechanism. In

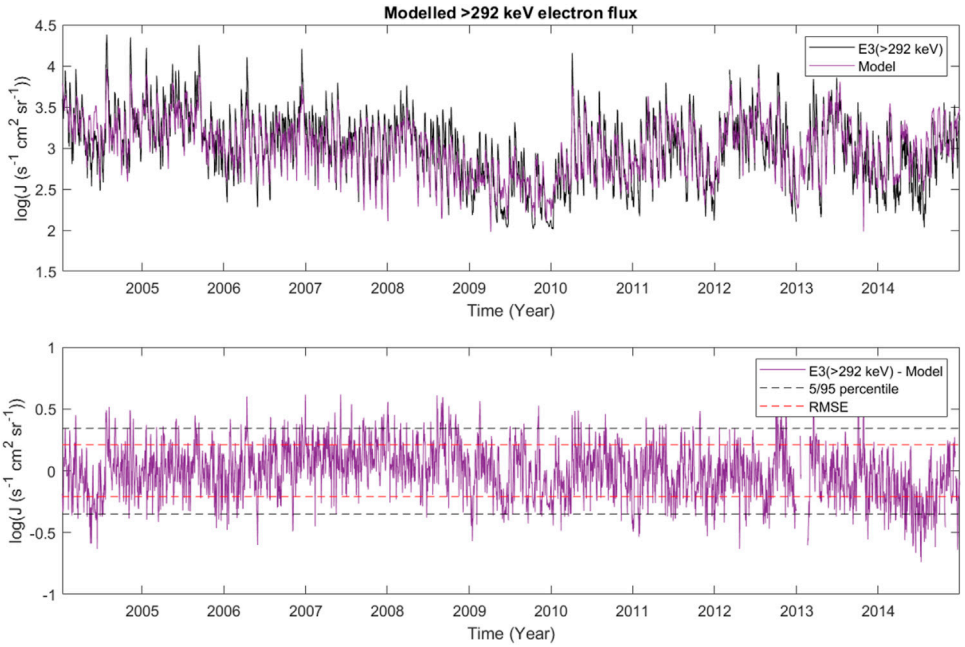


FIGURE 10 | The upper panel shows the observed (black) and modelled (purple) daily resolved fluxes >292 keV in the period from 2004 to 2014. The lower panel shows the difference between the observed and modelled fluxes.

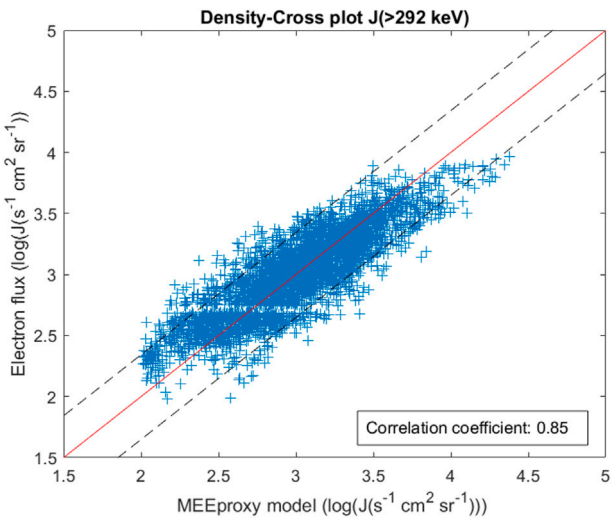


FIGURE 11 | Scatter plot of a linear fit of the logarithmic value of the optimized MEE_{proxy} and logarithmic value of the daily >292 keV fluxes. The black, dashed lines show the 95 and 5 percentile of the model errors.

fact, Miyoshi et al. (2013) find that High Speed Solar Wind Streams (HSSWS) alone is not sufficient to cause relativistic electron flux enhancement in the outer radiation belt, but strongly depend on IMF-Bz. They state that this would not be the case if radial transport via ULF waves is the primary mechanism. Miyoshi and Kataoka (2008) suggested that the IMF-Bz dependence could be attributed to substorm occurrence during HSSWS events where the electrons are accelerated via VLF waves. This is in line with the relativistic electron flux enhancements found during intervals of prolonged substorm activity operating on a timescale of the order of days (Bühler & Desorgher, 2002; Meredith et al., 2003).

The lifetimes applied in the MEE_{proxy} are impacted by the lifespan of the MEE particles in the outer radiation belt. The lifespan depends on the energy, radial distance from Earth, and the level of geomagnetic activity. The lifetimes for 100 keV electrons at a radial distance of about four are approximately 3.6 days and 13 h for quiet and active geomagnetic conditions, respectively, and are increasing rapidly with energy to about 131 and 17 days for 1 MeV electrons (Orlova et al., 2016). The expected lifetime can, however, be rapidly reduced in the case of magnetopause shadowing where trapped particles over several radial distances are lost to the magnetopause. This is a consequence of a sudden dynamic pressure increase in the solar wind, alongside convection driven outward radial transport (Turner et al., 2012). Applying a fixed lifetime as suggested in the MEE_{proxy} is therefore unrealistic. The optimized lifetime applied in the MEE_{proxy} is thus only the empirical average based on the applied data. It does, however, demonstrate the potential of an AE based MEE_{proxy}, where the precipitation fluxes are an accumulated effect of both the current and previous geomagnetic activity.

This study reveals the high predictive capabilities of the AE index for MEE precipitation, and how to account for the delayed response of the high energy tail (> 300 keV). Hence, it offers a potential improvement to the current MEE parameterization included in CMIP6 recommendation (Matthes et al., 2017). Nesse Tyssøy et al. (2019) compares the loss cone estimate to

TABLE 3 | The Pearson correlation coefficient between daily resolved AE based MEE_{proxy} and the logarithmic value of >43, >114, and >292 keV loss cone fluxes over the 55°–70° CGM latitude band for the years 2004–2014.

Correlation coefficient between the AE based MEE proxy and MEE fluxes					
Energy	**0–6 MLT**	**6–12 MLT**	**12–18 MLT**	**18–24 MLT**	**All MLT**
>43 keV	0.91	0.92	0.91	0.84	0.93
>114 keV	0.87	0.89	0.91	0.89	0.90
>292 keV	0.84	0.84	0.85	0.85	0.85

the CMIP recommendation and shows an overall underestimation of basic flux strength about one order of magnitude arises from utilizing 0° detector electron fluxes. As this is the same data used to develop the MEE_{proxy} model it is likely that the same assessment will apply if compared to the CMIP recommendation. Furthermore, Nesse Tyssøy et al. (2019) showed that the CMIP recommendation generally captured the initial phase of the storm fluxes, but fell short in respect to reproducing elevated flux levels during the recovery phase of CIR-driven storms. As such, the energy dependent lifetimes applied in the MEE_{proxy}, taking into account the accumulated geomagnetic activity, is likely to avoid this pitfall.

However, for AE to be used as a proxy for MEE precipitation in a more advanced MEE precipitation model, the seasonal bias needs further examination as it could be a source of unequal distribution between the two hemispheres. In addition, **Figures 6**, **8**, **10** show a potential solar cycle bias of a general underestimation in the declining phase. To which extent this is due to the dynamical expansion of the auroral oval and the equatorward shift of the electrojets, where the AE-stations cannot reliably monitor their intensity, needs to be explored. The small number of magnetometer stations and their uneven spatial distribution implies that small perturbations (e.g., isolated substorms and pseudo-breakups) can be undetected and large deflections underestimated if they are constrained in longitude or are located at latitudes poleward or equatorward of the AE station network (Gjerloev et al., 2004). Similarly, the MEE precipitation region does not cover a fixed latitude band, and its dependence with geomagnetic activity is explored in a parallel study. Alternatively, the solar cycle bias might reflect the type of solar wind driver responsible for the geomagnetic disturbances as Corotating Interaction Region (CIR)/ High Speed Solar Wind Streams (HSSWS) and Coronal Mass Ejection (CME) driven geomagnetic storms dominate different phases of the solar cycle. For example, the lifetime applied in the MEE_{proxy} can vary in weak but long lasting CIR/HSSWS compared to a short but powerful CME event.

In summary, this study demonstrates that simple AE based MEE-proxies have the capability of explaining at 72–86% of the detected MEE precipitation variance on a daily scale. The model shows, however, caveats in respect to the solar cycle and extreme events that summon further investigations. Nevertheless, 90% of the modelled flux values deviate less than a factor of 2.5 from the observed NOAA/ POES MEPED fluxes throughout a full solar cycle. By evaluating the different energy channels, > 43, >114, and >292 keV, independently, the model enables a realistic description of the time dependent energy spectrum. This finding will form the base of a new MEE model to be used for future studies of the energetic electron precipitation impact on the atmosphere.

DATA AVAILABILITY STATEMENT

Publicly available datasets were analyzed in this study. This data can be found here: https://www.ngdc.noaa.gov/stp/satellite/poes/dataaccess.html http://wdc.kugi.kyoto-u.ac.jp/wdc/Sec3.html https://supermag.jhuapl.edu/substorms/

AUTHOR CONTRIBUTIONS

HNT conceived idea of this paper, in charge of the analysis, and writing as lead author. NP contributed to the idea of this paper and editing of the manuscript. EMB is responsible for constructing the MLT dependent daily resolved electron flux and editing of the manuscript. CS-J contributed to editing of the manuscript. JAS contributed to editing of the manuscript.

FUNDING

The study is supported by the Norwegian Research Council (NRC) under contract 223252, 302040 and 287427. HNT further acknowledge the Young CAS (Centre for Advanced Studies) fellow program.

ACKNOWLEDGMENTS

The NOAA/POES data used in this study are available from the National Oceanic and Atmospheric Administration (https://www.ngdc.noaa.gov/stp/satellite/poes/dataaccess.html). The AE index used in this paper was provided by the WDC for Geomagnetism, Kyoto (http://wdc.kugi.kyoto-u.ac.jp/wdc/Sec3.html). We also acknowledge the substorm timing list identified by the Newell and Gjerloev technique (Newell and Gjerloev, 2011), the SMU and SML indices (Newell and Gjerloev, 2011); and the SuperMAG collaboration (Gjerloev, 2012) (https://supermag.jhuapl.edu/substorms/).

REFERENCES

Ahn, B.-H., Kroehl, H. W., Kamide, Y., and Kihn, E. A. (2000). Seasonal and Solar Cycle Variations of the Auroral Electrojet Indices. *J. Atmos. Solar-Terrestrial Phys.* 62 (14), 1301–1310. doi:10.1016/s1364-6826(00)00073-0

Andersson, M. E., Verronen, P. T., Wang, S., Rodger, C. J., Clilverd, M. A., and Carson, B. R. (2012). Precipitating Radiation belt Electrons and Enhancements of Mesospheric Hydroxyl during 2004-2009. *J. Geophys. Res.* 117 (D9). doi:10.1029/2011JD017246

Beharrell, M. J., Honary, F., Rodger, C. J., and Clilverd, M. A. (2015). Substorm-induced Energetic Electron Precipitation: Morphology and Prediction. *J. Geophys. Res. Space Phys.* 120 (4), 2993–3008. doi:10.1002/2014ja020632

Borovsky, J. E., and Yakymenko, K. (2017). Substorm Occurrence Rates, Substorm Recurrence Times, and Solar Wind Structure. *J. Geophys. Res. Space Phys.* 122 (3), 2973–2998. doi:10.1002/2016ja023625

Boynton, R. J., Balikhin, M. A., Billings, S. A., Wei, H. L., and Ganushkina, N. (2011). Using the Narmax Ols-Err Algorithm to Obtain the Most Influential Coupling Functions that Affect the Evolution of the Magnetosphere. *J. Geophys. Res. Space Phys.* 116 (A5). doi:10.1029/2010ja015505

Boynton, R. J., Balikhin, M. A., Sibeck, D. G., Walker, S. N., Billings, S. A., and Ganushkina, N. (2016). Electron Flux Models for Different Energies at Geostationary Orbit. *Space Weather* 14 (10), 846–860. doi:10.1002/2016sw001506

Bühler, P., and Desorgher, L. (2002). Relativistic Electron Enhancements, Magnetic Storms, and Substorm Activity. *J. Atmos. Solar-Terrestrial Phys.* 64 (5), 593–599. doi:10.1016/s1364-6826(02)00017-2

Clilverd, M. A., Rodger, C. J., van de Kamp, M., and Verronen, P. T. (2020). Electron Precipitation from the Outer Radiation belt during the St. Patrick's Day Storm 2015: Observations, Modeling, and Validation. *J. Geophys. Res. Space Phys.* 125 (2), e2019JA027725. doi:10.1029/2019ja027725

Dai, L., Wygant, J. R., Cattell, C. A., Thaller, S., Kersten, K., Breneman, A., et al. (2014). Evidence for Injection of Relativistic Electrons into the Earth's Outer Radiation belt via Intense Substorm Electric fields. *Geophys. Res. Lett.* 41 (4), 1133–1141. doi:10.1002/2014gl059228

Davis, T. N., and Sugiura, M. (1966). Auroral Electrojet Activity indexAEand its Universal Time Variations. *J. Geophys. Res.* 71 (3), 785–801. doi:10.1029/jz071i003p00785

Evans, D. S., and Greer, M. S. (2004). *Polar Orbiting Environmental Satellite Space Environment Monitor - 2: Instrument Descriptions and Archive Data Documentation*. Boulder, Colorado: NOAA Technical Memorandum, 93. version 1.4

Gjerloev, J. W., Hoffman, R. A., Friel, M. M., Frank, L. A., and Sigwarth, J. B. (2004). Substorm Behavior of the Auroral Electrojet Indices. *Ann. Geophys.* 22 (6), 2135–2149. doi:10.5194/angeo-22-2135-2004

Gjerloev, J. W. (2012). The Supermag Data Processing Technique. *J. Geophys. Res. Space Phys.* 117 (A9), 9213. doi:10.1029/2012ja017683

Jaynes, A. N., Baker, D. N., Singer, H. J., Rodriguez, J. V., Loto'aniu, T. M., Ali, A. F., et al. (2015). Source and Seed Populations for Relativistic Electrons: Their Roles in Radiation belt Changes. *J. Geophys. Res. Space Phys.* 120 (9), 7240–7254. doi:10.1002/2015ja021234

Katsavrias, C., Aminalragia–Giamini, S., Papadimitriou, C., Sandberg, I., and Jiggens, P. (2021). Daglis, I.,and Evans, HOn the Interplanetary Parameter Schemes Which Drive the Variability of the Source/seed Electron Population at Geo. Journal of Geophysical Research. *Space Phys.* 126 (6), e2020JA028939. doi:10.1029/2020ja028939

Kauristie, K., Morschhauser, A., Olsen, N., Finlay, C. C., McPherron, R. L., Gjerloev, J. W., et al. (2017). On the Usage of Geomagnetic Indices for Data Selection in Internal Field Modelling. *Space Sci. Rev.* 206, 61–90. doi:10.1007/s11214-016-0301-0

Kennel, C. F., and Petschek, H. E. (1966). Limit on Stably Trapped Particle Fluxes. *J. Geophys. Res. (1896-1977)* 71 (1), 1–28. doi:10.1029/jz071i001p00001

Li, L. Y., Cao, J. B., Zhou, G. C., and Li, X. (2009). Statistical Roles of Storms and Substorms in Changing the Entire Outer Zone Relativistic Electron Population. *J. Geophys. Res. Space Phys.* 114 (A12). doi:10.1029/2009ja014333

Maliniemi, V., Asikainen, T., and Mursula, K. (2016). Effect of Geomagnetic Activity on the Northern Annular Mode: Qbo Dependence and the holton-tan Relationship. *J. Geophys. Res. Atmospheres* 121 (17), 10043–10055. doi:10.1002/2015jd024460

Matthes, K., Funke, B., Andersson, M. E., Barnard, L., Beer, J., Charbonneau, P., et al. (2017). Solar Forcing for CMIP6 (v3.2). *Geosci. Model. Dev.* 10, 2247–2302. doi:10.5194/gmd-10-2247-2017

McPherron, R. L. (2015). "Earth's Magnetotail," in *Magnetotails in the Solar System* (American Geophysical Union), 61–84. doi:10.1002/9781118842324.ch4

Meredith, N. P., Cain, M., Horne, R. B., Thorne, R. M., Summers, D., and Anderson, R. R. (2003). Evidence for Chorus-Driven Electron Acceleration to Relativistic Energies from a Survey of Geomagnetically Disturbed Periods. *J. Geophys. Res. Space Phys.* 108 (A6). doi:10.1029/2002ja009764

Mironova, I. A., Artamonov, A. A., Bazilevskaya, G. A., Rozanov, E. V., Kovaltsov, G. A., Makhmutov, V. S., et al. (2019). Ionization of the Polar Atmosphere by Energetic Electron Precipitation Retrieved from Balloon Measurements. *Geophys. Res. Lett.* 46 (2), 990–996. doi:10.1029/2018gl079421

Miyoshi, Y., and Kataoka, R. (2008). Flux Enhancement of the Outer Radiation belt Electrons after the Arrival of Stream Interaction Regions. *J. Geophys. Res. Space Phys.* 113 (A3). doi:10.1029/2007ja012506

Miyoshi, Y., Kataoka, R., Kasahara, Y., Kumamoto, A., Nagai, T., and Thomsen, M. F. (2013). High-speed Solar Wind with Southward Interplanetary Magnetic Field Causes Relativistic Electron Flux Enhancement of the Outer Radiation belt via Enhanced Condition of Whistler Waves. *Geophys. Res. Lett.* 40 (17), 4520–4525. doi:10.1002/grl.50916

Mourenas, D., Artemyev, A. V., and Zhang, X. J. (2019). Impact of Significant Time-Integrated Geomagnetic Activity on 2-MeV Electron Flux. *J. Geophys. Res. Space Phys.* 124 (6), 4445–4461. doi:10.1029/2019ja026659

Nesse Tyssøy, H., Haderlein, A., Sandanger, M. I., and Stadsnes, J. (2019). Intercomparison of the POES/MEPED Loss Cone Electron Fluxes with the CMIP6 Parametrization. *J. Geophys. Res. Space Phys.* 124, 628–642. doi:10.1029/2018JA025745

Nesse Tyssøy, H., Sandanger, M. I., Ødegaard, L.-K. G., Stadsnes, J., Aasnes, A., and Zawedde, A. E. (2016). Energetic Electron Precipitation into the Middle Atmosphere—Constructing the Loss Cone Fluxes from Meped Poes. *J. Geophys. Res. Space Phys.* 121 (6), 5693–5707. doi:10.1029/2004JA010485

Newell, P. T., and Gjerloev, J. W. (2011). Evaluation of SuperMAG Auroral Electrojet Indices as Indicators of Substorms and Auroral Power. *J. Geophys. Res.* 116 (A15). doi:10.1029/2011JA016779

Ødegaard, L.-K. G., Tyssøy, H. N., Sandanger, M. I. J., Stadsnes, J., and Søraas, F. (2016). Space Weather Impact on the Degradation of Noaa Poes Meped Proton Detectors. *J. Space Weather Space Clim.* 6, A26. doi:10.1051/swsc/2016020

Ødegaard, L. K. G., Tyssøy, H. N., Søraas, F., Stadsnes, J., and Sandanger, M. I. (2017). Energetic Electron Precipitation in Weak to Moderate Corotating Interaction Region-driven Storms. *J. Geophys. Res. Space Phys.* 122 (3), 2900–2921. doi:10.1002/2016ja023096

Orlova, K., Shprits, Y., and Spasojevic, M. (2016). New Global Loss Model of Energetic and Relativistic Electrons Based on Van allen Probes Measurements. *J. Geophys. Res. Space Phys.* 121 (2), 1308–1314. doi:10.1002/2015ja021878

Partamies, N., Tesema, F., Bland, E., Heino, E., Nesse Tyssøy, H., and Kallelid, E. (2021). Electron Precipitation Characteristics during Isolated, Compound, and Multi-Night Substorm Events. *Ann. Geophys.* 39 (1), 69–83. doi:10.5194/angeo-39-69-2021

Pettit, J. M., Randall, C. E., Peck, E. D., Marsh, D. R., Kamp, M., Fang, X., et al. (2019). Atmospheric Effects of >30-keV Energetic Electron Precipitation in the Southern Hemisphere Winter during 2003. *J. Geophys. Res. Space Phys.* 124 (10), 8138–8153. doi:10.1029/2019ja026868

Rodger, C., Carson, B., Cummer, S., Gamble, R., Clilverd, M., Green, J., et al. (2010). Contrasting the Efficiency of Radiation belt Losses Caused by Ducted and Nonducted Whistler-Mode Waves from Ground-Based Transmitters. *J. Geophys. Res. Space Phys.* 115 (A12). doi:10.1029/2010ja015880

Rodger, C. J., Cresswell-Moorcock, K., and Clilverd, M. A. (2016). Nature's Grand Experiment: Linkage between Magnetospheric Convection and the Radiation Belts. *J. Geophys. Res. Space Phys.* 121 (1), 171–189. doi:10.1002/2015ja021537

Sandanger, M. I., Ødegaard, L. K. G., Nesse Tyssøy, H., Stadsnes, J., Søraas, F., Oksavik, K., et al. (2015). In-flight Calibration of NOAA POES Proton Detectors-Derivation of the MEPED Correction Factors. *J. Geophys. Res. Space Phys.* 120 (11), 9578–9593. doi:10.1002/2015ja021388

Sætre, C., Stadsnes, J., Nesse, H., Aksnes, A., Petrinec, S. M., Barth, C. A., et al. (2004). Energetic Electron Precipitation and the No Abundance in the Upper

Atmosphere: A Direct Comparison during a Geomagnetic Storm. *J. Geophys. Res. Space Phys.* 109 (A9). doi:10.1029/2004JA010485

Seppälä, A., Clilverd, M. A., Beharrell, M. J., Rodger, C. J., Verronen, P. T., Andersson, M. E., et al. (2015). Substorm-induced Energetic Electron Precipitation: Impact on Atmospheric Chemistry. *Geophys. Res. Lett.* 42 (19), 8172–8176. doi:10.1002/2015gl065523

Seppälä, A., Lu, H., Clilverd, M. A., and Rodger, C. J. (2013). Geomagnetic Activity Signatures in Wintertime Stratosphere Wind, Temperature, and Wave Response. *J. Geophys. Res. Atmos.* 118 (5), 2169–2183. doi:10.1002/jgrd.50236

Sinnhuber, M., Friederich, F., Bender, S., and Burrows, J. P. (2016). The Response of Mesospheric NO to Geomagnetic Forcing in 2002-2012 as Seen by SCIAMACHY. *J. Geophys. Res. Space Phys.* 121, 3603–3620. doi:10.1002/2015JA022284

Smirnov, A. G., Kronberg, E. A., Latallerie, F., Daly, P. W., Aseev, N., Shprits, Y. Y., et al. (2019). Electron Intensity Measurements by the Cluster/RAPID/IES Instrument in Earth's Radiation Belts and Ring Current. *Space Weather* 17 (4), 553–566. doi:10.1029/2018sw001989

Stepanov, N. A., Sergeev, V. A., Sormakov, D. A., Andreeva, V. A., Dubyagin, S. V., and Ganushkina, N. (2021). Superthermal Proton and Electron Fluxes in the Plasma Sheet Transition Region and Their Dependence on Solar Wind Parameters. Journal of Geophysical Research. *Space Phys.* 126 (4), e2020JA028580. doi:10.1029/2020ja028580

Tanskanen, E. (2009). A Comprehensive High-Throughput Analysis of Substorms Observed by Image Magnetometer Network: Years 1993–2003 Examined. *J. Geophys. Res. Space Phys.* 114 (A5). doi:10.1029/2008ja013682

Tanskanen, E., Pulkkinen, T. I., Koskinen, H. E. J., and Slavin, J. A. (2002). Substorm Energy Budget during Low and High Solar Activity: 1997 and 1999 Compared. *J. Geophys. Res. Space Phys.* 107 (A6). doi:10.1029/2001ja900153

Theodoridis, G. C., and Paolini, F. R. (1967). Pitch Angle Diffusion of Relativistic Outer belt Electrons. *Ann. Geophys.*, 375–381.

Turner, D. L., Shprits, Y., Hartinger, M., and Angelopoulos, V. (2012). Explaining Sudden Losses of Outer Radiation belt Electrons during Geomagnetic Storms. *Nat. Phys* 8, 208–212. doi:10.1038/nphys2185

Turunen, E., Verronen, P. T., Seppälä, A., Rodger, C. J., Clilverd, M. A., and Tamminen, J. (2009). . . . Ulich, TImpact of Different Energies of Precipitating Particles on Nox Generation in the Middle and Upper Atmosphere during Geomagnetic Storms. *J. Atmos. Solar-Terrestrial Phys.* 71 (10), 1176–1189. doi:10.1016/j.jastp.2008.07.005

van de Kamp, M., Seppälä, A., Clilverd, M. A., Rodger, C. J., Verronen, P. T., and Whittaker, I. C. (2016). A Model Providing Long-Term Data Sets of Energetic Electron Precipitation during Geomagnetic Storms. *J. Geophys. Res. Atmos.* 121, 12520–12540. doi:10.1002/2015JD024212

Yando, K., Millan, R. M., Green, J. C., and Evans, D. S. (2011). A Monte Carlo Simulation of the Noaa Poes Medium Energy Proton and Electron Detector Instrument. Journal of Geophysical Research:. *Space Phys.* 116 (A10). doi:10.1029/2011ja016671

Zawedde, A. E., Nesse Tyssøy, H., Hibbins, R., Espy, P. J., Ødegaard, L.-K. G., Sandanger, M. I., et al. (2016). The Impact of Energetic Electron Precipitation on Mesospheric Hydroxyl during a Year of Solar Minimum. *J. Geophys. Res. Space Phys.* 121 (6), 5914–5929. doi:10.1002/2016ja022371

Conflict of Interest: The authors declare that the research was conducted in the absence of any commercial or financial relationships that could be construed as a potential conflict of interest.

Publisher's Note: All claims expressed in this article are solely those of the authors and do not necessarily represent those of their affiliated organizations, or those of the publisher, the editors and the reviewers. Any product that may be evaluated in this article, or claim that may be made by its manufacturer, is not guaranteed or endorsed by the publisher.

Copyright © 2021 Tyssøy, Partamies, Babu, Smith-Johnsen and Salice. This is an open-access article distributed under the terms of the Creative Commons Attribution License (CC BY). The use, distribution or reproduction in other forums is permitted, provided the original author(s) and the copyright owner(s) are credited and that the original publication in this journal is cited, in accordance with accepted academic practice. No use, distribution or reproduction is permitted which does not comply with these terms.

frontiers in Astronomy and Space Sciences

ORIGINAL RESEARCH
published: 04 October 2021
doi: 10.3389/fspas.2021.745927

Electron Microbursts Induced by Nonducted Chorus Waves

Lunjin Chen[1], Xiao-Jia Zhang[2], Anton Artemyev[2,3], Liheng Zheng[1], Zhiyang Xia[1], Aaron W. Breneman[4] and Richard B. Horne[5]*

[1]Department of Physics, The University of Texas at Dallas, Richardson, TX, United States, [2]Department of Earth, Planetary, and Space Sciences, University of California, Los Angeles, Los Angeles, CA, United States, [3]Space Research Institute, RAS, Moscow, Russia, [4]NASA Goddard Space Flight Center, Greenbelt, MD, United States, [5]British Antarctic Survey, Cambridge, United Kingdom

Microbursts, short-lived but intense electron precipitation observed by low-Earth-orbiting satellites, may contribute significantly to the losses of energetic electrons in the outer radiation belt. Their origin is likely due to whistler mode chorus waves, as evidenced by a strong overlap in spatial correlation of the two. Despite previous efforts on modeling bursty electron precipitation induced by chorus waves, most, if not all, rely on the assumption that chorus waves are ducted along the field line with zero wave normal angle. Such ducting is limited to cases when fine-scale plasma density irregularities are present. In contrast, chorus waves propagate in a nonducted way in plasmas with smoothly varying density, allowing wave normals to gradually refract away from the magnetic field line. In this study, the interaction of ducted and nonducted chorus waves with energetic electrons is investigated using test particle simulation. Substantial differences in electron transport are found between the two different scenarios, and resultant electron precipitation patterns are compared. Such a comparison is valuable for interpreting low Earth-orbiting satellite observations of electron flux variation in response to the interaction with magnetospheric chorus waves.

Keywords: chorus, microbursts, radiation belts, precipitation, wave-particle interaction

OPEN ACCESS

Edited by:
Jean-Francois Ripoll,
CEA DAM Île-de-France, France

Reviewed by:
Chris Colpitts,
University of Minnesota Twin Cities, United States
Peter Haesung Yoon,
University of Maryland, United States

****Correspondence:***
Lunjin Chen
lunjin.chen@gmail.com

Specialty section:
This article was submitted to Space Physics, a section of the journal Frontiers in Astronomy and Space Sciences

Received: *22 July 2021*
Accepted: *13 September 2021*
Published: *04 October 2021*

Citation:
Chen L, Zhang X-J Artemyev A, Zheng L, Xia Z, Breneman AW and Horne RB (2021) Electron Microbursts Induced by Nonducted Chorus Waves. Front. Astron. Space Sci. 8:745927. doi: 10.3389/fspas.2021.745927

1 INTRODUCTION

Microbursts are impulsive (typically lasting a few tenths of a second) precipitation of energetic electrons (~30 keV to >1 MeV) from the magnetosphere into the atmosphere. They have been detected indirectly through X-ray counts on balloons (e.g., Anderson and Milton, 1964; Parks et al., 1979; Millan, 2011), and directly through particle detectors onboard rockets (e.g., Lampton, 1967) and low-Earth-orbiting satellites (e.g., Imhof et al., 1992; Douma et al., 2017). Their existence at <100 keV energies has been known for decades, and at higher energies is known only relatively recently. It has been suggested that microburst precipitation into the upper atmosphere may play an important role in radiation belt electron losses (Lorentzen et al., 2001; O'Brien et al., 2004; Millan and Thorne, 2007; Breneman et al., 2017). Recently, bouncing packets in an apparent form of microbursts have been reported by Shumko et al. (2018), suggesting a mixture of precipitating and trapped fluxes in the observation of microbursts (Chen et al., 2020). Blake and O'Brien (2016) discovered that microbursts might not just be temporal bursts of precipitation but may sometimes be very narrow curtain structures of precipitation.

Whistler-mode chorus waves in the Earth's magnetosphere have received great attention because of their dual role in energizing electrons and precipitating them into the lower atmosphere (Horne et al., 2003; Katoh and Omura, 2007; Ni et al., 2011; Reeves et al., 2013; Thorne et al., 2013). Whistler mode waves originate around the magnetic equator, often with nearly field-aligned propagation (e.g., LeDocq et al., 1998; Lauben et al., 2002; Santolík et al., 2005; Li et al., 2009) and they are excited by energetic electrons with anisotropic velocity distribution injected from the magnetotail (e.g., Kennel and Petschek, 1966; Tsurutani and Smith, 1974). Chorus waves often exhibit unique time-frequency spectrograms consisting of discrete rising (or sometimes falling) tones (e.g., Burtis and Helliwell, 1969; Burton and Holzer, 1974; Li et al., 2011a). Numerical theory and simulation studies have demonstrated that nonlinear resonant interactions with a coherent whistler mode wave leads to electron phase trapping, resulting in wave frequency chirping when the background magnetic field is inhomogeneous (Omura and Matsumoto, 1982; Nunn et al., 1997; Katoh and Omura, 2006; Omura and Summers, 2006; Omura et al., 2009; Tao, 2014; Gao et al., 2016). Chorus waves typically occur in the frequency range 0.1–0.8 f_{ce} (f_{ce} is the equatorial electron cyclotron frequency), often separated into distinct lower and upper bands with a wave power gap near $f_{ce}/2$ (e.g., Tsurutani and Smith, 1974; Li et al., 2016a). Statistically, the duration of individual chorus element spectra varies from 0.1 to 1 s, with peak occurrence at ~0.4 s at dayside and ~0.12 s at nightside (Teng et al., 2017). The spatial scales of individual chorus waves have been unavailable until recently when wave measurements over multiple nearby satellites are present. The estimate of the transverse spatial scale, based on individual event studies, ranges from 7–100 km at L ~4.5 (Santolík and Gurnett, 2003), ~500 km at L ~ 4.7 (Shumko et al., 2018), 600–800 km at L ~ 6 (Agapitov et al., 2017), to ~3,000 km in the outer magnetosphere (L ~ 10) (Agapitov et al., 2010). The statistical analysis based on 11-years THEMIS wave measurement shows the transverse scale is mostly in the range of ~250–800 km over 2 < L < 10 (Agapitov O. et al., 2018), which is consistent with Shen et al. (2019) results from Van Allen Probes and THEMIS, where the averaged transverse size is ~315 km over 5 < L < 6. These new observational features more thoroughly characterize the temporal and spatial scales of these individual elements, allowing for better modeling of the interaction of chorus waves with energetic electrons.

Whistler-mode chorus waves in the Earth's magnetosphere are suggested to be the primary drivers of relativistic microbursts, creating them by resonant scattering into the loss cone. This association comes from numerous observational and theoretical studies that focus on spatial (L, MLT) (Oliven and Gurnett, 1968; Lam et al., 2010) and temporal similarities (e.g., Lorentzen et al., 2001; Kersten et al., 2011), as well as plausibility of scattering mechanism (to name a few, Chang and Inan, 1983; Rosenberg et al., 1990; Saito et al., 2012; Chen et al., 2020). Statistically, whistler-mode chorus waves are a potential driver of relativistic microbursts (Douma et al., 2017) and the majority of microbursts are shown to have sizes consistent with the sizes of chorus waves (Shumko et al., 2020). Previous simulation with self-consistent chorus waves (Hikishima et al., 2010) has demonstrated a one-to-one correspondence between microbursts of precipitating electrons and chorus elements. Due to finite transverse scale, individual chorus element will illuminate an area of electron precipitation in the lower atmosphere. Statistically, electron microburst size distribution ranges from 2 to 100 km (Shumko et al., 2020), which is consistent with the size estimate for individual microbursts (Blake et al., 1996; Crew et al., 2016; Shumko et al., 2018), and most occurrences are over a few tens of km, which is about 200 km in size when mapped to the magnetic equator. Such size is comparable to the size of chorus wave packets mentioned above.

The most intense chorus waves are typically confined to within 10–20° of their source near the magnetic equator (e.g., Meredith et al., 2012; Agapitov et al., 2013), while relativistic microbursts (>100 keV) are observed at much higher latitudes (Breneman et al., 2017). Therefore, chorus wave properties at higher latitudes are critically important for modeling microbursts. Depending on wave propagation, the chorus wave intensity off the equator will differ. In the presence of fine-scale density irregularities, chorus waves can be ducted along the field line, with much less attenuated wave intensity away from the equator when compared with the nonducted case in a medium with smoothly varying plasma density. A schematic picture of ducted and nonducted propagation is shown in **Figure 1**. There exists a number of studies on microburst modeling due to the ducted waves (e.g., Hikishima et al., 2010; Saito et al., 2012; Chen et al., 2020), while few focus on the case of nonducted chorus waves. Colpitts et al. (2020) recently showed the first direct observations of individual chorus elements propagating from the equatorial source to higher latitudes, and confirmed with ray tracing that the waves propagated in the nonducted mode. As nonducted chorus waves propagate away from the equator, three important physical processes occur when compared with ducted waves. First, waves experience refraction in the inhomogeneous magnetosphere with wave normal becoming increasingly oblique along the propagation path (e.g., Chen et al., 2013a; Lu et al., 2019; Colpitts et al., 2020). Therefore, oblique whistler-mode mode waves propagate not only along, but also across magnetic field lines. This means that chorus waves at a given field line at high latitude may originate from a different field line at the equator, and thus chorus wave modeling requires the knowledge of their transverse sizes at the equator. Unlike ducted chorus waves, nonducted chorus waves may induce electron precipitation over a broader range of field lines than the range at the equator. Second, chorus waves experience Landau damping as their wave normal angles increase, which will limit the wave intensity at middle latitudes, and high latitudes if accessible (e.g., Chen et al., 2013b; Watt et al., 2013; Colpitts et al., 2020). Third, multiple-harmonics resonances (whose resonance condition is $\omega - k_z v_z = n\Omega/\gamma$ with n being an integer) become effective, when waves becomes oblique and field polarization becomes elliptical (instead of circular), while only the principal resonance ($n = -1$) is effective for ducted

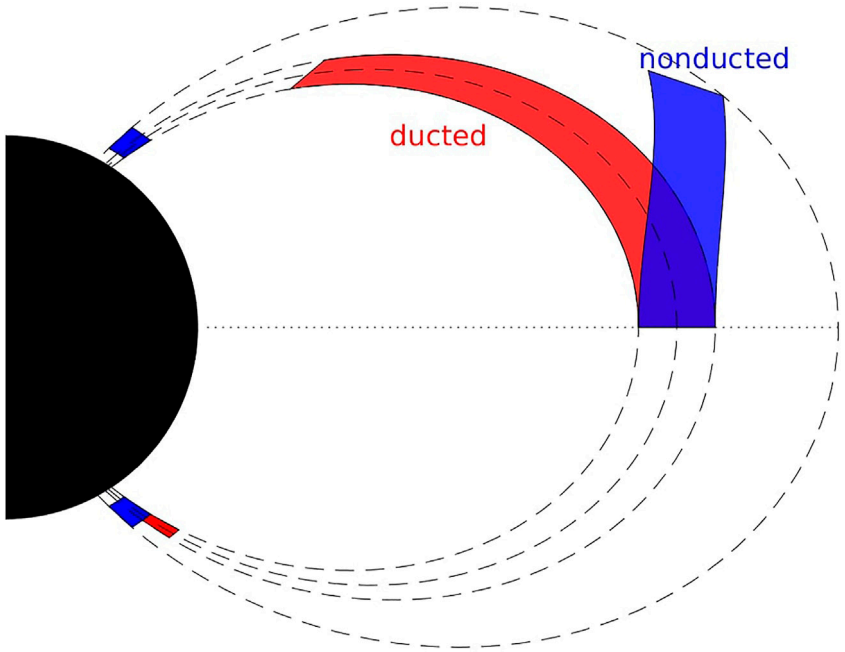


FIGURE 1 | Schematic illumination regions of electron precipitation due to interaction with ducted (shaded by red color) and nonducted (shaded by blue color) chorus waves that propagate northward. Dashed lines denotes the dipole magnetic field lines. The schematic diagram is not scaled. Ducted chorus waves here only induce electron precipitation in the southern hemisphere while nonducted chorus waves induce electron precipitation in both hemispheres.

waves. Here ω and k_z are wave angular frequency and parallel component of the wavenumber vector respectively, v_z, Ω and γ are electron parallel velocity, non-relativistic gyrofrequency and Lorentz factor respectively. Thus for northward propagation (as shown in **Figure 1**), nonducted chorus waves could induce electron precipitation in the northern hemisphere (through the resonances with, e.g., $n = 0$ and $+1$) and the southern hemisphere (through the resonance with $n = -1$) while ducted chorus waves could only induce precipitation in the southern hemisphere (through the resonance with $n = -1$). The three physics processes are important for modeling relativistic microbursts due to nonducted chorus waves with oblique wave normal angles (e.g., Artemyev et al., 2016).

In this study, a nonducted chorus wave model is developed as an extension of the ducted chorus wave model (Chen et al., 2020). We will look into the characteristics of electron precipitation due to a nonducted chorus element seen by virtual LEO satellites, which will be compared with that due to a ducted chorus element. In addition to temporal structures, spatial structures of microburst due to the nonducted chorus element will be revealed.

2 TEST PARTICLE MODEL

The dynamics of electrons in a dipole magnetic field with prescribed chorus wave fields is modeled by the following test particle equations along a dipole field line with a given L value (Chen et al., 2020):

$$\frac{dP_z}{dt} = -\frac{\mu}{\gamma}\frac{dB}{dz} + \Sigma_j\left[qe_{jz} - qv_\perp\left(b_{jx}\sin\theta_g - b_{jy}\cos\theta_g\right)\right] \quad (1)$$

$$\frac{dP_\perp}{dt} = \frac{\mu}{\gamma}\frac{P_z}{P_\perp}\frac{dB}{dz} + \Sigma_j\left[qv_z\left(b_{jx}\sin\theta_g - b_{jy}\cos\theta_g\right) + q\left(e_{jx}\cos\theta_g + e_{jy}\sin\theta_g\right)\right] \quad (2)$$

$$\frac{dz}{dt} = v_z \quad (3)$$

$$\frac{d\theta_g}{dt} = -\Omega/\gamma + \Sigma_j\frac{q}{P_\perp}\left[\left(e_{jy}\cos\theta_g - e_{jx}\sin\theta_g\right) + v_z\left(b_{jx}\cos\theta_g + b_{jy}\sin\theta_g\right)\right] \quad (4)$$

where B is the background dipole magnetic field strength, nonrelativistic electron gyrofrequency $\Omega = \frac{qB}{m}$, magnetic moment $\mu = P_\perp^2/(2\,mB)$, and q, m, v, P, and γ are electron charge ($q < 0$ for electrons), static mass, velocity, momentum, and Lorentz factor, respectively. The first terms on the right side of **Eqs. 1**, **2** represent adiabatic changes due to the background magnetic field, which lead to bounce motion. z, denoting the location of the guiding center along the field line, represents dipole field line arc length with $z = 0$ defined at the equator. The subscripts z and $\perp$ denote directions parallel and perpendicular to the background magnetic field, respectively, while the subscripts x and y denote the radially outward direction and azimuthal direction toward the east, respectively. The set of $\hat{\mathbf{x}}$, $\hat{\mathbf{y}}$ and $\hat{\mathbf{z}}$ axes constitute the field-aligned coordinate system, a local right-handed Cartesian coordinate system. θ_g is the gyrophase denoting the direction of $\mathbf{v}_\perp$ with the respect to the x axis. The subscript j

denotes the jth chorus element with wave electric field $\mathbf{e}_j$ and magnetic field $\mathbf{b}_j$ at the electron's actual location $\mathbf{r}$. $\mathbf{e}_j$, and $\mathbf{b}_j$ can be represented as $\Re(\tilde{\mathbf{e}}_j e^{i\phi_j(\mathbf{r},t)})$ and $\Re(\tilde{\mathbf{b}}_j e^{i\phi_j(\mathbf{r},t)})$, respectively, where $\Re$ denotes the real part, and $\tilde{\mathbf{e}}_j$ and $\tilde{\mathbf{b}}_j$ are complex amplitudes. These six-component complex amplitudes, which are linearly related, will be scaled by the magnetic field wave amplitude A_w, and the ratio of any two of the six is determined by the linear whistler mode dispersion relation (e.g., Tao and Bortnik, 2010).

Eqs. 1–4 are integrated over a time scale of several electron bounce periods (on the order of 1 s), which is sufficient to describe the interaction between chorus waves and electron gyromotion and to model electron precipitation induced by the chorus waves. Therefore it is safe to neglect drift motion of electrons across magnetic field lines. That is, electrons are trapped by the same field line (with constant L and magnetic local time). Hereafter, we investigate the effect of a single chorus element, either ducted or nonducted, on electron dynamics, and therefore the subscript j and the summation over j will be dropped. For the equations above, gyrophase-averaging on the wave force is not performed, and nonlinear wave particle interaction is included (as the wave phase ϕ depends on z). When test particles reach the atmospheric loss boundary, which is set to an altitude of 100 km, they are considered as lost (precipitated into the upper atmosphere) and no longer traced afterward.

To solve the test particle **Eqs. 1–4** and examine the effect of chorus waves, either ducted or nonducted, on the dynamics of particles at a given field line, it is necessary to find a solution of chorus wave field along that field line (that is, for a given L value in the case of dipole magnetic field). The solution should describe wave phase ϕ and wave amplitude as a function of z and t.

The derivatives of $\phi(\mathbf{r}, t)$ provide definition of wave angular frequency ω and wave normal vector $\mathbf{k}$ through:

$$\frac{\partial \phi}{\partial t} = -\omega(\mathbf{r}, t) \tag{5}$$

$$\frac{\partial \phi}{\partial \mathbf{r}} = \mathbf{k}(\mathbf{r}, t) \tag{6}$$

Given $\omega(\mathbf{r}, t)$ and $\mathbf{k}(\mathbf{r}, t)$, the two equations above can be solved for $\phi(\mathbf{r}, t)$.

$\phi(\mathbf{r}, t)$ can be conveniently rewritten in terms of the guiding center location $\mathbf{r_c}$ as

$$\phi(\mathbf{r}, t) = \phi(\mathbf{r_c}, t) + \mathbf{k}_\perp \cdot \mathbf{r}_{\mathbf{g}\perp} \tag{7}$$

where $\phi(\mathbf{r_c}, t)$ is the wave phase at the guiding center $\mathbf{r_c}$ along the field line and the second term on the right denotes the wave phase variation experienced due to the test particle's gyromotion. Oscillatory gyro-radius vector $\mathbf{r}_{\mathbf{g}\perp}$, defined as $\mathbf{r}-\mathbf{r_c}$, can be written as $(-\sin\theta_g\hat{\mathbf{x}} + \cos\theta_g\hat{\mathbf{y}})v_\perp/\Omega$. The term $\mathbf{k}_\perp\cdot\mathbf{r}_{\mathbf{g}\perp}$ here is known as the finite Larmor radius effect, which gives rise to harmonic resonances other than $n = -1$. When $k_\perp = 0$ (e.g., for ducted waves), this term vanishes, so do multiple harmonic resonances except $n = -1$.

Initially, test particles are launched at a given L with N_g (= 120) different gyrophases of equal spacing $\Delta\theta_g = 2\pi/N_g$, N_b(= 120) bounce phases of equal spacing $\Delta\phi_b = 2\pi/N_b$, N_E (=51) energies of equal logarithmic spacing $\Delta \ln E$ from 50 keV to 1 MeV, and $N_{\alpha_{eq}}$ (= 66) equatorial pitch angles from the equatorial loss cone α_{LC}, which for example is 3.3° at $L = 5.5$, to ~ 10° with a non-equal spacing $\Delta\alpha_{eq}$ (See further explanation below). In total, 4.8×10^7 electrons are traced. For minimizing the discrete nature of the test particle simulation, and thus modeling continuously varying electron flux, each test particle represents a group of ΔN particles located inside the magnetic flux tube of interest and with a range of $\Delta\theta_g$, $\Delta\phi_b$, $\Delta\alpha_{eq}$, and ΔE. Given the initial flux distribution F_0 (α_{eq}, E), $\Delta N = F_0\Delta t\Delta A\Delta E\Delta\Omega'$, where $\Delta\Omega' = \sin\alpha\Delta\alpha\Delta\theta_g$ (α is the local pitch angle), $\Delta A = \Delta A_\Phi/\cos\alpha$, $\Delta t = \Delta\phi_b/\omega_b$ (ω_b is electron bounce angular frequency), and $\Delta E = E\Delta\ln E$. The cross section area of the magnetic flux tube (a constant magnetic flux $\Delta\Phi_m$) $\Delta A_\Phi = \Delta\Phi_m/B$. Virtual LEO satellites are placed at the southern and northern footpoints of the field line L at a given altitude of 650 km. Electron fluxes at these footpoints as a function of pitch angle, energy and time t are reconstructed from the test particle results of those 4.8×10^7 electrons. To better model the electron flux variations at the LEO satellite locations as a function of pitch angles, a non-equal spacing $\Delta\alpha_{eq}$ is used so that sufficient number of α_{eq} grids covers both the following two α_{eq} ranges, one from the equatorial loss cone α_{LC} to the value of $\alpha_{eq,mirror}$ corresponding to the mirroring location at the LEO altitude and the other one from $\alpha_{eq,mirror}$ to ~ 10°. Following Chen et al. (2020), we adopt an anisotropic initial distribution as $F_0 = F_{0E}(E)\sin^2\alpha_{eq}$, where the energy dependent $F_{0E}(E)$ is obtained from the Van Allen Probes flux observation at pitch angle 90° shown in **Figure 2** of Breneman et al. (2017). Such simplified adoption of the electron anisotropy may affect the magnitude of electron fluxes, but is not critical for addressing general characteristics of electron flux variations.

3 DUCTED CHORUS WAVES

Ducted chorus waves are guided along a field line, say L_c, by keeping wavevector parallel or antiparallel to the field line. During ducted propagation, chorus waves follow:

$$\mathbf{k}_\perp = 0 \tag{8}$$

$$D(k_z, \omega, z) = 0 \tag{9}$$

$$\frac{\partial\omega}{\partial t} + v_{gz}\frac{\partial\omega}{\partial z} = 0 \tag{10}$$

$$\frac{\partial A_w}{\partial t} + v_{gz}\frac{\partial A_w}{\partial z} = 0 \tag{11}$$

where the first equation describes the constraint of parallel propagation, the second equation describes the local dispersion relation D, which adopts one for whistler mode in the cold plasma at the location z, and the third and fourth equations state the conservation of wave frequency and wave amplitude along the propagation path. The parallel component of group velocity $v_{gz} = -(\partial D/\partial k_z)/(\partial D/\partial\omega)$. These equations, assuming parallel propagation, have been widely used for chorus wave modeling (e.g., Furuya et al., 2008; Tao et al., 2012; Chen et al., 2020). For such "ideally" ducted propagation ($\mathbf{k}_\perp = 0$), it is implicitly assumed

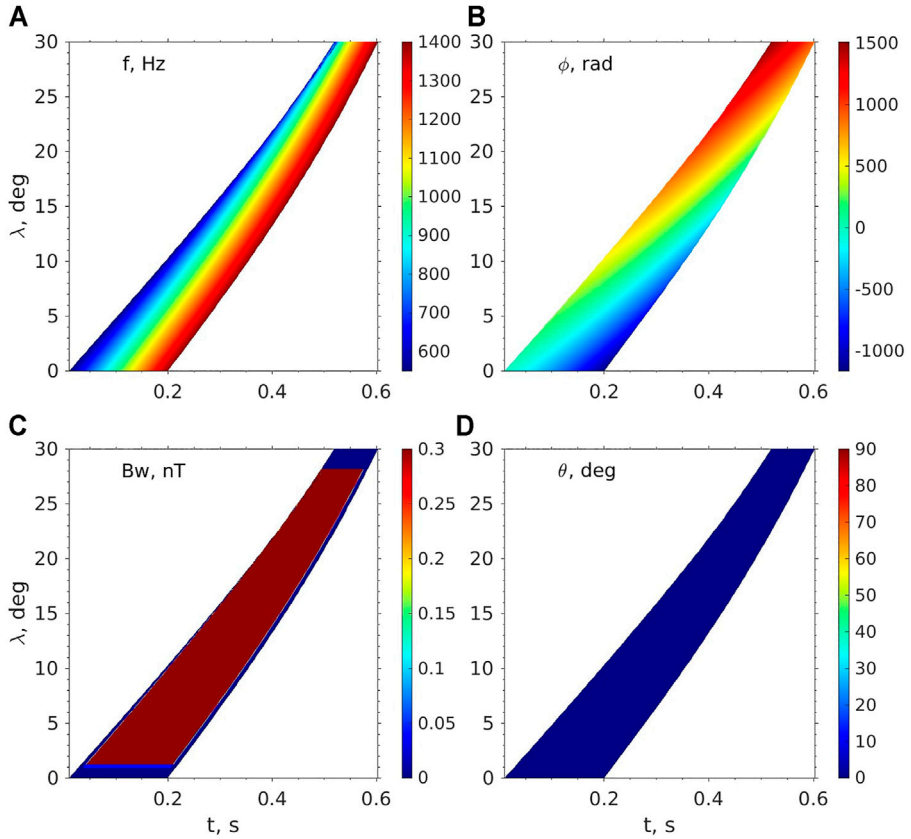


FIGURE 2 | Solution of a ducted chorus element along a dipole magnetic field at L = 5.5. **(A)** wave frequency f **(B)** wave phase ϕ, **(C)** wave magnetic amplitude B_w, and **(D)** wave normal angle θ as a function of time t and magnetic latitude λ.

that there exists a density duct with density gradients that perfectly overcome wave refraction due to magnetic field inhomogeneity. This implicit assumption places a constraint on the density gradients of the duct, whose solution, fortunately, is not required for modeling the ideally ducted propagation. For a more realistic ducted propagation (a non-ideal case, e.g., Liu et al., 2021), wave normal direction would experience oscillation near the parallel direction and so do ducted ray paths.

Let $\omega_0(t)$ be the prescribed chorus wave frequency-time profile in the equatorial source region. Then the one-sided boundary condition at the equator can be provided as

$$\omega(z = 0, t) = \omega_0(t). \tag{12}$$

Equations 10–12 can be solved for $\omega(z, t)$ using the method of characteristics (e.g., Furuya et al., 2008; Tao et al., 2012). With $\omega(z, t)$ solved, **Eq. 9** yields the solution of k_z (z, t). Then the solution of wave phase $\phi(z, t)$ can be numerically integrated by the following two constituent equations:

$$\frac{\partial \phi}{\partial t} = -\omega(z, t) \tag{13}$$

$$\frac{\partial \phi}{\partial z} = k_z(z, t) \tag{14}$$

For the calculation of the dispersion relation (D in **Eq. 9**), background plasma density is required. We adopt the modified diffusive equilibrium density model (Bortnik et al., 2011). The same initial condition $\omega_0(t)$ as Chen et al. (2020) is used, with the wave frequency f rising from 550 to 1,400 Hz over an interval of 0.2 s. The solution of wave frequency and wave phase is shown in **Figures 3A,B**. At λ = 0, wave frequency chirps over a duration of 0.2 s, while as λ increases, the wave duration becomes shorter due to frequency dispersion. In **Figure 3B**, wave phase ϕ increases with λ and decreases with t, as shown by **Eqs. 13**, **14**. The wave normal angle θ is zero, as expected (**Figure 3D**).

To represent a chorus element of a flexible amplitude, the initial amplitude profile is implemented as $A_{w0}(f, \lambda) = A_{w,max} G(f; f_1, f_2, \delta f_1, \delta f_2)$, where λ is magnetic latitude and $A_{w,max}$ is the maximum wave amplitude. The function G has a Gaussian-like profile with a flat-top and four control parameters (x_1, x_2, δx_1, δx_2). Specifically, G (x; x_1, x_2, δx_1, δx_2) is defined as $= \exp\left(-(x - x_1)^2/\delta x_1^2\right)$ for $x < x_1$, $= \exp(-(x - x_2)^2/\delta x_2^2)$ for $x > x_2$, with values equal to unity for $x_1 \le x \le x_2$. Further explanation on the G function can be found in the **Supplementary Material**. We set $A_{w,max}$ = 300 pT (corresponds to intense chorus waves in the radiation belts (e.g., Agapitov O. V. et al., 2018; Zhang et al., 2018;

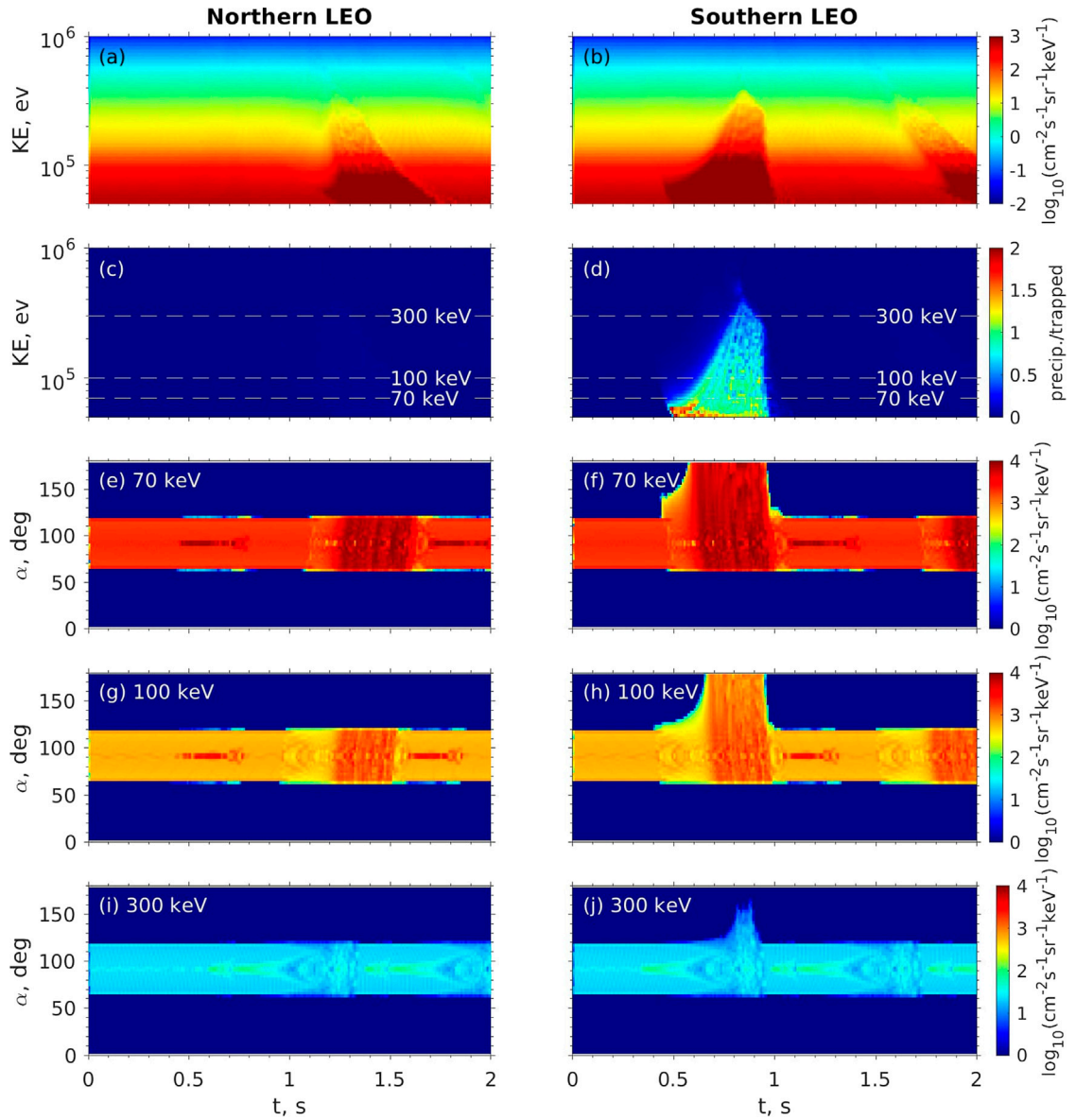


FIGURE 3 | Modeled electron fluxes at virtual northern **(left column)** and southern **(right column)** LEO satellites due to the presence of the ducted wave shown in **Figure 3**. **(A, B)** omni-directional differential flux over the energy range from 50 keV to 1 MeV. **(C, D)** the ratio of precipitating and trapped electron fluxes over the energy range from 50 keV to 1 MeV. Local pitch angle distribution of electron fluxes at three selected electron kinetic energies **(E, F)** 70 keV, **(G, H)** 100 keV and **(I, J)** 300 keV. The three energies are also marked by the horizontal white dashed lines in panels c-d.

Tyler et al., 2019)), f_1 = 600 Hz, f_2 = 1,350 Hz, δf_1 = 10 Hz, and δf_2 = 10 Hz. With A_w0 given, **Eq. 11** is solved for A_w. To represent latitudinal characteristics for field-aligned propagating chorus waves, an additional factor of a latitudinal profile of the wave amplitude is added as $G(\lambda; \lambda_1, \lambda_2, \delta\lambda_1, \delta\lambda_2)$, with $\lambda_1 = 1^\circ$, $\lambda_2 = 28^\circ$, $\delta\lambda_1 = 0.1^\circ$, and $\delta\lambda_2 = 0.1^\circ$. Using the prescribed amplitude profile and the obtained wave phases, complex amplitudes of the six electromagnetic components can be obtained and then test particle equations above can be solved.

Figure 3C shows the solution for the ducted chorus wave amplitude. The wave amplitude B_w is nearly constant in the z–t regime of the chorus wave field, expect the lower and higher latitude boundaries due to the introduced latitude-dependence term $G(\lambda; \lambda_1, \lambda_2, \delta\lambda_1, \delta\lambda_2)$ and the lower and higher time boundaries due to the frequency-dependence term $G(f; f_1, f_2, \delta f_1, \delta f_2)$. The introduction of the latitude-dependence term mimics the chorus growth near the equator and ensures the test particles are launched before the chorus

wave field perturbation occurs, and the test particles, if not reaching the atmospheric loss boundary, are terminated after the chorus wave field perturbation ends. By doing so, the effect of chorus wave field perturbation on electron flux can be evaluated.

Figure 2 shows modeled electron distribution at two virtual LEO satellites, which are placed at northern and southern foot points of L = 5.5 at 500 km altitude. The electrons accessing these locations are reorganized to obtain the full velocity distribution as a function of t at the two locations, respectively. The distribution is then used to calculate derived quantities, such as omni-directional differential flux, precipitating flux (the averaged flux over the solid angle within the loss cone), and trapped flux (the averaged flux over the solid angle beyond the loss cone). **Figures 2A,B** shows the omni-directional differential flux at the two, northern and southern, LEO satellite locations. One can see flux enhancement with energy from 50 up to 400 keV. The flux enhancement first appears 0.5–1 s at the southern location (**Figure 2B**), then over 1.2–1.7 s at the northern location (**Figure 2A**), and then again near 1.7 s at the southern location (**Figure 2B**). Such a series have been identified previously (e.g., Chen et al., 2020) as bouncing microburst packet. The initial flux enhancement is caused by cyclotron resonance of southward moving electrons with a northward propagating chorus element, which leads to a net transport towards smaller pitch angle. To resonate with the northward propagating chorus wave, electrons must be counter-moving to the south in order to satisfy the Doppler-shifted resonance condition with $n = -1$. Such initial flux enhancement occurs for both precipitating flux and trapped flux near 0.5–1 s in the southern hemisphere (**Figure 2D**). The subsequent flux enhancements, which corresponds to enhanced trapped flux only (**Figures 2C,D**), is caused by bounce motions of the enhanced trapped flux in the initial flux enhancement (See more detailed explanation on electron bouncing packets in Chen et al. (2020)). The ratio of precipitating to trapped flux is only significant in the southern location during the initial enhancement. The ratio decreases for higher energy, from as high as 2 at 50 keV, near 1 at 100 keV, and to a fraction near 300 keV (**Figure 2D**). The ratio exceeding unity at the low energy demonstrates nondiffusive transport in pitch angle, as a signature of nonlinear wave-particle interaction (Chen et al., 2020). **Figures 2E–J** shows the pitch angle distribution of electron unidirectional different flux at 70 keV, 100 and 300 keV. One can see full loss cone distribution (at electron energy, e.g., 70 keV in **Figure 2F** and 100 keV in 3 h) when the ratio of precipitating to trapped flux is 1 and above while partial loss cone corresponds to the case with the ratio being a fraction (at electron energy, e.g., 300 keV in **Figure 2J**). As expected, the ratio is zero for a completely empty loss cone. The simultaneous enhancement of trapped flux and precipitating flux (**Figures 2F,H,J**) is caused by the induced transport from the larger α_{eq} into the loss cone. Although short-lived, the chorus element can produce the permanent change to trapped electron distribution via bouncing packets, in addition to impulsive precipitation.

4 NONDUCTED CHORUS WAVES

An extension is made from the ducted chorus wave case to the case allowing nonducted propagation of chorus waves across magnetic field lines. Nonducted propagation is modeled by solving the following ray tracing equations (e.g., Horne, 1989):

$$\frac{d\mathbf{r}}{dt} = -\frac{\partial D}{\partial \mathbf{k}} \Big/ \frac{\partial D}{\partial \omega} \tag{15}$$

$$\frac{d\mathbf{k}}{dt} = \frac{\partial D}{\partial \mathbf{r}} \Big/ \frac{\partial D}{\partial \omega} \tag{16}$$

$$\frac{d\omega}{dt} = 0 \tag{17}$$

$$\frac{dA_w}{dt} = \gamma_L A_w \tag{18}$$

where D ($\mathbf{k}$, ω, $\mathbf{r}$) = 0 is the local dispersion relation, the right-handed side of the first equation is the general definition of the wave group velocity $\mathbf{v_g}$, and the fourth equation for wave amplitude A_w takes into account wave attenuation as a result of Landau damping due to the suprathermal electron population during oblique propagation. The suprathermal electron model used is based on THEMIS statistical observations of electron distribution over the energy range from ~0.1 to 26 keV (see detail in **Section 3** of Chen et al., 2013a). The ray tracing HOTRAY code (Horne, 1989) is used to calculate the nonducted propagation paths of whistler mode waves in a smoothly-varying plasma, and to evaluate the path integrated gain, which represents the relative change of wave amplitude. The ray tracing method assumes that the spatial scales of the medium, notably the plasma density and magnetic field, are large compared to the wavelength, and that their spatial gradients remain continuous. Like **Section 3**, the diffusive equilibrium density model (Bortnik et al., 2011) is used.

Say a ray with frequency ω_0 is launched at a source location $\mathbf{r}_0$ and initial wave vector $\mathbf{k}_0$ at time t_0. The ray is labeled by the set of initial parameters (ω_0, t_0, $\mathbf{r}_0$, $\mathbf{k}_0$), subject to two constraints. First, the launch time t_0 depends on ω_0 according to the prescribed chorus frequency-time profile at the source location $\mathbf{r}_0$. Second, the local dispersion relation is satisfied initially, D ($\mathbf{k}_0$, ω_0, $\mathbf{r}_0$) = 0. The ray tracing equations are solved numerically; the solution can be obtained: $\omega = \omega_0$, and symbolically $\mathbf{r} = \mathbf{r}$ (t; ω_0, t_0, $\mathbf{r}_0$, $\mathbf{k}_0$), $\mathbf{k} = \mathbf{k}$ (t; ω_0, t_0, $\mathbf{r}_0$, $\mathbf{k}_0$), and $A_w = A_w$ (t; ω_0, t_0, $\mathbf{r}_0$, $\mathbf{k}_0$), subject to the constraint D ($\mathbf{k}$, ω, $\mathbf{r}$) = 0.

It should be noted that the solution of $\mathbf{r} = \mathbf{r}$ (t; ω_0, t_0, $\mathbf{r}_0$, $\mathbf{k}_0$) provides characteristic curves (ray paths) for the following two equations for ω and A_w

$$\frac{\partial \omega}{\partial t} + \mathbf{v_g} \cdot \frac{\partial \omega}{\partial \mathbf{r}} = 0 \tag{19}$$

$$\frac{\partial A_w}{\partial t} + \mathbf{v_g} \cdot \frac{\partial A_w}{\partial \mathbf{r}} = \gamma_L A_w. \tag{20}$$

The two equations are equivalent to **Eqs. 17**, **18**, with the directive derivative $d/dt = \frac{\partial}{\partial t} + \mathbf{v_g} \cdot \frac{\partial}{\partial \mathbf{r}}$. With the aid of **Eqs. 5**, **6**, ϕ along the ray path $\mathbf{r} = \mathbf{r}$ (t; ω_0, t_0, $\mathbf{r}_0$, $\mathbf{k}_0$) can be obtained as

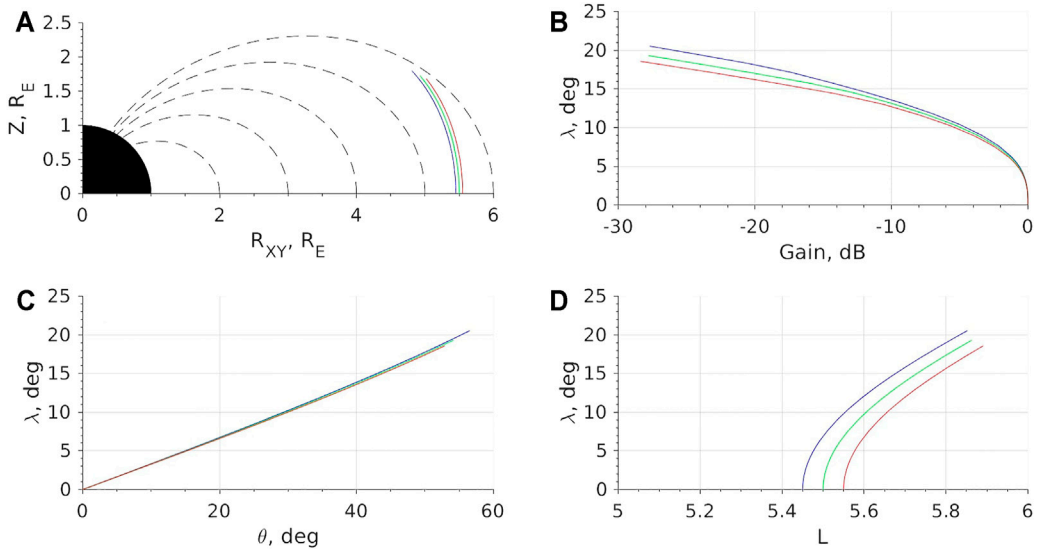


FIGURE 4 | Examples of ray tracing simulation for rays with 700 Hz. **(A)** ray paths of rays launched at the equator with initial L = 4.45 (blue), 5.5 (green) and 5.55 (red). **(B)** wave gain, **(C)** wave normal angle and **(D)** L-shell as a function of magnetic latitude λ.

$$\phi(t;\omega_0,t_0,\mathbf{r}_0,\mathbf{k}_0)=\phi_0+\int_{\text{raypath}}\mathbf{k}\cdot d\mathbf{r}-\omega(t-t_0), \tag{21}$$

where $\phi_0=\phi_0(t_0,\mathbf{r}_0)$ is the initial phase at $\mathbf{r}_0$ and at $t=t_0$. The solution of A_w can be written in an alternative fashion as

$$A_w(t;\omega_0,t_0,\mathbf{r}_0,\mathbf{k}_0)=A_{w0}\exp\left(\int_{\text{raypath}}\gamma_L dt\right), \tag{22}$$

where $A_{w0}=A_{w0}(t_0,\mathbf{r}_0)$ is the initial amplitude at $\mathbf{r}_0$ and at $t=t_0$.

For 3D space in $\mathbf{r}$, the initial conditions A_{w0} and ϕ_0 over a 2D spatial area (spanned by $\mathbf{r}_0$) of the wave source are needed as input. For a simpler case of 2D propagation on the meridian plane at a fixed local time, the initial conditions over a 1D curve (spanned by $\mathbf{r}_0$) of the wave source are needed. Hereafter we will limit the nonducted propagation on a meridian plane. Let us consider a chorus element at the equator at magnetic local time (MLT) of 6 h with wave amplitude peak at a L-shell value of L_c = 5.5 and a Gaussian width of δL = 0.05 R_E (corresponding to 320 km). The chosen location is consistent with the location of the microburst occurrence rate peak during geomagnetic active conditions (Douma et al., 2017) and the choice of the δL value is consistent with the mean spatial width of chorus wave elements (Shen et al., 2019). The source wave amplitude $A_{w0}(f,L_0)=A_{w,max}\times G(f;f_1,f_2,\delta f_1,\delta f_2)\times G(L_0;L_c,L_c,\delta L,\delta L)$. Without the loss of generality, the initial wave phase ϕ_0 is set to 0. To ensure sufficient chorus rays, we use 51 launch locations with L_0 from 5.25 to 5.75 in the spacing of 0.01 and 81 frequencies f from 600 to 1,400 Hz with spacing of 10 Hz. In total, 4,131 ray paths (characteristic curves) are traced. ϕ, A_w, and $\mathbf{k}$ along those paths are interpolated to reconstruct the corresponding 3D distributions in time t and position $\mathbf{r}$ (on the meridian plane), which are then fed into the test particle **Eqs. 1–4**.

Figure 4 shows examples of three rays launched at the equator on different field lines. As the rays propagate away from the equator, wave normals refract outward due to the dipole magnetic field (**Figure 4C**), i.e., $\mathbf{k}_\perp$ is pointed outward during wave propagation. Whether whistler-mode ray paths bend outward or inward depends on perpendicular wave group velocity ($\mathbf{v}_{g\perp}$) direction (e.g., Smith et al., 1960), which depends on wave frequency and wave normal angle. For $\omega>\Omega/2$, $\mathbf{v}_{g\perp}$ is always anti-parallel to $\mathbf{k}_\perp$ and thus is pointed inward. For $\omega<\Omega/2$, when the wave normal angle is smaller (larger) than the Gendrin angle, the $\mathbf{v}_{g\perp}$ direction is parallel (anti-parallel) with $\mathbf{k}_\perp$, which corresponds to outward (inward) bending of ray paths. Therefore, ray paths of the lower band chorus waves with initially parallel wave normal at the equator generally bend outward and toward larger L (as shown in **Figures 4A–D**). As wave normal increases, so does Landau damping. At the latitude of 20°, wave normal angles reach above 50° and path-integrated gain reaches below −20 dB. The same features can be also seen in the solution of nonducted chorus wave amplitude and wave normal angles as shown in **Figure 5**. In addition, chorus wave intensity is maximized at L = 5.5 near the equator, as chorus wave propagates outward, wave intensity peak is weakened and shifts toward higher latitude with more oblique wave normal angles. During wave propagation away from the equator, the nonducted chorus wave can extend to a higher L-shell, beyond the transverse range at the equator, and consequently is capable of interacting with electrons over a larger L range than the ducted chorus wave. However, due to Landau damping, the nonducted chorus wave intensity is mostly confined over $\lambda<20°$ and $L<5.8$. It is also noted that the chorus wave above $\lambda\sim10°$ is available only beyond L = 5.5 because of the outward propagation of wave energy and the limited chorus transverse size, while the chorus wave is

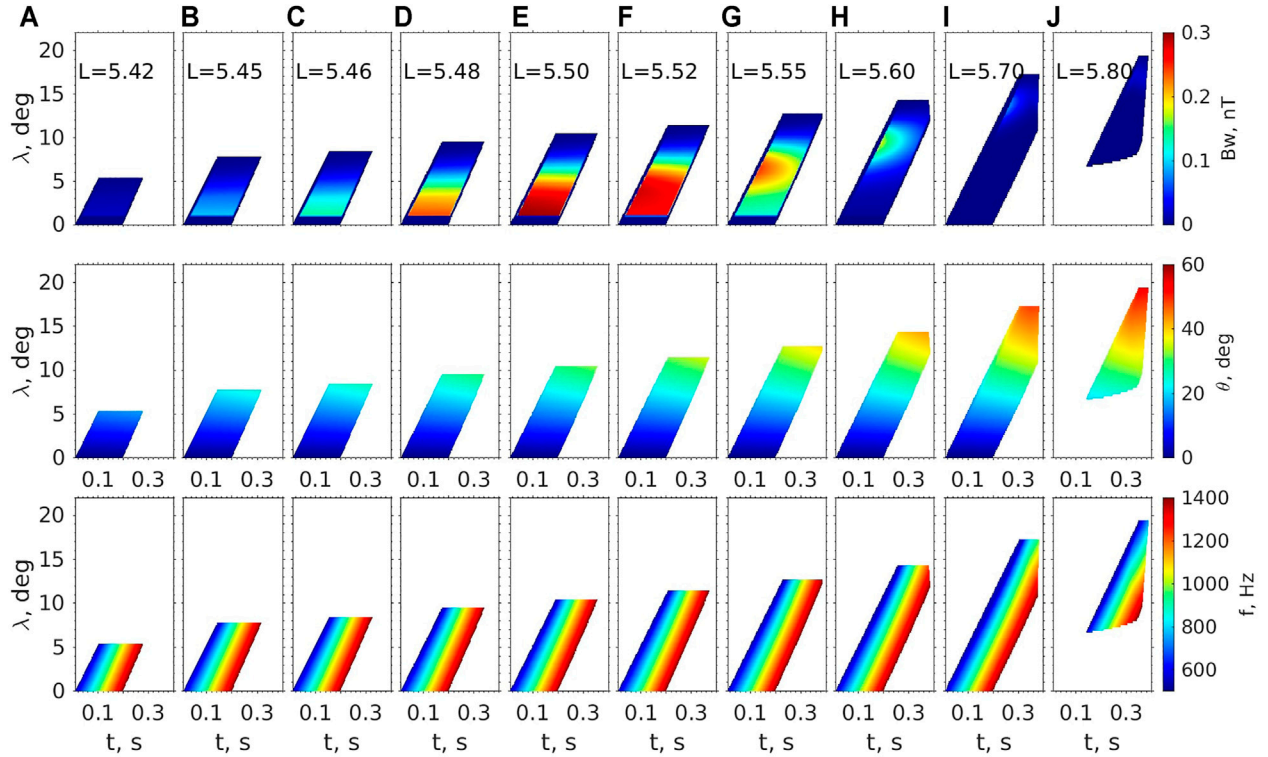


FIGURE 5 | Solution of nonducted chorus elements, wave amplitude B_w **(top panels)**, wave normal angles **(middle panels)**, and wave frequency **(bottom panels)** as a function of t and λ, along selected field lines with L values from 5.42 to 5.80 **(A–J)**.

confined near the equator near $L \sim 5.5$. Bottom panels of **Figure 5** show the corresponding solution for wave frequency. One can see frequency chirping evolve as chorus waves propagate away from the equator.

Figure 6 shows the response of electron omni-directional fluxes at the two LEO satellite locations along different L values (represented by different columns). Due to the tendency of outward propagation of nonducted chorus waves, the responses are asymmetric with respect to the central location L_c of the equatorial chorus wave source, with more pronounced flux enhancement over a broader energy range outside L_c than inside L_c. The chorus waves are capable of inducing electron responses at the southern footpoints over a L range from 5.45 to 5.7, a factor of 5 greater than the transverse size δL (= 0.05) of the equatorial chorus waves. The perturbation of the omni-directional flux is hardly visible in the northern footpoints. The corresponding ratios of precipitating to trapped electron fluxes are shown in **Figure 7**. The ratios at the southern footpoints can be on the order of 1 over the energy range of 50–70 keV over the L range from 5.45 to 5.6. For higher energy range, the ratios becomes smaller and the corresponding L range becomes narrower. Such enhancement in electron precipitation at the southern hemisphere is induced by the principal cyclotron resonance ($n = -1$) with the chorus waves. At the northern footpoints, the enhanced electron precipitating-to-trapped flux ratios are on the order of 0.01–0.1 at the outer L-shell with $L > 5.5$, which was caused by anomalous cyclotron resonance with $n = +1$ (requiring northward moving electrons). The anomalous cyclotron resonance requires significant wave intensity at oblique angles, and therefore favors the outer L shells. These ratios are lower than those associated with the $n = -1$ resonance because the intensity of the oblique waves is less than that of the equatorial waves. **Figure 8** shows pitch angle distribution of electron fluxes at a selected energy 70 keV. One can see partial and full loss cone (over the local pitch angle range from 118° to 180°) at the southern footpoints over the L range where chorus wave intensity remains strong, while at the northern footpoints, the loss cone in the pitch angle range below 62° is only slightly filled. The comparison of those pitch angle distributions is consistent with the precipitating-to-trapped flux ratio values shown in **Figure 7**.

The following four points are worth-noting when making comparison between ducted chorus waves and nonducted chorus waves. First, ducted chorus waves are capable of reaching higher latitude than nonducted chorus waves, and therefore are capable of inducing the electron precipitation at higher energy. Second, nonducted chorus waves can spread wave energy toward outer L-shell and becomes more oblique, Therefore, the electron precipitation, although at lower energy, will be induced over a spatial region a factor of

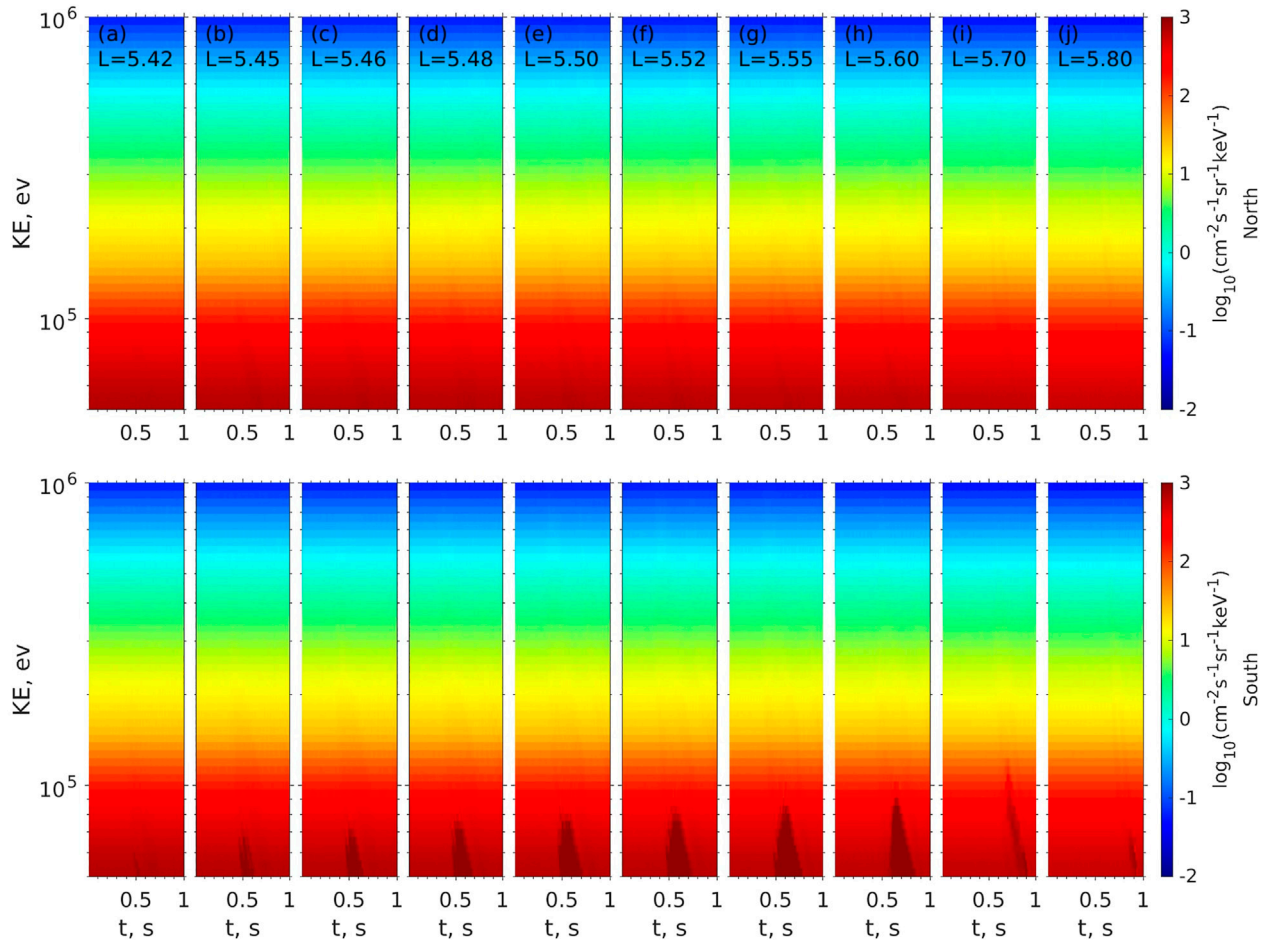


FIGURE 6 | Modeled electron fluxes at virtual northern **(top panels)** and southern **(bottom panels)** LEO satellites due to the presence of the nonducted wave shown in **Figure 5** at selected field lines with L values from 5.42 to 5.80 **(A–J)**.

several larger than the size of source chorus waves at the equator. Third, because of obliqueness, nonducted chorus waves introduce additional anomalous cyclotron resonance, as well as many higher order resonances that are generally less effective in electron scattering for moderately oblique waves (e.g., Shprits and Ni, 2009). The degree of outward propagation and wave obliqueness depends on the strength of Landau damping, which increases with L and Kp index and which is greater at nightside than dayside (Chen et al., 2013b). For a strong Landau damping case (such as nightside), one may expect more confinement of chorus waves at the equator, narrower L-shell spreading, less anomalous cyclotron resonance effect, and electron precipitation at lower energy. On the other hand, for a weak Landau damping case (such as morning side), one may expect more wave energy at higher latitudes, and spreaded wave intensity over a broader L range, electron precipitation at higher energy, and more significant anomalous cyclotron resonance effect. One can see the effects of the reduced Landau damping by comparing **Figure 7** with **Supplementary Figure S2** of **Supplementary Material**, where the Landau damping rate γ_L is halved. Fourth, for a given energy, nonducted chorus waves tend to introduce a narrower microburst duration compared with the ducted waves. That is because nonducted chorus waves at any given frequency only retain wave energy at a given L over a latitudinal range much narrower than the ducted waves along the same field. This reason also explains the difference in the energy dispersion of electron microbursts due to the ducted (**Figure 2B**) and nonducted chorus waves (**Figure 6**).

5 CONCLUSION AND DISCUSSION

We model electron flux response (including trapped and precipitating electrons) due to ducted and nonducted chorus elements and make comparison of the induced electron precipitation between the two cases. Our principal conclusions are summarized as follows:

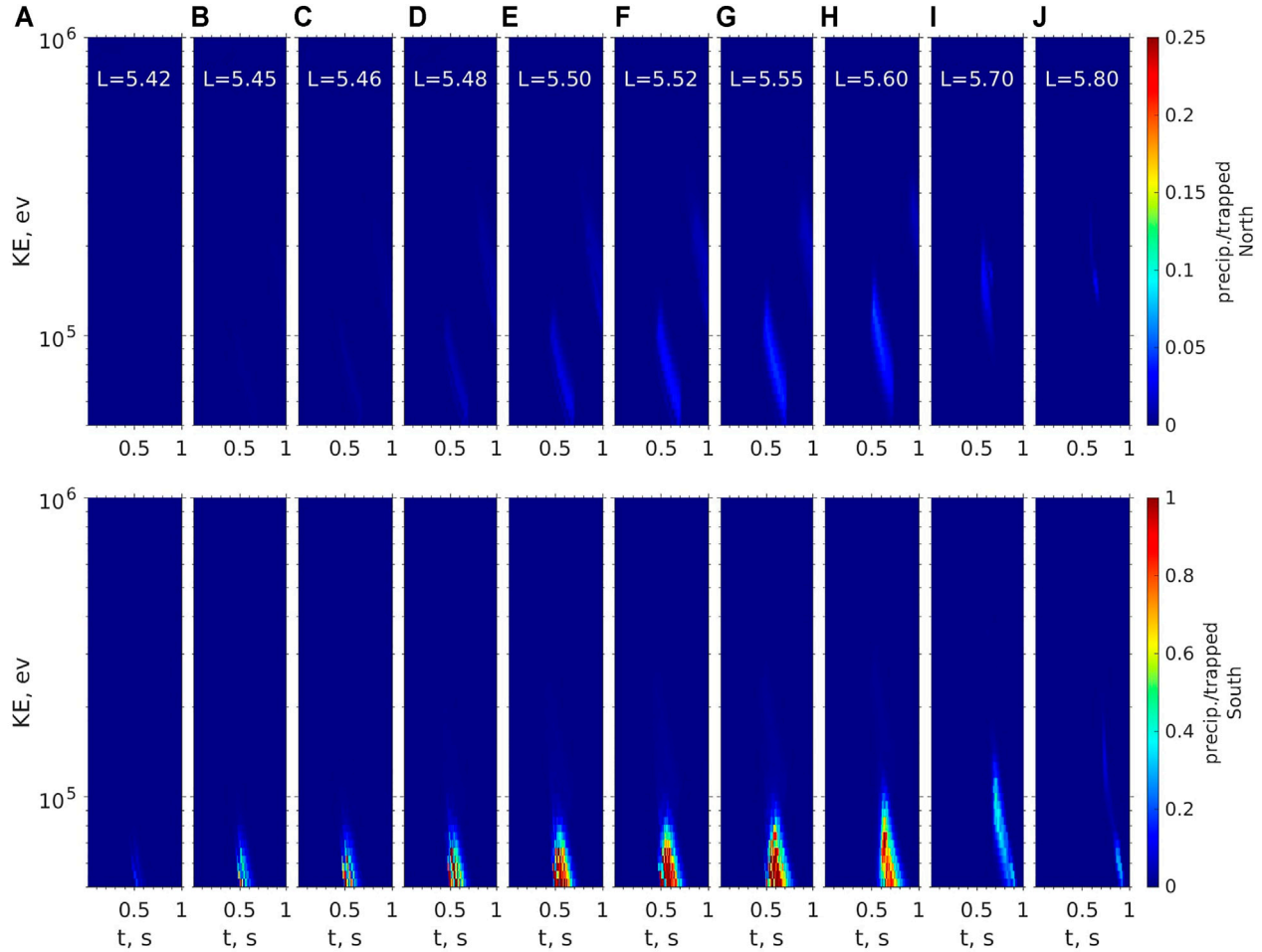


FIGURE 7 | Modeled ratio of precipitating to trapped electron fluxes at virtual northern **(top panels)** and southern **(bottom panels)** LEO satellites due to the presence of the nonducted wave shown in **Figure 5** at selected field lines with L values from 5.42 to 5.80 **(A–J)**.

- A dynamic model of nonducted chorus propagation is developed. In comparison with ducted chorus, nonducted chorus tends to be more confined near the equator, with wave energy decaying and propagating outward while propagating away from the equator.
- A numerical model of electron flux variation to nonducted chorus elements is developed. Such a model is valuable when interpreting the cause of microburst flux and predicting electron flux variation at a virtual observation.
- Distinct electron precipitation patterns due to the nonducted chorus waves are identified. Comparing with ducted chorus waves, nonducted waves tend to produce electron microbursts at lower energy, over a shorter duration, and over a broader L-shell region, and can trigger different resonance mechanisms (in additional to the principal resonance with $n = -1$).

There exist three factors that affect nonducted wave propagation and wave intensity. First, Landau damping shows strong dependence on L and MLT and Kp (Chen et al., 2012). Severe Landau damping limits the chorus wave intensity at high latitude and reduces the obliqueness of chorus waves. Second, wave propagation depends on the background plasma density variation, such as strong density gradient near the plasmapause. Third, the transverse size δL of equatorial chorus waves is another important factor. For a larger size, the off-equatorial chorus waves can obtain higher intensity. One can see the effects of increased δL by comparing **Figure 7** with **Supplementary Figure S3** of **Supplementary Material**, where δL is doubled.

Our study is limited to the case of nonducted propagation on the meridian plane here. Whistler waves have been shown to be confined near a meridian plane except there exists strong azimuthal density gradient such as near the plasmapause or near the plume region. When needed for those cases, our model is capable of extending to a more general three spatial-dimension case. The presented comparison of microburst characteristics due to ducted and nonducted

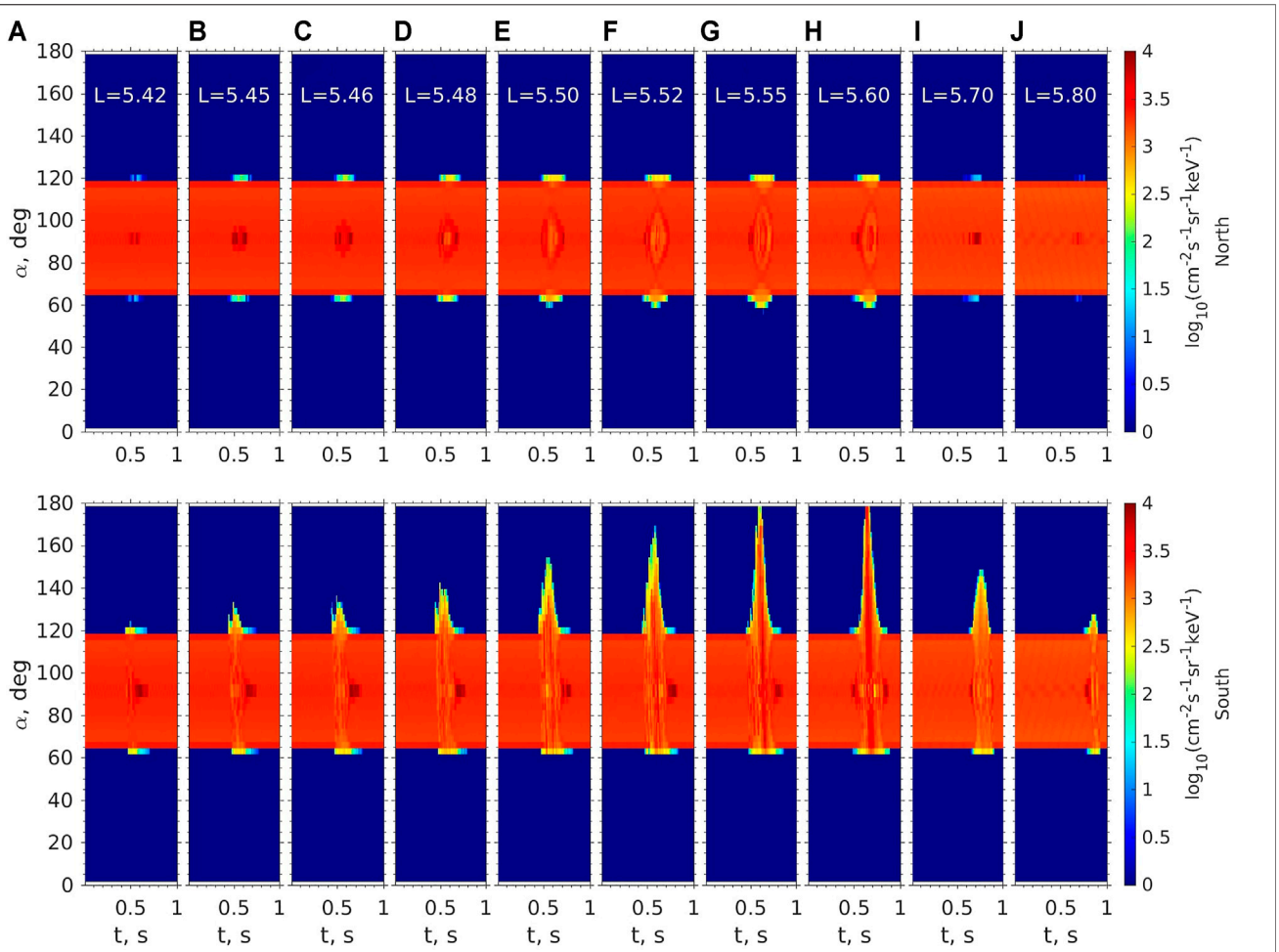


FIGURE 8 | Modeled pitch angle distribution of electron fluxes for a fixed energy 70 keV at virtual northern **(top panels)** and southern **(bottom panels)** LEO satellites due to the presence of the nonducted wave shown in **Figure 5** at selected field lines with L values from 5.42 to 5.80 **(A–J)**.

chorus waves will be valuable when interpreting the LEO observation of microburst structures. Our model is capable of revealing both temporal and spatial structures of induced electron precipitation.

The Landau damping can be significantly reduced by field-aligned electron beams or plateaus (see Ma et al., 2017) that are frequently observed around chorus generation regions (probably as an ionospheric response to electron precipitation by whistler waves, see Nishimura et al. (2015); Artemyev and Mourenas (2020)). Such reduced damping is associated with observations of very oblique chorus waves around the equatorial plane (e.g., Agapitov et al., 2016; Li et al., 2016b) and at middle latitudes Agapitov et al. (2013). The presented model results suggest that very oblique wave generation and propagation without significant damping also may generate microburst precipitation. Further simulations and model comparison with low-altitude spacecraft measurements will be required to reveal relative contributions of electron losses by different chorus wave modes (ducted waves, nonducted moderately and strongly oblique waves) for different electron energy ranges and geomagnetic conditions. To assess overall contribution of chorus waves to the radiation belt losses, relative occurrences of different chorus wave modes should be quantified separately, which is left for future exploration.

Finally, the development of nonducted chorus wave model, which is based on the solution of ray tracing, can be applied to model other coherent plasma waves, such as whistler waves due to lightning activities and from ground transmitter signals. The wave model allows flexible input on initial wave properties, and therefore is ideal for modeling a specific event with constraint by the observation. The general test particle equations can be used for modeling the effect of nonlinear wave particle interaction over a time scale of bounce periods. Results of such short-term simulation can be generalized for a long-term evolution due to nonlinear wave-particle interaction, by including test particle results into the modified Fokker-Planck equation describing phase trapping as a probabilistic process through the Green function approach (e.g., Omura et al., 2015), nonlocal transport operator (e.g., Artemyev et al., 2018), or the Markov chain method (e.g., Zheng et al., 2019).

DATA AVAILABILITY STATEMENT

No observational data were used in this study. Figure data are available at https://doi.org/10.5281/zenodo.5123390.

AUTHOR CONTRIBUTIONS

LC proposed the research idea, ran the simulation, and wrote the article. XZ and AA improved the idea and provided consultation on the interaction with ducted and nonducted chorus waves. LZ and ZX assisted with 1D and 2D chorus wave models. AB provided consultation on electron microbursts. RH developed the HOTRAY code and instructed its usage. All authors reviewed the article.

FUNDING

This work at UTD was supported by the NASA grants 80NSSC18K1224, 80NSSC19K0282, 80NSSC19K0283, 80NSSC21K0728, and 80NSSC21K1320. XZ and AA were supported by NSF grant 1914594. RH was supported by NERC Highlight Topic Grant NE/P01738X/1 (Rad-Sat) and NERC grant NE/V00249X/1 (Sat-Risk).

SUPPLEMENTARY MATERIAL

The Supplementary Material for this article can be found online at: https://www.frontiersin.org/articles/10.3389/fspas.2021.745927/full#supplementary-material

REFERENCES

Agapitov, O., Artemyev, A., Krasnoselskikh, V., Khotyaintsev, Y. V., Mourenas, D., Breuillard, H., et al. (2013). Statistics of Whistler Mode Waves in the Outer Radiation belt: Cluster STAFF-SA Measurements. *J. Geophys. Res. Space Phys.* 118, 3407–3420. doi:10.1002/jgra.50312

Agapitov, O., Blum, L. W., Mozer, F. S., Bonnell, J. W., and Wygant, J. (2017). Chorus Whistler Wave Source Scales as Determined from Multipoint Van allen Probe Measurements. *Geophys. Res. Lett.* 44, 2634–2642. doi:10.1002/2017GL072701

Agapitov, O., Krasnoselskikh, V., Zaliznyak, Y., Angelopoulos, V., Le Contel, O., and Rolland, G. (2010). Chorus Source Region Localization in the Earth's Outer Magnetosphere Using THEMIS Measurements. *Ann. Geophys.* 28, 1377–1386. doi:10.5194/angeo-28-1377-2010

Agapitov, O., Mourenas, D., Artemyev, A., Mozer, F. S., Bonnell, J. W., Angelopoulos, V., et al. (2018a). Spatial Extent and Temporal Correlation of Chorus and Hiss: Statistical Results from Multipoint Themis Observations. *J. Geophys. Res. Space Phys.* 123, 8317–8330. doi:10.1029/2018JA025725

Agapitov, O. V., Mourenas, D., Artemyev, A. V., and Mozer, F. S. (2016). Exclusion Principle for Very Oblique and Parallel Lower Band Chorus Waves. *Geophys. Res. Lett.* 43, 112–120. doi:10.1002/2016GL071250

Agapitov, O. V., Mourenas, D., Artemyev, A. V., Mozer, F. S., Hospodarsky, G., Bonnell, J., et al. (2018b). Synthetic Empirical Chorus Wave Model from Combined Van allen Probes and Cluster Statistics. *J. Geophys. Res. Space Phys.* 123, 297–314. doi:10.1002/2017ja024843

Anderson, K. A., and Milton, D. W. (1964). Balloon Observations of X Rays in the Auroral Zone: 3. High Time Resolution Studies. *J. Geophys. Res.* 69, 4457–4479. doi:10.1029/JZ069i021p04457

Artemyev, A., Agapitov, O., Mourenas, D., Krasnoselskikh, V., Shastun, V., and Mozer, F. (2016). Oblique Whistler-Mode Waves in the Earth's Inner Magnetosphere: Energy Distribution, Origins, and Role in Radiation Belt Dynamics. *Space Sci. Rev.* 200, 261–355. doi:10.1007/s11214-016-0252-5

Artemyev, A. V., and Mourenas, D. (2020). On Whistler Mode Wave Relation to Electron Field-Aligned Plateau Populations. *J. Geophys. Res. Space Phys.* 125, e27735. doi:10.1029/2019JA027735

Artemyev, A. V., Neishtadt, A. I., Vasiliev, A. A., and Mourenas, D. (2018). Long-term Evolution of Electron Distribution Function Due to Nonlinear Resonant Interaction with Whistler Mode Waves. *J. Plasma Phys.* 84, 905840206. doi:10.1017/S0022377818000260

Blake, J. B., Looper, M. D., Baker, D. N., Nakamura, R., Klecker, B., and Hovestadt, D. (1996). New High Temporal and Spatial Resolution Measurements by Sampex of the Precipitation of Relativistic Electrons. *Adv. Space Res.* 18, 171–186. doi:10.1016/0273-1177(95)00969-8

Blake, J. B., and O'Brien, T. P. (2016). Observations of Small-scale Latitudinal Structure in Energetic Electron Precipitation. *J. Geophys. Res. Space Phys.* 121, 3031–3035. doi:10.1002/2015JA021815

Bortnik, J., Chen, L., Li, W., Thorne, R. M., and Horne, R. B. (2011). Modeling the Evolution of Chorus Waves into Plasmaspheric Hiss. *J. Geophys. Res.* 116, a–n. doi:10.1029/2011JA016499

Breneman, A. W., Crew, A., Sample, J., Klumpar, D., Johnson, A., Agapitov, O., et al. (2017). Observations Directly Linking Relativistic Electron Microbursts to Whistler Mode Chorus: Van allen Probes and Firebird Ii. *Geophys. Res. Lett.* 44, 11,265–11,272. doi:10.1002/2017GL075001

Burtis, W. J., and Helliwell, R. A. (1969). Banded Chorus-A New Type of VLF Radiation Observed in the Magnetosphere by OGO 1 and OGO 3. *J. Geophys. Res.* 74, 3002–3010. doi:10.1029/JA074i011p03002

Burton, R. K., and Holzer, R. E. (1974). The Origin and Propagation of Chorus in the Outer Magnetosphere. *J. Geophys. Res.* 79, 1014–1023. doi:10.1029/ja079i007p01014

Chang, H. C., and Inan, U. S. (1983). A Theoretical Model Study of Observed Correlations between Whistler Mode Waves and Energetic Electron Precipitation Events in the Magnetosphere. *J. Geophys. Res.* 88, 10053–10064. doi:10.1029/ja088ia12p10053

Chen, L., Bortnik, J., Li, W., Thorne, R. M., and Horne, R. B. (2012). Modeling the Properties of Plasmaspheric Hiss: 1. Dependence on Chorus Wave Emission. *J. Geophys. Res.* 117, 1. doi:10.1029/2011JA017201

Chen, L., Breneman, A. W., Xia, Z., and Zhang, X.-j. (2020). Modeling of Bouncing Electron Microbursts Induced by Ducted Chorus Waves. *Geophys. Res. Lett.* 47, e2020GL089400. doi:10.1029/2020GL089400

Chen, L., Thorne, R. M., Li, W., and Bortnik, J. (2013a). Modeling the Wave normal Distribution of Chorus Waves. *J. Geophys. Res. Space Phys.* 118, 1074–1088. doi:10.1029/2012ja018343

Chen, L., Thorne, R. M., Shprits, Y., and Ni, B. (2013b). An Improved Dispersion Relation for Parallel Propagating Electromagnetic Waves in Warm Plasmas: Application to Electron Scattering. *J. Geophys. Res. Space Phys.* 118, 2185–2195. doi:10.1002/jgra.50260

Colpitts, C., Miyoshi, Y., Kasahara, Y., Delzanno, G. L., Wygant, J. R., Cattell, C. A., et al. (2020). First Direct Observations of Propagation of Discrete Chorus Elements from the Equatorial Source to Higher Latitudes, Using the Van allen Probes and Arase Satellites. *J. Geophys. Res. Space Phys.* 125, e2020JA028315. doi:10.1029/2020JA028315

Crew, A. B., Spence, H. E., Blake, J. B., Klumpar, D. M., Larsen, B. A., O'Brien, T. P., et al. (2016). First Multipoint *In Situ* Observations of Electron Microbursts: Initial Results from the Nsf Firebird Ii mission. *J. Geophys. Res. Space Phys.* 121, 5272–5283. doi:10.1002/2016JA022485

Douma, E., Rodger, C. J., Blum, L. W., and Clilverd, M. A. (2017). Occurrence Characteristics of Relativistic Electron Microbursts from Sampex Observations. *J. Geophys. Res. Space Phys.* 122, 8096–8107. doi:10.1002/2017JA024067

Furuya, N., Omura, Y., and Summers, D. (2008). Relativistic Turning Acceleration of Radiation belt Electrons by Whistler Mode Chorus. *J. Geophys. Res.* 113. doi:10.1029/2007ja012478

Gao, X., Mourenas, D., Li, W., Artemyev, A. V., Lu, Q., Tao, X., et al. (2016). Observational Evidence of Generation Mechanisms for Very Oblique Lower Band Chorus Using Themis Waveform Data. *J. Geophys. Res. Space Phys.* 121, 6732–6748. doi:10.1002/2016JA022915

Hikishima, M., Omura, Y., and Summers, D. (2010). Microburst Precipitation of Energetic Electrons Associated with Chorus Wave Generation. *Geophys. Res. Lett.* 37, a–n. doi:10.1029/2010GL042678

Horne, R. B., Glauert, S. A., and Thorne, R. M. (2003). Resonant Diffusion of Radiation belt Electrons by Whistler-Mode Chorus. *Geophys. Res. Lett.* 30, 1. doi:10.1029/2003gl016963

Horne, R. B. (1989). Path-integrated Growth of Electrostatic Waves: The Generation of Terrestrial Myriametric Radiation. *J. Geophys. Res.* 94, 895–909. doi:10.1029/ja094ia07p08895

Imhof, W. L., Voss, H. D., Mobilia, J., Datlowe, D. W., Gaines, E. E., McGlennon, J. P., et al. (1992). Relativistic Electron Microbursts. *J. Geophys. Res.* 97, 13829–13837. doi:10.1029/92JA01138

Katoh, Y., and Omura, Y. (2007). Relativistic Particle Acceleration in the Process of Whistler-Mode Chorus Wave Generation. *Geophys. Res. Lett.* 34, 1. doi:10.1029/2007gl031335

Katoh, Y., and Omura, Y. (2006). Simulation Study on Nonlinear Frequency Shift of Narrow Band Whistler-Mode Waves in a Homogeneous Magnetic Field. *Earth Planet. Sp* 58, 1219–1225. doi:10.1186/BF03352013

Kennel, C. F., and Petschek, H. E. (1966). Limit on Stably Trapped Particle Fluxes. *J. Geophys. Res.* 71, 1–28. doi:10.1029/jz071i001p00001

Kersten, K., Cattell, C. A., Breneman, A., Goetz, K., Kellogg, P. J., Wygant, J. R., et al. (2011). Observation of Relativistic Electron Microbursts in Conjunction with Intense Radiation belt Whistler-Mode Waves. *Geophys. Res. Lett.* 38, 1. doi:10.1029/2011gl046810

Lam, M. M., Horne, R. B., Meredith, N. P., Glauert, S. A., Moffat-Griffin, T., and Green, J. C. (2010). Origin of Energetic Electron Precipitation >30 Kev into the Atmosphere. *J. Geophys. Res.* 115, a–n. doi:10.1029/2009JA014619

Lampton, M. (1967). Daytime Observations of Energetic Auroral-Zone Electrons. *J. Geophys. Res.* 72, 5817–5823. doi:10.1029/JZ072i023p05817

Lauben, D. S., Inan, U. S., Bell, T. F., and Gurnett, D. A. (2002). Source Characteristics of ELF/VLF Chorus. *J. Geophys. Res.* 107, 1429. doi:10.1029/2000ja003019

LeDocq, M. J., Gurnett, D. A., and Hospodarsky, G. B. (1998). Chorus Source Locations from VLF Poynting Flux Measurements with the Polar Spacecraft. *Geophys. Res. Lett.* 25, 4063–4066. doi:10.1029/1998GL900071

Li, W., Mourenas, D., Artemyev, A. V., Bortnik, J., Thorne, R. M., Kletzing, C. A., et al. (2016a). Unraveling the Excitation Mechanisms of Highly Oblique Lower Band Chorus Waves. *Geophys. Res. Lett.* 43, 8867–8875. doi:10.1002/2016gl070386

Li, W., Santolik, O., Bortnik, J., Thorne, R. M., Kletzing, C. A., Kurth, W. S., et al. (2016b). New Chorus Wave Properties Near the Equator from Van allen Probes Wave Observations. *Geophys. Res. Lett.* 43, 4725–4735. doi:10.1002/2016GL068780

Li, W., Thorne, R. M., Angelopoulos, V., Bortnik, J., Cully, C. M., Ni, B., et al. (2009). Global Distribution of Whistler-Mode Chorus Waves Observed on the THEMIS Spacecraft. *Geophys. Res. Lett.* 36, L09104. doi:10.1029/2009GL037595

Li, W., Thorne, R. M., Bortnik, J., Shprits, Y. Y., Nishimura, Y., Angelopoulos, V., et al. (2011a). Typical Properties of Rising and Falling Tone Chorus Waves. *Geophys. Res. Lett.* 38, a–n. doi:10.1029/2011GL047925

Liu, X., Gu, W., Xia, Z., Chen, L., and Horne, R. B. (2021). Frequency-Dependent Modulation of Whistler-Mode Waves by Density Irregularities during the Recovery Phase of a Geomagnetic Storm. *Geophys. Res. Lett.* 48, e2021GL093095. doi:10.1029/2021GL093095

Lorentzen, K. R., Blake, J. B., Inan, U. S., and Bortnik, J. (2001). Observations of Relativistic Electron Microbursts in Association with VLF Chorus. *J. Geophys. Res.* 106, 6017–6027. doi:10.1029/2000JA003018

Lu, Q., Ke, Y., Wang, X., Liu, K., Gao, X., Chen, L., et al. (2019). Two-Dimensional gcPIC Simulation of Rising-Tone Chorus Waves in a Dipole Magnetic Field. *J. Geophys. Res. Space Phys.* 124, 4157–4167. doi:10.1029/2019JA026586

Ma, Q., Artemyev, A. V., Mourenas, D., Li, W., Thorne, R. M., Kletzing, C. A., et al. (2017). Very Oblique Whistler Mode Propagation in the Radiation Belts: Effects of Hot Plasma and Landau Damping. *Geophys. Res. Lett.* 44, 057–066. doi:10.1002/2017GL075892

Meredith, N. P., Horne, R. B., Sicard-Piet, A., Boscher, D., Yearby, K. H., Li, W., et al. (2012). Global Model of Lower Band and Upper Band Chorus from Multiple Satellite Observations. *J. Geophys. Res.* 117, A10225. doi:10.1029/2012ja017978

Millan, R. M., and Thorne, R. M. (2007). Review of Radiation belt Relativistic Electron Losses. *J. Atmos. Solar-Terrestrial Phys.* 69, 362–377. doi:10.1016/j.jastp.2006.06.019

Millan, R. M. (2011). Understanding Relativistic Electron Losses with Barrel. *J. Atmos. Solar-Terrestrial Phys.* 73, 1425–1434. doi:10.1016/j.jastp.2011.01.006

Ni, B., Thorne, R. M., Shprits, Y. Y., Orlova, K. G., and Meredith, N. P. (2011). Chorus-driven Resonant Scattering of Diffuse Auroral Electrons in Nondipolar Magnetic fields. *J. Geophys. Res.* 116, a–n. doi:10.1029/2011JA016453

Nishimura, Y., Bortnik, J., Li, W., Liang, J., Thorne, R. M., Angelopoulos, V., et al. (2015). Chorus Intensity Modulation Driven by Time-varying Field-aligned Low-energy Plasma. *J. Geophys. Res. Space Phys.* 120, 7433–7446. doi:10.1002/2015JA021330

Nunn, D., Omura, Y., Matsumoto, H., Nagano, I., and Yagitani, S. (1997). The Numerical Simulation of Vlf Chorus and Discrete Emissions Observed on the Geotail Satellite Using a Vlasov Code. *J. Geophys. Res.* 102, 27083–27097. doi:10.1029/97JA02518

O'Brien, T. P., Looper, M. D., and Blake, J. B. (2004). Quantification of Relativistic Electron Microburst Losses during the Gem Storms. *Geophys. Res. Lett.* 31, 1. doi:10.1029/2003GL018621

Oliven, M. N., and Gurnett, D. A. (1968). Microburst Phenomena: 3. An Association between Microbursts and Vlf Chorus. *J. Geophys. Res.* 73, 2355–2362. doi:10.1029/JA073i007p02355

Omura, Y., Hikishima, M., Katoh, Y., Summers, D., and Yagitani, S. (2009). Nonlinear Mechanisms of Lower-Band and Upper-Band Vlf Chorus Emissions in the Magnetosphere. *J. Geophys. Res. Space Phys.* 114, 1. doi:10.1029/2009ja014206

Omura, Y., and Matsumoto, H. (1982). Computer Simulations of Basic Processes of Coherent Whistler Wave-Particle Interactions in the Magnetosphere. *J. Geophys. Res.* 87, 4435–4444. doi:10.1029/ja087ia06p04435

Omura, Y., Miyashita, Y., Yoshikawa, M., Summers, D., Hikishima, M., Ebihara, Y., et al. (2015). Formation Process of Relativistic Electron Flux through Interaction with Chorus Emissions in the Earth's Inner Magnetosphere. *J. Geophys. Res. Space Phys.* 120, 9545–9562. doi:10.1002/2015JA021563

Omura, Y., and Summers, D. (2006). Dynamics of High-Energy Electrons Interacting with Whistler Mode Chorus Emissions in the Magnetosphere. *J. Geophys. Res.* 111, 1. doi:10.1029/2006JA011600

Parks, G. K., Gurgiolo, C., and West, R. (1979). Relativistic Electron Precipitation. *Geophys. Res. Lett.* 6, 393–396. doi:10.1029/GL006i005p00393

Reeves, G. D., Spence, H. E., Henderson, M. G., Morley, S. K., Friedel, R. H. W., Funsten, H. O., et al. (2013). Electron Acceleration in the Heart of the Van allen Radiation Belts. *Science* 341, 991–994. doi:10.1126/science.1237743

Rosenberg, T. J., Wei, R., Detrick, D. L., and Inan, U. S. (1990). Observations and Modeling of Wave-Induced Microburst Electron Precipitation. *J. Geophys. Res.* 95, 6467–6475. doi:10.1029/JA095iA05p06467

Saito, S., Miyoshi, Y., and Seki, K. (2012). Relativistic Electron Microbursts Associated with Whistler Chorus Rising Tone Elements: Gemsis-Rbw Simulations. *J. Geophys. Res.* 117, a–n. doi:10.1029/2012JA018020

Santolík, O., Gurnett, D. A., Pickett, J. S., Parrot, M., and Cornilleau-Wehrlin, N. (2005). Central Position of the Source Region of Storm-Time Chorus. *Planet. Space Sci.* 53, 299–305. doi:10.1016/j.pss.2004.09.056

Santolík, O., and Gurnett, D. A. (2003). Transverse Dimensions of Chorus in the Source Region. *Geophys. Res. Lett.* 30. doi:10.1029/2002GL016178

Shen, X. C., Li, W., Ma, Q., Agapitov, O., and Nishimura, Y. (2019). Statistical Analysis of Transverse Size of Lower Band Chorus Waves Using Simultaneous Multisatellite Observations. *Geophys. Res. Lett.* 46, 5725–5734. doi:10.1029/2019gl083118

Shprits, Y. Y., and Ni, B. (2009). Dependence of the Quasi-Linear Scattering Rates on the Wave normal Distribution of Chorus Waves. *J. Geophys. Res.* 114, a–n. doi:10.1029/2009JA014223

Shumko, M., Johnson, A. T., Sample, J. G., Griffith, B. A., Turner, D. L., O'Brien, T. P., et al. (2020). Electron Microburst Size Distribution Derived with Aerocube-6. *J. Geophys. Res. Space Phys.* 125, e2019JA027651. doi:10.1029/2019JA027651

Shumko, M., Sample, J., Johnson, A., Blake, B., Crew, A., Spence, H., et al. (2018). Microburst Scale Size Derived from Multiple Bounces of a Microburst Simultaneously Observed with the Firebird-Ii Cubesats. *Geophys. Res. Lett.* 45, 8811–8818. doi:10.1029/2018gl078925

Smith, R. L., Helliwell, R. A., and Yabroff, I. W. (1960). A Theory of Trapping of Whistlers in Field-Aligned Columns of Enhanced Ionization. *J. Geophys. Res.* 65, 815–823. doi:10.1029/JZ065i003p00815

Tao, X. (2014). A Numerical Study of Chorus Generation and the Related Variation of Wave Intensity Using the Dawn Code. *J. Geophys. Res. Space Phys.* 119, 3362–3372. doi:10.1002/2014JA019820

Tao, X., and Bortnik, J. (2010). Nonlinear Interactions between Relativistic Radiation belt Electrons and Oblique Whistler Mode Waves. *Nonlin. Process. Geophys.* 17, 599–604. doi:10.5194/npg-17-599-2010

Tao, X., Bortnik, J., Thorne, R. M., Albert, J. M., and Li, W. (2012). Effects of Amplitude Modulation on Nonlinear Interactions between Electrons and Chorus Waves. *Geophys. Res. Lett.* 39, a–n. doi:10.1029/2012GL051202

Teng, S., Tao, X., Xie, Y., Zonca, F., Chen, L., Fang, W. B., et al. (2017). Analysis of the Duration of Rising Tone Chorus Elements. *Geophys. Res. Lett.* 44, 074–082. doi:10.1002/2017GL075824

Thorne, R. M., Li, W., Ni, B., Ma, Q., Bortnik, J., Chen, L., et al. (2013). Rapid Local Acceleration of Relativistic Radiation-belt Electrons by Magnetospheric Chorus. *Nature* 504, 411–414. doi:10.1038/nature12889

Tsurutani, B. T., and Smith, E. J. (1974). Postmidnight Chorus: A Substorm Phenomenon. *J. Geophys. Res.* 79, 118–127. doi:10.1029/JA079i001p00118

Tyler, E., Breneman, A., Cattell, C., Wygant, J., Thaller, S., and Malaspina, D. (2019). Statistical Distribution of Whistler Mode Waves in the Radiation Belts with Large Magnetic Field Amplitudes and Comparison to Large Electric Field Amplitudes. *J. Geophys. Res. Space Phys.* 124, 6541–6552. doi:10.1029/2019JA026913

Watt, C. E. J., Degeling, A. W., and Rankin, R. (2013). Constructing the Frequency and Wave normal Distribution of Whistler-Mode Wave Power. *J. Geophys. Res. Space Phys.* 118, 1984–1991. doi:10.1002/jgra.50231

Zhang, X.-J., Thorne, R., Artemyev, A., Mourenas, D., Angelopoulos, V., Bortnik, J., et al. (2018). Properties of Intense Field-Aligned Lower-Band Chorus Waves: Implications for Nonlinear Wave-Particle Interactions. *J. Geophys. Res. Space Phys.* 123, 5379–5393. doi:10.1029/2018JA025390

Zheng, L., Chen, L., and Zhu, H. (2019). Modeling Energetic Electron Nonlinear Wave-Particle Interactions with Electromagnetic Ion Cyclotron Waves. *J. Geophys. Res. Space Phys.* 124, 3436–3453. doi:10.1029/2018JA026156

Conflict of Interest: The authors declare that the research was conducted in the absence of any commercial or financial relationships that could be construed as a potential conflict of interest.

Publisher's Note: All claims expressed in this article are solely those of the authors and do not necessarily represent those of their affiliated organizations, or those of the publisher, the editors and the reviewers. Any product that may be evaluated in this article, or claim that may be made by its manufacturer, is not guaranteed or endorsed by the publisher.

Copyright © 2021 Chen, Zhang, Artemyev, Zheng, Xia, Breneman and Horne. This is an open-access article distributed under the terms of the Creative Commons Attribution License (CC BY). The use, distribution or reproduction in other forums is permitted, provided the original author(s) and the copyright owner(s) are credited and that the original publication in this journal is cited, in accordance with accepted academic practice. No use, distribution or reproduction is permitted which does not comply with these terms.

frontiers in Physics

ORIGINAL RESEARCH
published: 11 October 2021
doi: 10.3389/fphy.2021.744298

Estimating Precipitating Energy Flux, Average Energy, and Hall Auroral Conductance From THEMIS All-Sky-Imagers With Focus on Mesoscales

Christine Gabrielse[1], Toshi Nishimura[2], Margaret Chen[1], James H. Hecht[1], Stephen R. Kaeppler[3], D. Megan Gillies[4], Ashton S. Reimer[5], Larry R. Lyons[6], Yue Deng[7], Eric Donovan[4] and J. Scott Evans[8]*

[1]The Aerospace Corporation, El Segundo, CA, United States, [2]Department of Electrical and Computer Engineering, Boston University, Boston, MA, United States, [3]Department of Physics and Astronomy, Clemson University, Clemson, SC, United States, [4]Department of Physics and Astronomy, University of Calgary, Calgary, AB, Canada, [5]SRI International, Menlo Park, CA, United States, [6]Atmospheric and Oceanic Sciences Department, UCLA, Los Angeles, CA, United States, [7]Department of Physics, University of Texas, Arlington, TX, United States, [8]Computational Physics, Inc, Springfield, VA, United States

OPEN ACCESS

Edited by:
Olga V. Khabarova,
Institute of Terrestrial Magnetism Ionosphere and Radio Wave Propagation (RAS), Russia

Reviewed by:
Renata Lukianova,
Space Research Institute (RAS), Russia
Nickolay Ivchenko,
Royal Institute of Technology, Sweden

***Correspondence:**
Christine Gabrielse
christine.gabrielse@aero.org

Specialty section:
This article was submitted to Space Physics, a section of the journal Frontiers in Physics

Received: 20 July 2021
Accepted: 20 September 2021
Published: 11 October 2021

Citation:
Gabrielse C, Nishimura T, Chen M, Hecht JH, Kaeppler SR, Gillies DM, Reimer AS, Lyons LR, Deng Y, Donovan E and Evans J (2021) Estimating Precipitating Energy Flux, Average Energy, and Hall Auroral Conductance From THEMIS All-Sky-Imagers With Focus on Mesoscales. Front. Phys. 9:744298. doi: 10.3389/fphy.2021.744298

Recent attention has been given to mesoscale phenomena across geospace (~10 s km to 500 km in the ionosphere or ~0.5 R_E to several R_E in the magnetosphere), as their contributions to the system global response are important yet remain uncharacterized mostly due to limitations in data resolution and coverage as well as in computational power. As data and models improve, it becomes increasingly valuable to advance understanding of the role of mesoscale phenomena contributions—specifically, in magnetosphere-ionosphere coupling. This paper describes a new method that utilizes the 2D array of Time History of Events and Macroscale Interactions during Substorms (THEMIS) white-light all-sky-imagers (ASI), in conjunction with meridian scanning photometers, to estimate the auroral scale sizes of intense precipitating energy fluxes and the associated Hall conductances. As an example of the technique, we investigated the role of precipitated energy flux and average energy on mesoscales as contrasted to large-scales for two back-to-back substorms, finding that mesoscale aurora contributes up to ~80% (~60%) of the total energy flux immediately after onset during the early expansion phase of the first (second) substorm, and continues to contribute ~30–55% throughout the remainder of the substorm. The average energy estimated from the ASI mosaic field of view also peaked during the initial expansion phase. Using the measured energy flux and tables produced from the Boltzmann Three Constituent (B3C) auroral transport code (Strickland et al., 1976; 1993), we also estimated the 2D Hall conductance and compared it to Poker Flat Incoherent Scatter Radar conductance values, finding good agreement for both discrete and diffuse aurora.

Keywords: aurora, precipitation, mesoscale, conductance, energy flux, average energy, all-sky-imagers, substorms

INTRODUCTION

A fundamental question at the heart of the dynamics and coupling of Earth's magnetosphere-ionosphere system is, "How is energy deposited into the ionosphere from the magnetosphere?" That itself has a complex answer comprised of multiple parts such as electromagnetic energy, particle precipitation, and waves. Great strides have been made in characterizing the global energy input due to precipitation; for example, Newell et al. [1] built an empirical precipitation model using Defense Meteorological Satellite Program (DMSP) statistics to determine the auroral power from diffuse, monoenergetic discrete, and broadband discrete aurora as a function of solar wind coupling. Results were binned by magnetic local time (MLT) and latitude. Their work has been useful for describing auroral power at large spatial scales, but does not explain contribution of specific scale sizes or provide event-based numbers that could be used in global climate models to investigate the ionosphere-thermosphere response to an intense, mesoscale (~10 s–500 km) auroral form. DMSP statistics-based modeling has been improved over the years, leading to the construction of the Oval Variation, Assessment, Tracking, Intensity, and Online Nowcasting (OVATION) models [2–4] to the current state-of-the art version, OVATION Prime, all of which still excel at the more global precipitation response without capturing the spatially and temporally dynamic aurora that occur on mesoscales.

In a newly developed empirical model, Auroral Spectrum and High-Latitude Electric field and variability (ASHLEY) [5], there is no assumed spectra distribution for the precipitating particles, and the DMSP observed energetic particles in 19-energy channels have been directly binned according to the geomagnetic local time, latitude, and solar wind conditions. ASHLEY has shown some advantage to specify the soft electron precipitation, but is still limited to the large-scale phenomena. Another very recent DMSP statistics-based modeling work employed machine learning techniques to build a new total electron energy flux particle precipitation nowcast model called PrecipNet [6]. PrecipNet better captures the dynamic changes of the auroral flux than OVATION Prime, improving capabilities to reconstruct mesoscale phenomena and making great progress towards nowcasting and forecasting auroral response to solar wind driving.

Though these and other works make great strides towards resolving the role of mesoscale auroral precipitation, the field still lacks a rigorous understanding and characterization of the contribution of the dynamic and energetic mesoscale auroral forms that are embedded within the large-scale system. These are important to resolve, as studies such as Deng et al. [7] and Sheng et al. [8] have illustrated with the Global Ionosphere-Thermosphere model (GITM) how mesoscale phenomena in the ionosphere can vastly alter the ionospheric and mesospheric response.

A major reason for the continued deficiency in mesoscale characterization has been inadequate data sources to fully resolve spatial and temporal ambiguities. The DMSP examples above are perhaps one of the best-suited datasets because they provide *in situ* measurements of the particle flux and energy, as well as 2D views of the aurora from above as the satellite flies overhead. However, statistics must be employed, since orbiting spacecraft measurements lack continuous coverage over a given 2D area. It is not possible to investigate auroral evolution over a short time in the region of interest. DMSP orbits are also not often optimized for covering the nightside auroral oval, as most of their measurements are made near the dawn-dusk meridian.

In contrast, ground-based observations consistently observe the same geographic location over time, allowing for the temporal changes to be recorded. However, most datasets do not have sufficiently high resolution for observing the aurora's spatial evolution with a wide spatial coverage in the nightside auroral oval. For example, meridian scanning photometers (MSPs), which observe multiple wavelengths (such as blue, green, and redline aurora), are limited to a line of constant longitude. Incoherent Scatter Radar (ISR) can measure electron densities to determine the precipitated energy, energy flux, and resulting changes in conductance in 1D or 2D (e.g., [9,10]), but the measurement area is limited to ~100 s km in horizontal spatial extent at 100 km altitude.

All-sky-imagers (ASIs) provide auroral intensity evolution in 2D space as well as over time. ASIs have been used to resolve auroral arcs and to obtain local 2D precipitation information such as energy flux (e.g., [11–16]), Pedersen conductance (e.g., [17]), and arc occurrence and distribution information (e.g., [18]). For example, Lam et al. [17] used the THEMIS ASI at Fort Yukon to demonstrate a relationship between the Pedersen conductance (as determined from Poker Flat Incoherent Scatter Radar (PFISR) data) to white light intensity within 3 mho or 40%. They assumed that the Pedersen conductance is proportional to the square root of the white light intensity, based on Kosch et al. (1998) who argued for this relationship after making the approximations that auroral optical intensity is proportional to ion production rate and that electron production is approximately equal to the electron loss.

Since 2006, NASA's THEMIS mission has provided an array of white-light ASIs across Canada and Alaska that monitor the majority of the nightside auroral oval at a 3 s cadence and up to 1 km resolution, providing a global view at temporal and spatial resolutions required to study the aurora on mesoscales [19]. This allows us to expand upon previous demonstrations of ASI capabilities to estimate precipitated energy flux and average energy in 2D, but on a continental scale. Our recent work has shown that the THEMIS ASI array can observe evolution of precipitating energy flux over the whole size of a substorm and that it is possible to estimate contributions of mesoscale precipitation over large-scale precipitation [20].

In this paper, we describe the technique that utilizes the white-light ASI array that was not detailed in Nishimura et al. [20], including important upgrades made through the present work, supplemented by MSPs and auroral transport code calculations, to estimate precipitating energy flux, average energy, and Hall conductance, as well as what percent of the energy flux is contributed by mesoscale auroral forms during two back-to-back substorms.

METHODOLOGY

Background and Overview

One method to estimate the precipitating energy flux and average energy utilizes the ratio of auroral intensities at different wavelengths (colors). When electrons precipitate into the upper atmosphere, the more energetic ones reach lower altitudes before encountering high enough atmospheric densities to thermalize, whereas the less energetic electrons are stopped and thermalize at higher altitudes. Therefore, the red aurora occurring at higher altitudes are produced by less energetic populations colliding with atomic oxygen, whereas the green and blue aurora occurring at lower altitudes are caused by more energetic populations colliding with oxygen and molecular nitrogen, respectively. Methodologies that utilize the intensity ratios between the different auroral color wavelengths have been developed to determine the integrated energy flux and the average energy of the precipitating particle distribution (e.g., [21–25]); for example, more red than blue light indicates a less energetic population, whereas more blue than red light indicates the opposite.

Janhunen [13] used the figures that plotted intensity ratios from Rees and Luckey [21] and Strickland et al. [22] to develop an inversion method that determines precipitating energy flux from multiwavelength ASIs. They found that the energy flux reconstructed from only the green images was very good, almost indistinguishable from the reconstructions that included the red images. When comparing the reconstructed arc energy flux with energy flux measured by the FAST satellite, they found a good agreement (12 mW m^{-2} vs. 10 mW m^{-2}, respectively). Kauristie et al. [14] used the methods laid out by Janhunen [13] to estimate the energy flux measured by the All-Sky Camera in Kilpisjärvi and compared those values against those measured by the incoherent scatter radar EISCAT, finding a correlation of r = 0.72 between datasets. Partamies et al. [15] further tested the technique by comparing 100 All-Sky Camera images at Longyearbyen with EISCAT energy fluxes, finding that in 35% of all of the blue and green image inversions the relative errors were less than 50%, and in 90% of the blue and green image inversions relative errors were less than 100%. Dahlgren et al. [16] also developed an inversion technique to determine both energy flux and average energy from ASIs combined with EISCAT data. Instead of relying on Rees and Luckey [21], which assumes all secondary, etc., electrons dissipate their energy locally, they determined the average energies of the precipitating electrons from Auroral Structure and Kinetics narrow angle camera emission ratios modelled with the Southampton ion chemistry and electron transport model (described in [11,26]), using atmospheric parameters for the conditions during their case study.

Hecht et al. [24,25] also presented relationships between different auroral wavelength ratios and the average energy of the precipitation using the B3C auroral electron transport code [27,28]. Strickland et al. [22,27,28] made a detailed attempt to investigate dependencies of red line emission on key parameters, unlike Rees and Luckey [21] who did not incorporate knowledge of O abundance relative to N2, which is necessary when using the red line emission. We rely upon and slightly update the methodologies developed by Strickland et al. [22] and Hecht et al. [23–25], which are described in *Determining Energy Flux and Average Energy From Aurora Color Ratios*. These methodologies, which utilize a model atmosphere to incorporate the appropriate physics and chemistry, improve calculations of the emissions and conductance as functions of the incident energy flux and average energy as compared to Rees and Luckey [21], which Nishimura et al. [20] used. We note that our techniques additionally include more physics and chemistry than the techniques employed by Kosch et al. (1998) and Lam et al. [17], who did not calculate emissions, energy flux, or average energy, but deduced the Pedersen conductance assuming that it is proportional to the square root of the white light intensity.

In order to employ the network of THEMIS ASIs, we developed log-log linear analytical functions to convert from white light counts to red (630.0 nm), green (557.7 nm), and blue (427.8 nm) intensities using overlapping meridian scanning photometer (MSP) data to calibrate. The steps we took are detailed in *Converting White Light Intensities to Color Intensities*. After obtaining the ratios, we estimated the precipitating electron energy flux and average energy. Using the 2D capabilities of the ASI mosaic, we determined what percentage of the energy flux is contributed by various mesoscales (*Results*).

From the energy flux and average energy, we estimated the Hall conductance in 2D over time (*Determining the Hall Conductance*) and compared to Poker Flat Incoherent Scatter Radar (PFISR) data (*Results*). Because the white light can be related to the OI (557.7 nm) greenline and (427.8 nm) blueline (shown in *Converting White Light Intensities to Color Intensities*), it does well estimating energy flux (Q). At higher average electron energies that are associated with intense aurora (>5 keV), the Hall conductivity scales very well with Q with little dependence on average electron energy (see Figure 16.5fig165 of [29] and **Supplementary Figure S1**). At lower energies, there is an energy dependence; but within a factor of two, the major dependent variable is still Q. Since this paper is focused on mesoscales associated with the more intense precipitation events, the Hall conductivities become a byproduct of a measurement of Q.

Instrumentation

THEMIS All-Sky-Imagers

The THEMIS all-sky-imager (ASI) array consists of about 20 unfiltered (white light) fish-eye cameras at any given time spanning Canada and Alaska, covering a large section of the auroral oval with up to 1 km resolution near zenith, 3 km at a 40° elevation angle, 10 km at a 20° elevation angle, and 25 km at a 10° elevation angle (see Figure 6 from [19]). The ASIs are time synchronized with a 3 s cadence. During northern winter, continuous coverage is available from about 00:00–15:00 UT covering approximately 17-07 MLT for each individual site. Data collection began in 2006 and continues to present day [19]. For this study, because ASIs do not differentiate between particle species, we assume the visible light is due to precipitating electrons. Hecht et al. [30] discuss that the electron flux Q can be derived from the blue intensity, and that the proton flux is a small fraction of the electron flux. As we will show, the white light and blueline are well-correlated, so this assumption carries through.

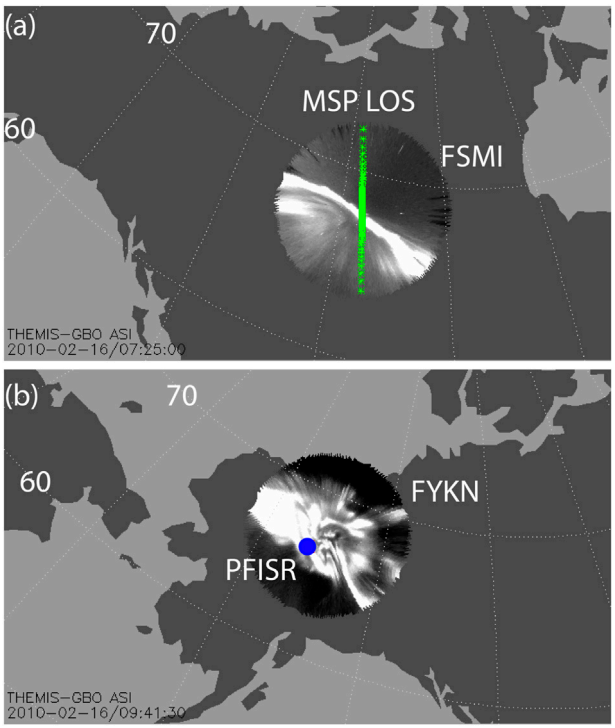


FIGURE 1 | (A) Green line depicts the NORSTAR MSP line of sight (LOS) superimposed on top of the THEMIS ASI at Fort Smith, Canada on 2010-02-16 at 07:25 UT. The locations were mapped to 110 km altitude. The white within the ASI FOV is the aurora. Some treetops are visible on the edges of the FOV as black spikes. The stars seen as single white dots are removed in our methodology. **(B)** The blue dot depicts the PFISR location within the Fort Yukon (FYKN), Canada FOV on 2010-02-16 at 09:41:30 UT. Both panels label the 60° and 70° magnetic latitude lines.

Before we continue, we highlight the caution one needs to take with ASI data at low elevation angles. For studies that require low error in energy flux, energy, or conductance magnitudes, elevation angles above ~70° will be more trustworthy as they look approximately up the magnetic field line local to the station. The farther from zenith in the ASI field of view (low elevation angles), the more flux tubes the line-of-sight observation cuts through. Because the image is 2D, aurora at different heights may not be observed integrally, but are spread out over several latitudes (and/or longitudes) in the image. This is because all white light is mapped to 110 km altitude and then projected onto the 2D plane. To address the question of mesoscale contribution to auroral precipitation, however, we require a larger field of view; otherwise, the ASIs do not contribute additional perspectives to what we can surmise from, say, ISRs. The uncertainty in mapping can be mitigated in cases where multiple ASI field of views (FOVs) overlap by validating and/or adjusting the mapping altitude to match aurora locations viewed from different imagers. For this study, as will be shown in *Results*, the arcs were well-aligned between different imagers. Lastly, a future work could be to try further calibrating ASI data to DMSP data, which does not have the low elevation angle error.

NORSTAR Meridian Scanning Photometer

The NORSTAR Meridian Scanning Photometer (MSP) array consists of four ground-based photometers designed to simultaneously measure luminosity in four key auroral bands (470.9, 486.1, 557.7, and 630.0 nm). To use the color ratio relationships discussed in *Determining Energy Flux and Average Energy From Aurora Color Ratios*, we converted the 470.9 nm intensity to 427.8 nm by multiplying the former by 4.5 [31]. As Omholt [32] showed, the ratio is constant between these auroral emissions. Each MSP utilizes a high speed, 8-channel filter wheel (to observe auroral plus background channels), coupled to a highly sensitive photo-multiplier tube (PMT) which mechanically scans from near horizon-to-horizon in the North-South direction. Each scan consists of approximately 544 elevation steps, taking 30 s to complete a full horizon to horizon scan in high resolution mode. PMT counts from these scans are then background subtracted and converted into units of Rayleighs (R). The green 557.7 nm, blue 470.9 nm, and 486.1 nm emissions are projected to an altitude of 110 km and the red 630.0 nm emission is typically projected to 230 km. We plotted the Fort Smith (FSMI) MSP line of sight (LOS) on top of the FSMI THEMIS ASI field of view (FOV) in **Figure 1A**, mapped to 110 km.

Poker Flat Incoherent Scatter Radar

In order to test how well our optical methods are able to determine the Hall conductance, we compared to the conductance determined from the Poker Flat Incoherent Scatter Radar (PFISR) altitude resolved electron density data. From this perspective the PFISR observations are considered a "truth" dataset, at least for the calculation of the Hall conductance. We plotted the PFISR location on top of the Fort Yukon (FYKN) THEMIS ASI FOV in **Figure 1B**. The PFISR electron density observations used in this study were estimated from received power measured using the Barker Coded pulses in the 121-beam "Grid11x11_11" mode on 16 February 2010. In this mode, the radar transmitted long-pulses and Barker codes, which are optimize for F region and lower E region observations, respectively, but it did not include alternating code pulses that are optimized for the whole E-region. This 121-beam mode uses a 130 μs, 13 baud Barker Code sampled at 5 μs, which provides electron density observations every 0.75 km with a range resolution of 1.5 km and achieves 48 samples per beam in 14.157 s. The electron density data was post-integrated to achieve ~30 s integration time. This mode does not provide a vertical beam, so the highest elevation angle beam, 89°, was used to compute conductance.

The Barker code is a pulse-compression code that only decodes properly when the correlation time of the target is longer than the time length of the pulse (e.g., [33]). ISR theory (e.g., [34]) predicts that the correlation time of ionospheric plasma depends strongly on the ion temperature resulting in a decrease of the correlation time as the ion temperature increases. For a 130 μs pulse and given the ion temperature observed by PFISR during the event under study, we expect the performance of the Barker code to significantly decrease for the top of the E region, e.g., above ~120 km. Above this altitude, the Barker code electron density observations will underestimate the electron

density, but the Barker code observations should well-cover the electron densities contributing to the Hall conductance. However, it can be shown that the Pedersen conductivity has a peak at the location where the ratio of the ion cyclotron frequency to ion neutral collision frequency equals one; this altitude typically occurs at ~120 km (e.g., Sangalli et al., 2009; Burchill et al., 2011; Oyama et al., 2012). Therefore, for this event in particular, a significant portion of the Pedersen conductivity is not well-resolved with the ISR observations, and the Barker code observations from PFISR would underestimate the Pedersen conductivities. Preliminary analysis (not shown) of the PFISR long pulse data shows that there is in fact greater density at altitudes above ~120 km that contribute to the Pedersen conductance. Unfortunately, the long pulse data has low range resolution (~72 km) and would require deconvolution (e.g., [35]) to be more useful for conductance calculations. We therefore focus only on the Hall conductance. This works to the strength of the ASI method, since the Hall conductance is essentially a function of Q when average energies exceed 5 keV [29]. Q is essentially a function of the blueline emission [22], which we show later is well-resolved with white light data.

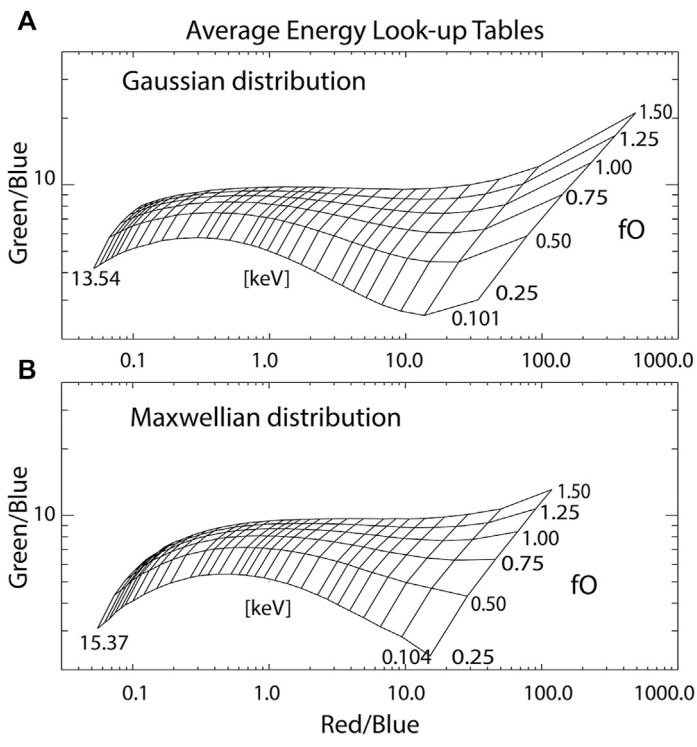
We calculated the Hall conductivity using **Eq. 10** from [36],

$$\sigma_H(z) \approx \frac{en_e(z)}{B\left[1 + \frac{\Omega_i^2}{\nu_{in}^2}\right]} \quad (1)$$

where $\Omega_i$corresponds to the ion cyclotron frequency, B corresponds to the magnetic field, e corresponds to the elementary charge, and z represents the altitude. The altitude resolved electron density, $n_e(z)$, is obtained using PFISR. The ion neutral collision frequency, ν_{in}, is calculated using equation 4.88 from Schunk and Nagy [37] for the non-resonant ion neutral collision frequencies and expressions in Table 4.5tbl45 of Schunk and Nagy [37] for the resonant ion-neutral collision frequencies. This formula has been implemented in the "flipchem" *Python* package. **Eq. 8** is approximately valid above 80 km altitude [36]. To obtain conductance, we perform an altitude integration of conductivity using a Simpson method integration routine. These formulas have been validated with previous results presented in Kaeppler et al. [9]. Results are discussed in *Results*.

Determining Energy Flux and Average Energy From Aurora Color Ratios

Following Hecht et al. [24,25], we used the B3C auroral electron transport code [27,28] to calculate lookup tables that allow the integrated energy flux (Q; erg cm^{-2} s^{-1}), the average energy ($\overline{E}$; keV), and the oxygen scaling factor (fO) to be derived from measurements of the green, red, and blue emissions (see **Figure 2**). Since the publication of Hecht et al. [24], the transport code has been updated especially with respect to the green line emission. Hence, the table reproduced below in



Gaussian [keV]	Maxwellian [keV]
0.101	0.104
0.242	0.262
0.364	0.391
0.482	0.525
0.592	0.656
0.704	0.787
0.814	0.921
0.924	1.06
1.14	1.34
1.37	1.62
1.57	1.91
1.794	2.15
2.08	2.39
2.281	2.67
2.50	2.9
2.731	3.18
3.14	3.67
3.593	4.15
4.040	4.69
4.424	5.14
5.52	6.37
6.531	7.56
7.62	8.70
8.584	9.81
9.44	10.86
10.30	11.61
11.21	12.61
11.847	13.75
12.74	14.33
13.54	15.37

FIGURE 2 | Plots of $\overline{E}$ and fO as a function of the green/blue vs. red/blue ratios for a MSIS90 atmosphere (daily Ap of 22, F10.7 of 85.5 and average F10.7 of 84.7 over Fort Smith, Canada) for electron precipitation characterized by **(A)** a Gaussian energy distribution with high and low energy tails [28] and **(B)** a Maxwellian energy distribution. Average energies ($\overline{E}$) are represented by the semi-vertical lines and are listed on the right for both distributions. The fO value is listed at the end of each semi-horizontal line.

Figure 2 differs somewhat from the corresponding **Figure 8** in the earlier publication. The B3C code solves the coupled set of linear Boltzmann equations for electrons, H^+, and H atom fluxes with full collisional processes [38] for a given set of cross sections and neutral densities for altitudes from 500 km down to 90 km. The B3C calculations are made with atmospheric neutral densities provided by the empirical MSIS90 model [39] that is parameterized by the geomagnetic Ap and solar flux F10.7 indices. (MSIS90 describes the neutral temperature and densities in Earth's atmosphere from ground to thermospheric heights.) The code accepts a choice of either a Maxwellian or a Gaussian incident precipitating electron flux spectrum and the associated Q and $\overline{E}$ for each geographic latitude and longitude of interest. We ran B3C for Gaussian and Maxwellian distributions to provide values for both discrete (Gaussian) and diffuse (Maxwellian) aurora. **Figure 2A** depicts the Gaussian distribution's average energies as a function of green to blue and red to blue ratios; **Figure 2B** depicts the Maxwellian version. A more complete discussion of the MSIS model is given in *Background and Overview* and *Determining Energy Flux and Average Energy From Aurora Color Ratios* of Hecht et al. [25].

The specific attributes of the model in this work are as follows. MSIS90 was run for 16 February 2010, the date of our event study. The location was chosen as Fort Smith, Canada at 60.0°N, 248.2°E, which is where our primary instrumentation were located. The F10.7 was 85.5, F10.7 average was 84.7, and the daily Ap was 22 (we also incorporated the other six Ap values for 16 February 2010). The reference O/N2 (an fO of 1) for a column density of 10^{17} (cm^{-2}) of N2, following Strickland et al. [40], is 0.53. This reference value allows a comparison of fO values for different model runs. This is a disturbed atmosphere for higher latitudes as would be suggested by comparing the reference O/N2 (0.53) with the quiet (0.91) and disturbed (0.45) values used in Hecht et al. [30]. **Figure 1** of Hecht et al. [30] suggests that uncertainties in the chosen model atmosphere will affect the derived $\overline{E}$ values. However, for the $\overline{E}$ values of interest here we would expect the derived values of $\overline{E}$ might be lower by 10–20% if the actual atmosphere were somewhat more disturbed than the chosen reference model. The exact bias on the derived $\overline{E}$ and fO values depends upon the area on the plot in **Figure 1** being considered.

To determine the average energies more precisely from the non-uniformly gridded look-up table, we first interpolated the 6 × 30 [fO × $\overline{E}$] look-up table values across log-log space to a 50 × 50 array, allowing for 50 red/blue values and 50 green/blue values, each with a corresponding $\overline{E}$ and fO value. Q was determined by dividing the 427.8 nm intensity (in Rayleighs) by the yield (Rayleigh/erg cm^{-2} s^{-1}), which is a function of $\overline{E}$ and fO [22] and is another output from the B3C run.

Converting White Light Intensities to Color Intensities

In order to use the methods described in *Determining Energy Flux and Average Energy From Aurora Color Ratios*, we had to first convert the ASI white light counts to red (630.0 nm), green (557.7 nm), and blue (427.8 nm) intensities. We accomplished this by fitting log-log linear functions *via* ordinary least-squares linear regression [41] to scatter plots of white light counts vs. green light intensity at the longitude line where the ASI data overlaps the NORSTAR MSP data at Fort Smith, NWT. We then fit scatter plots of the MSP blue light vs. green light, and the MSP red light vs. green light. We fit the data points from 07:00–10:00 UT on 16 February 2010.

Before developing the fits, we processed the ASI data by removing background light by subtracting a quiet-time snapshot from each station. The snapshot was chosen from a dark period immediately preceding any aurora observed in the ASI field of view, prior to the substorm. Starlight was removed by applying a median filter, since the starlight moves over time from the original dark sky snapshot. We ignored MSP data with <50 Rayleighs to avoid color ratio spikes that can occur when the denominator is near zero.

We performed the fitting in log-log space. In fitting the green to the white, we performed an ordinary least squares fit bisector (minimizing the sum of the squares of both white and green residuals [41]) to the median line over the white light range of 600–20,000 counts, to put the weight in the brighter aurora and because count levels below 600 show increased scatter and signal-to-noise ratio (see **Figure 3A**). (Above 20,000 counts had too few data points per bin.) **Figure 3A** plots the median and quartiles in yellow (using a white count bin size of 50 counts) and the fitted line in green. The quartiles (dashed yellow lines) are included to demonstrate the spread (uncertainty) in the data. We slightly altered the fit line below 600 counts so it would lay at or above the lower quartile, which still weights the higher counts but doesn't ignore the shift in median slope below 600 counts completely. When we tried shifting the fit below 600 counts so that it matched the median line, the result was that we frequently over-estimated the green light at low emissions, making it impossible to model low energies (since the green light median does not approach zero when the white light approaches zero).

Instead of fitting the white light counts to blue and red, we fit the blue and red intensities to the green intensity to calibrate colors using the same instrument (the MSP) at the exact same location (removing cross-instrument related errors). **Figure 3B** plots the blue vs. green fit in blue, and the median and quartiles in yellow (using a bin size of 50 R to calculate the medians and quartiles). We applied the three main methods for OLS described in Isobe et al. [41] that minimizes the sum of the squares of the green residuals, the blue residuals, and both green and blue, finding that minimizing the green residuals resulted in the smallest variance in both the slope and the *y*-intercept. There is no blue light below 225 R in the fitting because, as mentioned above, we did not include MSP data under 50 R and we converted the 470.9 nm intensity to 427.8 nm by multiplying the former by 4.5.

We next show the red vs. green fitting (**Figure 3C**). We split the fitting into three functions, described in **Eq. 5–7**. The largest deviation in the fit from the median is between the green line intensities 10^3–10^4 R, where the redline scatter is greatest. We initially tried fitting to the median line within 10^3–10^4 R by splitting the fitting even further, but discovered that because the slope is approximately zero in this range, the

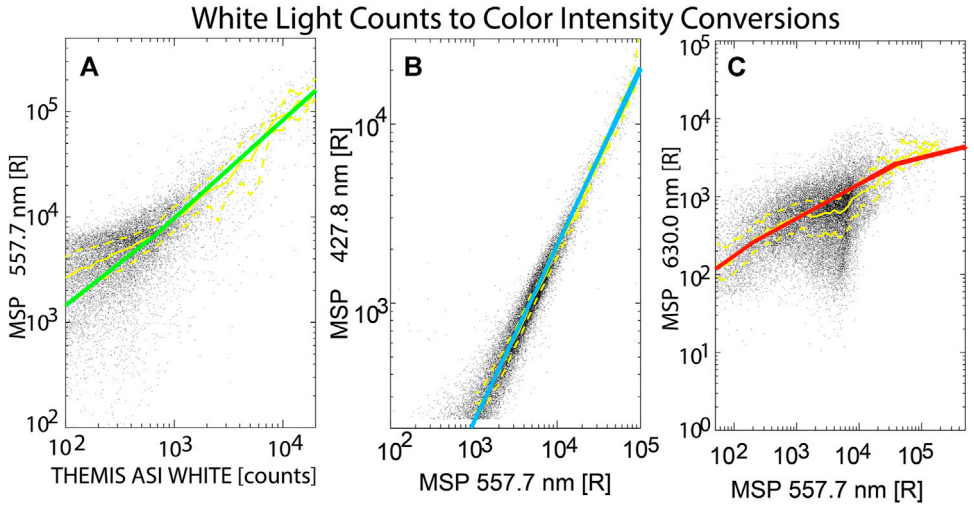


FIGURE 3 | (A) Scatter plot of green light intensity vs. white light counts from 07:00–10:00 UT. Solid yellow line shows median whereas dashed yellow lines show quartiles of green intensity for a given white light bin 50 counts wide. The green line represents the functional fit. **(B)** Scatter plot of blue light intensity vs. green light intensity. Solid yellow line shows median whereas dashed yellow lines show quartiles of blue intensity for a given green light bin 50 R wide. Blue line represents the functional fit. **(C)** Scatter plot of red light intensity vs. green light intensity. Solid yellow line shows median whereas dashed yellow lines show quartiles of red intensity for a given green light bin 50 R wide. Red line represents the functional fit.

red light did not vary according to what was seen in the MSPs during the active events. We therefore fit to the overall median line of the red vs. green scatterplot, which connected the two fits at lower and higher green light intensities (**Eq. 5**, **7**) with **Eq. 6**. The large scatter of the data points may be because different types or time of aurora had somewhat different color ratios. It is our future work to examine dependence of fitting on auroral types or time.

The conversion functions are as follows:

$$\text{Green 557.7 nm } [R] \text{ (where white} > 600 \text{ cts)} = 10^{\left(1.20+0.93 log_{10}\left(\text{white light cts}\right)\right)} \quad (2)$$

$$\text{Green 557.7 nm } [R] \text{ (where white} < 600 \text{ cts)} = 10^{\left(1.54+0.81 log_{10}\left(\text{white light cts}\right)\right)} \quad (3)$$

$$\text{Blue 427.8 nm } [R] = 10^{\left(-0.61+0.98 log_{10}\left(\text{green intensity}\right)\right)} \quad (4)$$

$$\text{Red 630.0 nm } [R] \text{ where green} > 4.e4 \text{ } [R] = 10^{\left(2.50+0.20 log_{10}\left(\text{green intensity}\right)\right)} \quad (5)$$

$$\text{Red 630.0 nm } [R] \text{ where } \left(\text{green} < 4.e4 \text{ [R] and green} > 200\right) = 10^{\left(1.40+0.44 log_{10}\left(\text{green intensity}\right)\right)} \quad (6)$$

$$\text{Red 630.0 nm } [R] \text{ where green} < 200 \text{ } [R] = 10^{\left(0.98+0.62 log_{10}\left(\text{green intensity}\right)\right)} \quad (7)$$

The variances in the slope and the y-intercept [41], respectively, in the log-log space are as follows:

Eq. 2: 0.000336 and 0.00589.

Eq. 3: 0.018 and 0.071 (when compared to the median line below 400 cts).

Eq. 4: 5.5e-6 and 7.6e-5.

Eq. 5: 0.0020 and 0.0521.

Eq. 6: 9.40e-5 and 0.0008.

Eq. 7: 0.0040 and 0.0185.

We note that in early iterations of our fitting process, we discovered that the red and green aurorae—especially at the time of the bright auroral arc seen in **Figure 4** from ~07:18–07:25 UT—were morphologically offset from one another, with the red mapping to lower latitudes than the green (see **Supplementary Figure S1**). The result was an unphysical situation in which the green overtook the red at a higher latitude and the red overtook the green at a lower latitude, and the artificial result was much higher average energies where the green arc mapped and much lower average energies where the red arc mapped. To align the 630.0 and 557.7 nm emissions, the effective altitude was found to be 160 km. This is below the expected emission altitude close to 200 km (e.g., Solomon, 1988; [42]). This effective altitude may appear lower than expected due to horizontal winds which are known to blow the redline emission (e.g., [43]). Ultimately, because the point of comparing red to green was to obtain an analytical relationship between intensities, we mapped the red to 160 km to match auroral morphologies and to build the scatterplot in **Figure 3C**.

The scatterplot in **Figure 3C** shows that the red and the green intensities are fairly uncorrelated, which may be due to several factors. First, the red to green ratio depends on both the average energy of the precipitating electron distribution and the energy flux. For Gaussian electron distributions that follow the Knight relation [44,45], Q and $\overline{E}$ should be broadly correlated; but for Maxwellians they are not [30,46,47]. Furthermore, the redline and greenline chemistries have different dependences on atomic oxygen density, which also decreases the correlation. This uncertainty in the average energy

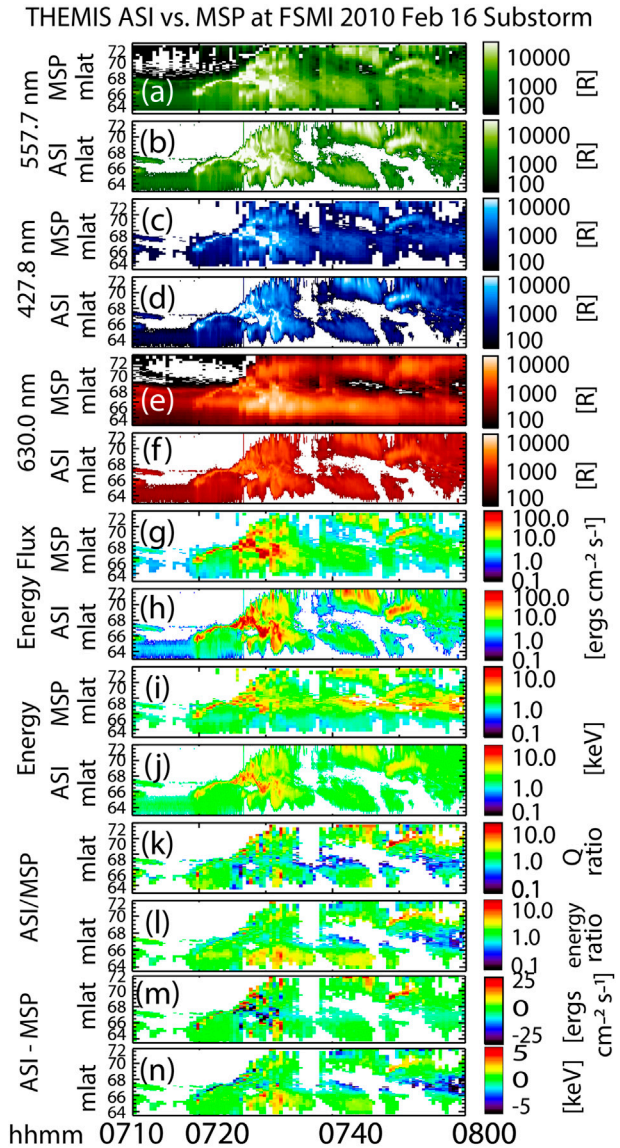


FIGURE 4 | Comparison between MSP data and THEMIS ASI data. Plots are keograms, which display magnetic latitude on the *y*-axis and time on the *x*-axis. The visual is therefore the auroral evolution along a single line of longitude over time. **(A)** MSP 557.7 nm intensity [R]. **(B)** ASI 557.7 nm intensity [R]. **(C)** MSP 427.8 nm intensity [R]. **(D)** ASI 427.8 nm intensity [R]. **(E)** MSP 630.0 nm intensity [R]. **(F)** ASI 630.0 nm intensity [R]. **(G)** MSP determined energy flux using color ratios as input to the B3C-generated look-up table described in *Background and Overview*. **(H)** ASI determined energy flux using color ratios as input to the B3C-generated look-up table described in *Background and Overview*. **(I)** MSP-determined energy using color ratios as input to the B3C-generated look-up table described in section 2.1. **(J)** ASI-determined energy using color ratios as input to the B3C-generated look-up table described in *Background and Overview*. **(K)** The ratio between ASI (interpolated) and MSP energy fluxes, or panel h divided by panel g. **(L)** The ratio between ASI (interpolated) and MSP average energies, or panel j divided by panel i. **(M)** The difference between ASI (interpolated) and MSP energy fluxes, or panel h minus panel g. **(N)** The difference between ASI (interpolated) and MSP average energies, or panel j minus panel i.

estimation could be explored further in future studies by defining when and where discrete aurora occur in order to build a functional relationship between green and red only during discrete auroral times. **Figure 4**, discussed below, as well as **Supplementary Figures S3, S4** do however show the energy comparison between MSP and ASI datasets to be relatively consistent. See also **Table 1** and **Supplementary Tables S1, S2** which quantify the differences between ASI and MSP derived average energies, along with other parameters.

Figure 4 plots the MSP data (**Figures 4A,C,E**) next to the THEMIS ASI-derived auroral colors (**Figures 4B,D,F**) for comparison and validation. Additionally, we determined the energy flux and average energy using the methods described in *Background and Overview* with the MSP color ratios as input (**Figures 4G,I**) and the ASI color ratios as input (**Figures 3H,J**). Visually the comparison is good, but to quantify the differences we interpolated the THEMIS-derived products to match the MSP location and cadence and calculated the ratio and the difference. The mean, standard deviation, median, and upper and lower quartiles of the ratios and the differences are compiled in **Table 1** for both the **Figure 4** time window (07:10–08:00 UT) and the full time window used for the calibration (07:00–10:00 UT). We present the ratios, the differences, and a similar table that compares the ASI and MSP color intensities in the supplemental materials (**Supplementary Figure S3** and **Supplementary Table S1**). Finally, we also present the percent differences between the ASI and MSP measured and derived quantities in **Supplementary Figure S4** and **Supplementary Figure S2**.

Table 1 tells us, for example, that on average, the ASI energy flux underestimates the MSP energy flux by 1.1 erg cm^{-2} s^{-1} with a standard deviation of 12.6 erg cm^{-2} s^{-1} for the **Figure 4** timeframe (07:10–08:00). For the entire calibration time (07:00–10:00), the ASI energy flux underestimates the MSP energy flux by only 0.6 erg cm^{-2} s^{-1} on average with a standard deviation of 7.2 erg cm^{-2} s^{-1}. **Table 1** also tells us that the average of the ratio of average energies is 1.0, with a median of 0.9 and upper and lower quartiles of 1.2 and 0.6, respectively, for the **Figure 4** timeframe. These and the rest of **Table 1** indicate the level of uncertainty assuming the MSP data as "truth". The very slight underestimation in the differences may be due to the fact we did not remove the <600 R greenline data points from the comparison which were not heavily weighted in **Figure 3** for the calibrations. As is shown in **Supplementary Figure S2**, for the full calibration time (07:00–10:00 UT), the percent differences are: for Q, 47.5 ±36.1% with median 39.6% and quartiles 18.4 and 68.6%; for $\overline{E}$, 46.0 ± 38.2% with median 35.3% and quartiles 15.8 and 67.6%. We also present the green, blue, and red percent differences in the **Supplementary Material**.

With these relationships to estimate the color ratios, we determined the energy flux and average energy for all pixels that comprise the ASI mosaic. The energy flux and average energy were then interpolated to a 400 × 400 uniform geographic grid with 0.1° latitude and 0.4° longitude resolution (see **Figure 5** for

TABLE 1 | The mean, standard deviation, median, and upper and lower quartiles of the ratios and the differences between ASI- and MSP-determined energy flux (Q) and average energy ($\bar{E}$). The first four lines are for the Figure 4 time window (07:10–08:00 UT). The bottom four lines are for the full time window used for the calibration (07:00–10:00 UT).

	Mean	Std Dev	Median	Lower quartile	Upper quartile
07:10–08:00 UT					
Q_{ASI}-Q_{MSP} [erg cm^{-2} s^{-1}]	−1.1	12.6	−0.7	−2.8	0.6
$\bar{E}_{ASI}$-$\bar{E}_{MSP}$ [keV]	−0.5	1.8	−0.2	−1.1	0.4
Q_{ASI}/Q_{MSP}	1.1	1.2	0.8	0.5	1.2
$\bar{E}_{ASI}/\bar{E}_{MSP}$	1.0	0.6	0.9	0.6	1.2
07:00–10:00 UT					
Q_{ASI}-Q_{MSP} [erg cm^{-2} s^{-1}]	−0.6	7.2	−0.6	−2.0	0.7
$\bar{E}_{ASI}$-$\bar{E}_{MSP}$ [keV]	−1.1	2.2	−0.5	−1.6	0.1
Q_{ASI}/Q_{MSP}	1.0	0.9	0.8	0.6	1.2
$\bar{E}_{ASI}/\bar{E}_{MSP}$	0.8	0.5	0.8	0.5	1.1

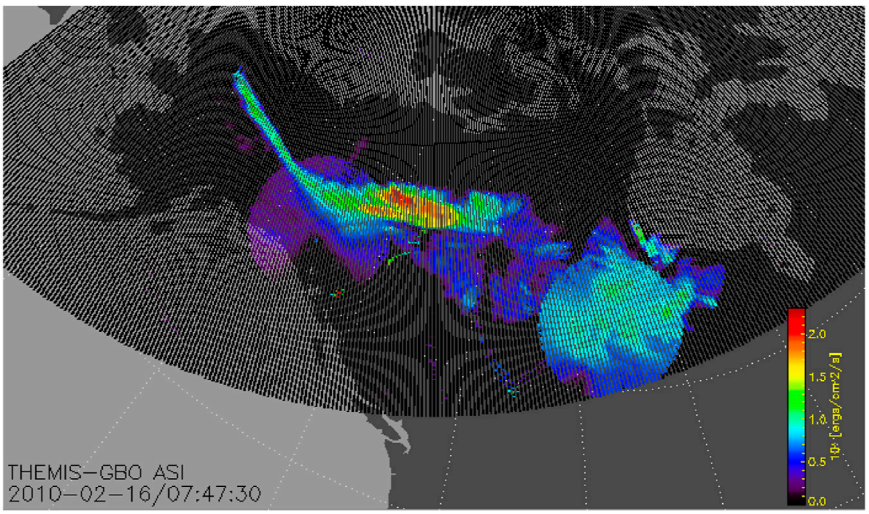


FIGURE 5 | Example of the energy flux saved into the 400 × 400 grid. Note that the plot energy flux (color) is in log space, with energy fluxes ranging from 1–200 ergs cm^{-2} s^{-1}).

an example). Any points at elevation angles lower than 10° were dropped

We first applied 2D median filtering with a window size of 3 pixels in both directions. Where more than one ASI fields of view overlap, the pixel with the brightest value usually comes from the imager with better viewing conditions (e.g., higher elevation angle and clearer sky conditions), which are more reliable. We therefore assigned each of the 400 × 400 grid points the maximum energy flux (or maximum energy) value found in any pixel that fell within ±0.05° latitude and ±0.2° longitude of the grid point. The uniform grid system is much simpler than the imager-dependent coordinates that overlap with surrounding imagers.

The data in the uniform grid system is used to calculate total energy flux and average energy across the imager coverage (see *Results*). Conductance maps are also obtained. Data in this coordinate system are also used to provide data to users. (Note that this grid could be altered to a different desired resolution, e.g., 500 × 500 or 300 × 300.)

Determining the Hall Conductance

We calculated the height-integrated Hall conductance from the incident precipitating electron flux energy spectrum using the B3C auroral transport code for the same F10.7 and Ap values used in *Determining Energy Flux and Average Energy From Aurora Color Ratios*. The code was run for either a Maxwellian or a Gaussian incident precipitating electron flux spectrum with an associated integrated energy flux and an average energy for each geographic latitude and longitude of interest. A Maxwellian distribution is representative of diffuse auroral electron precipitation whereas a Gaussian distribution is descriptive of an accelerated distribution associated with discrete auroral precipitation [48].

Similar to our methods to obtain energy flux and energy in *Determining Energy Flux and Average Energy From Aurora Color Ratios*, we used B3C to create a look-up table of conductances given various inputs. The B3C height-integrated Hall conductance was calculated for an incident precipitating electron Maxwellian distribution with combinations of average energies of 0.173, 0.875, 1.81, 3.49, 8.27, 15.7 and 21.9 keV and

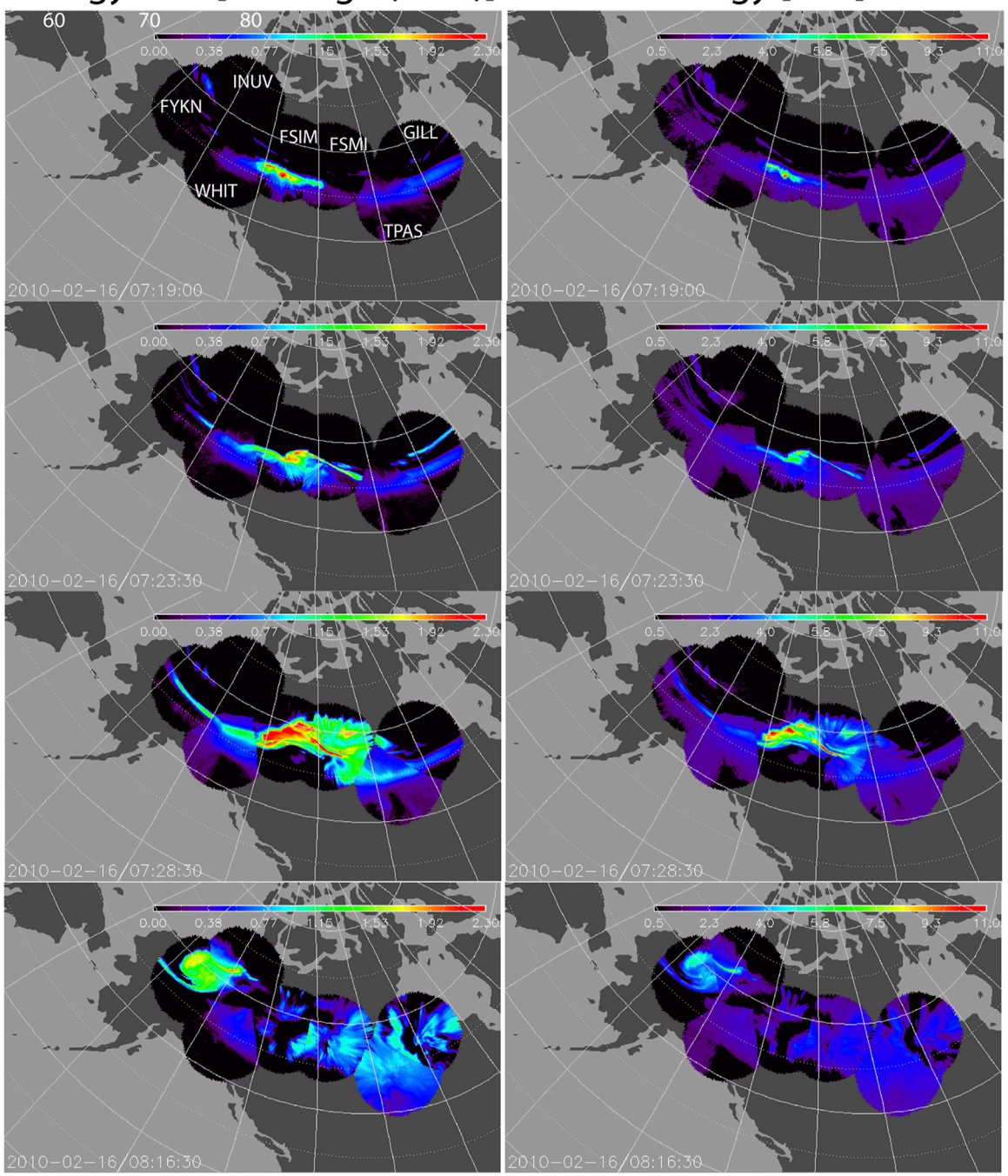


FIGURE 6 | Snapshots in time shortly after substorm onset through substorm poleward expansion and westward traveling surge. **Left column:** Energy flux (plotted logarithmically) from 1–200 erg cm^{-2} s^{-1}. **Right column:** Average energy (plotted linearly) from 0.5–11 keV. Magnetic latitudes and station names are marked in the first panel.

integrated electron energy flux of 1, 10, and 100 erg cm^{-2} s^{-1}. Similarly, the B3C height-integrated conductances are calculated for an incident precipitating electron Gaussian distribution with combinations of average energies of 0.101, 0.477, 0.924, 1.79, 4.42, 8.58, and 16.7 keV and integrated electron energy flux of 1, 10, and 100 erg cm^{-2} s^{-1}. The model was run for these various energy fluxes and energies at four different locations across Canada and Alaska: (56.2428°, 280.429°), (55.4554°, 255.580°), (61.3852°, 232.96°), and (65.2333°, 211.044°) in geographic latitude and longitude, respectively.

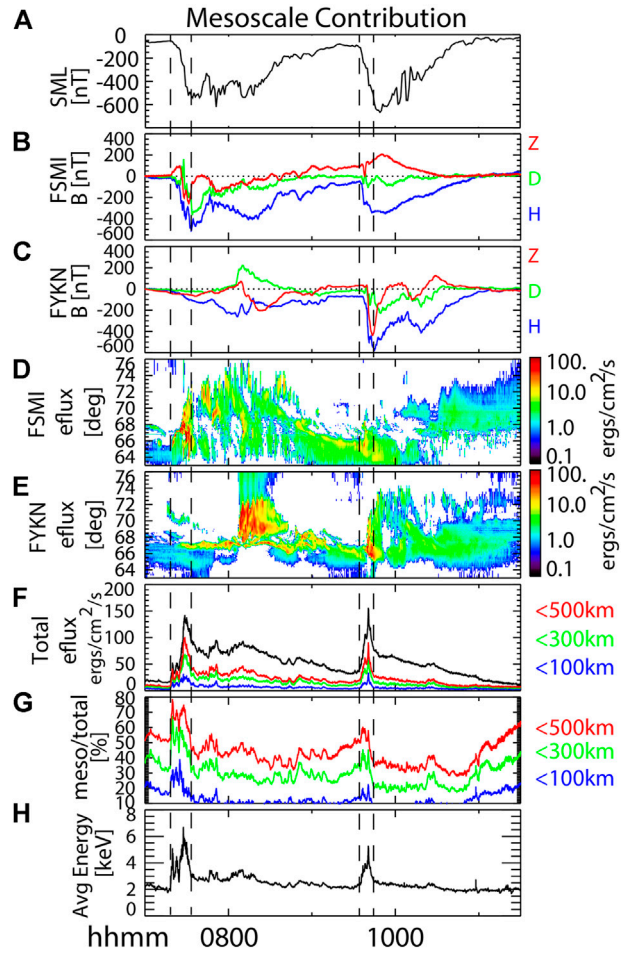


FIGURE 7 | (A) SML index. **(B)** Magnetometer data from Fort Smith, near the first substorm onset. **(C)** Magnetometer data from Fort Yukon, which was closer to the second substorm's onset. **(D)** Keogram of Fort Smith energy flux. **(E)** Keogram of Fort Yukon energy flux. **(F)** Total energy flux observed by the ASI mosaic plotted in black. Total energy flux contributed by scale sizes under 500 km, 300 and 100 km plotted in red, green, and blue, respectively. **(G)** Percent of the total energy flux contributed by scale sizes under 500 km, 300 km, and 100 km plotted in red, green, and blue, respectively. **(H)** Average of the average energy observed over the ASI mosaic. The vertical dashed lines mark the start of the sharp increase in total energy flux and the end of the sharp decrease in total energy flux that occurs during the substorm expansion phase for each substorm (07:18 and 07:33:20 for the first, 09:34:52 and 09:45 UT for the second).

The Hall conductance was then determined across the 400 × 400 ASI grid by interpolating the look-up table to the given parameters. The energy flux and energies in the B3C look-up table that correspond to a conductance value were treated as a uniform 2D grid that could be interpolated to each observed energy flux and energy stored in the ASI grid. Next, the geographic location in the look-up table closest to the given ASI point (found using the haversine between two geographic points) was used.

Although conductance is computed rigorously with the B3C auroral transport code, for contextual purposes we also calculated the Hall (Σ_H) conductance with the widely-used Robinson et al. (1987) formulae, where Σ_P is the Pedersen conductance:

$$\Sigma_P = \frac{40\overline{E}}{16 + \overline{E}^2} Q_E^{\frac{1}{2}} \tag{8}$$

$$\frac{\Sigma_H}{\Sigma_P} = 0.45\overline{E}^{0.85} \tag{9}$$

In this case, we simply used the energy flux and average energy value at each of the 400 × 400 grid points as inputs to the formulae. We did this for both the Gaussian and Maxwellian versions, but recognize that the Robinson formulae were intended to provide simple approximations of the conductance.

RESULTS

Figure 6 displays snapshots of the energy flux and average energies determined by the THEMIS ASIs throughout the first substorm lasting from ~07:18–09:30 UT. The values are from the Gaussian distribution; we include the Maxwellian version in the supplemental material as **Supplementary Figure S5**. Movies of the substorm are also included in the supplemental material (**Supplementary Movies S1–S4**). The ASIs capture the substorm onset, expansion, and westward-traveling surge as the vortical auroral form that has elevated energy flux and propagated westward. Note the relatively good agreement in arc location, energy flux, and energy across different ASI FOVs, suggesting overall the mapping is good. We also note that the strongest energy fluxes and average energies come in mesoscales during the expansion phase (e.g., 07:28:30 UT).

We next interpolated the data onto the 400 × 400 pixel grid to determine the total energy flux deposited in the ASI FOV (above 10° elevation) as well as the average of the average energy. The total energy flux at any given point in time was found by integrating the grid points over the 2D area:

$$Q_{Total} = \sum_{pixel_1}^{pixel_n} ((Q_n)(Area_n)) \tag{10}$$

We ran the ASI grid through a 2D median filter to determine what amount of the total energy flux was deposited as mesoscale auroral forms. For example, to determine the amount of energy flux contributed by scale sizes 500 km and less, for each pixel we found the median across 500 km in 2D (both latitude and longitude directions). We then found the total for that scale size by applying **Eq. 10** to the median filtered data, and subtracted that total from the total energy flux:

$$Q_{Total}(< 500\ km) = \sum_{pixel_1}^{pixel_n} ((Q_n)(Area_n)) - \sum_{pixel_1}^{pixel_n} ((Q_n)(Area_n))_{median\ 500km} \tag{11}$$

We weighted the average energies by the energy flux to perform a weighted average of the average energies:

$$\overline{E_{avg}} = \sum_{pixel_1}^{pixel_n} ((Q_n)(energy_n)) \Big/ \sum_{pixel_1}^{pixel_n} Q_n \tag{12}$$

This puts emphasis on the energies that comprise the aurora.

Figure 7 displays these results alongside the magnetograms (**Figures 7B,C**) and keograms (**Figures 7D,E**) from the two selected stations that saw the substorm onsets: FSMI and

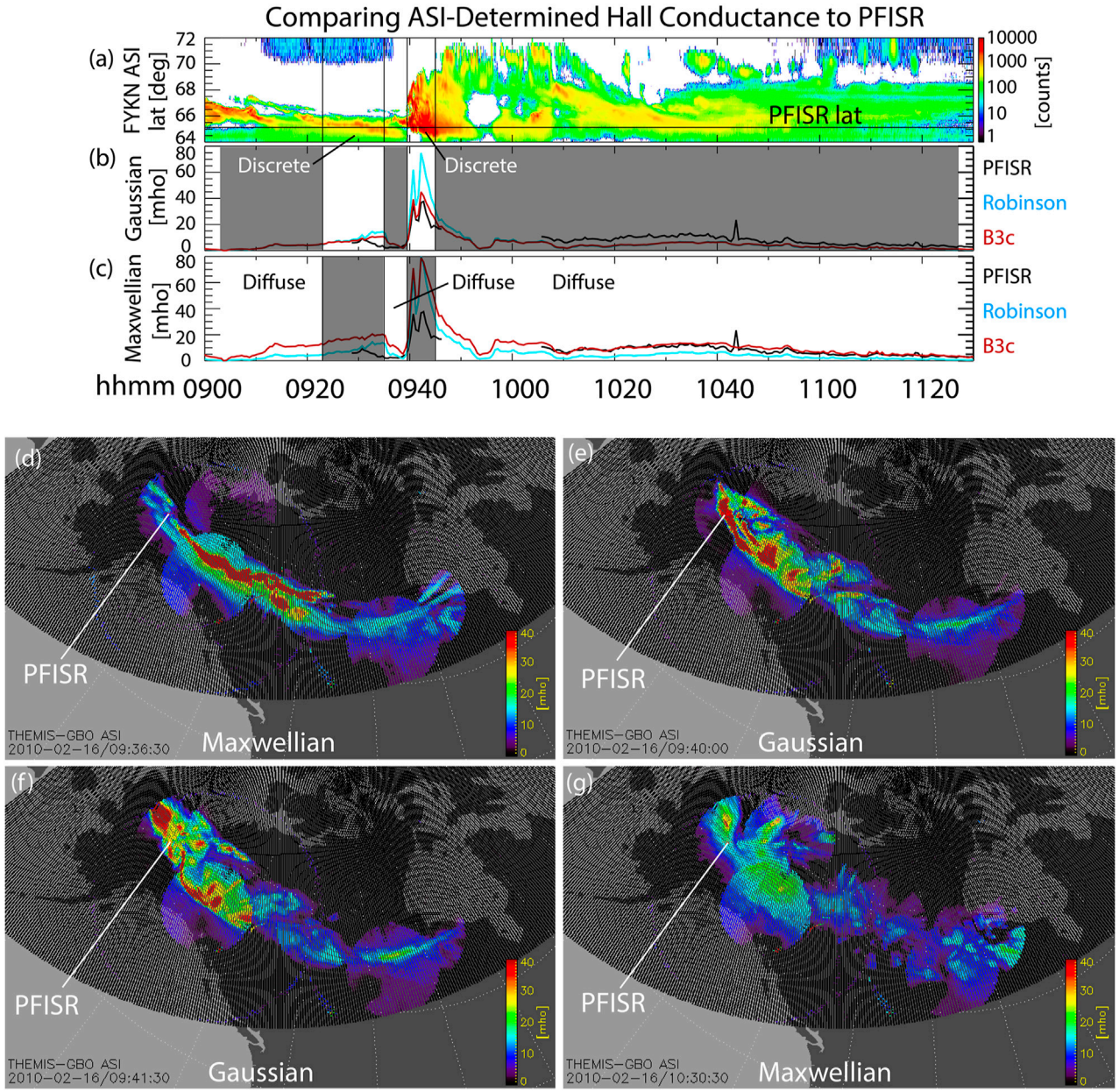


FIGURE 8 | Comparing the ASI-determined Hall conductance to PFISR-determined Hall conductance. The discrete and diffuse aurora are marked in panels a–c. The Gaussian distribution was used to determine the conductance related to discrete aurora, and the Maxwellian distribution was used for the diffuse aurora. **(A)** The FYKN white light intensity keogram at the PFISR longitude. The PFISR latitude line is drawn horizontally. **(B)** Hall conductance using the Gaussian energy fluxes and average energies from the ASI as input to B3C (red) and Robinson formula (blue) alongside the PFISR-determined result (black). **(C)** Hall conductance using the Maxwellian energy fluxes and average energies from the ASI as input to B3C (red) and Robinson formula (blue) alongside the PFISR-determined result (black). **(D)** 2D snapshot of Hall conductance assuming a Maxwellian distribution at 09:36:30 UT. **(E)** 2D snapshot of Hall conductance assuming a Gaussian distribution at 09:40:00. **(F)** 2D snapshot of Hall conductance assuming a Gaussian distribution at 09:41:30. **(G)** 2D snapshot of Hall conductance assuming a Maxwellian distribution at 10:30:30 UT.

FYKN. **Figure 7A** displays the SML index [49], which is a measure of the global substorm evolution and strength. The first substorm starts at ~07:18 UT as a bright, narrow arc that propagates poleward across FSMI's field of view until the westward traveling surge moves over the keogram longitude (at ~7:30 UT), showing auroral expansion both poleward and equatorward. The tertiary expansion is seen in **Figure 7E** as the westward traveling surge brightens and travels over FYKN after 08:00 UT. A bright, latitudinally narrow arc forms at ~66° magnetic latitude (mlat) during the recovery phase and moves equatorward (seen in **Figure 7D** from ~08:45–09:33 UT) until the second substorm onset at ~09:33 UT, seen in **Figure 7E**. **Figure 7F** displays the total energy flux deposited within all available THEMIS ASIs in black, the total energy flux from scale

TABLE 2 | The mean and standard deviations, median and quartiles of the differences, ratios, and percent differences between the various B3C informed by ASI (ASIB3C) and PFISR results.

	Mean	Std Dev	Median	Lower quartile	Upper quartile
Gaussian Distribution (Discrete)					
Difference (ASI_{B3C}-PFISR) [mho]	4.5	3.1	4.7	1.6	7.2
Ratio (ASI_{B3C}/PFISR)	1.5	0.7	1.3	1.2	1.6
Percent Difference [%]	34.8	32.0	24.2	17.7	47.1
Maxwellian Distribution (Diffuse)					
Difference (ASI_{B3C}-PFISR) [mho]	1.6	3.4	1.0	0.3	2.1
Ratio (ASI_{B3C}/PFISR)	1.3	0.9	1.2	1.0	1.3
Percent Difference [%]	23.6	26.2	18.1	8.4	27.2

sizes under 500 km, 300 km, and 100 km in red, green, and blue, respectively. **Figure 7G** displays the percentage of the total energy flux that is contributed by those three scale sizes. **Figure 7H** displays the average of the average energy.

The main take-aways from **Figure 7** are that the mesoscales (<500 km scale sizes) are important in the deposition of energy flux to the ionosphere, particularly so immediately after substorm onset during the rapid expansion phase where they contribute up to ~80 and ~60% of the total energy flux in substorms 1 and 2, respectively (**Figure 7G**, at 07:20 UT and 09:36–09:38). Even the <100 km scale sizes, which only contribute ~10% of the energy flux throughout the substorm on average, contribute >30% of the energy flux during the rapid expansion phase. Because the difference between the <500 km and <300 km total energy flux is roughly 10%, whereas the difference between the <100 km and <300 km total energy flux is roughly 20%, we can also surmise that more of the energy flux is deposited between 100–300 km scale sizes than 300–500 km scale sizes. The rapid expansion phase is also the most energetic, as the average of the average energy spikes then for both substorms at ~6.75 and ~5 keV, respectively (**Figure 7H**). The maximum average energy is of course, higher. The mesoscale contribution begins to decrease towards the end of the expansion phase, dropping significantly by the beginning of the recovery phase. From **Figure 7** and Movies 1-2mmc1-2, we see this is a combination of the mesoscale auroral forms evolving into larger-scale auroras as well as becoming less intense.

These results are related to those presented by Partamies et al. [18], who studied the substorm evolution of auroral arc structures. They found that auroral arcs occur in all conditions as the main element of the aurora, leading to the expectation that mesoscale auroral forms should play an important role in the total precipitating energy flux. They also found that auroral arcs occupy 8.7% of the total growth phase duration, 13.2% of the total expansion phase duration, and 9.2% of the total recovery phase duration. These percentages indicate the prevalence of arcs during the expansion phase—which is when we found the most contribution from mesoscales to the total energy flux. Partamies et al. [50] showed that the average auroral emission intensity is lower during the growth phases of substorms than the bright arcs during the expansion phases, which also aligns with our results showing the total energy flux is lower during the growth phase than the expansion phase.

Auroral arcs in the form of longitudinally localized poleward boundary intensifications and streamers have been correlated to mesoscale plasma sheet fast flows (on the scale of a few R_E) (e.g., [51]; [52-53]; [54–56]). These mesoscale fast flows were shown to play a large role in magnetotail magnetic flux transport [57,58], and now look to also play an important role in providing the precipitated energy flux during substorms. Further analysis to determine the nature of the mesoscale auroral forms—whether or not they are streamers—could be done to investigate how much of the mesoscale contribution to precipitated energy flux is due to these mesoscale plasma sheet fast flows.

We also see that the peak total energy flux of each substorm occurs in the middle of the rapid expansion phase, immediately after the peak in mesoscale contribution (**Figure 7F**). The vertical dashed lines mark the start of the sharp increase in total energy flux and the end of the sharp decrease in total energy flux that occurs during the substorm expansion phase for each substorm (07:18 and 07:33:20 for the first, 09:34:52 and 09:45 UT for the second). Note that these are coincident with the sharp increase and decrease of the mesoscale contribution. They are also approximately coincident with the substorm onset and the end of the substorm expansion phase, defined by the SML index. The SML index also shows that the first substorm had two more expansions before the final recovery, during each of which there was an increase in total energy flux as well as an increase in mesoscale contribution.

Analyzing the **Supplementary Movie S1**, the increased mesoscale contribution at the end of the first substorm (~09:18–09:34:42 UT) appears to be due to the latitudinally narrow, pre-onset arc that formed and moved equatorward prior to the second substorm. The increased mesoscale contribution at the end of the second substorm (~10:51 UT onward) appears to be from the aurora breaking up and the formation of pulsating aurora (e.g., [59]), a common occurrence after substorms due to whistler mode chorus waves in the magnetosphere.

Figure 8 plots the Hall conductance as determined by PFISR, B3C with ASI inputs, and Robinson formula with ASI inputs (methods described in *Poker Flat Incoherent Scatter Radar*and *Determining the Hall Conductance*). We used the FYKN ASI to determine when a discrete auroral arc was over PFISR, during which times we used the Gaussian distribution to determine average energy and energy flux. For other times, we used the Maxwellian distribution. **Figure 8A** plots the FYKN ASI keogram at the PFISR longitude. The horizontal line represents the PFISR latitude. Mapping the aurora to 110 km, the PFISR measurements lie somewhere between a 31–35° elevation angle in the FYKN field

of view. Note that there were gaps in the PFISR data, which is when the black line in **Figures 8B,C** disappears. **Figures 8D–G** illustrates the Hall conductance from B3C plotted in the 400 × 400 grid with the PFISR location marked. **Figure 8D** (09:36:30 UT) is a 2D snapshot of the Hall conductance assuming a Maxwellian distribution, during the time prior to the large increase in conductance due to the bright discrete auroral arc seen in **Figure 8F**. **Figures 8F,G** (09:40 and 09:41:30 UT) plot the Hall conductance assuming a Gaussian distribution while the discrete auroral arc is overhead. We see a decrease in conductance when the arc moves slightly away from PFISR in **Figure 8G**. **Figure 8H** (10:30:30 UT) again plots the Hall conductance assuming a Maxwellian distribution after the diffuse aurora has returned.

Because PFISR measurements are at a lower elevation angle within the FYKN ASI FOV, there is a greater likelihood of introducing error. First, it is possible that an arc maps to a higher or lower altitude than 110 km, in which case a narrow arc above PFISR could be incorrectly mapped in latitude. However, comparing the ASI-informed conductance with the PFISR-determined conductance, we see that the ASIs reproduce relative variations in conductance that is derived from PFISR very well. The fact that the conductances vary at the same time for both the ASI- and PFISR-informed values suggests the mapping is not a primary issue in this case.

Additionally, the ASI is not looking up the magnetic field line at that latitude, whereas PFISR and B3C are integrating along the field line. The result is that not all of the auroral intensity that is actually above PFISR will be mapped to the PFISR latitude and some intensity that is not above PFISR could be mapped to the PFISR latitude, which can result in an under- or over-estimation of the average energy and/or energy flux by the ASI. However, we see that the B3C model informed by the ASIs does exceptionally well at supplying the Hall conductance magnitudes, as it closely follows the PFISR Hall conductance during both discrete and diffuse aurora. Therefore, although the above cautions remain, in this case the methods do well. In contrast, the ASI-informed Robinson formula overestimated the Hall conductance during discrete aurora and underestimated during diffuse aurora. This highlights the improvements physics-based atmospheric modeling provides.

We list the mean and standard deviations, median and quartiles of the differences, ratios, and percent differences between the various B3C informed by ASI (ASI_{B3C}) and PFISR results in **Table 2**. Plots of the percent differences over time are included in **Supplementary Figure S6**. The diffuse aurora (Maxwellian) has a better match than the discrete, which is expected because discrete aurora is more variable and comes on smaller scale sizes, which are more likely to be mapped less precisely for the purposes of exact comparison between datasets. For the discrete aurora, the median percent difference is 24.2% whereas for the diffuse aurora the median percent difference is 18.1%.

SUMMARY

This paper presented a new methodology to utilize the mosaic of THEMIS all-sky-imagers to study auroral precipitation in 2D over time, estimating parameters such as energy flux, average energy, and Hall conductance. Using two consecutive substorms for a case study, results demonstrated the importance of mesoscale auroral forms (10 s km to 500 km scale sizes) to the overall energy flux deposition to the ionosphere, particularly during the initial expansion phase immediately after onset. Roughly 60–80% of the total energy flux immediately after onset, and ~30–55% thereafter, is from mesoscale auroral forms. These results confirm what we may have hypothesized from the Partamies et al. [18,50] observations, since they had found that auroral arcs occupy the greatest percentage of the substorm expansion phase duration (contrasted with the growth and recovery phases) and are brighter than during the growth phase.

Because prior work highly relied upon statistics or single ASIs, the mesoscale contribution has not been so well-resolved before over a continental scale, especially for specific case studies. The results indicate the importance of including mesoscale auroral forms in global models to appropriately capture the related physics. Additionally, the paper demonstrated the 2D time series data product that can be provided to modelers when ASI data are available, allowing for case-specific data-informed modeling.

The methods showed a good comparison between the calibrated ASI data and the MSP data, as were quantified in **Table 1** and **Supplementary Tables S1, S2**. As expected, the greatest scatter is in 630.0 nm wavelength. As a future work, the redline ASI cameras that are currently coming online as part of the TREx array of ASIs could be used to specify the 630.0 nm wavelength more accurately (https://www.ucalgary.ca/aurora/projects/trex). Comparing and/or calibrating to DMSP energy fluxes and average energies would also provide additional information on the uncertainties and/or improve our estimates. We do point out as mentioned above that the inversion method in Janhunen [13] found little difference in the energy flux results when the red aurora was included, since the energy flux is mostly related to the blue intensity [22,30], which is a close function of the green intensity (**Figure 3**).

The Hall conductance was well-captured by the B3C auroral transport code, informed by ASI energy fluxes and average energies, when compared to PFISR-determined Hall conductance. The ASI-informed Robinson formula overestimated the Hall conductance during discrete aurora and underestimated during diffuse aurora. As expected, the conductance increased during the intense discrete aurora. These values are not well-constrained in current models that rely on global, diffuse aurora as precipitation input only. These data could therefore be useful to modelers who want to include the larger conductance values that result from mesoscale, discrete aurora. As a future work, a date should be selected when PFISR can provide alternating code observations of the whole E region for a better comparison, and also to include the Pedersen conductance.

DATA AVAILABILITY STATEMENT

Publicly available datasets were analyzed in this study. This data can be found here: THEMIS ASI: themis.ssl.berkeley.edu. NORSTAR MSP: https://data-portal.phys.ucalgary.ca/msp/

summary_plots; http://data.phys.ucalgary.ca/sort_by_project/other/publication_datasets/Gabrielse2021/. PFISR: http://isr.sri.com/madrigal/. SML index: supermag.jhuapl.edu.

AUTHOR CONTRIBUTIONS

CG led the work, updated techniques developed by TN, performed the analyses, and wrote the paper. TN devised the original ASI-MSP techniques and advised CG on the details. MC ran the B3C code to provide the conductance look-up table for CG to use with ASI inputs, and described the methods in the text. JHH ran the B3C code to provide Figure 1 and the look-up table to determine energy fluxes and average energies from color ratios, as well as the associated text in the manuscript. SK calculated the conductance from the PFISR data and contributed to writing the PFISR section. DMG provided processed MSP data and text describing the instruments. AR provided processed PFISR data and text describing the instrument and dataset. LL contributed discussions about mesoscale auroral phenomena. YD contributed discussions about mesoscale phenomena in the ionosphere and insights on what parameters are important to specify. ED runs THEMIS-ASI in Canada, and contributed discussions on our methodology and use of the MSP data. JE manages the B3C code and gives permission and guidance for its use. All co-authors contributed comments, edits, and text to the manuscript.

FUNDING

The work in this paper was gratefully funded by NASA grants 80NSSC20K0725, 80NSSC18K0657, 80NSSC20K0604, 80NSSC20K0195, and 80NSSC20K1786, AFOSR Grant FA9559-16-1-0364, and NSF grants AGS 1602862 and AGS-1907698. The THEMIS mission is supported by NASA contract NAS5-02099, NSF grant AGS-1004736, and CSA contract 9F007-046101. This material is based upon work supported by the Poker Flat Incoherent Scatter Radar which is a major facility funded by the National Science Foundation through cooperative agreement AGS-1840962 to SRI International.

ACKNOWLEDGMENTS

We gratefully acknowledge the SuperMAG collaborators (https://supermag.jhuapl.edu/info/?page=acknowledgement). The ASI, PFISR and SuperMAG data are available at themis.ssl.berkeley.edu, isr.sri.com/madrigal, and supermag.jhuapl.edu.

SUPPLEMENTARY MATERIAL

The Supplementary Material for this article can be found online at: https://www.frontiersin.org/articles/10.3389/fphy.2021.744298/full#supplementary-material

REFERENCES

1. Newell PT, Sotirelis T, and Wing S. Diffuse, Monoenergetic, and Broadband aurora: The Global Precipitation Budget. *J Geophys Res* (2009) 114:a–n. doi:10.1029/2009JA014326
2. Newell PT, Sotirelis T, and Wing S. Seasonal Variations in Diffuse, Monoenergetic, and Broadband aurora. *J Geophys Res* (2010) 115:a–n. doi:10.1029/2009ja014805
3. Newell PT, Sotirelis T, Liou K, Lee AR, Wing S, Green J, et al. Predictive Ability of Four Auroral Precipitation Models as Evaluated Using Polar UVI Global Images. *Space Weather* (2010) 8:a–n. doi:10.1029/2010sw000604
4. Newell PT, Lee AR, Liou K, Ohtani S-I, Sotirelis T, and Wing S. Substorm Cycle Dependence of Various Types of aurora. *J Geophys Res* (2010) 115:a–n. doi:10.1029/2010ja015331
5. Zhu Q, Deng Y, Maute A, Kilcommons LM, Knipp DJ, and Hairston M. ASHLEY: A New Empirical Model for the High-Latitude Electron Precipitation and Electric Field. *Space Weather* (2021) 19:e2020SW002671. doi:10.1029/2020SW002671
6. McGranaghan RM, Ziegler J, Bloch T, Hatch S, Camporeale E, Lynch K, et al. Toward a Next Generation Particle Precipitation Model: Mesoscale Prediction through Machine Learning (A Case Study and Framework for Progress). *Space Weather* (2021) 19:e2020SW002684. doi:10.1029/2020SW00268
7. Deng Y, Heelis R, Lyons LR, Nishimura Y, and Gabrielse C. Impact of Flow Bursts in the Auroral Zone on the Ionosphere and Thermosphere. *J Geophys Res Space Phys* (2019) 124:10459–67. doi:10.1029/2019JA026755
8. Sheng C, Deng Y, Gabrielse C, Lyons LR, Nishimura Y, Heelis RA, et al. Sensitivity of Upper Atmosphere to Different Characteristics of Flow Bursts in the Auroral Zone, Submitted to. *J Geophys Res* ().
9. Kaeppler SR, Hampton DL, Nicolls MJ, Strømme A, Solomon SC, Hecht JH, et al. An Investigation Comparing Ground-based Techniques that Quantify Auroral Electron Flux and Conductanceflux and Conductance. *J Geophys Res Space Phys* (2015) 120:9038–56. doi:10.1002/2015JA021396
10. Sivadas N, Semeter J, Nishimura Y, and Mrak S. Optical Signatures of the Outer Radiation belt Boundary. *Geophys Res Lett* (2019) 46:8588–96. doi:10.1029/2019GL083908
11. Lanchester BS, Palmer JR, Rees MH, Lummerzheim D, Kaila K, and Turunen T. Energy Flux and Characteristic Energy of an Elemental Auroral Structure. *Geophys Res Lett* (1994) 21:2789–92.
12. Gustavsson B, Steen A, Sergienko T, and Brändström BUE. ¨Estimate of Auroral Electron Spectra, the Power of Ground-Based Multi-Station Optical Measurements. *Phys Chem Earth* (2001) 26:189–94. doi:10.1016/S1464-1917(00)00106-9
13. Janhunen P. Reconstruction of Electron Precipitation Characteristics from a Set of Multiwavelength Digital All-Sky Auroral Images. *J Geophys Res* (2001) 106:18505–16. doi:10.1029/2000JA000263
14. Kauristie K, Partamies N, Makinen S, Kuula R, and Strømme A. Energy Flux of Electron Precipitation as Monitored by an All-Sky Camera. *Int Conf Substorms* (2006) 8:123–6.
15. Partamies N, Janhunen P, Kauristie K, Mäkinen S, and Sergienko T. Testing an Inversion Method for Estimating Electron Energy Fluxes from All-Sky Camera Images. *Ann Geophys* (2004) 22:1961–71. doi:10.5194/angeo-22-1961-2004
16. Dahlgren H, Gustavsson B, Lanchester BS, Ivchenko N, Brändström U, Whiter DK, et al. Energy and Flux Variations across Thin Auroral Arcs. *Ann Geophys* (2011) 29:1699–712. doi:10.5194/angeo-29-1699-2011
17. Lam MM, Freeman MP, Jackman CM, Rae IJ, Kalmoni NME, Sandhu JK, et al. How Well Can We Estimate Pedersen Conductance from the THEMIS White-Light All-Sky Cameras. *J Geophys Res Space Phys* (2019) 124:2920–34. doi:10.1029/2018JA026067
18. Partamies N, Juusola L, Whiter D, and Kauristie K. Substorm Evolution of Auroral Structures. *J Geophys Res Space Phys* (2015) 120:5958–72. doi:10.1002/2015JA021217
19. Mende SB, Harris SE, Frey HU, Angelopoulos V, Russell CT, Donovan E, et al. The THEMIS Array of Ground-Based Observatories for the Study of

Auroral Substorms. *Space Sci Rev* (2008) 141:357–87. doi:10.1007/s11214-008-9380-x
20. Nishimura Y, Deng Y, Lyons LR, McGranaghan RM, and Zettergren MD. Multiscale Dynamics in the High-Latitude Ionosphere. In: C Huang, G Lu, Y Zhang, and LJ Paxton, editors. *Ionosphere Dynamics and Applications* (2021) p. 49–65. doi:10.1002/9781119815617.ch3
21. Rees MH, and Luckey D. Auroral Electron Energy Derived from Ratio of Spectroscopic Emissions 1. Model Computations. *J Geophys Res* (1974) 79(NO. 34):5181–6. doi:10.1029/JA079i034p05181
22. Strickland DJ, Meier RR, Hecht JH, and Christensen AB. Deducing Composition and Incident Electron Spectra from Ground-Based Auroral Optical Measurements: Theory and Model Results. *J Geophys Res* (1989) 94(13):13527–13539. doi:10.1029/JA094iA10p13527
23. Hecht JH, Christensen AB, Strickland DJ, and Meier RR. Deducing Composition and Incident Electron Spectra from Ground-Based Auroral Optical Measurements: Variations in Oxygen Density. *J Geophys Res* (1989) 94:13553–13563. doi:10.1029/JA094iA10p13553
24. Hecht JH, Strickland DJ, and Conde MG. The Application of Ground-Based Optical Techniques for Inferring Electron Energy Deposition and Composition Change during Auroral Precipitation Events. *J Atmos Solar-Terrestrial Phys* (2006) 68(13):1502–19. doi:10.1016/j.jastp.2005.06.022
25. Hecht JH, Mulligan T, Correira JT, Clemmons JH, Strickland DJ, Walterscheid RL, et al. A Multiyear (2002-2006) Climatology of O/N2in the Lower Thermosphere from TIMED GUVI and Ground-Based Photometer Observations. *J Geophys Res* (2012) 117:a–n. doi:10.1029/2011JA017146
26. Lanchester BS, Rees MH, Lummerzheim D, Otto A, Frey HU, and Kaila KU. Large Fluxes of Auroral Electrons in Filaments of 100 M Width. *J Geophys Res* (1997) 102:9741–8. doi:10.1029/97ja00231
27. Strickland DJ, Book DL, Coffey TP, and Fedder JA. Transport Equation Techniques for the Deposition of Auroral Electrons. *J Geophys Res* (1976) 81(16):2755–64. doi:10.1029/ja081i016p02755
28. Strickland DJ, Daniell RE, Jasperse JR, and Basu B. Transport-Theoretic Model for the Electron-Proton-Hydrogen Atom Aurora, 2. Model Results. *J Geophys Res* (1993) 98(A12):21533–48. doi:10.1029/93JA01645
29. Khazanov GV, Sibeck DG, and Chu M. Magnetosphere-Ionosphere Coupling of Precipitating Electrons and Ionospheric Conductance. *Magnetospheres in the Solar System*. American Geophysical Union (2021) p. 229–42. doi:10.1002/9781119815624.ch16
30. Hecht JH, Mulligan T, Strickland DJ, Kochenash AJ, Murayama Y, Tanaka Y-M, et al. Satellite and Ground-Based Observations of Auroral Energy Deposition and the Effects on Thermospheric Composition during Large Geomagnetic Storms: 1. Great Geomagnetic Storm of 20 November 2003. *J Geophys Res* (2008) 113:a–n. doi:10.1029/2007JA012365
31. Xu B-L, Samson JC, and Liu WW. Observations of Optical Aurora Modulated by Resonant Alfvén Waves. *J Geophys Res* (1993) 98:11531–11541. doi:10.1029/93ja00435
32. Omholt A. *The Optical Aurora*. chap. 4. New York: Springer-Veriag (1971). p. 96.
33. Richards MA, James AS, Jim S, and William AH. *Principles of Modern Radar: Basic Principles*, Vol. 1. Savoy Place, London: Institution of Engineering and Technology (2010). ISBN 1613532016, 9781613532010.
34. Kudeki E, and Milla MA. Incoherent Scatter Spectral Theories-Part I: A General Framework and Results for Small Magnetic Aspect Angles. *IEEE Trans Geosci Remote Sensing* (2011) 49(1):315–28. doi:10.1109/TGRS.2010.2057252
35. Vadas SL, and Nicolls MJ. Temporal Evolution of Neutral, Thermospheric Winds and Plasma Response Using PFISR Measurements of Gravity Waves. *J Atmos Solar-Terrestrial Phys* (2009) 71(Issues 6–7):744–70. doi:10.1016/j.jastp.2009.01.011
36. Boström R. A Model of the Auroral Electrojets. *J Geophys Res* (1964) 69:4983–99. doi:10.1029/JZ069i023p04983
37. Schunk RW, and Nagy AF. *Ionospheres: Physics, Plasma Physics and Chemistry*. 2nd ed. Cambridge, U. K: Cambridge Univ. Press (2009).
38. Basu B, Jasperse JR, Strickland DJ, and Daniell RE. Transport-Theoretic Model for the Electron-Proton-Hydrogen Atom Aurora, 1. Theory. *J Geophys Res* (1993) 98(A12):21517–32. doi:10.1029/93JA01646
39. Hedin AE. Extension of the MSIS Thermosphere Model into the Middle and Lower Atmosphere. *J Geophys Res* (1991) 96(A2):1159–72. doi:10.1029/90JA02125
40. Strickland DJ, Evans JS, and Paxton LJ. Satellite Remote Sensing of Thermospheric O/N2 and Solar EUV: 1. *Theory, J Geophys Res* (1995) 100:12217–12226. doi:10.1029/95ja00574
41. Isobe T, Feigelson ED, Akritas MG, and Babu GJ. Linear Regression in Astronomy. *ApJ* (1990) 364(1):104–13. doi:10.1086/169390
42. Megan Gillies D, Donovan DE, Jackel B, Gillies R, and Spanswick E. Identifying the 630 Nm Auroral Arc Emission Height: A Comparison of the Triangulation, FAC Profile, and Electron Density Methodsle, and Electron Density Methods. *J Geophys Res Space Phys* (2017) 122:8181–97. doi:10.1002/2016JA023758
43. Gustavsson B, Kosch M, Wong A, Pedersen T, Heinselman C, Mutiso C, et al. First Estimates of Volume Distribution of HF-Pump Enhanced Emissions at 6300 and 5577 Å: a Comparison between Observations and Theory. *Ann Geophys* (2008) 26:3999–4012. doi:10.5194/angeo-26-3999-2008
44. Knight S. Parallel Electric fields. *Planet Space Sci* (1973) 21:741–50. doi:10.1016/0032-0633(73)90093-7
45. Lyons LR. Generation of Large-Scale Regions of Auroral Currents, Electric Potentials, and Precipitation by the Divergence of the Convection Electric Field. *J Geophys Res* (1980) 85(A1):17–24. doi:10.1029/JA085iA01p00017
46. Christensen AB, Lyons LR, Hecht JH, Sivjee GG, Meier RR, and Strickland DG. Magnetic Field-Aligned Electric Field Acceleration and the Characteristics of the Optical aurora. *J Geophys Res* (1987) 92:6163–7. doi:10.1029/ja092ia06p06163
47. Strickland DJ, Hecht JH, Christensen AB, and Kelly J. Relationship between Energy Flux Q and the Mean Energy ⟨E⟩ of Auroral Energy Spectra Based on Radar Data from the 1987 CEDAR Campaign at Sondre Stromfjord, Greenland, Disturbance. *J Geophys Res* (1994) 99:19467–19473. doi:10.1029/94ja01901
48. McIntosh RC, and Anderson PC. Maps of Precipitating Electron Spectra Characterized by Maxwellian and Kappa Distributions. *J Geophys Res Space Phys* (2014) 119(12):10116–10132. doi:10.1002/2014JA020080
49. Gjerloev JW. The SuperMAG Data Processing Technique. *J Geophys Res* (2012) 117:a–n. doi:10.1029/2012JA017683
50. Partamies N, Juusola L, Tanskanen E, Kauristie K, Weygand JM, and Ogawa Y. Substorms during Different Storm Phases. *Ann Geophys* (2011) 29:2031–43. doi:10.5194/angeo-29-2031-2011
51. Henderson MG, Reeves GD, and Murphree JS. Are north-south Aligned Auroral Structures an Ionospheric Manifestation of Bursty Bulk Flows. *Geophys Res Lett* (1998) 25:3737–40. doi:10.1029/98gl02692
52. Sergeev VA, Liou K, Newell PT, Ohtani S-I, Hairston MR, and Rich F. Auroral Streamers: Characteristics of Associated Precipitation,convection and Field-Aligned Currents. *Ann Geophys* (2004) 22:537–48. doi:10.5194/angeo-22-537-2004
53. Sergeev VA, Sauvaud J-A, Popescu D, Kovrazhkin RA, Liou K, Newell PT, et al. Multiple-spacecraft Observation of a Narrow Transient Plasma Jet in the Earth's Plasma Sheet. *Geophys Res Lett* (2000) 27(6):851–4. doi:10.1029/1999gl010729
54. Lyons LR, Nagai T, Blanchard GT, Samson JC, Yamamoto T, Mukai T, et al. Association between Geotail Plasma Flows and Auroral Poleward Boundary Intensifications Observed by CANOPUS Photometers. *J Geophys Res* (1999) 104:4485–500. doi:10.1029/1998ja900140
55. Lyons LR, Zesta E, Xu Y, Sanchez ER, Samson JC, Reeves GD, et al. Auroral Poleward Boundary Intensifications and Tail Bursty Flows: A Manifestation of a Large-Scale ULF Oscillation. *J Geophys Res* (2002) 107(A11):1352. doi:10.1029/2001JA000242
56. Kauristie K, Sergeev VA, Kubyshkina M, Pulkkinen TI, Angelopoulos V, Phan T, et al. Ionospheric Current Signatures of Transient Plasma Sheet Flows. *J Geophys Res* (2000) 105:10677–10688. doi:10.1029/1999ja900487
57. Angelopoulos V, Kennel CF, Coroniti FV, Pellat R, Kivelson MG, Walker RJ, et al. Statistical Characteristics of Bursty Bulk Flow Events. *J Geophys Res* (1994) 99(A11):21257–5721. doi:10.1029/94JA01263
58. Angelopoulos V, Phan TD, Larson DE, Mozer FS, Lin RP, Tsuruda K, et al. Magnetotail Flow Bursts: Association to Global Magnetospheric Circulation, Relationship to Ionospheric Activity and Direct Evidence for Localization. *Geophys Res Lett* (1994) 24:2271–4. doi:10.1029/97GL02355

59. Li W, Bortnik J, Nishimura Y, Thorne RM, and Angelopoulos V. *The Origin of Pulsating Aurora: Modulated Whistler Mode Chorus Waves*. Washington DC American Geophysical Union Geophysical Monograph Series (2012). p. 197.

Conflict of Interest: JE was employed by the company Computational Physics, Inc.

The remaining authors declare that the research was conducted in the absence of any commercial or financial relationships that could be construed as a potential conflict of interest.

Publisher's Note: All claims expressed in this article are solely those of the authors and do not necessarily represent those of their affiliated organizations, or those of the publisher, the editors and the reviewers. Any product that may be evaluated in this article, or claim that may be made by its manufacturer, is not guaranteed or endorsed by the publisher.

Copyright © 2021 Gabrielse, Nishimura, Chen, Hecht, Kaeppler, Gillies, Reimer, Lyons, Deng, Donovan and Evans. This is an open-access article distributed under the terms of the Creative Commons Attribution License (CC BY). The use, distribution or reproduction in other forums is permitted, provided the original author(s) and the copyright owner(s) are credited and that the original publication in this journal is cited, in accordance with accepted academic practice. No use, distribution or reproduction is permitted which does not comply with these terms.

frontiers in Astronomy and Space Sciences

ORIGINAL RESEARCH
published: 11 October 2021
doi: 10.3389/fspas.2021.759431

Reproducibility of the Geomagnetically Induced Currents at Middle Latitudes During Space Weather Disturbances

Takashi Kikuchi[1,2]*, *Yusuke Ebihara*[2], *Kumiko. K. Hashimoto*[3], *Kentaro Kitamura*[4,5] and *Shin-Ichi Watari*[6]

[1]Institute for Sun-Earth Environmental Research, Nagoya University, Nagoya, Japan, [2]Research Institute for Sustainable Humanosphere, Kyoto University, Kyoto, Japan, [3]School of Agriculture, Kibi International University, Minamiawaji, Japan, [4]National Institute of Technology, Tokuyama College, Shunan, Japan, [5]Graduate School of Engineering, Kyushu Institute of Technology, Kitakyushu, Japan, [6]National Institute of Information and Communications Technology, Koganei, Japan

OPEN ACCESS

Edited by:
Toshi Nishimura,
Boston University, United States

Reviewed by:
Larry Lyons,
UCLA Atmospheric and Oceanic Sciences, United States
Hermann Lühr,
German Research Centre for Geosciences, Germany

***Correspondence:**
Takashi Kikuchi
kikuchi@isee.nagoya-u.ac.jp

Specialty section:
This article was submitted to Space Physics, a section of the journal Frontiers in Astronomy and Space Sciences

Received: 16 August 2021
Accepted: 02 September 2021
Published: 11 October 2021

Citation:
Kikuchi T, Ebihara Y, Hashimoto KK, Kitamura K and Watari S-I (2021) Reproducibility of the Geomagnetically Induced Currents at Middle Latitudes During Space Weather Disturbances. Front. Astron. Space Sci. 8:759431. doi: 10.3389/fspas.2021.759431

Watari et al. (Space Weather, 2009, 7) found that the geomagnetically induced current (GIC) in Hokkaido, Japan (35.7° geomagnetic latitude (GML)), is well correlated with the y-component magnetic field (B_y) (correlation coefficients >0.8) and poorly correlated with $B_{x,z}$ and $dB_{x,y,z}/dt$. The linear correlation with B_y would help predict the GIC, if we have capabilities of reproducing the magnetosphere–ionosphere currents during space weather disturbances. To validate the linear correlation with B_y for any periods (T) of disturbances, we made correlation analyses for the geomagnetic sudden commencements and pulsations (T = 1–10 min), quasi-periodic DP2 fluctuations (30 min), substorm positive bays (60 min), geomagnetic storms (1–20 h), and quiet-time diurnal variations (8 h). The linear correlation is found to be valid for short periods (cc > 0.8 for T < 1 h) but not for long periods (cc < 0.3 for T > 6 h). To reproduce the GIC with any periods, we constructed one-layer model with uniform conductor and calculated the electric field (IEF) induced by B_y using the convolution of dB_y/dt and the step response of the conductor. The IEF is found to be correlated with the GIC for long periods (cc > 0.9), while the GIC-B_y correlation remains better for short periods. To improve the model, we constructed a two-layer model with highly conductive upper and less conductive lower layers. The IEF is shown to reproduce the GIC with cc > 0.9 for periods ranging from 1 min to 24 h. The model is applied to the GIC measured at lower latitudes in Japan (25.3° GML) with strong B_y dependence. The mechanism of the strong B_y dependence of the GIC remains an issue, but a possible mechanism for the daytime GIC is due to the zeroth-order transverse magnetic (TM_0) mode in the Earth-ionosphere waveguide, by which the ionospheric currents are transmitted from the polar to equatorial ionosphere.

Keywords: geomagnetically induced current (GIC), middle latitude, polar-equatorial ionospheric currents, TM0 mode in the earth-ionosphere waveguide, induced electric field in the two-layer conductivity model, geomagnetic by dependence of GIC

KEY POINTS

1. The geomagnetically induced currents in Hokkaido, Japan (35.7° GML), are correlated with B_y (cc > 0.8) for short periods (T < 1 h), while the correlation is poor (cc < 0.3) for long periods (T > 6 h).
2. The GICs with periods of 1 min to 24 h are well correlated with the electric field, E_x, induced by B_y in the semi-infinite one-layer conductivity model (cc > 0.85) and two-layer model (cc > 0.95) composed of highly conductive upper layer.
3. The strong B_y dependence of the GIC is also observed at lower latitude in Japan (25.3° GML) with cc > 0.85.
4. The B_y dependence of the midlatitude GIC may be associated with the ionosphere-ground currents transmitted by the TM_0 mode waves in the earth-ionosphere waveguide from high latitude to the equator.

INTRODUCTION

Geomagnetic disturbances have been known to induce electric fields on the surface of the Earth, which create a potential difference between transformers in the power transmission line system. The potential difference drives electric currents [geomagnetically induced currents (GICs)] in the power lines through the Earthing lines of the transformers (Pirjola, 1983). The GIC is a quasi-steady current, compared to the frequency (50 Hz or 60 Hz) of the power system, and has the larger magnitude at higher latitudes, particularly at the auroral latitudes where the auroral electrojets cause large-amplitude disturbances in the northward magnetic field (B_x) on the ground. The magnetic disturbances often go over 2000 nT and occasionally cause blackouts of the power system, as actually occurred in Canada and USA in March 1989 (Bolduc, 2002).

The GIC is derived from formula relating the GIC and the surface electric field; $GIC = aE_x(t) + bE_y(t)$, where $E_{x,y}$ is the surface electric field measured or calculated from the surface magnetic fields, and a and b are the parameters, which depend on the topology and the electrical characteristics of the system (Pulkkinen et al., 2007; Viljanen et al., 2012; Wei et al., 2013). The surface impedance has been widely used to estimate the electric fields from the magnetic fields through the relationship; $E_{x,y} = Z \cdot B_{y,x}/\mu$, where $B_{y,x}$, μ, and Z are the horizontal magnetic field, magnetic permeability, and surface impedance, respectively. The surface impedance is derived from the ground conductivity and layer thickness through the complex-image method (Boteler and Pirjola, 1998) and from the measured GIC and surface magnetic fields (Pulkkinen et al., 2007).

On the other hand, it was reported that the GIC is much more closely related to time derivatives (dB/dt) than B (deflection from the pre-event value) (Viljanen, 1997; Trichtchenko and Boteler, 2006) and the GIC has been evaluated by quite a few papers from dB/dt using the Faraday's law (Viljanen, 1997; Pirjola, 2000; Carter et al., 2016; Kozyreva et al., 2018). It should be noted, on the other hand, that dB/dt is related to the spatial derivative of the electric field, E, in the Faraday's law. No clear correspondence between the GIC and $dB_{x,y}/dt$ reported by Pirjola (1983) may be an example of an inappropriate application of dB/dt to the GIC. The dB/dt method has been used to assess the GIC even under the equatorial electrojet where the GIC has never been measured (Ngwira et al., 2013; Carter et al., 2016). It should be noted that the induction theory tells us that dB/dt should be convolved with the function of $1/\sqrt{t}$ (t: time) (Cagniard, 1953; Viljanen and Pirjola, 1989) that is a response of the conductor to step function-like magnetic field changes (Cheng, 1959). Thus, the sole usage of dB/dt does not meet the induction theory except that the model is composed of two layers with less conductive upper layer over the highly conductive lower layer (Pirjola, 2010).

Watari et al. (2009) demonstrated that the middle latitude GIC in Hokkaido (35.7° GML), Japan, is not correlated with $dB_{x,y,z}/dt$ nor with the x-component magnetic field, B_x(deflection from the pre-event value), but very well correlated with the y-component magnetic field, B_y, with the correlation coefficients (cc) > 0.8. This result meets the two-layer model with the highly conductive upper layer (Pirjola, 2010). Concerning the strong $B_y$dependence, Watari et al. (2009) suggested that the GIC is a return current of the ionospheric currents carried by the TM_0 mode waves in the Earth-ionosphere waveguide, which was applied to explain the instantaneous transmission of the polar electric field and currents to the equator (Kikuchi et al., 1978). Brändlein et al. (2012) also suggested that the GIC is closely associated with the ionospheric currents by showing diurnal and seasonal variations of the GIC observed at low latitude in northern Chile.

The Hokkaido GIC has been reproduced from the ground magnetic fields using the surface impedance (Pulkkinen et al., 2010). Furthermore, Love and Swidinski (2015) reproduced the geoelectric field (GEF) measured at Kakioka, Japan (27.8° GML), from the magnetic fields at Kakioka using the convolution of dB/dt and the response of the semi-infinite one-dimensional flat Earth. Love and Swidinski (2014) solved the diffusion equation using the Laplace transformation and applied the function of $\sqrt{t}$ named linear ramp function for the convolution with dB/dt. The reproduced IEF was plotted in good shape with the observed GEF, but the correlation is not evaluated quantitatively.

As overviewed above, there are various methods to reproduce the GIC/GEF from the surface magnetic field such as from B_y, dB/dt, surface impedance and from the convolution of dB/dt and response functions. The variety of the method may be due to many factors affecting the GIC such as directions of power lines and coastlines, 3-D structures of Earth's conductivities (Goto, 2015; Nakamura et al., 2018; Ivannikova et al., 2018), and the propagation mode that transports magnetic disturbances from the ionosphere and magnetosphere into the Earth. In this study, we revisit the GIC in Hokkaido to construct a model that reproduces the GIC from the observed magnetic field, B_y. The model is not to clarify the structure of the Earth's conductivity that has been made by other methods like the magneto-telluric (MT) method but is rather a tool designed so as to reproduce the GIC from the surface magnetic field as accurately as possible. As a next step to the accomplishment of the good correlations between the GIC and B_y (Watari et al., 2009), we examine if the GIC-B_y correlations are valid for any space weather disturbances with

different period/time scales ranging from 1 min to 24 h. As shown in the following sections, we found that the GIC-B_y correlation depends on the period of disturbances such that cc > 0.8 for short periods (<1 h) and cc < 0.3 for long periods (>6 h). To construct a model capable of reproducing the long period GIC, we calculated the IEF, $E_{x,y}$ using the convolution of $dB_{y,x}/dt$ and the step response of the semi-infinite one-layer conductivity model. The GIC-E_x correlation is shown to be much better (cc (GIC-E_x) > 0.9) than cc (GIC-B_y) for long periods, while cc (GIC-B_y) is still better than cc (GIC-E_x) for short periods. To construct a model covering both short and long periods, we built the two-layer model composed of highly conductive upper layer over less conductive semi-infinite lower layer. The two-layer model is shown to reproduce the GIC with cc > 0.9 for periods ranging from 1 min to 24 h. In ***Derivation of the IEF from the Observed Magnetic field***, we formulate equations that derive the IEF from the observed magnetic field in one- and two-layer models. Then, we calculate correlation coefficients of the GIC with $B_{x,y}$ and $E_{y,x}$ induced in the one- and two-layer models in ***Correlations among Observed GIC, $B_{x,y}$ and $E_{y,x}$***. In order to evaluate the capability of the model for various types of space weather events, we analyzed impulsive geomagnetic sudden commencement (SC), short-period (1 min) geomagnetic Pi2 pulsations, longer-period (30 min-8 hours) DP2 fluctuations, and solar quiet diurnal variations (Sq), isolated substorm magnetic bays, and long-lasting storm disturbances (1–24 h). To examine the generality of the model, we applied the model to the GIC measured at the Shin-Yamaguchi (SYG) substation of the Chugoku Electric Company located at lower latitudes in Japan (25.3° GML). We found that the model well reproduced the GIC at SYG with high correlation coefficients (cc = 0.87–0.95) for DP2 and SC events with strong B_y dependence. In ***Discussion***, we discuss that the daytime GIC can be connected with the ionospheric currents by the TM_0 mode waves in the Earth-ionosphere waveguide, which carry the ionospheric currents from the polar ionosphere to the equator (Kikuchi et al., 1978; Kikuchi, 2014). We further stress that large-amplitude GICs tend to occur around the midnight during substorms, which raises an issue on the propagation mode from the magnetospheric currents to the ground on the nightside.

DERIVATION OF THE IEF FROM THE OBSERVED MAGNETIC FIELD

Convolution Theorem

The magnetic field, B_y, propagates downward in the Earth (a conducting medium) as described by the diffusion equation derived from the Faraday's law, Ampere's law, and Ohm's law. To solve the equations, we use the Laplace transformation that transforms differential equations into algebraic equations and convolution into multiplication. In the transformed equations, the time derivative is multiplication of s (s is the complex number used in the Laplace transformation), and integration is multiplication of $1/s$. Following the theory of response of the linear system (Cheng, 1959), the induced electric field (IEF), $E_x(t)$, is a response of the linear system (conductor) to the external excitation (applied $B_y(t)$). Letting the Laplace transforms of $E_x(t)$ and $B_y(t)$ be $e_x(s)$ and $b_y(s)$, respectively, we express $e_x(s)$ as a product of the excitation transform, $b_y(s)$ and the transfer function, $f(s)$ (Laplace transform of the impulse response function, $F(t)$) as shown below.

$$e_x(s) = f(s) \cdot b_y(s). \tag{1}$$

Here, we note that the impulse response is a response of the system to the external excitation in a form of the delta function, $\delta(t)$, of which Laplace transform is 1. The inverse Laplace transformation of **Eq. 1** gives $E_x(t)$ in a form of the convolution integral of the impulse response, $F(t)$ and the external excitation, $B_y(t)$ as given by

$$E_x(t) = F(t) * B_y(t) = \int_0^t F(t-\tau) B_y(\tau) d\tau, \tag{2}$$

where $*$ refers to the convolution of two functions. The convolution (2) implies that $E_x(t)$ is a sum of impulse responses of the system excited by B_y recorded from $\tau = 0$ to t.

We may write the **Eq. 1** in a different form including 1/s (time integral) and s (time derivative) as

$$e_x(s) = \left[\frac{1}{s} f(s)\right] \cdot \left[s b_y(s)\right]. \tag{3}$$

Using **Eq. 3**, we can write the convolution **(2)** in a different form as

$$E_x(t) = G(t) * \frac{dB_y(t)}{dt} = \int_0^t G(t-\tau) \frac{dB_y(\tau)}{d\tau} d\tau + B_y(0) G(t), \tag{4}$$

where $G(t)$ denotes the step response of the conductor, a response to the excitation function in a form of the unit step function, $U(t)$(= 1 for t > 0 and = 0 otherwise) and $B_y(0)$ is the initial value of B_y. In the following, $B_y(0)$ is assumed to be zero since $t = 0$ is set to the quiet time before the arrival of the disturbances. The convolution **(4)** is identical to the Eq. 12 of Cagniard (1953). It should be stressed that the IEF is obtained from dB/dt convolved with the step response of the conductor. In the following, we use **Eq. 4** to derive the IEF, while **Eq. 2** works the same way. Since the GIC and magnetometer data at Memambetsu (MMB), Hokkaido are sampled every one second, the time t is discrete, and the time derivative and integral in **Eq. 4** are replaced with a difference and summation, respectively, as follows.

$$E_x(t) = \sum_{i=1}^{t} \Big(G[t-i] \big(B_y[i] - B_y[i-1] \big) \Big) \qquad (i = 1, 2, 3, , , t), \tag{5}$$

where we start the summation from $i = 1$ since $B_y(t \le 0) = 0$ is assumed.

IEF in One-Layer Model

The diffusion equation in the conductor is derived from the Faraday's law, Ampere's law, and Ohm's law as listed below.

$$\begin{aligned} \nabla \times \boldsymbol{E} &= -\frac{\partial \boldsymbol{B}}{\partial \boldsymbol{t}} \\ \nabla \times \boldsymbol{B} &= \mu \boldsymbol{J} \\ \boldsymbol{J} &= \sigma \boldsymbol{E} \end{aligned} \quad , \tag{6}$$

where σ and $\boldsymbol{J}$ are electric conductivity and current in the conductor, respectively.

The **Eq. 6** leads to the following diffusion equations for B_y and E_x propagating toward the z-direction in the coordinates; x, y, and z directed toward the north, east, and down, respectively.

$$\begin{aligned} \frac{\partial^2 B_y}{\partial z^2} - \mu\sigma \frac{\partial B_y}{\partial t} &= 0 \\ \frac{\partial B_y}{\partial z} + \mu\sigma E_x &= 0 \end{aligned} \quad . \tag{7}$$

The Laplace transforms of **Eq. 7** are given by

$$\begin{aligned} \frac{\partial^2 b_y}{\partial z^2} - \mu\sigma s b_y &= 0 \\ \frac{\partial b_y}{\partial z} + \mu\sigma e_x &= 0 \end{aligned} \quad , \tag{8}$$

where the initial value of B_y is assumed to be zero as mentioned above. Transformed solutions are obtained in the following form:

$$\begin{aligned} b_y &= a_1 e^{-z\sqrt{\mu\sigma s}} + a_2 e^{z\sqrt{\mu\sigma s}} \\ e_x &= \frac{a_1\sqrt{s}}{\sqrt{\mu\sigma}} e^{-z\sqrt{\mu\sigma s}} + \frac{a_2\sqrt{s}}{\sqrt{\mu\sigma}} e^{z\sqrt{\mu\sigma s}} \end{aligned} . \tag{9}$$

We give the unit step function for $B_y(t)$ at $z = 0$ to obtain the step response function, which is used to derive the IEF from the convolution with dB_y/dt. The coefficients $a_{1,2}$ are determined from the following boundary conditions: $B_y(t) = U(t)$ at $z = 0$ and $B_y(t) = 0$ at $z = \infty$. We note that B_y in the convolution integral **(4)** is the magnetic field observed at the surface of the Earth, which therefore includes effects of induced currents as well as external currents flowing in the ionosphere and magnetosphere. Whatever the source currents are, the observed B_y is the boundary value for the diffusion equation in the ground.

We thus have the transformed solutions as

$$\begin{aligned} b_y &= \frac{1}{s} e^{-z\sqrt{\mu\sigma s}} \\ e_x &= \frac{1}{\sqrt{\mu\sigma}} \frac{1}{\sqrt{s}} e^{-z\sqrt{\mu\sigma s}} \end{aligned} , \tag{10}$$

Substituting $z = 0$ for **Eq. 10** and applying the inverse transformation, $L^{-1}\{1/\sqrt{s}\} = 1/\sqrt{\pi t}$, we obtain the step response function, $G(t)$ for E_x as

$$G(t) = \frac{1}{\sqrt{\pi\mu\sigma}} \frac{1}{\sqrt{t}} U(t). \tag{11}$$

Substituting (11) for (5), we obtain the IEF as

$$E_x(t) = \frac{1}{\sqrt{\pi\mu\sigma}} \sum_{i=1}^{t} \left(\frac{1}{\sqrt{t-i}} U[t-i]\big(B_y[i] - B_y[i-1]\big) \right). \tag{12}$$

E_y induced by B_x is calculated by replacing B_y with -B_x in the **Eq. 12**. We calculated E_x and E_y with the conductivity, $\sigma = 10^{-4}$ mho/ m, and as will be shown, the GIC is well correlated with E_x (cc > 0.9) for long-period disturbances, whereas the correlation is still better with B_y than with E_x for short periods. This result would raise a problem that requires us to use two models to reproduce the GIC, depending on the period of disturbances. To address this problem, we construct a two-layer model as shown in the next subsection.

IEF in the Two-Layer Model

Using the earth-currents and magnetometer data, Owada (1972) showed that the subterranean electric conductivity at Memambetsu has a structure of three layers with depths of 8–20 km, 20–90 km, and 90–170 km and with conductivities higher in the top layer than in the lower layers. The MT method has revealed inhomogeneous distribution of the Earth's conductivity in Hokkaido not only in the vertical but also in the horizontal directions (Satoh et al., 2000; Uyeshima et al., 2001; Uyeshima, 2007). However, since our purpose is to construct a model that is capable of reproducing the observed GIC, we pay our attention to the vertical profile of Owada (1972)'s results and construct a two-layer model with thickness, d = 20 km and $\sigma_1 = 10^{-4}$mho/m in the upper layer (layer 1) over the semi-infinite less conductive ($\sigma_2 = 10^{-8}$ mho/ m) layer (layer 2). The parameter dependence of the model will be discussed in the discussion section.

We assume the magnetic field be a fixed value at $z = 0$ in the same way as in the one-layer model, and the magnetic permeability is common in both layers. The Laplace-transformed solutions in the layer 1 and layer 2 are given as follows:

$$\begin{aligned} b_{y1} &= a_{11} e^{-z\sqrt{\mu\sigma_1 s}} + a_{12} e^{z\sqrt{\mu\sigma_1 s}} \\ e_{x1} &= \frac{a_{11}\sqrt{s}}{\sqrt{\mu\sigma_1}} e^{-z\sqrt{\mu\sigma_1 s}} - \frac{a_{12}\sqrt{s}}{\sqrt{\mu\sigma_1}} e^{z\sqrt{\mu\sigma_1 s}} \\ b_{y2} &= a_{21} e^{-z\sqrt{\mu\sigma_2 s}} \\ e_{x2} &= \frac{a_{21}\sqrt{s}}{\sqrt{\mu\sigma_2}} e^{-z\sqrt{\mu\sigma^2 s}} \end{aligned} \tag{13}$$

We give the unit step function for B_y at $z = 0$ and employ the boundary conditions at $z = d$ as b_y and e_x being continuous across the boundary. Then, we have the following relations among the coefficients:

$$\begin{aligned} a_{11} + a_{12} &= \frac{1}{s} \\ a_{11} e^{-d\sqrt{\mu\sigma_1 s}} + a_{12} e^{d\sqrt{\mu\sigma_1 s}} &= a_{21} e^{-d\sqrt{\mu\sigma^2 s}} \\ \frac{a_{11}\sqrt{s}}{\sqrt{\mu\sigma_1}} e^{-d\sqrt{\mu\sigma_1 s}} - \frac{a_{12}\sqrt{s}}{\sqrt{\mu\sigma_1}} e^{d\sqrt{\mu\sigma_1 s}} &= \frac{a_{21}\sqrt{s}}{\sqrt{\mu\sigma_2}} e^{-d\sqrt{\mu\sigma_2 s}} \end{aligned} \tag{14}$$

We obtain

$$a_{11} = \frac{1}{s} + k_{12}\left(1 - k_{12}e^{-2d\sqrt{\mu\sigma_1 s}}\right)^{-1}\frac{1}{s}e^{-2d\sqrt{\mu\sigma_1 s}}$$

$$a_{12} = -k_{12}\left(1 - k_{12}e^{-2d\sqrt{\mu\sigma_1 s}}\right)^{-1}\frac{1}{s}e^{-2d\sqrt{\mu\sigma_1 s}}$$

$$a_{21} = \left(1 - k_{12}\left(1 - e^{-2d\sqrt{\mu\sigma_1 s}}\right)\left(1 - k_{12}e^{-2d\sqrt{\mu\sigma_1 s}}\right)^{-1}\right)\frac{1}{s}e^{-d\sqrt{\mu s}\left(\sqrt{\sigma_1}-\sqrt{\sigma_2}\right)} \quad (15)$$

where

$$k_{12} = \frac{\left(\sqrt{\sigma_1} - \sqrt{\sigma_2}\right)}{\left(\sqrt{\sigma_1} + \sqrt{\sigma_2}\right)} \quad (16)$$

Under the condition, $\left|k_{12}e^{-2d\sqrt{\mu\sigma_1 s}}\right| < 1$ $(t \geq 1)$, we can use the following series expansion that represents reflections at the boundary between the two layers.

$$\left(1 - k_{12}e^{-2d\sqrt{\mu\sigma_1 s}}\right)^{-1} = 1 + \sum_{j=1}^{n}\left(k_{12}e^{-2d\sqrt{\mu\sigma_1 s}}\right)^{j} \quad (n \to \infty) \quad (17)$$

where j refers to the number of reflections and n is chosen so that the summation approaches a steady value ($n = 50$ in the calculation below). Then, we have the coefficients as follows:

$$a_{11} = \frac{1}{s}\sum_{j=0}^{n} k_{12}^{j}e^{-2jd\sqrt{\mu\sigma_1}\sqrt{s}}$$

$$a_{12} = -\frac{1}{s}\sum_{j=1}^{n} k_{12}^{j}e^{-2jd\sqrt{\mu\sigma_1}\sqrt{s}}$$

$$a_{21} = (1 - k_{12})\frac{1}{s}\sum_{j=0}^{n} k_{12}^{j}e^{-\left((2j+1)d\sqrt{\mu\sigma_1} - d\sqrt{\mu\sigma_2}\right)\sqrt{s}} \quad (18)$$

Substituting **Eq. 18** for **Eq. 13**, we obtain the transformed solutions as follows:

$$b_{y1} = \frac{1}{s}e^{-z\sqrt{\mu\sigma_1}\sqrt{s}} + \sum_{j=1}^{n} k_{12}^{j}\left(\frac{1}{s}e^{-\left(2jd+z\right)\sqrt{\mu\sigma_1}\sqrt{s}} - \frac{1}{s}e^{-\left(2jd-z\right)\sqrt{\mu\sigma_1}\sqrt{s}}\right)$$

$$e_{x1} = \frac{1}{\sqrt{\mu\sigma_1}}\left(\frac{1}{\sqrt{s}}e^{-z\sqrt{\mu\sigma_1 s}} + \sum_{j=1}^{n} k_{12}^{j}\left(\frac{1}{\sqrt{s}}e^{-\left(2jd+z\right)\sqrt{\mu\sigma_1}\sqrt{s}} + \frac{1}{\sqrt{s}}e^{-\left(2jd-z\right)\sqrt{\mu\sigma_1}\sqrt{s}}\right)\right)$$

$$b_{y2} = (1 - k_{12})\sum_{j=0}^{n} k_{12}^{j}\frac{1}{s}e^{-\left((2j+1)d\sqrt{\mu\sigma_1} + (z-d)\sqrt{\mu\sigma_2}\right)\sqrt{s}}$$

$$e_{x2} = (1 - k_{12})\frac{1}{\sqrt{\mu\sigma_2}}\sum_{j=0}^{n} k_{12}^{j}\frac{1}{\sqrt{s}}e^{-\left((2j+1)d\sqrt{\mu\sigma_1} + (z-d)\sqrt{\mu\sigma_2}\right)\sqrt{s}} \quad (19)$$

The Laplace transform of the step response function, $g(s)$, is obtained by substituting $z = 0$ for e_{x1} as

$$g(s) = \frac{1}{\sqrt{\mu\sigma_1}}\left(\frac{1}{\sqrt{s}} + 2\sum_{j=1}^{n} k_{12}^{j}\frac{1}{\sqrt{s}}e^{-\left(2jd\right)\sqrt{\mu\sigma_1}\sqrt{s}}\right) \quad (20)$$

Using the inverse Laplace transform, $L^{-1}\left\{\frac{1}{\sqrt{s}}e^{-\left(2jd\right)\sqrt{\mu\sigma_1}\sqrt{s}}\right\} = \frac{1}{\sqrt{\pi t}}e^{-\frac{(jd)^2\mu\sigma_1}{t}}$, we obtain the step response of the two-layer model as

$$G[t] = \frac{1}{\sqrt{\pi\mu\sigma_1}}\frac{1}{\sqrt{t}}\left(1 + 2\sum_{j=1}^{n} k_{12}^{j}e^{-\frac{(jd)^2\mu\sigma_1}{t}}\right)U(t) \quad (21)$$

Using **Eq. 21** in **Eq. 5**, we obtain the IEF from the convolution,

$$E_x[t] = \frac{1}{\sqrt{\pi\mu\sigma_1}}\left\{\sum_{i=1}^{t}\frac{1}{\sqrt{t-i}}\left(1 + 2\sum_{j=1}^{n} k_{12}{}^{j}e^{-\frac{(jd)^2\mu\sigma_1}{t-i}}\right)U[t-i]\left(B_y[i] - B_y[i-1]\right)\right\} \quad (22)$$

E_y induced by B_x is calculated by replacing B_y with -B_x in the **Eq. 22**.

CORRELATIONS AMONG OBSERVED GIC, $B_{X,Y}$, AND $E_{Y,X}$

The GIC was measured on the grounding conductor in the transformer of the 187 kV power line systems at the Memambetsu substation of Hokkaido Electric Power Co. Inc. (35.7° GML). The direction of the power line is southwestward, and the length of the line is approximately 100 km (Watari et al., 2009). The magnetometer observations were made at the Memambetsu magnetic observatory (http://www.kakioka-jma.go.jp/en/index.html) close to the GIC measurements.

Pi2 and SC (1–10 min)

To confirm the high correlation between the GIC and B_y (Watari et al., 2009), we picked out a Pi2 event with the period of 1 min recorded at Memambetsu (MMB) in the morning sector (0600 MLT) and a geomagnetic sudden commencement (SC) with the preliminary impulse (PI, 1 min) followed by the main impulse (MI, 5–10 min) in the morning sector (0630 MLT). **Figure 1** shows B_x and B_y at MMB (top left) and the GIC (bottom left) observed during the Pi2 event. The GIC is well correlated with B_y (cc = 0.90), while almost nothing with B_x (cc = -0.21). The Pi2 often occurs on the nightside during substorms, while also observed on the dayside as the event in **Figure 1** is the case (e.g., Han et al., 2004). The daytime Pi2 has been attributed to ionospheric currents flowing from the polar ionosphere to the equator carried by the TM_0 mode waves in the Earth-ionosphere waveguide (Sutcliffe and Lühr, 2010; Imajo et al., 2015). The TM_0 mode waves propagating southward (-x direction) have the magnetic field B_y perpendicular to the propagation plane and the electric fields,$E_{x,z}$ in the propagation plane, which transport the ionospheric and ground surface currents with north-south direction (Kikuchi and Araki, 1979). The good correlation between the GIC and B_y may indicate that the GIC is the ground surface current transported by the TM_0 mode waves as suggested by Watari et al. (2009) and Brändlein et al. (2012).

Figure 1 also shows the IEF in one-layer model, $E_{x\mathrm{I}}$ and $E_{y\mathrm{I}}$ induced by B_y and B_x, respectively (top right), and the IEF in the two-layer model, $E_{x\mathrm{II}}$ and $E_{y\mathrm{II}}$ (bottom right). The correlation coefficient of the GIC with $E_{x\mathrm{I}}$ is $cc(GIC - E_{x\mathrm{I}}) = 0.77$, less than $cc(GIC - B_y) = 0.90$, but the correlation with $E_{x\mathrm{II}}$ is

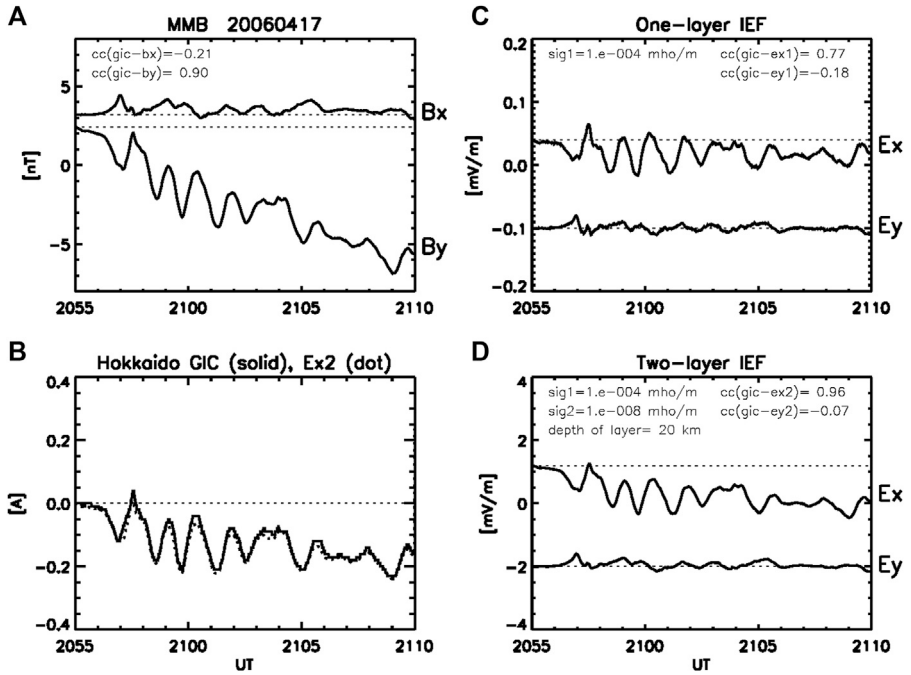


FIGURE 1 | (A) X- and Y-components of the magnetic field (B_x, B_y) observed at the Memambetsu (MMB) magnetic observatory during the Pi2 event with the period of 1 min in the morning sector (21 UT, 06 MLT). **(B)** GIC observed at the Memambetsu substation of the Hokkaido Electric Company (solid curve). E_{x2} scaled to the GIC is plotted with the dotted curve in the frame of the GIC, so that one can see the high correlation between the GIC and E_{x2}. **(C, D)** The induced electric fields (IEF), $E_{y,x}$ induced by $B_{x,y}$ at the surface of the Earth in the one- and two-layer models. Sig1 = 10^{-4} mho/ m in the one-layer model denotes the conductivity of the semi-infinite uniform conductor. The parameters of the two-layer model are sig1 = 10^{-4} mho/ m and depth = 20 km of the upper layer and sig2 = 10^{-8} mho/ m of the semi-infinite lower layer. The cc refers to the correlation coefficient between the GIC and $B_{x,y}/E_{y,x}$.

$cc(GIC - E_{xII}) = 0.96$, indicating that the GIC can be reproduced almost perfectly by the two-layer model. E_{xII} is plotted in the frame of the GIC with the dotted curve, whereE_{xII} is scaled to the GIC so that one can see the correlation with the GIC visually. On the other hand, the correlations with E_{yI} and E_{yII} are almost nothing (cc = -0.18 and -0.07) in the same way as the correlation with B_x, indicating that the GIC has no relations with B_x.

Figure 2 shows the SC event with the positive PI followed by the negative MI in B_x and negative PI followed by the positive MI in B_y. The GIC is well correlated with B_y (cc = 0.91) in the same manner as the Pi2 event. The PI and MI in B_x are caused by ionospheric Hall currents driven by the dusk-to-dawn and dawn-to-dusk electric fields, respectively, while those in B_y are due to north-south Pedersen currents flowing from the polar to the equatorial ionosphere (Kikuchi et al., 2001). The MI of SC in B_x is primarily composed of a stepwise increase caused by the magnetopause currents, superimposed by negative deflections due to the ionospheric Hall current in the morning sector (2130 UT, 0630 MLT) (Kikuchi et al., 2001). Since the Pedersen currents of the PI and MI are transmitted by the TM_0 mode waves (Kikuchi, 2014), the GIC is consistent with being the ground surface currents carried by the TM_0 mode waves.

Figure 2 (right panels) shows the IEF in one- and two-layer models. The correlation of the GIC with E_{xI}, $cc(GIC - E_{xI}) = 0.88$, is less than the correlation with B_y, $cc(GIC - B_y) = 0.91$, but the correlation with E_{xII} is extremely good as $cc(GIC - E_{xII}) = 0.99$. The GIC can be reproduced almost perfectly by the two-layer model as shown with the solid and dotted curves in the frame of GIC. In the following sections, we examine the correlations for longer period/time scale disturbances, ranging up to 24 h.

Quasi-Periodic DP2 Fluctuations (30 min)

Figure 3 shows periodic fluctuations with periods of 30 min in both B_x and B_y observed in the evening (10-12 UT, 19-21 MLT). The fluctuations are accompanied by Pi2 pulsations in the rising phase of each bay-like increase, which may imply that the fluctuations are associated with repetitive substorms (Sutcliffe and Lyons, 2002). Therefore, the fluctuations are quasi-magnetostatic field of the substorm current wedge that can be calculated using the Biot-Savart formula, although the 30-min period is shorter than the typical recurrence period (1–2 h) of substorms (Akasofu, 1964; Freeman and Morley, 2004; Borovsky and Yakymenko, 2017).

The correlation of the GIC with B_y is $cc(GIC - B_y) = 0.54$, and the correlation with B_x is almost nothing as $cc(GIC - B_x) = -0.07$. The $cc(GIC - B_y)$ is much less than the previous event, probably because the fluctuations are superimposed by the background gradual increase that may not have affected the GIC. However, the correlations with E_{xI}

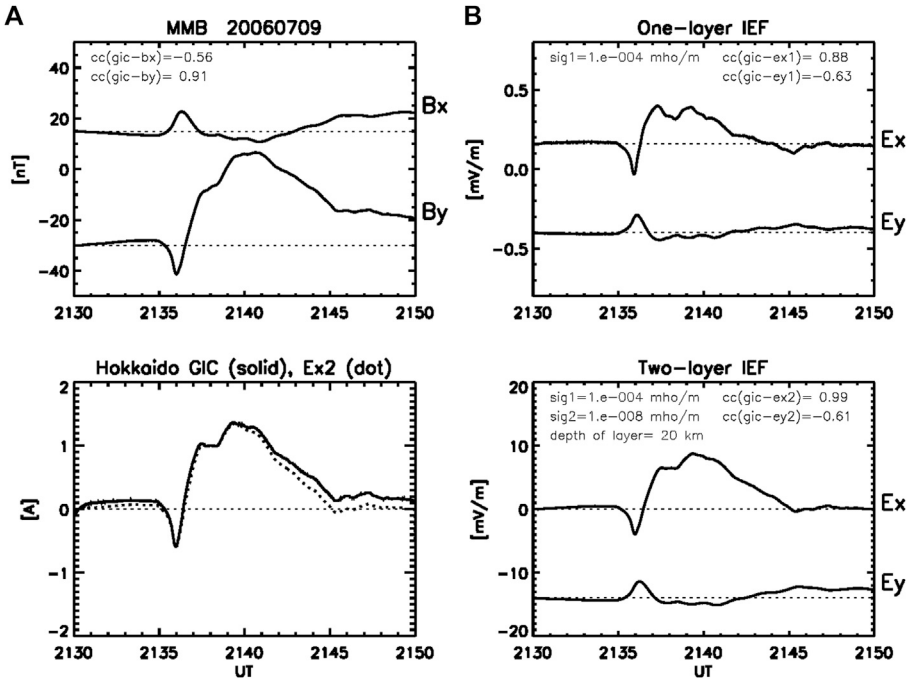


FIGURE 2 | (A) B_x, B_y and GIC observed at MMB, and **(B)** E_x and E_y calculated in the one- and two-layer models for the SC event with time scales of 1–10 min observed in the morning sector (2130 UT, 0630 MLT). The parameters and formats of the plots are the same as in **Figure 1**.

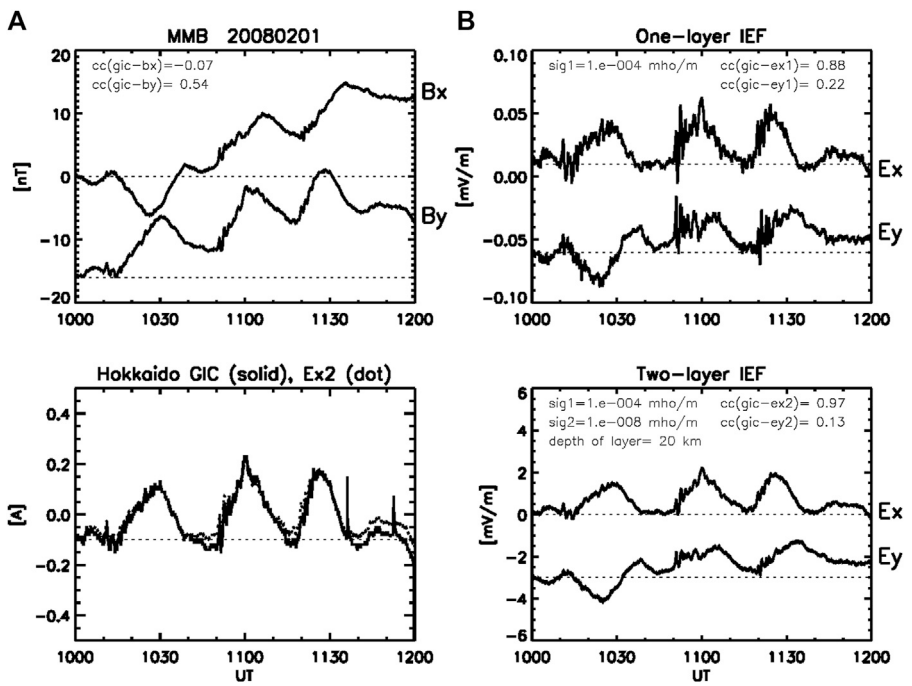


FIGURE 3 | (A) B_x, B_y and GIC observed at MMB, and **(B)** E_x and E_y calculated in the one- and two-layer models for the DP2 fluctuation event with periods of 30 min in the evening sector (10-12 UT, 19-21 MLT). The parameters and formats of the plots are the same as in **Figure 1**.

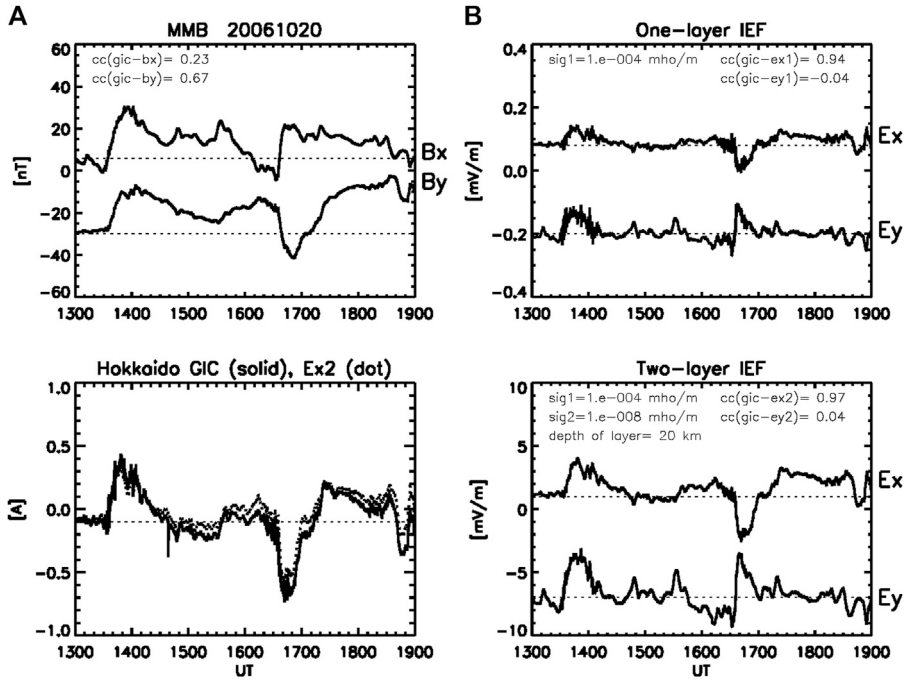


FIGURE 4 | (A) B_x, B_y and GIC observed at MMB, and **(B)** E_x and E_y calculated in the one- and two-layer models for the substorm positive bay events with time scales of 60 min in the pre-midnight (14 UT, 23 MLT) and post-midnight (17 UT, 02 MLT). The parameters and formats of the plots are the same as in **Figure 1**.

are much better as $cc(GIC - E_{xI}) = 0.88$ and almost perfect with E_{xII} as $cc(GIC - E_{xII}) = 0.97$. Consequently, the two-layer model well reproduces the GIC for the 30-min period fluctuations in the same way as for the Pi2 and SC.

Substorm Bays (60 min)

Figure 4 shows two successive substorm positive bays in B_x(top left). The first bay event occurred in the pre-midnight (1330UT, 2230MLT), and the second in the post-midnight (1630UT, 0130 MLT). The magnetic bays in B_x are positive in both events, while B_y is positive in the first and negative in the second events. The positive bay in B_x is caused by the wedge-type field-aligned currents flowing downward in the post-midnight and upward in the pre-midnight (McPherron et al., 1973). The positive and negative bays in B_y are due to the location of MMB station being close to the upward and downward FACs in the pre- and post-midnight, respectively. The GIC (bottom left) resembles the B_y in both events, and their correlation, $cc(GIC - B_y) = 0.67$, is better than $cc(GIC - B_x) = 0.23$ in the same manner as for the short-period disturbances, while the correlation is not so good as for the SC and Pi2. In contrast, the correlation with E_{xI} is much better as $cc(GIC - E_{xI}) = 0.94$, and furthermore, the two-layer model almost perfectly reproduces the GIC as $cc(GIC - E_{xII}) = 0.97$. The change in sign of the GIC across the midnight again indicates that the GIC has no association with B_x. The B_y-dependence of the nighttime bay events raises a question on the TM_0 mode wave scenario since the magnetic bays on the nightside are caused not by ionospheric currents but primarily by field-aligned currents. It remains an issue what kind of propagation mode explains the B_y dependence of the GIC on the nightside.

Geomagnetic Storms (1–20 h)

Figure 5 shows a geomagnetic storm event, where B_x shows the ring current development (00-10UT) and decay (12-18UT) superimposed by the substorm positive bay (10-11UT). The correlation of the GIC with B_y, $cc(GIC - B_y) = 0.65$ is better than $cc(GIC - B_x) = -0.17$. The correlations with the IEF, $cc(GIC - E_{xI}) = 0.92$ and $cc(GIC - E_{xII}) = 0.97$ are much better than $cc(GIC - B_y) = 0.65$. Thus, the two-layer model reproduces the GIC almost perfectly during the geomagnetic storm lasting over 20 h.

Solar Quiet Geomagnetic Variations (8 h)

Figure 6 shows an example of the solar quiet geomagnetic variations (Sq). The period of Sq is 24 h, while significant changes occur over 8 h in the daytime (00-08 UT, 09-17 MLT). B_x and B_y are caused by the ionospheric currents driven by the thermospheric tidal motions (Kelley, 1989). It is remarkable that the correlation of the GIC with B_y, $cc(GIC - B_y) = 0.27$ is much lower than those for the shorter period disturbances. Furthermore, the correlation with B_y is even less than the correlation with B_x, $cc(GIC - B_x) = 0.66$. The better correlation with B_x does not necessarily mean that the GIC was caused by B_x, since the temporal variations of the GIC resemble those of B_y, if the time of B_y is shifted ahead. On the other hand, the correlations with the IEF are extremely good as

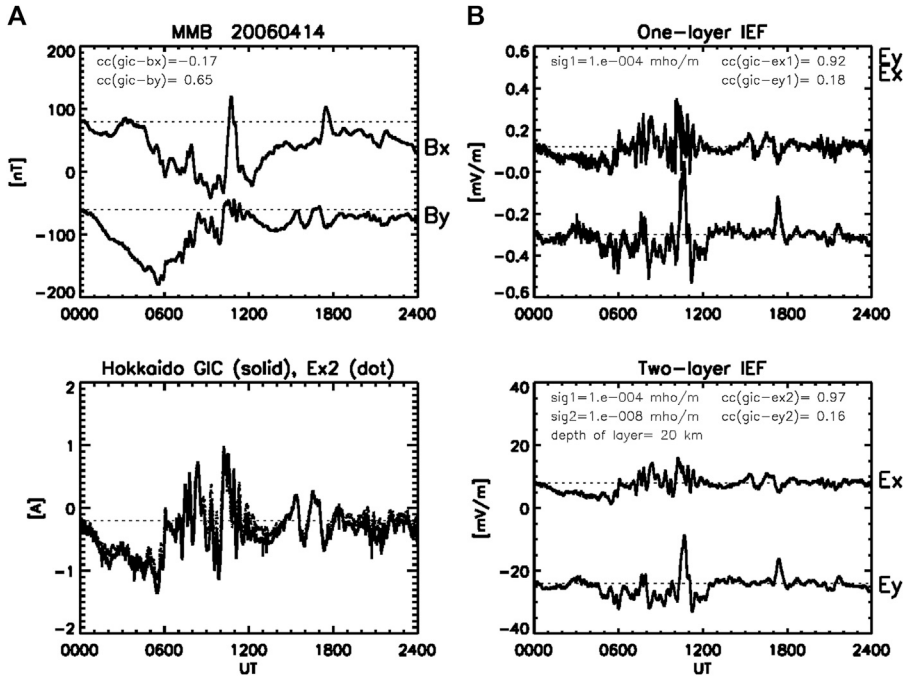


FIGURE 5 | (A) B_x, B_y and GIC observed at MMB, and **(B)** E_x and E_y calculated in the one- and two-layer models for the geomagnetic storm events with the main phase (00-10 UT, 09-19 MLT) followed by the recovery phase (10-18 UT, 19-03 MLT) superimposed by the substorm positive bay (10-11 UT, 19-20 MLT). The parameters and formats of the plots are the same as in **Figure 1**.

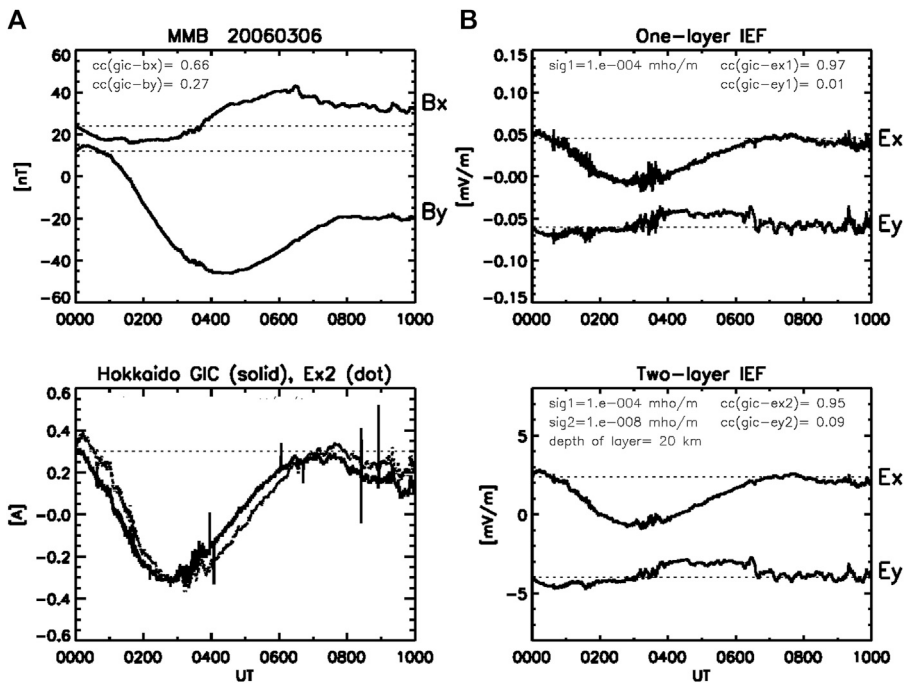


FIGURE 6 | (A) B_x, B_y and GIC observed at MMB, and **(B)** E_x and E_y calculated in the one- and two-layer models for the solar quiet diurnal variations with time scales of 8 h (00-08 UT, 09-17 MLT). The parameters and formats of the plots are the same as in **Figure 1**.

TABLE 1 | Correlation coefficients between the GIC and surface magnetic fields, B_x and B_y and the electric field, E_y and E_x induced by B_x and B_y, respectively, calculated in one (I)- and two (II)-layer models for space weather (SW) events with periods ranging from 1min to 24 h.

SW events	B_x	B_y	E_{xI}	E_{yI}	E_{xII}	E_{yII}
Pi2 (1 min)	−0.21	0.90	0.77	−0.18	0.96	−0.07
Sc (1–10 min)	−0.56	0.91	0.88	−0.63	0.99	−0.61
DP2 (30 min)	−0.07	0.54	0.88	0.22	0.97	0.13
Substorm (60 min)	0.23	0.67	0.94	−0.04	0.97	0.04
Storm (1–24 h)	−0.17	0.65	0.92	0.18	0.97	0.16
Sq (8 h)	0.66	0.27	0.97	0.01	0.95	0.09

$cc(GIC - E_{xI}) = 0.97$ and $cc(GIC - E_{xII}) = 0.95$, which show close connection of the GIC with B_y even under quiet conditions.

DISCUSSION

The GIC in Hokkaido, Japan, can be reproduced from B_y with high correlation coefficients as shown by Watari et al. (2009). We have further shown that the reproducibility strongly depends on the period of disturbances. As summarized in **Table 1**, the correlation with B_y is high for short periods, e.g., SC (cc = 0.91), but not for long periods, e.g., geomagnetic storm (cc = 0.65) and Sq (cc = 0.27). In particular, the correlation with $B_y$of the Sq is even lower than the correlation with B_x, $cc(GIC - B_x) = 0.66$. Using the one-layer model composed of the semi-infinite uniform conductor with the flat surface of the ground, we have calculated the IEF, E_x induced by B_y. The IEF is found to be highly correlated with the GIC as cc = 0.92 and 0.97 for the geomagnetic storm and Sq, respectively. This result implies that the long-period disturbances penetrated deep into the Earth, and the Earth can be considered to be uniform conductor. However, despite of the success with the one-layer model for long periods, the linear correlation with B_y (cc = 0.90) is still better than that with E_{xI} (cc = 0.77) for short period Pi2. This raises an issue on the period dependence of the reproducibility of the GIC.

To address this issue, we constructed the two-layer model composed of higher conductivity in the upper layer, following the

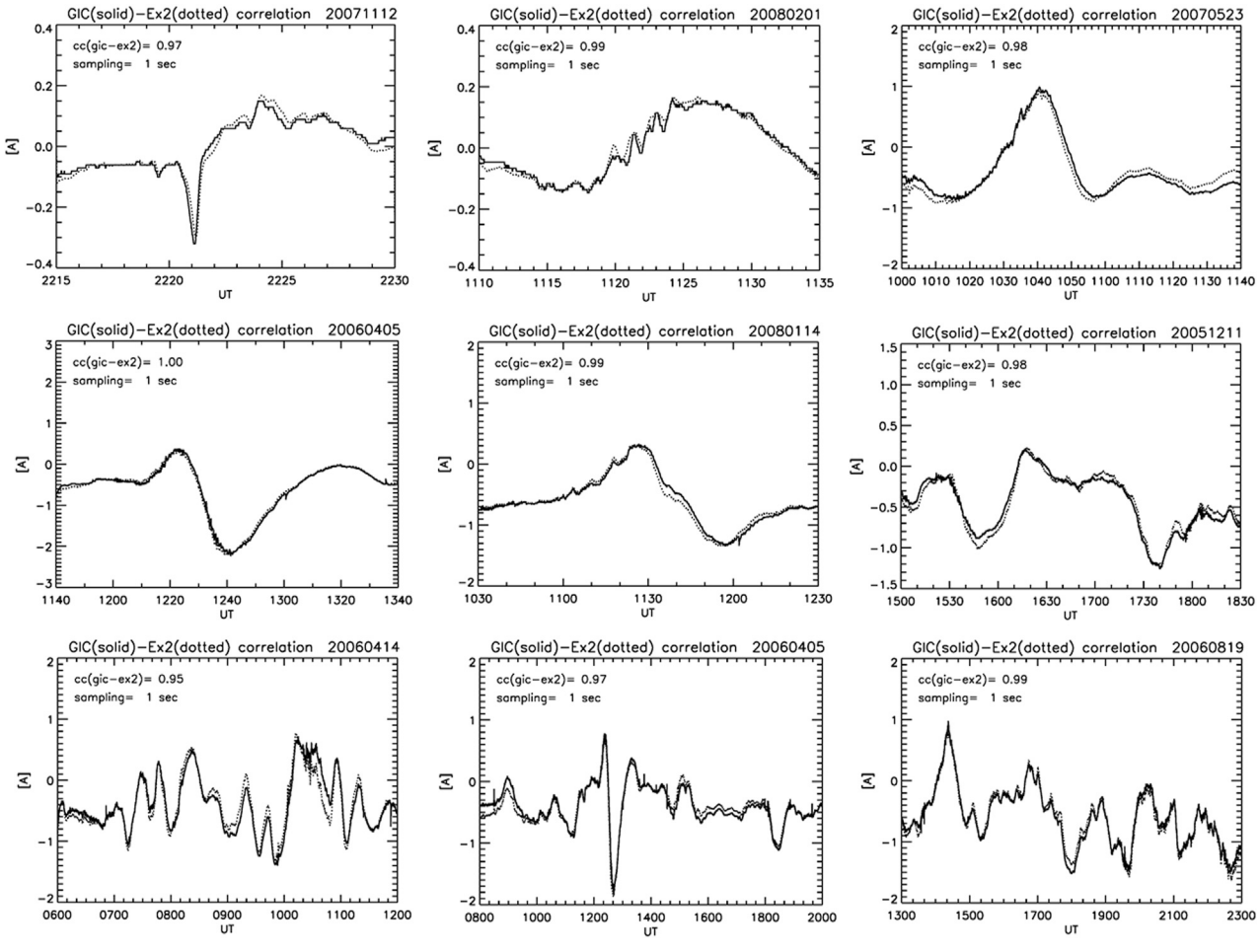


FIGURE 7 | Observed GIC (solid curve) and E_{x2} scaled to the GIC (dotted curve) during space weather disturbances; SC, Pi2, substorms, and storms with different time scales. The cc (gic-ex2) refers to the correlation coefficient between the GIC and E_{x2}, and sampling = 1 s refers to that the original 1 s sampled GIC and B_y data are used. Note that MLT = UT + 9.

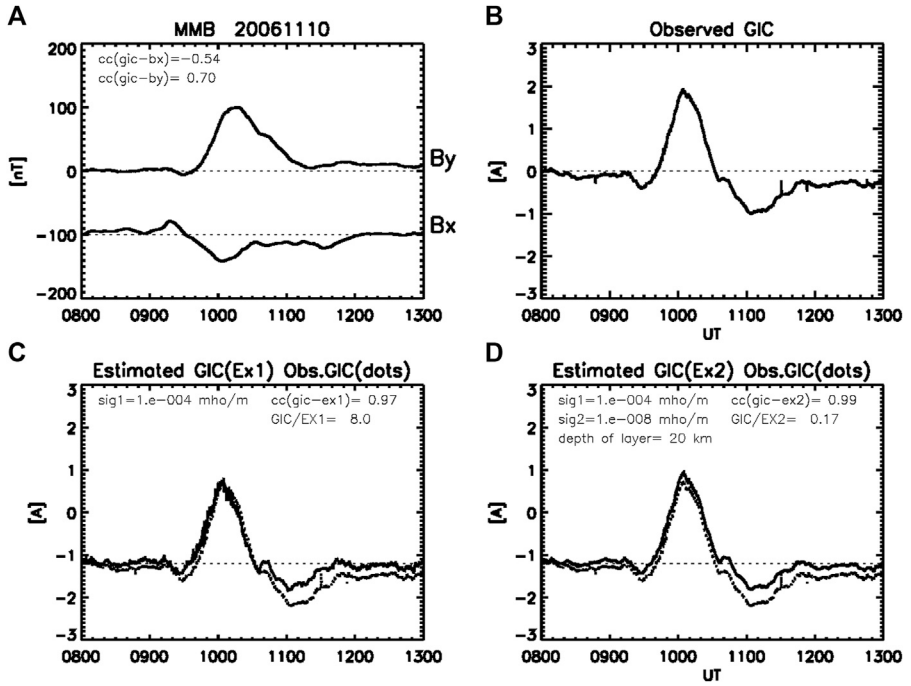


FIGURE 8 | (A, B) B_x, B_y and GIC observed at MMB in the evening (10 UT, 19 MLT) during the substorm bay event. **(C)** GIC estimated from E_{x1} scaled to the GIC with the scale factor, k_1 = 8.0 [A/(mV/m)] (solid line) and observed GIC (dotted line). **(D)** GIC estimated from E_{x2} scaled to the GIC with the scale factor, k_2 = 0.17 [A/(mV/m)] (solid line) and observed GIC (dotted line).

previous works on the geoelectric conductivity at Memambetsu (Owada, 1972). Fujii et al. (2015), using the MT method, clarified that the apparent resistivity of the Earth increases with an increasing period of geomagnetic disturbances at Memambetsu. This result is qualitatively consistent with the two-layer model with lower conductivity in the lower layer. The two-layer model with higher conductivity in the upper layer well explains the linear relationship with B (Pirjola, 2000). As summarized in **Table 1**, the induced electric field in the two-layer model, $E_{x\mathrm{II}}$, well reproduces the GIC with cc > 0.95 for both short- and long-period disturbances. To confirm the reproducibility with more events, we plotted the GIC and $E_{x\mathrm{II}}$ for other nine events in **Figure 7**, where impulsive, periodic, isolated, and long-lasting disturbances on both the day and night sides are shown. The GIC (solid curve) well coincides with the $E_{x\mathrm{II}}$ (dotted curve) that is scaled to the GIC. In particular, the peak of the GIC is well reproduced, which would help predict the GIC responsible for serious damages in the power transmission line.

We here check parameter dependence of the correlation coefficients (cc) in the two-layer model. Provided that the conductivities are fixed, major parameters responsible for cc are the number of reflections (n) and the depth of the upper layer (d_1) in the **Eq. 22**. Using the DP2 event in **Figure 3**, we calculated cc with d_1 = 20 km and different n. The cc increases as n increases such that cc = 0.94, 0.96, 0.96, 0.97, 0.97 for n = 20, 30, 40, 50, 100, respectively. We then calculated cc with fixed n = 50 and different d_1. The cc increases as d_1 increases such that cc = 0.94, 0.96, 0.97, 0.97 for d_1 = 10, 15, 20, 30 km, respectively. Thus, we fixed n = 50 and d_1 = 20 km in the two-layer model used for the calculation of the correlation coefficients.

Here, we make a brief comment on the singularity of $1/\sqrt{t}$ at t = 0 included in the step response function. Love and Swidinsky (2014), Love and Swidinsky (2015) introduced the ramp function, $\sqrt{t}$, derived from the inverse transform of $1/s\sqrt{s}$, to avoid the inconvenience in manipulating the singularity of $1/\sqrt{t}$. By using the time difference of $\sqrt{t}$, Love and Swidinsky (2015) reproduced the geoelectric field from the surface magnetic field in their two-layer model. The observed and calculated electric fields show fairly good coincidence, which may indicate success in using the ramp function. In our calculations, we replaced t with t + 0.0001 to avoid $1/\sqrt{t} = \infty$ at t = 0. This approximation worked well to achieve the excellent correlations between the IEF and GIC, while it is just technical so that 0.0001 can be replaced with another small value.

We next examine if we can estimate the GIC that could have occurred during the past major storms. For this examination, we fix scale factors, k_1 (GIC/E_{x1}) = 8.0 [A/(mV/m)] and k_2 (=GIC/E_{x2}) = 0.17 [A/(mV/m)], derived from the isolated substorm event in **Figure 8**. The observed GIC is well reproduced by both the one-layer and two-layer models with cc (GIC- E_{x1}) = 0.97 and cc (CIC- E_{x2}) = 0.99 as shown in the bottom left and right panels of **Figure 8**, respectively. For the sake of visual comparison, the observed GIC is plotted with dotted curves in each of the panels. Then, we used the scale factors, k_1 and k_2, to reproduce the GIC observed during the SC event (**Figure 2**). As shown in **Figure 9**, the GIC is well reproduced by the two-layer model with the same amplitude and high cc (=0.99), whereas the GIC is not well

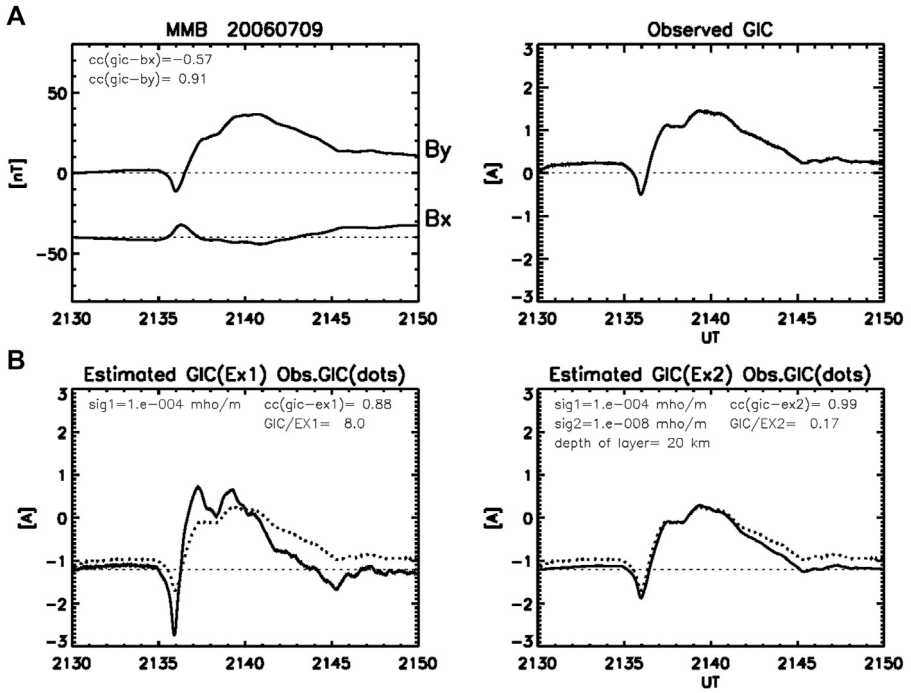


FIGURE 9 | (A) B_x, B_y and GIC observed at MMB during the SC event same as in **Figure 2**. **(B)** GIC estimated from E_{x1} and E_{x2} scaled with the same scale factors as in **Figure 8**.

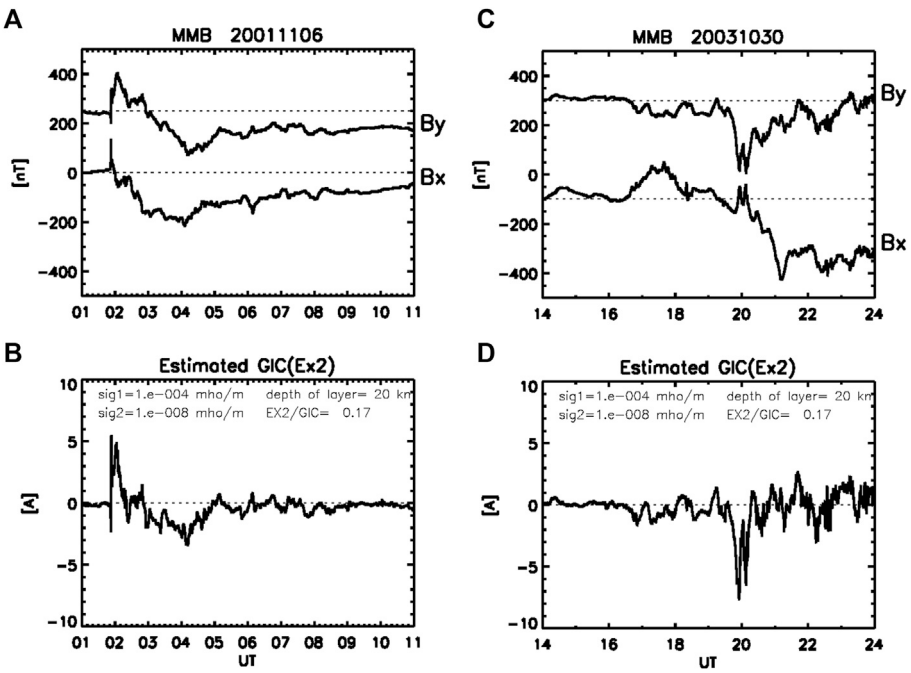


FIGURE 10 | (A) Geomagnetic storms recorded at MMB in the daytime (01-09 UT, 10-18 MLT) on November 06, 2001 and **(B)** in the midnight-morning (16-24 UT, 01-09 MLT) on October 30, 2003. **(C) (D)** GICs estimated from E_{x2} with the scale factor same as in **Figures 8**, **9**.

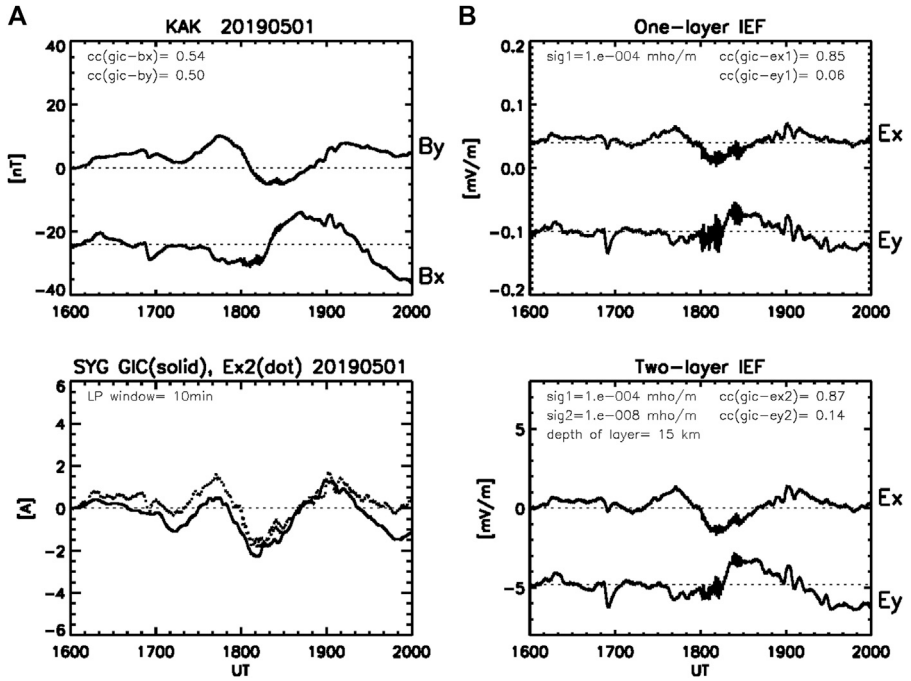


FIGURE 11 | (A) B_x and B_y observed at the Kakioka (KAK) magnetic observatory and GIC observed at the Shin-Yamaguchi (SYG) substation of the Chugoku Electric Power Company during the DP2 fluctuation event with periods of 60–80 min in the early morning (16-20 UT, 01-05 MLT). The GIC data is smoothed by applying the moving average over 10 min. **(B)** E_x and E_y calculated in one- and two-layer models. The parameters in the frames are the same as in **Figure 1** except that the depth of the upper layer of the two-layer model is 15 km.

reproduced by the one-layer model with lower cc (= 0.88) and overestimation of the rapid changes at the onset of the SC. The good correlation between the GIC and E_{x2} for the bay and SC events would allow us to use the scale factor k_2 to estimate the GIC for the past major storms. **Figure 10** shows two examples of the estimated GIC during the storms on November 6, 2001 (panel (a)) and October 30, 2003 (panel (b)). It is interesting to note that the GIC estimated for the October 2003 storm has the largest magnitude at 20 UT because of the large magnitude of B_y, when the storm ring current had not fully developed yet. This result suggests strong local time dependence of the GIC at MMB, which raises an important issue from the space weather forecasting point of view.

The parameters used in the two-layer model may not represent the ones estimated by the MT method (Fujii et al., 2015), but the excellent correlations in **Table 1** allow us to use the model to reproduce the GIC from the observed magnetic field disturbances. Therefore, the model should be referred to as an empirical model that works for MMB. Although the model is not a commonly applicable model, we check the model with GICs measured at the Shin-Yamaguchi (SYG) substation of the Chugoku Electric Power Company in Yamaguchi prefecture in the western-southern part of Japan (34.16°N, 131.09°E GR; 25.25°N, 201.67°E GM). The power transmission line extends in the east-west direction along the coastline. **Figure 11** shows a DP2 fluctuation event (T = 80 min) observed at Kakioka (KAK, 36.23°N,140.19°E GR; 27.95°N,209.77°E GM) and the GIC at SYG, where the high frequency components are removed by applying the moving average over the window of 10 min. The KAK observatory is separated from SYG by 2.7° in GML, but the GIC is well correlated with the IEF such that cc (GIC-E_{xI}) = 0.85 and cc (GIC-E_{xII}) = 0.87. The model parameters are the same as used in the calculations for MMB except for the depth of the upper layer of the two-layer model being 15 km. **Figure 12** shows an SC event with time scales of 1–10 min, where the window for the moving average is 30s. The correlation coefficients are better than those of the DP2 event such that cc (GIC-E_{xI}) = 0.93 and cc (GIC-E_{xII}) = 0.95. The correlation coefficients of the GIC with B_x/E_{yII} are not so good; cc = 0.54/0.14 and 0.27/0.51 for the DP2 and SC events, respectively. It is remarkable that the GIC at SYG is strongly dependent on B_y/E_x, similarly to the GIC at MMB. Furthermore, there is no big difference between the one- and two-layer models, suggesting us to use the simple one-layer model to estimate the GIC at SYG during the past major storms. Using the models constructed in the present study, we would be able to predict the GIC during space weather disturbances with the aid of the global simulations. Ebihara et al. (2014) successfully reproduced ground magnetic disturbances due to the equatorial electrojet driven by the penetration electric fields during substorms. Furthermore, Tanaka et al. (2020) reproduced magnetic disturbances due to field-aligned currents as well as the ionospheric currents during the SC and substorm.

The power transmission line in Hokkaido is directed southwestward (Watari et al., 2009), which would predict that the GIC is affected equally by both B_x and B_y. However, as shown above, the GIC depends only on B_y or E_x. Furthermore, the GIC depends on the B_y/E_x at SYG, where the power line and coastline

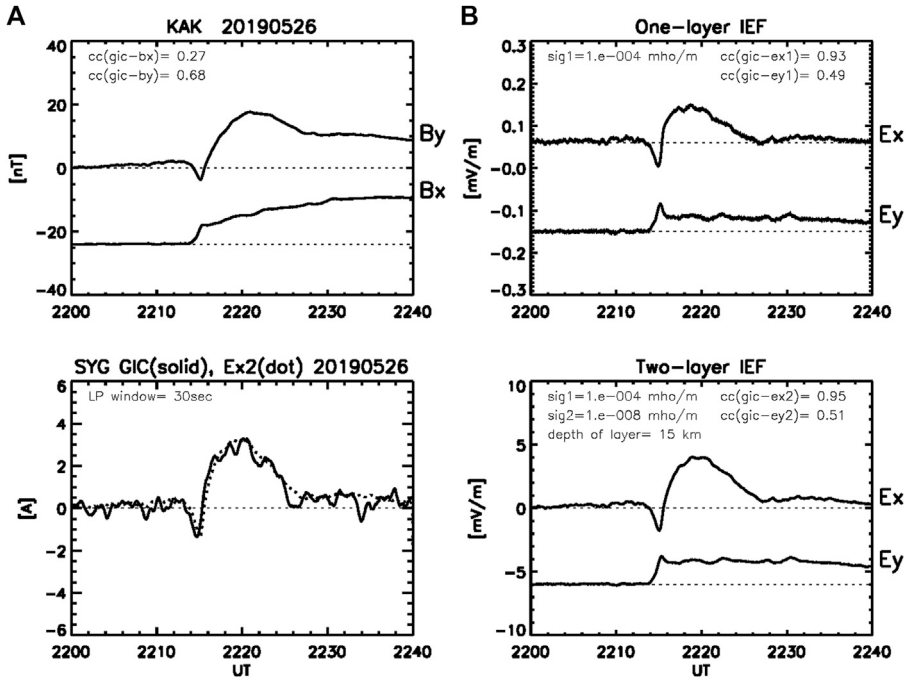


FIGURE 12 | (A) B_x and B_y observed at KAK in the morning (2220 UT, 0720 MLT) and GIC at SYG during the SC event (T = 1–10 min) with the same parameters as in **Figure 11**, except that the GIC data is smoothed over 30s. **(B)** IEFs in the same format as in **Figure 1**.

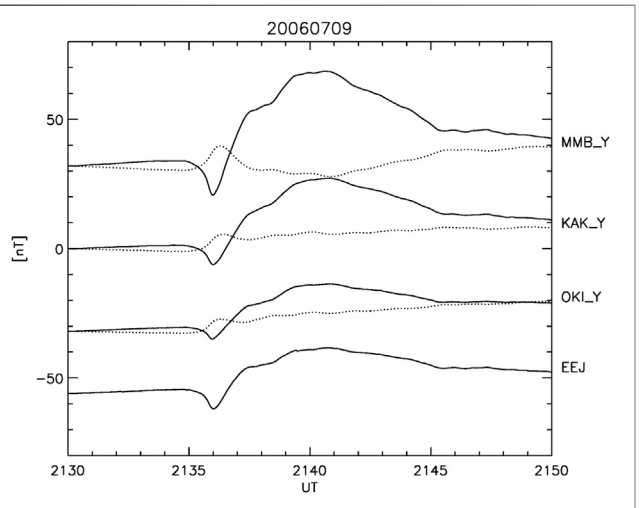


FIGURE 13 | Bx (dotted lines) and By (solid lines) recorded during the SC event (**Figure 2**) at Memambetsu (MMB, 35.7°GML), Kakioka (KAK, 27.8°GML), Okinawa (OKI, 17.0°GML), and the magnetic deflection caused by the equatorial electrojet (EEJ) defined as the difference between Bx (YAP, 0.5°GML) and Bx (OKI). All the stations are in the same local time zone (0630 MLT).

are in the east-west direction. Two possible mechanisms may explain the strong B_y dependence. One is that the GIC is a ground surface current induced by the TM_0 mode waves in the Earth-ionosphere waveguide (Watari et al., 2009; Brändlein et al., 2012). The TM_0 mode wave transmits the B_y and $E_{x,z}$ perpendicular and parallel to the (x-z) propagation plane, respectively, carrying the ionospheric currents and ground surface currents from high latitude to the equator (Kikuchi et al., 1978; Kikuchi, 2014). The TM_0 mode propagates at the speed of light and explains the simultaneous occurrence of the PI of SC (Araki, 1977) and DP2 fluctuations (Kikuchi et al., 1996) at high latitude and equator. In **Figure 13**, we show the equatorial electrojet (EEJ) defined as difference in B_x between Yap, Micronesia (YAP, 0.5° GML), and Okinawa, Japan (OKI, 17.0° GML) (Kikuchi et al., 1996) together with B_x (dots) and B_y (solid) at MMB, KAK, and OKI. It is remarkable that the EEJ is well correlated with B_y at MMB, KAK, and OKI, of which amplitude decreases as the latitude decreases. The latitudinal features may indicate that the Pedersen currents responsible for B_y at middle latitudes flow into the equatorial ionosphere. Since the TM_0 mode waves induce ionospheric currents and ground surface currents (Kikuchi, 2014), it would be reasonable to attribute B_y and the GIC to the TM_0 mode waves. It should be noted, however, that the TM_0 mode wave scenario may not be valid on the nightside, since ground magnetic fields are caused by magnetospheric currents in addition to the ionospheric currents during substorms (Ritter et al., 2008). Among these currents, the field-aligned currents transport the electromagnetic energy from the magnetosphere to the polar ionosphere. Therefore, a question arises, what kind of propagation mode transports the electromagnetic energy from the foot of the field-aligned currents or directly from the magnetosphere to the power transmission line at middle latitudes on the nightside? This will be a challenging issue of the magnetosphereionosphere coupling at middle latitudes.

The other possible mechanism is the effects of the geometry such as the direction of power lines and coastlines and of the 3-D structures of Earth's conductivities (Fujii et al., 2015; Goto, 2015; Nakamura et al., 2018). Ivannikova et al. (2018) found that much of Great Britain was affected by coastal effects owing to the strong conductivity gradient between the land and the ocean. The coastline effects on the GIC are also significant in Hokkaido as deduced from the model calculations (Nakamura et al., 2018). Furthermore, Fujii et al. (2015) clarified that the MT response at Memambetsu shows that B_y affects the induction in x-direction more strongly than B_x does in y-direction. The MT-deduced anisotropy is explained by means of the spatial inhomogeneity of the Earth's conductivity. Thus, both effects of the coastline and inhomogeneous distribution of the Earth's conductivity should have affected the anisotropic response of the GIC to the surface magnetic field. We would need to take into account the inhomogeneous conductivity distribution even in a thin layer model (e.g., McKirdy and Weaver, 1984). However, the horizontally uniform models employed in the present study well explain the GIC-B_y/E_x correlations. The consistency between the MT and GIC results and the inconsistency between the nonuniform and uniform models remain a question to be addressed in future studies.

CONCLUSION

1) We have shown that the GIC at Memambetsu in Hokkaido (35.7° GML) is linearly correlated with the y-component geomagnetic field, B_y, for the short-period disturbances such as the geomagnetic sudden commencements (cc = 0.91) and Pi2 pulsations (cc = 0.90), while the correlation was found to become worse as the period of disturbances increases, such that cc = 0.67 for the substorm and cc = 0.27 for the solar quiet diurnal variations.
2) The induced electric field in the one-layer model with the semi-infinite conductor ($\sigma = 10^{-4}$ mho/ m) well reproduces the GIC with cc = 0.94 for the substorm and 0.97 for the solar quiet variations. But, the correlation with B_y(cc = 0.91) is still better than the correlation with the induced electric field (cc = 0.88) for short period, SC.
3) We constructed the two-layer model with higher conductivity in the upper layer ($\sigma_1 = 10^{-4}$, $\sigma_2 = 10^{-8}$ mho/ m), which is found to be capable of reproducing the GIC with high correlations for both short periods, cc = 0.99 for SC, and for long periods, cc = 0.95 for Sq.
4) The GIC at Shin-Yamaguchi, Japan (25.3° GML) is well correlated with B_y/E_{xII} similarly to the GIC at MMB, such that cc = 0.87 and 0.95 for the DP2 and SC events, respectively.
5) The strong B_y dependence of the GIC could be associated with the TM_0 mode in the Earth-ionosphere waveguide, which carries B_y and ionosphere-ground surface currents from high latitude to the equator. This mechanism should be valid on the dayside, but it remains an issue to explain the B_y dependence on the nightside, where the magnetospheric current effects dominate over the ionospheric current effects.

DATA AVAILABILITY STATEMENT

The raw data supporting the conclusions of this article will be made available by the authors, without undue reservation.

AUTHOR CONTRIBUTIONS

TK built the one- and two-layer models and wrote the whole sections of the manuscript. YE contributed to creating the GIC database and to the calculation of the IEF in the models. KKH performed space weather event studies with magnetometer data and contributed to establishing the data acquisition system from SYG substation. KK installed the GIC meter and calibrated the data at SYG. S-IW contributed to recording the GIC at MMB. All authors contributed to manuscript revision, read, and approved the submitted version.

ACKNOWLEDGMENTS

The measurement of the GIC at Memambetsu substation of the Hokkaido Electric Power Co., Inc., was carried out under contract with the National Institute of Information and Communications Technology (NICT) and Institute for Sun-Earth Environmental Research (ISEE), Nagoya University. This contract is subject to the data sharing restrictions defined under the Memorandum of Understanding signed by the four organizations, including the NICT (S-IW) and Nagoya University (TK). We would like to thank Mr. Yuji Watanabe, Research and Development Department, the Hokkaido Electric Power Co., Inc., for supporting the GIC measurement at Memambetsu substation. The measurement of the GIC at Shin-Yamaguchi substation of the Chugoku Electric Power Co., Inc. was carried out under contract with the National Institute of Technology/Tokuyama College (TCT) and Kibi International University (KIUI). This contract is subject to the data sharing restrictions defined under the Memorandum of Understanding signed by the three organizations, including the TCT (KK) and KIUI (K.KH). We would like to thank Mr. K. Fujii at the Chugoku Electric Power Co., Inc., for supporting the GIC measurement at the Shin-Yamaguchi substation. Those who are interested in the data may contact with any one of TK at ISEE (kikuchi@isee.nagoya-u.ac.jp), S-IW at NICT (watari@nict.go.jp), and K.KH (hashi@kiui.ac.jp). The magnetometer data at Memambetsu and Kakioka are provided by the Kakioka Magnetic Observatory of the Japan Meteorological Agency (www.kakioka-jma.go.jp). The magnetometer data at Yap and Okinawa are from the Space Weather Magnetometer Network of the NICT. This study is supported by the grants-in-aid for Scientific Research (15H05815, 20H01960) of Japan Society for the Promotion of Science (JSPS), Electric Technology Research Foundation of Chugoku, and Wesco Scientific Promotion Foundation. The works of T.K. are supported by the joint research programs of the Institute for Space-Earth Environmental Research, Nagoya University and the Research Institute for Sustainable Humanosphere, Kyoto University.

REFERENCES

Akasofu, S.-I. (1964). The Development of the Auroral Substorm. *Planet. Space Sci.* 12, 273–282. doi:10.1016/0032-0633(64)90151-5

Araki, T. (1977). Global Structure of Geomagnetic Sudden Commencements. *Planet. Space Sci.* 25, 373–384. doi:10.1016/0032-0633(77)90053-8

Bolduc, L. (2002). GIC Observations and Studies in the Hydro-Québec Power System. *J. Atmos. Solar-Terrestrial Phys.* 64, 1793–1802. doi:10.1016/s1364-6826(02)00128-1

Borovsky, J. E., and Yakymenko, K. (2017). Substorm Occurrence Rates, Substorm Recurrence Times, and Solar Wind Structure. *J. Geophys. Res. Space Phys.* 122, 2973–2998. doi:10.1002/2016JA023625

Boteler, D. H., and Pirjola, R. J. (1998). The Complex-Image Method for Calculating the Magnetic and Electric fields Produced at the Surface of the Earth by the Auroral Electrojet. *Geophys. J. Int.* 132, 31–40.

Brändlein, D., Lühr, H., and Ritter, O. (2012). Direct Penetration of the Interplanetary Electric Field to Low Geomagnetic Latitudes and its Effect on Magnetotelluric Sounding. *J. Geophys. Res.* 117. doi:10.1029/2012JA018008

Cagniard, L. (1953). Basic Theory of the Magneto-telluric Method of Geophysical Prospecting. *Geophysics* 18 (3), 605–635. doi:10.1190/1.1437915

Carter, B. A., Yizengaw, E., Pradipta, R., Weygand, J. M., Piersanti, M., Pulkkinen, A., et al. (2016). Geomagnetically Induced Currents Around the World during the 17 March 2015 Storm. *J. Geophys. Res. Space Phys.* 121. doi:10.1002/2016JA023344

Cheng, D. K. (1959). *Analysis of Linear Systems*. Addison-Wesley world student series edition.

Ebihara, Y., Tanaka, T., and Kikuchi, T. (2014). Counter Equatorial Electrojet and Overshielding after Substorm Onset: Global MHD Simulation Study. *J. Geophys. Res. Space Phys.* 119, 7281–7296. doi:10.1002/2014JA020065

Freeman, M. P., and Morley, S. K. (2004). A Minimal Substorm Model that Explains the Observed Statistical Distribution of Times between Substorms. *Geophys. Res. Lett.* 31. doi:10.1029/2004GL019989

Fujii, I., Ookawa, T., Nagamachi, S., and Owada, T. (2015). The Characteristics of Geoelectric fields at Kakioka, Kanoya, and Memambetsu Inferred from Voltage Measurements during 2000 to 2011. *Earth Planet. Sp.* 67, 62. doi:10.1186/s40623-015-0241-z

Goto, T.-n. (2015). Numerical Studies of Geomagnetically Induced Electric Field on Seafloor and Near Coastal Zones Incorporated with Heterogeneous Conductivity Distributions. *Earth Planet. Sp.* 67, 193. doi:10.1186/s40623-015-0356-2

Han, D.-S., Iyemori, T., Nose, M., McCreadie, H., Gao, Y., Yang, F., et al. (2004). A Comparative Analysis of Low-Latitude Pi2 Pulsations Observed by Ørsted and Ground Stations. *J. Geophys. Res.* 109, A10209. doi:10.1029/2004JA010576

Imajo, S., Yoshikawa, A., Uozumi, T., Ohtani, S., Nakamizo, A., Marshall, R., et al. (2015). Pi2 Pulsations Observed Around the Dawn Terminator. *J. Geophys. Res. Space Phys.* 120, 2088–2098. doi:10.1002/2013JA019691

Ivannikova, E., Kruglyakov, M., Kuvshinov, A., Rastätter, L., and Pulkkinen, A. (2018). Regional 3-D Modeling of Ground Electromagnetic Field Due to Realistic Geomagnetic Disturbances. *Space Weather.* 16, 476–500. doi:10.1002/2017SW001793

Kelley, M. (1989). *The Earth's Ionosphere, Plasma Physics and Electrodynamics*. Akademic Press, Inc.

Kikuchi, T., and Araki, T. (1979). Horizontal Transmission of the Polar Electric Field to the Equator. *J. Atmos. Terrestrial Phys.* 41, 927–936. doi:10.1016/0021-9169(79)90094-1

Kikuchi, T., Araki, T., Maeda, H., and Maekawa, K. (1978). Transmission of Polar Electric fields to the Equator. *Nature* 273, 650–651. doi:10.1038/273650a0

Kikuchi, T., Lühr, H., Kitamura, T., Saka, O., and Schlegel, K. (1996). Direct Penetration of the Polar Electric Field to the Equator during aDP2 Event as Detected by the Auroral and Equatorial Magnetometer Chains and the EISCAT Radar. *J. Geophys. Res.* 101, 17161–17173. doi:10.1029/96ja01299

Kikuchi, T. (2014). Transmission Line Model for the Near-Instantaneous Transmission of the Ionospheric Electric Field and Currents to the Equator. *J. Geophys. Res. Space Phys.* 119, 1131–1156. doi:10.1002/2013JA019515

Kikuchi, T., Tsunomura, S., Hashimoto, K., and Nozaki, K. (2001). Field-aligned Current Effects on Midlatitude Geomagnetic Sudden Commencements. *J. Geophys. Res.* 106 (15), 555. doi:10.1029/2001ja900030

Kozyreva, O. V., Pilipenko, V. A., Belakhovsky, V. B., and Sakharov, Y. A. (2018). Ground Geomagnetic Field and GIC Response to March 17, 2015, Storm. *Earth Planet. Sp.* 70, 157. doi:10.1186/s40623-018-0933-2

Love, J. J., and Swidinsky, A. (2014). Time Causal Operational Estimation of Electric fields Induced in the Earth's Lithosphere during Magnetic Storms. *Geophys. Res. Lett.* 41, 2266–2274. doi:10.1002/2014GL059568

Love, J. J., and Swidinsky, A. (2015). Observatory Geoelectric fields Induced in a Two-Layer Lithosphere during Magnetic Storms. *Earth Planet. Sp.* 67, 58. doi:10.1186/s40623-015-0213-3

McKirdy, D. M., and Weaver, J. T. (1984). Induction in a Thin Sheet of Variable Conductance at the Surface of a Stratified Earth -- I. Two-Dimensional Theory. *Geophys. J. Int.* 78, 93–103. doi:10.1111/j.1365-246x.1984.tb06473.x

McPherron, R. L., Russell, C. T., and Aubry, M. P. (1973). Satellite Studies of Magnetospheric Substorms on August 15, 1968: 9. Phenomenological Model for Substorms. *J. Geophys. Res.* 78 (16), 3131–3149. doi:10.1029/ja078i016p03131

Nakamura, S., Ebihara, Y., Fujita, S., Goto, T., Yamada, N., Watari, S., et al. (2018). Time Domain Simulation of Geomagnetically Induced Current (GIC) Flowing in 500-kV Power Grid in Japan Including a Three-Dimensional Ground Inhomogeneity. *Space Weather.* 16, 1946–1959. doi:10.1029/2018SW002004

Ngwira, C. M., Pulkkinen, A., Wilder, F. D., and Crowley, G. (2013). Extended Study of Extreme Geoelectric Field Event Scenarios for Geomagnetically Induced Current Applications. *Space Weather.* 11, 121–131. doi:10.1002/swe.20021

Owada, S. (1972). On the Subterranean Electric Conductivity Near Memambetsu Deduced by the Magneto-Telluric Method (Japanese with English Abstract). *Mem. Kakioka Magn. Observatory.* 14 (No.2), 77–85.

Pirjola, R. (2010). Derivation of Characteristics of the Relation between Geomagnetic and Geoelectric Variation fields from the Surface Impedance for a Two-Layer Earth. *Earth Planet. Sp.* 62, 287–295. doi:10.5047/eps.2009.09.002

Pirjola, R. (2000). Geomagnetically Induced Currents during Magnetic Storms. *IEEE Trans. Plasma Sci.* 28 (6), 1867–1873. doi:10.1109/27.902215

Pirjola, R. (1983). Induction in Power Transmission Lines during Geomagnetic Disturbances. *Space Sci. Rev.* 35, 185–193. doi:10.1007/978-94-009-7063-2_14

Pulkkinen, A., Kataoka, R., Watari, S., and Ichiki, M. (2010). Modeling Geomagnetically Induced Currents in Hokkaido, Japan. *Adv. Space Res.* 46, 1087–1093. doi:10.1016/j.asr.2010.05.024

Pulkkinen, A., Pirjola, R., and Viljanen, A. (2007). Determination of Ground Conductivity and System Parameters for Optimal Modeling of Geomagnetically Induced Current Flow in Technological Systems. *Earth Planet. Sp.* 59, 999–1006. doi:10.1186/bf03352040

Ritter, P., and Lühr, H. (2008). Near-Earth Magnetic Signature of Magnetospheric Substorms and an Improved Substorm Current Model. *Ann. Geophys.* 26, 2781–2793. Available at: www.ann-geophys.net/26/2781/2008/. doi:10.5194/angeo-26-2781-2008

Satoh, H., Nishida, Y., Ogawa, Y., Takada, M., and Uyeshima, M. (2001). Crust and Upper Mantle Resistivity Structure in the Southwestern End of the Kuril Arc as Revealed by the Joint Analysis of Conventional MT and Network MT Data. *Earth Planet. Sp* 53, 829–842. doi:10.1186/BF03351680

Sutcliffe, P. R., and Lühr, H. (2010). A Search for Dayside Geomagnetic Pi2 Pulsations in the CHAMP Low-Earth-Orbit Data. *J. Geophys. Res.* 115. doi:10.1029/2009JA014757

Sutcliffe, P. R., and Lyons, L. R. (2002). Association between Quiet-Time Pi2 Pulsations, Poleward Boundary Intensifications, and Plasma Sheet Particle Fluxes. *Geophys. Res. Lett.* 29 (9), 7–1. doi:10.1029/2001gl014430

Tanaka, T., Ebihara, Y., Watanabe, M., Den, M., Fujita, S., Kikuchi, T., et al. (2020). Reproduction of Ground Magnetic Variations during the SC and the Substorm from the Global Simulation and Biot-Savart's Law. *J. Geophys. Res. Space Phys.* 125, e2019JA027172. doi:10.1029/2019ja027172

Trichtchenko, L., and Boteler, D. (2006). Response of Power Systems to the Temporal Characteristics of Geomagnetic Storms. *Can. Conf. Electr. Comp. Eng.* doi:10.1109/CCECE.2006.277733

Uyeshima, M. (2007). EM Monitoring of Crustal Processes Including the Use of the Network-MT Observations. *Surv. Geophys.* 28, 199–237. doi:10.1007/s10712-007-9023-x

Uyeshima, M., Utada, H., and Nishida, Y. (2001). Network-magnetotelluric Method and its First Results in central and Eastern Hokkaido, NE Japan. *J. Int.* 146, 1–19. doi:10.1046/j.0956-540x.2001.01410.x

Viljanen, A., and Pirjola, R. (1989). Statistics on Geomagnetically-Induced Currents in the Finnish 400kV Power System Based on Recordings of Geomagnetic Variations. *J. Geomagn. Geoelec.* 41, 411–420. doi:10.5636/jgg.41.411

Viljanen, A., Pirjola, R., Wik, M., Ádám, A., Prácser, E., Sakharov, Y., et al. (2012). Continental Scale Modelling of Geomagnetically Induced Currents. *J. Space Weather Space Clim.* 2, A17. doi:10.1051/swsc/2012017

Viljanen, A. (1997). The Relation between Geomagnetic Variations and Their Time Derivatives and Implications for Estimation of Induction Risks. *Geophys. Res. Lett.* 24, 631–634. doi:10.1029/97gl00538

Watari, S., Kunitake, M., Kitamura, K., Hori, T., Kikuchi, T., Shiokawa, K., et al. (2009). Measurements of Geomagnetically Induced Current in a Power Grid in Hokkaido, Japan. *Space Weather* 7. doi:10.1029/2008SW000417

Wei, L. H., Homeier, N., and Gannon, J. L. (2013). Surface Electric fields for North America during Historical Geomagnetic Storms. *Space Weather* 11, 451–462. doi:10.1002/swe.20073

Conflict of Interest: The authors declare that the research was conducted in the absence of any commercial or financial relationships that could be construed as a potential conflict of interest.

Publisher's Note: All claims expressed in this article are solely those of the authors and do not necessarily represent those of their affiliated organizations, or those of the publisher, the editors and the reviewers. Any product that may be evaluated in this article, or claim that may be made by its manufacturer, is not guaranteed or endorsed by the publisher.

Copyright © 2021 Kikuchi, Ebihara, Hashimoto, Kitamura and Watari. This is an open-access article distributed under the terms of the Creative Commons Attribution License (CC BY). The use, distribution or reproduction in other forums is permitted, provided the original author(s) and the copyright owner(s) are credited and that the original publication in this journal is cited, in accordance with accepted academic practice. No use, distribution or reproduction is permitted which does not comply with these terms.

frontiers in Astronomy and Space Sciences

ORIGINAL RESEARCH
published: 14 October 2021
doi: 10.3389/fspas.2021.740811

On the Saturation (or Not) of Geomagnetic Indices

*Joseph E. Borovsky**

Center for Space Plasma Physics, Space Science Institute, Boulder, CO, United States

Most geomagnetic indices are associated with processes internal to the magnetosphere-ionosphere system: convection, magnetosphere-ionosphere current systems, particle pressure, ULF wave activity, etc. The saturation (or not) of various geomagnetic indices under various solar-wind driver functions (a.k.a. coupling functions) is explored by examining plots of the various indices as functions of the various driver functions. In comparing an index with a driver function, "saturation" of the index means that the trend of stronger geomagnetic activity with stronger driving weakens in going from mid-range driving to very strong driving. Issues explored are 1) whether the nature of the index matters (i.e., what the index measures and how the index measures it), 2) the relation of index saturation to cross-polar-cap potential saturation, and 3) the role of the choice of the solar-wind driver function. It is found that different geomagnetic indices exhibit different amounts of saturation. For example the SuperMAG auroral-electrojet indices SME, SML, and SMU saturate much less than do the auroral-electrojet indices AE, AL, and AU. Additionally it is found that different driver functions cause an index to show different degrees of saturation. Dividing a solar-wind driver function by the theoretical cross-polar-cap-potential correction (1+Q) often compensates for the saturation of an index, even though that index is associated with internal magnetospheric processes whereas Q is derived for solar-wind processes. There are composite geomagnetic indices $E_{(1)}$ that show no saturation when matched to their composite solar-wind driver functions $S_{(1)}$. When applied to other geomagnetic indices, the composite $S_{(1)}$ driver functions tend to compensate for index saturation at strong driving, but they also tend to introduce a nonlinearity at weak driving.

Keywords: geomagnetic indices, polar cap saturation, solar wind—magnetosphere—ionosphere coupling, geomagnetic activity, reconnection

OPEN ACCESS

Edited by:
Scott Alan Thaller,
University of Colorado Boulder,
United States

Reviewed by:
Jeffrey Love,
United States Geological Survey
(USGS), United States
Jay R. Johnson,
Andrews University, United States

***Correspondence:**
Joseph E. Borovsky
jborovsky@spacescience.org

Specialty section:
This article was submitted to Space Physics, a section of the journal Frontiers in Astronomy and Space Sciences

Received: *13 July 2021*
Accepted: *20 September 2021*
Published: *14 October 2021*

Citation:
Borovsky JE (2021) On the Saturation (or Not) of Geomagnetic Indices. Front. Astron. Space Sci. 8:740811. doi: 10.3389/fspas.2021.740811

INTRODUCTION

It is well known that the cross-polar-cap potential in the ionosphere "saturates" under strong driving by the solar wind (e.g., Wygant et al., 1983; Reiff and Luhmann, 1986; Weimer et al., 1990a; Myllys et al., 2017), where saturation means that the ionospheric potential is systematically lower than expected for the observed solar-wind-driving conditions. The magnitude of the polar-cap potential saturation is well described by a parameter $Q \propto v_A \Sigma_P$ (cf. Ober et al., 2003; Borovsky et al., 2009; Gao et al., 2013) (see *Cross-Polar-Cap Potential Saturation* section), where v_A is the Alfven speed in the unperturbed solar wind and Σ_P is the height-integrated Pedersen conductivity of the polar-cap ionosphere. When looking at a plot of a geomagnetic index as a function of the strength of a solar-wind driver function, in the strong-driving regime (which also tends to be the large-Q regime) a

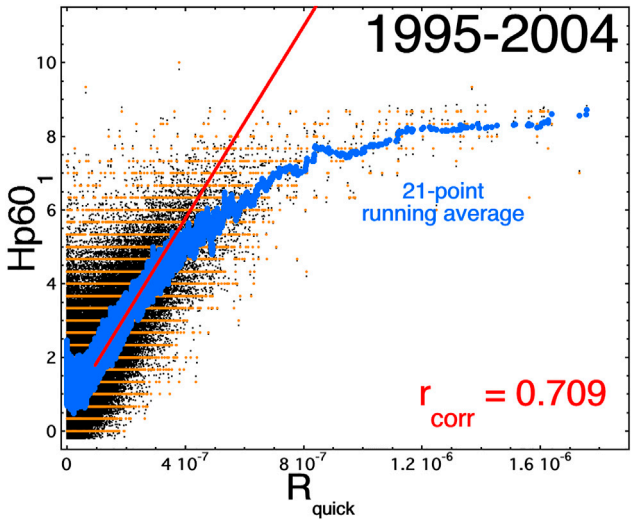


FIGURE 1 | The 1-h -lagged Hp60 index is plotted as a function of R_{quick} for the years 1995–2004. The orange points are the HP60 index and the black points are the HP60 index with small random numbers added to spread the points off the lines. Each orange point and each black point is 1 h of data. The blue points are 21-point running averages of the orange points. The thick red line is a least-squares linear-regression fit to $Hp60_1$ over the 50th–90th percentile of the R_{quick} values, and the red line is extended to larger R_{quick} values. The Pearson linear correlation coefficient r_{corr} between $Hp60_1$ (orange points) and R_{quick} is indicated in red.

saturation of the index is often seen wherein the index tends to stop increasing (or shows reduced increase) as the driver strength increases.

An example of an index that saturates appears in **Figure 1** where the Hp60 geomagnetic index is plotted as a function of the solar-wind driver function R_{quick}

$$R_{quick} = 6.9 p^{1/2} n_{sw}^{1/2} v_{sw}^{2} \sin^2(\theta_{clock}/2) M_A^{-1.35} \left[1 + 680 M_A^{-3.30}\right]^{-1/4} \quad (1)$$

where m_p is the mass of a proton, n_{sw} is the solar-wind proton number density, θ_{clock} is the IMF clock angle with respect to the Earth's dipole, and $M_A = v_{sw}/v_A$ is the solar-wind Alfven Mach number, which is a function of v_{sw}, B_{sw}, and n_{sw}. The values of R_{quick} are constructed using the 1-h-resolution OMNI2 solar-wind data set (King and Papitashvili, 2005). Hp60 is essentially the Kp index with a 60-min time resolution rather than a 3-h time resolution. $Hp60_1$ is Hp60 with a 1-h time lag from the solar wind. Like Kp (Thomsen, 2004), Hp60 is a measure of the internal convection in the magnetosphere. R_{quick} is the quick (simplified) derivation of the Cassak-Shay reconnection-rate equation (Cassak and Shay, 2007; Borovsky, 2008) applied at the nose of the magnetosphere written in terms of upstream solar-wind parameters (Borovsky and Birn, 2014; Borovsky and Yakymenko, 2017). The full derivations (Borovsky, 2008, 2013) produce more-accurate driver functions but result in algebraically much-more-complicated driver functions. Each orange point and each black point in **Figure 1** represents 1 h of data from the years 1995–2004 and the blue points are 21-point running averages of the orange points. (To spread the orange points vertically so that they do not lie on discrete lines, a small random value has been added to $Hp60_1$ when it is plotted as the black points.) Over the range of the 50th–90th percentiles of the R_{quick} values a least-squares linear-regression fit is made to the hourly values (black points) of $Hp60_1$ as a function of R_{quick} and that line is plotted in red. The line is extended to large R_{quick} values. The running average shows the vertical-versus-horizontal trend underlying the orange points: note for strong driving (large R_{quick}) that the running average flattens out instead of following the linear-regression fit: this is an example of a geomagnetic index saturating. In this report saturation of an index will be indicated by the index having a not-linear behavior going from mid-range driving to the strongest driving with the strength of the index weakening: this will be indicated by comparing the red-line fit for mid-range driving with the blue 21-point running averages going into the strongest driving.

Note that throughout this paper, 21-point running averages of the data will be plotted, as in **Figure 1**, with the unaveraged data typically not plotted. The 21-point running averages are to guide the eye about trends (such as bends) in the underlying un-averaged data. Often the trend in the data is not discernable on a plot without the running average. To obtain the 21-point running averages the data is sorted according to the magnitude of the driver-function value (horizontal axis) and then the running average is performed on the index (vertical axis). Hence, each point of the running average is the average value of the index for the 21 values of the driver function that are the closest in magnitude. 21 points was chosen as a compromise. With much more that 21 points, the running average curve does not extend into the strong-driving region of the plot. With much less than 21 points there is no advantage to averaging the data since the averaging curve will be as noisy as the underlying data. Note also that whenever correlations, etc., are calculated, they are calculated using the un-averaged data.

One motivation for investigating the nature of geomagnetic-index saturation is the development of composite geomagnetic indices (Borovsky and Denton, 2018; Borovsky and Osmane, 2019) that do not exhibit saturation at strong driving, even though some of the geomagnetic indices used to create the composite indices do exhibit saturation.

In the investigation of geomagnetic-index saturation, this paper will explore questions about 1) whether the nature of the index matters (what it measures and how it is measured), 2) the relation of index saturation to polar-cap potential saturation, and 3) the role of the choice of the solar-wind driver function.

CROSS-POLAR-CAP POTENTIAL SATURATION

Several mechanisms have been suggested for the cause of the saturation of the cross-polar-cap potential (cf. reviews by Borovsky et al., 2009; Gao et al., 2013; Myllys et al., 2017), but there is no community consensus as to which of the mechanisms is correct or dominant.

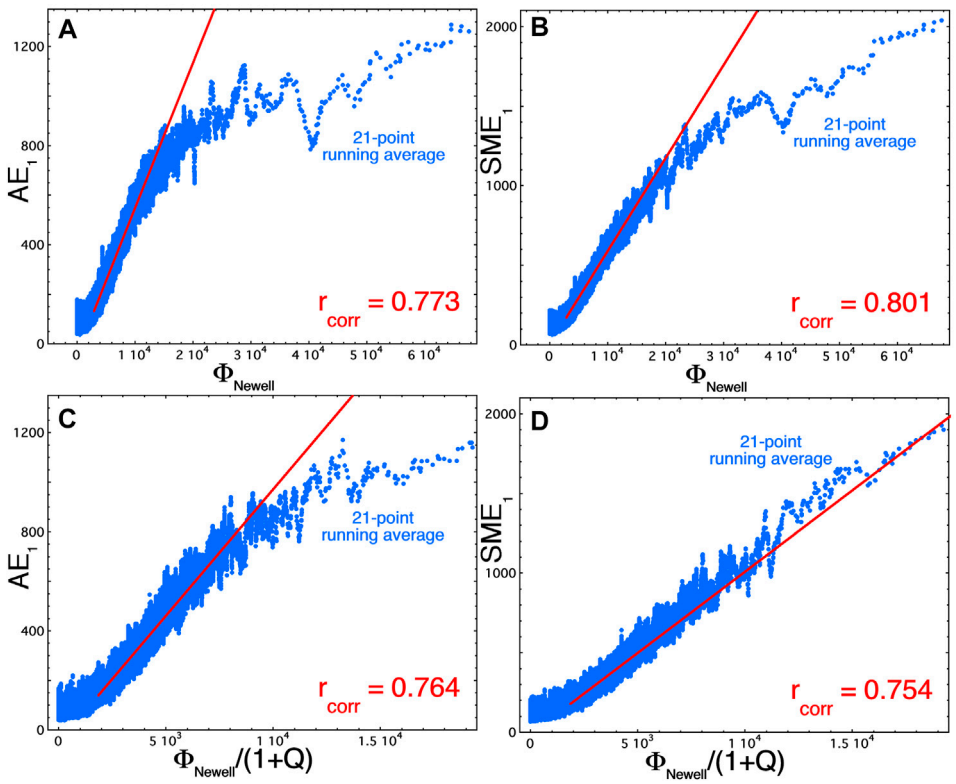


FIGURE 2 | For the years 1995–2004, the 1-h-lagged AE and SME indices are plotted as functions of the Newell driver function Φ_{Newell}. The blue points are 21-point running averages of the (unplotted) 1-h values. The red lines are a least-squares linear-regression fits over the 50th–90th percentile of the driver-function values, and the red lines are extended to larger driver-function values.

The reduction of the cross-polar-cap potential can be expressed as a multiplicative factor $(1+Q)^{-1}$ (Lavraud and Borovsky, 2008) where Q is a dimensionless parameter. Two physical arguments about polar-cap saturation lead to essentially the same formula for Q. Both arguments concern the solar wind, the magnetopause, and the polar-cap (open-field-line) ionosphere. First, Siscoe et al. (2004) argue that the high-latitude magnetopause current closes across the polar-cap ionosphere and that the magnetopause current is limited in magnitude by the amount of j×B force needed to halt the ram pressure of the solar wind. That derivation (Eqs 1–3 in Siscoe et al. (2004) with $\xi = 3.5$) yields

$$Q = V_A \Sigma_p / 892 \quad (2)$$

where v_A is the Alfven speed in the unperturbed solar wind in units of km/s and Σ_P is the height-integrated Pedersen conductivity of the polar-cap ionosphere in units of mho. Second, in a current-starvation (Alfven wing) argument (Goertz and Boswell, 1979; Kivelson and Ridley, 2008), to apply a potential ϕ across the polar cap a Pedersen current proportional to the Pedersen conductivity Σ_P must be supplied from field-aligned currents, with those field-aligned currents supplied to the polar cap by the solar-wind plasma. That parallel current is fed by an ion-polarization-drift current in the solar wind plasma. The Alfven speed of a plasma is governed by the strength of the ion-polarization-drift current (Nicholson, 1983), so the supply of parallel current is limited and proportional to v_A^{-1}. Hence the parameter

$$Q = V_A \Sigma_p / 795 \quad (3)$$

[Eq. 23 of Goertz and Boswell (1979)] describes the potential reduction of the polar cap caused by the inability of the solar wind to supply the required Pedersen current. Both arguments lead to essentially the same formula for Q since they both argue that the magnetopause current connects to the cross-polar-cap current: in the second argument the ion-polarization drift in the solar wind is the Alfvenic rotational discontinuity of the magnetopause propagating into the solar-wind plasma.

Note that large Q values tend to occur for low-Mach-number solar wind (Lavraud and Borovsky, 2008) where low values of the Alfven Mach number $M_A = v_{sw}/v_A$ are produced by high values of v_A. Low-Mach-number solar wind corresponds to the passage of a magnetic cloud (Borovsky and Denton, 2006).

SATURATION AND THE NATURE OF THE GEOMAGNETIC INDEX

In exploring why (or why not) a geomagnetic index saturates, it is suggested that the cause of the saturation could be 1) nature of the

index, 2) a relation to cross-polar-cap potential saturation, or 3) the use of the wrong driver function or an incomplete driver function. The nature of the index is what activity in the magnetosphere-ionosphere system the index measures and how the index measures that activity.

An example of how an activity is measured appears in **Figure 2**, where the auroral-electroject indices AE and SME are explored. Both AE and SME are indices that measure the intensity of the auroral-electrojet current; AE is measured with a modest number of ground magnetometer stations located in a ring around the Earth at high (northern) latitudes (Davis and Sugiura, 1966) whereas the SuperMAG SME is measured with a large network of ground magnetometer stations over a rang of latitudes (Newell and Gjerloev, 2011; Bergin et al., 2020). Both the nightside and the dayside auroral zones map into closed field regions within the magnetosphere (cf. Feldstein and Galperin, 1985; Frey et al., 2019). It is well known that the AE index saturates under strong driving (Weimer et al., 1990a,b). In the panels (a) and (b) of **Figure 2** the AE_1 and SME_1 (1-h lagged from the solar wind) indices in the years 1995–2004 are plotted as functions of the Newell driver function Φ_{Newell}

$$\Phi_{Newell} = V_{sw}^{4/3} B_{\perp}^{2/3} \sin^{8/3}(\theta_{clock}/2) \quad (4)$$

(Newell et al., 2007). Only the 21-point running averages (blue) of the hourly points are plotted in the four panels, along with a least-squares linear-regression fit to the hourly points in the 50th–90th percentile range of the driver function Φ_{Newell} (red). Panel (a) is AE_1 versus Φ_{Newell}: the 21-point running average shows a very strong saturation (flattening) for large values of Φ_{Newell}. Panel (b) is SME_1 versus Φ_{Newell}: SME_1 in panel (b) shows much less saturation than does AE_1. In each panel of **Figure 2** the Pearson linear-correlation coefficient r_{corr} for all 1-h data points is noted in red. Note higher Pearson linear correlation coefficients r_{corr} for SME_1 than for AE_1. Cross-polar-cap potential saturation can be largely corrected (mathematically accounted for) by dividing the solar-wind driver function by (1+Q) (Ober et al., 2003; Borovsky et al., 2009). In panels (c) and (d) of **Figure 2** the driver function $\Phi_{Newell}/(1+Q)$ is used to correlate with AE_1 and with SME_1. Here, Q is calculated as $Q = v_A \Sigma_P/795$ with $\Sigma_P = 0.77\ F_{10.7}^{1/2}$ (Ober et al., 2003). Comparing panels (a) and (c) it is seen that dividing the solar-wind driver by (1+Q) does not fully account for the observed saturation of AE_1, but comparing panels (b) and (d) it is seen that dividing the solar-wind driver by (1+Q) pretty much fully accounts for the saturation of SME_1. Hence, the saturation of AE appears to be in part related to the cross-polar-cap potential saturation plus another effect, whereas the milder saturation of SME appears to be solely related to the cross-polar-cap potential saturation. The additional saturation of AE may be caused by the fact that when driving is very strong the auroral oval expands to lower latitudes (e.g., Gussenhoven et al., 1983; Penskikh et al., 2021) away from the high-latitude ring of AE magnetometer stations, reducing the magnetic perturbations measured by those stations. The more-extensive network of SuperMAG ground magnetometer stations apparently does not suffer from this deficiency (cf. Bergin et al., 2020).

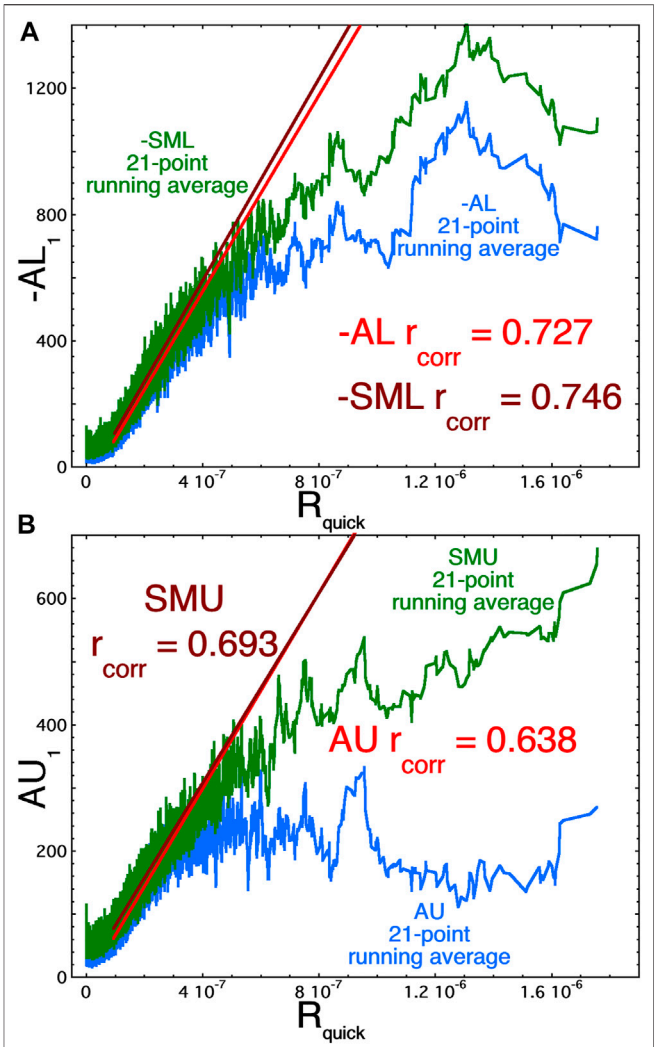


FIGURE 3 | For the years 1995–2004, the -AL index [panel **(A)**] and the AU index [panel **(B)**] are plotted as a function of R_{quick}. The blue points are 21-point running averages of the (unplotted) 1-h values. The red lines are a least-squares linear-regression fits over the 50th–90th percentile of the R_{quick} values, and the red lines are extended to larger R_{quick} values.

Note in **Figure 2** that dividing the solar-wind driver by (1+Q) helps to eliminate the appearance of saturation at strong driving, however it typically reduces the overall (all-points) linear correlation coefficient r_{corr} between the index and the solar-wind driver function.

The saturation of the auroral-electrojet indices is further explored in **Figure 3** where the behavior of the AU and AL indices is compared with the behavior of the SuperMAG SMU and SML indices. The solar-wind driver function used is R_{quick} [expression (1)]. The auroral-electrojet index AE is the sum of two other indices AE = AU − AL where AU is predominantly a positive number and AL is predominantly a negative number. AL is the maximum intensity of the eastward auroral electrojet and AU is the maximum intensity of the westward auroral electrojet: typically AL is recorded on the nightside of the auroral oval and

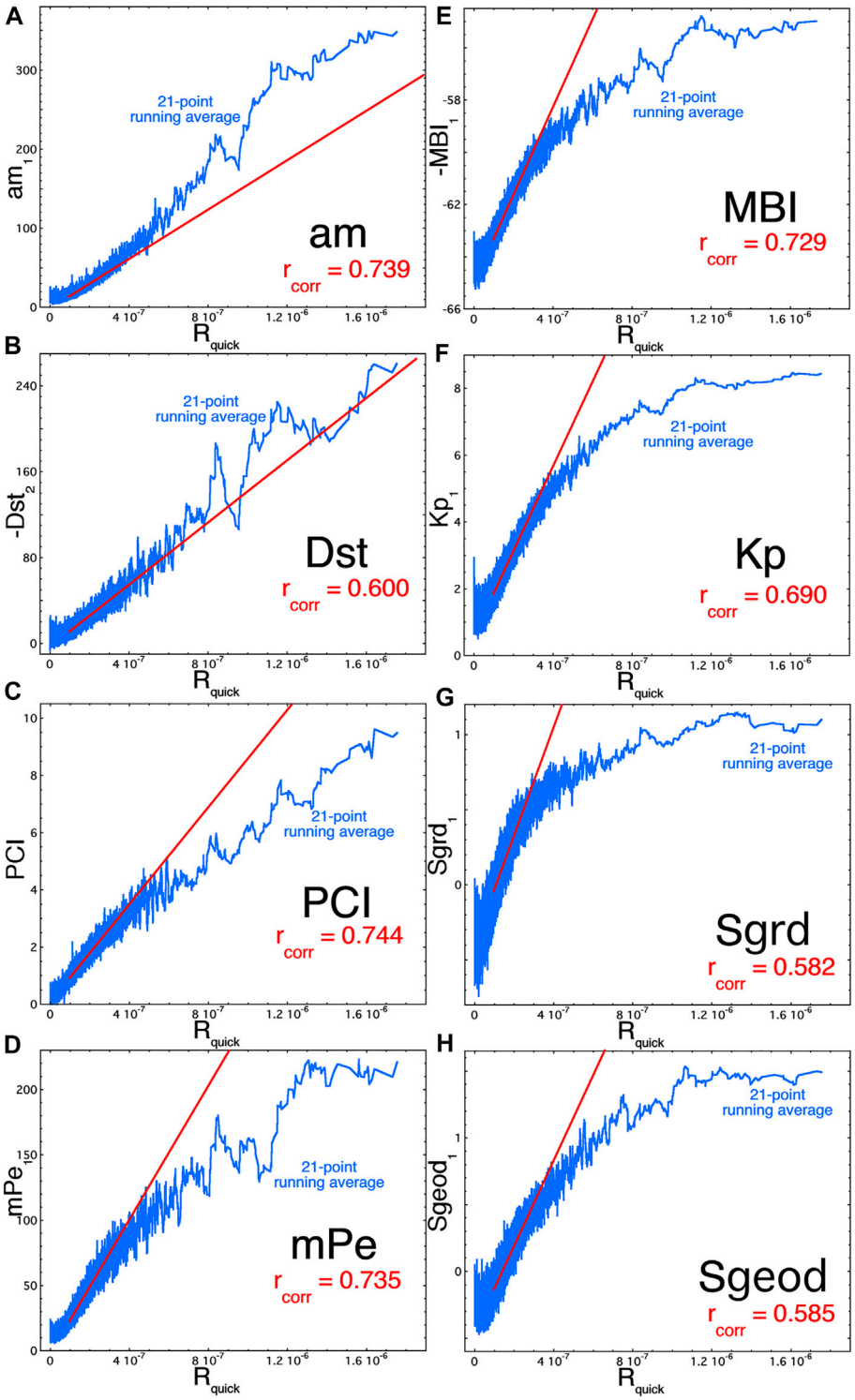


FIGURE 4 | For the years 1995–2004, eight geomagnetic indices are plotted as a function of R_{quick}. Hourly. The blue points are 21-point running averages of the (unplotted) 1-h values. The red lines are a least-squares linear-regression fits over the 50th–90th percentile of the R_{quick} values, and the red lines are extended to larger R_{quick} values.

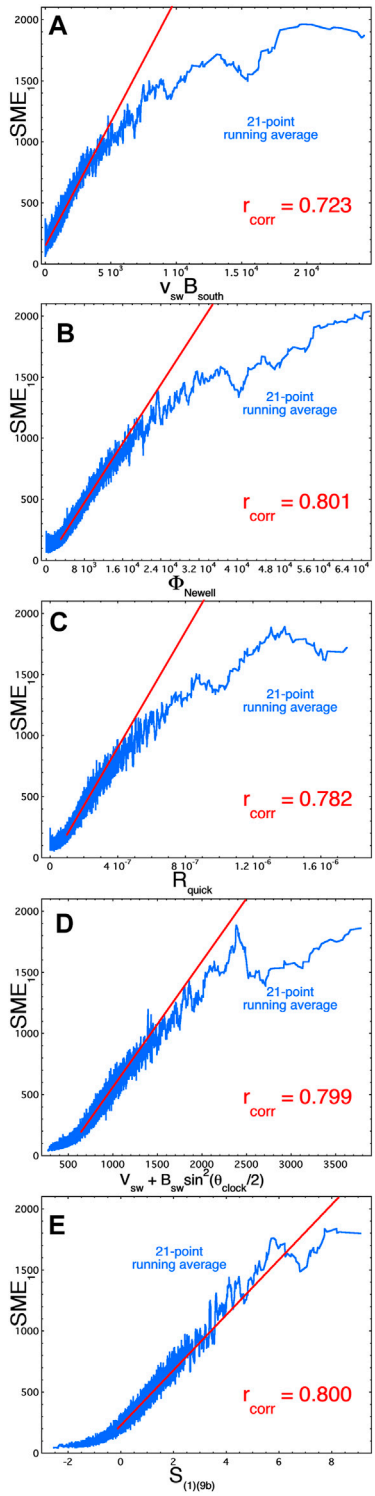


FIGURE 5 | For the years 1995–2004, the 1-h-lagged SME index is plotted as a function of five different solar-wind driver functions. The blue points are 21-point running averages of the (unplotted) 1-h values. The red lines are a least-squares linear-regression fits over the 50th–90th percentile of the driver-function values, and the red lines are extended to larger driver-function values.

typically AU is recorded on the dayside of the auroral oval (e.g., Goertz et al., 1993). The blue curve in **Figure 3A** is the 21-point running average of hourly values from the years 1995–2004 of $-AL_1$ (1-h lagged) and of AU_1 (1-h lagged) in **Figure 3B**. The red line in both panels is a least-squares linear-regression fit to the hourly values in the 50th–90th percentile range of R_{quick}. In **Figure 3A** it is seen that the AL index saturates, but note in **Figure 3B** that fractionally the AU index saturates much more strongly. The green curves in **Figure 3** are the 21-point running averages for the SuperMAG SML_1 index [panel (a)] and for the SuperMAG SMU_1 index [panel (b)]. Note that SML and SMU saturate less than AL and AU do. Presumably the stronger saturations of AL and AU are caused by the equatorward expansion of the auroral oval away from the ring of high-latitude stations that measure AL and AU. Note in the two panels of **Figure 3** the higher correlation coefficients r_{corr} between the indices SML and SMU with R_{quick} versus of coefficients between AL and AU with R_{quick}.

In **Figure 4** the behavior of 8 geomagnetic indices with respect to the magnitude of the solar-wind driver function R_{quick} is examined. With the exception of PCI in panel (c), the other 7 indices are associated with processes internal to the magnetosphere. In each panel of **Figure 4** the 21-point running average of the individual 1-h data points are plotted (blue) along with a least-squares linear-regression fit (red) to the individual points in the 50th–90th percentile range of R_{quick}. Saturation of an index will appear as a decrease of the slope of the running average as the magnitude of R_{quick} increases. In **Figures 4A,B** it is seen that the planetary range index am (cf. Mayaud, 1980) (1-h lagged from the solar wind) and the Dst index (2-h lagged from the solar wind) do not saturate under the action of the R_{quick} driver. **Figure 4C** indicates that the polar cap index PCI (Troshichev et al., 1988) (no time lag from the solar wind) saturates only mildly, i.e., its slope decreases by it does not flatten (See also Weimer et al., 2017 for no saturation of the field-aligned currents feeding the polar cap.). Similarly, the index of the mean electron precipitation mPe (Emery et al., 2009) (1-h lagged from the solar wind) only saturates mildly in **Figure 4D**. The midnight boundary index MBI (Gussenhoven et al., 1983) (1-h lagged from the solar wind) in **Figure 4E** and the Kp index (1-h lagged from the solar wind) in **Figure 4F** both show strong saturation for the R_{quick} driver function. In **Figures 4G,H** S_{grd} and S_{geod} are detrended ULF indices from ground (gr) measurements and from geosynchronous-orbit (geo) measurements (Romanova et al., 2007; Kozyreva et al., 2007; Romanova and Pilipenko, 2009), with the detrending described in Borovsky and Denton (2014). S_{grd} and S_{geod} show strong saturation. Note that although am, MBI, and Kp are all measures of the strength of magnetospheric convection, am does not saturate while MBI and Kp do saturate.

INDEX SATURATION AND THE SOLAR-WIND DRIVER FUNCTION

In **Figure 5** the saturation of the 1-h-lagged SuperMAG SME_1 index is examined for 5 different solar-wind driver functions. In

each panel of **Figure 5** the blue curve is the 21-point running average of the individual 1-h data points for the years 1995–2004 and the red line is a least-squares linear-regression fit to the individual 1-h data points in the 50th–90th percentile range of the driver strength. In each panel the Pearson linear correlation coefficient r_{corr} is indicated in red. In **Figure 5A** SME_1 is plotted as a function of the driver function $v_{sw}B_{south}$, which is $v_{sw}B_{south} = -v_{sw}B_z$ for B_z (GSM coordinates) southward (negative) and $v_{sw}B_{south} = 0$ for B_z northward (positive). The blue curve in **Figure 5A** indicates a very strong saturation at large values of $v_{sw}B_{south}$. **Figure 5B** examines SME_1 as a function of the Newell driver function Φ_{Newell} [expression (4)]: for Φ_{Newell} the degree of saturation of SME_1 is less dramatic than the saturation under $v_{sw}B_{south}$ in **Figure 5A**. **Figure 5C** examines SME_1 as a function of the reconnection driver function R_{quick}: again, the saturation for R_{quick} is less than the saturation for $v_{sw}B_{south}$ in **Figure 5A**. There are a number of solar-wind driver functions that have functional forms that seem unphysical in terms of the suspected physical processes by which the solar wind drives the Earth's magnetosphere (cf. Borovsky, 2014): $v_{sw} + 75B_{sw}\sin^2(\theta_{clock}/2)$ (where v_{sw} is in units of km/s and B_{sw} is in units of nT) is one of them. In **Figure 5D** the reaction of SME_1 to the solar-wind driver function $v_{sw} + 75B_{sw}\sin^2(\theta_{clock}/2)$ is plotted: the deviation of the 21-point running average (blue) from the linear regression (red) commences at higher values of the driver function than in panels (a)–(c). Hence, the saturation of SME_1 to the driver $v_{sw} + 75B_{sw}\sin^2(\theta_{clock}/2)$ only occurs at the highest values of the driver function. **Figure 5E** displays the relation between SME_1 and the canonical solar-wind driver function $S_{(1)(9b)}$, which is a composite of multiple solar-wind variables given by Eq. 9b of Borovsky and Denton (2014) [and see expression (5b) below]. As can be seen in **Figure 5E**, there is little or no saturation of SME_1 under solar-wind driving described by $S_{(1)(9b)}$.

New composite geomagnetic indices are possible derived with the use of canonical correlation analysis (vector-vector correlation) (Borovsky, 2014, 2020a; Borovsky and Denton, 2014, 2018; Borovsky and Osmane, 2019). The technique reduces a multidimensional time-dependent solar-wind state vector and a multidimensional time-dependent magnetospheric-system state vector to a time-dependent driver scalar and a time-dependent magnetospheric scalar (a composite index), with the composite index describing the global response of the magnetospheric system to the solar wind. The magnetospheric state vector contains multiple measures of the magnetospheric system, typically multiple geomagnetic indices plus spacecraft measurements of the states of various magnetospheric particle populations. This system description that is a reduction from the state vectors has advantages: compactness, low noise, and high prediction efficiency. Most important for the present study, the composite index shows linearity in the description of the magnetospheric system response to the solar-wind driver. I.e., the composite magnetospheric scalar does not exhibit saturation at strong driving by its matching composite scalar solar-wind driver. Here we will examine a case when only multiple geomagnetic indices are used in the magnetospheric state vector. The example

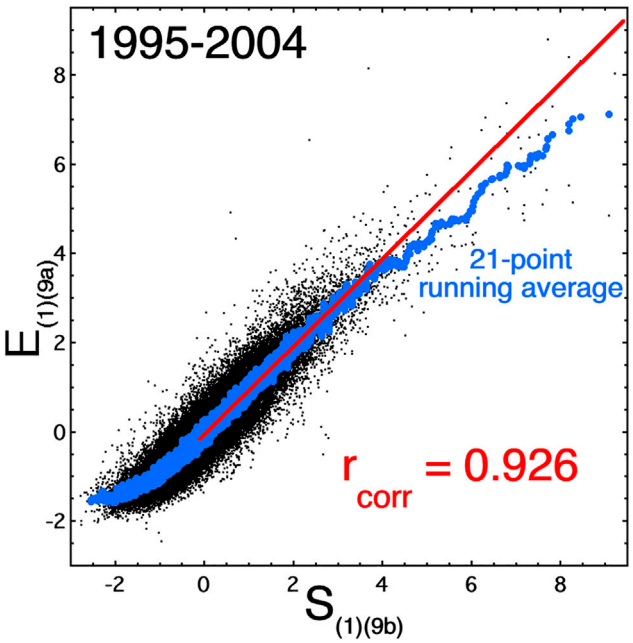


FIGURE 6 | For the years 1995–2004, the composite geomagnetic index $E_{(1)(9a)}$ is plotted as a function of the composite solar-wind driver function $S_{(1)(9b)}$. The black points are 1-h values and the blue points are 21-point running averages of the black points. The red lines are a least-squares linear-regression fits over the 50th–90th percentile of the $S_{(1)(9b)}$ values, and the red lines are extended to larger $S_{(1)(9b)}$ values.

is shown in **Figure 6**, where the composite magnetospheric scalar $E_{(1)(9a)}(t)$ ("E" representing Earth) is plotted as a function of its solar-wind driver scalar $S_{(1)(9b)}(t)$. The formula to create $E_{(1)(9a)}$ from 9 geomagnetic indices and the formula to create $S_{(1)(9b)}$ from 9 solar-wind variables are given by Eqs 9a, 9b of Borovsky and Denton (2014), which are repeated here:

$$E_{(1)(9a)} = 0.176\log(AE_1)^* + 0.036AU_1^* + 0.03Al_1^* + 0.244PCI_1^* + 0.166KP_1^* - 0.235MBI_1^* - 0.236Dst_1^* + 0.057S_{grd1}^* + 0.048S_{god1}^* \quad (5a)$$

$$S_{(1)(9b)} = 0.725\log(n_{sw}v_{sw}^2)^* - 0.535\log(n_{sw})^* - 0.357B_z^* + 0.274\langle\sin^2(\theta_{clock}/2)\rangle_{3^*} + 0.233\int^{22hr} R_{quick}\,dt^* + 0.189B_{sw}^* + 0.087\langle\theta_{Bn}\rangle_{3^*} - 0.070\log(M_A)^* + 0.064\log(F_{10.7})^* \quad (5b)$$

The asterisks in expressions (5a) and (5b) mean that the variable is standardized (mean value subtracted off followed by division by the standard deviation) and the numerical subscripts are the hrs of time lag of the magnetospheric variables from the solar-wind variables. Since the variables are standardized, either the base-e or the base-10 logarithms can be used. In expression (5b) the term $\int^{22\,h} R_{quick}\,dt$ is a 22-h time integral (into the past) of the reconnection driver function R_{quick}; this term in $S_{(1)}$ represents the past history of driving geomagnetic activity and acts to correct a slight hysteresis in the solar-wind driving of the

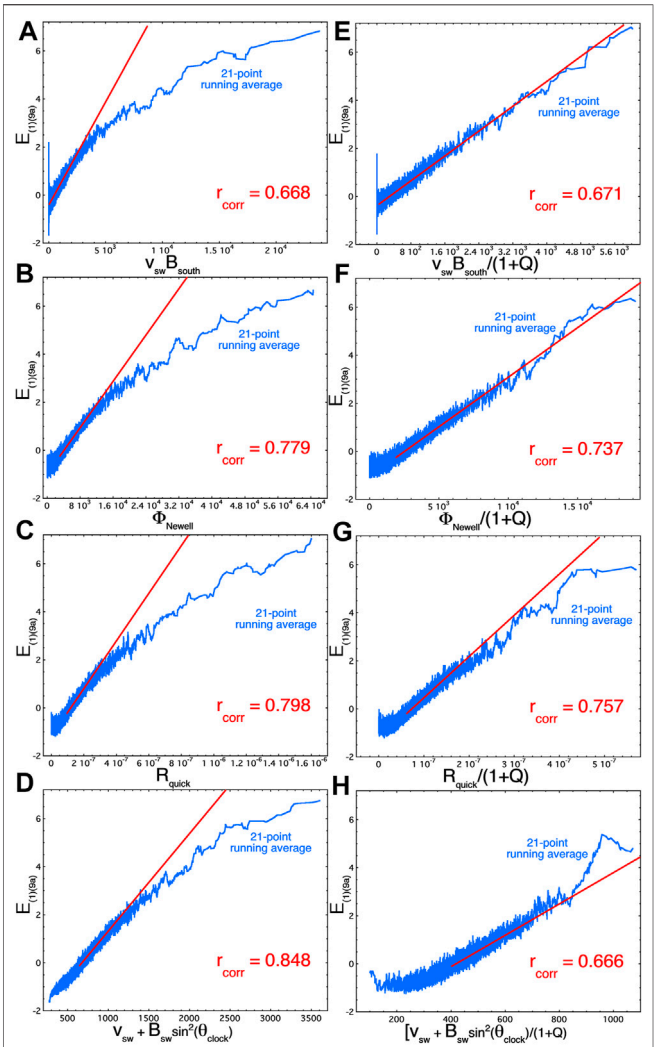


FIGURE 7 | For the years 1995–2004 the composite geomagnetic index $E_{(1)(9a)}$ is plotted as a function of four solar wind driver functions **(left column)** and as a function of the same driver functions divided by the factor (1+Q) **(right column)**. The blue points are 21-point running averages of the (unplotted) 1-h values. The red lines are a least-squares linear-regression fits over the 50th–90th percentile of the driver-function values, and the red lines are extended to larger driver-function values.

magnetosphere (which might be an atmospheric flywheel effect (e.g., Richmond and Matsushita, 1975). In **Figure 6** the hourly points of $E_{(1)(9a)}$ as a function of $S_{(1)(9b)}$ for the years 1995–2005 are plotted in black, a 21-point running average of the black points is plotted in blue, and a least-squares linear-regression fit to the black points in the 50th–90th percentile range of $S_{(1)(9b)}$ is plotted in red. Note the b) ely high Pearson linear correlation coefficient of 0.926 between $E_{(1)(9a)}$ and $S_{(1)(9b)}$. **Figure 6** shows the linearity for all strengths of the driving, with the running average (blue) tracking the linear fit (red). Note that other $E_{(1)}$ and $S_{(1)}$ variables composed of other geomagnetic indices and other solar-wind variables (with and without a $\int R_{quick}dt$ term) also show linearity in the response (no saturation): c.f. Figure 1 of Borovsky (2014), Figure 2A of Borovsky and Denton (2018), and Figure 1 of Borovsky and Osmane (2019). Note that the variable $F_{10.7}$ (which is used to construct a Q value) is not used in the $S_{(1)}$ values for these three referenced figures [cf. Eq. 2a of Borovsky (2014), Eq. 8 of Borovsky and Denton (2018), and Eq. 1a of Borovsky and Osmane (2019)], hence the lack of saturation in these cases is not dependent on the ability of the solar-wind driver function to know the value of Q.

An obvious question about the composite magnetospheric index $E_{(1)(9a)}$ is: How does the composite magnetospheric index $E_{(1)(9a)}$ behave in reaction to other solar-wind driver functions besides $S_{(1)(9b)}$? This is explored in **Figure 7** for four other driver functions. In **Figures 7A–D** of the reaction of $E_{(1)(9a)}$ to the solar-wind drivers $v_{sw}B_{south}$, Φ_{Newell}, R_{quick}, and $v_{sw} + 75B_{sw}\sin^2(\theta_{clock}/2)$ are examined by plotting the 21-point running averages (blue) of the hourly data points for the years 1995–2004 and comparing with linear-regression fits (red) in the 50th–90th percentile range of each driver function. In all four panels (a)–(d) the running averages indicate a saturation of $E_{(1)(9a)}$ for the four driver functions at strong levels of driving. In **Figures 7E–H** the four driver functions are each divided by (1+Q): this appears to more-or-less correct (or overcorrect) for the strong-driving saturation of $E_{(1)(9a)}$ for the four driver functions.

Comparing **Figure 6** for driver $S_{(1)(9b)}$ where there is no saturation with **Figures 7A–D** with other drivers where there is saturation, it seems that $S_{(1)(9b)}$ compensates for saturation (This is also the case in **Figure 5**). This implies that $S_{(1)(9b)}$ has the (1+Q) information in it. However, $F_{10.7}$ was not one of the solar-wind variables used to derive $S_{(1)(9b)}$ [see expression (5b)] and none of the other solar-wind variables in expression (5b) would seem to serve as a good proxy for $F_{10.7}$.

Figures 8, **9** examines the relation of the composite solar-wind driver function $S_{(1)(9b)}$ to 12 geomagnetic indices (similar to **Figures 3**, **4** for R_{quick} and various indices). With the exception of PCI in panel (c), all geomagnetic indices in **Figure 8** pertain to processes internal to the magnetosphere-ionosphere system. In each panel of **Figure 8** the blue curve is a 21-point running average of the 1-h data points and the red line is a linear-regression fit to the index as a function of $S_{(1)(9b)}$ in the 50th–90th percentile range of the $S_{(1)(9b)}$ values (with the red line extended to larger $S_{(1)(9b)}$ values). Comparing **Figure 8** with **Figures 3**, **4** it is seen that $S_{(1)(9b)}$ compensates for the strong-driving saturation of indices more than R_{quick} does. At strong driving $S_{(1)(9b)}$ reduces the saturation of PCI, mPe, MBI, Kp, SML, SMU, S_{grd} and S_{geod}. $S_{(1)(9b)}$ tends to overcompensate at strong driving for the indices am and Dst. Note that the all-points Pearson linear correlation coefficients are much higher for $S_{(1)(9b)}$ and the indices in **Figure 8** than they are for R_{quick} and the indices in **Figures 3**, **4**. Note also in comparing the 21-point running averages of **Figure 8** with the running averages of **Figures 3**, **4** that $S_{(1)(9b)}$ tends to introduce a nonlinearity at weak driving, with the index values being larger than a linear trend between $S_{(1)(9b)}$ and the index.

SUMMARY AND DISCUSSION

In this report some simple observations were made about the reactions of several geomagnetic indices to several solar-wind driver functions with the focus on whether or not the indices

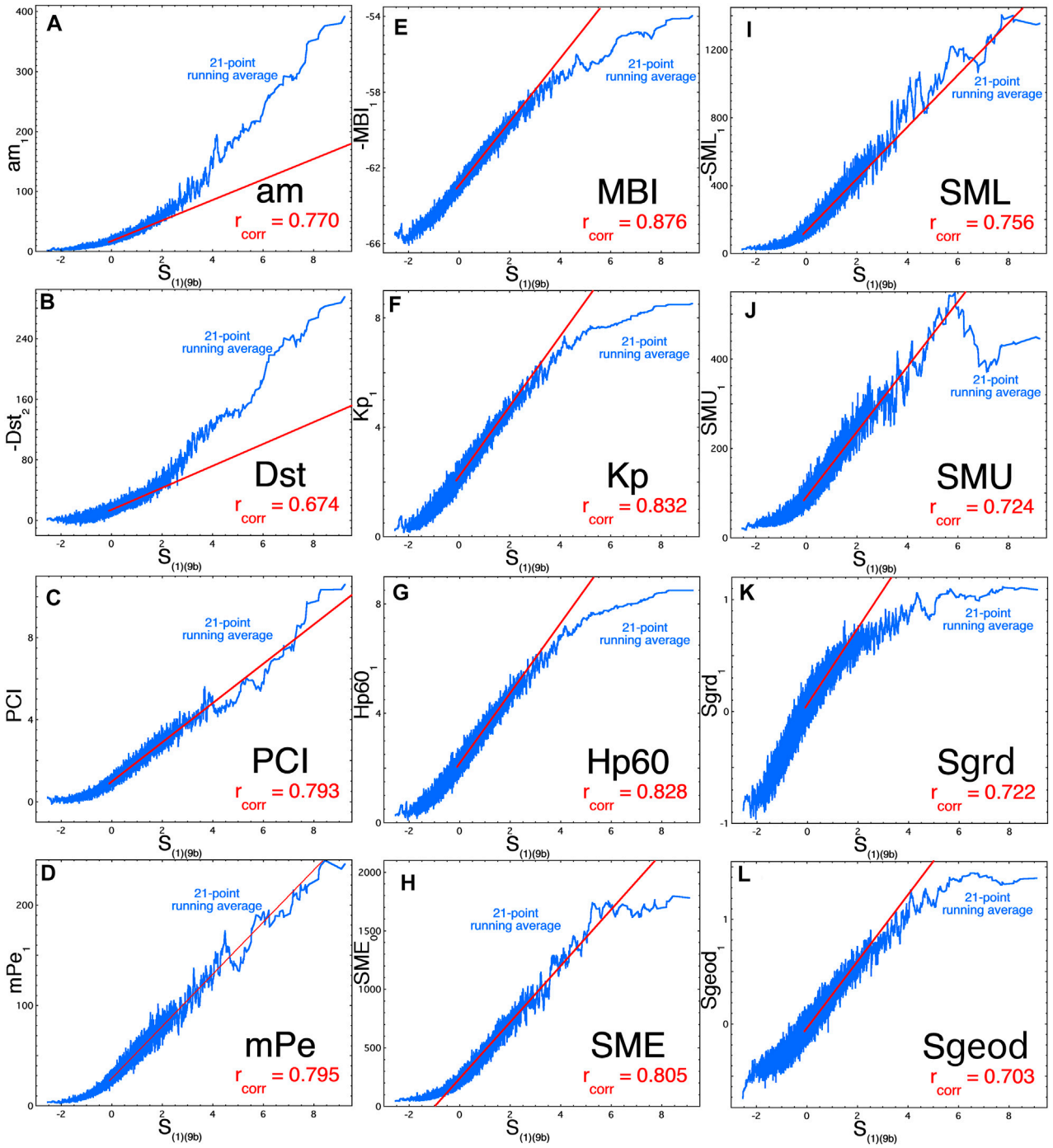


FIGURE 8 | For the years 1995–2004, 12 geomagnetic indices are plotted as a function of the composite driver function $S_{(1)(9b)}$. The blue points are 21-point running averages of the (unplotted) 1-h values. The red lines are a least-squares linear-regression fits over the 50th–90th percentile of the $S_{(1)(9b)}$ values, and the red lines are extended to $S_{(1)(9b)}$ values.

exhibit saturation for strong driving. Those observations are summarized as follows.

1) In plotting the strength of a geomagnetic index I(t) as a function of the strength of the solar-wind driver function D(t) and paying attention to the slope d|I|/dD of |I| as a function of the strength of D, saturation of the index is a reduction of the slope going from the region of moderate driving to the region of very strong driving.
2) Different geomagnetic indices show different degrees of saturation. E.g., for the solar-wind driver function R_{quick}

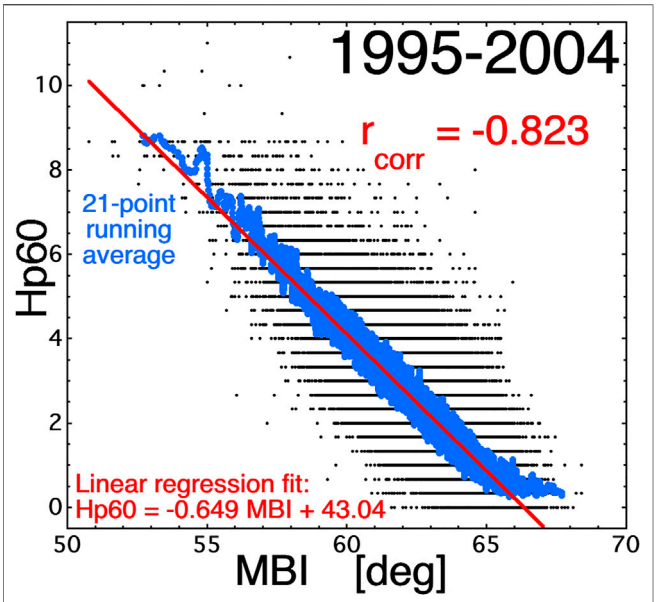


FIGURE 9 | For the years 1995–2004 the Hp60 index is plotted as a function of the MBI index (black points). A 21-point running average of Hp60 is plotted as the blue points and a linear-regression fit to the black points is plotted as the red line.

the indices am and Dst show no saturation, the PCI index shows mild saturation, and the indices mPe, MBI, Kp, Hp60, AE, AL, and AU show strong saturation.

3) Using the SuperMAG auroral-electrojet indices SME, SML, and SMU reduces the saturation seen with the AE, AL, and AU auroral-electrojet indices.
4) The degree of saturation of a geomagnetic index depends on the solar-wind driver function used.
5) Dividing a driver function by the theoretical polar-cap-saturation function (1+Q) can sometimes compensate the saturation of an index at strong driving, although sometimes it overcompensates. Although the derivations of Q are based on solar-wind/ionosphere arguments, the Q factor often compensates for geomagnetic indices that are associated with internal magnetospheric processes. The linear correlation coefficient between the index and the driver function often decreases when the driver function is divided by (1+Q), even in cases when saturation at high-driving is successfully corrected.
6) Derived composite indies $E_{(1)}$ do not exhibit saturation with their composite solar-wind driver functions $S_{(1)}$. $E_{(1)}$ does saturate under other solar-wind driver functions (e.g., $v_{sw}B_{south}$, Φ_{Newell}, R_{quick}) and dividing those driver functions by (1+Q) tends to compensate for the saturation of $E_{(1)}$.
7) The discussion subsections below concern difficulties in determining the strength of the driving of the magnetosphere by the solar wind and the difficulties in measuring the reaction of the magnetosphere-ionosphere system to that driving. Those discussions can be summarized as follows. The strength of the driving of the magnetosphere-ionosphere system by the solar wind is difficult to quantify and there is a lack of quantification of physical processes ongoing in the system's reaction to the solar-wind driving. We have predictions of the driving strength (via solar-wind driver functions) and proxy measurements of physical processes (via geomagnetic indices). Working with these indirect predictions and proxies make the causes of saturation difficult to interpret.
8) Two unsolved issues are: 1) Why is the saturation of various geomagnetic indices related to cross-polar-cap potential saturation? 2) Why are some composite solar-wind driver functions $S_{(1)}$ able to compensate for saturation without access to $F_{10.7}$ or other variables that would predict ionospheric conductivity?

Driving of the Magnetosphere-Ionosphere System

There is much that is not understood about the coupling of the solar wind to the Earth's magnetosphere and about the resulting driving of magnetospheric activity (e.g., Borovsky, 2021). Two important questions here are: 1) What do we mean by strength of driving? and 2) How do we measure the strength of driving?

We imagine that the total dayside reconnection rate (total amount of magnetic flux reconnected per unit time) would be a good indicator of the strength of driving of the magnetosphere by the solar wind. As of yet, we have no way of measuring the total dayside reconnection rate, we can only predict the rate from a knowledge of solar-wind parameters via the use of a variety of solar-wind driver functions.

The reconnection-rate function R_{quick} derived from the Cassak-Shay reconnection-rate equation is incomplete. R_{quick} only applies at the nose of the magnetosphere. To get the total reconnection rate along the entire dayside reconnection line we need the magnetospheric and magnetosheath plasma and field parameters along the entire reconnection line, which among other things requires a knowledge of where on the magnetopause the reconnection line is. Additionally, an accounting is needed for the effects of magnetosheath-magnetosphere velocity shear on the local reconnection rate. Also, we are completely lacking systematic information about the magnetospheric-plasma mass density ρ_{mag} at the dayside magnetosphere (Borovsky et al., 2013), which is in the denominator of the Cassak-Shay equation. And if we knew all that, we would still have only a prediction of the total reconnection rate, not an actual measurement.

Borovsky and Birn (2014) (see also Borovsky et al., 2008) argue that the concept of the solar-wind motional electric field controlling the dayside reconnection rate is mistaken (But see Lopez, 2016 for a response to this argument). The dayside reconnection rate has the dimensions of an electric field and for decades it has been assumed that reconnection electric field is proportional to the solar-wind motional electric field (e.g., Gonzalez and Mozer, 1974; Kan and Lee, 1979; Gonzalez and Gonzalez, 1981; Sergeev and Kuznetsov, 1981): reconnection

simulations by Birn and Hesse (2007) directly demonstrated that the two electric fields are not related.

Using global MHD simulation codes can be helpful for measuring the strength of driving, but the design of the simulation numerical scheme must guarantee that the MHD code gets the reconnection rate correct (cf. Borovsky et al., 2008).

A direct measure of the total dayside reconnection rate is the total ionospheric plasma flow (with ionospheric magnetic field) crossing the dayside open-closed boundary in the ionosphere: however, discerning where exactly that open-closed boundary is in ionospheric radar flow maps is difficult. Another measure of the total dayside reconnection rate is via the cross-polar-cap potential, however that cross-polar-cap potential is also affected by the nightside reconnection rate (Cowley and Lockwood, 1992) and there can be time delays between the reconnection rate and the polar-cap potential (Siscoe et al., 2011).

Note also that the assumption that the total dayside reconnection rate is a measure of the driving is ignoring any viscous driving of the magnetosphere by the solar wind (e.g., Lockwood and Moen, 1999; Farrugia et al., 2001), and questions about how to measure (Mozer, 1984; Drake et al., 2009) or predict (Vasyliunas et al., 1982; Borovsky, 2013) that portion of the driving.

Measuring the Reaction of the Magnetosphere-Ionosphere System to Driving

To understand quantitatively the reaction of the magnetosphere-ionosphere system to the solar wind, direct measures of the strengths of various magnetospheric physical processes is desirable. Instead we typically have proxy measures (e.g., geomagnetic indices) of diverse current systems.

One direct measure that we do have of a physical process is the cross-polar-cap potential in the ionosphere: however, as mentioned above that potential is affected by solar-wind driving and by reconnection in the magnetotail. Another physical quantity to focus on is the strength of magnetospheric convection, but a difficulty is directly measuring the strength of that convection. Specifically the total rate of convection might be defined as the amount of magnetic flux carried at the E-cross-B drift speed from the nightside magnetosphere into the dayside magnetosphere. The low-latitude-boundary-layer flow of flux antiSunward would not be included in that measure: that flow would be a measure of the driving in addition to the dayside reconnection rate. But there would be a difficulty in directly measuring the total convection rate in the magnetosphere with a limited number of spacecraft: a local measure of E-cross-B would need to be put into the context of the estimated time-dependent morphology of the magnetosphere to get a total convection from a local convection. Ionospheric radar convection maps may be a promising option.

Expectation of a Linear Reaction to Driving

In **Figures 1–8** a lot of linear response is seen between various geomagnetic indices and various solar-wind driver functions, particularly for mid-strength driving. Maybe it is surprising that we see so much linear behavior (Also, see the next subsection for a discussion of linearity and Kp.).

What measured reactions of the Earth do we expect to be linear with the strength of solar-wind driving? Is there a physical process in the magnetosphere that has a linear response and do we have a measure of the strength of that process that is also linear? (And still, what do we mean by strength of driving?)

If the rate of magnetospheric convection varies linearly with something like the total dayside reconnection rate, how do we measure it? For instance the MBI index is a measure of convection. MBI is the latitudinal position of the lower-latitude edge of the diffuse-auroral precipitation, which magnetically maps to the distance from the Earth of the inner edge of the electron plasma sheet penetrating from the magnetotail into the nightside of the dipole. The stronger the magnetospheric convection, the deeper the hot electrons E-cross-B drift into the dipole, and the lower the latitude of the diffuse-electron precipitation. However, the equatorial magnetic-field strength in the dipole varies as r^{-3}: Do we expect this penetration depth to be linear with the strength of the magnetospheric convection? Other measures of convection strength are indices such as am and Kp, which measure the strength of magnetotail currents and the proximity of the ionospheric closure currents to ground magnetometer stations (e.g., Thomsen, 2004) (See also the next subsection).

Note also that there are timescale complications to seeing a linear reaction of magnetospheric convection to dayside reconnection. The clock angle of the solar-wind magnetic field can vary drastically on a 10-min timescale (Borovsky, 2020b) and nightside reconnection can be bursty (Angelopoulos et al., 1994), however using hourly averaged measurements of the solar wind and the magnetosphere reduces these variabilities. There are, however, multiple time lags in the magnetospheric system (Borovsky, 2020a).

It might also be surprising that the auroral-electrojet indices show linear behavior with driving (Again, what do we mean by driving?) The large-scale nightside auroral currents are generated from the dipole-tail transition region probably by plasma flows and ion pressure gradients (Strangeway, 2012). The magnetospheric current-generation mechanisms for the smaller-scale auroral-arc currents are not known (Borovsky et al., 2020). As magnetospheric driving by the solar wind commences, the nightside magnetosphere undergoes a time evolution of morphology, as do the nightside currents and the particle populations. One would expect to see little in the way of a linear reaction of the current intensities with the strength of driving. Further, there is a feedback between the current intensities and the ionospheric conductivity (Weimer et al., 1990a) that may further ruin linearity. However, the use of hourly-averaged data may integrate out some of these time-evolution complexities to yield linearity at the 1-h-resolution examination of the dynamics.

In this report saturation of an index is gauged by a deviation from a linear trend in an algebraic relation between the index and a solar-wind driver function. Often this saturation can be "corrected" or "compensated for" by dividing the driver function by (1+Q), a method developed based on physical intuition of how the magnetosphere responds to the solar wind. Future studies could be performed to mathematically explore the explicit non-linear response of the magnetosphere to the solar wind: theses studies could explore integro-differential coupling relations rather than

algebraic functions (e.g., Borovsky, 2017; Mourenas et al., 2019) or they could use techniques that are well versed for nonlinear response such as information theory or conditional probability (e.g., Wing et al., 2016; Wing and Johnson, 2019).

What Does Hp60 (or Kp) Measure that Is Linear with the Strength of Earth Driving?

The indices Kp and Hp60 are based on the logarithm of the magnetic-field variation (range) seen at ground observatories. For example, a fit to the data in Table 6 of Mayaud [1980] yields Kp = $1.554\log_e(r_m)$ - 0.748, where r_m is the range (difference between the highest and lowest value) of the horizontal magnetic field in a 3-hr time interval. This Kp fit is accurate except for Kp < 0.3. The question arises as to why these "logarithmic" indices Kp and Hp60 show such a linear response to solar wind driving as displayed in **Figures 1**, **4f**, **8f**, and **8g**.

Thomsen [2004] argued that Kp is a measure of the latitude of the auroral zone. Figs. 6 and 7 of Thomsen [2004] (also Fig. 14 of Mayaud [1980] and Fig. 6 of Menvielle and Berthelier [1991]) points out the sensitivity of the magnetic variance range on the latitudinal distance of a subauroral magnetometer station from the location of the auroral current. If the current source (auroral zone) changes latitude the magnetic variance measured at a station will change substantially, approximately as 1/L where L is the latitude difference of the station from the current source. Since Kp and Hp60 are approximately the logarithm of the magnetic variance, they change less drastically than the variance changes. **Figure 9** demonstrates this argument (see also Fig. 1 of Thomsen [2004]). In **Figure 9** the Hp60 index is plotted (black points) as a function of the midnight boundary index MBI [Gussenhoven et al., 1983] for the years 1995-2004: MBI is a measure of the position of the lower-latitude edge of the auroral zone obtained from electron-precipitation measurements onboard the multiple DMSP spacecraft. The Pearson linear correlation coefficient between the plotted values of Hp60 and MBI is r_{corr} = -0.823. A 21-point running average of Hp60 is plotted as the blue points and a linear-regression fit of Hp60 as a function of MBI is plotted as the red line: the obtained fit is Hp60 = −0.649MBI + 43.04. According to this fit, the Hp60 index changes by unity, on average, when the midnight latitude of the auroral zone changes by 1/0.649 = 1.54°. Note however that the auroral zone latitudinal displacement with changes in Kp (convection) are less at local times other than midnight (e.g. compare Figs. 4a and 4b of Gussenhoven et al. [1983] where the auroral-zone latitudinal shift with Kp at local noon is about half the size of the latitudinal shift at local midnight. In **Figure 9** the linear-regression fit (red) tracks the running average (blue), indicting the linearity of the relationship of Hp60 to the latitudinal location of the auroral zone. The latitudinal location of the auroral zone is sensitive to the strength of magnetospheric convection [Gussenhoven et al., 1981; Elphic et al., 1999; Denton et al., 2005; Penskikh et al., 2021], i.e. how deep into the nightside dipolar portion of the magnetosphere magnetotail electron plasma sheet penetrates owing to global convection fighting co-rotation [Volland, 1973; Korth et al., 1999]. **Figure 1** indicates the linearity of Hp60 as a function of R_{quick} (at least until the linear relation saturates at strong driving levels). **Figure 4e** similarly shows a linearity of MBI with R_{quick}. The solar-wind-driving function Rquick was derived to be an estimate (from solar-wind variables) of the magnetic-reconnection rate at the nose of the magnetosphere [Borovsky, 2008; Borovsky and Birn, 2014]. The total magnetospheric convection, i.e. the return of magnetic flux from the magnetotail to the dayside of the dipole, should be linearly proportional to R_{quick}.

Other Issues

The focus of our thinking has been on dayside reconnection as the driver in solar-wind/magnetosphere coupling. Post-reconnection effects (such as current starvation) that might disconnect the reaction strength from the driving strength have not been considered. Additionally, viscous driving by the solar wind has not been considered.

Some different aspects of reconnection driving have not been separated: e.g., magnetospheric convection driven by the removal of magnetic flux from the dayside, magnetospheric convection driven by the accumulation of magnetic flux in the magnetotail, and magnetospheric convection driven by antisunward ionospheric convection in the polar cap directly driven by the solar wind (Siscoe and Siebert, 2006).

Finally, the preconditioning of the magnetosphere (Borovsky and Steinberg, 2006; Lavraud et al., 2006), which will alter the reaction of the magnetosphere to driving, and solar-wind/magnetosphere feedback loops (Borovsky and Valdivia, 2018; Walsh and Zou, 2021), which will produce a time-dependent reaction to steady driving, have not been considered.

DATA AVAILABILITY STATEMENT

Publicly available datasets were analyzed in this study. This data can be found here: http://supermag.jhuapl.edu/indices ftp://ftp.gfz-potsdam.de/pub/home/obs/Hpo https://omniweb.gsfc.nasa.gov.

AUTHOR CONTRIBUTIONS

JB initiated this project, performed the analysis, and wrote the manuscript.

FUNDING

This work was supported at the Space Science Institute by the NSF GEM Program via grant AGS-2027569, by the NASA Heliophysics LWS program via award NNX16AB75G by the NSF SHINE program via grant AGS-1723416, and by the NASA Heliophysics Guest Investigator Program via award NNX17AB71G.

ACKNOWLEDGMENTS

The author thanks Mick Denton and Jürgen Matzka for help. The author also acknowledges the SuperMAG team; the SuperMAG auroral-electrojet indices are available at http://supermag.jhuapl.edu/indices. The author also acknowledges GFZ Potsdam for the Hp60 index, which is available at ftp://ftp.gfz-potsdam.de/pub/home/obs/Hpo.

REFERENCES

Angelopoulos, V., Kennel, C. F., Coroniti, F. V., Pellat, R., Kivelson, M. G., Walker, R. J., et al. (1994). Statistical Characteristics of Bursty Bulk Flow Events. *J. Geophys. Res.* 99, 21257–21280. doi:10.1029/94ja01263

Bergin, A., Chapman, S. C., and Gjerloev, J. W. (2020). AE, Dst, and Their superMAG Counterparts: The Effects of Improved Spatial Resolution in Geomagnetic Indices. *J. Geophys. Res.* 125, e2020JA027828. doi:10.1029/2020ja027828

Birn, J., and Hesse, M. (2007). Reconnection Rates in Driven Magnetic Reconnection. *Phys. Plasmas* 14, 082306. doi:10.1063/1.2752510

Borovsky, J. E. (2020a). A Survey of Geomagnetic and Plasma Time Lags in the Solar-Wind-Driven Magnetosphere of Earth. *J. Atmos. Solar-Terrestrial Phys.* 208, 105376. doi:10.1016/j.jastp.2020.105376

Borovsky, J. E., Birn, J., Echim, M. M., Fujita, S., Lysak, R. L., Knudsen, D. J., et al. (2020). Quiescent Discrete Auroral Arcs: A Review of Magnetospheric Generator Mechanisms. *Space Sci. Rev.* 216, 1. doi:10.1007/s11214-019-0619-5

Borovsky, J. E., and Birn, J. (2014). The Solar Wind Electric Field Does Not Control the Dayside Reconnection Rate. *J. Geophys. Res. Space Phys.* 119, 751–760. doi:10.1002/2013ja019193

Borovsky, J. E. (2014). Canonical Correlation Analysis of the Combined Solar Wind and Geomagnetic index Data Sets. *J. Geophys. Res. Space Phys.* 119, 5364–5381. doi:10.1002/2013ja019607

Borovsky, J. E., Denton, M. H., Denton, R. E., Jordanova, V. K., and Krall, J. (2013). Estimating the Effects of Ionospheric Plasma on Solar Wind/magnetosphere Coupling via Mass Loading of Dayside Reconnection: Ion-Plasma-Sheet Oxygen, Plasmaspheric Drainage Plumes, and the Plasma Cloak. *J. Geophys. Res. Space Phys.* 118, 5695–5719. doi:10.1002/jgra.50527

Borovsky, J. E., and Denton, M. H. (2006). Differences between CME-Driven Storms and CIR-Driven Storms. *J. Geophys. Res.* 111, A07S08. doi:10.1029/2005ja011447

Borovsky, J. E., and Denton, M. H. (2018). Exploration of a Composite index to Describe Magnetospheric Activity: Reduction of the Magnetospheric State Vector to a Single Scalar. *J. Geophys. Res. Space Phys.* 123, 7384–7412. doi:10.1029/2018ja025430

Borovsky, J. E., and Denton, M. H. (2014). Exploring the Cross Correlations and Autocorrelations of the ULF Indices and Incorporating the ULF Indices into the Systems Science of the Solar Wind-Driven Magnetosphere. *J. Geophys. Res. Space Phys.* 119, 4307–4334. doi:10.1002/2014ja019876

Borovsky, J. E., Hesse, M., Birn, J., and Kuznetsova, M. M. (2008). What Determines the Reconnection Rate at the Dayside Magnetosphere. *J. Geophys. Res.* 113, A07210. doi:10.1029/2007ja012645

Borovsky, J. E. (2021). Is Our Understanding of Solar-Wind/Magnetosphere Coupling Satisfactory. *Front. Astron. Space Sci.* 8, 634073. doi:10.3389/fspas.2021.634073

Borovsky, J. E., Lavraud, B., and Kuznetsova, M. M. (2009). Polar Cap Potential Saturation, Dayside Reconnection, and Changes to the Magnetosphere. *J. Geophys. Res.* 114, A03224. doi:10.1029/2009ja014058

Borovsky, J. E., and Osmane, A. (2019). Compacting the Description of a Time-dependent Multivariable System and its Multivariable Driver by Reducing the State Vectors to Aggregate Scalars: the Earth's Solar-Wind-Driven Magnetosphere. *Nonlin. Process. Geophys.* 26, 429–443. doi:10.5194/npg-26-429-2019

Borovsky, J. E. (2013). Physics-based Solar Wind Driver Functions for the Magnetosphere: Combining the Reconnection-Coupled MHD Generator with the Viscous Interaction. *J. Geophys. Res. Space Phys.* 118, 7119–7150. doi:10.1002/jgra.50557

Borovsky, J. E., and Steinberg, J. T. (2006). The "calm before the Storm" in CIR/magnetosphere Interactions: Occurrence Statistics, Solar Wind Statistics, and Magnetospheric Preconditioning. *J. Geophys. Res.* 111, A07S10. doi:10.1029/2005ja011397

Borovsky, J. E. (2008). The Rudiments of a Theory of Solar-Wind/magnetosphere Coupling Derived from First Principles. *J. Geophys. Res.* 113, A08228. doi:10.1029/2007ja012646

Borovsky, J. E. (2017). Time-integral Correlations of Multiple Variables with the Relativistic-Electron Flux at Geosynchronous Orbit: The strong Roles of the Substorm-Injected Electrons and the Ion Plasma Sheet. *J. Geophys. Res.* 122, 11961. doi:10.1002/2017ja024476

Borovsky, J. E., and Valdivia, J. A. (2018). The Earth's Magnetosphere: A Systems Science Overview and Assessment. *Surv. Geophys.* 39, 817–859. doi:10.1007/s10712-018-9487-x

Borovsky, J. E. (2020b). What Magnetospheric and Ionospheric Researchers Should Know about the Solar Wind. *J. Atmos. Solar-Terrestrial Phys.* 204, 105271. doi:10.1016/j.jastp.2020.105271

Borovsky, J. E., and Yakymenko, K. (2017). Systems Science of the Magnetosphere: Creating Indices of Substorm Activity, of the Substorm-Injected Electron Population, and of the Electron Radiation belt. *J. Geophys. Res.* 122, 10012. doi:10.1002/2017ja024250

Cassak, P. A., and Shay, M. A. (2007). Scaling of Asymmetric Magnetic Reconnection: General Theory and Collisional Simulations. *Phys. Plasmas* 14, 102114. doi:10.1063/1.2795630

Cowley, S. W. H., and Lockwood, M. (1992). Excitation and Decay of Solar Wind-Driven Flows in the Magnetosphere-Ionosphere System. *Ann. Geophys.* 10, 103.

Denton, M. H., Thomsen, M. F., Korth, H., Lynch, S., Zhang, J. C., and Liemohn, M. W. (2005). Bulk Plasma Properties at Geosynchronous Orbit. *J. Geophys. Res.* 110, A07223. doi:10.1029/2004ja010861

Drake, K. A., Heelis, R. A., Hairston, M. R., and Anderson, P. C. (2009). Electrostatic Potential Drop across the Ionospheric Signature of the Low-Latitude Boundary Layer. *J. Geophys. Res.* 114, A04215. doi:10.1029/2008ja013608

Elphic, R. C., Thomsen, M. F., Borovsky, J. E., and McComas, D. J. (1999). Inner Edge of the Electron Plasma Sheet: Empirical Models of Boundary Location. *J. Geophys. Res.* 104, 22679–22693. doi:10.1029/1999ja900213

Emery, B. A., Richardson, I. G., Evans, D. S., and Rich, F. J. (2009). Solar Wind Structure Sources and Periodicities of Auroral Electron Power over Three Solar Cycles. *J. Atmos. Solar-Terrestrial Phys.* 71, 1157–1175. doi:10.1016/j.jastp.2008.08.005

Farrugia, C. J., Gratton, F. T., and Torbert, R. B. (2001). Viscous-type Processes in the Solar Wind Wind-Magnetosphere Interaction. *Space Sci. Rev.* 95, 443–456. doi:10.1023/a:1005288703357

Feldstein, Y. I., and Galperin, Y. I. (1985). The Auroral Luminosity Structure in the High-Latitude Upper Atmosphere: Its Dynamics and Relationship to the Large-Scale Structure of the Earth's Magnetosphere. *Rev. Geophys.* 23, 217. doi:10.1029/rg023i003p00217

Frey, H. U., Han, D., Kataoka, R., Lessard, M. R., Milan, S. E., Nishimura, Y., et al. (2019). Dayside aurora. *Space Sci. Rev.* 215, 51. doi:10.1007/s11214-019-0617-7

Gao, Y., Kivelson, M. G., and Walker, R. J. (2013). Two Models of Cross Polar Cap Potential Saturation Compared: Siscoe-Hill versus Kivelson-Ridley Model. *J. Geophys. Res.* 118, 1. doi:10.1002/jgra.50124

Goertz, C. K., and Boswell, R. W. (1979). Magnetosphere-ionosphere Coupling. *J. Geophys. Res.* 84, 7239. doi:10.1029/ja084ia12p07239

Goertz, C. K., Shan, L.-H., and Smith, R. A. (1993). Prediction of Geomagnetic Activity. *J. Geophys. Res.* 98, 7673–7684. doi:10.1029/92ja01193

Gonzalez, W. D., and Gonzalez, A. L. C. (1981). Solar Wind Energy and Electric Field Transfer to the Earth's Magnetosphere via Magnetopause Reconnection. *Geophys. Res. Lett.* 8, 265–268. doi:10.1029/gl008i003p00265

Gonzalez, W. D., and Mozer, F. S. (1974). A Quantitative Model for the Potential Resulting from Reconnection with an Arbitrary Interplanetary Magnetic Field. *J. Geophys. Res.* 79, 4186–4194. doi:10.1029/ja079i028p04186

Gussenhoven, M. S., Hardy, D. A., and Burke, W. J. (1981). DMSP/F2 Electron Observations of Equatorward Auroral Boundaries and Their Relationship to Magnetospheric Electric fields. *J. Geophys. Res.* 86, 7868–8778. doi:10.1029/ja086ia02p00768

Gussenhoven, M. S., Hardy, D. A., and Heinemann, N. (1983). Systematics of the Equatorward Diffuse Auroral Boundary. *J. Geophys. Res.* 88, 5692. doi:10.1029/ja088ia07p05692

Kan, J. R., and Lee, L. C. (1979). Energy Coupling Function and Solar Wind-Magnetosphere Dynamo. *Geophys. Res. Lett.* 6, 577–580. doi:10.1029/gl006i007p00577

King, J. H., and Papitashvili, N. E. (2005). Solar Wind Spatial Scales in and Comparisons of Hourly Wind and ACE Plasma and Magnetic Field Data. *J. Geophys. Res.* 110, 2104. doi:10.1029/2004ja010649

Kivelson, M. G., and Ridley, A. (2008). Saturation of the Polar Cap Potential: Inference from Alfven wing Arguments. *J. Geophys. Res.* 113, A05214. doi:10.1029/2007ja012302

Korth, H., Thomsen, M. F., Borovsky, J. E., and McComas, D. J. (1999). Plasma Sheet Access to Geosynchronous Orbit. *J. Geophys. Res.* 104, 25047–25061. doi:10.1029/1999ja900292

Kozyreva, O., Pilipenko, V., Engebretson, M. J., Yumoto, K., Watermann, J., and Romanova, N. (2007). In Search of a New ULF Wave index: Comparison of Pc5 Power with Dynamics of Geostationary Relativistic Electrons. *Planet. Space Sci.* 55, 755–769. doi:10.1016/j.pss.2006.03.013

Lavraud, B., and Borovsky, J. E. (2008). Altered Solar Wind-Magnetosphere Interaction at Low Mach Numbers: Coronal Mass Ejections. *J. Geophys. Res.* 113, A00B08. doi:10.1029/2008ja013192

Lavraud, B., Thomsen, M. F., Borovsky, J. E., Denton, M. H., and Pulkkinen, T. I. (2006). Magnetosphere Preconditioning under Northward IMF: Evidence from the Study of Coronal Mass Ejection and Corotating Interaction Region Geoeffectiveness. *J. Geophys. Res.* 111, A09208. doi:10.1029/2005ja011566

Lockwood, M., and Moen, J. (1999). Reconfiguration and Closure of Lobe Flux by Reconnection during Northward IMF: Possible Evidence for Signatures in Cusp/cleft Auroral Emissions. *Ann. Geophys.* 17, 996–1011. doi:10.1007/s00585-999-0996-2

Lopez, R. E. (2016). The Integrated Dayside Merging Rate Is Controlled Primarily by the Solar Wind. *J. Geophys. Res. Space Phys.* 121, 4435–4445. doi:10.1002/2016ja022556

Mayaud, P. N. (1980). *Derivation, Meaning, and Use of Geomagnetic Indices. Sect*, 5.2. Washington DC: American Geophysical Union.

Menvielle, M., and Berthelier, A. (1991). The K-derived Planetary Indices: Description and Availability. *Rev. Geophys.* 29, 415–432. doi:10.1029/91rg00994

Mourenas, D., Artemyev, A. V., and Zhang, X. J. (2019). Impact of Significant Time-Integrated Geomagnetic Activity on 2-MeV Electron Flux. *J. Geophys. Res. Space Phys.* 124, 4445–4461. doi:10.1029/2019ja026659

Mozer, F. S. (1984). Electric Field Evidence on the Viscous Interaction at the Magnetopause. *Geophys. Res. Lett.* 11, 135–138. doi:10.1029/gl011i002p00135

Myllys, M., Kipua, E. K. J., and Lavraud, B. (2017). Interplay of Solar Wind Parameters and Physical Mechanisms Producing the Saturation of the Cross Polar Cap Potential. *Geophys. Res. Lett.* 44, 3019–3027. doi:10.1002/2017gl072676

Newell, P. T., and Gjerloev, J. W. (2011). Evaluation of SuperMAG Auroral Electrojet Indices as Indicators of Substorms and Auroral Power. *J. Geophys. Res.* 116, A12211. doi:10.1029/2011ja016779

Newell, P. T., Sotirelis, T., LiouMeng, K. C. I., and Rich, F. J. (2007). A Nearly Universal Solar Wind-Magnetosphere Coupling Function Inferred from 10 Magnetospheric State Variables. *J. Geophys. Res.* 112, A01206. doi:10.1029/2006ja012015

Nicholson, D. R. (1983). *Introduction to Plasma Theory. Sect. 2.5*. New York: Wiley.

Ober, D. M., Maynard, N. C., and Burke, W. J. (2003). Testing the Hill Model of Transpolar Potential Saturation. *J. Geophys. Res.* 108, 1467. doi:10.1029/2003ja010154

Penskikh, Y., Lunyushkin, S., and Kapustin, V. (2021). Geomagnetic Method for Automatic Diagnostics of Auroral Oval Boundaries in Two Hemispheres of Earth. *Solar-terr. Phys.* 7, 57–69. doi:10.12737/stp-72202106

Reiff, P. H., and Luhmann, J. G. (1986). "Solar Wind Control of the Polar-Cap Voltage," in *Solar Wind-Magnetosphere Coupling*. Editors Y. Kamide and J. A. Slavin (Tokyo: Terra Scientific), 453–476. doi:10.1007/978-94-009-4722-1_33

Richmond, A. D., and Matsushita, S. (1975). Thermospheric Response to a Magnetic Substorm. *J. Geophys. Res.* 80, 2839–2850. doi:10.1029/ja080i019p02839

Romanova, N., and Pilipenko, V. (2009). ULF Wave Indices to Characterize the Solar Wind-Magnetosphere Interaction and Relativistic Electron Dynamics. *Acta Geophys.* 57, 158–170. doi:10.2478/s11600-008-0064-4

Romanova, N., Plipenko, V., Crosby, N., and Khabarova, O. (2007). ULF Wave index and its Possible Applications in Space Physics. *Bulg. J. Phys.* 34, 136.

Sergeev, V. A., and Kuznetsov, B. M. (1981). Quantitative Dependence of the Polar Cap Electric Field on the IMF Bz-Component and Solar Wind Velocity. *Planet. Space Sci.* 29, 205–213. doi:10.1016/0032-0633(81)90034-9

Siscoe, G. L., Farrugia, C. J., and Sandholt, P. E. (2011). Comparison between the Two Basic Modes of Magnetospheric Convection. *J. Geophys. Res.* 116, A05210. doi:10.1029/2010ja015842

Siscoe, G. L., and Siebert, K. D. (2006). Bimodal Nature of Solar Wind-Magnetosphere-Ionosphere-Thermosphere Coupling. *J. Atmos. Solar-Terrestrial Phys.* 68, 911–920. doi:10.1016/j.jastp.2005.11.012

Siscoe, G., Rader, J., and Ridley, A. J. (2004). Transpolar Potential Saturation Models Compared. *J. Geophys. Res.* 109, A09203. doi:10.1029/2003ja010318

Strangeway, R. J. (2012). The Relationship between Magnetospheric Processes and Auroral Field-Aligned Current Morphology. *Geophys. Monog. Ser.* 197, 355. doi:10.1029/2012GM001211

Thomsen, M. F. (2004). Why Kp Is Such a Good Measure of Magnetospheric Convection. *Space Weath* 2, S11044. doi:10.1029/2004sw000089

Troshichev, O. A., Andrezen, V. G., Vennerstrøm, S., and Friis-Christensen, E. (1988). Magnetic Activity in the Polar Cap-A New index. *Planet. Space Sci.* 36, 1095–1102. doi:10.1016/0032-0633(88)90063-3

Vasyliunas, V. M., Kan, J. R., Siscoe, G. L., and Akasofu, S.-I. (1982). Scaling Relations Governing Magnetospheric Energy Transfer. *Planet. Space Sci.* 30, 359–365. doi:10.1016/0032-0633(82)90041-1

Volland, H. (1973). A Semiempirical Model of Large-Scale Magnetospheric Electric fields. *J. Geophys. Res.* 78, 171–180. doi:10.1029/ja078i001p00171

Walsh, B. M., and Zou, Y. (2021). The Role of Magnetospheric Plasma in Solar Wind-Magnetosphere Coupling: A Review. *J. Atmos. Solar-Terrestrial Phys.* 219, 105644. doi:10.1016/j.jastp.2021.105644

Weimer, D. R., Edwards, T. R., and Olsen, N. (2017). Linear Response of Field-aligned Currents to the Interplanetary Electric Field. *J. Geophys. Res. Space Phys.* 122, 8502–8515. doi:10.1002/2017ja024372

Weimer, D. R., Maynard, N. C., Burke, W. J., and Liebrecht, C. (1990b). Polar Cap Potentials and the Auroral Electrojet Indices. *Planet. Space Sci.* 38, 1207–1222. doi:10.1016/0032-0633(90)90028-o

Weimer, D. R., Reinleitner, L. A., Kan, J. R., Zhu, L., and Akasofu, S.-I. (1990a). Saturation of the Auroral Electrojet Current and the Polar Cap Potential. *J. Geophys. Res.* 95, 18981. doi:10.1029/ja095ia11p18981

Wing, S., and Johnson, J. R. (2019). Applications of Information Theory in Solar and Space Physics. *Entropy* 21, 140. doi:10.3390/e21020140

Wing, S., Johnson, J. R., Camporeale, E., and Reeves, G. D. (2016). Information Theoretical Approach to Discovering Solar Wind Drivers of the Outer Radiation belt. *J. Geophys. Res. Space Phys.* 121, 9378–9399. doi:10.1002/2016ja022711

Wygant, J. R., Torbert, R. B., and Mozer, F. S. (1983). Comparison of S3-3 Polar Cap Potential Drops with the Interplanetary Magnetic Field and Models of Magnetopause Reconnection. *J. Geophys. Res.* 88, 5727. doi:10.1029/ja088ia07p05727

Conflict of Interest: The author declares that the research was conducted in the absence of any commercial or financial relationships that could be construed as a potential conflict of interest.

Publisher's Note: All claims expressed in this article are solely those of the authors and do not necessarily represent those of their affiliated organizations, or those of the publisher, the editors and the reviewers. Any product that may be evaluated in this article, or claim that may be made by its manufacturer, is not guaranteed or endorsed by the publisher.

Copyright © 2021 Borovsky. This is an open-access article distributed under the terms of the Creative Commons Attribution License (CC BY). The use, distribution or reproduction in other forums is permitted, provided the original author(s) and the copyright owner(s) are credited and that the original publication in this journal is cited, in accordance with accepted academic practice. No use, distribution or reproduction is permitted which does not comply with these terms.

frontiers in Astronomy and Space Sciences

ORIGINAL RESEARCH
published: 21 October 2021
doi: 10.3389/fspas.2021.738507

Direct Connection Between Auroral Oval Streamers/Flow Channels and Equatorward Traveling Ionospheric Disturbances

Larry R. Lyons[1], Yukitoshi Nishimura[2], Shunrong Zhang[3], Anthea Coster[3], Jiang Liu[1,4], William A. Bristow[5], Ashton S. Reimer[6], Roger H. Varney[6] and Don L. Hampton[7]*

[1]Department of Atmospheric and Oceanic Sciences, University of California, Los Angeles, Los Angeles, CA, United States, [2]Center for Space Physics and Department of Electrical and Computer Engineering, Boston University, Boston, MA, United States, [3]Haystack Observatory, Massachusetts Institute of Technology, Cambridge, MA, United States, [4]Department of Earth, Planetary and Space Sciences, University of California, Los Angeles, Los Angeles, CA, United States, [5]Department of Meteorology and Atmospheric Science, The Pennsylvania State University, State College, PA, United States, [6]Center for Geospace Studies, SRI International, Menlo Park, CA, United States, [7]Geophysical Institute, University of Alaska Fairbanks, Fairbanks, AK, United States

OPEN ACCESS

Edited by:
Georgios Balasis, National Observatory of Athens, Greece

Reviewed by:
Massimo Materassi, National Research Council (CNR), Italy
Octav Marghitu, Space Science Institute, Romania

***Correspondence:**
Larry R. Lyons
larry@atmos.ucla.edu

Specialty section:
This article was submitted to Space Physics, a section of the journal Frontiers in Astronomy and Space Sciences

Received: *08 July 2021*
Accepted: *15 September 2021*
Published: *21 October 2021*

Citation:
Lyons LR, Nishimura Y, Zhang S, Coster A, Liu J, Bristow WA, Reimer AS, Varney RH and Hampton DL (2021) Direct Connection Between Auroral Oval Streamers/Flow Channels and Equatorward Traveling Ionospheric Disturbances. Front. Astron. Space Sci. 8:738507. doi: 10.3389/fspas.2021.738507

We use simultaneous auroral imaging, radar flows, and total electron content (TEC) measurements over Alaska to examine whether there is a direct connection of large-scale traveling ionospheric disturbances (LSTIDs) to auroral streamers and associated flow channels having significant ground magnetic decreases. Observations from seven nights with clearly observable flow channels and/or auroral streamers were selected for analysis. Auroral observations allow identification of streamers, and TEC observations detect ionization enhancements associated with streamer electron precipitation. Radar observations allow direct detection of flow channels. The TEC observations show direct connection of streamers to TIDs propagating equatorward from the equatorward boundary of the auroral oval. The TIDs are also distinguished from the streamers to which they connect by their wave-like TEC fluctuations moving more slowly equatorward than the TEC enhancements from streamer electron precipitation. TIDs previously observed propagating equatorward from the auroral oval have been identified as LSTIDs. Thus, the TIDs here are likely LSTIDs, but we lack sufficient TEC coverage necessary to demonstrate that they are indeed large scale. Furthermore, each of our events shows TID's connection to groups of a few streamers and flow channels over a period in the order of 15 min and a longitude range of ~15–20°, and not to single streamers. (Groups of streamers are common during substorms. However, it is not currently known if streamers and associated flow channels typically occur in such groups.) We also find evidence that a flow channel must lead to a sufficiently large ionospheric current for it to lead to a detectable LSTID, with a few tens of nT ground magnetic field decreases not being sufficient.

Keywords: TIDs, flow channels, auroral streamers, substorms, magnetosphere–ionophere coupling

1 INTRODUCTION

Heating and momentum transfer to the upper atmosphere within the auroral oval can lead to neutral atmospheric gravity waves. While shorter-period (≲30 min) waves are dampened and thus cannot propagate far from their source (Richmond, 1978), longer-period waves (≳60 min) can move large distances from the auroral region toward the equator. As a result of ion–neutral collisions, these neutral atmospheric waves can be seen in the ionosphere as waves in electron density (Hines, 1960; Francis, 1975; Richmond, 1978; Hunsucker, 1982), referred to as large-scale traveling ionospheric disturbances (LSTIDs). These large-scale waves may be important for transporting auroral region energy to mid- and low-latitudes (Richmond, 1979). The total electron content (TEC) from the Global Navigation Satellite System (GNSS) receiver network gives the two-dimensional and temporal structure of LSTIDs (Zakharenkova et al., 2017, and references therein; Zhang et al., 2019a), and has shown their spatial sizes to be larger than 1,000 km and horizontal speeds of 400–1,000°m/s. LSTID's spatial and temporal structure has also been investigated using 630 nm airglow emissions (Kubota et al., 2001; Ogawa et al., 2002; Shiokawa et al., 2007), SuperDARN HF radars (e.g., Bristow et al., 1994; Hayashi et al., 2010; Frissell et al., 2014), and multipoint ionosondes (e.g., Shiokawa et al., 2002).

It is well known that auroral zone disturbances (e.g., Hajkowicz, 1991) with magnetic bays (e.g., Ding et al., 2008) can lead to LSTIDs propagating equatorward from the nightside auroral oval. Occurrence rates increase with increasing geomagnetic activity (Tsugawa et al., 2004), and duration of activity has been associated with the duration of LSTID activity (Davis, 1971). Magnetic bays result from different classes of auroral disturbances, including substorms and poleward boundary intensifications (known as "PBIs"), which are intensifications along the auroral poleward boundary. Auroral forms that extend equatorward from PBIs to lower latitudes are known as "auroral streamers" and can give large magnetic bays (Lyons, 2000; Lyons et al., 2013) as can omega bands (Jorgensen et al., 1999), which appear in the midnight to dawn sector. Substorms include auroral streamers, with the streamers being the dominant contributor to the magnetic bays of the substorm expansion phase (Nishimura et al., 2012; Lyons et al., 2013), but streamers are also common without the occurrence of a substorm.

Previous studies had used ground magnetic observations without auroral observations to detect auroral disturbances, and thus were not able to identify the specific type of disturbance that leads to a nightside LSTID. To overcome this limitation, in our previous study (Lyons et al., 2019), we used auroral images from the white-light all sky imager (ASI) array of the Time History of Events and Macroscale Interactions during Substorms (THEMIS), giving high temporal and spatial resolution continent-scale coverage over the North American auroral zone (Mende et al., 2008) and allowing the identification of the different types of auroral oval disturbances. We related these disturbances to LSTIDs as seen in vertical total electron content (TEC) measurements over North America (Coster et al., 2003; Rideout and Coster, 2006; Vierinen et al., 2016) and in 630 nm emissions from the Midlatitude Allsky-imaging Network for Geospace Observations (MANGO) ASI array over the western United States. Time periods with LSTIDs were found to start and stop with the initiation and cessation of overall periods of geomagnetic activity, consistent with the well-established association of LSTIDs with activity. Furthermore, many of LSTIDs were found to be associated with appropriate time delay to a specific auroral disturbance, suggesting that individual LSTIDs can be driven by identifiable auroral disturbances. We found LSTIDs to be associated with substorms and with auroral streamers in the absence of a substorm. Due to ground magnetic field depressions during substorms being directly related to streamers (Lyons et al., 2013), we suggested that auroral streamer disturbances may be the primary driver of individual LSTIDs seen on the nightside, independent of whether the streamers occur during a substorm. Auroral streamers result from the electron precipitation lying approximately adjacent to mesoscale flow channels (Gallardo-Lacourt et al., 2014), which are related to electric fields that map along field lines from the ionosphere to the magnetosphere (where they are often referred to as flow bursts) and move with an equatorward (earthward) component within the ionosphere (magnetosphere). Thus, the above suggestion would imply that the flows, electric fields, and electron precipitation associated with mesoscale flow channels drive the heating and momentum transfer that gives rise to the neutral atmospheric gravity waves that appear as LSTIDs. In the study by Lyons et al. (2019), we also found indications that a disturbance should have sufficiently large ground magnetic perturbation (ΔB) in order to lead to a detectable LSTID.

In the present study, we take advantage of simultaneous oval imaging, radar flows, and TEC over Alaska to examine whether, as suggested in our previous study, there is a direct connection of LSTIDs to auroral streamers and associated flow channels having a significant ΔB. The auroral observations allow us to identify auroral streamers, and the TEC observations allow us to detect TEC variations by both the electron precipitation associated with the streamers and by TIDs propagating equatorward from the equatorward boundary of the auroral oval. Radar observations, when available, allow us to directly detect the flow channels. Furthermore, the observations over Alaska allow us to take advantage of TEC coverage in both auroral and subauroral latitudes to see how TEC first increases within the auroral oval and then connects to TIDs propagating to lower latitudes. This overcomes the limitation in our previous study from the latitudinal gap between the ASIs within the auroral zone and the mid-latitude TEC measurements over the continental United States. Since the TIDs we observe are propagating equatorward from the auroral oval as in our previous study, they are likely LSTIDs. However, we do not have the continent-wide TEC coverage necessary to demonstrate that they are large scale.

2 METHODOLOGY

We started with 14 nights that were selected for having good auroral viewing from Poker Flat, Alaska. Of these, 11 were used in

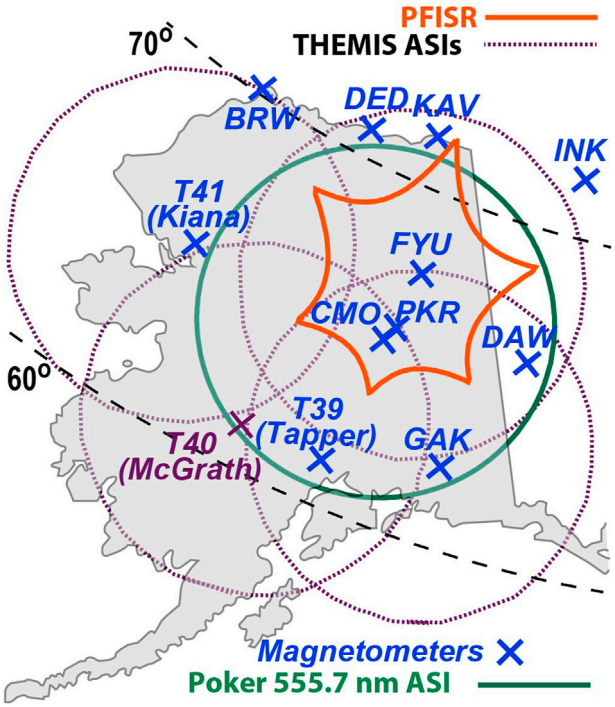


FIGURE 1 | FOVs of the Poker Flat 557.7 nm images, the THEMIS ASIs in the Alaskan sector, and the PFISR radar. Also shown are ground magnetometer locations. These include the THEMIS ASI stations, except that we do not use magnetometer data from T40. IAGA station names are used (see https://supermag.jhuapl.edu/ for station details).

our previous substorm-related studies (Lyons, et al., 2021a; Lyons et al., 2021b), and the three others had been selected for other studies. We narrowed this list to seven nights that had clear observable flow channels and/or auroral streamers and did not have ambiguities due to multiple flow channels and streamers.

We use the Poker Flat Incoherent Scatter Radar (PFISR) data product that gives flow vectors along the radar magnetic meridian from a best fit to line-of-sight (LOS) flow velocities along all PFISR beams using the assumption that longitudinal variations within the radar field-of-view (FOV) can be neglected (Nicolls and Heinselman, 2007). We use only flow vectors having an estimated error magnitude less than both the flow magnitude and 1 km/s. Super Dual Auroral Radar Network (SuperDARN) observations are also included when and where echoes are available. We show these observations as maps of flow vectors obtained with the Bristow et al. (2016) technique, which gives spatial resolution that is set by the underlying measurements rather than by the smoothing inherent in the global fits using a coarse grid that are typically used for global SuperDARN convection maps. The vectors are determined by the local LOS observations and the divergence-free condition. They are not strongly influenced by information beyond a few grid cell's distance so that localized steep gradients can be obtained without significantly influencing the remainder of the vector domain.

Figure 1 displays the coverage of the PFISR radar beams over Alaska (orange contour), and the Poker Flat green line (green circle) and THEMIS white light (dashed circles) ASIs having coverage that includes Alaska. Locations of ground magnetometer stations from which we show data are indicated.

To detect traveling ionospheric disturbances, we analyze global navigation satellite system (GNSS) TEC observations of differential TEC values of ΔTEC, as described in the study by Zhang et al. (2017) and Coster et al. (2017) and used in our previous study. They were derived at 1 min cadence by subtracting a smooth background TEC variation determined by a low-pass Savitzky–Golay filter (Savitzky and Golay, 1964). The filter uses least squares fitting of successive subsets of windows of a given length (e.g., 30 or 60 min) involving time-adjacent TEC data points from the same GNSS satellite–receiver pair and a linear basis function set. Thus, this filter removes high-frequency fluctuation from data while maximizing the preservation of the original shape and features of the signal. A 15° cutoff elevation for ground–satellite ray paths was used to eliminate data close to the horizon where the measurement uncertainty can be large. Data at the start and the end of each continuous segment from the same GNSS satellite–receiver pair were disregarded to avoid potential "edge" effects (Zhang et al., 2019b). Similar differential TEC analysis methods have been employed extensively (e.g., Saito et al., 1998; Tsugawa et al., 2007; Ding et al., 2008; Azeem et al., 2015). The accuracy of this method is based on the accuracy of the GNSS phase measurement, which is less than 0.03 TEC units (Coster et al., 2012), as all satellite and receiver bias terms cancel out.

Note that using a 30-min window could inhibit the detection of anything other than the first wave of a chain of waves with period larger than 30 min. However, Ding et al. (2008) found that most (79%) LSTID waves are solitary waves (i.e., a single perturbation pulse), and only 21% appear to be part of a wave chain. We are examining waves directly driven by a flow channel, and these waves would likely be initiated impulsively. If a flow channel were to lead to a chain of waves, we might only detect the first and largest one. But it is the impulsive response that we are looking for as a test of the proposed direct driving.

3 ANALYSIS

We start with two events for which the TEC coverage shows the best two-dimensional evidence for a direct connection between streamers and ensuing TIDs. The next three events show the direct connection for events having radar coverage, showing the flow channels associated with streamers and their connection to TIDs. The final two events have clear flow channels but substantially weaker ground magnetic depressions. These indicate that a flow channel must be associated with a sufficiently large ionospheric current to lead to a detectable LSTID.

3.1 March 2 and 1, 2017: Two-Dimensional TEC Coverage Showing Clear TIDs

Figure 2 shows an overview of observations from a period that included a substorm with onset at 0955:30 UT on March 2, 2017. The keograms on the left are, from top to bottom, 557.7 nm

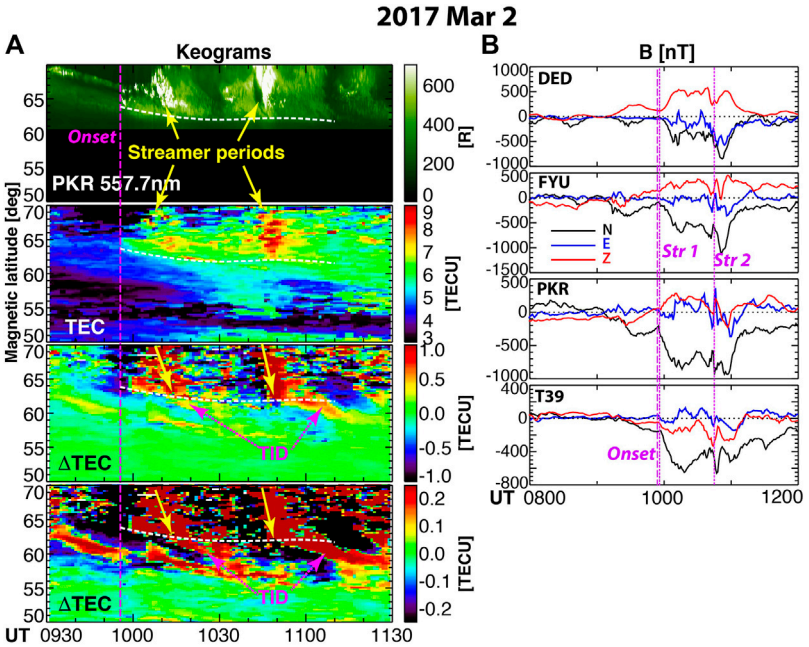


FIGURE 2 | Overview of observations from a period that included a substorm with onset at 0,955:30 UT on March 2, 2017. Keograms on the **(A)** are, from top to bottom, 557.7 nm emissions from the Poker Flat ASI, vertical TEC, and vertical ΔTEC with two different scales along the PFISR magnetic meridian. Ground magnetometer observations are shown on the panel **(B)** from stations approximately along the Poker Flat meridian stacked from lower to higher latitudes.

emissions from the Poker Flat ASI, vertical TEC, and vertical ΔTEC with two different scales. The keograms are along the PFISR magnetic meridian and cover available data over the entire range of Alaska magnetic longitudes (240–285°).

The substorm onset appears as a small brightening within the equatorward portion of the auroral oval at magnetic latitude Λ ~ 64°. As seen in the full ASI images in the movie **Additional File S1**, multiple streamers started soon before 10 UT, and then a large streamer near the Poker Flat meridian extended equatorward from the poleward expanded auroral poleward boundary starting at ~1006 UT and reached the auroral equatorward boundary at ~1010 UT. This streamer can be seen in the auroral keogram of **Figure 2** and also, as a result of ionization from the electron precipitation, in the TEC keogram and quite clearly in the upper ΔTEC keogram (−1 to +1 TECU scale). The auroral activity decreased at ~1020 UT, and then another group of streamers initiated at ~1040 UT. As seen by the magnetograms in **Figure 2B**, the northward ground N-component (local magnetic north) started an abrupt substantial several hundred nT drop with the initiation of the two periods of streamers.

Notice that the equatorward moving TEC enhancements associated with the streamers do not stop at the oval equatorward boundary but appear to continue equatorward at reduced levels below that boundary. (The white dashed curves in the left side of **Figure 2** show the estimated equatorward boundary of the auroral oval based on the ASI and TEC measurements.) The continuation is seen clearly in the lower ΔTEC panel (−0.2 to + 0.2 TECU scale) of **Figure 2**, where the dark red color of the streamers along the PFISR meridian can be seen to directly connect to equatorward moving dark red features having a lower slope (slower equatorward speed) than those of the streamers. The equatorward moving region equatorward of the oval is not the streamer-related flow channel and is supported by its different equatorward speed, implying a transition to the equatorward phase speed of a TID related to the streamer. This indicates a direct connection between the auroral streamers and a TID.

Figure 3 shows a sequence of the auroral images during the period of interest (557.7 nm emissions from the Poker Flat ASI with THEMIS ASI white light emissions in regions outside the Poker Flat ASI field-of-view, FOV) overlaid with all available ΔTEC measurements over the Alaska sector. **Additional File S1** shows these panels every 30°s as a movie. Just at the time of substorm onset (**Figure 3A**), at Λ ≈ 66°, ΔTEC shows no enhancement within the auroral oval. ΔTEC can be seen to have enhanced within the oval after onset (**Figure 3B**) as the oval expanded poleward and equatorward extending streamers formed. Clearly discernible streamers are identified by yellow arrows in **Figures 3B–D**. A longitudinally extended region of ΔTEC enhancement then starts to move equatorward from the oval at ~1002 UT, as encircled qualitatively with a yellow curve in **Figure 3C** (1007 UT). As encircled by the yellow curves in **Figures 3D–H**, this region continues to move equatorward as a detectable TID (most likely a LSTID) until ~1054 UT. Following the initiation of the second group of streamers at ~1040 UT (clearly discernible streamers are identified in **Figures 3G,H**), a second TID can clearly be seen moving equatorward from near the equatorward boundary of the auroral oval starting at ~1050

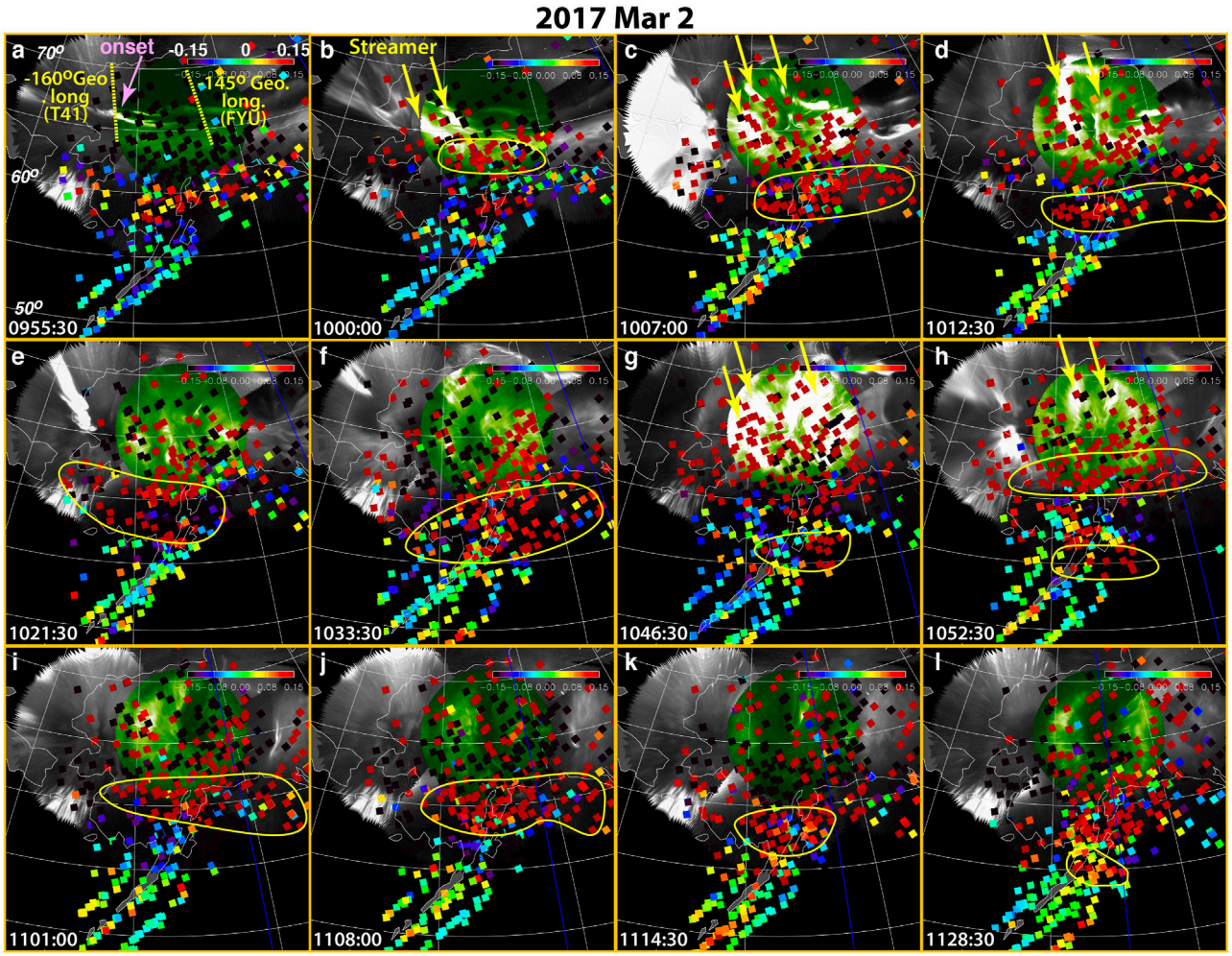


FIGURE 3 | Sequence of the auroral images during the period of interest on March 2, 2017 (557.7 nm emissions from the Poker Flat ASI with THEMIS ASI white light emissions in regions outside the Poker Flat ASI field-of-view, FOV), overlaid with all available ΔTEC measurements over the Alaska sector. Yellow curves encircle equatorward moving regions of ΔTEC enhancements equatorward of the auroral oval. Dark blue line is the magnetic midnight meridian and longitude lines are spaced 15° apart.

UT. This TID is identified by the second set of encircling yellow curves in **Figures 3H,I** and continued to be discernible until ~1129 UT. Both TIDs can be seen to have propagated from the equatorward boundary of the auroral oval at $\Lambda \approx 62^{\circ}$– $\Lambda \approx 55^{\circ}$, with data coverage being more limited at lower Λ.

A different way to visualize the connection between the streamers and the TID is given in **Figure 4**, which shows all TEC and ΔTEC data points within 5° geographic longitude bins from west of, to near, Poker Flat (−147.4° longitude). This covers the longitude range of the first set of streamers, as seen in **Figure 3** and **Supplementary Material S1** (note the longitude lines in these plots are spaced by 15°). The second set of streamers also extends over this longitude range and additionally somewhat further to the east. In the TEC panels, we can see these two equatorward moving regions of enhanced ionization, the first from ~1000 to 1020 UT and the second from ~1035 to 1100 UT. These periods correspond to the two streamer periods, indicating that they result from the electron precipitation producing the streamer auroral emissions.

The black solid curves in **Figure 4** give an approximation of the equatorward boundary of the electron auroral oval based on the auroral emissions in **Figures 2**, **3** and the TEC measurements. Note that the two regions of enhanced TEC appear to extend equatorward of the black curves but move equatorward at a different (slower) speed than does the enhancement due to the streamers. These are the TIDs identified in **Figures 2**, **3**. The connection between the two streamer TEC enhancements and the more equatorward TEC enhancements of the TIDs can be seen clearly in the ΔTEC panels in the lower half of **Figure 4**. Here, initial time edges of the streamer regions as visually estimated from the plots are marked with a yellow longer dashed line (black dashed in the TEC panels), and the initial edges of the more equatorward regions are marked by a yellow shorter dashed line. The change of slope can be seen to have occurred quite near the black curves, indicating the direct connection

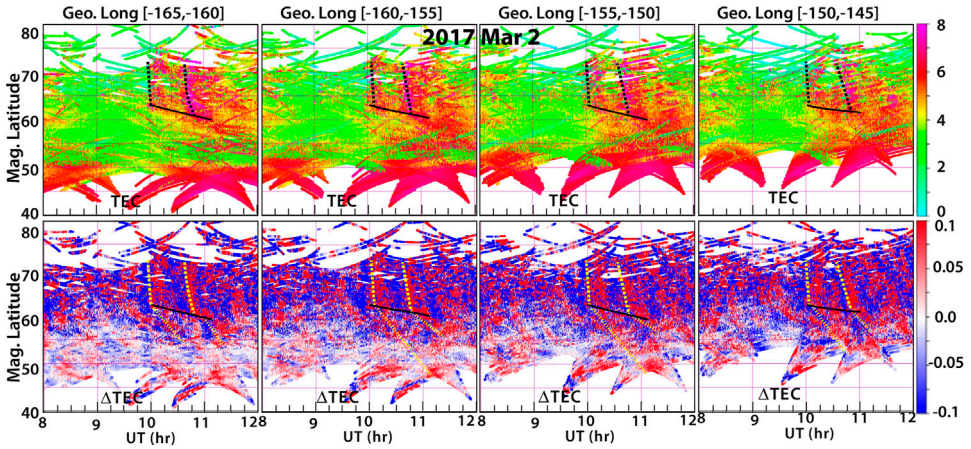


FIGURE 4 | All TEC and ΔTEC data points within 5° geographic longitude bins from west of, to near, Poker Flat (−147.4° longitude) on March 2, 2017. The black solid curves give an approximation of the equatorward boundary of the electron auroral oval based on the auroral emissions in **Figures 2**, **3**. The initial time edges of streamer ΔTEC enhancement regions are marked with yellow longer dashed lines (black dashed in the TEC panels). Initial edges of the more equatorward regions of equatorward moving ΔTEC enhancement are marked by yellow shorter dashed lines.

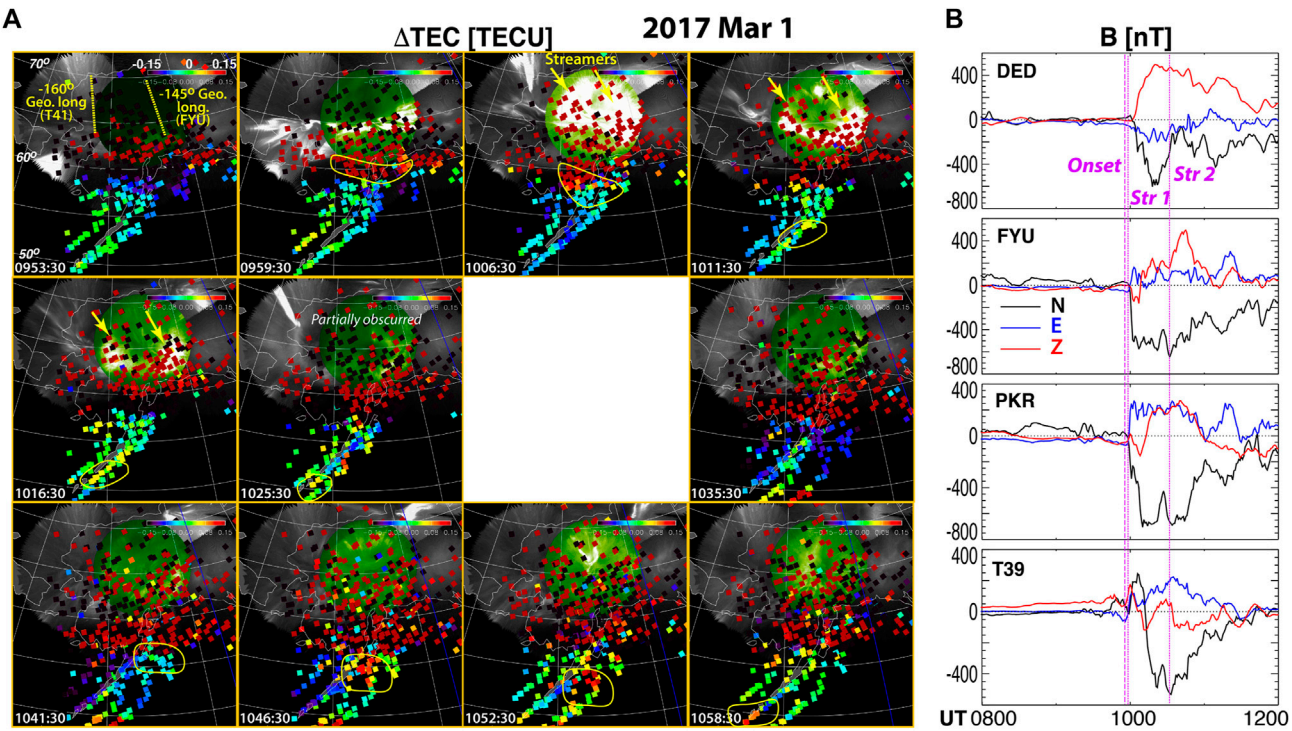


FIGURE 5 | (A) Sequence of the auroral images during the period of interest on March 1, 2017 (557.7 nm emissions from the Poker Flat ASI with THEMIS ASI white light emissions in regions outside the Poker Flat ASI field-of-view, FOV), overlaid with all available ΔTEC measurements over the Alaska sector. Yellow curves encircle equatorward moving regions of ΔTEC enhancements equatorward of the auroral oval. The blank square separates the time periods of the two TIDs. Dark blue line is the magnetic midnight meridian, and longitude lines are spaced 15° apart. **(B)** Ground magnetometer observations from stations approximately along the Poker Flat meridian stacked from lower to higher latitudes.

between the sets of streamers and the two TIDs. In this case, it appears to not be single streamers that drive the TIDs but groups of streamers extending over a sector ~15–20° wide in longitude and associated with fairly strong ground N magnetic decreases and thus fairly strong westward currents in the ionosphere. This can be seen from the auroral images in **Figure 3** and **Supplementary Material**

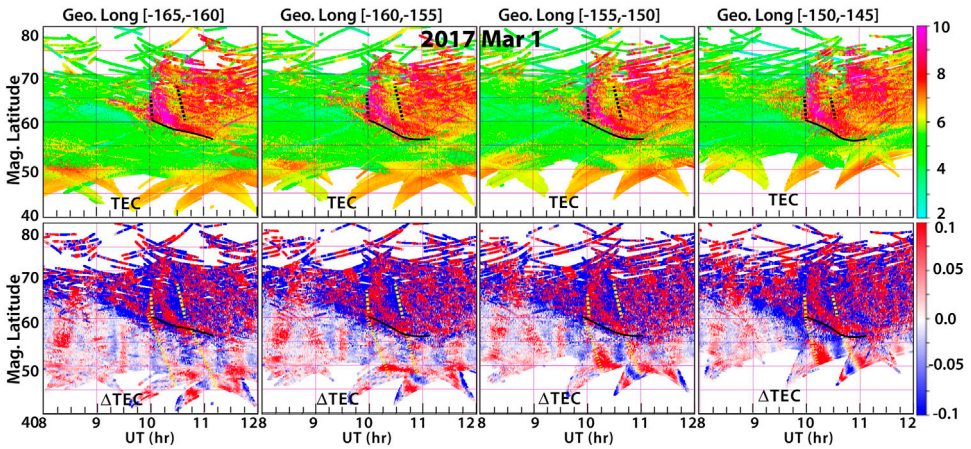


FIGURE 6 | Average TEC and ΔTEC over 5° geographic longitude increments from west of, to near, Poker Flat on March 1, 2017, in the same format as **Figure 4**.

S1, and from the TEC enhancements of the streamers occurring over the 15–20° of longitude included in **Figure 4**.

Figure 5 shows a sequence of the auroral images overlaid with all available ΔTEC measurements over the Alaska sector during the period of interest of a substorm with onset at 0954:00 UT on March 1, 2017. **Additional File S2** shows these panels every 30°s as a movie. As with the previous event, there were two separate periods of streamers, with the first extending from ~0955 UT (soon after onset) to ~1020 UT, and, while viewing conditions were partially obscured by clouds, the second started at ~1035 UT. Hundreds of nT ground N-component decreases were observed for both.

Figure 6 shows the TEC and ΔTEC data within 5° geographic longitude bins from west of, to near, Poker Flat. The two sets of streamers extended over and somewhat further to the east of this longitude range. In the TEC and ΔTEC panels, we can see these two equatorward moving regions of enhanced ionization. A connection to the two equatorward propagating TIDs can be seen in the ΔTEC panels, and the slower equatorward speed of the TIDs than that of the TEC enhancement of the streamers is clearly seen. The front edge of the TID shows in the ΔTEC plots as a transition from dark blue to dark red as in **Figure 4** for the second TID and for the first TID below $\Lambda \approx 56^{\circ}$. For the first TID, the transition at the auroral equatorward boundary is more subtly from blue to mostly white (ΔTEC = 0), with the transition still being near to somewhat above the 0.03 resolution of the ΔTEC measurements. This is because of the region of strong auroral TEC seen in the TEC panels that brings the auroral equatorward boundary equatorward from ~10 to ~1030 UT. This enhances the sliding 30 min average that is subtracted to obtain the ΔTEC values, thus reducing the magnitude that is calculated for the ΔTEC of the TID. As with the previous case, it appears that each TID is driven by a group of streamers extending over a longitude sector ~15–20° in longitude and associated with fairly strong ground N magnetic decreases.

3.2 November 21, 2012, and March 15 and 9, 2013: Radar Coverage of Flow Channels

Figure 7 shows observations on November 21, 2012, when there was a substorm onset at 0803:20 UT during a period when PFISR was operating, and there were sufficient SuperDARN echoes available in regions of interest to provide some two-dimensional flow coverage. The top left portion of the figure shows Poker Flat ASI 557.7 nm emissions with THEMIS ASI white light emissions in regions outside the Poker Flat ASI FOV overlaid with PFISR flow vectors along the radar magnetic meridian. The lower portion shows broader THEMIS ASI mosaics over a larger area overlaid with SuperDARN flow vectors. Flow vectors are scaled by color and length, with the foot of the arrow being at the location of the measurement. Heavier flow vector arrows are at points with a LOS flow measurement. The further from a region of heavier arrows, the more the flows revert to a statistical model.

Both the PFISR and SuperDARN flow measurements show an enhancement of an equatorward component of the flows pointing to near the location of substorm onset as seen in the aurora, which is a common feature signifying an earthward flow channel within the plasma sheet that likely leads to the onset (Nishimura et al., 2010; Lyons et al., 2021a). An enhancement of eastward flow is seen just poleward of the aurora after onset that is likely the dawnside flow enhancement recently referred to as dawnside polarization streams (DAPS, Liu et al., 2020). Neither of these flows are associated with a significant ground magnetic perturbation. Starting in the 0816 UT panels, 13 min after onset, we can see the formation of auroral streamers near and to the west of Poker Flat as identified by yellow arrows in the 0816 UT and subsequent panels. A strong equatorward flow adjacent to one of these streamers is very clearly seen with the PFISR flow vectors, and identified by the orange arrows. The SuperDARN flow vectors show the two-dimensional structure of streamer-related flow channels that continued until ~0828 UT.

Unlike the onset-related flow channel, the streamer-related flow channels from ~0816 to 0828 UT led to ~300 nT magnetic perturbations on the ground as seen in the **Figure 7B**. The fact that this group of streamers connected to an equatorward moving TID can be seen in **Figure 8**, which shows the TEC and ΔTEC within 5° geographic longitude bins from west of, to near, Poker Flat for the event on November 21, 2012. Unlike the previous two

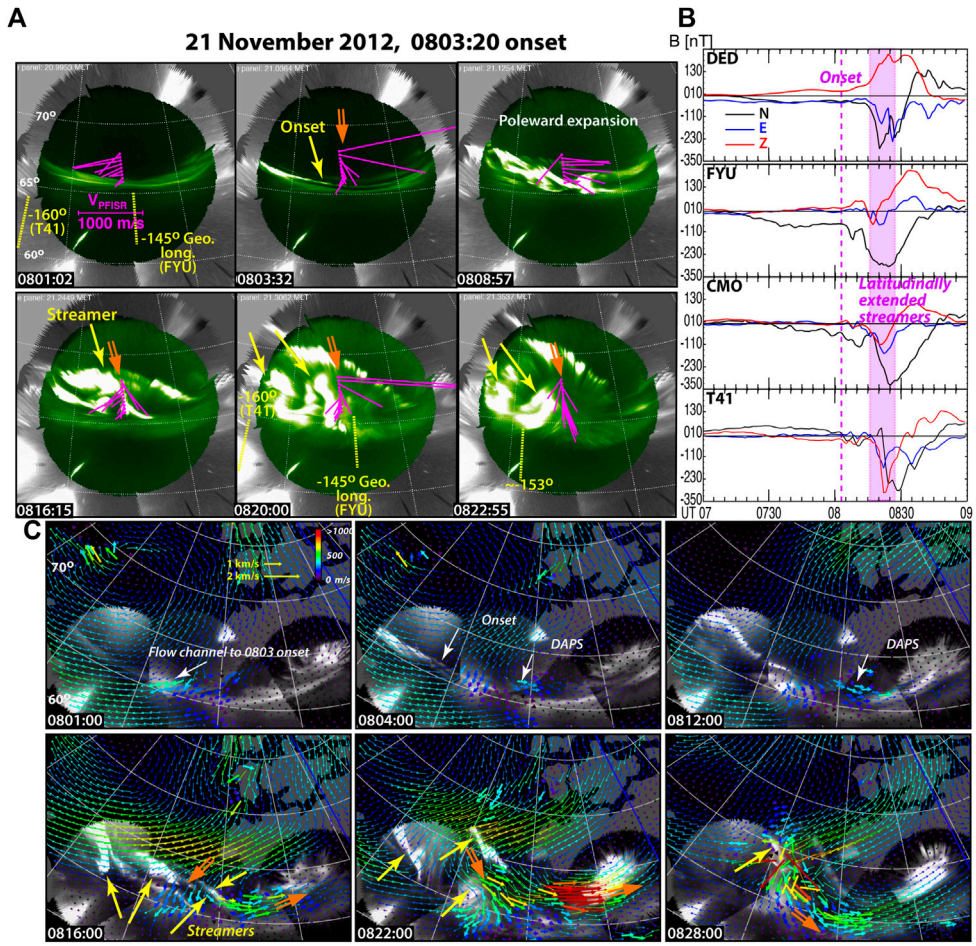


FIGURE 7 | Observations on November 21, 2012, during a period when PFISR was operating, and there were sufficient SuperDARN echoes available in regions of interest to provide some two-dimensional flow coverage. **(A)** Poker Flat ASI 557.7 nm emissions with THEMIS ASI white light emissions in regions outside the Poker Flat ASI FOV overlaid with PFISR flow vectors along the radar magnetic meridian. **(B)** Ground magnetometer observations from stations approximately along the Poker Flat meridian stacked from lower to higher latitudes. **(C)** THEMIS ASI mosaics over a larger area overlaid with SuperDARN flow vectors. Flow vectors are scaled by color and length, with the foot of the arrow being at the location of the measurement. Dark blue line is the magnetic midnight meridian, and longitude lines are spaced 15° apart. Heavier flow vector arrows are at points with a LOS flow measurement. The further from a region of heavier arrows, the more the flows revert to a statistical model. Yellow arrows point toward streamers and orange arrows indicate observed streamer-related flows.

cases, the signature is not to the darkest red color of the color bar. However, a slanted transition from blue shades to red shades that is near to somewhat above the 0.03 resolution of the ΔTEC measurements is discernible as indicated in the figure. Note again the difference in equatorward speeds of the streamer-related TEC enhancement and the TID propagation equatorward of the estimated equatorward boundary of the electron auroral oval.

Figures 9, **10** show observations from an event with onset at 1051:15 UT on March 15, 2013. In this case, the onset was west of Poker Flat and a streamer moved into the PFISR FOV as the substorm expansion-phase auroral bulge moved eastward. The flow channel associated with this streamer was seen by both PFISR and SuperDARN from ~1103 to 1117 UT and was accompanied by an ~300 nTN-component ground magnetic decrease as seen in **Figure 9**. Again, a direct connection between the streamer and an equatorward propagating TID can be seen in the ΔTEC panels in **Figure 10**. While the streamer-related TEC enhancement can be seen in the TEC panels to the equatorward boundary of the auroral oval, fairly intense post-midnight aurora persisted after the streamer within the two more eastern longitude sectors. This led to a few degrees in latitude gap between the TEC enhancement of the streamer and ΔTEC of the TID in those two sectors, with this effect in ΔTEC being the result of the background subtraction using a 30-min sliding average.

Figure 11 shows a somewhat more complicated event with onset at 0902:55 UT on March 9, 2013. Onset was to the east of Poker Flat, and, as seen in the 0,909:47 panel. PFISR saw enhanced flows in the SAPS region associated with the westward expansion of the onset brightening and eastward flow toward the head of the oncoming westward traveling surge, as discussed in the study by Lyons et al. (2021b). As identified on the Poker Flat ASI images/ground magnetic field plots on the left/right portion of the figure, three periods of

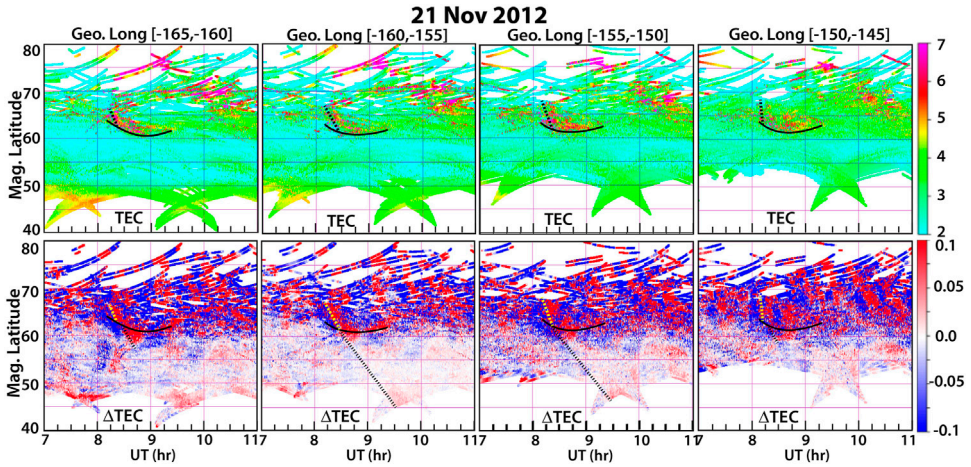


FIGURE 8 | Average TEC and ΔTEC over 5° geographic longitude increments from west of, to near, Poker Flat on November 21, 2012 in the same format as **Figure 4**.

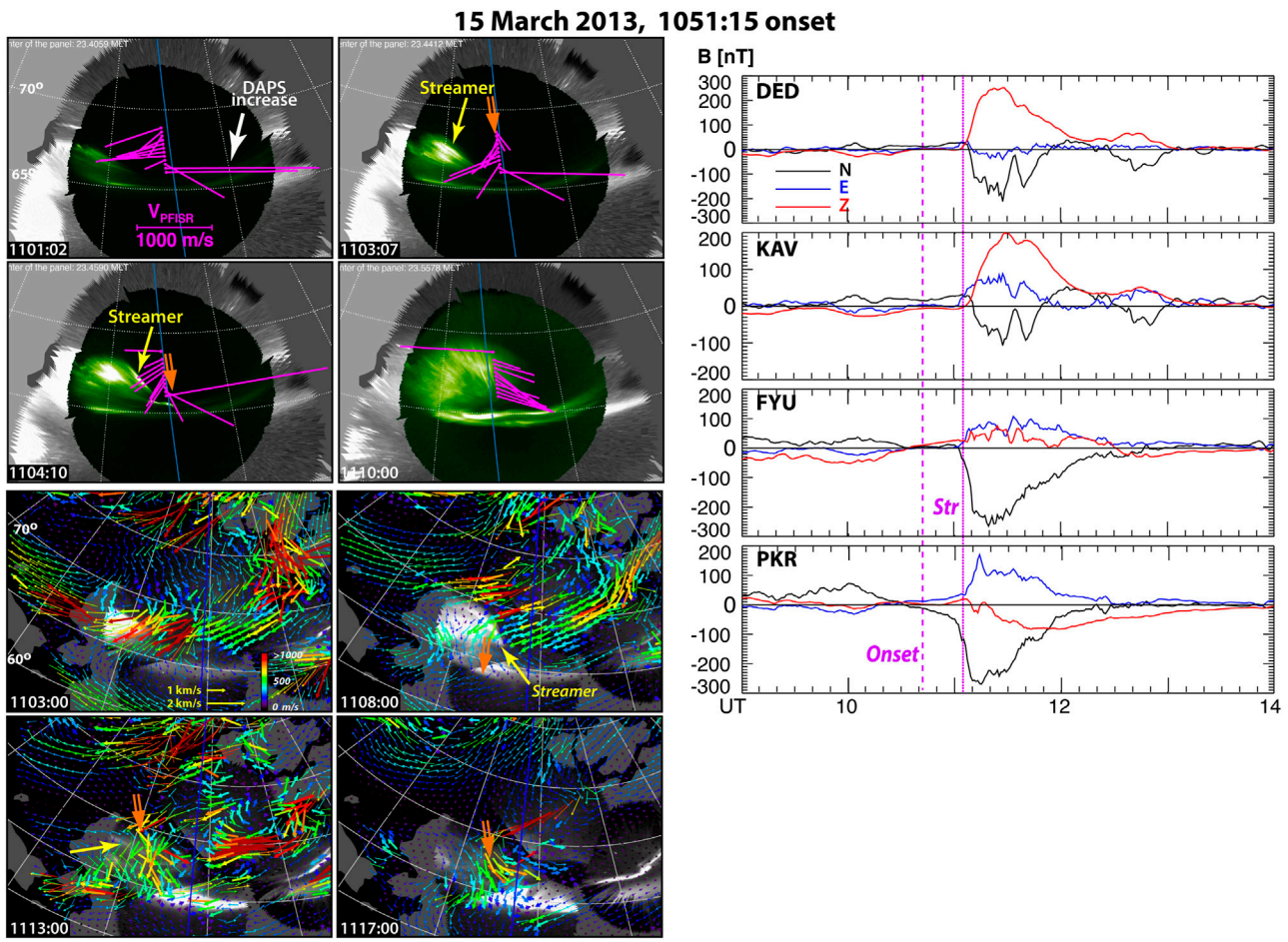


FIGURE 9 | Observations on March 15, 2013 during a period when PFISR was operating, and there were sufficient SuperDARN echoes available in regions of interest to provide some two-dimensional flow coverage. Format is the same as **Figure 7**.

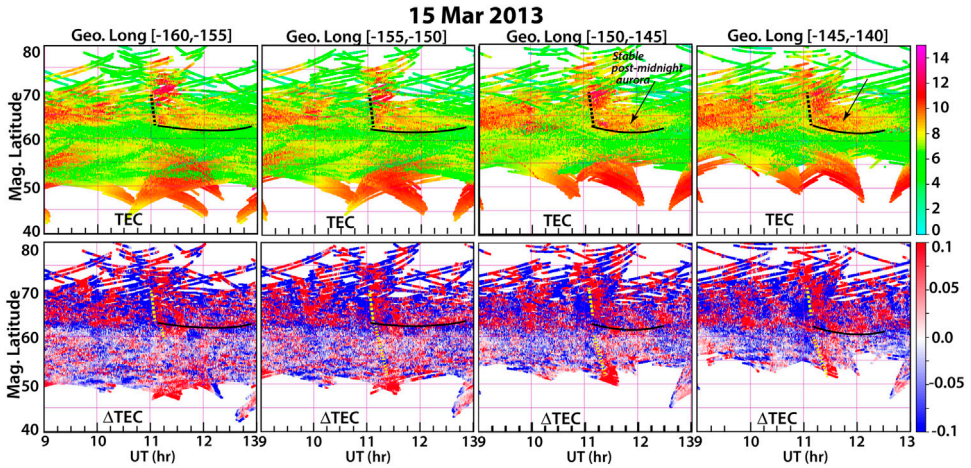


FIGURE 10 | Average TEC and ΔTEC over 5° geographic longitude increments from west of, to 5° east of, Poker Flat on March 15, 2017, in the same format as **Figure 4**.

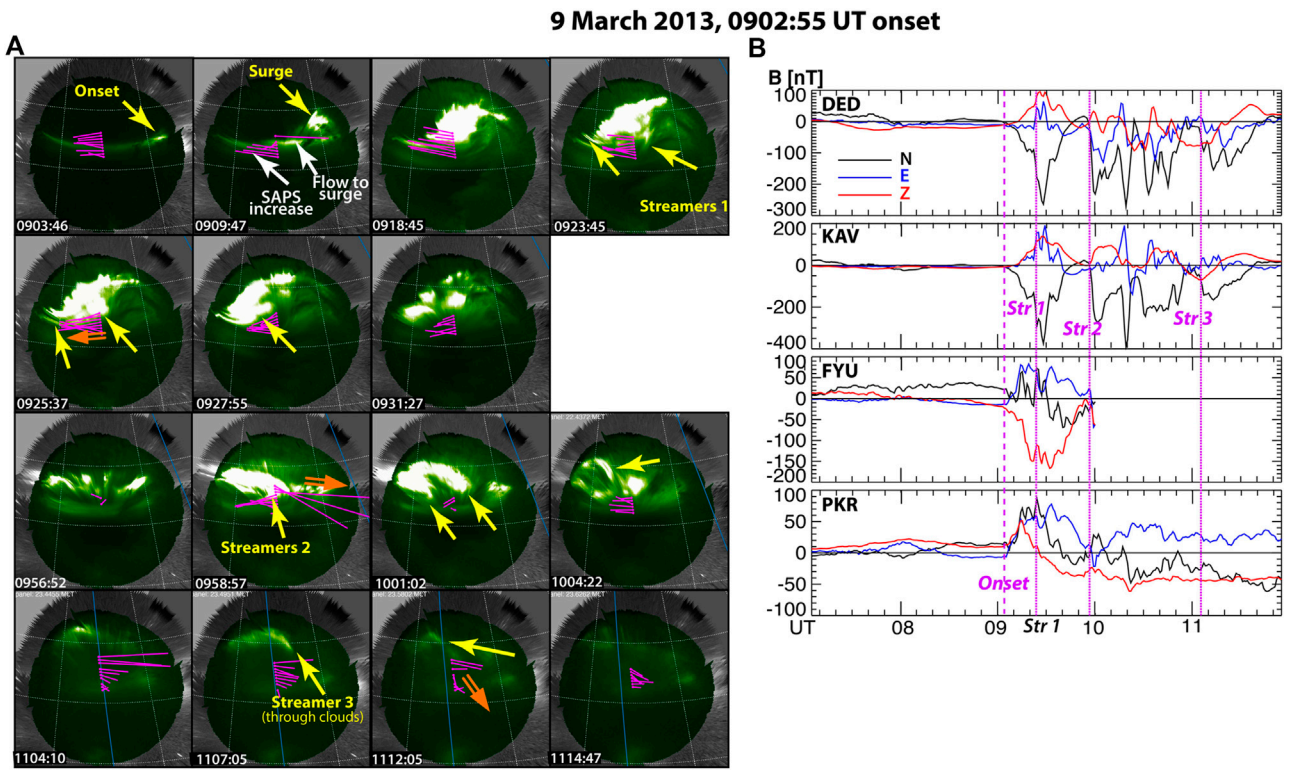


FIGURE 11 | Observations on March 9, 2013, during a period when PFISR was operating. **(A)** Poker Flat ASI 557.7 nm emissions with THEMIS ASI white light emissions in regions outside the Poker Flat ASI FOV overlaid with PFISR flow vectors along the radar magnetic meridian. **(B)** Ground magnetometer observations from stations approximately along the Poker Flat meridian stacked from lower to higher latitudes. "Str" is abbreviation for "streamer." Yellow arrows point toward streamers, and orange arrows indicate observed streamer-related flows. Observations from the period before and during the first streamer period are shown in the top two rows, and observations from the second and third streamer period are shown in the third and fourth rows, respectively.

streamers were identified after the surge head moved westward over Poker Flat with ~100–300 ground N-component magnetic field decreases. Flow enhancements roughly parallel to the local streamer orientation were seen in the PFISR measurements for each as indicated by orange arrows, the enhanced flows being southwestward and just equatorward of the southwestward

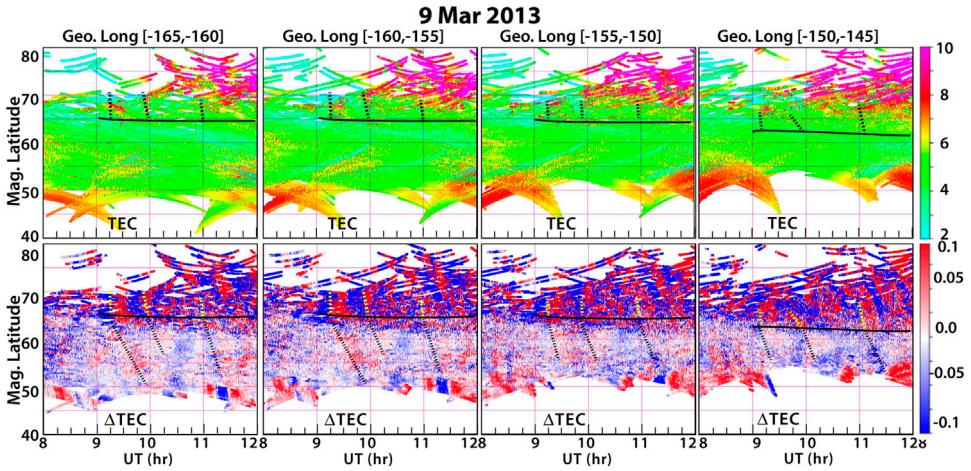


FIGURE 12 | Average TEC and ΔTEC over 5° geographic longitude increments from west of, to near, Poker Flat on March 9, 2013, in the same format as **Figure 4**.

extending portion of the first streamers, southeastward and just poleward of the southeastward extending portion of one of the second group of streamers, and equatorward with the more north–south–oriented third streamer that was seen through increasingly cloudy skies.

Turning to **Figure 12**, we can see the ionization from the three sets of streamers more clearly in the ΔTEC panels than in the TEC panels. Each of the streamer-related equatorward moving ΔTEC enhancements can be seen to connect to an equatorward propagating ΔTEC enhancement as indicated by the dashed lines, and thus to a TID at latitudes below the auroral oval. (In a few locations, the ΔTEC transitions, such as that for the first TID in the left column, are from white or light red to deeper red. But these still represent an increase near to somewhat above the 0.03 resolution of the ΔTEC measurements.)

3.3 November 11, 2012, and August 22, 2014: Weak Magnetic Depression

The two examples in **Figure 13** have well-defined flow channels as seen in the SuperDARN flow vectors. Two separate flow channels are shown from November 11, 2012, one near 0956 UT and the other near 1030 UT. The flow channels both turn westward around a poleward boundary intensification seen in the aurora images and also eastward in the region of DAPS. The flow channel on August 22, 2014 is shown over a ~15 min period and quite clearly moved into the auroral oval from the polar cap and turned eastward at Λ ~65–67° into what is likely the DAPS region. As can be seen by the SuperMAG L index (SML), there were no ground magnetic field decreases exceeding a few tens of nT with these flow channels. While there are some TEC variations as seen within the auroral oval in the ΔTEC panels, there are no discernible equatorward moving regions of ΔTEC below the roughly (due to the weak TEC enhancement from the weak auroral precipitation) estimated equatorward boundary of the auroral oval near the times of the flow channels. (On November 11, 2012, the feature near 10 UT is approximately vertical in the plot, and thus cannot be an equatorward propagating TID. The features at 11 UT, and maybe also at 1130 UT, could be TIDs, but those are well after the time of the flow channels.) This lends support to our previous suggestion (Lyons et al., 2019) that a sufficiently large ionospheric current is necessary for a flow channel to lead to an LSTID, with a few tens of nT ground magnetic field decreases not being sufficient.

4 SUMMARY AND CONCLUSION

LSTIDs are often viewed as a chain of waves having a period such as the 1.8 h average as in the study by Ding et al. (2008). However, Ding et al. noted that 79% of the events they detected were a single perturbation pulse, suggesting that LSTIDs may be generated impulsively. Consistent with this, the wave periods in their **Figure 1** do not show a tendency for an intrinsic period. Instead, the periods are essentially distributed uniformly from ~0.5 to ~3 h. This suggests that most LSTIDs are generated impulsively. While Ding et al. only considered storm periods, it is reasonable that this result also applies to non-stormtime conditions. In the present study, we have taken advantage of the existence over Alaska of simultaneous auroral imaging with the Poker Flat and THEMIS ASIs, radar flow measurements with PFISR and SuperDARN, and TEC measurements. This has allowed us to test our previous suggestion that there may be a direct connection of LSTIDs to auroral streamers and associated flow channels having a significant ΔB. Such a connection would indicate that LSTIDs are often generated impulsively by the flow channels and their associated auroral precipitation.

We considered seven nights of observations from our previous studies that had good auroral viewing and clear observations of flow channels and/or streamers. 12 separate relatively ideal events were analyzed, and these events have allowed us to minimize ambiguities in looking for the direct connection of streamers with TIDs. Based on previous studies, TIDs propagating equatorward from the auroral oval in association with auroral zone

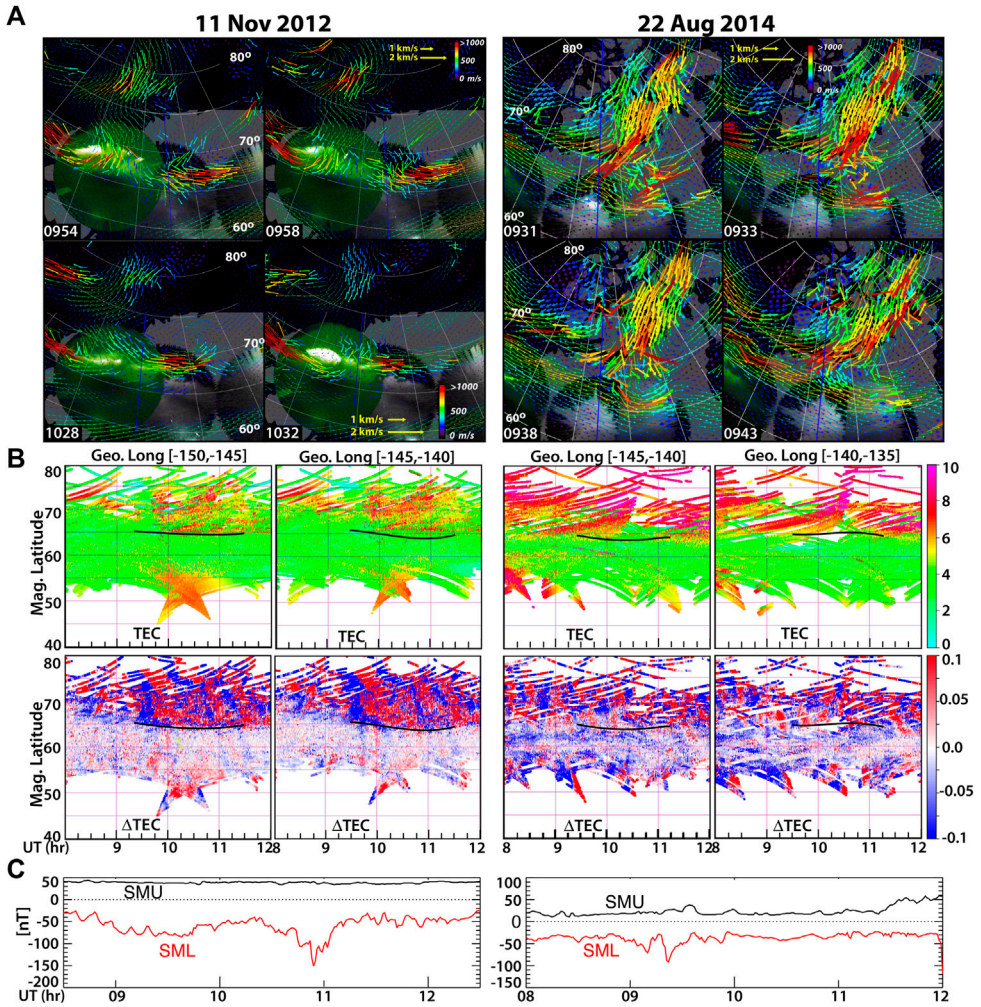


FIGURE 13 | Examples having well defined flow channels as seen in the SuperDARN flow vectors. **(A)** Two separate flow channels are shown from November 11, 2012, one near 0956 UT and the other near 1030 UT and one from August 22, 2014. **(B)** Average TEC and ΔTEC over 5° geographic longitude increments from near and 5° east of, Poker Flat on the above two dates in the same format as **Figure 4**, except without dashed lines identifying features. **(C)** SuperMAG U and L indices (SMU and SML) for the above two dates.

disturbances are LSTIDs. Thus, the events analyzed here are likely LSTIDs, although we do not have sufficient TEC coverage to demonstrate that the events we observed are indeed large scale.

We started with two nights in 2017 for which the TEC coverage is the best, allowing for two-dimensional images that show the TEC enhancements from streamers and their ensuing connection to TIDs. For the four events on these nights, a longitudinally extended region of TEC enhancement was observed to start to move equatorward from the auroral oval as a group of streamers contacted the equatorward boundary of the oval, thus showing a direct connection covering the approximate range of longitude of the streamers. During the next three nights considered, we saw a direct connection of the streamer-associated ionization and a TID for five events having radar coverage, showing the flow channels associated with the streamers and their connection to TIDs.

For all the above events, these TID regions moved equatorward below the auroral equatorward boundary, and, for each event, the TID region moved at a slower speed than did the TEC enhancements due to the electron precipitation of the associated streamers. These observations indicate that the TID is indeed a different feature from the streamer precipitation. They further indicate that there is a direct connection between the streamers together with their flow channels within the auroral oval and an ensuing TID that propagates equatorward more slowly than does the streamer ionization enhancement. This is consistent with the possibility that heating and momentum transfer from the streamer-related precipitation and flow are responsible for forming the gravity waves that produce the TIDs arising from the nightside auroral-oval, as seen in the flow channel simulations in the study by Deng et al. (2019). Note that we have recently found interesting azimuthal diversion and expansion of flow channels as they approach the equatorward

portion of the auroral oval/near-Earth plasma sheet (Wang et al., 2018; Lyons et al., 2021c) that has not yet been included in simulations to determine its effects on TID formation.

All the above events had ground magnetic N-component decreases of a few hundred nT. In contrast, the final two events we examined had clear flow channels in the SuperDARN data but substantially weaker ground magnetic depressions, and a discernible TID was not observed in association with these flow channels. These indicate that a flow channel must lead to a sufficiently large ionospheric current for it to lead to a detectable LSTID, with a few tens of nT ground magnetic field decreases not being sufficient.

Our results give evidence that LSTIDs can be generated impulsively by the flow channels and their associated auroral precipitation, offering a plausible explanation for Ding et al.'s (2008) results that the large majority of LSTID events are a single perturbation pulse. The fact that Ding et al.'s results are available for many events suggests that the impulsive generation by flow channels may be quite common. However, we have examined only 12 events so that further testing of this conclusion is warranted. We note One final point is that we had anticipated that we might see an association between individual flow channels and TIDs. However, we never observed just a single flow channel or streamer. Each of our events consisted of a few streamers and flow channels over a period on the order of 15 min and a longitude range of ~15–20°. Such groups of streamers are common during substorms. However, to the best of our knowledge, there have not been studies of whether or not streamers and their associated flow channels typically occur in groups.

DATA AVAILABILITY STATEMENT

Publicly available datasets were analyzed in this study. These data can be found here: SuperDARN data are accessible *via* http://vt.superdarn.org/tiki-index.php?page=Data+AccessSML, and SMU indices used here are available *via* the SuperMAG at http://supermag.jhuapl.edu/. The University of Alaska ASI data are available at http://optics.gi.alaska.edu/optics/. The THEMIS ASI data are available at http://themis.ssl.berkeley.edu/themisdata/. The PFISR data are available at amisr.com/database and isr.sri.com/madrigal.

AUTHOR CONTRIBUTIONS

LL: all aspects of the paper; YN: all aspects of the paper; SZ: TEC and TID evaluation; AC: TEC and TID evaluation; WB: SuperDARN radar data analysis; AR: PFISR radar data analysis; RV: PFISR radar data analysis; DH: Poker Flat ASI data analysis. All authors contributed to the article and approved the submitted version.

ACKNOWLEDGMENTS

The study at UCLA has been supported by NSF grants 1907483 and 2055192, NASA grant 80NSSC20K1314 and AFOSR FA9559-16-1-0364, at Boston University by AFOSR FA9559-16-1-0364, NASA NNX17AL22G, NSF AGS-1737823, and AFOSR FA9550-15-1-0179. This material is based upon the study supported by the Poker Flat Incoherent Scatter Radar which is a major facility funded by the National Science Foundation through cooperative agreement AGS-1840962 to SRI International. SuperDARN work at Penn State was supported by AFOSR FA9559-16-1-0364. SuperDARN data are accessible *via* http://vt.superdarn.org/tiki-index.php?page=Data+Access. SuperDARN is a collection of radars funded by the National Scientific Funding Agencies of Australia, Canada, China, France, Italy, Japan, Norway, South Africa, the United Kingdom, and the United States. Operation of the Kodiak and Adak radars, and processing of the SuperDARN data for this study were supported by the NSF grant AGS1934410 to the University of Alaska Fairbanks. The study at MIT to produce GNSS TEC data products and provide access to them through the Madrigal distributed data system has been supported by the NSF Geospace Facility program under an agreement AGS-1952737. Additional support came from AFOSR FA9559-16-1-0364, NASA LWS funding NNX15AB83G, and AGS-2033787. We thank the SuperMAG and PI Jesper W. Gjerloev for making the ground magnetic field data and SML and SMU indices used here available *via* the SuperMAG at http://supermag.jhuapl.edu/. The data we have used here are from THEMIS, CARISMA (Mann et al., 2008), the University of Alaska, and USGS (https://www.usgs.gov/natural-hazards/geomagnetism/science/observatories?qt-science_center_objects=0#qt-science_center_objects). The University of Alaska ASI data are available at http://optics.gi.alaska.edu/optics/, and the THEMIS ASI data are available at http://themis.ssl.berkeley.edu/themisdata/. The PFISR data are available at amisr.com/database and isr.sri.com/madrigal.

SUPPLEMENTARY MATERIAL

The Supplementary Material for this article can be found online at: https://www.frontiersin.org/articles/10.3389/fspas.2021.738507/full#supplementary-material

REFERENCES

Azeem, I., Yue, J., Hoffmann, L., Miller, S. D., Straka, W. C., and Crowley, G. (2015). Multisensor Profiling of a Concentric Gravity Wave Event Propagating from the Troposphere to the Ionosphere. *Geophys. Res. Lett.* 42 (19), 7874–7880. doi:10.1002/2015GL065903

Bristow, W. A., Greenwald, R. A., and Samson, J. C. (1994). Identification of High-Latitude Acoustic Gravity Wave Sources Using the Goose Bay HF Radar. *J. Geophys. Res.* 99 (A1), 319–331. doi:10.1029/93JA01470

Bristow, W. A., Hampton, D. L., and Otto, A. (2016). High-spatial-resolution Velocity Measurements Derived Using Local Divergence-Free Fitting of SuperDARN Observations. *J. Geophys. Res. Space Phys.* 121 (2), 1349–1361. doi:10.1002/2015JA021862

Coster, A., Herne, D., Erickson, P., and Oberoi, D. (2012). Using the Murchison Widefield Array to Observe Midlatitude Space Weather. *Radio Sci.* 47 (6), a–n. doi:10.1029/2012RS004993

Coster, A. J., Foster, J. C., and Erickson, P. J. (2003). Monitoring the Ionosphere with GPS. *GPS World* 14 (5), 42–45.

Coster, A. J., Goncharenko, L., Zhang, S. R., Erickson, P. J., Rideout, W., and Vierinen, J. (2017). GNSS Observations of Ionospheric Variations During the 21 August 2017 Solar Eclipse. *Geophys. Res. Lett.* 44 (24), 12041–12048. doi:10.1002/2017GL075774

Davis, M. J. (1971). On Polar Substorms as the Source of Large-Scale Traveling Ionospheric Disturbances. *J. Geophys. Res.* 76 (19), 4525–4533. doi:10.1029/JA076i019p04525

Deng, Y., Heelis, R., Lyons, L. R., Nishimura, Y., and Gabrielse, C. (2019). Impact of Flow Bursts in the Auroral Zone on the Ionosphere and Thermosphere. *J. Geophys. Res. Space Phys.* 124 (12), 10459–10467. doi:10.1029/2019JA026755

Ding, F., Wan, W., Liu, L., Afraimovich, E. L., Voeykov, S. V., and Perevalova, N. P. (2008). A Statistical Study of Large-Scale Traveling Ionospheric Disturbances Observed by GPS TEC during Major Magnetic Storms over the Years 2003-2005. *J. Geophys. Res.* 113 (A3), a–n. doi:10.1029/2008JA013037

Francis, S. H. (1975). Global Propagation of Atmospheric Gravity Waves: A Review. *J. Atmos. Terrestrial Phys.* 37, 1011–1054. doi:10.1016/0021-9169(75)90012-4

Frissell, N. A., Baker, J. B. H., Ruohoniemi, J. M., Gerrard, A. J., Miller, E. S., Marini, J. P., et al. (2014). Climatology of Medium-Scale Traveling Ionospheric Disturbances Observed by the Midlatitude Blackstone SuperDARN Radar. *J. Geophys. Res. Space Phys.* 119 (9), 7679–7697. doi:10.1002/2014JA019870

Gallardo-Lacourt, B., Nishimura, Y., Lyons, L. R., Zou, S., Angelopoulos, V., Donovan, E., et al. (2014). Coordinated Superdarn Themis ASI Observations of Mesoscale Flow Bursts Associated with Auroral Streamers. *J. Geophys. Res. Space Phys.* 119 (1), 142–150. doi:10.1002/2013JA019245

Hajkowicz, L. A. (1991). Auroral Electrojet Effect on the Global Occurrence Pattern of Large Scale Travelling Ionospheric Disturbances. *Planet. Space Sci.* 39 (8), 1189–1196. doi:10.1016/0032-0633(91)90170-F

Hayashi, H., Nishitani, N., Ogawa, T., Otsuka, Y., Tsugawa, T., Hosokawa, K., et al. (2010). Large-scale Traveling Ionospheric Disturbance Observed by superDARN Hokkaido HF Radar and GPS Networks on 15 December 2006. *J. Geophys. Res.* 115 (A6), a–n. doi:10.1029/2009JA014297

Hines, C. O. (1960). Internal Atmospheric Gravity Waves at Ionospheric Heights. *Can. J. Phys.* 38 (11), 1441–1481. doi:10.1139/p60-150

Hunsucker, R. D. (1982). Atmospheric Gravity Waves Generated in the High-Latitude Ionosphere: A Review. *Rev. Geophys.* 20 (2), 293–315. doi:10.1029/RG020i002p00293

Jorgensen, A. M., Spence, H. E., Hughes, T. J., and McDiarmid, D. (1999). A Study of omega Bands and Ps6 Pulsations on the Ground, at Low Altitude and at Geostationary Orbit. *J. Geophys. Res.* 104 (A7), 14705–14715. doi:10.1029/1998JA900100

Kubota, M., Fukunishi, H., and Okano, S. (2001). Characteristics of Medium- and Large-Scale TIDs over Japan Derived from OI 630-nm Nightglow Observation. *Earth Planet. Sp* 53 (7), 741–751. doi:10.1186/BF03352402

Liu, J., Lyons, L. R., Wang, C. P., Hairston, M. R., Zhang, Y., and Zou, Y. (2020). Dawnside Auroral Polarization Streams. *J. Geophys. Res. Space Phys.* 125 (8), e2019JA027742. doi:10.1029/2019JA027742

Lyons, L. R. (2000). Geomagnetic Disturbances: Characteristics of, Distinction between Types, and Relations to Interplanetary Conditions. *J. Atmospheric Solar-Terrestrial. Phys.* 62 (12), 1087–1114. doi:10.1016/s1364-6826(00)00097-3

Lyons, L. R., Liu, J., Nishimura, Y., Reimer, A. S., Bristow, W. A., Hampton, D. L., et al. (2021a). Radar Observations of Flows Leading to Substorm Onset Over Alaska. *J. Geophys. Res. Space Phys.* 126 (2), e2020JA028147. doi:10.1029/2020JA028147

Lyons, L. R., Liu, J., Nishimura, Y., Wang, C. P., Reimer, A. S., Bristow, W. A., et al. (2021b). Radar Observations of Flows Leading to Longitudinal Expansion of Substorm Onset Over Alaska. *J. Geophys. Res. Space Phys.* 126 (2), e2020JA028148. doi:10.1029/2020JA028148

Lyons, L. R., Nishimura, Y., Donovan, E., and Angelopoulos, V. (2013). Distinction between Auroral Substorm Onset and Traditional Ground Magnetic Onset Signatures. *J. Geophys. Res. Space Phys.* 118 (7), 4080–4092. doi:10.1002/jgra.50384

Lyons, L. R., Nishimura, Y., Wang, C.-P., Liu, J., and Bristow, W. A. (2021c). Two-Dimensional Structure of Flow Channels and Associated Upward Field-Aligned Currents: Model and Observations. *Front. Astron. Space Sci.* 8, 143. doi:10.3389/fspas.2021.737946

Lyons, L. R., Nishimura, Y., Zhang, S. R., Coster, A. J., Bhatt, A., Kendall, E., et al. (2019). Identification of Auroral Zone Activity Driving Large-Scale Traveling Ionospheric Disturbances. *J. Geophys. Res. Space Phys.* 124 (1), 700–714. doi:10.1029/2018JA025980

Mann, I. R., Milling, D. K., Rae, I. J., Ozeke, L. G., Kale, A., Kale, Z. C., et al. (2008). The Upgraded CARISMA Magnetometer Array in the THEMIS Era. *Space Sci. Rev.* 141 (1–4), 413–451. doi:10.1007/s11214-008-9457-6

Mende, S. B., Harris, S. E., Frey, H. U., Angelopoulos, V., Russell, C. T., Donovan, E., et al. (2008). The THEMIS Array of Ground-Based Observatories for the Study of Auroral Substorms. *Space Sci. Rev.* 141 (1–4), 357–387. doi:10.1007/s11214-008-9380-x

Nicolls, M. J., and Heinselman, C. J. (2007). Three-dimensional Measurements of Traveling Ionospheric Disturbances with the Poker Flat Incoherent Scatter Radar. *Geophys. Res. Lett.* 34 (21). doi:10.1029/2007GL031506

Nishimura, Y., Lyons, L. R., Kikuchi, T., Angelopoulos, V., Donovan, E., Mende, S., et al. (2012). Formation of Substorm Pi2: A Coherent Response to Auroral Streamers and Currents. *J. Geophys. Res.* 117, a–n. doi:10.1029/2012JA017889

Nishimura, Y., Lyons, L. R., Zou, S., Xing, X., Angelopoulos, V., Mende, S. B., et al. (2010). Preonset Time Sequence of Auroral Substorms: Coordinated Observations by All-Sky Imagers, Satellites, and Radars. *J. Geophys. Res.* 115, a–n. doi:10.1029/2010JA015832

Ogawa, T., Balan, N., Otsuka, Y., Shiokawa, K., Ihara, C., Shimomai, T., et al. (2002). Observations and Modeling of 630 Nm Airglow and Total Electron Content Associated with Traveling Ionospheric Disturbances over Shigaraki, Japan. *Earth Planet. Sp* 54 (1), 45–56. doi:10.1186/BF03352420

Richmond, A. D. (1978). Gravity Wave Generation, Propagation, and Dissipation in the Thermosphere. *J. Geophys. Res.* 83 (A9), 4131–4145. doi:10.1029/JA083iA09p04131

Richmond, A. D. (1979). Large-amplitude Gravity Wave Energy Production and Dissipation in the Thermosphere. *J. Geophys. Res.* 84 (A5), 1880–1890. doi:10.1029/JA084iA05p01880

Rideout, W., and Coster, A. (2006). Automated GPS Processing for Global Total Electron Content Data. *GPS Solut* 10 (3), 219–228. doi:10.1007/s10291-006-0029-5

Saito, A., Fukao, S., and Miyazaki, S. (1998). High Resolution Mapping of TEC Perturbations with the GSI GPS Network over Japan. *Geophys. Res. Lett.* 25 (16), 3079–3082. doi:10.1029/98GL52361

Savitzky, A., and Golay, M. J. E. (1964). Smoothing and Differentiation of Data by Simplified Least Squares Procedures. *Anal. Chem.* 36 (8), 1627–1639. doi:10.1021/ac60214a047

Shiokawa, K., Lu, G., Otsuka, Y., Ogawa, T., Yamamoto, M., Nishitani, N., et al. (2007). Ground Observation and AMIE-TIEGCM Modeling of a Storm-Time Traveling Ionospheric Disturbance. *J. Geophys. Res.* 112 (A5), a–n. doi:10.1029/2006JA011772

Shiokawa, K., Otsuka, Y., Ogawa, T., Balan, N., Igarashi, K., Ridley, A. J., et al. (2002). A Large-Scale Traveling Ionospheric Disturbance during the Magnetic Storm of 15 September 1999. *J. Geophys. Res.* 107 (A6), SIA 5-1–SIA 5-11. doi:10.1029/2001JA000245),

Tsugawa, T., Otsuka, Y., Coster, A. J., and Saito, A. (2007). Medium-scale Traveling Ionospheric Disturbances Detected with Dense and Wide TEC Maps over North America. *Geophys. Res. Lett.* 34 (22). doi:10.1029/2007GL031663

Tsugawa, T., Saito, A., and Otsuka, Y. (2004). A Statistical Study of Large-Scale Traveling Ionospheric Disturbances Using the GPS Network in Japan. *J. Geophys. Res.* 109 (A6). doi:10.1029/2003JA010302

Vierinen, J., Coster, A. J., Rideout, W. C., Erickson, P. J., and Norberg, J. (2016). Statistical Framework for Estimating GNSS Bias. *Atmos. Meas. Tech.* 9 (3), 1303–1312. doi:10.5194/amt-9-1303-2016

Wang, C. P., Gkioulidou, M., Lyons, L. R., and Wolf, R. A. (2018). Spatial Distribution of Plasma Sheet Entropy Reduction Caused by a Plasma Bubble: Rice Convection Model Simulations. *J. Geophys. Res. Space Phys.* 123 (5), 3380–3397. doi:10.1029/2018JA025347

Zakharenkova, I., Astafyeva, E., and Cherniak, I. (2016). GPS and GLONASS Observations of Large-Scale Traveling Ionospheric Disturbances during the 2015 St. Patrick's Day Storm. *J. Geophys. Res. Space Phys.* 121 (12), 12138–12156. doi:10.1002/2016JA023332

Zhang, S. R., Coster, A. J., Erickson, P. J., Goncharenko, L. P., Rideout, W., and Vierinen, J. (2019b). Traveling Ionospheric Disturbances and Ionospheric Perturbations Associated With Solar Flares in September

2017. *J. Geophys. Res. Space Phys.* 124 (7), 5894–5917. doi:10.1029/2019JA026585

Zhang, S. R., Erickson, P. J., Coster, A. J., Rideout, W., Vierinen, J., Jonah, O., et al. (2019a). Subauroral and Polar Traveling Ionospheric Disturbances During the 7-9 September 2017 Storms. *Space Weather* 17 (12), 1748–1764. doi:10.1029/2019SW002325

Zhang, S. R., Erickson, P. J., Goncharenko, L. P., Coster, A. J., Rideout, W., and Vierinen, J. (2017). Ionospheric Bow Waves and Perturbations Induced by the 21 August 2017 Solar Eclipse. *Geophys. Res. Lett.* 44 (24), 12067–12073. doi:10.1002/2017GL076054

Conflict of Interest: The authors declare that the research was conducted in the absence of any commercial or financial relationships that could be construed as a potential conflict of interest.

Publisher's Note: All claims expressed in this article are solely those of the authors and do not necessarily represent those of their affiliated organizations, or those of the publisher, the editors, and the reviewers. Any product that may be evaluated in this article, or claim that may be made by its manufacturer, is not guaranteed or endorsed by the publisher.

Copyright © 2021 Lyons, Nishimura, Zhang, Coster, Liu, Bristow, Reimer, Varney and Hampton. This is an open-access article distributed under the terms of the Creative Commons Attribution License (CC BY). The use, distribution or reproduction in other forums is permitted, provided the original author(s) and the copyright owner(s) are credited and that the original publication in this journal is cited, in accordance with accepted academic practice. No use, distribution or reproduction is permitted which does not comply with these terms.

frontiers in Astronomy and Space Sciences

ORIGINAL RESEARCH
published: 27 October 2021
doi: 10.3389/fspas.2021.746459

Mesoscale Features in the Global Geospace Response to the March 12, 2012 Storm

Mayowa Adewuyi[1], *Amy M. Keesee*[1,2]*, *Yukitoshi Nishimura*[3], *Christine Gabrielse*[4] *and Roxanne M. Katus*[5]

[1]Department of Physics and Astronomy, University of New Hampshire, Durham, NH, United States, [2]Space Science Center, Institute for Earth, Oceans, and Space, University of New Hampshire, Durham, NH, United States, [3]Department of Electrical and Computer Engineering and Center for Space Physics, Boston University, Boston, MA, United States, [4]The Aerospace Corporation, El Segundo, CA, United States, [5]Department of Mathematics and Statistics, Eastern Michigan University, Ypsilanti, MI, United States

The geospace response to coronal mass ejections includes phenomena across many regions, from reconnection at the dayside and magnetotail, through the inner magnetosphere, to the ionosphere, and even to the ground. Phenomena occurring in each region are often connected to each other through the magnetic field, but that field undergoes dynamic changes during storms and substorms. Improving our understanding of the geospace response to storms requires a global picture that enables us to observe all the regions simultaneously with both spatial and temporal resolution. Using the Energetic Neutral Atom (ENA) imager on the Two Wide-Angle Imaging Neutral-Atom Spectrometers (TWINS) mission, a temperature map can be calculated to provide a global view of the magnetotail. These maps are combined with *in situ* measurements at geosynchronous orbit from GOES 13 and 15, auroral images from all sky imagers (ASIs), and ground magnetometer measurements to examine the global geospace response of a coronal mass ejection (CME) driven event on March 12th, 2012. Mesoscale features in the magnetotail are observed throughout the interval, including prior to the storm commencement and during the main phase, which has implications for the dominant processes that lead to pressure buildup in the inner magnetosphere. Auroral enhancements that can be associated with these magnetotail features through magnetosphere-ionosphere coupling are observed to appear only after global reconfigurations of the magnetic field.

Keywords: geomagnetic storm, substorm, magnetotail, particle injections, mesoscale phenomena

OPEN ACCESS

Edited by:
Hermann Lühr,
Helmholtz Centre Potsdam, Germany

Reviewed by:
Evgeny Panov,
Austrian Academy of Sciences, Austria
Huishan Fu,
Beihang University, China

***Correspondence:**
Amy M. Keesee
amy.keesee@unh.edu

Specialty section:
This article was submitted to Space Physics, a section of the journal Frontiers in Astronomy and Space Sciences

Received: *23 July 2021*
Accepted: *13 October 2021*
Published: *27 October 2021*

Citation:
Adewuyi M, Keesee AM, Nishimura Y, Gabrielse C and Katus RM (2021) Mesoscale Features in the Global Geospace Response to the March 12, 2012 Storm. Front. Astron. Space Sci. 8:746459. doi: 10.3389/fspas.2021.746459

INTRODUCTION

During geomagnetic storms and substorms, magnetic reconnection in Earth's magnetotail can accelerate ions and electrons both Earthward and tailward (e.g. Hoshino et al., 2001; Drake et al., 2006; Fu et al., 2019). Bursty bulk flows (BBFs) and dipolarization fronts (DFs) are Earthward traveling features that can result from this reconnection-driven acceleration (Baumjohann et al., 1990, 1999; Angelopoulos et al., 1992, 1994; Nakamura et al., 2002; Runov et al., 2009; Fu et al., 2013). BBFs are continuous segments of magnetotail flow enhancement (~10 min), punctuated by ~1 min long intense flow and electric field bursts (V > 400 km/s, VBz > 2 mV/m). DFs are a sharp increase in

Bz with thickness on the order of the ion inertial length. Statistical analysis by Fu et al. (2012) showed that these DFs have a peak occurrence at a radial distance of approximately 15 R_E, and occurrence decreases rapidly inside r ~ 10 R_E. Using simulation results, Merkin et al. (2019a) demonstrated the correlation between substorm onset and abrupt increase in DF counts, noting this increase as a characteristic of the substorm onset. These reconnection fast flows and related DFs are narrow--on the order of a few R_E wide (Sergeev et al., 1996; Nakamura et al., 2004). These phenomena in the tail are associated with particle injections-observed as rapid increases in energetic particle fluxes-in the near tail and inner magnetosphere (Birn et al., 1997).

There is debate about whether the buildup of the ring current pressure is caused by these mesoscale phenomena or by broad earthward convection resulting from a southward *z*-component of the interplanetary magnetic field (IMF). Menz et al. (2017) used Van Allen Probes measurements and drift trajectory modeling to show that adiabatic convection was sufficient to explain the ring current pressure buildup for two storms. However, the fast flows and DFs have been shown to carry >60% of the measured earthward transport of mass, energy and magnetic flux using a statistical study of *in situ* measurements (Angelopoulos et al., 1994). Because of their narrow nature, it is extremely difficult to put BBFs into the global context for a specific event with only single-point *in situ* satellite measurements that will easily miss the signature. Modeling of several idealized storms demonstrated a similar contribution from mesoscale phenomena (~61% for intense storms) and that these injections were required to recreate observed ring current enhancements in the simulations (Yang et al., 2015; 2016). A global view of the near-Earth region is needed to provide context to localized measurements and validate simulations.

The plasma sheet where these mesoscale phenomena occur magnetically maps to the ionosphere. Many studies have shown the connection between phenomena in the magnetotail and auroral enhancements (e.g. Elphinstone et al., 1995; Henderson et al., 1998; Sergeev et al., 2000, 2004) and we discuss a few highlights here. Motoba et al. (2012) used conjugate auroral observations in the northern and southern hemispheres to demonstrate that auroral beads (wave-like structures) appearing in the initial brightening arc just before substorm onset have a source in the magnetotail with scales on the order of the 1–10 keV proton gyroradius. Spanswick et al. (2017) used THEMIS and FAST satellite-based measurements and ground-based proton aurora images to statistically determine that most of the proton aurora originates from 6–10 R_E. Lyons et al. (2012) demonstrated a connection between dipolarization fronts in the plasma sheet and aurora streamers and discussed the implications for substorm onset. Ge et al. (2012) found connections between dipolarization fronts and proton aurora observations and used magnetohydrodynamics (MHD)-based simulations to determine that proton aurora enhancements were caused by ion reflection at the front. Nishimura et al. (2014) connected transient flow bursts in the magnetotail and ring current injections measured by THEMIS with proton aurora observed by all sky imagers. Nakamura et al. (2001) used Geotail measurements and Polar UVI images to show that auroral streamers correspond to field aligned currents on the dusk side of earthward flow bursts. Auroral streamers have been used to demonstrate that BBFs are seen to enter and terminate within the transition region from stretched to dipolar-like field lines in the tail (Kauristie et al., 2003). It is in this transition region that Gabrielse et al. (2019) showed minutes-long ion injections with flux enhancements that lasted approximately for the duration of the earthward flow. Both the flow and the ion injection were quenched when the global dipolarization (and associated substorm auroral expansion seen in the THEMIS ASIs) expanded over the observing satellites. Donovan et al. (2013) notes that more observations of this transition region are needed to better understand the physics of this region, particularly to understand substorm onset.

All of these studies supplemented and informed the ionosphere observations with localized *in situ* measurements in the magnetotail that provide limited spatial coverage. While comparison to simulations can provide more context to the global response of the system, global measurements are needed to provide validation. Energetic neutral atom (ENA) imaging can provide this needed global view of the magnetosphere. Ion temperature maps can be calculated using ENA measurements (Scime et al., 2002; Keesee et al., 2008) and used to look for heated ions associated with phenomena in the magnetotail. This technique requires active intervals for sufficient ENA signal (McComas et al., 2002; Keesee et al., 2014). DFs are associated with a gradual increase in ion temperature ahead of the front (Runov et al., 2011) due to the acceleration and reflection of ions in the plasma sheet ahead of the front (Zhou et al., 2010). Ukhorskiy et al. (2018) found that this energization is higher than would be expected from an adiabatic process. Ion temperatures tend to remain elevated for a longer time interval than the short time scales during which the flow bursts occur (Angelopoulos et al., 1992). The dipolarization of the magnetic field associated with substorms and injections also results in energization of ions through a process similar to betatron acceleration (Birn et al., 1997).

Keesee et al. (2014) observed regions of energized ions in the magnetotail during the Galaxy-15 substorm using TWINS energetic neutral atom (ENA) data to calculate ion temperature maps. These energized regions are observed to move Earthward and are deflected azimuthally near geosynchronous orbit. Keesee et al. (2020) compared TWINS ion temperature maps, MMS data, and MHD simulations for an interval during August 3, 2016. Multiple regions of enhanced ion temperatures are observed during this period across the tail in the TWINS maps. One of these regions occurred on the dusk side of the tail near the location of the MMS satellites. This region increased from ~5 to >10 keV as calculated from TWINS data. During this interval MMS4 observed increased ion energies, Earthward flow bursts (Vx), increased ion temperatures, and a dipolarization of Bz. The MHD simulations of this interval also had increased ion temperatures and flows associated with substorm activity. However, the heating in the simulations was less than that observed in the data, demonstrating that global

ENA imaging is critical to validating models and improving our understanding of substorm dynamics.

In this study, we combine global ENA imaging with *in situ* measurements in the inner magnetosphere and auroral imaging to improve our understanding of mesoscale phenomena in the magnetotail and their connections to the inner magnetosphere and ionosphere.

DATA AND METHODOLOGY

TWINS Ion Temperature Maps

The Two Wide-angle Imaging Neutral atom Spectrometers (TWINS) mission (McComas et al., 2009) provides energetic neutral atom data from two satellites in high inclination Molniya orbits. Ion temperature maps are calculated by projecting ENA flux with energies of 1–36 keV along the line of sight to the equatorial plane and fitting to a Maxwellian distribution for parent ions (Scime et al., 2002; Keesee et al., 2008). The resulting mapped area is a combination of the instrument field of view and a modeled magnetosphere boundary using Shue et al. (1997). The map is a grid of 0.5 × 0.5 R_E bins that are populated by flux from a varying number of projected instrument pixels, resulting in a spatial resolution that decreases with increasing distance from Earth (Keesee et al., 2014, 2011). A database of temperature maps at 10-min cadence during storms is available at CDAWeb (Keesee et al., 2020) and the projection and temperature analysis codes are available in the UNH Scholar's Repository (Keesee et al., 2019). For this study, temperature maps were created using a ~3-min cadence.

In Situ Measurements

Inner magnetosphere measurements during the storm are available from the Time History of Events and Macroscale Interactions during Substorm (THEMIS) mission (Angelopoulos, 2008) and NOAA Geostationary Operational Environmental Satellite (GOES) 13 and 15. THEMIS consists of three identically-instrumented satellites with apogees of ~12 R_E. Ion flux measurements are provided by the electrostatic analyzer (ESA) (5 eV–25 keV ions) (McFadden et al., 2008) and the Solid State Telescope (SST) (30 to >700 keV ions) (Angelopoulos et al., 2008) and magnetic field measurements from the fluxgate magnetometer (FGM) (Auster et al., 2008). The GOES satellites include a Space Environment Monitor (SEM) instrument subsystem that obtains magnetometer, energetic particle, and soft X-ray data (Singer et al., 1996; Onsager et al., 1996).

Auroral Imagers

The THEMIS mission includes an array of 20 white light auroral imagers across Greenland, Canada, and Alaska (Harris et al., 2008; Mende et al., 2008). These All Sky Imagers (ASI) provide images with several km spatial resolution and 3 s temporal resolution. ASI images cannot be used to distinguish between electron and proton aurora, but conjugate observations from satellites such as THEMIS and GOES electron and proton fluxes can be used to identify proton aurora in the images (Nishimura et al., 2014).

Ground Magnetometers

Ground magnetic field perturbations are obtained from the SuperMAG database (Gjerloev, 2012). Data was obtained from 201 magnetometer stations. Station location is used to determine magnetic local time.

RESULTS

A CME-driven storm occurred on March 12, 2012 (Keesee and Scime, 2015) with a sudden storm commencement beginning at 9:16 UT and a minimum Sym-H index of -67 nT at 16:55 UT. The overall evolution of the storm is shown in **Figure 1**, including interplanetary magnetic field (IMF) *z*-component, AE index, solar wind pressure, Sym-H index, proton flux from GOES 13 and 15, average plasma sheet ion temperature from TWINS, and average ground magnetic field perturbations from SuperMag stations for mid (50–60) and high (> 60) latitudes. The overall trend in the temperature of the plasma sheet corresponds with the trends in the AE index and SuperMAG ground magnetic field perturbations, showing connections between the plasma sheet and the ionosphere. There are three separate peaks observed in these variables, one at the beginning of the storm, the second associated with a southward turning of the IMF Bz, and the third following a prolonged period of strong southward Bz.

A sudden storm commencement (SSC) can be observed around 9:15 UT (vertical line 1 in **Figure 1**), with a very strong (>50 nT) increase to the Sym-H index driven by the high solar wind pressure. We note that the increase in Sym-H (**Figure 1D**) appears prior to the increase in solar wind pressure (**Figure 1C**) which may be due to inaccurate propagation of the data measured at the Lagrangian L1 point to the bow shock. An increase in the proton flux was measured by *in situ* satellites shortly after the SSC, with GOES 13 observing the flux increase slightly before GOES 15. During this time interval, GOES 13 was located pre-dawn at approximately −5.5 R_E in Y and −3 R_E in X (GSM coordinates), while GOES 15 was located near midnight at approximately −0.1 R_E in Y and −5.8 R_E in X (see GOES and THEMIS orbital locations in the **Supplementary Material**). Both GOES satellites observed a simultaneous increase in flux across all energies for both protons and electrons (electrons not shown). THEMIS satellites located toward the dawn flank from GOES 13 observed similar flux increases (see **Supplementary Material**). This is typically interpreted as a signature of the plasma sheet's earthward boundary moving earthward of the satellite location by magnetosphere compression and global E x B convection. However, as we will describe in the Discussion, this could be a signature of dispersionless injection. The SSC was preceded by consistent southward IMF Bz for approximately 90 min. A northward turning of the IMF Bz can be seen around 9:45 UT (vertical line 2 in **Figure 1**), with the AE index also decreasing around the same time and the Sym-H index remaining near zero. A

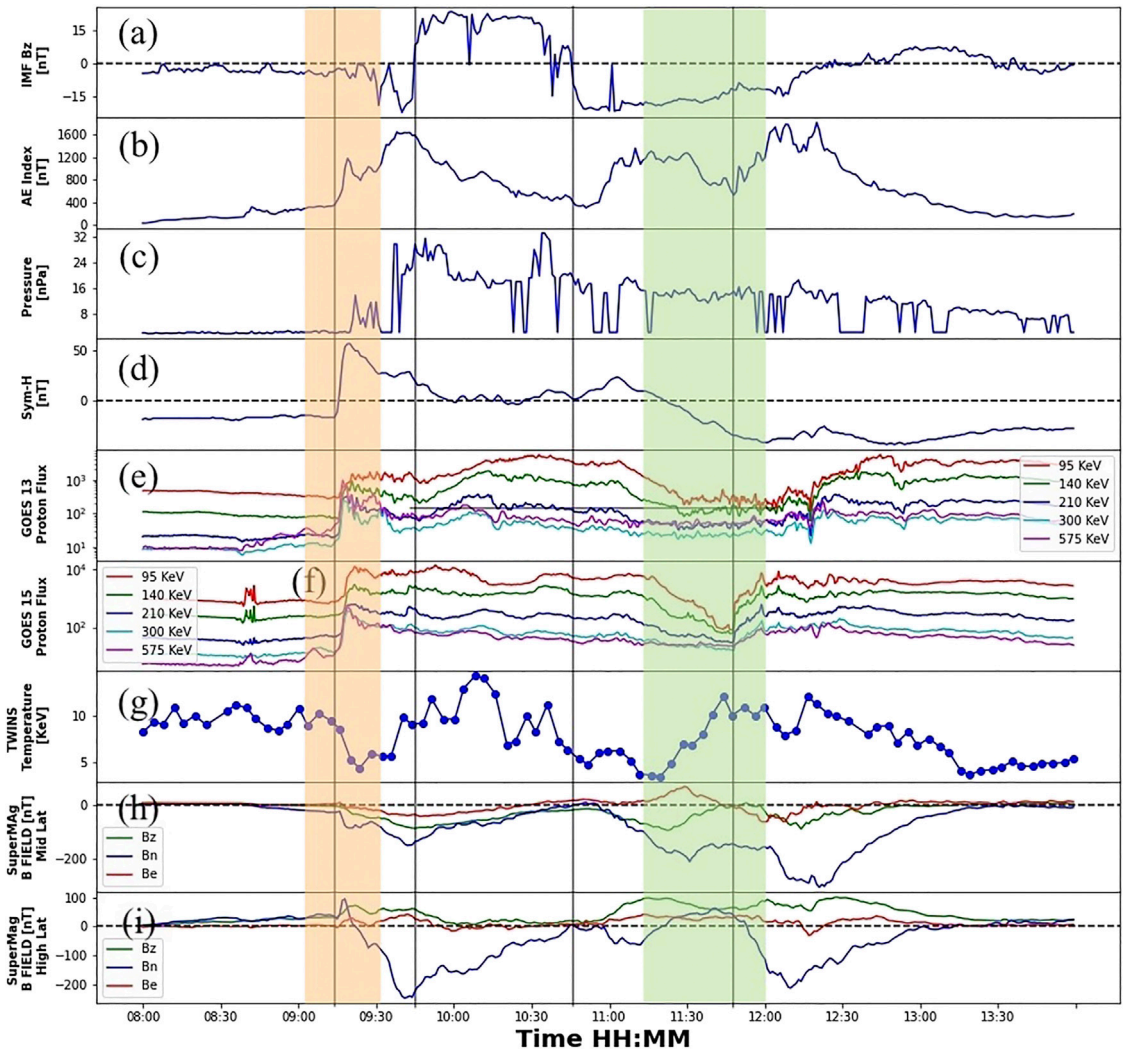


FIGURE 1 | (A) IMF Bz, **(B)** AE index, **(C)** solar wind pressure, and **(D)** Sym-H index from OMNIWeb, GOES **(E)** 13 and **(F)** 15 proton flux [p/cm2 s sr keV], **(G)** TWINS average plasma sheet ion temperature, SuperMAG ground magnetic field perturbations averaged for **(H)** mid and **(I)** high latitude stations for March 12, 2012, 8: 00–14:00 UT. Vertical lines indicate times referenced in the text. The shaded regions correspond to intervals discussed in the text and highlighted in **Figures 2**, **3** (orange) and **Figures 4**, **5** (green).

decrease in the temperature of the plasma sheet occurred shortly afterwards at around 10:15 UT. Ground perturbations were observed at the SSC, with the averaged SuperMag magnetic field changing in response, especially in the local magnetic north component. The high latitude SuperMAG average was positive for about 4 min after the SSC, before a negative bay that peaked around 9:45 UT. The mid latitude stations experienced a less intense perturbation that peaked at the same time.

Figure 2 shows a sequence of ion temperature maps calculated from TWINS for 9:04–9:33 UT (orange highlighted interval in **Figure 1**). This series of temperature maps give a global observation of the plasma sheet during the interval surrounding the SSC. The average temperature shown in **Figure 1** is calculated from these maps by selecting the area from 5 to 20 R_E and magnetic local time (MLT) from 20:00 to 4:00. A movie of ion temperature maps for the entire storm interval is in the **Supplementary Material**. Regions of increased ion temperatures are observed prior to the SSC, likely due to the steady southward IMF Bz prior to the shock arrival driving tail reconnection and earthward flows (as evidenced by the AE index increasing to ~400 nT in **Figure 1B**). At the time of the SSC, the plasma sheet temperatures drop significantly across the entire field of view, as seen in **Figure 2D**. Regions of increased ion temperature begin appearing again in the 9:22–9:26 UT interval (**Figure 2F**) with the most intense region occurring in the dusk half of the magnetotail. These regions appear localized across the magnetotail and elongated along the tail and move towards the inner magnetosphere, indicative

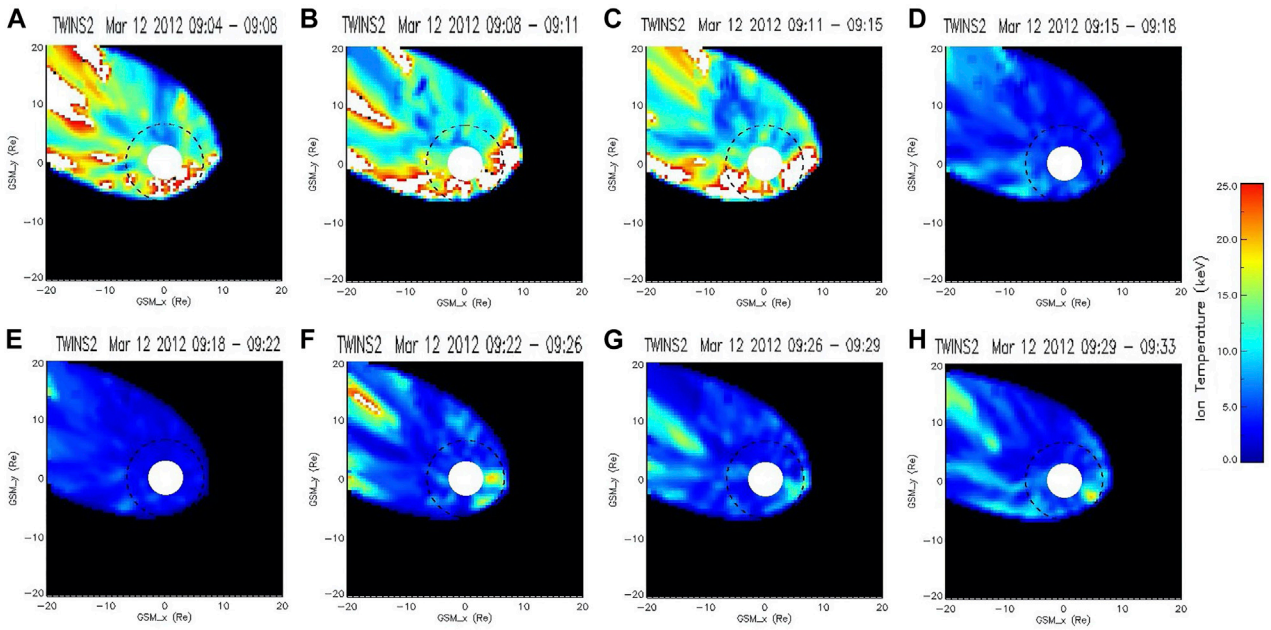


FIGURE 2 | Ion temperature maps of the GSM xy-plane calculated from TWINS measurements for 9:04–9:33 UT. The Sun is to the right, the white disc has a radius of 3 Re and is centered at Earth and the dashed line indicates geosynchronous orbit.

of narrow flow channels. Note, however, that because the temperature maps are ~3 min averages the flows do not necessarily exist across the entire length for the full interval.

The THEMIS All Sky Imagers can provide spatial and temporal evolution of ionospheric activity. The ASI movie is in the **Supplementary Material**. To compare locations of observations to TWINS measurements, the TS01 model was used to map THEMIS ASI images and the locations of the *in situ* spacecraft to the GSM equatorial plane. The magnetic field model is not necessarily accurate, particularly at outer L-shells. As such, we do not intend to make pixel-to-pixel comparisons, and instead compare overall morphology. A sequence of mapped ASI images and the associated globe projections for 9:05–9:30 UT are shown in **Figure 3**. Despite the continuous southward IMF Bz, the auroral activity is minimal (the moonlight is blocked and appears white) until after the SSC at 9:15 UT (**Figure 3C**) with initial brightening occurring in the region mapping to post-midnight. A poleward boundary intensification (PBI) is observed prior to SSC (**Figure 3B**). Streamers are identified in each interval after the SSC. At 9:25 UT (**Figure 3E**), brightening occurs in the pre-midnight region and extends to post-midnight. This brightening is identified as a streamer in the pre-midnight region of the ASI.

The IMF Bz turned southward around 10:45 UT (vertical line 3 in **Figure 1**) resulting in moderate increases in the AE index, plasma sheet temperatures, and ground magnetic field perturbations approximately 10–15 min later. As the Bz remained strongly southward, the plasma sheet ion temperature increased and dispersionless ion injections were observed at geosynchronous orbit. A strong response was seen in the SuperMAG data, and the AE and Sym-H indices peaked about 10 min after the injection observed at GOES 15.

A sequence of ion temperature maps calculated from TWINS from 11:13–11:56 UT (green highlighted interval in **Figure 1**) is shown in **Figure 4**. This series shows the plasma sheet during the interval of strong southward IMF Bz. Regions of increased ion temperatures are observed in the plasma sheet, primarily on the dawn (post-midnight) side of the tail. These regions appear to first reach geosynchronous orbit in the 11:20–11:24 UT interval (**Figure 4C**). As time continues, there are more regions and they increase in size across the tail. The flux dropout observed by GOES-15 (located post-midnight) at 11:20–11:47 UT corresponds to the substorm growth phase during the southward IMF, when the magnetic field stretched, resulting in the satellite moving away from the central plasma sheet (**Figure 1F**). A dispersionless injection is observed by GOES-15 at 11:47 UT (vertical line 4 in **Figure 1**). GOES-13 (located at dawn) observed a flux dropout similar to GOES-15 (**Figure 1E**). The magnetic field at this location didn't change much, so the flux variations don't seem to be due to magnetic field stretching. The lower energy ion fluxes dropped, while high energy ion fluxes didn't change much, which could be indicative of magnetopause shadowing.

The sequence of ASI projections for 11:15–12:00 UT is shown in **Figure 5**. Auroral activity is minimal until 11:45 UT (**Figure 5G**), after which the enhancements in the post-midnight imager expand tailward.

To understand the spatial correlation between signatures in the temperature maps and the ground observations, plots of magnetic perturbation as a function of MLT and UT are shown in **Figure 6** for low (0–50°), mid (50–60°), and high

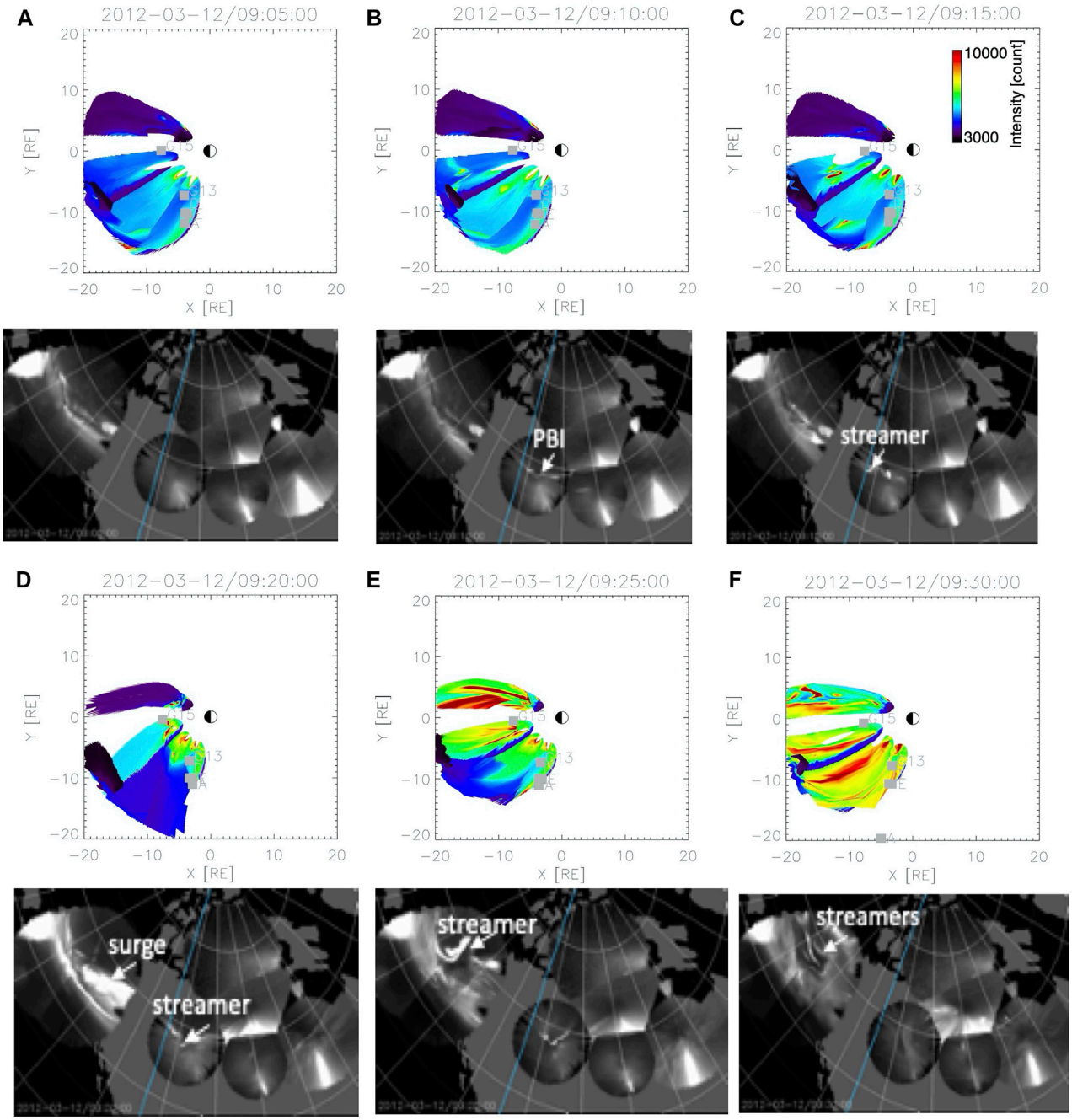


FIGURE 3 | THEMIS ASI auroral images mapped to the GSM equatorial plane using TS01 **(top)** and globe projections **(bottom)** for 9:05–9:30 UT. The colorbar in panel **(C)** applies to all panels. Symbols indicate the mapped location of the GOES 13 (G13), GOES 15 (G15), and THEMIS (A, D, E) satellites.

(60–90°) latitudes. Very weak perturbations in the magnetic field at low latitudes (**Figure 6A**) can be seen, with the strongest perturbation reaching about 400 nT in magnitude. The mid latitude stations (**Figure 6B**) observed some stronger perturbations, going as far up as 1600 nT. The location of the highest magnetic field perturbations was also confined within the 0–10 MLT (i.e., post-midnight). The high latitude stations (**Figure 6C**) observed the strongest perturbations, with some stations going up to 2000 nT in magnitude. The locations of the highest changes in the fields were broader in comparison to the mid latitude stations, going from about 18 to 10 MLT. Across all latitudes, three distinct temporal regions of increased perturbations can be seen, starting from the SSC at 9:15 UT, and then at 11:00 UT, with a final increase occurring shortly afterwards at approximately 12:00 UT. While the first

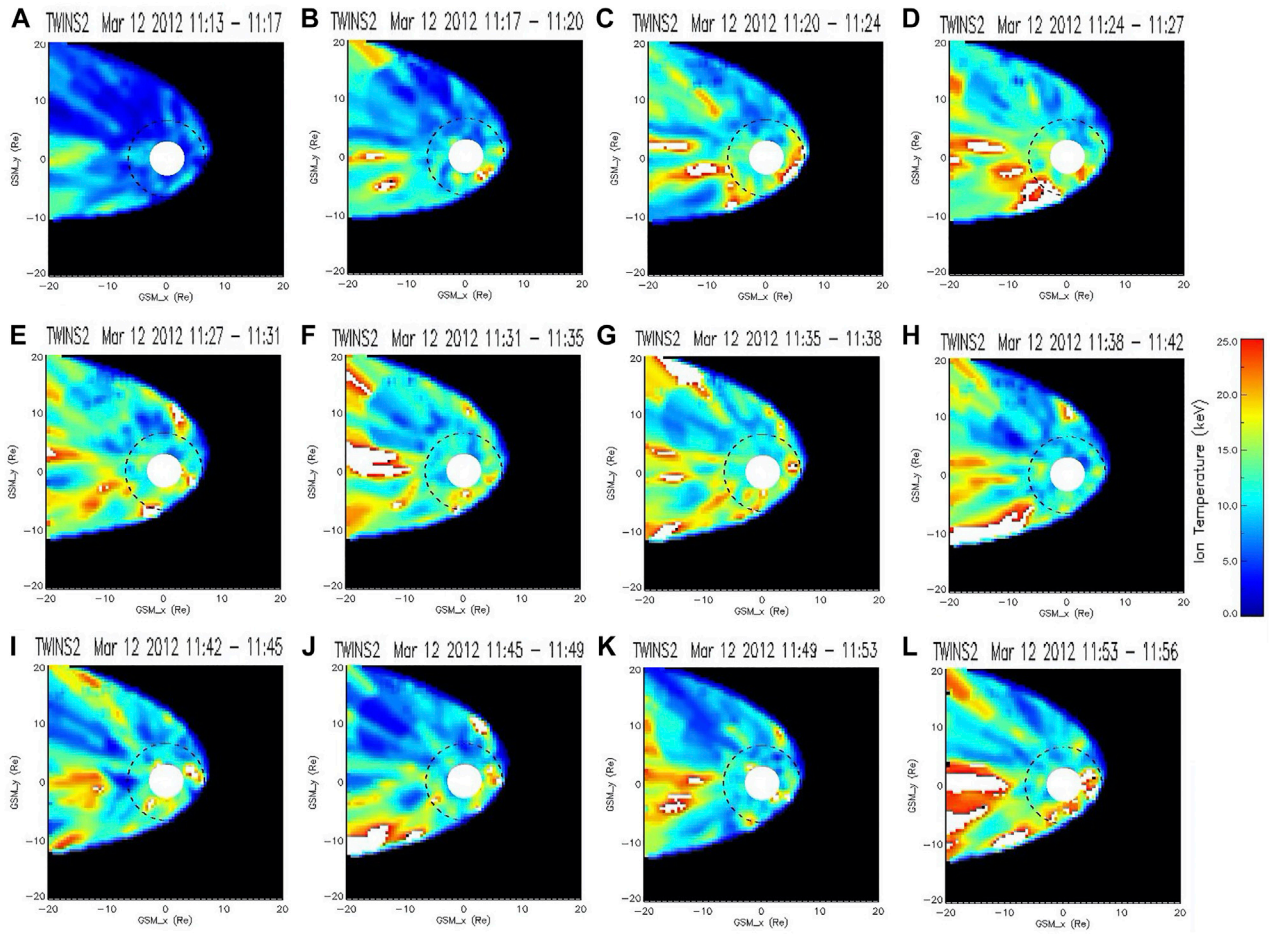


FIGURE 4 | Ion temperature maps of the GSM xy-plane calculated from TWINS measurements for 11:13–11:56. The Sun is to the right, the white disc has a radius of 3 Re and is centered at Earth and the dashed line indicates geosynchronous orbit.

two peaks appear to stay mostly stationary in MLT, the third peak appears to move toward noon over time.

DISCUSSION

Using a multi-perspective global view, we found that mesoscale phenomena played a significant role during this storm. As described above, the initial flux increase at the SSC is typically interpreted as a global phenomenon due to compression of the magnetosphere. However, there were multiple mesoscale features observed in the TWINS maps prior to the SSC that could have led to particle injections to the inner magnetosphere. The Sym-H response to the SSC was significantly stronger than typical storms, perhaps indicating that a combination of changes, including injection of particles, was occurring to the inner magnetosphere. A decrease in the ion temperature across the magnetosphere was also observed at the time of the SSC. It is unclear if this is a physical result or a reduction in ENA flux to the instrument due to global reconfiguration of the magnetic field. More studies using global imaging are needed to compare pre-storm plasma sheet conditions and the resulting inner magnetosphere SSC response.

While the southward turning of the IMF Bz at ~10:45 UT resulted in moderate activity, as observed by the ground observations and AE index, more significant activity was observed following prolonged southward Bz while the plasma sheet had the opportunity to heat up. The average plasma sheet temperature begins to decrease at the same time as the GOES 13 (located at dawn) flux begins to decrease (~11:10 UT in **Figure 1E–G**). Then, the temperature increase begins at the same time as the flux decrease at GOES 15 (located post-midnight) began (~11:20 in **Figure 1F,G**). An injection is observed at GOES 15 and the AE begins to increase to its highest value during the storm just after the plasma sheet reaches its peak temperature. This agrees with the findings by Forsyth et al. (2014) that plasma sheet ion temperatures during the substorm growth phase increase with solar wind driving and also correlate with substorm size. The multiple mesoscale features observed by TWINS during the growth phase agrees qualitatively with simulations

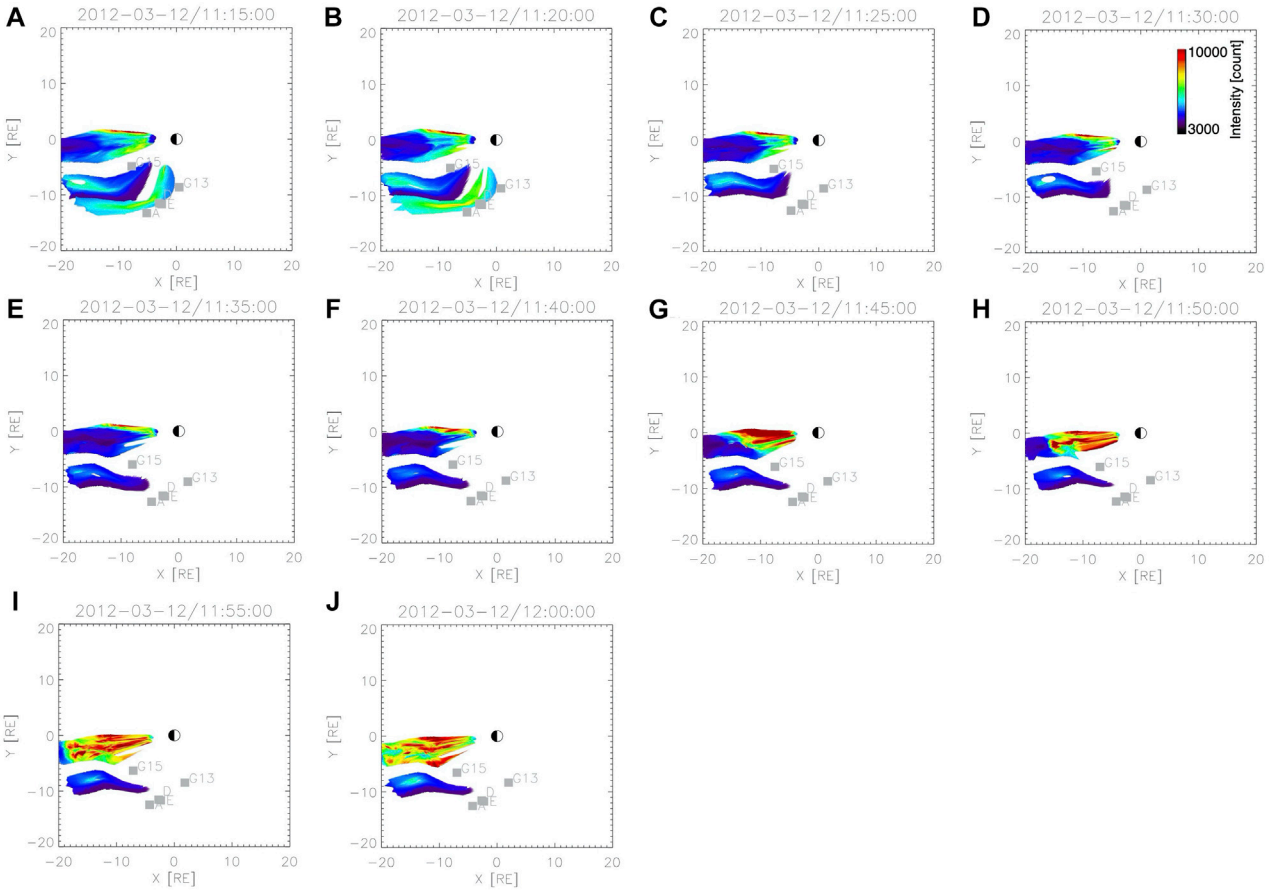


FIGURE 5 | THEMIS ASI auroral images mapped to the GSM equatorial plane using TS01 for 9:15–12:00 UT. The colorbar in panel **(D)** applies to all panels. Symbols indicate the mapped location of the GOES 13 (G13), GOES 15 (G15), and THEMIS (A, D, E) satellites.

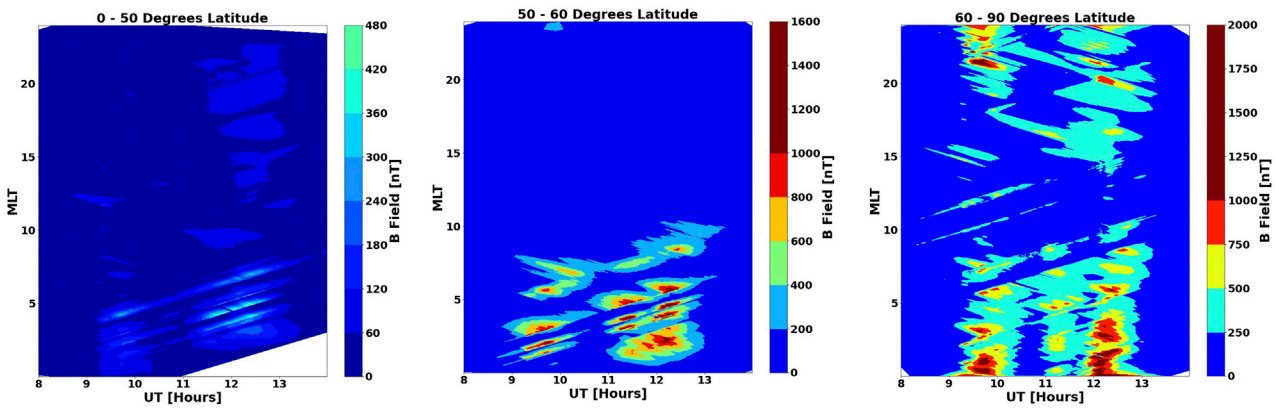


FIGURE 6 | Ground magnetic field north component perturbations as a function of location (MLT) and time (UT) for **(A)** low, **(B)** mid, and **(C)** high latitudes using SuperMAG data. Note that each plot is on the same color scale, but the colorbar indicates the range of values within the plot.

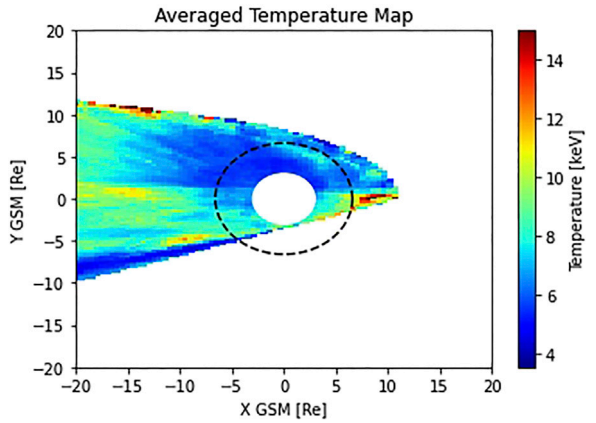


FIGURE 7 | Average temperature map for the entire storm interval, 8:00–13:30 UT. The white disk has a radius of 3 Re centered on Earth, while the dashed circle indicates geosynchronous orbit. The color bar limit goes up only to 15 keV, as opposed to 25 keV from the previous temperature maps.

by Merkin et al. (2019b), and direct comparisons of such simulations with TWINS temperature maps during the same interval would be useful for future studies.

We note that the increased temperatures occur predominantly on the dawn (post-midnight) side of the magnetotail during the ~11–12 UT interval (**Figure 4**), which makes this storm unique in that it contrasts with the majority of fast flows and injections that have been observed on the dusk (pre-midnight) side (McPherron et al., 2011; Liu et al., 2013; Walsh et al., 2014; Gabrielse et al., 2017). To emphasize this, an ion temperature map averaged over the entire storm is shown in **Figure 7**. While this average over 5.5 h demonstrates some variations due to instrumental effects (the TWINS ENA instrument consists of two sensor heads), recall that primarily dusk-side regions are observed early in the storm (**Figure 2**). Additionally, the localization of the enhancements in the ASI projections and mid-latitude ground perturbations to the post-midnight sector corresponds to the predominance of increased plasma sheet temperatures to the same region.

As noted in the description of **Figure 6**, the third overall increase in ground magnetic perturbations (starting just before 12:00 UT) showed movement in MLT toward noon over time. This is indicative of particles flowing around Earth, and can also be observed in the ion temperature maps (see movie in **Supplementary Material**). This is in contrast to the first two increases, and only occurred after the heating of the plasma sheet, demonstrating the role that plasma sheet dynamics have in particle motion in the inner magnetosphere.

The regions of increased ion temperatures observed in the plasma sheet were observed to first reach geosynchronous orbit in the 11:20–11:24 UT interval (**Figure 4C**). However, increases in flux are not observed at GOES until 11:47 UT, though as indicated GOES is probably outside of the central plasma sheet due to magnetic field stretching. Thus, the global imaging from TWINS enables us to see that particles are likely entering the inner magnetosphere earlier than is observable by the *in situ* measurements. However, the ASI enhancements are also observed at about the same time as the GOES flux increase. At the time when GOES observes the flux increase, both TWINS and ASI observed enhancements in the post-midnight region (**Figures 4J**, **5G**). GOES 15 mapped to a location −6.7 Re in X, and −6.6 Re in Y, just on the edge of the region of hot ion plasma seen in the temperature map. A flux increase in the GOES 15 data can be seen across all energy levels. Since the regions of heated ions are observed in the plasma sheet prior to the injection at GOES but no significant features were observed in the aurora until after the injection, the reconfiguration of the magnetic field caused by the substorm must have provided a stronger connection between the plasma sheet and ionosphere after than time. A similar reconfiguration appears to occur at the beginning of the storm since the auroral brightening occurs after SSC despite the observation of heated ions in the plasma sheet prior to it.

CONCLUSION

We have analyzed the global response of the geospace system, from the plasma sheet in the magnetotail to the ground, for the storm on March 12, 2012. By taking advantage of global imaging techniques, spatial and temporal signatures of the plasma sheet's response to the CME driven event was observed. Observations of the plasma sheet before the SSC show signatures of flow channels coming in from the magnetotail, indicating the importance of mesoscale injections to the inner magnetosphere at SSC. This may have combined with global convection to result in a strong Sym-H response at SSC. The temperature maps during the storm main phase showed a flow channel bias towards the post-midnight sector. This bias towards this sector was also seen in the ground observations, with regions within 18 MLT to 10 MLT experiencing stronger magnetic perturbations. Comparison with auroral images demonstrates a change in magnetosphere-ionosphere coupling upon both the commencement of the storm and the onset of a substorm.

DATA AVAILABILITY STATEMENT

Publicly available datasets were analyzed in this study. This data can be found here: The TWINS and THEMIS datasets analyzed for this study can be found at CDAWeb (https://cdaweb.gsfc.nasa.gov/index.html/). GOES datasets can be found at NOAA (https://www.ngdc.noaa.gov/stp/satellite/goes/dataaccess.html). Ground magnetometer data is available at the SuperMAG site (https://supermag.jhuapl.edu). Solar wind, IMF, and geomagnetic indices can be found at OMNIWeb (https://omniweb.gsfc.nasa.gov).

AUTHOR CONTRIBUTIONS

MA and AK conducted the primary analysis and writing of the manuscript. YN and RK contributed to data analysis and figure creation. YN and CG contributed to data interpretation. YN, CG, and RK reviewed the draft and provided input.

FUNDING

Funding provided by NASA Awards 80NSSC19K0755, 80NSSC20K0701, 80NSSC18K0657, 80NSSC20K0604, 80NSSC20K0725 and NSF Awards 2109543, AGS-1602862, AGS-1907698, and AFOSR Grant FA9559-16-1-0364.

ACKNOWLEDGMENTS

The authors would like to thank Victor Pinto for helpful discussions.

SUPPLEMENTARY MATERIAL

The Supplementary Material for this article can be found online at: https://www.frontiersin.org/articles/10.3389/fspas.2021.746459/full#supplementary-material

REFERENCES

Angelopoulos, V., Baumjohann, W., Kennel, C. F., Coroniti, F. V., Kivelson, M. G., Pellat, R., et al. (1992). Bursty Bulk Flows in the Inner Central Plasma Sheet. *J. Geophys. Res.* 97 (A4), 4027–4039. doi:10.1029/91ja02701

Angelopoulos, V., Kennel, C. F., Coroniti, F. V., Pellat, R., Kivelson, M. G., Walker, R. J., et al. (1994). Statistical characteristics of bursty bulk flow events. *J. Geophys. Res.* 99 (A11), 21257. doi:10.1029/94JA01263

Angelopoulos, V., Sibeck, D., Carlson, C. W., McFadden, J. P., Larson, D., Lin, R. P., et al. (2008). First results from the THEMIS mission. *Space Sci. Rev.* 141 (1–4), 453–476. doi:10.1007/s11214-008-9378-4

Angelopoulos, V. (2008). The THEMIS Mission. *Space Sci. Rev.* 141 (1–4), 5–34. doi:10.1007/s11214-008-9336-1

Auster, H. U., Glassmeier, K. H., Magnes, W., Aydogar, O., Baumjohann, W., Constantinescu, D., et al. (2008). The THEMIS fluxgate magnetometer. *Space Sci. Rev.* 141 (1–4), 235–264. doi:10.1007/s11214-008-9365-9

Baumjohann, W., Hesse, M., Kokubun, S., Mukai, T., and Nagai, T. (1999). Substorm dipolarization and recovery Baumjohann et did a superposed epoch observed fast earthward flows in the plasma sheet sis of substorm phase signatures in the How- boundary layer starting at the beginning of the recovery ever. *since the the AMPTE*/104, 995–1000. doi:10.1029/1999ja900282

Baumjohann, W., Paschmann, G., and Lühr, H. (1990). Characteristics of high-speed ion flows in the plasma sheet. *J. Geophys. Res.* 95 (A4), 3801–3809. doi:10.1029/ja095ia04p03801

Birn, J., Thomsen, M. F., Borovsky, J. E., Reeves, G. D., McComas, D. J., Belian, R. D., et al. (1997). Substorm ion injections: Geosynchronous observations and test particle orbits in three-dimensional dynamic MHD fields. *J. Geophys. Res.* 102 (A2), 2325–2341. doi:10.1029/96JA03032

Donovan, E., Spanswick, E., Liang, J., Grant, J., Jackel, B., and Greffen, M. (2013). Magnetospheric Dynamics and the Proton Aurora. *Earth and Other Planets*, 365–378. doi:10.1029/2012GM001241

Drake, J. F., Swisdak, M., Phan, T. D., Cassak, P. a., Shay, M. a., Lepri, S. T., et al. (2009). Ion heating resulting from pickup in magnetic reconnection exhausts. *J. Geophys. Res.* 114 (A5), a–n. doi:10.1029/2008JA013701

Elphinstone, R. D., Hearn, D. J., Cogger, L. L., Murphree, J. S., Singer, H., Sergeev, V., et al. (1995). Observations in the vicinity of substorm onset: Implications for the substorm process. *J. Geophys. Res.* 100 (A5), 7937. doi:10.1029/94ja02938

Forsyth, C., Watt, C. E. J., Rae, I. J., Fazakerley, a. N., Kalmoni, N. M. E., Freeman, M. P., et al. (2014). Increases in plasma sheet temperature with solar wind driving during substorm growth phases. *Geophys. Res. Lett.* doi:10.1002/2014GL062400

Fu, H. S., Cao, J. B., Khotyaintsev, Y. V., Sitnov, M. I., Runov, A., Fu, S. Y., et al. (2013). Dipolarization fronts as a consequence of transient reconnection: *In situ* evidence. *Geophys. Res. Lett.* 40 (23), 6023–6027. doi:10.1002/2013GL058620

Fu, H. S., Khotyaintsev, Y. V., Vaivads, A., André, M., and Huang, S. Y. (2012). Occurrence rate of earthward-propagating dipolarization fronts. *Geophys. Res. Lett.* 39, L10101. doi:10.1029/2012GL051784

Fu, H. S., Xu, Y., Vaivads, A., and Khotyaintsev, Y. V. (2019). Super-efficient Electron Acceleration by an Isolated Magnetic Reconnection. *ApJ* 870 (2), L22. doi:10.3847/2041-8213/aafa75

Gabrielse, C., Runov, A., Angelopoulos, V., Spanswick, E., and Turner, D. L. (2017). Premidnight preponderance of dispersionless ion and electron injections. *Dawn-Dusk Asymmetries Planet. Plasma Environments*, 171–185. doi:10.1002/9781119216346.ch13

Gabrielse, C., Spanswick, E., Artemyev, A., Nishimura, Y., Runov, A., Lyons, L., et al. (2019). Utilizing the Heliophysics/Geospace System Observatory to Understand Particle Injections: Their Scale Sizes and Propagation Directions. *J. Geophys. Res. Space Phys.* 124, 5584–5609. doi:10.1029/2018ja025588

Ge, Y. S., Zhou, X.-Z., Liang, J., Raeder, J., Gilson, M. L., Donovan, E., et al. (2012). Dipolarization fronts and associated auroral activities: 1. Conjugate observations and perspectives from global MHD simulations. *J. Geophys. Res.* 117 (10), a–n. doi:10.1029/2012JA017676

Gjerloev, J. W. (2012). The SuperMAG data processing technique. *J. Geophys. Res.* 117 (9), A09213. doi:10.1029/2012JA017683

Harris, S. E., Mende, S. B., Angelopoulos, V., Rachelson, W., Donovan, E., Jackel, B., et al. (2008). THEMIS ground based observatory system design. *Space Sci. Rev.* 141 (1–4), 213–233. doi:10.1007/s11214-007-9294-z

Henderson, M. G., Reeves, G. D., and Murphree, J. S. (1998). Are north-south aligned auroral structures an ionospheric manifestation of bursty bulk flows. *Geophys. Res. Lett.* 25 (19), 3737–3740. doi:10.1029/98GL02692

Hoshino, M., Mukai, T., Terasawa, T., and Shinohara, I. (2001). Suprathermal electron acceleration in magnetic reconnection. *J. Geophys. Res.* 106 (A11), 25979–25997. doi:10.1029/2001ja900052

Kauristie, K., Sergeev, V. A., Amm, O., Kubyshkina, M. V., Jussila, J., Donovan, E., et al. (2003). Bursty bulk flow intrusion to the inner plasma sheet as inferred from auroral observations. *J. Geophys. Res.* 108 (A1), 1–9. doi:10.1029/2002JA009371

Keesee, A. M., Buzulukova, N., Goldstein, J., Mccomas, D. J., Scime, E. E., Spence, H., et al. (2011). Remote observations of ion temperatures in the quiet time magnetosphere. *Geophys. Res. Lett.* 38, L03104. doi:10.1029/2010GL045987

Keesee, A. M., Buzulukova, N., Mouikis, C., and Scime, E. E. (2021). Mesoscale Structures in Earth's Magnetotail Observed Using Energetic Neutral Atom Imaging. *Geophys. Res. Lett.* 48, e2020GL091467. doi:10.1029/2020gl091467

Keesee, A. M., Chen, M. W., Scime, E. E., and Lui, A. T. Y. (2014). Regions of ion energization observed during the Galaxy-15 substorm with TWINS. *J. Geophys. Res. Space Phys.* 119, 8274–8287. doi:10.1002/2014JA020466

Keesee, A. M., Katus, R. M., Floyd, M., and Scime, E. E. (2020). Database of Storm Time Equatorial Ion Temperatures in Earth's Magnetosphere Calculated from Energetic Neutral Atom Data. *J. Geophys. Res. Space Phys.* 125, e2020JA028266. doi:10.1029/2020JA028266

Keesee, A. M., and Scime, E. E. (2015). Database of ion temperature maps during geomagnetic storms. *Earth Space Sci.* 2, 39–46. doi:10.1002/2014EA000061

Keesee, Amy. M., Scime, E., and Moldwin, M. B. (2008). Remote measurements of ion temperatures in the terrestrial magnetotail. *J. Geophys. Res. Space Phys.* 113, A00A03. doi:10.1029/2008JA013130

Keesee, A., Scime, E., Zaniewski, A., and Katus, R. (2019). 2D Ion Temperature Maps from TWINS ENA data: IDL scripts. *UNH Scholars' Repository*. doi:10.34051/c/2019.1

Liu, J., Angelopoulos, V., Runov, A., and Zhou, X.-Z. (2013). On the current sheets surrounding dipolarizing flux bundles in the magnetotail: The case for wedgelets. *J. Geophys. Res. Space Phys.* 118 (5), 2000–2020. doi:10.1002/jgra.50092

Lyons, L. R., Nishimura, Y., Xing, X., Runov, A., Angelopoulos, V., Donovan, E., et al. (2012). Coupling of dipolarization front flow bursts to substorm expansion phase phenomena within the magnetosphere and ionosphere. *J. Geophys. Res.* 117, A02212. doi:10.1029/2011JA017265

McComas, D. J., Allegrini, F., Baldonado, J., Blake, B., Brandt, P. C., Burch, J., et al. (2009). The Two Wide-angle Imaging Neutral-atom Spectrometers (TWINS) NASA Mission-of-Opportunity. *Space Sci. Rev.* 142 (1–4), 157–231. doi:10.1007/s11214-008-9467-4

McComas, D. J., Valek, P., Burch, J. L., Pollock, C. J., Skoug, R. M., and Thomsen, M. F. (2002). Filling and emptying of the plasma sheet: Remote observations with 1-70 keV energetic neutral atoms. *Geophys. Res. Lett.* 29 (22), 2079. doi:10.1029/2002GL016153

McFadden, J. P., Carlson, C. W., Larson, D., Ludlam, M., Abiad, R., Elliott, B., et al. (2008). The THEMIS ESA Plasma Instrument and In-flight Calibration. *Space Sci. Rev.* 141 (1–4), 277–302. doi:10.1007/s11214-008-9440-2

McPherron, R. L., Hsu, T.-S., Kissinger, J., Chu, X., and Angelopoulos, V. (2011). Characteristics of plasma flows at the inner edge of the plasma sheet. *J. Geophys. Res.* 116 (4), 1–19. doi:10.1029/2010JA015923

Mende, S. B., Harris, S. E., Frey, H. U., Angelopoulos, V., Russell, C. T., Donovan, E., et al. (2008). The THEMIS array of ground-based observatories for the study of auroral substorms. *Space Sci. Rev.* 141 (1–4), 357–387. doi:10.1007/s11214-008-9380-x

Menz, A. M., Kistler, L. M., Mouikis, C. G., Spence, H. E., Skoug, R. M., Funsten, H. O., et al. (2017). The role of convection in the buildup of the ring current pressure during the 17 March 2013 storm. *J. Geophys. Res. Space Phys.* 122 (122), 475–492. doi:10.1002/2016JA023358

Merkin, V. G., Panov, E. V., Sorathia, K. A., and Ukhorskiy, A. Y. (2019a). Contribution of Bursty Bulk Flows to the Global Dipolarization of the Magnetotail during an Isolated Substorm. *J. Geophys. Res. Space Phys.* 124, 8647–8668. doi:10.1029/2019JA026872

Merkin, V. G., Panov, E. V., Sorathia, K. A., and Ukhorskiy, A. Y. (2019b). Contribution of Bursty Bulk Flows to the Global Dipolarization of the Magnetotail during an Isolated Substorm. *J. Geophys. Res. Space Phys.* 124 (11), 8647–8668. doi:10.1029/2019JA026872

Motoba, T., Hosokawa, K., Kadokura, A., and Sato, N. (2012). Magnetic conjugacy of northern and southern auroral beads. *Geophys. Res. Lett.* 39, L08108. doi:10.1029/2012GL051599

Nakamura, M. S., Matsumoto, H., and Fujimoto, M. (2002). Interchange instability at the leading part of reconnection jets. *Geophys. Res. Lett.* 29 (8). doi:10.1029/2001GL013780

Nakamura, R., Baumjohann, W., Mouikis, C., Kistler, L. M., Runov, A., Volwerk, M., et al. (2004). Spatial scale of high-speed flows in the plasma sheet observed by Cluster. *Geophys. Res. Lett.* 31, L09804. doi:10.1029/2004GL019558

Nakamura, R., Baumjohann, W., Schödel, R., Brittnacher, M., Sergeev, V. A., Kubyshkina, M., et al. (2001). Earthward flow bursts, auroral streamers, and small expansions. *J. Geophys. Res.* 106 (A6), 10791–10802. doi:10.1029/2000ja000306

Nishimura, Y., Bortnik, J., Li, W., Lyons, L. R., Donovan, E. F., Angelopoulos, V., et al. (2014). Evolution of nightside subauroral proton aurora caused by transient plasma sheet flows. *J. Geophys. Res. Space Phys.* 119 (7), 5295–5304. doi:10.1002/2014JA020029

Onsager, T., Grubb, R., Kunches, J., Matheson, L., Speich, D., Zwickl, R. W., Sauer, H., et al. (1996). "Operational Uses of the GOES Energetic Particle Detectors," in SPIE's 1996 International Symposium on Optical Science, Engineering, and Instrumentation, Denver, CO, October 18, 1996 (Denver, CO: SPIE) 2812. doi:10.1117/12.254075

Runov, A., Angelopoulos, V., Sitnov, M. I., Sergeev, V. a., Bonnell, J., McFadden, J. P., et al. (2009). THEMIS observations of an earthward-propagating dipolarization front. *Geophys. Res. Lett.* 36 (14), L14106. doi:10.1029/2009GL038980

Runov, A., Angelopoulos, V., Zhou, X.-Z., Zhang, X.-J., Li, S., Plaschke, F., et al. (2011). A THEMIS multicase study of dipolarization fronts in the magnetotail plasma sheet. *J. Geophys. Res.* 116 (A5), A05216. doi:10.1029/2010JA016316

Scime, E. E., Keesee, A. M., Jahn, J.-M., Kline, J. L., Pollock, C. J., and Thomsen, M. (2002). Remote ion temperature measurements of Earth's magnetosphere: Medium energy neutral atom (MENA) images. *Geophys. Res. Lett.* 29 (10), 1438. doi:10.1029/2001gl013994

Sergeev, V. A., Angelopoulos, V., Gosling, J. T., Cattell, C. A., and Russell, C. T. (1996). Detection of localized, plasma-depleted flux tubes or bubbles in the midtail plasma sheet. *J. Geophys. Res.* 101 (A5), 10817–10826. doi:10.1029/96ja00460

Sergeev, V. A., Liou, K., Newell, P. T., Ohtani, S.-I., Hairston, M. R., and Rich, F. (2004). Auroral streamers: characteristics of associated precipitation,convection and field-aligned currents. *Ann. Geophys.* 22, 537–548. doi:10.5194/angeo-22-537-2004

Sergeev, V. A., Sauvaud, J.-A., Popescu, D., Kovrazhkin, R. A., Liou, K., Newell, P. T., et al. (2000). Multiple-spacecraft observation of a narrow transient plasma jet in the Earth's plasma sheet. *Geophys. Res. Lett.* 27 (6), 851–854. doi:10.1029/1999GL010729

Shue, J.-H., Chao, J. K., Fu, H. C., Russell, C. T., Song, P., Khurana, K. K., et al. (1997). A new functional form to study the solar wind control of the magnetopause size and shape. *J. Geophys. Res.* 102 (A5), 9497–9511. doi:10.1029/97JA00196

Singer, H., Matheson, L., Grubb, R., Newman, A., and Bouwer, D. (1996). "Monitoring Space Weather with the GOES Magnetometers," in SPIE's 1996 International Symposium on Optical Science, Engineering, and Instrumentation, Denver, CO, October 18, 1996 (Denver, CO: SPIE) 2812, 299–308. doi:10.1117/12.254077

Spanswick, E., Donovan, E., Kepko, L., and Angelopoulos, V. (2017). The Magnetospheric Source Region of the Bright Proton Aurora. *Geophys. Res. Lett.* 44 (2010), 094. doi:10.1002/2017GL074956

Ukhorskiy, A. Y., Sorathia, K. A., Merkin, V. G., Sitnov, M. I., Mitchell, D. G., and Gkioulidou, M. (2018). Ion Trapping and Acceleration at Dipolarization Fronts: High-Resolution MHD and Test-Particle Simulations. *J. Geophys. Res. Space Phys.* 123 (7), 5580–5589. doi:10.1029/2018JA025370

Walsh, A. P., Haaland, S., Forsyth, C., Keesee, a. M., Kissinger, J., Li, K., et al. (2014). Dawn-dusk asymmetries in the coupled solar wind-magnetosphere-ionosphere system: a review. *Ann. Geophys.* 32 (7), 705–737. doi:10.5194/angeo-32-705-2014

Yang, J., Toffoletto, F. R., and Wolf, R. A. (2016). Comparison study of ring current simulations with and without bubble injections. *J. Geophys. Res. Space Phys.* 121, 374–379. doi:10.1002/2015JA021567

Yang, J., Toffoletto, F. R., Wolf, R. A., and Sazykin, S. (2015). On the contribution of plasma sheet bubbles to the storm time ring current. *J. Geophys. Res. Space Phys.* 120, 7416–7432. doi:10.1002/2016JA023362

Zhou, X.-Z., Angelopoulos, V., Sergeev, V. a., and Runov, a. (2010). Accelerated ions ahead of earthward propagating dipolarization fronts. *J. Geophys. Res.* 115 (May), a–n. doi:10.1029/2010JA015481

Conflict of Interest: CG was employed by The Aerospace Corporation.

The remaining authors declare that the research was conducted in the absence of any commercial or financial relationships that could be construed as a potential conflict of interest.

Publisher's Note: All claims expressed in this article are solely those of the authors and do not necessarily represent those of their affiliated organizations, or those of the publisher, the editors and the reviewers. Any product that may be evaluated in this article, or claim that may be made by its manufacturer, is not guaranteed or endorsed by the publisher.

Copyright © 2021 Adewuyi, Keesee, Nishimura, Gabrielse and Katus. This is an open-access article distributed under the terms of the Creative Commons Attribution License (CC BY). The use, distribution or reproduction in other forums is permitted, provided the original author(s) and the copyright owner(s) are credited and that the original publication in this journal is cited, in accordance with accepted academic practice. No use, distribution or reproduction is permitted which does not comply with these terms.

frontiers in Astronomy and Space Sciences

ORIGINAL RESEARCH
published: 01 November 2021
doi: 10.3389/fspas.2021.761875

The Role of Mesoscale Plasma Sheet Dynamics in Ring Current Formation

K. A. Sorathia[1], A. Michael[1], V.G. Merkin[1], A.Y. Ukhorskiy[1], D. L. Turner[1], J.G. Lyon[2], J. Garretson[1], M. Gkioulidou[1] and F.R. Toffoletto[3]*

[1]The Johns Hopkins University Applied Physics Laboratory, Laurel, MD, United States, [2]Department of Physics and Astronomy, Dartmouth College, Hanover, NH, United States, [3]Department of Physics and Astronomy, Rice University, Houston, TX, United States

During geomagnetically active periods ions are transported from the magnetotail into the inner magnetosphere and accelerated to energies of tens to hundreds of keV. These energetic ions, of mixed composition with the most important species being H+ and O+, become the dominant source of plasma pressure in the inner magnetosphere. Ion transport and acceleration can occur at different spatial and temporal scales ranging from global quasi-steady convection to localized impulsive injection events and may depend on the ion gyroradius. In this study we ascertain the relative importance of mesoscale flow structures and the effects of ion non-adiabaticity on the produced ring current. For this we use: global magnetohydrodynamic (MHD) simulations to generate self-consistent electromagnetic fields under typical driving conditions which exhibit bursty bulk flows (BBFs); and injected test particles, initialized to match the plasma moments of the MHD simulation, and subsequently evolved according to the kinetic equations of motion. We show that the BBFs produced by our simulation reproduce thermodynamic and magnetic statistics from *in situ* measurements and are numerically robust. Mining the simulation data we create a data set, over a billion points, connecting particle transport to characteristics of the MHD flow. From this we show that mesoscale bubbles, localized depleted entropy regions, and particle gradient drifts are critical for ion transport. Finally we show, using identical particle ensembles with varying mass, that O+ non-adiabaticity creates qualitative differences in energization and spatial distribution while H+ non-adiabaticity has non-negligible implications for loss timescales.

Keywords: plasma sheet, ring current, buoyancy, mesoscale, bursty bulk flows, injections, geospace

OPEN ACCESS

Edited by:
Jean-Francois Ripoll,
CEA DAM Île-de-France, France

Reviewed by:
Fabio Bacchini,
University of Colorado Boulder, United States
Victor Sergeev,
Saint Petersburg State University, Russia

****Correspondence:***
K. A. Sorathia
kareem.sorathia@gmail.com

Specialty section:
This article was submitted to Space Physics, a section of the journal Frontiers in Astronomy and Space Sciences

Received: *20 August 2021*
Accepted: *11 October 2021*
Published: *01 November 2021*

Citation:
Sorathia KA, Michael A, Merkin VG, Ukhorskiy AY, Turner DL, Lyon JG, Garretson J, Gkioulidou M and Toffoletto FR (2021) The Role of Mesoscale Plasma Sheet Dynamics in Ring Current Formation. Front. Astron. Space Sci. 8:761875. doi: 10.3389/fspas.2021.761875

1 INTRODUCTION

The modern understanding of transport processes, and their multiscale nature, through the magnetotail transition region has advanced considerably in the decades following the early work that first recognized their importance (e.g., Mauk and McIlwain, 1974). The definition of what constitutes the transition region varies in the literature (e.g., Ohtani and Motoba, 2017; Sergeev et al., 2018); for the purposes of this work we will take a more expansive definition of the magnetotail transition region, $\sim 8-20R_E$ tailwards of Earth. It is now known that much of the plasma transport in the transition region occurs by means of transient (~ 10 minute), fast (~ 400 km/s) bursty bulk flows (BBFs; Baumjohann et al., 1990; Angelopoulos et al., 1992, Angelopoulos et al., 1994). These flow bursts have typical cross-tail sizes of 1–3R_E (e.g., Nakamura et al., 2004; Liu et al., 2013), which we will refer to here as mesoscale to distinguish them from both global and kinetic scales in the

magnetosphere. Increasingly these BBFs have been connected to localized ion injections into the ring current (Turner et al., 2017; Gabrielse et al., 2019) which can provide a substantial source of ring current pressure during stormtime (Gkioulidou et al., 2014).

A theoretical description of these flow bursts was provided by Pontius and Wolf. (1990) who identified fast flows as entropy-depleted "bubbles" that would be interchange unstable within the ambient entropy profile radially-decreasing away from Earth. Confirming that flow bursts are bubbles using *in situ* data is complicated by both the sparsity of spacecraft in the transition region and the necessity of extrapolating flux tube entropy from point measurements of fast flows (e.g., Wolf et al., 2006). However, it has been found that inferred entropy-depletion from spacecraft measurements is a good predictor of the penetration depth of flow bursts (Dubyagin et al., 2011; Kim et al., 2012). This interpretation was supported by regional modeling, i.e., localized subdomains of the global magnetosphere, which highlighted the role of reconnection, and the resultant reduction in flux tube volume, in creating bubbles (e.g., Birn et al., 2009, 2011; Liu et al., 2014) and the role of buoyancy (e.g., Yang et al., 2010, Yang et al., 2015; Sadeghzadeh et al., 2021) in the subsequent transport of these bubbles into the inner magnetosphere.[1]

Despite these advances, a full multiscale understanding of the transition region has remained elusive due to both observational and modeling limitations. Important questions remain regarding: the relative role of large-scale versus mesoscale convection; the statistical distribution of bubble lengthscales and the physical mechanisms that govern the size of bubbles; and the mechanisms of ion energization. Sparse spacecraft coverage of the transition region makes it difficult to spatially localize injections, although there has been progress using multi-mission conjunctions (Turner et al., 2017) and remote imaging (Keesee et al., 2021). Modeling multiscale transport in the transition requires: energy-dependent drifts, not included in global magnetohydrodynamic (MHD) models which approximate the bulk flow with the $E \times B$ drift; fast flows outside the quasi-static slow-flow approximation of typical ring current models (see e.g., Toffoletto, 2020, and references therein); global models that produce mesoscale magnetotail structures (Wiltberger et al., 2015; Cramer et al., 2017; Merkin et al., 2019), requiring high spatial resolution and low dissipation algorithms; a representation of wave-particle interactions that contribute to ion heating (e.g., Chaston et al., 2014; Cheng et al., 2020); and finite gyroradius effects, as H+ in the transition region is known to be quasi-adiabatic (Runov et al., 2017), while heavier ion species like O+, likely exhibit highly non-adiabatic behavior (e.g., Moebius et al., 1987; Delcourt et al., 1997; Nosé et al., 2000; Keika et al., 2013; Bingham et al., 2020). The latter point is particularly important. While the details of the O+ energization mechanisms and transport into the ring current are not yet fully understood (Ohtani et al., 2011; Keika et al., 2013; Gkioulidou et al., 2019), O+ is known to contribute a significant, if not dominant, amount of the total ring current energy density during increasingly disturbed geomagnetic conditions (Nosé et al., 2005).

[1]See Sitnov et al. (2019) for a more comprehensive review.

Given these challenges it is perhaps not surprising that there has been little work studying bubble-mediated transport through the transition region in a global context. Ukhorskiy et al. (2018) used global MHD and test particle modeling to investigate particle interactions with a single bubble to demonstrate the importance of the mesoscale structure of the bubbles to trap the particles, whereas Cramer et al. (2017) performed a more expansive study over a range of stormtime events to demonstrate the importance of bubbles in transport. In a series of papers representing the most self-consistent work to date (Lin et al., 2017, 2021; Cheng et al., 2020), global hybrid simulations were used to demonstrate that reconnection creates depleted bubbles that are anisotropic, non-Maxwellian, and not in equilibrium. However, spatial rescaling is necessary for global hybrid simulations to be computationally tractable and even then the duration of these simulations remains limited.

Regional modeling has been used to reveal many aspects regarding transport through the transition region, while global modeling faces substantial intrinsic difficulties. Despite this, global modeling of the transition region is necessary to probe the complex magnetosphere-ionosphere coupling that binds the two geospace domains together. Mesoscale plasma sheet injections have global-scale consequences through their role in the ring current build-up. The partial ring current drives "Region 2" field-aligned currents (FACs; e.g., Roelof, 1989) into the ionosphere where they connect to the "Region 1" currents driven by magnetospheric processes at higher-latitudes. The mutual closure of these currents in the ionosphere occurs across the electrojets (Baumjohann, 1982), the most intense electrical currents in the ionosphere. It is in these auroral regions where strong Joule heating and momentum transfer between the ions and neutrals occur, stirring up the thermosphere. Changes in the high-latitude neutral temperature and winds are transmitted to lower latitudes through non-linear, coupled, dynamical processes, causing global-scale variations in neutral temperature, winds and composition (Li et al., 2019). This alters global ionospheric plasma densities through chemistry and plasma transport (e.g., Fuller-Rowell et al., 1994; Wang et al., 2010; Lu et al., 2016). Changes in plasma densities are also produced by energetic particle precipitation at different altitudes, depending on their energy spectra. All this results in complex ionospheric conductivity changes and electrodynamic feedback to the magnetosphere. Furthermore, Joule heating, soft electron precipitation, and plasma transport cause upwelling of ionospheric ions that enables mass coupling with the magnetosphere by providing the source for ion outflow. Therefore a systems-level understanding of geospace requires a self-consistent and cross-scale (global, meso-, and ion kinetic) treatment of the transition region.

It is the goal of this work, which extends aspects of Wiltberger et al. (2015) and Ukhorskiy et al. (2018), to better inform what aspects of the transition region transport are most critical for a global, self-consistent model to capture. To this end we utilize an approach combining MHD and test particle simulations wherein we create a test particle "mirror" of the plasma sheet, matching the spatiotemporal variations of density and temperature, whose evolution we can follow to gauge the importance of certain kinetic effects. This approach allows us to include the self-consistent

formation and propagation of BBFs, within the framework of the MHD approximation, and the effects of drift physics and particle non-adiabaticity, within the framework of test particle trajectories. However, as these are test particles, there is no kinetic feedback to the global MHD electromagnetic fields. This caveat must be taken into account in the interpretation of these results. Nevertheless, our approach allows us to use very highly-resolved fluid models that produce mesoscale flow structures and to study their implications on ion transport and acceleration in the transition region.

With the appropriate caveats in mind, we will assess the importance of flow and particle characteristics to the transport of ions across the transition region. In particular we consider: flow characteristics like entropy-depletion and mesoscale structure; and particle characteristics like energy, and consequently energy-dependent drifts, and gyroradius. With the combined MHD and test particle approach we employ, we are able to mine simulation data to construct a database, exceeding a billion points, of instantaneous correlations between the inward radial transport of particle energy and properties of the ambient MHD flow. Given the importance of entropy, we find it critical to investigate the ability of our simulation to accurately reproduce the thermodynamic plasma properties of BBFs, which we verify by comparing with the THEMIS-based study of Runov et al. (2015). Next, by comparing identical test particle ensembles whose initial state is informed by MHD and are subsequently evolved with varying gyroradii, we are able to quantitatively assess the importance of non-adiabaticity and its implications to both the build-up and decay of the ring current.

This work is an extension of Ukhorskiy et al. (2018) but incorporates significant advances to the methodology. Ukhorskiy et al. (2018) seeded test particles into a single bubble and followed the evolution for ~10 minutes while using a fiducial plasma sheet temperature to assess the implications to ring current buildup. Therefore, that work did not directly assess the comparative evolution of particles inside versus outside of bubbles or the result of particles interacting with multiple bubbles over longer timescales. Additionally, in this work we use flux tube entropy as a metric to explicitly study the connection between the sharp magnetic field gradients, identified as important by Ukhorskiy et al. (2018), to depleted entropy bubbles. This work is also a natural extension to the statistical data-model comparison performed by Wiltberger et al. (2015), where they used statistics derived from an idealized steady magnetospheric convection, or SMC-like period, to construct a superposed epoch analysis which they compared to Ohtani et al. (2004). The analysis of Wiltberger et al. (2015) was limited in its ability to disentangle whether the data and model differed due to differences in the properties of flow bursts or in the ambient state of the plasma sheet in their idealized simulation. Here we construct our data-model comparison to assess the relative properties of the bubbles to the ambient plasma sheet to focus on the ability of our model to reproduce how depleted bubbles are and how deeply into the inner magnetosphere they will therefore penetrate.

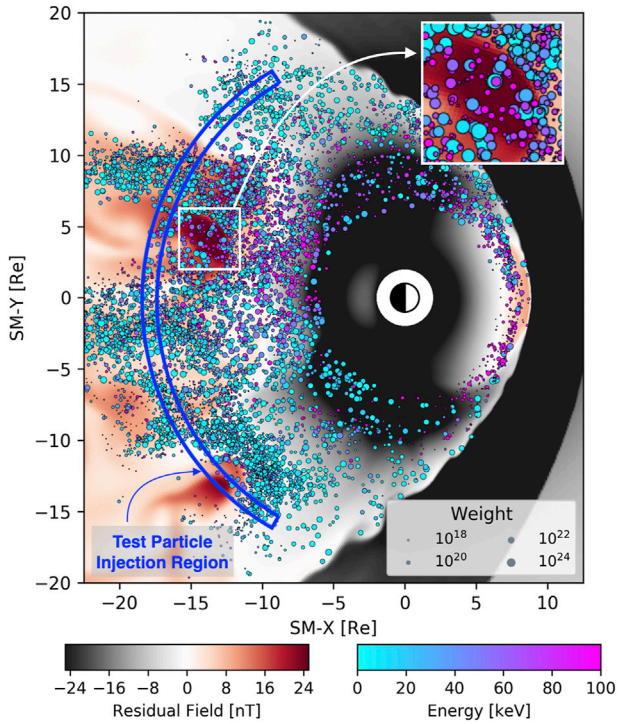


FIGURE 1 | Simulation at a glance. Combined visualization of the MHD simulation and test particle data. Background color (bottom let color bar) denotes residual, i.e., non-dipolar, vertical magnetic field. Test particles are marked at the location of their field-line projection to the equatorial plane, colored by their energy (bottom right color bar), and denoted with a marker whose surface area is proportional to the logarithm of their weight. The region where test particles are seeded is marked in blue. Figure inset shows a close-up view of the test particle population in a typical BBF.

Having outlined the goals and limitations of our study, we now describe the plan for the remainder of the paper. In the next section, we provide an overview of the MHD (**Section 2.1**) and test particle (**Section 2.2**) simulations as well as the diagnostics (**Section 2.3**) we employ. Our main results are presented in **Section 3** and include: a comparison of the thermodynamic properties of our modeled BBFs to observations (**Section 3.1**); a statistical study of the correlation between flow and particle properties to the transport and acceleration of test particle energy into the inner magnetosphere (**Section 3.2**); and a study of the effects of increasing non-adiabaticity relative to a guiding center ensemble (**Section 3.3**). Finally, we present a discussion of our results and their implications for future magnetospheric modeling in **Section 4**.

2 METHODOLOGY

Our technical approach combines two simulation methods: GAMERA (Zhang et al., 2019; Sorathia et al., 2020), a global MHD model, is used to generate electromagnetic fields; and CHIMP (Sorathia et al., 2018), a test particle code, is used to calculate particle trajectories through the time-dependent MHD

electromagnetic fields and weight the test particles to match a specified phase space density (PSD). In the remainder of this section we will describe in turn the details of the global magnetospheric simulation (**Section 2.1**), the test particle parameters and weighting (**Section 2.2**), and the diagnostics we will employ (**Section 2.3**). For convenience, however, we will provide a brief, high-level overview here. We drive the global magnetospheric simulation in an idealized configuration using pure southward interplanetary magnetic field (IMF), following a period of preconditioning. Within that global magnetospheric simulation we continuously seed new test particles in a thin arc on the nightside and weight them using the instantaneous density and temperature from the MHD simulation. In other words, we create a test particle "mirror" of the MHD flow moving through the nightside injection region. This is a mirror only within the injection region, upon moving inwards the test particles will evolve differently than the MHD flow they were created to mimic due to the kinetic equations of motion they are governed by. We seed test particles for a period of 1 h, beginning at $T = -1$ h and ending at $T = 0$ h, and continue to evolve those test particles that remain in the closed field region for an additional 1 h period, ending at $T = +1$ h. Finally, we look at the instantaneous correlation between the transport of test particle energy into the inner magnetosphere and the properties of the ambient MHD flow. In particular, we focus on the importance of the characteristic lengthscale of the ambient magnetic field, assessing the multiscale flows of the transition region, and the deviation of the flux tube entropy from an averaged background value, i.e., buoyancy, to assess the role of bubbles.

A visualization of the combined model output half-way through the simulation is illustrated in **Figure 1**. It depicts both the residual, or non-dipolar, magnetic field calculated by GAMERA, defined as the northward component (B_Z) with dipole contribution subtracted, and a sample of test particles with markers denoting the projection from their 3*D* position along the local magnetic field to the equator with the marker colored by energy and sized so that its diameter is proportional to the logarithm of the test particle's weight. The thin nightside region where test particles are continuously seeded for $T < 0$ is marked in blue. The inset of **Figure 1** shows a zoomed-in view of a BBF having recently moved through the test particle injection region; the test particles inside the BBF are higher energy and lower weight than those outside, reflecting, as expected, the hotter, less dense plasma inside the BBF.

2.1 Global Magnetosphere

The first step in our model pipeline is the generation of electromagnetic fields and plasma moments using our global magnetosphere model GAMERA. The details of GAMERA's core MHD numerics and its validation via a standard portfolio of MHD test problems (e.g., Stone et al., 2008) were presented in detail by Zhang et al. (2019) and its first magnetospheric application by Sorathia et al. (2020). Zhang et al. (2019) also showed the critical importance of algorithmic details beyond simply the size of grid cells. In particular, the use of high-order spatial reconstruction can dramatically improve the preservation of sharp structures compared to lower-order schemes on an otherwise identical spatial grid (see Zhang et al., 2019, **Section 4**). For typical MHD test problems they find that lower-order reconstruction (e.g. 2^{nd}-order) requires 4–8× finer grid resolution as the higher-order (7^{th}- or 8^{th}-order) reconstruction used by GAMERA for the same effective resolving capability. Mapped to 3*D*, 4–8× the grid resolution becomes a factor of $\sim 250 - 4000$ the computational cost. As we will show below, this extra resolving power is critical to capture sharp flow structures and their subsequent effect on particle evolution.

As a first study of particle transport with GAMERA, we adopt a similar approach used in previous BBF studies with GAMERA's predecessor LFM (Lyon et al., 2004). As in Wiltberger et al. (2015), we utilize an idealized magnetospheric configuration to generate an SMC-like period. Specifically, after a preconditioning phase of alternating northward and southward IMF, the IMF turns southward and remains so for the remainder of the simulation. The solar wind driving uses typical values: 5/cc density, 400 km/s velocity with only an SM-X component, and an IMF of 5 nT directed either northwards or southwards. Two hours after the final southward IMF turning, at which point steady reconnection has begun producing regular BBFs moving earthward, we begin injecting test particles whose properties are described below (**Section 2.2**). The inner boundary condition of the simulation is imposed at a spherical surface of $2R_E$ via closing the field-aligned currents through a thin-shell ionosphere as described by Merkin and Lyon. (2010). In the idealized configuration we present here, we use a constant Pedersen conductance of $\Sigma_P = 10$ S with no Hall conductance and an ionospheric grid of $1^\circ \times 1^\circ$. It is important to note that these are ideal MHD simulations without an explicit resistivity, although there is numerical resistivity that allows reconnection. While this can have an effect on the specific details of reconnection onset (e.g., Raeder et al., 2001), we do not expect this to affect the transport and acceleration of our test particles that are seeded earthward of the reconnection line.

GAMERA, like LFM before it, uses for its magnetospheric simulations a warped spherical grid, whose spherical axis is aligned with the SM-X axis. The grid encompasses a region extending sunward to $30R_E$ and tailward to $-350R_E$, and to $120R_E$ radius in the YZ-plane. The warped grid is distorted to maximize resolution in the regions where it is most important, e.g. the bow shock, the magnetopause, and the near-Earth plasma sheet. This simulation was run using $192 \times 192 \times 256$ cells in the radial, polar, and azimuthal directions and is comparable to the highest-resolution capability of LFM, known as "OCT" resolution, which has been used to study mesoscale plasma sheet flows before (Wiltberger et al., 2015; Merkin et al., 2019). In particular, the nominal resolution in the near-Earth plasma sheet is approximately 600 km.

2.2 Test Particles and Weighting

2 h after the final southward turning, we begin injecting test particles continuously into an arc tailward of Earth (see **Figure 1**). The arc is of width $\Delta R = 1R_E$ and centered on $R = 18R_E$, extending azimuthally 8 h in MLT centered at midnight. We refer to the beginning of test particle injections as $T = -1$ h, and inject test particles continuously into the arc for a period of 1 h. At $T = 0$, the

injections are ceased and the existing particles are evolved until $T = +1$ h. Over the hour of continuous injection we create $20M$ test particles, or ~5000 per second. These test particles are created with randomly chosen pitch angles, varying between field-aligned and anti-aligned, and energies, varying between 100 eV and 100 keV.

The numerical details of how test particle trajectories are calculated and how each test particle is weighted are described in detail in Sorathia et al. (2018) and more recent improvements to the interpolation of GAMERA electromagnetic fields by CHIMP in Sorathia et al. (2019). We, however, provide a brief overview here for convenience. For ion trajectories we advance the particle position using the Lorentz force and Boris integrator. For electrons or positrons, we use a mixed integrator alternating between a guiding center formulation, utilizing the conservation of the first invariant, and the Lorentz trajectory depending on the ratio of the particle gyroradius to local magnetic field lengthscale. When a test particle encounters a region where $\epsilon > 10^{-2}$, where ϵ is the ratio of particle gyroradius to magnetic field lengthscale (Sorathia et al., 2018, **Eq. (3)**), a random gyrophase is chosen and the test particle is subsequently evolved using the full Lorentz equations of motion. The test particle can be converted back to the guiding center approximation when $\epsilon < 10^{-2}$ by calculating an approximate guiding center location, which we do in the manner of Snicker et al. (2010), and the first invariant at the guiding center location.

In the work we present here we consider the evolution of an ensemble of test particles with identical initial conditions, but evolved as either positrons, i. e a guiding center ring current (GCRC), H+ (PRC), or heavy ions (HRC), specifically O+. This will allow us investigate separately the adiabatic interaction of particles with MHD-produced flow structures (GCRC), as well as the effects of increasing non-adiabaticity (PRC and HRC). Note that while we use the terminology RC for ring current because our ultimate interest is the role of these particles in building the ring current, our investigation includes their behavior throughout the nightside near-Earth plasma sheet. Data Sets S1-S3 contain a random sample of test particle trajectories for GCRC, PRC, and HRC respectively.

Given a collection of test particles and their trajectories, we assign each particle a weight such that the overall collection reproduces a desired initial condition for the PSD. Here the test particle weights represent the number of real particles each test particle acts as a proxy for, i.e. macroparticles. Note, however the weighting does not alter the underlying statistics of the test particles themselves it merely assigns weights to each pre-existing test particle. The flexibility of this approach is that if we have a collection of test particles that properly samples the phase space then we can easily change the choice of PSD initial condition, and thus the weighting, without recalculating any test particle trajectories.

For this study our PSD initial condition is directly informed by the MHD flow properties. Test particles are weighted using a κ-distribution with the density and temperature of the MHD flow in the location and time of the test particles injection. Here we use $\kappa = 6$ consistent with ion observations for this region of the near-Earth tail (Runov et al., 2015). We note that we use the same κ value across all species so as to focus on the role of non-adiabaticity on an otherwise identical ensemble, although we do not expect sensitivity to the choice of κ (Ukhorskiy et al., 2018).

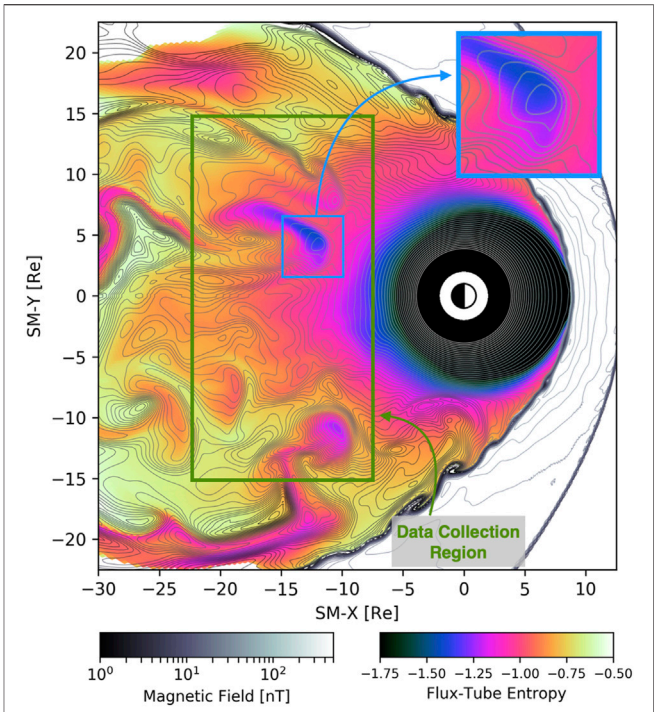


FIGURE 2 | MHD flow structures in the transition region. Snapshot of the simulation at the same time as **Figure 1** showing the integrated flux tube entropy (logarithmic scale) in the equatorial plane and contours of constant total magnetic field strength. Green boundary depicts the domain from which we compile statistics of transport and acceleration in the transition region. Figure inset shows a typical "magnetic island" field structure exhibited by BBFs in MHD.

Weighting is done on a $4D$ discretized phase space spanning cylindrical radius, MLT, pitch angle, and energy. The phase space is reduced by one in each of its spatial and momentum components: phase space densities are averaged over entire flux tubes, corresponding to the radius and MLT of their equatorial crossing; and over gyrophase. In this work we use a phase space, $\Gamma(R, \phi, \alpha_{EQ}, K)$, spanning [3, 22] R_E, [0, 2π], [0, π], and [0.1, 500] keV respectively. The phase space grid is discretized linearly in the angular variables with $N_\phi = 72$ and $N_\alpha = 36$ and logarithmically in radius and energy with $N_R = 30$ and $N_K = 30$. Newly-seeded test particles are weighted collectively at a cadence of $\delta T = 5$ s. We ensure that the resolution of the phase space and number of test particles are appropriate by verifying the approximate invariance of the results when changing the discretization or number of test particles used for weighting.

While there are a number of technical details involved in this process, the result is merely to constrain the test particles in the injection region (**Figure 1**, blue arc) so that they reproduce, up to the phase space discretization chosen, the distribution corresponding to a κ-distribution using the MHD moments. Effectively we create a test particle mirror of the MHD flow passing through the test particle

injection region. This is similar to Sorathia et al. (2018), which used three discrete wedge-shaped injection regions on the nightside but with much finer spatial granularity.

2.3 Diagnostics

Our goal in this study is to connect properties of the background MHD flow, e.g., deviations of integrated flux tube entropy from the background, to metrics quantifying the transport and acceleration of test particles within those flow regions, e.g., the velocity of the equatorial crossing of a test particle. Here we will define the metrics we use for the background MHD flow and the test particles. Our primary interest is the "transition region," which for our purposes we define in an expansive way to encompass the region where fast flows and particle drift physics are both non-negligible. We define a "Data Collection Region", marked in **Figure 2**, as $-22.5 \le X \le -8$ and $|Y| \le 15$ from which we will take statistics.

Interchange instability, due to flux tube entropy imbalance, has long been believed to play an important role in the earthward transport of plasma (see recent review by Toffoletto, 2020, and references therein). To identify interchange unstable regions, we use the entropy function (e.g. Birn et al., 2009):

$$\mathcal{S}(R,\phi) = \int p(s)^{1/\gamma} \frac{ds}{B(s)}, \tag{1}$$

where the integral is taken along the flux tube that contains the cylindrical coorinate (R, ϕ, $z = 0$). The quantity $\mathcal{S}$ is conserved in ideal MHD and related, but not identical, to the thermodynamic entropy of a flux tube (Birn et al., 2009). This distinction is not relevant for this work and we will simply refer to **Eq. (1)** as the flux tube entropy (FTE). **Figure 2** shows a representative equatorial distribution of flux tube integrated entropy, including examples of low-entropy intruding bubbles. **Supplementary Video S1** is an animation of the simulation data in the same format as **Figure 2**.

Interchange instability is governed by deviation of the local entropy from the background (Rosenbluth and Longmire, 1957), which we can quantify using what we henceforth refer to as the "relative buoyancy",

$$\delta\mathcal{S}(R,\phi,t) = \frac{\mathcal{S}(R,\phi,t) - S_0(R,\phi,t)}{S_0(R,\phi,t)}, \tag{2}$$

where $\mathcal{S}_0$ is an average background entropy calculated using a sliding time window, namely

$$\mathcal{S}_0(R,\phi,t) = \frac{1}{\Delta t}\int_{t-\Delta t}^{t+\Delta t} \mathcal{S}(R,\phi,\tau)d\tau, \tag{3}$$

with Δt = 10 min. The timescale for averaging is chosen to lie between the timescales characterizing the propagation of individual bubbles and those governing global reconfiguration of the tail during the SMC-like event we simulate. **Eq. (2)**, the relative buoyancy, quantifies the fractional deviation of the local entropy from the background. Negative relative buoyancy corresponds to regions that will tend to move earthwards, i.e. bubbles, and positive relative buoyancy regions will tend to move outward, i.e. blobs.

An example of the relative buoyancy, $\delta\mathcal{S}(R,\phi)$, at the same time as **Figures 1**, **2** is shown in **Supplementary Figure S1**. An example of the manner of evolution of this quantity is shown in **Supplementary Figure S2**, which depicts $\delta\mathcal{S}(\phi,t)$, i.e. as a function of MLT and time, at selected fixed radii.

Previous work (Gabrielse et al., 2017; Ukhorskiy et al., 2017; Sorathia et al., 2018; Ukhorskiy et al., 2018) has identified the role of mesoscale magnetic structures within BBFs to induce "trapping" of sufficiently energetic particles within closed contours of constant magnetic field strength. An example of these "magnetic islands" can be seen in the inset of **Figure 2**. To identify these types of mesoscale structures in the background flow, we define the quantity

$$L_{\nabla B} = \frac{|\vec{B}|}{\left|\nabla_{x,y}\vec{B}\right|}, \tag{4}$$

where the denominator is taken to be the L_2 norm of the Jacobian, restricted to equatorial derivatives, of the magnetic field.

Turning now to the test particles, we seek to investigate the correlation of particle transport and acceleration to properties of the background flow. To this end we consider the motion of each test particle's equatorial crossing point through the nominal transition region highlighted in **Figure 2**. For this exercise we focus on GCRC as our interest is really in the motion of the equatorial crossing point of the particle guiding center, and using GCRC allows us to remove the additional noise that would be introduced by gyromotion. We accomplish this by projecting each test particle to the equator at a temporal cadence of ΔT = 5 s, with $(X_{EQ}, Y_{EQ}, K)^{i,p}$ designating the equatorial projection of particle p at time $T = T_0 + i\Delta T$ and its kinetic energy. Similarly we can calculate for each particle at each time: ΔR_{EQ}, the rate of change of the radial equatorial crossing point; ΔK, the rate of change of energy; and α_{EQ}, the equatorial pitch angle of the projected test particle, assuming conserved first invariant. Finally, we join to each tuple of test particle characteristics the flow characteristics at the equatorial projection, i.e. $L_{\nabla B}(X, Y)$ and $\delta\mathcal{S}(X,Y)$. In this manner we create a large collection of data points of the form,

$$(X_{EQ}, Y_{EQ}, K, \alpha_{EQ}, \Delta R_{EQ}, \Delta K, L_{\nabla B}, \delta\mathcal{S}), \tag{5}$$

which we restrict to those for which (X_{EQ}, Y_{EQ}) lie in our nominal transition region. A randomly selected subset of these is included in Data Set S4.

The collection defined this way, i.e. tuples of the form given by **Eq. (5)** for which (X_{EQ}, Y_{EQ}) is in the nominal transition region, creates a data set of over a billion points. Our data analysis benefited from the use of fast-histogram[2] as intrinsic numpy routines were often insufficient to handle data at this scale. From this data set we construct statistical populations defined by a membership criteria and weighting of each data point. These statistical populations are:

- Population ($\mathcal{P}$): All tuples with weights given by w_p, the standard weight of test particle p.

[2]https://github.com/astrofrog/fast-histogram.

- Transport ($\mathcal{T}$): All tuples for which $\Delta R_{EQ} < 0$, i.e. instances of inward radial transport, with weights given by $w_p K \Delta R_{EQ}$
- Acceleration ($\mathcal{A}$): All tuples for which $\Delta K > 0$, i.e. instances of particle acceleration, with weights given by $\Delta K w_p$

With these definitions, $\mathcal{P}$ represents simply the occurrence ratio. The collection $\mathcal{T}$ represents all instances of inward radial transport and the weighting is such that we consider the relevance of each data point to the total keV $-R_E$ of energy transport. In other words, one 20 keV particle transported inwards 5 R_E is equivalent to ten 5 keV particles transported inwards 2 R_E. Finally, population $\mathcal{A}$ represents all instances of individual particle acceleration and the weighting quantifies the importance of each data point to the bulk energization that occurs in the nominal transition region.

3 RESULTS

In the sections that follow we use weighted test particles to study particle transport and acceleration due to the global and mesoscale flow, as captured by our combined MHD and test particle simulations. In our model, test particles are weighted based on the density, temperature, and flux tube volume in the MHD simulation at the location and time of their injection. Therefore, prior to our discussion of particle transport, we show that the statistical properties of the BBFs, particularly those related to the quantities used in particle weighting, produced by our model are in agreement with observations (**Section 3.1**). Having established this, we next turn to an investigation of energetic, but adiabatic, particle transport through the transition region (**Section 3.2**). Here we show the critical role of energetic particle drifts and entropy-depleted bubbles. Given the importance of the latter, we also discuss the sensitivity of our results to numerical resolution. Finally, we go beyond the guiding center approximation and quantify the effects of increasing particle gyroradius (**Section 3.3**). We find that non-adiabaticity results in significant and qualitative differences in particle behavior for heavier ions, and that even for H+ there are non-negligible effects.

3.1 Bursty Bulk Flows in Global Magnetohydrodynamics and Observations

In the context of a study of BBFs using GAMERA's predecessor, the LFM, and a similar global magnetosphere simulation to ours Wiltberger et al. (2015) used simulation data to conduct a superposed epoch analysis mirroring the Geotail study of Ohtani et al. (2004). Wiltberger et al. (2015) found that the model was able to qualitatively reproduce statistical profiles of velocity, magnetic field, and density within the BBFs. Before moving on to an analysis of particle transport and acceleration, we pause here to expand upon the validation efforts of Wiltberger et al. (2015) in a similar statistical manner.

Runov et al. (2015) have conducted a statistical study, using THEMIS data over a 2 year period, quantifying the relative thermodynamic and magnetic properties of intruding regions, or dipolarizing flux bundles (DFBs), to the background flow. They identify intruding regions using a criteria informed by large dB_z/dt and maximum B_z, indicating a sharp magnetic front, small B_x to exclude events when the spacecraft are in the lobes, and decreasing number density, to help select for depleted flux tubes. These criteria select approximately 300 events which are separated based into 4 groups based on their equatorial radius: $R < 9.5$, $R \in [9.5, 12]$, $R \in [12, 15.5]$, and $R \in [15.5, 25]$. Within each of these radial groups they calculate the ratio of density, temperature, and vertical magnetic field between the intruding to background populations. Their results (see Runov et al., 2015, **Table 1**) are reproduced here in **Table 1** under the "DATA" columns, and demonstrate clear statistical relationships that are observed in nature.

In this paper, our approach to model validation is to consider data-model comparison as a question of whether the model can reproduce observed statistical relationships. This statistical approach helps alleviate, but not eliminate, the difficulties associated with comparing *in situ* measurements, characterized by low spatial density over a long time duration, with high-resolution models, featuring high spatial density over a very limited temporal duration. Runov et al. (2015) use 300 measurements collected over 2 years, whereas we (as described below) can generate millions, or even billions when including test particles, of measurements over only 2 hours of, in this case, synthetic southward IMF driving. Care must be taken in how we interpret comparisons of a population with sparse sampling of a large event space to dense sampling of a very limited event space. With these caveats in mind, we return to the data from our simulation.

To construct our statistics, we calculate flux tube entropy throughout the nominal transition region defined in **Section 2.3** at a cadence of 5 s. We identify the intruding population using a criteria defined by the relative buoyancy and density depletion, although we return to the significance of the latter criterion shortly. The background population is defined by $|\delta\mathcal{S}| < 0.05$ and the intruding population is defined based on the criteria $\delta\mathcal{S} < -0.075$ and density depletion of 10% relative to the background. We note here that in principle we can identify everything for which $\delta\mathcal{S} < 0$ as a bubble. However, we find that for small $\delta\mathcal{S}$ the time-varying background $\mathcal{S}(R, \phi, t)$ complicates reliably separating bubbles from background. Therefore we use the stricter criterion $\delta\mathcal{S} < -0.075$ to identify bubbles. We also note that the use of a density depletion criterion only appreciably affects the results in the innermost radial bin ($R < 9.5$), outside of that the ratios we get with and without the additional density depletion criterion are largely unchanged. We attribute this to the fact that there are fewer bubbles that penetrate this deeply (**Supplementary Figure S2**) and that the statistics of the innermost region are skewed by the induced effects of bubbles, e.g. background plasma displaced from its entropy equilibrium by braking bubbles (e.g., Toffoletto et al., 2020). This interpretation is supported by the long-wavelength striations of oscillating relative buoyancy seen inside $R = 8R_E$ (**Supplementary Figure S2C**).

With the criteria as defined above we generate approximately 10^7 total data points, of which $\approx 10^6$ are identified as intruding.

TABLE 1 | Data-model comparison of BBF statistics. Shown are the results of a statistical study (DATA; Runov et al., 2015) looking at the relative density, temperature and magnetic field strength of BBFs to the background plasma. We construct analogous, although not identical, statistics (MODEL) from our simulation to compare against.

Radial Domain [R_E]	Intruding-Background Ratio of Flow Properties					
	Density		Temperature		Vertical Magnetic Field	
	DATA	MODEL	DATA	MODEL	DATA	MODEL
R < 9.5	0.60 ± 0.30	0.48	1.40 ± 0.03	1.20	1.38 ± 0.01	1.55
[9.5,12]	0.60 ± 0.30	0.46	1.30 ± 0.02	1.37	1.59 ± 0.02	1.57
[12,15.5]	0.60 ± 0.30	0.60	1.30 ± 0.07	1.34	2.00 ± 0.10	1.92
R > 15.5	0.60 ± 0.30	0.81	1.40 ± 0.08	1.22	2.10 ± 0.20	1.98

The fraction of intruding to background is of course higher in the model than the observational data as we are focused only on the nominal transition region during an SMC-like period. The ratios of the average density, temperature, and magnetic field between the intruding and background populations are then calculated in each of the radial groups (**Table 1**) under "MODEL". The statistical relationships inferred from the data, as characterized by **Table 1** can be summarized as follows: the intruding regions are depleted of mass, typically exhibiting 60% of the background mass, this relationship is largely independent of radius but exhibits large deviations; the intruding regions are hotter than the background, typically by 40%; and the intruding regions are dipolarizing, i.e. exhibit stronger magnetic fields than the background, typically twice as strong outside of $R = 12\ R_E$ and decreasing within. As can be seen in the comparison of MODEL and DATA shown in **Table 1**, our model can, for the most part, quantitatively reproduce these relationships.

The quantities we have considered in our data-model comparison are of direct relevance to how we weight test particles: the thermodynamic quantities directly inform the κ-distribution function used as an initial condition of the PSD; and the magnetic field, via the flux tube volume, is included in the phase space volume element. Beyond their importance to the initial configuration of the test particles, we expect these flow characteristics to shape their subsequent development. Hotter flows will have a higher fraction of their energy density carried by particles whose energy-dependent drifts, i.e. gradient and curvature, are comparable to the bulk $E \times B$ flow (see e.g., Sorathia et al., 2017, Figure 12). More strongly magnetized flows may have lower flux tube volumes and possibly lower flux tube entropy, $\mathcal{S}$, which can result in deeper penetration of the flow (Dubyagin et al., 2011; Kim et al., 2012). Therefore our ability to reproduce these statistics in the MHD flow do not just reflect our ability to accurately create particles at the tailward edge of the transition region but to evolve those particles throughout the transition region.

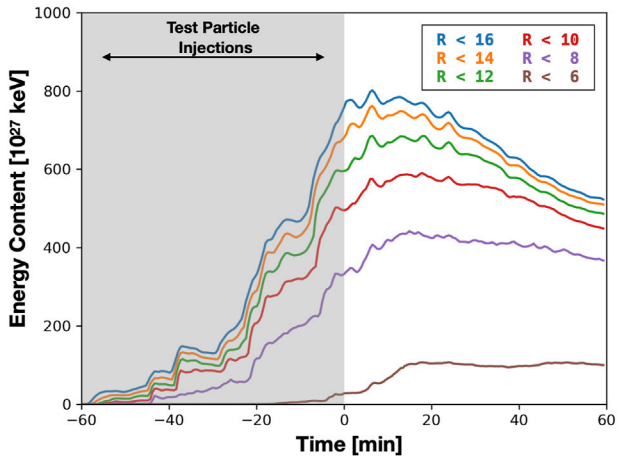


FIGURE 3 | Total energy content from injected guiding center test particles (GCRC) as a function of time for different (cylindrical) radial shells based on equatorial projection of 3*D* test particle location. Shaded region denotes period where test particles are being actively injected into the nightside arc at $R \approx 18$.

3.2 Role of Mesoscale Flow Structures in Ring Current Energization and Transport

The first particle study we consider is the transport of particle energy in the adiabatic limit. To this end we use positrons, which we refer to as "GCRC" for guiding center ring current, whose gyro- and bounce-frequencies are much higher than the MHD frequencies. An animation of the combined MHD and test particle simulation is shown in **Supplementary Video S2** in the same format as **Figure 1**. In **Figure 3** we show the evolution of energy content contained within various equatorial shells. The energy content within a shell of (cylindrical) radius R is simply $\sum w_p K_p$ where the sum is taken over all test particles whose equatorial projection is within the given radius. The shaded region in **Figure 3** denotes the period in which new test particles are being continuously created ($T < 0$), whereas for $T > 0$ only the existing test particles within the domain are evolved. For the outer radial shells, $R > 8$, there is a drop off between the maximum energy content shortly after $T = 0$ to the energy content at the end of the simulation. This is due to the loss, without replacement, of particles on open drift orbits. Inside of $R = 8$ the energy content increases during the period of active injection and is largely flat afterwards as particles that penetrate that far reach closed drift orbits and remain trapped. This highlights how sensitive the energy content of the inner magnetosphere is to the penetration depth of the injected particles.

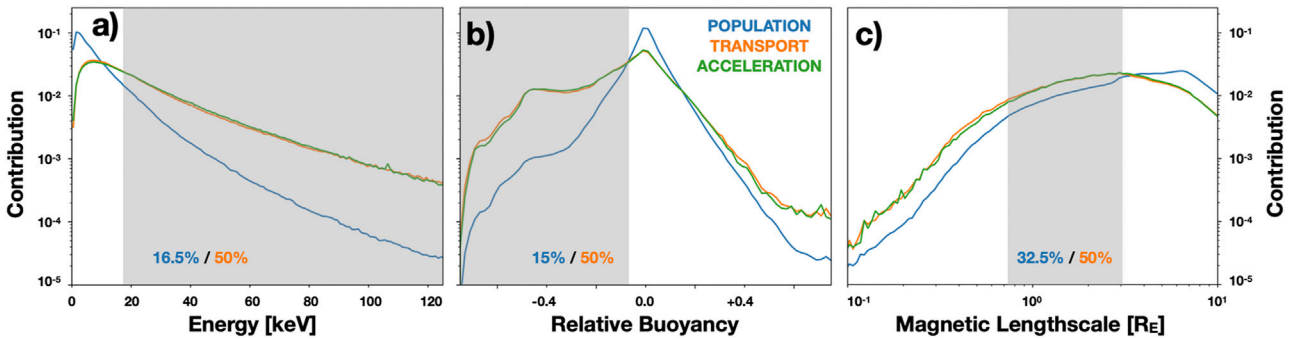


FIGURE 4 | Efficiency of transport and acceleration in the transition region. Here we compare for various particle and flow properties their fraction of: the total population, the total inward energy transport, and the total energization as defined in **Section 2.3**. Regions where the contribution of a quantity to transport/acceleration is greater than population are "efficient" for ring current buildup. Shown are particle energy **(A)**, relative buoyancy **Eq. (2)**; **(B)**, and magnetic lengthscale **Eq. (4)**; **(C)**. In each panel the shaded region is chosen to highlight approximately 50% of the total energy transport.

Next we turn to one of our core goals in this study, namely the identification of the ambient flow properties that lead to the transport and acceleration of particle energy into the inner magnetosphere, i.e. the formation of the ring current. Using the method we describe in **Section 2.3** we construct $\sim 10^9$ data-points representing the instantaneous correlation between: a test particle state, through its equatorial projection, energy, and pitch angle; its transport and acceleration, through the change in its equatorial projection and energy; and the ambient MHD flow properties, through the characteristic magnetic field lengthscale (**Eq. 4**) and the relative buoyancy (**Eq. 2**).

Each of the statistical samples we defined in **Section 2.3** are a collection of tuples of the form of **Eq. (5)**, defined via a sample-dependent membership criteria and weight. We define the contribution of a quantity, Q in the range $Q_0 + \Delta Q$, as the weighted-sum of the elements that satisfy both the sample membership criteria and $Q \in [Q_0, Q_0 + \Delta Q]$. In other words, the contribution of a given relative buoyancy is: to population ($\mathcal{P}$), the probability of finding a particle in a flow with that property; to transport ($\mathcal{T}$), the fraction of all particle energy transport that occurs in regions of the flow with that property; and to acceleration ($\mathcal{A}$), the fraction of the total bulk energization of the particles that occurs in regions of the flow with that property.

Absent any correlation between the particle or flow characteristic to transport, the population contribution and transport contribution would be the same. Regions for which the contribution to transport/acceleration is higher than the contribution to the population represents a characteristic favorable to the delivery of energy to the inner magnetosphere, e.g., we find that particles with energies above 10 keV "punch above their weight" and contribute more to transport and acceleration than their fraction of the population. **Figure 4** compares the relative contribution of particles of different energies (**Figure 4A**) and in different ambient flows (**Figures 4B,C**) to the overall population versus transport and acceleration. Before proceeding to the more fine-grained discussion of the individual characteristics, we note that contribution to transport, specifically inward radial transport from the $w_p K \Delta R_{EQ}$ weighting, correlates almost identically with that of acceleration. This is perhaps unsurprising as the transition region bridges the stretched tail and dipolar inner magnetosphere and therefore adiabatic transport (for GCRC) across it would lead to both betatron and Fermi acceleration via conservation of the first and second adiabatic invariant.

In each panel of **Figure 4**, the shaded region corresponds to a contribution of 50% of the total transport of energy through the transition region. The overlaid percentages represent the contribution within the shaded region to the population and the 50% contribution to transport. We can summarize the results of **Figure 4** as follows: ambient flows that exhibit depleted entropy or spatial mesoscale structure of the magnetic field are particularly effective at delivering particle energy into the inner magnetosphere; similarly, particles with energies above ~ 10 keV are particularly effective at carrying that energy into the inner magnetosphere. In the remainder of this section we analyze more closely these transport critical flow structures and the characteristics of the particles they delivery into the inner magnetosphere.

From **Figure 4a**, particles with $K > 20$ keV account for half the energy transport in the statistical sample despite making up only $\sim 16.5\%$ of the population. Previous modeling work using test particles has identified the importance of the energy-dependent gradient drift, V_∇, whose relative importance to the energy-independent $E \times B$ drift, also the MHD bulk flow, increases with energy (Gabrielse et al., 2017, 2016; Ukhorskiy et al., 2017, Ukhorskiy et al., 2018). As a simple estimate we can approximate the magnitudes of the $E \times B$ and gradient drifts as $V_{EB} \sim E/B$ and

$$V_\nabla \sim \frac{K}{q} \frac{1}{L_{\nabla B}} \frac{1}{B}, \tag{6}$$

respectively, and define

$$K_\nabla \sim qE \times L_{\nabla B}, \tag{7}$$

the energy for which the two velocities are equal (see Sorathia et al., 2017, Figure 12). For typical values inferred from the MHD

simulation, $E = 2.5$ mV/m and $L_{\nabla B} = 2R_E$, $K_\nabla \sim 25$ keV. This is an estimate of the energy at which gradient drift magnitude would exceed the bulk flow, it would be non-negligible for lower energies.

Using the statistics we have derived from this simulation, we can more quantitatively assess the role of particles whose trajectories deviate appreciably from the bulk flow. We find that the fraction of transport that occurs for $V_\nabla/V_{EB} > 0.5$ and $V_\nabla/V_{EB} > 1$ is 48 and 30% respectively. In other words, we find that the majority of transport through the transition region is via particles with non-negligible energy-dependent drift speed. Ukhorskiy et al. (2018) show that for particles with $K >$ 10 keV, comparable to where we find the contribution to transport exceeds population (**Figure 4A**), magnetic gradient trapping is necessary to confine particles within azimuthally localized flow long enough to reach the inner magnetosphere. While we do not try to distinguish magnetic gradient trapping in individual cases of our billion data points, the importance of $K >$ 10 keV particles (**Figure 4A**) and $L_{\nabla B} < 3R_E$ (**Figure 4C**) strongly suggests the potential importance of this mechanism.

Focusing now on **Figure 4B** we see the critical role of entropy in particle transport. Low-entropy "bubbles", which we define here conservatively as $\delta\mathcal{S} < -0.075$, account for approximately half the energy transport in the sample while making up only $\sim 15\%$ of the population. Less conservatively, $\delta\mathcal{S} < 0$ accounts for $\sim 50\%$ and $\sim 65\%$ of population and transport, respectively. The efficiency increases as we consider only deeply depleted bubbles, $\delta\mathcal{S} < -0.2$, which correspond to 3 and 30% of the population and energy transport respectively. This is similar to previous studies using RCM (e.g., Lemon et al., 2004; Yang et al., 2010, Yang et al., 2015) and coupled RCM-MHD (e.g., Pembroke et al., 2012; Cramer et al., 2017) which have highlighted the importance of entropy-depleted flux tubes to ring current buildup. Of note is that we find that in addition to depleted entropy regions that there is, perhaps counter-inuitively, some inward transport in regions with $\delta\mathcal{S} > 0$. We attribute this effect, as pointed out by Yang et al. (2011), to regions directly ahead of the depleted bubbles that are initially neutrally buoyant but pushed inwards by the bubble (see also **Supplementary Figure S2**). However, we can see from this analysis that while those regions do contribute to more transport than their fraction of the population, the overall effect is much smaller than the bubbles themselves.

Finally, we consider the importance of the characteristic lengthscale of the ambient magnetic field as shown in **Figure 4C**. Here we find that while regions with $L_{\nabla B} < 3R_E$ are efficient, the effect beyond their contribution to the population is not as significant as that of particle energy or depleted entropy. From **Figure 2** (inset) we see that regions of smaller magnetic lengthscale may correspond to: the interior of the depleted entropy bubble, which is particularly efficient at transport; the region ahead of the bubble, which is somewhat efficient; or the regions azimuthally adjacent to the flow channel for which we expect, if anything, outwards flow from the vorticity at the edges of the flow channel. We can instead consider the magnetic lengthscale statistics differently and look at the characteristic lengthscales of deeply depleted bubbles, $\delta\mathcal{S} < -0.2$. We find that

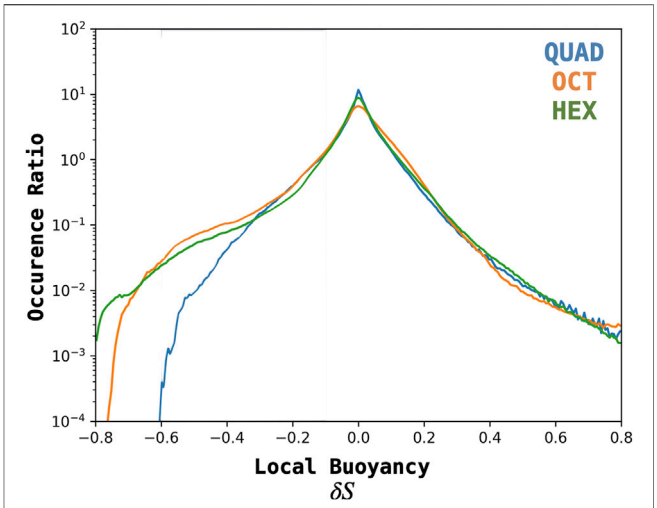


FIGURE 5 | Grid resolution study of the statistics of bubble depletion during SMC-like activity. Shown are statistics calculated using a grid 2× coarser (QUAD) and 2× finer (HEX) than the grid resolution we use elsewhere in this paper (OCT).

the vast majority of deeply depleted bubbles are mesoscale, between 0.5–3R_E. Specifically

$$\Pr(R_E/2 < L_{\nabla B} < 3R_E \mid \delta\mathcal{S} < -0.2) = 80\%, \tag{8}$$

with $\Pr(A|B)$ denoting the conditional probability of A given B. **Supplementary Figure S3** shows the probability distribution of magnetic lengthscales for all bubbles, $\delta\mathcal{S} < -0.075$, and deeply depleted bubbles, $\delta\mathcal{S} < -0.2$. For both we find a largely similar distribution of magnetic lengthscales: sharply peaked at $L_{\nabla B} \approx 1.75R_E$, very similar to observationally-inferred values (e.g. Nakamura et al., 2004; Liu et al., 2013), and transitioning to a rapid decline for $L_{\nabla B} > 4R_E$.

Taken together, we find: bubbles are very efficient at transport, bubbles are mesoscale, and that bubbles transport particles whose energy-dependent drifts are comparable to the ambient flow. Given the critical role of buoyancy in transporting particle energy across the transition region, and consequently building the ring current, understanding the role of numerical resolution in producing these bubbles is vital. To this end we show in **Figure 5** a resolution study of the buoyancy statistics for simulations with resolutions 2× coarser (QUAD) and 2× finer (HEX) than the simulation we consider in this paper (OCT). An analogous comparison of $L_{\nabla B}$ is shown in **Supplementary Figure S4**.

From our resolution study, we find that the lowest resolution differs most notably from the two higher resolutions, and that the two higher resolution simulations are largely similar for all but the most depleted bubbles, $\delta\mathcal{S} < -0.7$, which account for only $\approx 1\%$ of the total energy transport in our test particle statistics at OCT resolution. By contrast we find that the lowest resolution simulation differs appreciably for $\delta\mathcal{S} < -0.3$, which corresponds to $\approx 20\%$ of the total energy transport in the OCT simulation. From this, the lower resolution simulation would clearly be

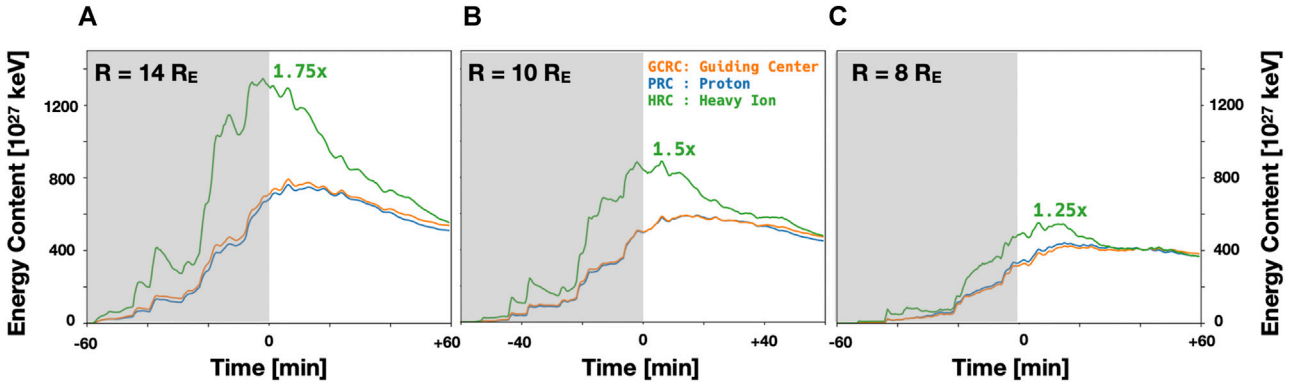


FIGURE 6 | Comparison of total energy content for identical test particle ensembles evolved with increasing gyroradius within equatorial radius $R = 14$ **(A)**, $R = 10$ **(B)**, and $R = 8$ **(C)**. Shaded region denotes period where test particles are being actively injected into the nightside arc at $R \approx 18$. Overlaid text is the approximate ratio of energy content at peak between HRC and PRC.

missing a non-trivial amount of energy transport assuming it behaved otherwise similarly to the higher resolution simulation. We return to this point in **Section 4**, but expect that the lower resolution simulation misses much more due to the depressed manifestation of $L_{\nabla B} < 3$ R_E flow structures (**Supplementary Figure S4**).

3.3 Sensitivity to Larmor Radius

In the preceding section we considered the transport and acceleration of positrons (GCRC) as a proxy for adiabatic ion processes. Here we broaden our experiment to assess the role of non-adiabatic effects by considering more realistic ion masses. To this end we consider the exact same ensemble of created test particles, defined by their location and time of seeding, energy, and pitch angle and evolve them with a different mass. In addition to positrons (GCRC), we also include H+ (PRC), and heavier *O*+ ions (HRC). While the GCRC test particles are evolved using a hybrid guiding-center and Lorentz trajectory approach, for PRC and HRC we solely use the Lorentz trajectories. The formulation of our experiment is solely to explore the role of non-adiabaticity in the evolution of an otherwise identical ensemble of particles. It does not attempt to account for differences in plasma sheet ion properties due to different source populations, e.g. ionospheric *O*+ versus solar wind H+. Animations of the MHD and test particle simulations for PRC and HRC are shown in **Supplementary Video S2 and S3** in the same format as **Figure 1**.

A comparison of the energy content at different penetration depths across the test particle ensembles of varying mass is shown in **Figure 6**, where the shaded region denotes the period of active test particle seeding. While the bulk energization and spatial distribution of H+ (PRC) evolve relatively similarly to positrons (GCRC), there is a qualitative change in behavior when going to heavier ions (HRC). We find that HRC is more energetic at further distances and during the period of active seeding, with the deviation between HRC and GCRC/PRC diminishing closer to Earth and rapidly in time after the source of newly-injected particles is shut off.

The overlaid text on each panel of **Figure 6** is approximately the ratio of energy content at peak between HRC and PRC, which we find to be: 1.75× ($14R_E$), 1.5× ($10R_E$), 1.25× ($8R_E$). Recall that in this comparison we have evolved the same ensemble of test particles using varying mass, so the excess energy content of HRC is a proxy for the effects of non-adiabaticity in these particles interactions with the same flow structures. While not a precise analog, we can use the *O*+ enhancement factor introduced by Moebius et al. (1987) and studied as a function of downtail distance using Geotail statistics by Nosé et al. (2000). The *O*+ enhancement factor, $E_{O+} = R_{O+}/R_{H+}$, where R_X is the ratio of the differential flux os species *X* prior to and following substorm onset. By comparing the ratio of ratios, the enhancement factor helps control for ambient differences in the properties of different ion species, e.g., due to their different sources, and makes it a good metric for comparison with our simulation that neglects these potential differences. In their study, Nosé et al. (2000) find E_{O+} to be, averaging over ± $1R_E$: $E_{O+} = 1.77$ ($14R_E$), $E_{O+} = 1.35$ ($12R_E$), and $E_{O+} = 1.26$ ($10R_E$). This is very much in line with the results of our simulation, although we do find that the comparison of HRC to PRC energy content decreases more slowly towards Earth than these statistics. We suspect this is due to differences in ambient conditions; the ratio of HRC to PRC energy content in the simulation is taken after several hours of southward IMF as compared to the Geotail statistics of local dipolarizations over 3 years. In particular it is likely that our simulation has a less stretched magnetotail configuration after several hours of SMC-like activity as compared to the broader statistical sample and this in turn would affect where and how strongly *O*+ ions are scattered.

As can be seen in **Figure 6**, the significant excess energy content of HRC that penetrates inside $14R_E$ is largely absent from the region inside $8R_E$, i.e. the majority of this excess energy is lost prior to reaching the inner magnetosphere. **Supplementary Video S2** through **Supplementary Video S4** show the evolution of GCRC, PRC, and HRC respectively and **Supplementary Figure S5** shows a comparison of the state of

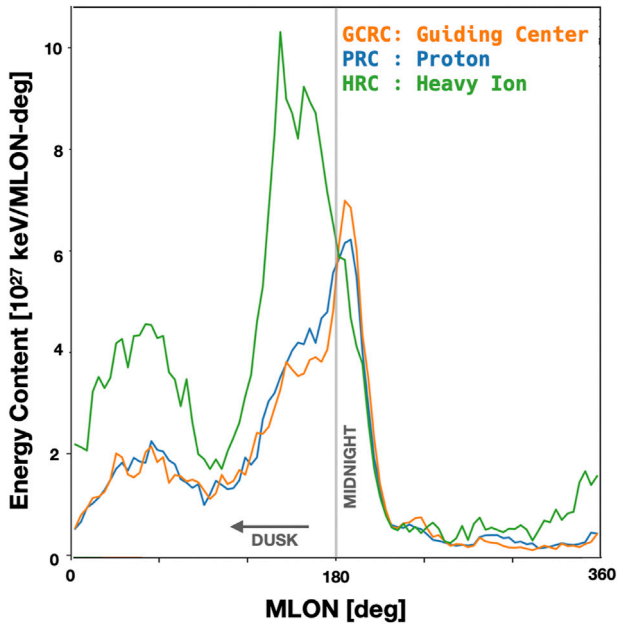


FIGURE 7 | Comparison of the magnetic longitude distribution of total energy content, within R = 12 at T = 0, for identical test particle ensembles evolved with increasing gyroradius.

GCRC, PRC, and HRC at T = 0. Most evident in these comparisons is the strong duskward skew of the highly non-adiabatic HRC. To make this more quantitative we show in **Figure 7** a comparison of the MLT distribution of energy inside $R = 12R_E$ at T = 0 for the three ensembles. There is a broad similarity across all the ensembles: a dominant peak near midnight sharply falling off towards dawn and more gradually towards dusk, and a smaller secondary peak in the post-noon sector, approximately 1400 MLT. However, we find an appreciably stronger duskward bias in HRC as compared to GCRC/PRC. The primary pressure peak of HRC is shifted several hours of MLT duskward with a broader pre-midnight extension with the secondary pressure peak extending across the dayside into the pre-noon sector. The exaggerated dawn-dusk asymmetry due to non-adiabaticity is consistent with observational statistics of plasma sheet O+ (e.g., Ohtani et al., 2011).

The duskward bias of HRC evident in **Figure 7** provides a clue to the ultimate fate of the HRC energy content inside $R = 14R_E$ (**Figure 6A**) that is largely missing at $R = 8R_E$ (**Figure 6C**). Test particles are evolved until the end of the simulation or until the test particle leaves the simulation domain, in this case a spherical annulus spanning 2–30 R_E. When the test particles exit the domain, they are marked out of bounds at the location they intersected the boundary. Therefore we can identify lost energy content and distinguish its manner of exit either through precipitation, for particles lost to the inner boundary, or the dusk or dawn flank based on the sign of the SM–Y coordinate. For PRC, we find the lost energy content is distributed 20%/70%/10% to precipitation, dusk, and dawn flank respectively. For HRC, we find approximately 4× more lost energy content compared to PRC and the distribution to be approximately 10%/85%/5% to precipitation, dusk, and dawn. In other words, HRC provides a great deal of non-adiabatic energy relative to PRC which reside primarily on open drift shells that lead to significant magnetopause losses on the dusk flanks. This excess energy content is rapidly lost when the source population is extinguished.

The non-adiabatic effects we find in HRC result in a dramatic difference when compared to GCRC. Additionally, despite the fact that **Figure 6** shows that GCRC and PRC have very similar overall energy content and spatial distribution, we find that there are subtle but important differences in how that energy density is distributed in momentum space, i.e. pitch angle and energy spectrum.

That there should be some degree of non-adiabaticity is perhaps unsurprising as both data (e.g., Runov et al., 2017) and particle simulations (e.g., Birn et al., 2013; Ukhorskiy et al., 2018) have shown that ions at dipolarization fronts are only quasi-adiabatic. Here we find that for the energy content inside of $8R_E$ at the end of the simulation: the energy-weighted mean equatorial pitch angle, $\bar{\alpha}$, goes from $\approx 45°$ (GCRC) to $\approx 50°$ (PRC); and the energy-weighted mean energy, $\bar{K}$, goes from $\approx$ 50 keV (GCRC) to $\approx$ 60 keV (PRC). In other words we find that PRC is hotter and exhibits some perpendicular anisotropy relative to GCRC, due to the proton non-adiabaticity. The latter is potentially important as perpendicular anisotropy provides a free energy source for electromagnetic ion cyclotron (EMIC) waves known to be important in the inner magnetosphere.

For trapped ring current ions it is generally believed that charge exchange (CX) is the dominant loss mechanism for typical magnetospheric conditions (e.g., Jordanova, 2020, and references therein). The CX lifetime can be estimated as,

$$\tau_{CX} = \frac{1}{< n_G > \sigma_{CX} v}, \tag{9}$$

where $< n_G >$ is the bounce-averaged geocorona density, σ_{CX} is the CX cross-section (Lindsay and Stebbings, 2005), and v is the particle velocity. The cross-section exhibits a great deal of sensitivity to energy with $\sigma_{CX}(\bar{K}_{PRC})/\sigma_{CX}(\bar{K}_{GCRC}) \approx 0.6$ for the mean energies calculated for PRC and GCRC above (Lindsay and Stebbings, 2005). The other critical term of τ_{CX} is the bounce-averaged geocorona density, which will be lower for more equatorial particles whose smaller mirror latitude limits their exposure to the highest geocorona densities.

Both the equatorial anisotropy and hotter distribution will tend to increase τ_{CX}. Here we make a simple estimate of the combined effect using the energy-weighted mean pitch angle and energy as properties of a fiducial particle at L = 8 combined with: the geocorona density at L = 8 from Østgaard et al. (2003), and the approximation (Smith and Bewtra, 1976),

$$\tau_{CX} = \tau_{EQ} \cos^{3.5}(\lambda_M), \tag{10}$$

where τ_{EQ} is the lifetime of an equatorial particle and λ_M is the actual mirror latitude. This yields $\tau^{PRC}/\tau^{GCRC} \approx 1.6$, an

appreciable change in the typical particle lifetime, which has important implications for longer-term ring current decay in the aftermath of active periods. This only serves to further complicate the already difficult modeling of ring current decay due to the sensitivity to different geocorona density models (Ilie et al., 2013).

4 DISCUSSION AND CONCLUSION

We have presented results of tracing a large number of test particles (20 M per species) in a high resolution MHD simulation of an idealized SMC-like period (**Section 2.1**), where particles were initialized to "mirror" the bulk properties of the MHD plasma in the plasma sheet. We continuously seed test particles in a thin ($\Delta R = 1R_E$) nightside arc at $R \approx 18$ R_E and weight those test particles using the density, temperature, and flux tube volume calculated from the MHD flow at that time and location (**Section 2.2**). Due to the importance of the MHD flow quantities to the weighting of test particles we begin with a statistical validation exercise comparing the relative thermodynamics and magnetization of BBFs in our simulation to similar statistics derived from *in situ* data. We use the correlations between test particles and MHD flow properties to study the transport of particle energy through the transition region, where we use an expansive definition of the transition region to encompass the domain where both fast flows and particle drift physics are both non-negligible. These correlations generate a massive database, over a billion data points connecting particle energy transport, via the motion of the equatorial projection of a particle, and local flow properties, via the magnetic lengthscale and local buoyancy (**Section 2.3**). Finally, we consider the importance of non-adiabaticity by comparing the evolution, using increasing mass, of identical test particle ensembles, as defined by their initial configuration and weights. Our key results are summarized as follows:

- The mesoscale bursty bulk flows (BBFs) in our global MHD simulation yield thermodynamics, magnetization, and spatial scales (**Table 1** and **Supplementary Figure S3**) that largely reproduce statistics from *in situ* THEMIS measurements (Nakamura et al., 2004; Runov et al., 2015). We further demonstrated that the transport-critical properties of the modelled BBFs are principally independent of the simulation resolution, as long as the simulation possesses sufficient resolving power (**Figure 5** and **Supplementary Figure S4**).
- Mesoscale bubbles, or localized regions of depleted entropy, are critical to particle energy transport through the transition region and, for a significant fraction of the particles, the gradient and curvature drifts are non-negligible.
- The effects of ion non-adiabaticity (**Section 3.3**), i.e. finite gyroradius, for heavy ions (O+) are consistent with *in situ* measurements of relative enhancement (Nosé et al., 2000) and create qualitative differences in the bulk energization and spatial distribution (radial and MLT) of the heavy ion energy density. The overall energization and spatial distribution of H+ is largely similar to the adiabatic control run, however differences in the momentum space distribution, i.e. energy and pitch angle, have implications for recovery timescales that are non-negligible.

Although we find that MHD is able to create BBFs that reproduce observed statistical properties, this is only at sufficiently high resolution and using a low-dissipation algorithm. The importance of proper resolution to building the ring current is likely even higher than suggested in **Section 3.2**, where we estimate 20% of the energy transport would be lost in the lower versus higher resolution simulation by considering the energy transport for $\delta\mathcal{S} < -0.3$. However, **Supplementary Figure S4** adds a corollary that the lower resolution simulation manifests far less structure at scales between 0.5–3 R_E, which are critical for bubbles in our simulation (**Supplementary Figure S3**) and typically associated with *in situ* measurements of flow bursts (Nakamura et al., 2004). Furthermore, the larger typical lengthscale will increase K_∇ (**Eq. (7)**), the characteristic energy at which energy-dependent and $E \times B$ drifts are comparable; consequently, less energy density in the transition region will undergo gradient-drift dependent processes like trapping (Gabrielse et al., 2017; Ukhorskiy et al., 2017, Ukhorskiy et al., 2018), which may result in depressed transport. In fact, we found this to be the case in our early experiments (Sorathia et al., 2018). There we demonstrated, when comparing test particle transport in simulations with the same low and high resolutions as presented in this paper, that even though the lower resolution simulation exhibited overall higher global earthward mass flux, the test particle energy density inside of $R = 8$ R_E was only half that of the higher resolution simulation. In other words, the inclusion of adiabatic particle physics without mesoscale plasma sheet dynamics will not build the same ring current. Further, these effects are not limited to the ring current. Mesoscale processes shape the wave populations of the inner magnetosphere: anisotropic ion injections provide free energy for the EMIC wave population and low energy electron injections play a similar role for VLF wave growth (e.g., Jaynes et al., 2015). The evolving plasmaspheric population correlates with the relative distribution of whistler-mode hiss and chorus waves, with important consequences to flux enhancements of energetic trapped particles in the radiation belts (e.g., Ripoll et al., 2020).

We also have found here that adiabatic particle dynamics is insufficient to capture the building, and subsequent decay, of the ring current. For H+ non-adiabaticity plays a minor role in the bulk energization and spatial distribution of particle energy in the inner magnetosphere, but even relatively small alterations to the momentum space distribution can have important implications. Non-adiabaticity leads to a more anisotropic distribution, with perpendicular bias, which can provide free energy to the wave populations of the inner magnetosphere, and a harder energy spectrum. Taken together, the more equatorial and higher energy distribution will decay more slowly due to charge exchange (**Section 3.3**).

More dramatic, although not unexpected (e.g., Moebius et al., 1987; Nosé et al., 2000; Delcourt et al., 1997; Keika et al., 2013; Bingham et al., 2020) is the non-adiabaticity exhibited by O+. Our results show that O+ non-adiabaticity creates an excess energy density, exceeding 1.5× the adiabatic energy density for $R > 10$ R_E

(**Figure 6**), whose contribution to the ring current is qualitatively different than H+. For O+ versus H+ we find: shallower penetration depth, greater duskward-biased asymmetry, and a rapid depletion of the excess when the source in the plasma sheet is shut off. The inclusion of O+ in ring current composition is known to affect recovery timescales via charge exchange (e.g., Hamilton et al., 1988; Ilie et al., 2013; Jordanova, 2020), due to the disparate collision cross-sections and their dependence on energy. We see here that recovery timescales via magnetopause losses will also be affected by O+ composition due to non-adiabaticity. In their review, Keika et al. (2013) discuss possible mechanisms to explain the stronger O+ energization as compared to H+. These include: direct finite gyroradius particle processes, e.g. Speiser orbits or interactions with transient and localized electric fields, which will result in preferential duskward deflection; resonant interaction with inner magnetospheric waves; and differences in the underlying source population. Of these, our simulations only include the first but produce O+ enhancement factors with similar radial dependence as observed (Nosé et al., 2000), highlighting the importance of non-adiabatic interactions with the background flow. Given the importance of O+ energy density in the ring current during disturbed geomagnetic conditions (Nosé et al., 2005), modeling these non-adiabatic effects is crucial.

In the simulation presented here we did not include ring current feedback on the global magnetosphere simulation. For the relatively undisturbed magnetospheric configuration we have considered here this omission is likely acceptable. However, expanding this type of study to more disturbed periods, such as storms, will require at least coupling to an inner magnetosphere model. Even so, our work shows that models coupling global MHD magnetosphere and ring current models, while the current state of the art for simulating typical geospace timescales, are insufficient in the transition region, where both fast flows, excluded from typical inner magnetosphere models, and energy-dependent drifts, missing from MHD, are important. The results of this work stress the importance of comprehensive modeling of ion transport across the transition region which requires: producing numerically robust mesoscale bubbles with appropriate entropy depletion; resolving energetic particle interactions with the sharp boundaries and internal magnetic structure of these mesoscale bubbles; and including the effects of non-adiabatic ion particle dynamics, particularly for heavier ion species. In other words, to properly model the buildup of the H+ ring current in the inner magnetosphere, a model must account for both fast flows and energy-dependent drifts in the transition region as the transport processes operate more effectively on the higher-energy tail of the thermal distribution. Further, for heavier ions, e.g. O+, including non-adiabatic effects is necessary as they qualitatively change the character of the contribution, in the magnitude and distribution of energy density, to the ring current.

DATA AVAILABILITY STATEMENT

The datasets presented in this study can be found in online repositories. The names of the repository/repositories and accession number(s) can be found in the article/**Supplementary Material**. Supporting information (Movies S1–S4 and Datasets S1–S4) are archived and available online (via https://doi.org/10.5281/zenodo.5542601). In addition, raw simulation data are preserved on the Cheyenne supercomputer and can be made available upon request.

AUTHOR CONTRIBUTIONS

All authors listed have made a substantial, direct, and intellectual contribution to the work and approved it for publication.

FUNDING

This work was supported by NASA grants 80NSSC19K0241, 80NSSC20K1833, 80NSSC17K0679, NNX16AG73G, NNX17AI54G, and 80NSSC19K0071; the Van Allen Probes contract NNN06AA01C and by the NASA DRIVE Science Center for Geospace Storms (CGS) under grant 80NSSC20K0601.

ACKNOWLEDGMENTS

We would like to acknowledge the use of computational resources (doi:10.5065/D6RX99HX) at the NCAR-Wyoming Supercomputing Center provided by the National Science Foundation and the State of Wyoming and supported by NCAR's Computational and Information Systems Laboratory.

SUPPLEMENTARY MATERIAL

The Supplementary Material for this article can be found online at: https://www.frontiersin.org/articles/10.3389/fspas.2021.761875/full#supplementary-material

REFERENCES

Angelopoulos, V., Baumjohann, W., Kennel, C. F., Coroniti, F. V., Kivelson, M. G., Pellat, R., et al. (1992). Bursty Bulk Flows in the Inner central Plasma Sheet. *J. Geophys. Res.* 97, 4027–4039. doi:10.1029/91ja02701

Angelopoulos, V., Kennel, C. F., Coroniti, F. V., Pellat, R., Kivelson, M. G., Walker, R. J., et al. (1994). Statistical Characteristics of Bursty Bulk Flow Events. *J. Geophys. Res.* 99, 21257–21280. doi:10.1029/94ja01263

Baumjohann, W. (1982). Ionospheric and Field-Aligned Current Systems in the Auroral Zone: a Concise Review. *Adv. Space Res.* 2, 55–62. Proceedings of the Topical Meeting of the COSPAR Interdisciplinary Scientific Commission C of the COSPAR Twenty-fourth Plenary Meeting. doi:10.1016/0273-1177(82)90363-5

Baumjohann, W., Paschmann, G., and Lühr, H. (1990). Characteristics of High-Speed Ion Flows in the Plasma Sheet. *J. Geophys. Res.* 95 (1978–2012), 3801–3809. doi:10.1029/ja095ia04p03801

Bingham, S. T., Nikoukar, R., Cohen, I. J., Mauk, B. H., Turner, D. L., Mitchell, D. G., et al. (2020). Evidence for Non-adiabatic Oxygen Energization in the Near-Earth Magnetotail from MMS. *Geophys. Res. Lett.* 20. doi:10.1029/2020JA028144

Birn, J., Hesse, M., Nakamura, R., and Zaharia, S. (2013). Particle Acceleration in Dipolarization Events. *J. Geophys. Res. Space Phys.* 118, 1960–1971. doi:10.1002/jgra.50132

Birn, J., Hesse, M., Schindler, K., and Zaharia, S. (2009). Role of Entropy in Magnetotail Dynamics. *J. Geophys. Res.* 114, n/a. doi:10.1029/2008ja014015

Birn, J., Nakamura, R., Panov, E. V., and Hesse, M. (2011). Bursty Bulk Flows and Dipolarization in MHD Simulations of Magnetotail Reconnection. *J. Geophys. Res.* 116, a–n. doi:10.1029/2010ja016083

Chaston, C. C., Bonnell, J. W., and Salem, C. (2014). Heating of the Plasma Sheet by Broadband Electromagnetic Waves. *Geophys. Res. Lett.* 41, 8185–8192. doi:10.1002/2014gl062116

Cheng, L., Lin, Y., Perez, J. D., Johnson, J. R., and Wang, X. (2020). Kinetic Alfvén Waves from Magnetotail to the Ionosphere in Global Hybrid Simulation Associated with Fast Flows. *J. Geophys. Res. Space Phys.* 125. doi:10.1029/2019ja027062

Cramer, W. D., Raeder, J., Toffoletto, F. R., Gilson, M., and Hu, B. (2017). Plasma Sheet Injections into the Inner Magnetosphere: Two-Way Coupled OpenGGCM-RCM Model Results. *J. Geophys. Res. Space Phys.* 122. doi:10.1002/2017ja024104

Delcourt, D. C., Sauvaud, J.-A., and Moore, T. E. (1997). Phase Bunching during Substorm Dipolarization. *J. Geophys. Res.* 102, 24313–24324. doi:10.1029/97ja02039

Dubyagin, S., Sergeev, V., Apatenkov, S., Angelopoulos, V., Runov, A., Nakamura, R., et al. (2011). Can Flow Bursts Penetrate into the Inner Magnetosphere?: FAST FLOW PENETRATION. *Geophys. Res. Lett.* 38. doi:10.1029/2011gl047016

Fuller-Rowell, T. J., Codrescu, M. V., Moffett, R. J., and Quegan, S. (1994). Response of the Thermosphere and Ionosphere to Geomagnetic Storms. *J. Geophys. Res.* 99, 3893–3914. doi:10.1029/93ja02015

Gabrielse, C., Angelopoulos, V., Harris, C., Artemyev, A., Kepko, L., and Runov, A. (2017). Extensive Electron Transport and Energization via Multiple, Localized Dipolarizing Flux Bundles. *J. Geophys. Res. Space Phys.* 122, 5059–5076. doi:10.1002/2017ja023981

Gabrielse, C., Harris, C., and Angelopoulos, V. (2016). The Role of Localized Inductive Electric fields in Electron Injections Around Dipolarizing Flux Bundles. *Physics, Geology.* 16 doi:10.1002/2016ja023061

Gabrielse, C., Spanswick, E., Artemyev, A., Nishimura, Y., Runov, A., Lyons, L., et al. (2019). Utilizing the Heliophysics/Geospace System Observatory to Understand Particle Injections: Their Scale Sizes and Propagation Directions. *J. Geophys. Res. Space Phys.* 124, 5584–5609. doi:10.1029/2018ja025588

Gkioulidou, M., Ohtani, S., Ukhorskiy, A. Y., Mitchell, D. G., Takahashi, K., Spence, H. E., et al. (2019). Low-Energy (. *J. Geophys. Res. Space Phys.* 124, 405–419. doi:10.1029/2018ja025862

Gkioulidou, M., Ukhorskiy, A. Y., Mitchell, D. G., Sotirelis, T., Mauk, B. H., and Lanzerotti, L. J. (2014). The Role of Small-Scale Ion Injections in the Buildup of Earth's Ring Current Pressure: Van Allen Probes Observations of the 17 March 2013 Storm. *J. Geophys. Res. Space Phys.* 119, 7327–7342. doi:10.1002/2014ja020096

Hamilton, D. C., Gloeckler, G., Ipavich, F. M., Stüdemann, W., Wilken, B., and Kremser, G. (1988). Ring Current Development during the Great Geomagnetic Storm of February 1986. *J. Geophys. Res.* 93, 14343–14355. doi:10.1029/ja093ia12p14343

Ilie, R., Skoug, R. M., Funsten, H. O., Liemohn, M. W., Bailey, J. J., and Gruntman, M. (2013). The Impact of Geocoronal Density on Ring Current Development. *J. Atmos. Solar-Terrestrial Phys.* 99, 92–103. doi:10.1016/j.jastp.2012.03.010

Jaynes, A. N., Baker, D. N., Singer, H. J., Rodriguez, J. V., Loto'aniu, T. M., Ali, A. F., et al. (2015). Source and Seed Populations for Relativistic Electrons: Their Roles in Radiation belt Changes. *J. Geophys. Res. Space Phys.* 120, 7240–7254. doi:10.1002/2015ja021234

Jordanova, V. K. (2020). "Ring Current Decay," in *Ring Current Investigations*. Editors V. K. Jordanova, R. Ilie, and M. W. Chen (Elsevier), 181–223. doi:10.1016/B978-0-12-815571-4.00006-8

Keesee, A. M., Buzulukova, N., Mouikis, C., and Scime, E. E. (2021). Mesoscale Structures in Earth's Magnetotail Observed Using Energetic Neutral Atom Imaging. *Geophys. Res. Lett.* 48. doi:10.1029/2020gl091467

Keika, K., Kistler, L. M., and Brandt, P. C. (2013). Energization of O+ Ions in the Earth's Inner Magnetosphere and the Effects on Ring Current Buildup: A Review of Previous Observations and Possible Mechanisms. *J. Geophys. Res. Space Phys.* 118, 4441–4464. doi:10.1002/jgra.50371

Kim, H.-S., Lee, D.-Y., Ohtani, S., Park, M.-Y., and Ahn, B.-H. (2012). On Near-Tail Bubble Penetration into Geosynchronous Altitude. *J. Geophys. Res.* 117, a–n. doi:10.1029/2012ja017749

Lemon, C., Wolf, R. A., Hill, T. W., Sazykin, S., Spiro, R. W., Toffoletto, F. R., et al. (2004). Magnetic Storm Ring Current Injection Modeled with the Rice Convection Model and a Self-Consistent Magnetic Field. *Geophys. Res. Lett.* 31, a–n. doi:10.1029/2004gl020914

Li, J., Wang, W., Lu, J., Yue, J., Burns, A. G., Yuan, T., et al. (2019). A Modeling Study of the Responses of Mesosphere and Lower Thermosphere Winds to Geomagnetic Storms at Middle Latitudes. *J. Geophys. Res. Space Phys.* 124, 3666–3680. doi:10.1029/2019ja026533

Lin, Y., Wang, X. Y., Fok, M. C., Buzulukova, N., Perez, J. D., Cheng, L., et al. (2021). Magnetotail-Inner Magnetosphere Transport Associated with Fast Flows Based on Combined Global-Hybrid and CIMI Simulation. *J. Geophys. Res. Space Phys.* 126. doi:10.1029/2020ja028405

Lin, Y., Wing, S., Johnson, J. R., Wang, X. Y., Perez, J. D., and Cheng, L. (2017). Formation and Transport of Entropy Structures in the Magnetotail Simulated with a 3-D Global Hybrid Code. *Geophys. Res. Lett.* 44, 5892–5899. doi:10.1002/2017gl073957

Lindsay, B. G., and Stebbings, R. F. (2005). Charge Transfer Cross Sections for Energetic Neutral Atom Data Analysis. *J. Geophys. Res.* 110, A12213. doi:10.1029/2005ja011298

Liu, J., Angelopoulos, V., Runov, A., and Zhou, X.-Z. (2013). On the Current Sheets Surrounding Dipolarizing Flux Bundles in the Magnetotail: The Case for Wedgelets. *J. Geophys. Res. Space Phys.* 118, 2000–2020. doi:10.1002/jgra.50092

Liu, Y. H., Birn, J., Daughton, W., Hesse, M., and Schindler, K. (2014). Onset of Reconnection in the Near Magnetotail: Pic Simulations. *J. Geophys. Res. Space Phys.* 119, 9773–9789. doi:10.1002/2014JA020492

Lu, G., Richmond, A. D., Lühr, H., and Paxton, L. (2016). High-latitude Energy Input and its Impact on the Thermosphere. *J. Geophys. Res. Space Phys.* 121, 7108–7124. doi:10.1002/2015ja022294

Lyon, J. G., Fedder, J. A., and Mobarry, C. M. (2004). The Lyon-Fedder-Mobarry (LFM) Global MHD Magnetospheric Simulation Code. *J. Atmos. Solar-Terrestrial Phys.* 66, 1333–1350. doi:10.1016/j.jastp.2004.03.020

Mauk, B. H., and McIlwain, C. E. (1974). Correlation ofKpwith the Substorm-Injected Plasma Boundary. *J. Geophys. Res.* 79, 3193–3196. doi:10.1029/ja079i022p03193

Merkin, V. G., Panov, E. V., Sorathia, K., and Ukhorskiy, A. (2019). Contribution of Bursty Bulk Flows to the Global Dipolarization of the Magnetotail during an Isolated Substorm. *J. Geophys. Res. Space Phys.* 19. doi:10.1029/2019ja026872

Merkin, V., and Lyon, J. (2010). Effects of the Low-Latitude Ionospheric Boundary Condition on the Global Magnetosphere. *J. Geophys. Res. Space Phys.* 115. doi:10.1029/2010ja015461

Moebius, E., Scholer, M., Klecker, B., Hovestadt, D., and Gloeckler, G. (1987). Acceleration of Ions of Ionospheric Origin in the Plasma Sheet during Substorm Activity. 231–234.

Nakamura, R., Baumjohann, W., Mouikis, C., Kistler, L. M., Runov, A., Volwerk, M., et al. (2004). Spatial Scale of High-Speed Flows in the Plasma Sheet Observed by Cluster. *Geophys. Res. Lett.* 31, a–n. doi:10.1029/2004gl019558

Nosé, M., Lui, A. T. Y., Ohtani, S., Mauk, B. H., McEntire, R. W., Williams, D. J., et al. (2000). Acceleration of Oxygen Ions of Ionospheric Origin in the Near-Earth Magnetotail during Substorms. *J. Geophys. Res.* 105 (1978–2012), 7669–7677. doi:10.1029/1999ja000318

Nosé, M., Taguchi, S., Hosokawa, K., Christon, S. P., McEntire, R. W., Moore, T. E., et al. (2005). Overwhelming O+contribution to the Plasma Sheet Energy Density during the October 2003 Superstorm: Geotail/EPIC and IMAGE/LENA Observations. *J. Geophys. Res.* 110 (1978–2012), 110. doi:10.1029/2004ja010930

Ohtani, S.-I., Shay, M. A., and Mukai, T. (2004). Temporal Structure of the Fast Convective Flow in the Plasma Sheet: Comparison between Observations and Two-Fluid Simulations. *J. Geophys. Res.* 109, A03210. doi:10.1029/2003ja010002

Ohtani, S., and Motoba, T. (2017). Equatorial Magnetic Field of the Near-Earth Magnetotail. *J. Geophys. Res. Space Phys.* 122, 8462–8478. doi:10.1002/2017ja024115

Ohtani, S., Nosé, M., Christon, S. P., and Lui, A. T. Y. (2011). Energetic O+and H+ions in the Plasma Sheet: Implications for the Transport of Ionospheric Ions. *J. Geophys. Res.* 116, a–n. doi:10.1029/2011ja016532

Østgaard, N., Mende, S. B., Frey, H. U., Gladstone, G. R., and Lauche, H. (2003). Neutral Hydrogen Density Profiles Derived from Geocoronal Imaging. *J. Geophys. Res.* 108 (1978–2012), 108. doi:10.1029/2002ja009749

Pembroke, A., Toffoletto, F., Sazykin, S., Wiltberger, M., Lyon, J., Merkin, V., et al. (2012). Initial Results from a Dynamic Coupled Magnetosphere-Ionosphere-Ring Current Model. *J. Geophys. Res.* 117, a–n. doi:10.1029/2011ja016979

Pontius, D. H., and Wolf, R. A. (1990). Transient Flux Tubes in the Terrestrial Magnetosphere. *Geophys. Res. Lett.* 17, 49–52. ISSN 0094-8276. doi:10.1029/gl017i001p00049

Raeder, J., McPherron, R. L., Frank, L. A., Kokubun, S., Lu, G., Mukai, T., et al. (2001). Global Simulation of the Geospace Environment Modeling Substorm challenge Event. *J. Geophys. Res.* 106, 381–395. doi:10.1029/2000ja000605

Ripoll, J. F., Claudepierre, S. G., Ukhorskiy, A. Y., Colpitts, C., Li, X., Fennell, J. F., et al. (2020). Particle Dynamics in the Earth's Radiation Belts: Review of Current Research and Open Questions. *J. Geophys. Res. Space Phys.* 125. doi:10.1029/2019ja026735

Roelof, E. C. (1989). Remote Sensing of the Ring Current Using Energetic Neutral Atoms. *Adv. Space Res.* 9, 195–203. doi:10.1016/0273-1177(89)90329-3

Rosenbluth, M. N., and Longmire, C. L. (1957). Stability of Plasmas Confined by Magnetic fields. *Ann. Phys.* 1, 120–140. doi:10.1016/0003-4916(57)90055-6

Runov, A., Angelopoulos, V., Artemyev, A., Birn, J., Pritchett, P. L., and Zhou, X. Z. (2017). Characteristics of Ion Distribution Functions in Dipolarizing Flux Bundles: Event Studies. *J. Geophys. Res. Space Phys.* 122, 5965–5978. doi:10.1002/2017ja024010

Runov, A., Angelopoulos, V., Gabrielse, C., Liu, J., Turner, D. L., and Zhou, X. Z. (2015). Average Thermodynamic and Spectral Properties of Plasma in and Around Dipolarizing Flux Bundles. *J. Geophys. Res. Space Phys.* 120, 4369–4383. doi:10.1002/2015ja021166

Sadeghzadeh, S., Yang, J., Wang, C. P., Mousavi, A., Wang, W., Sun, W., et al. (2021). Effects of Bubble Injections on the Plasma Sheet Configuration. *J. Geophys. Res. Space Phys.* 126. doi:10.1029/2021ja029127

Sergeev, V. A., Gordeev, E. I., Merkin, V. G., and Sitnov, M. I. (2018). Does a Local B-Minimum Appear in the Tail Current Sheet during a Substorm Growth Phase?. *Geophys. Res. Lett.* 45, 2566–2573. doi:10.1002/2018gl077183

Sitnov, M., Birn, J., Ferdousi, B., Gordeev, E., Khotyaintsev, Y., Merkin, V., et al. (2019). Explosive Magnetotail Activity. *Space Sci. Rev.* 215, 31. doi:10.1007/s11214-019-0599-5

Smith, P. H., and Bewtra, N. K. (1976). Dependence of the Charge Exchange Lifetimes on Mirror Latitude. *Geophys. Res. Lett.* 3, 689–692. doi:10.1029/gl003i011p00689

Snicker, A., Kurki-Suonio, T., and Sipila, S. K. (2010). Realistic Simulations of Fast-Ion Wall Distribution Including Effects Due to Finite Larmor Radius. *IEEE Trans. Plasma Sci.* 38, 2177–2184. doi:10.1109/tps.2010.2056705

Sorathia, K. A., Merkin, V. G., Panov, E. V., Zhang, B., Lyon, J. G., Garretson, J., et al. (2020). Ballooning-Interchange Instability in the Near-Earth Plasma Sheet and Auroral Beads: Global Magnetospheric Modeling at the Limit of the MHD Approximation. *Geophys. Res. Lett.* 47 18. doi:10.1029/2020gl088227

Sorathia, K. A., Merkin, V. G., Ukhorskiy, A. Y., Allen, R. C., Nykyri, K., and Wing, S. (2019). Solar Wind Ion Entry into the Magnetosphere during Northward Imf. *J. Geophys. Res. Space Phys.* 124, 5461–5481. doi:10.1029/2019ja026728

Sorathia, K. A., Merkin, V. G., Ukhorskiy, A. Y., Mauk, B. H., and Sibeck, D. G. (2017). Energetic Particle Loss through the Magnetopause: A Combined Global MHD and Test-Particle Study. *J. Geophys. Res. Space Phys.* 122, 9329–9343. doi:10.1002/2017ja024268

Sorathia, K. A., Ukhorskiy, A. Y., Merkin, V. G., Fennell, J. F., and Claudepierre, S. G. (2018). Modeling the Depletion and Recovery of the Outer Radiation Belt during a Geomagnetic Storm: Combined MHD and Test Particle Simulations. *J. Geophys. Res. Space Phys.* 123, 5590–5609. doi:10.1029/2018ja025506

Sorathia, K., Ukhorskiy, A. Y., and Merkin, V. G. (2018). The Role of Mesoscale Electrodynamics in Ring Current Evolution: Global MHD and Test Particle Simulations. In AGU Fall Meeting Abstracts. vol. 2018,, 2018 SM22A–06.

Stone, J. M., Gardiner, T. A., Teuben, P., Hawley, J. F., and Simon, J. B. (2008). Athena: A New Code for Astrophysical MHD. *Astrophys J. Suppl. S* 178, 137–177. doi:10.1086/588755

Toffoletto, F. (2020). "Modeling Techniques," in *Ring Current Investigations*. Editors V. K. Jordanova, R. Ilie, and M. W. Chen (Elsevier), 99–151. doi:10.1016/B978-0-12-815571-4.00004-4

Toffoletto, F. R., Wolf, R. A., and Schutza, A. M. (2020). Buoyancy Waves in Earth's Nightside Magnetosphere: Normal-Mode Oscillations of Thin Filaments. *J. Geophys. Res. Space Phys.* 125, 17–20. doi:10.1029/2019ja027516

Turner, D. L., Fennell, J. F., Blake, J. B., Claudepierre, S. G., Clemmons, J. H., Jaynes, A. N., et al. (2017). Multipoint Observations of Energetic Particle Injections and Substorm Activity during a Conjunction between Magnetospheric Multiscale (MMS) and Van Allen Probes. *J. Geophys. Res. Space Phys.* 122, 11,481–11,504. doi:10.1002/2017ja024554

Ukhorskiy, A. Y., Sitnov, M. I., Merkin, V. G., Gkioulidou, M., and Mitchell, D. G. (2017). Ion Acceleration at Dipolarization Fronts in the Inner Magnetosphere. *J. Geophys. Res. Space Phys.* 122, 3040–3054. doi:10.1002/2016ja023304

Ukhorskiy, A. Y., Sorathia, K., Merkin, V. G., Sitnov, M. I., Mitchell, D. G., and Gkioulidou, M. (2018). Ion Trapping and Acceleration at Dipolarization Fronts: High-Resolution MHD and Test-Particle Simulations. *J. Geophys. Res. Space Phys.* 27, 1–5589. doi:10.1029/2018ja025370

Wang, W., Lei, J., Burns, A. G., Solomon, S. C., Wiltberger, M., Xu, J., et al. (2010). Ionospheric Response to the Initial Phase of Geomagnetic Storms: Common Features. *J. Geophys. Res. Space Phys.* 115. doi:10.1029/2009ja014461

Wiltberger, M., Merkin, V., Lyon, J. G., and Ohtani, S. (2015). High-resolution Global Magnetohydrodynamic Simulation of Bursty Bulk Flows. *J. Geophys. Res. Space Phys.* 120, 4555–4566. doi:10.1002/2015ja021080

Wolf, R. A., Kumar, V., Toffoletto, F. R., Erickson, G. M., Savoie, A. M., Chen, C. X., et al. (2006). Estimating Local Plasma sheetPV5/3from Single-Spacecraft Measurements. *J. Geophys. Res.* 111. doi:10.1029/2006ja012010

Yang, J., Toffoletto, F. R., and Song, Y. (2010). Role of Depleted Flux Tubes in Steady Magnetospheric Convection: Results of RCM-E Simulations. *J. Geophys. Res.* 115, a–n. doi:10.1029/2010ja015731

Yang, J., Toffoletto, F. R., Wolf, R. A., and Sazykin, S. (2015). On the Contribution of Plasma Sheet Bubbles to the Storm Time Ring Current. *J. Geophys. Res. Space Phys.* 120, 7416–7432. doi:10.1002/2015ja021398

Yang, J., Toffoletto, F. R., Wolf, R. A., and Sazykin, S. (2011). RCM-E Simulation of Ion Acceleration during an Idealized Plasma Sheet Bubble Injection. *J. Geophys. Res.* 116, 4027. doi:10.1029/2010ja016346

Zhang, B., Sorathia, K. A., Lyon, J. G., Merkin, V. G., Garretson, J. S., and Wiltberger, M. (2019). Gamera: A Three-Dimensional Finite-Volume Mhd Solver for Non-orthogonal Curvilinear Geometries. *ApJS* 244, 20. doi:10.3847/1538-4365/ab3a4c

Conflict of Interest: The authors declare that the research was conducted in the absence of any commercial or financial relationships that could be construed as a potential conflict of interest.

Publisher's Note: All claims expressed in this article are solely those of the authors and do not necessarily represent those of their affiliated organizations, or those of the publisher, the editors and the reviewers. Any product that may be evaluated in this article, or claim that may be made by its manufacturer, is not guaranteed or endorsed by the publisher.

Copyright © 2021 Sorathia, Michael, Merkin, Ukhorskiy, Turner, Lyon, Garretson, Gkioulidou and Toffoletto. This is an open-access article distributed under the terms of the Creative Commons Attribution License (CC BY). The use, distribution or reproduction in other forums is permitted, provided the original author(s) and the copyright owner(s) are credited and that the original publication in this journal is cited, in accordance with accepted academic practice. No use, distribution or reproduction is permitted which does not comply with these terms.

frontiers in Astronomy and Space Sciences

ORIGINAL RESEARCH
published: 05 November 2021
doi: 10.3389/fspas.2021.728531

Links of the Plasmapause With Other Boundary Layers of the Magnetosphere: Ionospheric Convection, Radiation Belt Boundaries, Auroral Oval

V. Pierrard[1,2]*, *E. Botek*[1], *J.-F. Ripoll*[3,4], *S. A. Thaller*[5], *M. B. Moldwin*[6], *M. Ruohoniemi*[7] and *G. Reeves*[8]

[1]Solar Terrestrial Center of Excellence, Space Physics, Royal Belgian Institute for Space Aeronomy, Brussels, Belgium, [2]Center for Space Radiations (CSR) and Georges Lemaître Centre for Earth and Climate Research (TECLIM), Earth and Life Institute (ELI), Université Catholique de Louvain (UCLouvain), Louvain-La-Neuve, Belgium, [3]CEA, DAM, DIF, Arpajon, France, [4]UPS, CEA, LMCE, Bruyères-le-Châtel, France, [5]Laboratory for Atmospheric and Space Physics, University of Colorado, Boulder, CO, United States, [6]University of Michigan-Ann Arbor, Ann Arbor, MI, United States, [7]SuperDARN Laboratory, Blacksburg, VA, United States, [8]Los Alamos Nat. Lab., Mexico, VA, United States

OPEN ACCESS

Edited by:
Philip J Erickson,
Massachusetts Institute of Technology, United States

Reviewed by:
Nickolay Ivchenko,
Royal Institute of Technology, Sweden
Binbin Ni,
Wuhan University, China
Jerry Goldstein,
Southwest Research Institute (SwRI), United States

***Correspondence:**
V. Pierrard
viviane.pierrard@aeronomie.be

Specialty section:
This article was submitted to Space Physics, a section of the journal Frontiers in Astronomy and Space Sciences

Received: 21 June 2021
Accepted: 18 October 2021
Published: 05 November 2021

Citation:
Pierrard V, Botek E, Ripoll J-F, Thaller SA, Moldwin MB, Ruohoniemi M and Reeves G (2021) Links of the Plasmapause With Other Boundary Layers of the Magnetosphere: Ionospheric Convection, Radiation Belt Boundaries, Auroral Oval. Front. Astron. Space Sci. 8:728531. doi: 10.3389/fspas.2021.728531

The plasmapause marks the limit of the plasmasphere and is characterized by a sudden change in plasma density. This can influence the other regions of the magnetosphere, including due to different waves circulating inside and outside the plasmasphere. In the present work, we first compare the positions of the plasmapause measured by the NASA Van Allen Probes in 2015 with those of the Space Weather Integrated Forecasting Framework plasmasphere model (SPM). Using the Van Allen Probes and other satellite observations like PROBA-V, we investigate the links that can exist with the radiation belt boundaries. The inward motion of the outer radiation belt associated with sudden flux enhancements of energetic electrons can indeed be directly related to the plasmapause erosion during geomagnetic storms, suggesting possible links. Moreover, the position of the plasmapause projected in the ionosphere is compared with the ionospheric convection boundary. The equatorward motion of the plasmapause projected in the ionosphere is related to the equatorward edge motion of the auroral oval that goes to lower latitudes during storms due to the geomagnetic perturbation, like the low altitude plasmapause and the outer radiation belt. The links between these different regions are investigated during quiet periods, for which the plasmasphere is widely extended, as well as during geomagnetic storms for which plumes are generated, and then afterwards rotates with the plasmasphere. The magnetic local time dependence of these boundaries is especially studied on March 14, 2014 after a sudden northward turning of the interplanetary magnetic field (IMF) and for the geomagnetic storm of August 26, 2018, showing the importance of the magnetic field topology and of the convection electric field in the interactions between these different regions eventually leading to the coupling between magnetosphere and ionosphere.

Keywords: plasmapause, ionospheric convection, radiation belts, auroral oval, boundaries, magnetosphere, plasmasphere, geomagnetic storm

INTRODUCTION

The plasmasphere is the extension of the ionosphere at low and mid-latitudes and is filled by low energy plasma (Lemaire and Gringauz, 1998; Darrouzet et al., 2009 for reviews). Plasmaspheric ion temperature is species dependent, with H^+ and He^+ typically in the range 0.1–1 eV and O^+ warmer in the range 1–10 eV (Comfort et al., 1985; Comfort, 1996; Goldstein et al., 2019). The outer surface of the plasmasphere is often characterized by a "knee", i.e., a sharp decrease of the plasma density: the plasmapause (Carpenter, 1963). Depending on the strength of the level of geomagnetic activity, usually parameterized or measured by the value of the Kp index (Bartels and Veldkamp, 1949), the equatorial position of the observed plasmapause can change from 7 Re to 2 Re, for low and high activity respectively (e.g., Pierrard et al., 2009 for a review). Analyses of ground-based whistler waves and *in situ* satellite observations of the cold plasma density show that the plasmapause forms closer to Earth when the geomagnetic activity level is enhanced (e.g., Pierrard and Cabrera, 2005). Above the plasmapause, the region of the plasmaspheric trough is characterized by much lower densities, generally below 10 cm^{-3}.

The plasmapause boundary plays an important role in magnetospheric dynamics. In the present article, we study the links and possible coupled feedback mechanisms of the plasmapause with three other regions of the magnetosphere, i.e., the ionosphere, the radiation belts and the auroral oval. These regions and their interactions in the magnetosphere are described, for instance, in the review paper of Borovsky and Valdivia (2018) and in the book chapter of Fuselier et al. (2019).

Links between the inner edge of the outer radiation belt electrons and the innermost plasmapause location were first reported by Li et al. (2006) by using 12 years of 30-days averaged measurements of MeV electrons from both CRRES and SAMPEX satellites. The study was recently revisited in Khoo et al. (2018) with focus on storms. Links between the inner edge of the outer radiation belt and the plasmapause were also identified with previous observations from the LEO satellite SAC-C (Pierrard and Benck, 2012) and with CLUSTER (Darrouzet et al., 2013). Goldstein et al. (2016) quantified the outer belt and plasmapause position for the 5-day period of 15–20 January 2013 and found that for this event, electron fluxes earthward of belt's peak are anti-correlated with cold plasma density. Here we will investigate such links using the Van Allen Probes and PROBA-V data, as well as some models.

We also study the links between the Magnetic Local Time (MLT) distribution of the plasmapause, the ionospheric convection boundary (using SuperDARN), the radiation belts for different energies from 10 keV to 8 MeV, and the auroral oval during two specific events: March 14, 2014 corresponding to a quiet period with a sudden Northward turning of the IMF, and August 26, 2018 corresponding to a geomagnetic storm. We start in *Data and Models* with the description of the satellite data and models used. In *Long Term Variations of the Plasmapause: Comparison Between Observations and the Space Weather Integrated Forecasting Framework plasmasphere model Model*, we compare the plasmapause observed by two satellites (Van Allen Probes and CRRES) with the plasmapause positions obtained from the dynamical SPM model (Pierrard and Lemaire, 2004). We show that long term plumes observed during long storm periods are reproduced by the model. Then, we discuss the long-term links of the plasmapause with the other regions of the magnetosphere, and especially with the radiation belts in *Links Between the Plasmapause and the Radiation Belt Boundaries* before analyzing specific cases. In *Links Between the Plasmapause, Ionospheric Convection Boundary, Radiation Belts and Auroral Oval During a Quiet Period: March 14, 2014*, we analyze the quiet period of March 14, 2014 to determine the relations between the radial distance, the latitude, and the MLT distribution of the plasmapause, the ionospheric convection boundary, the radiation belt boundaries and the auroral oval. In *Links Between the Plasmapause, Ionospheric Convection Boundary, Radiation Belts and Auroral Oval During the Storm Event of August 26, 2018*, we show the evolution of these links during the geomagnetic storm of August 26, 2018, and show the strong decrease in latitude of all these boundaries during the main phase of the storm in the framework of the global magnetospheric dynamics and its effects on the ionosphere-atmosphere. The links between the different boundaries and their MLT distribution are discussed in *Discussion About the Links Between the Boundaries and Their the Magnetic Local Time Distribution* and the results of the present work are summarized in the concluding section.

DATA AND MODELS

Satellite and Radar Data

Van Allen Probes

Data from the Van Allen Probes mission (Mauk et al., 2013) are used in this study. The NASA Van Allen Probes mission, formerly called RBSP (Radiation Belt Storm *Probes* A and B) was launched in 2012, enabling unprecedented studies of the electron radiation belt variability in response to solar activity. The two spacecraft of the Van Allen Probes mission flew on a low inclination (<20°) elliptical orbit ranging from 600 to 30,600 km. We will use three of the Van Allen Probes mission instruments, enabling us simultaneous observations of the radiation belts and the plasmapause. A review of recent radiation belt studies involving Van Allen Probes data is available in Ripoll J. F. et al. (2020).

The NASA Van Allen Probes have four magnetic spectrometers aboard each of the two spacecraft, one low-energy unit (20–240 keV), two medium-energy units (80–1,200 keV), and a high-energy unit (800–4,800 keV), which compose the MagEIS (Magnetic Electron Ion Spectrometer) instrument used to measure the radiation belt flux. MagEIS data are background corrected (Claudepierre et al., 2015). This instrument is part the Energetic Particle, Composition, and Thermal Plasma (ECT) suite (Spence et al., 2013), which combines the HOPE (Funsten et al., 2013), MagEIS (Blake et al., 2013), and REPT (Baker et al., 2012) instruments. We use the Level 2 ECT flux combined data (Boyd et al., 2019) which combine the data of these three instruments to bring a view

of the radiation belt flux over the whole energy range. This study makes also use of data from the Electric and Magnetic Field Instrument Suite and Integrated Science (EMFISIS) instrument suite (Kletzing et al., 2013) and the Electric Fields and Waves instrument (Wygant et al., 2013). Their measurement of electromagnetic waves allows the deduction of the cold plasma electron density and, then, the deduction of the plasmapause position.

PROBA-V/EPT Data

We use the Energetic Particle Telescope (EPT) on board the ESA PROBA-V satellite to provide radiation belt electron flux. PROBA-V operated simultaneously with the Van Allen Probes from 2013 to 2019, so that both data sets allow direct comparison of the electron radiation belt variability in response to solar activity. The EPT instrument has been developed to obtain the best discrimination between the particle species and determine uncontaminated particle spectra useful for space weather predictions (Cyamukungu et al., 2014). It was launched on May 7, 2013 to a polar orbit at an altitude of 820 km onboard the ESA satellite PROBA-V with an inclination of 98.73°, an orbital rotation period of 101.21 min and 10:30 AM as nominal local time at the descending node (Pierrard et al., 2014). The detector measures the particle fluxes for seven virtual channels for electrons, 11 channels for protons and 11 channels for helium ions.

Combined Release and Radiation Effects Satellite Data

We make use of some of the data from the Combined Release and Radiation Effects Satellite (CRRES) (e.g., Johnson and Kierein, 1992). The CRRES mission took place between August 1990 and October 1991. We use the Moldwin et al. (2002) CRRES database for nearly 1,000 orbits of the observed plasmapause positions sorted by the maximum geomagnetic index Kp during the previous 12 h. The plasmapause locations were identified as the innermost sharp density gradient of at least a factor of five within a radial distance of 0.5 L.

Super Dual Auroral Radar Network Observations

We use the SuperDARN (Super Dual Auroral Radar Network) network consisting of more than 30 low-power high frequency (HF) radars that observe the Earth's upper atmosphere, beginning at mid-latitudes and extending into the polar regions (Ruohoniemi and Baker, 1998). SuperDARN serves to establish the ionospheric convection that, in part, defines the various boundaries we study.

Models

Plasmapause and Plasmasphere Model

Pierrard and Lemaire (2004) have developed a model for the formation of the plasmapause based on the influence of the convection electric field and the interchange instability mechanism. They showed that the plasmapause is formed in the post-midnight MLT sector (typically at MLT = 2h00) and is then propagated by co-rotation to other MLT sectors. This MLT dependence of the plasmapause was also confirmed by Bandic et al. (2016), Bandic et al. (2017) and Verbanac et al. (2018) with CRRES and THEMIS plasmapause observations. The plasmapause is related to Kp and Dst, as well as to other geomagnetic and solar wind indices (Verbanac et al., 2015).

The model has been improved to give not only the position of the plasmapause, but also the density and the temperature of the particles inside and outside the plasmasphere (Pierrard and Stegen, 2008). Later, it has been coupled to an ionosphere model (Pierrard and Voiculescu, 2011) in the framework of the SWIFF (Space Weather Integrated Forecasting Framework) project that allowed coupling of models for different regions of the magnetosphere (Lapenta et al., 2013). The SPM (SWIFF Plasmasphere model) provides daily nowcasts on the ESA SSA (Space Situational Awareness) website (https://swe.ssa.esa.int/space-radiation).

Auroral Oval Model

The OVATION (Oval Variation, Assessment, Tracking, Intensity, and Online Nowcasting) model is an empirical model of the intensity of the aurora (Newell et al., 2002, 2010; Machol et al., 2012). It gives a short-term forecast of the intensity of the auroral oval for both the Northern and the Southern hemispheres. It is based on the solar wind and IMF conditions as measured by the DSCOVR spacecraft. The OVATION model is used here to generate the intensity and location of the auroral oval in the Northern hemisphere for cases of quiet and disturbed periods.

Radiation Belt Model

We make use of the empirical radiation belt model AE-8MAX (Vette, 1991; Fung, 1996) to illustrate the meridian view of the radiation belt during maximum solar activity. This model incorporates satellite measurements that date back into the 1960s from many orbital regimes, e.g., low Earth orbit LEO, (middle) MEO, (high) HEO and (geostationary) GEO.

LONG TERM VARIATIONS OF THE PLASMAPAUSE: COMPARISON BETWEEN OBSERVATIONS AND THE SWIFF PLASMASPHERE MODEL

Van Allen Probes Plasmapause Observations

The EMFISIS instrument on board of Van Allen Probes measures the upper hybrid resonance frequency allowing us to determine the plasma density (Kurth et al., 2015). When EMFISIS density is unavailable, the density is derived from spacecraft floating potential data, which has been calibrated against previous plasma densities determined from the upper hybrid resonance frequency (Thaller et al., 2015). Spacecraft floating potential is measured by the Electric Fields and Waves (EFW) instrument (Wygant et al., 2013). Here, the plasmapause locations (Lpp) are computed from the spacecraft floating potential measured by EFW onboard Probe B of the Van Allen Probes and are equal to the first minimum L-shell at which the density drops below the 100 cm^{-3} level within a 4-h temporal bin (Ripoll et al., 2020, 2021).

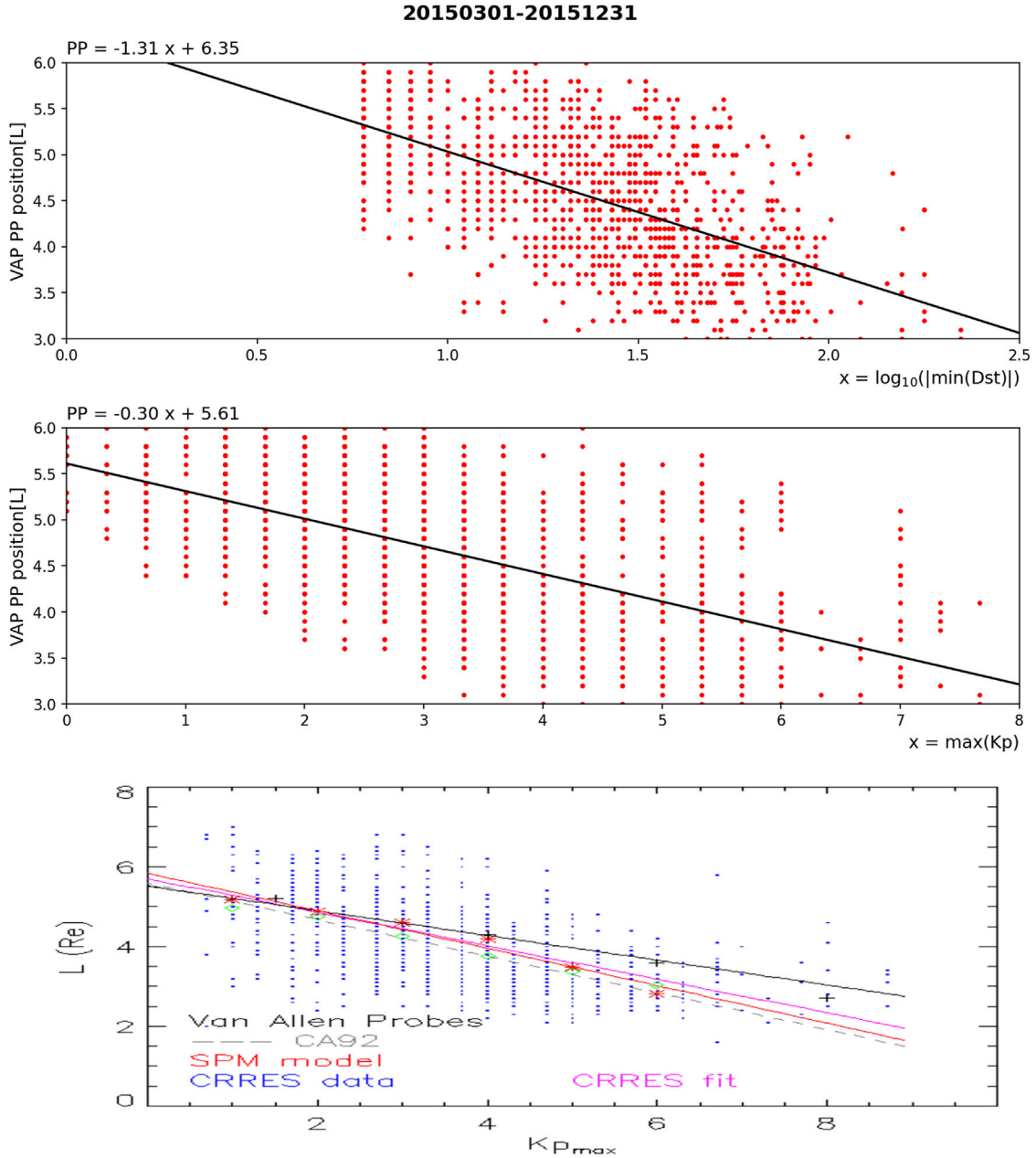


FIGURE 1 | Upper panel: Plasmapause observed by Probe B of the Van Allen Probes from 1-3-2015 to 31-12-2015 as a function of the logarithm of the minimum value of Dst observed during the previous 24 h. The best linear relation is provided by the black line for which the expression is shown above the panel. **Middle panel:** Same plasmapause observed by Probe B of the Van Allen Probes from 1-3-2015 to 31-12-2015 as a function of max (Kp) during the previous 24 h. The best linear relation is provided by the black line for which the expression is shown above the panel. **Bottom panel:** (Blue dots) Plasmapause Lpp observed by CRRES as a function of Kp maximum during the previous 12 h (Green diamonds) Averaged values of CRRES Lpp as a function of Kp. (Pink line) Plasmapause linear relation found by Moldwin et al. (2002) in the 21-03 h MLT sector. (Gray dashed line) Plasmapause linear relation found by Carpenter and Anderson (1992) from ISEE data. (Black crosses) Mean plasmapause measured by Van Allen Probes from 2012 to 2019 for four Kp ranges in the night side. (Black line) Plasmapause linear relation found in top panel with Van Allen Probes data from March to end December 2015. (Red stars) Plasmapause positions found with the SPM model as a function of Kp. (Red line) Plasmapause linear relation found with the SPM model.

This method allows us to determine the plasmapause location (Lpp) from 1-3-2015 to 31-12-2015 represented in **Figure 1** as a function of the logarithm of the minimum of Dst during the last 24 h (top panel). In the present study, we also determine the best linear relation for these data:

$$\mathrm{Lpp} = -1.31 \log 10\left|\min \mathrm{Dst}_{24h}\right| + 6.35 \quad (1)$$

with err (a) = 0.054 is the standard error on the regression coefficient, err (b) = 0.077 is the standard error on the constant and the Root Mean Square Error RMSE = 0.610. Even if the linear

trend is obvious, the dispersion is quite high. Here we have kept all MLT to have enough data for the fit. During this period, Van Allen Probes apogee varied from 21 MLT to 11 MLT and the outbound crossing of the L = 3 field line varied from 17 MLT to 7 MLT, making the above law representative of more dusk and day side plasmapause.

Similarly, we derive the expression of the plasmapause position for this same period as a function of Kp (middle panel) and find the best linear fit:

$$\mathrm{Lpp} = -0.30\left|\max \mathrm{Kp}_{24h}\right| + 5.61 \quad (2)$$

with lower errors err(a) = 0.010, err(b) = 0.036 and RMSE = 0.601.

Comparison With CRRES Satellite

These new results can be compared with previous observations and fits. Moldwin et al. (2002) selected in the database of CRRES observations all orbits where a sharp density gradient indicated the presence of a well-defined plasmapause. The L-value of the observed plasmapause positions were ranked according to the maximum geomagnetic index Kp during the previous 12 h. The bottom panel of **Figure 1** shows these plasmapause positions (blue dots) observed for all local time sectors as a function of the maximum value of Kp. The scatter of the observed values of Lpp is rather wide but there is a clear trend confirming that the plasmapause forms closer to the Earth when Kp is large. The green diamonds symbols in **Figure 1** correspond to the mean value of the observed plasmapause positions for $\mathrm{Kp}_{\mathrm{jmax}}$ between $\mathrm{Kp_j} - 0.4$ and $\mathrm{Kp_j} + 0.4$.

This trend is evidenced in all local time sectors, but the slope of this relationship is local time dependent (Moldwin et al., 2002). O'Brien and Moldwin (2003) determined linear fits of the average plasmapause locations as a function of Kp for four local time sectors for various time delays between 12 and 36 h. They found lower RMSE in the dawn and day sectors in comparison with dusk and night. Different studies have shown that it is around 2–3 h in MLT that the link between the plasmapause and geomagnetic indices is the clearest because it is the MLT sector where the plasmapause is formed due to a higher convection electric field (Pierrard and Cabrera, 2006; Reinisch et al., 2009). The linear relation found by Moldwin et al. (2002) in the MLT sector corresponding to 21-3 h is represented in magenta on **Figure 1** (bottom) and is given by:

$$\mathrm{Lpp} = -0.4204\,\mathrm{Kp}_{\max 12} + 5.704 \quad (3)$$

As a comparison, taking the Probe B of the Van Allen Probes mission in 09/2012–07/2019 in the night sector (21–3 h), we find that the mean plasmapause position (defined as the 100 #/cc level of the EFW density) is: Lpp = 2.7 for all events with Kp > 7, Lpp = 3.6 for Kp in]5,7], Lpp = 4.3 for Kp in]3,5], and Lpp = 5.2 for Kp < 3. These values are represented by the black crosses in **Figure 1** (bottom panel), and the linear relation **Eq. 2** that was found with the Van Allen Probes for 2015 is illustrated by the black line.

An empirical relationship between Lpp and Kp had also been deduced previously from ISEE one data for 0–15 LT (Carpenter and Anderson, 1992):

$$\mathrm{Lpp} = -0.46\,\mathrm{Kp}_{\max 24} + 5.6 \quad (4)$$

where $\mathrm{Kp}_{\mathrm{max24}}$ is the maximum value during the preceding 24 h. This best fit linear relationship is shown by the gray dashed line in the bottom panel of **Figure 1**.

Other authors have derived empirical relations between the plasmapause equatorial distance (Lpp), and a variety of geomagnetic indices such as Kp, Dst or AE. O'Brien and Moldwin (2003) for instance used CRRES data for all MLT and found:

$$\mathrm{Lpp} = -1.57\mathrm{Log10}\left|\min \mathrm{Dst}_{24h}\right| + 6.3. \quad (5)$$

The large dispersion of the measurements from the linear fits (clearly visible in **Figure 1**) highlights that any plasmapause prediction based only on such linear relation could differ by up to 1 $\mathrm{R_E}$ from the actual locations depending on the events. A more sophisticated model is thus necessary for predictions, as the SPM model that takes into account the MLT dependence of the plasmapause and uses the historical variation of the Kp index during the 24 previous hours instead of its maximum value only.

Modeling the Plasmapause Position

The red stars in the bottom panel of **Figure 1** show the theoretical plasmapause position $\mathrm{M_j}$ determined by our numerical SPM model (Pierrard and Lemaire, 2004) for a set of stationary values of the Kp index ranging from one to 6. They correspond to the average position of the plasmapause predicted by the theoretical model based on the mechanism of plasma interchange driven unstable by the enhancement of centrifugal effects and using McIlwain's Kp-dependent electric field model E5D and his M2 equatorial magnetic field model to calculate the magnetospheric convection velocity (Pierrard and Stegen, 2008). The plasmapause position in the SPM model depends on the historical evolution of the geomagnetic index Kp during the previous days. The plasmapause is formed at MLT = 2 and is transmitted to other MLT sectors due to the plasma motion dominated almost entirely by corotation. It is thus necessary to have the Kp evolution during at least 24 h to determine the plasmapause in all MLT sectors. In **Figure 1**, stationary values of Kp during the previous 24 h are used to obtain the plasmapause position averaged on all MLT in the model.

We find with the model a best linear relation (red line on bottom panel of **Figure 1**) corresponding to

$$\mathrm{Lpp} = -0.47\,\mathrm{Kp} + 5.84 \quad (6)$$

This relation based on averaged values can be used for long term comparisons, but the actual plasmapause positions given by the model are of course more precise since they take into account the historical evolution of Kp during the previous hours and the MLT sector of the plasmapause observation.

Discussion About the Long Term Plasmapause

The linear fits of the equatorial plasmapause positions versus Kp that are shown in the bottom panel of **Figure 1** (Van Allen Probes black **Eq. 2**, CRRES magenta **Eq. 3**, ISEE1 gray **Eq. 4**, SPM model

red **Eq. 6**) are rather similar for the satellite observations and the model. The slope for the Van Allen Probes data is lower than the others. This is probably due to the lower number of observations and to the fact that the computation is not restricted to the night side. In comparison, the four mean plasmapause positions (black crosses) given as a function of Kp established over the whole Van Allen Probes mission and restricted to the night side are closer to the other observations and models. The large scatter of the experimental data indicates that the actual plasmapause is a rather irregular and dynamic surface (cf. density plots for the case study in *Links Between the Plasmapause, Ionospheric Convection Boundary, Radiation Belts and Auroral Oval During a Quiet Period: March 14, 2014 and Links Between the Plasmapause, Ionospheric Convection Boundary, Radiation Belts and Auroral Oval During the Storm Event of August 26, 2018*). It indicates that simulations based on quasi-stationary E-field models with a 3-h time resolution may grasp the general trend but not the small dynamical features. Furthermore, the position of the plasmapause does not depend only on the value of Kp, but is also influenced by the history of the short time variations of the magnetospheric electric and magnetic fields (Pierrard et al., 2008). Moreover, as shown in the next section, the MLT sector can play an important role as the plasmapause can be very asymmetric, especially during geomagnetic storms and substorms, when plumes are created in the afternoon-dusk MLT sector.

Long Term Plumes

Large scale structures like plasmaspheric plumes are reproduced by the SPM numerical simulations as a result of enhancements of the overall convection velocities correlated with enhanced geomagnetic activity (Pierrard and Lemaire, 2004). The plumes rotate with the plasmasphere and are not only confined in the dusk sector, as in the ideal MHD simulation of Grebowsky (1970). Plume merging is one theoretical way of generating fine plasmaspheric structure from successive layers of wrapped residual plumes which merge with newer plumes, creating on the long term layers of filamentary density structure over multiple cycles (e.g., Goldstein et al., 2003; Sandel et al., 2003). In our dynamical model, plumes are convected around the Earth as indeed observed by the EUV/IMAGE experiment (Spasojevic et al., 2004; Pierrard and Cabrera, 2005, 2006; Darrouzet et al., 2006).

The SPM model can determine the plasmapause and the plasmaspheric density for any date. Only the knowledge of the Kp index for the 24 h before the date to be simulated is required to determine the position of the plasmapause at any MLT during stormy periods. This does not mean that plumes generated during storms do not have long term duration. Plumes can remain visible during several days, as we now discuss.

Figure 2 shows the results of the SPM density and plasmapause model for the period of May 1, 1994 to May 7, 1994 at different universal times (UT). For this period, Borovsky et al. (2014) reported observations of long duration plumes from the spacecraft 1989–046 at geosynchronous orbit. They observed dense plasmaspheric plasma advecting sunward toward the dayside magnetopause during more than 10 days. Such long-term plume is reproduced by the SPM model, as visible by the tails appearing in the afternoon MLT sector in the bottom of the left panels of **Figure 2**. The model shows that it is due to Kp remaining very high all along this 10-day period, always above Kp = 4 (cf. top panels of **Figure 2**) as soon as the first expansion on May 1, 1994 occurred.

Note that a longer period of historical evolution of Kp than 24 h is necessary in the most recent version of the model (Pierrard

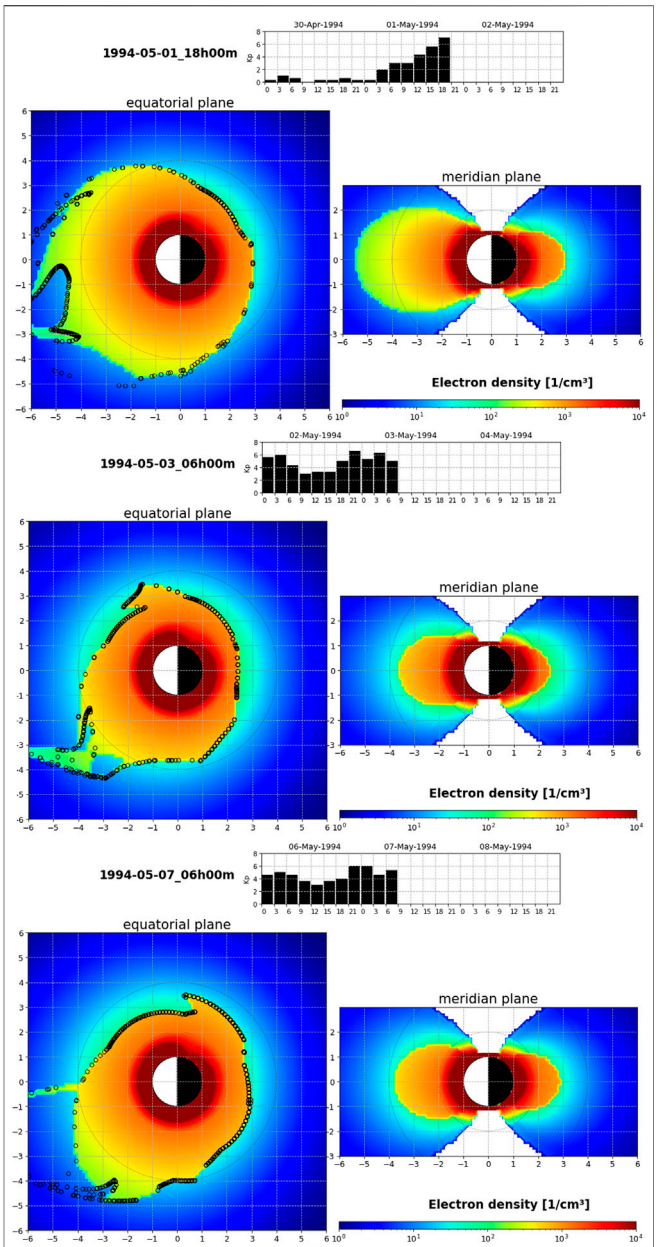


FIGURE 2 | Plasmapause (black circles) and electron number density (color scale) in the plasmasphere obtained with the SPM model in the equatorial plane **(left panels)** and in the meridian plane **(right panels)** on May 1, 1994 18 h UT **(top)**, May 3, 1994 6 h UT **(middle)**, and May 7, 1994 6 h UT **(bottom)**. These simulations are examples showing that plumes are reproduced in a continuous manner during the first weeks of May 1994 with the SPM model. Plume occurrence is due to the high values of the Bartels geomagnetic index Kp which is shown at the top of each panel.

et al., 2021a) to take into account the refilling that takes around two or 3 days after the storm erosion (Gallagher et al., 2021) and the plasmaspheric wind appearing during prolonged quiet periods (Lemaire and Schunk, 1992).

LINKS BETWEEN THE PLASMAPAUSE AND THE RADIATION BELT BOUNDARIES

The plasmapause is not the only boundary that is clearly correlated to the Dst index. Pierrard et al. (2020) obtained Dst-based relationships of the inner and the outer edges of the outer radiation belt for electrons of energy above 1 MeV. The position of the inner edge of the outer belt is very energy-dependent due to the dependence on electron lifetimes. This study also shows a correlation between the motion of the inner edge of outer belt and that of the innermost plasmapause location. This previous work indicates that it is useful to compare the plasmapause position with the position of the inner edge of the outer belt, as done in the next two sections with the observations of both the Van Allen Probes and the LEO PROBA-V satellite.

Van Allen Probes/MAGEIS and PROBA-V/EPT Observations of the Radiation Belts During 10 months in 2015

The top panel of **Figure 3** represents the Van Allen Probes/MagEIS (Blake et al., 2013) electron fluxes (color scale) at 2.28 MeV as a function of the McIlwain (1966) parameter L in Earth radii from 1st March to December 31, 2015. The second panel of **Figure 3** shows simultaneous observations of the Energetic Particle Telescope (EPT) instrument on board the PROBA-V satellite for E = 1–2.4 MeV for the active year 2015 that was especially studied with EPT in Pierrard and Lopez Rosson (2016). The inner and outer edges of the outer radiation belt are characterized by very sharp transitions, so that they are clearly visible by color changes from red to blue in **Figure 3**. The equatorial observations of MagEIS flux and the LEO observations of PROBA-V/EPT at higher latitude show similar electron flux variations, with fast increase during storms (easily identified by Dst inverted peaks given in the third panel of **Figure 3**) and slower decay afterwards. Differences in flux level and sensitivity to the pitch angle is discussed in Pierrard et al. (2020). The black line represents the plasmapause position that is discussed in the next section.

Links Between Plasmapause and Radiation Belts Observations

The solid black line on the top panel of **Figure 3** corresponds to the plasmapause position measured by the Van Allen Probes as previously discussed. The dotted black line on the second panel corresponds to the plasmapause position estimated by the linear **Equation 6** deduced from the SPM model. Both are superposed in the fourth panel of **Figure 3**. Spearman correlation gives a moderate coefficient of 0.36 and RMSE = 0.817. One can see that the linear relation deduced from the SPM plasmapause model based on the geomagnetic activity index Kp gives positions of the plasmapause close to the Van Allen Probes observations with quite similar time variations and a maximum L < 6.2. During the strongest events, the model gives lower plasmapause than what is observed, while on the contrary, some more moderate events show an observed plasmapause further than what predicted by the model. This can be due to the MLT sector anisotropy not taken into account in the comparison.

During moderate and big storms (e.g., in March 2015), the plasmapause (obtained by the model, as well as that observed by Van Allen Probes) is formed closer to the Earth and shows an inward motion similar to the inward motion of the inner edge of the outer belt, which appears only for the strongest events for the radiation belt. The plasmapause is clearly much more mobile than the inner edge of the outer belt.

Often in the top panel of **Figure 3** (e.g., in April 2015), the plasmapause is located close to the outer edge of the outer belt for E = 2.28 MeV, especially during quiet periods longer than several days. During the main phase of storms (with Dst < 50 nT, e.g., mid-March 2015) and even for substorms (inverted Dst peak with 50 nT < minimum Dst < 30 nT), the plasmapause comes closer to the Earth.

The bottom panel of **Figure 3** compares the plasmapause with the inner edge of the outer radiation belt for 1–2.4 MeV electrons during storms. The blue dots in the bottom panel show the lowest L-shell (Lm) value of flux penetration of electrons with E = 1–2.4 MeV (Ch 5) observed in the slot region by PROBA-V/EPT during the 47 strongest storms appearing from May 2013 to December 2019. The lower edges Lm of the outer radiation belt during storms are identified using the methodology explained in Pierrard et al. (2020) (see their **Figures 8–10**), i.e. by determining the lowest L-shell where the flux exceeds the threshold of 2. e2 electrons/(cm^2 s sr MeV) in the slot region. The Lm positions are here represented as a function of log10|min Dst_24 h|, like the plasmapause in **Figure 1** (panel 1). The black line shows the best fit function for these Lm obtained to be

$$\mathrm{Lm} = -1.4\mathrm{Log10}\left|\min \mathrm{Dst}_{24h}\right| + 6.0 \quad (7)$$

with err(a) = 0.272, err(b) = 0.529 and RMSE = 0.25. The linear relation is very similar to **Eq. 5** obtained for the plasmapause with CRRES observations and represented in green on the bottom panel of **Figure 3**. This shows a clear link between the radiation belt boundary for the 1–2 MeV energy range and the plasmapause position. Van Allen Probes plasmapause fit (**Eq. 1**) is also represented in green and shows a similar slope but a position typically 0.8 Re higher, may be due to the lower threshold of 100 cm^{-3} level used to define the plasmapause with Van Allen Probe data.

Independently of the nature of the acceleration, both inner boundary of ultra-relativistic peak flux and plasmapause are related during the storm main phase. A similar inward motion of the inner edge of the outer belt and the plasmapause is observed, but only for the biggest storms with Dst < 50 nT. In that case, the inward motion of the plasmapause during the storm

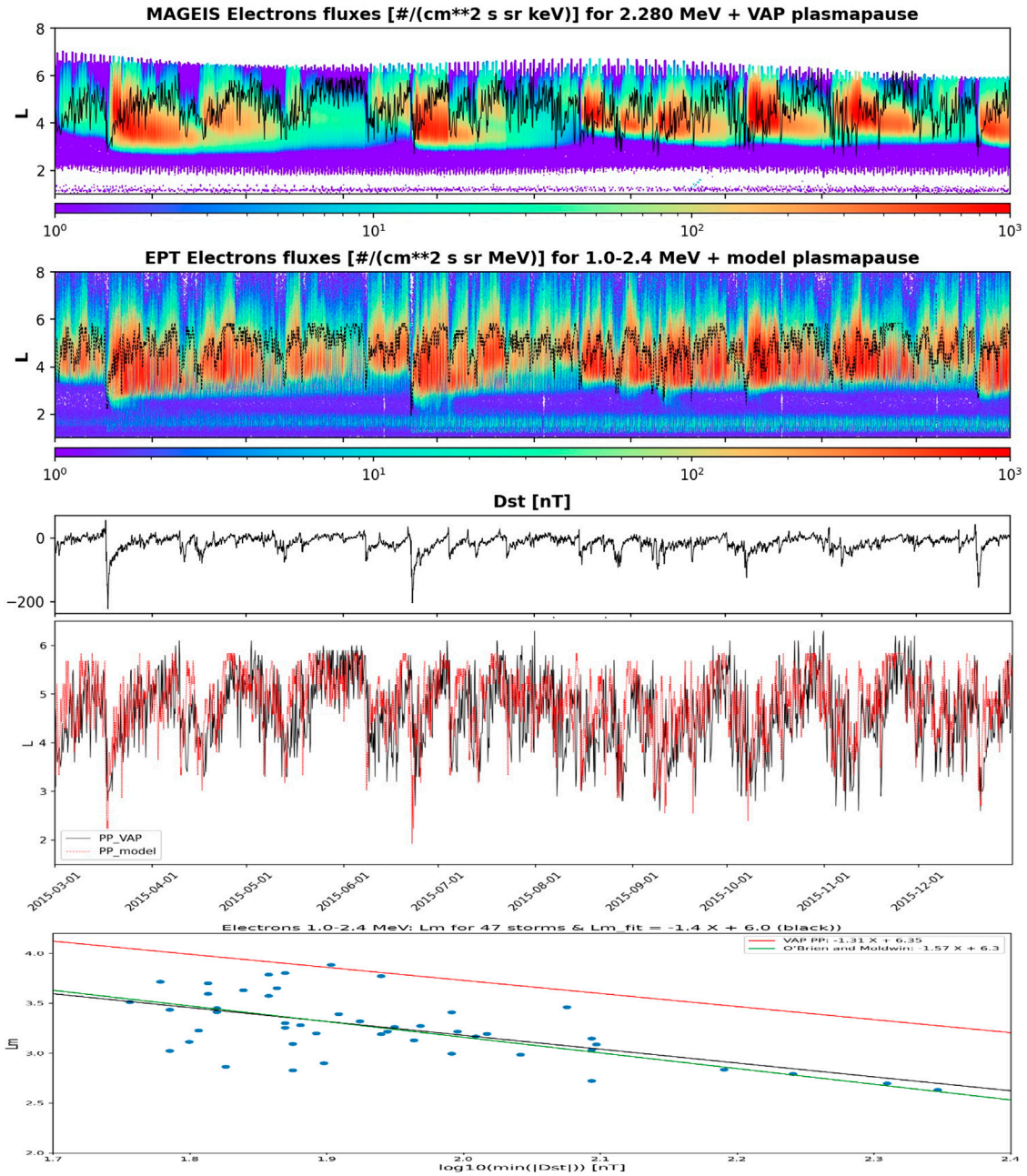


FIGURE 3 | Upper panel: Electron flux measured by MagEIS on board the Van Allen Probes at 2.28 MeV from March 1, 2015 to December 31, 2015. The black line corresponds to the plasmapause computed from spacecraft charging measured by EFW on board the Van Allen Probes. **Second panel:** Electron flux measured by PROBA-V/EPT at 1–2.4 MeV from March 1, 2015 to December 31, 2015. The black line corresponds to the plasmapause obtained from the SPM model. **Third panel:** Observed Dst index from March 1, 2015 to December 31, 2015. **Fourth panel:** Comparison of the plasmapause observed by Van Allen Probes (black line) with the plasmapause obtained from the SPM model (red line) from March 1, 2015 to December 31, 2015. **Bottom panel:** Blue dots: lowest position Lm of the flux injected in the slot during the 47 biggest storms observed by PROBA-V/EPT Ch5 (1–2.4 MeV) from May 2013 to December 2019, as a function of log10|min Dst_24 h|. Black line: best linear fit function for Lm. Red line: Best fit of plasmapause position as a function of log10|min Dst_24 h| as observed by Van Allen Probes (**Eq. 1**). Green line: Best fit of plasmapause position as observed with CRRES (**Eq. 5**).

gives a minimum position very close to that of the inner edge of the outer belt for 1 MeV electrons. During the recovery phase, the plasmapause goes gradually further away from the Earth due to ionospheric refilling that takes several days. Top panels of **Figure 3** show no link between the plasmapause and the radiation belt boundary during these recovery times, since the inner edge of the outer belt remains close to the Earth during more extended periods from several days to weeks. Spearman correlation coefficients between the plasmapause and the flux of the radiation belts measured by PROBA-V/EPT do not show

significant relation, except may be for 1–2.4 MeV (see **Figure 14** in Pierrard et al., 2020).

In summary, we observe that the plasmapause corresponds with the inner edge of relativistic outer radiation belt electrons for E = 1–2.4 MeV during the storm main phase only, while it extends up to the outer edge of ultra-relativistic outer radiation belt electrons during prolonged quiet periods. We do not conclude in general that the depth of penetration of the outer radiation belt electrons into the inner magnetosphere is associated with the innermost plasmapause position as Li et al. (2006), a theory which has been revisited since then (Khoo et al., 2018). Here, in **Figure 3**, the only link we find is a coincident position of the plasmapause with the 1–2.4 MeV electron outer radiation belt during the storm main phase. No link is found during recovery periods, between the storm and the established quiet times, during which both edges evolve with their own dynamics, one driven by ionospheric refilling, the other by wave-particle interactions.

The inward motion of the outer radiation belt associated with sudden flux enhancements of energetic electrons (e.g., Turner et al., 2015) seems directly related to the plasmapause erosion during geomagnetic storms (e.g., October 2015 in **Figure 3**). The similar position of the plasmapause and the edges of the energetic outer belt suggests a link between these different populations. The plasmasphere can contribute to explain the impenetrable barrier discovered at L~2.7 (Baker et al., 2014) through which ultra-relativistic energetic Van Allen belt electrons cannot migrate (Fennell et al., 2015). This barrier is seen during prolonged periods after enhancements at very high energy and could be generalized for lower energies at lower L down to the inner belt (Pierrard et al., 2020). The different waves that are generated inside and outside the plasmasphere and close to the plasmapause position are also able to contribute to the loss and acceleration of outer belt electrons, therefore changing its edges and spectrum (e.g., Reeves et al., 2016; Ripoll et al., 2016; Turner et al., 2019; Pierrard et al., 2020; 2021b). The two-belt radiation structure has been explained as arising from strong electron interactions with plasmaspheric hiss, existing from the inside of the plasmasphere up to the plasmapause boundary, with the inner edge of the outer radiation zone corresponding to the minimum plasmapause location just after the storm (Ripoll et al., 2017). Since during strong storms, the plasmasphere is eroded down to low L, local acceleration of MeV electrons by chorus waves can reach the new region outside of the plasmasphere that was previously located in the slot region and inner belt. On the other hand, during the early storm recovery, the quick recovery of the plasmasphere allows outer belt electrons to be situated in the plasmasphere where intense plasmaspheric hiss can scatter them (e.g., Ripoll et al., 2019).

LINKS BETWEEN THE PLASMAPAUSE, IONOSPHERIC CONVECTION BOUNDARY, RADIATION BELTS AND AURORAL OVAL DURING A QUIET PERIOD: MARCH 14, 2014

Radar and satellite observations for specific dates, as well as models, allow us also to analyze the MLT distribution of different boundaries, i.e., the position of the plasmapause, the limits of the outer belt and the limits of the auroral oval. We start in this section with a quiet period for which we have different observations (March 14, 2014) and we will analyze in the following section 6 the case of a geomagnetic storm (August 26, 2018).

Links Between the Plasmapause and the Ionospheric Convection Boundary

Plasmasphere Model

Figure 4 illustrates the electron density of the plasmasphere obtained with the SPM model on March 14, 2014 at 15h30 UT in the equatorial and meridian plane. The density is provided in geocentric solar magnetospheric (GSM) coordinates. Since Kp = 2 at 15h30 UT and Kp < 3 during the previous 24 h, the activity was low and the plasmasphere was quite extended with Lpp~4.5 Re and almost circular in the equatorial plane. The meridian view shows clearly that the plasmapause is not only present in the equatorial plane, but also at all latitudes along the magnetic field lines, resulting in a high density gradient at low altitude, and thus also in the ionosphere. As shown on the right panel of **Figure 5**, a plasmapause between L = 4 and L = 5.2 in the equatorial plane corresponds to a latitude between 60° and 64° when projected in the ionosphere along the magnetic field line.

Ionospheric Convection Observed by Super Dual Auroral Radar Network

The ionospheric convection pattern measured by the SuperDARN radars on March 14, 2014 at 15h30 UT is illustrated in **Figure 5**. The ionospheric convection boundary, Heppner Maynard Boundary (HMB), determined by SuperDARN (green line in **Figure 5**) can be used as a proxy for the geographic latitude of the auroral oval (Imber et al., 2013). The HMB delimits the latitudinal extent of the polar ionospheric convection and has also links with the plasmapause, as found by Matar (2021). The convection is less extended in the Northern hemisphere (NH left panel) than in the Southern hemisphere (SH right panel). The convection induced by the solar wind directly controls the different processes within the magnetosphere such as the aurora, the plasmasphere, and radiation belts response.

This is a period of contraction of the auroral zone following a northward turning of the IMF appearing around 13h00 UT, as illustrated in **Figure 5** third panel. The bottom panel of **Figure 5** shows a time series of the HMB from the NH from 9h00–18h00 UT on March 14, 2014. A sudden northward turning measured at the satellite just after 13h00 UT resulted in a steady rise of the HMB to higher latitudes, consistent with the contraction. The selected map (15h30 UT) from the NH looks like a good representation of this development with L_{HMB} = 69°, except in the noon sector where it is located at higher geographic latitude around 75° due to the compression of the magnetic field lines in the day side. The MLT is provided by the *x* axis, with 0h00 MLT (midnight) corresponding to the bottom of the top panels in **Figure 5**.

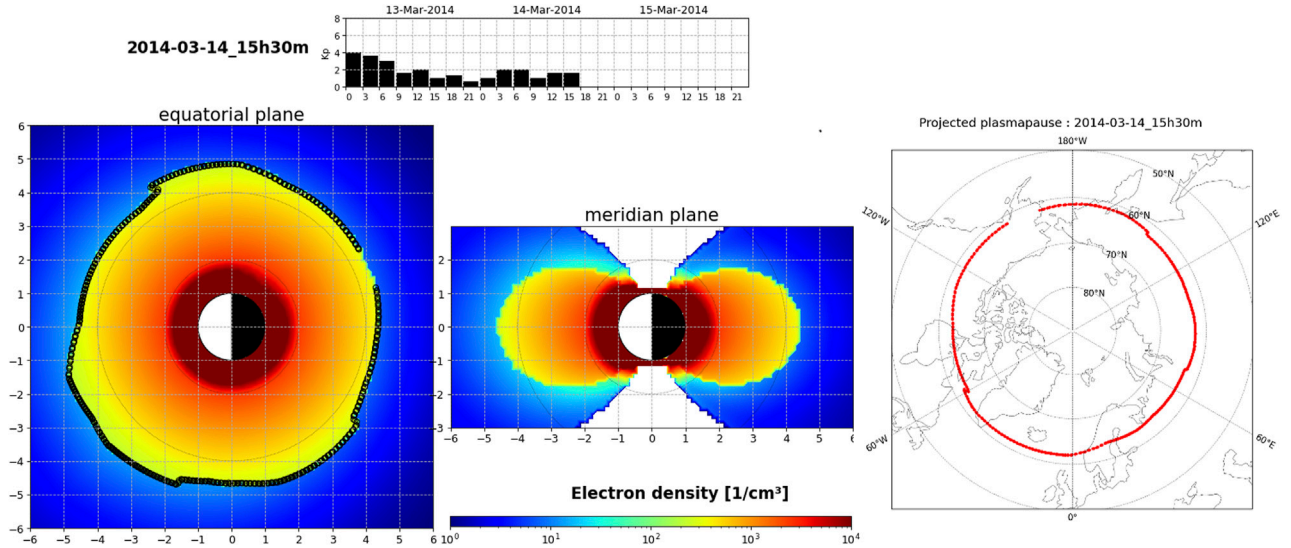


FIGURE 4 | The electron density of the plasmasphere obtained with the SPM model on March 14, 2014 at 15 h 30 UT in the **(left)** equatorial and **(middle)** meridian plane. The right panel illustrates the footprint of the plasmapause projected at high latitude in the Northern ionosphere. The top panel shows the geomagnetic activity index Kp observed from 13 to March 15, 2014.

The sequence in the SH is consistent with that in the NH and with some sign of residual plasma convection surviving at somewhat lower latitudes L_{HMB} = 65°. Note that the reconstructed convection pattern from SuperDARN is given by models in addition to the observations, leading to a HMB very different in the Northern and the Southern hemisphere, and a HMB located at higher latitudes in the noon MLT sector than at other MLT, due to strong compression of the terrestrial magnetic field associated to solar wind pressure. The HMB is found to be located at higher latitudes than the ionospheric footprint of the equatorial plasmapause obtained with the SPM model in both hemispheres, at all MLT but especially at noon. The accuracy of the SuperDARN convection pattern reconstruction is to large extent driven by the underlying model.

Radiation Belts

Flux Evolution Observed by PROBA-V/EPT

Figure 6 shows the electron fluxes measured by EPT on PROBA-V from 14 to March 20, 2014 during a quiet period. The SPM model gives a plasmapause position located around L = 5 that is located inside the outer radiation belt for the energies 500–600 keV and 1–2.4 MeV. For higher energies, the outer belt is less extended than at lower energies and the plasmapause around L = 5 lies beyond the outer edge of the outer belt, as also illustrated in **Figure 7** with the 1.6 MeV channel. The plasmapause obtained by the model is very stable around L~5 during this quiet period, which is confirmed by Van Allen Probes measurements of the local density (see bottom panel of **Figure 7**) showing a plasmapause oscillating between L = 4 (at the Dst minimum) and L = 6.

Flux Evolution Observed by Van Allen Probes

Figure 7 shows Van Allen Probes/ECT Level 2 combined fluxes (Boyd et al., 2019). Fluxes are binned by temporal bins of 4 h corresponding to half an orbit, which allows to fill all (or almost) the L-shell of that bin (from perigee to apogee) with a flux value. Flux observations are then interpolated in the time direction to produce a smooth representation. This treatment produces a continuous view of the radiation belts (albeit time is frozen within a 4 h bin) for a wide range of energies, here, for a quiet magnetosphere (a similar treatment will be applied to disturbed time fluxes in the next section). At sub-relativistic and relativistic energy, the radiation belt is concentrated in the outer belt above L~4. Fluxes are low compared with more active times (cf. *Van Allen Probes/MAGEIS and PROBA-V/EPT Observations of the Radiation Belts During 10 months in 2015*) and gradually decaying with time. The 1 MeV fluxes and above are closer to the inner belt than sub-relativistic electron fluxes, which is due to the fact that sub-relativistic electrons are more sensitive to whistler-mode hiss waves than higher energy electrons and thus are more scattered during extended quiet periods. This forms a remnant denser pocket of MeV electrons in the outer belt explained in Ripoll et al. (2019), which forms the top part of a structure called S-shape when plotted in the (L, E) plane (Reeves et al., 2016; Ripoll et al., 2016).

At lower energy, between 10 and 100 keV, fluxes are much higher and injections are more visible on 14–15 and on 18–20 March 2014, although the activity is very mild as shown by the Dst index in **Figure 6**. At these low energies, the inner belt reaches L~4. At 10 keV, the slot fully disappears. These electrons are considered as potential source for *in-situ* VLF (very low frequency) whistler waves generation, ultimately able to produce local acceleration of hundreds of keV electrons to MeV energies (Tu et al., 2014; Jaynes et al., 2015).

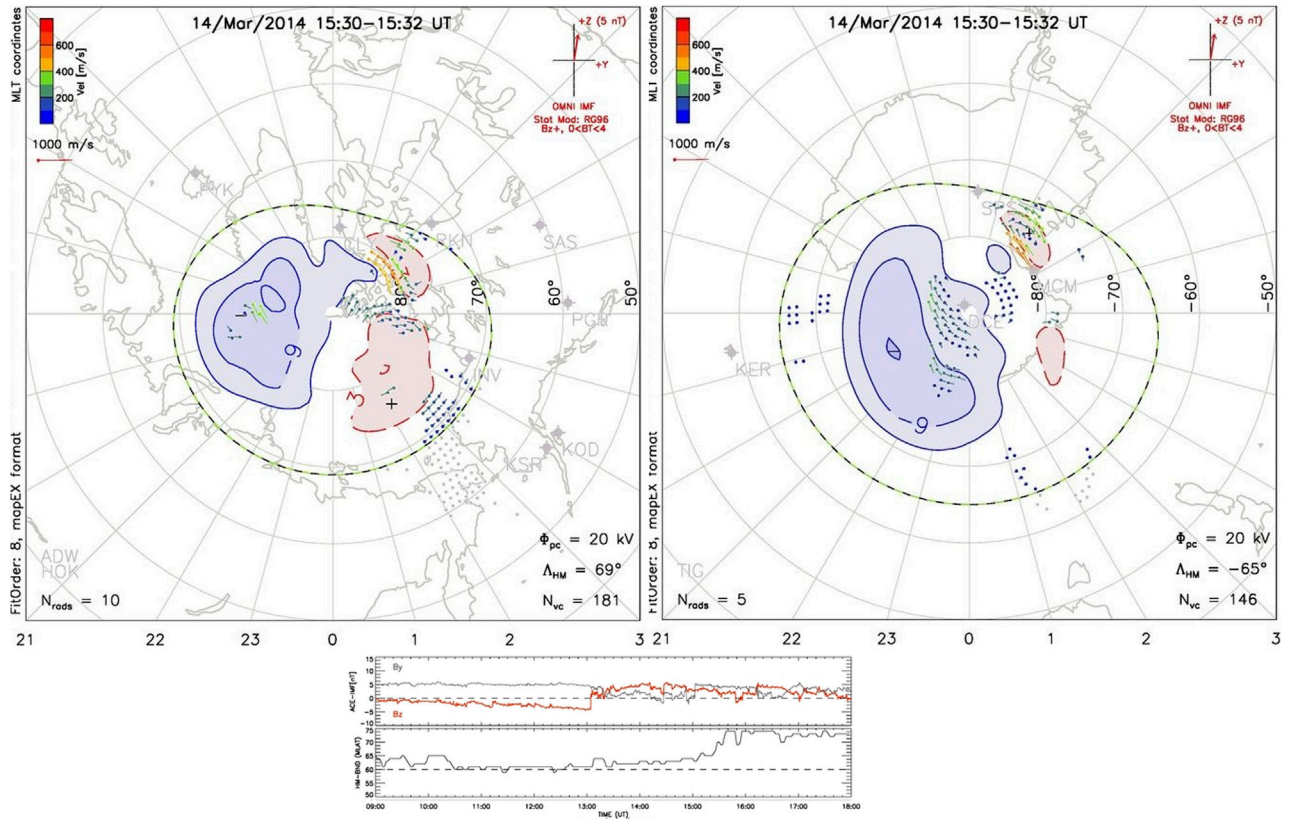


FIGURE 5 | Top panels: ionospheric convection pattern measured by SuperDARN in the Northern hemisphere **(left panel)** and in the Southern hemisphere **(right panel)** on March 14, 2014 at 15 h 30 UT. The *x*-axis gives the MLT. The green lines represent the Heppner-Maynard Boundary (HMB). The blue-red shades show the ionospheric potential. **Bottom panel:** Time evolution from 9h00 to 18h00 UT of the HMB boundary on 14 March 2014 estimated by SuperDARN in degrees of geomagnetic latitude at 0h00 MLT.

For all these energies during this period of quiet geomagnetic activity, the plasmapause boundary measured by EMFISIS on RBSP A (magenta line) does not seem to correspond to any specific boundary of the electron fluxes. It varies between L = 4 and L = 6 during this time period and is much more irregular than the radiation belt boundaries.

Meridian View From AE8 Model

Van Allen Probes and PROBA-V observations do not give a meridian view due to their limited latitude coverage. That is why to illustrate the meridian view of the integral electron flux with E > 1 MeV in **Figure 8**, we use the empirical model AE-8MAX (Vette, 1991) to better see the radiation belts from the side view (see Loridan et al. (2019) for more latitudinal representations of the radiation belt dynamics). The slot region (yellow region) appears clearly between the inner belt and the outer belts (red regions). The boundaries depend on the geomagnetic activity, as shown in **Figure 3**, but also on the energy as shown in **Figure 7**. Typically, the slot in the AE8 model is located between L = 2 and L = 3 for E = 0.5–7 MeV with quite sharp boundaries. At lower energy, from 40 to 500 keV, the slot is a little bit higher between L = 2.5 and L = 3.5 with more gradual boundaries. This is consistent with the theoretical energy-dependent structure of the radiation belts (Lyons and Thorne, 1973; Reeves et al., 2016; Ripoll et al., 2016). The plasmasphere generally overlaps the radiation belts during low geomagnetic activity. Otherwise, there could not be interactions between plasmaspheric waves and the trapped electrons, and, thus, the observed energetic structure of the radiation belts would not exist.

High-Latitude Magnetic Local Time Maps

The top panels of **Figure 9** illustrate the EPT observations of electron fluxes for E = 500–600 keV at 820 km from 14 to March 20, 2014 in the Northern hemisphere (left) and Southern hemisphere (right). At this altitude, the radiation belt population is constituted by low equatorial pitch angle particles, ready to be or soon scattered in the ionosphere. This is different from **Figure 7** previously discussed, which showed equatorial electrons, which distribution is dominated by high pitch angle trapped particles. Detailed comparison between polar EPT and equatorial Van Allen Probe observations is made in Pierrard et al. (2020, 2021b).

Figure 9 (top) allows visualization of the oval formed by the outer belt when penetrating at 820 km. The bottom right map in latitude-longitude shows that the outer belt corresponds to the high latitude band located above Scandinavia in the Northern hemisphere. The fluxes are always artificially low above Europe

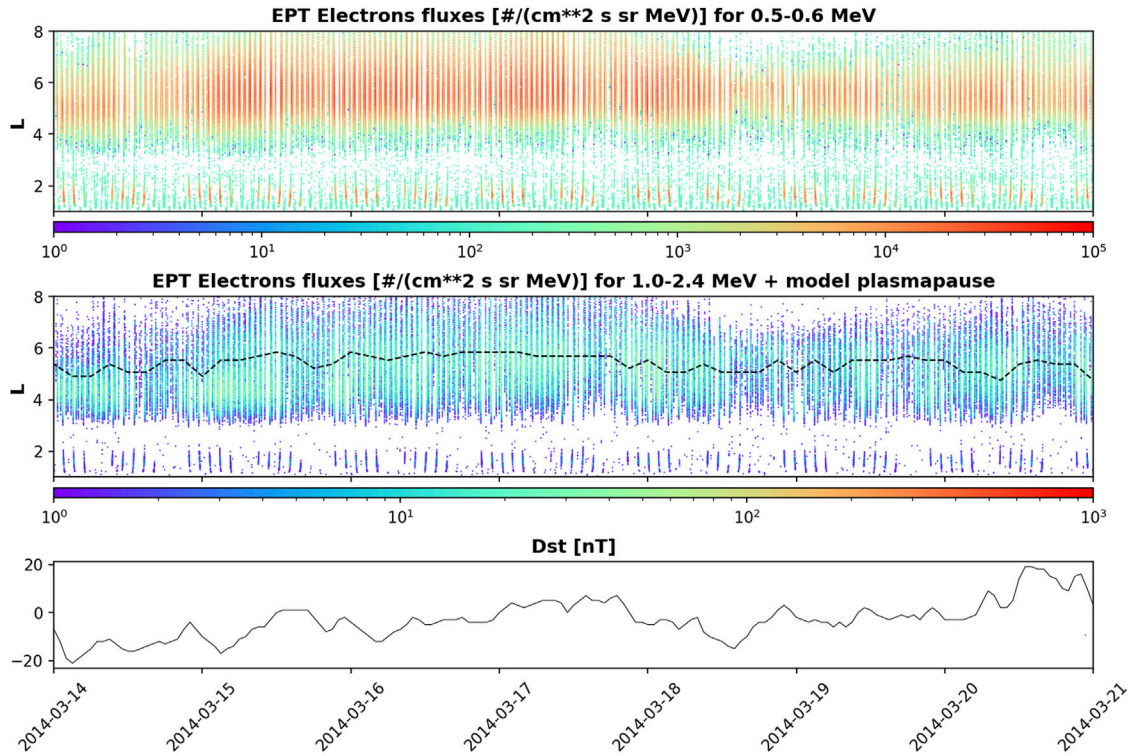


FIGURE 6 | Upper panel: Electron flux measured by PROBA-V/EPT at 500–600 keV from 14 to March 20, 2014. **Middle panel:** Electron flux measured by PROBA-V/EPT at 1–2.4 MeV from 14 to March 20, 2014. The black dotted line in the middle panel corresponds to the plasmapause obtained from the SPM model. **Bottom panel:** Observed Dst index during the same period.

with EPT due to the pause in the measurements during the transmission of the data to the Belgian station of Redu.

One can see that in the Northern hemisphere, the radiation oval is located between L = 3.5 and 8.5 represented by the black dots in the bottom map. The South Atlantic Anomaly SAA is visible in the Southern hemisphere (top right) and in the latitude-longitude map (bottom). Due to the characteristics of the orbit of the PROBA-V satellite that has a period of 101 min (thus about 14 orbits around the Earth per day), it is necessary to accumulate the observations during several days to obtain good coverage on the maps. Here, the data are shown from 14 to March 20, 2014. This accumulation time is consistent with gradual mild loss occurring in both the slot and the outer belt at 500–600 keV (see, for instance, **Figure 5** of Ripoll et al. (2019)). As such, **Figure 9** represents the total loss accumulated during 6 days in the whole radiation belts region. Further integration (not attempted) would lead to the computation of the total radiation belt electron content (TRBEC) (e.g., Forsyth et al., 2016).

Auroral Oval

The bottom left panel of **Figure 9** illustrates a map of the intensity and location of the auroral oval as obtained with the OVATION model in the Northern hemisphere for March 14, 2014 at 15h30. It shows the polar cap energy flux and combines discrete and diffuse electron precipitation, as well as proton precipitation producing the aurora. Boundaries of the auroral oval are clearly visible for direct comparison with the position of the outer belt shown in **Figure 9** (top left panel). We find that the auroral oval is located at higher latitudes [from 70° to 80° at 0°–180° of longitude (right side) and from 60° to 70° at 180–360° of longitude (left side)] than the outer radiation belt oval [from 60° to 75° from 0° to 180° of longitude (right side) and from 50° to 60° from 180° to 360° of longitude (left side)] at this date. The auroral oval is at higher latitudes than Scandinavia for instance. The lower (equatorward) edge of the auroral oval corresponds to the outer (polar) edge of the outer belt, even if some overlap is partially observed. Both ovals have similar shape slightly elongated at lower latitudes for longitudes >180°, due to the configuration of the magnetic field. The auroral oval is located at higher latitude than the oval of the outer radiation belt for E = 500–600 keV measured from PROBA-V/EPT.

Thus, to summarize our findings up to now, the auroral oval is located at higher latitudes than the outer radiation belt, as expected since the plasma sheet is located at larger distances in the elongated tail than the inner magnetosphere regions. Globally, we observe that the inner (equatorial) edge of aurora as obtained by OVATION is close to the outer (polar) edge of the outer belt for E = 500–600 keV. Only for sufficiently long quiet periods, the plasmapause also lies beyond the polar edge of the outer belt, only for E > 1.6 MeV. For lower energies, the outer radiation belt is generally more extended than the plasmasphere.

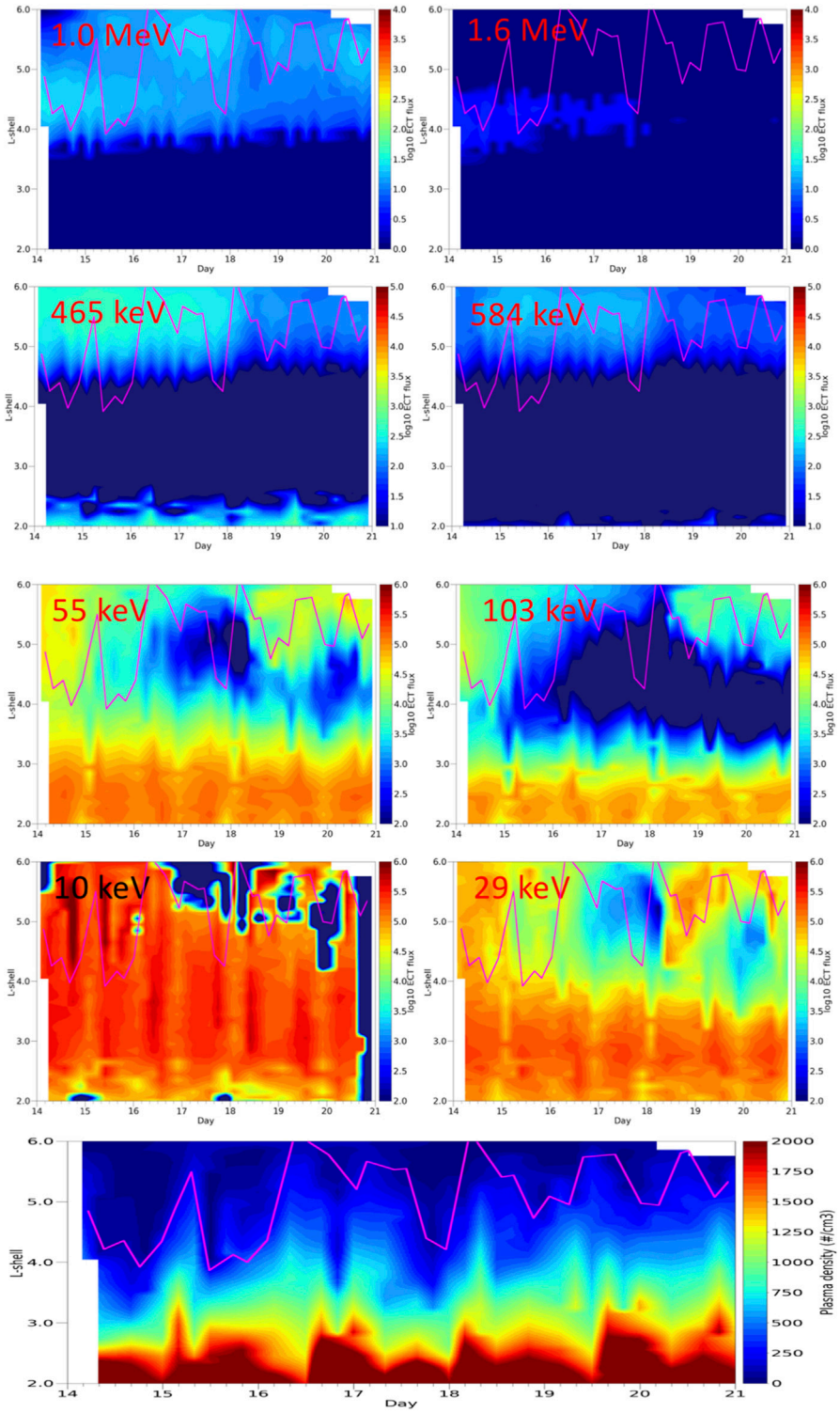


FIGURE 7 | (Top four panels) Radiation belt flux versus time and L-shell for sub-relativistic and relativistic electrons for the quiet period of 14–20 March 2014 measured by the Van Allen Probes/ECT suite in the magnetic equatorial plane. **(Next four panels)** Low energy seed electrons (10–100 keV), which contribute to the electromagnetic environment and as source of aurora. The magenta line corresponds to the plasmapause position measured by EMFISIS on RBSP A. **(Bottom panel)** Density measured by RBSP A/EMFISIS during the same period.

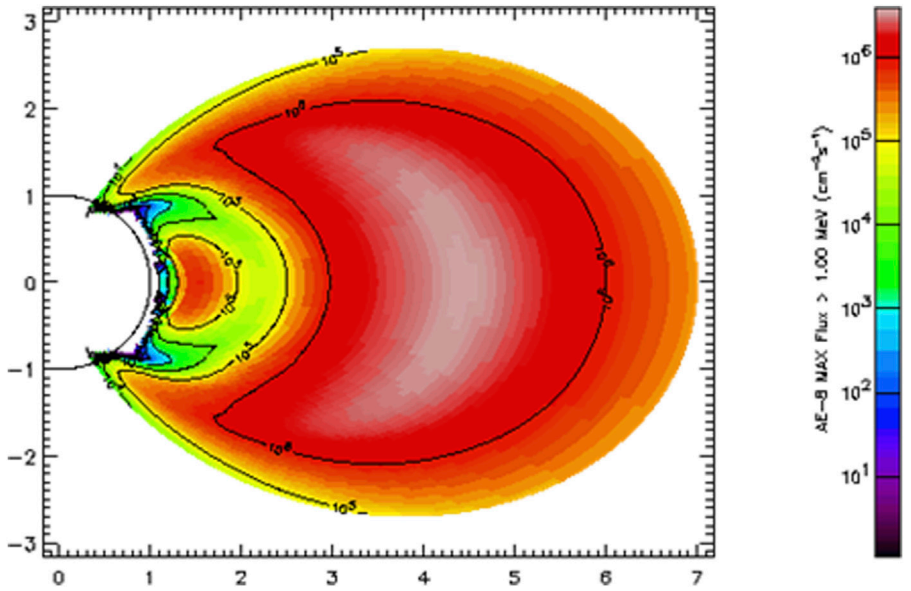


FIGURE 8 | Electron flux obtained with the empirical model AE-8MAX for 1 MeV.

The plasmapause located far from the Earth during prolonged low activity periods is still generally below the equatorial edge of the auroral oval for most MLT. The energy of the particles is essential to explain the observed differences and some particular overlap of these regions, since the particle's energy determines the particle drift velocity, therefore influences the MLT repartition, as well as the (trapped or not) position in the inner magnetosphere.

LINKS BETWEEN THE PLASMAPAUSE, IONOSPHERIC CONVECTION BOUNDARY, RADIATION BELTS AND AURORAL OVAL DURING THE STORM EVENT OF AUGUST 26, 2018

The August 26, 2018 storm is one of the three most powerful geomagnetic storms, which occurred since the launch of PROBA-V in 2013 (see **Figure 1** in Pierrard et al. (2020) for a 7-years representation). For this storm, Kp exceeded 6 (see **Figure 10**) and Dst reached -174 nT, as illustrated in **Figure 12**.

Links Between the Plasmapause and the Ionospheric Convection Boundary

Plasmasphere Model

Figure 10 illustrates how the position of the plasmapause varies with the geomagnetic activity before (top panels) and during (bottom panels) this storm. The plasmasphere electron density (in cm^{-3}) is obtained in the equatorial (MLT distribution) and meridian planes with the SPM model on August 24, 2018 at 22h30, before the storm and on August 26, 2018 at 4h30 during the storm. The plasmapause develops structures like plumes and shoulders depending on the Kp variations (e.g., Pierrard and Lemaire, 2004; Bandic et al., 2020). A plume is clearly visible forming in the dusk sector on 26 August during the storm. The eroded and more anisotropic plasmasphere is also associated to an ionospheric projection of the plasmapause located at higher latitudes during the storm, as clearly visible on the right panels. Storm enhanced density observed in the ionosphere has been identified as ionospheric signature of plasmaspheric plumes (Foster et al., 2002). We will confirm in *Flux Evolution Observed by Van Allen Probes* that the plasmasphere observed by Van Allen Probes is highly dynamics for this period.

Ionospheric Convection Observed by Super Dual Auroral Radar Network

We quantify the intensity of convection before and during the storm case of August 26, 2018 in **Figure 11** showing ionospheric convection patterns measured by the SuperDARN radars. The convection is much stronger after the storm (bottom panels) than before (top panels). The ionospheric convection boundary HMB determined by SuperDARN is shown by the green line on **Figure 11**.

On August 24, 2018 at 22h30 before the storm, the plots are taken from an extended period of stable IMF and the pattern is fairly fixed in orientation through the 22–23 UT interval, giving high confidence. The pattern is characteristic of By-conditions. In the NH, we have $L_{HMB} = 65^{\circ}$, in the SH, $L_{HMB} = 69^{\circ}$. The amount of data in the SH is very limited (59 vectors), so we can only say that $L_{HMB} \leq 69^{\circ}$ as the equatorward limit of the convection zone could extend equatorward of 69°.

On August 26, 2018 at 4h30 during the major storm, there are many vectors observed in the NH. They show that the convection zone is greatly expanded and $L_{HMB} = 50^{\circ}$. Under such extreme

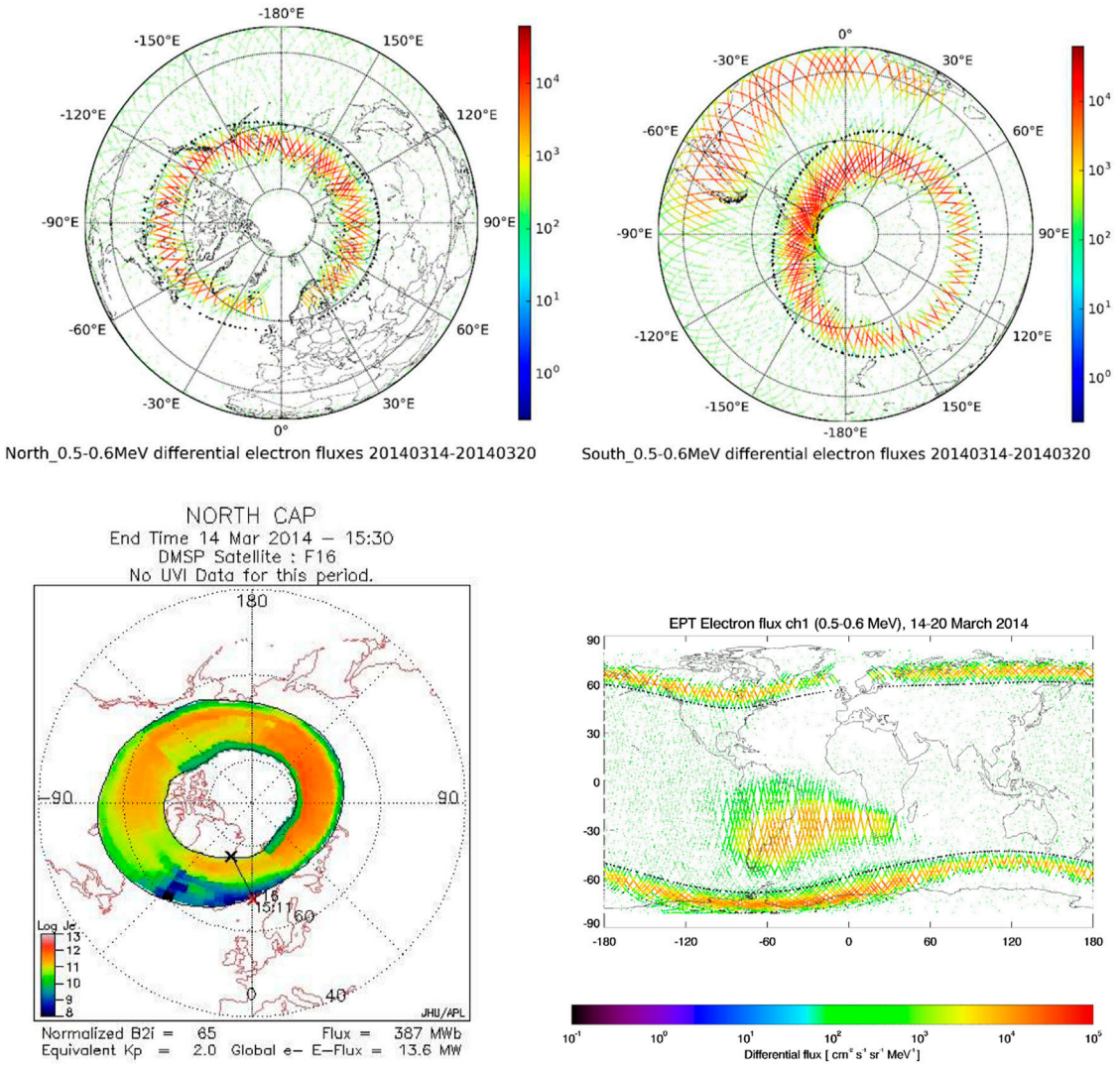


FIGURE 9 | Top panels: EPT observations at 820 km of electron fluxes 500–600 keV from 14 to March 20, 2014 in the Northern hemisphere **(left)** and Southern hemisphere with the South Atlantic Anomaly SAA **(right)**. The black circles with increasing radius correspond to constant latitudes of 80°, 60° and 30°. Bottom panels: **(Left)** The auroral oval as obtained with the OVATION model in the Northern hemisphere for March 14, 2014 at 15h30. The color scale indicates the energy flux producing the aurora. The dotted circles correspond to constant latitudes of 80°, 60° and 40°. **(Right)** The EPT observations of electron fluxes represented on a latitude/longitude map with the SAA at low latitudes and the outer belt at high latitudes. The black dots correspond to L = 3.5 (inner equatorward edge) and L = 8.5 (outer polar edge).

conditions, SuperDARN may not be seeing the equatorward limit of convection. The problem is that the radar fields of view are limited to latitudes >50° due to the dynamic range of the instrument. So here $L_{HMB} \leq 50°$. In the SH, there is evidence as well of a greatly expanded convection zone. Note the vectors that extend almost to the site of the Kerguelen radar (KER). With fewer radars operating at lower latitudes in the south, there is less scope for detecting the equatorward limit, and so here $L_{HMB} \leq 55°$. Like the plasmapause, the HMB migrates to higher latitudes during storm, but with a different latitude and MLT distribution that depends significantly on the magnetic field model used to reconstruct the SuperDARN convection pattern.

Radiation Belts

Flux Evolution Observed by PROBA-V/EPT

Figure 12 shows the electron flux measured by PROBA-V/EPT at 500–600 keV (top), 1–2.4 MeV (second) and 2.4–8 MeV (third) from August 1, 2015 to September 20, 2018. The white regions correspond to periods when no observations are available. The black dashed lines (middle panels) shows the plasmapause position obtained with the SPM model. The inward motion of the plasmapause to lower L is clearly visible on August 26, 2018, and leads to a L ~ 2.5 for E = 1–2.4 MeV similar to the lowest position of the inner edge of the outer belt during the storm. This position of the plasmapause close to the Earth is nevertheless lower than the lowest penetration of the inner edge of the outer

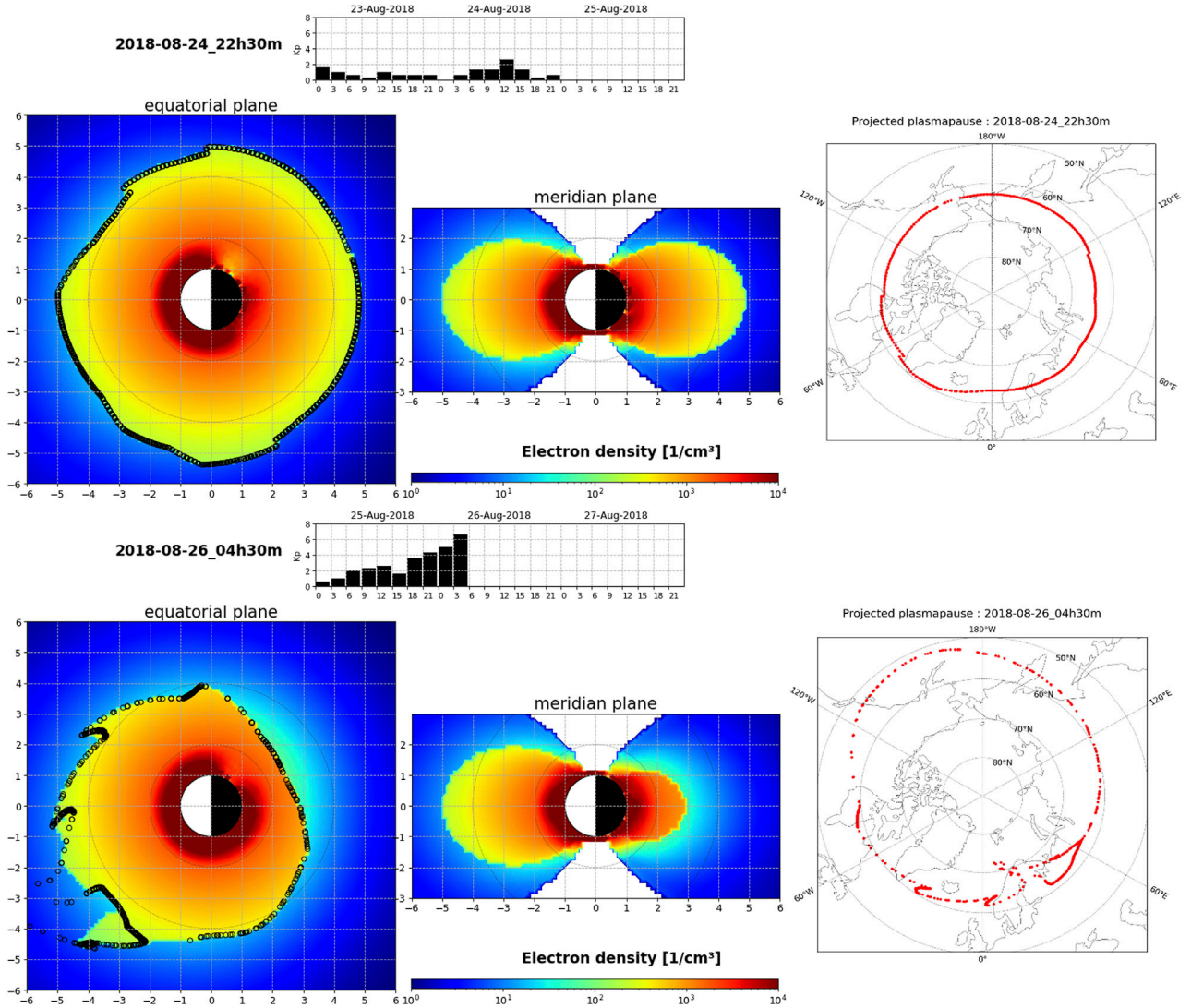


FIGURE 10 | Plasmasphere electron density in cm^{-3} in **(left)** the equatorial plane and in **(middle)** the meridian plane, as well as the ionospheric footprint of the plasmapause at high latitude **(right)** obtained with the SPM model on **(top panel)** August 24, 2018 at 22h30, before the storm, and on **(bottom panel)** August 26, 2018 at 4h30 during the storm. The Kp index measured between 23 and August 26, 2018 4h30 is also shown in the top figure of each panel.

belt for higher energy (around L~3 for 2.4–8 MeV for instance). On the contrary, for 500–600 keV, the injection penetrates deeper, almost down to the inner belt, until a new slot forms 10 days later around L = 3. Note also the dropouts that appear during each substorm and penetrate down to L = 4 on August 26, 2018, due to magnetopause shadowing (e.g., Pierrard et al., 2020).

Flux Evolution Observed by Van Allen Probes

This feature is confirmed in **Figure 13** that shows the radiation belts prior and after the storm as observed by Van Allen Probes for different energies. The storm produced enhanced 1 MeV flux for 8 days, forming a hard-spectrum outer belt notably different from the quiet outer belt of the beginning of August 2018 (or the one shown previously in **Figure 7**). The 1 MeV belt reaches as low as L = 2.5 on 28 August. The injection of sub-relativistic electrons deep in the inner belt reaches almost 600 keV. This is quite rare. For comparison, the average energy of substorm injections is ~250 keV (e.g., Turner et al., 2015). At low energy (30–100 keV), the injections are intense and repeated before and after the 26 August storm. The small substorm occurring on August 15, 2018 does not generate sub-relativistic injections but does inject low energy electrons. Below 30 keV, the inner belt and the outer belt start merging to form a unique active region surrounding the Earth. The waves creating the slot region separating the radiation belts are thus not effective at 10 keV and below.

Last panel of **Figure 13** shows the plasma density and the plasmapause extracted from it, also reported on the flux.

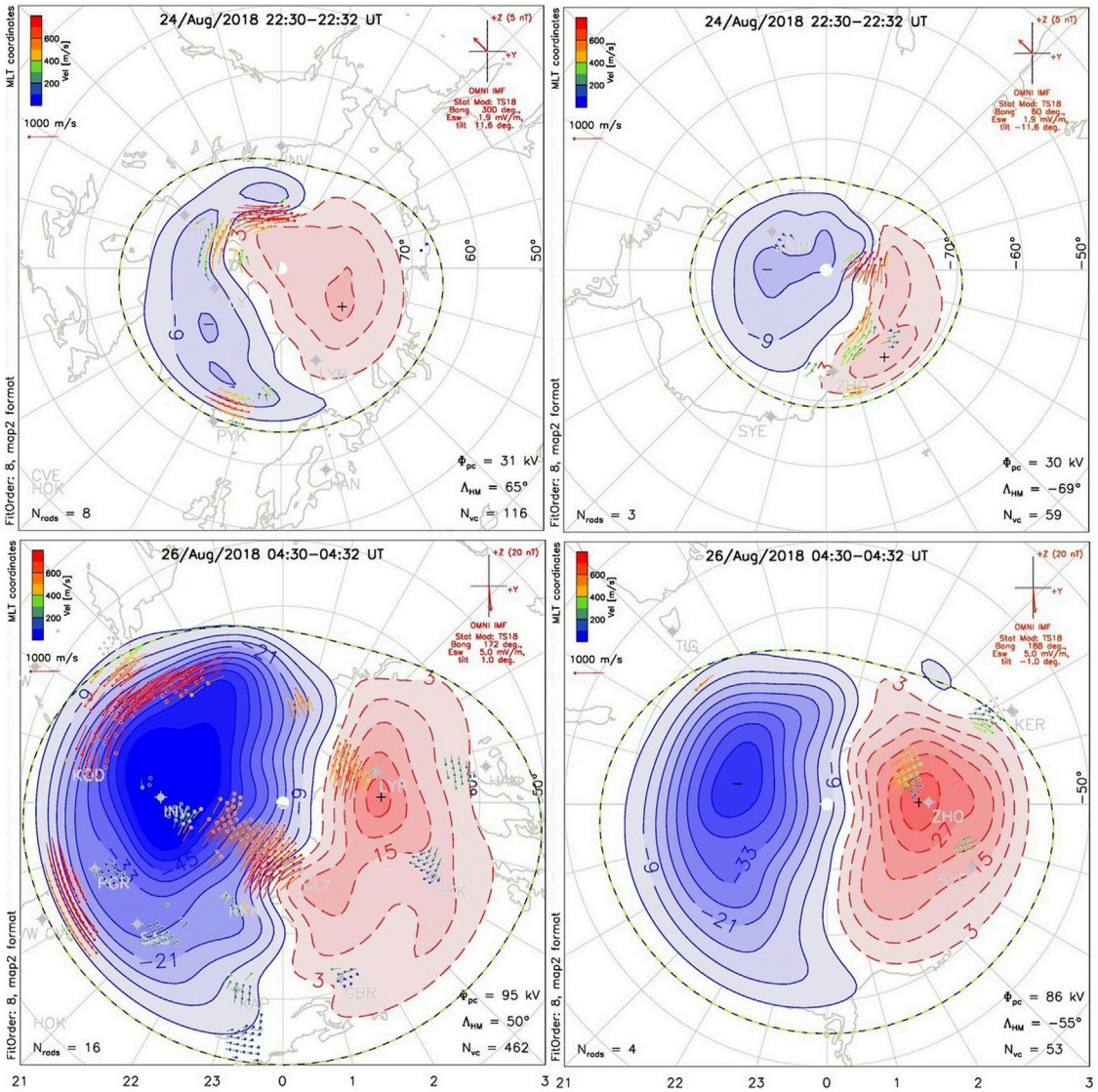


FIGURE 11 | Ionospheric convection pattern measured by SuperDARN in the Northern hemisphere **(left panels)** and in the Southern hemisphere **(right panels)** on **(top)** August 24, 2018 at 22h30 before the storm and **(bottom)** during the storm of August 26, 2018 at 4h30. The green lines represent the ionospheric Heppner-Maynard Boundary (HMB). Arrows represent the measured ionospheric convection velocity (most seen on the Northern hemisphere during the storm). The blue-red shades show the ionospheric potential.

There is a good coincidence of the plasmapause location with the 1.6 MeV channel during the couple of days of the storm recovery (26–28 August 2018), both reaching L = 3. Lower energy electrons penetrate deeper than the Lpp as shown in **Figure 13**. This confirms the claims made in section *Links Between the Plasmapause and the Radiation Belt Boundaries*. In August-September 2018, RBSP apogee is at ~23–22 MLT and cross the L = 3 field line at 19–18 MLT so that the modeled minimum Lpp at 2.5 and the observed minimum plasmapause at L~3 are consistent. The complex structure of the modeled density is confirmed by the filamentary structure of the observations with various detached regions of dense plasma and high variability in time as the probes scan a different region from one pass to another. After the early recovery period, both the outer radiation belt and the plasmasphere evolve at their own rates and no link exists anymore.

High-Latitude Magnetic Local Time Maps of the Outer Radiation Belt by PROBA-V/EPT

Figure 14 shows complementing polar maps of the 1–2.4 MeV electron differential flux measured by PROBA-V/EPT at 820 km of altitude in the Northern hemisphere (left panels) and in the Southern hemisphere (right panels). We show a new way to illustrate how radiation belts in the equatorial magnetosphere project and map at high latitudes. Before the

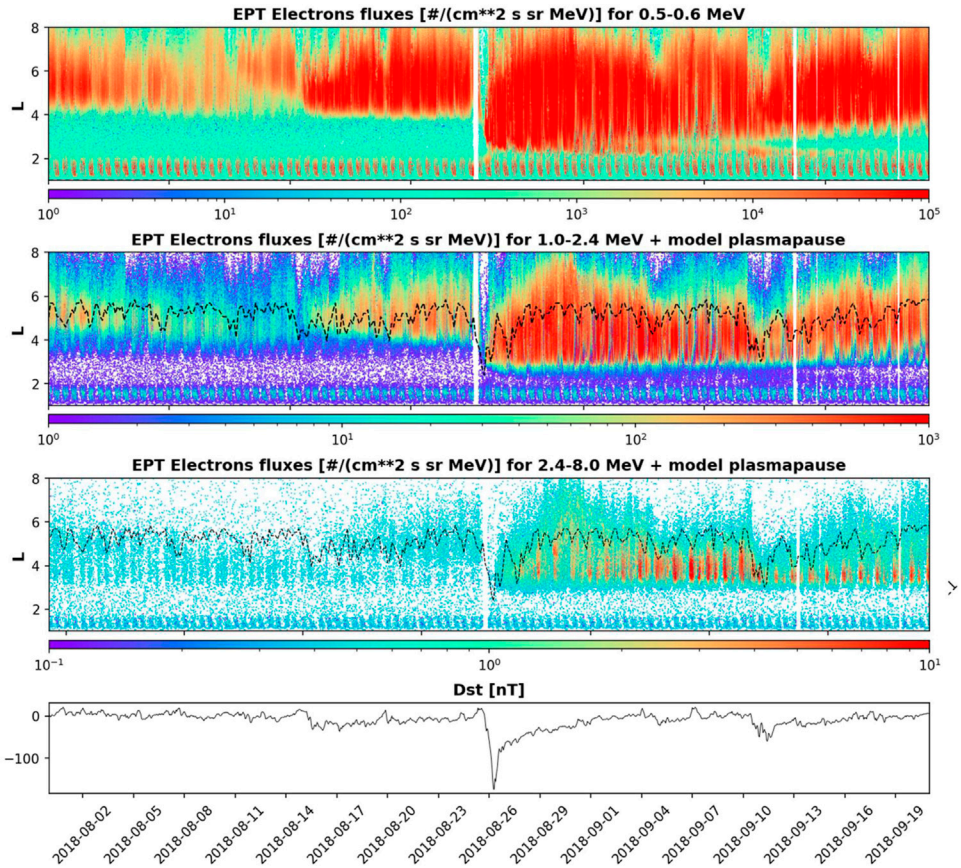


FIGURE 12 | Electron flux measured by PROBA-V/EPT at 500–600 keV from 1 August to September 20, 2018. **Second panel:** Electron flux measured by PROBA-V/EPT at 1–2.4 MeV from 1 August to September 20, 2018. The black dotted line corresponds to the plasmapause obtained from the SPM model. **Third panel:** Same as second panel but for 2.4–8 MeV. **Bottom panel:** Observed Dst index.

storm, from 1 to August 24, 2018 (top panels), the outer radiation belt oval is thin. After the storm, (here accumulated from 25 August to September 20, 2018 on bottom panels), the outer radiation belt oval is more intense and extends at lower latitudes than before the storm, typically 10° lower, as also found for other storms (Pierrard and Lopez Rosson, 2016). It is interesting to note that losses in the slot are only slightly enhanced by the storm times. This is due to the high energy channel (>1 MeV) and the rarity of these particles in the deep slot region, although we note that these electrons reached L = 3 at the Dst peak of the storm (cf. **Figure 12**).

During the storm, the lowest boundary of the outer radiation belt oval for the high energy 1–2.4 MeV reaches 40° of latitude for longitudes between 60° and 120° West in the Northern hemisphere, and a latitude of 40° for longitudes between 60° and 180° East. The boundary is located at higher latitudes for other longitudes due to the configuration of the magnetic field.

Auroral Oval by the OVATION Model

Figure 15 illustrates the Northern hemisphere auroral oval as predicted by the OVATION model on 24-8-2018 at 22h25 UT (upper left) before the storm, and successively for three times following the storm. One can see that the auroral oval is very thin and faint before the storm, and becomes brighter and broader during the storm. The position of the oval and its intensity are very dependent on the MLT sector: the aurora is not visible at 12h00 MLT in the dayside, even during the storm, while the probability of auroral visibility oval is the most intense and wide in the nightside shown by the black background region. Already before the storm on 24-8-2018 at 22h25 and during the storm on 25-8-2018 at the same time, Sweden and Norway (easy to identify on **Figure 15**) are located under the auroral oval, as well as under the radiation belt oval as shown in **Figure 14**, showing that overlap between these regions are possible. On 26-8-2018 at 10h25 (bottom right), Sweden and Norway are located in the dayside so that the auroral oval does not cover these countries. As illustrated by **Figures 14**, **15** respectively, intensification and broadening of the auroral oval during storms are common characteristics with the outer radiation belt oval, but there are major differences concerning the position of the boundaries and the MLT distribution that are detailed in the next section, discussing also the plasmapause position and convection pattern during magnetic disturbances.

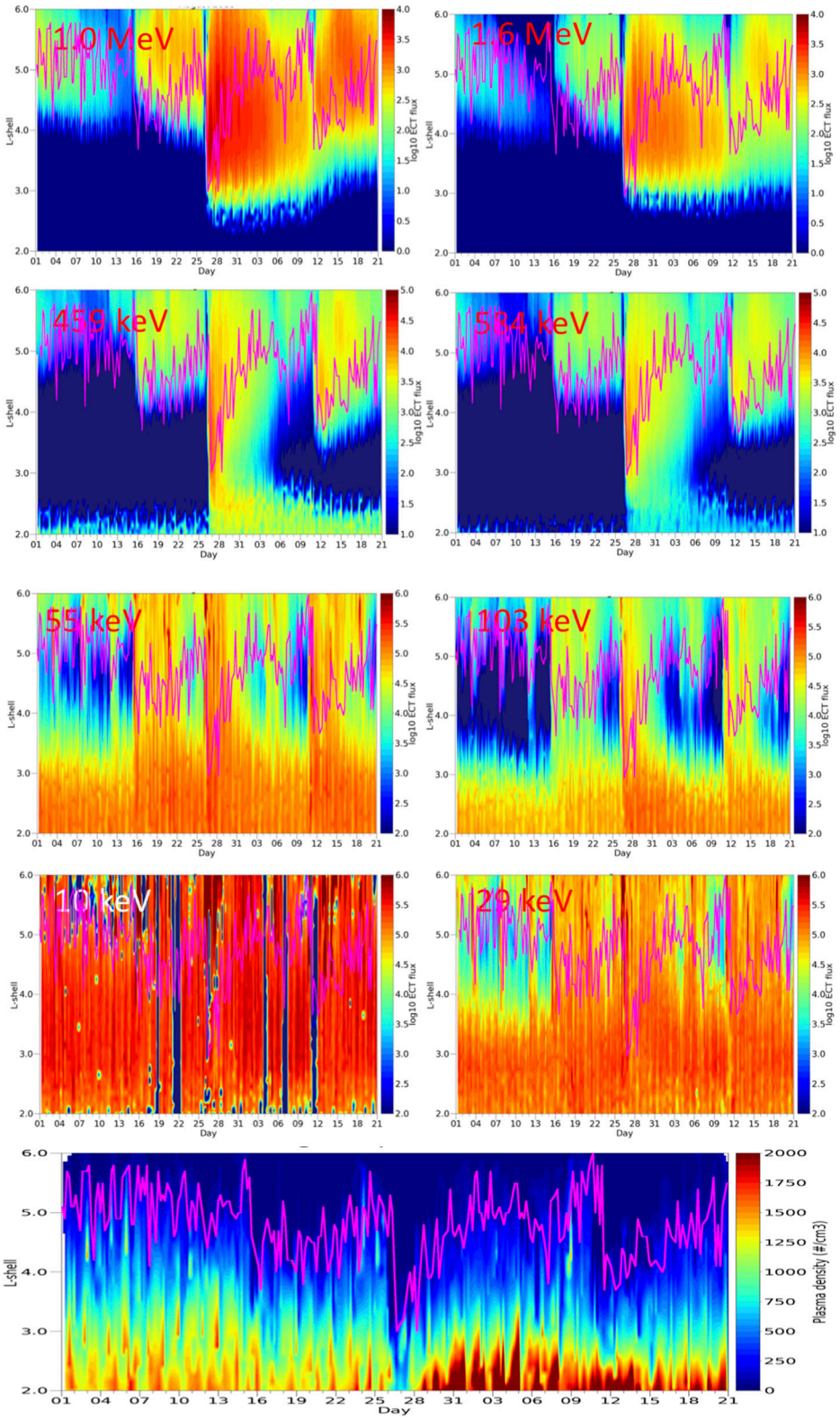


FIGURE 13 | Level 2 ECT combined radiation belt spin-averaged flux plotted versus time and L-shell from 1 August to September 20, 2018 measured by the ECT suite of Van Allen Probes in the magnetic equatorial plane. The magenta line corresponds to the plasmapause position measured by EMFISIS on RBSP B. **(Top 4)** sub-relativistic and relativistic electrons. **(Next 4)** low energy seed electrons (10–100 keV). **(Bottom panel)** Plasma density of RBSP B/EMFISIS computed as explained in section *Van Allen Probes Plasmapause Observations*, from 1 August to September 21, 2018.

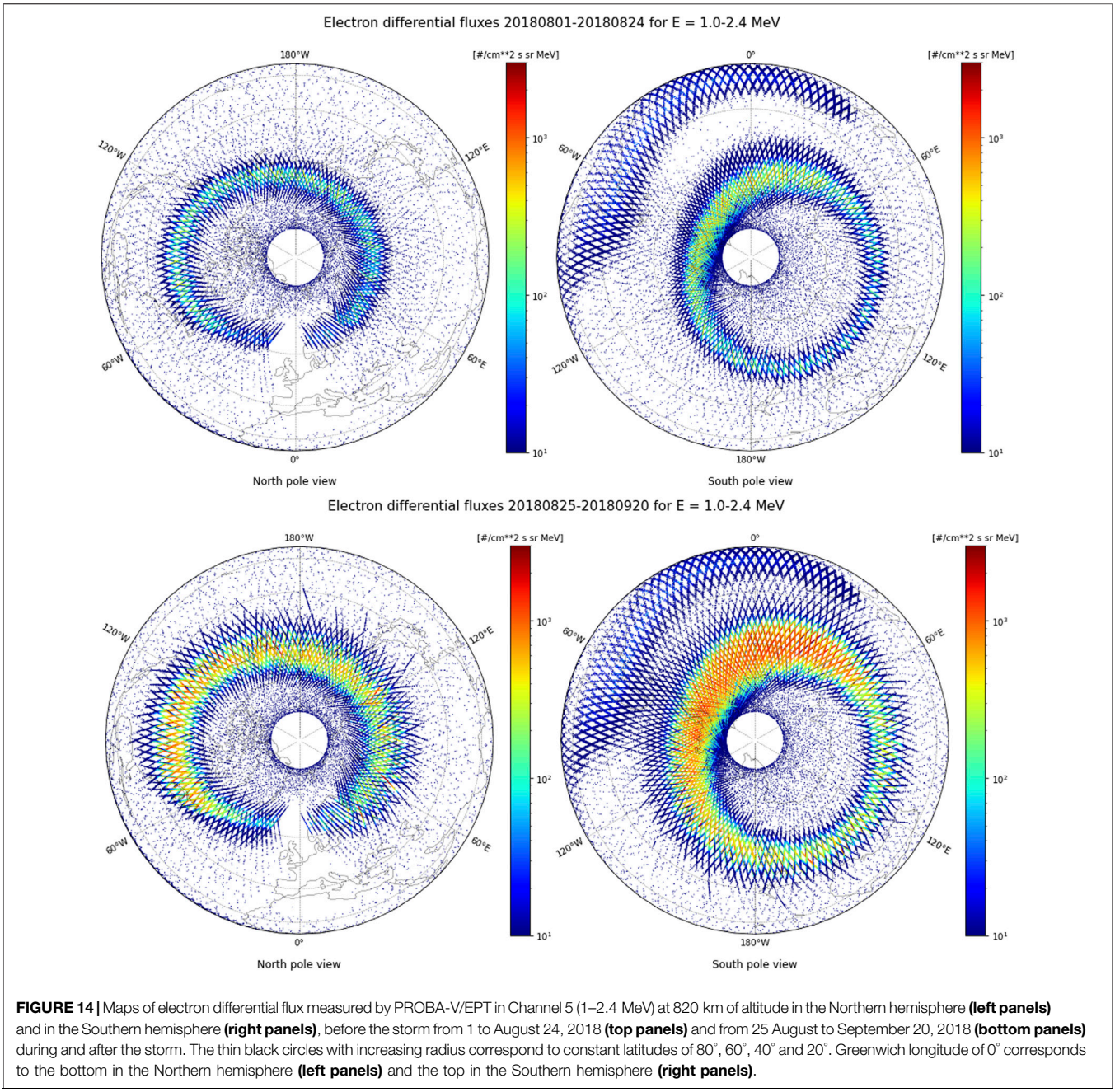


FIGURE 14 | Maps of electron differential flux measured by PROBA-V/EPT in Channel 5 (1–2.4 MeV) at 820 km of altitude in the Northern hemisphere **(left panels)** and in the Southern hemisphere **(right panels)**, before the storm from 1 to August 24, 2018 **(top panels)** and from 25 August to September 20, 2018 **(bottom panels)** during and after the storm. The thin black circles with increasing radius correspond to constant latitudes of 80°, 60°, 40° and 20°. Greenwich longitude of 0° corresponds to the bottom in the Northern hemisphere **(left panels)** and the top in the Southern hemisphere **(right panels)**.

DISCUSSION ABOUT THE LINKS BETWEEN THE BOUNDARIES AND THEIR MAGNETIC LOCAL TIME DISTRIBUTION

Links Between the Plasmapause and the Radiation Belt Boundaries

Empirical relations between the plasmapause and Dst have been found, as shown in *Data and Models*. Similar empirical relations exist also for the inner and outer edges of the radiation belts (for different energies) with the Dst index (Pierrard et al., 2020), indicating a possible link between these positions and the ring current responsible for the Dst decrease during storms. As shown in *Long Term Variations of the Plasmapause: Comparison Between Observations and the Space Weather Integrated Forecasting Framework plasmasphere model Model*, the plasmapause is located close to the inner edge of the energetic outer belt for E ~ 1 MeV during the storm main phase and generally above the outer edge of the outer belt for E > 1.6 MeV after sufficiently prolonged quiet periods (Pierrard et al., 2020). The convection electric field that depends on the geomagnetic activity seems also implicated in the dynamics affecting these different regions.

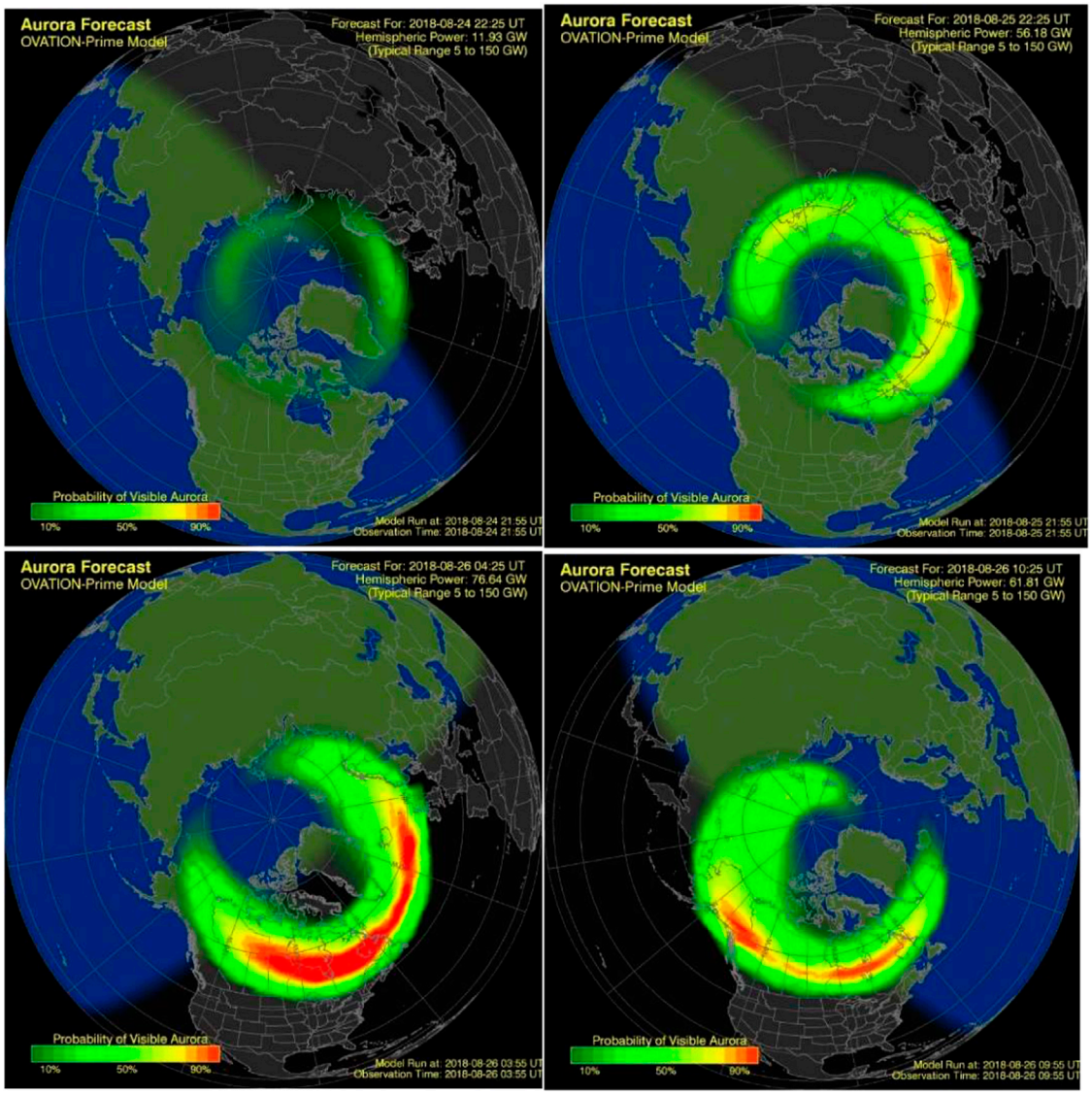


FIGURE 15 | Northern hemisphere probability of aurora visibility as predicted by the OVATION model before the storm **(upper left)** on 24-8-2018 at 22h25, and then during the storm on **(upper right)** 25-8-2018 at 22h25, on **(bottom left)** 26-8-2018 at 4h25 and on **(bottom right)** 26-8-2018 at 10h25. Greenwich longitude of 0° is located in the right side of the panels.

Links between the plasmasphere and the radiation belts can be determinant for the global dynamics of the magnetosphere. The plasmapause boundary determines the electromagnetic waves that circulate in the plasma and may cause energization and loss of the particles. Outside the plasmasphere, whistler-mode chorus waves have been found to play an important role in the enhancement and precipitation of electrons (e.g., Thorne et al., 2013). Inside the plasmasphere, whistler-mode hiss waves can cause the slow decay of radiation belts electrons with loss time scales on the order of 5–10 days (e.g., Ripoll et al., 2019) and rarely contribute to local acceleration. In general, the plasmapause separates chorus waves outside the plasmasphere and hiss waves inside the plasmasphere (e.g., Thorne, 2010). Therefore, changes in plasmapause location can cause drastic change in the hardening or softening of the radiation belt flux. Poloidal ULF (ultra-low frequency) pulsations have also been investigated near the dayside plasmapause and these studies revealed that the wave field is confined in the Alfvén resonator at the outer edge of the plasmapause (Schäfer et al., 2007, 2008). O'Brien et al. (2003) found that electron acceleration at low L shells is closely associated with both ULF activity and MeV microbursts and thereby probably also with chorus activity. Electron flux enhancements across the outer radiation belt are, in general, related to both ULF and VLF/ELF activity. These authors suggest that electron flux peaks observed at $L \sim 4.5$ are likely caused by VLF/ELF wave acceleration which appears to be excluded from the plasmasphere, while ULF activity probably produces the dominant electron acceleration at geosynchronous

orbit and beyond. Intense local acceleration can occur outside of the plasmasphere from chorus waves (Thorne et al., 2013; Li et al., 2016), bringing very quickly sub-relativistic electrons (E < 500 keV) to ultra-relativistic energies (E > 2 MeV), using the terminology in Drozdov et al. (2015). While this is a classic scenario, with available chorus observations during the March 2015 storm for both a THEMIS spacecraft and Van Allen Probes (Li et al., 2016), there is still a debate on the respective importance of local acceleration and adiabatic transport (Ozeke et al., 2019).

Links Between the Plasmapause and Its Footprint in the Ionosphere

The plasmapause boundary has been shown to be related to mid-latitude ionospheric troughs (e.g., Lemaire, 2001). Such mid-latitude troughs, also called main ionospheric light ion troughs, are density depletions observed in the ionosphere in the F region above 150 km of altitude (e.g., Rycroft and Burnell, 1970). Because the low latitude boundary of the trough corresponds to the projection of the plasmapause into the ionosphere, the mid-latitude troughs have been proven to be a good indicator of the plasmapause location (Yizengaw and Moldwin, 2005; Anderson et al., 2008), including for recent events like the September 2017 storm (Obana et al., 2019). A new study compares the location of the mid-latitude trough and plasmapause boundary using Van Allen Probe observations (Weygand et al., 2021). Their results indicate that the mid-latitude trough observed within vertical total electron content maps represents an additional means of identifying the plasmapause boundary location.

Mid-latitude troughs have to be differentiated from high-latitude ionospheric troughs that are sometimes observed inside and poleward of the auroral oval. They are due to auroral precipitation processes (Collis and Haggstrom, 1988; Voiculescu et al., 2016).

Links Between the Radiation Belts and the Location of the Auroral Oval

We have found that the auroral oval is generally located at higher latitude than the oval of the outer radiation belt. This can be explained by the fact that auroras are due to particles coming from a ring located at larger distances in the equatorial plane than the radiation belts for electrons with E > 500 keV. This ring surrounds the Earth at geocentric distances from ~7 Re to the magnetopause, near noon, and to~10–13 Re near midnight, where it corresponds to the plasma sheet (Riazanteseva et al., 2018). Electric potential differences cause the precipitation of energetic particles from the plasma sheet along the elongated magnetic field lines located mainly in the night side, where the auroral oval is thus brighter (Pierrard et al., 2007). It is expected that the energetic ions originate from the ring current and can be scattered by the electromagnetic Ion Cyclotron (EMIC) waves through cyclotron resonance (Sigsbee et al., 2020 and references therein). The energetic electrons can also be precipitated by non-resonant interactions between the electrons and EMIC waves (e.g., Denton et al., 2019). Other studies show the link of proton auroral and plasmaspheric plumes through these same processes (Spasojevic et al., 2004). And several studies have shown that proton aurora spot sources are often located in the vicinity of the plasmapause (Yahnin et al., 2013; Zhou et al., 2019).

Riazanteseva et al. (2018) found that the high-latitude boundary of the outer radiation belt (>100 keV) can be located both inside the auroral oval or equatorward of the low-latitude boundary of the auroral precipitation zone. They also found that for slightly disturbed geomagnetic conditions, the polar boundary of the outer radiation belt is almost always located inside the auroral oval. This is important since the position of the trapping boundary for energetic electrons in the outer radiation belt contains information about the topology of the magnetic field lines of the Earth.

The scenario is different for diffuse aurora since they are caused by precipitations of electrons from 10–30 keV (e.g., Nishimura et al., 2020) and can occur where chorus waves are present. Chorus waves can also cause acceleration of hundreds of keV radiation belt electrons at a lower L-shell. Since chorus are mainly located outside the plasmasphere, this would lead to diffuse aurora being poleward of the plasmapause. Note also that some studies have shown that electron cyclotron harmonic (ECH) waves can also contribute to the formation of diffuse aurora (e.g. Zhang et al., 2015).

Magnetic Local Time Distribution of the Different Regions

The particles of the plasmasphere, of the auroral regions and of the radiation belts are all trapped in the magnetic field of the Earth, giving them a toroidal shape around the Earth in the meridian plane. When projected at low altitude, they correspond to different ovals, at very high latitude for the aurora and at mid-latitudes for the radiation belts and the plasmapause. Nevertheless, their shape is quite different due to their different energy that give them different motion.

The low energy particles (around 1 eV) of the plasmasphere are located in the same region of the inner magnetosphere as the inner and outer belt (500 keV–5 MeV) during quiet periods. The plasmasphere is almost in co-rotation with the Earth. In fact, the velocity of the ionosphere and the low altitude plasmasphere has sometimes a small lag (80–90% of corotation) (Burch et al., 2004; Lejosne and Mozer, 2016). The causes of sub-corotation variability have been explored by Galvan et al. (2010). The azimuthal drift is dominated by the electric force: v_{drift}= (ExB)/B^2. It takes thus approximately 24 h for the particles to make a complete rotation. The plasmapause and the plasmasphere density are thus highly dependent on MLT, with the development of some specific structures like plumes in the afternoon-dusk MLT sector.

The plasma sheet electrons *with an energy from 100 eV to several keV* causing the aurora are located in the nightside tail and are thus also very dependent on MLT. The auroral oval is clearly broader and brighter in the midnight sector, as shown in **Figure 15**. For the energetic particles of the radiation belts (E > 500 keV), the drift velocity is not dominated by the electric force anymore, but by the Lorentz force due to the gradient of B and the curvature of the magnetic field lines (Roederer, 1970). This force depends on the energy of the particles. A 1 MeV electron at L = 1.5 Re (respectively L

= 6) takes approximately 45 (respectively 11) minutes to rotate around the Earth in the equatorial plane. The longitudinal dependence of the radiation belt is thus more determined by the configuration of the magnetic field than by the MLT. The MLT plays nevertheless a fundamental role in the radiation belts, because, for instance, magnetopause shadowing on the day side is responsible for particle dropouts during the main phase of the storms, highly affecting the outer edge of the outer belt (e.g., Pierrard et al., 2020) and wave-particle interactions determining the radiation belt structure are strongly MLT-dependent (cf. review of Ripoll et al. (2019)).

Since the energies of the particles filling the auroral regions, the radiation belts and the plasmasphere are very different, their drift velocity is also different and can explain some of the differences observed in MLT. The physical processes of plasmapause formation and auroral injections are related to the convection electric field that increases during the storm. The very energetic particles of the radiation belt are less affected by the electric field since their drift velocity is dominated by the effects of the magnetic (gradient and curvature) force during quiet times.

The MLT sector plays an important role for the distribution of the particles trapped in the terrestrial magnetic field. The plasmapause is formed in the post-midnight sector due to the plasma convection and is transmitted to the other MLT sectors by co-rotation (Pierrard and Lemaire, 2004). The formation of plumes in the afternoon-dusk sector and their rotation toward other MLT can influence the other regions. As shown by Imber et al. (2013), the ionospheric convection boundary, Heppner Maynard Boundary (HMB), measured by SuperDARN can be used as a proxy for the latitude of the auroral oval and is magnetically related to the plasmapause, in turn reflecting itself the topology of the system. Matar (2021) observed, by analyzing geomagnetic storms, that the plasmasphere density correlates with the open magnetic flux associated to reconnection, confirming the links we discussed in the present work between the plasmasphere and the aurora.

Global Motion During Storms

The different ovals (aurora, outer radiation belt at low altitude, footprint of the plasmapause projection in the ionosphere, and ionospheric convection pattern) have to be considered within a global view of the magnetosphere as they are all part of this dynamic system. The equatorward motion of the different regions of the magnetosphere during storms, i.e., the plasmapause, inner edge of the outer belt and inner edge of the auroral oval, implies some possible intersections of these different regions at particular times (as seen in *Links Between the Plasmapause, Ionospheric Convection Boundary, Radiation Belts and Auroral Oval During a Quiet Period: March 14, 2014* for quiet times and *Links Between the Plasmapause, Ionospheric Convection Boundary, Radiation Belts and Auroral Oval During the Storm Event of August 26, 2018* for storms), possibly linking them, all reflecting at their own scales a same magnetic topology of the system.

As shown in Auroral Oval by the OVATION Model, the auroral zone shifts poleward at times of low solar activity, while during periods of high solar activity, the auroral oval moves to lower latitudes (thus southward in the Northern hemisphere). This southward motion during storms and substorm is very similar to the motion of the plasmapause and of the outer radiation belt toward lower latitudes during the same disturbed periods, as shown in *Links Between the Plasmapause, Ionospheric Convection Boundary, Radiation Belts and Auroral Oval During the Storm Event of August 26, 2018*. The primary source mechanism of the polar aurora is nevertheless different since it is related to reconnection in the magnetotail that extends on the nightside (e.g., Kivelson and Russell, 1995). Reconnection of the geomagnetic field with the IMF mostly occurs when the IMF is directed southward and generates substorm injections. The plasmasphere and the outer belts are in turn also affected by such substorm injection events.

CONCLUSION

In the present work, we study and compare the positions (with respect to L-shell and magnetic local time) of the plasmapause, of the ionospheric convection, of the radiation belt boundaries and of the auroral oval, on the long term during a 10 months period of 2015 and also during two specific periods: one period of quiet geomagnetic activity in March 2014 and one period of disturbed geomagnetic activity associated with the geomagnetic storm of August 26, 2018. We combine different satellite observations (the NASA Van Allen Probes for the plasmapause and the radiation belts, and the ESA PROBA-V for the radiation belts at LEO), radar observations (SuperDARN for the ionospheric convection), and various models (the SPM plasmasphere model, OVATION for aurora, AE-8MAX for radiation belts). We show the dynamics of these regions in three dimensions, i.e., radially, in MLT, and as a function of the latitude. This is done by combining meridian, equatorial and polar maps. We show a similar equatorward motion of the plasmapause, the outer belt and the auroral oval during storms, suggesting a link due to the magnetic field topology and the convection electric field that increases during storms and substorms.

Maps in geographic coordinates allow direct comparison of the different boundaries in MLT sectors at the same UT times during quiet and active periods. We discuss links between the plasmapause and the projection of the plasmapause in the ionosphere. The plasmapause is located at similar distance as the outer edge of the outer belt, but only for E~1.6 MeV and after sufficiently long quiet periods, and as the inner edge of the outer belt during the main phase of the storms, but only for E~1 MeV. The radiation belt boundaries are strongly dependent on the energy of the particles. At lower energies, the plasmapause is located inside the outer radiation belt.

The equatorial edge of the auroral oval is often located close to the outer (polar) edge of the outer energetic belt, and to the plasmapause during quiet periods. There is often overlap between the plasmasphere region, the outer radiation belt and equatorward part of the auroral oval, especially in the nightside. During storms, the auroral oval position decreases in latitude, similarly to the plasmapause, the ionospheric trough, the ionospheric convection

boundary and the inner edge of the outer belt. All these regions seem related by the magnetic field and the convection electric field.

The boundaries are dependent on the energy of the particles, especially for the outer radiation belt that include electrons from 100 keV to several MeV. The MLT dependence is also different for the plasmasphere, the auroral oval, and the radiation belts due to the relative contributions of convective and magnetic of the particles at different energies.

Recent research studies show the need of a more global view of the magnetosphere dynamics that takes into account the interactions between these different regions. The links between the plasmapause, the ionospheric convection, the boundaries of the radiation belts, and the auroral oval certainly need further investigations. In that perspective and to know further, links between compressions of the plasmapause, multi-keV electrons injections, and luminous phenomena reported in the ionosphere are discussed in Cully et al. of this special issue. Nevertheless, they remain difficult to explore due to the lack of simultaneous observations. Three dimensional dynamic models of different regions of the magnetosphere help providing some vision and understanding global and coupled dynamics between the magnetosphere and the ionosphere, with still the need to validate them from more observations.

DATA AVAILABILITY STATEMENT

Publicly available datasets were analyzed in this study. The SPM model nowcast images are available on the ESA SSA (Space Situational Awareness) website (https://swe.ssa.esa.int/space-radiation). Ovation model, developed at the Johns Hopkins University, Applied Physics Lab by Patrick Newell and co-workers, and validated by NASA Polar satellite data, is available on NOAA, Colorado: https://www.swpc.noaa.gov/products/aurora-30-minute-forecast. EPT data are publicly available at the ESA website http://swe.ssa.esa.int/space-radiation. All RBSP-ECT data are publicly available at the Web site http://www.RBSP-ect.lanl.gov/. The EFW spacecraft potential is available from the University of Minnesota Van Allen Probes EFW site http://www.space.umn.edu/rbspefw-data/. EMFISIS data can be obtained from http://emfisis.physics.uiowa.edu. The authors acknowledge the use of on-line plotting tools hosted by the Virginia Tech SuperDARN group at their website (http://vt.superdarn.org/tiki-index.php?page=Conv+map+overview). The CRRES Plasmapause Data (Data set) have been put in repository by Moldwin, M., O'Brien, P., University of Michigan - Deep Blue: https://doi.org/10.7302/mwy1-v326.

AUTHOR CONTRIBUTIONS

PV has written this article, has developed the SPM model, and contributed to the analysis of the data, including for EPT as co-I. EB contributed to improve the SPM model and to realize some plots. J-FR computed the plasmapause location from the EFW and EMFISIS density, and provided the ECT combined flux. J-FR contributed to the analysis of the data and to the writing of the article. ST provided the EFW electron density and GR checked the electron fluxes of Van Allen Probes. MM provided the CRRES plasmapause data set. MR provided and checked the SuperDARN data.

FUNDING

The SafeSpace project has received funding from the European Union's Horizon 2020 research and innovation program under grant agreement No 870437. The project Plasmasphere ionosphere Thermosphere Integrated Research Environment and Access services: a Network of Research Facilities PITHIA-NRF (https://www.pithia-nrf.eu/) has received funding from INFRAIA-02–2020, ID 101007599. Processing and analysis of the (HOPE, MagEIS, REPT, or ECT) data was supported by Energetic Particle, Composition, and Thermal Plasma (RBSP-ECT) investigation funded under NASA's Prime contract no. NAS5-01072.

ACKNOWLEDGMENTS

The authors thank the editors for their invitation to contribute to this special issue about on Coupled Feedback Mechanisms in the Magnetosphere-Ionosphere System. The authors thank the EFW and EMFISIS teams of the Van Allen Probes mission for their support. Van Allen Probes wave data used in this work are available from the EFW and EMFISIS team websites (which one can link to http://rbspgway.jhuapl.edu). The authors thank the ECT team of the Van Allen Probes mission for their support. VP thanks the team of Center for Space Radiations for the validation of the EPT data. JFR thanks M. Cosmides for her contribution to the ECT combined flux figures. The authors thank the International Space Sciences Institute (ISSI) and the participants in a 2020 ISSI workshop for the project "Radiation belts physics". The authors acknowledge the use of SuperDARN data. SuperDARN is a collection of radars funded by national scientific funding agencies of Australia, Canada, China, France, Italy, Japan,Norway, South Africa, United Kingdom and the United States.

REFERENCES

Anderson, P. C., Johnston, W. R., and Goldstein, J. (2008). Observations of the Ionospheric Projection of the Plasmapause. *Geophys. Res. Lett.* 35, L15110. doi:10.1029/2008GL033978

Baker, D. N., Jaynes, A. N., Hoxie, V. C., Thorne, R. M., Foster, J. C., Li, X., et al. (2014). An Impenetrable Barrier to Ultrarelativistic Electrons in the Van Allen Radiation Belts. *Nature* 515, 531–534. doi:10.1038/nature13956

Baker, D. N., Kanekal, S. G., Hoxie, V. C., Batiste, S., Bolton, M., Li, X., et al. (2012). The Relativistic Electron-Proton Telescope (REPT) Instrument on Board the Radiation Belt Storm Probes (RBSP) Spacecraft: Characterization of Earth's Radiation Belt High-Energy Particle Populations. *Space Sci. Rev.* 179, 337–381. doi:10.1007/s11214-012-9950-9

Bandić, M., Verbanac, G., Moldwin, M. B., Pierrard, V., and Piredda, G. (2016). MLT Dependence in the Relationship between Plasmapause, Solar Wind, and Geomagnetic Activity Based on CRRES: 1990-1991. *J. Geophys. Res. Space Phys.* 121, 4397–4408. doi:10.1002/2015JA022278

Bandić, M., Verbanac, G., Pierrard, V., and Cho, J. (2017). Evidence of MLT Propagation of the Plasmapause Inferred from THEMIS Data. *J. Atmos. Solar-Terrestrial Phys.* 161, 55–63. doi:10.1016/j.jastp.2017.05.005

Bandić, M., Verbanac, G., and Pierrard, V. (2020). Relationship between Global Plasmapause Characteristics and Plasmapause Structures in the Frame of Interchange Instability Mechanism. *J. Geophys. Res. Space Phys.* 125, e2019JA026768. doi:10.1029/2019JA026768

Bartels, J., and Veldkamp, J. (1949). International Data on Magnetic Disturbances, First Quarter, 1949. *J. Geophys. Res.* 54 (3), 295–299. doi:10.1029/JZ054i003p00295

Blake, J. B., Carranza, P. A., Claudepierre, S. G., Clemmons, J. H., Crain, W. R., Dotan, Y., et al. (2013). The *Magnetic Electron Ion Spectrometer* (MagEIS) Instruments Aboard the Radiation Belt Storm Probes (RBSP) Spacecraft. *Space Sci. Rev.* 179, 383–421. doi:10.1007/s11214-013-9991-8

Borovsky, J. E., and Valdivia, J. A. (2018). The Earth's Magnetosphere: A Systems Science Overview and Assessment. *Surv. Geophys.* 39 (5), 817–859. doi:10.1007/s10712-018-9487-x

Borovsky, J. E., Welling, D. T., Thomsen, M. F., and Denton, M. H. (2014). Long-lived Plasmaspheric Drainage Plumes: Where Does the Plasma Come from. *J. Geophys. Res. Space Phys.* 119 (8), 6496–6520. doi:10.1002/2014JA020228

Boyd, A. J., Reeves, G. D., Spence, H. E., Funsten, H. O., Larsen, B. A., Skoug, R. M., et al. (2019). RBSP-ECT Combined Spin-Averaged Electron Flux Data Product. *J. Geophys. Res. Space Phys.* 124, 9124–9136. doi:10.1029/2019JA026733

Burch, J. L., Goldstein, J., and Sandel, B. R. (2004). Cause of Plasmasphere Corotation Lag. *Geophys. Res. Lett.* 31 (L05802), 1–4. doi:10.1029/2003GL019164

Carpenter, D. L., and Anderson, R. R. (1992). An ISEE/whistler Model of Equatorial Electron Density in the Magnetosphere. *J. Geophys. Res.* 97 (A2), 1097–1108. doi:10.1029/91ja01548

Carpenter, D. L. (1963). Whistler Evidence of a 'knee' in the Magnetospheric Ionization Density Profile. *J. Geophys. Res.* 68, 1675–1682. doi:10.1029/jz068i006p01675

Claudepierre, S. G., O'Brien, T. P., Blake, J. B., Fennell, J. F., Roeder, J. L., Clemmons, J. H., et al. (2015). A Background Correction Algorithm for Van Allen Probes MagEIS Electron Flux Measurements. *J. Geophys. Res. Space Phys.* 120, 5703–5727. doi:10.1002/2015JA021171

Collis, P. N., and Häggström, I. (1988). Plasma Convection and Auroral Precipitation Processes Associated with the Main Ionospheric Trough at High Latitudes. *J. Atmos. Terrestrial Phys.* 50, 389–404. doi:10.1016/0021-9169(88)90024-4

Comfort, R. H. (1996). Thermal Structure of the Plasmasphere. *Adv. Space Res.* 17, 175–184. doi:10.1016/0273-1177(95)00710-V

Comfort, R. H., Waite, J. H., Jr., and Chappell, C. R. (1985). Thermal Ion Temperatures from the Retarding Ion Mass Spectrometer on DE 1. *J. Geophys. Res.* 90, 3475. doi:10.1029/JA090iA04p03475

Cyamukungu, M., Benck, S., Borisov, S., Gregoire, G., Cabrera, J., Bonnet, J.-L., et al. (2014). The Energetic Particle Telescope (EPT) on Board Proba-V: Description of a New Science-Class Instrument for Particle Detection in Space. *IEEE Trans. Nucl. Sci.* 61 (6), 3667–3681. doi:10.1109/TNS.2014.2361955

Darrouzet, F., De Keyser, J., Décréau, P. M. E., Gallagher, D. L., Pierrard, V., Lemaire, J. F., et al. (2006). Analysis of Plasmaspheric Plumes: CLUSTER and IMAGE Observations. *Ann. Geophys.* 24, 1737–1758. doi:10.5194/angeo-24-1737-2006

F. Darrouzet, J. De Keyser, and V. Pierrard (Editors) (2009). *The Earth's Plasmasphere: Cluster and IMAGE – A Modern Perspective* (Springer), 296.

Darrouzet, F., Pierrard, V., Benck, S., Lointier, G., Cabrera, J., Borremans, K., et al. (2013). Links between the Plasmapause and the Radiation belt Boundaries as Observed by the Instruments CIS, RAPID, and WHISPER Onboard Cluster. *J. Geophys. Res. Space Phys.* 118, 4176–4188. doi:10.1002/jgra.50239

Denton, R. E., Ofman, L., Shprits, Y. Y., Bortnik, J., Millan, R. M., Rodger, C. J., et al. (2019). Pitch Angle Scattering of Sub-MeV Relativistic Electrons by Electromagnetic Ion Cyclotron Waves. *J. Geophys. Res. Space Phys.* 124, 5610–5626. doi:10.1029/2018JA026384

Drozdov, A. Y., Shprits, Y. Y., Orlova, K. G., Kellerman, A. C., Subbotin, D. A., Baker, D. N., et al. (2015). Energetic, Relativistic, and Ultrarelativistic Electrons: Comparison of Long-Term VERB Code Simulations with Van Allen Probes Measurements. *J. Geophys. Res. Space Phys.* 120, 3574–3587. doi:10.1002/2014JA020637

Fennell, J. F., Claudepierre, S. G., Blake, J. B., O'Brien, T. P., Clemmons, J. H., Baker, D. N., et al. (2015). Van Allen Probes Show that the Inner Radiation Zone Contains No MeV Electrons: ECT/MagEIS Data. *Geophys. Res. Lett.* 42, 1283–1289. doi:10.1002/2014GL062874

Forsyth, C., Rae, I. J., Murphy, K. R., Freeman, M. P., Huang, C.-L., Spence, H. E., et al. (2016). What Effect Do Substorms Have on the Content of the Radiation Belts. *J. Geophys. Res. Space Phys.* 121, 6292–6306. doi:10.1002/2016JA022620

Foster, J. C., Erickson, P. J., Coster, A. J., Goldstein, J., and Rich, F. J. (2002). Ionospheric Signatures of Plasmaspheric Tails. *Geophys. Res. Lett.* 29 (13), 1–4. doi:10.1029/2002GL015067

Fung, S. F. (1996). "Recent Development in the NASA Trapped Radiation Models," in *Radiation Belts: Models and Standards, Geophys. Monogr. Ser., 97* (Washington, D. C: AGU), 79–91.

Funsten, H. O., Skoug, R. M., Guthrie, A. A., MacDonald, E. A., Baldonado, J. R., Harper, R. W., et al. (2013). Helium, Oxygen, Proton, and Electron (HOPE) Mass Spectrometer for the Radiation Belt Storm Probes Mission. *Space Sci. Rev.* 179, 423–484. doi:10.1007/s11214-013-9968-7

Fuselier, S., McPherron, D. B., Kletzing, C., and Pierrard, V. (2019). "Geomagnetism, Aeronomy and Space Weather: a Journey from the Earth's Core to the Sun," in *IAGA Book*. Editors M. Mandea, M. Korte, A. Yau, and E. Petrovsky (Cambridge University Press). doi:10.1017/9781108290135

Gallagher, D. L., Comfort, R. H., Katus, R. M., Sandel, B. R., Fung, S. F., and Adrian, M. L. (2021). The Breathing Plasmasphere: Erosion and Refilling. *J. Geophys. Res. Space Phys.* 126, 4. doi:10.1029/2020ja028727

Galvan, D. A., Moldwin, M. B., Sandel, B. R., and Crowley, G. (2010). On the Causes of Plasmaspheric Rotation Variability: IMAGE EUV Observations. *J. Geophys. Res.* 115 (A01214), 1–4. doi:10.1029/2009JA014321

Goldstein, J., Baker, D. N., Blake, J. B., De Pascuale, S., Funsten, H. O., Jaynes, A. N., et al. (2016). The Relationship between the Plasmapause and Outer belt Electrons. *J. Geophys. Res. Space Phys.* 121, 8392–8416. doi:10.1002/2016JA023046

Goldstein, J., Gallagher, D., Craven, P. D., Comfort, R. H., Genestreti, K. J., Mouikis, C., et al. (2019). Temperature Dependence of Plasmaspheric Ion Composition. *J. Geophys. Res. Space Phys.* 124, 6585–6595. doi:10.1029/2019ja026822

Goldstein, J., Sandel, B. R., Hairston, M. R., and Reiff, P. H. (2003). Control of Plasmaspheric Dynamics by Both Convection and Sub-auroral Polarization Stream. *Geophys. Res. Lett.* 30 (24), 2243. doi:10.1029/2003GL018390

Grebowsky, J. M. (1970). Model Study of Plasmapause Motion. *J. Geophys. Res.* 75, 4329–4333. doi:10.1029/JA075i022p04329

Imber, S. M., Milan, S. E., and Lester, M. (2013). The Heppner-Maynard Boundary Measured by SuperDARN as a Proxy for the Latitude of the Auroral Oval. *J. Geophys. Res. Space Phys.* 118 (2), 685–697. doi:10.1029/2012ja018222

Jaynes, A. N., Baker, D. N., Singer, H. J., Rodriguez, J. V., Loto'aniu, T. M., Ali, A. F., et al. (2015). Source and Seed Populations for Relativistic Electrons: Their Roles in Radiation belt Changes. *J. Geophys. Res. Space Phys.* 120, 7240–7254. doi:10.1002/2015ja021234

Johnson, M. H., and Kierein, J. (1992). Combined Release and Radiation Effects Satellite (CRRES): Spacecraft and Mission. *J. Spacecraft Rockets* 29 (4), 556–563. doi:10.2514/3.55641

Khoo, L. Y., Li, X., Zhao, H., Sarris, T. E., Xiang, Z., Zhang, K., et al. (2018). On the Initial Enhancement of Energetic Electrons and the Innermost Plasmapause Locations: Coronal Mass Ejection-Driven Storm Periods. *J. Geophys. Res. Space Phys.* 123, 9252–9264. doi:10.1029/2018JA026074

Kivelson, M., and Russell, C. T. (1995). *Introduction to Space Physics*. New York: Cambridge University Press.

Kletzing, C. A., Kurth, W. S., Acuna, M., MacDowall, R. J., Torbert, R. B., Averkamp, T., et al. (2013). The Electric and Magnetic Field Instrument Suite and Integrated Science (EMFISIS) on RBSP. *Space Sci. Rev.* 179 (1-4), 127–181. doi:10.1007/s11214-013-9993-6

Kurth, W. S., De Pascuale, S., Faden, J. B., Kletzing, C. A., Hospodarsky, G. B., Thaller, S., et al. (2015). Electron Densities Inferred from Plasma Wave Spectra Obtained by the Waves Instrument on Van Allen Probes. *J. Geophys. Res. Space Phys.* 120 (2), 904–914. doi:10.1002/2014JA020857

Lapenta, G., Pierrard, V., Keppens, R., Markidis, S., Poedts, S., Šebek, O., et al. (2013). SWIFF: Space Weather Integrated Forecasting Framework. *J. Space Weather Space Clim.* 3 (1), A05–A17. doi:10.1051/swsc/2013027

Lejosne, S., and Mozer, F. S. (2016). Van Allen Probe Measurements of the Electric Drift E × B/B 2 at Arecibo's L = 1.4 Field Line Coordinate. *Geophys. Res. Lett.* 43, 6768–6774. doi:10.1002/2016GL069875

Lemaire, J. F. (2001). The Formation of the Light-Ion Trough and Peeling off the Plasmasphere. *J. Atmos. Solar-Terrestrial Phys.* 63, 1285–1291. doi:10.1016/s1364-6826(00)00232-7

Lemaire, J., and Gringauz, K. I. (1998). *The Earth's Plasmasphere*. Cambridge: Cambridge University Press.

Lemaire, J., and Schunk, R. W. (1992). Plasmaspheric Wind. *J. Atmos. Terr. Phys.* 54 (3-4), 467–477. doi:10.1016/0021-9169(92)90026-H

Li, W., Ma, Q., Thorne, R. M., Bortnik, J., Zhang, X. J., Li, J., et al. (2016). Radiation belt Electron Acceleration during the 17 March 2015 Geomagnetic Storm: Observations and Simulations. *J. Geophys. Res. Space Phys.* 121, 5520–5536. doi:10.1002/2016JA022400

Li, X., Baker, D. N., O'Brien, T. P., Xie, L., and Zong, Q. G. (2006). Correlation between the Inner Edge of Outer Radiation belt Electrons and the Innermost Plasmapause Location. *Geophys. Res. Lett.* 33, L14107. doi:10.1029/2006GL026294

Loridan, V., Ripoll, J. F., Tu, W., and Cunningham, G. S. (2019). On the Use of Different Magnetic Field Models for Simulating the Dynamics of the Outer Radiation belt Electrons during the October 1990 Storm. *J. Geophys. Res. Space Phys.* 124, 6453–6486. doi:10.1029/2018ja026392

Lyons, L. R., and Thorne, R. M. (1973). Equilibrium Structure of Radiation belt Electrons. *J. Geophys. Res.* 78 (13), 2142–2149. doi:10.1029/JA078i013p02142

Machol, J. L., Green, J. C., Redmon, R. J., Viereck, R. A., and Newell, P. T. (2012). Evaluation of OVATION Prime as a Forecast Model for Visible Aurorae. *Space Weather* 10, a–n. doi:10.1029/2011SW000746

Matar, J. (2021). "Effect of Magnetic Reconnection over the Earth's Space Environment,". PhD thesis (Liège: University of Liège).

Mauk, B. H., Fox, N. J., Kanekal, S. G., Kessel, R. L., Sibeck, D. G., and Ukhorskiy, A. (2013). Science Objectives and Rationale for the Radiation Belt Storm Probes mission. *Space Sci. Rev.* 179, 3–27. doi:10.1007/s11214-012-9908-y

McIlwain, C. E. (1966). Magnetic Coordinates. *Space Sci. Rev.* 5, 585–598. doi:10.1007/BF00167327

Moldwin, M. B., Downward, L., Rassoul, H. K., Amin, R., and Anderson, R. R. (2002). A New Model of the Location of the Plasmapause: CRRES Results. *J. Geophys. Res.* 107 (1339), 1–9. doi:10.1029/2001ja009211

Newell, P. T., Sotirelis, T., Ruohoniemi, J. M., Carbary, J. F., Liou, K., Skura, J. P., et al. (2002). OVATION: Oval Variation, Assessment, Tracking, Intensity, and Online Nowcasting. *Ann. Geophys.* 20, 1039–1047. doi:10.5194/angeo-20-1039-2002

Newell, P. T., Sotirelis, T., and Wing, S. (2010). Seasonal Variations in Diffuse, Monoenergetic, and Broadband aurora. *J. Geophys. Res.* 115, a–n. doi:10.1029/2009JA014805

Nishimura, Y., Lessard, M. R., Katoh, Y., Miyoshi, Y., Grono, E., Partamies, N., et al. (2020). Diffuse and Pulsating Aurora. *Space Sci. Rev.* 216, 4. doi:10.1007/s11214-019-0629-3

O'Brien, T. P., Lorentzen, K. R., Mann, I. R., Meredith, N. P., Blake, J. B., Fennell, J. F., et al. (2003). Energization of Relativistic Electrons in the Presence of ULF Power and MeV Microbursts: Evidence for Dual ULF and VLF Acceleration. *J. Geophys. Res.* 108 (A8), 1329. doi:10.1029/2002JA009784

O'Brien, T. P., and Moldwin, M. B. (2003). Empirical Plasmapause Models from Magnetic Indices. *Geophys. Res. Lett.* 30, 1152. doi:10.1029/2002GL016007

Obana, Y., Maruyama, N., Shinbori, A., Hashimoto, K. K., Fedrizzi, M., Nosé, M., et al. (2019). Response of the Ionosphere-plasmasphere Coupling to the September 2017 Storm: What Erodes the Plasmasphere So Severely. *Space Weather* 17, 861–876. doi:10.1029/2019SW002168

Ozeke, L. G., Mann, I. R., Claudepierre, S. G., Henderson, M., Morley, S. K., Murphy, K. R., et al. (2019). The March 2015 Superstorm Revisited: Phase Space Density Profiles and Fast ULF Wave Diffusive Transport. *J. Geophys. Res. Space Phys.* 124, 1143–1156. doi:10.1029/2018JA026326

Pierrard, V., and Benck, S. (2012). The Dynamics of the Terrestrial Radiation Belts and its Links to the Plasmasphere. *AIP Conf. Proc.* 1500, 216. doi:10.1063/1.4768769

Pierrard, V., Botek, E., and Darrouzet, F. (2021a). Improving Predictions of the 3D Dynamic Model of the Plasmasphere. *Front. Astron. Space Sci.* 8, 681401. doi:10.3389/fspas.2021.681401

Pierrard, V., Botek, E., Ripoll, J. F., and Cunningham, G. (2020). Electron Dropout Events and Flux Enhancements Associated with Geomagnetic Storms Observed by PROBA-V/Energetic Particle Telescope from 2013 to 2019. *J. Geophys. Res. Space Phys.* 125, 12. doi:10.1029/2020JA028487

Pierrard, V., and Cabrera, J. (2005). Comparisons between EUV/IMAGE Observations and Numerical Simulations of the Plasmapause Formation. *Ann. Geophys.* 23 (7), 2635–2646. doi:10.5194/angeo-23-2635-2005

Pierrard, V., and Cabrera, J. (2006). Dynamical Simulations of Plasmapause Deformations. *Space Sci. Rev.* 122 (1-4), 119–126. doi:10.1007/s11214-006-5670-3

Pierrard, V., Goldstein, J., André, N., Jordanova, V. K., Kotova, G. A., Lemaire, J. F., et al. (2009). Recent Progress in Physics-Based Models of the Plasmasphere. *Space Sci. Rev.* 145, 193–229. doi:10.1007/978-1-4419-1323-4_7

Pierrard, V., Khazanov, G. V., Cabrera, J., and Lemaire, J. (2008). Influence of the Convection Electric Field Models on Predicted Plasmapause Positions during Magnetic Storms. *J. Geophys. Res.* 113, 1. doi:10.1029/2007JA012612

Pierrard, V., Khazanov, G. V., and Lemaire, J. F. (2007). Current-voltage Relationship. *J. Atmos. Solar-Terrestrial Phys.* 69 (12), 2048–2057. doi:10.1016/j.jastp.2007.08.005

Pierrard, V., and Lemaire, J. F. (2004). Development of Shoulders and Plumes in the Frame of the Interchange Instability Mechanism for Plasmapause Formation. *Geophys. Res. Lett.* 31 (5), a–n. doi:10.1029/2003GL018919

Pierrard, V., Lopez Rosson, G., Borremans, K., Lemaire, J., Maes, J., Bonnewijn, S., et al. (2014). The Energetic Particle Telescope: First Results. *Space Sci. Rev.* 184, 87–106. doi:10.1007/s11214-014-0097-8

Pierrard, V., and Lopez Rosson, G. (2016). The Effects of the Big Storm Events in the First Half of 2015 on the Radiation Belts Observed by EPT/PROBA-V. *Ann. Geophys.* 34, 75–84. doi:10.5194/angeo-34-75-2016

Pierrard, V., Ripoll, J. F., Cunningham, G., Botek, E., Santolik, O., Thaller, S., et al. (2021b). Observations and Simulations of Dropout Events and Flux Decays in October 2013: Comparing MEO Equatorial with LEO Polar Orbit. *J. Geophys. Res. Space Phys.* 126, e2020JA028850. doi:10.1029/2020JA028850

Pierrard, V., and Stegen, K. (2008). A Three-Dimensional Dynamic Kinetic Model of the Plasmasphere. *J. Geophys. Res.* 113, A10209. doi:10.1029/2008ja013060

Pierrard, V., and Voiculescu, M. (2011). The 3D Model of the Plasmasphere Coupled to the Ionosphere. *Geophys. Res. Lett.* 38, a–n. doi:10.1029/2011GL047767

Reeves, G. D., Friedel, R. H. W., Larsen, B. A., Skoug, R. M., Funsten, H. O., Claudepierre, S. G., et al. (2016). Energy-dependent Dynamics of keV to MeV Electrons in the Inner Zone, Outer Zone, and Slot Regions. *J. Geophys. Res. Space Phys.* 121, 397–412. doi:10.1002/2015ja021569

Reinisch, B. W., Moldwin, M. B., Denton, R. E., Gallagher, D. L., Matsui, H., Pierrard, V., et al. (2009). Augmented Empirical Models of Plasmaspheric Density and Electric Field Using IMAGE and CLUSTER Data. *Space Sci. Rev.* 145, 231–261. doi:10.1007/s11214-008-9481-6

Riazanteseva, M. O., Antonova, E. E., Stepanova, M. V., Marjin, B. V., Rubinshtein, I. A., Barinova, V. O., et al. (2018). Relative Positions of the Polar Boundary of the Outer Electron Radiation belt and the Equatorial Boundary of the Auroral Oval. *Ann. Geophys.* 36, 1131–1140. doi:10.5194/angeo-36-1131-2018

Ripoll, J.-F., Denton, M. H., Hartley, D. P., Reeves, G. D., Malaspina, D., Cunningham, G. S., et al. (2021). Scattering by Whistler-Mode Waves during a Quiet Period Perturbed by Substorm Activity. *J. Atmos. Solar-Terrestrial Phys.* 215, 105471. doi:10.1016/j.jastp.2020.105471

Ripoll, J.-F., Denton, M., Loridan, V., Santolík, O., Malaspina, D., Hartley, D. P., et al. (2020b). How Whistler Mode Hiss Waves and the Plasmasphere Drive the Quiet Decay of Radiation Belts Electrons Following a Geomagnetic Storm. *J. Phys. Conf. Ser.* 1623, 012005. doi:10.1088/1742-6596/1623/1/012005

Ripoll, J.-F., Loridan, V., Denton, M. H., Cunningham, G., Reeves, G., Santolík, O., et al. (2019). Observations and Fokker-Planck Simulations of the L-Shell, Energy, and Pitch Angle Structure of Earth's Electron Radiation Belts during Quiet Times. *J. Geophys. Res. Space Phys.* 124, 1125–1142. doi:10.1029/2018ja026111

Ripoll, J.-F., Reeves, G. D., Cunningham, G. S., Loridan, V., Denton, M., Santolík, O., et al. (2016). Reproducing the Observed Energy-dependent Structure of

Earth's Electron Radiation Belts during Storm Recovery with an Event-specific Diffusion Model. *Geophys. Res. Lett.* 43, 5616–5625. doi:10.1002/2016GL068869

Ripoll, J. F., Claudepierre, S. G., Ukhorskiy, A. Y., Colpitts, C., Li, X., Fennell, J. F., et al. (2020a). Particle Dynamics in the Earth's Radiation Belts: Review of Current Research and Open Questions. *J. Geophys. Res. Space Phys.* 125, e2019JA026735. doi:10.1029/2019JA026735

Ripoll, J. F., Santolík, O., Reeves, G. D., Kurth, W. S., Denton, M. H., Loridan, V., et al. (2017). Effects of Whistler Mode Hiss Waves in March 2013. *J. Geophys. Res. Space Phys.* 122, 7433–7462. doi:10.1002/2017JA024139

Roederer, J. G. (1970). "Dynamics of Geomagnetically Trapped Radiation," in *Physics and Chemistry in Space*, Editors J. G. Roederer and J. Zahringer (Berlin: Springer). doi:10.1007/978-3-642-49300-3

Ruohoniemi, J. M., and Baker, K. B. (1998). Large-scale Imaging of High-Latitude Convection with Super Dual Auroral Radar Network HF Radar Observations. *J. Geophys. Res. Space Phys.* 103 (A9), 20797–20811. doi:10.1029/98JA01288

Rycroft, M. J., and Burnell, S. J. (1970). Statistical Analysis of Movements of the Ionospheric Trough and the Plasmapause. *J. Geophys. Res.* 75, 5600–5604.

Sandel, B. R., Goldstein, J., Gallagher, D. L., and Spasojevic, M. (2003). Extreme Ultraviolet Imager Observations of the Structure and Dynamics of the Plasmasphere. *Space Sci. Rev.* 109, 25–46. doi:10.1023/b:spac.0000007511.47727.5b

Schäfer, S., Glassmeier, K. H., Eriksson, P. T. I., Mager, P. N., Pierrard, V., Fornaçon, K. H., et al. (2008). Spatio-temporal Structure of a Poloidal Alfvén Wave Detected by Cluster Adjacent to the Dayside Plasmapause. *Ann. Geophys.* 26, 1805–1817. doi:10.5194/angeo-26-1805-2008

Schäfer, S., Glassmeier, K. H., Eriksson, P. T. I., Pierrard, V., Fornaçon, K. H., and Blomberg, L. G. (2007). Spatial and Temporal Characteristics of Poloidal Waves in the Terrestrial Plasmasphere: A CLUSTER Case Study. *Ann. Geophys.* 25, 1011–1024. doi:10.5194/angeo-25-1011-2007

Sigsbee, K., Kletzing, C. A., Faden, J. B., Jaynes, A. N., Reeves, G. D., and Jahn, J. M. (2020). Simultaneous Observations of Electromagnetic Ion Cyclotron (EMIC) Waves and Pitch Angle Scattering during a Van Allen Probes Conjunction. *J. Geophys. Res. Space Phys.* 125 (4), e219JA0277424. doi:10.1029/2019ja027424

Spasojević, M., Frey, H. U., Thomsen, M. F., Fuselier, S. A., Gary, S. P., Sandel, B. R., et al. (2004). The Link between a Detached Subauroral Proton Arc and a Plasmaspheric Plume. *Geophys. Res. Lett.* 31, L04803. doi:10.1029/2003GL018389

Spence, H. E., Reeves, G. D., Baker, D. N., Blake, J. B., Bolton, M., Bourdarie, S., et al. (2013). Science Goals and Overview of the Radiation Belt Storm Probes (RBSP) Energetic Particle, Composition, and Thermal Plasma (ECT) Suite on NASA's Van Allen Probes Mission. *Space Sci. Rev.* 179, 311–336. doi:10.1007/s11214-013-0007-5

Thaller, S. A., Wygant, J. R., Dai, L., Breneman, A. W., Kersten, K., Cattell, C. A., et al. (2015). Van Allen Probes Investigation of the Large-scale Duskward Electric Field and its Role in Ring Current Formation and Plasmasphere Erosion in the 1 June 2013 Storm. *J. Geophys. Res. Space Phys.* 120, 4531–4543. doi:10.1002/2014ja020875

Thorne, R. M., Li, W., Ni, B., Ma, Q., Bortnik, J., Chen, L., et al. (2013). Rapid Local Acceleration of Relativistic Radiation-belt Electrons by Magnetospheric Chorus. *Nature* 504 (7480), 411–414. doi:10.1038/nature12889

Thorne, R. M. (2010). Radiation belt Dynamics: The Importance of Wave-Particle Interactions. *Geophys. Res. Lett.* 37, a–n. doi:10.1029/2010GL044990

Tu, W., Cunningham, G. S., Chen, Y., Morley, S. K., Reeves, G. D., Blake, J. B., et al. (2014). Event-specific Chorus Wave and Electron Seed Population Models in DREAM3D Using the Van Allen Probes. *Geophys. Res. Lett.* 41, 1359–1366. doi:10.1002/2013gl058819

Turner, D. L., Claudepierre, S. G., Fennell, J. F., O'Brien, T. P., Blake, J. B., Lemon, C., et al. (2015). Energetic Electron Injections Deep into the Inner Magnetosphere Associated with Substorm Activity. *Geophys. Res. Lett.* 42, 2079–2087. doi:10.1002/2015gl063225

Turner, D. L., Kilpua, E. K. J., Claudepierre, S. G., O'Brien, T. P., and Fennell, J. F. (2019). The Response of Earth's Electron Radiation Belts to Geomagnetic Storms: Statistics from the Van Allen Probes Era Including Effects from Different Storm Drivers. *J. Geophys. Res. Space Phys.* 124, 1013–1034. doi:10.1029/2018JA026066

Verbanac, G., Bandić, M., Pierrard, V., and Cho, J. (2018). MLT Plasmapause Characteristics: Comparison between THEMIS Observations and Numerical Simulations. *J. Geophys. Res. Space Phys.* 123, 2000–2017. doi:10.1002/2017JA024573

Verbanac, G., Pierrard, V., Bandić, M., Darrouzet, F., Rauch, J.-L., and Décréau, P. (2015). The Relationship between Plasmapause, Solar Wind and Geomagnetic Activity between 2007 and 2011. *Ann. Geophys.* 33, 1271–1283. doi:10.5194/angeo-33-1271-2015

Vette, J. I. (1991). *The AE-8 Trapped Electron Model Environment*. Greenbelt: NSSDC/WDC-A-R&S, 91–24.

Voiculescu, M., Nygren, T., Aikio, A., Vanhamaki, H., and Pierrard, V. (2016). Post Midnight Troughs at High Latitudes in Summer. *J. Geophys. Res. Space Phys.* 121, 12171–12185. doi:10.1002/2016ja023360

Weygand, J. M., Zhelavskaya, I., and Shprits, Y. (2021). A Comparison of the Location of the Mid-Latitude Trough and Plasmapause Boundary. *J. Geophys. Res. Space Phys.* 126, e2020JA028213. doi:10.1029/2020JA028213

Wygant, J. R., Bonnell, J. W., Goetz, K., Ergun, R. E., Mozer, F. S., Bale, S. D., et al. (2013). The Electric Field and Waves Instruments on the Radiation Belt Storm Probes mission. *Space Sci. Rev.* 179 (1-4), 183–220. doi:10.1007/978-1-4899-7433-4_6

Yahnin, A. G., Yahnina, T. A., Frey, H., and Pierrard, V. (2013). Sub-oval Proton aurora Spots: Mapping Relatively to the Plasmapause. *J. Atmos. Solar-Terrestrial Phys.* 99, 61–66. doi:10.1016/j.jastp.2012.09.018

Yizengaw, E., and Moldwin, M. B. (2005). The Altitude Extension of the Mid-latitude Trough and its Correlation with Plasmapause Position. *Geophys. Res. Lett.* 32, L09105. doi:10.1029/2005GL022854

Zhang, X.-J., Angelopoulos, V., Ni, B., and Thorne, R. M. (2015). Predominance of ECH Wave Contribution to Diffuse aurora in Earth's Outer Magnetosphere. *J. Geophys. Res. Space Phys.* 120, 295–309. doi:10.1002/2014JA020455

Zhou, S., Luan, X., Pierrard, V., and Han, D. (2019). Isolated Auroral Spots Observed by DMSP/SSUSI. *J. Geophys. Res. Space Phys.* 124 (11), 8416–8426. doi:10.1029/2019JA026853

Conflict of Interest: The authors declare that the research was conducted in the absence of any commercial or financial relationships that could be construed as a potential conflict of interest.

Publisher's Note: All claims expressed in this article are solely those of the authors and do not necessarily represent those of their affiliated organizations, or those of the publisher, the editors and the reviewers. Any product that may be evaluated in this article, or claim that may be made by its manufacturer, is not guaranteed or endorsed by the publisher.

Copyright © 2021 Pierrard, Botek, Ripoll, Thaller, Moldwin, Ruohoniemi and Reeves. This is an open-access article distributed under the terms of the Creative Commons Attribution License (CC BY). The use, distribution or reproduction in other forums is permitted, provided the original author(s) and the copyright owner(s) are credited and that the original publication in this journal is cited, in accordance with accepted academic practice. No use, distribution or reproduction is permitted which does not comply with these terms.

frontiers in Astronomy and Space Sciences

ORIGINAL RESEARCH
published: 02 December 2021
doi: 10.3389/fspas.2021.776992

Early-Time Non-Equilibrium Pitch Angle Diffusion of Electrons by Whistler-Mode Hiss in a Plasmaspheric Plume Associated with BARREL Precipitation

R. M. Millan[1]*, *J.-F. Ripoll*[2,3], *O. Santolík*[4,5] *and W. S. Kurth*[6]

[1]Department of Physics and Astronomy, Dartmouth College, Hanover, NH, United States, [2]CEA, DAM, DIF, Arpajon, France, [3]UPS, CEA, LMCE, Bruyeres-le-Chatel, France, [4]Department of Space Physics, Institute of Atmospheric Physics of the Czech Academy of Sciences, Prague, Czechia, [5]Faculty of Mathematics and Physics, Charles University, Prague, Czechia, [6]Department of Physics and Astronomy, University of Iowa, Iowa City, IA, United States

OPEN ACCESS

Edited by:
Olga V. Khabarova,
Institute of Terrestrial Magnetism Ionosphere and Radio Wave Propagation (RAS), Russia

Reviewed by:
Kyung-Chan Kim,
Chungbuk National University, South Korea
Arvind Kumar Tripathi,
Indian Institute of Technology (BHU), India

***Correspondence:**
R. M. Millan
Robyn.Millan@dartmouth.edu

Specialty section:
This article was submitted to Space Physics, a section of the journal Frontiers in Astronomy and Space Sciences

Received: 14 September 2021
Accepted: 28 October 2021
Published: 02 December 2021

Citation:
Millan RM, Ripoll J-F, Santolík O and Kurth WS (2021) Early-Time Non-Equilibrium Pitch Angle Diffusion of Electrons by Whistler-Mode Hiss in a Plasmaspheric Plume Associated with BARREL Precipitation. Front. Astron. Space Sci. 8:776992. doi: 10.3389/fspas.2021.776992

In August 2015, the Balloon Array for Radiation belt Relativistic Electron Losses (BARREL) observed precipitation of energetic (< 200 keV) electrons magnetically conjugate to a region of dense cold plasma as measured by the twin Van Allen Probes spacecraft. The two spacecraft passed through the high density region during multiple orbits, showing that the structure was spatial and relatively stable over many hours. The region, identified as a plasmaspheric plume, was filled with intense hiss-like plasma waves. We use a quasi-linear diffusion model to investigate plume whistler-mode hiss waves as the cause of precipitation observed by BARREL. The model input parameters are based on the observed wave, plasma and energetic particle properties obtained from Van Allen Probes. Diffusion coefficients are found to be largest in the same energy range as the precipitation observed by BARREL, indicating that the plume hiss waves were responsible for the precipitation. The event-driven pitch angle diffusion simulation is also used to investigate the evolution of the electron phase space density (PSD) for different energies and assumed initial pitch angle distributions. The results show a complex temporal evolution of the phase space density, with periods of both growth and loss. The earliest dynamics, within the ~5 first minutes, can be controlled by a growth of the PSD near the loss cone (by a factor up to ~2, depending on the conditions, pitch angle, and energy), favored by the absence of a gradient at the loss cone and by the gradients of the initial pitch angle distribution. Global loss by 1-3 orders of magnitude (depending on the energy) occurs within the first ~100 min of wave-particle interaction. The prevalence of plasmaspheric plumes and detached plasma regions suggests whistler-mode hiss waves could be an important driver of electron loss even at high L-value (L ~6), outside of the main plasmasphere.

Keywords: radiation belt, wave-particle interaction, electron precipitation, plasmaspheric plume, whistler-mode hiss/chorus, quasi-linear diffusion

1 INTRODUCTION

On August 10, 2015, BARREL balloon payload 3 A observed bremsstrahlung x-rays (~5–150 keV) attributed to precipitation of energetic electrons with energies < 200 keV. The balloon was located over Kiruna, Sweden, and magnetically conjugate to the Van Allen Probes (RBSP) spacecraft as they entered a region of high plasma density. The high density region was spatially confined and persisted for multiple orbits indicating that it is a plasmaspheric plume or detached plasma region. Strong whistler-mode hiss waves were observed by both spacecraft in the high density region.

Plasmaspheric hiss is a major driver of radiation belt loss inside the plasmasphere, contributing to the creation of the slot region between the inner and outer radiation belts (Lyons and Thorne, 1973). These low-frequency (~50 Hz-2 kHz) electromagnetic whistler-mode waves are broadband and incoherent. Their power is also proportional to the density, with more power in dense regions (Malaspina et al., 2016; Malaspina et al., 2018). Recent RBSP observations and simulations demonstrate the importance of hiss waves; these waves generate major loss up to L = 5.5 from pitch angle diffusion when the plasmasphere is widely extended during quiet times (Ripoll et al., 2016; Ripoll et al., 2017; Ripoll et al., 2019). More information about hiss waves and the dynamics of the radiation belts can be found in the review of Ripoll et al. (2020a).

Outside the plasmasphere, at higher L-values, energetic electron precipitation has been primarily attributed to whistler mode chorus waves or electromagnetic ion cyclotron (EMIC) waves [e.g., Millan and Thorne (2007); Thorne (2010)]. Recent work suggests that hiss may also be active at higher L-values in dense plasmaspheric plumes and detached plasma regions. A plasmaspheric plume (also called a "tail" in the literature) is a narrow region of dense cold plasma that extends out from the main plasmasphere at Earth. The EUV instrument on the IMAGE spacecraft provided the first global observations of plasmaspheric plumes, their formation and evolution (Sandel et al., 2001; Goldstein, 2004). Plume evolution is driven by changes in the dawn-dusk convection electric field due to changes in the solar wind (Grebowsky, 1970; Lemaire, 2000). A sudden increase in the convection electric field causes the plasmapause boundary to move inward leaving behind plasma that $E \times B$ drifts towards the dayside, forming a dayside plume that is wide in magnetic local time (MLT). With a subsequent decrease in the convection electric field, the plume wraps around Earth and the MLT extent narrows. Spacecraft passing through a plume observe a localized increase in cold plasma density over a narrow range in MLT. In the absence of global imaging, the twin Van Allen Probes spacecraft, moving in similar orbits - one following the other, provide an opportunity to distinguish between temporal and spatial variations, helping to identify spatial density structures like plumes.

Properties of hiss waves in plumes have been statistically characterized in Shi et al. (2019). The occurrence rate of hiss in plumes has a clear dependence on MLT and geomagnetic activity, peaking near the dusk sector during active times. These waves are more powerful in plumes than inside the plasmasphere, particularly during active times, and have low wave normal angles compared to the wide wave distribution function in the plasmasphere. Plume whistler-mode waves were frequently observed by Van Allen Probes and may be an efficient loss mechanism for radiation belt seed electrons (Zhang et al., 2019). Zhang et al. (2018) calculated loss rates due to observed hiss emissions in a nightside plume and found that such emissions may result in fast (few hours) loss of 10–100 keV electrons at L in [4.5, 5.5] and a slower decay of higher energy particles. Li et al. (2019) examined a particular event and found that plume whistler mode waves are an effective pitch-angle scattering mechanism, particularly for electrons with energies from tens to hundreds of keV.

In this paper, we investigate plume whistler-mode hiss waves as the primary cause of the energetic electron precipitation observed by BARREL balloon 3 A on 10 August, 2015. The observations are described in **Section 2.1**. Data from Van Allen Probes are used to precisely determine the properties of observed waves, trapped electrons, and cold plasma density. An event-driven quasi-linear diffusion model is then used (**Section 2.2**) to investigate wave-particle interactions between the plume whistler-mode waves and the trapped electrons, seeking to identify the theoretical energy of the precipitating electrons. We further investigate the time evolution of the electron phase space density.

2 MATERIALS AND METHODS

2.1 Data and Observations

In this study, we use data from BARREL Campaign 3 and the two Van Allen Probes spacecraft to characterize observed electron precipitation and *in situ* plasma and wave properties respectively. BARREL measures electron precipitation by detecting the bremsstrahlung x-rays produced as electrons collide with the neutral atmosphere [see e.g., Sample et al. (2020) for review]. Each BARREL payload carries a single 3" diameter by 3" tall sodium-iodide scintillator nominally sensitive to x-rays from 20 keV to 10 MeV (Millan et al., 2013). Several BARREL data products are available as described in Woodger et al. (2015). In the present study, we use the fast spectra (FSPC) with 50 ms x-ray count rates, available in six energy channels covering 3–1300 keV. Note that the nominal FSPC energy range is 25–1500 keV but the Level 2 data product used here is calibrated to account for temperature-dependent gain shifts. GPS timing and positioning are transmitted using the Iridium satellite network along with the science and other housekeeping data. The third BARREL campaign was carried out at the Esrange facility near Kiruna, Sweden in August 2015. A total of seven balloons were launched over 16 days. Here, we use data from BARREL 3 A which was launched on 10 August at 13:50 UT and terminated on 10 August at 21:18 UT.

The twin Van Allen Probes (here also referred to as RBSP-A and RBSP-B) were launched on 30 August 2012 into nearly-equatorial orbits with 618 km perigee and 30,414 km apogee, providing two passes through the outer radiation belts every

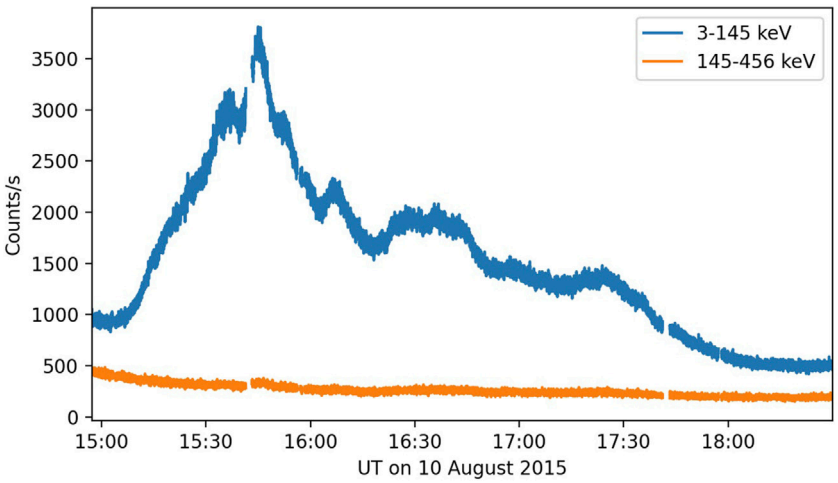


FIGURE 1 | BARREL Payload 3 A x-ray count rate versus time in two energy ranges: 3–145 keV (blue) and 145–456 keV (orange), observed on August 10, 2015. The 50 ms FSPC data have been summed to a 1 s cadence.

roughly 9 h. Each spacecraft carries a comprehensive suite of instrumentation to study particles and plasma waves throughout the inner magnetosphere (Mauk et al., 2013). In this study, we use data from the EMFISIS (Electric and Magnetic Field Instrument Suite and Integrated Science) (Kletzing et al., 2013), and MagEIS (Magnetic Electron Ion Spectrometer) instruments (Blake et al., 2013).

The EMFISIS waves instrument uses a tri-axial search coil magnetometer and electric field measurements from the EFW (Electric Field/Waves) instrument. A 6-channel waveform receiver (WFR) provides electric and magnetic field power from 10 Hz to 12 kHz. A single channel high frequency receiver (HFR) covers 10–500 kHz. For this study, we use Level 4 CDF files for cold plasma density, and the Level 2 WFR Spectral matrix product CDF files for wave observations, obtained from https://emfisis.physics.uiowa.edu/data/index/. The analysis used to determine the wave properties is described in more detail in **Section 2.2** below. For more information about EMFISIS, see Kletzing et al. (2013).

The MagEIS instrument consists of four magnetic spectrometers, one low-energy unit (20–240 keV), two medium-energy units (80–1200 keV), and a high-energy unit (800–4800 keV). For this study, we use Level 3 CDF files from: https://www.rbsp-ect.lanl.gov/data_pub/rbspa/mageis/level3/ which combine low, medium and high data into pitch-angle resolved electron flux. For more information about the MagEIS instrument design see Blake et al. (2013).

BARREL 3 A began to detect an increase in the 3–145 keV x-ray count rate (obtained by summing the FPSC 1a, 1b, and 1c energy channels) at 1505 UT (**Figure 1**, blue trace) just after the balloon reached a float altitude of 37 km. The energy of the precipitating electrons producing the x-rays was primarily below 145 keV as can be seen by the lack of count rate increase in the FSPC2 (145–456 keV) channel (**Figure 1**, orange trace). Precipitation was observed for about 3 h. Note that precipitation may have begun prior to 1505 UT while the balloon was ascending and thus not sensitive to these low energy x-rays. At the onset of the observed precipitation, BARREL 3 A was located at L ~6, MLT ~1740 (T89 magnetic field model with Kp = 2), just east of the RBSP-B magnetic footpoint. BARREL is nearly fixed geographically and thus moves in MLT as earth rotates.

Figure 2 shows EMFISIS data for just over two RBSP orbits on 10 August 2015. The two spacecraft were in similar orbits with RBSP-B (bottom panel) leading RBSP-A (top panel) by about 45 min. The white trace shows plasma density derived from the upper hybrid frequency (Kurth et al., 2015). At 1150 UT, RBSP-B exits the plasmasphere, as indicated by a steep decrease in plasma density. At 1445 UT, it encounters a localized region of increased density (~80 cm^{-3}). About 40 min later, at 1525 UT, RBSP-A encounters a similar localized increase in density. Both spacecraft encountered the high density region near apogee (L = 5.9) and in the same magnetic local time range (~16–17 MLT), indicating that the density increase was a stable spatial structure which we identify as a plasmaspheric plume or detached plasma region. The high density region was also present on the previous orbit but with more spatial variation (**Figure 2**).

Both RBSP spacecraft detected wave power between roughly 50 Hz-1 kHz, identified as whistler-mode hiss waves, throughout the high density plume region (**Figure 2**, color spectrogram). There was substantial variability of the observed wave amplitude, with values ranging from ~50–200 pT. For comparison, mean hiss amplitudes are between 10 and 30 pT depending on geomagnetic conditions (e.g., (Malaspina et al., 2018)). Large amplitude whistler waves similar to those shown here are also reported in the statistics of Shi et al. (2019). The wave analysis and properties are discussed in more detail in **Section 2.2** below.

We also examined electron data from the RBSP MagEIS instrument (**Figure 3**). A small substorm injection between 54–132 keV was observed starting at 1430 UT, just before RBSP-B entered the plume region. The injection shows some energy dispersion at both RBSP spacecraft. Data from the LANL

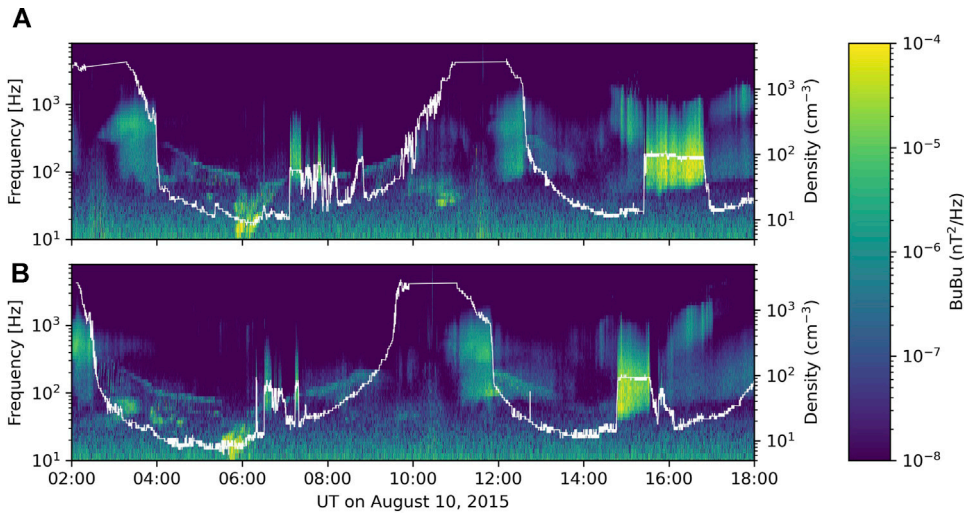


FIGURE 2 | RBSP-A **(A)** and RBSP-B **(B)** EMFISIS data on 10 August 2015. The spectrogram shows the WFR cross spectrum diagonal matrix element, BuBu (spacecraft spin plane component of magnetic field), between 10 Hz and 8 kHz. Plasma density derived from the upper hybrid frequency is shown with the white trace.

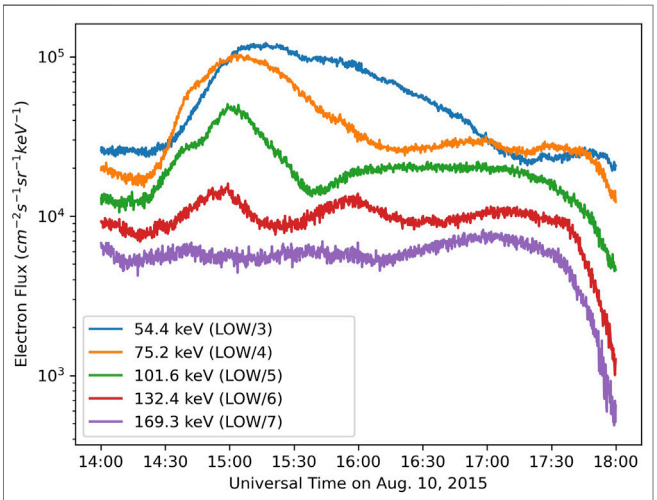


FIGURE 3 | Electron intensity near the loss cone ($\alpha = 24.5°$) in five energy channels as measured by the RBSP-B MagEIS instrument.

geosynchronous spacecraft also show evidence of a substorm injection, with the spacecraft closer to midnight (e.g., LANL-02 A) observing a dispersionless injection at around 1330 UT (not shown). This is consistent with the RBSP observations of a dispersed injection a bit later, since the RBSP spacecraft were in the afternoon sector. **Figure 4** shows example MagEIS pitch angle and energy distributions with superposed fits that are used in the modeling analysis described below.

2.2 Analysis and Model Description

To investigate whether the observed plume hiss waves are the cause of the precipitation observed by BARREL, we use an event-driven quasi-linear diffusion model. Wave properties (mean frequency, frequency cut-offs, wave normal angle, and wave amplitude) over the time interval 1440–1700 UT on 10 August were generated from the EMFISIS data. We first compute the characteristic magnetic field amplitudes of whistler-mode waves using the trace of the magnetic-field power-spectral matrix calculated onboard RBSP-A from 3D measurements of the EMFISIS search coil antennas. The data were further processed into the Level 4 WNA data set (Kletzing et al., 2013) which serves as a basis for our analysis and additionally provides wave-normal angles. We select waves which propagate in the whistler mode and are right-hand polarized with ellipticity above 0.2 (Santolík and Gurnett, 2002). We restrict the analysis to a frequency range typical for plasmaspheric hiss from 50 Hz to 2 kHz (Santolík et al., 2001; Li W. et al., 2013; Thorne et al., 1973). The total power spectral density is therefore integrated over this frequency band. Mean frequency, mean frequency width, and wave normal angle are defined by equations (2)-(4) in (Ripoll et al., 2017) (not repeated here for brevity).

The average wave properties are shown in **Table 1** for RBSP-A and RBSP-B. Although we use only RBSP-A values for the quasi-linear computations described below, the wave properties measured by RBSP-B are also shown in **Table 1** to illustrate the stability and small variations of the wave system within the high density plume as measured by both spacecraft. We note that the waves have relatively small wave normal angles (last column in **Table 1**) in accordance with the statistical behavior found by Shi et al. (2019). The median frequency is also quite low, in agreement with observations of low frequency hiss (Malaspina et al., 2017), which favors interactions with higher energy electrons. Cold plasma density, derived from the upper hybrid frequency as measured by EMFISIS (Kurth et al., 2015), is reported in **Table 2**, along with the normalized wave parameters.

Diffusion coefficients are computed with the CEVA code originally developed by Réveillé et al. (2001). In this code, bounce averaged diffusion coefficients were computed following the method and equations of Lyons et al. (1972),

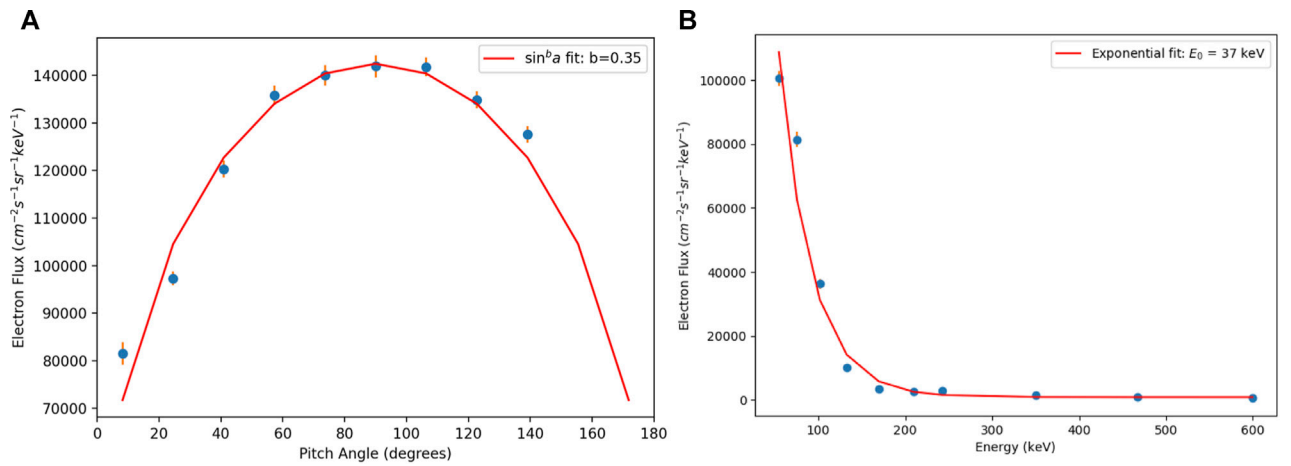


FIGURE 4 | Example pitch angle **(A)** and energy **(B)** distributions from the RBSP-B MagEIS instrument with superposed fits. The pitch angle distribution is shown for ~75 keV electrons and the energy distribution is shown near the loss cone at $\alpha \sim 8^{\circ}$.

TABLE 1 | Average wave parameters obtained from both Van Allen Probe spacecraft during the event interval. θ is the wave normal angle.

Spacecraft	Time	Amplitude	f_{median}	f_{min}	f_{max}	θ
RBSP	UT	(pT)	(Hz)	(Hz)	(Hz)	(degrees)
A	1500–1700	140	154	76	313	11
B	1440–1540	92	150	63	400	12

TABLE 2 | Average plasma and normalized wave parameters during the event interval. ω_{med} is the median wave angular frequency calculated using f_{median} from **Table 1**.

Spacecraft	n_e	ω_{pe}	ω_{ce}	ω_{med}/ω_{ce}	$\omega_{med}\omega_{ce}/\omega_{pe}^2$
RBSP	(cm^{-3})	$\times 10^5 s^{-1}$	$\times 10^3 s^{-1}$	$\times 10^{-1}$	$\times 10^{-5}$
A	79.4	5.03	4.26	0.97	1.63
B	79.4	5.03	4.26	0.94	1.59

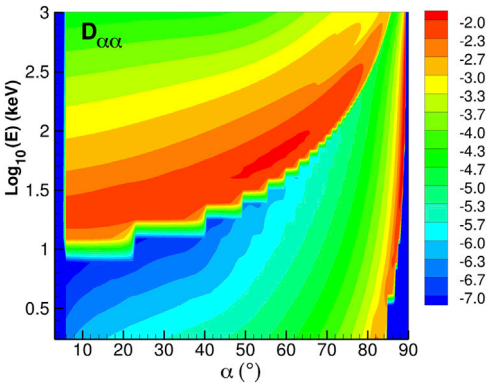


FIGURE 5 | Bounce averaged diffusion coefficient (1/s, log10 scale) with respect to energy (E) and equatorial pitch angle (α) at L = 5.9 for the plume conditions observed by RBSP-A on 10 August, 2015 1500–1700 (cf. **Tables 1**, **2**.).

which account for a sum over all harmonics (-n. . ., 0, . . ., n), a wave normal integration, and bounce averaging between the mirror points. Equations 2 to 8 of Lyons et al. (1972) define the diffusion coefficients. The limit of low frequency ($\omega_{med}/\omega_{ce} < 1$) and high-density ($\omega_{med}\omega_{ce}/\omega_{pe}^2 \ll 1$) that are assumed in these computations are satisfied (cf. **Table 2**, last two columns). A more synthetic and modern expressions of the diffusion coefficients is available through Equations 8, 9 in Ripoll and Mourenas (2013) using the notations of Albert (2005). Verification by comparison with diffusion coefficients computed with the codes from the US AFRL and BAS (e.g.,Albert (1994, 2008); Meredith et al. (2007)) have been performed in Ripoll and Mourenas (2013). Validation studies include Ripoll et al. (2016, 2017, 2019), Ripoll et al. (2020b), Ripoll et al. (2020c), and Loridan et al. (2019).

Diffusion coefficients were calculated using the average wave and plasma parameters from RBSP-A. They are based on the observed size of the high density region (~1 h MLT) and there is no MLT-averaging (e.g., Spasojevic et al. (2015)) that accounts for the wave variations throughout the drift path (cf. more comments below). The inclusion of the available ambient measurements produces so-called event-driven diffusion coefficients which are today the most sophisticated method for reproducing radiation belt observations (see also Thorne et al. (2013); Tu et al. (2014); Ripoll et al. (2020b); Pierrard et al. (2021)). In doing so, we attempt to quantify the accuracy of this type of modeling. The calculated diffusion coefficients are discussed in **Section 3** below.

We also investigate the evolution of the electron phase space density (PSD) using the calculated diffusion coefficients in a pitch angle diffusion based Fokker-Planck equation (e.g. Ripoll et al. (2017)). The initial electron distribution was taken to be dependent on pitch angle following the RBSP-B observations. A convolution with the energy spectrum can be performed after the computation is made (in the absence of energy

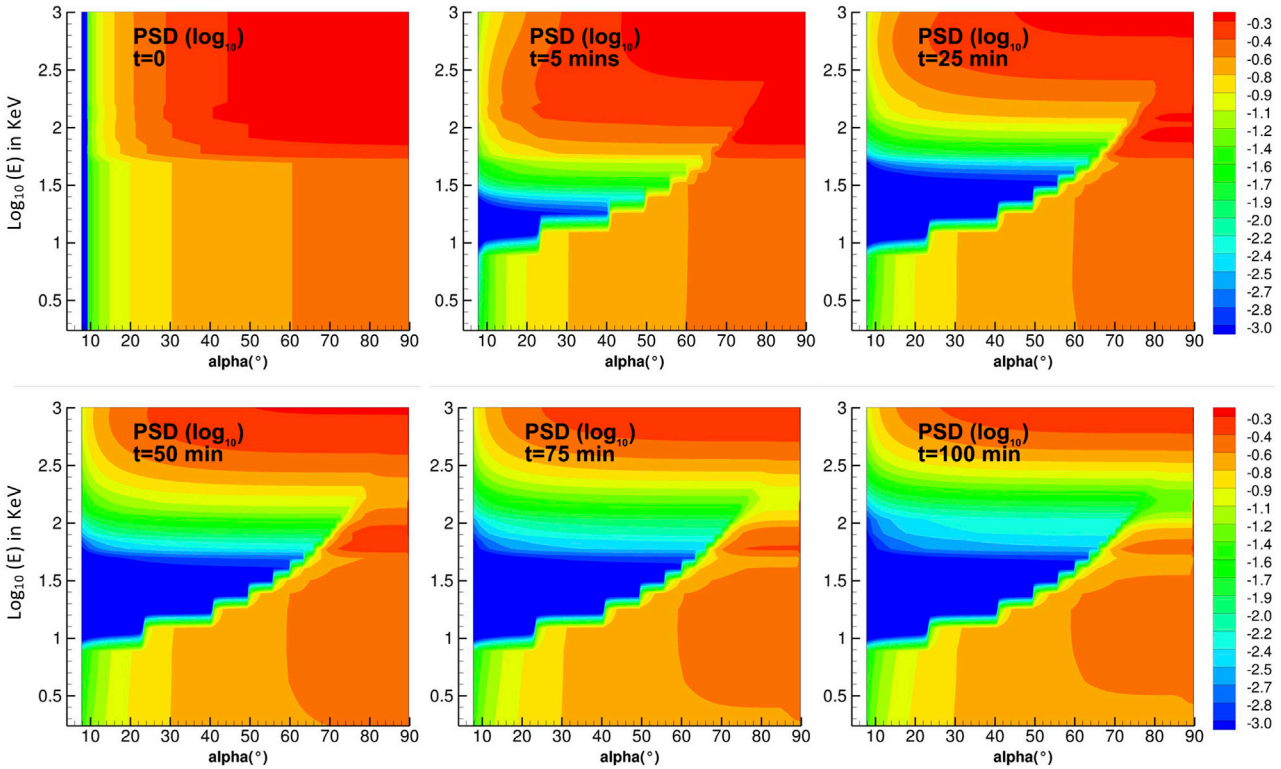


FIGURE 6 | Phase space density versus energy (log10 in keV) and equatorial pitch angle (degrees) plotted at t = 0, 5, 25, 50, 75, 100 min. This PSD is the solution of the Fokker-Planck pitch angle diffusion equation.

diffusion). For each MagEIS energy channel, the pitch angle distribution was fit with a $\sin^{b}(\alpha)$ function with a power $b(E)$ depending on energy (example shown for 75 keV in left panel of **Figure 4**). We find $b(E)$ = [0.15, 0.35, 0.52, 0.8, 0.6] for E = [54, 75, 102, 132, 169] keV. The initial condition is regularized in a continuous manner within the loss cone using the expression $f(t = 0, E) = \sin^{b(E)}(\alpha) - \sin^{b(E)}(\alpha_{lc})$ (Li Z. et al. (2013)).

3 RESULTS

Figure 5 shows the bounce averaged diffusion coefficients calculated using the input parameters described above. At large L-shell (e.g., in the outer belt or in plasmaspheric plumes, $L \sim 6$), hiss waves will predominantly act on low energy electrons. Here, the diffusion coefficient for small pitch angle particles is largest between ~10–150 keV, consistent with the energy of x-rays observed by BARREL. As mentioned previously, the diffusion coefficient is not drift-averaged and is representative of the wave particle interactions only within the plume. The waves were observed only within the plume region, extending ~1 h of MLT, thus drift-bounce-averaged diffusion coefficients would be a factor 1/24 lower in amplitude. Here, due to the intense wave amplitude and the absence of MLT-averaging, diffusion coefficients reach very high rates with $D_{\alpha\alpha} \sim 10^{-2}\ s^{-1}$. Since BARREL was located in the northern hemisphere, it observed predominantly local precipitation. This local bounce loss comes from the immediate and intense (low pitch angle) precipitation within the plume (thus proportional to the local wave amplitude squared) and is not the result of wave particle interactions all along the drift path (that would be proportional to the MLT-averaged squared amplitude, a factor 1/24 lower in this case).

Figure 6 shows the evolution of the phase space density for electrons as a function of energy, E, and equatorial pitch angle, α, from t = 0 to t = 100 min of interaction with hiss waves in the high-density region. The initial condition (top left panel) is $f(t = 0, E) = \sin^{b(E)}(\alpha) - \sin^{b(E)}(\alpha_{lc})$. Sudden loss of 10–30 keV electrons occurs almost immediately, within the first 5 min, in the vicinity of the loss cone (**Figure 6**, top middle). Loss of 100 keV electrons by one order of magnitude takes 25 min of interaction. After 100 min (**Figure 6**, bottom right), the phase space density has vanished by ~2 (resp. 1) orders of magnitude for all pitch angles below 70° for E in [20, 70] keV (resp [70, 200] keV). Note that electrons, particularly of higher energy, may interact with the plume multiple times as they gradient-curvature drift around Earth in order to reach a total of 100 min of interaction. 10 keV electrons with small pitch angle take ~40 min to drift across the plume, thus the rapid loss of low energy electrons within the first 5 min occurs upon their first encounter with the plume. The predicted range of energies of the main loss are also in agreement with the range of energy found by Shi et al. (2019). Some loss of

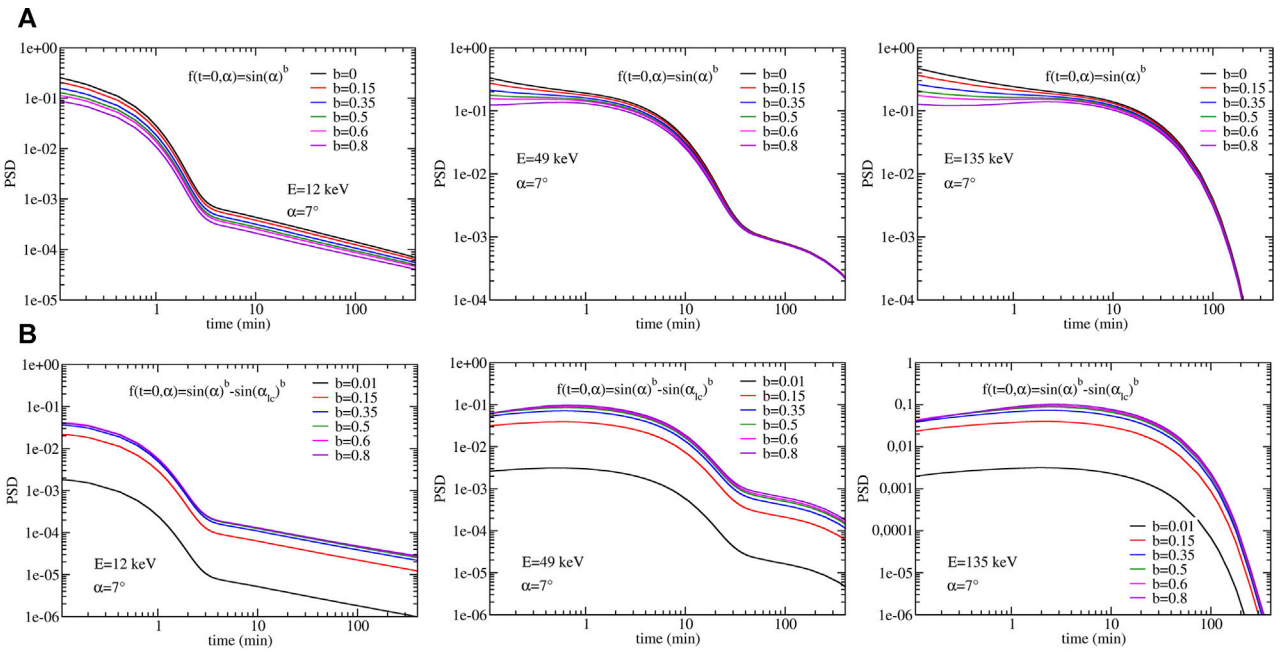


FIGURE 7 | Phase space density versus time for different initial conditions. Initial conditions without **(A)** and with **(B)** regularization at the loss cone for E = 12, 49, and 135 keV. Within each plot, the initial pitch angle distribution varies with a power b ranging from $b \sim 0$ (for which it tends toward $f(t = 0) = 1$) to $b \sim 1$ for which $f(t = 0) = \sin(\alpha)$. For certain energies and b(E) power, the initial condition induces a growth of the PSD prior to a decaying phase. The decay itself presents various phases with different slopes. Changes of slope indicate the steady state has not been reached.

high energy electrons up to 1 MeV within the vicinity of the loss cone are also computed.

We also study the influence of the initial conditions on the loss and on the dynamics at early times, when pitch angle diffusion has not yet reached an equilibrium state. **Figure 7** shows the evolution of the PSD in the vicinity of the loss cone (at $\alpha = 7.95°$, rounded to 7° in the figure's label) during the first 100 min of interaction with hiss waves. Comparing the top and bottom rows of **Figure 7** illustrates the important role of the loss cone regularization. Comparing lines within each figure allows to see the influence of the $b(E)$ power index, with two limits bounding the variations. The low limit $b(E) \rightarrow 0$ (i.e. $b = 0.01$) is equivalent to the widely used and standard $f(t = 0, \alpha) = 1$ initial condition, either dropping abruptly from one for $\alpha \neq \alpha_{lc}$ to 0 for $\alpha = \alpha_{lc}$ if there is no regularization (top row) or going continuously from one to 0 if regularized (bottom row). The second limit of $b(E) \rightarrow 1$ is a PSD approaching $\sin(\alpha)$ and with significant gradient at intermediate pitch angle. **Figure 7** provides interesting new insight into the dynamics and how they are modeled. First, as expected, the larger the gradient at the loss cone, the more intense will be the loss in the vicinity of the loss cone and at the earliest times (generally below 1 min for our case, depending on energy). The regularization, which can be seen as a continuous process to fill out the loss cone, limits the gradient and thus the intensity of the earliest loss. In turn, large $b(E)$ power index leads to intermediate pitch angle diffusion that will make the overall loss-gain budget at fixed pitch angle to lean in favor of a temporary growth of the PSD level during the earliest times. This is better seen in the presence of the regularization (since loss

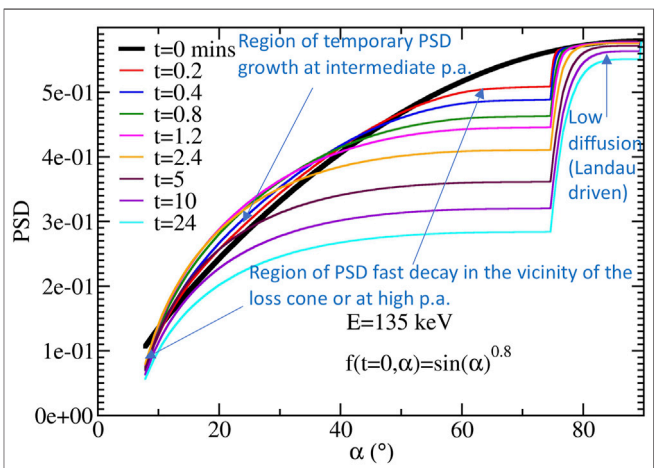


FIGURE 8 | Phase space density of 135 keV electrons versus pitch angle for different times (in min) with four pitch angle regions of different dynamics that are indicated with arrows.

is even milder). On the contrary, without regularization the loss can dominate for certain low energy and $b(E)$, and temporary growth can no longer exist. Most past parameter studies in the literature have been done with $f(t = 0, \alpha) = 1$ and $f(t = 0, \alpha_{lc}) = 0$ (e.g., Shprits et al. (2008)) so that PSD growth could not be seen. This is because the infinite gradient at the loss cone creates intense sudden loss, and the absence of other gradients with respect to pitch angle make the appearance of

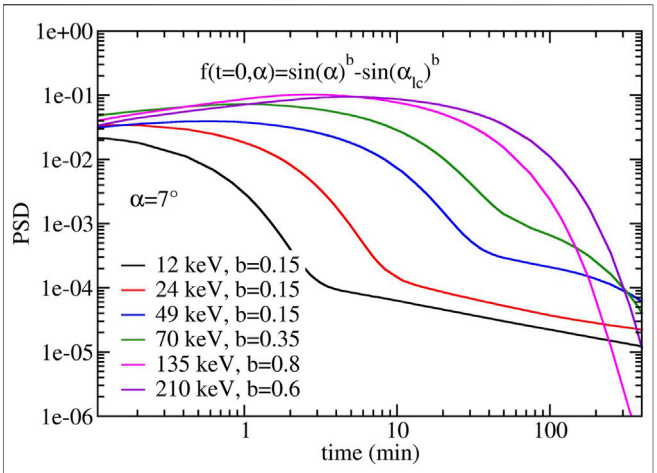


FIGURE 9 | Predicted phase-space density at the loss cone edge (α = 7.95°) for a range of energies (E = 12, 24, 49, 70, 135, 210 keV). PSD growth can occur during the first ~10 min after which the PSD starts decaying abruptly.

temporary PSD growth impossible. This explains why this particular behavior has not been discussed in the past (to the authors' knowledge).

The temporary growth of the PSD can be best analyzed and understood looking at **Figure 8** in which we see a temporary growth happening for times below 5 min at 135 keV for equatorial pitch angle between ~12 and ~40°. The growth is due to the diffusion coefficient whose maximum (first cyclotron resonance) is located above 40° for 135 keV (cf. **Figure 5**). That diffusion turns out to be faster than the diffusion of the lower pitch angles below 40°and outside the loss cone vicinity region. High pitch angle electrons (40°–75°) thus diffuse faster and fill out lower pitch angles (~12°–40°) causing the flux at low pitch angles to rise progressively during the first 3–5 min. That type of diffusion explains the various growths of PSD we see happening in time in **Figure 7**. Comparison of **Figure 8** with **Figure 7** also shows that the growth cannot happen at ~7° for this energy and initial condition for which the absence of regularization in this example increases the gradient at the loss cone and favors the loss.

Figure 9 shows the evolution of the PSD using the specific energy-dependent $b(E)$ observed by RBSP-B. In addition, we plot in **Figure 10** the respective instantaneous growth ($\tau > 0$) and loss rates ($\tau < 0$), previously discussed. We define these rates as $1/\tau = |\Delta f(t)/\Delta t|$ in units of hours. The considerable variation of τ with time (including a change of sign) shows that steady state, which defines the general electron lifetime (Lyons et al., 1972), is not reached within the first 100 min for most of the energies below 200 keV. At 74 keV, we see, for instance, a fast loss rate of ~12 min persisting during ~30 min, which signifies that the flux decreases by a factor e^1 every 12 min during 30 min, i.e. a factor of $e^{(30/12)} = 12$ after 30 min. The constant loss rate during that time is controlled by the largest gradients, which flatten as diffusion occurs. After 30 min, the loss rate of 74 keV starts to increase and reaches a plateau value at ~80 min, which is the steady state value. This is in agreement with the theoretical lifetime from direct steady state computation for 74 keV electron that is 90 min for this problem. Therefore, during the first 30 min that followed the growth phase, the loss is 7.5 times faster than the lifetime would predict. After 100 min, the 49 and 74 keV electron flux are reduced by two orders of magnitude and the 100–200 keV electron flux is reduced by ~1 order of magnitude. The initial electron energy distribution observed by RBSP is exponential and also strongly weighted towards lower energies (**Figure 4**), thus the precipitation observed by BARREL was also dominated by these energies.

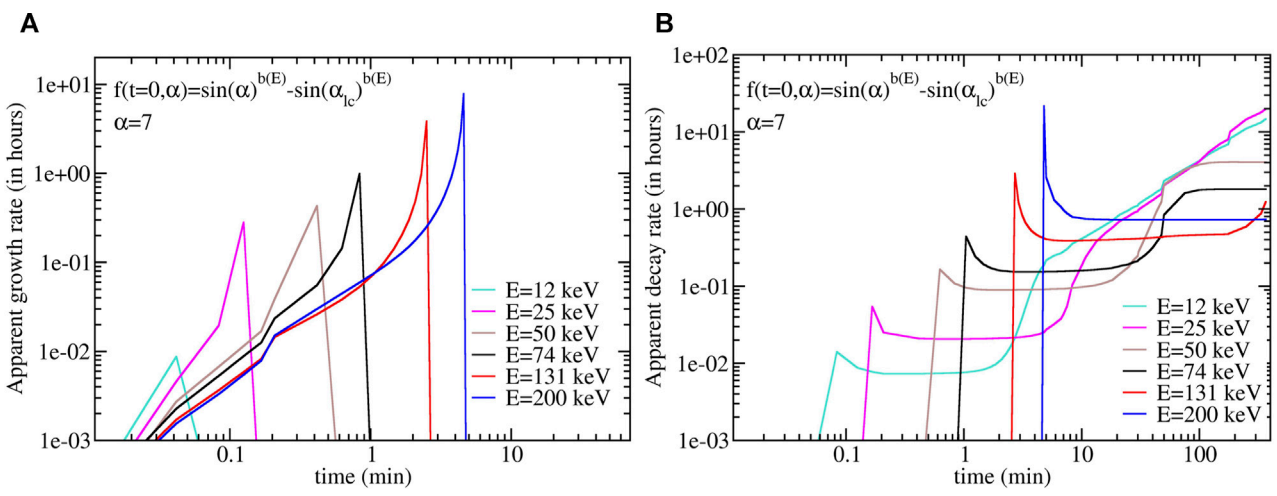


FIGURE 10 | Evolution of the instantaneous growth ($\tau > 0$) **(A)** and decay ($\tau < 0$) **(B)** timescales, defined as $1/\tau(t) = -\Delta f(t)/\Delta t$, for pitch angle in the vicinity of the loss cone. The growth exists during the five first minutes and is entirely due to the initial condition, favored by the absence of an abrupt gradient at the loss cone, which allows the low pitch angle population to be populated from higher pitch angle electrons diffusing toward the loss cone.

4 DISCUSSION

An event-based study was conducted to investigate wave-particle interactions in the radiation belts. A fortuitous magnetic conjunction between the RBSP spacecraft and BARREL balloon payload 3 A provided a rare opportunity to study pitch-angle scattering by plume whistler-mode hiss waves. A quasi-linear pitch angle diffusion model was developed using wave and plasma parameters observed by RBSP as they passed through a stable region of dense cold plasma (n ~80 cm^{-3}) near L = 6. The model results show that interaction with the plume hiss waves leads to rapid loss of electrons over the same energy range observed by BARREL. Moreover, a significant decrease in the trapped electron flux can occur within 2 h for electrons of pitch angle up to 70° for E in [50, 100] keV.

We also examined the effects of the initial pitch-angle distribution that is assumed when evolving the phase space density. Many previous studies assume a completely empty initial loss cone distribution which leads to an artificially rapid loss rate due to the very steep gradient at the loss cone. Regularization of the loss cone distribution reduces this effect and also reveals how diffusion from larger pitch angles can actually cause an initial increase in flux near the loss cone. This effect is very sensitive to the initial pitch angle distribution assumed for a given energy. These results illustrate the importance of modeling the dynamic evolution of the PSD; the assumption of steady-state loss lifetimes is not accurate for event-based studies such as this one, since the event duration is comparable to the time to reach a steady state. We incorporated the observed pitch angle distribution into the dynamic model of PSD. The present study did not include the effects of the energy-dependent drift time for electrons, rather examined the evolution of the PSD as a function of total interaction time with the waves. The lowest energy (~10 keV) electrons spend ~ 40 min within the wave region (the plume) while higher energy (~100 keV) electrons drift across the plume more quickly and may encounter the plume several times as they drift around Earth. In order to more accurately model the energy spectrum observed by BARREL, these effects must be included. The development of the model presented here will allow for such future work.

Recent work from the Van Allen Probes mission has revealed the prevalence of whistler-mode hiss waves in plasmaspheric plumes, and several studies have suggested that plume hiss waves could lead to strong loss of electrons. The event examined here occurred during a substorm injection of electrons into the radiation belts as observed by the RBSP MagEIS instruments. Thus it was not possible to separate the effects of acceleration and loss in order to quantify the overall impact of this plume on the radiation belts. However, the loss rate indicated by this study suggests that scattering by plume whistler-mode hiss waves, which is currently not included in radiation belt models, could be an important loss mechanism, particularly for radiation belt seed electrons. In particular, the plume investigated in this study was stable and persisted for several RBSP orbits. Electrons gradient-curvature drift around the earth many times per day and thus experience multiple encounters with such high-density plumes and the hiss waves they support. Future work should investigate the overall impact of plumes as a loss mechanism for radiation belt electrons and the seed particles that generate them.

DATA AVAILABILITY STATEMENT

Publicly available datasets were analyzed in this study. This data can be found here: https://cdaweb.gsfc.nasa.gov/pub/data/barrel/, https://emfisis.physics.uiowa.edu/Flight/, and https://rbsp-ect.newmexicoconsortium.org/science/DataDirectories.php.

AUTHOR CONTRIBUTIONS

RM and J-FR together developed the study concept. RM carried out the basic data analysis and produced figures from BARREL and Van Allen Probes to characterize the observations. OS provided further analysis of the Van Allen Probes wave data to obtain wave parameters used in the modeling. WK processed EMFISIS data to provide cold plasma density. J-FR developed the quasi-linear diffusion model and produced the model result figures. RM and J-FR together wrote the first draft of the manuscript. All authors contributed to manuscript revision, read, and approved the submitted version.

FUNDING

RM is supported by Dartmouth College through the Margaret Anne and Edward Leede '49 Distinguished Professorship. OS acknowledges support from the LTAUSA17070 Inter-Excellence project and from the European Union's Horizon 2020 research and innovation programme under grant agreement No 870437. WK receives funding from JHU/APL contract 921647 under NASA prime contract NAS5-0107.

ACKNOWLEDGMENTS

The authors thank the International Space Sciences Institute (ISSI) and the participants in a 2020 ISSI workshop for the project "Radiation belts physics". We acknowledge the BARREL, and RBSP EMFISIS and ECT teams for use of their data.

REFERENCES

Albert, J. M. (2008). Efficient Approximations of Quasi-Linear Diffusion Coefficients in the Radiation Belts. *J. Geophy. Res.*, 113, A06208. doi:10.1029/2007ja012936

Albert, J. M. (2005). Evaluation of Quasi-Linear Diffusion Coefficients for Whistler Mode Waves in a Plasma with Arbitrary Density Ratio. *J. Geophy. Res.* 110, A03218. doi:10.1029/2004ja010844

Albert, J. M. (1994). Quasi-linear Pitch Angle Diffusion Coefficients. *Retaining high harmonics* 99, 23741. doi:10.1029/94ja02345

Blake, J. B., Carranza, P. A., Claudepierre, S. G., Clemmons, J. H., Crain, W. R., Dotan, Y., et al. (2013). The Magnetic Electron Ion Spectrometer (Mageis) Instruments Aboard the Radiation belt Storm Probes (Rbsp) Spacecraft. *Space Sci. Rev.* 179, 383–421. doi:10.1007/s11214-013-9991-8

Goldstein, J. (2004). Simultaneous Remote Sensing and *In Situ* Observations of Plasmaspheric Drainage Plumes. *J. Geophys. Res.* 109. doi:10.1029/2003ja010281

Grebowsky, J. M. (1970). Model Study of Plasmapause Motion. *J. Geophys. Res.* 75, 4329–4333. doi:10.1029/ja075i022p04329

Kletzing, C. A., Kurth, W. S., Acuna, M., MacDowall, R. J., Torbert, R. B., Averkamp, T., et al. (2013). The Electric and Magnetic Field Instrument Suite and Integrated Science (Emfisis) on Rbsp. *Space Sci. Rev.* 179, 127–181. doi:10.1007/s11214-013-9993-6

Kurth, W. S., Pascuale, S. D., Faden, J. B., Kletzing, C. A., Hospodarsky, G. B., Thaller, S., et al. (2015). Electron Densities Inferred from Plasma Wave Spectra Obtained by the Waves Instrument on Van allen Probes. *J. Geophys. Res. Space Phys.* 120, 904–914. doi:10.1002/2014ja020857

Lemaire, J. (2000). The Formation Plasmaspheric Tails. *Phys. Chem. Earth, C: Solar, Terrestrial Planet. Sci.* 25, 9–17. doi:10.1016/s1464-1917(99)00026-4

Li, W., Shen, X.-C., Ma, Q., Capannolo, L., Shi, R., Redmon, R. J., et al. (2019). Quantification of Energetic Electron Precipitation Driven by Plume Whistler Mode Waves, Plasmaspheric Hiss, and Exohiss. *Geophys. Res. Lett.* 46, 3615–3624. doi:10.1029/2019gl082095

Li, W., Thorne, R. M., Bortnik, J., Reeves, G. D., Kletzing, C. A., Kurth, W. S., et al. (2013a). An Unusual Enhancement of Low-Frequency Plasmaspheric Hiss in the Outer Plasmasphere Associated with Substorm-Injected Electrons. *Geophys. Res. Lett.* 40, 3798–3803. doi:10.1002/grl.50787

Li, Z., Millan, R. M., and Hudson, M. K. (2013b). Simulation of the Energy Distribution of Relativistic Electron Precipitation Caused by Quasi-Linear Interactions with Emic Waves. *J. Geophys. Res. Space Phys.* 118, 7576–7583. doi:10.1002/2013JA019163

Loridan, V., Ripoll, J.-F., Tu, W., and Cunningham, G. S. (2019). On the Use of Different Magnetic Field Models for Simulating the Dynamics of the Outer Radiation belt Electrons during the October 1990. *storm* 124, 6453–6486. doi:10.1029/2018ja026392

Lyons, L. R., and Thorne, R. M. (1973). Equilibrium Structure of Radiation belt Electrons. *J. Geophys. Res.* 78, 2142–2149. doi:10.1029/ja078i013p02142

Lyons, L. R., Thorne, R. M., and Kennel, C. F. (1972). Pitch-angle Diffusion of Radiation belt Electrons within the Plasmasphere. *J. Geophys. Res.* 77, 3455–3474. doi:10.1029/JA077i019p03455

Malaspina, D. M., Jaynes, A. N., Boulé, C., Bortnik, J., Thaller, S. A., Ergun, R. E., et al. (2016). The Distribution of Plasmaspheric Hiss Wave Power with Respect to Plasmapause Location. *Geophys. Res. Lett.* 43, 7878–7886. doi:10.1002/2016GL069982

Malaspina, D. M., Jaynes, A. N., Hospodarsky, G., Bortnik, J., Ergun, R. E., and Wygant, J. (2017). Statistical Properties of Low-Frequency Plasmaspheric Hiss. *J. Geophys. Res. Space Phys.* 122, 8340–8352. doi:10.1002/2017JA024328

Malaspina, D. M., Ripoll, J.-F., Chu, X., Hospodarsky, G., and Wygant, J. (2018). Variation in Plasmaspheric Hiss Wave Power with Plasma Density. *Geophys. Res. Lett.* 45, 9417–9426. doi:10.1029/2018GL078564

Mauk, B. H., Fox, N. J., Kanekal, S. G., Kessel, R. L., Sibeck, D. G., and Ukhorskiy, A. (2013). Science Objectives and Rationale for the Radiation belt Storm Probes mission. *Space Sci. Rev.* 179, 3–27. doi:10.1007/s11214-012-9908-y

Meredith, N. P., Horne, R. B., Glauert, S. A., and Anderson, R. R. (2007). *Slot Region Electron Loss Timescales Due to Plasmaspheric Hiss and Lightning-Generated Whistlers*, 112. doi:10.1029/2007ja012413

Millan, R. M., McCarthy, M. P., Sample, J. G., Smith, D., Thompson, L. D., McGaw, D. G., et al. (2013). The Balloon Array for Rbsp Relativistic Electron Losses (Barrel). *Space Sci. Rev* 179, 503–530. doi:10.1007/s11214-013-9971-z

Millan, R. M., and Thorne, R. M. (2007). Review of Radiation belt Relativistic Electron Losses. *J. Atmos. Solar-Terrestrial Phys.* 69, 362–377. doi:10.1016/j.jastp.2006.06.019

Pierrard, V., Ripoll, J.-F., Cunningham, G., Botek, E., Santolik, O., Thaller, S., et al. (2021). Observations and Simulations of Dropout Events and Flux Decays in October 2013: Comparing Meo Equatorial with leo Polar Orbit. *J. Geophys. Res. Space Phys.* 126, e2020JA028850. doi:10.1029/2020JA028850

Réveillé, T., Bertrand, P., Ghizzo, A., Simonet, F., and Baussart, N. (200118894). *Dynamic Evolution of Relativistic Electrons in the Radiation Belts*, 106, 18883. doi:10.1029/2000ja900177

Ripoll, J.-F., Claudepierre, S. G., Ukhorskiy, A. Y., Colpitts, C., Li, X., Fennell, J. F., et al. (2020a). Particle Dynamics in the Earth's Radiation Belts: Review of Current Research and Open Questions. *J. Geophys. Res. Space Phys.* 125, e2019JA026735. doi:10.1029/2019JA026735

Ripoll, J.-F., Denton, M., Hartley, D., Reeves, G., Malaspina, D., Cunningham, G., et al. (2020b). Scattering by Whistler-Mode Waves during a Quiet Period Perturbed by Substorm Activity. *J. Atmos. Solar-Terrestrial Phys.* 215, 105471. doi:10.1016/j.jastp.2020.105471

Ripoll, J.-F., Denton, M., Loridan, V., Santolík, O., Malaspina, D., Hartley, D. P., et al. (2020c). *How Whistler Mode Hiss Waves and the Plasmasphere Drive the Quiet Decay of Radiation Belts Electrons Following a Geomagnetic Storm*, 1623. doi:10.1088/1742-6596/1623/1/012005

Ripoll, J.-F., Loridan, V., Denton, M. H., Cunningham, G., Reeves, G., Santolik, O., et al. (2019). Observations and Fokker-Planck Simulations of the L-Shell, Energy, and Pitch Angle Structure of Earth's Electron Radiation Belts during Quiet Times. *J. Geophys. Res. Space Phys.* 124, 1125–1142. doi:10.1029/2018JA026111

Ripoll, J.-F., and Mourenas, D. (2013). "High-energy Electron Diffusion by Resonant Interactions with Whistler Mode Hiss," in *Dynamics of the Earth's Radiation Belts and Inner Magnetosphere* (American Geophysical Union), 281–290. doi:10.1029/2012gm001309

Ripoll, J.-F., Reeves, G. D., Cunningham, G. S., Loridan, V., Denton, M., Santolik, O., et al. (2016). Reproducing the Observed Energy-dependent Structure of Earth's Electron Radiation Belts during Storm Recovery with an Event-specific Diffusion Model. *Geophys. Res. Lett.* 43, 5616–5625. doi:10.1002/2016GL068869

Ripoll, J.-F., Santolik, o., Reeves, G., Kurth, W. S., Denton, M. H., Loridan, V., et al. (2017). Effects of Whistler Mode Hiss Waves in March 2013. *J. Geophys. Res. Space Phys.* 122, 7433—–7462. doi:10.1002/2017JA024139

Sample, J. G., Millan, R. M., and Woodger, L. A. (2020). "Nanosat and Balloon-Based Studies of Radiation belt Loss: Low-Cost Access to Space," in *The Dynamic Loss of Earth's Radiation Belts* (Elsevier), 121–144.

Sandel, B. R., King, R. A., Forrester, W. T., Gallagher, D. L., Broadfoot, A. L., and Curtis, C. C. (2001). Initial Results from the IMAGE Extreme Ultraviolet Imager. *Geophys. Res. Lett.* 28, 1439–1442. doi:10.1029/2001gl012885

Santolík, O., and Gurnett, D. A. (2002). Propagation of Auroral Hiss at High Altitudes. *Geophys. Res. Lett.* 29, 119–121. doi:10.1029/2001gl013666

Santolík, O., Parrot, M., Storey, L. R. O., Pickett, J. S., and Gurnett, D. A. (2001). Propagation Analysis of Plasmaspheric Hiss Using Polar PWI Measurements. *Geophys. Res. Lett.* 28, 1127–1130. doi:10.1029/2000gl012239

Shi, R., Li, W., Ma, Q., Green, A., Kletzing, C. A., Kurth, W. S., et al. (2019). Properties of Whistler Mode Waves in Earth's Plasmasphere and Plumes. *J. Geophys. Res. Space Phys.* 124, 1035–1051. doi:10.1029/2018JA026041

Shprits, Y. Y., Subbotin, D. A., Meredith, N. P., and Elkington, S. R. (2008). Review of Modeling of Losses and Sources of Relativistic Electrons in the Outer Radiation belt Ii: Local Acceleration and Loss. *J. Atmos. Solar-Terrestrial Phys.* 70, 1694–1713. doi:10.1016/j.jastp.2008.06.014

Spasojevic, M., Shprits, Y. Y., and Orlova, K. (2015). Global Empirical Models of Plasmaspheric Hiss Using Van allen Probes. *J. Geophys. Res. Space Phys.* 120 (10370–10), 383. doi:10.1002/2015JA021803

Thorne, R. M., Li, W., Ni, B., Ma, Q., Bortnik, J., Chen, L., et al. (2013). Rapid Local Acceleration of Relativistic Radiation-belt Electrons by Magnetospheric Chorus. *Nature* 504, 411–414. doi:10.1038/nature12889

Thorne, R. M. (2010). Radiation belt Dynamics: The Importance of Wave-Particle Interactions. *Geophys. Res. Lett.* 37, 22107.

Thorne, R. M., Smith, E. J., Burton, R. K., and Holzer, R. E. (1973). Plasmaspheric Hiss. *J. Geophys. Res.* 78, 1581–1596. doi:10.1029/ja078i010p01581

Tu, W., Cunningham, G. S., Chen, Y., Morley, S. K., Reeves, G. D., Blake, J. B., et al. (2014). Event-specific Chorus Wave and Electron Seed Population Models in Dream3d Using the Van allen Probes. *Geophys. Res. Lett.* 41, 1359–1366. doi:10.1002/2013GL058819

Woodger, L. A., Halford, A. J., Millan, R. M., McCarthy, M. P., Smith, D. M., Bowers, G. S., et al. (2015). A Summary of the Barrel Campaigns: Technique for Studying Electron Precipitation. *J. Geophys. Res. Space Phys.* 120, 4922–4935. doi:10.1002/2014JA020874

Zhang, W., Fu, S., Gu, X., Ni, B., Xiang, Z., Summers, D., et al. (2018). Electron Scattering by Plasmaspheric Hiss in a Nightside Plume. *Geophys. Res. Lett.* 45, 4618–4627. doi:10.1029/2018GL077212

Zhang, W., Ni, B., Huang, H., Summers, D., Fu, S., Xiang, Z., et al. (2019). Statistical Properties of Hiss in Plasmaspheric Plumes and Associated Scattering Losses of Radiation belt Electrons. *Geophys. Res. Lett.* 46, 5670–5680. doi:10.1029/2018gl081863

Conflict of Interest: The authors declare that the research was conducted in the absence of any commercial or financial relationships that could be construed as a potential conflict of interest.

Publisher's Note: All claims expressed in this article are solely those of the authors and do not necessarily represent those of their affiliated organizations, or those of the publisher, the editors and the reviewers. Any product that may be evaluated in this article, or claim that may be made by its manufacturer, is not guaranteed or endorsed by the publisher.

Copyright © 2021 Millan, Ripoll, Santolík and Kurth. This is an open-access article distributed under the terms of the Creative Commons Attribution License (CC BY). The use, distribution or reproduction in other forums is permitted, provided the original author(s) and the copyright owner(s) are credited and that the original publication in this journal is cited, in accordance with accepted academic practice. No use, distribution or reproduction is permitted which does not comply with these terms.

frontiers in Astronomy and Space Sciences

ORIGINAL RESEARCH
published: 02 February 2022
doi: 10.3389/fspas.2022.810792

Pitch-Angle Diffusion in the Earth's Magnetosphere Organized by the Mozer-Transformed Coordinate System

Joseph E. Borovsky[1]*, *Gian Luca Delzanno*[2] *and Kateryna N. Yakymenko*[3,4]

[1]Center for Space Plasma Physics, Space Science Institute, Boulder, CO, United States, [2]Theoretical Division, Los Alamos National Laboratory, Los Alamos, NM, United States, [3]Center for Nonlinear Studies, Los Alamos National Laboratory, Los Alamos, NM, United States, [4]Intelligence and Space Research Division, Los Alamos National Laboratory, Los Alamos, NM, United States

In the Earth's dipole magnetosphere finite-gyroradius effects produce a shift of the atmospheric loss cone away from the direction of the magnetic field. This loss-cone shift is theoretically described by the "Mozer transform" [Mozer, F. S. (1966). Proton trajectories in the radiation belt. J. Geophys. Res. 71:2701], which is based upon the curvature drift of particles crossing the equatorial plane. For positive ions the northern and southern loss cones both shift westward and for electrons the northern and southern loss cones both shift eastward. This loss-cone shift is part of a coordinate-system transform, with the transformed coordinates better organizing the behavior of particle orbits in the dipole magnetic field (e.g. first adiabatic invariants, mirror heights, and bounce times). In this report it is demonstrated that the transformed coordinate system also properly organizes pitch-angle diffusion. This improved organization of the diffusion is true whether the angular scattering is produced by plasma-wave scattering or by field-line-curvature (FLC) scattering. It is shown that FLC scattering and the loss cone shift are linked, so that if FLC scattering is occurring, there is a loss cone shifted away from the magnetic-field direction and the Mozer-transformed coordinates are needed.

Keywords: magnetospheres, pitch-angle scattering, particle orbits, radiation belts, field-linecurvature scattering, adiabatic invariants

OPEN ACCESS

Edited by:
Jean-Francois Ripoll,
CEA DAM Île-de-France, France

Reviewed by:
Yiqun Yu,
Beihang University, China
Nickolay Ivchenko,
Royal Institute of Technology, Sweden

***Correspondence:**
Joseph E. Borovsky
jborovsky@spacescience.org

Specialty section:
This article was submitted to Space Physics, a section of the journal Frontiers in Astronomy and Space Sciences

Received: *07 November 2021*
Accepted: *03 January 2022*
Published: *02 February 2022*

Citation:
Borovsky JE, Delzanno GL and Yakymenko KN (2022) Pitch-Angle Diffusion in the Earth's Magnetosphere Organized by the Mozer-Transformed Coordinate System. Front. Astron. Space Sci. 9:810792. doi: 10.3389/fspas.2022.810792

INTRODUCTION

For energetic charged particles in the Earth's dipole magnetic field a finite-gyroradius effect causes the atmospheric loss cone to shift away from the direction of the magnetic field (Porazik et al., 2014; Borovsky et al., 2022). Defining the equatorial pitch angle α_o to be the angle between the particle's velocity vector when it crosses the equatorial plane and the equatorial magnetic-field vector, this shift means that the loss cone is not centered at $\alpha_o = 0^o$ as it is for very-low-energy particles. For positive ions the northern and southern loss cones both shift westward and for electrons the loss cones both shift eastward. Note that with this shift the two loss cones are no longer 180^o apart.

The loss-cone shift (aberration) is simply described using the "Mozer transform" (Mozer, 1966), which points out that the angular shift is

$$\theta_{shift} = \arcsin\left(v_{curve}/v_o\right) = \arctan\left(v_{curve}/v_{||}\right) \quad (1)$$

where v_o is the particle's total velocity, $v_{||}$ is the component of the particle's velocity that is parallel to the magnetic field, and v_{curve} is the curvature drift velocity of the particle

$$\underline{\mathbf{v}}_{curve} = (m\gamma c/qB^3)v_{||}^2(\underline{\mathbf{B}}\times\nabla B) \quad (2)$$

[cf. eq. (2.17) of Roederer and Zhang (2014)], where m is the mass of the particle, q the signed charge of the particle, c the speed of light, and $\gamma = (1-(v_o^2/c^2))^{-1/2}$ is the relativistic factor. At the equator of the dipole magnetic field, the curvature drift speed is

$$v_{curve} = 3\gamma mcv_{||}^2/qBr, \quad (3)$$

where r is the distance from the dipole center. Borovsky et al. (2020a,b) used the Mozer transform to explore the loss cone shift for space experiments with energetic electron beams. Borovsky et al. (2022) extensively explored the loss-cone shift and the organization of particle-orbit properties using the Mozer transform. Earlier Porazik et al. (2014) explored the loss-cone shift in a more-complicated fashion using the Gardner-expansion (Gardner, 1966) for the first adiabatic invariant μ. (See also Sanchez et al. (2019), Powis et al. (2019), and Willard et al. (2019) for discussions of the loss-cone shift in terms of the Gardner expansion.)

Looking beyond the shift of the loss cone, in this paper an angular coordinate system will be explored that organizes the behavior of energetic ions and electrons bouncing in the Earth's dipole. This coordinate system differentially aberrates the standard equatorial pitch-angle α_o gyrophase-angle ϕ_o coordinate system, with the aberration angle being maximum for the center of the loss cone near $\alpha_o = 0^o$ and the aberration angle going to zero for $\alpha_o = 90^o$ particles. It will be shown in particular that this aberrated coordinate system better describes the action of the pitch-angle scattering (angular scattering) of particles in the dipole than does the standard α_o–ϕ_o coordinate system.

EXPLORING THE ABERRATED COORDINATE SYSTEM

In the low-energy limit (the zero-gyroradius limit) the contours of equal mirror height (and the atmospheric loss cone) are concentric circles in α_o–ϕ_o (pitch angle - gyrophase angle) coordinates as seen from the equatorial plane. The centers of these low-energy circles are all at $\alpha_o = 0^o$, which is the direction of the magnetic field. Further, in that low-energy limit the instantaneous value of the first-adiabatic invariant $\mu = \gamma mv_\perp^2\tau_g$ at the equatorial plane is equal to $\mu = \gamma mv_\perp^2\tau_g$ at the mirror point [where τ_g is the particle's gyroperiod and $v_\perp = v_o\sin(\alpha)$]. (Note that, as in Borovsky et al. (2022), the definition of the first adiabatic invariant from the action integral $\mu = \int \underline{\mathbf{P}}_\perp \bullet d\underline{\mathbf{L}} = (1/2)\int \gamma mv_\perp^2\, dt$ for the gyromotion [cf. eq. (12.64) of Jackson (1975)] is used rather than the magnetic moment, where $\underline{\mathbf{P}}_\perp$ is the transverse-to-$\underline{\mathbf{B}}$ canonical momentum and where the integral is over a full gyroperiod: the two definitions of μ differ by the constant mc/q.) For energetic particles in a dipolar magnetic field, finite-gyroradius effects make $\mu = (1/2)\,\gamma mv_\perp^2\tau_g$ and $\mu = (1/2)\int \gamma mv_\perp^2\, dt$ not useful for describing orbits (Borovsky et al., 2022). This was clearly pointed out by Mozer (1966) and by Il'in et al. (1992) where part of the particle's perpendicular velocity $\underline{\mathbf{v}}_\perp$ does not participate in gyromotion and mirroring. Because of finite-gyroradius effects, for energetic particles in a dipolar (or stretched) magnetic field the polar coordinate system α - ϕ becomes distorted. An aberrated coordinate system better organizes the properties of particle orbits in terms of equatorial α_o and ϕ_o. This aberrated coordinate system organizes bounce periods, values of $\mu = \gamma mv_\perp^2\tau_g$ at the mirror points, and the mirror height (Borovsky et al., 2022). The aberrated coordinate system also locates the atmospheric loss cone, which is aberrated (displaced) away from 0^o equatorial pitch angle. In the aberrated coordinate system, the angular area of loss cone as seen from the equatorial plane stays approximately constant. Note that the amount of aberration of the coordinate system depends on the kinetic energy and mass of the particle [cf. expressions (**Eq. 1**) and (**Eq. 3**)].

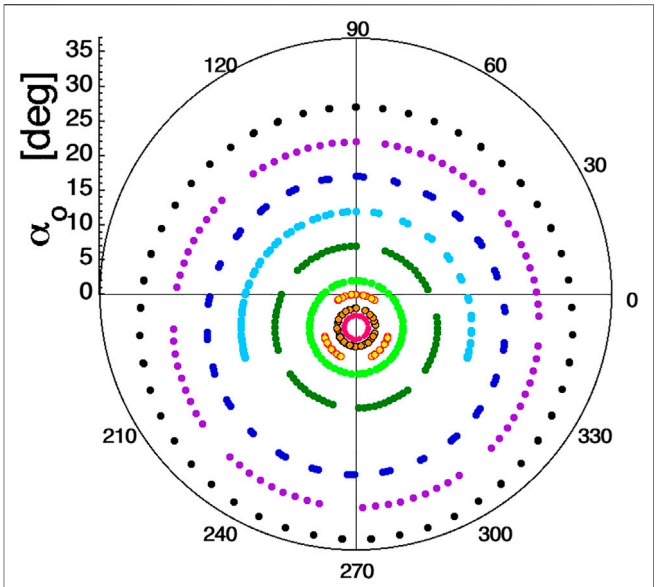


FIGURE 1 | For nine 700-keV protons launched at the geosynchronous orbit (L = 6.6) equator with nine different initial equatorial pitch angles, the pitch angle α_o and gyrophase angle ϕ_o of the protons at the times of their northward-going equatorial crossings is plotted. The magnetic-field direction vector is at $\alpha_o = 0^o$, where the black cross-hairs intersect.

The coordinate system is explored by integrating particle orbits in the Earth's dipole magnetic field. The equations

$$\underline{\mathbf{B}} = (M/r^5)(3xz, 3yz, 2z^2 - x^2 - y^2) \quad (4a)$$

$$d(\gamma m\mathbf{v})/dt = (q/c)\,\underline{\mathbf{v}}\times\underline{\mathbf{B}} \quad (4b)$$

$$d\,\underline{\mathbf{r}}/dt = \underline{\mathbf{v}}, \quad (4c)$$

where $\underline{\mathbf{r}} = (x, y, z)$ is the location of the particle, q is the charge of the particle, m is the mass of the particle, c is the speed of light, $\underline{\mathbf{v}}$ is the particle's velocity vector, $\gamma = [1-(v^2/c^2)]^{-1/2}$ is the relativistic factor, $\underline{\mathbf{B}} = \underline{\mathbf{B}}(\underline{\mathbf{r}})$ is the magnetic field vector at the location of the particle, and $M = \times 7.9510^{25}$ G cm^3 is the dipole moment of the

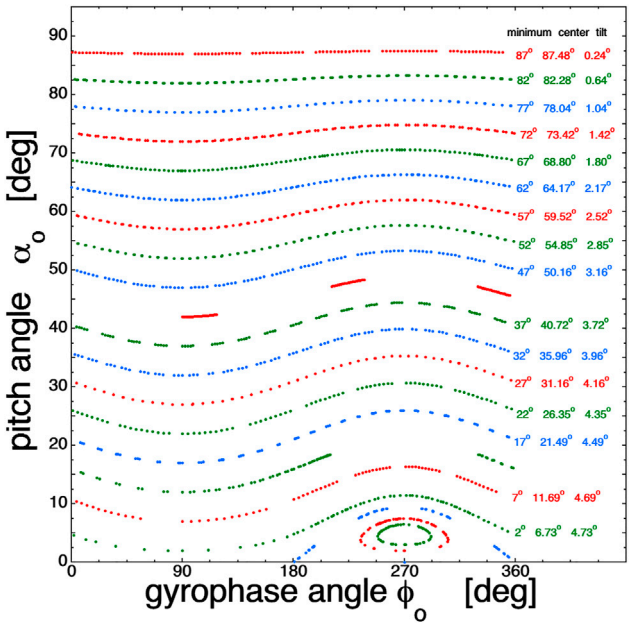


FIGURE 2 | The α_o and ϕ_o coordinates of the northward-going equatorial crossings of twenty 700-keV protons at geosynchronous orbit (**Figure 1**) are plotted in Cartesian fashion.

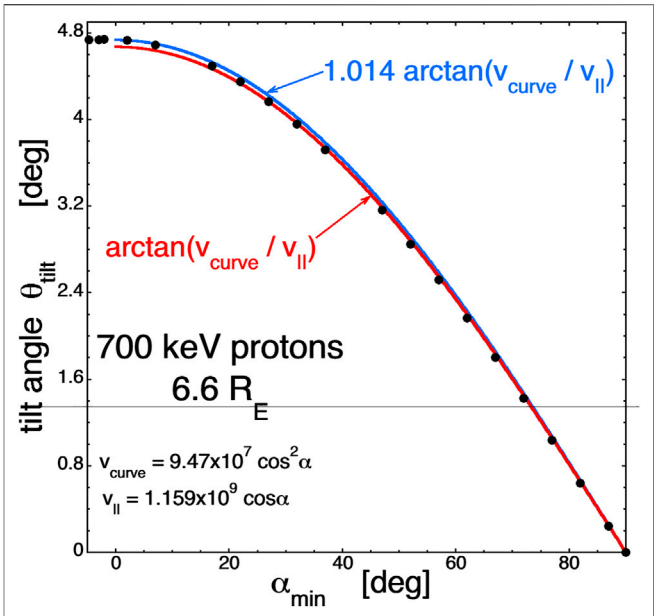


FIGURE 3 | The data from **Figure 2** is plotted and fitted. (See text for an explanation.)

Earth. Expressions (4) are numerically solved with a time-centered predictor-corrector scheme with a typical time step of 2.5×10^{-8} s for protons.

Following Mozer's logic, the aberration angle for the coordinate system is found to be governed by the curvature drift speed v_{curve} at the equator [cf. expression **(Eq. 1)**], which is a function of the particle velocity, the particle's equatorial pitch angle α_o, and the particle's distance r from the dipole center [cf. expression **(Eq. 3)**]. Mozer's transformation can be demonstrated by looking at the orbit of a particle with initial velocity at the equatorial plane such that $\underline{v}_\perp = \underline{v}_{curve}$. This orbit exhibits no gyromotion and indeed it is at the center of the aberrated equatorial loss cone. (In the literature, this orbit with $\underline{v}_\perp = \underline{v}_{curve}$ at the equatorial plane has been denoted as the "central trajectory" (Il'in et al. (1992); Il'ina et al., 1993; Borovsky et al., 2022).) As a single mirroring particle in the Earth's magnetic field repeatedly crosses the equatorial plane, its direction vector repeatedly lies on an aberrated circle in α_o–ϕ_o coordinates. Each time the particle crosses the equatorial plane, the particle's phase angle on that circle advances by the same increment. Hence one can assume that particles mirroring in a dipole are "gyrotropic" on each aberrated circle. This is demonstrated in **Figure 1**, where the (α_o, ϕ_o) coordinates of nine different 700-keV protons injected at the geosynchronous-orbit equator are plotted as each proton repeatedly crosses the equatorial plane traveling northward. The initial (α_o, ϕ_o) coordinates of the nine ions were (3°, 270°) (red points), (2°, 270°) (orange points), (0°, 270°) (yellow points), (2°, 90°) (light-green points), (7°, 90°) (green points), (12°, 90°) (light-blue points), (17°, 90°) (blue points), (22°, 90°) (purple points), and (27°, 90°) (black points). Note that the (α_o, ϕ_o) equatorial crossing points of each ion lie on a circle. Each time an ion crosses the equatorial plane, the phase angle on its circle increases by the same fixed amount: this constant added phase angle gives rise to the clumping patterns of the points in **Figure 1**. Note that the circles of **Figure 1** are aberrated away from $\alpha_o = 0°$ in the direction of $\phi_o = 270°$ (westward).

It is instructive to look at these equatorial-crossing coordinates in Cartesian (α_o,ϕ_o) coordinates. In **Figure 2** the northward-traveling equatorial-plane crossings of 21 different 700-keV protons at geosynchronous orbit are plotted. Note that the displaced (aberrated) circles of **Figure 1** become wavy curves in **Figure 2**. Note also that the waviness of the curves in **Figure 2** decreases as the equatorial pitch angle $\alpha_o \rightarrow 90°$. This indicates that the transformation of the equatorial (α_o,ϕ_o) coordinates from the $\alpha_o = 0°$ direction that organizes the orbits is not a simple rotation, but rather differential rotation with the rotation being largest near the central trajectory and the loss cone and the rotation being zero at $\alpha_o = 90°$.

For each curve of **Figure 2**, the tilt angle θ_{tilt} of each circle in **Figure 1** is plotted in **Figure 3** as a function of the minimum pitch angle α_{min} of that circle. For each wavy curve in **Figure 2**, the tilt angle is given by $\theta_{tilt} = (\alpha_{max}-\alpha_{min})/2$. For the closed contours in **Figure 1**, the α_o angles are plotted as negative values. **Figure 3** clearly shows that the tilt (aberration) angle is maximum for the loss-cone center and the tilt goes to zero for $\alpha_o = 90°$. The red curve in **Figure 3** is arctan ($v_{curve}/v_{||}$) at the equator, where for the 700-keV protons at L = 6.6 the quantities are $v_{curve} = \cos^2\alpha\ 9.47 \times 10^7$ cm/s and $v_{||} = \cos\alpha\ 1.159 \times 10^9$ cm/s. The blue curve is 1.014 times the red curve. (It is not known why multiplying by 1.014 yields a better fit.) As can be seen, these curves fit the black data points in **Figure 3** fairly well and so the formula

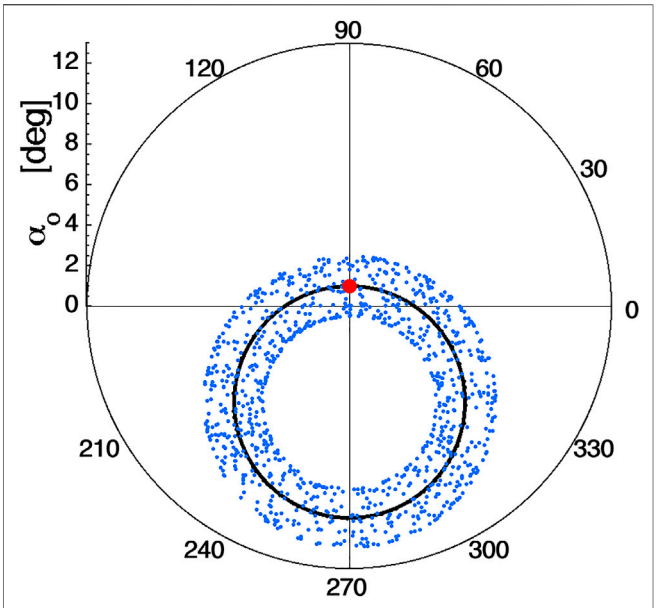


FIGURE 4 | For 1,000 protons of energy 700-keV all launched from the equatorial plane at L = 6.6 with $(\alpha_o, \phi_o) = (1^o, 90^o)$ (marked with the large red dot), the (α_o, ϕ_o) values for the first northward-going equatorial crossing is plotted as a blue point. Each ion was subjected to a 3° deflection when it was halfway to its first mirror point. The black circle is the circle of (α_o, ϕ_o) values for ions that are not subjected to angular scatterings.

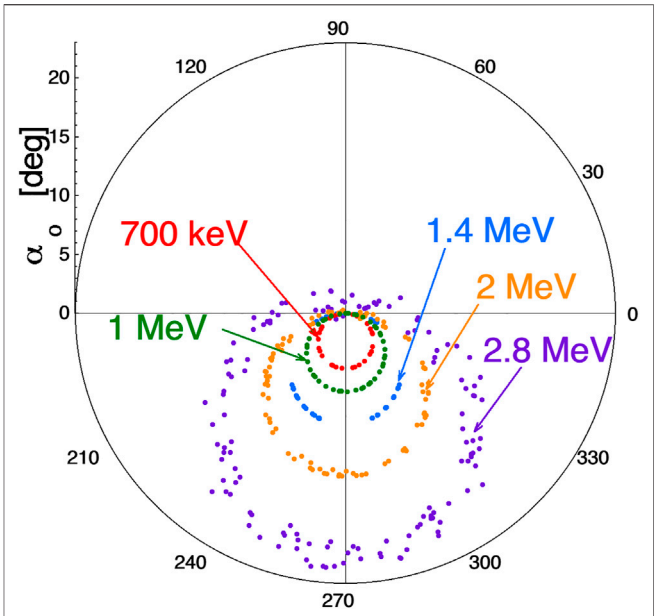


FIGURE 5 | Five protons with five different kinetic energies (colors) are launched from the geosynchronous-orbit equator with $\alpha_o = 0^o$ and the (α_o, ϕ_o) values of their northward-gong equatorial crossings are plotted as the points.

$$\theta_{tilt} = \arctan\left(v_{curve}/v_{||}\right) \quad (5)$$

can be used to calculate the aberration (tilt) of the coordinate system relative to the standard α_o–ϕ_o coordinates.

Note that in $\theta_{tilt} = \arctan(v_{curve}/v_{||})$, the gradient-B drift $v_{grad} = \sin^2\alpha\ 4.36 \times 10^7$ cm/s does not seem to play a role in the aberration of the improved coordinate system. This is observed in the analysis of the particle orbits, but is not yet fully understood. Borovsky et al. (2022) demonstrated that the sum of the curvature drift v_{curve} plus the gradient drift v_{grad} is the proper numerator in the Mozer transform [expression **(Eq. 1)**] for better conservation of the first adiabatic invariant $\mu = \gamma m v_{\perp}^2 \tau_g$.

PITCH-ANGLE SCATTERING ORGANIZED BY THE ABERRATED COORDINATE SYSTEM

As seen in **Section 2**, the equatorial-crossing circles aberrated by the Mozer transform organize the behavior of the orbits and the loss cone. When angular scattering is added along the ion's orbit away from the equator, the aberrated circles also organize the description of the scattering in equatorial pitch-angle and gyrophase-angle coordinates. This is demonstrated in **Figure 4**. In **Figure 4** the (α_o,ϕ_o) coordinates at the equatorial crossings of 1,000 protons are shown. Each proton is launched northward from the dipole equator at $r = 6.6\ R_E$ with an $\alpha_o = 1^o$ pitch angle at a gyrophase angle of $\phi_o = 90^o$ and with a kinetic energy of 700 keV. The launch angles $(\alpha_o,\phi_o) = (1^o, 90^o)$ of the 1,000 protons are plotted as the large red point in **Figure 4**. Each proton, when it has traveled for exactly a time 2.282 s (halfway in time to its first mirror point), is given a 3° deflection in its velocity vector in a random direction normal to its instantaneous velocity vector, keeping its kinetic energy constant. (This could represent the interaction of the particle with some wave along the particle's orbit, although in a very controlled and idealized way.) The equatorial pitch angles and gyrophase angles of the first northward equatorial crossings of the 1,000 protons that each experienced a single 3° deflection are plotted as the blue points in **Figure 4**. The black circle in the figure is the circle that unscattered (unperturbed) protons make as they bounce and cross the equatorial plane. As seen in **Figure 4**, the aberrated black circle is uniformly broadened by off-equatorial pitch-angle scattering, and the black aberrated circle organizes the behavior (diffusion) of the non-equatorial scattering in equatorial pitch angle and gyrophase angle.

Another form of angular scattering is field-line-curvature (FLC) scattering. FLC scattering is parameterized by the "adiabaticity parameter" $\varepsilon = r_{gyro}/R_c$ at the equator, where r_{gyro} is the gryroradius of the particle with pitch angle 90° and R_c is the equatorial radius of curvature of the field lines. $\varepsilon = r_{gyro}/R_c = 3\gamma m c v_o/eB$ is related to the loss-cone shift at the equator $\theta_{tilt} = \arctan(v_{curve}/v_{||}) = \arctan(3\gamma m c v_o \cos(\alpha_o)/eB)$. At small angles α_o, $\varepsilon \approx \theta_{tilt}$. Hence, the strength of FLC scattering is parameterized by the size of the loss-cone tilt (Borovsky et al., 2022). If the $\varepsilon = r_{gyro}/R_c$ value of a particle is larger than 0.1–0.2, the particle begins to stochastically scatter each time it crosses the equatorial region of the dipole (e.g. Dragt and Finn, 1976; Birmingham, 1984; Tagare, 1986; Jung and Sholz, 1988; Chrikov, 1987; Anderson et al., 1997; Young et al., 2002, 2008; Artemyev et al., 2015; Borovsky et al., 2022). An example of this is

shown in **Figure 5**, where five protons with five different kinetic energies are launched at the geosynchronous-orbit equator with initial equatorial pitch angle of 0^o. The northward-traveling equatorial crossings of the five protons are plotted as the points in **Figure 5**. The colors are 700 keV ($\varepsilon = 0.08$) in red, 1 MeV ($\varepsilon = 0.113$) in green, 1.4 MeV ($\varepsilon = 0.16$) in blue, 2 MeV ($\varepsilon = 0.23$) in orange, and 2.8 MeV ($\varepsilon = 0.32$) in purple. As can be seen, with increasing energy the westward angular tilt of the loss cone increases since v_{curve}/v_o in expression **(Eq. 1)** is approximately proportional to v_o and $v_o \propto E^{1/2}$, with E being the kinetic energy. At energies of 2-MeV and higher in the figure a scattering of the crossings can be seen. (also Figure 6 of Borovsky et al., (2022).). Note in **Figure 5** that the aberrated circles organize the FLC scattering as they did the off-equatorial angular scattering in **Figure 4**. As pointed out in Borovsky et al., (2022), FLC scattering and the loss-cone shift are both finite-gyroradius effects and the two are linked. Hence, if FLC scattering (values of $\varepsilon \geq 0.15$) is occurring, there is also a shift of the loss cone ($\theta_{shift} \geq 10^o$).

One might worry that if FLC scattering is going on and first adiabatic invariants are being broken, that the Mozer transform [expression **(Eq. 1)**] does not work because the concept of calculating the curvature drift is a guiding-center concept and that is being violated. This is extensively explored in Borovsky et al. (2022). The Mozer transform accurately predicts the loss cone shift for shift values up to about 10^o, which are ε values of about 0.15 or less. As ε increases further (where FLC scattering commences), the loss-cone shift in pitch angle deviates slightly from the prediction of the Mozer transform and the loss-cone shift picks up an earthward component in gyrophase angle. When epsilon goes beyond about 0.5, the Mozer transform looses accuracy in predicting the loss-cone shift, but in this $\varepsilon > 0.5$ regime the shift angle still increases monotonically as ε increases. Even though with FLC scattering occurring the first adiabatic invariants are breaking upon crossing the equator, a particle's kinetic energy and its ε value are both conserved and the loss cone for that particle has the same shift as seen from the equator. The magnitude of the loss-cone shift and the FLC scattering are still linked: independent of the value of ε the loss cone shift and the FLC scattering strength both increase monotonically as the value of ε increases.

DISCUSSION

In this report it was demonstrated that the Mozer-transformed coordinates organize the bounce motion of charged particles and they also organize the behavior of charged particles undergoing pitch angle scattering in the dipole magnetic field, whether that scattering is caused by 1) scattering centers encountered during the bounce motion or 2) finite-gyroradius effects in the dipole. The Mozer-transformed coordinate system was explored and shown to be a differential aberration of the commonly used α_o-ϕ_o pitch-angle gyrophase-angle coordinate system.

This organization of the angular scattering indicates that there is the possibility that the Mozer-transformed coordinate system can provide a path forward to correct bounce-averaged pitch-angle-diffusion calculations in the presence of the displaced atmospheric loss cone.

For pitch-angle diffusion by plasma waves, one inherent difficulty with this plan for correction is that 1) plasma-wave-driven pitch-angle-scattering calculations are naturally performed in a coordinate system that is aligned with the local magnetic-field direction whereas 2) the particle orbits and pitch-angle diffusion are organized in a coordinate system that is aberrated (rotated) away from the local magnetic-field direction. For FLC scattering this difficulty does not exist: both the FLC scattering and the particle orbits are organized by the aberrated (Mozer-transformed) coordinate system. In fact, the magnitude of FLC scattering and the magnitude of the aberration of the coordinates are linked.

A future investigation will explore the plausibility and estimate the magnitude of this pitch-angle-diffusion correction.

For future thinking, a question arises. If a magnetospheric particle population exhibits an empty loss cone that is offset from the magnetic-field direction, can a kinetic plasma-wave instability arise?

DATA AVAILABILITY STATEMENT

The original contributions presented in the study are included in the article/Supplementary Material, further inquiries can be directed to the corresponding author.

AUTHOR CONTRIBUTIONS

JB initiated this project, performed the numerical orbit calculations, and wrote the first draft of the manuscript. GD and KY separately checked the numerical calculations with their codes and helped to finalize the manuscript.

FUNDING

JB was supported at the Space Science Institute by the NSF GEM Program *via* grant AGS-2027569, by the NASA Heliophysics LWS program *via* award NNX16AB75G, by the NASA HERMES Interdisciplinary Science Program *via* grant 80NSSC21K1406, and by the NASA Heliophysics Guest Investigator Program *via* award NNX17AB71G. The work of GD was supported by the Laboratory Directed Research and Development (LDRD) Program of Los Alamos National Laboratory under project number 2020007DR. KY acknowledges the support of the Center for Non Linear Studies through the LDRD Program under project number 20190496DR. Los Alamos National Laboratory is operated by Triad National Security, LLC, for the National Nuclear Security Administration of U.S. Department of Energy (Contract No. 89233218CNA000001).

ACKNOWLEDGMENTS

The authors thank Jay Johnson and Ennio Sanchez for helpful conversations.

REFERENCES

Anderson, B. J., Decker, R. B., Paschalidis, N. P., and Sarris, T. (1997). Onset of Nonadiabatic Particle Motion in the Near-Earth Magnetotail. *J. Geophys. Res.* 102, 17553–17569. doi:10.1029/97ja00798

Artemyev, A. V., Agapitov, O. V., Mozer, F. S., and Spence, H. (2015). Butterfly Pitch Angle Distribution of Relativistic Electrons in the Outer Radiation belt: Evidence of Nonadiabatic Scattering. *J. Geophys. Res. Space Phys.* 120, 4279–4297. doi:10.1002/2014ja020865

Birmingham, T. J. (1984). Pitch Angle Diffusion in the Jovian Magnetodisc. *J. Geophys. Res.* 89, 2699–2707. doi:10.1029/ja089ia05p02699

Borovsky, J. E., Delzanno, G. L., Dors, E. E., Thomsen, M. F., Sanchez, E. R., Henderson, M. G., et al. (2020a). Solving the Auroral-Arc-Generator Question by Using an Electron Beam to Unambiguously Connect Critical Magnetospheric Measurements to Auroral Images. *J. Atmos. Solar-Terrestrial Phys.* 206, 105310. doi:10.1016/j.jastp.2020.105310

Borovsky, J. E., Delzanno, G. L., and Henderson, M. G. (2020b). A mission Concept to Determine the Magnetospheric Causes of aurora. *Front. Astron. Space Sci.* 7, 595292. doi:10.3389/fspas.2020.595929

Borovsky, J. E., Yakymenkno, K. N., and Delzanno, G. L. (2022). Modification of the Loss Cone for Energetic Particles in the Earth's Inner Magnetosphere. *Submitted J. Geophys. Res.*, 2021JA030106.

Chrikov, B. V. (1987). Particle Confinement and Adiabatic Invariance. *Proc. Roy. Soc. Lond. A.* 413, 145–156. doi:10.1098/rspa1987.0106

Dragt, A. J., and Finn, J. M. (1976). Insolubility of Trapped Particle Motion in a Magnetic Dipole Field. *J. Geophys. Res.* 81, 2327–2340. doi:10.1029/ja081i013p02327

Gardner, C. S. (1966). Magnetic Moment to Second Order for Axisymmetric Static Field. *Phys. Fluids* 9, 1997–2000. doi:10.1063/1.1761557

Il'in, V. D., Kuznetsov, S. N., Yushkov, B. Y., and Il'in, I. V. (1992). Quasiadiabatic Model of Charged-Particle Motion in a Dipole Magnetic Confinement System under Conditions of Dynamic Chaos. *JETP Lett.* 55, 645–649.

Il'ina, a. N., Il'in, V. D., Kuznetsov, S. N., Ysushkov, B. Y., Amirkhanov, I. V., and Il'in, I. V. (1993). Model of Nonadiablatic Charged Particle Mostion in the Field of a Magnetic Dipols. *JETP* 77, 246–252.

Jackson, J. D. (1975). *Classical Electrodynamics, Second Edition*. New York, NY: John Wiley and Sons.

Jung, C., and Scholz, H.-J. (1988). Chaotic Scattering off the Magnetic Dipole. *J. Phys. A: Math. Gen.* 21, 2301–2311. doi:10.1088/0305-4470/21/10/010

Mozer, F. S. (1966). Proton Trajectories in the Radiation Belts. *J. Geophys. Res.* 71, 2701–2708. doi:10.1029/jz071i011p02701

Porazik, P., Johnson, J. R., Kaganovich, I., and Sanchez, E. (2014). Modification of the Loss Cone for Energetic Particles. *Geophys. Res. Lett.* 41, 8107–8113. doi:10.1002/2014gl061869

Powis, A. T., Porazik, P., Greklek-Mckeon, M., Amin, K., Shaw, D., Kaganovich, I. D., et al. (2019). Evolution of a Relativistic Electron Beam for Tracing Magnetospheric Field Lines. *Front. Astron. Space Sci.* 6, 69. doi:10.3389/fspas.2019.00069

Roederer, J. G., and Zhang, H. (2014). *Dynamics of Magnetically Trapped Particles*. Berlin: Springer-Verlag.

Sanchez, E. R., Powis, A. T., Kaganovich, I. D., Marshall, R., Porazik, P., Johnson, J., et al. (2019). Relativistic Particle Beams as a Resource to Solve Outstanding Problems in Space Physics. *Front. Astron. Space Sci.* 6, 71. doi:10.3389/fspas.2019.00071

Tagare, S. G. (1986). Motion of Charged Particles in an Axisymmetric Magnetic Mirror. *Phys. Rev. A.* 34, 1587–1590. doi:10.1103/physreva.34.1587

Willard, J. M., Johnson, J. R., Snelling, J. M., Powis, A. T., Kaganovich, I. D., and Sanchez, E. R. (2019). Effect of Field-Line Curvature on the Ionospheric Accessibility of Relativistic Electron Beam Experiments. *Front. Astron. Space Sci.* 6, 56. doi:10.3389/fspas.2019.00056

Young, S. L., Denton, R. E., Anderson, B. J., and Hudson, M. K. (2002). Empirical Model for μ Scattering Caused by Field Line Curvature in a Realistic Magnetosphere. *J. Geophys. Res.* 107, 1069. doi:10.1029/2000ja000294

Young, S. L., Denton, R. E., Anderson, B. J., and Hudson, M. K. (2008). Magnetic Field Line Curvature Induced Pitch Angle Diffusion in the Magnetosphere. *J. Geophys. Res.* 113, A03210. doi:10.1029/2006ja012133

Conflict of Interest: The authors declare that the research was conducted in the absence of any commercial or financial relationships that could be construed as a potential conflict of interest.

Publisher's Note: All claims expressed in this article are solely those of the authors and do not necessarily represent those of their affiliated organizations, or those of the publisher, the editors and the reviewers. Any product that may be evaluated in this article, or claim that may be made by its manufacturer, is not guaranteed or endorsed by the publisher.

Copyright © 2022 Borovsky, Delzanno and Yakymenko. This is an open-access article distributed under the terms of the Creative Commons Attribution License (CC BY). The use, distribution or reproduction in other forums is permitted, provided the original author(s) and the copyright owner(s) are credited and that the original publication in this journal is cited, in accordance with accepted academic practice. No use, distribution or reproduction is permitted which does not comply with these terms.

frontiers in Astronomy and Space Sciences

ORIGINAL RESEARCH
published: 17 February 2022
doi: 10.3389/fspas.2022.823695

Radial Transport of Energetic Electrons as Determined From the "Zebra Stripes" Measured in the Earth's Inner Belt and Slot Region

Solène Lejosne[1]*, *Bela G. Fejer*[2], *Naomi Maruyama*[3] and *Ludger Scherliess*[2]

[1]Space Sciences Laboratory, University of California, Berkeley, Berkeley, CA, United States, [2]Center for Atmospheric and Space Sciences, Utah State University, Logan, UT, United States, [3]Laboratory for Atmospheric and Space Physics, University of Boulder, Boulder, CO, United States

OPEN ACCESS

Edited by:
Jean-Francois Ripoll,
CEA DAM Île-de-France, France

Reviewed by:
Theodore Sarris,
Democritus University of Thrace, Greece
Clare Watt,
Northumbria University, United Kingdom

***Correspondence:**
Solène Lejosne
solene@berkeley.edu

Specialty section:
This article was submitted to Space Physics, a section of the journal Frontiers in Astronomy and Space Sciences

Received: 28 November 2021
Accepted: 13 January 2022
Published: 17 February 2022

Citation:
Lejosne S, Fejer BG, Maruyama N and Scherliess L (2022) Radial Transport of Energetic Electrons as Determined From the "Zebra Stripes" Measured in the Earth's Inner Belt and Slot Region. Front. Astron. Space Sci. 9:823695. doi: 10.3389/fspas.2022.823695

The "zebra stripes" are drift-periodic structures present in the form of peaks and valleys in energetic (tens to hundreds of keV) electron spectrograms in the Earth's inner belt and slot region. Their characteristics inform of preceding electric field disturbances. Specifically, their amplitude contains information on the radial transport of trapped particles generated by azimuthal electric field disturbances. We introduce a method to quantify radial transport from the measured amplitude of the zebra stripes, and we apply it to the zebra stripes observed on 16 February 2014. The findings are compared with results from a particle tracing code that leverages an empirical analytical model for the electric field disturbances. The measured amplitude of the zebra stripes indicates that the electric field disturbances transported the trapped population coherently, over radial distances spanning several hundreds to thousands of kilometers. The magnitude of radial transport is shown to depend on angular drift frequency and initial location (equatorial radial distance and magnetic local time) in the disturbance. The model-observation comparison suggests that the timing for electric field variations provided by the model is valid for studying radial transport in the inner belt and slot region. On the other hand, we found discrepancies when comparing radial transport magnitudes. When assuming that radial transport varies as L^3, as weakly suggested by the data for set angular drift frequencies, and extrapolating observations to L = 1, the amount of experimental transport obtained is two to three times greater than numerical estimates. Outputs from the standalone version of the Rice Convection Model (RCM) suggests that the electric field disturbances are likely greater than the estimates provided by the empirical model. RCM also supports the idea that radial transport driven by the prompt penetration of magnetospheric convection varies as L^3 in the inner belt and slot region.

Keywords: radial transport, prompt penetration electric fields, disturbance electric fields, trapped particles, Earth's inner radiation belt, van allen probes

1 INTRODUCTION

The Van Allen Probes mission (Mauk et al., 2013) has provided large amounts of measurements of the zebra stripes below an equatorial altitude of about three Earth Radii (L < 3, i.e. < 54° in magnetic latitude for the field line footpoint). The zebra stripes are drift-periodic structures in the form of well-defined peaks and valleys in the spectrograms of energetic (tens to hundreds of keV) electrons. They are usually present over continuous portions (several Earth radii) of the inner belt and slot region (Imhof and Smith, 1965; Ukhorskiy et al., 2014). Similar structures have also been detected in the inner magnetosphere of Saturn, where they were used to provide information on magnetospheric convection (Sun et al., 2021). Indeed, zebra stripe generation mechanisms usually assume that some spatial and/or temporal variations of the magnetospheric electric field modify trapped particles' drift motion depending on drift phase (e.g. Sauvaud et al., 2013; Ukhorskiy et al., 2014; Lejosne and Roederer, 2016; Liu et al., 2016; Selesnick et al., 2016).

One of the feature of the zebra stripes is that the drift frequency separation between successive stripes decreases with time (Lejosne and Roederer, 2016; Liu et al., 2016). This characteristic has been leveraged recently to demonstrate that the time at which zebra stripes are generated is usually associated with substorm onset (Lejosne and Mozer, 2020a). As a result, the zebra stripes are now thought to be routinely generated by the magnetospheric electric field disturbances occurring around substorm onset. To modify drift motion depending on drift phase, the electric field disturbance needs to vary rapidly enough to violate the third adiabatic invariant of trapped energetic electrons. In other words, it needs to have a characteristic timescale shorter than a couple of hours (that is, the drift period timescale).

Magnetospheric electric fields and conjugate ionospheric electric fields are usually related under the assumption of equipotential field lines, as is the case within the plasmasphere (e.g. Mozer, 1970; Lejosne and Mozer, 2016). Ionospheric electric field disturbances associated with magnetic activity have been well studied experimentally (e.g. Fejer et al., 2017 and references therein). They are usually viewed as the combination of two processes: 1) a large, sudden and relatively short-lived (<a couple of hours) perturbation associated with the prompt penetration of high-latitude electric fields and 2) a perturbation occurring on a slower timescale due to the dynamo action of storm time winds. In that context, the zebra stripes are now thought to be a mark of the radial transport associated with the prompt penetration of magnetospheric convection.

Radial transport in the absence of significant magnetic field perturbations is primarily due to time variations of the azimuthal component of the electric field (e.g. Fälthammar, 1965). This component has been most accurately measured at the geomagnetic equator in the ionosphere, where the magnetic field lines are typically aligned in the north-south direction and the vertical ion drift can be easily converted into a zonal electric field. Years of radar observations of the ionospheric drift resulted in a relatively simple analytical model for the storm time dynamics of the disturbance electric fields over Jicamarca, Peru (Fejer and Scherliess, 1997). This analytical model is leveraged in the following.

The objective of this study is to demonstrate that the zebra stripes contain information on important, yet mostly uncharted drivers of the Earth's inner radiation belt and slot region. Namely, we show that the zebra stripes contain information: 1) on the dynamics of electric field disturbances, and 2) on the irreversible radial transport of trapped populations. Observational and modeling resources are introduced in **Section 2**. In particular, we describe the analytical empirical model for electric field disturbances over Jicamarca. We also detail how to quantify radial transport from measured fluctuations in trapped particles' directional differential fluxes in **Section 2**. We apply the method in **Section 3**. We show that the analysis of the zebra stripes of 16 February 2014 suggests radial transport up to a few thousands of kilometers, variable as a function of drift frequency and initial location, yet consistent over a broad range of L values ($\Delta L > 1$). We leverage the model for ionospheric electric field disturbances at the equator to compute radial transport of notionally trapped particles at L = 1. A comparison between model and observation is presented in **Section 3**, and it is discussed in **Section 4** in the light of additional results from the Rice Convection Model (RCM).

2 MATERIALS AND METHODS

We present the system of equations relative to drift motion and radial transport for trapped energetic particles (**Section 2.1**) and the empirical electric field model chosen to solve them (**Section 2.2**). Both elements are used in a particle tracing code, whose outputs are compared with experimental estimates. In **Section 2.3**, we present the equation to implement in order to determine radial transport from measured fluctuations in directional differential fluxes. The assumptions underlying the theoretical framework are also provided in **Section 2.3**.

2.1 Trapped Particles' Drift Motion in the Inner Belt and Slot Region

The objective of this Section is to present the theoretical framework necessary to describe drift motion and radial transport in the inner belt and slot region.

2.1.1 Trapped Particles' Azimuthal Drift Motion

In the absence of significant time variation of the magnetic and electric fields, trapped energetic electrons drift eastward around the Earth, along closed surfaces known as drift shells. There is on average no radial transport as they remain at about the same equatorial distance from the Earth. The frequency of this periodic drift motion, $\Omega/2\pi$, is the sum of a relatively small contribution due to the action of the electric field, $\Omega_E/2\pi$, and a main magnetic contribution, $\Omega_B/2\pi$:

$$\Omega = \Omega_E + \Omega_B \tag{1}$$

The electric drift frequency is mostly constant and equal to co-rotation frequency ($\Omega_E = 2\pi/24 \sim 0.26\, rad/hr$). It can slightly (~10%) decrease during active times (e.g. Sandel et al., 2003; Lejosne and Mozer, 2018). On the other hand, the magnetic drift

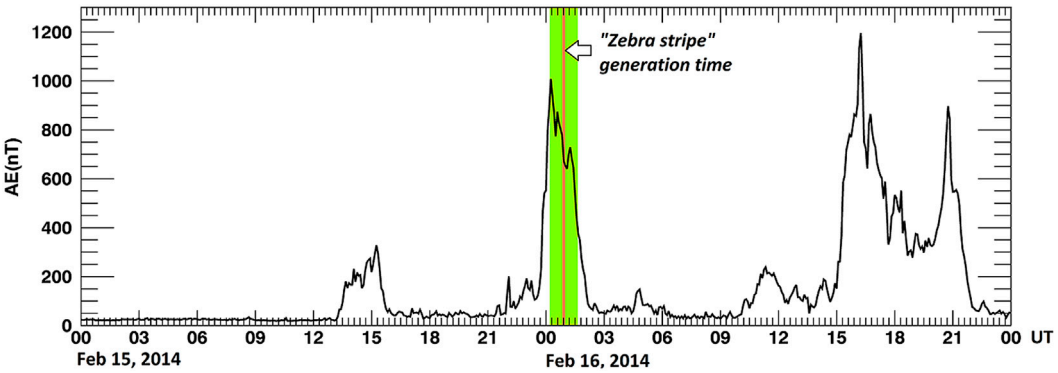


FIGURE 1 | The time evolution of the AE index on 15 February 2014 and 16 February 2014. The estimated time for the generation of zebra stripes is indicated by an orange line. The standard deviation of the estimate is shaded in green. A substorm onset occurred during this time interval, at 00:15 UT on 16 February 2014 according to the criteria set by Newell and Gjerloev (2011).

frequency is a function of the magnetic field topology (magnitude, gradient, and curvature of the magnetic field). The magnetic drift frequency also depends on the particles' characteristics (kinetic energy, charge, and to a lesser extent, pitch angle). In the case of electrons trapped in a magnetic dipole field:

$$\Omega_B(T, L, y) = \frac{3LT}{eB_E R_E^2}\left(\frac{\gamma+1}{\gamma}\right)\frac{\mathcal{D}(y)}{\mathcal{T}(y)} \tag{2}$$

Where T is the kinetic energy, γ is the Lorentz factor, $R_E = 6400\,km$ is one Earth radius, L is the normalized equatorial radial distance, $L = r/R_E$, $B_E = 30,000$ nT is the magnetic equatorial field at the surface of the Earth, e is the elementary charge, and $\mathcal{D}$ and $\mathcal{T}$ are functions of the sine of the equatorial pitch angle, y. The ratio $\mathcal{D}(y)/\mathcal{T}(y)$ lies between 1/3 and 1/2. It is equal to 1/2 for equatorial particles ($y = 1$) and it decreases monotonically with decreasing pitch angle (Schulz and Lanzerotti, 1974; see also Lejosne and Mozer, 2020a, 2020b for the definitions of $\mathcal{D}$ and $\mathcal{T}$).

The value of the sine of the equatorial pitch angle, y, is related to the pitch angle measured along the same field line, α, through conservation of the first adiabatic invariant: $y = \sin\alpha\sqrt{B_o/B}$ where B is the local magnetic field magnitude, and B_o is the magnetic field magnitude at the magnetic equator of the same field line. In this study, the ratios between B and B_o are calculated according to the International Geomagnetic Reference Field to which the Kp-driven Tsyganenko (1989) magnetic field model is superimposed. Because the analysis is in the Earth's inner belt and slot region (L < 3), the choice of the magnetic field model is unimportant provided that it remains consistent with the assumption of a magnetic field that is mainly dipolar.

2.1.2 Trapped Particles' Radial Motion

While the magnetic field of the inner belt and slot region remains essentially equal to the internal geomagnetic field, the electric field varies with time, t, driving radial transport. In polar coordinates (r, φ), the radial transport of trapped particles is described by the following set of equations of motion:

$$\begin{cases} \dfrac{dr}{dt} = \dfrac{E_\varphi(r, \varphi; t)}{B_o} \\ \dfrac{d\varphi}{dt} = \Omega \end{cases} \tag{3}$$

where E_φ is the azimuthal component of the time varying electric field at the magnetic equator, r is the equatorial radial location, and φ is the drift phase, i.e., the magnetic local time of the trapped particles. In this formulation, radial motion due to the internal geomagnetic multipoles (Roederer et al., 1973) and to the quiet time wind dynamo (Richmond et al., 1980) is assumed to be small in comparison with radial motion driven by the time-varying electric fields. The main cause of drift shell distortion for energetic particles of the inner belt, the quiet time wind dynamo, provides 6–8 kV for the average dawn-to-dusk electric potential variation at L = 1.30 (Lejosne et al., 2021), and local time dependent distortion of $\Delta L \sim 0.01$, i.e., several tens of kilometers (see also: Selesnick et al., 2016).

To solve this system of equations, information on the spatio-temporal variations of the azimuthal component of the electric field is required. We use an empirical model for the time varying electric fields of the equatorial ionosphere. It is introduced in the following (**Section 2.2**).

2.2 Analytical Empirical Model for the Azimuthal Electric Field Disturbances of the Equatorial Ionosphere

A mathematical formula for the azimuthal storm time ionospheric electric field disturbances at the geomagnetic equator has been developed by Fejer and Scherliess (1995), Fejer and Scherliess (1997) leveraging 20 years (1968–1988) and nearly five thousand hours of radar measurements of the F-region vertical plasma drift (300–400 km) over Jicamarca, Peru. The formulation with the highest time resolution uses the time history of the 15 min averaged AE index to provide a description of the prompt penetration and disturbance dynamo electric fields. The magnitude of the local time dependent prompt penetration electric fields is determined by the AE variations over the past

15 min $(AE(t) - AE(t - 15min))$, at 30 min time delay $(AE(t - 15min) - AE(t - 45min))$, and at 75 min time delay $(AE(t - 45min) - AE(t - 105min))$. The electric fields generated by the disturbance wind dynamo arise from shorter term (1–12 h) and longer term (22–28 h) disturbance dynamo effects. The short-term effects are represented using two parameters $AE_d(1 - 6\,hours)$ and $AE_d(7 - 12\,hours)$, which denote the average value of the AE index above a value of 130 nT from 1 to 6 h before the time t, and from 7 to 12 h prior the time t, respectively. The longer term disturbance dynamo electric fields $AE_d(22 - 28\,hours)$ arise when the average AE index from 22 to 28 h prior to the time t is greater than 200 nT. The model informs the dynamics of the azimuthal (i.e. zonal) component of the electric field in the equatorial region of the ionosphere above the radar location $(B = 25,000\,nT)$. In the following, we assume that the model remains valid at the magnetic equator of $L = 1$ $(B = 30,000\,nT)$

On 16 February 2014, zebra stripes were noticeable below $L = 3$ in the energetic electron spectrograms measured by both Van Allen Probes, for more than 10 h starting 05:40 UT (Liu et al., 2016). The analysis of the drift frequency separation between successive stripes suggested that the features were generated by fast electric field variations occurring at 00:55 UT ± 42 min on 16 February 2014 (Lejosne and Mozer, 2020a), a time interval that coincides with substorm onset–at 00:15 UT on 16 February 2014 according to the criteria set by Newell and Gjerloev (2011a). The concurrence between substorm onset and generation time is a characteristic feature of the zebra stripes (Lejosne and Mozer, 2020a). The time series of the Auroral Electrojet (AE) index from NASA/GSFC's OMNI data set through OMNIWeb (https://omniweb.gsfc.nasa.gov/) is provided with a 5 min time resolution in **Figure 1**. This time series is the input to the model for equatorial electric field disturbances. The AE index increases sharply at the beginning of 16 February 2014 (+900 nT in less than an hour). It reaches a maximum of 1,008 nT at 00:15 UT. Then, it decreases by about −300 nT in 1 hour before decreasing even faster $(-740\,nT/hr)$ and reaching quiet time value levels below 100 nT by 02:10 UT.

The mostly quiet AE values of 15 February 2014 and the fast variations measured around substorm onset indicates that the main source of electric field disturbances for this event is the prompt penetration of magnetospheric convection.

2.3 Relating Measured Fluctuations in Trapped Particles' Directional Differential Fluxes and Radial Transport

Sudden variations of the fields produce drift echoes (e.g., Lanzerotti et al., 1967), that is, drift-periodic fluctuations in flux measurements. The amplitude of the fluctuation is related to the radial transport for trapped populations below $L = 3$ (Lejosne and Mozer, 2020b):

$$\frac{\delta j}{j}(T, y, L) = \psi(T, y, L)\frac{dL}{L} \tag{4}$$

where $\delta j = j(T, y, L; t^+) - j(T, y, L; t^-)$ is the fluctuation in directional differential flux, j, and t^- and t^+ are times before and after the occurrence of electric field disturbances, respectively. The denominator, j, is the flux, measured at t^-. This equation is equivalent to detailing the conservation of phase space density, f, along the dynamical paths of particles assuming conservation of the first two adiabatic invariants. The function ψ controls how radial transport, dL, shows up in flux measurements. It is defined as:

$$\psi(T, y, L) = -\frac{6\mathcal{D}(y)}{\mathcal{T}(y)}\left(1 - \frac{\gamma + 1}{2\gamma}\frac{\partial \ln j}{\partial \ln T}\right) - \frac{\partial \ln j}{\partial \ln L} - \frac{\mathcal{Y}(y)}{4\mathcal{T}(y)}\frac{1 - x^2}{x^2}\frac{\partial \ln j}{\partial \ln x} \tag{5}$$

Where j is measured at t^-, $x = \sqrt{1 - y^2}$ is the cosine of the equatorial pitch angle, and $\mathcal{Y}$ is Schulz and Lanzerotti (1974)'s dipole bounce function (see also Lejosne and Mozer, 2020b for a detailed derivation of **Eq 4**). The main assumptions underlying this equation are that:

- There is no significant source or loss mechanism on the time scale of many hours (i.e. multiple drift periods), so that the phase space density $f = j/p^2$ is constant along the continuous trajectories of the system in phase space (Liouville's theorem);
- The timescale for electric field variations is such that the drift motion is the only perturbed motion: in other words, the first and second adiabatic invariants are conserved;
- There is no time variation of the magnetic field and the magnetic field is mainly dipolar.

2.4 Data Set and Data Processing

2.4.1 Van Allen Probes Data Set

We analyze directional differential fluxes between $L = 1.5$ and $L = 3$ in the 50–400 keV energy range provided by the Radiation Belt Storm Probes Ion Composition Experiment (RBSPICE) instruments (Mitchell et al., 2013) onboard the two Van Allen Probes. The data products (level 3 Pitch Angle and Pressure High-Energy resolution, Low Time resolution, Electron Species Rates, lev-3-PAP_ESRHELT) offer high energy resolution (dE/E ~ 0.065) over 17 pitch angle channels with a 10° resolution in almost every bin (15° in the first and last bins).

The Van Allen Probes had a perigee at ~600 km, an apogee at ~5.8 R_E, a period of ~9 h and an inclination of ~10°. They crossed the inner belt and slot region multiple times per day, providing consecutive observations of the time evolution of the zebra stripes close to the magnetic equator. At the beginning of the year 2014, the inbound crossings of the region of interest (1.5 < L < 3) were in the dusk sector (16–19.5 MLT) while the outbound crossings were in the dawn sector (5–8 MLT).

2.4.2 Data Processing

To compute the fluctuations in directional differential fluxes, δj, it is necessary to determine the differential flux before the occurrence of electric field disturbances, $j(t^-)$ (**Eq 4**). Because the event occurs at the beginning of 16 February 2014, we analyzed Van Allen Probes data during 15 February 2014. While fluxes of trapped energetic electrons have been shown to vary with magnetic local time due to drift shell distortion by the quiet time wind dynamo (e.g., Selesnick et al., 2016; Lejosne et al., 2021), this effect is found to be unimportant for the range of L values (1.5 < L < 3) and kinetic

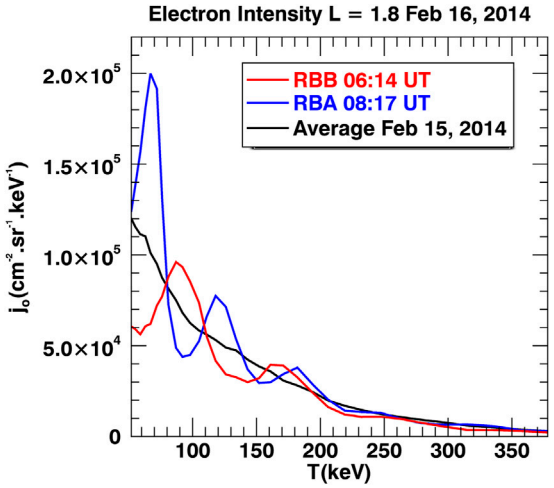


FIGURE 2 | Zebra stripes observed during two successive inbound crossings of L = 1.8 (18 MLT), at 06:14 UT by Van Allen Probes B (RBB, in red) and at 08:17 UT by Van Allen Probes A (RBA, in blue). The time-varying equatorial electron intensity is compared with the average equatorial intensity at L = 1.8 of 15 February 2014 (in black) and shows 100% fluctuations in equatorial electron intensity at low energies (~70 keV).

energy (50–400 keV) considered in this study: $\Delta j/j$, the relative difference between equatorial fluxes measured in the dawn and dusk sectors of the same L value, decreases with L value and kinetic energy. It is less than 10% on average at L = 1.5, and less than 5% on average at L = 1.7. This simplifies the analysis as the magnetic local time dimension does not need to be taken into account when determining the differential flux before the occurrence of electric field disturbances, $j(t^-)$. For every L value (+/- 0.05) between 1.5 and 3, and for each energy channel between 50 and 400 keV, the directional differential fluxes measured are represented as a function of the sine of the equatorial pitch angle, y. A linear least square regression is performed for the logarithm of the flux, j, as a function of the logarithm of the sine of the equatorial pitch angle, y, to find the best fitting sets of parameters $(\overline{j_o}, n)$ so that $j(T, y, L; t^-) \cong \overline{j_o}\, y^n \equiv \bar{j}$. The error of the estimate is quantified by the root mean square error in every pitch angle bin $(x + / - 0.05)$. Because the energetic electron fluxes did not vary significantly with time and magnetic local time on 15 February 2014, the fitting of the fluxes is relatively good: The error is of the order of 10% for near equatorial particles, and it increases with decreasing pitch angle – up to 50+% for the most field aligned particles. Information on the fitting parameters $(\overline{j_o}, n)$ is then leveraged to estimate the function $\psi(T, y, L)$ (**Eq 5**). The partial derivatives $\partial \ln j/\partial \ln T$, $\partial \ln j/\partial \ln L$ and $\partial \ln j/\partial \ln x$ are estimated locally by computing the slopes of the linear fits between $\ln \bar{j}$ and $\ln T$, $\ln L$ and $\ln x$ in bins of size $0.1L$, $0.12T$ and $0.1x$, respectively.

Figure 2 shows the equatorial electron intensity at L = 1.8 during two successive inbound crossings on 16 February 2014 at 06:14 UT for Van Allen Probes B (18:14 MLT) and at 08:17 UT for Van Allen Probes A (18:23 MLT). The reference equatorial electron intensity, $\overline{j_o}$, is superimposed. The comparison between the different curves shows the presence of time-varying, energy-dependent fluctuations in the equatorial electron intensity, $\delta j/j$, up to 100% for ~70 keV electrons.

3 RESULTS

3.1 Radial Transport From the Analysis of the Zebra Stripes

Figure 3 illustrates how (**Section 2.3**) information on trapped particles' radial transport can be retrieved from an analysis of fluctuations in directional differential fluxes observed at a later time. The fluxes are similar to the ones shown in **Figure 2**. The fluctuations (**Figure 3A**) are divided by the function $\psi(T, y, L)$ to provide information on radial transport (**Figure 3B**). The oscillations in kinetic energy arise because the radial transport magnitude varies with the drift phase (i.e., magnetic local time) at

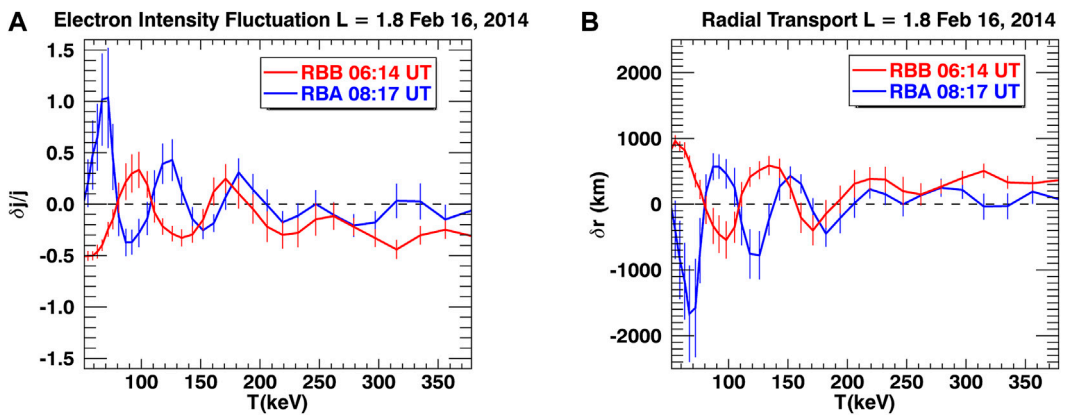


FIGURE 3 | (A) Electron intensity fluctuations, $\delta j/j$, in the 90° pitch angle channel at L = 1.8 on 16 February 2014 at 06:14 UT according to Van Allen Probes B (RBB, in red) and at 08:17 UT according to Van Allen Probes A (RBA, in blue) and **(B)** corresponding radial transport in km, $\delta r = R_E dL$. The error bars are mainly due to the uncertainty in the magnitude of the flux before the occurrence of the electric field disturbances, $j(t^-)$.

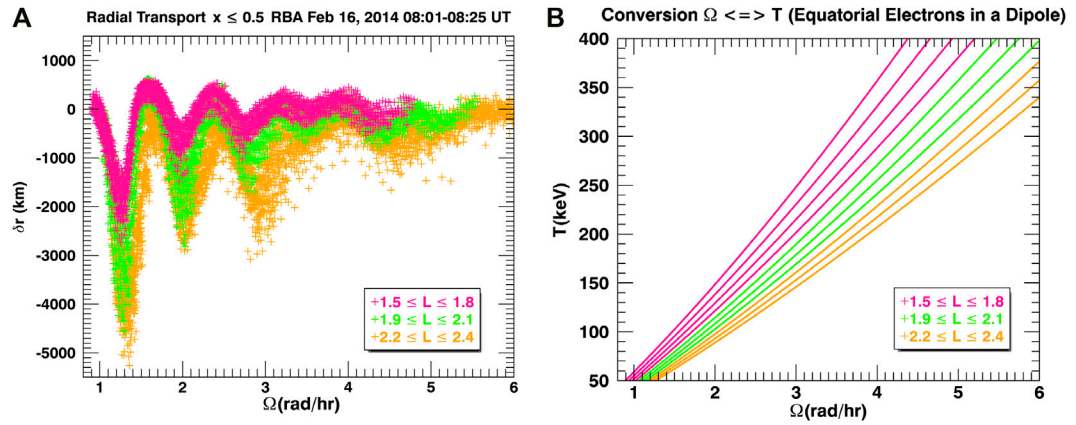


FIGURE 4 | (A) Radial transport, $\delta r = R_E dL$, caused by the electric field disturbances at the beginning of 16 February 2014 and estimated from an analysis of fluctuations in electron intensity (50–400 keV, equatorial pitch angle of 90° + / − 30°) measured by Van Allen Probes A 7 hours after the event. Three L regions between L = 1.5 and L = 2.4 are represented by three colors to highlight the increase of radial transport with L ($1.5 \leq L \leq 1.8$ is in pink, $1.9 \leq L \leq 2.1$ is in green and $2.2 \leq L \leq 2.4$ is in orange). **(B)** Conversion between angular drift frequency and kinetic energy in the case of equatorial electrons trapped at various L values ($1.5 < L < 2.5$) in a dipole field.

the time of the event, t_i, and this magnetic local time, $\varphi(t_i)$, is a function of kinetic energy: $\varphi(t_i) = \varphi - \Omega(t - t_i)$, where φ is the magnetic local time of the observation at time, t, and Ω is the angular drift frequency (**Eq. 1**). **Figure 3B** suggests that the electric field disturbances generated radial transport of the order a thousand kilometers peak-to-peak at $L = 1.8$ ($dL/L \sim 0.1$). This is at least one order of magnitude greater than the effect of the quiet time wind dynamo, that generates radial distortion of the drift shell between dawn and dusk of the order of several tens of kilometers at L = 1.3 (**Section 2.1.2**, see also Lejosne et al., 2021; Selesnick et al., 2016).

The approach illustrated in **Figure 3** is applied to all inbound and outbound crossings of the inner belt and slot region during the morning of 16 February 2014. **Figure 4A** shows how radial transport generated multiple (~7) hours before observations is determined from an analysis of fluxes measured during one crossing of $1.5 < L < 2.5$. The illustration is for trapped particles with a cosine of the equatorial pitch angle, x, below 0.5 (equatorial pitch angles between 60° and 120°) and below $L = 2.5$, to focus on estimates with relatively small error bars. **Figure 4B** provides the kinetic energy, T, associated with the angular drift frequency, Ω, in the case of equatorial electrons trapped at various L values ($1.5 < L < 2.5$) in a dipole field (**Eq. 1** and **Eq. 2**).

Figure 4A shows how radial transport oscillates with angular drift frequency, Ω (**Eq. 1** and **Eq. 2**) and increases with increasing L values. These findings are consistent with the picture in which the prompt penetration of high latitude electric fields quickly modifies trapped particles' drift motion, coherently over a large (>1L) portion of the inner belt and slot region, and with an effect that depends on the trapped particles' location at the time of the event. The oscillation with angular drift frequency indicates that the amount of radial transport depends on the initial magnetic local time of the electrons in the disturbance. Indeed, the angular drift frequencies that correspond to the same phase of the periodic signal share the same initial magnetic local time, $\varphi(t_i)$. The increase with L values indicates that radial transport is most efficient at higher L values. We emphasize that radial transport is not expected to depend on pitch angle in the electrostatic case (e.g., Fälthammar, 1968).

The radial transport estimates shown in **Figure 4** as a function of the angular drift frequency do not oscillate symmetrically around a value of zero: They are negative (i.e. inward) on average. One possible interpretation of this observation is that the drift motion of the trapped particles has also been altered by a slower (occurring on a time scale greater than trapped particles' drift periods) variation of the electric fields. A slow inward transport of the trapped particles requires a relatively steady westward component for the time varying electric fields (**Eq. 3**). This could be due to the disturbance dynamo action of the storm time winds for instance.

We further investigate the dependence of radial transport with equatorial radial distance, L, by performing a series of linear least

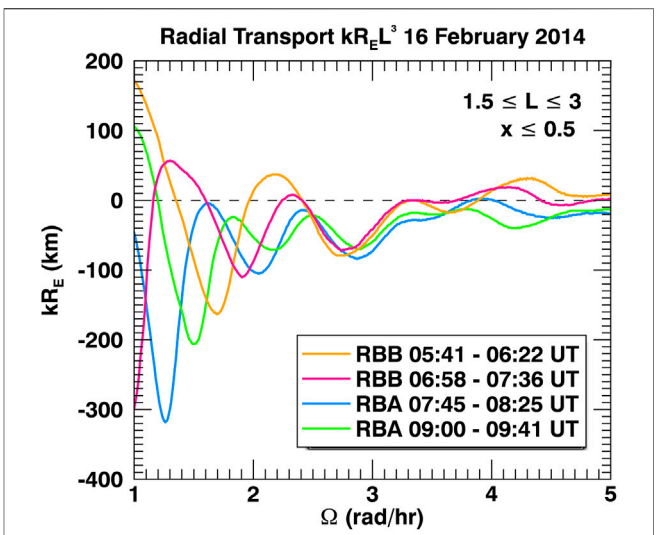


FIGURE 5 | Radial transport, $\delta r = kR_E$, caused by the electric field disturbances at the beginning of 16 February 2014, estimated at L = 1, assuming that the radial transport varies as L^3, i.e., $\delta r(L) = kR_E L^3$.

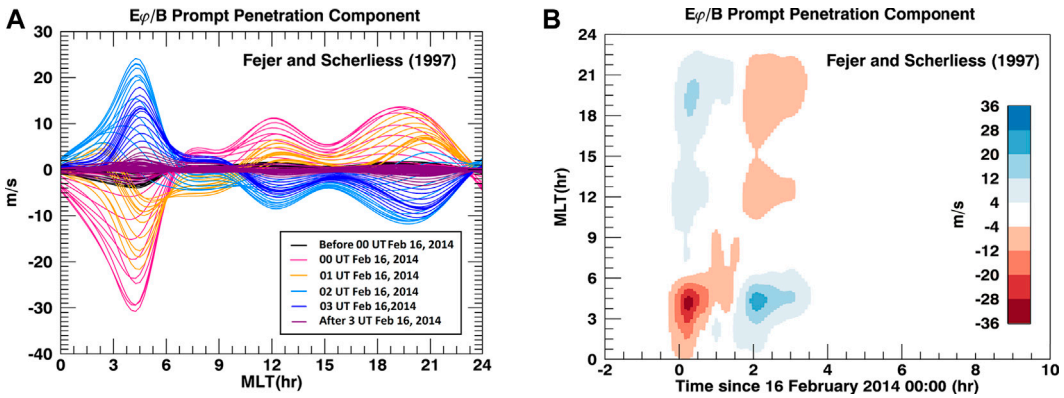


FIGURE 6 | 12 h of radial drift motion driven by the prompt penetration of magnetospheric convection between 15 February 2014, 22 UT and 16 February 2014, 10 UT, according to the analytical empirical model developed by Fejer and Scherliess (1997). **(A)** The amplitude is represented as a function of magnetic local time, MLT, for different times. **(B)** The amplitude is color-coded as a function of the number of hours since 16 February 2014, 00 UT and the magnetic local time, MLT.

square regressions. For every angular drift frequency, Ω (+/ − 0.1 rad/hr), and for every crossings of the inner belt and slot region (1.5 < L < 3), we collect information on average radial transport as a function of L (+/ − 0.1). Because radial transport is not expected to depend on pitch angle in the electrostatic case (e.g., Fälthammar, 1968), we collect all data points relative to trapped particles with equatorial pitch angle of 90° + / − 30° ($x \leq 0.5$). Because radial transport is expected to vary as a power of L, $\delta r = kR_E L^n$, we perform linear least square regressions between ln $|\delta r|$ and ln L to determine the best sets of k and n parameters for each angular drift frequency and inner belt crossing time. We find estimates for the power of L associated with radial transport, n, that are variable when considering all inbound and outbound crossings of the inner belt and slot region during the morning of 16 February 2014. The median value is of the order of n = 3, with an interquartile range of 3 (value of the first quartile: 2; value of the third quartile: 5). Considering that radial transport is proportional to L^3 is equivalent to assuming that the electric field disturbances is uniform in the inner belt and slot region (**Eq. 3**), a finding seemingly consistent with the prompt penetration of magnetospheric convection.

The estimates for the k parameters are obtained by minimizing the least squares of $\delta r/R_E L^3$. The results, provided in **Figure 5**, correspond to radial transport extrapolated to L = 1. It is of the order of 300 km peak-to-peak for $\Omega \sim 1$ rad/hr and decreases to a few tens of kilometers for $\Omega \geq 3$ rad/hr. Decreasing (resp. increasing) the assumed power of L by one unit in the least square fit ($n' = n \mp 1$) increases (resp. decreases) the resulting peak-to-peak amplitude of radial transport at L = 1 by factor ~2.

3.2 Radial Transport at L = 1 From Particle Tracing

We apply the model developed by Fejer and Scherliess to compute the perturbation in radial motion (i.e., the ionospheric meridional drift disturbance) based on the time history of the AE index. According to the model, the prompt penetration electric fields are by far the main contributors to the perturbation in radial motion (**Section 2.2**). The spatial and temporal variations of the electric drift associated with prompt penetration of magnetospheric dynamo electric field is represented in **Figure 6**. The time interval is from 15 February 2014, 22 UT to 16 February 2014, 10 UT. The sharp increase in the AE index at the beginning of 16 February 2014 is associated with a strong inward motion around 5 MLT (with a maximum magnitude of ~ −30 m/s). Similarly, the sharp decrease in AE index around two UT is associated with a strong outward motion around 5 MLT (with a maximum magnitude of 24 m/s, i.e., 0.6 mV/m). In comparison, the perturbation in radial motion velocity associated with the disturbance dynamo remains smaller than 6 m/s (0.15 mV/m) throughout the same time interval. With this model, the characteristic time for the variation of the fields is shorter than the drift period (<1 h vs. 1.25hr–6.3hr for Ω between 1 rad/hr and 5 rad/hr).

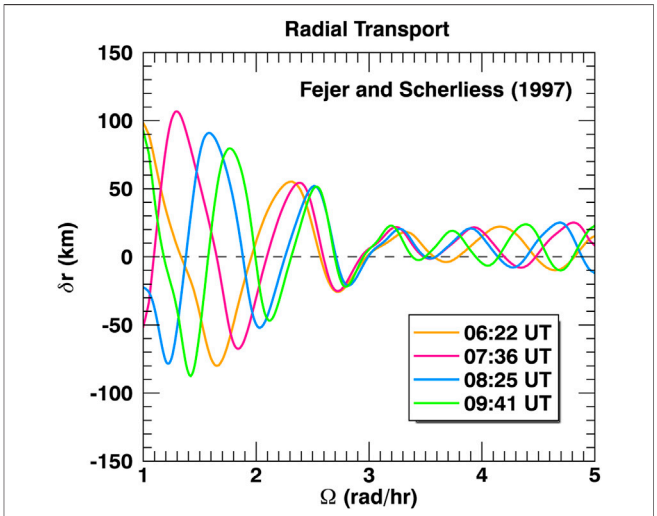


FIGURE 7 | Radial transport modeled at L = 1, at the time and magnetic local time zones of Van Allen probes' crossings (i. e. 5-8 MLT for the inbound passes at 06:22 UT and 08:25 UT and 16–19.5 MLT for the outbound passes at 07:36 UT and 09:41 UT). The electric field disturbances are provided by the analytical empirical formula of Fejer and Scherliess (1997).

We use these outputs to solve the dynamics of particles unrealistically trapped at L = 1. Using **Eq. 3**, we launch particles with different angular drift velocities, Ω, and different drift phases at L = 1 on 15 February 2014, 22 UT. At the time of the end of every crossing (06:22 UT, 07:36 UT, 08:25 UT and 09:41 UT), we select the particles that are in the same magnetic local time zone as the one scanned by the Van Allen Probes and we store information relative to their radial transport, δr. The results are provided in **Figure 7**.

The radial transport computed using the modeled electric field disturbances (prompt penetration and disturbance wind dynamo) varies as expected with time, magnetic local time, and angular drift velocity, Ω. It is of the order of 150 km peak-to-peak for $\Omega \sim 1-2$ rad/hr, and decreases to a few tens of kilometers for $\Omega \geq 3$ rad/hr.

3.3 Model-Observation Comparison

The comparison of **Figure 5** and **Figure 7** shows that the local minima and maxima seen in the experimental estimates for radial transport correspond to the ones obtained numerically. The Pearson correlation coefficient, cc, between the two series (experimental and numerical estimates of radial transport) is high during the first pass, and then decreases with time (06:22UT cc = 0.76; 07:36 UT cc = 0.52; 08:25 UT cc = 0.49; 09:41 UT cc = 0.39). The good agreement between the locations of the extrema and the similitude in the overall shapes of the envelopes suggest that the timing for electric field variations provided by the model is valid for studying radial transport in the inner belt and slot region. On the other hand, the amount of radial transport provided by the model (**Figure 7**) is smaller than the one resulting from the extrapolation of radial transport experimental estimates down to L = 1 (**Figure 5**), by approximately a factor 2–3. Because the numerical model comes from an average over many scenarios, it is possible that the penetration electric fields are underestimated in this case. Another difference is that the experimental estimates for radial transport are predominantly negative while the numerical estimates oscillate around zero. This negative offset is present during both inbound passes in the dusk sector and outbound passes in the dawn sector. This rules off the quiet time wind dynamo as the cause of the offset, since the effect of the quiet time wind dynamo depends on local time. Even though the effect of the electric fields due to the disturbance wind dynamo are taken into account in the particle tracing, this discrepancy suggests that their effect is greater than predictions. It could be that the effect of the dynamo electric fields increases with equatorial radial distance in the magnetosphere.

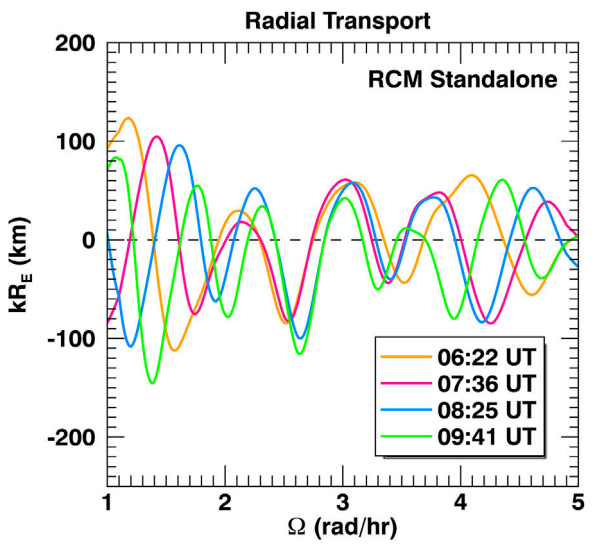


FIGURE 8 | Radial transport modeled at L ~ 1, at the time and magnetic local time zones of Van Allen probes' crossings (i. e. 5-8 MLT for the inbound passes at 06:22 UT and 08:25 UT and 16–19.5 MLT for the outbound passes at 07:36 UT and 09:41 UT). The electric field disturbances are provided by the standalone version of RCM at L = 1.03.

4 DISCUSSION

4.1 Comparing With Radial Transport Based on the Electric Field Dynamics Provided by the Rice Convection Model

We further investigate the model-data discrepancies by running the University of Colorado's version of the standalone Rice Convection Model (RCM) for 15–16 February 2014 (e.g, Maruyama et al., 2011). The data gaps in the OMNI solar wind parameters are filled using WIND measurements. The modeled prompt penetration electric fields are provided at 100 km altitude, and they are mapped to the magnetic equator assuming equipotential field lines in a magnetic dipole (e.g., Lejosne and Mozer, 2016). Specifically, for the azimuthal electric field component: $E_\varphi = E_{\varphi,iono}\, L^{-3/2}$, where $E_{\varphi,iono}$ is the ionospheric eastward electric field. The time resolution for model outputs is 10 min. The magnitude of the peak inward motion increases from a value of −65 m/s at 04:30 MLT around 00 UT on 16 February 2014 to a value of up to 38 m/s at 00:20 UT at 03:15 MLT. These magnitudes are ~2 times larger than the extrema provided by the analytical empirical model (**Figure 6A**). In addition, the electric field variations occur on a shorter timescale with RCM (+100 m/s within 20 min for RCM versus +50 m/s within 2 h for the analytical empirical model). The results of the particle tracing at L = 1 using RCM electric field disturbances are presented in **Figure 8**.

The quality of the agreement between model and data is lesser here than in **Section 3.3**, with correlation coefficients below 0.5 in all passes (06:22UT cc = 0.38; 07:36 UT cc = 0.35; 08:25 UT cc = 0.42; 09:41 UT cc = 0.14). That the amplitude of radial transport does not decrease with the angular drift frequency indicates that the characteristic timescale for the variations of the field is faster than the drift period in all cases. This is in contrast with the experimental result, where radial transport decreases and reaches values of the order of a few tens of kilometers for $\Omega \geq 3$ rad/hr (**Figure 5**). This discrepancy suggests that the electric fields vary too rapidly in the simulation.

We leverage the fact that RCM informs on electric field dynamics at all magnetic latitudes to determine the power of L, n, associated with radial transport in the simulations. The

average value is of the order of $n = 3$, with an interquartile range of 0.6, in agreement with results from the experimental data analysis (**Section 3.1**).

4.2 Other Considerations

4.2.1 Instrument Resolution

An instrument with a high-energy resolution is required when it comes to resolving and analyzing drift echoes such as the zebra stripes (e.g., Hartinger et al., 2018). Particles with slightly different kinetic energies sharing the same energy channel will have mixed adiabatically on a time scale of the order of $2\pi/d\Omega$ (Schulz and Lanzerotti, 1974), i.e. of the order of $2\pi/(\Omega(\mathrm{dE/E}))$. This effect can preclude the application of the method introduced in **Section 2.3** when the time interval between the event and the observation of the resulting flux variations is too long. The resolution of the RBSPICE instruments is dE/E of ~0.06. Thus, for trapped particles with angular drift velocities of $5\,rad/hr$, the timescale for adiabatic mixing is ~20 h. That said, damping in the amplitude of the zebra stripes occurs on shorter timescales. For instance, the zebra stripes observed in the afternoon of 16 February 2014 have significantly smaller peak-to-peak amplitudes than the ones observed during the morning. That is why they were omitted from this study.

4.2.2 Radial Diffusion in the Inner Belt and Slot Region

The power of L associated with radial transport informs the power of L associated with radial diffusion, since $D_{LL} = [(\Delta L)^2]/2\Delta t$, where ΔL corresponds to the normalized radial transport after a time Δt. This analysis suggests that radial diffusion associated with the prompt penetration of magnetospheric convection has a power of L equal to 6 in the inner belt and slot region. A statistical analysis of zebra stripe events is necessary to determine the frequency and average magnitude of radial transport, both of which are needed to quantify radial diffusion driven by magnetic activity below L = 3.

DATA AVAILABILITY STATEMENT

Publicly available datasets were analyzed in this study. This data can be found here: http://rbspice.ftecs.com/Data.html (RBSPICE database). Simulation outputs can be obtained by contacting NM.

AUTHOR CONTRIBUTIONS

The first author is the lead and corresponding author. All other authors are listed in alphabetical order. We describe contributions to the paper using the CRediT (Contributor Roles Taxonomy) categories (Brand et al., 2015). Conceptualization, Formal Analysis, Writing—Original Draft, Visualization and Project Administration: SL Funding acquisition, Methodology: SL and NM Resources, Software: SL, BF, NM, and LS. Investigation: SL, BF and LS. Writing-Review & Editing: SL, BF, NM and LS.

FUNDING

SL work was performed under NASA Grant Awards 80NSSC18K1223 and 80NSSC20K1351. The work of BF was supported by the NASA H-LWS program through grant 80NSSC17K71.

ACKNOWLEDGMENTS

The use of OMNI data and NASA/GSFC's Space Physics Data Facility's OMNIWeb (https://omniweb.gsfc.nasa.gov/) service is acknowledged. We also acknowledge the substorm timing list identified by the Newell and Gjerloev technique (Newell and Gjerloev, 2011a), the SMU and SML indices (Newell and Gjerloev, 2011b); and the SuperMAG collaboration (Gjerloev, 2012). SL thanks C. Huang for a helpful discussion about ionospheric E-field measurements. SL and NM thank Mariangel Fedrizzi for a helpful discussion about filling data gaps in solar wind measurements.

REFERENCES

Brand, A., Allen, L., Altman, M., Hlava, M., and Scott, J. (2015). Beyond Authorship: Attribution, Contribution, Collaboration, and Credit. *Learn. Pub.* 28, 151–155. doi:10.1087/20150211

Fälthammar, C.-G. (1965). Effects of Time-Dependent Electric fields on Geomagnetically Trapped Radiation. *J. Geophys. Res.* 70 (11), 2503–2516. doi:10.1029/JZ070i011p02503

Fälthammar, C.-G. (1968). "Radial Diffusion by Violation of the Third Adiabatic Invariant," in *Earth's Particles and fields*. Editor B. M. McCormac (New York: Reinhold), 157–169.

Fejer, B. G., and Scherliess, L. (1995). Time Dependent Response of Equatorial Ionospheric Electric fields to Magnetospheric Disturbances. *Geophys. Res. Lett.* 22 (7), 851–854. doi:10.1029/95GL00390

Fejer, B. G., and Scherliess, L. (1997). Empirical Models of Storm Time Equatorial Zonal Electric fields. *J. Geophys. Res.* 102 (A11), 24047–24056. doi:10.1029/97JA02164

Fejer, B. G., Blanc, M., and Richmond, A. D. (2017). Post-Storm Middle and Low-Latitude Ionospheric Electric Fields Effects. *Space Sci. Rev.* 206, 407–429. doi:10.1007/s11214-016-0320-x

Gjerloev, J. W. (2012). The SuperMAG Data Processing Technique. *J. Geophys. Res.* 117, A09213. doi:10.1029/2012JA017683

Hartinger, M. D., Claudepierre, S. G., Turner, D. L., Reeves, G. D., Breneman, A., Mann, I. R., et al. (2018). Diagnosis of ULF Wave-Particle Interactions with Megaelectron Volt Electrons: The Importance of Ultrahigh-Resolution Energy Channels. *Geophys. Res. Lett.* 45, 11,883–11,892. doi:10.1029/2018GL080291

Imhof, W. L., and Smith, R. V. (1965). Observation of Nearly Monoenergetic High-Energy Electrons in the Inner Radiation Belt. *Phys. Rev. Lett.* 14, 885–887. doi:10.1103/PhysRevLett.14.885

Lanzerotti, L. J., Roberts, C. S., and Brown, W. L. (1967). Temporal Variations in the Electron Flux at Synchronous Altitudes. *J. Geophys. Res.* 72 (23), 5893–5902. doi:10.1029/JZ072i023p05893

Lejosne, S., and Mozer, F. S. (2016). Typical Values of the Electric Drift E × B/B 2 in the Inner Radiation belt and Slot Region as Determined from Van Allen Probe Measurements. *J. Geophys. Res. Space Phys.* 121, 12014–12024. doi:10.1002/2016JA023613

Lejosne, S., and Mozer, F. S. (2018). Magnetic Activity Dependence of the Electric Drift below L = 3. *Geophys. Res. Lett.* 45, 3775–3782. doi:10.1029/2018GL077873

Lejosne, S., and Mozer, F. S. (2020a). Experimental Determination of the Conditions Associated with "Zebra Stripe" Pattern Generation in the Earth's

Inner Radiation Belt and Slot Region. *J. Geophys. Res. Space Phys.* 125, e2020JA027889. doi:10.1029/2020JA027889

Lejosne, S., and Mozer, F. S. (2020b). Inversion of the Energetic Electron "Zebra Stripe" Pattern Present in the Earth's Inner Belt and Slot Region: First Observations and Interpretation. *Geophys. Res. Lett.* 47, e2020GL088564. doi:10.1029/2020GL088564

Lejosne, S., and Roederer, J. G. (2016). The "Zebra Stripes": An Effect of *F* Region Zonal Plasma Drifts on the Longitudinal Distribution of Radiation belt Particles. *J. Geophys. Res. Space Phys.* 121, 507–518. doi:10.1002/2015JA021925

Lejosne, S., Fedrizzi, M., Maruyama, N., and Selesnick, R. S. (2021). Thermospheric Neutral Winds as the Cause of Drift Shell Distortion in Earth's Inner Radiation Belt. *Front. Astron. Space Sci.* 8, 725800. doi:10.3389/fspas.2021.725800

Liu, Y., Zong, Q.-G., Zhou, X.-Z., Foster, J. C., and Rankin, R. (2016). Structure and Evolution of Electron "Zebra Stripes" in the Inner Radiation belt. *J. Geophys. Res. Space Phys.* 121, 4145–4157. doi:10.1002/2015JA022077

Maruyama, N., Fuller-Rowell, T. J., Codrescu, M. V., Anderson, D., Richmond, A. D., Maute, A., et al. (2011). "Modeling the Storm Time Electrodynamics," in *Aeronomy of the Earth's Atmosphere and Ionosphere, IAGA Special Sopron Book Series*. Editors M. Abdu and D. Pancheva (Dordrecht: Springer), 2, 455–464. doi:10.1007/978-94-007-0326-1_35

Mauk, B. H., Fox, N. J., Kanekal, S. G., Kessel, R. L., Sibeck, D. G., and Ukhorskiy, A. (2013). Science Objectives and Rationale for the Radiation Belt Storm Probes Mission. *Space Sci. Rev.* 179, 3–27. doi:10.1007/s11214-012-9908-y

Mitchell, D. G., Lanzerotti, L. J., Kim, C. K., Stokes, M., Ho, G., Cooper, S., et al. (2013). Radiation Belt Storm Probes Ion Composition Experiment (RBSPICE). *Space Sci. Rev.* 179, 263–308. doi:10.1007/s11214-013-9965-x

Mozer, F. S. (1970). Electric Field Mapping in the Ionosphere at the Equatorial Plane. *Planet. Space Sci.* 18, 259–263. doi:10.1016/0032-0633(70)90161-3

Newell, P. T., and Gjerloev, J. W. (2011a). Evaluation of SuperMAG Auroral Electrojet Indices as Indicators of Substorms and Auroral Power. *J. Geophys. Res.* 116, A12211. doi:10.1029/2011JA016779

Newell, P. T., and Gjerloev, J. W. (2011b). Substorm and Magnetosphere Characteristic Scales Inferred from the SuperMAG Auroral Electrojet Indices. *J. Geophys. Res.* 116, A12232. doi:10.1029/2011JA016936

Richmond, A. D., Blanc, M., Emery, B. A., Wand, R. H., Fejer, B. G., Woodman, R. F., et al. (1980). An Empirical Model of Quiet-Day Ionospheric Electric Fields at Middle and Low Latitudes. *J. Geophys. Res.* 85, 4658–4664. doi:10.1029/JA085iA09p04658

Roederer, J. G., Hilton, H. H., and Schulz, M. (1973). Drift Shell Splitting by Internal Geomagnetic Multipoles. *J. Geophys. Res.* 78 (1), 133–144. doi:10.1029/JA078i001p00133

Sandel, B. R., Goldstein, J., Gallagher, D. L., and Spasojevic, M. (2003). Extreme Ultraviolet Imager Observations of the Structure and Dynamics of the Plasmasphere. *Space Sci. Rev.* 109, 25–46. doi:10.1023/b:spac.0000007511.47727.5b

Sauvaud, J.-A., Walt, M., Delcourt, D., Benoist, C., Penou, E., Chen, Y., et al. (2013). Inner Radiation belt Particle Acceleration and Energy Structuring by Drift Resonance with ULF Waves during Geomagnetic Storms. *J. Geophys. Res. Space Phys.* 118, 1723–1736. doi:10.1002/jgra.50125

Schulz, M., and Lanzerotti, L. J. (1974). *Particle Diffusion in the Radiation Belts*. Berlin, Heidelberg: Springer-Verlag. doi:10.1007/978-3-642-65675-0

Selesnick, R. S., Su, Y. J., and Blake, J. B. (2016). Control of the Innermost Electron Radiation belt by Large-scale Electric fields. *J. Geophys. Res. Space Phys.* 121, 8417–8427. doi:10.1002/2016JA022973

Sun, Y. X., Roussos, E., Hao, Y. X., Zong, Q.-G., Liu, Y., Lejosne, S., et al. (2021). Saturn's Inner Magnetospheric Convection in the View of Zebra Stripe Patterns in Energetic Electron Spectra. *J. Geophys. Res. Space Phys.* 126, e2021JA029600. doi:10.1029/2021ja029600

Tsyganenko, N. A. (1989). A Magnetospheric Magnetic Field Model with a Warped Tail Current Sheet. *Planet. Space Sci.* 37 (1), 5–20. doi:10.1016/0032-0633(89)90066-4

Ukhorskiy, A. Y., Sitnov, M. I., Mitchell, D. G., Takahashi, K., Lanzerotti, L. J., and Mauk, B. H. (2014). Rotationally Driven 'Zebra Stripes' in Earth's Inner Radiation belt. *Nature* 507, 338–340. doi:10.1038/nature13046

Conflict of Interest: The authors declare that the research was conducted in the absence of any commercial or financial relationships that could be construed as a potential conflict of interest.

Publisher's Note: All claims expressed in this article are solely those of the authors and do not necessarily represent those of their affiliated organizations, or those of the publisher, the editors and the reviewers. Any product that may be evaluated in this article, or claim that may be made by its manufacturer, is not guaranteed or endorsed by the publisher.

Copyright © 2022 Lejosne, Fejer, Maruyama and Scherliess. This is an open-access article distributed under the terms of the Creative Commons Attribution License (CC BY). The use, distribution or reproduction in other forums is permitted, provided the original author(s) and the copyright owner(s) are credited and that the original publication in this journal is cited, in accordance with accepted academic practice. No use, distribution or reproduction is permitted which does not comply with these terms.

frontiers | Frontiers in Astronomy and Space Sciences

ORIGINAL RESEARCH
published: 02 May 2022
doi: 10.3389/fspas.2022.731925

Statistical Analysis of Bifurcating Region 2 Field-Aligned Currents Using AMPERE

H. K. Sangha [1]†, S. E. Milan [1,2]*, B. J. Anderson [3] and H. Korth [3]*

[1]School of Physics and Astronomy, University of Leicester, Leicester, United Kingdom, [2]Birkeland Centre for Space Science, University of Bergen, Bergen, Norway, [3]The Johns Hopkins University Applied Physics Laboratory, Laurel, MD, United States

OPEN ACCESS

Edited by:
Philip J. Erickson, Massachusetts Institute of Technology, United States

Reviewed by:
Octav Marghitu, Space Science Institute (Romania), Romania
Angeline G. Burrell, United States Naval Research Laboratory, United States

***Correspondence:**
H. K. Sangha
hs0103@uah.edu
S. E. Milan
steve.milan@leicester.ac.uk

†Present Address:
H. K. Sangha, Center for Space Plasma and Aeronomic Research (CSPAR), University of Alabama in Huntsville, Huntsville, AL, United States

Specialty section:
This article was submitted to Space Physics, a section of the journal Frontiers in Astronomy and Space Sciences

Received: *28 June 2021*
Accepted: *05 April 2022*
Published: *02 May 2022*

Citation:
Sangha HK, Milan SE, Anderson BJ and Korth H (2022) Statistical Analysis of Bifurcating Region 2 Field-Aligned Currents Using AMPERE. Front. Astron. Space Sci. 9:731925. doi: 10.3389/fspas.2022.731925

We present a statistical analysis of the occurrence of bifurcations of the Region 2 (R2) Field-Aligned Current (FAC) region, observed by the Active Magnetosphere and Planetary Electrodynamics Response Experiment (AMPERE). Previously, these have been shown to occur as the polar cap contracts after substorm onset, the beginning of the growth phase. During this phase both the Region 1 (R1) and R2 currents move equatorwards as the polar cap expands. Following onset, the R1 FAC region contracts polewards but the R2 FAC continues to expand equatorwards before eventually fading. At the same time, a new R2 FAC develops equatorwards of the R1 FAC. We have proposed that the bifurcated FACs formed during substorms are associated with plasma injections from the magnetotail into the inner magnetosphere, and that they might be the FAC signature associated with Sub-Auroral Polarization Streams (SAPS). We investigate the seasonal dependence of the occurrence of bifurcations from 2010 to 2016, determining whether they occur predominantly at dawn or dusk. Region 2 Bifurcations (R2Bs) are observed most frequently in the summer hemisphere and at dusk, and we discuss the possible influence of ionospheric conductance. We also discuss a newly discovered UT dependence of the R2B occurrences between 2011 and 2014. This dependence is characterized by broad peaks in occurrence near 09 and 21 UT in both hemispheres. Reasons for such a preference in occurrence are explored.

Keywords: bifurcated field-aligned currents, region 2 field-aligned currents, AMPERE, ionosphere, sub-auroral polarization streams

1 INTRODUCTION

When studying the Solar Wind-Magnetosphere-Ionosphere-Thermosphere (SWMIT) coupled system, it is important to note the role played by Field-Aligned Currents (FACs), also known as Birkeland currents, in stress balance. For instance, they transmit stress from the magnetosphere to excite ionospheric flows in response to the Dungey cycle of convection (Dungey 1961). Observed initially by Iijima and Potemra (1976a), Iijima and Potemra (1976b), Iijima and Potemra (1978), the Region 1 (R1) FACs are located at higher latitudes and the Region 2 (R2) FACs occur equatorwards of the R1 FAC system. They both have an associated upward and downward FAC. The dawnside R1 and duskside R2 currents are directed downward, and the duskside R1 and dawnside R2 currents are directed upward. Iijima and Potemra were able to build up the FAC distribution using data collected from multiple orbits by the Triad satellite. Not only are the FACs situated in the auroral region,the upward FACs form a significant component of the aurorae

with the electrons precipitating down the field lines and interacting with the atmospheric neutrals.

Studying the FACs gives us a unique perspective on magnetospheric processes that are occurring in the SWMIT system. When the Interplanetary Magnetic Field (IMF) is directed southward (IMF $B_Z < 0$), dayside reconnection initiates the Dungey cycle, convecting field lines and plasma within the magnetosphere (Dungey 1961). Dayside reconnection also increases the amount of open flux within the system, and causes the polar cap (the region with open field lines inside the auroral oval) to expand. The location of the FACs provide an effective proxy for the polar cap. The FACs move to lower and higher latitudes in correspondence with geomagnetic activity levels–more disturbed geomagnetic activity sees the FACs travel further equatorward. This can also be seen in the changing latitudes of the aurorae. This behavior is due to the polar cap expanding and contracting under different rates of dayside and nightside reconnection (explained by the Expanding/Contracting Polar Cap (ECPC) model, described by Cowley and Lockwood (1992); Milan et al. (2007), Milan et al. (2017); Clausen et al. (2012) and references therein).

The modulation of the polar cap size can indicate the occurrence of substorm cycles within the magnetosphere. During levels of increased open flux within the system–when dayside reconnection dominates over nightside reconnection–the polar cap expands. At this point, energy from the solar wind can be stored in the magnetotail. This is known as the "substorm growth phase". Field lines in the magnetotail subsequently reconnect, releasing the stored energy during the "substorm expansion phase". When this happens, the polar cap begins to contract, and there is an increase in the auroral activity and the precipitation of energetic particles. This release of stored energy allows the magnetosphere to return to a quiet state, known as the "substorm recovery phase", at which point the polar cap has fully returned to a contracted state (Akasofu and Chao 1979; McPherron 1979; Rostoker et al., 1980; McPherron 1991). The convection associated with substorms leads to injections of plasma from the magnetotail into the inner magnetosphere (Eastman et al., 1984; Daglis et al., 1999), giving rise to the formation of a partial ring current, which closes through the ionosphere carried by R2 FACs (Daglis et al., 1999).

Sangha et al. (2020) discussed a novel feature in the FAC data measured by the Active Magnetosphere and Planetary Electrodynamics Response Experiment (AMPERE); namely, the development of a second pair of R2 FACs. This second R2 FAC, which fits the description of R2 FAC Bifurcations (R2Bs), is shown in **Figure 1**. This figure contains a series of eight northern AMPERE polar plots, from 06:50 to 08:12 UT on 2 June 2011. Each plot is oriented with noon at the top and dawn on the right, with the upward FACs shown in red and downward FACs in blue. The dashed box in the 06:50 UT panel shows the dawn-dusk region (right-left), and the arrows at 08:06 UT show the location of the R2B signatures. From 06:50 to 07:44 UT, the polar cap can be seen to contract. At 07:44 UT, the dawn and dusk R2 FACs have developed a second peak in the current density, equatorward of the original one. By 08:06 UT the R2 FACs have bifurcated, and by 08:12 UT the duskside R2 FAC has completely disconnected from the original R2 FAC. This plot is described in more detail in Sangha et al. (2020), where it was first published. These substorm-related events were seen as predominantly a duskside phenomenon, favoring the summer hemisphere. Utilizing both the Defense Meteorological Satellite Program's (DMSP) Special Sensor Ultraviolet Spectrographic

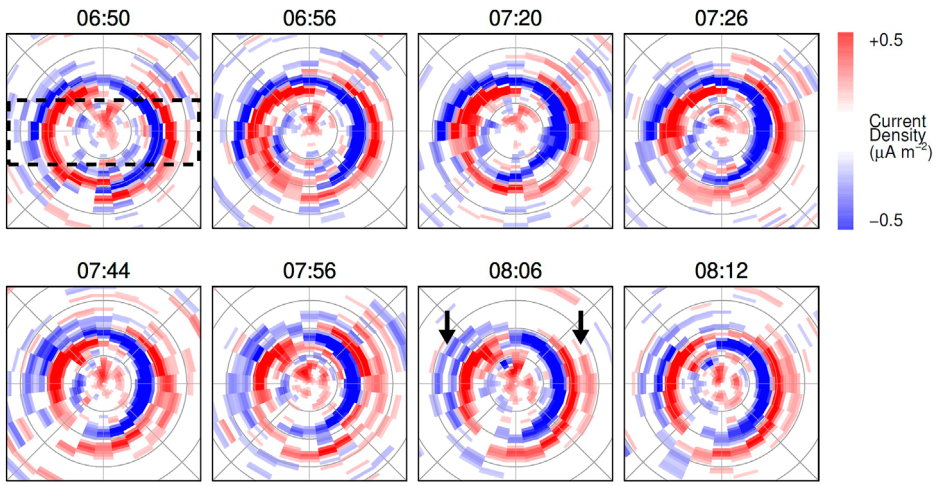


FIGURE 1 | A series of eight northern hemisphere polar plots from Sangha et al. (2020), showing the development of AMPERE field-aligned current densities during a FAC bifurcation event, from 06:50 to 08:12 UT on 2 June 2011. The color scale shows upward (red) and downward (blue) FACs, saturating at ±0.5 μA m^{-2}. The gray concentric rings show the colatitude in steps of 10°, up to 35°. 12 MLT (local noon) is located at the top of the plots, with 06 MLT (dawn) on the right. The dashed box indicates the axis of interest - the dawn-dusk axis. The locations of interest are indicated with the black arrows in the 08:06 UT panel, where there are R2Bs present in both the dawn and dusk regions. The first panel shows the standard R1/R2 pattern, which evolves and by 07:44 UT the polar cap is seen to have contracted, with R2Bs clearly evident ~25° to 30° (Sangha et al., 2020).

Imager (SSUSI) auroral data, and Super Dual Auroral Radar Network (SuperDARN) ionospheric convection data, they were able to deduce that the R2Bs were a subauroral feature and were associated with fast ionospheric flows. This led to the conclusion of a relationship between the R2Bs and Sub-Auroral Polarization Streams (SAPS)–fast westward directed flows occurring in the ionosphere equatorward of the main auroral oval. SAPS are believed to form due to a polarization electric field produced in the sub-auroral ionosphere causing ionospheric convection. They are also associated with the region of low ionospheric conductance. They suggest that these R2Bs are the closure currents associated with SAPS (Foster and Burke 2002; Huang et al., 2006; Clausen et al., 2012; Lejosne and Mozer 2017; Sangha et al., 2020).

In this paper, we describe further analyses of the occurrence of R2Bs. In **Section 2** we describe the instrumentation that has been used for these studies. We then include a more in-depth study of the seasonal variations of the R2Bs in **Section 3**, as well as the UT dependence that we have discovered in **Section 4**. We currently do not know the reason for this dependence. However, we mention some possible causes of this distribution in **Section 5**. We conclude in **Section 6**.

2 INSTRUMENTATION

The work that we present in this paper uses data from AMPERE, collected from the Iridium satellite constellation. Iridium consists of 66 satellites in six polar orbital planes circling the Earth at low altitudes of 780 km. The satellites cross both the North and South polar regions, allowing for the FAC density to be determined for both the northern and southern auroral regions, with a cadence of a few minutes (Anderson et al., 2000, Anderson et al., 2002). The FACs are inferred from measurements of magnetic field perturbations via engineering magnetometers on-board the satellites. These data are used to constrain a spherical harmonic fit, from which the FAC density can be computed (Anderson et al., 2000; Waters et al., 2001; Green et al., 2006; Coxon et al., 2014a, Coxon et al., 2014b, Coxon et al., 2018).

3 SEASONAL AND INTERHEMISPHERIC VARIABILITY

Sangha et al. (2020) discussed the dawn-dusk and interhemispheric variabilities between the occurrences of the R2Bs. An initial analysis of the seasonal occurrence distribution was also discussed.

Following on from this initial study in Sangha et al. (2020), we now present the results of our complete seasonal analysis. To conduct this study, we identified the number of occurrences of R2Bs throughout 2010 to 2016 during the different seasons. This was done by using data from the months of June and July (northern hemisphere summer solstice), March and September (equinoxes), and December and January (southern hemisphere summer solstice). The R2B occurrences were identified by plotting keograms (time-latitude plots) of the AMPERE data

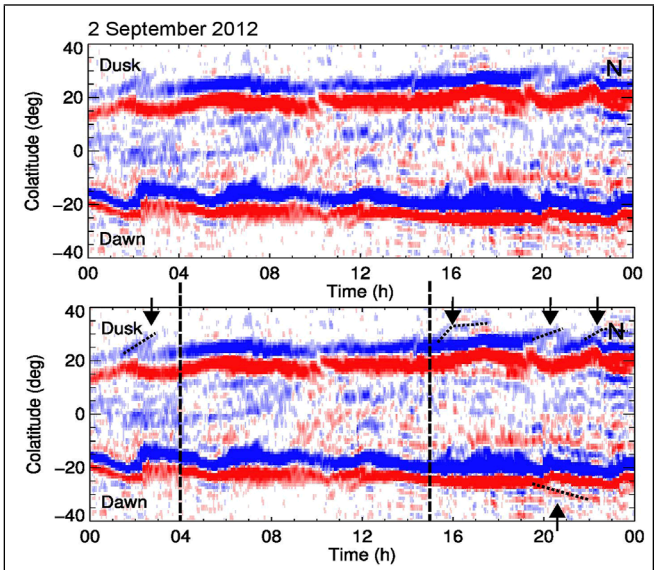


FIGURE 2 | An example of an AMPERE FAC keogram used to identify R2Bs. The data were taken from 2 September 2012, in particular the dawn-dusk axis. Upward FACs are shown in red and downward FACs in blue, in the same scale as **Figure 1**. Both plots are showing the same data, with the second showing the annotated version allowing for the R2Bs to be clearly identified. The arrows indicate the dawn and dusk R2B occurrences at 20 UT and 02, 16, 20, and 22 UT, respectively. The dotted lines follow the evolution of the events throughout the day. The time between the dashed lines (04 and 15 UT) shows the period with no R2B activity occurring.

(shown here in **Figure 2** and in Figure 5 of Sangha et al. (2020)), and analyzing the plots by eye. The requirements for R2B identification were that the R2 FACs needed to diverge by at least 5° away from the original R2 current, extending above 20° colatitude at dusk and below −20° colatitude at dawn. The R2B had to persist for at least 30 min, and be seen in at least two adjacent MLT sectors.

Figure 2 shows an example of the AMPERE keograms created for the identification of the R2Bs. This example shows FAC data from 2 September 2012, where a small number of R2B events occurred, as well as a period of no R2B activity. These data were taken from the dawn-dusk axis. The direction of the currents are shown in the range of red to blue, where red identifies the upward FACs and blue identifies the downward FACs in the same scale as **Figure 1**. The top and bottom panels are showing the same keogram, the second of which has been annotated to denote the key features. The arrows indicate the locations of the bifurcations at 02, 16, 20 and 22 UT in the dusk sector, and 20 UT in the dawn sector. The development of the R2B occurrences are shown with the dotted lines within the features. The period between 04 and 15 UT (within the dashed lines) shows no bifurcation activity occurring. The R2Bs can be seen as the R2 current extending to lower latitudes away from the R1/R2 boundary. During the period of no bifurcations, the R2 current remains continuous and alongside the R1 current.

In total, 275 R2B events were observed during June and July, 243 events during March and September, and 216 events

TABLE 1 | Table showing the ratio of occurrences of R2Bs in the months of January, December (southern summer solstice), March, September (equinox), and June, July (northern summer solstice).

Months	Both Hemispheres (%)	Northern Hemisphere Only (%)	Southern Hemisphere Only (%)	Total Number of Events
January	56.19	12.38	31.43	105
March	77.40	15.04	7.52	133
June	46.38	50.00	3.62	138
July	49.64	49.64	0.73	137
September	70.91	25.45	3.64	110
December	60.36	6.31	33.33	111

during December and January. In each case, we noted if an event was observed simultaneously in both hemispheres, or just in one hemisphere. The proportion of events observed in each hemisphere is summarized in **Table 1**.

From the table, we can deduce that on average ~50% of events are seen in both hemispheres conjugately (this percentage is higher during the months of equinox). Of the events that only appear in one hemisphere, for both the northern and southern summer months, the events favor the summer hemisphere. Specifically, during June/July, ~50% of R2Bs identified were seen only in the summer hemisphere, with ~2% of events being seen in the winter hemisphere alone. During December/January, these numbers change to ~32% of R2B occurrences being seen only in the summer hemisphere, and ~9% in the winter hemisphere. This suggests that the ionospheric conductance, which is primarily produced by solar illumination, plays a significant role in modulating the occurrence of R2Bs in each hemisphere.

For the equinox months, March and September, we would expect to see events appearing more often than not in both hemispheres simultaneously. This is due to the fact that this time of year is when the ionospheric conductance is most equal between the two hemispheres. This is indeed the case, with ~75% being seen conjugately. However, those single-hemisphere events seem to have a preference for the northern hemisphere. ~20% of R2Bs seen in one hemisphere were seen in the northern hemisphere, and ~6% were identified in the southern hemisphere alone. This is more evident in the autumn equinox than the spring equinox. The autumn equinox saw ~7% fewer events seen conjugately, and ~10% more events identified solely in the northern hemisphere. These results suggest that ionospheric conductance plays a predominant role in controlling the occurrence of R2Bs, but that the R2Bs also show a preference for occurring in the northern hemisphere. This is discussed further in **Section 5**.

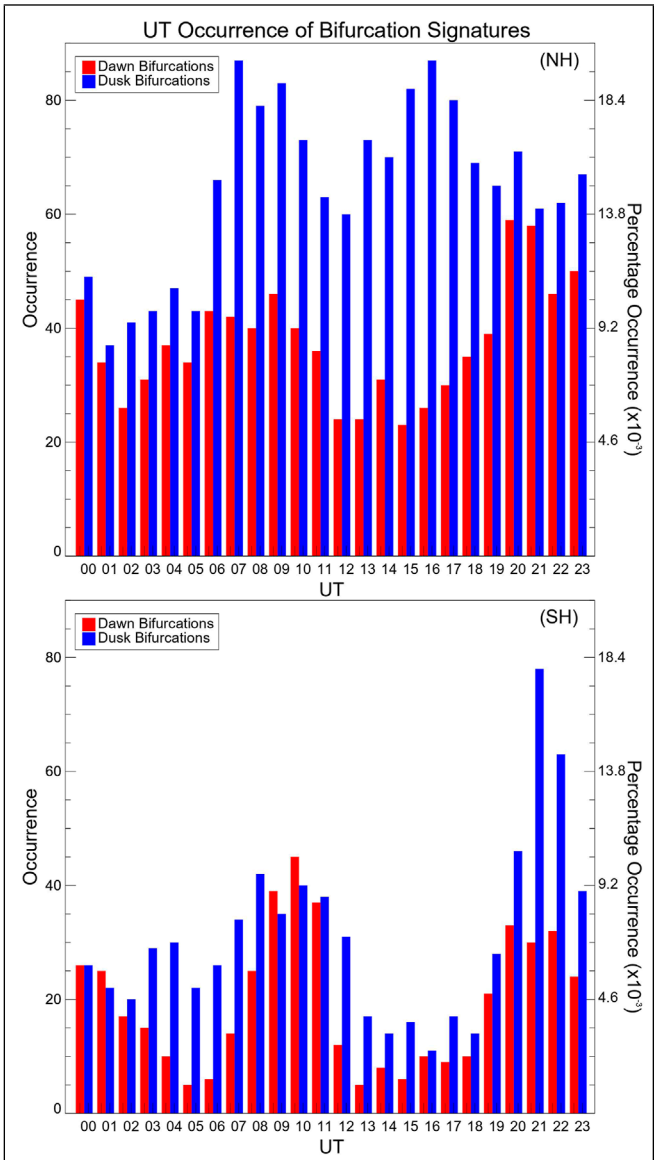


FIGURE 3 | Universal time (UT) occurrence distribution of the bifurcation signatures from 2011 to 2014, in (top) the northern hemisphere and (bottom) the southern hemisphere. The right-hand axis shows the percentage occurrence of the R2Bs. In both plots, the red shows the dawn bifurcations and the blue shows the dusk bifurcations.

4 BIFURCATION UT DEPENDENCE

In this section, we investigate the UT occurrence of R2Bs for both the northern and southern hemispheres. 24 hour-long bins were used to created this distribution. We used data from 2011 to 2014 for the same seasonal months (Jan/Mar/Jun/Jul/Sep/Dec). In this time period, there were 601 days where AMPERE data were available for both the northern and southern hemispheres, from which the keograms were created and analyzed. If an R2B signature was identified, it was included in this distribution by adding it to the UT bin in which the signature was present. If the same event spanned over multiple hours of UT, the event was incorporated into each UT where the signature was present. For example, if an event was identified at 06 UT, and persisted until 09 UT, then that event would be included in the 06, 07, and 08 UT bins for this distribution. The distributions are shown in **Figure 3**. The top plot shows the distribution for the R2B events observed

in the North, and the bottom plot shows the same for the South. The dawn R2B events are shown in red, and the dusk R2Bs are shown in blue.

What is immediately clear when looking at the plots, is that the R2B occurrence rate is not uniformly distributed. The distributions in both hemispheres show two peaks in occurrences at both the dawn and dusk. This could indicate the superposition of two effects–one from the northern hemisphere and one from the southern hemisphere, which are being added together. This would suggest that the R2Bs may then be impacted by conditions in both the northern and southern ionospheres.

The UT distributions were further sub-divided by season; the northern seasonal distributions are shown in **Figure 4**. The top panel shows the distribution for the R2B events from northern hemisphere winter (December and January), the middle panel shows the R2B events for the northern equinox (March and September), and the last panel shows the R2B events for the northern summer (June and July). In all panels, the red shows the dawnside R2Bs, and the blue shows the duskside R2Bs. By looking at these histograms, we were able to identify the peaks within each of the distributions.

Looking at the overall distribution for the northern hemisphere (top plot from **Figure 3**), we can see the location

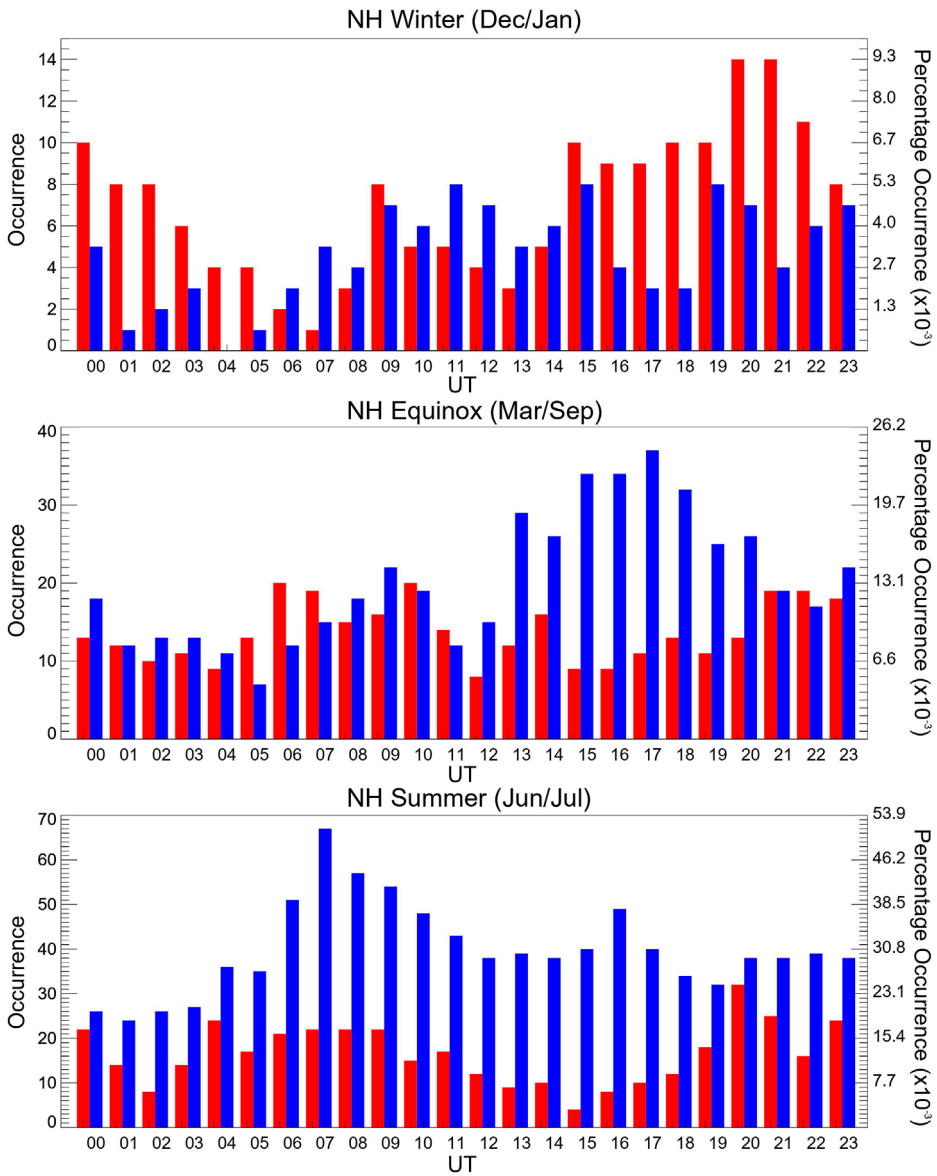


FIGURE 4 | The UT occurrence distribution of R2Bs from 2011 to 2014, for the northern hemisphere split by season: (top) northern winter (December/January) (middle) northern equinox (March/September), and (bottom) northern summer (June/July). The right-hand axis shows the percentage occurrence. Red showing dawn and blue showing dusk R2Bs.

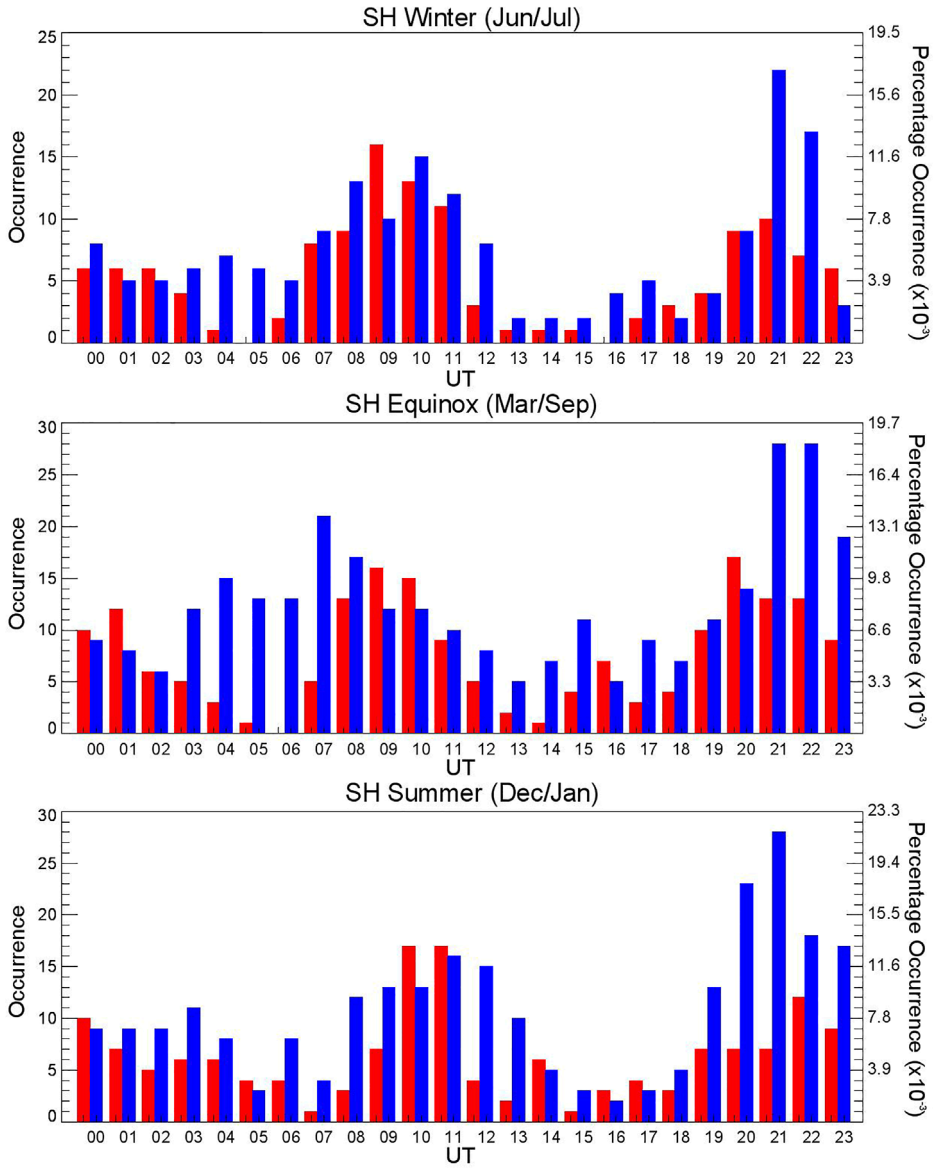


FIGURE 5 | The UT occurrence distribution of R2Bs from 2011 to 2014, for the southern hemisphere split by season: (top) southern winter (June/July) (middle) southern equinox (March/September), and (bottom) southern summer (December/January). The right-hand axis shows the percentage occurrence. Red showing dawn and blue showing dusk R2Bs.

of the distinct peaks in the distributions. The two peaks in the dawn R2Bs are roughly: 07 UT and 21 UT, with two peaks for the dusk R2Bs being roughly: 07 UT and 16 UT. Looking to the seasons now in **Figure 4**, one thing to note is the difference in the number of events. The peak number of events in the northern hemisphere winter distribution is 14, whereas in the equinoxes it is 37, and in the summer this peak reaches 67. This further confirms that the FACs favor the summer hemisphere.

As can be seen from **Figure 4**, almost all of the plots also have the appearance of two peaks in the R2B distributions, with little overlap. Northern hemisphere winter is the only one without a double peaked distribution. It has a single peak in the dawn R2Bs at ~20 UT, and a clear minima at 04 UT in the dusk R2Bs followed by several peaks of nearly equal magnitude between 09 and 23 UT. However, the distributions for northern hemisphere equinox and summer do present two peaks. For equinox, the dawn peaks are: ~10 UT and ~22 UT, and the dusk peaks are: 09 UT and 17 UT. For northern hemisphere summer, the dawn peaks are: ~08 UT and ~19 UT, and the dusk peaks are: ~07 UT and ~16 UT.

By directly comparing the peaks in the seasonal plots to the total distribution for the northern hemisphere, we can see that they coincide. That is, for the peak in the dawn R2B occurrences from northern hemisphere winter at 20 UT, there is a clear peak

in the overall distribution of dawnside events. For the peak in the equinoxes duskside occurrences at 17 UT, there is a peak in the overall distribution of the duskside events at 17 UT also.

We now consider the southern hemisphere distributions. These are shown in **Figure 5**, in the same layout as **Figure 4**. We have the southern hemisphere winter at the top, equinox in the middle, and southern hemisphere summer in the bottom panel. The red shows dawnside occurrences, and blue shows duskside occurrences.

The total distribution (bottom panel in **Figure 3**) shows a clearer double peak than for the northern hemisphere. There are clear dawnside peaks at: 10 UT and 20 UT, and clear duskside peaks at: 08 UT and 21 UT. Initial analysis of the seasonal plots shows a smaller change between the number of peak R2B occurrences between the seasons. **Figure 5** shows that southern hemisphere winter has a peak of 22 events, equinox has a peak of 28, and southern hemisphere summer has a peak of 28.

The southern hemisphere UT distributions are more consistent between seasons than in the northern hemisphere. For southern hemisphere winter, the dawnside peaks are: 09 UT and 21 UT, with the duskside peaks being located at: 10 UT and 21 UT. The equinox sees dawnside peaks at: 09 UT and 20 UT, and duskside peaks of: 07 UT and 21 UT. Finally, for southern hemisphere summer, we have dawn peaks at: 10 UT and 22 UT, and duskside peaks at: 11 UT and 21 UT.

These distributions suggest that the occurrence of R2Bs is modulated by hemisphere, season, and UT. It also appears as though both the northern and southern hemispheres contribute to this modulation. One possible explanation is the conductance of the ionospheres, as discussed in the next section.

5 DISCUSSION

In this paper, we have presented the seasonal dependence and UT occurrence of Region 2 Field-Aligned Current Bifurcations (R2Bs). The occurrence of R2Bs maximizes at dawn and dusk, though with a preference for dusk events. R2Bs are observed most frequently in the summer hemisphere suggesting that ionospheric conductance plays a role in modulating the occurrence. Furthermore, the occurrence in UT tends to be double-peaked in both northern and southern hemispheres, possibly with a lower probability of observation when the conductance is a maximum in either hemisphere.

In approximately 50% of occurrences, R2Bs were observed simultaneously in both hemispheres. In the remainder of cases, the events favored the summer hemisphere suggesting that ionospheric conductance, which increases with greater solar illumination, is a significant influencer of R2Bs in each hemisphere.

Furthermore, during the equinoctial months (when the ionospheric conductance is thought to be most similar between the two hemispheres) we would expect the R2Bs to mostly appear in both hemispheres, which is true for ~74% of the events. We expect the other occurrences to be split relatively evenly between the hemispheres, which is not the case. In fact, of the events seen in a single hemisphere, there were ~8–22% more seen in the northern hemisphere compared to the southern hemisphere for equinox. This is consistent with the results of Coxon et al. (2016), Laundal et al. (2017), Workayehu et al. (2019) and others, who showed that on average the FACs are stronger in the northern hemisphere than the southern hemisphere. As mentioned in **Section 3**, the single-hemisphere detected R2Bs show a larger North-South asymmetry in the autumn equinox over the spring equinox. ~10% more events were shown to have a preference for the northern hemisphere during the autumn equinox over the spring equinox. Work by Workayehu et al. (2020) showed the interhemispheric differences of the FACs varies with season. During local winter and autumn the asymmetry is larger than during local summer and spring, which could be the same effect we are seeing in the occurrences of the R2Bs. During the majority of the time in the southern summer months (December/January), the R2Bs are seen in both hemispheres simultaneously. For the single hemisphere observations, they are more often seen in the southern (summer) hemisphere. However, the difference between occurrences in the northern hemisphere versus the southern hemisphere is smaller for the southern summer than for the northern summer. This suggests that the FAC imbalance between the northern and southern hemisphere is also impacting the occurrence of R2B events.

The UT distributions in the two hemispheres showed two distinct peaks. This could suggest that there are preferred longitudes for the occurrence of R2Bs. However, as the peaks occur at about the same UTs for both dawn and dusk R2Bs, this seems unlikely. Rather, we suggest that the location of the solar terminator is a possible controlling factor, because it will affect dawn and dusk similarly through its influence on ionospheric conductance (i.e., height-integrated conductivity). These double-peaked distributions also suggest that the occurrence of R2Bs is modulated by season and by UT, and that both the northern and southern hemispheres contribute to this modulation. In what follows, we discuss the impact of conductivity on the occurrence of R2Bs, along with other factors which may contribute to a UT dependence, including dayside reconnection geometries and neutral winds.

We start by discussing ionospheric conductance. Enhanced ionospheric conductivity, which is associated with solar illumination, leads to larger FACs (Ohtani et al., 2005). As solar illumination (and ionospheric conductance) is greatest in the summer months, we would expect the R2Bs to be more visible in these months; this is indeed the case. As the Earth rotates, the geomagnetic pole moves towards and away from the Sun, shifting the polar regions towards the sunlight-produced ionospheric conductance. This conductance may be expected to have an influence on R2Bs. The magnetic pole faces towards the Sun at ~17 UT for the northern hemisphere and 05 UT for the southern hemisphere (Coxon et al., 2016). This means that when the pole is facing the Sun, there is increased solar illumination for that time compared to the rest of the day. This increases the ionospheric conductance in that hemisphere, i.e., in the North the conductance will be a maximum at 17 UT, and in the South it will be maximum at 05 UT. We might, therefore, expect to see a single peak in the northern hemisphere and southern hemisphere at 17 and 05 UT, respectively. However, the peaks

that our distributions are showing are: northern hemisphere dawn–07 UT and 21 UT, northern hemisphere dusk–07 UT and 16 UT, southern hemisphere dawn–10 UT and 20 UT, southern hemisphere dusk–08 UT and 21 UT. As there are two peaks seen, it suggests that the conductance in each hemisphere has an influence on the visibility of the R2Bs in both hemispheres. The peaks seen here are slightly offset from the times of the poles pointing towards the Sun suggesting there are other impacting factors involved, some of which are discussed further below.

The predominant focus of this analysis was in reference to the location of the peaks. However, the location of the troughs can be identified as being roughly at 05 and 17 UT, which is clearer to see in the distribution for the southern hemisphere. These are the times corresponding to the southern and northern hemisphere magnetic dipoles pointing toward the Sun, respectively (Coxon et al., 2016). As discussed in **Section 1**, we believe that R2Bs are connected to SAPS flows. This is because the DMSP SSUSI imager showed the R2Bs occurring in the sub-auroral ionosphere, predominantly in the dusk region, and SuperDARN indicated an association with fast ionospheric flows (Sangha et al., 2020). SAPS are associated with periods of low auroral conductance. During these times of low conductance, the ionospheric polarization electric fields can increase, which leads to SAPS flows forming. However, during the times specified, the conductance increases due to solar illumination, which can suppress this process and reduce the number of SAPS flows.

One reason as to why the conductance in one hemisphere could have an influence on the visibility of R2Bs in the other, is if the R2Bs were forming on closed field lines, impacting both hemispheres simultaneously. Another reason could be that high conductance in one hemisphere may also suppress the R2Bs in both hemispheres. The rise in overall conductance would lead to a smaller region of low conductance (where the R2Bs form). This would explain the small peaks seen midway between 05 and 17 UT, when the conductance is not a maximum in the either hemisphere. However, it is not clear as to why this mechanism would impact the dawn and dusk R2Bs differently. Another possible reason for the difference in behavior between the hemispheres, is that the magnetic pole is displaced further from the rotation pole in the South than in the North, so the UT variation in conductance will be larger (but not by a huge amount) (Bruinsma et al., 2006; Cnossen and Richmond 2012). An increase in conductance during certain hours of UT could cause a decrease in the number of R2B events occurring, as seen in our distributions.

We now discuss dayside reconnection geometries. Increased dayside reconnection ultimately leads to the occurrence of substorms, of which R2Bs seem to be a new facet. Variations in IMF geometry, as it approaches the magnetosphere, can have an impact on reconnection rates. For example, when IMF B_Z is negative, that is the IMF is directed southward, then dayside reconnection increases. Alternatively, changes in the orientation of IMF B_Y can also impact the resulting ionospheric flows and cusp regions (Holzworth and Meng 1984; Erlandson et al., 1988; Candidi et al., 1989; Newell et al., 1989; Cowley et al., 1991). Although we have not currently checked the B_Y dependence of dawn/dusk R2Bs, this would certainly be an interesting avenue for future research. Additionally, the speed of the solar wind has also been seen to impact the rate of dayside reconnection (Milan et al., 2012). Periods of higher dayside reconnection could lead to an increase in R2B events developing. This may be having an impact on the results presented in this paper.

There are seasonal variations that also effect the dayside reconnection rates. Geomagnetic activity peaks are seen roughly at the equinoctial months. The Russell-McPherron effect states that the more southward the IMF, the more magnetic activity occurs. At the equinoxes, geomagnetic activity is increased due to the dipole tilt being the largest (enabling the angle between the IMF and the dipole to be the largest). When the southward component of the IMF is most negative, it can couple more efficiently with the terrestrial magnetic field. This would increase the rate of reconnection, and hence geomagnetic activity. The time of day in which the effective average southward component of the IMF is most negative changes based on what month of the year we are currently in (see Figure 5 in Russell and McPherron (1973)) (Russell and McPherron 1973; Zhao and Zong 2012; Lockwood et al., 2020b). These seasonal variations may be effecting the occurrence of R2Bs.

There are also longitudinal variations in space weather that change as the Earth travels around the Sun. The Earth's magnetic poles oscillate during the day, moving to point toward and away from the Sun (as already discussed) (Coxon et al., 2016). There are also offsets of the rotational and magnetic poles, which are different in the two hemispheres. These can cause longitudinal variations in space weather (Cnossen and Richmond 2012; Lockwood et al., 2020b,a,c, 2021). Although longitudinal variations may play some role in creating this UT distribution, it is unlikely to cause changes between the longitudes that is drastic enough to account for the UT distribution found.

Finally, we mention neutral winds. Electric fields, and hence ionospheric currents, depend on the relative motion of the ionosphere and neutral background. Neutral winds will influence this relative motion, so can increase or decrease the horizontal currents, in turn affecting the FACs (Lu et al., 1995). Seasonal variations in prevalent neutral winds could hence influence the occurrence of R2Bs. The authors do not currently have an in-depth understanding of these prevalent winds, so will be leaving these for a future study.

Further study is required to understand these UT and seasonal variations of the R2B occurrences.

6 CONCLUSION

We have confirmed the dawn-dusk and the interhemispheric asymmetry in the occurrence of R2Bs, the proposed FAC signature of SAPS reported in Sangha et al. (2020). The R2Bs favor the dusk region and the summer hemisphere. The occurrence of R2Bs shows an interhemispheric asymmetry: 50% of R2Bs occur simultaneously in both hemispheres, but in other cases they favor the summer hemisphere. There is also a preponderance of R2Bs occurring in the northern

hemisphere, reflecting the stronger average FACs observed in the North (Coxon et al., 2016). Similar double-peaked UT occurrence distributions are seen in both hemispheres, with peaks near 09 and 21 UT for both dawn and dusk R2Bs. These suggest that the occurrence of R2Bs in one hemisphere is also influenced by conditions in the conjugate hemisphere. As these R2Bs may be related to the SAPS phenomena, these results may also show a potential relationship between SAPS and seasonal/UT variations. We suggest that ionospheric conductance, controlled by seasonal and UT changes in solar illumination, plays a role in modulating the occurrence of R2Bs. However, the relationship is not a simple one and further work must be done to understand it.

DATA AVAILABILITY STATEMENT

Publicly available datasets were analyzed in this study. This data can be found here: http://ampere.jhuapl.edu.

AUTHOR CONTRIBUTIONS

HKS identified the Region 2 Bifurcation occurrences, and created the analyses as described in this paper. SEM aided with the methods and analyses of the work, and with editing the paper. BJA and HK provided the data to be analyzed.

FUNDING

HKS was supported by a studentship from the Science and Technology Facilities Council (STFC), United Kingdom; SEM was supported by STFC grant no. ST/N000749/1.

ACKNOWLEDGMENTS

This research used the SPECTRE High Performance Computing Facility at the University of Leicester.

REFERENCES

Akasofu, S.-I., and Chao, J. K. (1979). Prediction of the Occurrence and Intensity of Magnetospheric Substorms. *Geophys. Res. Lett.* 6, 897–899. doi:10.1029/GL006i011p00897

Anderson, B. J., Takahashi, K., Kamei, T., Waters, C. L., and Toth, B. A. (2002). Birkeland Current System Key Parameters Derived from Iridium Observations: Method and Initial Validation Results. *J. Geophys. Res.* 107, 1–13. doi:10.1029/2001JA000080

Anderson, B. J., Takahashi, K., and Toth, B. A. (2000). Sensing Global Birkeland Currents with Iridium Engineering Magnetometer Data. *Geophys. Res. Lett.* 27, 4045–4048. doi:10.1029/2000GL000094

Bruinsma, S., Forbes, J. M., Nerem, R. S., and Zhang, X. (2006). Thermosphere Density Response to the 20-21 November 2003 Solar and Geomagnetic Storm from CHAMP and GRACE Accelerometer Data. *J. Geophys. Res.* 111. doi:10.1029/2005JA011284

Candidi, M., Mastrantonio, G., Orsini, S., and Meng, C.-I. (1989). Evidence of the Influence of the Interplanetary Magnetic Field Azimuthal Component on Polar Cusp Configuration. *J. Geophys. Res.* 94, 13585–13591. doi:10.1029/JA094iA10p13585

Clausen, L. B. N., Baker, J. B. H., Ruohoniemi, J. M., Greenwald, R. A., Thomas, E. G., Shepherd, S. G., et al. (2012). Large-scale Observations of a Subauroral Polarization Stream by Midlatitude SuperDARN Radars: Instantaneous Longitudinal Velocity Variations. *J. Geophys. Res.* 117, a–n. doi:10.1029/2011JA017232

Cnossen, I., and Richmond, A. D. (2012). How Changes in the Tilt Angle of the Geomagnetic Dipole Affect the Coupled Magnetosphere-Ionosphere-Thermosphere System. *J. Geophys. Res.* 117, a–n. doi:10.1029/2012JA018056

Cowley, S. W. H., and Lockwood, M. (1992). Excitation and Decay of Solar Wind-Driven Flows in the Magnetosphere-Ionosphere System. *Ann. Geophysicae* 10, 103–115.

Cowley, S. W. H., Morelli, J. P., and Lockwood, M. (1991). Dependence of Convective Flows and Particle Precipitation in the High-Latitude Dayside Ionosphere on theXandYcomponents of the Interplanetary Magnetic Field. *J. Geophys. Res.* 96, 5557–5564. doi:10.1029/90JA02063

Coxon, J. C., Milan, S. E., and Anderson, B. J. (2018). *A Review of Birkeland Current Research Using AMPERE*. American Geophysical Union, 257–278. doi:10.1002/9781119324522.ch16

Coxon, J. C., Milan, S. E., Carter, J. A., Clausen, L. B. N., Anderson, B. J., and Korth, H. (2016). Seasonal and Diurnal Variations in AMPERE Observations of the Birkeland Currents Compared to Modeled Results. *J. Geophys. Res. Space Phys.* 121, 4027–4040. doi:10.1002/2015JA022050

Coxon, J. C., Milan, S. E., Clausen, L. B. N., Anderson, B. J., and Korth, H. (2014b). A Superposed Epoch Analysis of the Regions 1 and 2 Birkeland Currents Observed by AMPERE during Substorms. *J. Geophys. Res. Space Phys.* 119, 9834–9846. doi:10.1002/2014JA020500

Coxon, J. C., Milan, S. E., Clausen, L. B. N., Anderson, B. J., and Korth, H. (2014a). The Magnitudes of the Regions 1 and 2 Birkeland Currents Observed by AMPERE and Their Role in Solar Wind-magnetosphere-ionosphere Coupling. *J. Geophys. Res. Space Phys.* 119, 9804–9815. doi:10.1002/2014JA020138

Daglis, I. A., Thorne, R. M., Baumjohann, W., and Orsini, S. (1999). The Terrestrial Ring Current: Origin, Formation, and Decay. *Rev. Geophys.* 37, 407–438. doi:10.1029/1999RG900009

Dungey, J. W. (1961). Interplanetary Magnetic Field and the Auroral Zones. *Phys. Rev. Lett.* 6, 47–48. doi:10.1103/PhysRevLett.6.47

Eastman, T. E., Frank, L. A., Peterson, W. K., and Lennartsson, W. (1984). The Plasma Sheet Boundary Layer. *J. Geophys. Res.* 89, 1553–1572. doi:10.1029/JA089iA03p01553

Erlandson, R. E., Zanetti, L. J., Potemra, T. A., Bythrow, P. F., and Lundin, R. (1988). IMFBydependence of Region 1 Birkeland Currents Near Noon. *J. Geophys. Res.* 93, 9804–9814. doi:10.1029/JA093iA09p09804

Foster, J. C., and Burke, W. J. (2002). SAPS: A New Categorization for Sub-auroral Electric fields. *Eos Trans. AGU* 83, 393–394. doi:10.1029/2002EO000289

Green, D. L., Waters, C. L., Anderson, B. J., Korth, H., and Barnes, R. J. (2006). Comparison of Large-Scale Birkeland Currents Determined from Iridium and SuperDARN Data. *Ann. Geophys.* 24, 941–959. doi:10.5194/angeo-24-941-2006

Holzworth, R. H., and Meng, C.-I. (1984). Auroral Boundary Variations and the Interplanetary Magnetic Field. *Planet. Space Sci.* 32, 25–29. doi:10.1016/0032-0633(84)90038-2

Huang, C., Sazykin, I., Spiro, R., Goldstein, J., Crowley, G., and Ruohoniemi, J. M. (2006). Storm-time Penetration Electric fields and Their Effects. *Eos Trans. AGU* 87, 131. doi:10.1029/2006EO130005

Iijima, T., and Potemra, T. A. (1976b). Field-aligned Currents in the Dayside Cusp Observed by Triad. *J. Geophys. Res.* 81, 5971–5979. doi:10.1029/JA081i034p05971

Iijima, T., and Potemra, T. A. (1978). Large-scale Characteristics of Field-Aligned Currents Associated with Substorms. *J. Geophys. Res.* 83, 599–615. doi:10.1029/JA083iA02p00599

Iijima, T., and Potemra, T. A. (1976a). The Amplitude Distribution of Field-Aligned Currents at Northern High Latitudes Observed by Triad. *J. Geophys. Res.* 81, 2165–2174. doi:10.1029/JA081i013p02165

Laundal, K. M., Cnossen, I., Milan, S. E., Haaland, S. E., Coxon, J., Pedatella, N. M., et al. (2017). North-south Asymmetries in Earth's Magnetic Field. *Space Sci. Rev.* 206, 225–257. doi:10.1007/s11214-016-0273-0

Lejosne, S., and Mozer, F. S. (2017). Subauroral Polarization Streams (SAPS) Duration as Determined from Van Allen Probe Successive Electric Drift Measurements. *Geophys. Res. Lett.* 44, 9134–9141. doi:10.1002/2017GL074985

Lockwood, M., Haines, C., Barnard, L. A., Owens, M. J., Scott, C. J., Chambodut, A., et al. (2021). Semi-annual, Annual and Universal Time Variations in the Magnetosphere and in Geomagnetic Activity: 4. Polar Cap Motions and Origins of the Universal Time Effect. *J. Space Weather Space Clim.* 11, 15. doi:10.1051/swsc/2020077

Lockwood, M., McWilliams, K. A., Owens, M. J., Barnard, L. A., Watt, C. E., Scott, C. J., et al. (2020a). Semi-annual, Annual and Universal Time Variations in the Magnetosphere and in Geomagnetic Activity: 2. Response to Solar Wind Power Input and Relationships with Solar Wind Dynamic Pressure and Magnetospheric Flux Transport. *J. Space Weather Space Clim.* 10, 30. doi:10.1051/swsc/2020033

Lockwood, M., Owens, M. J., Barnard, L. A., Haines, C., Scott, C. J., McWilliams, K. A., et al. (2020b). Semi-annual, Annual and Universal Time Variations in the Magnetosphere and in Geomagnetic Activity: 1. Geomagnetic Data. *J. Space Weather Space Clim.* 10, 23. doi:10.1051/swsc/2020023

Lockwood, M., Owens, M. J., Barnard, L. A., Watt, C. E., Scott, C. J., Coxon, J. C., et al. (2020c). Semi-annual, Annual and Universal Time Variations in the Magnetosphere and in Geomagnetic Activity: 3. Modelling. *J. Space Weather Space Clim.* 10, 61. doi:10.1051/swsc/2020062

Lu, G., Richmond, A. D., Emery, B. A., and Roble, R. G. (1995). Magnetosphere-ionosphere-thermosphere Coupling: Effect of Neutral Winds on Energy Transfer and Field-Aligned Current. *J. Geophys. Res.* 100, 19643–19659. doi:10.1029/95JA00766

McPherron, R. L. (1979). Magnetospheric Substorms. *Rev. Geophys.* 17, 657–681. doi:10.1029/RG017i004p00657

McPherron, R. L. (1991). "Physical Processes Producing Magnetospheric Substorms and Magnetic Storms," in *Geomagnetism*. Editor Jacobs, J. A. (Cambridge, MA: Academic Press), 593–739. doi:10.1016/b978-0-12-378674-6.50013-3

Milan, S. E., Clausen, L. B. N., Coxon, J. C., Carter, J. A., Walach, M.-T., Laundal, K., et al. (2017). Overview of Solar Wind-Magnetosphere-Ionosphere-Atmosphere Coupling and the Generation of Magnetospheric Currents. *Space Sci. Rev.* 206, 547–573. doi:10.1007/s11214-017-0333-0

Milan, S. E., Gosling, J. S., and Hubert, B. (2012). Relationship between Interplanetary Parameters and the Magnetopause Reconnection Rate Quantified from Observations of the Expanding Polar Cap. *J. Geophys. Res.* 117, a–n. doi:10.1029/2011JA017082

Milan, S. E., Provan, G., and Hubert, B. (2007). Magnetic Flux Transport in the Dungey Cycle: A Survey of Dayside and Nightside Reconnection Rates. *J. Geophys. Res.* 112, a–n. doi:10.1029/2006JA011642

Newell, P. T., Meng, C.-I., Sibeck, D. G., and Lepping, R. (1989). Some Low-Altitude Cusp Dependencies on the Interplanetary Magnetic Field. *J. Geophys. Res.* 94, 8921–8927. doi:10.1029/JA094iA07p08921

Ohtani, S., Ueno, G., and Higuchi, T. (2005). Comparison of Large-Scale Field-Aligned Currents under Sunlit and Dark Ionospheric Conditions. *J. Geophys. Res.* 110. doi:10.1029/2005JA011057

Rostoker, G., Akasofu, S.-I., Foster, J., Greenwald, R. A., Kamide, Y., Kawasaki, K., et al. (1980). Magnetospheric Substorms-Definition and Signatures. *J. Geophys. Res.* 85, 1663–1668. doi:10.1029/JA085iA04p01663

Russell, C. T., and McPherron, R. L. (1973). Semiannual Variation of Geomagnetic Activity. *J. Geophys. Res.* 78, 92–108. doi:10.1029/JA078i001p00092

Sangha, H., Milan, S. E., Carter, J. A., Fogg, A. R., Anderson, B. J., Korth, H., et al. (2020). Bifurcated Region 2 Field-Aligned Currents Associated with Substorms. *J. Geophys. Res. Space Phys.* 125, e2019JA027041. doi:10.1029/2019JA027041

Waters, C. L., Anderson, B. J., and Liou, K. (2001). Estimation of Global Field Aligned Currents Using the Iridium System Magnetometer Data. *Geophys. Res. Lett.* 28, 2165–2168. doi:10.1029/2000GL012725

Workayehu, A. B., Vanhamäki, H., and Aikio, A. T. (2019). Field-Aligned and Horizontal Currents in the Northern and Southern Hemispheres from the Swarm Satellite. *J. Geophys. Res. Space Phys.* 124, 7231–7246. doi:10.1029/2019JA026835

Workayehu, A. B., Vanhamäki, H., and Aikio, A. T. (2020). Seasonal Effect on Hemispheric Asymmetry in Ionospheric Horizontal and Field-Aligned Currents. *J. Geophys. Res. Space Phys.* 125, e2020JA028051. doi:10.1029/2020JA028051

Zhao, H., and Zong, Q.-G. (2012). Seasonal and Diurnal Variation of Geomagnetic Activity: Russell-Mcpherron Effect during Different IMF Polarity And/or Extreme Solar Wind Conditions. *J. Geophys. Res.* 117, a–n. doi:10.1029/2012JA017845

Conflict of Interest: The authors declare that the research was conducted in the absence of any commercial or financial relationships that could be construed as a potential conflict of interest.

Publisher's Note: All claims expressed in this article are solely those of the authors and do not necessarily represent those of their affiliated organizations, or those of the publisher, the editors and the reviewers. Any product that may be evaluated in this article, or claim that may be made by its manufacturer, is not guaranteed or endorsed by the publisher.

Copyright © 2022 Sangha, Milan, Anderson and Korth. This is an open-access article distributed under the terms of the Creative Commons Attribution License (CC BY). The use, distribution or reproduction in other forums is permitted, provided the original author(s) and the copyright owner(s) are credited and that the original publication in this journal is cited, in accordance with accepted academic practice. No use, distribution or reproduction is permitted which does not comply with these terms.

frontiers | Frontiers in Physics

ORIGINAL RESEARCH
published: 05 May 2022
doi: 10.3389/fphy.2022.786639

Machine Learning Methods Applied to the Global Modeling of Event-Driven Pitch Angle Diffusion Coefficients During High Speed Streams

G. Kluth [1,2], J.-F. Ripoll [1,2], S. Has [3], A. Fischer [3], M. Mougeot [4] and E. Camporeale [5,6]*

[1]CEA, DAM, DIF, F-91297, Arpajon, France, [2]UPS, CEA, LMCE, F-91680, Bruyères-le-Châtel, France, [3]LPSM UMR 8001, Université de Paris, Paris, France, [4]Centre Borelli UMR 9010, ENS Paris-Saclay, ENSIIE, Gif, France, [5]CIRES, University of Colorado, Boulder, CA, United States, [6]NOAA Space Weather Prediction Center, Boulder, CA, United States

Whistler-mode waves in the inner magnetosphere cause electron precipitation in the atmosphere through the physical process of pitch-angle diffusion. The computation of pitch-angle diffusion relies on quasi-linear theory and becomes time-consuming as soon as it is performed at high temporal resolution from satellite measurements of ambient wave and plasma properties. Such an effort is nevertheless required to capture accurately the variability and complexity of atmospheric electron precipitation, which are involved in various Earth's ionosphere-magnetosphere coupled problems. In this work, we build a global machine-learning model of event-driven pitch-angle diffusion coefficients for storm conditions based on the data of a variety of storms observed by the NASA Van Allen Probes. We first proceed step-by-step by testing 8 nonparametric machine learning methods. With them, we derive machine learning based models of event-driven diffusion coefficients for the storm of March 2013 associated with high-speed streams. We define 3 diagnostics that allow highlighting of the properties of the selected model and selection of the best method. Three methods are retained for their accuracy/efficiency: spline interpolation, the radial basis method, and neural networks (DNN), the latter being selected for the second step of the study. We then use event-driven diffusion coefficients computed from 32 high-speed stream storms in order to build for the first time a statistical event-driven diffusion coefficient that is embedded within the retained DNN model. We achieve a global mean event-driven model in which we introduce a two-parameter dependence, with both the Kp-index and time kept as in an epoch analysis following the storm evolution. The DNN model does not entail any issue to reproduce quite perfectly its target, i.e., averaged diffusion coefficients, with rare exception in the Landau resonance region. The DNN mean model is then used to analyze how mean diffusion coefficients behave compared with individual ones. We find a poor performance of any mean models compared with individual events, with mean diffusion coefficients computing the general trend at best, due to their large variability. The DNN-based model allows simple and fast data exploration of pitch-angle diffusion among its multiple variables. We finally discuss how to conduct uncertainty quantification of Fokker-Planck simulations of storm conditions for space weather nowcasting and forecasting.

Keywords: machine learning, pitch angle diffusion, event-driven, data exploration, high speed streams

OPEN ACCESS

Edited by:
Georgios Balasis, National Observatory of Athens, Greece

Reviewed by:
Jorge Amaya, KU Leuven, Belgium
Dedong Wang, GFZ German Research Centre for Geosciences, Germany
Antoine Brunet, Université de Toulouse, France

****Correspondence:***
G. Kluth
gilles.kluth@cea.fr

Specialty section:
This article was submitted to Space Physics, a section of the journal Frontiers in Physics

Received: *30 September 2021*
Accepted: *21 February 2022*
Published: *05 May 2022*

Citation:
Kluth G, Ripoll J-F, Has S, Fischer A, Mougeot M and Camporeale E (2022) Machine Learning Methods Applied to the Global Modeling of Event-Driven Pitch Angle Diffusion Coefficients During High Speed Streams. Front. Phys. 10:786639. doi: 10.3389/fphy.2022.786639

1 INTRODUCTION

Pitch angle diffusion is one of the major mechanisms that drive the structure of the Van Allen radiation belts and cause the well-known two belt structure. Whistler-mode hiss waves are responsible for the scattering of energetic electrons by wave-particle interactions and their subsequent precipitation into the atmosphere, forming a region devoid of electrons in the inner magnetosphere, known as the slot region, between the two radiation belts [1]. Observations of the dynamics of the slot from the NASA Van Allen Probes [2] are, for instance, presented in Reeves et al. [3]. Radiation dose received by the electronics of orbiting spacecraft is then reduced in the slot region. In the atmosphere, Breneman et al. [4] have observed a direct correlation between the pulsation of the whistler-mode hiss waves and precipitated electrons at ~100 km observed from a balloon of the BARREL mission [5]. Linking directly precipitations and wave activity remains an open research subject of the ionosphere-magnetosphere system [6]. The recent review in Ripoll et al. [7] and references therein brings more insight on radiation belt physics and current open questions.

Pitch angle scattering can be computed either from statistical models derived from years of satellite observations of the hiss waves properties, e.g., from missions such as CRRES (e.g., [8]), the Van Allen Probes (e.g., [9]), and combined missions (e.g., [10]), or directly from the evolving observations of the ambient properties for a particular event (e.g., [11,12]). The latter method is called the event-driven approach (e.g., [13]) and is the focus of this article. It consists in feeding a quasi-linear Fokker-Planck model (here, we use the CEVA code developed originally by Réveillé [14]) with *in-situ* measurements of wave properties and the plasma density observations made by the Van Allen Probes in order to produce pitch angle diffusion coefficients, $D_{\alpha\alpha}(t)$ at a high temporal resolution. The high temporal resolution comes from refreshing the coefficient values from the temporally updated parameters, with this new evaluation made at best at every pass of the satellite and properties assumed as constant between two passes. Results of Watt et al. [15] have shown that updating the diffusion coefficients at a time rate of less than 9 h (representing one Van Allen Probes orbit) was producing the best accuracy. In return, a computational step requires massively parallel computations in order to calculate bounced-averaged pitch angle diffusion coefficients at each satellite pass time, t, and location, L, i.e., $D_{\alpha\alpha}(t, L, E, \alpha) = D_{\alpha\alpha}(w_i(t, L), n_e(t, L), E, \alpha)$, with the locally measured wave properties denoted here as w_i (t, L) for $i = 1, \ldots 5$, and the plasma density, n_e (t, L), for any electron at time t, L-shell L, of energy E, and equatorial pitch angle α. The index $i = 1, \ldots 5$ includes the four main wave properties, which determine the distribution of a given wave both in frequency and wave normal angle, i.e., the wave mean frequency, frequency width, wave normal angle, and wave normal angle width. The fifth parameter is the wave power, with a quadratic dependence of the diffusion coefficient on wave power. General and technical explanations about the computation of the diffusion coefficients are given in the second section of this article. For further details of this method the reader is referred to Ripoll et al. [12,16,17].

Once diffusion coefficients are computed for a given event, one can repeat the procedure for many events of the same kind (here applied to high speed stream storms) and derive statistical event-driven diffusion coefficients $\tilde{D}_{\alpha\alpha}(w_i, n_e, L, E, \alpha)$, with $\tilde{D}$ denoting, for instance, a temporal average. For comparison, the classic statistical approach, for which the mean of the properties is used, produces instead $D_{\alpha\alpha}(\tilde{w}_i, \tilde{n}_e, L, E, \alpha)$. In statistical methods, a binning on the geomagnetic conditions (using the Kp geomagnetic index [18,19] or sometimes the AE index [8,10]) is commonly introduced in order to reflect at least partially the dynamics of the wave-particle interaction. Conversely, our method allows keeping the non-linearity of the functional form of the diffusion coefficients and the coupling between all parameters since we compute means of diffusion coefficients $\tilde{D}_{\alpha\alpha}$ rather than diffusion coefficients of mean properties. We believe this is required to capture accurately the variability and complexity of atmospheric electron precipitation, which is crucial for studying the Earth's ionosphere-magnetosphere coupling. Similarly to statistical methods, we will also re-introduce a binning with respect to the geomagnetic indices once we generate statistics of event-driven diffusion coefficient below, i.e., means of diffusion coefficients $\tilde{D}_{\alpha\alpha}$ per geomagnetic activity bin, with the use of machine learning techniques.

Machine-learning (ML) techniques have been used for different problems related to ionospheric physics, such as ionospheric scintillation [20,21], the estimation of maps of total electron content (TEC) [22–24], the modeling of the foF2 parameter (which is the highest frequency that reflects from the ionospheric F2-layer) [25], the generation of maps of the thermosphere density [26], and the forecast of electron precipitation [27].

For radiation belt physics, neural networks (NN) are among the most popular machine learning methods. NN have been used for geomagnetic indices prediction, such as Dst/SYM-H, K_p, AE, and AL [28–31] (see also review in [32]). Models of plasmaspheric density have been developed in Zhelavskaya et al. [12,33,35] and Chu et al. [36,37], using NN in order to compensate the lack of density data in radiation belt Fokker-Planck simulations. For instance, Ma et al. [38] computed pitch angle and energy diffusion coefficients using the NN-based density model of Chu et al. [36,37], in the dusk sector where density can be hard to infer, and used them afterward in Fokker-Planck simulations. Malaspina et al. [39] use the NN-plasmasphere model of Chu et al. [36] to quantify the importance of the density for parameterized maps of whistler-mode hiss waves, and Camporeale et al. [40] provide estimates of the uncertainty for the predictions of that NN-plasmasphere model. Other neural network-based models of plasmaspheric density have been developed in Zhelavskaya et al. [12,33,35] and then used in radiation belt Fokker-Planck simulations. For instance, Wang et al. [41] have performed simulations using plasmapause positions inferred from a combination of empirical and Zhelavskaya's NN-based density model and showed the importance of the plasmapause positions on the dynamics of relativistic electrons. For a detailed review of machine learning methods applied to both ionospheric and magnetospheric problems, the reader is referred to the review in Camporeale [42].

In this article, we will show that we can construct a ML model for a single storm based on assimilating the pitch-angle diffusion coefficient $D_{\alpha\alpha}(t, L, E, \alpha)$. Ideally, in order to extend that model to the prediction of any storm, we would need quantities that describe the electromagnetic waves and the plasma conditions for each ongoing storm, which does not exist in practice. Here, we derive the simplest possible global event-driven model encompassed within a ML model and built on an existing large database of event-driven diffusion coefficients. This means that we have to do prediction-error experiments, trying to model pitch angle diffusion for storms for all their given variables, evaluate model errors with the reference data, and modify the type or the number of the used variables to improve the model at best. A similar problem was addressed in Zhelavskaya et al. [33] for a different quantity: the prediction of the cold electron density, training multiple neural networks with different variables and producing different time-averages. Time averaging is also at stake when constructing a global model: the longer the averaging period, the more regularized the model. With a regularized model, the machine learning model is easier to obtain, but its predictive ability is degraded considering a sample event. Yet, regularization should also help in generalizing the model to out-of-sample events.

As a first step, we construct a specific-event model using data from one storm (i.e., March 1, 2013). In other words, we build a regression model for $D_{\alpha\alpha}(L, E, \alpha)$ in 3 dimensions. We compare the results of 8 machine learning methods, such as deep neural networks, functional approximation, and tree-based models, and we use different sizes of training dataset to test each model.

As a second step, we construct a global event-driven model $D_{\alpha\alpha}(t, K_p, L, E, \alpha)$ with a deep neural network using data from the 32 high-speed streams (HSS) storms. For each storm, we extract the geomagnetic index K_p evolving in time during the 3 days of the main and recovery phases of the HSS storms [43]. Time will be kept as a main parameter and serve to produce a superposed epoch analysis of diffusion during the 3 first days of the HSS storms. This is based on the recognition that each storm has a time history, considering, for instance, that two storms having the same geomagnetic activity index at the beginning of the storm, or at the end, can still give different pitch-angle diffusion coefficients (as the data show). The deep neural network is thus used to learn from a giant diffusion coefficient database and construct the first statistical event-driven model diffusion coefficient by whistler-mode hiss waves during HSS events, parameterized by both epoch time and Kp index. The machine learning model is thus used to replace averages and interpolations of the database elements, which one would perform usually by hand, by a numerical expression, which is afterward extremely easy to call for any epoch time, K_p index, location, energy, and pitch angle, without notably altering the accuracy of the initial database. The article is organized as follows. After the introduction in **Section 1**, we present in **Section 2** the dataset and the machine learning methods that are used and tested in this study. In **Section 3**, we present our results first for all methods for the March 1, 2013, storm with regularized data and, then, for the global, i.e., statistical, even-driven model diffusion coefficient of HSS events made from a database of 32 HSS storms. In **Section 4**, we discuss the global DNN pitch angle diffusion model and its use for exploration of the database. Conclusions are given in **Section 5**.

2 MATERIALS AND METHODS

2.1 Description of Datasets

2.1.1 Pitch Angle Diffusion Coefficients

The diffusion coefficient represents the diffusive effect of a given electromagnetic wave (defined by its wave properties) on an energetic electron (with energy E and pitch angle α) trapped on a magnetic field line at a L-shell L in a medium containing cold electrons of density n_e. Eqs 2–8 of Lyons et al. [44] define the diffusion coefficients as they are used here. A more synthetic and modern expression of the diffusion coefficients is available through Eqs (8, 9) in Mourenas and Ripoll [45] using the notations of Albert [46]. One can see that the coefficient directly and explicitly depends on wave amplitude, wave frequency distribution (defined by a mean frequency and a mean frequency width), a wave normal distribution (defined by a mean wave normal angle and mean wave-normal-angle), and plasma density. Diffusion coefficients are computed with the CEVA code originally developed by [47]. In this code, bounce averaged diffusion coefficients are computed following the method and equations of Lyons et al. [44], which account for a sum over all harmonics ($-n$ ... , 0, ... , n), a wave normal integration, and bounce averaging between the mirror points. The limit of low frequency ($\omega_{med}/\omega_{ce} < 1$) and high-density ($\omega_{med}\omega_{ce}/\omega_{pe}^2 \ll 1$) are assumed in these computations. (See also Albert [48] where this model is derived within these approximations and analyzed). Drift averaging is then performed in order to produce mean diffusion coefficients over the full electron drift. Verification by comparison with diffusion coefficients computed with the codes from the US AFRL and BAS (e.g., [49–51]) have been performed in Ripoll and Mourenas [52]. Validation studies of the CEVA code include [6,11,12,17,53].

Diffusion coefficients are evaluated from observed properties in a dynamic way so as to generate event-driven pitch angle diffusion coefficients. Event-driven diffusion coefficients are computed by temporal bins of 8 h each day (3 bins a day). As time is frozen within an 8-h bin and corresponds to roughly a full orbit of the Van Allen Probes, this allows to have frozen parameters for the whole L-shell range (from apogee to perigee of the probes) during each temporal bin. This is made to be able to solve the Fokker-Planck equation over the entire radiation belt regions through which trapped electrons are transported during storms and where they can interact with electromagnetic ambient waves (albeit the wave is present). An 8-h temporal resolution also allows to account for short timescales causing non-equilibrium diffusion effects (i.e., solutions far from steady states) (e.g., [6,15,54]). This means that we evaluate the diffusion coefficients with new properties each 8 h during the few days the storm lasts. We use Van Allen Probes observations of wave amplitude, mean frequency, mean frequency width, mean wave normal angle,

mean wave-normal-angle, and plasma density so that all parameters are data-driven. Each one of these ambient properties changes with time and L-shells as the satellite observes a new value at each pass. In between two passes, we assume conditions are stable enough so that we can keep all parameters constant. This assumption is forced by the lack of available satellite data at higher rates. Eventually, the diffusion coefficients are specific to particular chosen events and qualified as "event-driven" or "event-specific."

All the wave properties, which were listed above as $w_i\,(t, L)$ for $i = 1, \ldots 5$, have been extracted from data of whistler-mode hiss waves (0.05–2 kHz; e.g., [55]). These primitive data are taken from measurements by the Electric and Magnetic Field Instrument Suite and Integrated Science (EMFISIS) Waves instrument aboard the Van Allen Probes [56]. As we do, a Magnetic Local Time (MLT) dependence of the wave amplitude (i.e., the square root of the power) is taken into account by rescaling the locally observed wave amplitude by the MLT-dependence derived statistically from 4 ears of Van Allen Probes data by Spasojevic et al. [57]. The latter approximation is required to account for the great variability of the wave amplitude with MLT (since measurements at all MLTs do not exist) but may introduce temporal inaccuracies due to the use of a statistical model. The MLT rescaling produces diffusion coefficients that apply over the full azimuthal drift of the electron. Similarly, dependence of the diffusion coefficient with the cold electron plasma density ($n_e(t, L)$) is accounted for by using either the density deduced from the upper hybrid line measured by EMFISIS [58] or the density computed from spacecraft charging [59] measured by the Electric Field Wave instrument (EFW) [60] aboard the Van Allen Probes. We note that the wave properties are taken from past measured events and that they are unknown for future events so that any model of diffusion coefficients cannot be made with the wave properties set as mathematical variable. Wave properties remain mandatory parameters that one can either take from direct measurements as here or from statistical models (e.g., [9,18,19,38,41,57,61]). Prediction can then be made from postulating a temporal series of one (or more) geomagnetic index for a given period of time or a known type of event.

Once the diffusion coefficients have been generated from all the primitive ambient properties, they only remain dependent on time t, L-shell L, energy, E, and equatorial pitch angle, α. The original spatial grid of the diffusion coefficients, $D_{\alpha\alpha}\,(t, L, E, \alpha)$, is composed of 43 uniformly distributed bins in L-shell, from L = 1.3 to L = 5.5. The energy grid is composed of 60 logarithmically distributed bins from E = 50 keV to E = 6 MeV. The pitch angle grid is composed of 256 uniformly distributed pitch angles, from the loss cone pitch angle to 90°. This leads to 660480 values per time of interest.

Due to the large variability of the ambient properties, geomagnetic conditions, and position, the values of interest of the pitch-angle diffusion coefficient spread over many decades (from 10^{-19} to 10^{-4} s^{-1}) so that all our machine learning models will output the logarithm of the diffusion coefficient. However, all averages will be made directly on the pitch-angle diffusion coefficient, since averaging instead its logarithm would have weighted excessively the lowest diffusion coefficients and biased them.

During the storm evolution, some of the highest L-shells are located outside the plasmasphere where hiss waves are absent, which produces at best a null (when there are traces of the wave in some denser detached regions) or undefined diffusion coefficients (when the absence of the wave makes the main parameters missing). In this case, the coefficients need to be kept as a null pitch-angle diffusion coefficient in the database and in the statistics. If they were removed from the data, it would result in the rare events in which the wave are presents wrongly dominating the statistics.

2.1.2 Original Full Dataset

In this study, we consider either 1 or 32 storms, 1 or 9 time intervals, 43 positions, 60 energies, and 256 pitch angles. This corresponds to 190 million data points, which we call the full dataset, DS1, in **Table 1**. This original set is too large for the herein regression in dimension 3 (i.e., L, E, α) or 5 (i.e., t, geomagnetic index, L, E, α) and the first task is a strategy to reduce the amount of data.

In this article, we first restrain the dataset by choosing values of L at a few discrete points L = 2, 3, 4 and 5, which gives around 18 million data. Five L-shells are enough to be representative of the general behavior of the diffusion coefficients, i.e., the spread of the cyclotron component over pitch angle, in order to first focus on the reduction in (E, α) at fixed L. This dataset is called DS2; see **Table 1**. The reduction method in (E, α) is then directly extended to a finer grid in L in the case of the 32 storms global model (cf. **Section 2.1.4**).

2.1.3 Dataset for the Storm of March 2013

The dynamics of the electron radiation belts during the month of March 2013 have been subject to much attention (e.g., [3,11,12,16,62,63]). The storm of March 1, 2013, is associated with a high-speed solar wind stream that created strong erosion of the plasmasphere and resulted in outer belt flux dropout events. The storm was followed by enhancements of relativistic electrons in the slot region and outer belt during the 3 days. An extended period of quiet solar wind conditions persisted then for the 11 next days, with the plasmasphere expanding outward to $L \sim 5.5$. For this event, Ripoll et al. [11] showed the electron depletion in both the slot region and the outer belt was caused by pitch angle scattering from whistler mode hiss waves. Ripoll et al. [16] extended the demonstration to a global analysis of the 3D (L, E, α) structure of the radiation belts during the quiet times from March 4–15 and compared the output of event-driven Fokker-Planck simulations to pitch angle-resolved Van Allen Probes flux observations with good agreement.

In this section, we focus on the specific storm of March 1, 2013, and we use the event-driven diffusion coefficients database that was generated for the studies of Ripoll et al. [16]. Specific parameters of the diffusion coefficients are given there and not recalled here. These coefficients use the local wave and data parameters and as such can contain the noise and the variability of the measurements. But since the expression of the diffusion coefficients is made of the combination of

TABLE 1 | List and properties of the various datasets in use.

Name	# Of storm	Time	L	E	α	# Data	Comment
DS1	32	9	43	60	256	1.90E8	Raw data
DS2_L	1		37	5	60	1E4	Storm of March 2013, from DS1
DS2	32	9	4	60	256	1.8E7	Filtered in L, from DS1
DS3_M13	1		4	60	256	6.1E4	Storm of March 2013, from DS2
DS3_AVG	avg	9	4	60	256	2.3E6	Averaged (from DS2) global data

TABLE 2 | The datasets used for training (2 first rows) and testing (3 last rows). Test data are obtained by subtracting the training and validation datasets from the data, and all points that are outside the bounds of these training and validation datasets, so as to avoid extrapolation in the test.

Name	Obtained from	How	# Data	Comment
TRAIN_M13	DS3_M13	84 chosen α $8 \leq \alpha \leq 89$	20,160	all models trained
TRAIN_AVG	DS3_AVG	shuffled sampling	230,000	DNN trained (only)
TEST_M13_L	DS2_L	shuffled sampling subtraction of TRAIN_M13	5,000	High resolution in L
TEST_M13	DS3_M13	by subtracting TRAIN_M13	40,000	Test (L, E, α)
TEST_AVG	DS3_AVG	shuffled sampling subtraction of TRAIN_AVG	230,000	Test (K_p, t, L, E, α)

tractable mathematical expressions, with some oscillating Bessel functions, and a series of summation (over the harmonics) and integration (over both frequency and wave normal angle) (e.g., Albert [48]), the database ends up being quite smooth and not too noisy. This will be a key property of the data for choosing or developing an adapted machine learning method. In addition, the diffusion coefficients are also time-averaged from March 1 to March 5 in order to provide a single diffusion coefficient defined for L-shell L, energy E, and pitch angle α. This time-averaging made over 5 days (representing 15 temporal bins of 8-h averaged together) produces smoothed data, i.e., a regularized dataset, which may otherwise be more variable over time and less smooth (e.g., **Figure 5** in Ripoll et al. [12]). As we average, we mix different geomagnetic conditions and create a mean diffusion coefficient for that 5-days event. The time-averaging is only done in this section and will not be done in the HSS section in which we will keep time as another variable. Absence of noise and regularized data make our problem specific. On the contrary, in general, data have uncertainties coming either from our partial knowledge of the variables, or from data variability. In our case, we can have experimental and simulation uncertainties. In such cases, machine learning models have to avoid over-fitting, by not being too close to the data during training. In this article, regularization of data was such that over-fitting was not an issue.

For this storm, we use 4 positions, 60 energies, 256 pitch-angles, i.e., 61440 data points for (L, E, α, $D_{\alpha\alpha}$) listed as DS3_M13 in **Table 1**. We extract a subset of DS3_M13 that is composed of 84 pitch angles and 60 energies bins, thus 20,160 data points, listed as TRAIN_M13 in **Table 2**. This dataset is used for training and calibrating the internal parameters of the various machine learning models using cross-validation.

To evaluate the ability of the machine learning models that we trained on the TRAIN_M13 dataset, to generalize on new data, we consider 2 test datasets; see **Table 2**. The first dataset TEST_M13_L contains more values in the L input. The model was trained with 4 L-values (L = 2, 3, 4, 5), and here we have 37 values from L = 2 to L = 5: thus we test the interpolation between the discretization used during the training in the case of a very low resolution. The other test dataset (TEST_M13) has full resolution in angles and energies, but the same resolution in L. The test datasets have no intersection with the training dataset. We have also excluded all extrapolation points (with an exception for K_p in **Section 3.2.3**), signifying that we bound the test datasets with the bounds of the corresponding training datasets, when evaluating errors.

2.1.4 Dataset for the 32 HSS Storms

In this section, we extend massively the previous problem from 1 storm to 32 storms. We choose storms all among the same family of storms called high-speed streams (HSS) so that we can compare them together, characterize the differences, and compute relevant statistics. By doing so, we try to optimize our chances to address similar physical processes and their spatio-temporal timescales. These 32 HSS were each identified in Turner et al. [43] between September 2012 and December 2016 (listed in **Table 3**). Each storm is observed at various MLT positions, changing with the Probes orbit. When Van Allen Probe B is at its apogee, the corresponding MLT is reported in the right column of **Table 3**. This MLT corresponds roughly to the most observed MLTs from L above ~ 4 up to L ~ 6. The 32 storms are such that we have 10 events observed from the night side (MLT = 21–3), 11 from the dusk side (MLT = 15–21), 4 from the day side (MLT = 9–15), and 7 from the dawn side (MLT = 3–9). Some of the differences we found may be attributed to MLT variations, though keep in mind that the statistical MLT-rescaling of the wave power makes the coefficients valid and comparable over all MLTs.

TABLE 3 | From left to right: number, Date and time, minimum Sym-H index (i.e., high resolution Dst index) and MLT of the apogee of probe B of the Van Allen Probes for each of the 32 high speed streams between September 2012 and December 2016 of this study (reported from the selection of the HSS events of Turner et al. [2019]).

Event #	Minimum date/Time	Min. SYM-H	MLT
1	2013–01-26/22:19:00.000	–6.2e+01	2.9
2	2013–04-24/18:11:00.000	–5.2e+01	23.1
3	2013–08-05/02:20:00.000	–5.6e+01	15.5
4	2013–08-16/04:29:00.000	–5.4e+01	15.1
5	2013–08-27/21:43:00.000	–6.4e+01	18.8
6	2013–10-15/03:18:00.000	–5.2e+01	17.2
7	2013–12-08/08:30:00.000	–7.2e+01	15.2
8	2014–02-23/22:48:00.000	–6.3e+01	12
9	2014–08-27/18:18:00.000	–9.0e+01	5.5
10	2014–10-14/18:38:00.000	–5.2e+01	3.7
11	2014–10-20/17:10:00.000	–5.7e+01	3.5
12	2014–11-16/07:24:00.000	–5.1e+01	2.5
13	2015–02-17/23:55:00.000	–7.0e+01	23.3
14	2015–02-24/03:36:00.000	–7.6e+01	23
15	2015–04-16/23:29:00.000	–8.8e+01	21.1
16	2015–05-13/06:59:00.000	–9.8e+01	20
17	2015–05-19/02:55:00.000	–6.4e+01	19.7
18	2015–06-08/07:45:00.000	–1.05e+02	18.9
19	2015–07-05/04:52:00.000	–5.8e+01	17.8
20	2015–07-23/07:28:00.000	–8.3e+01	17.1
21	2015–08-23/08:34:00.000	–6.2e+01	15.8
22	2015–10-04/07:33:00.000	–5.2e+01	14.3
23	2015–12-14/19:04:00.000	–6.0e+01	12
24	2016–02-18/00:28:00.000	–6.0e+01	9.5
25	2016–03-16/23:41:00.000	–6.9e+01	8.4
26	2016–04-13/01:09:00.000	–7.0e+01	7.3
27	2016–05-08/08:15:00.000	–1.05e+02	6.3
28	2016–06-06/06:47:00.000	–5.5e+01	5.3
29	2016–08-23/21:13:00.000	–8.3e+01	2.8
30	2016–10-25/22:57:00.000	–8.1e+01	0.4
31	2016–10-29/07:25:00.000	–7.8e+01	0.3
32	2016–11-25/06:38:00.000	–5.3e+01	23.2

For each observed storm, we extract wave and plasma data from the Van Allen Probes during 3 days, every 8 h, which gives 9 intervals of 8 h. The timescale of 3 days is representative of the HSS main and recovery phases seen in Turner et al. [43]. The measurements are used as inputs in the simulations of the quasi-linear pitch-angle diffusion coefficients Ripoll et al. [16] outputted at this rate, producing the full database DS1.

For each storm and for a given time bin, we have a discretized grid (L, E, α) of the diffusion coefficient. For each temporal bin, we store the K_p index (itself averaged over the 8 h bin duration). The Kp-index is the global geomagnetic activity index that is based on 3-h measurements from ground-based magnetometers around the world. The Kp-index ranges from 0 (very little geomagnetic activity) to 9 (extreme geomagnetic storms). The Kp index is largely used in the radiation belt models as a main parameter of wave models driving radiation belt simulations (e.g., Cervantes et al. [61]; Sicard-Piet et al. [18]; Wang et al. [41]). Here, it works as a measure of the storm strength at a given time. We define averages per K_p index and regroup the diffusion coefficients per K_p. The K_p index then becomes the 5th variable, which was first meant to replace the time variable, as any K_p average model, but we will explain later that time was nevertheless kept. As such, we have 18 million data points in (t, K_p, L, E, α, $D_{\alpha\alpha}$), which gives data set DS2.

We build a first set of averaged diffusion coefficients by considering all the 32 storms, each defined at 9 temporal bins, which now define 9 epoch times. For a given temporal bin $j = 1..9$, for a given $K_p = 0, \ldots 6$, we average $D_{\alpha\alpha}(L, E, \alpha)$ over all the storms. We obtained this way 2,300 000 data points, listed as DS3_AVG in **Table 1**. The model is defined for (t, K_p, L, E, α). Averages are made at fixed K_p for each t_j. (If we were averaging without binning by the K_p index, we would produce a superposed epoch model of diffusion coefficients.) Here, the approach produces a superposed epoch model of the diffusion coefficient, further binned by K_p. Such an approach allows the diffusion coefficients to evolve in time, keeping within its origins ambient properties that are consistent with each other, always keeping the coupling between the electron plasma density and all wave properties. This approach is different from making a superposed epoch model of the wave properties of HSS and computing afterwards a single diffusion coefficient from them. The latter approach has low numerical cost but neglects correlations between all the properties of the ambient domain and, therefore, introduces some error (e.g., Ripoll et al. [17]). From a machine learning perspective, the Kp averaging helps produce smoothed data, acting as a regularization of the solution that makes the solution less fluctuating, i.e., less noisy from a ML-perspective, similarly to the temporally-averaged data of the March 2013 storm (as discussed in **section 2.1.3**). From DS3_AVG, we train on 10% of the data, listed as TRAIN_AVG in **Table 2**. All datasets are described in **Table 1**, training and validation datasets in **Table 2** (2 first rows), and test datasets in **Table 2** (3 last rows).

2.2 Machine Learning Methods

In this section we briefly describe the several statistical and machine learning methods that we used to build the various models of this study. We considered methods based on local evaluation (k-nearest neighbors and kernel regression), tree-based methods (regression tree, bagging and random forest), neural networks, and function approximations (Radial basis and splines). All are nonparametric so that we make no assumption about the distribution of the data. A detailed description of all these machine learning methods can be found in Hastie et al. [64], and complementary information about neural networks can be found in Géron [65]and Goodfellow et al. [66].

2.2.1 *K*-Nearest Neighbors

A key idea in many supervised machine learning methods is to think that the targets associated to nearby inputs should be close to each other. Based on this idea, to predict the target of any new input data points, it is reasonable to look at the target values of their surrounding neighbors. This is the whole framework of k-nearest neighbors machine learning method which predicts the target of new input data by averaging the target values of its k-nearest neighbors, measured using the Euclidean distance (see, for example, Fix and Hodges [67]; Altman [68] and Hastie et al. [64]). The number of nearest neighbors k is the key parameter and it is very crucial to tune it using cross-validation technique

described in the following. On one hand, if k is too large, a large number of observations, among which not very representative ones, contribute to the prediction, resulting in too rough predictions. On the other hand, if k is too small, the prediction is made relying only on a small number of neighbors of the query point, resulting in high variance.

2.2.2 Kernel Regression

The k-nearest neighbors procedure may be modified to obtain a smoother method, which gives more weight to the closest points and less to the furthest: instead of specifying a number of neighbors, the neighborhood is defined according to a distance notion, via a kernel function, that is a function K: $\mathbf{R}^d \to \mathbf{R}_+$, such that $K(x) = L(\|x\|)$, where $x \mapsto L(x)$ is nonincreasing. More specifically, a prediction $\hat{y}$ of a new data point x is obtained by setting:

$$\hat{y} = \frac{\sum_{i=1}^{n} K_h(X_i - x) Y_i}{\sum_{i=1}^{n} K_h(X_i - x)},$$

where the kernel K_h is defined by $K_h(x) = K(x/h)$, with h the bandwidth of the kernel, and (X_i, Y_i), $i = 1, 2, \ldots, n$, denotes the input-output training data. Here, a Gaussian kernel has been considered:

$$K(x) = \exp\left(-\|x\|^2/\sigma^2\right),$$

for some $\sigma > 0$. For more about the method see, for example, Nadaraya [69] and Watson [70].

2.2.3 Regression Tree

Another nonparametric model commonly used in regression problems is regression tree. It is an iterative partitioning algorithm aiming at each step to split the input space along the value of a chosen predictor and threshold, minimizing the target variance on both parts of the split (see Breiman et al. [71]). Growing a tree is equivalent to partitioning the input space into smaller and smaller regions containing lesser and lesser points. The prediction of a new data point is the average target values of the points falling into the same region as the query point. Growing a single deep depth tree on the training data (small terminal nodes or small region) will most likely lead to overfitting. Moreover, a deep depth tree can be very sensitive (high variance) meaning that a small change in splitting the training data can result in a very different structure of the tree. It is then important to tune the depth of the tree, which is the key parameter. This may be done using cross validation technique.

2.2.4 Bagging

The aim of this method is to reduce the variance of regression trees by introducing bootstrap samples from the training data. A regression tree is grown on each bootstrap sample, and the final prediction is the average of the predictions of all the trees (see Breiman [72]). This method is shown to be significantly more accurate in generalization capability. The parameters of the method are the number and the depth of the trees to be constructed on the bootstrap samples.

2.2.5 Random Forest

As each tree in Bagging method is constructed using a bootstrap sample of the training data, the constructed trees are likely to be quite correlated. Random forests have been proposed to enhance reduction of the variance. They aim at producing uncorrelated trees by randomly selecting only a subset of features at each split in the process of growing the trees. In regression problems, the size of the set of features to be randomly selected at each split is usually taken around $\sqrt{p}$, where p is the total number of features (see, for instance, Ho [73] and Breiman [74]). In addition to the number of selected features, the parameters of the method are the depth and the number of trees.

2.2.6 Neural Networks (DNN)

We use feed-forward neural networks as a regression model. A neuron is the composition of a nonlinear function (here we use $Relu(x) = \max(0, x)$) and a linear function. All inputs enter the $N1$ neurons of the first layer. Then each neuron gives an output, and each output connects to the $N2$ neurons of the second layer. We do the same for all the layers (the number of such layers is the depth of the network), and we end with a layer of one neuron (because we have one output, the pitch-angle diffusion coefficient), which has no nonlinear function. It has been shown [75] that any reasonable function may be approximated by one layer of neurons, but the practice has shown that it is better to go deep, which means to use a lot of layers (which entails a lot of composition of nonlinear functions, that is to say a lot of interactions between the inputs).

The coefficients of the linear functions of all the neurons are tuned by an optimization algorithm. This phase is called the training. We use a variant of the stochastic gradient descent method (the Adam optimizer) to minimize the mean square error between data and predictions.

Neural networks are accurate for regression problems and extend well to a huge dataset or to high dimension problems. One difficulty is that such a model involves a lot of hyperparameters, and many combinations of these hyperparameters may give low accuracy results. For example, we have to choose the architecture (number of layers and neurons per layer), the initialization of the linear coefficients, the optimization algorithm, the number of epochs (iterations of the algorithm) and batches (splitting of the data to calculate gradients in the stochastic gradient descent). In order to optimize these choices, an original specificity of our DNN model is to use a data-driven method for selecting all these hyperparameters [76,77]. It uses random forest methods (which has a few hyperparameters, see **Section 2.2.5**) and a mapping between the obtained trees and the architecture of an ensemble of neural networks. We obtain this way accurate neural networks with only 2 hyperparameters, the depth and the number of trees. When we obtain this accurate network, we may search for higher accuracy by playing with other hyperparameters that were fixed in the first step.

2.2.7 Thin Plate Spline

Thin plate splines, introduced by [78], may be seen as an extension of cubic smoothing splines to the multivariate case [79]. In the one-dimensional case, cubic smoothing splines are used to construct new points within the boundaries of a set of

observations. They are fitted using a penalized least squares criterion, with the penalty based on the second derivative. The interpolation function consists of several piecewise cubic polynomials. Fitting low-degree polynomials to small subsets of values instead of fitting a single high-degree polynomial to all data allows us to avoid the Runge phenomenon, that is, oscillation between points occurring with high-degree polynomials. Cubic smoothing splines are widely used since they are easy to implement and the resulting curve seems very smooth. More specifically, if we observe data $(X_1, Y_1), \ldots, (X_n, Y_n)$, the quantity to be minimized is defined by

$$\|\mathbf{Y} - \mathbf{f}\|^2 + \lambda \int \left(f''(t)\right)^2 dt,$$

where $\mathbf{Y}$ is the vector of observed outputs $Y_1, \ldots, Y_n$ and $\mathbf{f} = (f(X_1), \ldots, f(X_n))$. In the general case, the main part of the criterion remains the same, but the shape of the penalty is far more involved, based on several partial derivatives. Thin plate splines are given as functions $\mathbf{f}$ minimizing

$$\|\mathbf{Y} - \mathbf{f}\|^2 + \lambda \text{pen}(\mathbf{f}),$$

where

$$\text{pen}(\mathbf{f}) = \int_{\mathbf{R}^d} \sum_{\nu_1 + \cdots + \nu_d = m} \frac{m!}{\nu_1! \ldots \nu_d!} \left(\frac{\partial^m \mathbf{f}}{\partial u_1^{\nu_1} \ldots \partial u_d^{\nu_d}} \right)^2 du,$$

and the factor λ drives the weight on the penalty. Here, m is such that $2m - d > 0$, and the ν_i's are nonnegative integers such that $\sum_{i=1}^{d} \nu_i = m$.

2.2.8 Radial Basis Function Interpolation

A Radial Basis Function (RBF) is a function that depends only on the distance between the input and a predetermined fixed point, called a node. We can use RBF as a basis for an interpolator in the form:

$$f(x) = \sum_{i=1}^{N} h_i \phi_i(x), \tag{1}$$

where N is the number of nodes, h_i are unknown coefficients, and $\phi_i(x) = \|x - x_i\|$, with x_i the coordinates of the ith node. Here, we use all the points in the training set as nodes. The training consists in finding the values of the coefficients h_i by imposing that the interpolant passes exactly through the targets in the training set, that is $f(x_i) = Y(x_i)$. This amounts to solve the linear system $\mathbf{X}\vec{h} = \vec{Y}$ for the vector $\vec{h} = (h_1, \ldots, h_N)^T$, where $\mathbf{X}$ is the $N \times N$ symmetric matrix containing all the distances between nodes. Once we have the coefficients h_i, the targets in new data points can be evaluated directly by using the interpolator in Eq. 1. Even though the RBF could be generalized by introducing hyper-parameters (called in this context shape parameters), for instance defining $\phi_i(x) = \|x - x_i\| + c_i$, in this work we have not investigated more general choices of RBF and used only the form in 1.

2.2.9 Cross-Validation

Each method depends on some key smoothness parameters (usually called hyperparameters) that need to be tuned properly to get a good performance. This is done via cross-validation. K-fold cross-validation consists of breaking down the training data into K folds $\{F_k: k = 1, 2, \ldots, K\}$, and for a given candidate parameter, the corresponding model is constructed using as training set the $K - 1$ folds where the remaining fold is treated as a validation dataset. Thus, for a given value of parameter β, the corresponding model f is trained K times (K different combination of $K - 1$ folds choosing from the total K folds). We then measure the performance of f at the choice of parameter β using the cross-validation error defined by

$$\text{CVE}(\beta) = \frac{1}{K} \sum_{k=1}^{K} \sum_{x_i \in F_k} \left(f(x_i) - y_i\right)^2$$

In the particular case where each data subset only contains one single observation, the method is called leave-one-out cross validation.

Roughly speaking, this provides the average performance of f associated with the parameter β on K different unseen folds of the training data. The parameter $\hat{\beta}$ minimizing this cross-validation error would be a suitable one to be used as a global parameter in predicting the real testing dataset.

For k-nearest neighbors, kernel regression, regression tree, bagging, and random forest, a 10-fold cross validation was used. For thin plate splines, the penalty coefficient is estimated through generalized cross validation, which may be regarded as an approximation to leave-one-out. For the neural networks, the training data set was randomly cut in 3 parts: 80% for the training, 10% for checking over-fitting during the training, and 10% for selecting the final network. After that hyperparameters selection, all results presented in this article are obtained on a huge separated test dataset, as showed in **Table 2**.

2.2.10 Complexity of the Training and Computational Time

Training phases are very different between all methods: for KNN there is only a search over the existing space of data. In tree-based methods the training corresponds to the construction of the trees. In DNN the training corresponds to the search for the weighting factors in the interconnections. All training phases agreed in the choice of the hyperparameters: as data have no uncertainties, and are somehow regularized, our methods have to fit to the training data. This means for tree-based methods to grow deep trees (one point in the final node), to be very localized for the k-nearest neighbors method ($K = 2$) and kernel regression, and to go deep with neural networks, with many epochs. Ensemble methods do not need to be pushed too far: for tree-based methods, we used 100 trees, and for neural networks, we averaged the outputs of around 5 networks. Moreover, thin plate splines are specifically dedicated to interpolation.

Even if the methods depend on the choice of hyperparameters, we can still say that the cpu-cost of training is about a minute for both regression tree and k-nearest neighbours, about 10 min for bagging and random forests, and 2 h for neural networks, with each method using around 20,000 data. Predictions are fast for all methods, meaning they take a few seconds maximum for 60,000 data.

TABLE 4 | Performances of all the methods trained on TRAIN_M13 and tested on TEST_M13. We consider the absolute error $|e_i|$ and report the mean error, standard deviation, first quartile, median error, third quartile, and maximal error.

	Mean	Std	Q_1	Med	Q_3	Max
Tree	0.014	0.026	0.001	0.005	0.014	0.620
Bag	0.012	0.025	0.001	0.004	0.012	0.483
RF	0.012	0.025	0.001	0.004	0.012	0.448
KNN	0.010	0.017	0.002	0.006	0.011	0.420
KerReg	0.005	0.014	0.000	0.001	0.003	0.466
RBF	0.002	0.009	0.000	0.000	0.001	0.349
Spline	0.002	0.009	0.000	0.000	0.001	0.394
DNN	0.003	0.008	0.001	0.002	0.003	0.302

3 RESULTS

3.1 Results for the Storm of March 2013

The numerical results reported in the following tables and figures present an analysis of the distribution of the errors: $e_i = y_i - \hat{y}_i$, for $i = 1, 2, \ldots, n$, for the different investigated methods, where $y_i = \log(D_{\alpha\alpha})$, $\hat{y}_i$ is the prediction of the considered model, and n is the size of the considered test dataset. We train our models on the TRAIN_M13 data set, containing 20,160 samples.

The TEST_M13 test data set is detailed in pitch-angles and energies but contains only 4 discrete L-shells values ($L = 2, 3, 4, 5$). The TEST_M13_L data set is however detailed in L and contains L-shell values regularly spaced from $L = 1.6$ to $L = 5.2$ by 0.1 step (37 values) and a few angles and energies values. These datasets are sampled on a grid and there is no uncertainty on the points. Hence, as already mentioned, all models are trained until reaching a small error value on the training data set. We first start by addressing the error with respect to the (E,α) resolved grids and then on the grid resolved in L-shell.

3.1.1 Variation With (E, α)

Results in **Table 4** show that the Spline, the RBF, and the DNN models outperform with the lowest mean and maximal absolute error. We also observe that the Spline and the RBF have very low medians which show that they are very good on many samples,

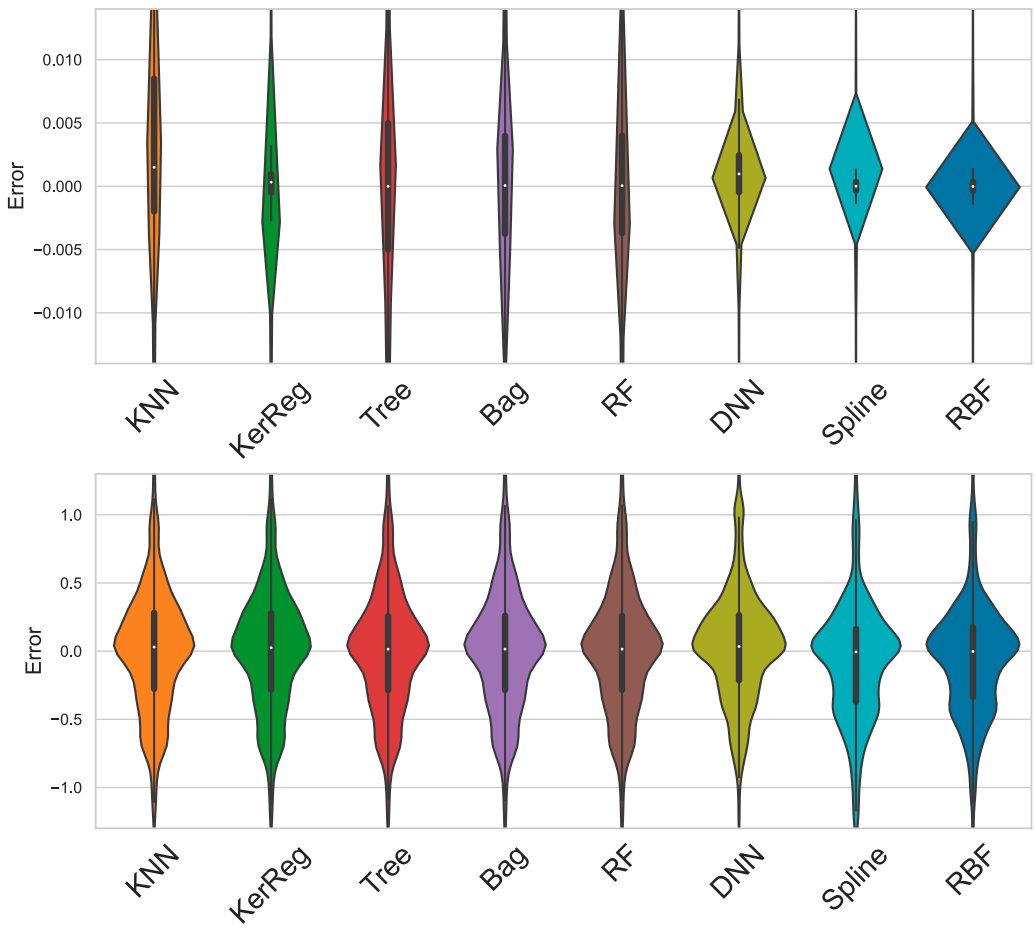


FIGURE 1 | Violinplots of error $e_i = y_i - \hat{y}_i$ evaluated on (top) TEST_M13 and (bottom) TEST_M13_L of all the methods, trained on TRAIN_M13. For each ML-method, the outside envelop is the smoothed distribution of error, symmetric for visualization consideration, with a box-whiskers plot inside (median with a white circle, 1st and 3rd quartiles are represented by the border of the box).

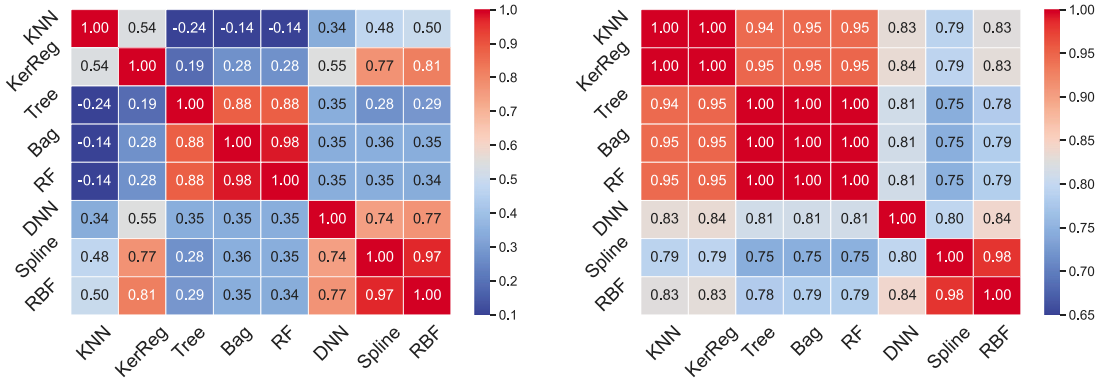


FIGURE 2 | Correlations of error $e_i = y_i - \hat{y}_i$ evaluated on (left) TEST_M13 and (right) TEST_M13_L for all methods, trained on TRAIN_M13.

TABLE 5 | Performances of all the methods trained on TRAIN_M13 and tested on TEST_M13_L. We consider the absolute error $|e_i|$ and report the mean error, standard deviation, first quartile, median error, third quartile, and maximal error.

	Mean	Std	Q_1	Med	Q_3	Max
Tree	0.371	0.419	0.102	0.265	0.521	4.451
Bag	0.372	0.418	0.102	0.269	0.524	4.448
RF	0.372	0.418	0.102	0.267	0.525	4.459
KNN	0.364	0.378	0.108	0.279	0.520	4.374
KerReg	0.363	0.379	0.111	0.280	0.512	4.350
Spline	0.339	0.320	0.099	0.255	0.462	2.332
RBF	0.316	0.297	0.100	0.234	0.440	2.587
DNN	0.315	0.306	0.100	0.237	0.439	3.063

but have also many outliers, with big error. The DNN shows a median error close to the mean.

The violin plots in the top panel of **Figure 1** complement well **Table 4** in showing that the underlying statistical distributions of the errors differ from one method to the other. DNN, Splines, and RBF have the most concentrated distributions at low errors, especially both the Splines and RBF methods, with spline with a mode around the mean and RBF with a mode around the median. As seen on **Table 4** with the maximal error, this hides more outliers with Splines and RBF than with DNN.

These results start to exhibit two main families of methods: on one hand the Tree family (Tree, Bag, RF) with KNN and KerReg, and on the other the RBF, spline, and DNN methods.

In order to get insights on the differences and similarities between the machine learning models, we now compute the correlation between the errors provided by a couple of different models. The correlation errors are given in **Figure 2** for TEST_M13, on the left. First, **Figure 2** confirms the 3 methods (Tree, Bag, RF) fall into the same family, with high correlation (> 0.8). We will see in the next section that KNN and KerReg will join this same family, but this is not obvious from the correlation errors of the left part of **Figure 2**. On the contrary, we see the specificity of the DNN method which errors do not correlate with any of the other methods. The closest methods to DNN are the spline and RBF methods. Similarly, the spline and RBF methods correlate less with the forest tree method family.

Finally, this study was also conducted at low resolution with 13 energies and 14 pitch angle resolution, representing 728 data points (results not shown). Although some small changes of behavior either within or among the methods were visible, the conclusions were similar, for an admissible accuracy of the diffusion coefficients. Machine learning methods can thus be used to find an optimum between accuracy and resolution, reducing this way the high original cost of computation of the diffusion coefficients.

3.1.2 Variation With L-Shell

In this section, we consider each method for its ability to capture the L-shell dependence. It should be noticed that all methods have been trained on a very crude L-shell resolution, containing 5 L-shells only, and that they are now tested against data fully resolved in L-shell. This test is therefore very challenging and only made to gain insight on the properties of the ML methods. If a full model in (L, E, α) had to be generated (cf. **Section 3.2**), the approach would be to train on a higher L-shell resolution and not to interpolate a low resolution grid.

Table 5 presents the main error global metrics, with errors much higher than in the previous section due to the initially low L-shell resolution. The mean error gradually decays from the Forest tree family to DNN (from top to bottom). However, the median error remains more similar, still decaying from top to bottom. Best performances are always obtained from either the Spline, the RBF, or the DNN method.

Violin plots of the distributions of errors have been generated (on the bottom of **Figure 1**). All the distributions are found very alike in their global shape, with only subtle differences. Some methods show two or even three modes which appear as peculiar oscillations on the edge of the distribution.

Figure 2 (on the right) shows the error correlation among the couples of models for the test with respect to L-shell. The main families previously mentioned remain, this time with KNN and KerReg performing similarly to the Forrest tree family. Based on these results and the one of the previous section, all 5 models (Tree, Bag, RF, KNN, KerReg) are regrouped into the same family.

We finalize this series of tests by **Figure 3**, in which we compare the forest tree family (represented by the RF

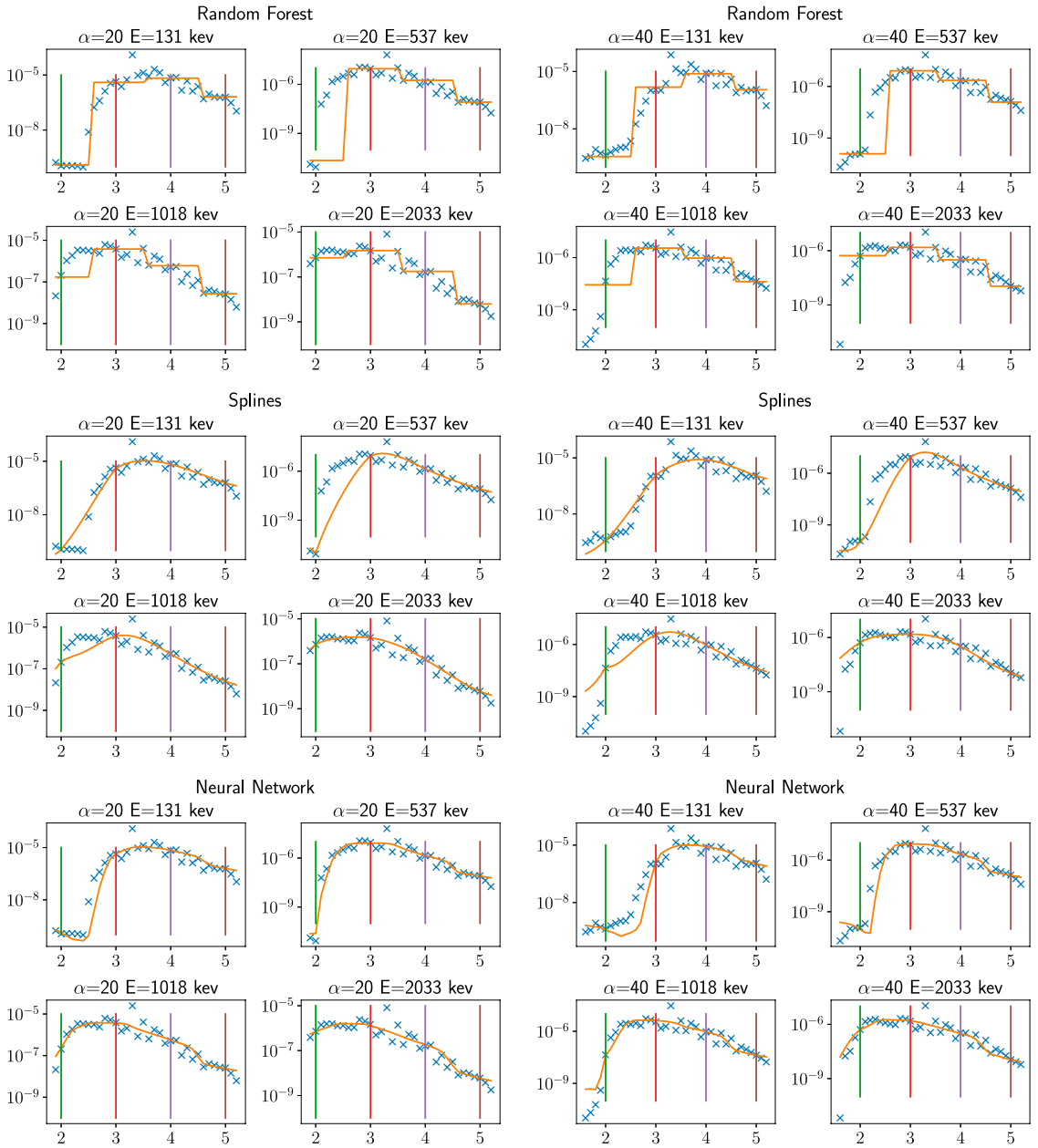


FIGURE 3 | Machine learning pitch angle diffusion coefficients ($D_{\alpha\alpha}(L)$ in s^{-1} on the *Y*-axis) for the March 2013 storm plotted in orange color versus L-shell (*X*-axis) for various pitch-angles (20° and 40°) and energies (131, 537, 1,018, 2,033 Kev) computed from (top) random forest, (center) thin plate spline, (bottom) neural network. The blue dots are the reference original diffusion coefficients (points of TEST_M13_L which were not used in the training and testing phase). Vertical lines represent the location of the training data of TRAIN_M13 ($L = 2, 3, 4, 5$). These plots were made with methods that were trained on a subset of TRAIN_M13: we used fewer points in energy and pitch-angles.

method), the spline method, and the DNN method for a few selected (E, α) but resolved in L-shell. The training phase being done at $L = 2, 3, 4, 5$ (indicated by vertical bars), we see all models provide an exact answer at these points. Everything in between these points is modeled (orange line plots) and compared with the exact solution (blue crosses). The random forest model plotted in **Figure 3** (left) uses constant approximation around the training points so that the approximation is made by step functions and is extremely crude. It is the same for tree-based methods, *k*-nearest neighbor, and kernel regression (not shown). The spline method does much better in **Figure 3** (center), but cannot approximate brutal variations, as for radial basis model (not shown). The DNN method in **Figure 3** (right) seems to us the most capable for this difficult exercise, which confirms the global metrics of **Table 5**.

We conclude that without any prior assumption on a physical phenomenon and on the database, it is difficult to advise the use

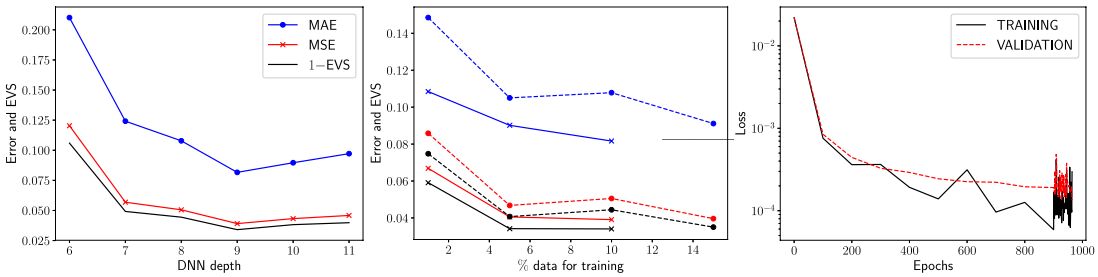


FIGURE 4 | Errors calculated on the dataset *TEST_AVG* are plotted for different DNN models, with various depth on the left, and various sizes of training dataset on the middle. On the left, models are trained on 10% of the data, meaning around 230,000 data. On the middle, dot lines with circles are for a model of depth 8, and continuous lines with crosses for a model of depth 9. In blue, we plot the Mean Average Error, in red the Mean Square Error, and in black one minus the Explained Variance Score. On the right, the loss function (MSE) is plotted during the training, evaluated on the training dataset, and on the validation dataset. We see at the end that we make more often evaluations of these errors, and the training stops selecting the more accurate model in the last epochs. Note that this loss may not be compared with anything in this article, as it is given on scaled data.

of a particular machine learning model. One main reason is the data used to train the model have a big influence on the model performance, which makes it hard to generalize the capabilities of a given model. Here, we believe the different series of tests and comparisons are explicit enough to conclude that the DNN method is a good candidate to perform the rest of the study and to generate a more global model.

3.2 Results for the Global Model of Pitch Angle Diffusion During HSS Storms

In this section, we use the data from 32 storms in order to build a database of statistical event-driven diffusion coefficients that is embedded within a machine learning model for facilitating its use. The method relies on constructing first an averaged model and then using the deep neural network (DNN) previously selected to learn and output the solution of the averaged model. As in the previous sections, we will see the machine learning model does not entail any issue to interpolate and reproduce the averaged model. Questions arise more about the physical choices we make to build the averaged model (cf. discussion below and in **Section 4.1**). Interestingly, the machine learning model was of great help for the various investigations we conducted. As the training step was quite fast (based on the knowledge acquired during the March 2013 storm study), we could test different ways of manipulating and averaging the data when iterating to choose how to best parametrize the statistical model. Another strength of the machine learning approach is the simplicity of performing comparisons with the model since it delivers continuous maps of the solution with a simple numerical subroutine able to output a 5 to 6 dimensions solution. On the contrary, manipulating directly the database and using discrete points is very constraining. It can also be source of direct errors or interpretation errors when it is a given plotting software (e.g., Python subroutines) that carries intrinsic ad-hoc interpolation with integrated smoothing procedures.

3.2.1 Training the DNN Global Model

The data used to generate the global model is DS3_AVG described in **Section 2.1.4** with 2.3*e*6 data points. We then use TRAIN_AVG (2.3*e*5 data points), unless specified differently for training and validation, and TEST_AVG (2.3*e*5 data points) for test.

The training of the global model $D_{\alpha\alpha}(K_p, t, L, E, \alpha)$ was not harder than the model previously trained for the storm of March 2013 in **Section 3.1**. The two more dimensions of the input space entailed a larger neural network. The bigger amount of data (from 20,000 to 230,000) caused a longer training. Generating the whole model took a few hours of computation on a standard computer. For comparison the simple generation of a mean model, without machine learning and performing only means throughout the whole database, took a few days on the same computer. Again for comparison, computing 19.3M diffusion coefficients for around 10-days event takes around 15,600 h spread over 1,300 processors on a CEA massively parallel supercomputer [17]. This brings another advantage of machine learning methods to be able to manipulate simply and at low cost a large database, with the possibility to operate on them basic statistical operations useful for the understanding of the database.

In **Figure 4** (left), we represent the mean average error (MAE), the mean square error (MSE), and one minus the explained variance score (EVS) computed when the model is evaluated against the TEST_AVG test dataset (230,000 data not used during the training phase performed with the TRAIN_AVG dataset). Because the dataset contains little noise, we can train neural networks going deep, with depths of the network going from 6 to 11 hidden layers on the x-axis. We see an optimum of low values of the three metrics is found for a depth of 9.

The same three quantities are plotted in **Figure 4** (center) using different sizes of training dataset (from 1 to 15% of the TRAIN_AVG dataset), with DNN of depth 8 or 9. From these results, we selected the neural network of depth 9 trained with 10% of the data. As over-fitting is not an issue here, we could reach better accuracy by taking a more important capacity for the model, or just by taking more epochs as discussed next. This is not obvious on **Figure 4** as with a higher depth, error is growing (after depth 9), but it is possible to be more accurate by varying all hyper-parameters. However, we have also seen that the loss of

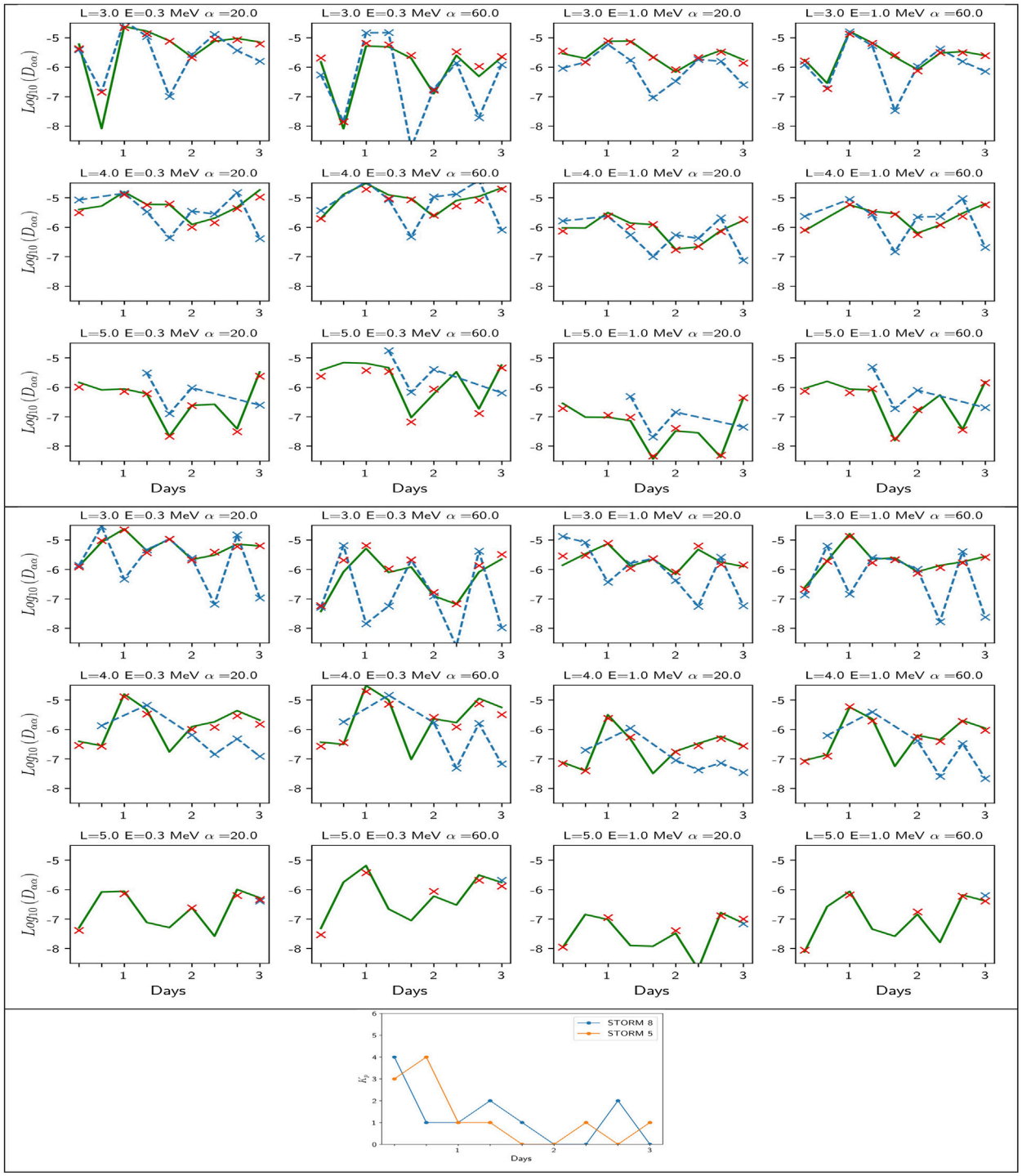


FIGURE 5 | Pitch angle diffusion coefficients for (1–3 rows) storms 8 and (4–6 rows) storm 5. The first 6 panels show historic pitch-angle diffusion coefficient's at different (L, E, α) values, with (blue crosses and lines) the raw data of event-driven coefficients (red crosses) the averaged data (on the 32 storms at given (K_p, t, L, E, α)), and (green lines) the DNN model. The average data (in red) and the DNN model (in green) (trained on a subset of the average model) are run from the Kp(t) sequence of each storm plotted at the bottom panel for each of the 9 temporal bins. The good agreement between red crosses and the green line shows the success of the DNN model at matching its target. Both capture levels and variations, but are not very accurate compared with the event-driven diffusion reference values in blue, showing the limits of a mean model.

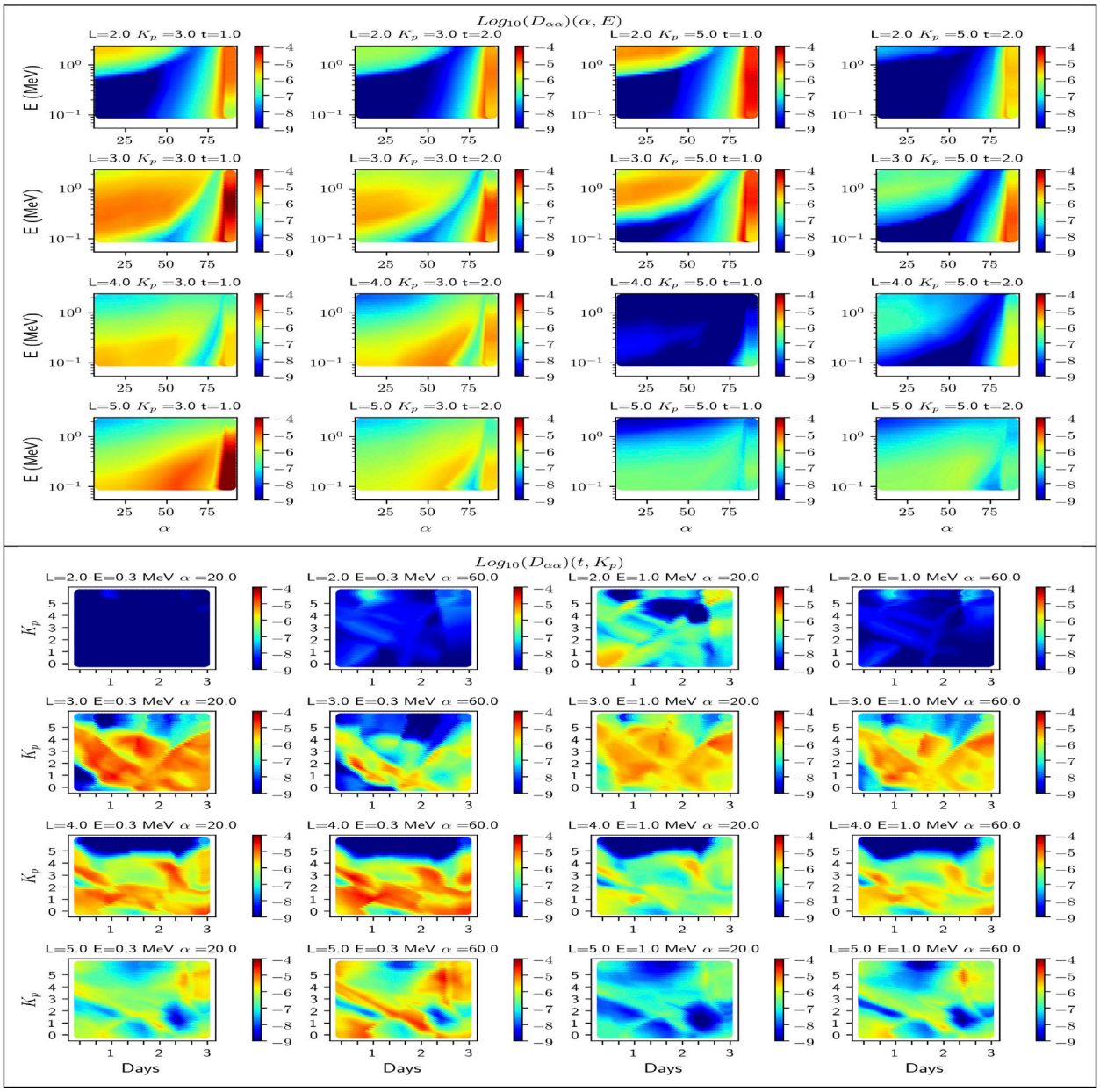


FIGURE 6 | The DNN model of ($D_{\alpha\alpha}$) (Log_{10} of s^{-1}) in the (top) (α, E) plane at fixed (L, K_p, t) and (bottom) (t, K_p) plane at fixed (L, E, α).

accuracy due to the DNN model is less the issue than the loss of accuracy caused by an averaged statistical approach (cf. discussion in **Section 3.2.2**).

Figure 4 (right) represents the loss function during the training and the validation phases of the model of depth 9 over 10% of the data. The loss function is the minimal MSE computed over all the data and evolving according to the epoch number, which represents the number of cycles the data are used in a training or validation step. After 900 epochs, we evaluate more often the loss function, because we stop at the best loss value obtained on the validation dataset.

3.2.2 Accuracy of the DNN Global Model

We present in **Figure 5** the obtained deep neural network (DNN) global model of diffusion coefficients, which is plotted in green for two of the 32 selected storms. We choose for illustration storm 8 (3 top rows) as event-driven and average diffusion coefficients agree quite well and storm 5 because the opposite occurs. We also plot in red the average model, which represents what the DNN model (in green) has to reproduce. Each storm is decomposed in 9 times with its K_p index history (as shown in the bottom panel of **Figure 5**) and the DNN model is played for the (t,K_p(t)) sequence of this storm. Results are presented at L = 3, 4, 5. We omit L = 2

for the sake of brevity since diffusion is limited to high energy (see discussion in **Section 3.2.3** and **Figure 6** top row).

As we can see for storm 8, the DNN model is very close to the average model, as it should be, as soon as the intrinsic interpolation rules of the model have been learnt well. This is confirmed for storm 5 in **Figure 5**, which ends our demonstration that the restitution of the DNN model is accurate. Figures like **Figure 5** (3 top rows) have been generated for each of the 32 HSS storms (not shown), which allows us to reach an individual view of each of them and confirm the accuracy of the DNN approach. This occurs at all L-shells used to derive the DNN model.

We now use the DNN mean model to analyze how mean coefficients behave compared with individual ones. An important physical question arising in space weather forecasting is the ability of an average model (e.g., from the DNN approach or directly from averaged data) to precisely predict the history of the diffusion during the storm. We thus compare in **Figure 5** the DNN statistical model (in green) with the event-driven diffusion coefficients (blue cross). We find the average procedure captures quite well the global variations of the pitch-angle diffusion coefficient in general for storm 8 but fails by a significant factor at various (t,L,E,α). This way we start to enlighten the difference between an event-driven approach and a mean approach thanks to the machine learning interface. We see for instance an interesting strong departure at (L = 3, E = 0.3 MeV, α =60°, t= 1.6 days) for storm 8 between both the average models (green and red) and the event driven model (blue). Readers will understand in the next section (based on **Figure 6** top, left) that α =60° falls right at the sharp edge between significant diffusion of the cyclotron harmonics and absence of diffusion for E = 0.3 MeV electrons at L = 3. Both average models capture thus (on average) significant diffusion while for storm 8 at t = 1.6 days the diffusion is negligible, causing an error by more than 2 orders of magnitude. Note that all models agree for the time before (t = 1.3) and after (t = 2.). This is likely due to the particularity of the wave conditions at t = 1.6. Conversely, Storm 5 (fourth to sixth rows of **Figure 5**) is an example of the opposite, with a storm for which the diffusion coefficient behavior (in blue) is opposite to the mean behavior (red and green). The error between the average model and the event-driven coefficient is often large, up to 2 orders of magnitude. We see the same feature as for storm 8 at L = 3, E = 0.3 MeV, α =60. Large errors at L = 2 (not shown) for 1 MeV electrons are also likely due to the average model missing the particularity of a local increase of diffusion close to a strong gradient region. At L = 5, we see the absence of the event-driven coefficients for that case, except for the point at the latest time, at t = 3 days. This can be due to the plasmasphere that has not recovered up to L = 5 during the first 2.6 days and the absence of hiss waves, to the absence of measurements for that event, or both. The average model returns low diffusion most of the time (below 10^{-6}), except for E = 0.3 MeV and α = 60.

3.2.3 Exploring the DNN Global Model

We now explore and discuss the main physical characteristics of the statistical mean model of pitch angle diffusion coefficients for HSS storms thanks to the DNN encapsulation.

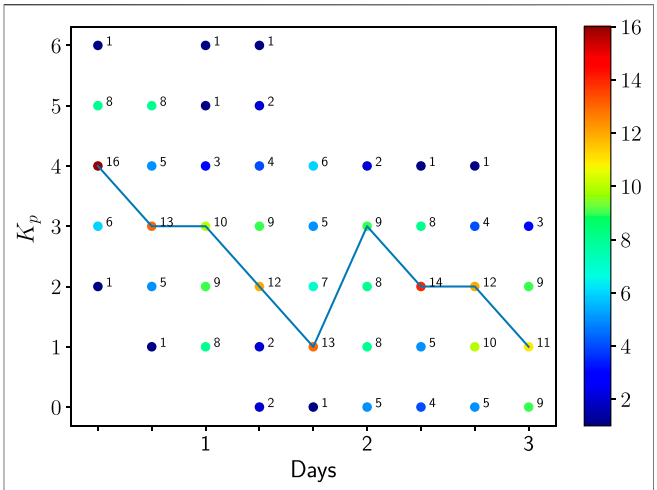


FIGURE 7 | Numbers of storms that have K_p and t values. The number of storms in each (t,Kp) bin is written and colored and represents the number of elements averaged together per (t,Kp).

At fixed (t, K_p), we see pitch angle diffusion occurs at lower energy as L increases in **Figure 6** (four top rows). At low L-shell (L < 3), we see a wide region of negligible diffusion in the (E, α) plane. This region of no interaction is due to the first cyclotron harmonic that does not reach pitch angles higher than the loss cone pitch angle [12]. The DNN model has thus to learn more very low values at low L-shell. This absence of pitch angle diffusion explains why electrons are not scattered out by hiss waves and remain trapped at low L-shell in the inner belt. With the storms compressing the plasmapause, the model allows us to see better if there is more effect at low L-shell. **Figure 6** shows diffusion is non negligible above ≃ 700 keV at L = 2 and becomes stronger for active conditions (K_p = 5 at t = 1, first row and third column) when hiss power is localized deep inside the plasmasphere. For Landau diffusion (pitch angle above 80°) of electron below 300 keV, we notice a transition between significant Landau diffusion and an absence of diffusion for the highest pitch angle (above 85°) at K_p = 3 and t = 1 day, which is likely the DNN model reaching its limit. We will come back on this negative feature in the next section.

At higher L shell ($L \geq 3$) and fixed energy, the minimum pitch angle diffusion occurs between first cyclotron harmonic and the Landau (n = 0) harmonic (e.g., between α = 75 at L = 4, E = 200 keV, K_p =3, and t = 1). At fixed L shell, the maximal pitch angle diffusion from cyclotron harmonics occurs at higher energy as pitch angle increases. The sharp gradients that occur for given (L, E, α) values in the region of transition between Landau and cyclotron resonance reduces as L increases, but it remains a region of possible errors as commented in the previous section for L = 3, E = 0.3 MeV, and α =60 in the third row of **Figure 5**.

One could wonder why the diffusion at L = 4 and K_p = 5 is negligible at t = 1. This is due to the fact that for such active condition the center of the plasmasphere where hiss is dominant (e.g.,[39]) is located at lower L-shell, while L = 4 is in a region of minimal hiss activity, likely in the vicinity of the plasmapause (if beyond, the wave would not be defined and the diffusion would be null). Further

investigation in **Section 4.1** and **Figure 7** will show that there exists only once case of storm having $K_p = 5$ and t = 1 so that the mean DNN model has learnt the solution shown in **Figure 6** (two top rows and third column) from a single storm event. As interesting is the absence of storms with $K_p = 5$ at t = 2 days (cf. **Figure 7**) so that the model is extrapolating with respect to K_p in **Figure 6**(two top rows and fourth column). At t = 2 days, the model statistically predicts some waves with some power due to the fact that likely the plasmasphere has often recovered to above L = 4 at that time, bringing some hiss power. We understand the model could learn such behavior from the data. But would that be occurring in reality if K_p was still as high as $K_p = 5$ on the second day of a HSS storm? We cannot tell from the current data.

Looking at fixed (L, E, α) values in **Figure 6** (two bottom rows), we see any storm can be represented by its evolving path in the (t, K_p) space, with possibly great differences from one time to another although each storm belongs to the same kind. There is a large variability of pitch angle diffusion coefficients with respect to time looking at a horizontal line of fixed K_p. The diversity of the wave and plasma conditions leads to decay rates varying by orders of magnitude and although the K_p indices are the same. This contributes to explain why storms can be so different from one event to the other (e.g., [80]). This brings the question of the time resolution of K_p (here 8 h) and the pertinence of this index when considered as the only parameter of geomagnetic activity. The MLT location of all the observations could also explain the differences. Time plays a crucial role in the solution (cf. the discussion on the interpretation of time in **section 4.1**), while diffusion coefficients do not depend on time in most common space weather simulations (e.g., [61]) in which only K_p remains in both the wave models and the diffusion coefficients (sometime even in the absence of the L-shell dependence (e.g., [81]). The variability of the wave parameters calls for the use of at least two geomagnetic indices or one geomagnetic index and another relevant parameter (here, directly time).

For a given (L,E), we see in **Figure 6** (two bottom rows) the pattern and shape in at fixed (E, α) is roughly conserved while the levels changes. This is true because the solution is presented at not too low L-shell ($L \leq 3$) such that the region of minimal diffusion at moderately high pitch angle between the Landau and cyclotron resonance is narrower than at lower L-shell (Ripoll et al. [12]). Nevertheless, there exist regions in the (E, α) with shapes and variations that differ from the main general trend, as, for instance, illustrated in **Figure 6** (two top rows).

Further exploration of pitch angle diffusion during HSS events is discussed in Ripoll et al. [82] and, in particular, the variability of diffusion within a same Kp index bin. This exploration of the DNN model leads us to look at which diffusion is predicted by the model during sustained HSS yet unobserved.

4 DISCUSSION

4.1 Average vs. Event-Driven Models

The number of storms for each activity (K_p, t) is represented in **Figure 7**. The specificity of storms (e.g., [80]) appears clearly with a few or none events for some combinations of (K_p, t). For instance, there is no HSS storm that has a mean $K_p = 0$ within the 8 first hours. However, there is one HSS storm (over 32) for which $K_p = 1$ occurs within the second period of 8 h of the storm. In great majority, HSS storms have a mean K_p index of $K_p = 4$ during the first 8 h. 2.6 days after the storm 70% of HSS storms (22 over 32) have K_p between 1 and 2, indicative of a quite fast recovery. We also see that averages are made at fixed K_p on a maximum of 16 storms (over 32) at best for a single (K_p, t). This maximum is reached at $K_p = 4$ in the first temporal 8 h bin (t = 0.33). The second bin with the largest number of data is ($t = 2.3$ days, $K_p = 2$) with 14 storms. The largest spread in K_p is for the second day with 5–9 storms in each of the K_p = 0,1,2,3 bin. We have only 3 HSS storms reaching $K_p = 6$, each at 3 different times. One of them has $K_p = 6$ within the first 8 h. **Figure 7** also shows the most probable activity history of HSS, which is K_p = 4, 3, 3, 2, 1, 3, 2, 2, 1. This is quite the activity of storm 12 for which we confirm we have good agreement between the event-driven diffusion coefficients and the average models (DNN and data) (not shown but similar to the results of storm 8 in **Figure 5**). The most probable activity history of HSS shows interestingly a main decay followed by a second milder peak of activity (with a mean Kp reaching Kp = 3 again) after 48 h. This second peak is then followed by a decay to quiet times within the next 24 h.

As we see that the error is caused by the use of averages, the immediate question arising is why averaging when making the DNN model? This is necessary here because of the way our problem is defined. If one wanted to learn directly from the individual diffusion coefficients of the 32 storms, the problem becomes multi-valued and cannot be treated by any machine learning method (unless one DNN model is done for each storm at each time, which asks then the question on how to aggregate n DNN models together). For a given (t, L, E, α), or a given (K_p, L, E, α) we found there exist multiple values of the diffusion coefficient $D_{\alpha\alpha}$. We can solve this issue by two ways: either by using more input parameters, or by averaging data. The K_p-only model is too rough and causes too much error as we will discuss next, and thus $D_{\alpha\alpha}(t, K_p, L, E, \alpha)$ was retained. Here, time could be interpreted as representing any other geomagnetic index (or some global measure of them). Similarly, one could have use 2 (e.g., Dst and K_p) or 3 (or more) geomagnetic indices and their history ($Dst^\star = max_{24\ h}\,(Dst(t))$, $Kp^\star = max_{24\ h}\,(K_p(t))$) or characteristic quantities (such as solar wind velocity, dynamic pressure, etc.) so that the problem becomes single valued, without averaging. In principle, one could also use all wave parameters as entry parameters of the unitary diffusion coefficients $D_{\alpha\alpha}(t, L, E, \alpha)$ since they were used for the generation of the single diffusion coefficients. In that case, the complexity of merging and coupling correctly various complex database together becomes an issue. Another is the knowledge of predicted wave parameters in order to use them in the model (as they are yet non unknown). Adding parameters, we reduce the possibility of encountering prohibitive multi-valued solutions, and we expect it will improve the accuracy of single events.

There are still in turn 3 drawbacks to increase the data size that can alter accuracy, in particular if too many parameters were chosen. First, it increases the problem dimensions, thus the

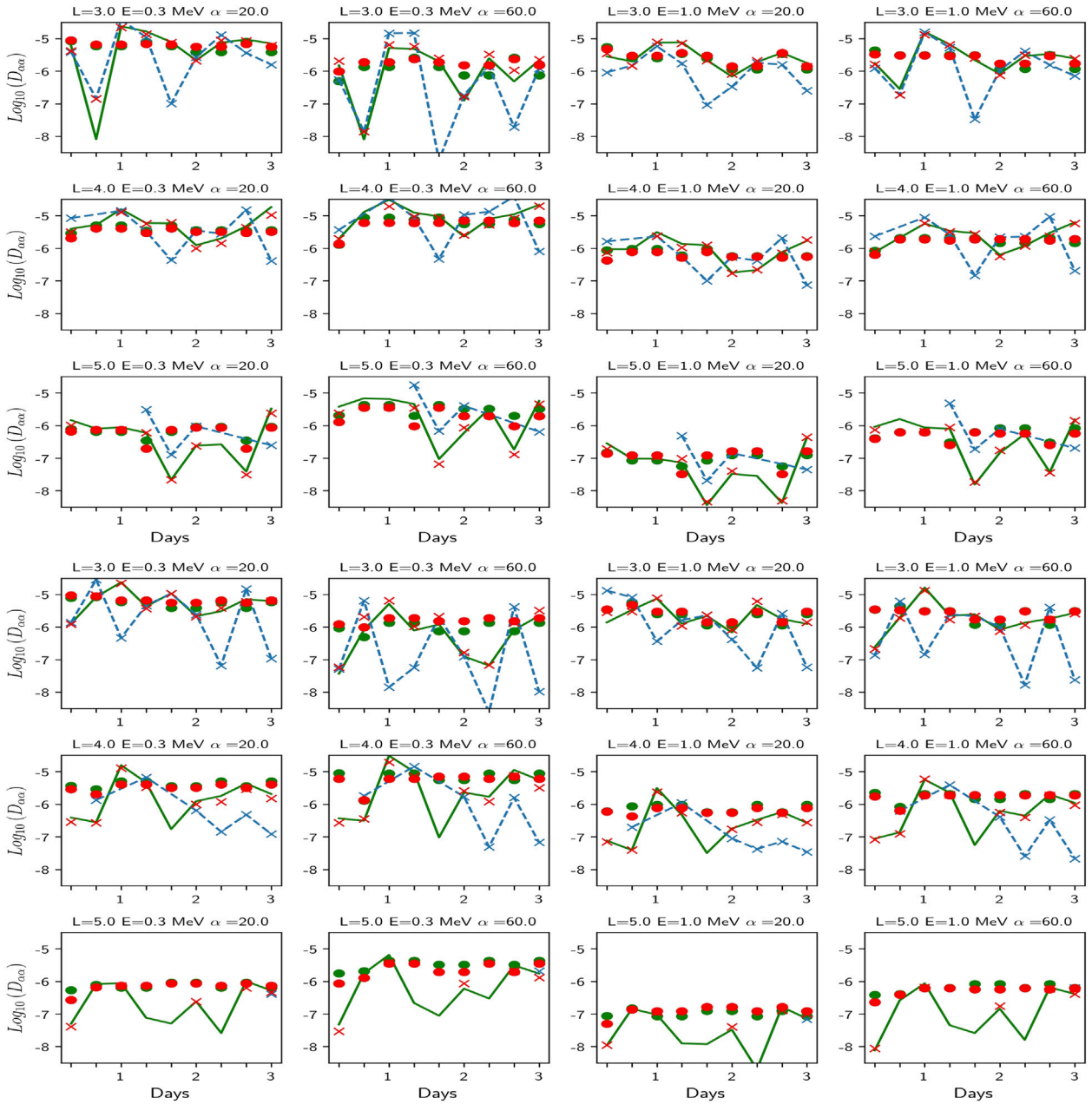


FIGURE 8 | History of the storms 8 and 5. We plot here the same results as in **Figure 5** (blue: raw data, red crosses (K_p, t, L, E, α) average model, green crosses (K_p, t, L, E, α) DNN model) to which we added circles obtained from averaging in time either the average data (red) or directly the DNN model (green); it produces a K_p-dependent (only) model. The DNN model approaches well its target (the average data) but both have a degraded accuracy compared to the event-driven model (in blue), particularly visible for storm 5 in which diffusion coefficients depart significantly from the average.

numerical cost, which should not be a problem for methods such as neural networks. Machine learning methods relying on solving for a linear system (such as the RBF method) become, however, unusable with too large matrices. Dimensionality is an issue for methods that require the computation of geometrical distances, as KNN, and methods that solve for a linear system as RBF. The DNN method does not suffer from this issue and has been used in problems with hundreds and thousands of different input features. Second, there will be a larger domain in the parameter space with sparse data that will cause loss of accuracy in the region of rare occurrence. Third, increasing too much the dimension can cause over fitting of the problem, in the sense that the model loses its ability to be general and represents new events.

When going to more input variables, there is also a trade-off to find between the expected model accuracy and the variability we

do not want to keep in the model, such as the dispersion caused by some measurements or very specific geophysical parameters that may be spurious. This trade-off can be quantified by the same method we use to avoid over-fitting during the training phase of the machine-learning models. The way is to start by testing models on storms that have not been seen during the training phase. When the chosen model has reached enough learning capacity, its error on these new storms will not improve, and will even grow, signifying that the learning limit has been reached.

That is why the approach we present in this article is not unique. Although we retained an approach parametrized with two parameters, i.e., (K_p, t), the approach should be repeated for different various set of other relevant parameters, comparisons among them performed, and ultimately a choice can be made of the best parametrization reproducing the variability of the diffusion coefficients (more generally of the targeted quantity). That is why the simplest, most efficient, and accurate machine learning method has to be chosen in the first place since the method needs to be implemented quickly and replicated multiple times for different choices until eventually reaching a more definitive and more robust model.

4.2 On a K_p-Only Model

Before the retained average model presented above, we tried a simpler model, based only on K_p, i.e., $D_{\alpha\alpha}(K_p, L, E, \alpha)$, as the modeling of pitch-angle diffusion is not time-dependent in most common space weather simulations and follows only the dynamics of a single index, such as the K_p or AE index. Interestingly, $D_{\alpha\alpha}(K_p, L, E, \alpha)$ can be obtained in three different ways: averaging the whole data DS2 over times and storms, averaging DS3_AVG over time (cf. **Section 2.1.4**), or by averaging the machine learning model over time. The two first methods require to run through the dataset many times and to select the right data in order to perform the proper averages. These operations are prone to errors. On the other hand, averaging the DNN model is extremely seductive because it is immediate and simple to perform. It may contain errors due to the DNN intrinsic errors, but this is compensated by the simplicity. This gives another example of positive outcome of machine learning methods.

Figure 8 shows the performance of the $D_{\alpha\alpha}(K_p, L, E, \alpha)$ approach for storm 8, with the DNN mean-K_p model plotted with green circles and the mean-K_p averaged data plotted with red circles (all plotted on top of the data represented in **Figure 5** for illustrating the departure from the time-varying solution). First the DNN mean-K_p model and the mean-K_p averaged data agree well together which shows the success of the data assimilation by the DNN method. This also confirms a simple way to perform further global averages is to directly average the DNN model rather than to further average the data (lowering the risk of errors and simplifying greatly the task). However, both mean-K_p models gives a very rough approximation of the diffusion for a given event. They predict almost a flat curve giving only at best the central tendency. The globally low accuracy is more visible for storm 5 (which diffusion is further away to the mean diffusion) than for storm 8 (closer to the mean). This confirms the deterioration of the accuracy by any form of average; the bigger the ensemble, the higher the error.

4.3 Model Limitations and Future Improvements

The data we use were not created specifically for this study and, as such, the discretization is not best optimized for further encapsulation by a machine learning method. The original set is too large for the herein regression in dimension 3 or 5 and the first task is a necessary strategy to reduce the amount of data. Moreover, when generating data for the purpose of machine learning modeling, an adaptive sampling strategy should be preferred. Such a method consists in optimizing at which variable in (L, E, α) the diffusion coefficient should be computed. This task is left for a future improvement of the model.

The present DNN model of HSS storms has been computed for 5 L-shells with a $\Delta L = 1$. One of the next tasks is to generalize the method to 50 L-shells covering the whole domain with $\Delta L = 0.1$. One way is to repeat the study but spread the teaching onto randomly chosen L-shells in order to keep the same resolution or to increase the sampling size, which remains possible with DNN.

Landau diffusion is the highest diffusion we see for pitch angle above $\alpha_L > \sim 80^\circ$ in **Figure 6** (top, left). At lower pitch angle, Landau diffusion is well defined but negligible (cf Mourenas and Ripoll [45] for an approximation of α_L for a given L-shell and energy). For very large pitch angle, Landau diffusion is strong almost everywhere in the (L, E) plane, but this strong diffusion is surrounded by very weak diffusion outside $[\alpha_L, 90 - \epsilon]$, which traps and diffuses the particle within that pitch angle range. Only coupled energy-pitch angle diffusion effects can then change the electron pitch angle outside of that range [83]. The region of Landau diffusion is a region with a distinct behavior that requires particular attention and can cause the DNN network to make higher local errors (as discussed previously). There can be various strategies to avoid that difficulty. One can either choose to generate two distinct DNN models, one for low and moderate pitch angles (which has the effect to focus on cyclotron resonance) and the other for larger ones (above $\alpha_L > \sim 80^\circ$ where Landau generally occurs). This strategy can be tricky because the exact position of the Landau resonance varies also with the wave and density properties [45] leading to a dependence with (t, K_p, L, E). The better and simpler strategy, which our study brings, is to separate the sum of the n-cyclotron harmonics of the diffusion coefficient from the Landau harmonic ($n = 0$) when the diffusion coefficients are computed and to store both. Then, it is straightforward and more accurate to build a DNN model for each of the two components: one for the n-cyclotron and one for the Landau component. The full model is then made by the sum of both models. The only drawback is the increase of the memory storage by a factor 2.

Finally, machine learning models provide a wide and continuous model in a high dimensional space, which can produce extrapolation and surprising results (right or wrong) in particular for rare events and in the various high-dimensional corners of the model. These solutions always require for verification to go back to the database and to explore it more

and more to the point of knowing (or trying to know) the data in all its aspects. This is often very time consuming, if not practically impossible, even if facilitated by the machine learning method in use. These difficulties call for reliable and robust testing methods and metrics to be able to rely more and more on the machine learning method with less and less verification of the database. In this work, even though the DNN model has shown a good accuracy, we do not think we have yet reached this level as, for instance, there are some remaining issues due to strong gradients (e.g., associated to Landau diffusion) or there is no possibility to verify and validate the behavior of the model for special configuration (e.g., low K_p in the first time of the HSS storm). The second point may call for using a given mean model simultaneously with its variance, which signifies using DNN that propagate the distribution of the data. A mean answer would be given with a confidence index based on the variance. The generation of DNN-based median, quartile, and standard deviation of the diffusion coefficients is thus a promising next step to help selecting a given model. A second important application brought by the knowledge of both the mean and variance is the ability to perform with them uncertainty analysis of Fokker Planck simulation (e.g., [40]) and better establish the variability caused by storms and better rank the best possible scenarios for given conditions.

5 CONCLUSION

In this work, we consider 8 nonparametric methods of machine learning based on local evaluation (k-nearest neighbors and kernel regression), tree-based methods (regression tree, bagging and random forest), neural networks, and function approximations (Radial basis and splines). With them, we derive machine learning based models of event-driven diffusion coefficients first for the storm of March 2013 associated to high-speed streams. We present an approach that exhibits some selected properties of the machine learning models in order to select the best method for our problem among the 8 methods. The approach is based on 3 diagnostics: compute the main global metrics (including mean, median, minimum, maximum, standard deviation, and quartiles errors) at various resolution of the database, generate violin plots for analyzing the error distribution, and compute the correlation of each method with the other to enlighten their differences and exhibit the main families. We find that neural networks (DNN), radial basis functions, and splines methods performed the best for this storm, with DNN retained for the next steps of the study.

We then use the diffusion coefficients computed from 32 high-speed storms in order to build a statistical event-driven diffusion coefficient that is embedded within the retained DNN model. This is the first model of that kind for two reasons. First the machine learning model encapsulates the statistical event-driven diffusion coefficients. Second, this is the first statistical diffusion coefficients made from averaging event-driven coefficients. The common approach is to rather build statistical wave and plasma properties and to compute single diffusion coefficients from them.

The statistics of the event-driven diffusion coefficients are based on the mean with a double parametrization in epoch time and K_p. The double parametrization is chosen to keep both the strength of the storm and follow its history through epoch time. In comparison, a K_p-only model is found too inaccurate compared with specific event-driven diffusion coefficients (by 1–2 orders of magnitudes depending on the event). The machine learning model step is made for greatly facilitating the use of the mean model, for instance, in providing a continuous solution in a high dimensional space [e.g., (t, L, E, α, K_p)]. We find the DNN model does not entail any issue to interpolate the averaged model and reproduces quite perfectly its target. Some small deviations are found at very high pitch angle for Landau resonance for which we propose a future solution to bypass this difficulty. We then use the DNN mean model to analyze how mean diffusion coefficients behave compared with individual ones. We find a poor performance of any mean models compared with individual events, with mean models computing the general trend at best. Degradation of the accuracy of mean diffusion coefficients comes for the large variance of event-driven diffusion coefficients. Mean models can easily deviate by 2 orders of magnitude. This is shown to occur, for instance, in region of strong gradients of the diffusion coefficients, basically delimited by the edge of the first cyclotron resonance in the (E, α) plane.

The strength of the DNN approach is the simplicity of performing comparisons since the model delivers a continuous map of the solution with a simple numerical subroutine for a problem with 5–6 dimensions here. This is illustrated by model exploration provided in **Section 3.2.3**. Plotting diffusion coefficients in the (t, K_p) plane, for instance, shows a wide variety of solutions, contributing to explain why storms can be so different from one event to the other.

Machine learning methods and the easily accessible numerical procedures that favor their use have a wide potential for the type of problems we presented, whether it is for manipulating, interpolating, representing, or for analyzing a huge database of event-driven diffusion coefficients and, more generally, database of diffusion coefficients combined with the main parameters used to compute them, such as plasma density and wave parameters. An inherent drawback is the human involvement required to analyze these huge databases in order to potentially identify regions of model deviance or model breakthrough.

The DNN method that is proposed here has the advantage to be extended to more parameters characterizing storms (including OMNI solar wind and geomagnetic index data), which should improve the accuracy and predictability of global models. DNN can similarly be used to derive DNN-based median, quartile, and standard deviation of the diffusion coefficients. With them, one can perform uncertainty analysis of Fokker Planck simulation and better establish the variability caused by storms and better rank the best possible scenarios for given conditions. We expect this approach to take more importance in the coming years.

DATA AVAILABILITY STATEMENT

Publicly available datasets were used in this study. EMFISIS data was obtained from https://emfisis. physics.uiowa.edu/Flight/. Data are also available at NASA CDAWeb https://cdaweb. gsfc.nasa.gov/index.html/. Datafiles and both RBF and KerReg models are hosted on https://github.com/ ML-Space-Weather/ PADiffusion-HSS. For DNN models, we used DJINN package https: //github.com/LLNL/DJINN. It is based on scikit-learn and tensorflow library. The tree- based and local evaluation methods are based on sklearn library. We use both the tree and the neighbors functions for Regression tree and KNN, respectively. We use both BaggingRegressor and RandomForestRegressor functions of ensemble module (sklearn.ensemble) of sklearn, respectively. And we use KFold function of model selection module from sklearn to perform K-fold cross validation in selecting the hyperparameters of the methods. Lastly, the Thin Plate Spline regression was implemented in R software using Tps function of fields library https://cran. r-project.org/package= fields.

AUTHOR CONTRIBUTIONS

All authors contributed to the manuscript and the data analysis, with a synthesis made by GK. Data were constructed by J-FR and processed by GK. J-FR, and EC brought their expertise in geophysics. SH, AF, MM, EC, and GK in machine learning. Models were made by SH, AF, MM, except for the radial basis model (EC) and the deep neural network learning model (GK). GK, and J-FR together wrote the first draft of the manuscript. J-FR performed the physical analysis. All authors contributed to manuscript revision, read, and approved the submitted version.

FUNDING

EC is partially funded by the National Aeronautics and Space Administration under grant 80NSSC20K1580 "SWQU: Ensemble Learning for Accurate and Reliable Uncertainty Quantification."

REFERENCES

1. Lyons LR, Thorne RM. Equilibrium Structure of Radiation belt Electrons. *J Geophys Res* (1973) 78:2142–9. doi:10.1029/JA078i013p02142
2. Mauk BH, Fox NJ, Kanekal SG, Kessel RL, Sibeck DG, Ukhorskiy A. Science Objectives and Rationale for the Radiation belt Storm Probes mission. *Space Sci Rev* (2013) 179:3–27. doi:10.1007/s11214-012-9908-y
3. Reeves GD, Friedel RHW, Larsen BA, Skoug RM, Funsten HO, Claudepierre SG, et al. Energy-dependent Dynamics of keV to MeV Electrons in the Inner Zone, Outer Zone, and Slot Regions. *J Geophys Res Space Phys* (2016) 121: 397–412. doi:10.1002/2015JA021569
4. Breneman AW, Halford A, Millan R, McCarthy M, Fennell J, Sample J, et al. Global-scale Coherence Modulation of Radiation-belt Electron Loss from Plasmaspheric Hiss. *Nature* (2015) 523:193–5. doi:10.1038/nature14515
5. Millan RM, McCarthy MP, Sample JG, Smith DM, Thompson LD, McGaw DG, et al. The Balloon Array for Rbsp Relativistic Electron Losses (Barrel). *Space Sci Rev* (2013) 179:503–30. doi:10.1007/s11214-013-9971-z
6. Millan RM, Ripoll J-F, Santolík O, Kurth WS. Early-time Non-equilibrium Pitch Angle Diffusion of Electrons by Whistler-Mode Hiss in a Plasmaspheric Plume Associated with Barrel Precipitation. *Front Astron Space Sci* (2021) 8. doi:10.3389/fspas.2021.776992
7. Ripoll J-F, Claudepierre SG, Ukhorskiy AY, Colpitts C, Li X, Fennell JF, et al. Particle Dynamics in the Earth's Radiation Belts: Review of Current Research and Open Questions. *J Geophys Res Space Phys* (2020) 125:e2019JA026735. doi:10.1029/2019JA026735
8. Meredith NP, Horne RB, Glauert SA, Baker DN, Kanekal SG, Albert JM. Relativistic Electron Loss Timescales in the Slot Region. *J Geophys Res Space Phys* (2009) 114. doi:10.1029/2008ja013889
9. Li W, Ma Q, Thorne RM, Bortnik J, Kletzing CA, Kurth WS, et al. Statistical Properties of Plasmaspheric Hiss Derived from Van allen Probes Data and Their Effects on Radiation belt Electron Dynamics. *J Geophys Res Space Phys* (2015) 120:3393–405. doi:10.1002/2015JA021048
10. Meredith NP, Horne RB, Kersten T, Li W, Bortnik J, Sicard A, et al. Global Model of Plasmaspheric Hiss from Multiple Satellite Observations. *J Geophys Res Space Phys* (2018) 123:4526–41. doi:10.1029/2018JA025226
11. Ripoll J-F, Reeves GD, Cunningham GS, Loridan V, Denton M, Santolík O, et al. Reproducing the Observed Energy-dependent Structure of Earth's Electron Radiation Belts during Storm Recovery with an Event-specific Diffusion Model. *Geophys Res Lett* (2016) 43:5616–25. doi:10.1002/ 2016GL068869
12. Ripoll JF, Santolík GD, Kurth WS, Denton MH, Loridan V, et al. Effects of Whistler Mode Hiss Waves in March 2013. *J Geophys Res Space Phys* (2017) 122:7433–62. doi:10.1002/2017JA024139
13. Thorne RM, Li W, Ni B, Ma Q, Bortnik J, Chen L, et al. Rapid Local Acceleration of Relativistic Radiation-belt Electrons by Magnetospheric Chorus. *Nature* (2013) 504:411–4. doi:10.1038/nature12889
14. Réveillé T. *Etude de mécanismes de pertes de particules dans les ceintures artificielles de van allen.* FranceNancy-I: Univ. Henri Poincaré (1997). Ph.D. Thesis.
15. Watt CEJ, Allison HJ, Thompson RL, Bentley SN, Meredith NP, Glauert SA, et al. The Implications of Temporal Variability in Wave-Particle Interactions in Earth's Radiation Belts. *Geophys Res Lett* (2021) 48:e2020GL089962. doi:10. 1029/2020GL089962
16. Ripoll JF, Loridan V, Denton MH, Cunningham G, Reeves G, Santolík O, et al. Observations and Fokker-Planck Simulations of the L -Shell, Energy, and Pitch Angle Structure of Earth's Electron Radiation Belts during Quiet Times. *J Geophys Res Space Phys* (2019) 124:1125–42. doi:10.1029/2018JA026111
17. Ripoll J-F, Denton MH, Hartley DP, Reeves GD, Malaspina D, Cunningham GS, et al. Scattering by Whistler-Mode Waves during a Quiet Period Perturbed by Substorm Activity. *J Atmos Solar-Terrestrial Phys* (2021) 215:105471. doi:10.1016/j.jastp.2020.105471
18. Sicard-Piet A, Boscher D, Horne RB, Meredith NP, Maget V. Effect of Plasma Density on Diffusion Rates Due to Wave Particle Interactions with Chorus and Plasmaspheric Hiss: Extreme Event Analysis. *Ann Geophys* (2014) 32:1059–71. doi:10.5194/angeo-32-1059-2014
19. Horne RB, Kersten T, Glauert SA, Meredith NP, Boscher D, Sicard-Piet A, et al. A New Diffusion Matrix for Whistler Mode Chorus Waves. *J Geophys Res Space Phys* (2013) 118:6302–18. doi:10.1002/jgra.50594
20. Linty N, Farasin A, Favenza A, Dovis F. Detection of Gnss Ionospheric Scintillations Based on Machine Learning Decision Tree. *IEEE Trans Aerospace Electron Syst* (2018) 55:303–17.
21. McGranaghan RM, Mannucci AJ, Wilson B, Mattmann CA, Chadwick R. New Capabilities for Prediction of High-Latitude Ionospheric Scintillation: A Novel Approach with Machine Learning. *Space Weather* (2018) 16:1817–46. doi:10. 1029/2018sw002018
22. Tulunay E, Senalp ET, Radicella SM, Tulunay Y. Forecasting Total Electron Content Maps by Neural Network Technique. *Radio Sci* (2006) 41. doi:10. 1029/2005rs003285
23. Sun W, Xu L, Huang X, Zhang W, Yuan T, Chen Z, et al. Forecasting of Ionospheric Vertical Total Electron Content (Tec) Using Lstm Networks. 2017 International Conference on Machine Learning and Cybernetics (ICMLC). IEEE (2017). 2. 340–4. doi:10.1109/icmlc.2017.8108945

24. Cesaroni C, Spogli L, Aragon-Angel A, Fiocca M, Dear V, De Franceschi G, et al. Neural Network Based Model for Global Total Electron Content Forecasting. *J Space Weather Space Clim* (2020). doi:10.1051/swsc/2020013
25. Oyeyemi E, Poole A, McKinnell L. On the Global Model for Fof2 Using Neural Networks. *Radio Sci* (2005) 40. doi:10.1029/2004rs003223
26. Pérez D, Wohlberg B, Lovell TA, Shoemaker M, Bevilacqua R. Orbit-centered Atmospheric Density Prediction Using Artificial Neural Networks. *Acta Astronautica* (2014) 98:9–23.
27. McGranaghan RM, Ziegler J, Bloch T, Hatch S, Camporeale E, Lynch K, et al. *Toward a Next Generation Particle Precipitation Model: Mesoscale Prediction through Machine Learning (A Case Study and Framework for Progress)*. Space Weather (2021), 19. p. e2020SW002684.
28. Gruet MA, Chandorkar M, Sicard A, Camporeale E. Multiple-hour-ahead Forecast of the Dst index Using a Combination of Long Short-Term Memory Neural Network and Gaussian Process. *Space Weather* (2018) 16:1882–96. doi:10.1029/2018sw001898
29. Siciliano F, Consolini G, Tozzi R, Gentili M, Giannattasio F, De Michelis P. Forecasting Sym-H index: A Comparison between Long Short-Term Memory and Convolutional Neural Networks. *Space Weather* (2021) 19: e2020SW002589. doi:10.1029/2020sw002589
30. Takalo J, Timonen J. Neural Network Prediction of Ae Data. *Geophys Res Lett* (1997) 24:2403–6. doi:10.1029/97gl02457
31. Bala R, Reiff P. Improvements in Short-Term Forecasting of Geomagnetic Activity. *Space Weather* (2012) 10. doi:10.1029/2012sw000779
32. Liemohn MW, McCollough JP, Jordanova VK, Ngwira CM, Morley SK, Cid C, et al. Model Evaluation Guidelines for Geomagnetic index Predictions. *Space Weather* (2018) 16:2079–102. doi:10.1029/2018sw002067
33. Zhelavskaya IS, Spasojevic M, Shprits YY, Kurth WS. Automated Determination of Electron Density from Electric Field Measurements on the Van allen Probes Spacecraft. *J Geophys Res Space Phys* (2016) 121: 4611–25. doi:10.1002/2015JA022132
34. Zhelavskaya IS, Shprits YY, Spasojević M. Empirical Modeling of the Plasmasphere Dynamics Using Neural Networks. *J Geophys Res Space Phys* (2017) 122:11227–11244. doi:10.1002/2017JA024406
35. Zhelavskaya IS, Shprits YY, Spasojevic M. Reconstruction of Plasma Electron Density from Satellite Measurements via Artificial Neural Networks. In: E Camporeale, S Wing, JR Johnson, editors. *Machine Learning Techniques for Space Weather*. Elsevier (2018). p. 301–27. doi:10.1016/B978-0-12-811788-0.00012-3
36. Chu XN, Bortnik J, Li W, Ma Q, Angelopoulos V, Thorne RM. Erosion and Refilling of the Plasmasphere during a Geomagnetic Storm Modeled by a Neural Network. *J Geophys Res Space Phys* (2017) 122:7118–29. doi:10.1002/2017JA023948
37. Chu X, Bortnik J, Li W, Ma Q, Denton R, Yue C, et al. A Neural Network Model of Three-dimensional Dynamic Electron Density in the Inner Magnetosphere. *J Geophys Res Space Phys* (2017) 122:9183–97. doi:10.1002/2017JA024464
38. Ma Q, Li W, Bortnik J, Thorne RM, Chu X, Ozeke LG, et al. Quantitative Evaluation of Radial Diffusion and Local Acceleration Processes during Gem challenge Events. *J Geophys Res Space Phys* (2018) 123:1938–52. doi:10.1002/2017JA025114
39. Malaspina DM, Ripoll JF, Chu X, Hospodarsky G, Wygant J. Variation in Plasmaspheric Hiss Wave Power with Plasma Density. *Geophys Res Lett* (2018) 45:9417–26. doi:10.1029/2018GL078564
40. Camporeale E, Chu X, Agapitov OV, Bortnik J. On the Generation of Probabilistic Forecasts from Deterministic Models. *Space Weather* (2019) 17:455–75. doi:10.1029/2018sw002026
41. Wang D, Shprits YY, Zhelavskaya IS, Effenberger F, Castillo AM, Drozdov AY, et al. The Effect of Plasma Boundaries on the Dynamic Evolution of Relativistic Radiation belt Electrons. *J Geophys Res Space Phys* (2020) 125:e2019JA027422. doi:10.1029/2019JA027422
42. Camporeale E. The challenge of Machine Learning in Space Weather: Nowcasting and Forecasting. *Space Weather* (2019) 17:1166–207. doi:10.1029/2018SW002061
43. Turner DL, Kilpua EKJ, Hietala H, Claudepierre SG, O'Brien TP, Fennel JF, et al. The Response of Earth's Electron Radiation Belts to Geomagnetic Storms: Statistics from the Van Allen Probes Era Including Effects from Different Storm Drivers. *J Geophys Res Space Phys* (2019) 124:1013–34. doi:10.1029/2018JA026066
44. Lyons LR, Thorne RM, Kennel CF. Pitch-angle Diffusion of Radiation belt Electrons within the Plasmasphere. *J Geophys Res* (1972) 77:3455–74. doi:10.1029/JA077i019p03455
45. Mourenas D, Ripoll J-F. Analytical Estimates of Quasi-Linear Diffusion Coefficients and Electron Lifetimes in the Inner Radiation belt. *J Geophys Res* (2012) 117. doi:10.1029/2011JA016985
46. Albert JM. Evaluation of Quasi-Linear Diffusion Coefficients for Whistler Mode Waves in a Plasma with Arbitrary Density Ratio. *J Geophys Res* (2005) 110. doi:10.1029/2004JA010844
47. Réveillé T, Bertrand P, Ghizzo A, Simonet F, Baussart N. Dynamic Evolution of Relativistic Electrons in the Radiation Belts. *J Geophys Res Space Phys* (2001) 106:18883–94. 10.1029/2000JA900177.
48. Albert JM. Analysis of Quasi-Linear Diffusion Coefficients. *J Geophys Res* (1999) 104:2429–41. doi:10.1029/1998JA900113
49. Albert JM. Quasi-linear Pitch Angle Diffusion Coefficients: Retaining High Harmonics. *J Geophys Res* (1994) 99:23741–5. doi:10.1029/94JA02345
50. Albert JM. Efficient Approximations of Quasi-Linear Diffusion Coefficients in the Radiation Belts. *J Geophys Res* (2008) 113:a–n. doi:10.1029/2007JA012936
51. Meredith NP, Horne RB, Glauert SA, Anderson RR. Slot Region Electron Loss Timescales Due to Plasmaspheric Hiss and Lightning-Generated Whistlers. *J Geophys Res* (2007) 112:a–n. doi:10.1029/2007JA012413
52. Ripoll J-F, Mourenas D. *High-Energy Electron Diffusion by Resonant Interactions with Whistler Mode Hiss*. American Geophysical Union AGU (2012). p. 281–90. doi:10.1029/2012GM001309
53. Loridan V, Ripoll JF, Tu W, Scott Cunningham G. On the Use of Different Magnetic Field Models for Simulating the Dynamics of the Outer Radiation belt Electrons during the October 1990 Storm. *J Geophys Res Space Phys* (2019) 124:6453–86. doi:10.1029/2018JA026392
54. Ripoll JF, Loridan V, Cunningham GS, Reeves GD, Shprits YY. On the Time Needed to Reach an Equilibrium Structure of the Radiation Belts. *J Geophys Res Space Phys* (2016) 121:7684–98. doi:10.1002/2015JA022207
55. Santolík O, Parrot M, Storey LRO, Pickett JS, Gurnett DA. Propagation Analysis of Plasmaspheric Hiss Using Polar Pwi Measurements. *Geophys Res Lett* (2001) 28:1127–30. doi:10.1029/2000GL012239
56. Kletzing CA, Kurth WS, Acuna M, MacDowall RJ, Torbert RB, Averkamp T, et al. The Electric and Magnetic Field Instrument Suite and Integrated Science (Emfisis) on Rbsp. *Space Sci Rev* (2013) 179:127–81. doi:10.1007/s11214-013-9993-6
57. Spasojevic M, Shprits YY, Orlova K. Global Empirical Models of Plasmaspheric Hiss Using Van allen Probes. *J Geophys Res Space Phys* (2015) 120:10370–10383. doi:10.1002/2015JA021803
58. Kurth WS, De Pascuale S, Faden JB, Kletzing CA, Hospodarsky GB, Thaller S, et al. Electron Densities Inferred from Plasma Wave Spectra Obtained by the Waves Instrument on Van allen Probes. *J Geophys Res Space Phys* (2015) 120: 904–14. doi:10.1002/2014JA020857
59. Thaller SA, Wygant JR, Dai L, Breneman AW, Kersten K, Cattell CA, et al. Van Allen Probes Investigation of the Large-scale Duskward Electric Field and its Role in Ring Current Formation and Plasmasphere Erosion in the 1 June 2013 Storm. *J Geophys Res Space Phys* (2015) 120:4531–43. doi:10.1002/2014JA020875
60. Wygant JR, Bonnell JW, Goetz K, Ergun RE, Mozer FS, Bale SD, et al. The Electric Field and Waves Instruments on the Radiation belt Storm Probes mission. *Space Sci Rev* (2013) 179:183–220. doi:10.1007/s11214-013-0013-7
61. Cervantes S, Shprits YY, Aseev NA, Allison HJ. Quantifying the Effects of Emic Wave Scattering and Magnetopause Shadowing in the Outer Electron Radiation belt by Means of Data Assimilation. *J Geophys Res Space Phys* (2020) 125:e2020JA028208. doi:10.1029/2020JA028208
62. Baker DN, Jaynes AN, Li X, Henderson MG, Kanekal SG, Reeves GD, et al. Gradual Diffusion and Punctuated Phase Space Density Enhancements of Highly Relativistic Electrons: Van allen Probes Observations. *Geophys Res Lett* (2014) 41:1351–8. doi:10.1002/2013GL058942

63. Li Z, Hudson M, Jaynes A, Boyd A, Malaspina D, Thaller S, et al. Modeling Gradual Diffusion Changes in Radiation belt Electron Phase Space Density for the March 2013 Van allen Probes Case Study. *J Geophys Res Space Phys* (2014) 119:8396–403. doi:10.1002/2014JA020359
64. Hastie T, Tibshirani R, Friedman J. *The Elements of Statistical Learning*. Springer (2009).
65. Géron A. Machine Learning Avec Scikit-Learn *(Dunod)* (2017).
66. Goodfellow I, Bengio Y, Courville A. *Deep Learning*. The MIT Press (2016).
67. Fix E, Hodges J. Discriminatory Analysis. Nonparametric Discrimination: Consistency Properties (Report). Tech. rep. (1951).
68. Altman NS. An Introduction to Kernel and Nearest-Neighbor Nonparametric Regression. *The Am Statistician* (1992) 46:175–85. doi:10.1080/00031305.1992.10475879
69. Nadaraya EA. On Estimating Regression. *Theor Probab. Appl.* (1964) 9:141–2. doi:10.1137/1109020
70. Watson GS. Smooth Regression Analysis. *Sankhyā: Indian J Stat Ser A* (1964) 26:359–72. doi:10.1136/hrt.26.6.755
71. Breiman L, Friedman JH, Olshen RA, Stone CJ. *Classification and Regression*. Trees, CA: Wadsworth and Brooks/Cole Advanced Books and Software (1984).
72. Breiman L. Bagging Predictors. *Mach Learn* (1996) 24:123–40. doi:10.1007/BF00058655
73. Ho TK. Random Decision Forests. Proceedings of the Third International Conference on Document Analysis and Recognition. 1. USA: IEEE Computer Society (1995). p. 278.
74. Breiman L. Random Forests. *Machine Learn* (2001) 45:5–32. doi:10.1023/A:1010933404324
75. Cybenko G. Approximations by Superpositions of Sigmoidal Functions. *Mathematics Control Signals ans Syst* (1989) 2. doi:10.1007/bf02551274
76. Humbird KD, Peterson JL, McClarren RG. Deep Neural Network Initialization with Decision Trees. *IEEE Trans Neural Netw Learn Syst* (2019) 30:1286–95. doi:10.1109/TNNLS.2018.2869694
77. Kluth G, Humbird K, Spears B, Peterson J, Scott H, Patel M, et al. Deep Learning for Nlte Spectral Opacities. *Phys plasma* (2020) 27. doi:10.1063/5.0006784
78. Duchon J. Splines Minimizing Rotation-Invariant Semi-norms in Sobolev Spaces. In: *Construction Theory of Functions of Several Variables*. Berlin: Springer (1977). doi:10.1007/bfb0086566
79. Green PJ, Silverman BW. *Nonparametric Regression and Generalized Linear Models: A Roughness Penalty Approach*. United Kingdom: Chapman & Hall (1994).
80. Reeves GD, Baker DN, Belian RD, Blake JB, Cayton TE, Fennell JF, et al. The Global Response of Relativistic Radiation belt Electrons to the January 1997 Magnetic Cloud. *Geophys Res Lett* (1998) 25:3265–8. doi:10.1029/98GL02509
81. Zhu H, Shprits YY, Spasojevic M, Drozdov AY. New Hiss and Chorus Waves Diffusion Coefficient Parameterizations from the Van allen Probes and Their Effect on Long-Term Relativistic Electron Radiation-belt Verb Simulations. *J Atmos Solar-Terrestrial Phys* (2019) 193:105090. doi:10.1016/j.jastp.2019.105090
82. Ripoll J-F, Kluth G, Has S, Fischer A, Mougeot M, Camporeale E. A Neural Network Model of Quasi-Linear Diffusion Coefficients during High-Speed Streams. Proceedings of the 3rd URSI AT-AP-RASC, Gran Canaria, 29 May – 3 June 2022 (2022).
83. Albert JM, Starks MJ, Horne RB, Meredith NP, Glauert SA. Quasi-linear Simulations of Inner Radiation belt Electron Pitch Angle and Energy Distributions. *Geophys Res Lett* (2016) 43:2381–8. doi:10.1002/2016GL067938

Conflict of Interest: The authors declare that the research was conducted in the absence of any commercial or financial relationships that could be construed as a potential conflict of interest.

Publisher's Note: All claims expressed in this article are solely those of the authors and do not necessarily represent those of their affiliated organizations, or those of the publisher, the editors, and the reviewers. Any product that may be evaluated in this article, or claim that may be made by its manufacturer, is not guaranteed or endorsed by the publisher.

Copyright © 2022 Kluth, Ripoll, Has, Fischer, Mougeot and Camporeale. This is an open-access article distributed under the terms of the Creative Commons Attribution License (CC BY). The use, distribution or reproduction in other forums is permitted, provided the original author(s) and the copyright owner(s) are credited and that the original publication in this journal is cited, in accordance with accepted academic practice. No use, distribution or reproduction is permitted which does not comply with these terms.

frontiers in Astronomy and Space Sciences

ORIGINAL RESEARCH
published: 19 May 2022
doi: 10.3389/fspas.2022.809367

Imaging Low-Energy Ion Outflow in the Auroral Zone

Douglas Rowland[1], Michael Collier[1†], John Keller[1], Robert Pfaff[1], Jeffrey Klenzing[1], Jason McLain[1], James Clemmons[2] and James Hecht[3]*

[1]NASA Goddard Space Flight Center, Greenbelt, MD, United States, [2]Physics Department, The University of New Hampshire, Durham, NH, United States, [3]The Aerospace Corporation, El Segundo, CA, United States

The VISualizing Ion Outflow via Neutral atom imaging during a Substorm (VISIONS) sounding rocket mission investigated the factors leading to ion outflow following a geomagnetic substorm. *In situ* and remote sensing instrumentation provided complementary measurements that have been combined to yield an in-depth look at the phenomena associated with ion outflow. In particular, the inclusion of instrumentation that provided high spatial and temporal resolution "images" of low-energy neutral atom (ENA) emissions from the nightside auroral zone following a substorm has led to new insights. The observed ENAs were spatially structured, and strongly associated with regions of intense 630.0 nm auroral emissions. The ENAs in the auroral zone were predominantly up-going, consistent with thick-target scattering in the region where the ENA mean free path is close to or less than the atmospheric scale height.

Keywords: magnetosphere-ionosphere coupling, ionosphere, plasma transport, particle energization, ion outflow

OPEN ACCESS

Edited by:
Scott Alan Thaller, University of Colorado Boulder, United States

Reviewed by:
Robert Wilkes Ebert, Southwest Research Institute (SwRI), United States
Weijie Sun, University of Michigan, United States

****Correspondence:***
Douglas Rowland
douglas.e.rowland@nasa.gov

†Deceased

Specialty section:
This article was submitted to Space Physics, a section of the journal Frontiers in Astronomy and Space Sciences

Received: *04 November 2021*
Accepted: *23 February 2022*
Published: *19 May 2022*

Citation:
Rowland D, Collier M, Keller J, Pfaff R, Klenzing J, McLain J, Clemmons J and Hecht J (2022) Imaging Low-Energy Ion Outflow in the Auroral Zone. Front. Astron. Space Sci. 9:809367. doi: 10.3389/fspas.2022.809367

1 INTRODUCTION

Ion outflow is one of the most critical two-way feedback mechanisms between the ionosphere/thermosphere and magnetosphere (see, e.g., Welling et al., 2015; Huddleston et al., 2005; Glocer et al., 2009; Glocer et al 2020). However, major questions remain about the conditions and mechanisms that drive ions, particularly heavy ions that should be gravitationally bound, from thermal energies of ~0.5 eV to escape velocities of a few to 10 eV and ultimately magnetospheric energies of 100 of eV to 100 of keV.

Numerous observations have revealed that plasma of ionospheric origin pervades geospace, and can at times be the dominant source of magnetospheric plasma (Shelley et al 1972; Chappell et al 1987; Haaland et al 2012a; Haaland et al 2012b; Gloeckler and Hamilton 1987). The critical "gate" that controls this vast ionospheric source of plasma—by regulating the mass flux that ultimately escapes to the magnetosphere—is the Exobase Transition Region (ETR). This ETR ranges from just below the exobase (~500 km) to where the ions achieve most of their peak escape flux (≤1,200 km). Within the ETR the ion mean free path becomes longer than the scale height, giving ions a chance to gain enough energy to overcome Earth's gravity. Thus, the ETR is a very important region that must be understood if we are to be able to ultimately understand and predict what controls the fluxes and locations of ionogenic plasma in the magnetosphere.

The ETR hosts two types of ion outflow: light ions (H^+, He^+) propelled upward via the polar wind [Banks and Holzer 1968] and heavier ions such as O^+ that must be heated from above to escape [Roberts et al 1987]. The most episodic and spatiotemporally variable of these flows are the heavy ion outflows, which are predominantly driven in the cusp/cleft region on the dayside, and in the nightside auroral zone.

Measurements throughout this ETR are sorely needed to understand two critical components of this escape process: *ionospheric source*, and *acceleration processes*. The *ionospheric source* consists of cold ions with energies from ~0.5 eV to tens of eV, the transition from gravitationally bound to unbound. This population is one of the least well studied because of the lack of proper measurements. Measurements of evolving cold ion distribution functions are essential to understand ion escape. The *acceleration processes* responsible for ETR ion heating derive their free energy from two major sources: 1) charged particle kinetic energy input, such as magnetospheric electron (e^-) precipitation, secondary production, and photoelectrons, and 2) electromagnetic energy input, such as magnetospheric Poynting flux, waves, and field-aligned currents.

While many studies have made *in situ* measurements capable of resolving details of ion distribution functions and (synoptically) their variation with altitude within the ETR, as well as many aspects of the energy sources and acceleration mechanisms that may contribute to ion energization and outflow [e.g., Yau et al., 1983; Chaston et al., 2004; Wilson et al., 2004, Lynch et al., 1996; Kintner et al., 1996; Moore et al., 1996], they typically lack the ability to study the spatiotemporal variations of the ion outflow over a finite volume, and to definitively link, on a case by case basis instead of statistically, the energy sources and acceleration mechanisms at work that drive instances of outflow. Studies with ground-based radars [e.g., Søraas et al., 1974, Thayer 1998], can examine many of the bulk properties (flows, densities, temperatures) of the ions and have high spatial and temporal resolution, but are inherently limited in field of view and cannot measure the detailed distribution function of the outflowing ions.

Recognizing the inherently local/one-dimensional nature of single-platform measurement approaches and the need for additional information about ion distribution function variations with altitude and over a larger volume, researchers have turned to energetic neutral atom (ENA) imaging, using the detected ENAs to infer the properties of the accelerated ions. This includes low-altitude low energy ENA imaging from spacecraft (primarily the Swedish microsatellite Astrid) [e.g., C:son Brandt et al., 2000, see also Rowland et al., 2011], or high-altitude low energy ENA imaging from spacecraft, primarily from IMAGE LENA (e.g., Fuselier et al., 2001; Wilson et al., 2003). These approaches demonstrated that it was possible to measure ENAs from low-altitude sources and to examine their spatiotemporal variation and their response to changes in driving.

These pioneering studies were made on fast-moving platforms (satellites), providing little integration time to gather the ENA signal and resolve it spatially (although the Astrid results did resolve low-altitude ENA emissions on regional scales). IMAGE, in particular, was sweeping through perigee quite rapidly, and spinning slowly, when it made its low-altitude measurements. The resulting IMAGE ENA measurements at low altitude show a generally featureless "sea" of low energy ENAs, that would be difficult or impossible to localize with respect to particular auroral features. In fact, a single pixel in the IMAGE reconstruction corresponds to the entire region sampled by VISIONS at much higher spatial resolution.

The VISIONS sounding rocket mission was designed to provide high-spatiotemporal resolution ENA imaging in a local volume (1,000 km × 1,000 km × 1,000 km) with good energy sensitivity, while simultaneously measuring ion distributions, auroral energy inputs (over a wide area), electric and magnetic fields (including wave modes thought to be critical for ion acceleration). With its slow horizontal motion, fast spin rate, and large-aperture ENA detector, as well as a suite of comprehensive and complementary measurements, VISIONS was designed to answer the following science questions:

- What are the spatial and temporal variations of ion outflow in and near an auroral arc?
- What is the total ion outflow in the remotely sensed volume, and what is its variation during the substorm life cycle?
- How do the relative contributions of the energy sources change during the substorm life cycle, and spatially, relative to the visible auroral arcs?
- How do regions of enhanced ion outflow compare in detail to the locations of field-aligned currents, optical auroral emissions, enhanced electric fields, energetic particle precipitation, wave activity, and regions of enhanced/depressed electron density?
- What are the altitudinal locations and extents of ion acceleration regions, and how do these parameters vary over time?

Because the auroral event VISIONS launched into was fairly stable in time (well past substorm onset) we have not been able to determine temporal variations, but the mission was successful in spatially localizing the region where outflow occurred and sheds some light on the relation of ion outflow regions to simultaneously measured auroral input as well as the detailed ion distributions that are associated with the remotely sensed ENAs.

This paper presents an overview of the mission and the initial results from the ENA instrument, showing its ability to spatially localize ion outflow regions at relatively high resolution. Detailed modeling of the ENAs and ion outflow will be presented in a follow-on work.

2 MATERIALS AND METHODS

The VISIONS sounding rocket mission was launched northwards from Poker Flat, AK at 08:21:00.0 UT on 7 Feb 2013, reaching an apogee of 753.8 km 495 s later. The launch occurred approximately 20 mins after the onset of a modest substorm (−400 nT), with breakup north of Poker Flat. The VISIONS rocket trajectory is shown in **Figure 1**. The left panel shows the geographic latitude and longitude of the instrument payload as a function of time in seconds since launch (blue dots). The right panel shows the altitude and latitude of the payload, with labels indicating the position at selected times since launch.

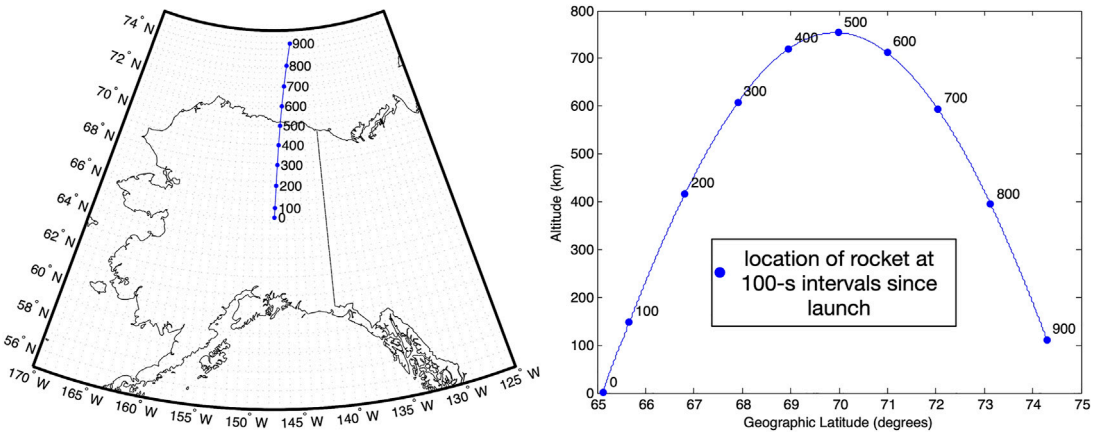


FIGURE 1 | Geometry of the VISIONS rocket experiment. Left: Geographic footpoint of the rocket along the trajectory. Right: Altitude vs. Geographic Latitude of the VISIONS-1 rocket along the trajectory. Data from various instruments exists from just before 200 s through the end of the flight. The dots represent the location of the rocket at 100 s intervals after launch.

TABLE 1 | VISIONS instrument capabilities.

Instrument	Purpose	Capability
MILENA	"Image" low-energy neutral atoms	Six 30° × 5° pixels, 50 eV to 3 keV spin sweeps out "full sky"
RAI	Image visible and near-IR auroral emissions	Nadir-viewing visible light imager with 90° FOV four narrowband wavelengths: 391.4, 630.0, 844.4, 486.1 nm images at 2 Hz rate
EEA	Measure energy-pitch angle distributions of energetic electrons	Energy-pitch angle distributions every 50 ms from 7 eV to 30 keV
EIA	Measure energy-pitch angle distributions of energetic ions	Energy-pitch angle distributions every 50 ms from 3.5 eV to 15 keV
FTP	Measure fields and thermal plasma density and temperature	DC Electric Fields, accuracy 1 mV/m Waves from ULF to 5 MHz Electron density and temperature DC magnetic field, accuracy 2 nT

VISIONS combined remote sensing and *in situ* instruments to provide a new view of ion outflow and its drivers in the nighttime auroral zone, shown in **Table 1**. A brief description of these instruments follows.

2.1 MILENA

The Miniaturized Imager for Low Energy Neutral Atoms (MILENA) is nearly identical to the MINI-ME instrument flown on the FASTSAT mission, launched in 2010 (Rowland et al., 2011). MILENA is essentially a standard top-hat electrostatic analyzer (Carlson, et al., 1983), with an additional front end consisting of a "Venetian blind" set of polished silicon conversion surfaces and an electrostatic charged particle rejector. The charged particle rejector serves to reject energetic electrons and to mechanically collimate the incoming ENAs. The Venetian blind conversion surfaces allow incoming O and H ENAs to capture an electron from the silicon via grazing incidence reflection at fairly high efficiencies (~few %). After electron capture, they become negative ions and are steered through the ESA, first to a microchannel plate, and then to a detector and counter. MILENA uses a "three-bounce" design with blackened interior surfaces to minimize UV background. VISIONS was launched at night, in moon-down conditions, further reducing the UV signal level that could enter the instrument.

MILENA had an energy range of 50 eV to 3 keV, and a responsivity of approximately 3×10^{-4} counts/s per neutrals/s-cm^2-sr-dE/E. MILENA's geometric factor was 0.044 sr, corresponding to a solid angle of 31.9 × 4.5° and an aperture of 4 cm^2. MILENA's energy resolution (dE/E) was 20%. MILENA's integration period was 16 ms, with 128 integrations per energy step (the total duration of each energy step was 2.048 s). The VISIONS rocket was kept nearly aligned to the background magnetic field (within about 8°) and spun at a rate of ~0.48 Hz.

VISIONS flew two identical MILENA instruments, M1 and M2. M1 stepped over the following eight energies: 50, 70, 100, 300, 500, 700, 1,000, and 3,000 eV, changing energies every 2.048 s. M2 alternated between 50 and 100 eV every 2.048 s. The instrument aperture plane contained the spin axis of the rocket, and so each imager swept out a "full sky" image every half-spin, or approximately once per second. The MILENA sectors

each had an angular extent of ~30° in polar angle (in the aperture plane), and there were six per instrument, with ~30° gaps between sectors. The angular acceptance in the azimuthal direction (perpendicular to the aperture plane) was approximately ±2.25°. Sectors 1 and 2 look downward, with sector centers at 30° from the rocket spin axis (which is aligned roughly to the magnetic field direction) and are the sectors closest to "nadir"). Sectors 3 and 6 look horizontally, with centers at 90° to the rocket spin axis. Sectors 4 and 5 look upward with centers at 30° from the rocket spin axis (opposite the magnetic field direction, these are the sectors closest to viewing in the zenith). Collier et al., 2015 highlights some initial measurements from VISIONS-1 MILENA.

2.2 RAI

The Rocket-borne Auroral Imager (RAI) consisted of four independent narrowband visible-light imagers, each tuned to a unique wavelength (Hecht et al., 2006). Each had an identical 90° wide field of view, achieved using telecentric optics that are consistent with the narrowband interference filters used. After onboard binning, the resulting images were captured twice per second at 128 × 128 pixel resolution. The instrument sensitivity was a few 100 Rayleighs in all four channels. The four wavelengths selected were 1) 391.4 nm, to measure energetic electron precipitation, 2) 630.0 nm, to measure softer electron precipitation, 3) 844.4 nm, to provide another measure of atomic oxygen density, and 4) 486.1 nm, H-beta, to look for proton precipitation and regions of albedo ENA production. These lines were selected to permit an estimation of electron energy flux and characteristic electron energy in each pixel, using the technique of Hecht et al. (2006). When the rocket was near apogee (~750 km), the RAI pixel size was approximately 10 km, assuming a projection height of 100 km. RAI was deployed on a sub-payload which was three-axis stabilized, to avoid motion or spin-blur effects on the image. The RAI apertures were kept pointing near the 100 km altitude point above Arctic Village, Alaska, with three updates to the pointing throughout the flight, to stay near this target.

2.3 EEA and EIA

The Energetic Electron Analyzer (EEA) and Energetic Ion Analyzer (EIA) [Clemmons et al., 2013] were top-hat electrostatic analyzers (Carlson et al., 1983) for measuring electrons and ions, respectively. These instruments had instrument aperture planes that contained the spin plane of the rocket. Since this rocket spin axis was kept nearly aligned to the magnetic field, this geometry permitted full pitch angle distribution measurements. The instruments each utilized twenty pixels of various sizes ranging from 3° (near 90° pitch angle on EIA to sample transverse ions, and near 0° pitch angle on EEA to sample precipitating electrons) to 12°. The instruments each had a geometric factor of 0.01 cm^2-s-sr keV/keV, energy resolution of 16%, and integration times of 1 ms per energy step. They swept over 50 energies in a total energy sweep time of 50 ms. EIA measured ions from 7.5 eV to 15 keV. EEA measured electrons from 15 eV to 30 keV. These instruments also mapped out a full three-dimensional distribution every half spin (approximately once per second).

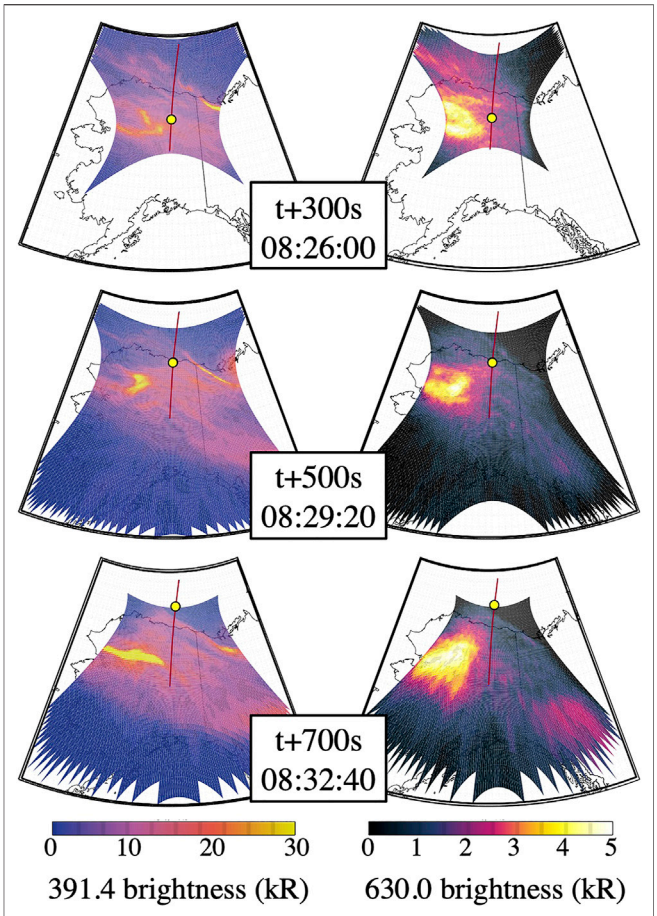


FIGURE 2 | Representative auroral images during VISIONS flight, with rocket trajectory (red line) superimposed. The yellow dot indicates the payload position at the time of the given auroral image. Each row represents the 391.4 emissions (left) and 630.0 nm emissions (right) measured onboard the VISIONS rocket by the nadir-viewing Rocket Auroral Imager (RAI), projected onto a geographic reference altitude of 120 km (391.4) or 200 km (630.0). Each column shows a separate time point during the flight ranging from t + 300 s since launch (top row) to t + 700 s since launch (bottom row). The important feature of this plot is that there is a large and persistent 630.0 nm emission feature to the west/southwest of the rocket trajectory, and bright 391.4 nm emissions from both the southwest and northeast of the trajectory, and these features persist throughout the entire rocket flight.

2.4 FTP

The Fields and Thermal Plasma instrument suite (FTP) consisted of a vector double-probe electric field instrument, a cylindrical Langmuir Probe, a dipole impedance probe, and a fluxgate magnetometer on the main payload and a single axis wave electric field double probe, magnetometer, and Langmuir probe on the sub-payload. For the purposes of this study, we focus on the fields and thermal plasma instruments on the main payload.

The double-probe instrument measured the electric field from quasi-static (DC) frequencies to 5 MHz perpendicular to the background magnetic field, along which the payload spin axis was oriented by the on-board attitude control system. Four spherical electric field sensors with embedded pre-amps were

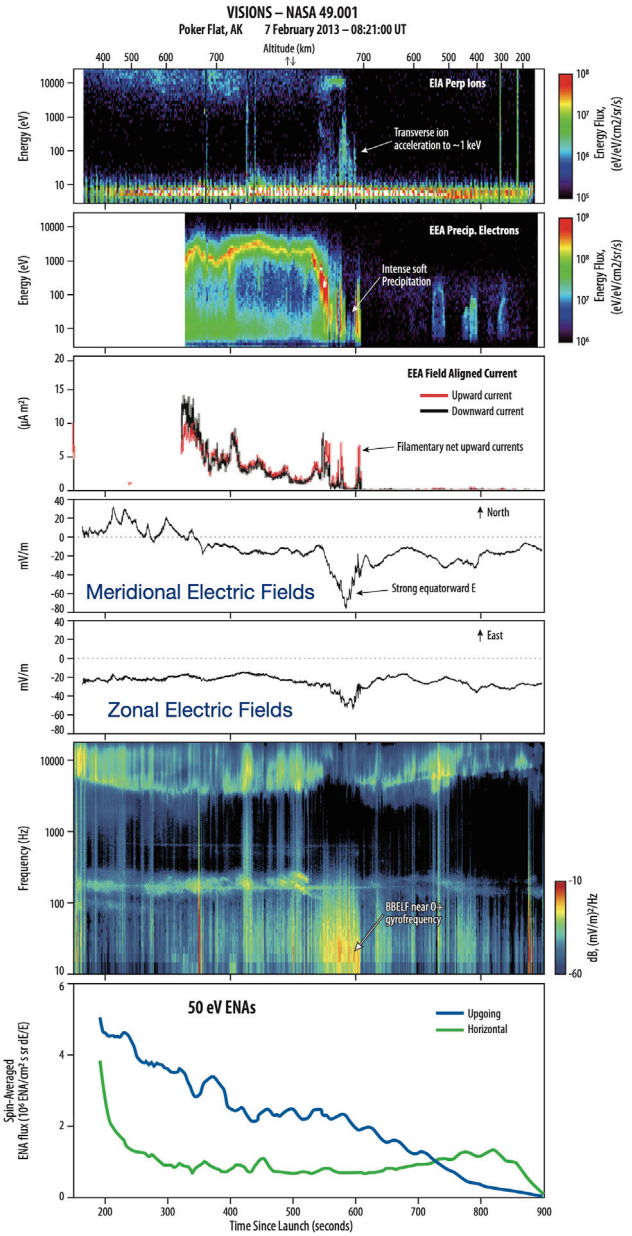


FIGURE 3 | Top six panels: *In situ* measurements of particles and fields along the VISIONS rocket track: Panel 1 presents energetic ion measurements from the VISIONS-1 Energetic Ion Analyzer for pitch angles near 90°, presented as an energy time-spectrum. Color indicates log scale of flux. Note the intense signal near and below 10 eV is the signal of rammed ions in the rocket frame. At higher energies (above a few keV) the signature of magnetospheric ions can be seen. There are several instances where TAIs (transversely accelerated ions) are observed, most prominently near t + 600 s, where flues of TAIs are observed up to 1 keV; Panel 2 shows an energy-time spectrogram of precipitating (pitch angle near 180°) electrons from the VISIONS-1 Energetic Electron Analyzer. Intense inverted-V structure, with precipitating electrons at energies 2–3 keV persists until about t + 550 s, where the rocket crosses the poleward boundary of the auroral zone, and encounters a region of intense soft electron precipitation with energies below 1 keV. Panel 3 shows field-aligned current computed by summing the upgoing and downgoing electrons over energy for appropriate pitch angles. Earlier in the flight, the net current is large in spatial scale and small amplitude or slightly downward, while in the region of soft electron precipitation the current is upgoing, stronger, and highly filamentary. Panels 4 and 5 show the meridional and zonal components of the electric field (in magnetic coordinates) measured by the double probe electric field experiment on VISIONS-1, showing an intense equatorward electric field in the region of soft precipitation and filamentary upward current, that exhibits the TAI signature. Panel 6 shows a Fourier spectrogram of the ELF/VLF electric field wave environment. Intense lower hybrid emissions with a sharp cutoff can be seen at the top of the figure, with an enhancement of broad-band ELF (BBELF) waves that span the O+ gyrofrequency in the region where TAIs are observed. Bottom panel: Spin-averaged (2 s average) fluxes of 50 eV energetic neutral atoms (ENAs) from one of the MILENA imagers. The blue trace indicates ENAs that are coming from primarily below the rocket (dominant before about 700 s), while the green are ENAs coming from primarily horizontal angles of arrival. The angle of arrival is measured using six angular sectors of 30° width with 30°-wide gaps between them.

(*Continued*)

deployed at the end of 3 m long "stacer" booms to form orthogonal 6 m tip-to-tip double probes in the spin plane. The electric field measurement was gathered continuously over a range of frequency bands, including: 1) "DC-coupled" channels with a sample rate of 2 kHz and a range of ±833 mV/m at 18-bit precision and an absolute accuracy of approximately 0.5 mV/m, 2) "AC-coupled" VLF channels with a high pass filter at 16 Hz that were sampled at 32 kHz at 18 bits, for which the most significant 15 bits were telemetered to the ground, over a range of ±45.7 mV/m, and 3) HF electric fields sampled at 5 Ms/s with a 12 bit analog-digital converter. The cylindrical Langmuir Probe was designed to measure the thermal electron density and temperature (during sweeps of the bias voltage) as well as small-scale variations in the ion density (during intervals when the probe was held at a negative bias voltage). It was sampled at 8 kHz, and the voltage sweep ran from −2 to +3 V over 256 ms, once every 10 seconds. The impedance probe measured the impedance of a short dipole antenna exposed to the plasma, from which observed resonances were used to measure the upper hybrid frequency and thus the electron number density (see, e.g., Jensen and Baker, 1992), approximately six times per second. The fluxgate magnetometer was a three-axis Bartington MAG-03MSB60, sampled at 18 bits at 2 kHz per channel. The absolute accuracy was approximately 2 nT.

3 RESULTS

3.1 RAI Auroral Images

Figure 2 shows the rocket trajectory superimposed on a set of representative images from the RAI instrument. In each column is shown a different wavelength, with 391.4 nm on the left and 630.0 nm on the right. Time increases down each column, and the three pairs of images span more than 6.5 min of the flight. The rocket trajectory is shown as a thin blue line, with a yellow dot indicating the payload position at the given time. The 391.4 nm image is projected to 120 km altitude, while the 630.0 nm image is projected to 200 km altitude. All images have undergone dark current subtraction and 3 × 3 median filtering from the original 128 × 128 pixel images.

The images show that VISIONS passed to the east of a large, stable region of intense precipitation, both hard (391.4) and soft (630.0), and to the west of a more dynamic feature that is more readily apparent in 391.4. The complete sequence of auroral images (not shown here) indicates that a dynamic set of arcs was forming and evolving near the polar cap boundary, including the poleward arc encountered by VISIONS. In addition, a combination of ground-based whitelight imagers and the full image sequence from VISIONS showed that the strong auroral feature to the west of the rocket trajectory is stable throughout the flight and for ~10 min before and >30 min after. Some of the apparent variation in the emissions (particularly in the 630.0 nm line, in the later portion of the flight is due to the changing viewing angle relative to the magnetic field and projection effects. See **Figure 5** for similar ground-based images of the persistence of the auroral features.

3.2 *In situ* Measurements of Particles and Fields

The *in situ* measurements from the VISIONS flight are shown in **Figure 3**. VISIONS was launched into a region of inverted-V electron precipitation (~2–3 keV electrons), as shown in the second panel. The inverted-V electron precipitation transitioned to a region of intense soft electron precipitation at the polar cap boundary, between about 500 and 600 s after launch (just after apogee), with electron energies at or below a few 100 eV. The polar cap boundary also exhibited signatures of transversely accelerated ions (panel 1), with energies up to 1 keV, coincident with the soft precipitation. This region also exhibited intense, filamentary field aligned currents (panel 3, net upward current of ~5–10 $\mu A/m^2$) as measured by the energetic particle instrument, strong equatorward DC electric fields (~90 mV/m, panel 4 and 5), and intense BBELF waves near the O+ gyrofrequency which was near 40 Hz at this location (panel 6). These intense filamentary upward currents may be capable of exciting O+ ion cyclotron waves in the range 400–1,000 km, depending on the details of the Te/Ti ratio and ion composition profiles, which were not directly measured by VISIONS (Kindel and Kennel, 1971). These are fairly typical signatures of the nightside auroral zone following a substorm [see, e.g., Lynch et al., 1996] and have been discussed further in a companion paper (Clemmons, 2014).

Taken together, these figures show that VISIONS flew through some regions with transversely accelerated ions and active aurora but did not encounter the regions of most intense auroral precipitation (or, presumably, ion acceleration). Throughout most of the flight, the largest, most intense region of precipitation was to the southwest of the rocket, with narrow arcs of harder precipitation at the polar cap and to the east.

3.3 ENA Measurements

To understand how these more distant regions of auroral precipitation might have driven ion energization, it is instructive to examine the ENA emissions observed by VISIONS. The ENAs, as described above, are generated as energetic ions charge exchange with the neutral atmosphere. These ENAs can be remotely observed at large distances from the parent ion population. The ENA fluxes can thus serve as proxies for the line of sight-integrated ion populations.

3.3.1 Spin-Averaged ENA Data

Panel 7 of **Figure 3** shows data from MILENA. In this case, the data shown are the 50 eV channel data from MILENA's M2 sensor, summed over a full 2-s energy step (nearly the same as the spin period) for two pairs of the six arrival angle sectors. The blue traces are for ENAs traveling within ±45° of the direction opposite to the magnetic field (up the field line). The green traces correspond to "horizontal" ENAs traveling within ±15° of the direction perpendicular to the magnetic field. The horizontal axis of the plot shows time since launch. The vertical axis represents the ENA number flux in a given pixel. The integration time was 2.048 s.

As the rocket ascends, in the early part of the flight before apogee (in the auroral zone, inverted-V region) the upgoing ENAs dominate over the horizontal and downgoing ENAs. The upgoing ENAs also diminish in intensity with time, presumably as the rocket moves farther away from the source region in distance, and potentially also reflecting the angular distribution of upgoing ENAs, reducing significantly out in the polar cap. The downgoing ENAs (not shown) are generally weak throughout the flight. The horizontal ENAs start out at high levels, as the rocket is near peak ENA production altitudes and also closest to the source in the early part of the flight, then remain stable and low once the rocket has reached higher altitudes where horizontal ENA production is lower, and then go on to increase when the rocket is on the descending portion of its trajectory in the polar cap, even though the rocket is farther from the source at this point. Indeed, the horizontal ENAs become dominant just after t + 800 s.

3.3.2 Angle-Resolved ENA Data

While the spin-averaged data is valuable and provides some important clues about the nature and sources of ENA production, it is the sub-spin "ENA imaging" data from MILENA that shows the promise of this technique. **Figure 4** shows four panels of subspin data (inset polar plots) from M2 50 eV data at each of four different times during the VISIONS flight: 1) t + 359 s, in the auroral zone, at 682 km; 2) t + 580 s near the polar cap boundary, at 727 km altitude; 3) t + 777 s, at 428 km altitude, in the polar cap; and 4) t + 847 s, 242 km altitude, below the exobase in the polar cap. In each panel, the combined count rate from each pair of matched pixels is shown as a function of arrival direction, using the same color scheme as **Figure 3**, with the addition of red traces showing downgoing ENAs (±45 of the direction of the magnetic field). North is to the top of each panel, and east to the right. The angle shown is the projection of that pixel's center look direction onto a horizontal plane as a function of time. The radial distance of each curve from the center of the panel indicates the counts measured by M2 at that angular location. For each panel, an arrow (blue for auroral zone, green for polar cap) is superimposed on the point on the rocket trajectory corresponding to that observation. Also superimposed is the RAI 630.0 nm image from t + 359 s, for

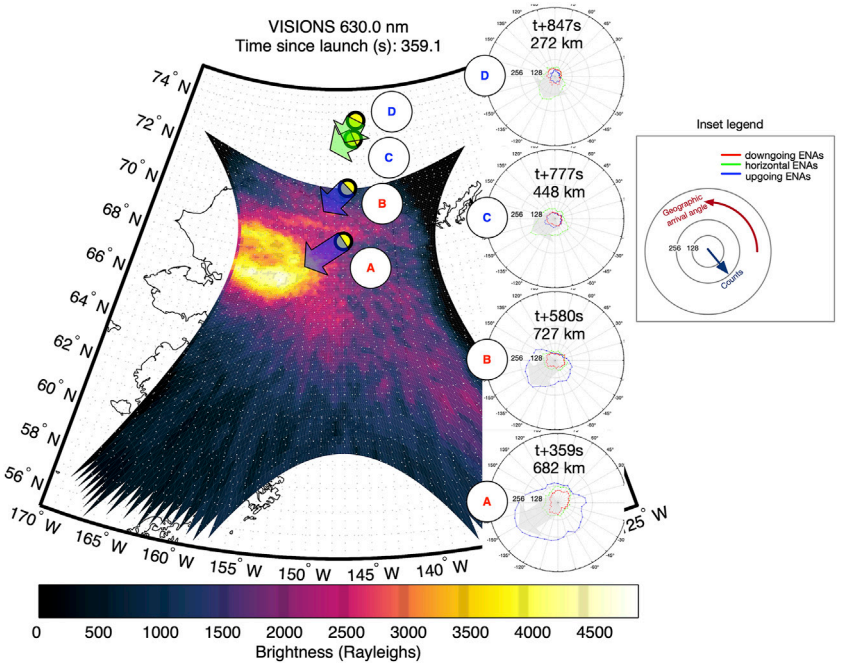


FIGURE 4 | The image presents the 630.0 nm emissions imaged by the VISIONS RAI at t + 359.1 s after launch, projected onto geographic coordinates, assuming an emission altitude of 200 km. The four circles marked "A" through "D" represent the rocket location at times t + 359, t + 580, t + 777, and t + 847 s since launch. Next to each circle is an arrow that points in the horizontal direction of the peak in the observed ENAs. These are colored blue if the dominant ENAs at that time are coming in from nadir-viewing sectors of the ENA instrument, and green if they are coming from sectors that look more towards the horizontal. The right hand insets show the detailed ENA arrival angle distribution (where radial distance is counts and polar angle is geographic direction of arrival) at each of those four time points. In each inset, there are three angular distributions: red for ENAs arriving from closer to the zenith/magnetic field direction, green for ENAs arriving from near horizontal directions, and blue for ENAs arriving from the nadir direction. VISIONS ENAs show consistent, coherent direction of arrival predominantly consistent with neutral atom source regions to the southwest. The amplitude of the ENA signal drops with distance from the bright 630.0 nm feature to the southwest of the trajectory, and goes from being primarily upgoing to being primarily horizontal, as would be expected for a distant source subject to thick-target scattering below the exobase and thin-target scattering above.

comparison and to show a representative distribution of auroral emissions. While these change slightly with time, the main feature (large emission region to the southwest of the rocket) does not vary significantly through the VISIONS flight. While there is some variation in the ENA arrival direction with time as the rocket moves along its trajectory, it is clear that the strongest signals are to the southwest of the rocket. The data are consistent with multiple weaker sources at other angular positions as well, in some cases. The transition from upgoing ENAs in the top two panels to horizontal ENAs in the bottom (lower altitude, polar cap) panels is quite clear.

In order to spatially localize the region of outflow, it is important to assess which magnetic flux tubes are associated with regions of outflow and how these outflow regions relate to regions of energy inputs, particularly auroral inputs. In so doing, we can collapse the (important) altitude dependence to answer the question—to first order, where are the ENAs coming from? This will be important both to address the VISIONS science questions and to develop improved techniques for reconstructing accelerated ion populations from ENA measurements in optically thick regions.

The usual technique for analyzing ENA data [see, e.g., Roelof, 1987 or Roelof and Skinner, 2000] assumes an optically thin medium, and takes the line integral of the product of the neutral atom density and ion flux along the line of sight, times the charge exchange cross section. Observations of this ENA source function along different lines of sight are used to tomographically reconstruct the ion population (or simulated ENA images are generated, compared with observations, and iterated until a match is achieved, see also Fok et al., 2003 and Wilson et al., 2003). As discussed in Roelof (1997), low-altitude ENA imaging must deal with the complications of an optically thick medium, including attenuation, scattering, re-ionization, and reverse charge exchange. For the VISIONS regime, near the exobase, the optically thin approximation is not strictly valid. A "thick target" approach, similar to that used by Bazell et al. (2010) would be a more rigorous approach, in terms of accounting for multiple scattering, charge exchange, stripping, and other effects.

3.3.3 Altitude Variations in ENA Production and "Thin Shell" Backtracing

However, to first order, since VISIONS is relatively close to the source, we can approximate the ENA source region as optically thin above about 400 km (where the mean free path for ENA-neutral collisions becomes >100 km, assuming no collisions in this optically thin region [see, e.g., C:son Brandt

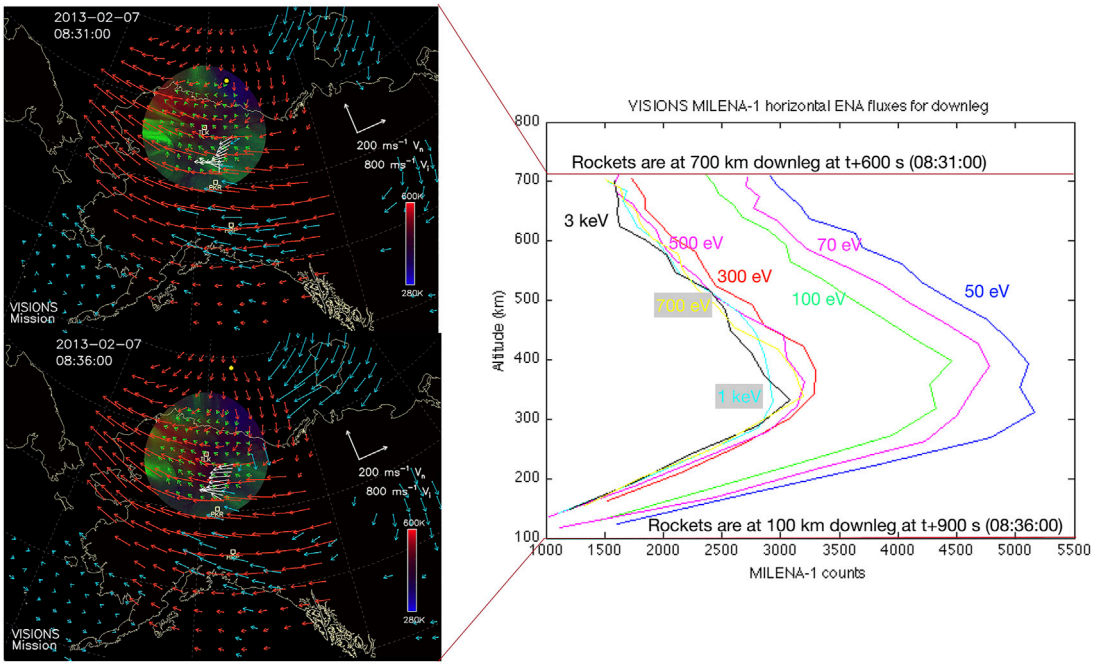


FIGURE 5 | Left panels (courtesy Prof. Mark Conde, University of Alaska, Fairbanks) show the aurora (green and red shading) SDI-derived F-region (red) and E-region (green) neutral wind vectors, SuperDARN convection patterns (blue arrows) and PFISR plasma velocities (white arrows) at two points during the VISIONS flight: (top) t + 600 s (08:31:00) and (bottom) t + 900 s (08:36:00). The auroral and electrodynamic conditions do not change significantly during this 5 min period. The right panel shows the altitude profile of horizontal ENAs, demonstrating that the majority are produced near 300–400 km. Shown are the summed counts for the downleg of the flight between t + 600 and t + 900 s, spanning the altitude range 700 to 100 km. The counts detected in each energy channel is shown by a separate trace. blue: 50 eV, magenta: 70 eV, green: 100 eV, red: 300 eV, magenta: 500 eV, yellow: 700 eV, cyan: 1 keV, black: 3 keV. All data are from the MILENA M1 imager, summed over pixels 3 and 6 (horizontal/perp to magnetic field) for a full energy step (nearly a full spin). All of the data obtained here are essentially northward of the auroral zone boundary and outside the region of energetic electron precipitation. Note that as the rocket moves from 700 to 400 km, it is traveling ~200 km/2° latitude downrange, and thus further from the ENA source, and yet the ENA signal is increasing. This is because the horizontal ENA signal is produced by charge exchange, and the neutral density increases with decreasing altitude, resulting in more ENAs per unit ion flux. The broad peak centered around 350 km is where the probability of multiple ENA-neutral collisions becomes largest—below this the horizontal ENA signal becomes attenuated due to the decreasing ENA mean free path that "filters" ENAs from reaching the rocket. VISIONS ENA images (dial plots) superimposed on VISIONS narrowband auroral emission images of 391.4 nm (left) and 630.0 nm (right) show strong correlation of projected ENA source with soft electron precipitation at ~ t + 360 s.

et al., (2001)]. We refer to this as a "thin shell" backtracing approach. Even though the ENAs are generated over a range of altitudes and ranges along the instrument's line of sight, we assume all ENAs originate from the boundary where the atmosphere becomes optically thick. Below about 400 km this condition is satisfied with mean free paths approaching 10 km near 300 km altitude. It is important to note that the point at which the ENA leaves the optically thick medium is not, in general, the same as where the original parent ion underwent charge exchange, as there can be a great deal of ENA-neutral scattering in this optically thick region, resulting in spatial smearing of features. This scattering also tends to degrade information on the initial parent ion's energy and pitch angle, which get heavily smeared by scattering in this layer. ENAs produced by charge exchange in the optically thin region (typically horizontally traveling ENAs) do not have this problem to the same extent.

To assess the validity of this "thin shell" approach, we examined the altitude dependence of the horizontal ENAs observed by VISIONS as it flew through the descending portion of its trajectory in the polar cap. **Figure 5** shows the sum of M1 pixels 3 and 6 (sidelooking pixels, perpendicular to magnetic field ± 15°) as a function of altitude for each of the eight M1 energy steps, summed over pixels 3 and 6 for each 2.048 s energy step (nearly a full spin). The energy spectrum is fairly constant with altitude, and is roughly consistent with a power law of slope −0.3, becoming harder at altitudes below 300 km, consistent with more energetic ENAs being able to reach the spacecraft when lower energy ENAs have their energy degraded and their flux attenuated by ENA-neutral collisions.

These data are plotted as a function of altitude, but the rocket is also moving northwards, during this interval (about 300 km northwards while the rocket descends from 700 to 300 km altitude). In addition, the charge exchange probability increases with decreasing altitude, an effect that is not corrected for here. Finally, the detailed ion population pitch angle, energy, and altitude distribution is not known over the entire ENA source region and can be expected to be variable in space and time over the energy input region. The left panels of **Figure 5** show the relative stability of the auroral and electrodynamic conditions during the 5 min period that corresponds to the rocket downleg descent from 700 to

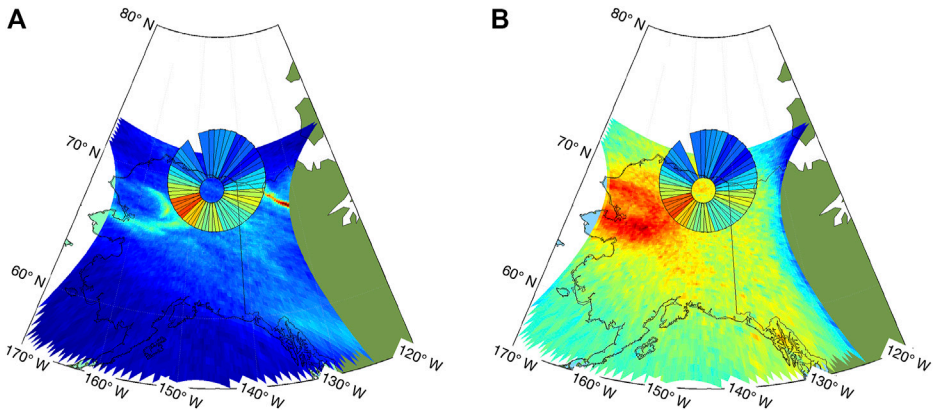


FIGURE 6 | VISIONS ENA images (dial plots) superimposed on VISIONS narrowband auroral emission images of 391.4 nm [panel **(A)**] and 630.0 nm [panel **(B)**] show strong correlation of projected ENA source with soft electron precipitation at ~ t + 360 s. The colorscale image represents the auroral emissions measured onboard the rocket and projected to 110 (left) and 200 (right) km altitude, analogous to **Figures 2**, **4**. The pixelated "dial plot" represents the geographical projection of the look direction for one of the "downlooking" MILENA M1 sectors as the rocket completes nearly a full spin. In each case the pixel is shaded with the number of counts that the detector received when looking in that direction. This is another way of representing the data of **Figure 4**, but this time allowing direct comparison between ENA locations and optical emission locations. Several features are evident: 1) there is a strong north-south gradient in the ENA emissions, as might be expected if ENAs are being produced south of the rocket location and the rocket is near the edge of the poleward boundary of the auroral zone; 2) There is a strong enhancement of the ENA signature to the southwest, where there are both bright 391.4 and 630.0 nm optical emissions; 3) In contrast, an even brighter 391.4 nm signature to the east produces only a weak flux of ENAs. This is consistent with soft precipitation being more efficient at producing escaping TAIs and associated ENAs, given the higher altitude at which their energy is deposited.

100 km. With all these issues in mind, this figure does show that the horizontal ENAs observed by VISIONS peak in the 300–400 km altitude range, consistent with our thin shell tracing to first order.

For an initial analysis, we thus assume that the upgoing ENAs observed by VISIONS come from a thin shell at 375 km. While the data in **Figure 5** show a range in altitudes where peak ENAs are observed, small differences in the assumed "thin shell" altitude do not substantially alter the backtracing, given the inherently low resolution of the ENA imager and the significant effects of ENA-neutral scattering. We backtrace the ENAs using straight-line trajectories (valid for energies significantly above escape velocity) and locate the point at which that backtraced trajectory intersects a 375 km altitude spherical surface.

The result is shown for a particular time in the flight (t + 360 s) in **Figure 6**. It is important to note that we do not have directly measured ion distributions on the flux tubes where the highest ENA counts seem to be coming from. The RAI images from **Figure 2** are shown again, with 391.4 nm on the left, and 630.0 nm on the right. Superimposed on these is a "dial plot" showing the projections of the M2 pixel "1" count rates onto the 375 km spherical surface. Color is used to indicate the count rate in each spin sector. The dial plots in the two panels are identical—they are repeated for clarity. In both panels, the strongest ENA emissions show a strong overlap with the region of strong auroral emissions (especially 630.0 nm) to the southwest of the rocket. There is also a slight enhancement in the ENA count rate associated with the narrow but intense 391.4 emissions to the east of the rocket. The asymmetric shape of the ENA pixels when projected to the reference altitude result from the fact that the payload is aligned near the magnetic field, which has a finite inclination.

4 DISCUSSION

The only other low energy (<1 keV) ENA observations near the nighttime auroral zone below 1,000 km come from the IMAGE LENA instrument (Moore et al., 2000), the PIPPI instrument on Astrid (Barabash et al., 1997), and the MINI-ME instrument on FASTSAT (Rowland et al., 2011). IMAGE LENA saw an omnipresent source of low energy ENAs of broad angular extent, including some that were coming from the nadir (Wilson et al., 2004). LENA did not have energy discrimination capability, and may have been susceptible to angular scattering of the rammed signal which tends to broaden the observed ENA signal. This featureless "sea" of low energy ENAs was also likely dominated by proton precipitation and dayside ENA emissions, since there were few IMAGE perigee passes during or immediately following an auroral substorm. PIPPI saw structured ENAs between 0.1 and 13 keV, with ENA "pitch angles" between 110° and 140° [C:son Brandt et al., 2001]. These emissions were at latitudes above the auroral zone, however. At higher altitudes, missions such as TWINS have seen higher energy (2 keV to tens of keV) "low altitude emissions" or LAEs [Bazell et al., 2010] coming from predominantly "ENA albedo" or backsplash from precipitating magnetospheric protons [e.g., Torr et al. (1974); Kozyra et al. (1982)]. These emissions have been observed primarily at near-horizontal ENA pitch angles, due to the required observing geometry.

Three main aspects of the VISIONS results are new and warrant further examination: 1) the predominance of upgoing

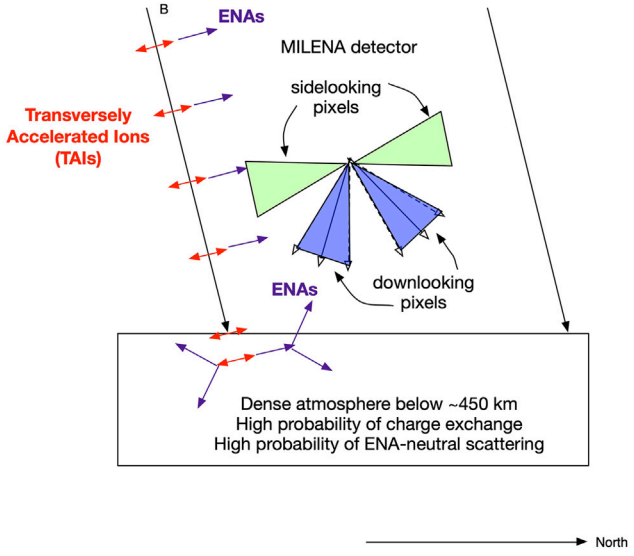


FIGURE 7 | This figure represents a typical viewing geometry for the VISIONS MILENA detectors. There are six detector sectors, each 30° wide, with 30° gaps between, Over half a rocket spin, these sectors sweep out the whole sky (with gaps). The alignment of the rocket (and instrument) axis with the magnetic field is shown. The green pixels view "horizontally" (perpendicular to B) while the blue pixels look "down" (to see upgoing ENAs). Indicated with red arrows are notional ions with near-90° pitch angles, as might be produced by transverse acceleration processes. Purple arrows indicate ENAs produced in charge exchange reactions, and also (below 450 km, where the ENA mean free path is relatively short) secondary ENAs produced by ENA-neutral scattering. Upgoing ENAs may be produced by ENA-neutral scattering below the rocket. For rocket measurements above the dense atmosphere, only the ENAs that are produced in the thin-target regime above ~450 km and the ones produced below 450 km that travel almost vertically (to minimize their attenuation) can be observed. The upgoing ones are primarily the result of significant ENA-neutral scattering.

ENAs in the auroral zone; 2) the altitudinal dependence of the ENAs in the polar cap; and 3) the spatial localization of the ENA emissions and its strong association with 630.0 nm auroral emissions.

4.1 Upgoing ENAs

Since the charge-exchange reaction is nearly conservative in momentum and energy, upgoing ENAs could be produced by upgoing ions with pitch angles near 180°. Since the upgoing ENAs observed by VISIONS are at energies of 50 eV and higher, this would require an energization mechanism active below 400 km (the lowest altitude on the upleg where we have MILENA data) that could energize ions to 50 eV with pitch angles >135°. Previous observations of TAIs [e.g., Kintner et al., 1996; Lynch et al., 1996] at low altitudes show distributions that are much more strongly peaked near 90°. In principle, a very strong energization mechanism could produce a significant upgoing ENA flux that was itself a small fraction of the 90° energization, with the low-altitude 90° ENAs not observable due to the experiment geometry and/or attenuation in the neutral atmosphere. We do not deem this explanation likely to be able to explain the VISIONS results.

The other explanations for strong fluxes of upgoing ENAs all involve ENA-neutral scattering. In these scenarios, a near-90° TAI (transversely accelerated ion) undergoes charge exchange, resulting in a near-90° "pitch angle" ENA. For this to result in a strong upgoing ENA flux, this ENA must scatter off of a cold neutral atom (or undergo multiple scattering) in the thermosphere. **Figure 7** shows the basic geometry, with magnetic field lines indicated in black, energetic ions schematically shown as red arrows, and purple arrows indicating ENAs. The rectangle at the bottom of the figure shows schematically the atmosphere below 400 km, which is "optically thick" and in which ENA-neutral scattering is likely. Four of the six MILENA pixels are also shown, for reference.

There are at least five ways in which this can happen: 1) local ENA-neutral scattering in the "optically thin" region above 400 km; 2) backscatter of "near 90°" ENAs that happen to have downward vertical velocities due to the magnetic declination; 3) albedo ENA generation from precipitating multi-keV ions (either plasma sheet ions or conjugate transversely accelerated/outflowing ions from the other hemisphere); 4) low altitude acceleration—when the TAIs are formed below 400 km when the mean free path is short; or 5) a "pressure cooker" scenario after Gorney et al., 1985.

In the local scattering scenario, the "near-90° pitch angle" ENA scatters off a cold neutral atom at high altitude (above 400 km), and then sometimes travels upwards where it can be detected by MILENA. This scenario is not very consistent with the fact that mean free paths above 400 km are on the order of 100 km or longer. There would have to be incredibly intense ion fluxes to produce the observed ENA fluxes in this scenario.

In the backscatter scenario, there will be a population of "downward" ENAs traveling down to the exobase, for certain gyrophases of the parent ion at the moment of charge exchange. Due to the finite magnetic declination (nearly 16° for VISIONS), "90° pitch angle" ENAs may have a range of vertical velocity angles relative to zenith/nadir, corresponding to ± 16° depending on the parent ion gyrophase. Some fraction of the ENAs thus produced will travel vertically downward (although at a shallow angle) and may then scatter off the dense atmosphere below the parent ion population. Some fraction of those scattered ENAs may then backscatter upwards, to be viewed by the VISIONS MILENA instrument. Due to the small declination, we would expect ENAs to preferentially be generated south of auroral features, and separated at some distance (a few 100 km away). Initial indications are that the northern edge of the auroral feature lines up well with the northern edge of the ENA emissions, but this will require more detailed analysis to rule out.

In the albedo ENA scenario (Roelof 1997) the precipitating energetic ions (6–8 keV) shown in **Figure 3** would generate ENAs as they (mostly) charge exchange near the exobase. The VISIONS *in situ* instruments recorded these multi-keV ions throughout the flight, with an intensification both in energy and flux right at the polar cap boundary in the region of transversely accelerated ions. We have no direct measurements regarding their presence or fluxes away from the rocket trajectory, but the H-β channel of the RAI (which was designed to measure emissions associated with proton precipitation—see, e.g., Søraas et al. [1996], Synnes et al.

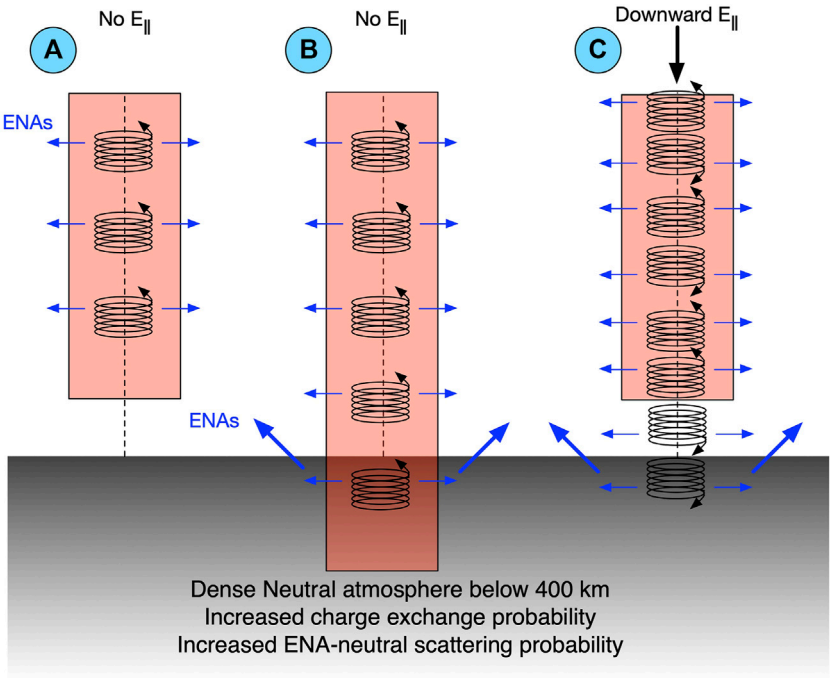


FIGURE 8 | This figure presents three scenarios for ENA production. In each case, the gray shaded region represents the dense neutral atmosphere below the exobase, where the ENA mean free path becomes short compared to the atmospheric scale height. The shaded red boxes are meant to indicate a notional altitude region where significant transverse ion acceleration is ongoing, and the helical symbols and blue arrows represent transverse ions and primary and secondary ENAs. The three panels show: **(A)** high altitude acceleration that does not extend into the dense atmosphere produces primarily horizontal ENAs as the mirror force pushes accelerated ions out. To the extent that the acceleration produces ions with slightly downgoing (but near 90) pitch angles, those ions will reach the dense atmosphere and can produce upgoing ENAs. **(B)** if the acceleration region extends to low-altitude, the acceleration produces mainly upgoing ENAs, and **(C)** High altitude parallel electric field pressure cooker reflects ions back down to the exobase, amplifying the weak upgoing signal from scenario "A".

[1998]) saw very low emissions during the flight (down to the sensitivity of the imager, channel, about 200 R) when the RAI was pointed to the nadir. At the end of the flight, the RAI viewed the limb, and limb brightening raised the H-beta signal to ~0.5 erg/cm^2/s on average, with a slightly brighter emission of ~1 erg/cm^2/s to the southwest, in a similar direction to the region of ENA production and strong 630.0 nm emission. In contrast, the electron fluxes in that region are on the order of 20 erg/cm^2/s.

This would imply that to the extent that the precipitating ions are present and generating ENAs, those ENAs would not be expected to be strongly structured, spatially. On the other hand, Synnes et al. (1998) demonstrated that incoming protons with energies of a few keV might be expected to "smear out" through charge exchange over spatial scales of a few 100 km, with up to 10% of incoming protons returning back to space as outgoing ENAs. We continue to model this effect to determine its relative contribution to the other scenarios, but believe that the highly spatially structured ENA emissions, with strong boundaries coincident with 630.0 nm emissions observed by MILENA cannot be explained by this effect.

Alternately, we could be seeing ENAs from lower energy TAIs that were energized at higher altitudes above the conjugate hemisphere, and which then propagate to the northern hemisphere, where they appear as predominantly downgoing energetic ions (with some change in pitch angle closer to 90° due to the magnetic mirror force). In this case, the ENAs we see could be primarily generated from ions that were accelerated over a relatively long pathlength in the conjugate hemisphere, up to several 100 eV or 1 keV, and which then mirror, precipitate, or charge exchange in the northern hemisphere. These ions could generate ENAs via charge exchange which would then be scattered from atmospheric neutrals up into the VISIONS detector.

This scenario is consistent with the local, *in situ* observations of primarily downgoing and transverse energetic ions at the polar cap boundary. The main problem with it is the inferred potential drop of ~1 keV above the spacecraft where the TAIs are locally observed by VISIONS [Clemmons et al., 2015]. If ions from the conjugate hemisphere fell through this potential drop, they would have a minimum energy of 1 keV, and a maximum energy larger than this. In addition, the bounce time for a keV electron near the polar cap boundary would likely be tens of minutes. Given the time it is expected to take for the initial heating process and upwelling/upflow of the low energy ions to the high-altitude wave-particle acceleration region, there is likely not enough time for these ions to be able to reach the northern hemisphere if they were accelerated in the southern hemisphere.

Figure 8 shows the basic geometry for the "standard picture" (panel A—ENAs generated mostly horizontally in optically thin

region), the "low altitude acceleration" scenario (panel B—wave acceleration region extends into region of dense neutral atmosphere) and the "pressure cooker" scenario, which is described in more detail, below.

The low altitude acceleration scenario would hold if the waves that are presumed to accelerate the TAIs extend to low altitudes (below 400 km, where the mean free path is short). In this case, the neutral density is high enough at these altitudes that any generated ENA would be expected to scatter one or more times before ascending to the optically thin region or being attenuated by the atmosphere to the side or below its generation point. This scenario suffers from the problem that there is a narrow "sweet spot" or range of altitudes where the neutral density is high enough to produce significant ENAs and ENA-neutral scatter without too much attenuation, as well as permitting efficient transverse acceleration by (e.g., BBELF, broadband Extremely Low Frequency) waves, where the wave frequency is several orders of magnitude higher than the ion-neutral collision frequency. Too low an altitude, and the transverse acceleration is not effective, too high and the ENA production and scattering cannot explain the observed upgoing ENAs.

With O+ gyrofrequencies of ~30–40 Hz at VISIONS altitudes, this condition is only satisfied around 350 km altitude (where the ion-neutral collision frequency falls to about 1 Hz). In this scenario, it is possible that the region of wave acceleration would extend to higher altitudes as well, but the ions would have to gain at least 50 eV between about 350 km and where they are observed by MILENA (as low as 400 km). Whalen et al. (1978) did observe a case where TAIs were seen with energies up to 533 eV below 428 km, but the peak in the pitch angle distribution at these altitudes was also just about 90°, suggesting that the particles were either locally accelerated, or near their mirror points after traveling down the field line from a higher altitude acceleration region.

Typical observations of BBELF waves associated with TAIs are generally limited to altitudes above about 600 km [e.g., Arnoldy et al., 1992] although this may be due to the fact that rocket measurements with the necessary instrumentation to observe TAIs typically encounter regions of TAIs and BBELF above 500 km. Indeed, VISIONS only measured intense BBELF waves near its apogee above about 700 km presumably because this is the only location along the trajectory where the payload encountered the localized region of TAIs. The VISIONS rockets did observe intense VLF waves along their entire trajectory (see **Figure 2**) which were associated with the broad regions of energetic electron precipitation essentially present during the entire flight. For low-altitude acceleration, one would expect to see transversely accelerated ions with a range of pitch angles, including upgoing ions. The actual transversely accelerated ions that VISIONS observed near the polar cap boundary were much more intense in the downgoing hemisphere relative to the upgoing hemisphere, suggesting that there was not much acceleration going on below the rocket in that region [Clemmons et al., 2014], although again, we do not have direct measurements of the region that seems to have produced the majority of the ENAs.

In the pressure cooker scenario, first proposed by Gorney et al. (1985), a high-altitude parallel electric field, pointing downwards, reflects upgoing ions back down towards the magnetic mirror point. In this model, the region where waves can transversely accelerate the ions gets traversed multiple times as ions bounce back and forth between the high-altitude potential drop and the magnetic mirror point. This continues until either the ion charge exchanges or gains enough energy to overcome the potential barrier and escapes (or until time variations in the electric potential remove the "lid" from the pressure cooker). This scenario decouples the wave-particle interaction region from the ENA production region, and can *in principle* explain the VISIONS observations. The analysis of these observations is as yet incomplete, and we have not been able to test whether a pressure cooker scenario exists in the remotely-sensed ENA production region.

It will be important for future studies to determine under what conditions and over how large a spatiotemporal extent pressure cooker geometries may exist, as they can dramatically affect the total ion outflow rate and characteristic energy of the outflowing ions.

More detailed modeling is needed in future to determine if this process is in fact operating during the VISIONS launch. The *in situ* measurements do suggest that the pressure cooker is operational in the region of ion acceleration that VISIONS directly flew through [Clemmons et al., 2014]—the high energy precipitating ion population above about 5 keV shown in **Figure 2** narrows and intensifies in the region of transverse ion acceleration, implying a downwards parallel electric field above the rocket. This implies that VISIONS flew through a local pressure cooker, though it is not likely the same region that produced the majority of the ENAs seen by the MILENA instrument.

4.2 Altitudinal Dependence of ENAs Observed in the Polar Cap

Synnes et al. (1998) modeled escaping ENA production as a function of altitude for the case of energetic precipitating protons. For precipitating protons of 1–20 keV, similar to those observed by VISIONS, and for magnetic tilt angle between 10 and 20° (matching the VISIONS geometry), their model predicts a broad altitude range of production for ENAs that eventually escape. For 2 keV precipitating protons, the predicted escaping ENA production altitude distribution had a sharp ledge near 250 km, and a two-peak structure, with maxima near 285 and 560 km. The double-peak structure was explained as due to efficient charge exchange at high altitudes producing the high altitude peak, with many of the ENAs thus produced traveling downwards, until they are re-ionized, scattered in pitch angle, and then produce additional ENAs at lower altitude. At 20 keV energy for the precipitating protons, their model predicts a single peak near 340 km in the altitude profile of escaping ENAs, with FWHM ~300 km. C:son Brandt et al. (2001) modeled the ENA production altitude for 100 eV ions as a function of ion "injection" height, and showed that for ions injected near 400 km, the ENA emissions should come from a thin altitudinal layer, about 100 km wide.

VISIONS traversed the altitude range from below the exobase up to 750 km, returning the first altitude-resolved low energy

ENA measurements in this region. The horizontal ENA fluxes as a function of altitude exhibit a single broad maximum at about 350 km. The VISIONS altitudinal profile is single-peaked, and broader (FWHM is >500 km) than either the idealized model of C:son Brandt et al. (2001) or the model of Synnes et al. (1998). This is likely due to two effects: broader pitch-angle distributions of the energetic ions, and subsequent ENA-neutral scattering. A broader pitch-angle distribution would tend to produce more ENAs at higher altitudes, compared to their modeled cases of 180° pitch angle. Subsequent ENA-neutral scattering following the initial charge exchange would tend to broaden the altitude profile and extend it to lower altitudes, until the ENA mean free path becomes significantly shorter than the distance to the rocket payload (in **Figure 5**, this occurs somewhere between 300 and 400 km). The fact that there are significant horizontal ENAs detected at lower altitudes (below typical mirror heights) implies that the ENA-neutral scattering process is important. This lends further support to the hypothesis that the ions and neutrals are interacting at low altitudes.

In addition to providing some validation for the use of the "thin shell" approximation to trace the ENA emissions to potential source regions, the altitude dependence of the ENA emissions provides important constraints on the energetic ion populations. For example, the energy spectra of the horizontal ENAs detected in the "optically thin" altitude range above 400 km should closely track the energy spectra of the parent ions, since there is very little ENA-neutral scattering at these altitudes over the few 100 km separating the source region from the rocket. The ENAs exhibit an approximate power law spectrum with slope −0.3. VISIONS ion measurements near the polar cap boundary along the rocket track are consistent with this slope in the energy range 50–500 eV [Clemmons et al., 2014]. The horizontal ENAs at high altitude should be more directly proportional to the outflowing ion flux, especially at energies above that of any hypothesized "lid" to the pressure cooker. In contrast, the upgoing ENAs observed earlier in the flight and the low-altitude horizontal ENAs are indicative of the total energetic ion population (though not simply proportional, due to the strong effects of ENA-neutral scattering).

4.3 Total Ion Outflow Over the Sampled Region

To estimate the ion outflow associated with this event, we assume the "horizontal" ENAs detected by MILENA in the polar cap have not undergone any scattering or attenuation at altitudes above 500 km (since the horizontal distance is significantly less than the ~1,000 km mean free path), and that the energetic ions that give rise to these ENAs have pitch angles near 90°. If we assume the horizontal scale size of the ENA producing region is ~200 km (based on the width of the 630.0 nm auroral feature), and that the ENAs are oxygen (O+-O charge exchange cross section at 50 eV approximately 24×10^{-16} cm^2 (Lindsay and Stebbings, 2005)), and that the O density at 500 km is ~6×10^6 cm^3, based on the NRL MSIS-E-90 Atm model (Picone et al., 2002), we can estimate the ion flux that produces the horizontal ENAs seen by VISIONS, using the "optically thin" approximation (Roelof, 1997):

$$j_{ena} = \int dl\, j_{ion}\, \sigma\, n \quad (1)$$

where σ is the charge exchange cross section, n is the neutral density (assumed pure O), and j_{ena} and j_{ion} are the ENA and ion fluxes, respectively, and the integral is over the line of sight between the ENA source region and the observer (assume $j_{ion} = 0$ outside of this region).

Based on the MILENA calibrations, the peak count rate of 5,000 counts/s corresponds to an ENA flux of ~7.5×10^7 neutrals/s/cm^2/sr. This ENA flux at 50 eV can be directly compared to that reported from Astrid measurements in the polar cap by C:son Brandt et al. (2000). Astrid saw ENA fluxes between 0.1 and 13 keV of 10^6 neutrals/s/cm^2/sr.

Taking into account the presumed ENA source region size and the mean free path for charge exchange in **Eq. 1**, we estimate an average ion flux in the source region (at 50 eV) of 2.6×10^8 ions/s cm^2/sr/dE/E. Assuming the parent ions have pitch angles within ± 15° of 90, this results in an estimate for the total ion flux of 5.5×10^8 ions/s/cm^2, similar to that previously reported by other researchers [e.g., Yau et al., 1983], and in line with the superposed epoch analysis of Wilson et al. (2004) as well as the FAST observations reported in Tung et al. (2001).

This inferred ion flux is ~×100 stronger than the more modest fluxes of transversely accelerated ions observed by VISIONS at the polar cap boundary [Clemmons et al., 2015]. This implies that the observed ENAs cannot be accounted for by the directly measured ions encountered by VISIONS. Instead, the majority of the ENA production was likely occurring to the southwest of the rocket, in the region not directly sampled by the *in situ* measurements. When integrated over the presumed ion source region, and over the ~60 min timescales measured in Wilson et al. (2004), this corresponds to ~20 kg of outflowing oxygen ions. This estimate is a lower limit, because we have not included ions at other pitch angles or other energies.

4.4 Spatial Localization of ENAs and Strong Correlation With 630.0 nm Emissions

The VISIONS MILENA data demonstrate that the low energy ENAs (50 eV) are strongly structured in longitude and latitude. The majority of these ENAs appear to emanate from a region to the southwest of the rocket trajectory. This is also the region where there are large-scale, intense auroral emissions, including strong 630.0 nm emissions. As described above, the IMAGE LENA results of Wilson et al. [2004] provided evidence consistent with a spatially broad, time varying (predominantly diurnal, but also depending on geomagnetic activity) background low energy ENA signal (including upgoing ENAs) at high latitudes. It is important to understand why these results seem so different. The differences are twofold: 1) higher resolution of VISIONS; and 2) targeted launch of VISIONS into an auroral substorm.

VISIONS had a horizontal velocity of 1–2 km/s, as opposed to the IMAGE perigee velocities of >8 km/s. Increasing the "dwell time" in the region of interest from 2 to 3 min (IMAGE) to ~15 min allowed VISIONS to sample the temporal variation of ion outflow over a significant fraction of the substorm life-cycle.

This slow velocity also increased the ENA image spatial and temporal resolution—MILENA produced a full sky image every second (every 1.5 km along track), and full energy distributions in 3-D every 16 s (24 km along track), compared to IMAGE, which had a 2-min spin period, and produced full-sky images every ~1,000 km along track near perigee. VISIONS also had the capability to resolve energies of the incoming ENAs, which IMAGE LENA lacked. This allows VISIONS to discriminate between, e.g., 50 eV ENAs and the lower energy "rammed" population, which may produce counts with significant angular scatter in the instrument.

Regarding the conditions under which VISIONS made its measurements—VISIONS was launched into an active aurora ~30 min after substorm onset. While IMAGE made ~130 perigee passes over the 3 months of data described in Wilson et al. (2004), these ranged over local times from dawn-dusk to noon-midnight. Also, while they were all in the local (southern) winter, each perigee pass was only in the nightside auroral zone for 2–3 min, every 14.2 h. This low duty cycle made it very unlikely for IMAGE LENA to directly observe substorm outflow near perigee within 30 min after onset. Thus, the IMAGE LENA data represents a climatology of the hot oxygen environment during quiet conditions, rather than representing the substorm response.

The main limitation of the thin shell tracing is that, due to scattering effects, it may produce significant errors in quantitatively estimating ion flux from measured upgoing ENA flux, and it does not provide detailed knowledge of the ion populations that produced the ENAs, primarily due to ENA-neutral scattering. Nonetheless, it is extremely useful in providing the first high resolution localization of the regions where significant ion acceleration is occurring at low altitudes in the ETR. Future efforts will need to self-consistently model ion and neutral populations to better understand the limitations and accuracies of the thin-shell approach, and improve our techniques for obtaining ion flux information from the ENA measurements.

4.5 Summary

The VISIONS sounding rocket provided the first height-resolved, high-resolution measurements of low energy neutral atoms (<1 keV) associated with transversely accelerated ions in the nightside auroral zone following substorm onset. The ENA emissions were most intense in the auroral zone, and were dominated there by upgoing ENAs, indicating a strong interaction between the energetic ions and the neutral atmosphere. The ENAs exhibited a strong altitudinal dependence, maximizing around 400 km "Thin shell" mapping of the ENAs to an idealized source region at 375 km revealed a strong association between 50 eV ENA emission and regions of strong 630.0 nm auroral emissions. The region of ENA production was well structured and had a long-term coherence over the ~10 min of observation. The estimated ion flux (for the component that leads to charge exchange and ENA generation) from the region of strong ENA emissions was $\sim 5.5 \times 10^8$ ions/s cm^2, and the ENA energy spectrum is consistent with a power-law with slope −0.3.

The *in situ* measurements detected a narrow region of transversely associated ions near 700 km altitude that were precisely observed in a localized region of enhanced broadband ELF waves suggesting that strong wave-particle interactions near the O^+ gyro frequency may have been operating to accelerate the oxygen ions.

The observations suggest that there exist large (~200 km horizontally) regions of efficient wave particle heating up to a few keV. Further work is needed to model the ion energization observed by VISIONS, and to produce simulated ENA images for comparison, as well as to model the ion acceleration and propagation to assess how much of the ion population ends up escaping to high altitudes, and how much is lost to charge exchange and precipitation.

ADDITIONAL REQUIREMENTS

For additional requirements for specific article types and further information please refer to Author Guidelines.

DATA AVAILABILITY STATEMENT

The raw data supporting the conclusions of this article can be downloaded from: https://doi.org/10.5281/zenodo.6326353.

AUTHOR CONTRIBUTIONS

All authors listed have made a substantial, direct, and intellectual contribution to the work and approved it for publication. DR led the thin-shell backtracing analysis. JK, MC, and JL provided the MILENA data. RP and JK provided the FTP data. JH provided the RAI data.

FUNDING

The authors would like to acknowledge funding support from the NASA Heliophysics Geospace SR&T/Low Cost Access to Space Program, including NASA Grant# NNX09AI51G, and NASA grant NNH14ZDA001N-HSR. DR and JK were supported by the NASA competed Internal Science Funding Model (ISFM).

ACKNOWLEDGMENTS

The authors would also like to acknowledge the contributions of the Sounding Rocket Project Office, the NSROC sounding rocket team, and the UAF Poker Flat Research Range. In addition, the authors would like to acknowledge particularly useful conversations with Alex Glocer and Katherine Garcia-Sage at NASA GSFC, Rick Chappell at Vanderbilt, Thomas Moore (retired NASA GSFC), and Matthew Zettergren (Embry-Riddle Aeronautical University).

REFERENCES

Arnoldy, R. L., Lynch, K. A., Kintner, P. M., Vago, J., Chesney, S., Moore, T. E., et al. (1992). Bursts of Transverse Ion Acceleration at Rocket Altitudes. *Geophys. Res. Lett.* 19 (4), 413–416. doi:10.1029/92gl00091

Barabash, S., Brandt, s., Norberg, R. Lundin, O. E. C., Mauk, C. J. C. B. H., and Koskinen, H. (1997). Energetic Neutral Atom Imaging by the Astrid Micro Satellite. *Adv. Space Res.* 20. doi:10.1016/s0273-1177(97)00560-7

Bazell, D., Roelof, E. C., Sotirelis, T., Brandt, P. C., Nair, H., Valek, P., et al. (2010). Comparison of TWINS Images of Low-Altitude Emission of Energetic Neutral Atoms with DMSP Precipitating Ion Fluxes. *J. Geophys. Res.* 115, a–n. doi:10.1029/2010JA015644

Brandt, P., Barabash, S., Roelof, E. C., Chase, C. J., and Wilson, G. R. (2000). Energetic Neutral Atom Imaging at Low (≤10 keV) Energies from Astrid: Observations and Simulations. *J. Atmos. Solar-Terrestrial Phys.* 62, 901–909. doi:10.1016/s1364-6826(00)00040-7

Brandt, P. C., Barabash, S., Roelof, E. C., and Chase, C. J. (2001). Energetic Neutral Atom Imaging at Low Altitudes from the Swedish Microsatellite Astrid: Observations at Low (≤10 keV) Energies. *J. Geophys. Res.* 106 (A11), 24663–24674. doi:10.1029/2000ja900119

Carlson, C. W., Curtis, D. W., Paschmann, G., and Michael, W. (1983). An Instrument for Rapidly Measuring Plasma Distribution Functions with High Resolution. *Adv. Space Res.* 2, 67.

Chappell, C. R., Moore, T. E., and Waite, J. H. (1987). The Ionosphere as a Fully Adequate Source of Plasma for the Earth's Magnetosphere. *J. Geophys. Res.* 92 (A6), 5896–5910. doi:10.1029/JA092iA06p05896

Chaston, C., Bonnell, J., Carlson, C., McFadden, J., Ergun, R., Strangeway, R., et al. (2004). Auroral Ion Acceleration in Dispersive Alfvén Waves. *J. Geophys. Res.* 109 (A04205). doi:10.1029/2003ja010053

Clemmons (2014) Paper to Be Submitted Describing VISIONS Pressure Cooker *In Situ* Measurements

Collier, M. R., Chornay, D., Clemmons, J., Keller, J. W., Klenzing, J., Kujawski, J., et al. (2015). VISIONS Remote Observations of a Spatially-Structured Filamentary Source of Energetic Neutral Atoms Near the Polar Cap Boundary during an Auroral Substorm. *Adv. Space Res.* 56, 2097–2105. doi:10.1016/j.asr.2015.08.010

Fok, M.-C., Moore, T. E., Wilson, G. R., Perez, J. D., Zhang, X. X., Brandt, P. C. S., et al. (2003). Global ENA Image Simulations. *Space Sci. Rev.* 109, 77–103. doi:10.1023/b:spac.0000007514.56380.fd

Fuselier, S. A., Ghielmetti, A. G., Moore, T. E., Collier, M. R., Quinn, J. M., Wilson, G. R., et al. (2001). Ion Outflow Observed by IMAGE: Implications for Source Regions and Heating Mechanisms. *Geophys. Res. Lett.* 28 (6), 1163–1166. doi:10.1029/2000gl012450

Glocer, A., Toth, G., Gombosi, T., and Welling, D. (2009). Modeling Ionospheric Outflows and Their Impact on the Magnetosphere, Initial Results. *J. Geophys. Res.* 114 (A5), A05216. doi:10.1029/2009ja014053

Glocer, A., Welling, D., Chappell, C. R., Toth, G., Fok, M. C., Komar, C., et al. (2020). A Case Study on the Origin of Near-Earth Plasma. *J. Geophys. Res. Space Phys.* 125 (11), 1–19. doi:10.1029/2020JA028205

Gloeckler, G., and Hamilton, D. C. (19871987). AMPTE Ion Composition Results. *Phys. Scr.* T18, 73–84. Number T18. doi:10.1088/0031-8949/1987/T18/009

Gorney, D. J., Chiu, Y. T., and Croley, D. R. (1985). Trapping of Ion Conics by Downward Parallel Electric fields. *J. Geophys. Res.* 90, 4205. doi:10.1029/ja090ia05p04205

Haaland, S., Eriksson, A., Engwall, E., Lybekk, B., Nilsson, H., Pedersen, A., et al. (2012a). Estimating the Capture and Loss of Cold Plasma from Ionospheric Outflow. *J. Geophys. Res.* 117, a–n. doi:10.1029/2012JA017679

Haaland, S., Li, K., Eriksson, A., André, M., Engwall, E., FöRster, M., et al. (2012b). "Cold Ion Outflow as a Source of Plasma for the Magnetosphere," in *Dynamics of the Earth's Radiation Belts and Inner Magnetosphere*. Editors D. Summers, I. R. Mann, D. N. Baker, and M. Schulz, and, 341–354. doi:10.1029/2012GM001317

Hecht, J. H., Strickland, D. J., and Conde, M. G. (2006). The Application of Ground-Based Optical Techniques for Inferring Electron Energy Deposition and Composition Change during Auroral Precipitation Events. *J. Atmos. Solar-Terrestrial Phys.* 68, 1502–1519. doi:10.1016/j.jastp.2005.06.022

Hecht (2014). *Paper to Be Submitted Describing VISIONS RAI Observations of O/N2 Depletions*.

Huddleston, M. M., Chappell, C. R., Delcourt, D. C., Moore, T. E., Giles, B. L., and Chandler, M. O. (2005). An Examination of the Process and Magnitude of Ionospheric Plasma Supply to the Magnetosphere. *J. Geophys. Res.* 110 (A12), A12202. doi:10.1029/2004JA010401

Jensen, M. D., and Baker, K. D. (1992). Measuring Ionospheric Electron Density Using the Plasma Frequency Probe. *J. Spacecraft Rockets* 29 (1), 91–95. doi:10.2514/3.26318

Kindel, J. M., and Kennel, C. F. (1971). Topside Current Instabilities. *J. Geophys. Res.* 76, 13.

Kintner, P. M., Bonnell, J., Arnoldy, R., Lynch, K., Pollock, C., and Moore, T. (1996). SCIFER-transverse Ion Acceleration and Plasma Waves. *Geophys. Res. Lett.* 23 (14), 1873–1876. doi:10.1029/96gl01863

Kozyra, J. U., Cravens, T. E., and Nagy, A. F. (1982). Energetic O+ Precipitation. *J. Geophys. Res.* 87, 2481.

Lindsay, B. G., and Stebbings, R. F. (2005). Charge Transfer Cross Sections for Energetic Neutral Atom Data Analysis. *J. Geophys. Res.* 110, A12213. doi:10.1029/2005JA011298

Lynch, K. A., Arnoldy, R. L., Kintner, P. M., and Bonnell, J. (1996). The AMICIST Auroral Sounding Rocket: A Comparison of Transverse Ion Acceleration Mechanisms. *Geophys. Res. Lett.* 23 (23), 3293–3296. doi:10.1029/96gl02688

Moore, T., Chandler, M., Pollock, C., Reasoner, D., Arnoldy, R., Austin, B., et al. (1996). Plasma Heating and Flow in an Auroral Arc. *J. Geophys. Res.* 101 (A3), 579. doi:10.1029/95ja03154

Moore, T. E., et al. (2000). "The Low Energy Neutral Atom Imager for IMAGE," in *The IMAGE Mission*. Editor J. L. Burch (Dordrecht, Netherlands: Kluwer Academic Publishers).

Picone, J. M., Hedin, A. E., Drob, D. P., and Aikin, A. C. (2002). NRLMSISE-00 Empirical Model of the Atmosphere: Statistical Comparisons and Scientific Issues. *J. Geophys. Res.* 107, 151468–151471. doi:10.1029/2002JA009430

Roelof, E. C. (1987). Energetic Neutral Atom Image of a Storm-Time Ring Current. *Geophys. Res. Lett.* 14, 652–655. doi:10.1029/gl014i006p00652

Roelof, E. C. (1997). Energetic Neutral Atom Imaging of Magnetospheric Ions from High- and Low-Altitude Spacecraft. *Adv. Space Res.* 20, 341–350. doi:10.1016/s0273-1177(97)00689-3

Roelof, E. C., and Skinner, A. J. (2000). Extraction of Ion Distributions from Magnetospheric ENA and EUV Images. *Space Sci. Rev.* 91, 437–459. doi:10.1007/978-94-011-4233-5_15

Rowland, D. E. (2011). Science of Opportunity: Heliophysics on the FASTSAT Mission and STP-S26. *IEEE Aerospace Conf. Proc.* 2011. March 5-12. doi:10.1109/aero.2011.5747235

Shelley, E. G., Johnson, R. G., and Sharp, R. D. (1972). Satellite Observations of Energetic Heavy Ions during a Geomagnetic Storm. *J. Geophys. Res.* 77 (31), 6104–6110. doi:10.1029/JA077i031p06104

Söraas, F., Lindalen, H. R., Måseide, K., Egeland, A., Sten, T. A., and Evans, D. S. (1974). Proton Precipitation and the Hβ Emission in a Postbreakup Auroral Glow. *J. Geophys. Res.* 79, 1851–1859. doi:10.1029/ja079i013p01851

Synnes, S. A., Søraas, F., and Hansen, J. P. (1998). Monte-Carlo Simulations of Proton aurora. *J. Atmos. Solar-Terrestrial Phys.* 60, 1695–1705.

Torr, M. R., Walker, J. C. G., and Torr, D. G. (1974). Escape of Fast Oxygen from the Atmosphere during Geomagnetic Storms. *J. Geophys. Res.* 79, 5267–5271. doi:10.1029/ja079i034p05267

Tung, Y.-K., Carlson, C. W., McFadden, J. P., Klumpar, D. M., Parks, G. K., Peria, W. J., et al. (2001). Auroral Polar Cap Boundary Ion Conic Outflow Observed on FAST. *J. Geophys. Res.* 106, 3603–3614. doi:10.1029/2000ja900115

Welling, D. T., Jordanova, V. K., Glocer, A., Toth, G., Liemohn, M. W., and Weimer, D. R. (2015). The Two-way Relationship between Ionospheric Outflow and the Ring Current. *J. Geophys. Res. Space Phys.* 120, 4338–4353. doi:10.1002/2015JA021231

Whalen, B. A., Bernstein, W., and Daly, P. W. (1978). Low-altitude Acceleration of Ionospheric Ions. *Geophys. Res. Lett.* 5, 1. doi:10.1029/gl005i001p00055

Wilson, G., Moore, T., and Collier, M. (2003). Low-energy Neutral Atoms Observed Near the Earth. *J. Geophys. Res.* 108 (A4). doi:10.1029/2002ja009643

Wilson, G., Ober, D., Germany, G., and Lund, E. (2004). Nightside Auroral Zone and Polar Cap Ion Outflow as a Function of Substorm Size and Phase. *J. Geophys. Res.* 109 (A02206). doi:10.1029/2003ja009835

Yau, A. W., Whalen, B. A., McNamara, A. G., Kellogg, P. J., and Bernstein, W. (1983). Particle and Wave Observations of Low-Altitude Ionospheric Ion Acceleration Events. *J. Geophys. Res.* 88, 341. doi:10.1029/ja088ia01p00341

Zettergren, M., Semeter, J., Blelly, P.-L., and Diaz, M. (2007). Optical Estimation of Auroral Ion Upflow: Theory. *J. Geophys. Res.* 112, a–n. doi:10.1029/2007JA012691

Conflict of Interest: Author JH was employed by the company The Aerospace Corporation.

The remaining authors declare that the research was conducted in the absence of any commercial or financial relationships that could be construed as a potential conflict of interest.

Publisher's Note: All claims expressed in this article are solely those of the authors and do not necessarily represent those of their affiliated organizations, or those of the publisher, the editors, and the reviewers. Any product that may be evaluated in this article, or claim that may be made by its manufacturer, is not guaranteed or endorsed by the publisher.

Copyright © 2022 Rowland, Collier, Keller, Pfaff, Klenzing, McLain, Clemmons and Hecht. This is an open-access article distributed under the terms of the Creative Commons Attribution License (CC BY). The use, distribution or reproduction in other forums is permitted, provided the original author(s) and the copyright owner(s) are credited and that the original publication in this journal is cited, in accordance with accepted academic practice. No use, distribution or reproduction is permitted which does not comply with these terms.

frontiers | Frontiers in Astronomy and Space Sciences

ORIGINAL RESEARCH
published: 16 June 2022
doi: 10.3389/fspas.2022.895514

Kelvin-Helmholtz Vortices as an Interplay of Magnetosphere-Ionosphere Coupling

K.-J. Hwang[1], J. M. Weygand[2], D. G. Sibeck[3], J. L. Burch[1], M. L. Goldstein[4], C. P. Escoubet[5], E. Choi[1], K. Dokgo[1], B. L. Giles[3], C. J. Pollock[6], D. J. Gershman[3], C. T. Russell[2], R. J. Strangeway[2] and R. B. Torbert[7]*

[1]Southwest Research Institute, San Antonio, TX, United States, [2]Institute of Geophysics and Planetary Physics, University of California, Los Angeles, Los Angeles, CA, United States, [3]NASA Goddard Space Flight Center, Greenbelt, MD, United States, [4]The Goddard Planetary Heliophysics Institute, University of Maryland, Baltimore County, MD, United States, [5]European Space Agency, Noordwijk, Netherlands, [6]Denali Scientific, LLC, Fairbanks, AK, United States, [7]Space Science Center, University of New Hampshire, Durham, NH, United States

OPEN ACCESS

Edited by:
Toshi Nishimura,
Boston University, United States

Reviewed by:
Xuanye Ma,
Embry–Riddle Aeronautical University, United States
Peter Haesung Yoon,
University of Maryland, College Park, United States
Scott Alan Thaller,
University of Colorado Boulder, United States

***Correspondence:**
K.-J. Hwang
jhwang@swri.edu

Specialty section:
This article was submitted to Space Physics, a section of the journal Frontiers in Astronomy and Space Sciences

Received: *13 March 2022*
Accepted: *11 May 2022*
Published: *16 June 2022*

Citation:
Hwang K-J, Weygand JM, Sibeck DG, Burch JL, Goldstein ML, Escoubet CP, Choi E, Dokgo K, Giles BL, Pollock CJ, Gershman DJ, Russell CT, Strangeway RJ and Torbert RB (2022) Kelvin-Helmholtz Vortices as an Interplay of Magnetosphere-Ionosphere Coupling. Front. Astron. Space Sci. 9:895514. doi: 10.3389/fspas.2022.895514

The solar wind-magnetosphere interaction drives diverse physical processes on the flanks of Earth's magnetopause, and in turn these processes couple to the ionosphere. We investigate simultaneous multipoint *in-situ* spacecraft and ground-based measurements to determine the role of Kelvin-Helmholtz waves at the Earth's magnetopause and the low-latitude boundary layer in the magnetosphere-ionosphere coupling process. Nonlinear Kelvin-Helmholtz waves develop into flow vortices that twist and/or shear flux tube magnetic fields, thereby generating localized field-aligned currents. Kelvin-Helmholtz vortices on the dusk (dawn) flanks of the magnetosphere generate clockwise (counter-clockwise) rotations and upward (downward) field-aligned currents inside the flux tubes, consistent with the region-1 field-aligned current. We present *in-situ* MMS and Cluster spacecraft observations of Kelvin-Helmholtz vortices at the magnetopause that map to the poleward edge of the auroral regions. The FAST spacecraft and the ground-based magnetometers from which spherical elementary currents (acting as a proxy for vertical currents) can be calculated observe corresponding field-aligned current signatures. This study demonstrates the role played by the Kelvin-Helmholtz waves in linking magnetopause boundary fluctuations to ionospheric phenomena.

Keywords: Kelvin-Helmholtz vortices, Kelvin-Helmholtz waves, magnetosphere-Ionosphere coupling, region 1 field-aligned current, magnetopause and boundary layers, flow vorticity

1 INTRODUCTION

In contrast to the Dungey (1961) model that refers to the transport of the solar wind into the Earth's magnetosphere *via* dayside-then-nightside magnetic reconnection, (Axford and Hines, 1961) proposed that there was a quasi-viscous interaction between the solar wind and the magnetosphere, powered by flow velocity shear. The Kelvin-Helmholtz instability (KHI) grows in such a velocity shear layer. Along the Earth's magnetopause, across which there is a significant velocity shear between the fast anti-sunward magnetosheath and the relatively stagnant magnetosphere, Kelvin-Helmholtz waves (KHWs) are generated. KHWs develop nonlinearly into large-scale rolled-up Kelvin-Helmholtz vortices (KHVs) when the shear flow energy is greater than the magnetic energy along the shear flow direction (Chandrasekhar, 1961;

Hasegawa, 1975). This KHI-unstable condition is often satisfied when the interplanetary magnetic field (IMF) is oriented nearly perpendicular to the shear flow direction, i.e., either due northward or southward. However, the magnetopause KHWs/KHVs have been less frequently observed during periods of the southward IMF (Kavosi and Raeder, 2015). Hwang et al. (2011) and Nakamura et al. (2020) explained this: there exist decay mechanisms such as magnetic reconnection and flux transfer events that lead to a quick decay of the vortex structures under southward IMF.

KHWs/KHVs affect the Earth's magnetosphere *via* various direct and indirect paths. Numerous studies have shown that nonlinear KHWs lead to mass, momentum, and energy transport across the magnetopause (Kivelson and Chen, 1995; Fairfield et al., 2000; Hasegawa et al., 2004; Faganello et al., 2008; Nakamura et al., 2013, 2017; Turkakin et al., 2013). In particular, large-scale KHVs promote solar wind entry into the magnetosphere *via* 1) magnetic reconnection between stretched magnetic field lines caused by the vortex motion (Otto and Fairfield, 2000; Nykyri and Otto, 2004; Cowee et al., 2010; Nakamura et al., 2011; Eriksson et al., 2016; Hwang et al., 2021) or mid-latitude reconnection between KHI-stable lobe fields and vortex-induced engulfed magnetosheath fields (Takagi et al., 2006; Faganello et al., 2012; Vernisse et al., 2016; Hwang et al., 2020; Eriksson et al., 2021), 2) diffusive transport through the turbulent decay of KHVs or coalescence of neighboring vortices (Matsumoto and Hoshino, 2004; Nakamura et al., 2004; Nakamura and Fujimoto, 2008; Cowee et al., 2009; Matsumoto and Seki, 2010), or 3) kinetic Alfvén waves or ion gyro-radius scale waves through a mode conversion from KH waves (Chaston et al., 2007; Yao et al., 2011). These processes result in plasma heating and the formation of a broad mixing layer along the flanks of the magnetosphere. Magnetohydrodynamic (MHD) simulations predict that flux tubes populated by plasmas of magnetosheath origin that enter the magnetosphere *via* KHVs can rapidly propagate toward the inner magnetosphere *via* an interchange instability (Wiltberger et al., 2000; Pembroke et al., 2012).

KHWs/KHVs can trigger ULF (ultra-low-frequency) pulsations in the Pc4-5 range with a frequency of ~2–22 mHz *via* the excitation of a global cavity/waveguide mode that can occur at locations where the geomagnetic field-line eigenfrequency equals the frequency of KHWs (Mathie and Mann, 2000; Agapitov et al., 2009). KHW-driven ULF waves facilitate radial diffusion and/or acceleration of radiation belt electrons through drift resonance (Claudepierre et al., 2008). Nonlinear fast-mode waves can also develop at the edges of KHWs, propagate into the magnetosphere, and interact with radiation belt and ring current plasmas (Lai and Lyu, 2010).

The main focus of this paper is to study the influence of KHWs/KHVs on magnetosphere-ionosphere coupling (MIC). Previously, ionospheric traveling convection vortices have been interpreted as an ionospheric manifestation of solar wind dynamic pressure enhancements or KHI-driven ULF perturbations (Glassmeier and Heppner, 1992; Samson and Pao, 1996; Mann et al., 2002). Observations of ULF field-line-resonance pulsations initiated by magnetopause KHWs and conjugate ground-based magnetometer/radar measurements have shown the enhancements of electron precipitation or net downward Poynting flux and associated energy deposition into the ionosphere at latitudes coupled to the resonance region (Mann et al., 2002; Rae et al., 2007).

Those studies indicated that KHWs/KHVs have a global influence on the dynamics of the coupled magnetosphere-ionosphere system. In this paper, we incorporate the data obtained from Cluster, MMS, FAST, and ground magnetometers and show that KHWs/KHVs generate field-aligned currents (FACs) *via* the vortical motion that twists magnetic field lines within flux tubes. The sense of flux-tube rotation and associated FACs and conjugate ionospheric currents mapped to the dawn vs. dusk magnetopause KHWs/KHVs are very consistent with the region-1 FAC. This study demonstrates that KHWs/KHVs are at least partially responsible for the region1 FAC.

We organize this paper by introducing a theoretical prediction in **Section 2**, briefly describing the *in-situ* spacecraft and ground-based data used for this study in **Section 3**, presenting case studies of the dusk/dawn magnetopause KHW/KHV events observed by Cluster and MMS in **Section 4** and **Section 5**, respectively. Discussion of Cluster/MMS case studies and conjugate ionospheric signatures and the implied roles and impact of KHWs/KHVs on MIC follow in **Section 6**.

2 THEORETICAL EXPECTATION

Nonlinear KHWs drive flow vortices that cause a twist or shear of magnetic field lines within the vortical flux tube. This process generates FACs within the flux tube (see Figure 19 of Birn et al., 2004) as predicted by Maxwell's equations:

$$\frac{\partial \mathbf{B}}{\partial t} = -\nabla\times \mathbf{E}\,, \mu_0 \mathbf{J} = \nabla\times \mathbf{B} \tag{1}$$

B and **E** are the magnetic and electric field, respectively. **J** is the electric current density, and μ_0 is the magnetic permeability of free space. Combining the two equations in **Eq. 1** gives

$$\frac{\partial \mathbf{J}}{\partial t} = -\frac{1}{\mu_0}\boldsymbol{\nabla} \times [\mathbf{B}\boldsymbol{\nabla}\cdot\mathbf{V} + \mathbf{V}\cdot\boldsymbol{\nabla}\mathbf{B} - \mathbf{B}\cdot\boldsymbol{\nabla}\mathbf{V}] \tag{2}$$

V represents the plasma velocity. In case of small perturbations, the first-order terms of **Eq. 2** for the component parallel to **B** yield (Paschmann et al., 2002)

$$\frac{\partial \mathbf{J}_{||}}{\partial t} = \frac{1}{\mu_0}\mathbf{B}\cdot\nabla\left(\nabla\times\mathbf{V}\right)_{||} \tag{3}$$

The parenthesis in the right-hand side term is defined as flow vorticity, $\Omega = \nabla\times V$. **Eq. 3** is also valid for large-scale structures such as KHVs without the small-perturbation approximation.

Eq. 3 tells us that the gradient of vorticity gives rise to the generation of FACs. The magnitude of Ω. becomes largest in the equatorial plane of the magnetosphere where a vortex flow develops driven by the KHI. The flow vortex decreases toward the northern/southern ionosphere along positive/negative **B**. The

sense of rotation, which determines the sign of $\Omega_.$, is clockwise at the dawn flank of the magnetosphere and counter-clockwise at dusk. Therefore, the right-hand side term is positive at dawn and negative at dusk. Corresponding FACs, $J_{||}$ in the left-hand side term of **Eq. 3** that build up within the flux tube with time are downward into the northern ionosphere at dawn and upward from the northern ionosphere at dusk. This corresponds to the presence of FACs of region-1 sense.

3 METHOD

To test the theoretical prediction extracted from **Eq. 3** observationally and to quantify how effectively and importantly KHV-driven FACs contribute to the region-1 current system, we use data from: the four Cluster spacecraft with the separation among the spacecraft greater than or equal to the ion gyroradius (ρ_i) or inertial length (λ_i), the four MMS spacecraft with interspacecraft separation down to the order of the electron scale, the FAST spacecraft, and THEMIS ground-based fluxgate magnetometers, which we call "gMAG" in this paper.

Both Cluster and MMS regularly fly through the dawn/dusk magnetopause and detect KHWs/KHVs. Their tetrahedral configuration facilitates the calculation of **J** using the curlometer technique (Dunlop et al., 2002). MMS further enables the direct estimation of Ω using high time-resolution plasma data (150-ms for ions and 30-ms for electrons in burst mode; 4.5 s in fast survey mode). We focus on the ion flow vorticity (the electron vorticity (Hwang et al., 2019) that is associated with microphysical processes is out of the scope of this study). The larger spacecraft separation of Cluster compared to MMS allows a test using plasma density to determine if the observed fluctuations are KHVs or not (**Section 4**).

FAST traversed the northern and southern ionosphere with an altitude ranging from hundreds km to ≲4,000 km. Its operation during ~12 years until 4 May 2009 enables conjunctions to be studied with KHWs/KHVs detected by Cluster. KHV events observed both by Cluster and most-recently-launched MMS can be coupled to ionospheric signatures recorded in ground magnetometers. Data obtained from 11 different magnetometer arrays (gMAG) allow us to calculate the (horizontal) equivalent ionospheric current (EIC) and the (vertical) spherical elementary current (SEC), which is a proxy for the field-aligned current, using the SEC technique outlined in Amm and Viljanen (1999) and Weygand et al. (2011).

From our coordinated case studies of *in-situ* magnetopause KHVs observed by Cluster and MMS and corresponding ionospheric responses identified by FAST or gMAG, we qualitatively test **Eq. 3** in the dusk sector (**Section 4**) vs. the dawn sector (**Section 5**).

4 DUSKWARD KHVS AND IONOSPHERIC FACS

4.1 Cluster Observations of Duskward KHVs

From 1,200 to 1300 UT on 20 November 2001 (**Figures 1A–C**) Cluster was located in the duskward magnetopause boundary layer. The four Cluster spacecraft (C1-4) were in a tetrahedral configuration and were separated by ~1968 km on average (**Figure 1D**) with its barycenter at ~[−5.3, 17.9, 3.2] Earth radii (R_E) in Geocentric Solar Ecliptic (GSE) coordinates. [GSE coordinates correspond to the boundary normal coordinates (LMN) obtained from Shue et al. (1997) model in this event.] The IMF was mostly northward during this period. **Figure 1** shows (A) the magnetic field (**B**) averaged over the four spacecraft and (B, C) the electric current density (**J**) obtained using the curlometer technique (x, y, and z components in blue, green, and red in GSE) and decomposed into parallel (red) and perpendicular (blue) components with respect to **B**. Both **B** and **J** show quasi-periodic fluctuations with a period of ~8–15 min that are most likely to be attributed to magnetopause KHWs.

To test if these fluctuations resulted from nonlinear KHWs, we expanded the C1 data from 1200 UT to 1215 UT in **Figures 1E–J**. On the top of **Figure 1E**, we denoted a *more*-magnetospheric region in a blue bar as characterized by a relatively larger B_z (**Figure 1E**), more flux of high-energy (≳1 keV) ions (**Figure 1F** showing the ion energy spectrogram), reduced anti-sunward flow velocity (V_x shown in blue; **Figure 1G**) and ion density (black in **Figure 1I**). The region of a smaller B_z accompanied by more flux of low-energy ions (<1 keV), increases in anti-sunward velocity and ion density represents a *more*-magnetosheath side (red bar). [Note that the energy spectrogram indicates that the boundary layer was rather in a mixed/turbulent state.] We marked the magnetosphere-to-magnetosheath transitions by 'A', 'B', 'C', and 'D' at the top of **Figure 1E** and vertical solid black lines. The magnetosheath-to-magnetosphere transitions are marked by 'a', 'b', 'c', and 'd' and vertical dashed black lines.

In a steady state of KHVs, the centrifugal force is balanced by the pressure force. Since the centrifugal force is radially outward in a rolled-up vortex, the pressure force should point inward to the vortex center. The high total pressure, then, builds up at the boundary from the more-magnetospheric side into the more-magnetosheath side crossing by Cluster (see Figure 19 of Hasegawa, 2012). And the total pressure is minimized close to the boundary from the more-magnetosheath side to the more-magnetospheric side crossing. **Figure 1H** shows this trend. The total pressure (black), i.e., the sum of plasma (red) and magnetic (blue) pressures, often peaks at boundaries toward the more-magnetosheath side ('H' letters in **Figure 1H**) and decreases at boundaries toward the more-magnetospheric side ('L').

Another characteristic of KHVs is the so-called density reversal (Hasegawa et al., 2004). For the rolled-up vortices, the density profile away from the nominal magnetopause (i.e., ~along + y_{GSE} for duskward KHV events) shows a layer of a higher density (of magnetosheath origin) sandwiched between layers of a lower density (of magnetosphere origin). As a result, the spacecraft can detect a lower-density magnetosphere-origin layer located outward of a higher-density magnetosheath-origin layer. **Figure 1I** shows the ion density measured by C1 (black), C3 (green), and C4 (blue). **Figure 1J** presents these observations by color with C1, C3, and C4 data arranged in terms of their distance away from the magnetopause, i.e., along + y_{GSE}. Red arrows in **Figure 1J** indicate the times when the density observed by C1

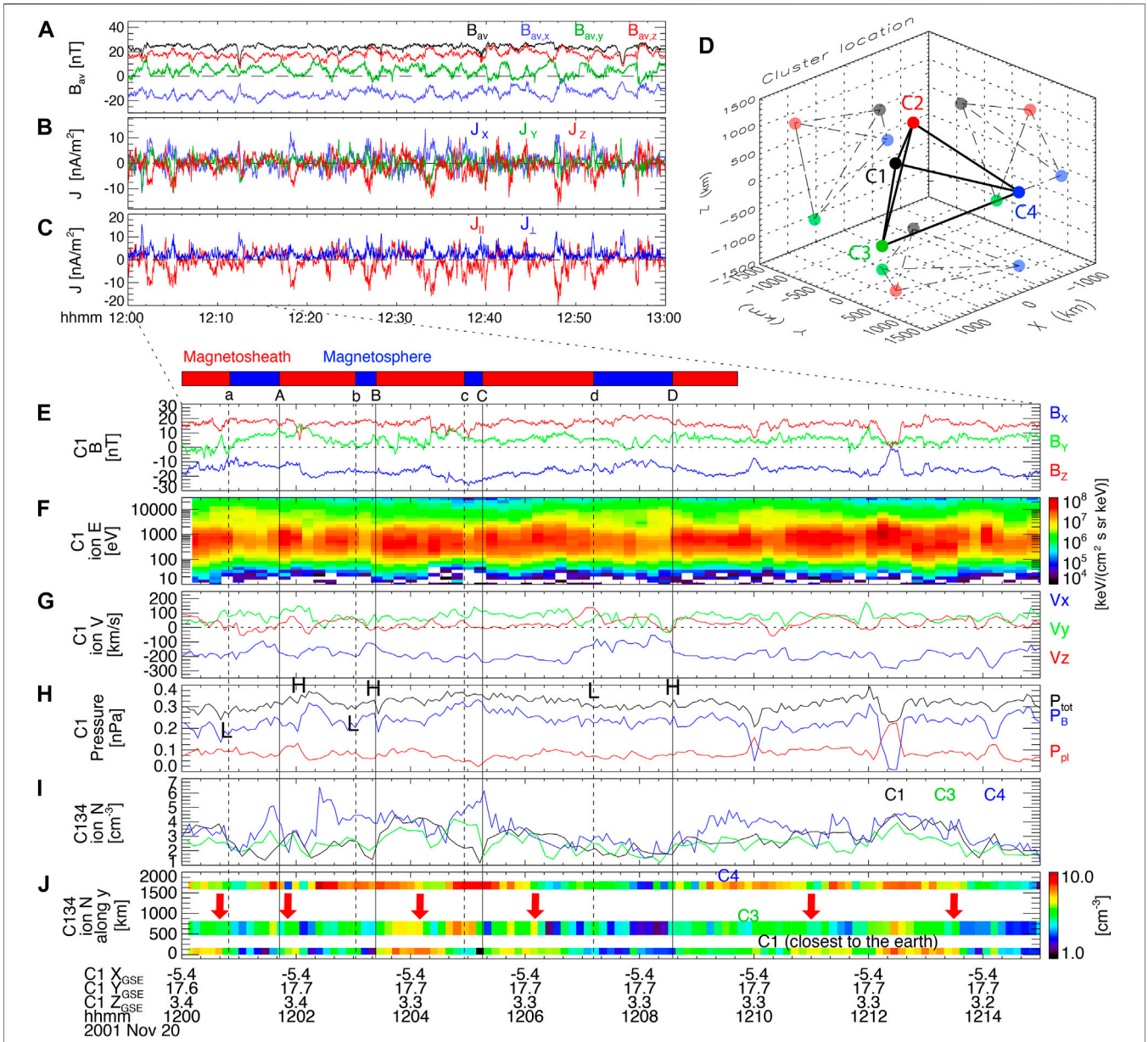


FIGURE 1 | Cluster observation of duskward KHVs: **(A)** the magnetic field and **(B,C)** the electric current density during 1,200–1300 UT on 20 November 2001; **(D)** the tetrahedral configuration of the four Cluster spacecraft around its barycenter at ~(–5.3, 17.9, 3.2) R_E in GSE. C1 observation from 1200 UT to 1215 UT on 20 November 2001: **(E)** the magnetic field; **(F)** the ion energy spectrogram; **(G)** the ion velocity; **(H)** the plasma (red) and magnetic (blue) pressures, and the sum (black) of these pressures; **(I)** the ion density measured by C1 (black), C3 (green), and C4 (blue); **(J)** the ion density (color) at C1, C3, and C4 arranged in terms of their distance away from the magnetopause (along y; e.g., C1 located closest to the earth).

(closest to the earth) is higher than that observed by C3 or C4 (further away from the earth).

Both features of total pressure (**Figure 1H**) and density reversal (**Figure 1J**) support the identification of KHVs. For the duskward KHV event such as **Figure 1**, we expect the development of the antiparallel current or, equivalently, upward FAC in the northern ionosphere. **Figure 1C**, indeed, shows that **J** is donimantly antiparallel throughout the event.

4.2 FAST Observations of Ionospheric FACs

The geomagnetic field models (Tsyganenko, 1989; Tsyganenko, 1995) predict that the magnetic field lines encountered by Cluster during the **Figure 1** event are mapped to the ionosphere at ~73° LAT and ~339° LON in geographic coordinates (GEO). FAST spacecraft fortuitously passed the northern ionosphere at/near the footprint of Cluster's location around the time of the event. **Figure 2** shows the energy spectrograms of down-going (with pitch angles of 0° ± 45°; A, C) and up-going (with pitch angles of

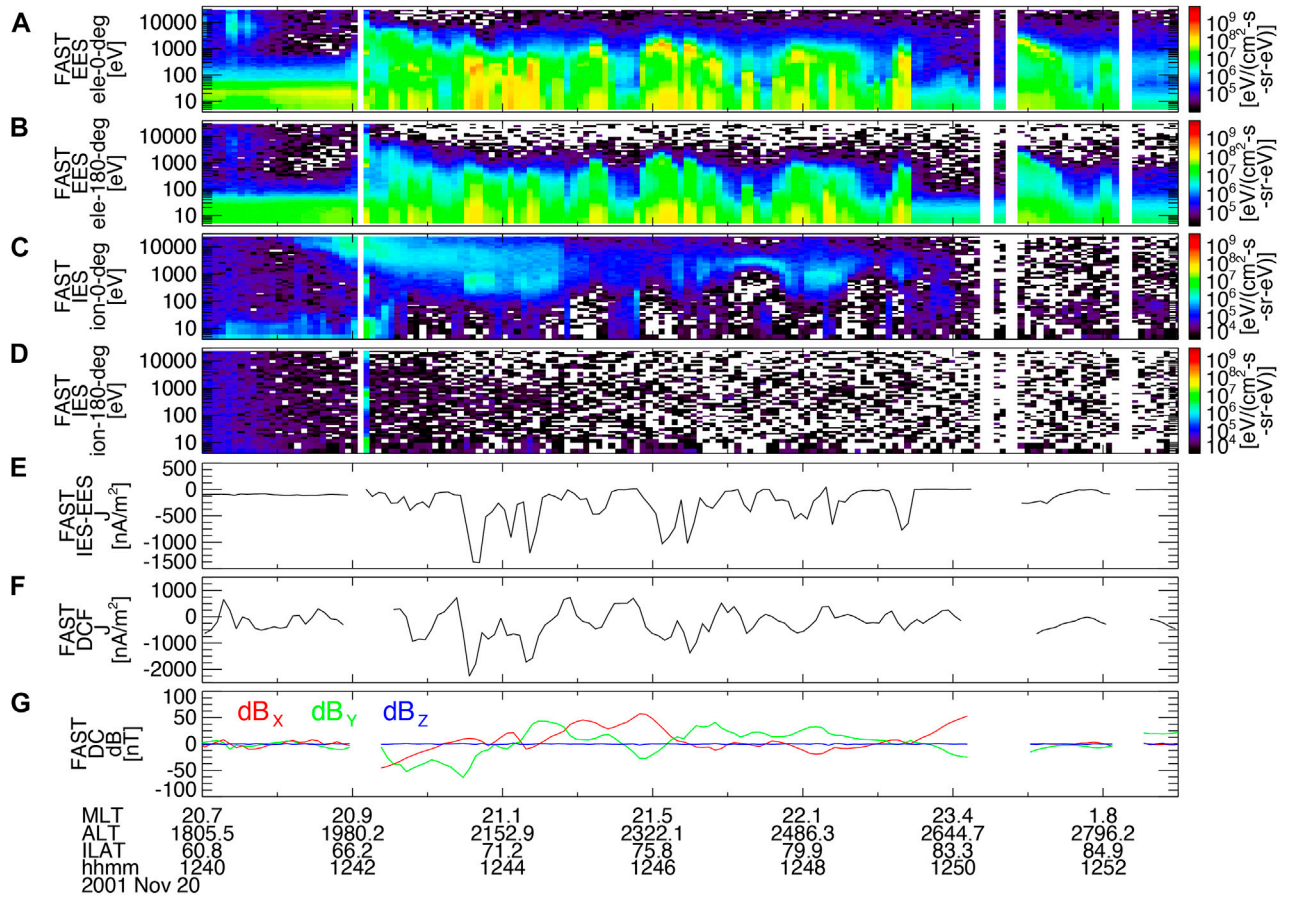


FIGURE 2 | FAST observation of the northern ionosphere conjugate to the Cluster observation of duskward KHVs (**Figure 1**): the energy spectrograms of down-going [with pitch angles of 0° ± 45°; **(A,C)**] and up-going [with pitch angles of 180° ± 45°; **(B,D)**] electrons **(A,B)** and ions **(C,D)**; the electric current density calculated **(E)** from the particle data and **(F)** from the perturbed magnetic field **(G)**.

180° ± 45°; B, D) electrons (A, B) and ions (C, D). Precipitating fluxes are larger than up-going fluxes for both electrons and ions. The difference between the ion and electron flux gives rise to the current density along **B** (**Figure 2E**) that is mostly upward from the ground, i.e., antiparallel to **B**. The perturbed magnetic field (d**B**; **Figure 2G**) also gives rise to a negative **J** (**Figure 2F**) from Ampere's law, demonstrating that FAST traversed the upward FAC region. **J** calculated from both particles and d**B** ranges from hundreds to ~2000 nA/m^2.

4.3 MMS Observations of Duskward KHVs

During ~1759–1809 UT on 1 October 2015, the MMS quartet with its barycenter at ~[3.9, 9.2, −4.1] R_E in Geocentric Solar Magnetospheric (GSM) coordinates encountered magnetopause fluctuations shown in **Figure 3**. The IMF was mostly southward during the period. A *more*-magnetosheath region is then identified by a mostly negative B_z (**Figure 3A**), more flux of <2 keV-energy ions (**Figure 3B**), larger anti-sunward flow (**Figure 3C**), enhanced ion density (**Figure 3D**), and reduced ion temperature (**Figure 3E**). We denoted such repeated regions by red bars on the top of **Figure 3A** (although the region between 'E' and 'e' at the top of **Figure 1** is a mixed region exhibiting a magnetospheric field and a magnetosheath plasma). Opposite trends represent a *more*-magnetospheric region as indicated by a blue bar.

We, again, marked magnetosphere-to-magnetosheath transitions by 'A', 'B', …, 'F' at the top of **Figure 3A** with vertical solid black lines and magnetosheath-to-magnetosphere transitions by 'a', 'b', …, 'f' with vertical dashed black lines. **Figure 3F** shows that the total pressure generally rises at/near magnetosphere-to-magnetosheath boundaries ('H' in **Figure 3F**) and lowers at/near magnetosheath-to-magnetosphere boundaries ('L'). This supports that the observed fluctuations are attributed to KHVs.

The average spacecraft separation of ~31 km during this event prevents us from testing the density reversal. Instead, we performed boundary normal analyses. As shown in **Figure 3K** (Hwang et al., 2011, 2020), boundaries of typical KHVs tilt from the initially-undisturbed magnetopause with its normal along **n**, showing a more-gentle waveform at the trailing edges (see black arrows at 'A', 'B', …, 'F' in **Figure 3K**) and a

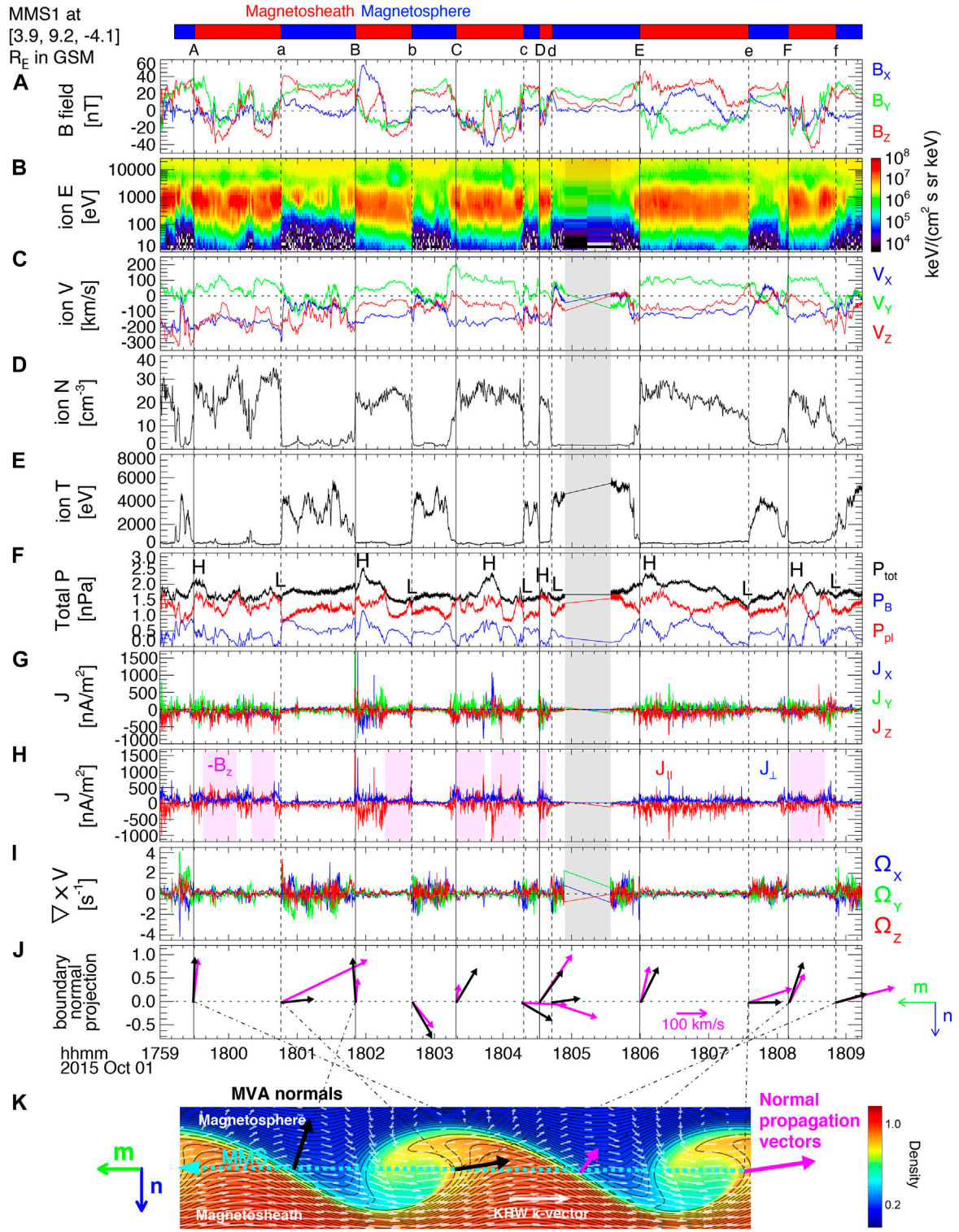


FIGURE 3 | MMS1 observation of duskward KHVs during 1759–1809 UT on 1 October 2015: **(A)** the magnetic field; **(B)** the ion energy spectrogram; **(C)** the ion velocity; **(D)** the ion density; **(E)** the ion temperature; **(F)** the plasma (red) and magnetic (blue) pressures, and the sum (black) of these pressures; **(G)** the current density, **J**; **(H)** **J** decomposed into parallel (red) and perpendicular (blue) components; **(I)** the ion vorticity; **(J)** the *mn*-plane projections of boundary normals (black arrows) and normal propagation velocities (magenta arrows) to be compared with **(K)** typical waveforms of duskward KHVs, when viewed from north, with color representing density. The gray shade in **(B–I)** indicates a gap in the burst-mode particle data.

TABLE 1 | Boundary normals and normal propagation vectors at the trailing (marked by vertical solid lines, A, B, . . ., F in **Figure 3**) and leading (vertical dashed lines, a, b, . . ., f) edges in LMN ($\lambda_{mid\text{-}min}$ is the medium-to-minimum eigenvalue ratio in the minimum variance calculation.).

	A	a	B	b	C	c	D	d	E	e	F	f
Time (UT)	~17: 59:30	~18: 00:44	~18: 01:51	~18: 02:40	~18: 03:20	~18: 04:19	~18: 04:31	~18: 04:42	~18: 06:00	~18: 07:34	~18: 08:10	~18: 08:51
Normal in LMN coordinates	$\lambda_{mid\text{-}min}$ = 2.71 [–0.007, –0.047, –0.998]	$\lambda_{mid\text{-}min}$ = 7.94 [–0.025, –0.996, –0.080]	$\lambda_{mid\text{-}min}$ = 14.5 [–0.176, 0.093, –0.980]	$\lambda_{mid\text{-}min}$ = 2.80 [–0.041, –0.622, 0.782]	$\lambda_{mid\text{-}min}$ = 4.40 [–0.244, –0.611, –0.753]	$\lambda_{mid\text{-}min}$ = 3.44 [0.081, –0.915, 0.396]	$\lambda_{mid\text{-}min}$ = 3.63 [0.008, –0.702, –0.712]	$\lambda_{mid\text{-}min}$ = 3.09 [–0.497, –0.863, –0.092]	$\lambda_{mid\text{-}min}$ = 9.49 [–0.342, –0.523, –0.781]	$\lambda_{mid\text{-}min}$ = 6.49 [–0.054, –0.998, –0.007]	$\lambda_{mid\text{-}min}$ = 29.4 [–0.222, –0.406, –0.886]	$\lambda_{mid\text{-}min}$ = 2.24 [–0.290, –0.936, –0.198]
Normal propagation velocity in LMN	v = 106 km/s [–0.372, –0.137, –0.918]	v = 280 km/s [–0.054, –0.941, –0.335]	v = 57.6 km/ s [0.341, –0.101, –0.935]	v = 86.5 km/ s [–0.169, –0.729, 0.663]	v = 43.4 km/ s [0.293, –0.177, –0.940]	v = 143 km/s [–0.326, –0.945, 0.033]	v = 145 km/s [–0.162, –0.667, –0.727]	v = 142 km/s [–0.143, –0.962, 0.233]	v = 86.8 km/ s [–0.270, –0.288, –0.918]	v = 166 km/s [0.581, –0.792, –0.188]	v = 79.9 km/ s [–0.192, –0.569, –0.800]	v = 199 km/s [–0.447, –0.878, –0.167]

steeper waveform at the leading edges (black arrows at 'a', 'b', ... 'f'). Also, since KHVs propagate tailward along the magnetopause (along – **m** or **k**-vector seen by a white arrow), normal propagation velocities (magenta arrows) are more aligned to the ± **n** direction with smaller speed at the trailing edges, and more perpendicular to **n** (or more parallel to **k**-vector) with larger speed at the leading edges. To test this, we determined the *nominal* boundary normal coordinates (LMN) derived from minimum variance analysis (MVA) (Sonnerup and Scheible, 1998; Siscoe and Suey 1972) for the magnetopause-crossing period from 1710 UT to 1730 UT prior to the occurrence of KHVs: l = [0.31, 0.34, 0.89], m = [0.59, –0.80, 0.10], and n = [0.75, 0.50, –0.44] in GSM. **Table 1** lists the normal propagation velocities derived from a four-spacecraft timing analysis (Paschmann and Daly, 1998) and the MVA (using **B**)-derived boundary normals in LMN together with the medium-to-minimum eigenvalue ratio.

Figure 3J displays the *mn*-plane projections of boundary normals shown as black arrows and normal propagation velocities as magenta arrows. Both the normals and normal propagation vectors generally show a repetitive pattern between leading and trailing edges, consistent with **Figure 3K**. This confirms the identification of KHVs for the **Figure 3** event.

Figure 3G shows **J** caculated from particle data (it is consistent with the curlometer-derived **J**) and **Figure 3H** shows parallel and perperdicular components of **J**. Both J_z and $J_{||}$, although fluctuating around zero, are mostly negative with magenta shades in **Figure 3H** representing $B_z < 0$ periods. Therefore, **J** mainly pointed opposite to the geomagnetic **B**, consistent with the upward FAC in the northern ionosphere for the duskward KHV event.

Figure 3I shows the ion vorticity, Ω. As expected in **Section 2** (**Eq. 3**), the z component of Ω. is relatively positive, indicating the counter-clockwise rotation of the duskward KHV. A quantitative test of **Eq. 3** requires another spacecraft quartet simultaneously crossing the KHV flux tube above/below the near-equatorial plane where MMS traversed. **Figures 3G–I**, however, demonstrate the sign/sense of J and Ω. We note that the larger inertia on the faster magnetosheath side than the magnetospheric side generally leads to a larger |J| and smaller |Ω.|

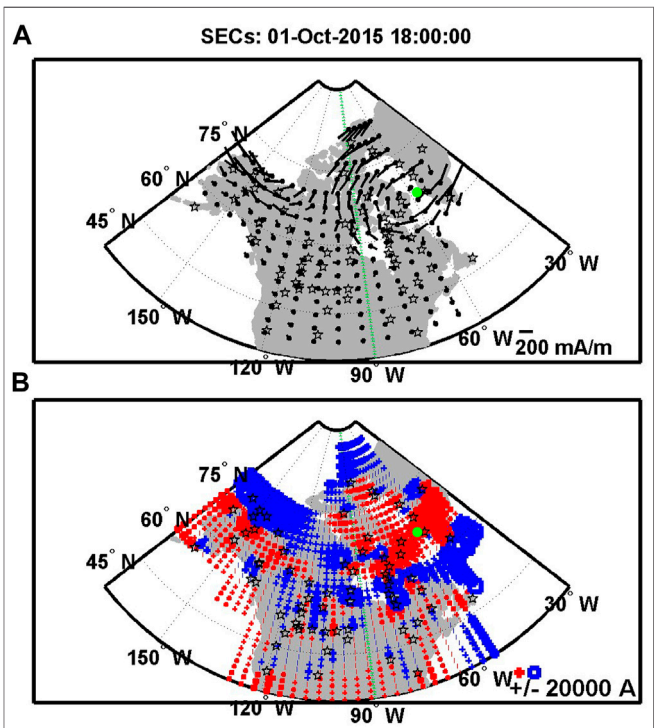


FIGURE 4 | Ground magentometer observation of the ionospheric currents calculated from the SEC technique (Amm and Viljanen, 1999; Weygand et al., 2011) at 1800 UT on 1 October 2015: The (horizonal) equivalent ionospheric current [EIC; **(A)**] and the vertical spherical elementary current [SEC; **(B)**], which is a proxy of the FAC. The MMS footprint corresponding to the duskward KHV event (**Figure 3**) is denoted by a green dot.

4.4 Ground Magnetometer Observations of Ionospheric FACs

The geomagnetic field model (Tsyganenko, 1989) predicts that the magnetic field lines encountered by MMS during the **Figure 3** event are mapped to the ionosphere at ~67° LAT and ~302° LON. We use the gMAG data to derive the equivalent ionospheric current (EIC) and spherical elementary current

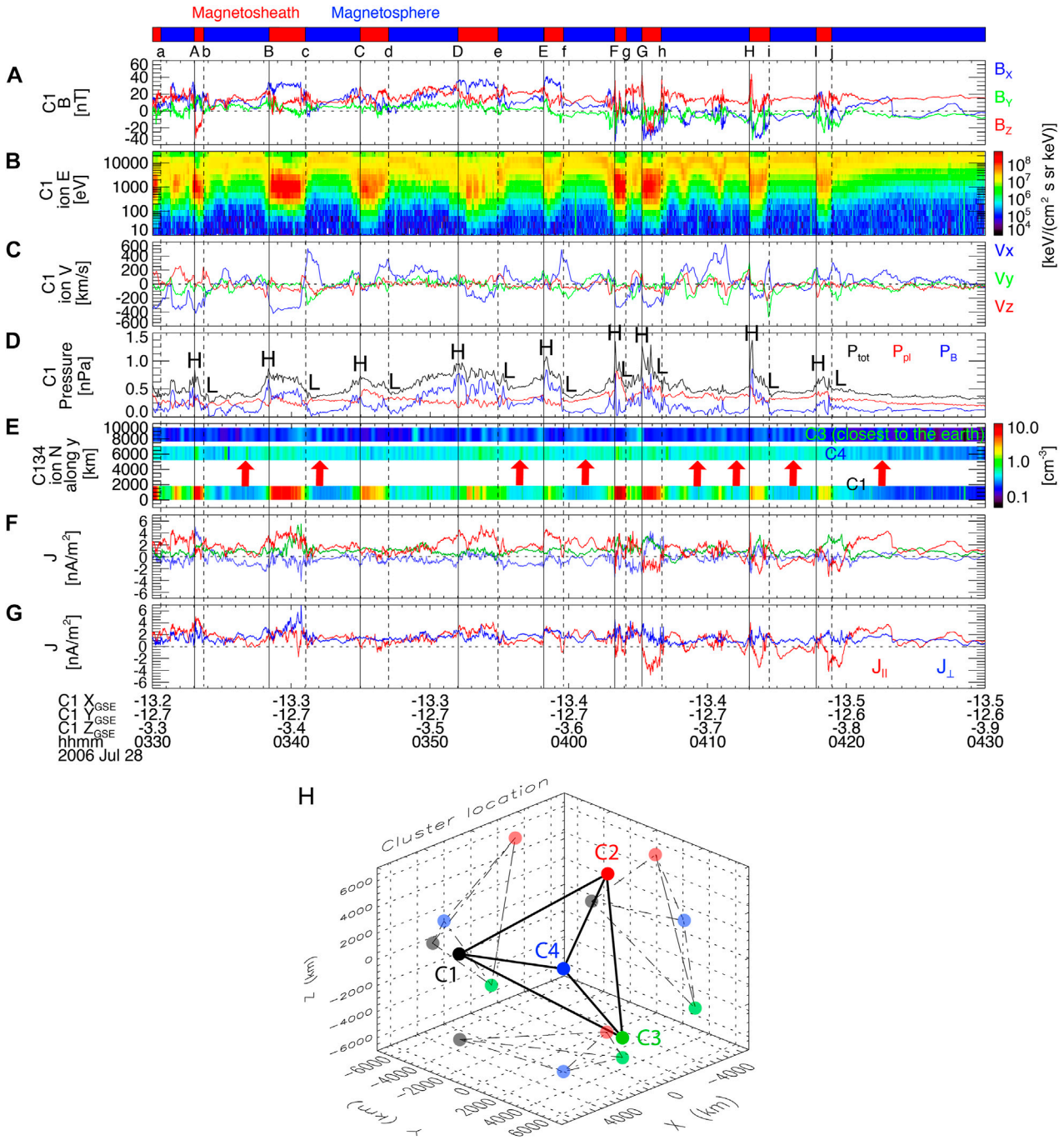


FIGURE 5 | Cluster observation of dawnward KHVs during 0330–0430 UT on 28 July 2006: **(A)** the magnetic field and **(B)** the ion energy spectrogram; **(C)** the ion velocity; **(D)** the plasma (red), magnetic (blue), and total (black) pressures; **(E)** the ion density (color) measured by C1, C3, and C4 arranged in terms of their distance away from the magnetopause (along−−y; e.g., C3 located closest to the earth); **(F)** the current density, **J**; **(G) J** decomposed into parallel (red) and perpendicular (blue) components; **(H)** the tetrahedral configuration of Cluster around its barycenter at ~[−13, −13, −3.0] R_E.

(SEC). The result is shown in **Figure 4**, where the MMS footprint is denoted by a green dot. A counter-clockwise rotation of EIC around the green dot (upper panel) indicates upward FACs. SEC (lower), a proxy of the vertical current for an altitude of 100 km, shows the upward FAC of ~18,400 A at the green dot. We note a bead-like structure in SEC indicative of upward FACs elongated in the east-west direction, possibly implying their generation *via* the duskward KHVs (**Figure 3**).

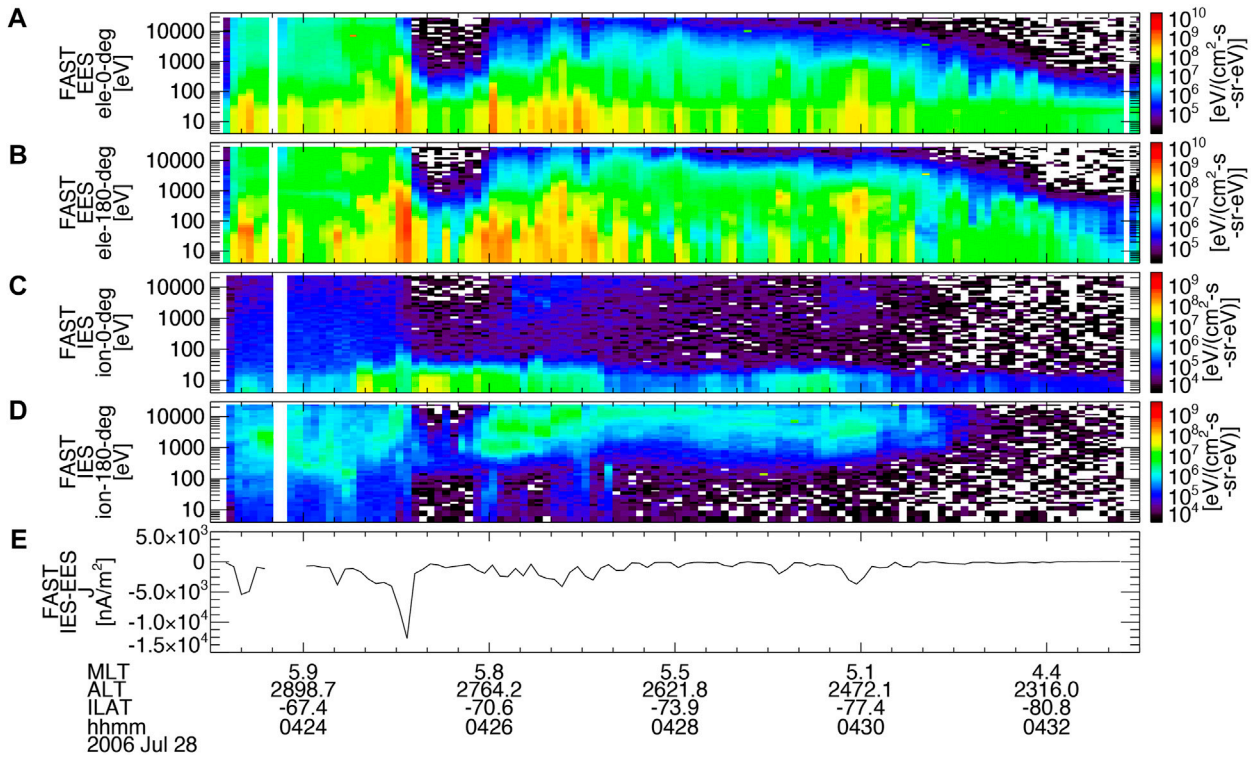


FIGURE 6 | FAST observation of the southern ionosphere conjugate to the Cluster observation of dawnward KHVs (**Figure 5**): the energy spectrograms of down-going (with pitch angles of 0° ± 45°; A, C) and up-going (with pitch angles of 180° ± 45°; B, D) electrons **(A,B)** and ions **(C,D)**; **(E)** the electric current density calculated from the difference between the ion and electron flux.

5 DAWNWARD KHVS AND IONOSPHERIC FACS

5.1 Cluster Observations of Dawnward KHVs

From ~0250 UT to ~0430 UT on 28 July 2006 Cluster located at ~ [−13, −13, −3.0] R_E in GSE observed KHV-induced magnetopause fluctuations (**Figure 5**) as reported by Hwang et al. (2011). [GSE coordinates that were close to GSM in this event correspond to the boundary normal coordinates (LMN) obtained from Shue et al. (1997) model.] The IMF was fluctuating with $B_z \leq 0$. On the top of **Figure 5A**, blue (red) bars represent a *more*-magnetospheric (*more*-magnetosheath) region with a larger (smaller or negative) B_z (**Figure 5A**), more (less) flux of high-energy ions (**Figure 5B**), reduced (enhanced) anti-sunward flow (**Figure 5C**). We, again, denoted the magnetosphere-to-magnetosheath transitions by 'A', 'B', . . ., 'I' with vertical solid black lines and the magnetosheath-to-magnetosphere transitions by 'a', 'b', . . ., 'j' with vertical dashed black lines.

The total pressure (black in **Figure 5D**) is maximized at/near the boundaries toward the more-magnetosheath region ('H') and minimized at boundaries toward the more-magnetospheric region ('L'). The four Cluster spacecraft in a tetrahedron were separated by > 1 R_E on average (**Figure 5H**), which enables us to test the density reversal. **Figure 5E** shows the ion density in color measured by C1/3/4 arranged in terms of their distance away from the magnetopause. Red arrows in **Figure 5H** mark the density-reversal times when the density observed by C4 or C3 (closer to the earth) is larger than that observed by C1 (further away from the earth). These observations confirm the dawnward-magnetopause KHVs for the **Figure 5** event.

For the dawnward KHV event, we expect the development of the parallel current or, equivalently, downward FAC in the northern ionosphere (**Section 2**). J_z is, indeed, mostly positive (**Figure 5F**) and $J_{||}$ is mainly parallel (**Figure 5G**) although the anti-paralell component becomes significant during later (near-) magnetosheath-side crossings ('G'-'h', 'H'-'i', around 'j'). The overall trend is consistent with the prediction.

5.2 FAST Observations of Ionospheric FACs

The geomagnetic field models (Tsyganenko, 1989; Tsyganenko, 1995) predict that the footprint of the magnetic field lines encountered by Cluster at ~0425 UT on 28 July 2006 falls at −69° LAT and ~72° LON in GEO. FAST spacecraft fortuitously passed the conjugate southern ionosphere. **Figure 6** shows the energy spectrograms of up-going (A, C) and down-going (B, D) electrons (A, B) and ions (C, D). During 0424:30-0426 UT precipitating fluxes of electrons are larger than up-going fluxes, and vice versa for ions. The difference between the ion and electron flux gives rise to the up-flowing FAC (**Figure 6E**) reaching −12,500 nA/m^2 (d**B** data is not available). The up-flowing FAC in the southern

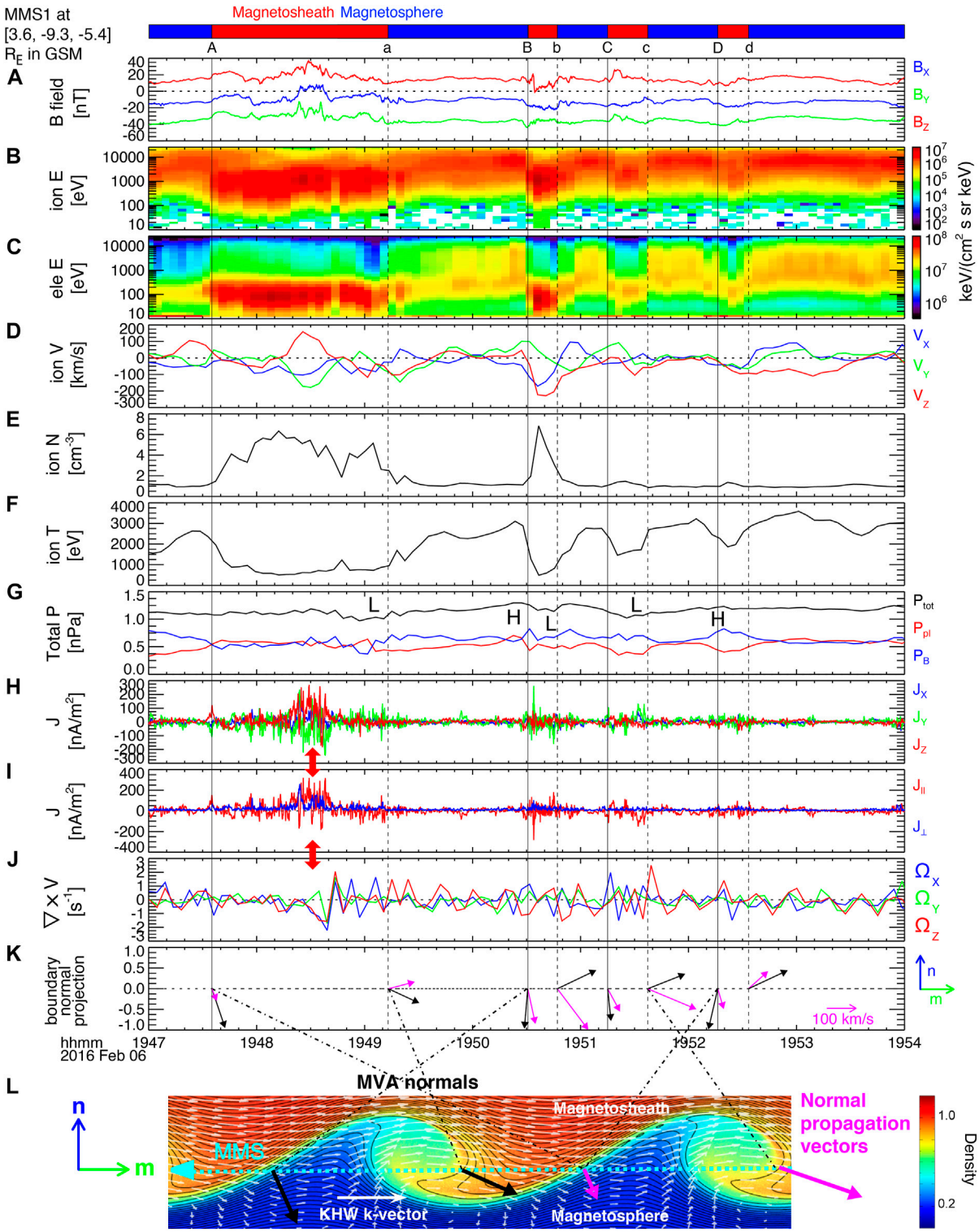


FIGURE 7 | MMS1 observation of dawnward KHVs during 1947–1954 UT on 6 February 2016: **(A)** the magnetic field; **(B)** the ion energy spectrogram; **(C)** the electron energy spectrogram; **(D)** the ion velocity; **(E)** the ion density; **(F)** the ion temperature; **(G)** the plasma (red), magnetic (blue), and total (black) pressures; **(H)** the current density, **J**; **(I) J** decomposed into parallel (red) and perpendicular (blue) components; **(J)** the ion vorticity; **(K)** the *mn*-plane projections of boundary normals (black arrows) and normal propagation velocities (magenta arrows) to be compared with **(L)** typical waveforms of dawnward KHVs, when viewed from north, with color representing density.

TABLE 2 | Boundary normals and normal propagation vectors at the trailing (marked by vertical solid lines, A, B, C, and D in **Figure 7**) and leading (vertical dashed lines, a, b, c, and d) edges in LMN ($\lambda_{mid\text{-}min}$ is the medium-to-minimum eigenvalue ratio in the minimum variance calculation.).

	A	a	B	b	C	c	D	d
Time (UT) Normal in LMN coordinates	~19:47:34 $\lambda_{mid\text{-}min}$ = 4.37 [–0.141, 0.301, –0.943]	~19:49:13 $\lambda_{mid\text{-}min}$ = 8.87 [0.625, 0.700, –0.345]	~19:50:31 $\lambda_{mid\text{-}min}$ = 3.40 [–0.280, –0.077, –0.957]	~19:50:47 $\lambda_{mid\text{-}min}$ = 4.04 [0.138, 0.883, 0.448]	~19:51:15 $\lambda_{mid\text{-}min}$ = 28.9 [–0.629, 0.075, –0.773]	~19:51:38 $\lambda_{mid\text{-}min}$ = 9.54 [–0.387, 0.850, 0.357]	~19:52:16 $\lambda_{mid\text{-}min}$ = 3.82 [–0.037, –0.214, –0.976]	~19:52:33 $\lambda_{mid\text{-}min}$ = 3.03 [0.083, 0.892, 0.443]
Normal propagation velocity in LMN	v = 39.8 km/s [–0.618, 0.282, –0.734]	v = 95.2 km/s [–0.754, 0.632, 0.177]	v = 93.2 km/s [–0.378, 0.186, –0.907]	v = 157 km/s [–0.635, 0.448, –0.630]	v = 74.7 km/s [–0.571, 0.373, –0.731]	v = 151 km/s [–0.596, 0.733, –0.326]	v = 58.5 km/s [0.503, 0.230, –0.833]	v = 86.7 km/s [–0.704, 0.516, 0.488]

ionosphere corresponds to the down-flowing FAC in the northern ionosphere, as expected for the dawnward KHVs of **Figure 5**.

5.3 MMS Observations of Dawnward KHVs

During ~1833–2015 UT on 6 February 2016, MMS observed the dawnward magnetopause/low-latitude boundary layer to be fluctuating. We focus on 7-min (1947–1954 UT) data when MMS with its average spacecraft separation of ~17 km was located in the boundary layer at ~[3.6, –9.3, –5.4]R_E in GSM (**Figure 7**). The IMF was mostly duskward for the period. On the top of **Figure 7A**, blue (red) bars represent a *more*-magnetospheric (*more*-magnetosheath) region with more (less) flux of high-energy ions and electrons (**Figures 7B,C**), reduced (enhanced) anti-sunward flow and ion density (**Figures 7D,E**), and enhanced (reduced) ion temperature (**Figure 7F**). The magnetosphere-to-magnetosheath transitions are denoted by 'A', 'B', 'C', and 'D' with vertical solid black lines and the magnetosheath-to-magnetosphere transitions by 'a', 'b', 'c', and 'd' with vertical dashed black lines.

The total pressure (black in **Figure 7G**) generally shows the typical 'H'/'L' trend at magnetosphere-to-magnetosheath/magnetosheath-to-magnetosphere boundaries. To test the unique signature of leading vs. trailing edges of KHVs, we determined the nominal boundary normal coordinates (LMN) using Shue et al. (1997) model: l = [0.27, –0.26, 0.93], m = [–0.70, –0.72, 0.00], and n = [0.66, –0.65, –0.38] in GSM. **Table 2** lists the normal propagation velocities derived using the four-spacecraft timing analysis and the MVA-derived boundary normals in LMN together with the medium-to-minimum eigenvalue ratio.

Figure 7K shows the *mn*-plane projection of boundary normals (black arrows) and normal propagation velocities (magenta arrows). Both the normals and normal propagation vectors are more aligned to−−**n** with smaller normal-propagation speed at the trailing edges, and more aligned to **k**-vector (white arrow in **Figure 7L**) with larger speed at the leading edges. Agreement with **Figure 7L** confirms the identification of KHVs.

Figures 7H,I shows **J** caculated from the curlometer technique (decomposed into parallel and perperdicular components). Both J_z and $J_{||}$ are mostly positive, in particular, during 'A'-'a' (red arrows between **Figures 7H,I**). **J** mainly points due the geomagnetic **B**, consistent with the downward FAC in the northern ionosphere for the dawnward KHV event.

The ion vorticity, Ω. (**Figure 7J**; note that there is no burst-mode ion data for this vent), although fluctuating around zero, shows—Ω_z during 'A'-'a' (red arrows between **Figures 7I,J**). This corresponds to the clockwise rotation of the dawnward KHV. Although a quantitative test of **Eq. 3** is not available, **Figures 7H–J** indicates a linkage (red arrows) between the FAC and the vorticity.

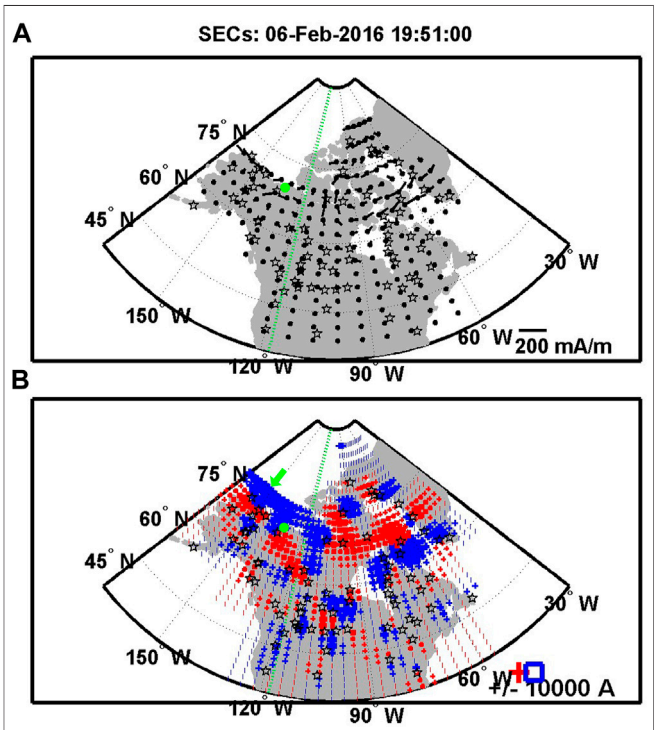


FIGURE 8 | Ground magentometer observation of the ionospheric currents calculated from the SEC technique (Amm and Viljanen, 1999; Weygand et al., 2011) at 1951 UT on 6 February 2016: The (horizonal) equivalent ionospheric current [EIC; **(A)**] and the vertical spherical elementary current [SEC; **(B)**], which is a proxy of the FAC. The MMS footprint prior to (at 1804 UT) and during the dawnward KHV event (**Figure 7**) is denoted by a green dot and a green arrow (presumed), respectively.

5.4 Ground Magnetometer Observations of Ionospheric FACs

Figure 8 shows the EIC (upper) and SEC (lower) at 1951 UT (corresponding to the **Figure 7** event) using the data from gMAG. The footprint of the magnetic field lines encountered by MMS at

TABLE 3 | List of coordinated Cluster/MMS observations of magnetopause KHVs and FAST/gMAG observations of ionospheric responses to those KHVs categorized into duskward (left columnes) vs. dawnward (right) events.

Duskward KHV events				Dawnward KHV events			
Time (UT)	**KHV-induced $J_{\|\|}$ (J_z) [nA/m^2]**	**FAST $J_{\|\|}$ [nA/m^2]**	**gMAG FAC [A]**	**Time (UT)**	**KHV-induced $J_{\|\|}$ (J_z) [nA/m^2]**	**FAST $J_{\|\|}$ [nA/m^2]**	**gMAG FAC [A]**
~12:43 UT 20 November 2001	Cluster Upward 1.2–11	Upward 500–2200 (0.14–0.62 MA)	N/A	~04:20 UT 28 July 2006	Cluster Downward 1.5–4.5	Downward 5000–12,000 (1.7–4.2 MA)	N/A
~18:00 UT 01 October 2015	MMS Upward 120–470	N/A	Upward 16,000–32,000	~19:51 UT 06 February 2016	MMS Downward 45–270	N/A	Downward 1,100–7800
~16:00 UT 14 September 2015	MMS Upward 50–196	N/A	Upward 72,000–110,000	~18:52 UT 07 February 2016	MMS Downward 23–84	N/A	Downward 10,000–23,000
~16:05 UT08 October 2015	MMS Upward 46–150	N/A	Upward 8,700–18,000	~17:49 UT 18 February 2016	MMS Downward 30–115	N/A	Downward 14,000–23,000
~18:37 UT 27 September 2016	MMS Upward 53–280	N/A	Upward 20,000–63,000	~15:38 UT 17 February 2017	MMS Downward 88–370	N/A	Downward 11,000–19,000

1804 UT, i.e., prior to the **Figure 7** event is predicted to sit on the ionosphere at ~70° LAT and ~230° LON in GEO from the Tsyganenko (1989) model (mapping failed after 1804 UT on 6 February 2016). A green dot in **Figure 8** denotes the MMS footprint at 1804 UT. A generally clockwise rotation of EIC around the green dot indicates downward FACs. SEC shows an azimuthally-extended band of downward FACs at/around the green dot. Considering ~1.8 h interval between 1804 UT and 1951 UT, it is likely that the footprint of MMS at 1951 UT falls within the downward FAC band (a green arrow), where the magnitude of downward FACs ranges from—−7800 A to−—1080 A. Again, a bead-like structure in SEC/FACs elongated in the east-west direction possibly implies the generation of the downward FACs *via* the dawnward KHVs (**Figure 7**).

6 DISCUSSION

In this paper, we report coordinated Cluster/MMS observations of magnetopause KHVs and FAST/gMAG observations of ionospheric responses to those KHVs categorized into duskward vs. dawnward events. Cluster and MMS events presented in **Section 4** and **Section 5** demonstrate that nonlinear KHWs on the dusk (dawn) flank of the magnetosphere develop into flow vortices, which twist or shear flux tube magnetic fields in counter-clockwise (clockwise) rotation, generating upward (downward) FACs in the northern ionosphere. The sense of rotations is consistent with the region-1 Birkeland current system.

Table 3 lists our statistics of duskward (left columns) and dawnward (right) events including **Figures 1–8** events. KHV-associated $J_{||}$ or J_z ranges are obtained after low-pass filtering highly-fluctuating **J** data. 'gMAG'-derived FAC ranges are obtained from the SEC data around the ionospheric footprint of MMS. For all MMS-gMAG conjunction events listed in **Table 3**, we identify the bead-like structure in SEC/FAC patterns elongated in the east-west direction (e.g., **Figures 4**, **8**). This might support the generation of FACs *via* corresponding KHVs. We speculate that the characteristic time scale of the build-up of FACs into the ionosphere induced by low-latitude magnetopause KHVs is on the order of the Alfvén transit time (Johnson et al., 2021; Ebihara and Tanaka, 2022). This is hardly measurable in our study due to a limited knowledge on the developmental phase of KHVs that are locally observed by the spacecraft.

We note that the current density obtained from Cluster is less than that obtained from MMS by up to 2 orders of magnitude. This might be due to larger spacecraft separation of Cluster than MMS by ~2 orders of magnitude. Since the size of a KHV (with a wavelength of ~1.5–15 R_E for the KHV events listed in **Table 3**; ~3°–11° latitudinal or longitudinal width on ground) corresponds to the Cluster separation, we assume that the average current density induced by KHVs ranges from ~1 to ~10 nA/m^2. The ratio between the current density associated with KHVs in the near-equatorial magnetopause (at Cluster) and in the ionosphere (at FAST) from **Table 3** ranges from ~200 to ~4,000. This is relatively consistent with the ratio of magnetic flux-tube cross-section area between *in-situ* KHV locations and their conjugate ionosphere (~1,000–6,000) based on the flux-tube current/magnetic-flux conservation.

Our statistics shown in **Table 3** indicate that KHV-induced FACs categorized by duskward vs. dawnward KHVs correspond to FACs of region-1 sense. Considering the size of a KHV mapped to the ionosphere for the two Cluster events, the magnitude of FAC ranges 0.14–4.2 MA. This is comparable to the FAC magnitude obtained from gMAG for the MMS KHV events listed in **Table 3**. The order of region-1 current magnitudes often ranges 10^{-1} to 1 MA. **Table 3**, thus, indicates that KHVs might significantly contribute to region-1 current.

Previous studies attributed the generation of the region-1 current to magnetospheric pressure gradients (Yang et al., 1994; Iijima, 1997; Mishin et al., 2011) or speculated the region-1 current driver to be anti-sunward flows in the magnetosphere (Tanaka, 1998). Wing et al. (2011) investigated the variations of region-1 and 2 FACs as a function of solar wind and IMF. They showed that the response of FACs to solar wind velocity is higher for southward than for northward IMF, which is attributed to the higher velocity shear across the magnetopause boundary layer. A theory connecting the low-latitude shear flow

or vortex and FACs in the ionosphere has been proposed (Johnson and Wing, 2015; Johnson et al., 2021). A theory-observation comparison was conducted by Johnson et al. (2021) and Petrinec et al. (2022). The theory is restricted to regions of upward region-1 FACs where a Knight current-voltage relation is generally valid.

So far as we know, our study presents the first observational evidence for the role played by KHVs in MIC, i.e., the generation of the global FAC system developed in both duskward and dawnward sectors: the magnetoapuse KHVs, at least partially and possibly significantly, contribute to the region-1 current system.

DATA AVAILABILITY STATEMENT

The datasets presented in this study can be found in online repositories. The names of the repository/repositories and accession number(s) can be found in the article/Supplementary Material. The data from MMS, Cluster, FAST, and EIC/SEC data used for the present study are accessible through the public links http://lasp.colorado.edu/mms/sdc/public/, https://cdaweb.gsfc.nasa.gov/, and http://vmo.igpp.ucla.edu/data1/SECS/.

AUTHOR CONTRIBUTIONS

K-JH found the research topic, analyzed the relevant data, and wrote the paper including tables and figures. JW provided/analyzed the EIC/SEC data. DS, JB, MG, EC, and KD assisted the data analysis and interpretation. CE, BG, CP, DG, CR, RS, and RT provided/assisted with the availability of the MMS data.

FUNDING

This study was supported, in part, by NASA's MMS project at SwRI, NASA 80NSSC18K1534, 80NSSC18K0570, 80NSSC18K0693, and 80NSSC18K1337, and ISSI program: MMS and Cluster observations of magnetic reconnection.

REFERENCES

Agapitov, O., Glassmeier, K.-H., Plaschke, F., Auster, H.-U., Constantinescu, D., Angelopoulos, V., et al. (2009). Surface Waves and Field Line Resonances: A THEMIS Case Study. *J. Geophys. Res.* 114, a–n. doi:10.1029/2008JA013553

Amm, O., and Viljanen, A. (1999). Ionospheric Disturbance Magnetic Field Continuation from the Ground to the Ionosphere Using Spherical Elementary Current Systems. *Earth Planet Sp.*, 51, 431–440. doi:10.1186/bf03352247

Axford, W. I., and Hines, C. O. (1961). A Unifying Theory of High-Latitude Geophysical Phenomena and Geomagnetic Storms. *Can. J. Phys.*, 39, 1433. doi:10.1139/p61-172

Birn, J., Raeder, J., Wang, Y. L., Wolf, R. A., and Hesse, M. (2004). On the Propagation of Bubbles in the Geomagnetic Tail. *Ann. Geophys.* 22, 1773–1786. doi:10.5194/angeo-22-1773-2004

Chandrasekhar, S. (1961). "Hydrodynamic and Hydromagnetic Stability," in *International Series of Monograph on Physics* (Oxford: Clarendon), 652.

Chaston, C. C., Wilber, M., Mozer, F. S., Fujimoto, M., Goldstein, M. L., Acuna, M., et al. (2007). Mode Conversion and Anomalous Transport in Kelvin-Helmholtz Vortices and Kinetic Alfvén Waves at the Earth's Magnetopause. *Phys. Rev. Lett.* 99, 1750044. doi:10.1103/PhysRevLett.99.175004

Claudepierre, S. G., Elkington, S. R., and Wiltberger, M. (2008). Solar Wind Driving of Magnetospheric ULF Waves: Pulsations Driven by Velocity Shear at the Magnetopause. *J. Geophys. Res.* 113, a–n. doi:10.1029/2007JA012890

Cowee, M. M., Winske, D., and Gary, S. P. (2010). Hybrid Simulations of Plasma Transport by Kelvin-Helmholtz Instability at the Magnetopause: Density Variations and Magnetic Shear. *J. Geophys. Res.* 115, a–n. doi:10.1029/2009JA015011

Cowee, M. M., Winske, D., and Gary, S. P. (2009). Two-dimensional Hybrid Simulations of Superdiffusion at the Magnetopause Driven by Kelvin-Helmholtz Instability. *J. Geophys. Res. Sp. Phys.* 144, 14222. doi:10.14573/altex.2012.4.41110.1029/2009ja014222

Dungey, J. W. (1961). Interplanetary Magnetic Field and the Auroral Zones. *Phys. Rev. Lett.* 6, 47–48. doi:10.1103/PhysRevLett.6.47

Dunlop, M. W., Balogh, A., and Robert, P. (2002). Four-point Cluster Application of Magnetic Field Analysis Tools: The Curlometer. *J. Geophys. Res.* 107, 1–14. doi:10.1029/2001JA005088

Ebihara, Y., and Tanaka, T. (2022). Where Is Region 1 Field-Aligned Current Generated? *JGR Space Phys.* 127, 1–15. doi:10.1029/2021ja029991

Eriksson, S., Ma, X., Burch, J. L., Otto, A., Elkington, S., and Delamere, P. A. (2021). MMS Observations of Double Mid-latitude Reconnection Ion Beams in the Early Non-linear Phase of the Kelvin-Helmholtz Instability. *Front. Astron. Space Sci.* 8, 1–24. doi:10.3389/fspas.2021.760885

Eriksson, S., Wilder, F. D., Ergun, R. E., Schwartz, S. J., Cassak, P. A., Burch, J. L., et al. (2016). Magnetospheric Multiscale Observations of the Electron Diffusion Region of Large Guide Field Magnetic Reconnection. *Phys. Rev. Lett.* 117, 15001. doi:10.1103/PhysRevLett.117.015001

Faganello, M., Califano, F., Pegoraro, F., and Andreussi, T. (2012). Double Mid-latitude Dynamical Reconnection at the Magnetopause: An Efficient Mechanism Allowing Solar Wind to Enter the Earth's Magnetosphere. *Epl* 100, 69001. doi:10.1209/0295-5075/100/69001

Faganello, M., Califano, F., and Pegoraro, F. (2008). Competing Mechanisms of Plasma Transport in Inhomogeneous Configurations with Velocity Shear: The Solar-Wind Interaction with Earth's Magnetosphere. *Phys. Rev. Lett.* 100, 1–4. doi:10.1103/PhysRevLett.100.015001

Fairfield, D. H., Otto, A., Mukai, T., Kokubun, S., Lepping, R. P., Steinberg, J. T., et al. (2000). Geotail Observations of the Kelvin-Helmholtz Instability at the Equatorial Magnetotail Boundary for Parallel Northward Fields. *J. Geophys. Res. Space Phys.*, 105. 21159–2117310. doi:10.1029/1999ja000316

Glassmeier, K.-H., and Heppner, C. (1992). Traveling Magnetospheric Convection Twin Vortices: Another Case Study, Global Characteristics, and a Model. *J. Geophys. Res.* 97, 3977. doi:10.1029/91JA02464

Hasegawa, A. (1975). *Plasma Instabilities and Non-linear Effects* 430. New York, NY: Springer-Verlag.

Hasegawa, H., Fujimoto, M., Phan, T.-D., Rème, H., Balogh, A., Dunlop, M. W., et al. (2004). Transport of Solar Wind into Earth's Magnetosphere through Rolled-Up Kelvin-Helmholtz Vortices. *Nature* 430, 755–758. doi:10.1038/nature02799

Hasegawa, H. (2012). Structure and Dynamics of the Magnetopause and its Boundary Layers. *Monogr. Environ. Earth Planets* 1, 71–119. doi:10.5047/meep.2012.00102.0071

Hwang, K.-J., Dokgo, K., Choi, E., Burch, J. L., Sibeck, D. G., Giles, B. L., et al. (2021). Bifurcated Current Sheet Observed on the Boundary of Kelvin-Helmholtz Vortices. *Front. Astron. Space Sci.* 8, 1–13. doi:10.3389/fspas.2021.782924

Hwang, K.-J., Kuznetsova, M. M., Sahraoui, F., Goldstein, M. L., Lee, E., and Parks, G. K. (2011). Kelvin-Helmholtz Waves under Southward Interplanetary Magnetic Field. *J. Geophys. Res.* 116, a–n. doi:10.1029/2011JA016596

Hwang, K. J., Choi, E., Dokgo, K., Burch, J. L., Sibeck, D. G., Giles, B. L., et al. (2019). Electron Vorticity Indicative of the Electron Diffusion Region of Magnetic Reconnection. *Geophys. Res. Lett.* 46, 6287–6296. doi:10.1029/2019GL082710

Hwang, K. J., Dokgo, K., Choi, E., Burch, J. L., Sibeck, D. G., Giles, B. L., et al. (2020). Magnetic Reconnection inside a Flux Rope Induced by Kelvin-Helmholtz Vortices. *J. Geophys. Res. Space Phys.* 125, 1–16. doi:10.1029/2019JA027665

Iijima, T., Potemra, T. A., and Zanetti, L. J. (1997). Contribution of Pressure Gradients to the Generation of Dawnside Region 1 and Region 2 Currents. *J. Geophys. Res.* 102, 27069–27081. doi:10.1029/97JA02462

Johnson, J. R., Wing, S., Delamere, P., Petrinec, S., and Kavosi, S. (2021). Field-Aligned Currents in Auroral Vortices. *J. Geophys. Res. Space Phys.* 126, 1–15. doi:10.1029/2020JA028583

Johnson, J. R., and Wing, S. (2015). The Dependence of the Strength and Thickness of Field-aligned Currents on Solar Wind and Ionospheric Parameters. *J. Geophys. Res. Space Phys.* 120, 3987–4008. doi:10.1002/2014JA020312

Kavosi, S., and Raeder, J. (2015). Ubiquity of Kelvin-Helmholtz Waves at Earth's Magnetopause. *Nat. Commun.* 6. doi:10.1038/ncomms8019

Kivelson, M. G., and Chen, S.-H. (1995). "The Magnetopause: Surface Waves and Instabilities and Their Possible Dynamical Consequences," in *Geophysical Monograph Series*, 257–268. doi:10.1029/GM090p0257

Lai, S. H., and Lyu, L. H. (2010). A Simulation and Theoretical Study of Energy Transport in the Event of MHD Kelvin-Helmholtz Instability. *J. Geophys. Res.* 115, a–n. doi:10.1029/2010JA015317

Mann, I. R., Voronkov, I., Dunlop, M., Donovan, E., Yeoman, T. K., Milling, D. K., et al. (2002). Coordinated Ground-Based and Cluster Observations of Large Amplitude Global Magnetospheric Oscillations during a Fast Solar Wind Speed Interval. *Ann. Geophys.*, 20, 405–426. doi:10.5194/angeo-20-405-2002

Mathie, R. A., and Mann, I. R. (2000). Observations of Pc5 Field Line Resonance Azimuthal Phase Speeds ' A Diagnostic of Their Excitation Mechanism. *J. Geophys. Res. Space Phys.* 105. 10713–10728. doi:10.1029/1999ja000174

Matsumoto, Y., and Hoshino, M. (2004). Onset of Turbulence Induced by a Kelvin-Helmholtz Vortex. *Geophys. Res. Lett.* 31, 1–4. doi:10.1029/2003GL018195

Matsumoto, Y., and Seki, K. (2010). Formation of a Broad Plasma Turbulent Layer by Forward and Inverse Energy Cascades of the Kelvin-Helmholtz Instability. *J. Geophys. Res.* 115, a–n. doi:10.1029/2009JA014637

Mishin, V. M., Förster, M., Kurikalova, M. A., and Mishin, V. V. (2011). The Generator System of Field-Aligned Currents during the April 06, 2000, Superstorm. *Adv. Space Res.* 48, 1172–1183. doi:10.1016/j.asr.2011.05.029

Nakamura, T. K. M., Daughton, W., Karimabadi, H., and Eriksson, S. (2013). Three-dimensional Dynamics of Vortex-Induced Reconnection and Comparison with THEMIS Observations. *J. Geophys. Res. Space Phys.* 118, 5742–5757. doi:10.1002/jgra.50547

Nakamura, T. K. M., and Fujimoto, M. (2008). Magnetic Effects on the Coalescence of Kelvin-Helmholtz Vortices. *Phys. Rev. Lett.*, 101, 1–4. doi:10.1103/PhysRevLett.101.165002

Nakamura, T. K. M., Hasegawa, H., Daughton, W., Eriksson, S., Li, W. Y., and Nakamura, R. (2017). Turbulent Mass Transfer Caused by Vortex Induced Reconnection in Collisionless Magnetospheric Plasmas. *Nat. Commun.* 8, 1–8. doi:10.1038/s41467-017-01579-0

Nakamura, T. K. M., Hasegawa, H., Shinohara, I., and Fujimoto, M. (2011). Evolution of an MHD-Scale Kelvin-Helmholtz Vortex Accompanied by Magnetic Reconnection: Two-Dimensional Particle Simulations. *J. Geophys. Res.* 116. doi:10.1029/2010JA016046

Nakamura, T. K. M., Hayashi, D., Fujimoto, M., and Shinohara, I. (2004). 92, 2–5. doi:10.1103/PhysRevLett.92.145001

Nakamura, T. K. M., Plaschke, F., Hasegawa, H., Liu, Y. H., Hwang, K. J., Blasl, K. A., et al. (2020). Decay of Kelvin-Helmholtz Vortices at the Earth's Magnetopause under Pure Southward IMF Conditions. *Geophys. Res. Lett.* 47, 87574. doi:10.1029/2020GL087574

Nykyri, K., and Otto, A. (2004). Influence of the Hall Term on KH Instability and Reconnection inside KH Vortices. *Ann. Geophys.* 22, 935–949. doi:10.5194/angeo-22-935-2004

Otto, A., and Fairfield, D. H. (2000). Kelvin-Helmholtz Instability at the Magnetotail Boundary: MHD Simulation and Comparison with Geotail Observations. *J. Geophys. Res.* 105, 21175–21190. doi:10.1029/1999ja000312

Paschmann, G., and Daly, P. W. (1998). *Analysis Methods for Multispacecraft Data*. Bern: International Space Science Institute. Scientific Report 001.

Paschmann, G., Haaland, S., and Treumann, R. (2002). Chapter 3 - Theoretical Building Blocks. *Space Sci. Rev.* 103, 41–92. doi:10.1023/A:1023030716698

Pembroke, A., Toffoletto, F., Sazykin, S., Wiltberger, M., Lyon, J., Merkin, V., et al. (2012). Initial Results from a Dynamic Coupled Magnetosphere-Ionosphere-Ring Current Model. *J. Geophys. Res.* 117, a–n. doi:10.1029/2011JA016979

Petrinec, S. M., Wing, S., Johnson, J. R., and Zhang, Y. (2022). Multi-Spacecraft Observations of Fluctuations Occurring along the Dusk Flank Magnetopause, and Testing the Connection to an Observed Ionospheric Bead. *Front. Astron. Space Sci.* 9, 1–15. doi:10.3389/fspas.2022.827612

Rae, I. J., J Watt, C. E., Fenrich, F. R., Mann, I. R., Ozeke, L. G., and Kale, A. (2007). Energy Deposition in the Ionosphere through a Global Field Line Resonance. Available at: www.ann-geophys.net/25/2529/2007/.doi:10.5194/angeo-25-2529-2007

Samson, J. C., and Cogger, L. L, and Pao, Q. (1996). Observations of field line resonances, auroral arcs, and auroral vortex structures. *J. Geophys. Res: Space Physics* 101. 17373-17383. doi:10.1029/96ja01086

Shue, J.-H., Chao, J. K., Fu, H. C., Russell, C. T., Song, P., Khurana, K. K., et al. (1997). A New Functional Form to Study the Solar Wind Control of the Magnetopause Size and Shape. *J. Geophys. Res.* 102, 9497–9511. doi:10.1029/97JA00196

Siscoe, G. L., and Suey, R. W. (1972). Significance Criteria for Variance Matrix Applications. *J. Geophys. Res.-Space* 77, 1321–1322. doi:10.1029/JA077i007p01321

Sonnerup, B., and Scheible, M. (1998). Minimum and Maximum Variance Analysis. *Anal. Methods Multi-Spacecr.*185, 220. Available at: http://www.issibern.ch/forads/sr-001-08.pdf%0Ahttp://ankaa.unibe.ch/forads/sr-001-08.pdf.

Takagi, K., Hashimoto, C., Hasegawa, H., Fujimoto, M., and Tandokoro, R. (2006). Kelvin-Helmholtz Instability in a Magnetotail Flank-like Geometry: Three-Dimensional MHD Simulations. *J. Geophys. Res.* 111, 1–10. doi:10.1029/2006JA011631

Tanaka, T. (1998). "Generation Mechanism of the Field-Aligned Currrent System Deduced From a 3-D MHD Simulation of the Solar Wind-Magnetosphere-Ionosphere Coupling," in *Magnetospheric Research With Advanced Techniques*, Editors R. L. Xu and A. T. Y. Lui. (Pergamon, 1998a) Vol. 9, 133.

Tsyganenko, N. A. (1989). A Magnetospheric Magnetic Field Model With a Warped Tail Current Sheet. *Planet. Space Sci.* 37 (1), 5–20. doi:10.1016/0032-0633(89)90066-4

Tsyganenko, N. A. (1995). Modeling the Earth's Magnetospheric Magnetic Field Confined within a Realistic Magnetopause. *J. Geophys. Res.* 100, 5599. doi:10.1029/94ja03193

Turkakin, H., Rankin, R., and Mann, I. R. (2013). Primary and Secondary Compressible Kelvin-Helmholtz Surface Wave Instabilities on the Earth's Magnetopause. *J. Geophys. Res. Space Phys.* 118, 4161–4175. doi:10.1002/jgra.50394

Vernisse, Y., Lavraud, B., Eriksson, S., Gershman, D. J., Dorelli, J., Pollock, C., et al. (2016). Signatures of Complex Magnetic Topologies from Multiple Reconnection Sites Induced by Kelvin-Helmholtz Instability. *J. Geophys. Res. Space Phys.* 121, 9926–9939. doi:10.1002/2016JA023051

Weygand, J. M., Amm, O., Viljanen, A., Angelopoulos, V., Murr, D., Engebretson, M. J., et al. (2011). Application and Validation of the Spherical Elementary Currents Systems Technique for Deriving Ionospheric Equivalent Currents with the North American and Greenland Ground Magnetometer Arrays. *J. Geophys. Res.* 116, 1–8. doi:10.1029/2010JA016177

Wiltberger, M., Pulkkinen, T. I., Lyon, G., and Goodrich, C. C. (2000). MHD Simulation of the Magnetotail during the December 10, 1996, Substorm. *J. Geophys. Res. Space Phys.* 105, 649–663. doi:10.1029/1999ja000251

Wing, S., Ohtani, S.-i., Johnson, J. R., Echim, M., Newell, P. T., Higuchi, T., et al. (2011). Solar Wind Driving of Dayside Field-Aligned Currents. *J. Geophys. Res.* 116, a–n. doi:10.1029/2011JA016579

Yang, Y. S., Spiro, R. W., and Wolf, R. A. (1994). Generation of Region 1 Currents by Magnetospheric Pressure Gradients. *J. Geophys. Res.* 99 (A1), 223–234. doi:10.1029/93JA02364

Yao, Y., Chaston, C. C., Glassmeier, K. H., and Angelopoulos, V. (2011). Electromagnetic Waves on Ion Gyro-radii Scales across the Magnetopause. *Geophys. Res. Lett.* 38, 1–5. doi:10.1029/2011GL047328

Conflict of Interest: Author, Dr. C. J. P is employed by Denali Scientific, LLC, Fairbanks, AK.

The remaining authors declare that the research was conducted in the absence of any commercial or financial relationships that could be construed as a potential conflict of interest.

The reviewer PY declared a shared affiliation with the author(s) MG to the handling editor at the time of review.

Publisher's Note: All claims expressed in this article are solely those of the authors and do not necessarily represent those of their affiliated organizations, or those of the publisher, the editors and the reviewers. Any product that may be evaluated in this article, or claim that may be made by its manufacturer, is not guaranteed or endorsed by the publisher.

Copyright © 2022 Hwang, Weygand, Sibeck, Burch, Goldstein, Escoubet, Choi, Dokgo, Giles, Pollock, Gershman, Russell, Strangeway and Torbert. This is an open-access article distributed under the terms of the Creative Commons Attribution License (CC BY). The use, distribution or reproduction in other forums is permitted, provided the original author(s) and the copyright owner(s) are credited and that the original publication in this journal is cited, in accordance with accepted academic practice. No use, distribution or reproduction is permitted which does not comply with these terms.

Advantages of publishing in Frontiers

OPEN ACCESS
Articles are free to read for greatest visibility and readership

FAST PUBLICATION
Around 90 days from submission to decision

HIGH QUALITY PEER-REVIEW
Rigorous, collaborative, and constructive peer-review

TRANSPARENT PEER-REVIEW
Editors and reviewers acknowledged by name on published articles

Frontiers
Avenue du Tribunal-Fédéral 34
1005 Lausanne | Switzerland

Visit us: www.frontiersin.org
Contact us: frontiersin.org/about/contact

REPRODUCIBILITY OF RESEARCH
Support open data and methods to enhance research reproducibility

DIGITAL PUBLISHING
Articles designed for optimal readership across devices

FOLLOW US
@frontiersin

IMPACT METRICS
Advanced article metrics track visibility across digital media

EXTENSIVE PROMOTION
Marketing and promotion of impactful research

LOOP RESEARCH NETWORK
Our network increases your article's readership